NASA/CR—2009-215441 FSEC–CR–1745–08

Hydrogen Research at Florida Universities

David L. Block and Ali T-Raissi
Florida Solar Energy Center, Cocoa, Florida

February 2009

NASA STI Program . . . in Profile

Since its founding, NASA has been dedicated to the advancement of aeronautics and space science. The NASA Scientific and Technical Information (STI) program plays a key part in helping NASA maintain this important role.

The NASA STI Program operates under the auspices of the Agency Chief Information Officer. It collects, organizes, provides for archiving, and disseminates NASA's STI. The NASA STI program provides access to the NASA Aeronautics and Space Database and its public interface, the NASA Technical Reports Server, thus providing one of the largest collections of aeronautical and space science STI in the world. Results are published in both non-NASA channels and by NASA in the NASA STI Report Series, which includes the following report types:

- TECHNICAL PUBLICATION. Reports of completed research or a major significant phase of research that present the results of NASA programs and include extensive data or theoretical analysis. Includes compilations of significant scientific and technical data and information deemed to be of continuing reference value. NASA counterpart of peer-reviewed formal professional papers but has less stringent limitations on manuscript length and extent of graphic presentations.

- TECHNICAL MEMORANDUM. Scientific and technical findings that are preliminary or of specialized interest, e.g., quick release reports, working papers, and bibliographies that contain minimal annotation. Does not contain extensive analysis.

- CONTRACTOR REPORT. Scientific and technical findings by NASA-sponsored contractors and grantees.

- CONFERENCE PUBLICATION. Collected papers from scientific and technical conferences, symposia, seminars, or other meetings sponsored or cosponsored by NASA.

- SPECIAL PUBLICATION. Scientific, technical, or historical information from NASA programs, projects, and missions, often concerned with subjects having substantial public interest.

- TECHNICAL TRANSLATION. English-language translations of foreign scientific and technical material pertinent to NASA's mission.

Specialized services also include creating custom thesauri, building customized databases, organizing and publishing research results.

For more information about the NASA STI program, see the following:

- Access the NASA STI program home page at *http://www.sti.nasa.gov*

- E-mail your question via the Internet to *help@sti.nasa.gov*

- Fax your question to the NASA STI Help Desk at 301–621–0134

- Telephone the NASA STI Help Desk at 301–621–0390

- Write to:
  NASA Center for AeroSpace Information (CASI)
  7115 Standard Drive
  Hanover, MD 21076–1320

NASA/CR—2009-215441 FSEC–CR–1745–08

Hydrogen Research at Florida Universities

David L. Block and Ali T-Raissi
Florida Solar Energy Center, Cocoa, Florida

Prepared under Grant NAG3–2751

National Aeronautics and
Space Administration

Glenn Research Center
Cleveland, Ohio 44135

February 2009

This work was sponsored by the Fundamental Aeronautics Program at the NASA Glenn Research Center.

Level of Review: This material has been technically reviewed by NASA technical management.

Available from

NASA Center for Aerospace Information
7115 Standard Drive
Hanover, MD 21076–1320

National Technical Information Service
5285 Port Royal Road
Springfield, VA 22161

Available electronically at http://gltrs.grc.nasa.gov

Contents

Hydrogen Research at Florida Universities

D. Block and A. T-Raissi
Florida Solar Energy Center
Cocoa, Florida 32922

March 2008

Abstract

This final report describes the R&D activities and projects conducted for NASA under the 6-year NASA Hydrogen Research at Florida Universities grant program. Contained within this report are summaries of the overall activities, one-page description of all the reports funded under this program and all of the individual reports from each of the 29 projects supported by the effort. The R&D activities cover hydrogen technologies related to production, cryogenics, sensors, storage, separation processes, fuel cells, resource assessments and education. In the span of 6 years, the NASA Hydrogen Research at Florida Universities program funded a total of 44 individual university projects, and employed more than 100 faculty and over 100 graduate research students in the six participating universities. Researchers involved in this program have filed more than 20 patents in all hydrogen technology areas and put out over 220 technical publications in the last 2 years alone.

This 6 year hydrogen research program was conducted by a consortium of six Florida universities: Florida International University (FIU) in Miami, Florida State University (FSU) and Florida A&M University (FAMU) in Tallahassee, University of Central Florida (UCF) in Orlando, University of South Florida (USF) in Tampa, and University of Florida (UF) in Gainesville. The Florida Solar Energy Center (FSEC) of the University of Central Florida managed the research activities of all consortium member universities except those at the University of Florida. This report does not include any of the programs or activities conducted at the University of Florida.

Program Summary

Florida Solar Energy Center (FSEC) of the University of Central Florida (UCF) was funded by GRC in March 2002 to conduct research and manage this NASA research grant program. Soon after, a Request for Proposals (RFP) was issued to all of the universities in the State University System of Florida. A total of 37 proposals were received of which 30 were selected for funding. Selections were made following review by a FSEC Review Committee and by the NASA program managers at both Glenn Research Center (GRC) and Kennedy Space Center (KSC). For each of the selected projects, other than those at FSEC, formal contracts to the corresponding university were issued by the UCF Division of Sponsored Research. These university contracts were overseen by the FSEC program managers. Work at the participating universities began in the August to December 2002 time frame. Table I presents the list of the initial 30 projects and the principal investigators for each project. The listing is presented by projects under each university.

Table 1. Projects funded for the initial year. (Listed in alphabetical order of project titles).

Florida Solar Energy Center

- Analysis of Alternative Hydrogen Production Processes Liquid Hydrogen Production via Hydrogen Sulfide Methane Reformation - Huang, C.; T-Raissi, A.
- Development of Tribological Coatings for Cryocoolers - Dhere, N.
- Experimental Design & Evaluation of ZBO Cryogenic Systems - Baik, J.
- Hydrogen Education and Outreach – Schleith, S., Henzmann, A.
- Hydrides for Hydrogen Purification and Recovery - Slattery, D.
- Hydrogen Production via Photocatalysis - Linkous, C.
- Hydrogen Purification and Storage Using Lithium Borohydride - Linkous, C.
- Local Hydrogen Production via Catalytic Reformation of Fossil and Renewable Resources - Muradov, N., Smith, F.
- Photoelectrochemical Water Splitting for Hydrogen Production Using Multiple Bandgap Combination of Photovoltaic Cells and Photocatalyst. - Dhere, N.
- R & D Processes for Increasing the Fluid Density of Cryogenic Liquids - Baik, J.
- Safety and Monitoring Systems - Alternate Methods of Operating H_2 Systems During Start-up and Shutdown - Elbaccouch, M., Bain, A.
- System Analysis of Hydrogen Production and Utilization at KSC - T-Raissi, A., Gu, L., Huang, C., Robertson, T.
- Technoeconomic Analysis of the Use of Densified Propellants in Storage and Transportation Systems - Baik, J.

University of Central Florida

- Development of Cryogenic Actuator Materials for Switches, Seals and Valves - Vaidyanathan, R.
- Development of Hydrogen Gas Sensor with High Sensitivity and Selectivity Based on Doped Nanocrystalline-nanoporous Metal/Metal Oxides for Space Explorations – Seal, S.
- Metal Alloys for Hydrogen Recovery and Purification - Hampton, M.
- Novel Technique for the Detection and Location of Hydrogen Leaks – Sellar, G.
- Quasicrystalline Materials for Hydrogen Recovery and Purification - Hampton, M.
- Two-Stage Cryocooler Development for Liquid Hydrogen Systems - Chow, L., Kapat, J.

Florida State University

- Development of Optical Mass Gauging Systems - Van Sciver, S.
- Experimental and Numerical Investigations of Solid Hydrogen Particles in Liquid Helium - Van Sciver, S.
- Measurement of Transport Properties of Densified LH_2 and LO_2 - Van Sciver, S.

Florida International University

- Assessment of Florida's Biomass Resources for Hydrogen Production Using GIS – Ebadian, M., Tachiev, G., Srivastave, R., Philippidis, G.

University of South Florida

- By Product Hydrogen Production - Krakow, B., Stefanakos, E., Moore, G.
- Development of a Numerical Simulation Model for Thermo-Fluid Analysis and Design Optimization of Cryogenic Storage Systems with Zero Boiloff - Rahman, J.
- Electrochemical Catalytic Cell for the Production of Hydrogen from Various Fuel Stocks – Benson, R., Wolan, J.
- Hydrogen Gas Sensors by Surface Acoustic Waves - Bhethanabotla, V., Bhansali, S., Joseph, B.
- Hydrogen Liquefaction by Metal Hydride Devices Powered by Low Grade Heat - Krakow, B., Rahman, M.
- Prototype and Simulation Model for a MEMS Magneto-caloric Refrigerator - Bhansali, S., Bhethanabotla, V., Rahman, M.

University of West Florida

- Software Agents and Knowledge Discovery and Data Mining for Enhanced Safety and Control of Hydrogen Operations - Bradshaw, J.; Glymore, C.; Bunch, L., Hanson, J.

A report for the first year's effort was completed by FSEC in November 2003 and sent to the NASA program managers at GRC and KSC. This 2003 report contained individual project activities for each of the funded projects.

During the initial year of the project, the NASA managers required periodic review meetings be held in order to appraise the projects goals, benefits to NASA and expected results. During the first year, two project review meetings were held, one on January 14-16, 2003 at the University of South Florida in Tampa and one on August 12-15, 2003 at the University of Florida in Gainesville. The project review meetings were to be held at all the participating universities and covered, in addition to project reviews, tours of the labs and facilities at the host university.

Each of the review meetings took 3 to 4 days due to the large number of project presentations. Each project presentation was given 20 minutes for the power point slides followed by a 10-minute question and answer period. Following all the presentations at each review meeting, FSEC program managers met with the five to six NASA reviewers that had attended the meeting to discuss individual projects. These discussions concerned the project's need, benefits and results and included recommended changes in the project direction and activity. Following the two first year review meetings, five projects were judged complete and six projects were added to the program. The added projects were either redirected projects from the first year or new efforts requested by NASA.

During the second year, the spring project review meetings were held on March 3-4, 2004 at Florida State University in Tallahassee and March 30-31, 2004 at the University of Central Florida in Orlando and the fall meeting on September 21-22, 2004 at the Florida Solar Energy Center in Cocoa.

A report for the activities at the end of year two was prepared for the NASA GRC program manager in November 2004. Following a NASA GRC management change, the November 2004 report was updated and sent to NASA GRC in June 2005. This report was named the project report for FY 2003 which then was published as NASA Contract Report #2006-214326. The projects covered in the NASA CR are given in Table 2.

Table 2. Projects published in NASA CR 2006-214326, June 2005.

Florida Solar Energy Center

- Analysis of Alternative Hydrogen Production Processes Liquid Hydrogen Production via Sub-Quality Natural Gases - Huang, C., T-Raissi, A.
- Characterization of Spin-Coated Terbium-Doped Strontium Cerate Thin Film Membranes - Elbaccouch, M., Mohajeri, N., T-Raissi, A.
- Development of Tribological Coatings for Cryocoolers - Dhere, D.
- Experimental Design and Evaluation of ZBO Cryogenic Systems - Baik, J.
- Hydrogen Education and Outreach - Schleith, S., Hall, P., Henzmann, A., Block, D.
- Hydrogen Production from Used Lube Oil via Supercritical Water Reformation - T-Raissi, A., Ramasamy, K.
- Hydrogen Production via Photocatalysis - Linkous, C., Bateman, C., Chan, Q.
- Hydrogen Purification and Storage Using Lithium Borohydride - Linkous, C.
- Hydrogen Storage and Recovery in Ammonia Borane Complex - T-Raissi, A., Mohajeri, N.
- Liquid Hydrogen Storage at Kennedy Space Center - Gu, L., Bokerman, G., T-Raissi, A.
- Local Hydrogen Production via Catalytic Reformation of Fossil and Renewable Feedstocks - Muradov, N., Smith, F.
- Photoelectrochemical Water Splitting for Hydrogen Production Using Multiple Bandgap Combination of Photovoltaic Cells and Photocatalyst. - Dhere, N.
- R & D Processes for Increasing the Fluid Density of Cryogenic Liquids - Baik, J.
- Smart Paints and Pigments for Hydrogen Sensing - Mohajeri, N., Bokerman, G., Muradov, N., T-Raissi, A.
- System Analysis of Hydrogen Production and Utilization at KSC - T-Raissi, A., Elbaccouch, M., Ramasamy, K.

University of Central Florida

- Development of Cryogenic Shape-Memory Actuator Materials for Switches, Seals and Valves - Vaidyanathan, R.
- High Selective Nano-MEMS Low Temperature Sensor - Seal, S., Shukla, S.
- Metal Hydrides for Hydrogen Separation, Recovery and Purification - Hampton, M., Slattery, D.
- Novel Technique for the Detection and Location of Hydrogen Leaks - Sellar, G.
- Reverse Turbo Brayton Cycle Cryocooler Development for Liquid Hydrogen Systems - Chow, L., Kapat, J., Chen, Q.

Florida State University

- Development of Optical Systems for Mass and Two Phase Flow Gauging - Van Sciver, S., Justak, J.
- Experimental and Numerical Investigations of Cryogenic Multiphase Flow - Van Sciver, S., Hussaini, Y.
- Measurement of Transport Properties of Densified LH_2 and LO_2 - Van Sciver, S., Celik, D., Hilton, D.

Florida International University

- Development and Demonstration of a Pilot-Scale Biomass Gasification Unit for Hydrogen Production - Srivastava, R., Mazumdar, A.

University of South Florida

- By Product Hydrogen Production - Stefanakos, E., Krakow, B., Moore, G., Wolan, J., Smith, M.
- Development of a Numerical Simulation Model for Thermo-Fluid Analysis and Design Optimization of Cryogenic Storage Systems with Zero Boiloff - Rahman, J., Ho, S.
- Development of Rectenna Solar Energy Conversion for Local Hydrogen Production - Buckle, K., Bhansali, S., Goswami, Y.
- Hydrogen Gas Sensors by Surface Acoustic Waves - Bhethanbotla, V., Joseph, B.
- Hydrogen Production via Methane Nonoxidative Aromation - Wolan, J., Kababji, A.
- Prototype and Simulation Model for a Magneto-Caloric Refrigerator - Bhansali, S., Bhethanabotla, V., Rahman, M.

University of West Florida

- Software Agents and Knowledge Discovery and Data Mining for Enhanced Safety and Control of Hydrogen Operations - Bunch, L.

Following the project review in September 2004, a decision was made by the FSEC and NASA project managers on continuation of the existing projects and the desire to add new activities. This led to issuance of a second RFP. This RFP allowed for submission of both continuing and for new projects. Following extensive FSEC and NASA review, six old projects were discontinued and six new ones were initiated. The new projects are given in Table 3.

Table 3. New projects began in January 2005

- Development of High Temperature Proton Exchange Membrane Electrolytes - Linkous, C. (FSEC)
- Genetic Engineering of Escherichia Coli to Enhance Biological Hydrogen Production from Biomass-Derived Sugars - Self, W (UCF)
- Modeling and Optimization of Fuel Cell Systems for Aircraft Applications - Ordonez, J. (FAMU)
- Smart Porous Metal-Organic Frameworks for Hydrogen Recovery and Storage - Eddaoudi, M. (USF)
- Solar Powered Hydrogen Production via a High Temperature Photocatalytic Water Splitting Cycle - Huang, C. (FSEC)
- Wireless Passive Sensors and Systems for Physical and Hydrogen Sensing Applications - Malocha, D. (UCF)

With regard to yearly reports, a report for FY 2004/2005 was prepared and sent to NASA GRC in June 2006. The next program change occurred in September 2006 when the fourth and last funding increment was received from NASA GRC. At this time, the program was to place more

emphasis on the development of fuel cells. The list of projects for the last phase of the program is given in Table 4. Table 4 also includes the final reports for four projects that were given in the FY 2004/2005 report. These projects were considered completed and, thus, are reported here. The projects listed in Table 4 are the ones presented in this report.

With regard to review meetings, the final two review meetings were held on May 11-15, 2005 at the University of Florida in Gainesville and on November 1-4, 2005 at the Florida Solar Energy Center in Cocoa.

Table 4. Project listing for the period of 2005 through 2007.

Florida Solar Energy Center

- Ammonia-Borane Complex for Hydrogen Storage - Mohajeri, N., T-Raissi, A., Ramasamy, K., Adebiyi, O., Bokerman, G.
- Ceramic Membranes of Mixed Ionic-Electronic Conductors for Hydrogen Separation - Elbaccouch, M., T-Raissi, A., Linkous, C., Mohajeri, N.
- Compact, Lightweight and Optimized Fuel cells for Space or Aircraft Power - Fenton, J, Choi, P., Bonville, L., Kunz, R.
- Gas Permeable Chemochromic Compositions for Hydrogen Sensing - Mohajeri, N., Muradov, M., Bokerman, G., T-Raissi, A., Captain, J., Peterson, B., Whitten, M.
- Hydrogen Education and Outreach – Schleith, S., Hall, P., Henzmann, A., Block, D.
- Hydrogen Production From Used Lube Oils - T-Raissi, A., Ramasamy, K.
- Hydrogen Production via Solar Thermochemical Water Splitting – T-Raissi, A., Huang, C., Muradov, N.
- Hydrogen-Powered Aeropropulsion: Compact, Lightweight and Efficient Fuel Cells for Space Power - Linkous, C., Pearman, B., Hall, D., Slattery, D., Baik, J.
- Integrated Fuel Cell Test Bed Facility - Slattery, D., Bonville, L., Fowler, R.
- Liquid Hydrogen Storage at Kennedy Space Center - Gu, L., Block, D., Bokerman, G., T-Raissi, A., Basarkar, M.
- Local Hydrogen Production via Catalytic Reformation of Fossil and Renewable Resources - Muradov, N., Smith, F.
- Photoelectrochemical Water Splitting for Hydrogen Production Using Multiple Bandgap Combination of Thin-Film- Photovoltaic Cells and Photocatalyst – Dhere, N.
- System Analysis of Hydrogen Production and Utilization at KSC - T-Raissi, A., Elbaccouch, M., Ramasamy, K., Baik, J.
- Zero-Boil-Off Liquid Hydrogen Storage Tanks - Baik, J.

University of Central Florida

- A Reliable, Efficient and Compact Reverse Turbo Brayton Cycle Cryocooler for Storage and Transport of Hydrogen in Spaceport and Space Vehicle Applications - Chow, L., Kapat, J., Chen, Q., An, L., Wu, T., Sundaram, K., Ham, C., Dhere, N.
- Development of Cryogenic Shape Memory Actuator Materials for Switches, Seals and Valves - Vaidyanathan, R.
- Genetic Engineering to Enhance Biological Hydrogen Production - Self, W., Ganyc, D., Halvorsen, L.
- Highly Selective Nano-Mems Low Temperature Hydrogen Sensor - Seal, S., Cho, H.
- Metal Hydrides for Hydrogen Separation, Recovery and Purification - Hampton, M., Slattery, D.
- Wireless Passive Sensors and Systems for Physical Sensors and Hydrogen Sensing Applications - Malocha, D.

Florida State University

- Densified LH_2 and LO_2: Transport Properties and Density - Van Sciver, S.
- Experimental and Numerical Investigations of Cryogenic Multiphase Flow - Van Sciver, S., Hussaini, Y., Justak, J.

Florida International University

- Improved Hydrogen Yield from Florida Specific Biomass Gasification Using a Pilot Scale Gasification Unit - Srivastava, R.

University of South Florida

- Numerical Simulation Model for Thermo-Fluid Analysis of Cryogenic Storage Systems with Zero Boiloff - Rahman, J., Ho, S.
- Prototype and Simulation Model for a Magneto-Caloric Refrigerator - Bhansali, S., Rahman, M., Kim, S., Ghirlanda, S., Hernandez, C., Adams, C., Bethala, B., Rosario, S., Sambandam, S.
- Smart Porous Metal-Organic Frameworks (MOFs) for Hydrogen Recovery and Storage - Eddaoudi, M., Zaworotko, M., Space, B., Eckert, J., T-Raissi, A., Mohajeri, N.
- Surface Acoustic Wave (SAW) Sensors for Hydrogen and Other Gas Detection - Bhethanabotla, V.
- Thermo Catalytic H2 Production via Oxygen-Free Methane Aromatization - Wolan, J., Stefanakos, E., Kababji, A.

Florida A & M University

- Modeling and Optimization of Fuel Cell systems for Aircraft Applications - Ordonez, J., Lungo, C.

As previously mentioned, this program covered research in a broad area of hydrogen technologies. A brief description of the final projects presented by hydrogen technology areas are as follows:

Hydrogen Production – In Florida, NASA KSC and Cape Canaveral Air Force Station will eventually require local production facilities because of economics, transportation safety and quantity requirements. Thus, local hydrogen production was a major task of the program. Eight projects were carried out under this general heading:

- Genetic Engineering to Enhance Biological Hydrogen Production - Self, W., Ganyc, D., Halvorsen, L. (UCF)
- Hydrogen Production from Used Lube Oils - T-Raissi, A., Ramasamy, K. (FSEC)
- Hydrogen Production via Solar Thermochemical Water Splitting – T-Raissi, A., Huang, C., Muradov, N. (FSEC)
- Improved Hydrogen Yield from Florida Specific Biomass Gasification Using a Pilot Scale Gasification Unit - Srivastava, R. (FIU)
- Local Hydrogen Production via Catalytic Reformation of Fossil and Renewable Resources - Muradov, N., Smith, F. (FSEC)
- Photoelectrochemical Water Splitting for Hydrogen Production Using Multiple Bandgap Combination of Thin-Film Photovoltaic Cells and Photocatalyst – Dhere, N. (FSEC)
- System Analysis of Hydrogen Production and Utilization at KSC – T-Raissi, A., Elbaccouch, M., Ramasamy, K., Baik, J. (FSEC)
- Thermo Catalytic H_2 Production via Oxygen-Free Methane Aromatization - Wolan, J., Stefanakos, E., Kababji, A. (USF)

Fuel Cells – Fuel cells offer new aircraft power options that can meet NASA's vehicle requirements. Of the five types of fuel cells, proton exchange membrane (PEM) fuel cells are the leading candidate for next generation space and aircraft power due to their high specific power output. This task addressed several innovative PEM fuel cell technologies as follows:

- Compact, Lightweight and Optimized Fuel cells for Space or Aircraft Power - Fenton, J., Choi, P., Bonville, L., Kunz, R. (FSEC)
- Hydrogen-Powered Aeropropulsion: Compact, Lightweight and Efficient Fuel Cells for Space Power - Linkous, C., Pearman, B., Hall, D., Slattery, D., Baik, J. (FSEC)
- Integrated Fuel Cell Test Bed Facility - Slattery, D., Bonville, L., Fowler, R. (FSEC)
- Modeling and Optimization of Fuel Cell Systems for Aircraft Applications - Ordonez, J., Lungo, C. (FAMU)

Hydrogen Sensors – Cost effective hydrogen sensor technologies that can deliver detection selectivity and sensitivity, dependability and durability, stability and reproducibility, and applicability in cryogenic LH_2 environment are needed. Projects conducted in this area were:

- Gas Permeable Chemochromic Compositions for Hydrogen Sensing - Mohajeri, N., Muradov, M., Bokerman, G., T-Raissi, A., Captain, J., Peterson, B., Whitten, M. (FSEC)
- Highly Selective Nano-Mems Low Temperature Hydrogen Sensor- Seal, S., Cho, H. (UCF)
- Surface Acoustic Wave (SAW) Sensors for Hydrogen and Other Gas Detection - Bhethanabotla, V. (USF)
- Wireless Passive Sensors and Systems for Physical Sensors and Hydrogen Sensing Applications - Malocha, D. (UCF)

Hydrogen Storage and Liquefaction – Use of hydrogen as an energy carrier and fuel for spaceport and vehicle applications requires that it be stored and transported. New and innovative technologies are needed for higher energy density and safe H_2 storage and transport. The storage and liquefaction projects were:

- A Reliable, Efficient and Compact Reverse Turbo Brayton Cycle Cryocooler for Storage and Transport of Hydrogen in Spaceport and Space Vehicle Applications - Chow, L., Kapat, J., Chen, Q., An, L., Wu, T., Sundaram, K., Ham, C., Dhere, N. (UCF)
- Ammonia-Borane Complex for Hydrogen Storage - Mohajeri, N., T-Raissi, A., Ramasamy, K., Adebiyi, O., Bokerman, G. (FSEC)
- Liquid Hydrogen Storage at Kennedy Space Center - Gu, L., Block, D., Bokerman, G., T-Raissi, A., Basarkar, M. (FSEC)
- Numerical Simulation Model for Thermo-Fluid Analysis of Cryogenic Storage Systems with Zero Boiloff - Rahman, J., Ho, S. (USF)
- Prototype and Simulation Model for a Magneto-Caloric Refrigerator - Bhansali, S., Rahman, M., Kim, S., Ghirlanda, S., Hernandez, C., Adams, C., Bethala, B., Rosario, S., Sambandam, S. (USF)
- Smart Porous Metal-Organic Frameworks (MOFs) for Hydrogen Recovery and Storage - Eddaoudi, M., Zaworotko, M., Space, B., Eckert, J., T-Raissi, A., Mohajeri, N. (USF/FSEC)
- Zero-Boil-Off Liquid Hydrogen Storage Tanks - Baik, J. (FSEC)

Cryogenics – NASA Glenn research engineers have been working in the field of high-energy, high-density cryogenic propellants for over two decades. This basic research area focused on developing handling capabilities and defining and measuring low temperature performance characteristics of cryogenic propellants.

- Development of Cryogenic Shape Memory Actuator Materials for Switches, Seals and Valves - Vaidyanathan, R. (UCF)
- Densified LH_2 and LO_2: Transport Properties and Density - Van Sciver, S. (FSU)
- Experimental and Numerical Investigations of Cryogenic Multiphase Flow - Van Sciver, S., Hussaini, Y. (FSU); Justak, J. (ATG)

Hydrogen Separation – Hydrogen is lost by NASA operations due to transfer, boil off and purging. In addition, prior to filling lines with liquid hydrogen, they must be precooled with liquid helium and then the helium is purged. Recovery of this lost hydrogen and helium could lead to substantial savings and led to these two projects.

- Ceramic Membranes of Mixed Ionic-Electronic Conductors for Hydrogen Separation - Elbaccouch, M., T-Raissi, A., Linkous, C., Mohajeri, N. (FSEC)
- Metal Hydrides for Hydrogen Separation, Recovery and Purification - Hampton, M., Slattery, D. (UCF/FSEC)

Hydrogen Education and Outreach

- Hydrogen Education and Outreach – Schleith, S., Hall, P., Henzmann, A., Block, D. (FSEC)

With reference to the above projects, it is noted that the projects for each of the hydrogen technologies were reasonably split with eight projects in production and two projects in separation.

It is also noted that ten projects began in 2002 and continued until the program end in 2007. These ten projects are shown in Table 5.

Table 5 - Projects covered the full grant time period.

- A Reliable, Efficient and Compact Reverse Turbo Brayton Cycle Cryocooler for Storage and Transport of Hydrogen in Spaceport and Space Vehicle Applications - Chow, L., Kapat, J., Chen, Q., An, L., Wu, T., Sundaram, K., Ham, C., Dhere, N. (UCF)
- Densified LH_2 and LO_2: Transport Properties and Density - Van Sciver, S. (FSU)
- Development of Cryogenic Shape Memory Actuator Materials for Switches, Seals and Valves - Vaidyanathan, R. (UCF)
- Highly Selective Nano-Mems Low Temperature Hydrogen Sensor- Seal, S., Cho, H. (UCF)
- Hydrogen Education and Outreach – Schleith, S., Hall, P., Henzmann, A., Block, D. (FSEC)
- Local Hydrogen Production via Catalytic Reformation of Fossil and Renewable Resources - Muradov, N., Smith, F. (FSEC)
- Numerical Simulation Model for Thermo-Fluid Analysis of Cryogenic Storage Systems with Zero Boiloff - Rahman, J., Ho, S. (USF)
- Prototype and Simulation Model for a Magneto-Caloric Refrigerator - Bhansali, S., Rahman, M., Kim, S., Ghirlanda, S., Hernandez, C., Adams, C., Bethala, B., Rosario, S., Sambandam, S. (USF)
- Surface Acoustic Wave (SAW) Sensors for Hydrogen and Other Gas Detection - Bhethanabotla, V. (USF)
- System Analysis of Hydrogen Production and Utilization at KSC - T-Raissi, A., Elbaccouch, M., Ramasamy, K., Baik, J. (FSEC)

As a final comment on the projects that were conducted, it is noted that each of the university participants have made educational activities a major part of their research program. The educational component has used the research projects as part of graduate student masters and PhD theses and training. The FSEC program expanded the education effort to include K-12 education and public outreach activities. Table 6 presents the totals for publications, presentations and students trained for each institution by their program.

Table 6. Publications, presentations and student by institution.

Institution	Publications	Presentations	Students
Florida Solar Energy Center	93	78	13
University of Central Florida	71	72	35
Florida State University	15	11	2
Florida International University	-	-	-
University of South Florida	33	28	24
Florida Agricultural & Mechanical University	10	7	22
Totals	222	196	96

To conclude this section on projects, one-page summaries of each of the 29 projects followed by the individual final reports are presented in the last two sections of this report. Detailed information on each of the projects is also available at: http:// www.fsec.ucf.edu/ hydrogen/new/ research/funded_nasa.htm and http://www.hydrogenresearch.org.

Projects Funded by Other Agencies or Industry

In the previous section, a listing of the projects that were conducted under the NASA grant was presented. One of the significant outcomes of the NASA grant was the development of strong R&D programs by many of the program PIs at each of the universities. These researchers have developed novel hydrogen and hydrogen related technologies that have the potential to become topics of interest to other funding agencies or industry. This section of the report presents a listing of those projects which have received additional funding from other agencies or industry and in which the research is still being conducted under the new agency funding. It is noted that these projects are not an official part of the NASA grant, but they are related to the NASA effort in that the NASA program initiated the effort which is now receiving additional support. For this area, there are twelve projects presented in Table 7.

Table 7. Related projects funded by other agencies/industries.

Project Title	Funding Amount	University	Funding Agency	Comments
Thermochemical Conversion of Biomass to Liquid Hydrocarbons as Substitutes for Petroleum-based Fuels	$998,000	FSEC	FL DACS/ FHI/DOE/ Chevron/EES	F-T conversion of biomass to diesel fuel
Smart Paints for Hydrogen Leaks	No funding	FSEC	KSC	Tape being tested for use on shuttle launch site.
Smart Paint Pigments for Hydrogen Sensing	$375,000	FSEC	U.S. Navy	Smart paints used for rapid testing storage materials.
Hydrogen Production by Solar Thermochemcial Water-Splitting Cycles	$2,500,000	FSEC	SAIC/U.S. DOE	Solar hydrogen production. Total DOE funding of $4.5 million over 4 years.
Nanocrystalline Al-Mg Alloys for Hydrogen Storage	$300,000	UF/FSEC	NSF	Fabricate nanocrystalline magnesium alloys for hydrogen storage.
Lunar Hydrogen - Metal Hydride System	$71,735	FSEC	ASRC/KSC	Design and test metal hydride systems for lunar mission.
Metal-Organic Frameworks for High Capacity Hydrogen Storage	$280,000	USF/FSEC	U.S. DOE	Develop MOFs for high capacity hydrogen storage.

On-site Reformation of Diesel Fuel for Hydrogen Fueling Station Applications	$500,000	FSEC	Chevron/FHI/U.S. DOE	Reform diesel fuel to hydrogen.
Hydrogen Sensor with High Selectivity and Sensitivity at Room Temperature	$102,000	UCF	NSF	Hydrogen sensing.
Nano-particles/tubes Integrated MEMS Device for Point Contact Highly Sensitive Hydrogen Sensor	$174,000	UCF	ASRC/KSC	Hydrogen sensing.
Technology Demonstration of a 100 KW Biomass Gasifier in El Salvador	$1,026,000	FIU	DOD	Hydrogen production in El Salvador.
GIS Assessment of Florida Biomass Resources for Local Energy Production	$9,500	FIU	FL DEP/FSEC	Biomass resource in Florida.
TOTAL ADDITIONAL FUNDING:	**$6,336,285**			

1. Thermochemical Conversion of Biomass to Liquid Hydrocarbons as Substitutes for Petroleum-based Fuels – The goal of this project is to further develop and demonstrate a process for generating clean-burning synthetic liquid hydrocarbon fuels made from Florida biomass resources as well as the large quantities of animal wastes available throughout the State. In this project, biomass feedstock will be gasified to form a bio-syngas suitable for reformation via Fischer Tropsch (F-T) synthesis to form synthetic liquid fuels, e.g., bio-gasoline and/or diesel. Both the gasification and F-T technology are well established industrial processes but mostly used for coal or natural gas conversion. In this project we intend to further develop and demonstrate the technology for converting biomass feedstock and various animal wastes to gasoline and diesel range fuels. This activity has been funded by the Florida Department of Agriculture and Consumer Services, Chevron Corp. and Environmental Energy Systems, Inc. of Hialeah, FL.

2. Smart Paints for Hydrogen Leaks – Monitoring hydrogen at the storage and usage sites for leakage is an important safety issue. FSEC has developed and filed for a U.S. patent on several formulations that act as smart paints for sensing hydrogen gas. Smart paints reveal, in an easy-to-see manner, the location of minute hydrogen leaks from pipes, flange joints, etc.

The dark spot on the "smart tape" indicates the location of hydrogen leak around this flange.

A roll of KSC fabricated "smart tape".

The “smart paint” in the form of a tape can be applied at the pipe connections, valve joints, or other areas susceptible to leaking. FSEC developed pigments that have been field tested at KSC for well over a year. And, KSC has also applied for a patent under this project.

FSEC researchers have also developed special tungsten-based pigments that revert to the original color after exposure to hydrogen has ceased. These special reversible pigments intended for “repeated use” applications, and they are also currently undergoing field-testing at KSC. KSC personnel have informed FSEC that KSC is planning in the near future to use the smart paint tape on the liquid hydrogen lines flowing from the storage tanks to the shuttle.

3. Smart Paint Pigments for Hydrogen Sensing – For a ‘hydrogen economy’, one of the major technology issues yet to be addressed involves its safe storage. If hydrogen can be stored safely and efficiently, it will open up many potential applications for its use. There are many potential candidate materials that can store hydrogen and identifying prospective candidates require a rapid and efficient material screening process.

FSEC researchers will design, fabricate, and test a high throughput-screening system based on the FSEC-developed hydrogen sensing polymers. The technique is applicable to a broad range of absorbents, including metal-organic frameworks (MOFs), various doped and undoped hydrides (e.g., alanates, alanes, etc.), among others.

FSEC’s hydrogen sensing membranes allow simple visual inspection of the chemochromic membranes after each dehydriding test. The change in the color of the membrane directly depicts the amount of hydrogen release from the samples. Under a new contract from the U.S. Navy, Defense Logistics Agency, FSEC researchers will be developing an apparatus and methods for high throughput combinatorial testing of hydrogen storage materials. The FSEC-developed technique reduces the time now required for screening for hydrogen storage materials from days down to a few minutes. The Navy funding for this project is $375,000.

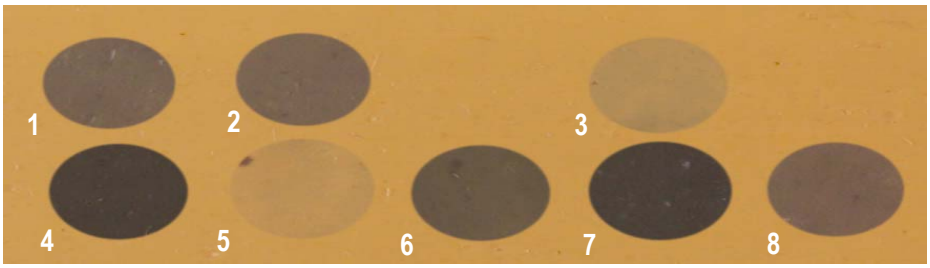

A 25-mil thick section of FSEC-developed chemochromic film after exposure to various quantities of hydrogen gas.

4. *Hydrogen Production by Solar Thermochemical Water-Splitting Cycles –* Past research in solar thermochemical cycles has focused on processes that utilize only the thermal component of the solar spectrum. FSEC’s approach employs the high-energy photons within the solar spectrum to drive ammonium sulfite/ammonium sulfate redox system for photocatalytic production of hydrogen from water. Thus, the cycle uses both the photonic and thermal energies. FSEC developed water splitting cycle has received the Innovative Technology Award at the 15th World Hydrogen Energy Conference held in Yokohama Japan in 2006 – the only such award given to researchers from the U.S.A. A patent on the cycle has been filed. For this

project, FSEC partnered with the Science Applications International Corporation of San Diego, CA. The U.S. DOE funding to FSEC for this project is $2.0 million plus cost share for the first year beginning August 2007. The total project effort is $4.5 million over four years.

Photoreactor for high temperature solar powered hydrogen production.

5. ***Nanocrystalline Al-Mg Alloys for Hydrogen Storage –*** The objectives of this effort are to fabricate nanocrystalline magnesium alloys (Al-Mg) in the form of powder via electrodeposition, characterize the microstructural evolution during hydrogenation and dehydrogenation, and then design an alloy powder with optimized characteristics. FSEC researchers have looked at alanates in the past. However, this new work involves nanocrystalline materials – materials with very tiny particles with a shorter path for the hydrogen, giving them a faster dehydriding rate. FSEC in a joint effort with the University of Florida investigating the use of metal hydrides for hydrogen storage. The project is funded by NSF at $300,000.

6. ***Lunar Hydrogen - Metal Hydride System –*** In 2005, NASA initiated the Regolith and Environment Science & Oxygen and Lunar Volatiles Extraction (RESOLVE) project to develop hardware under the NASA Exploration Technology Development Program (ETDP). The RESOLVE objective is to quantify volatiles released from lunar regolith (soils) and demonstrate in-situ resource utilization (ISRU) on a small scale by capturing the water and hydrogen volatiles. A metal hydride system has been initially designed for use in the system. However a more suitable metal hydride is needed because the current system does not work well at the desired temperatures. FSEC was tasked to identify a metal hydride based system that will capture hydrogen from a mixed gas stream and release the hydrogen when needed (a reversible system). The system captures 1.0 g of hydrogen in every cycle and is able to cycle 50 times. Ideally the system will absorb near room temperature, but absorption temperatures between 20-120 °C with desorption temperatures lower than 300 °C are desirable. FSEC has been funded by Arctic Slope Research Corp. at KSC for the amount of $71,735.

7. ***Metal-Organic Frameworks for High Capacity Hydrogen Storage –*** Metal-organic frameworks (MOFs) are a new class of metal-organic materials that exhibit desirable properties akin to zeolites, but also allow for tenability (pore size, organic functionality, choice of metallic constituents, inclusion of polar/ionic character) and rational design of desirable storage properties. These factors make MOFs a promising candidate for use as high capacity hydrogen storage materials. This project is concerned with developing and understanding new pathways aimed at synthesizing MOFs. The design strategy involves choosing the desired building blocks

for the assembly step in a “top-down design” process, followed by directed assembly, “bottom-up synthesis”. This project is a cooperative effort between Dr. M. Eddauodi of USF and FSEC. It is funded by the U.S. Department of Energy, Basic Energy Sciences, at $280,000 for 3 years.

8. ***On-site Reformation of Diesel Fuel for Hydrogen Fueling Station Applications –*** The objectives of this project are to develop a cost effective, energy efficient and near-term on-site fuel reformation process for producing hydrogen (particularly high purity H_2) from sulfurous liquid hydrocarbon fuels (e.g., diesel, kerosene and/or jet fuels). Once developed, the process will be used at the hydrogen fueling stations and for applications that involve remote fuel cell based electric power generation in areas without access to natural gas or grid power. This activity is a collaborative RD&D effort between FSEC and the Catalysis Group at Chevron Technology Ventures, LLC. The project is funded by the U.S. Department of Energy through the Florida Hydrogen Initiative at $500,000 with $200,000 in cost share from Chevron Corp. and UCF.

9. ***Hydrogen Sensor With High Selectivity and Sensitivity at Room Temperature –*** This University of Central Florida project is developing and studying the defect structure of oxides at the nano-level for the development of high performance hydrogen sensors. The project will also investigate the selectivity issues by using ceramic separation membranes and the effect of UV exposure on sensor cleaning is further investigated. The study will ascertain the underlying mechanism for exhibiting enhanced sensor response of doped oxide nanoparticles and nano-wires at room temperature. This aspect would be a significant step towards room temperature H_2 sensor. Funded by NSF for $102,000.

10. ***Nano-particles/tubes Integrated MEMS Device for Point Contact Highly Sensitive Hydrogen Sensor –*** The advanced concepts in H_2 separation and gas sensing technologies are merged for the development of a novel H_2 sensor consisting of porous, doped, nano-clustered particulate/fiber/rod shaped nanostructures. Additionally, the sensor will be a unique integration of nanomaterials and MEMS device, thus combining the faculty expertise from UCF’s materials, nanoscience, and MEMS fabrication technology. Funded by ASRC Corp. at KSC for $174,000.

11. ***Technology Demonstration of a 100 KW Biomass Gasifier in El Salvador –*** Florida International University (FIU) is assisting the U.S. Department of Defense (DOD) to facilitate the exchange of information and technology with western hemisphere nations under the auspices of the Western Hemisphere Information exchange (WHIX) program. An element of the WHIX program is the technology demonstration and validation of innovative technologies that further the efficient management of military installations and protect the environment while ensuring safety and occupational health of workers and residents. FIU has installed and operated a 100 KW biomass gasifier (wood chips) for the U.S. military base in El Salvador for a period of 6 months. Funded by the U.S. Department of Defense for $1,026,000.

12. ***GIS Assessment of Florida Biomass Resources for Local Energy Production –*** The Florida Energy Office (FEO) was tasked with mapping of the state’s potential biomass resources with the ultimate goal of prioritizing future development of resources and related technologies that will lead to a Florida bio-based economy. The Florida Solar Energy Center (FSEC) and the Applied Research Center at Florida International University assisted FEO with the creation of a statewide computer based compendium of biomass resource maps along with installed and potential biomass energy production capacity. GIS technology was used to create a portfolio of biomass resource maps and to identify installed and potential biomass energy production capacity statewide. Funded by Florida Department of Environmental Protection for $9,500.

The total external funding for the above twelve projects is **$6.336 million**.

Concluding Remarks

The NASA Hydrogen Research at Florida Universities program has demonstrated that six Florida universities within the State University System all working collaboratively can successfully address a major problem of national interest, hydrogen economy. Each of the partner universities has identified areas of expertise and interest while contributing to the overall success of the program. This final report has described the R&D activities and projects conducted for NASA under the 5-year NASA Hydrogen Research at Florida Universities grant program. The R&D activities cover hydrogen technologies related to production, cryogenics, sensors, storage, separation processes, fuel cells, resource assessments and education.

In the span of 6 years, the NASA Hydrogen Research at Florida Universities program funded a total of 44 individual university projects, and employed more than 100 faculty and over 100 graduate research students at the six participating universities. Program researchers have filed more than 20 patents in all hydrogen technology areas and put out well over 220 technical publications in the last 2 years alone. The NASA research grant has also led to the universities receiving over $6.336 million of additional funding from federal agencies for research on twelve projects - all related to the NASA funded effort.

Finally, it is noted that each of the university participants have made educational activities a major part of their research program. The educational component has used the research projects as part of graduate student masters and PhD theses and training. The numbers of students trained by this research were 15 PhD, 23 M.S., 2 post doctorial, 20 undergraduate and 36 unknown for a total of 96 students. The FSEC program expanded the education effort to include K-12 education and public outreach activities.

In the next two sections are one-page summaries of each of the 29 projects followed by the individual final reports. The reports are organized individually from each of the universities and presented in alphabetical order of the project title. These one-page summaries and the following complete reports are presented in the same order as the listing of reports given in Table 4. The complete name, title and affiliation of each project principal investigator are given in Appendix A.

Acknowledgements

Special thanks for this program are made to NASA Glenn Research Center (GRC) for its support and to the three program managers at GRC for their program guidance – James Burkhart and David Chato in the initial 2 years and Timothy Smith in the final 3 years. Thanks are also made to Ms. Syreeta Stewert of GRC for her administrative support and to David Bartine and H. T. Everett of NASA Kennedy Space Center for program guidance.

One Page Summaries

This section presents one page summaries of each of the projects as follows:

Florida Solar Energy Center

- Ammonia-Borane Complex for Hydrogen Storage - Mohajeri, N., T-Raissi, A., Ramasamy, K., Adebiyi, O., Bokerman, G.
- Ceramic Membranes of Mixed Ionic-Electronic Conductors for Hydrogen Separation - Elbaccouch, M., T-Raissi, A., Linkous, C., Mohajeri, N.
- Compact, Lightweight and Optimized Fuel cells for Space or Aircraft Power - Fenton, J., Choi, P., Bonville, L., Kunz, R.
- Gas Permeable Chemochromic Compositions for Hydrogen Sensing - Mohajeri, N., Muradov, M., Bokerman, G., T-Raissi, A., Captain, J., Peterson, B., Whitten, M.
- Hydrogen Education and Outreach – Schleith, S., Hall, P., Henzmann, A., Block, D.
- Hydrogen Production From Used Lube Oils - T-Raissi, A., Ramasamy, K.
- Hydrogen Production via Solar Thermochemical Water Splitting – T-Raissi, A., Huang, C., Muradov, N.
- Hydrogen-Powered Aeropropulsion: Compact, Lightweight and Efficient Fuel Cells for Space Power - Linkous, C., Pearman, B., Hall, D., Slattery, D., Baik, J.
- Integrated Fuel Cell Test Bed Facility - Slattery, D., Bonville, L., Fowler, R.
- Liquid Hydrogen Storage at Kennedy Space Center - Gu, L., Block, D., Bokerman, G., T-Raissi, A., Basarkar, M.
- Local Hydrogen Production via Catalytic Reformation of Fossil and Renewable Resources - Muradov, N., Smith, F.
- Photoelectrochemical Water Splitting for Hydrogen Production Using Multiple Bandgap Combination of Thin-Film- Photovoltaic Cells and Photocatalyst – Dhere, N.
- System Analysis of Hydrogen Production and Utilization at KSC - T-Raissi, A., Elbaccouch, M., Ramasamy, K., Baik, J.
- Zero-Boil-Off Liquid Hydrogen Storage Tanks - Baik, J.

University of Central Florida

- A Reliable, Efficient and Compact Reverse Turbo Brayton Cycle Cryocooler for Storage and Transport of Hydrogen in Spaceport and Space Vehicle Applications - Chow, L., Kapat, J., Chen, Q., An, L., Wu, T., Sundaram, K., Ham, C., Dhere, N.
- Development of Cryogenic Shape Memory Actuator Materials for Switches, Seals and Valves - Vaidyanathan, R.
- Genetic Engineering to Enhance Biological Hydrogen Production - Self, W., Ganyc, D., Halvorsen, L.
- Highly Selective Nano-Mems Low Temperature Hydrogen Sensor- Seal, S., Cho, H.
- Metal Hydrides for Hydrogen Separation, Recovery and Purification - Hampton, M., Slattery, D.
- Wireless Passive Sensors and Systems for Physical Sensors and Hydrogen Sensing Applications - Malocha, D.

Florida State University

- Densified LH_2 and LO_2: Transport Properties and Density - Van Sciver, S.
- Experimental and Numerical Investigations of Cryogenic Multiphase Flow - Van Sciver, S., Hussaini, Y., Justak, J.

Florida International University

- Improved Hydrogen Yield from Florida Specific Biomass Gasification Using a Pilot Scale Gasification Unit - Srivastava, R.

University of South Florida

- Numerical Simulation Model for Thermo-Fluid Analysis of Cryogenic Storage Systems With Zero Boiloff - Rahman, J., Ho, S.
- Prototype and Simulation Model for a Magneto-Caloric Refrigerator - Bhansali, S., Rahman, M., Kim, S., Ghirlanda, S., Hernandez, C., Adams, C., Bethala, B., Rosario, S., Sambandam, S.
- Smart Porous Metal-Organic Frameworks (MOFs) for Hydrogen Recovery and Storage - Eddaoudi, M., Zaworotko, M., Space, B., Eckert, J., T-Raissi, A., Mohajeri, N.
- Surface Acoustic Wave (SAW) Sensors for Hydrogen and Other Gas Detection - Bhethanabotla, V.
- Thermo Catalytic H_2 Production via Oxygen-Free Methane Aromatization - Wolan, J., Stefanakos, E., Kababji, A.

Florida A & M University

- Modeling and Optimization of Fuel Cell systems for Aircraft Applications - Ordonez, J., Lungo, C.

The complete name, title and affiliation of each project principal investigator are given in Appendix A.

Ammonia-Borane Complex for Hydrogen Storage

N. Mohajeri, A. T-Raissi, K. Ramasamy, O. Adebiyi, and G. Bokerman
Florida Solar Energy Center

Research Period: June 2002 to December 2007

Summary

The goal of this project was to develop a high-density hydrogen storage system based on ammonia borane (AB) complex. Due to their high hydrogen capacity, AB hydrides have been employed as disposable hydrogen (H_2) sources for fuel cell applications. The objectives of this project were to 1) identify viable amine-borane (AB) complexes for hydrogen storage at ambient conditions and 2) develop a cost-effective synthetic route for hydrogenation of borazine to cyclotriborazane - as a means of chemical hydrogen storage.

Ammonia borane (AB) complex is a chemical hydride that is stable in air and water, and contains very high hydrogen content (19.6 wt%) with a system-level H_2 energy storage density of about 2.74 kWh/L (vs. 2.36 kWh/L for a liquid hydrogen Dewar). AB is a promising material as a hydrogen carrier especially for power generation utilizing proton exchange membrane fuel cells (PEMFC). Release of hydrogen in the AB complex can occur by either thermolysis or hydrolysis. Thermolysis of AB generates, in addition to hydrogen, species such as borazine, monomeric aminoborane, and diborane. In the case of AB hydrolysis, ammonia is the byproduct of the reaction.

The results have shown the liberation of 2 moles of hydrogen by thermolysis of AB complex with relatively minor expenditure of energy. Without downstream treatment, some quantities of borazine and poly-aminoborane are also generated. The results have also shown that borazine generated can be effectively captured and removed from H_2 gas stream using a broad class of solid sorbents including carbons and mesoporous silica.

Results for pyrolysis of the AB complex have shown it to be an overall exothermic process that requires induction energy to initiate AB decomposition until about 0.3 moles of H_2 is released. At this point, the reaction is self sustaining and proceeds to completion with the additional release of 2 moles of hydrogen gas. Induction energy required to release 2 moles of H_2 is about 16.2 kJ/mol of AB or 8.1 kJ/mol of H_2, which corresponds to 3.35% of the chemical energy of hydrogen generated (on LHV basis).

Near room temperature hydrolysis of AB complex has been carried out using small amounts of K_2PtCl_6 salt. The AB hydrolytic reaction is exothermic and can be extremely fast, kinetically. The report also measures the thermal conductivities of composites formed by mixing fine aluminum powder with AB complex at temperatures in the range of 300-420 K. At 300 K, the thermal conductivity of pure AB is approximately 15 W/m-K. A composite pellet prepared by mixing 10% by weight aluminum powder with AB complex had a thermal conductivity that was a factor of 4 higher than that of pure AB.

The research has resulted in one patent, 9 publications and 7 presentations.

Ceramic Membranes of Mixed Ionic-Electronic Conductors for Hydrogen Separation

M. Elbaccouch, A. T-Raissi, C. Linkous, and N. Mohajeri
Florida Solar Energy Center

Research Period: April 2004 to September 2007

Summary

Mixed ionic-electronic conductors of perovskite-type structure ($A^{2+}B^{4+}O_3$) are of interest for hydrogen production and separation at high temperatures. The goal of this project was to develop ion transport separation and purification systems using mixed ionic-electronic conductors of perovskite-type structure ($A^{2+}B^{4+}O_3$-doped with a trivalent cation). The targeted membranes separate hydrogen from gas mixtures with 100% selectivity, high hydrogen flux, and good chemical stability in CO_2-rich mixture. The designed membranes are dense and free of pinholes. For the project, three tasks were conducted as follows.

Task 1 - Hydrogen Flux in Terbium (Tb) Doped Strontium Cerate ($SrCeO_3$) Disk Membranes. In task 1, hydrogen membranes of $SeCe_{0.95}Tb_{0.05}O_{3-\delta}$ were synthesized using the liquid-phase method, and hydrogen flux data was generated under different processing conditions. The results evaluated hydrogen permeability as a function of temperature, hydrogen partial pressure, hydrogen dry conditions, and water vapor pressure. Also, the influence of nickel deposition on hydrogen flux was evaluated.

Task 2 - Microstructural Analysis of Doped-Strontium Cerate Thin Film Membranes Fabricated via Polymer Precursor Techniques. This task synthesized nanocrystalline thin film membranes of terbium (Tb)-doped strontium cerate ($SrCeO_3$) via the polymer precursor techniques. Continuous and dense thin film membranes of composition $SrCe_{0.95}Tb_{0.05}O_{3-\delta}$ were prepared using spin-coating technique by utilizing ethylene glycol (EG)-based polymeric precursor. The polymeric precursor was deposited on silicon-based substrates, and converted to dense polycrystalline thin film ceramic membranes by sintering at relatively low temperatures. The study demonstrated that using the EG-based polymeric precursor, Tb-doped $SrCeO_3$ thin film membranes, having thicknesses in the range of 0.2-2 μm and average nanocrystallite size of 8-70 nm, can be effectively synthesized by controlling the number of spin-coating cycles and sintering temperature.

Task 3 - Development of Ceramic Oxide Thin Films Using Tape-Casting Process. This task fabricated a tubular membrane reactor that could be used at temperatures (above 550 °C) for hydrogen separation and purification. The tubular reactor was a mixed ionic-electronic conductive system with a doped perovskite structure ($A^{2+}B^{4+}O_3$-doped with a trivalent cation). The reactor consists of a porous $SrCeO_3$-NiO composite support and a dense thin film membrane of $SrCe_{0.95}Y_{0.05}O_{3-\alpha}$. The support material, composed of the ceramic powder, binder, plasticizer, and solvent, was formulated into homogeneously dispersed slurry with uniform structure. A tape-casting process was used to produce thin film support tapes. After drying, the tapes were cut and rolled on a rod producing a tubular geometry. Slow sintering and H_2 atmosphere exposure burned off the organic materials, producing a ceramic composite tube with appreciable porosity.

From this work, 5 publications have resulted.

Compact, Lightweight, and Optimized Fuel Cells for Space and Aircraft Power

J. Fenton, P. Choi, L. Bonville, and R. Kunz
Florida Solar Energy Center

Research Period: June 2005 to February 2008

Summary

Proton exchange membrane (PEM) fuel cells are potentially the most efficient energy conversion devices for space applications. Conventional PEM fuel cells use external humidification requiring cumbersome humidification devices, which increase the volume and complexity of the fuel cell system. The research objective of this project was to achieve efficient fuel cell operation without external humidification of reactant gases by developing highly efficient and compact fuel cell systems which include efficient membrane electrode assemblies and internal water management systems.

To accomplish the objective, techniques were developed for improving PEM fuel cell performance when operating on dry reactants that are known to harm performance. The use of reactant recirculation, water recirculation, and a cell with membrane additives were considered. For reactant recirculation, a simple mass balance model was used to determine the membrane inlet relative humidity (RH) for a fuel cell operating on dry reactant gases. Calculations were done to vary cell temperature, cell pressure, reactant stoichiometry and reactant recycle in order to generate strategies for internally humidifying the stack and for operation under conditions which maximize power density. These calculations showed the cathode recycle was much more effective than the anode recycle at increasing the membrane inlet relative humidity. They also showed that for reasonable total flow rates, the losses due to reduced reactant pressures were much higher than the gains for the increased membrane water content.

A simplified and compact fuel cell system with no external humidification was designed and operated. A model was developed for the system, which includes a combined analysis of the generation of water in the fuel cell and the diffusion of water from the wet side of humidifier to the dry feed stream. Single cell and stack experiments of the internal humidifier incorporated cell have shown improved performance of fuel cell compared to the dry feed operation. However, the performance was lower than that of externally humidified operation by 20 to 30% in a single cell experiment. Polymer membranes such as Nafion® and SPEEK have been successfully employed in the fuel cell system to provide the diffusion medium for the transport of water vapor from the humid exhaust gas to the dry feed stream. In order to improve the efficiency of the MEA, new composite membranes using inorganic acid were prepared and tested. The composite membrane showed higher performance, which may be attributed to the improved conductivity and lower ohmic resistance of the membrane.

The humidifier may be further improved by increasing the active area of diffusion and reducing the thickness of the membrane. The implementation of an internal humidifier with highly efficient MEAs provides the basis for a new compact fuel cell system for space applications.

The research has resulted in research for two graduate students, in one patent, in one publication and in two presentations.

Gas Permeable Chemochromic Compositions for Hydrogen Sensing

N. Mohajeri, N. Muradov, G. Bokerman, and A. T-Raissi
Florida Solar Energy Center

J. Captain
Nacional Aeronautics and Space Administration
Kennedy Space Center

B. Peterson
ASRC Aerospace Corporation

M. Whitten
University of Central Florida

Research Period: January 2004 to December 2007

Summary

The goal of this project was to develop a special powder material that can be applied like paint to the surfaces of cross-county lines at NASA-KSC and used for detecting hydrogen leaks. Operations at KSC require safety and the use of extremely pure hydrogen. The proposed technique provides a visual method to detect and locate possible hydrogen leaks that may occur in the field lines, flanges and joints for hydrogen transport and use. To detect the location of hydrogen leaks, a special chemochromic hydrogen (H_2) sensing material, called smart paint, has been researched, developed and patented by the Florida Solar Energy Center. The development of the smart paint sensors has also been done with close coordination and collaboration with scientists from NASA Kennedy Space Center.

The hydrogen (H_2) sensors are comprised of a gas permeable matrix material intermixed and encapsulating with at least one chemochromic pigment. The chemochromic pigment produces a detectable change in color of the overall sensor composition in the presence of H_2 gas. The hydrogen leaks are shown by changes in color from white to gray of the sensing material. Two types of sensors have been developed and field tested – one in which the color change is irreversible and one, called reversible, in which the changed color in the presence of H_2 is reversed to the original color when no H_2 is present.

The irreversible sensing material employs titania (TiO_2) supported palladium oxide (PdO) pigments encapsulated within a special silicone matrix. The results for the irreversible sensors determined the hydrogen activity of four different chemochromic TiO_2 supported PdO pigments, the chemochromic activity of the pigments as a function of the PdO particle size and level of PdO dispersion on theTiO_2 support surface and the materials kinetics and color contrast number.

The reversible H_2 sensors were formulated based on isopolycompounds (IPC) of tungsten and molybdenum, heteropolycompounds, HPC, all of which were synthesized and evaluated. For this case, results were determined for reversing enhancing agents polyoxometalates (POM) of W and Mo including silico-tungstic acid (STA) $H_4[SiW_{12}O_{40}]$, phospho-tungstic acid (PTA) $H_3[P(W_3O_{10})_4]$), and phospho-molybdic acid (PMA) $H_3[P(Mo_3O_{10})_4]$. POMs were doped with small amounts of Pt to catalyze the coloration-bleaching reactions. Two modifications of the reversible pigment were studied: (1) alumina-supported Pt-POM encapsulated in silicone matrix, and (2) Pt-POM supported on porous supports such as glass and paper filters. Both systems performed well during coloration and bleaching stages.

The research has resulted in one patent, one publication and two presentations.

Hydrogen Education and Outreach

S. Schleith, P. Hall, A. Henzmann, and D. Block
Florida Solar Energy Center

Research Period: June 2002 to December 2007

Summary

Education and outreach were extremely important components of the NASA hydrogen research program. These activities have supported four main areas: education of graduate and undergraduate engineering and science students, education for K-12 students and teacher professional development, participation in and offering of seminars and workshops, and a variety of public outreach activities.

Each of the university participants have made educational activities a major part of their research program. The universities have used the topics from the large variety of research projects for graduate student masters and PhD theses. In addition, the project's results are used for publications and presentations by university faculty members and their students to present the results to local, national and international audiences. The totals are 222 publications, 196 presentations and the support of 96 students.

The goal of incorporating hydrogen education into K-12 student and teacher programs at FSEC has been successfully accomplished through curriculum development, professional development for teachers and special events for K-12 students. These activities are ongoing and are being continually expanded. Over the course of the grant period, an average 310 teachers per year have participated in hydrogen education training opportunities facilitated by FSEC staff. The teacher opportunities include multi-day institutes, one-day workshops, and half-day experiences. Interest in hydrogen continues to grow amongst teachers, as evidenced by the popularity of the many hydrogen training events held for teachers by FSEC throughout the year. Field trips to the Florida Solar Energy Center are also popular with schools with nearly 800 students, their teachers and 60 parents per year visiting the facility for informal instruction on hydrogen, solar and energy efficiency.

Another major effort directed at graduate students and the technical community was the fuel cell short courses developed and offered for the past three years at the Florida Solar Energy Center. The courses are open to industry, academia and students and have drawn researchers and engineers from such places as NASA, UTC, Giner Electochemical, Lawrence Berkeley National Lab, and Savanah River National Lab. Most attendees were from the US but some came from as far away as Spain and Japan.

The outreach program has been accomplished publications, presentations, press releases and web site development, as well as personal interaction with the public. Outreach results in addition to publications and presentations include 21 press releases and the development of two hydrogen web sites.

Hydrogen Production From Used Lubricating Oils

A. T-Raissi and K. Ramasamy
Florida Solar Energy Center

Research Period: June 2005 to December 2007

Summary

Used lubricating oils present a valuable, readily available and cost-effective resource for local production of hydrogen at NASA-KSC. In Florida, the amount of used lubricating oil available for hydrogen production amounts to 45 million gallons per year at a relatively low cost of about 10 cents/gallon delivered. Used lube oils are a complex mixture of aliphatic and polycyclic hydrocarbons formulated to withstand high service temperatures in internal combustion engines. Both synthetic and mineral oils contain a high concentration of hydrogen (about 13–14 wt%). In this project, a process has been developed that converts used oils to hydrogen and other valuable low molecular weight hydrocarbons. The processes used were supercritical water reformation and steam pyrolysis.

The results show that hydrogen production from used lube oil via thermal cracking can be an attractive process both environmentally and economically. The performance of several dehydrogenation catalysts -- nickel, carbon, and an alkali based catalysts -- were investigated. Both nickel and carbon based catalysts performed poorly toward hydrogen production during steam assisted reformation of lube oils because of catalyst deactivation. Utilizing KOH as a catalyst for the reformation of lube oils increased the total yield of all the gaseous species produced with no noticeable degradation of the catalyst activity and with high selectivity toward hydrogen. However, the hydrogen yields were low.

Total gas produced and the yield of hydrogen were significantly higher during both steam assisted reformation and direct thermal cracking of the lube oils at 1 atm and reformer temperatures above 715 °C as compared with those obtained by supercritical water reformation (65% of hydrogen contained in oil, compared with only about 5% from supercritical water reformation). The high temperature, low pressure process also yielded lower concentrations of CO_2 and CO in the output gas (30% compared with only 1% by volume of gas produced by supercritical water reformation).

Results obtained from the direct thermolytic reformation of the virgin synthetic (Mobile One™) oil and used oil showed that, respectively, 58–65% and 40–63% of the total mass of hydrogen in the oil fed into the reformer was converted to H_2 in the output gas. Composition of the gaseous species generated by thermal cracking and steam reformation of lube oils were basically the same and included mainly hydrogen, methane and ethylene at 17–30%, 40–45%, and 15–25%, respectively. Under the experimental conditions of this investigation, the presence of water does not appear to affect the chemistry of the thermolysis of lube oils and only acts as a heat transfer medium. Direct thermolysis of lube oils requires less energy and produces about one third less disposable waste materials (compared to that from steam reformation process).

The research has resulted in 6 publications and 2 presentations.

Hydrogen Production via Solar Thermochemical Water Splitting

A. T-Raissi, C. Huang, and N. Muradov
Florida Solar Energy Center

Research Period: March 2004 to February 2008

Summary

One of the NASA objectives was to identify, characterize, and analyze a series of eco-friendly technologies that could be used for hydrogen production at NASA Kennedy Space Center (NASA-KSC) from locally available feedstock. One approach for hydrogen production that utilizes both local and renewable resources is splitting water using solar energy as the primary energy input. Technologies described in this project employ solar-driven thermochemical cycles for the direct (i.e., no intermediate electricity generation step is involved) production of hydrogen from solar energy and water. Any thermochemical water splitting cycle consists of two main steps: hydrogen and oxygen production steps. In this report, a new sulfur-family solar thermochemical water splitting cycle is described that utilizes the photonic portion of the solar spectrum for the production of hydrogen and the thermal part of the sunlight for the oxygen generation.

All sulfur-family thermochemical water splitting cycles rely on concentration and decomposition of sulfuric acid for the oxygen evolution step of the cycle. The sulfuric acid decomposition step presents serious materials and catalyst deactivation challenges. Thus, a new family of hybrid photo/thermo-chemical water splitting cycles based on a sulfur ammonia cycle has been developed.

Experimental results for the sulfur ammonia cycle show that the hydrogen generation step attains an efficiency of about 12% using precious metal doped cadmium sulfide photocatalyst. Due to the materials challenges of the sulfuric acid decomposition process, two new classes of cycles have been developed by modifying the original sulfur ammonia cycle to include 12 metal sulfate-ammonia (MSO_4-NH_3); and 3 metal pyrosulfate-ammonia ($M_2S_2O_7$-NH_3) based cycles. Experiments involving the zinc oxide catalyzed decomposition of ammonium sulfate using a thermogravimetric/ differential thermal analysis system couple to a mass spectrometer have shown the evolution of ammonia validating the feasibility of oxygen production via metal sulfate sub-cycles.

From this funded work, two patents, 8 publications and 8 presentations have resulted, and 1 post-doctoral and 2 graduate research students have been trained. This activity helped FSEC researchers secure a U.S. Department of Energy funding for $4.5 million (2007-2011) for a project entitled “Solar High-Temperature Water-Splitting Cycle with Quantum Boost.” This DOE awarded effort is a 50%-50% joint FSEC/Science Application International Corp. (SAIC) R&D program.

Hydrogen-Powered Aeropropulsion: Compact, Lightweight, and Efficient Fuel Cells for Space Power

C. Linkous, B. Pearman, D. Hall, D. Slattery, and J. Baik
Florida Solar Energy Center

Research Period: September 2004 to December 2007

Summary

Fuel cells have long been used in supplying space power, however, improvements are still required in terms of size, weight, and fuel efficiency. In this project, various strategies for increasing the specific power (kilowatts of power per kilogram of device weight) of fuel cells were studied. The major objective was to increase the state-of-the-art fuel cell power density from ~100 W/kg to 1.0 kW/kg and higher.

The approach to improving power density was to increase the current density. Current density is frequently limited by electrolyte conductivity, especially for solid electrolytes. Thus, the research targeted the ionic conductivity of the electrolyte as a significant barrier in the development of higher power density devices. The effect of temperature was clearly demonstrated, with conductivity values rising on order of 4x in going from room temperature to 100 °C. Another strong effect was the acid electrolyte concentration where additional improvements in conductivity by >30% are gained by lowering concentration of the acid from its maximum value to the 4-6 M range. The combined effects can potentially produce a conductivity greater than 5x of the ambient concentrated acid value.

Liquid electrolytes must be contained in a porous matrix. Hexagonal boron nitride, h-BN, was a strong contender in this regard, due to its chemical inertness and fine particle size. Conductivities as high 0.25 S/cm with a phosphoric acid/BN paste were obtained, some 2.5 times that obtained with conventional solid polymer electrolytes. Boron carbide, BC, and silicon nitride, SiN, gave comparable results.

The research also showed the use of FLUENT® computer program as a performance modeling tool and investigated the pros and cons of the use of microphotography, solvent permeation, and conductivity of solvent extract for monitoring oxidative resistance to peroxide attack on polymer membranes. It was determined that the conductivity of the peroxide soaking solution itself was the best way of comparing rates of membrane degradation among many disparate ionomer materials. Another way to improve the conductivity of a proton-conducting electrolyte was to increase the acidity of the acid groups or molecules contained within it. In this later case, the research found that the sulfonic acid derivative of a polyaryletherketone known as SPEEK (polyetheretherketone sulfonate) was not a strong acid. It was attempted to prepare the superacidic α,α-difluoromethanesulfonic acid of SPEEK, starting with monobromination of 2,5-diacetamido-trifluoromethylbenzene. Finding a solvent that would dissolve both the trisubstituted benzene and the BBr3 brominating agent and remain inert throughout the reaction proved to be a challenge.

The research resulted in 2 publications, 6 presentations and support of one visiting graduate student.

Integrated Fuel Cell Test Bed Facility

D. Slattery, L. Bonville, and R. Fowler
Florida Solar Energy Center

Research Period: January 2005 to December 2007

Summary

The goal of the Integrated Fuel Cell Test Bed (IFCT) facility was to create a proving ground and permanent test facility where fuel cell components and systems could be tested and their performance evaluated. The fully integrated test bed facility could also be used for determining figures of merit and performance metrics to include round trip efficiency, specific power (kW/kg), reliability for long duration operation (approximately 1 year), redundancy path development, waste heat/cooling/heating management, turn down effects, transients, and the development of 'expert' systems for the process control. The facility also gives researchers the ability to perform hands-on research in membrane and electrode fabrication, electrochemical testing, materials analyses and cell and device operation.

An analysis of site requirements at FSEC was conducted and an appropriate area to be refurbished into the IFCT was selected. State Fire Marshal regulations required that all laboratories must have an air handler system that uses 100% outside, non-recirculated air. As a result, it was necessary to install new air handlers for the IFCT. This was the single most challenging task, with many set backs before it was finally accomplished. Two labs were required for space.

The first lab was outfitted with two fume hoods, a 6-ft and an 8-ft. Four U-shaped benches were installed and much of the lab is devoted to analytical instrumentation. This includes an Altimira Thermal Programmed Desorption system, a PMI BET Surface Area Analyzer, a Perkin Elmer FT-IR Spectrophotometer, Perkin Elmer Differential Scanning Calorimeter, Dionex High Pressure Liquid Chromatograph, JEOL Gas Chromatograph/Mass Spectrometer/Mass Spectrometer, Shimadzu UV-Vis Spectrophotometer, a Perkin Elmer Thermal Gravimetric/Differential Thermal Analyzer with attached Mass Spectrometer, and a Hiden pct system for analysis of hydrogen storage materials. This 1800 ft^2 laboratory contains instrumentation for material science analysis of fuel cell components.

The second lab is a 1100 ft^2 fuel cell laboratory. This Class B lab has capabilities ranging from those required for membrane electrode assembly fabrication to complete in-situ electrochemical diagnostics. There are three Scribner 850C fuel cell test stands, one Teledyne Medusa unit coupled with a Scribner 890C, 2 poteniostats, a sonicator and homogenizer for catalyst ink preparation, a screen printer, an enclosure for catalyst spraying, a dry box for membrane fabrication, a hot press under a canopy hood, three extra deep fume hoods (4-ft, 6-ft, and 8-ft), a vacuum oven, and a high temperature oven.

Liquid Hydrogen Storage at Kennedy Space Center

L. Gu, D. Block, G. Bokerman, A. T-Raissi, and M. Basarkar
Florida Solar Energy Center

Research Period: September 2003 to September 2006

Summary

The liquid hydrogen and oxygen storage tanks at NASA Kennedy Space Center's (KSC) Pad A and Pad B have served the space launch operations for more than 40 years. Although these tanks are identical, the hydrogen boiloff rate was 750 gal/day for the Pad B tank and 300 gal/day for the Pad A tank. The main cause for the Pad B tank boiloff has been determined to be a void inside the vacuum space between inner and outer shells near the top of the tank caused by missing perlite insulation. The void area was discovered by viewing IR images taken at night by a KSC engineer. It is estimated that KSC losses approximately $1 million per year due to liquid hydrogen and oxygen boiloff.

KSC plans to renovate the Pad B tank in the near future. Although there are many possible tank renovation options, the objective of the present project was to find out which options would be more realistic and economical. For example, one of these options is to add external insulation over the void area. The questions raised are, how large should the coverage area be and what should be the level of the thermal resistance. A second issue had to do with the tank insulation. Hollow glass microspheres are the leading candidate for replacing the perlite insulation. The microspheres provide improved thermal performance. While perlite is known to compact with age, the microspheres are expected to remain as free flowing particles. However, their limited use in cryogenic applications and their crush strength in the large tank have raised questions about particle behaviors.

Thermal simulations provide the only cost effective method to answer these questions. Thus, the objective of this project was to develop a computer model to examine the thermal performance of the Pad B LH_2 tank and to measure the experimental parameters that are needed for modeling of the granular effects of using glass microspheres as tank insulation. A detailed 3-D model was developed to simulate thermal performance of the tank with a void, a vacuum space without perlite between inner and outer shells. The model was validated against measured data, including boiloff rates, IR images, point temperatures and heat flux measurements and then parametric studies were performed. Experimental data from 3M Corp were also sent to KSC to support KSC's model efforts.

Following the extensive modeling, twelve conclusions and recommendations were made to KSC based on the investigation. These conclusions showed simulation results using the 3-D mesh are comparable with measured data, the heat transfer coefficient at exterior surface plays an important role in determining surface temperature distribution, boiloff rate is proportional to effective void interior surface equivalent emissivity and ambient conditions, the most important impact on boiloff rate is void size and the external insulation coverage may not be an effective method to reduce boiloff rate. See report for other conclusions and details.

Local Hydrogen Production via Catalytic Reformation of Fossil and Renewable Feedstocks

N. Muradov and F. Smith
Florida Solar Energy Center

Research Period: June 2002 to December 2007

Summary

Economical, safety and other factors will eventually necessitate on-site manufacturing of liquid hydrogen at the NASA-KSC site. The objective of this project was to develop an economically viable process for local production of hydrogen from renewable and fossil-based methane-containing feedstocks with minimal environmental impact. In this project, research and development was conducted on two novel hydrogen production technologies: (i) direct reforming of landfill gas (LFG) to syngas and its further processing to H_2, and (ii) catalytic pyrolysis of methane to hydrogen and carbon.

The advantages of direct reforming of LFG are that it does not require preliminary recovery of methane from LFG, which simplifies the process. The thermodynamic analysis of CO_2 reforming of methane using AspenPlus™ chemical process simulator was conducted. Efficient and stable catalysts for the direct reforming of LFG were developed and tested. The catalytic activity of a number of commercial and synthesized transition metal catalysts (Ni, Fe, Pt, Pd, Ir, Ru, and Rh) was evaluated. Ni-based catalyst was down-selected for further evaluation and the operational conditions for its efficient and stable operation were determined. A pilot scale unit with the capacity of 1 SCFM of H_2 was designed, fabricated and successfully operated using CH_4:CO_2=1.3:1 mixture mimicking local (Cocoa) LFG composition. It was estimated that the local resources of LFG would be sufficient for production of 5 tons/day of hydrogen. A preliminary economic assessment indicates the cost range of liquid hydrogen product to be $3.00-$6.00 per kilogram depending upon the production capacity and whether or not carbon sequestration is added.

For the methane catalytic pyrolysis process, its advantage is that it allows production of hydrogen and clean carbon, with no or minimal CO_2 emissions. The thermodynamic analysis of methane pyrolysis in two different regimes (thermo-neutral and external heat input) using AspenPlus™ chemical process simulator was conducted. Experimental data showed fairly good agreement with the simulation results. Comprehensive catalyst and process development studies for the methane pyrolysis reaction were conducted. Characterization and structural studies of carbon products of the process were conducted and potential markets for carbon products were evaluated. The technical feasibility of converting citrus waste products (e.g., citrus pulp pellets, CPP) into high purity hydrogen with the yield of 0.55 L of H_2 per gram of CPP was also demonstrated.

The research output consisted of four patent applications, 27 publications, 17 presentations, and support for two graduate students.

Photoelectrochemical Water Splitting for Hydrogen Production Using Multiple Bandgap Combination of Thin-Film-Photovoltaic-Cells and Photocatalyst

N. Dhere
Florida Solar Energy Center

Research Period: July 2002 to September 2006

Summary

One of the NASA research activities was to identify, characterize, and simulate a series of technologies that could be used for hydrogen production at NASA Kennedy Space Center (KSC) using locally available sources. This project examined the production of hydrogen from solar energy. To produce hydrogen by water splitting, the operating voltage of conventional photovoltaic (PV) cells cannot supply the overvoltage required. Thus, the objective of this project was to research and develop photoelectrochemical (PEC) cells that can supply the required voltage for water splitting by constructing a multiple bandgap tandem PV cell and a photocatalyst that can be activated by infrared (IR) photons transmitted through the PV cell. The proposed concept is different from conventional PEC water splitting by using multiple band gap combinations. The advantages for this PEC cell concept is that the PV cells are not in contact with the electrolyte solution, thus reducing the problems of corrosion and the photocatalyst is not grown directly over the PV cell as is the case with solid-state tandem PV cells.

The research conducted in this project was based on development of CIGS2 polycrystalline-thin film solar cells for use in the PEC process. CIGS2 thin film solar cells have the advantages over other types of solar cells of lower cost potentials, achieving large area depositions and integral interconnects and they do not suffer from intrinsic degradation.

The research developed P-type transparent and conducting layers, CIGS2 and CdTe thin film cells with transparent and conducting back contacts, suitable electrolytes with high conductivity and ruthenium oxide, ruthenium sulfide and ruthenium-iron sulfide photoanodes. Over the course of the project, the results gave a photovoltaic efficiency of conventional CIGS2 cells of 11.99% at an open circuit voltage of 830 mV. The calculated PEC efficiency for this configuration was 8.78% (solar to hydrogen).

In another experiment, the PEC hydrogen generation efficiency using two CIGS2 thin-film solar cells on transparent and conducting back contacts, connected in series with a RuS_2 anode and a platinum cathode under AM1.5 illumination. The PEC efficiency was calculated as 2.99%. This efficiency is lower than the CIGS2 and CdTe cycle because of the lower operating voltage of the CIGS2 pair. This efficiency can be improved by optimization of the operating voltage and increasing the efficiency of the photoanode for oxygen evolution.

As a result of the research there were 9 technical papers, 4 graduate student theses and 14 presentations. The research supported 1 Ph.D and 3 M.S students.

System Analysis of Hydrogen Production and Utilization at KSC

A. T-Raissi, M. Elbaccouch, K. Ramasamy, and J. Baik
Florida Solar Energy Center

Research Period: January 2003 to December 2007

Summary

The objectives of this project were to identify, characterize, and simulate a technology for hydrogen production for NASA-KSC from locally available sources. This activity will establish a baseline for the future procurement and use of hydrogen propellants at NASA-KSC. Chemical Process Simulators (CPS) were used to generate highly detailed and accurate process models for use in chemical plant designs. Aspen Technology's Aspen Plus is among the most widely used CPS platforms by leading companies in the process industries. The approach of the project is to generate gaseous and liquid hydrogen, under steady state conditions, sufficient for several NASA space shuttle mission. The project consisted of two tasks as follows.

Task 1 -- Chemical Process Simulation of Used Oil for the Liquid Hydrogen Production. The objective of this task was to simulate an economically viable process for the production of liquid hydrogen by steam reforming used automotive lubricating oil. The simulation was carried out using Aspen Plus™, Aspen Adsim™, and Aspen Icarus™ chemical process simulators. The reformer was simulated as a Gibbs reactor to reform the large oil molecules. A water-gas shift unit, simulated as an equilibrium reactor, was used to enhance the production of hydrogen and a flash separator was used to remove excess water from the product stream. The off-gas is burned with air in a combustor and the generated energy is used to heat the processing units. Aspen Adsim™ was used to simulate the adsorption process of the pressure swing adsorption (PSA). A hydrogen liquefaction unit, simulated as a Claude densifier cycle, was used to produce liquid hydrogen. Aspen-Icarus™ is utilized to develop a detailed capital costs breakdown for the plant.

Task 2 -- Aspen Plus Process Model for the Production of Gaseous Hydrogen via SteamGasification of Bagasse. The objective of this task was to simulate a chemical plant for the production of hydrogen from bagasse using Aspen Plus Chemical Process Simulator with no heat generation. The goal of the simulation was to design and optimize the performance of a directly heated gasification system that converts bagasse into gaseous hydrogen. The Aspen model consists of four sections: 1) a dryer section to partially dry the bagasse, 2) a gasifier consists mainly of a bagasse combustion zone, and a gasification zone to volatilize the bagasse feedstock, 3) a gas clean up section to purify the hydrogen product, and 4) a pressure swing adsorption unit to recover the hydrogen at desired purity levels. A fraction of the bagasse was used as a fuel and directed into combustor reactors to fire up the plant. The temperatures of the combustor reactors in the gasifier section were set at 1550 °C, and the generated heat was used to heat up the plant's reactors and flow streams. All other process units operate adiabatically. 900 $kg.hr^{-1}$ of bagasse was used as the feed stock of the plant to produce 17.4 $kg.hr^{-1}$ ultra pure hydrogen product.

The research results in 13 publications and 11 presentations.

Zero-Boil-Off Liquid Hydrogen Storage Tanks

J. Baik
Florida Solar Energy Center

Research Period: September 2003 to September 2006

Summary

The Florida Solar Energy Center and NASA KSC have conducted a collaborative research project with the objective of increasing the density of cryogenic propellants for launch vehicle applications. Technologies that provide for the densification, conditioning, transfer and storage of cryogenic propellants can reduce gross lift-off weight of a launch vehicle by up to 20% thereby increasing the vehicle's payload capacity. NASA KSC has years of experience handling cryogenic propellants, but all with saturated liquids. This work focuses on using existing cryogenic technology to densify hydrogen, and developing a test bed where densified propellant handling techniques can be researched.

FSEC and NASA KSC have designed a densified liquid hydrogen test bed that uses a Gifford-McMahon cryocooler to refrigerate hydrogen inside a 150 liter storage tank. The test bed is located at FSEC and has an integrated refrigeration and storage system with multiple capabilities. The volume of inner storage vessel was limited to 150 liter by the facility safety regulation code. The aspect ratio of the vessel was optimized by vessel material, operating temperature, thermal analysis of heat conduction and radiation heat transfer from ambient. Heat pipe technology was selected to extend the cold head of cryocooler down to the bottom of storage vessel. Operating temperature, pressure and thermodynamic properties of working fluid in the heat pipe can provide heat pipe design parameters such as material choices and dimensions. A pressure build-up unit was employed to control internal vessel pressure by evaporating stored liquid hydrogen without any vent loss. It also allows self-pressurization of the system in a short period of time to drain and/or transfer stored liquid hydrogen to other storage tanks and applications. The top plate of the vessel and its dewar necks were designed to maximize reconfiguration flexibility with flanged connections on the cryocooler interface and the outer vessel. This design allows full access to reveal components such as the cryocooler cold head, heat pipe, and copper braids structures out of the vessel when repairs and future modifications are needed.

As a preliminary densification test, a nitrogen liquefaction and densification tests were performed to exercise subatmospheric operating condition for subcooled cryogen. Then, the test bed successfully demonstrated hydrogen liquefaction and densification processes at 16.5 K followed by long term ZBO liquid hydrogen storage. The test bed successfully performed 7.2~25 liter/day of 16.5 K densified liquid hydrogen demonstration from ambient gaseous hydrogen using a G-M cryocooler. A series of ZBO storage tests proved that the system can store densified liquid hydrogen without any boil-off loss by ~1 hr/day of the cryocooler operation.

The research resulted in 8 publications and 9 presentations.

A Reliable, Efficient and Compact Reverse Turbo Brayton Cycle (RTBC) Cryocooler for Storage and Transport of Hydrogen in Spaceport and Space Vehicle Applications

L. Chow, J. Kapat, Q. Chen, L. An, T. Wu, and K. Sundaram
University of Central Florida

C. Him
FSI

N. Dhere
Florida Solar Energy Center

Research Period: July 2002 to September 2007

Summary

The objective of this five year project was to design a reliable, compact, lightweight, and highly efficient cryocooler for distributed cooling of liquid hydrogen systems for spaceport applications and to develop an appropriate integrated compressor/motor system for the said cryocooler. For many NASA space missions, cooling capacities much higher than 2 watts are estimated to be required. This effort in developing a light weight, compact and higher cooling capacity cryocooler will be highly beneficial for these applications. To accomplish the objective project, a reverse turbo Brayton cycle cryocooler was researched and developed. A key component was on the development of an integrated motor/compressor designed for use in the cryocooler. This cryocooler will be capable of extracting a few tens of watts (20-30 watts) of heat at liquid hydrogen temperature (~18 K).

All the previous attempts of cryocoolers by NASA for zero boil off of cryogenic propellants in space have cooling powers of less than 2 watts at liquid hydrogen temperature. These versions of flight-like cryocoolers would be more appropriate for cooling of sensors and super conducting materials in a spacecraft. The cryocooler designed under this project with a few tens of watts of cooling power at liquid hydrogen temperature will be ideal for ZBO of cryogenic propellants in NASA's future robotic missions to Mars and for other human space missions. The R&D activities under this program cover the design and thermodynamics of a high efficient cryocooler and development of a highly efficient, compact, reliable, high-speed and light-weight integrated compressor/motor setup for the cryocooler. Suggestions for improvement in the integrated compressor/motor setup were provided in addition to heat exchanger (HEX) design and friction and wear reduction techniques that help in the betterment of the system performance. Applications of the designed cryocooler for future NASA needs were also addressed.

1) It is possible to support high speed machinery (integrated compressor/motor system) on off-the-shelf bearings with proper balancing, alignment and aerodynamic optimization.
2) It is not advisable to use a mechanical coupler for high-speed rotating machinery.
3) Less the number of rotating parts in conjunction, better is the design for high rigidity and rotordynamic stability.
4) Tip gap plays a very important role in deciding the performance of a mesoscale centrifugal compressor.
5) A proper diffuser design (without flow separation) is a must for realizing high compressor efficiency.
6) A high effectiveness HEX design is a key enabling technology for a high system COP.

The research resulted in one patent, 24 publications, 18 presentations, and support of ten graduate students.

Development of Cryogenic Shape Memory Actuator Materials for Switches, Seals, and Valves

R. Vaidyanathan
University of Central Florida

Research Period: July 2002 to October 2007

Summary

Shape memory alloy actuators are widely recognized as having the following advantages for space-related applications: (i) high power/weight and stroke length/weight ratios (ii) integration of sensor and actuator in a single element (iii) clean, debris-less, spark-free operation and (iv) ability to function in zero-gravity environments with small, controlled accelerations. Shape memory alloys (SMAs) when deformed can produce strains as high as 8%. Heating results in a phase transformation and associated recovery of all the accumulated strain, a phenomenon known as shape memory. This strain recovery can occur against large forces, resulting in their use as actuators.

The goal of this project was to lower the operating temperature range of shape memory alloys in order for them to be used in hydrogen related technologies. The immediate benefit to NASA is the development of a shape memory thermal conduction switch for application in cryogenic liquefaction, densification and zero boil-off systems. Even though a wide range of alloys are found to exhibit the shape memory effect, NiTi alloys are of particular interest owing to the best combination of material properties coupled with substantial strain recovery associated with the phase transformation. In NiTi, the phase transformation usually occurs in a single step from the high temperature austenite (B2, cubic) phase to the low temperature martensite (B19', monoclinic) phase or vice versa. Addition of Fe, introduces an intermediate trigonal R-phase. The emphasis of this project was on the R-phase transformation in NiTiFe alloys.

The project results made theoretical as well as applied contributions to understanding and using R-phase transformations in the ternary NiTiFe shape memory alloy system. Applied aspects include alloy development by recourse to arc melting followed by thermomechanical processing and a range of characterization techniques that include SEM, TEM, DSC, dilatometry, DMA, and indentation. The alloys were also used in prototype thermal conduction switches. Theoretical aspects include in situ neutron diffraction measurements during loading and cooling at Los Alamos National Laboratory. Thus, valuable information on deformation mechanisms was obtained.

From this funded work two patent applications have been filed and two patents have been disclosed. In addition, 12 publications and 21 presentations have resulted, and seven graduate students have been trained. Two of the students were awarded best theses awards in the UCF College of Engineering and Computer Science. Also various aspects of this project benefited from concurrent synergistic funded efforts from the National Science Foundation (a CAREER award), UCF-UF's Space Research Initiative (SRI), NASA KSC and Arctic Slope Regional Corporation (ASRC). A new project funded by NASA has just been initiated at UCF that leverages the knowledge and experience gained from this project for application to NiTiPt and NiTiPd alloys. Another separate project from ASRC is also expected to use NiTiFe springs in a convection-based heat-pipe type thermal switch.

Genetic Engineering to Enhance Biological Hydrogen Production

W. Self, D. Ganyc, and L. Halvorsen
University of Central Florida

Research Period: June 2005 to September 2007

Summary

Conversion of lignocellulosic biomass to hydrogen, and potentially other fuels, can be a vital part of NASA's goal of deep space exploration. Recent NASA directives include missions to the Moon as well as Mars. One of the limitations to these missions is long-term fuel supplies. The ability to recharge fuel cells will require novel technologies to supply renewable sources of hydrogen. These renewable sources can be achieved using biological sources. The development of biological catalysts that can convert any form of biomass to hydrogen (and other potential fuels such as ethanol) thus has great significance for long term exploration of space.

The goal of this project was to genetically engineer metabolic pathways in bacteria to enhance the hydrogen yield generated from oxidation of the polymers (sugars) by catalyzing the reduction of protons with electrons using enzymes termed hydrogenases. Using engineered bacteria, the fermentation of sugars derived from biomass can be coupled with hydrogen production. The project first demonstrated that genetic engineering of metabolic pathways can enhance hydrogen production in the model system of *Escherichia coli.* From this result, a similar strategy was implemented to develop a hydrogen producing microbe that can efficiently degrade plant biomass, *Erwinia chrysanthemi*. Next, optimization of the formate hydrogenlyase (FHL) complex was accomplished in order to determine whether the approach was feasible for long term hydrogen production from plant biomass and to ensure that the engineered system is applicable for *near term* hydrogen production from plant biomass

Results on the regulatory systems of the FHL complex have revealed a link between selenoprotein synthesis and the regulation of the FhlA transcriptional activator. This result implies that *E. coli* has some type of sensory mechanism that monitors the intracellular levels of available selenocysteine. This mechanism is in turn able to modulate the amount of selenocysteine requiring enzymes being transcribed by directly affecting the expression of the *fhlA* protein. Based on past research, the expected result was that the highest amount of FHL complex activity would result with the combined expression of *fhlA165* along with a *hycA* mutant background, however, our result showed the opposite. The combination of these two mutations results in a phenotype having no detectable FHL complex activity. However, the fact that increasing the capacity for selenoenzyme synthesis, by transforming into these same cells the pSUABC plasmid, fully recovers this phenotype and provides strong evidence that selenoprotein synthesis is involved.

The research has resulted in 1 publication, 3 presentations and work for two graduate students.

Highly Selective Nano-Mems Low Temperature Hydrogen Sensor

S. Seal and H. Cho
University of Central Florida

Research Period: September 2002 to September 2007

Summary

Hydrogen safety and handling remain as top priorities to NASA operations and these concerns have been the prime motivation for this proposed research. Thus, the objective of this research was to develop nanotechnology based room temperature and low energy hydrogen (H_2) sensors with high sensitivity, selectivity, repeatability and rapid response times.

Currently available sensors are a variety of experimental (metal-oxide-semiconductor (MOS)-based, catalytic resistor, acoustic wave and pyroelectric) and commercial (catalytic combustion, electrochemical, semiconductor, and thermal conductivity) based technologies. They are based on different principles, but each as major drawbacks. Normally these sensors work at high temperatures (>80 to 400 °C). The very low sensitivity of these sensors at room temperature and low concentrations of H_2 has resulted in poor responses and recovery times. In addition, there are only few manufacturers, which guarantee the cross sensitivity to other poisonous gases and no claims are made regarding the suitability of these sensor-devices for sensing H_2 on other planetary conditions, which is an essential requirement for NASA. Thus, the commercial sensors currently available in the market are designed only to meet the atmospheric conditions on the earth's surface and modifying the sensor material properties to meet the NASA's over all requirements is imperative.

In the recent years, nanotechnology has emerged as an attractive field for the development of novel materials having unusual properties. To solve the hydrogen sensing problem, we have developed sol-gel-nanocrystalline indium oxide (In_2O_3) doped tin oxide (SnO_2) sensors, in the form of thin film/nanowires/nanofibers, for room temperature hydrogen sensing. The nanocrystalline thin film sensor is incorporated into the microelectromechanical system (MEMS) device to achieve high hydrogen sensitivity and selectivity with fast detection and recovery at room temperature.

The effects of various parameters such as the air pressure, H_2 concentration as well as the MEMS design parameters such as the finger spacing and the number of fingers on the sensing characteristics have been evaluated. The present nano-micro integrated sensor shows large room temperature H_2 sensitivity (10^3-10^5, orders of magnitude) with high selectivity over carbon monoxide (CO) was able to detect H in He environment. The current H_2 detection and recovery time at room temperature lie within the range of 4-200 sec, depending on various parameters. New technological solutions for further reducing the response and the recovery time of the present nano-micro integrated sensor have been proposed. Nano-micro integrated sensor prototype has been successfully developed.

The research resulted in 1 patent, 23 publications, 25 presentations, and work for seven graduate students.

Metal Hydrides for Hydrogen Separation, Recovery and Purification

M. Hampton
University of Central Florida

D. Slattery
Florida Solar Energy Center

Research Period: June 2002 to September 2006

Summary

At NASA's Kennedy Space Center (KSC) hydrogen is used for the space shuttle and other launch vehicles. As a result, huge quantities of liquid hydrogen are transported, transferred and stored at KSC. During the transfer of the hydrogen from the trucks to the storage dewars, significant quantities of hydrogen are lost during the cool down of the transfer lines and from flash evaporation as the high pressure cryogenic liquid enters the low pressure dewars. Additionally, during storage, hydrogen is constantly lost because of boil off.

In addition to the hydrogen that is lost due to transfer operations and boil off, NASA also loses hydrogen during purge operations. Prior to filling lines with liquid hydrogen, they must be precooled with liquid helium. After an operation, the residual hydrogen is purged, again with helium, in order to safe the systems. Both the hydrogen and helium in these operations is currently not recovered, leading to additional losses. Recovery of this lost hydrogen and helium could lead to substantial savings.

It was the loss of KSC's hydrogen and helium that led to this project. The project objective was to research and develop a hydrogen storage system that can recover both hydrogen and helium. Hydriding alloys of the AB_5 type are suitable materials for hydrogen storage applications because of their large hydrogen capacity, easy activation and rapid hydriding/dehydriding rates. One of these representative compounds that has been extensively studied is $LaNi_5$ a compound that absorbs hydrogen rapidly, reversibly and selectively. As a result, it is capable of not only absorbing hydrogen as it vaporizes during transfer operations, but also is potentially useful for separating hydrogen from the helium purge gas. Selective removal of the hydrogen would allow recovery of helium, in high purity, for future use.

The results showed that the alloy, $LaNi_5$, had the kinetics and capacity needed to remove hydrogen from a flowing stream of hydrogen and helium, thus allowing purification of both gases. Other results showed that the addition of aluminum to the alloy up to a level of 47 mole% provided improvement in the kinetics of hydrogen absorption without significantly reducing capacity. This incorporation of aluminum into the lanthanum nickel alloy will enormously reduce the weight and cost of the alloy required to purify hydrogen and helium.

In addition to being used to purify helium and hydrogen, $LaNi_5$ could also be used to capture the hydrogen currently lost to boil-off. While the hydrogen recovered could not be used for shuttle functions because of the requirement for liquid hydrogen, it could be used for other functions at the space center, such as fueling automobiles or buses. The project recommended that a system based on lanthanum, nickel, aluminum alloy be implemented at KSC for the purification of hydrogen and helium and the recovery of boil-off hydrogen.

Wireless Passive Sensors and Systems for Physical Sensors and Hydrogen Sensing Applications

D. Malocha
University of Central Florida

Research Period: July 2005 to September 2007

Summary

The objective of this project was to develop passive, wireless and multi-sensor surface acoustic wave (SAW) sensors based piezoelectric materials. The NASA application's for these sensors cover a wide range of NASA needs that include temperature sensing in harsh environments of space or ground-based operations, liquid level sensing for hydrogen, oxygen, nitrogen or other cryogenic liquids, and hydrogen gas sensing.

The developed SAW sensors are passive, wireless, small and lightweight. SAW devices have no fundamental limitation in material or physical principles for wide temperature operation; from cryogenic temperatures to 1000 °C, with appropriate substrate material. In addition, the SAW sensors can be encoded to provide security and close proximity multi-sensor operation. Finally, the proposed SAW sensor is totally passive, which means there are no batteries or other source for a spark or ignition; critical for use in the hydrogen environment and the SAW device can be accessed remotely without external connections, removing cabling and interconnects to a sensor array.

The objectives of the research project were to build new and novel SAW wireless-passive sensors, to research the SAW components operation at cryogenic temperatures, to build new devices and test fixtures for hydrogen gas sensing, and to develop measurement and test procedures. The developed SAW devices use orthogonal frequency coded (OFC) SAW reflective structures to encode the signal and to send back the sensor information. The encoding technique is similar to multi-tone CDMA in terms of its implementation, where a transducer or reflector is built with the desired code A RF 250 MHz transceiver system has been built for sensor interrogation. This process shows the feasibility of a software-radio approach for data acquisition, post processing and sensor data extraction.

The use of OFC SAW sensor technology has been shown to be a viable platform for passive, wireless sensor systems. Initial work is very promising for the use of nano Pd thin films as a possible reversible room temperature sensor. New methods of the coding devices have been studied which will lead to lower collision effects in a multi-sensor system environment. Higher frequency devices have been demonstrated which will reduce the required antenna size and should increase range. Although great progress was made, more research is needed to make the SAW devices a commercial product.

Because of this effort, a number of NASA STTR proposals and contracts have been submitted and won. Nine students have been funded from this program, 11 publications and 5 presentations were done. In addition, collaborations are now established between the UCF group and NASA KSC, JSC, Langley, and Glenn. It is certainly our judgment that this has been an extremely fruitful program.

Densified LH_2 and LO_2: Transport Properties and Density

S. Van Sciver
Florida State University

Research Period: June 2002 to September 2007

Summary

The overall objective of this experimental program was to produce precision measured values for the thermal conductivity, viscosity and density of subcooled LO_2 and LH_2. The region of primary interest was subcooled liquid below the normal boiling point (56 K to 93 K for LO_2 and 14 K to 20 K for LH_2) and for pressures up to 0.7 MPa. The measurement precision was to be better than $\pm$1%. The second objective was to establish facilities that can be used to investigate transport values in other cryogenic fluids of interest. No other similar facilities are currently in operation in the U.S. The project had three tasks as follows.

Task 1—Determine the thermal conductivity of subcooled O_2 and H_2, The thermal conductivity of liquid oxygen and hydrogen have been studied extensively, however, available data do not extend below about 77 K in the case of oxygen and there are very few points below 20 K for hydrogen. These measured thermal conductivity values were obtained and were compared with the available experimental data in the literature and from Refprop, a NIST standard reference database code.

Task 2—Determine the dielectric coefficient and density measurement of subcooled O_2 and H_2. From the best knowledge, dielectric coefficients of liquid oxygen have only been measured either along the liquid-vapor saturation curve or above 100 K for compressed fluid. In addition for the case of subcooled liquid equilibrium hydrogen, the dielectric coefficient of has not been measured to very high accuracy and precision. These results give the dielectric coefficients measured for liquid oxygen below 95 K and for liquid hydrogen below 23 K both at pressures up to 1 MPa. The results are combined with the previously published data for liquid along the liquid-vapor saturation line to express the fluid density in terms of the dielectric coefficient embedded in the Clausius-Mossotti relation. This expression covers both the liquid and the gaseous state.

Task 3—Measure the kinematic viscosity of subcooled O_2 and H_2. Successfully measurements of the absolute dynamic viscosity of subcooled liquid oxygen over the desired the pressure and temperature domains was completed, but the measurements for liquid hydrogen were inaccurate.

The experimental effort developed three new measuring instruments. The first instrument was for measurements of the thermal conductivity (k) and dielectric coefficient (κ) of subcooled liquids. The second instrument was the development of a capillary tube viscometer and the third instrument was a dedicated ortho-para converter used to supply equilibrium hydrogen to both experiments.

The research produced 9 publications and 6 presentations.

Experimental and Numerical Investigations of Cryogenic Multiphase Flow

S. Van Sciver and Y. Hussaini
Florida State University

J. Justak
Advanced Technology Group

Research Period: June 2002 to December 2005

Summary

The purposes of this project were to experimentally measure and model solid hydrogen particle mass flow in liquid helium and two phase liquid/vapor flow or solid/liquid hydrogen flow for fluid handling systems. The project was a joint effort between the Cryogenics group at Florida State University (FSU), members of the School of Computational Sciences (SCS) at FSU and the Advanced Technology Group (a small business in Stewart, FL). The work focused on three main subtasks.

The first subtask was the development of an experimental test facility to produce and measure cryogenic multiphase flows. This facility is a flow visualization facility which has an overall length of 5 m and includes two visualization ports. Flow channels within the facility are suspended in a vacuum environment and surrounded by thermal radiation shields cooled by LN_2 and LHe natural circulation loops. The end stacks contain metal bellows pumps, each with a volume displacement of one liter and controlled by linear stepper motors. These components can force the liquid cryogens to flow in either direction at precisely controllable volume flow rates up to 0.3 liters/s. The two phase flow facility is also capable of studying flows consisting of a mixture of solid hydrogen particles (sH_2-p) and LHe. To support these measurements, researchers have developed the capability to inject sH_2 particles into liquid helium.

The second subtask was development of a numerical simulation program to provide a synergistic approach with the experiments to study the production of hydrogen particles of uniform size and shape, their storage in the LHe carrier, and the multi-phase flow characteristics of the slurry comprising sH_2 in LHe. The simulations are first validated by the experiments followed by a simulation-based parametric study to guide future experiments. Liquid hydrogen droplet formation has also been addressed within the context of the incompressible Navier-Stokes equations for multiphase flows with the surface-tension model properly incorporated.

The third subtask was the development of mass flow sensors for measurements in two phase cryogenic flows. As part of this program, Advanced Technologies Group (ATG) developed a Fluid Optical Quality Sensor (FOQS) for cryogenic fluids. The capability to measure cryogen depletion instantaneously is critical when operating cryogenic turbo-machinery. The Fluid Optical Quality Sensor (FOQS) provides a means of measuring fluid quality for a wide range of flow systems. In addition, a laminar two phase mass flow meter was developed at FSU. Both these mass flow sensors were tested in liquid nitrogen and liquid helium using the experimental multiphase flow facility at FSU.

This work produced 6 publications, 5 presentations, no patents, and 1 MS thesis.

Improved Hydrogen Yield From Florida Specific Biomass Gasification Using a Pilot Scale Gasification Unit

R. Srivastava
Florida International University

Research Period: July 2002 to September 2007

Summary

Local production of hydrogen is of interest to NASA KSC because of economic, transportation safety, and energy security considerations. Thus, this project conducted R&D on hydrogen production from biomass through thermochemical processes. Gasification (thermochemical methodology) yields fuel gas that can be used in variety of power options. During the initial phase, citrus peels and sugarcane bagasse were identified as promising local biomass resources in Florida due to their overabundance and favorable market value. The farmland acreage dedicated to citrus almost exceeds 800,000 acres and the citrus industry generates more than 1 million tons/year of citrus waste residue (dry basis). Biomass fuels consist of moisture ranging from 5 to 35%. At the temperature above 100 °C, the water is removed and converted into steam. Biomass does not experience any kind of decomposition in the drying stage. A key element in planning a biomass to hydrogen facility is to locate a plant that will have ready access to adequate feedstock supplies.

The primary objectives of the project were to design, fabricate, and operate a pilot-scale biomass gasification unit, validate the unit's performance and identify economic and technical barriers. The research was focused on the biomass gasification testing in a pilot-scale gasifier of 10 to 100 KW range. Effort was directed towards maximizing the hydrogen yield in the synthesis gas. Results assessed the technical and economic potential of producing hydrogen from citrus peels obtained from Citrus World Inc. in Lake Wales, FL. The citrus pellets had approximately 14 wt% moisture content.

Gasification is a two-step process in which a solid fuel (biomass) is thermochemically converted to a low- or medium-energy-content gas. A highly critical factor in the high-energy efficiency of the gasification process is that of the gasifier (primary reformer) which consists of four stages—drying, pyrolsis, oxidation and reduction. The gasifier used was procured from Community Power Corporation (CPC) of Littleton, Colorado. The gasifier is a downdraft unit, fully automated system that has the ability to convert a variety of woody biomass residues into syngas.

The report also includes results on the feedstock preparation, feedstock handling, feedstock performance, hydrogen yields and potential problems identified during the pilot scale experiments.

The results for biomass gasification of citrus pellets show that hydrogen can be produced economically at an average $7.54/GJ for 10 to 100 KW range pilot scale gasification unit. Previous literature studies have cited that hydrogen prices from $6 to $10/GJ can be realized.

Numerical Simulation Model for Thermo-Fluid Analysis of Cryogenic Storage Systems With Zero Boiloff

M. Rahman and S. Ho
University of South Florida

Research Period: September 2002 to September 2007

Summary

Conventional methods of storing hydrogen are either as a compressed gas or as a cryogenic liquid. Liquid storage of hydrogen has a very significant advantage over gaseous storage because of its much lower storage volume and ease of regeneration of the fuel with demand. Conventional cryogenic storage tanks suffer loss of hydrogen due to boil-off of the cryogen induced by heat loss from the tank to the surrounding environment. In order to keep the inner pressure within the structural limits of the tank, the stored fluid needs to be periodically vented. The Zero Boil-Off (ZBO) concept has evolved as a means of storage tank pressure control by a synergistic application of passive insulation, active heat removal, and forced mixing within the tank. The goal is that the fuel can be stored for a very long time with almost no loss.

This report presents a numerical simulation study of steady state fluid flow and heat transfer in a cryogenic storage tank for liquid hydrogen using two and three-dimensional models. The tank model includes a tank with cylindrical wall and oblate spheroidal top and bottom, a heat pipe located along the axis of the tank, and one or more pump-nozzle unit(s) that collects fluid at the suction inlet and discharges at its nozzle face onto the cool tip (evaporator) of the heat pipe in order to prevent the fluid to boil off.

For a number of pump-nozzle units, the numerical simulations were done using an axi-symmetric model because of the nearly axi-symmetric nature of the problem. For one pump-nozzle unit, a three-dimensional model was employed since the axi-symmetry was no longer the case. It was found that the normal speed at the nozzle and tank dimension parameters significantly affect the mixing, cooling, and boiling of the fluid inside the tank. These parameters can be used to optimize the performance of the cryogenic system.

The results from the simulations for both models show that the increasing of the fluid speed discharged at the nozzle face improves both mixing effectiveness (increase average speed, decrease maximum-average temperature difference) and zero-boiling-off effectiveness (decrease maximum temperature). The numerical simulations give better understanding of the fluid flow and heat transfer phenomena needed for the design of a cryogenic storage tank for liquid hydrogen.

Prototype and Simulation Model for a Magnetocaloric Refrigerator

S. Bhansali, M. Rahman, S. Kim, S. Ghirlanda, C. Hernandez, C. Adams,
B. Bethala, L. Rosario, and S. Sambandam
University of South Florida

Research Period: September 2002 to September 2007

Summary

Hydrogen liquefaction is necessary technology for satellite and space craft. The magnetocaloric refrigeration of this project is being explored as a highest efficient pathway for cooling hydrogen for storage and liquefaction. Realizing micro cryo-coolers that can operate at low temperature with high cooling capacity, and in a small size has been a challenge. This research makes a development of micro-cooling device which has compact size. This process required that magnetocaloric materials be exposed to an alternating magnetic field. Analysis and experimentation have positioned the investigators to both (a) demonstrate the feasibility of magnetocaloric refrigeration and (b) experimentally validate the critical parameters required for design of scalable cooling systems. Simulation of cooling hydrogen from 77 to 20 K suggests a multi-stage GdSiGe based magnetocaloric refrigeration system.

Thermodynamic analysis was carried out for a magnetic refrigeration system for near room temperature application using Gd as the magnetic material. The conceptual design and analysis of a magnetic refrigeration system near hydrogen liquefaction temperature was established based on two prototypes with circular and trapezoidal microchannels. In aspect of fabrication, the microfabrication processes and fabrication of trapezoidal flow channels in silicon was developed and tested.

The stability of Si_3N_4 as a diffusion barrier in deposition of GdSiGe thin films on Si was studied. Thin films of GdSiGe were deposited on PECVD nitride coated Si substrate. The films were annealed in vacuum to crystallize the GdSiGe desired phase. SIMS analysis of the interface of GdSiGe/Si_3N_4/Si films indicates a breakdown of the SiN diffusion barrier with depletion of GdSiGe films into silicon nitride and Si upon annealing at 1150 °C. It is hypothesized that the dangling hydrogen bonds in Si_3N_4 contribute to the breakdown. The AlN/SiO_2 layer is also used as barrier layer for GdSiGe annealing. The result shows that the layer has good role and it prevent diffusion of GdSiGe into the Si wafer.

The trapezoidal microchannels were designed with circular and trapezoidal microchannels. The eight microchannels with 150 μm deep in 2 in. wafer were fabricated using MEMS technology. The combined etching of 250 μm formed the inlet and outlet ports to flow refrigerant. The in-situ temperature sensors through deep impurity diffusion were installed into the wafer and tested by changing the temperature. GiSiGe block was assembled with the microchannel and its prototype of microcooler was shown in the presentation. The cooling test are carried out by applying electromagnetic field to the GdSiGe, and obtained temperature change. The constant temperature chamber was made by using insulating material and the lower temperature than room temperature was obtained by liquid nitrogen.

Smart Porous Metal-Organic Frameworks (MOFs) for Hydrogen Recovery and Storage

M. Eddaoudi, M. Zaworotko, and B. Space
University of South Florida

J. Eckert
Los Alamos National Laboratory

A. T-Raissi and N. Mohajeri
Florida Solar Energy Center

Research Period: January 2005 to November 2007

Summary

Advances in the fast growing field of microporous metal-organic frameworks (MOFs) have led to numerous developments. Specifically, the chemistry of MOFs has provided a range of low-cost porous crystalline materials assembled from molecular building blocks (MBBs) that exhibit high stability, tunable properties, and porosity. Synthesis of metal-carboxylate polyhedral frameworks and molecules based upon metal-carboxylate building blocks has attracted interest for their properties such as porosity, H_2 storage and magnetism. Though a myriad of crystalline porous carboxylate based MOFs have been synthesized and structurally characterized, many remain unexplored for their potential as H_2 storage media. The nature of these structures is such that they are simple and inexpensive to prepare, they are modular and can be designed to contain accessible windows and nanoscale cavities (often decorated with adjustable open metal sites) suitable for H_2 sorption.

Better hydrogen storage materials will have a far-reaching impact on future aerospace technology. Recently, applications of rigid MBBs have led to the development of a wide range of MOFs, from fused metal-organic polyhedra to zeolite-like MOFs (ZMOFs), with large accessible 3-D pores decorated with adjustable periodic organic and inorganic moieties suitable for hydrogen uptake. Most recently, systematic studies of MOFs have indicated that increasing the number of benzene rings in the scaffold of a MOF greatly improves the amount of hydrogen uptake. Furthermore, Inelastic Neutron Scattering (INS) studies suggest that MOFs can contain several types of hydrogen binding sites ranging from organic components to the metal constituents of the framework, including results that indicate open metal sites may increase H_2-framework interactions Preliminary studies have demonstrated that MOFs have the ability to store larger amounts of non-cryogenic hydrogen than amorphous porous carbon and inorganic zeolites. Further, the facile tunability of the MOF constituents and pore size has reinforced the belief that materials with superior H_2 storage capacity are achievable.

Thus, the specific objectives of this project were to synthesize and characterize viable porous MOFs for H_2 storage, to develop a better understanding of the interactions between sorbed hydrogen with the organic and inorganic constituents of the sorbent MOF by means of INS and computational studies and to construct made-to-order cost-effective MOFs that exhibit superior hydrogen storage capacity. The results of this project provide a basis for developing selected metal-organic frameworks as high-capacity hydrogen storage materials for onsite H_2 recovery, purification and storage.

The project's research output has included the award of a similar project by the U.S. Department of Energy (Project no. DE0FG02-07ER4670), 2 publications, and 3 presentations.

Surface Acoustic Wave (SAW) Sensors for Hydrogen and Other Gas Detection

V. Bhethanabotla
University of South Florida

Research Period: September 2002 to September 2007

Summary

Design, construction and testing of inexpensive, solid state sensors that respond sensitively, selectively and rapidly to hydrogen and other gases are a NASA need. Acoustic wave devices have been known for their use in sensor applications and are capable of meeting the above requirements, as well as providing passive and wireless operation. To achieve the objectives for hydrogen sensors, the research approach was one that combined surface acoustic wave (SAW) transducer technology with nanomaterial sensing layers. For these SAW devices to be practical, advances in device fabrication, wireless communication, device packaging and sensing materials were necessary. Solid-state SAW devices are mass produced in current cell phone, TV and other radio frequency uses, thus, a suitably designed hydrogen sensor can be similarly produced inexpensively.

The research approach was to leverage the mass, electroacoustic and elastic response mechanisms of SAW devices, with the advantages afforded by the nanomaterials of Pd-alloys as the sensing layers. The research constructed field devices using suitably designed high frequency SAW devices. Results of the research is summarized as (1) the setting up of an acoustic wave sensors laboratory with full sensor testing capabilities, (2) the development of several candidate prototypes for hydrogen sensors, (3) the development and evaluation of various nanomaterial sensing layers for hydrogen detection and sensing at room temperature in a surface acoustic wave sensor configuration, (4) the development of a high frequency (100 MHz) thickness shear mode organic vapor sensor demonstrating superior sensitivity, (5) multiple-scale modeling to understand sensor mechanisms, and (6) the development of a novel hexagonal multi-frequency surface acoustic wave sensor, useful in chemical and biological sensor applications.

Specifically, Pd-coated single walled carbon nanotubes (Pd-SWNTs) have been developed and are emerging to be the best sensing materials tested so far in hydrogen sensor applications. Preliminary results indicate that these Pd-SWNTs are capable of several times more sensitivity compared to pure Pd nanomaterial layers, and possess excellent repeatability upon cycling with hydrogen exposures.

A hexagonal SAW device development is nearly complete, and is being tested in the detection of multiple biomarkers in specific applications to ovarian cancer detection, collaboration with the Moffitt Cancer Research Center at USF. Future sensor research is expected to yield commercially viable results.

Thermo Catalytic Hydrogen Production via Oxygen-Free Methane Aromatization

J. Wolan, E. Stefanakos, and A. Kababji
University of South Florida

Research Period: April 2004 to September 2007

Summary

One of the NASA research activities were to identify, characterize, and simulate a series of technologies that could be used for hydrogen production at NASA Kennedy Space Center (KSC). This work investigates the production of hydrogen from a biomass by a process that is a direct gas to liquid. The most important benefit of this process is that it is highly selective to pure hydrogen production with no green-house gas by-products. The bimetallic catalyst developed is molybdenum promoted H-ZSM-5 zeolite modified with various transition metal ions (TMI). These catalysts are prepared by the incipient wetness co-impregnation of the ammonium form of the zeolite, calcined in air at 500 °C, and then reduced and activated following an in-house developed procedure.

For this project, bimetallic catalysts were prepared by incipient wetness co-impregnation of a ZSM-5 and H-ZSM-5 zeolite support. The supports were formulated and tested for use in methane non-oxidative aromatization to hydrogen and aromatic species. A novel 100% hydrogen-selective custom designed catalytic membrane reactor was utilized. In this design, no separation of products is required as hydrogen is selectively permeated through an internal membrane. This catalytic system has been designed to be selective for hydrogen production over benzene and thus is considered a novel technology as researched catalytic systems of this type are designed to be selective toward production of benzene.

In this study, the focus is on the production of hydrogen rather than the aromatic products which include ethylene, ethane, toluene and unreacted methane. The overall chemical reaction is considered highly endothermic, operating in the temperature range between 600 to 850 °C. The large activation energy and high temperature reactions has been shown to affect the catalyst performance adversely through sintering and/or coking of the catalyst bed. Therefore, catalyst design, fabrication and pretreatment are critical.

The results for the rate of hydrogen production are:

- At 500 °C up to 550 °C and after 1 hr on stream, H_2 production rate was 36 sccm (based on 100 sccm methane flow rate).
- At 600 °C up to 650 °C and after 1 hr 40 min total time on stream, H_2 production rate was about 10 sccm (based on 100 sccm methane flow rate).
- Membrane selectivity to H_2 is approximately 100%; the calculated selectivity data for different catalyst systems is shown below.
- Aromatic compounds including benzene, toluene, ethane, ethylene and cyclohexane rates of production have not been determined, but conversion results are presented. CO and CO_2 conversion versus temperature curves are also presented for different catalyst systems prepared.

Modeling and Optimization of Fuel Cell Systems for Aircraft Applications

J. Ordonez and C. Luongo
Florida Agricultural and Mechanical University-Florida State University

Research Period: March 2005 to September 2007

Summary

The use of fuel cells for aircraft is an ever-growing concept in today's environmentally conscious world. NASA studies have indicated that fuels cells are becoming reasonably practical for propulsion in small aircraft and could be promising in future large-scale commercial aircraft. For these applications, it is important to understand the fuel cell-based power system from a system integration and power management perspective. Optimizing the integration of each component into the system and understanding the overall power system compatibility is essential for a successful design. Thus, the main objective of this project was to research and develop design concepts for implementation of fuel-cells on aircraft by modeling and optimization of the fuel cell systems.

The project results gave four major outcomes:

1. A library of fuel cells and fuel cell power network components were development to facilitate a simulated test bed for fuel cell-based power systems. All of the models were developed in an electric network simulator (EMTDC) and include a solid oxide fuel cell (SOFC) stack, a proton exchange membrane (PEM) fuel cell stack, electrical converters (time-averaged models and switching models), and forms of energy storage. As a test case scenario, a fuel cell-based powertrain system was modeled and simulated for Cessna-like power range specifications.

2. Guidelines for the optimization PEM and SOFC internal structures were developed. Numerical results showed that the optimized single cells internal structure and stack external shape are "robust" with respect to changes in stoichiometric ratios, membrane water content, and total stack volume. The optimized internal structure and single cells thickness, and the stack external shape are results of an optimal balance between electrical power output and pumping power required to supply fuel and oxidant to the fuel cell through the stack headers and single-cell gas channels.

3. Models were developed and implemented in the Matlab-Simulink environment to guide the selection of hybrid fuel cell/gas turbine system configuration. A comparative study based upon performance parameters, such as SOFC power, turbine inlet temperature, and exhaust temperature was used to select a configuration among few candidates.

4. The modeling of renewable fuel cell (RFC*)* subsystems has been addressed. The models presented focus on the application of RFC subsystems to high altitude aircraft operations. Solid oxide cells were found to have performance disadvantages that prohibit dedicated galvanic and electrolytic cell configurations, specifically with respect to thermal management.

The full report (100+ pages) is available upon request. The research resulted in 10 publications, 7 presentations and the training of nine graduate students and thirteen undergraduate students.

Final Reports for Florida Solar Energy Center

- Ammonia-Borane Complex for Hydrogen Storage - Mohajeri, N., T-Raissi, A., Ramasamy, K., Adebiyi, O., Bokerman, G.
- Ceramic Membranes of Mixed Ionic-Electronic Conductors for Hydrogen Separation - Elbaccouch, M., T-Raissi, A., Linkous, C., Mohajeri, N.
- Compact, Lightweight and Optimized Fuel cells for Space or Aircraft Power - Fenton, J., Choi, P., Bonville, L., Kunz, R.
- Gas Permeable Chemochromic Compositions for Hydrogen Sensing - Mohajeri, N., Muradov, M., Bokerman, G., T-Raissi, A., Captain, J., Peterson, B., Whitten, M.
- Hydrogen Education and Outreach – Schleith, S., Hall, P., Henzmann, A., Block, D.
- Hydrogen Production from Used Lube Oils - T-Raissi, A., Ramasamy, K.
- Hydrogen Production via Solar Thermochemical Water Splitting – T-Raissi, A., Huang, C., Muradov, N.
- Hydrogen-Powered Aeropropulsion: Compact, Lightweight and Efficient Fuel Cells for Space Power - Linkous, C., Pearman, B., Hall, D., Slattery, D., Baik, J.
- Integrated Fuel Cell Test Bed Facility - Slattery, D., Bonville, L., Fowler, R.
- Liquid Hydrogen Storage at Kennedy Space Center - Gu, L., Block, D., Bokerman, G., T-Raissi, A., Basarkar, M.
- Local Hydrogen Production via Catalytic Reformation of Fossil and Renewable Resources - Muradov, N., Smith, F.
- Photoelectrochemical Water Splitting for Hydrogen Production Using Multiple Bandgap Combination of Thin-Film- Photovoltaic Cells and Photocatalyst – Dhere, N.
- System Analysis of Hydrogen Production and Utilization at KSC - T-Raissi, A., Elbaccouch, M., Ramasamy, K., Baik, J.
- Zero-Boil-Off Liquid Hydrogen Storage Tanks - Baik, J.

Ammonia-Borane Complex for Hydrogen Storage

N. Mohajeri, A. T-Raissi, K. Ramasamy, O. Adebiyi, and G. Bokerman
Florida Solar Energy Center

Research Period: June 2002 to December 2007

Abstract

Ammonia borane (AB) complex is a chemical hydride that is stable in air and water, and contains very high hydrogen content (19.6 wt%). AB is a promising material as a hydrogen carrier especially for power generation utilizing proton exchange membrane fuel cells (PEMFC). Release of hydrogen in the AB complex can occur by either thermolysis or hydrolysis. Thermolysis of AB generates, in addition to hydrogen, species such as borazine, monomeric aminoborane, and diborane. In the case of AB hydrolysis, ammonia is the byproduct of the reaction. All byproducts of these processes have adverse effect on the PEMFC operation and it is important to be sequestered from H_2 gas stream. In this report, hydrogen release results are presented for both release approaches. In addition, the thermal properties and conductivities of composites formed by mixing fine aluminum powder with AB complex at temperatures in the range of 300 to 420 K are presented.

Objectives

The objectives of this work were to 1) identify viable amine-borane (AB) complexes for hydrogen storage at ambient conditions and 2) develop a cost-effective synthetic route for hydrogenation of borazine to cyclotriborazane - as a means of chemical hydrogen storage.

The goal of this project is to develop a high-density hydrogen storage system based on ammonia borane (AB) complex for in-flight, LEAP applications, and any portable devices that use batteries as the energy source. Due to their high hydrogen capacity, these hydrides have been employed, in the past, as disposable H_2 sources for fuel cell applications. This project is intended to advance the Technology Readiness Level (TRL) of a special class of high-density hydrogen storage compounds based on the ammonia borane (AB) complex from the TRL 2 (technology concept formulated) to TRL 3 (proof of concept).

Introduction

Presently, rechargeable power sources are used for cell phones, PDAs, and laptop computers, among others. Secondary (rechargeable) batteries have improved over the years, but a non-rechargeable alkaline battery still delivers 50% more power than lithium-ion, one of the highest energy density secondary batteries in existence. Also, rechargeable batteries are vulnerable to the elements as well as extreme temperatures, humidity, and other exposures. While recent innovations in the technologies used in rechargeable batteries has reduced these risks, rechargeable batteries are not yet as powerful, rugged or reliable as primary batteries.

Despite their dependability and superior capacity, the one-time use constraint of primary batteries increases their cost to over thirty times that of rechargeable batteries. For certain applications, e.g., auxiliary power units (APU), among others, the need to constantly deliver new batteries is not desirable.

Hydrogen, in combination with proton exchange membrane fuel cells (PEMFC), can replace rechargeable batteries as the power source of choice in many applications including those requiring portable power for aerospace applications. This requires successful development of an energy dense, safe, reliable and convenient H_2 storage device.

Background

Compounds represented by the empirical formula $B_xN_xH_y$ have been known and used as high capacity hydrogen (H_2) carriers. Hydrogen generators based on such carriers can be employed for hydrogen on-demand applications. However, the hydrogen generated is often too impure for use in proton exchange membrane fuel cell (PEMFC) applications. In addition, the process yield is low and requires high temperatures (above 100 °C) for reasonable yield or environmentally harmful materials are produced.[1]

Ammonia borane (AB) complex has the highest material hydrogen content (about 19.6 wt%) with a system-level H_2 energy storage density of about 2.74 kWh/L (vs. 2.36 kWh/L for a liquid hydrogen Dewar). At near room temperatures and atmospheric pressure, AB is a white crystalline solid that is stable in both water and ambient air.

Thermolysis has been used as a method of choice to generate hydrogen from AB complex. There are several drawbacks to thermolytic release of hydrogen from AB complex. In practice, thermolysis of AB involves competing reactions leading to the formation of various by-products. For example, FTIR analysis of the evolved gases from the thermolysis of AB complex has shown that monomeric aminoborane (BH_2NH_2), borazine, and diborane are also produced. The aminoborane comprises poly-aminoborane, $(BH_2NH_2)_n$. Ammonia-borane pyrolysis begins at temperatures below 140 °C. However, to release substantial amount of the hydrogen contained in AB complex, temperatures above 500 °C are needed. The overall process is exothermic, but requires heat to be added to activate the AB complex. The overall reaction can be written as follows:

$$NH_3BH_3 + \text{Heat} \rightarrow BN + 3H_2 \quad (1)$$

Poly-aminoborane, the inorganic analog of polyethylene, is a nonvolatile white solid. These compounds are undesirable impurities that make hydrogen from direct thermolysis of AB complex unfit for PEMFC applications. Furthermore, formation of these species lowers H_2 yield from direct thermolysis of AB complex.

An alternative to thermolysis is provided by hydrolysis or methanolysis of AB complex. Hydrolytic or methanolic cleavage of amine-borane complexes provides 3 moles of hydrogen per mole of AB complex.[2-5]

Although this process has been used in the field of modern synthetic organic chemistry and for pharmaceutical applications, only recently has it been applied as a way of utilizing AB complex for the storage of hydrogen. Corresponding reactions are given below:

$$NH_3BH_3 + 3H_2O \rightarrow NH_3 + H_3BO_3 + 3H_2 \quad (2)$$

$$NH_3BH_3 + 3CH_3OH \rightarrow NH_3 + B(OCH_3)_3 + 3H_2 \quad (3)$$

As noted above, an AB complex is a stable adduct. Therefore, to date, the hydrogen generating reactions (2) and (3) have involved harsh acidic conditions such as refluxing in aqueous HCl or the use of heterogeneous catalysts based on palladium or nickel.

In this project, the methods for thermolysis and catalytic hydrolysis of AB complex for production of high purity hydrogen at low temperatures will be presented. In addition, experimental data for the apparent thermal conductivity of AB complex and composites formed by mixing fine aluminum powder with AB in the temperature range of 300 to 420 K will also be presented.

Experimental

General

AB complex (NH_3BH_3) and catalysts used in this study were purchased from Aldrich and used as received. Aluminum powder (0.1 micron) spherical, was purchased from Alfa Aesar and was handled inside a glove box. The AB complex was mixed and grinded with aluminum powder with a 10:1 mass ratio inside the glove box.

Instrumentation and Analytical

The X-ray Photoelectron Spectroscopy (ESCA) analysis was done using a Physical Electronic 5400 spectrometer and a Mg anode, at 300 watt power, high resolution scans from 1100 to 0 with eV step size 0.1 eV and dwell time of 50 micro seconds. In situ ^{11}B-NMR studies were conducted using a Varian VXR300. The GC/MS experiments were performed on a JEOL GCmate-II GC/MS-MS instrument. The carrier gas was helium and the flow rate was kept at 2.0 mL/min throughout the run. All the experiments were carried out in the splitless mode. The injector port and the interface were set at 60 °C and 250 °C, respectively. Thermogravimetric (TG) analysis was performed using a Perkin-Elmer, Diamond TG/DTA in an argon flow at a heating rate of 10 °C/min.

Hydrolysis Reactions

In a typical reaction, the catalyst was dissolved in water and then added on as received AB. The amount of hydrogen is measured volumetrically.

Kinetic Studies Using In Situ ^{11}B-NMR

For these studies, 0.01 g of AB complex was added to 7 mL of 5 mM, 10 mM, 30 mM, and 40 mM K_2Cl_6Pt in D_2O solution at 25 °C, 30 °C, and 35 °C. The NMR tube cap was modified to allow hydrogen release.

Thermal Conductivity Measurements

Figure 1 depicts the arrangement used for the measurement of the thermal conductivity of the as received AB. Two coaxial cylindrical bars were machined using aluminum 6061-T6 stock (thermal conductivity of 180 W/m-K). Both pieces had an outside diameter of 0.378 in. and were 0.181 in. long. They were used as the reference blocks for the measurement of heat flux (Q') through AB samples. The AB pellets (0.378 in. OD and three different thicknesses: 0.181 in., 0.261 in., and 0.223 in.) were placed between the two aluminum cylinders. Temperature measurements were made using four T-type thermocouples.

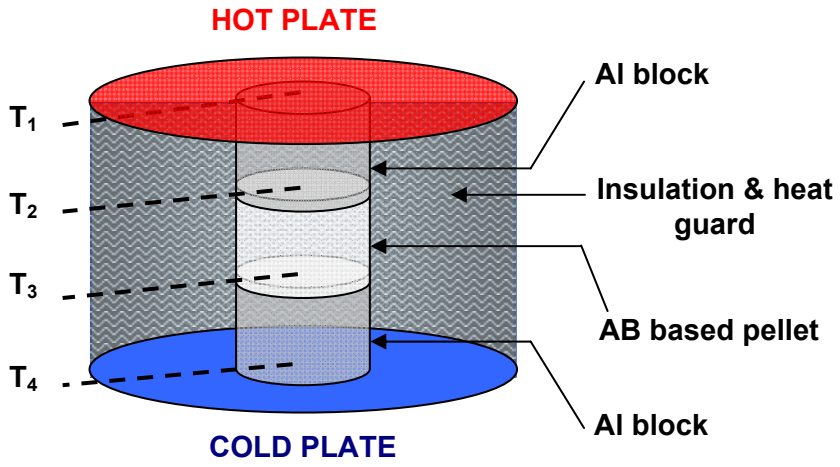

Figure 1. Setup for measuring thermal conductivity of AB complex.

Reactor Design for Ammonia Borane Thermolysis

Ammonia borane complex was purchased from Aviabor and used as received. Product gas from AB thermolysis was analyzed using JEOL GCmate™ II GC/MS-MS instrument.

Figure 2 provides a schematic diagram depicting the setup employed for AB thermolysis experiments. A cylindrical aluminum reaction vessel was used with inlet and outlet lines for the purge gas flow, a pressure gauge, a pressure relief valve set to 100 psia, and a gas collection line. Gas flowing in and out of the reactor was controlled via several valves as depicted in Figure 2. Furthermore, a gas sampling port was installed to allow occasional sampling of the effluent flow from reactor exit. Samples were heated in-situ by nichrome resistance wire (0.063 in. OD – 34 AWG) coiled around the AB pellet located inside the reactor. Electric wires connected to nichrome wire via two feed-through ports on the top of the reaction vessel.

A Carver laboratory press was used to compact the AB powders into various pellet sizes using 2000 psi applied pressure. The pellets were cylindrical (0.0875 in. diameter) with various thicknesses. The length of the nichrome wire used varied so that the desired amount of energy could be delivered to the AB pellets. The nichrome wire coiled AB pellet was bundled between two pieces of Thermcraft™ ceramic fiber insulation pads 0.5 in. thick. The same ceramic fiber material was also used and packed into the gas exit line from reactor to filter out poly-aminoborane, boron nitride (white solid particles) and other particulate matter released during AB thermolysis. This was done to prevent clogging of the gas lines, valves and gas sampling port.

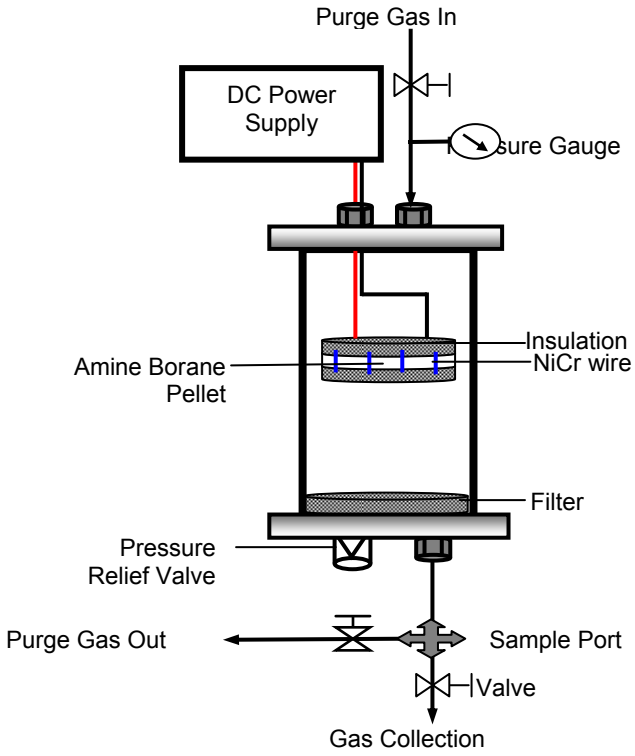

Figure 2. Experimental setup for thermolysis of AB complex.

Prior to each experiment, the reactor was purged with hydrogen and carefully leak tested at 90 psi internal pressure. All the experiments reported in this project were conducted in hydrogen filled reactor. The gas generated due to AB thermolysis remained in the reactor. At the conclusion of each test, the reactor was allowed to cool down to room temperature and then slowly depressurized releasing the product gas into a graduated gas collection cylinder to determine the total amount of H_2 produced.

Sorption Experiment

Figure 3 depicts the experimental arrangement used for fast screening of solid sorbents for borazine adsorption. Sorbents were heated to 200 °C and kept at that temperature in an Ar atmosphere for 2 hr. Samples of pre-weighed sorbent were transferred to a glass container and placed in a vial containing liquid borazine. The vial was capped and kept inside refrigerator at 5 to 7 °C for 24 hr. The sorbents were removed from the vial and weighed to determine the amount of borazine adsorbed.

A series of flow experiments were conducted by employing effluent generated from thermolysis of AB and allowing the flow to pass through the sorbent material.[6] Product stream from AB thermolysis was analyzed by taking gas samples at ports located before and after the sorbent material using JEOL GCmate™ II GC/MS-MS instrument. FT-IR spectra were collected on a Perkin Elmer Spectrum 100 FTIR instrument.

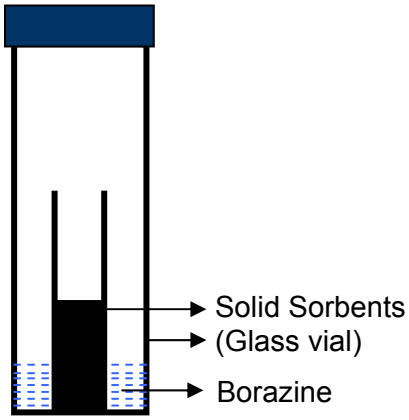

Figure 3. Experimental set-up for fast screening of solid sorbents for borazine take-up.

Results and Discussion

Molecular Modeling of Hydrogenation of Borazine to Cyclotriborazane

In this effort, the molecular modeling of hydrogenation of borazine ($H_3B_3N_3H_3$) to cyclotriborazane ($H_6B_3N_3H_6$) was investigated. Commercial processes for the production of ($H_3B_3N_3H_3$), an inorganic benzene analogue are available and molecular modeling studies have been performed to investigate possible aromatic behavior. No current studies have been performed on further hydrogenation of the molecule to ($H_6B_3N_3H_6$), and no modern molecular modeling results for this molecule exist. The goal is to assess the suitability of cyclotriborazane for high-capacity hydrogen storage.

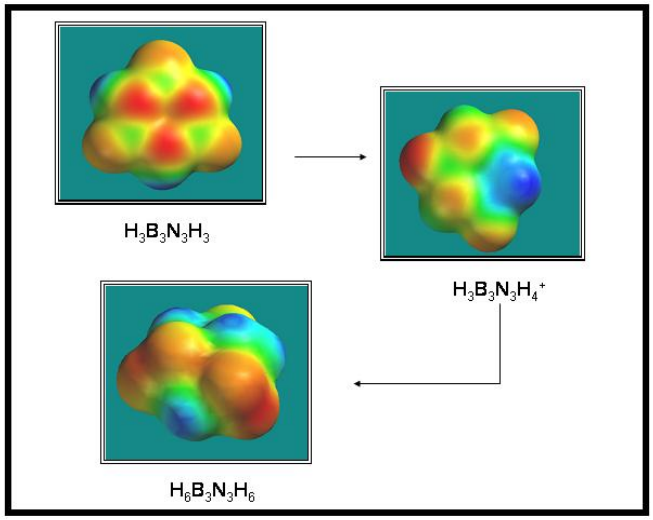

Figure 4. Electrostatic potential surfaces for isolated borazine ($H_3B_3N_3H_3$), protonated borazine, and cyclotriborazane ($H_6B_3N_3H_6$) molecules. Colors toward red correspond to a negative potential (a stabilizing interaction between the molecule and a positive charge), while colors toward blue indicate a positive potential.

***Spartan Software*—**For familiarization with and evaluation of the Spartan software, geometry optimization calculations were performed for borazine and compared to existing x-ray diffraction data (see Table 1).

Geometry optimizations generally give good results even at a low level of calculation. Single molecule calculations were performed for cyclotriborazane geometry, and showed good agreement. Further calculations for the lattice structure will be performed using clusters, as needed.

Table 1. Experimental and molecular orbital calculation results for borazine.

Basis set:	Experimental	MP2 (6-311+G**)
B-N bond length	1.436 Å	1.434 Å
N-H bond length	1.050 Å	1.010 Å
B-H bond length	1.258 Å	1.193 Å
B-N-B ∠	121.1°	122.97°
N-B-N ∠	117.7°	117.03°

Next, atomization energies, electron affinities, and ionization potentials for borazine and cyclotriborazane, along with proton affinity for borazine were calculated. The enthalpy of the reaction for borazine to cyclotriborazane was calculated as well. For borazine, NIST data gives ionization energy of approximately 10.1 eV, compared to our calculated 10.42 eV. For the proton affinity of borazine, a value of 190.4 kcal/mol versus 191.8 kcal/mol (NIST) was obtained. No NIST data is available for cyclotriborazane. These results indicate good agreement for this method and basis set.

All of the above calculations were carried out at an MP2 level, using the 6-311+G** basis set, and the appropriate scaling factor for the thermodynamic and zero point energy values. To test the applicability of this basis set, the gas phase basicity of borazine at 298.15 K was calculated. The calculation showed a discrepancy of several kilocalories per mole exists. A better result may be obtained using the coupled cluster single and double excitation method (CCSD(T)). However, using SPARTAN limits the basis set functionality, and certain basis sets cannot be used as per a suggestion in the literature for the types of molecules of interest.

Gaussian '03 Software—*Method*: Two levels of calculations were carried out using Gaussian '03 software. The two were Lee-Yang-Parr's DFT (Density Functional Theory) with a 6-31G basis set, cc-pVTZ, and Aug-cc-pVTZ correlation correction.

*Geometry of borazine and cyclotriborazane***—**The charge distribution and structure parameters for borazine, cyclotriborazane, benzene and cyclohexane are listed in Tables 2 through 5. BN bonds in borazine are of the same length, which is similar to C-C bonds in benzene. Although bond angles are slightly different for BNB and NBN in borazine molecule but they are very close to benzene CCC bond angel. Both in borazine and cyclotriborazane, B-H bonds are shorter than N-H bonds. This is due to higher electronegativity of nitrogen compared to boron. The structural parameters of borazine, cyclotriborazane, benzene, and cyclohexane, given below, are in good agreement with other reported computational results.[7]

*Thermochemistry***—**Using Gaussian '03 and DFT/B3LYP/6-31G and Aug-cc-pVTZ, the enthalpy of reaction, Δ*Hr*, for borazine hydrogenation was calculated to be 27.6 kcal/mol for 6-31G basis set and 28.9 kcal/mol for Aug-cc-pVTZ basis set (see Table 6**)**. The same levels of calculation

for benzene hydrogenation to cyclohexane was performed and resulted in Δ*Hr* = -35.8 kcal/mol and -32.1 kcal/mol. Note that the experimental value for benzene hydrogenation is -49.1 kcal/mol. At least two interesting observation can be made from these results. First, the level of calculation seems to have minimal affect on Δ*Hr* value calculated. Second, borazine hydrogenation is an endothermic process.

Table 2. Atomic charge distribution.

Molecule	**Atom**	**APT Charges**	
		6-31G	**Aug-cc-pVTZ**
Borazine	B	+0.87	+0.84
	N	-0.86	-0.84
	H_N	+0.20	+0.19
	H_B	-0.21	-0.20
Cyclotriborazane	B	+0.75	+0.73
	N	-0.59	-0.54
	H_N(ax)	+0.13	+0.12
	H_N(eq)	+0.19	+0.18
	H_B(ax)	-0.28	-0.27
	H_B(eq)	-0.21	-0.22
Benzene	C	-0.02	-0.03
	H	+0.02	+0.03
Cyclohexane	C	+0.1	+0.1
	H(ax)	-0.05	-0.05
	H(eq)	-0.05	-0.05

Table 3**.** Structural parameters calculated for borazine.

Method	**Dipole M. (debye)**	***d*$_1$ (A)**	***d*$_2$ (A)**	***d*$_3$ (A)**	**α ∠BNB**	**β ∠NBN**
B3LYP/Aug-cc-pVTZ	0.00	1.1913	1.4292	1.0059	122.97	121.48
B3LYP/6-31G	0.00	1.1935	1.4361	1.0113	122.76	121.38
Experimental	0.50 in benzene	1.258	1.436	1.050	121.10	117.07

Table 4. Structural parameters calculated for cyclotriborazane.

Method	**Dipole M. (debye)**	***d1a,d1e* (A)**	***d*$_2$ (A)**	***d3a,d3e* (A)**	**α ∠BNB**	**β ∠NBN**
B3LYP/Aug-cc-pVTZ	3.54	1.2097, 1.2007	1.5948	1.0167, 1.0154	118.02	107.71
B3LYP/6-31G	3.70	1.2143, 1.2037	1.6052	1.0241, 1.0228	117.36	108.14
Experimental	3.2 ± 0.10 in *p*-dioxane	1.12-1.16	1.575-1.5781	0.88-0.91	115.8-116.0	107.2, 107.3

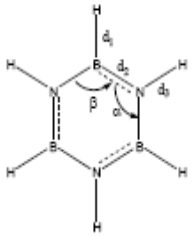

Borazine

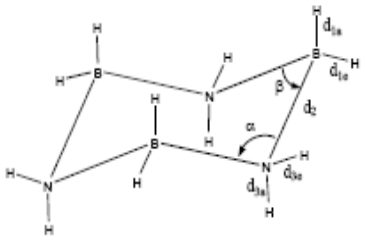

Cyclotriborazane

Table 5. Structural parameters calculated for benzene and cyclohexane.

Compound	Method	*d1* (A)	d_2 (A)	α ∠BNB
Benzene	B3LYP/cc-pVTZ	1.0818	1.3911	120.01
	B3LYP/6-31G	1.0996	1.3954	120.01
Cyclohexane	B3LYP/6-31G	1.0923	1.544	112.34
	B3LYP/6-31G	1.0978	1.554	112.15

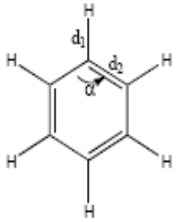

Benzene

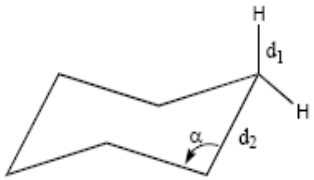

Cyclohexane

Table 6. Heat of the reaction for borazine and benzene hydrogenation.

Molecule	ΔH_r (kcal/mol)		
	Experimental	**6-31G**	**Aug-cc-pVYZ**
$B_3N_3H_6 + 3H_2 \rightarrow B_3N_3H_{12}$	N/A	27.6	28.9
$C_6H_6 + 3H_2 \rightarrow C_6H_{12}$	-49.06	-35.8	-32.1

Hydrolytic Cleavage of AB Complex

Catalyst Screening—At near room temperatures, AB complex was found to readily undergo hydrolytic cleavage in the presence of various platinum group metal (PGM) salts such as, $(NH_4)_2RuCl_6$, K_2Cl_6Pt, $(NH_4)_2PtCl_6$, and Na_3RhCl_6. Figure 5 depicts the volume of hydrogen generated vs. time for several PGM salts. It can be seen that among all the catalysts screened, Na_3RhCl_6 had the highest catalytic activity. For all catalysts tested, the reaction is fast and exothermic.

The rate of hydrolysis can be affected by varying the rate at which the catalyst solution is introduced to the AB powder. Temperature and heat transfer within the reacting material can

also affect the reaction rate. Figure 6 shows the amount of evolved H_2 as a function of time for hydrolytic dehydrogenation of AB complex at three different reaction conditions. Prior research has shown that AB bond cleavage is the rate-limiting step followed by rapid hydrolysis of BH_3.[8] Elevating the reactor temperature slightly from room temperature to 35 °C for 5 min, significantly increased the rate of hydrolysis of AB complex compared to that resulting from either insulated reactor or isothermal reactor set at 30 °C.

Kinetic Studies Using In Situ ^{11}B-NMR—In aqueous solutions of K_2Cl_6Pt, hydrolysis of the AB complex is first-order with respect to [AB]. The apparent first-order rate constant varies with the catalyst concentration as shown in Figure 7. Figure 8 depicts the rate of the AB hydrolysis versus time for $[K_2Cl_6Pt]$ in the range of 0.005 to 0.03 M.

The data indicate that hydrolysis of AB complex is second order with respect to concentration of the catalyst. Therefore, the overall rate of K_2Cl_6Pt catalyzed hydrolysis of AB complex is third-order and can be expressed as: $-d[AB]/dt = k'[AB][K_2Cl_6Pt]^2$. It is assumed that the concentration of water remains constant throughout the reaction, thus, $k'=k[H_2O]$.

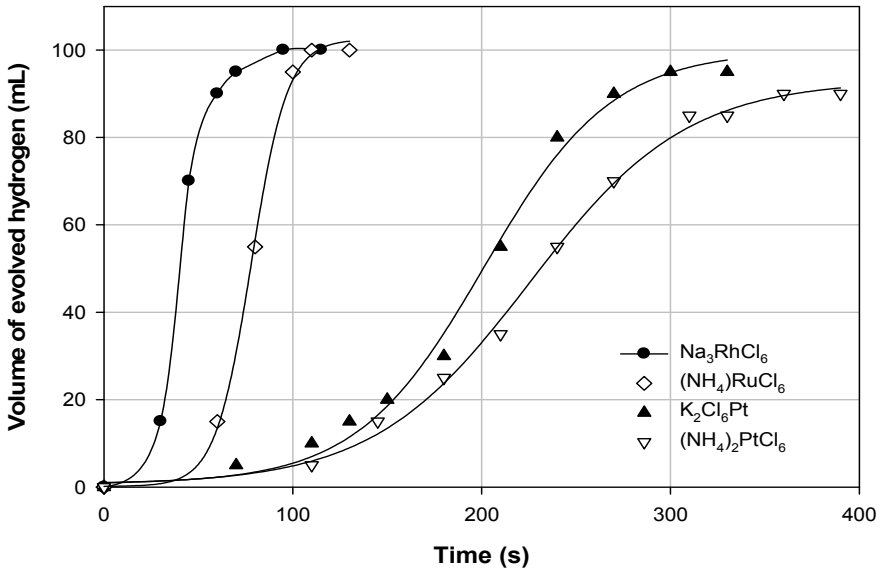

Figure 5. Hydrogen evolution vs. time for the hydrolytic dehydrogenation of AB complex (0.05 g) by 0.1 mL of 19 mM solution of various PGM catalysts at room temperature.

Figure 9 shows the temperature dependency (in the range of 25 to 35 °C) of the AB hydrolysis reaction rates. The first-order rate constants increase as the temperature increased from 25 to 35 °C (see Table 7).

Using the information given in Table 7, the pre-exponential factor (A) and the activation energy (E_a) were determined from Figure 10 using the Arrhenius equation, $\ln k = \ln A - E_a/RT$, to be: $A = 1.6 \times 10^{11}$ $Lmol^{-1}s^{-1}$ and $E_a = 86.6$ $kJmol^{-1}$.

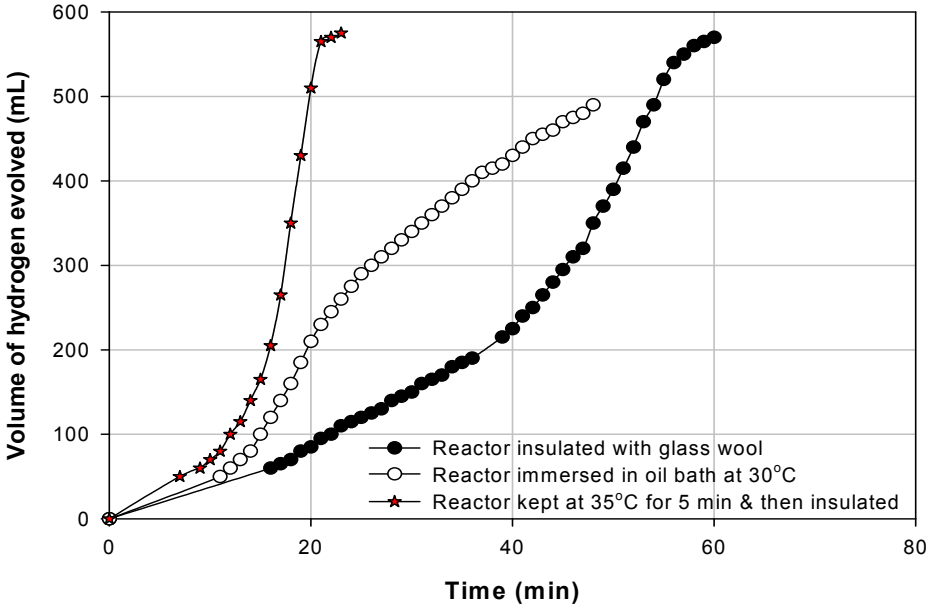

Figure 6. H_2 production vs. time for hydrolytic dehydrogenation of AB complex (0.3 g) by 0.1 mL H_2O and 0.44 mL of 19 mM K_2Cl_6Pt solution supplied at the rate of 0.02 mL/min at three different heating conditions.

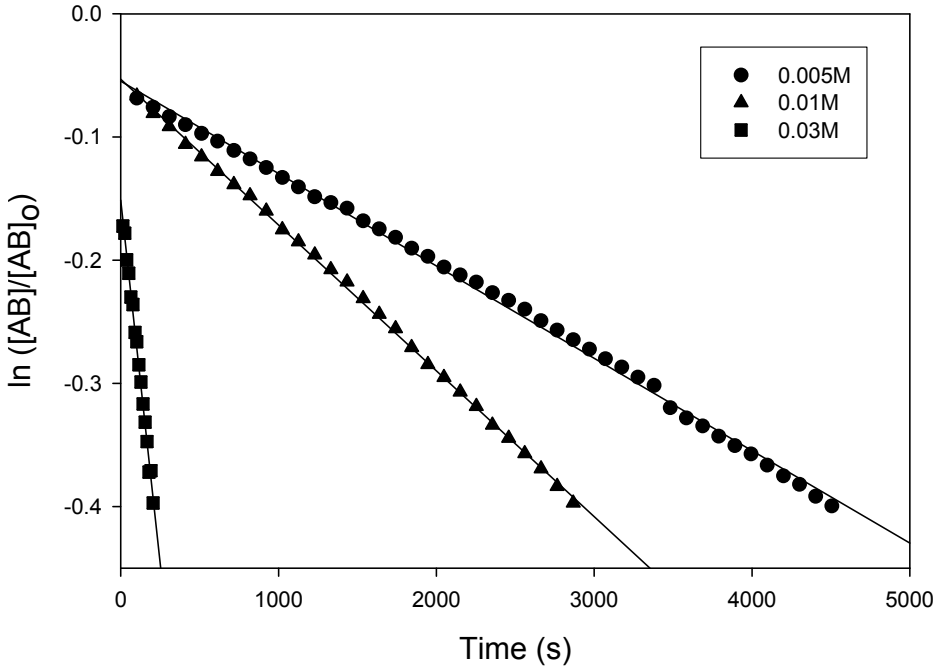

Figure 7. Rate of hydrolysis of the AB complex as a function of time at various concentration of the K_2Cl_6Pt in the solution (0.005, 0.01, and 0.03 M). The rate is first order with respect to $[NH_3BH_3]$.

ESCA Analysis of Spent Catalyst—Figure 11 depicts the ESCA spectra used to determine the state of Pt in the spent catalyst. The two binding energy peaks at 71.3 and 74.6 in the spectra are in good agreement with Pt^0 metal.[9] Results suggest that the platinum salt was reduced from Pt^{4+} to Pt^0 within the course of the reaction. We note that the metallic state of the PGM catalysts did not show significant catalytic activity for hydrolysis of AB complex.

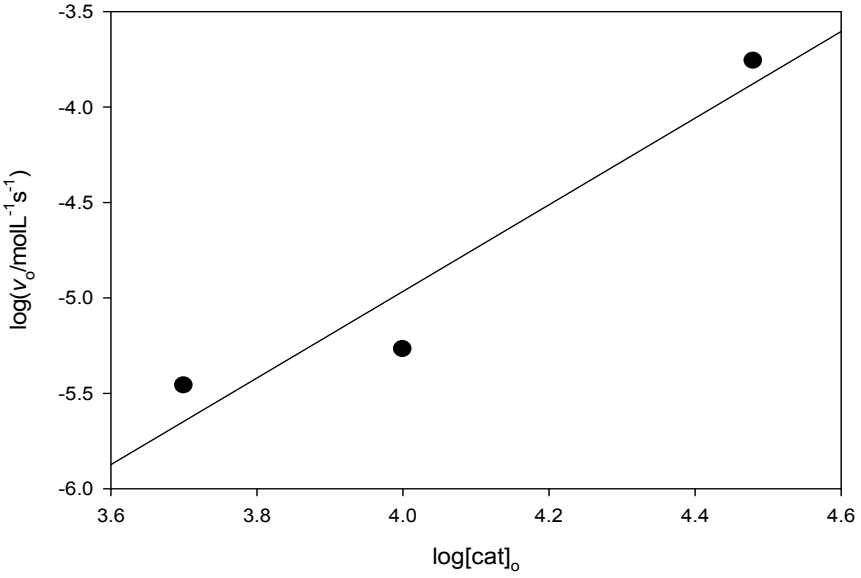

Figure 8. Rate of NH_3BH_3 hydrolysis in D_2O solutions at 25 °C for 0.005 to 0.03 M K_2Cl_6Pt catalyst concentration, slope = 2.27 (correlation coefficient = 0.92), $v_o = k'[AB]$.

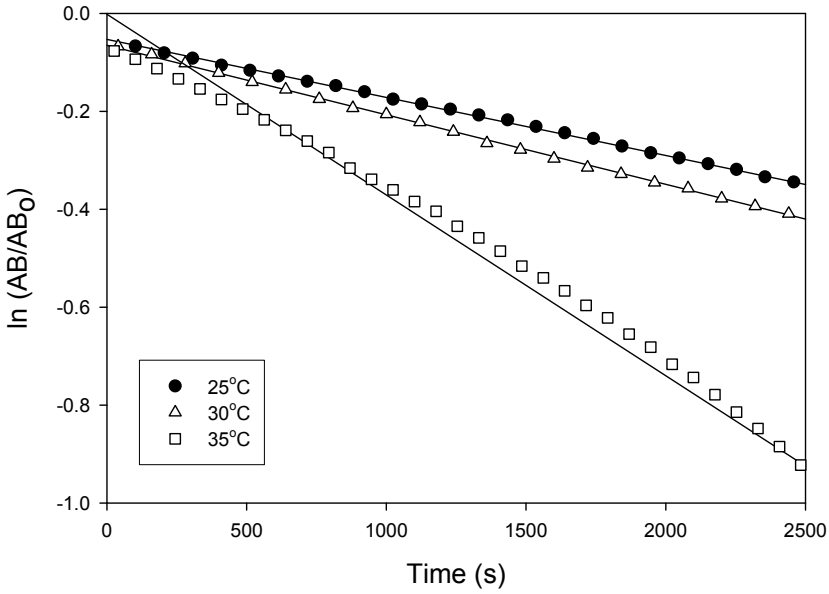

Figure 9. Rate constant of NH_3BH_3 hydrolysis at 25, 30, and 35 °C for a first order reaction with respect to [NH_3BH_3} using 0.01 M K_2Cl_6Pt solutions.

Table 7. Rate constants and correlation coefficients for the AB hydrolysis at T = 25, 30, and 35 °C.

T (°C)	k ($Lmol^{-1}s^{-1}$)	R^2
25	1.18×10^{-4}	0.999
30	1.42×10^{-4}	0.999
35	3.69×10^{-4}	0.987

Ammonia Sequestration—Hydrolytic cleavage of AB complex produces one equivalent weight of ammonia per equivalent weight of AB complex (Eq. 2). Ammonia can be split catalytically to generate more hydrogen (Eq. 4):

$$2NH_3 \rightarrow N_2 + 3H_2 \quad (4)$$

But, presently, there are no ammonia decomposition catalysts that provide high yields of hydrogen at temperatures below 400 °C. For small portable fuel cell applications, ammonia decomposition at high temperatures is generally not desired. Therefore, it is necessary to sequester NH_3 to avoid degradation of the PEMFC performance. Ammonia can be readily sequestered using sulfuric or phosphoric acid. For example, the stoichiometry for the production of hydrogen from AB complex using H_3PO_4 is as follows:

$$NH_3BH_3 + 3\ H_2O + \tfrac{1}{3}\ H_3PO_4 + \text{PGM catalyst} \rightarrow \tfrac{1}{3}\ (NH_4)_3PO_4 + B(OH)_3 + 3H_2 \quad (5)$$

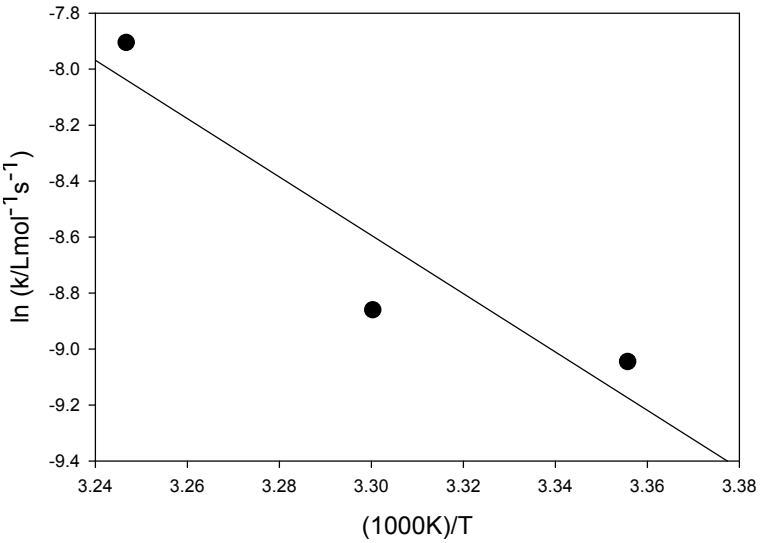

Figure 10. The Arrhenius plot for the hydrolysis of AB complex using K_2Cl_6Pt as the catalyst, correlation coefficient = 0.86.

Figure 12 depicts the GC/MS spectra for the total ammonia ion count (TIC) for the gas samples taken from the headspace of the AB hydrolysis reactor from tests with and without H_3PO_4 in the solution. The amount of ammonia detected in the reactor effluent was significantly less when phosphoric acid was used as the sequestering agent.

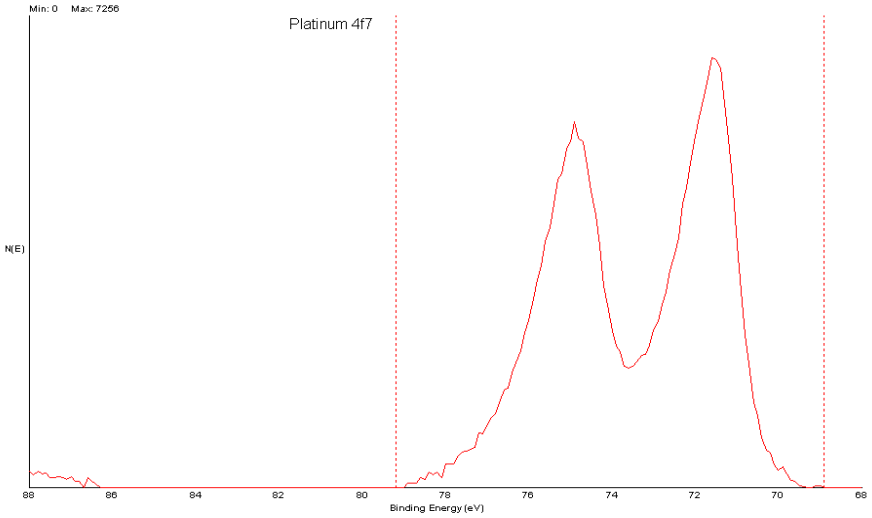

Figure 11. Pt 4f ESCA spectra of spent material from catalytic hydrolysis of AB complex.

Thermal Conductivity measurements of AB Complex

The rate of conductive heat transfer (Q') depends upon the temperature difference (T_{HOT} - T_{COLD}), distance (d), and the thermal conductivity of the material (*k*) as follows (Eq. 6):

$$Q' = k\,(T_{Hot} - T_{Cold})/d \qquad (6)$$

Apparent thermal conductivity was measured using the steady state method according to ASTM E 1225. A test sample is inserted under load between two similar specimens of known material thermal conductivity. A steady state temperature gradient is established in the test stack and heat losses minimized using a longitudinal heat guard subject to about the same temperature gradient. Under steady-state conditions, the thermal conductivity of the target specimen can be derived in terms of the temperature gradients in the respective specimens and the thermal conductivity of the reference material.

Figure 13 depicts the measured thermal conductivity of the AB pellet having a thickness of 0.181 in., in the temperature range of 300 to 420 K. At room temperature, thermal conductivity of the palletized AB was found to be approximately 15 W/m-K, comparable to that of dielectric materials such as alumina (*k* = 30 W/m-K) and calcium oxide (*k* = 16 W/m-K).[10]

The experimental error for these thermal conductivity measurements was determined by using two additional pellet thicknesses of 0.223 and 0.261 in. Table 8 depicts the measured values of the thermal conductivity of AB for the 0.223 and 0.261 in. pellets. Corresponding values of *k* for AB pellets having a thickness of 0.223 and 0.261 in. calculated using Figure 10 data are also given in Table 8.

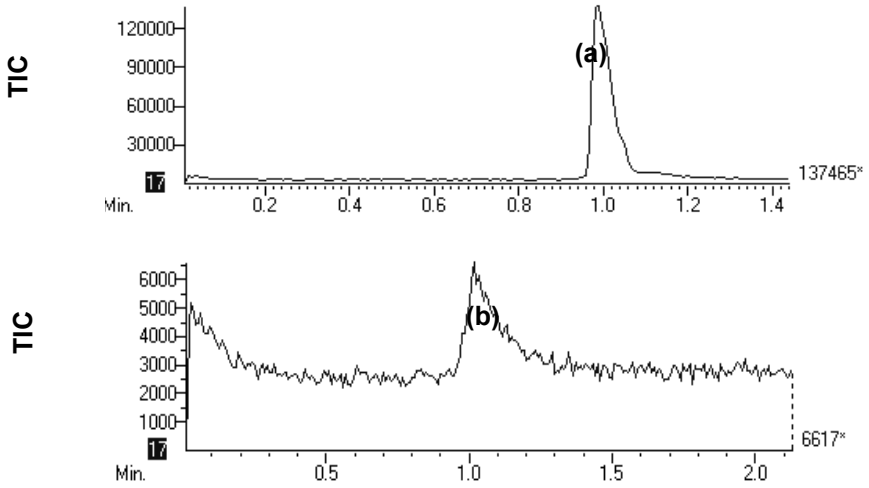

Figure 12. GC/MS spectra depicting the total ammonia ion counts for the gas samples AB hydrolysis reaction (a) without phosphoric acid and (b) with phosphoric acid.

Table 8. Thermal Conductivity of AB complex with different pellet thickness.

Pellet Thickness (inch)	**Temperature (K)**	**Measured *k* (W/m-K)**	**Calculated *k* (W/m-K) using Figure 10**
0.261	333	25.6	20.5
0.223	337	26.9	21.3

In an effort to increase the thermal conductivity of AB complex, we prepared AB composites by mixing fine aluminum powder with ammonia-borane. The apparent thermal conductivity of the composite AB/Al material increases by a factor of 4 over that of pure AB when 10% by weight of aluminum powder is added to AB material. This is shown in Figure 14 depicting the thermal conductivity of pure AB and AB-Al (10:1) composite in the temperature range of 300 to 420 K.

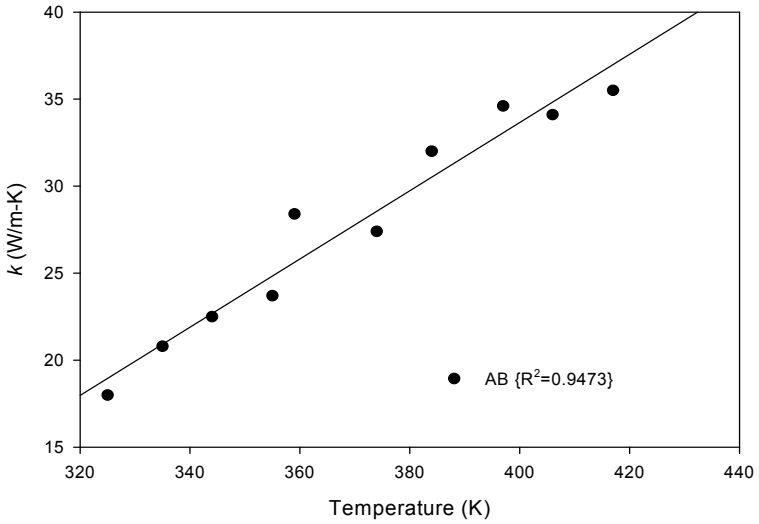

Figure 13. Thermal conductivity of AB complex as a function of temperature.

Finally, we conducted TG analysis of the AB/Al composites in order to measure the effect of Al addition on the dehydrogenation of AB complex. Typical results are shown in Figure 15. It can be seen that blending Al powder with AB complex results in a reduction in the overall AB mass loss from 33.9 to 25.4%. The difference can be attributed to the reduced levels of undesirable thermolysis products released, e.g., borazine, BH_2NH_2, diborane, etc.

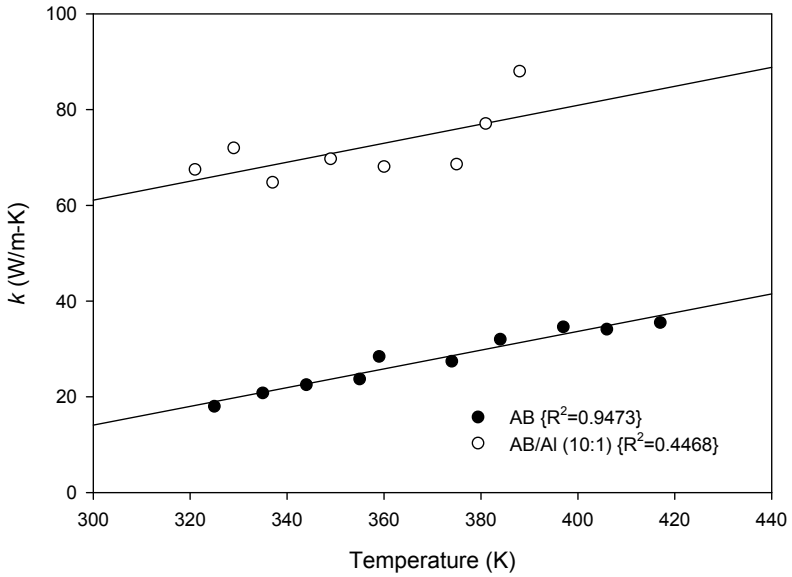

Figure 14. Thermal conductivity of AB complex and AB-Al (10:1) composite as a function of temperature.

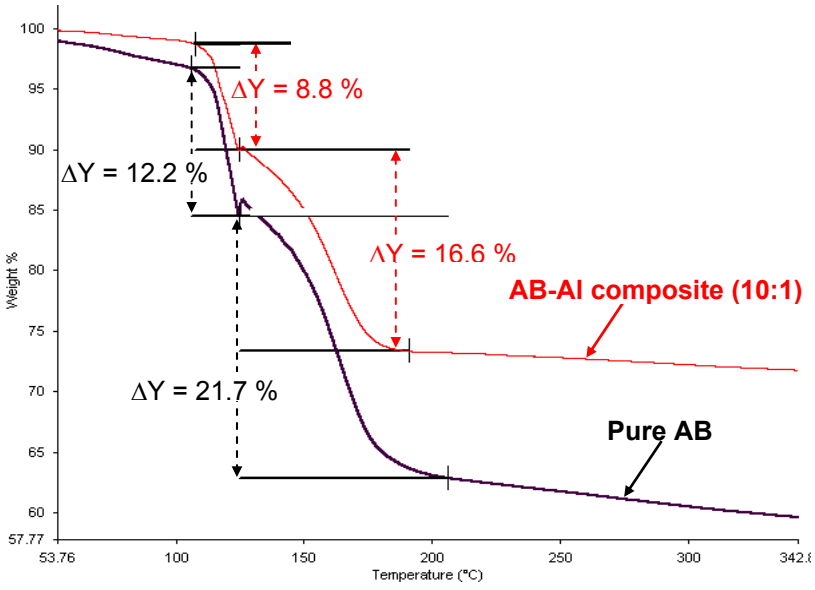

Figure 15. TG analysis of pure AB and AB/Al (10:1) composite.

It appears that the addition of aluminum powder to AB pellets improves the thermal conductivity of the material and as such affects the heat transfer through the AB/Al sample resulting in a more uniform temperature distribution and ultimately a higher level of hydrogen release and reduced amounts of undesirable volatile AB decomposition products.

Factors influencing Ammonia Borane Thermolysis

As noted before, the overall process for AB thermolysis is exothermic, but requires heating at the onset (i.e., induction energy) to initiate AB decomposition. A series of experiments were conducted to determine the induction energy needed for AB pyrolytic decomposition. In the first experiment, 1 g of AB was placed inside the reactor and heated for a period of time before the heating current was cut off - that is 1st induction period. After 10 s, the power to the heating element was turned on for a second time (2nd induction period) before cutting off the power, and so forth and so on. Table 9 depicts the amount of hydrogen evolved, in moles, for three tests all employing 1 g of AB complex, initially. Results of Table 9 imply that for 1 g AB sample, the induction energy required is about 556 joules leading to hydrogen release of about 0.3 moles. After that the reaction becomes self-sustaining and proceeds to completion–releasing about 2 moles of H_2 gas.

Next set of experiments was conducted to determine the minimum amount of energy required for 1 g of AB, at the lowest possible heating element temperature, to generate 0.3 moles of hydrogen from AB thermolysis allowing dehydrogenation and then the release of approximately 2 moles of H_2. Figure 16 represents the energy required to thermally decompose 1 g of AB at various Nichrome wire temperatures. The amount of borazine released from the AB pyrolysis is also given in Figure 16.

Table 9. H_2 production from AB thermal decomposition at various input power and induction times (at 954 °C).

1st induction		2nd induction		3rd induction	
Power Input (joules)	Mole H_2 Prod. (mL)	Power Input (joules)	Mole H_2 Prod. (mL)	Power Input (joules)	Mole H_2 Prod. (mL)
306	0.07	306	0.20	306	2.05
382	0.20	230	2.05	--	--
556	0.33	0	2.05	--	--

These results imply that at wire temperatures lower than 500 °C, AB thermolysis requires higher induction energy. Above 500 °C the Nichrome wire temperature doesn't affect the induction energy required to initiate AB thermolytic decomposition. Energy required to release 2 moles of H_2 from 1 g of AB is about 525 joules (16.2 kJ/mol of AB or 8.1 kJ/mol of H_2), which is about 3.35% of the chemical energy of hydrogen generated (on LHV basis). All of the experiments shown in Figure 16 generated about 2 moles of hydrogen with borazine concentration of about 6 vol% in the product gas.

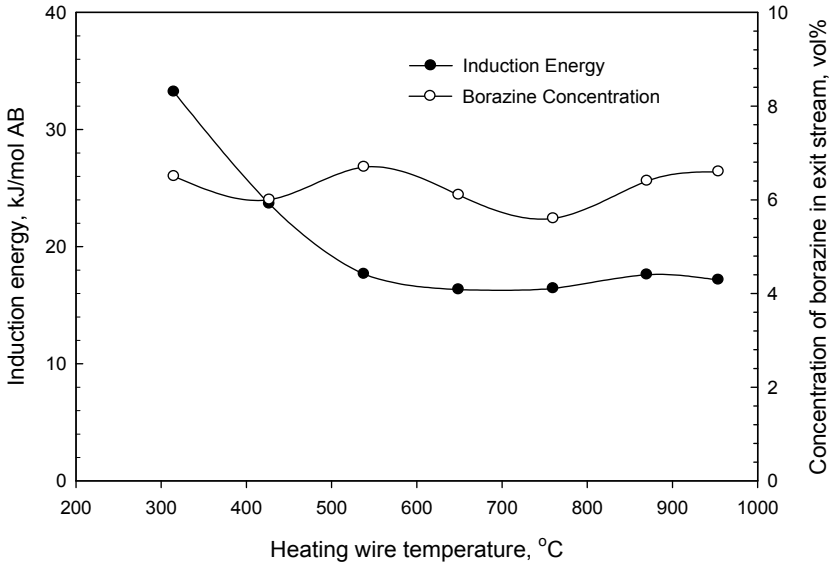

Figure 16. Induction energy requirement and concentration of borazine formed during thermolysis of AB complex.

Figure 17 depicts the extent of induction energy required and concentration of borazine in the exit stream of the reactor during pyrolysis of various amounts of AB complex at 954 °C wire temperature. Results of Figure 17 imply that the amount of induction energy needed is directly proportional to mass of AB pyrolyzed.

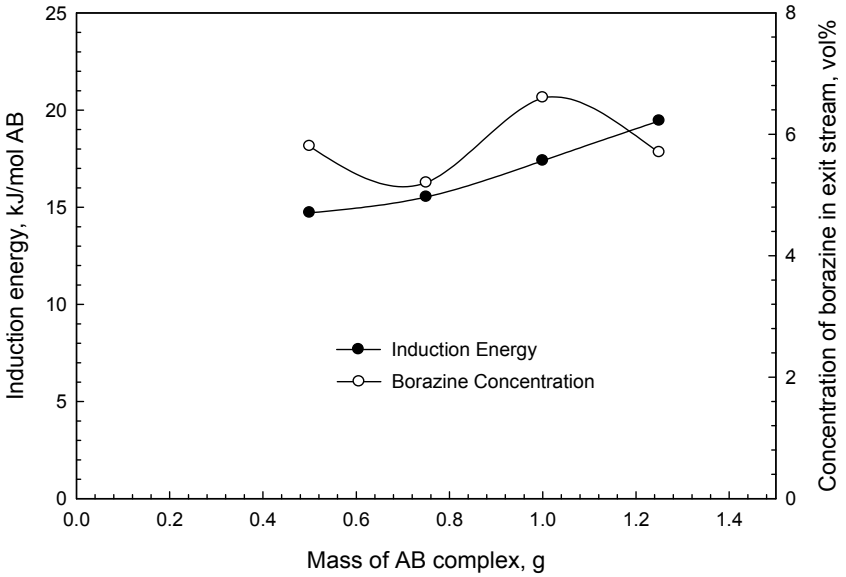

Figure 17. Induction energy and borazine concentration at 954 °C wire temperature for pyrolysis of different mass of AB complex.

Figure 18 shows the amount of induction energy required and concentration of borazine in the reactor outlet stream as a function of reactor pressures at 954 °C wire temperature and 0.5 g of AB. Hydrogen gas was used to elevate the reactor pressure. Results of Figure 18 indicate that the reactor pressure did not affect the borazine concentration. However, experiments conducted at 39.7 and 64.7 psia reactor pressure required less induction energy to react (for the same amount of AB consumed) and generate 2 moles of H_2 gas.

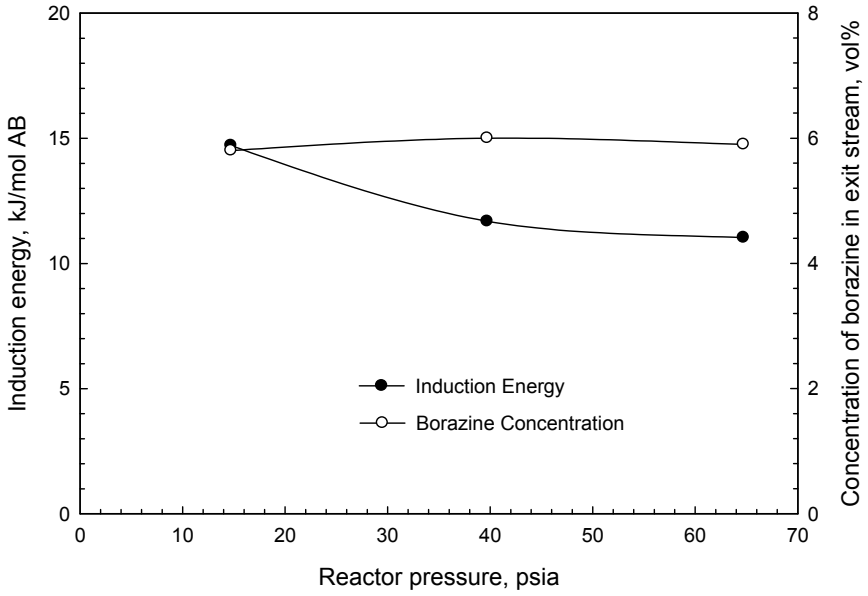

Figure 18. Induction energy and borazine concentration at 954 °C wire temperature for pyrolysis of AB at different reactor pressures.

Borazine Capture Utilizing Solid Sorbents

The results have already shown that thermolytic decomposition of AB at temperatures higher than 200 °C generates 2 moles of hydrogen per mole of AB pyrolyzed. Furthermore, the effluent released contains borazine at concentrations around 6 vol% of the total gas produced. Although liquid borazine readily decomposes at near room temperatures, vapor-phase borazine is very stable even at temperatures as high as 340 °C.[11] Additional tests have been conducted on a series of solid adsorbents to determine their ability to capture borazine from a gaseous stream. First, a rapid screening method depicted in Figure 3 was used to identify the best performing sorbents and then these candidates were tested by in a flow experiment using raw gas generated from thermolysis of AB complex in a manner described in the reference 6. Figure 19 shows the percentage of weight increase as a result of borazine uptake by various carbons, mesoporous silica powder, and calix(4)arene.

Amongst all materials tested, the carbon L was by far the best performing sorbent with measured 76.5% weight increase. All the other carbon samples except for carbon F and K showed an average weight increase of 23 to 40% when exposed to borazine. Non-carbonaceous mesoporous silica powder with 55% weight increase was the next best performing solid sorbent tested.

In order to confirm these results, carbon L was packed in a small tube and subjected to flow of 10 mL/min H_2 gas mixed with borazine, generated by direct pyrolysis of AB complex.[6] Again, gas samples were taken and analyzed at ports located before and after the scrubbing section until borazine breakthrough was observed. Based on GC/MS analysis, it was found that the borazine removal efficiency of 88% was achievable using carbon L material. In other words, 0.4 g of carbon L is required to effectively remove 88% of borazine generated from thermolysis of 1.0 g of AB complex (i.e., 9.3% by wt material-based H_2 storage or 1770 Wh/kg of AB – material basis).

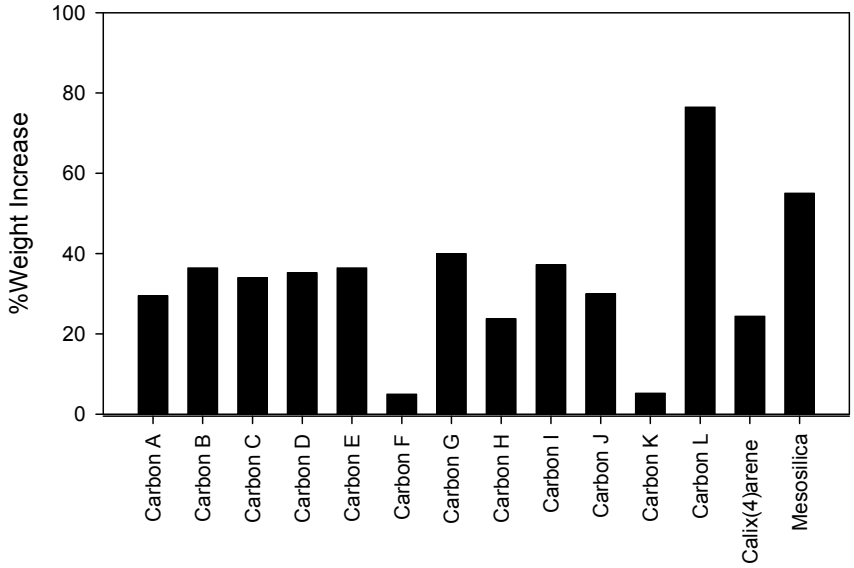

Figure 19. Borazine uptake by various solid sorbents using borazine in-vial measurement technique.

The nature of the adsorbed species on the surface of solid sorbents was also investigated using FT-IR attenuated total reflectance (ATR) technique. Figure 20 depicts the spectra of the surface bound species for several carbons tested. FT-IR spectra of borazine and BN are also given for comparison. Adsorbed species on carbons A and I have a very different structure than borazine or BN. Carbon C and K show a B-N stretch at 1450 cm^{-1} and small amount of B-H and N-H stretch for carbon C at 2600 cm^{-1} and 3550 cm^{-1}, respectively. Carbon L is the only carbon material that shows borazine molecules on its surface. Consecutive FT-IR analysis of carbon L showed than even after 10 days, borazine molecules adsorbed on its surface still remain and did not decompose to other species such as BN or polymeric $B_XN_XH_Y$. These findings are important as they point to a systematic approach for finding sorbents for borazine capture and removal from the off-gas of AB thermolysis reactor. Continuing activities are focused on the full characterization of these solid sorbents and their interactions with the adsorbed borazine and other species on their surface.

Conclusions

In this project, results have shown that a relatively minor expenditure of energy, can liberate 2 moles of hydrogen from thermolysis of AB complex. Without downstream treatment, some quantities of borazine and poly-aminoborane are also generated. At 954 °C wire temperature and 0.5 g of AB, borazine concentration in the reactor outlet stream was not affected by the reactor pressure. However, results obtained at pressures above 1 atm (i.e., 39.7 and 64.7 psia) showed that less energy was required to initiate AB thermolysis reaction and that the continuing reaction still resulted in production of 2 moles of hydrogen gas.

Other results have shown that borazine generated from direct thermolysis of ammonia borane complex can be effectively captured and removed from H_2 gas stream using a broad class of solid sorbents including carbons and mesoporous silica. In addition, FT-IR investigation of adsorbed species on the surface of these materials has shown that depending on the type of solid sorbent used, borazine can decompose or remain intact on the surface of sorbent material. Further research is underway to better understand the underlying chemistry involved in the

interactions between sorbent surface and adsorbed species so that a more effective material for borazine capture and removal can be formulated.

Pyrolysis of AB complex has been shown to be an overall exothermic process, but induction energy is required to initiate AB decomposition until about 0.3 moles of H_2 are released. At this point, the reaction is self sustaining and proceeds to completion with the release of about 2 moles of hydrogen gas. Induction energy required to release 2 moles of H_2 is about 16.2 kJ/mol of AB or 8.1 kJ/mol of H_2, which corresponds to 3.35% of the chemical energy of hydrogen generated (on LHV basis). Induction energy required for complete pyrolysis of AB complex is proportional to the mass of AB reacted.

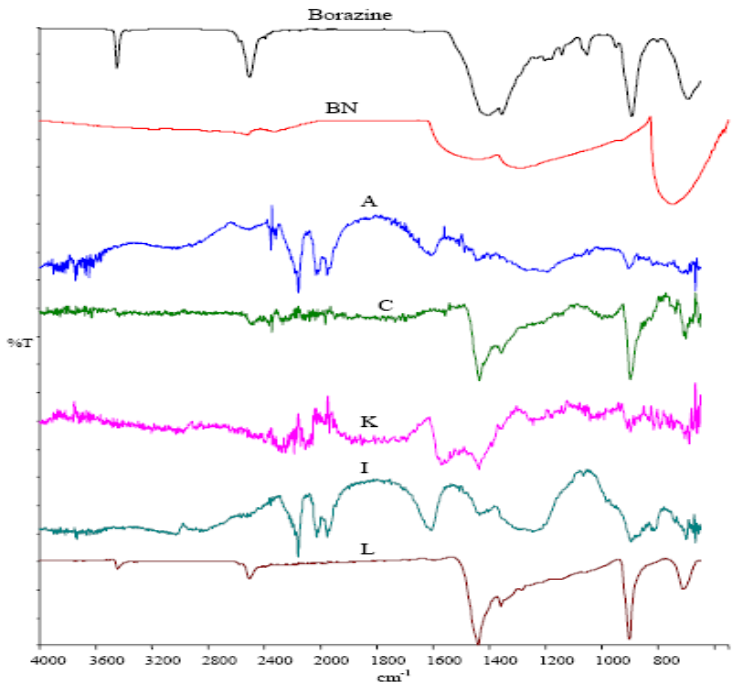

Figure 20. FT-IR spectra of adsorbed species on the surface of A, C, K, I, and L carbons. FT-IR spectra of borazine and BN are also given for comparison.

Near room temperature hydrolysis of AB complex has been carried out using small amounts of K_2PtCl_6 salt. The AB hydrolytic reaction is exothermic and can be extremely fast, kinetically. The kinetics of the AB hydrolysis in the presence of K_2PtCl_6 catalyst was studied using *in situ* ^{11}B-NMR spectroscopy. The overall reaction-order was estimated to be three with an apparent activation energy E_a = 86.6 kJmol^{-1}. XPS analysis of the spent material showed that the Pt in the catalyst is reduced to metallic state during the reaction and as such Pt did not display any catalytic activity. The XRD pattern for the residue of AB hydrolysis showed crystallized single-phase boric acid as the final product.

The thermal conductivity of AB complex, in the temperature range of 300 to 420 K, was measured experimentally using ASTM method E 1225. At 300 K, the thermal conductivity of pure AB is approximately 15 W/m-K. A composite pellet prepared by mixing 10% by weight aluminum powder with AB complex had a thermal conductivity that was a factor of 4 higher than that of pure AB. Weight loss due to pyrolysis of AB/Al composite was significantly less than that

of the pure AB complex indicating comparatively lower levels of volatile species formed as impurities (e.g., monomeric aminoborane, borazine, diborane, etc.) in the hydrogen generated.

References

1. A. T-Raissi, A Proc. Of the U.S. DOE Hydrogen Program Annual Review, Golden, CO, May 7, 2002, 537.
2. M. Couturier, J. Tucker, B. Anderson, P. Dubé, & J. Negri, Org. Lett. 2001, 3, 465.
3. H. Kelly, & V. Marriott, *Inorg. Chem.* 1979, 18, 2875.
4. G. Ryschkewitsch, & J., *Am. Chem. Soc.* 1960, 82, 3290.
5. J. Linechan, T. Autrey, J. Fulton, Y. Chen, & M. Balasubramanian, *Prep.Pap.-Am. Chem. Soc., Div. Fuel Chem.* 2005, 50(2), 540.
6. K. Ramasamy, G. Bokerman, N. Mohajeri, & A. T-Raissi, *Prep. Pap.-Am. Chem. Soc., Div. Fuel. Chem.* 2007, 52, (2).
7. (a) S. Peyerimhoff, & R. Buenker, *Theoret. Chim. Acta* 1970, 19, 1. (b) R. Findlay, *J. Chem. Soc. Dalton Trans. Inorg. Chem.* 1976, 10, 851. (c) B. Kiran, A. Phukan, & E. Jemmis, *Inorg. Chem.* 2001, 40, 3615. (d) S. Yang, H. Zhang, J. Soon, C. Lim, P. Wu, & K. Loh, *Diamond and Related Materials* 2003, 12(3-7), 1194-200.
8. H. Kelly, & V. Marriott, *Inorg. Chem. 1979, 18, 2875.*
9. G. Bancroft, I. Adams, L. Coatsworth, C. Bennewitz, J. Brown, & W. Westwood, *Anal. Chem.,* 1975, 47, 585.
10. D. Lide, *Handbook of Chemistry and Physics*, CRC Press, 1995.
11. A. Laubengayer, P. Moews, Jr., & R. Porter, *J. Am. Chem. Soc.* 1961, 83, 1337.

Publications

1. N. Mohajeri, & A. T-Raissi, “Hydrogen Storage in Ammonia Borane Complexes,” Proceedings of 15th World Hydrogen Energy Conference, June 27-July 2, 2004, Yokohama, Japan.
2. N. Mohajeri, & A. T-Raissi, ‘‘Regeneration of Ammonia Borane Complex for Hydrogen Storage,’’ Proceedings of 2005 MRS Spring Meeting, San Francisco, CA, March 28-April 1, 2005.
3. N. Mohajeri, O. Adebiyi, & A. T-Raissi, “Hydrolytic Cleavage of Ammonia Borane Complex for Hydrogen Production,” Proceeding of the 16th World Hydrogen Energy Conference, Lyon, France, 2006.
4. N. Mohajeri, & A. T-Raissi, “Novel Thermoneutral Catalytic Method for Dehydrogenation of Ammonia Borane Complex,” *Prepr. Pap.-Am. Chem. Soc., Div. Fuel Chem.* 2006, 51(1), 308.
5. N. Mohajeri, A. T-Raissi, & K. Ramasamy, “Thermal Conductivity of the Pure Ammonia Borane Complex and its Composites With Aluminum Powder,” *Prepr. Pap.-Am. Chem. Soc., Div. Fuel Chem.* 2006, 51(1), 309.
6. N. Mohajeri, A. T-Raissi, & K. Ramasamy, “Thermal Conductivity of Ammonia Borane Complex and its Composites With Aluminum Powder,” *Thermochimica Acta*, 2007, 452, 28.
7. N. Mohajeri, A. T-Raissi, & O. Adebiyi, “Hydrolytic Cleavage of Ammonia Borane Complex for Hydrogen Production,” *J. Power Sources*, 2007, 167, 482.
8. K. Ramasamy, G. Bokerman, N. Mohajeri, & A. T-Raissi, “Factors Influencing the Ammonia Borane Thermolysis,” *Prepr. Pap.-Am. Chem. Soc., Div. Fuel Chem.* 2007, 52(2), 565.
9. N. Mohajeri, K. Ramasamy, G. Bokerman, & A. T-Raissi, “Ammonia Borane Complex Thermolysis-Borazine Capture Utilizing Solid Sorbents,” *Prepr. Pap.-Am. Chem. Soc., Div. Fuel Chem.* 2007, 52(2), 557-558.

Patent

N. Mohajeri, A. T-Raissi, “Catalytic Dehydrogenation of Amine Borane Complexes,” (2007), U. S. Patent No. 7285142.

Presentations

1. N. Mohajeri, A. T-Raissi, “Regeneration of Ammonia-Borane Complex for Hydrogen Storage,” Proceedings of 2005 MRS Spring Meeting, March 28-April 1, 2005, San Francisco, CA.
2. N. Mohajeri, O. Adebiyi, & A. T-Raissi, “Hydrolytic Cleavage of Ammonia Borane Complex for Hydrogen Production,” WHEC16 Proceeding, June 13-16, 2006, Lyon, France.
3. N. Mohajeri, O. Adebiyi, J. Baik, G. Bokerman, & A T-Raissi, “An Ammonia Borane Based Hydrogen Storage System for Portable Applications,” Presented at ACS National Meeting, September 10-14, 2006, San Francisco, CA.
4. N. Mohajeri, & A. T-Raissi, “Novel thermoneutral catalytic method for dehydrogenation of ammoniaborane complex,” Presented at ACS National Meeting April 26-30, 2006, Atlanta, GA.
5. N. Mohajeri, A. T-Raissi, & K. Ramasamy, “Thermal Conductivity of the Pure Ammonia Borane Complex and its Composites with Aluminum Powder,” Presented at ACS National Meeting April 26-30, 2006, Atlanta, GA.
6. K. Ramasamy, G. Bokerman, N. Mohajeri, & A. T-Raissi, “Factors Influencing the Ammonia Borane Thermolysis,” Presented at ACS National Meeting, August 21, 2007, Boston, MA.
7. N. Mohajeri, K. Ramasamy, G. Bokerman, & A.T-Raissi, “Ammonia Borane Complex Thermolysis-Borazine Capture Utilizing Solid Sorbents,” Presented at ACS National Meeting, August 21, 2007, Boston, MA.

November 2007

Ceramic Membranes of Mixed Ionic-Electronic Conductors for Hydrogen Separation

M. Elbaccouch, A. T-Raissi, C. Linkous, and N. Mohajeri
Florida Solar Energy Center

Research Period: April 2004 to September 2007

Summary

This report presents a summary of the research and activities conducted for the U.S. National Aeronautics and Space Administration (NASA) under the NASA-Hydrogen Research at Florida Universities Program (Task III). The goal of the project is to develop ion transport systems for hydrogen separation and purification using mixed ionic-electronic conductors of perovskite-type structure ($A^{2+}B^{4+}O_3$-doped with a trivalent cation). The targeted membranes separate hydrogen from gas mixtures with 100% selectivity, high hydrogen flux, and good chemical stability in CO_2-rich mixture. The designed membranes are dense and free of pinholes.

The project approach to hydrogen gas purification is much more selective than permeation through polymeric membranes, yet much less expensive than metallic foils such as Pd. The project could open up an entirely new approach to the purification of hydrogen gas streams, especially for high temperature processes such as steam reformation of alkanes, gasification of coal, solid oxide fuel cells, and associated sensor technologies.

The followings are the three tasks of the project:

Task #1 Hydrogen Flux in Terbium (Tb) Doped Strontium Cerate ($SrCeO_3$) Disk-Type Membranes.

Task #2 Microstructural Analysis of Doped-Strontium Cerate Thin Film Membranes Fabricated via Polymer Precursor Technique.

Task #3 Development of Ceramic Oxide Thin Films Using Tape-Casting Process.

Introduction

Task #1: The objectives of this task are to synthesize hydrogen membranes of $SeCe_{0.95}Tb_{0.05}O_{3-\delta}$ using the liquid-phase method, and generate hydrogen flux data under different processing conditions. The membranes are of perovskite-type structure with mixed ionic-electronic conductivities. The membranes are dense providing 100% hydrogen selectivity. Hydrogen permeability is studied as a function of temperature, hydrogen partial pressure, hydrogen dry conditions, and water vapor pressure. Also, the influence of nickel deposition on hydrogen flux is evaluated.

Task #2: The objectives of this task are to synthesize nanocrystalline thin film membranes of terbium (Tb)-doped strontium cerate ($SrCeO_3$) via polymer precursor technique. The membranes are of interest in the hydrogen (H_2) separation and solid oxide fuel cells (SOFCs). Continuous and dense thin film membranes of composition $SrCe_{0.95}Tb_{0.05}O_{3-\delta}$ were prepared using spin-coating technique by utilizing ethylene glycol (EG)-based polymeric precursor. The polymeric precursor was deposited on silicon-based substrates, and converted to dense

polycrystalline thin film ceramic membranes by sintering at relatively low temperatures. The number of spin-coating cycles and sintering temperatures were systematically varied to study their effect on the film morphology, thickness, and crystallite size within the membranes. This study demonstrated that by using the EG-based polymeric precursor, dense and continuous Tb-doped $SrCeO_3$ thin film membranes, having thicknesses in the range of 0.2-2 μm and average nanocrystallite size of 8 to 70 nm, can be effectively synthesized by controlling the number of spin-coating cycles and sintering temperature.

Task#3: The objective of this task is to fabricate a tubular membrane reactor that could be used at high temperatures (above 550 °C) for hydrogen (H_2) separation and purification. The tubular reactor is a mixed ionic-electronic conductive system with a doped perovskite structure ($A^{2+}B^{4+}O_3$-doped with a trivalent cation). The reactor consists of a porous $SrCeO_3$-NiO composite support and a dense thin film membrane of $SrCe_{0.95}Y_{0.05}O_{3-\alpha}$. The support and membrane powders were synthesized by the solid state reaction method. The support material, composed of the ceramic powder, binder, plasticizer, and solvent, was formulated into homogeneously dispersed slurry with uniform structure. The tape-casting process was used to produce a thin film support tape by the shearing action of a doctor blade on the ceramic slurry. After drying, the tape was cut and rolled on a rod producing a tubular geometry. Slow sintering and H_2 atmosphere exposure burned off the organic materials, producing a ceramic composite tube with appreciable porosity.

Project Results

Task #1: Hydrogen Flux in Terbium (Tb) Doped Strontium Cerate ($SrCeO_3$) Disk-Type Membranes, M. Elbaccouch, & A. T-Raissi

Abstract—Hydrogen production membranes of $SeCe_{0.95}Tb_{0.05}O_{3-\delta}$ are synthesized using the liquid-phase method. The membranes are of perovskite-type structure with mixed ionic-electronic conductivities. The membranes are dense providing 100% hydrogen selectivity. Hydrogen permeability is studied as a function of temperature, hydrogen partial pressure, hydrogen dry conditions, and water vapor pressure. Also, the influence of nickel deposition on hydrogen flux is evaluated.

Introduction—Hydrogen production and separation using mixed ionic-electronic conductors of perovskite-type structure ($A^{2+}B^{4+}O_3$) are of great interest to the coal, natural gas, and petrochemical industries. The doped perovskite structure for hydrogen production has several attractive characteristics including, 100% pure hydrogen, external electrical power is not required, high thermal and energy efficiencies, cost-effective compared to palladium membranes, simple and flexible compared to pressure swing adsorption, and on-site hydrogen production.

Above 550 °C, the perovskite ceramic oxides exhibit ionic and electronic conductivities when the *B*-sites are doped with rare earth trivalent cations [1]. Ion transport in perovskite structures include three fundamental steps, a gas-solid interfacial reaction where hydrogen dissociate into protons and electrons, ion migration through the solid lattice, and solid-gas interfacial reaction where protons and electrons form hydrogen atoms [2].

The characteristics of ionic conductivity in perovskite-type ceramic oxides were first discovered in 1981 by Iwahara et al. [1]. Since then, various doped perovskite ceramics have been investigated including the respective cerates ($SrCeO_3$ [2-4] and $BaCeO_3$ [5-7]) and strontium zirconate ($SrZrO_3$ [4.8]). Evidence of proton conductivity in perovskite materials has been the

focus of many research programs [9-12]. $SrCeO_3$-based material is chosen for this investigation because it displays one of the highest proton conductivity.

In this work we report hydrogen permeability data of terbium doped strontium cerate oxide ($SrCe_{0.95}Tb_{0.05}O_{3-\delta}$) as a function of temperature (600 to 900 °C), hydrogen partial pressure (P_{H2}), and water vapor partial pressure (P_{H2O}). Also, the effect of metallic nickel impregnation on hydrogen flux is evaluated.

Experimental

Chemicals—Strontium nitrate ($Sr(NO_3)_2$) (99.995%) was purchased from Aldrich Chemical Co. 1.5 N cerium nitrate ($Ce(NO_3)_4.31H_2O$) solution, terbium nitrate ($Tb(NO_3)_3.6H_2O$) (99.9%), and citric acid (99%) were purchased from Alfa Aesar. Nitric acid (HNO_3) was obtained from Fisher Scientific. Distilled water was supplied by the Florida Solar Energy Center (FSEC). All chemicals were used as-received without further purifications.

Membrane Fabrication—Stoichiometric molar ratios of the metal nitrate precursors are mixed in distilled water to form 0.2 M solution. Nitric acid and excess citric acid (50% of total moles of metal ions) are added to the solution followed by stirring for 5 h in a reflux mode at 100 °C to initiate the polymerization process [13]. Water is evaporated on a hot plate and the solution is condensed to a gel-like material. The gel material is dried at 110 °C for 24 h to form a sponge-like brittle material. A self-ignition step is followed for about 40 min at 400 °C. The resulting powder is sieved twice to 90 μm and calcined at 600 and 800 °C for 24 hr to eliminate all organic residues. The powder is ground again to 90 μm and pressed under 130 Mpa hydraulic pressure into disks. Final sintering is carried out at 1200 °C for 24 h.

Hydrogen Permeation Apparatus—A schematic diagram of the permeation unit is represented in Figure 1 [14]. The set up consists of three interconnected alumina tubes (Coors Tek) used as the feed gas chamber (22 in. L x 1 in. D), sweep gas inlet chamber (15 in. L x 0.5 in. D), and sweep gas outlet chamber (17 in. L x 0.25 in. D). A ceramic sealant is used to obtain a gas-tight seal between the membrane disk and the sweep gas inlet alumina tube. The inlet feed gas and the argon sweep gas are introduced from opposite sides of the membrane and their flow rates are monitored using volumetric flow meters (Gilmont GF-1060). The upstream and downstream flow rates are maintained at atmospheric pressure and vacuum respectively. A gas chromatograph (SRI Instruments 8610) is used to analyze the product stream.

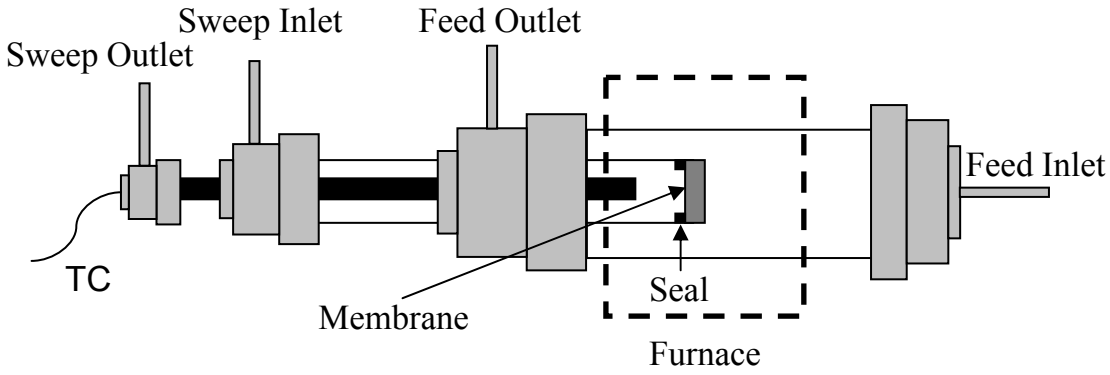

Figure 1. Hydrogen membrane permeation apparatus.

Results and Discussion

Leakage in the membrane disk due to pin-holes or incomplete membrane seal is checked by introducing helium in the feed stream as a tracer and measuring helium content in the product stream. The total hydrogen permeation rate (mol/s) is calculated from the hydrogen content in the argon sweep gas and argon flow rate. Hydrogen flux is calculated by dividing the permeation rates by the effective surface area (mol/cm^2 s).

Figure 2 represents hydrogen flux as a function of temperature (600 to 900 °C) for $SrCe_{0.95}Tb_{0.05}O_{3-\delta}$. The figure indicates that hydrogen flux increases linearly with temperature. The ceramic sealant and the gas-tight requirement of the membrane disk limit the upper temperature of the measurements to 900 °C.

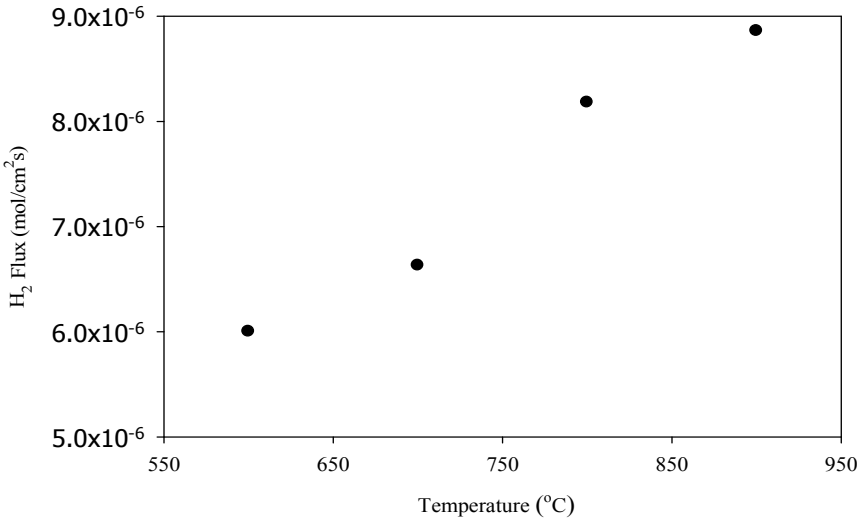

Figure 2. Temperature dependence of hydrogen flux for $SrCe_{0.95}Tb_{0.05}O_{3-\delta}$.

Figure 3 shows the influence of P_{H2} at different temperatures under dry conditions on hydrogen flux for $SrCe_{0.95}Tb_{0.05}O_{3-\delta}$. The figure shows that hydrogen flux increases as P_{H2} increases. The influence of P_{H2O} on hydrogen flux at 800 °C as a function of ΔP_{H2} of $SrCe_{0.95}Tb_{0.05}O_{3-\delta}$ is given in Figure 4. Hydrogen permeability decreases with increasing P_{H2O} due to increase in P_{O2}. It is expected that the flux for 100% dry hydrogen conditions to be higher than that of wet hydrogen conditions.

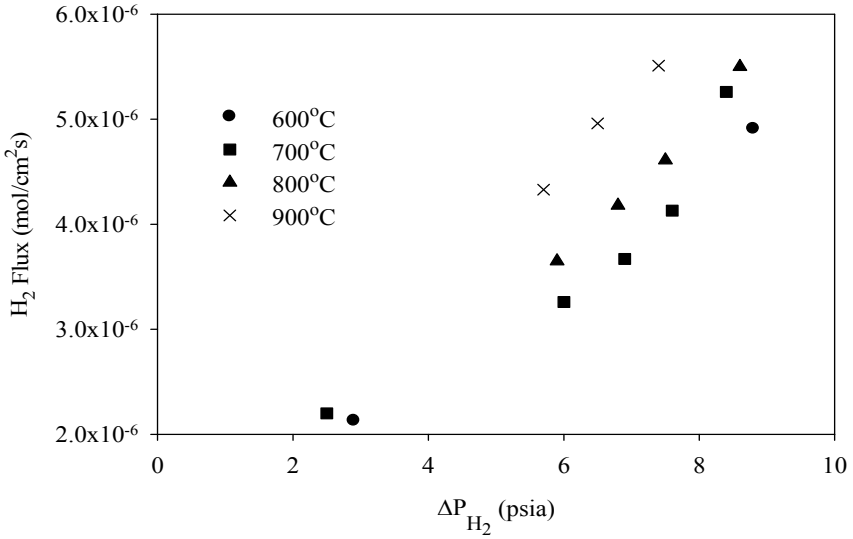

Figure 3. Influence of ΔP_{H2} at different temperatures under dry conditions on hydrogen flux for $SrCe_{0.95}Tb_{0.05}O_{3-\delta}$.

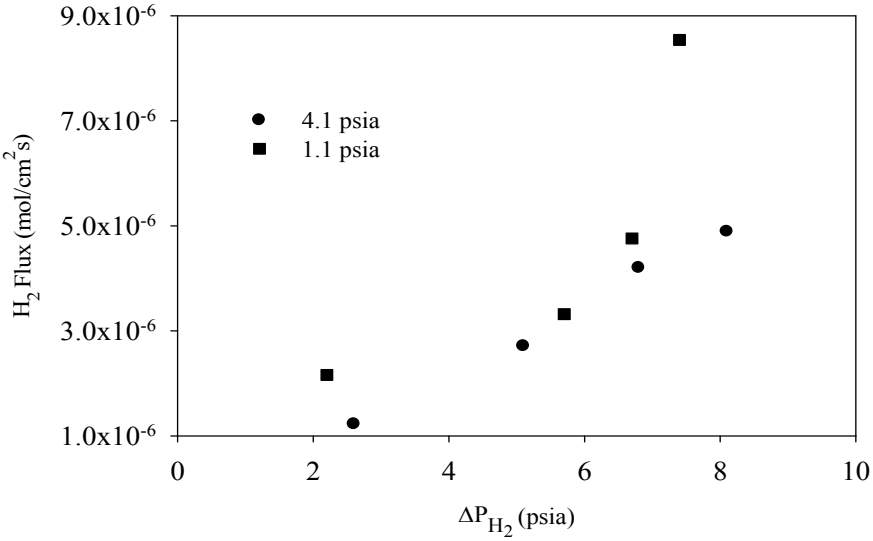

Figure 4. Influence of ΔP_{H2O} on hydrogen flux at 800°C for $SrCe_{0.95}Tb_{0.05}O_{3-\delta}$.

The hydrogen flux at 800 °C and 100% hydrogen dry conditions for $SrCe_{0.95}Tb_{0.05}O_{3-\delta}$ impregnated with nickel (2.3 mm) is 1.12×10^{-5} mol/(cm^2 s), while the hydrogen flux for a similar membrane disk (1.5 mm thick) without nickel is 8.18×10^{-6} mol/(cm^2 s). Although the nickel membrane sample has a larger thickness, it has a higher permeation rate. That is because nickel impregnation enhances hydrogen permeability by enhancing the catalytic activity at the solid-gas interfaces.

Conclusions

We developed high temperature dense ceramic oxide membranes of $SrCe_{0.95}Tb_{0.05}O_{3-\delta}$ with mixed ionic electronic conductors for hydrogen production and separation. Hydrogen permeability for $SrCe_{0.95}Tb_{0.05}O_{3-\delta}$ is presented as a function of temperature (600 to 900 °C), P_{H2}, and P_{H2O}. For the infinite hydrogen selectivity, the membrane needs to be dense, free of pin-holes (i.e., N_2 like molecules do not diffuse through), and free of cracks. Results indicate that hydrogen flux increases linearly with temperature. Also, hydrogen flux increases as P_{H2} increases. 100% dry hydrogen condition has higher H_2 permeability than wet H_2 conditions. Nickel impregnation enhances hydrogen permeability by enhancing the catalytic activity at the solid-gas interface. Experiments are in progress to generate H_2 flux data for $SrCeO_3$-based materials doped with yttrium, neodymium, and gadolinium trivalent cations.

References

[1] H. Iwahara, T. Esaka, H. Uchida, and N. Maeda, "Proton Conduction in Sintered Oxides and its Application to Steam Electrolysis for Hydrogen Production," *Solid State Ionics* 3/4, 359-363 (1981).

[2] S. Song, E. Wachsman, J. Rhodes, S. Dorris, & U. Balachandran. Hydrogen, "Permeability of $SrCe_{1-x}M_xO_{3-\delta}$ (x = 0.05, M = Eu, Sm)," *Solid State Ionics* 167, 99-105 (2004).

[3] X. Qi, & Y. Lin, "Electrical Conducting Properties of Proton-Conducting Terbium-Doped Strontium Cerate Membrane," *Solid State Ionics* 120, 85-93 (1999).

[4] S. Hamakawa, L. Li, A. Li, & E. Iglesia, "Synthesis and Hydrogen Permeation Properties of Membranes Based on Dense $SrCe_{0.95}Yb_{0.05}O_{3-\delta}$ Thin Films," *Solid State Ionics* 48, 71-81 (2002).

[5] R. Slade, & N. Singh, "Generation of Charge Carriers and H/D Isotope Effect in Proton-Conducting Doped Barium Cerate Ceramics," *J. Mater. Chem.* 1(3), 441-445 (1991).

[6] K. Takeuchi, C. Loong, J. Richardson Jr., J. Guan, S. Dorris, & U. Balachandran, "The Crystal Structure and Phase Transition in Y-Doped BaCeO3: Their Dependence on Y Concentration and Hydrogen Doping," *Solid State Ionics* 138, 63-77 (2000).

[7] V. Agarwal, & M. Liu, "Preparation of Barium Cerate-Based Thin Films Using a Modified Pechini Process," *J. mat. Sci.* 32, 619-625 (1997).

[8] J. Muller, K. Kreuer, J. Maier, S. Matsuo, & M. Ishigame, "A Conductivity and Thermal Gravimetric Analysis of a Y-Doped $SrZrO_3$ Single Crystal," *Solid State Ionics* 97, 421-427 (1997).

[9] J. Guan, "Ceramic Membranes of Mixed Ionic-Electronic Conductors for Hydrogen Separation," Ph.D. Thesis, Georgia Institute of Technology, (1986).

[10] K.D. Kreuer, Proton-Conducting Oxides, Annual Review Mater. Res. 33 (2003) 333-359.

[11] H. Iwahara, "High Temperature Proton Conductors Based on Perovskite-Type Oxides," in: Proton Conductors - Solids, Membranes and Gels-Materials and Devices, P. Colomban, Cambridge University Press, Cambridge, Chapter 8, P 122-137 (1992).

[12] S. Haile, G. Stanefe, & K. Ryu, "Non-Stoichiometry, Grain Boundary Transport and Chemical Stability of Proton Conducting Perovskites," *J. Membr. Sci.* 36, 1149-1160 (2001).

[13] D. Dionysiou, X. Qi, Y. Lin, G. Meng, & D. Peng, "Preparation and Characterization of Proton Conducting Terbium Doped Strontium Cerate Membranes," *J. membr. Sci.* 154, 143-153 (1999).

[14] F. Lau, & S. Doong, "Coal to Hydrogen: A Novel Membrane Reactor for Direct Extraction," Gas Technology Institute Presentation at GCEP Energy Workshops at Stanford University, April 26-27 (2004).

Task #2: Microstructural Analysis of Doped-Strontium Cerate Thin Film Membranes Fabricated via Polymer Precursor Technique *M. Elbaccouch N. Mohajeri, & A. T-Raissi (Florida Solar Energy Center); S. Shukla, & S. Seal (University of Central Florida)*

Abstract—A Nanocrystalline thin film membrane of terbium (Tb)-doped strontium cerate ($SrCeO_3$), which is of interest in the hydrogen (H_2) separation and solid oxide fuel cells (SOFCs), was synthesized via polymer precursor technique. Continuous and dense thin film membranes of composition $SrCe_{0.95}Tb_{0.05}O_{3-\delta}$ were prepared using spin-coating technique by utilizing ethylene glycol (EG)-based polymeric precursor. The polymeric precursor was deposited on silicon-based substrates, and converted to dense polycrystalline thin film ceramic membranes by sintering at relatively low temperatures. The number of spin-coating cycles and sintering temperatures were systematically varied to study their effect on the film morphology, thickness, and crystallite size within the membranes. Fourier transform infrared (FTIR) spectroscopy was utilized to study the changes in the polymer chemistry during the membrane processing. Thermogravimetric analysis (TGA) and differential thermal analysis (DTA) were used to examine thermal decomposition and thermodynamics of the synthesized precursor, respectively. The scanning electron microscopy (SEM) analysis was used to study the surface morphology and estimate average particle size as a function of number of spin-coating cycles and sintering temperatures. Atomic force microscope (AFM) was utilized to determine the roughness and quality of the spin-coated films. The membrane thickness, crystal structure, and nanocrystallite size were determined using focused ion-beam (FIB) milling and X-ray diffraction (XRD) techniques. Furthermore, the surface chemistry of the thin film membranes was studied by means of X-ray photoelectron spectroscopy (XPS). This study demonstrated that by using the EG-based polymeric precursor, dense and continuous Tb-doped $SrCeO_3$ thin film membranes, having thicknesses in the range of 0.2 to 2 μm and average nanocrystallite size of 8 to 70 nm, can be effectively synthesized by controlling the number of spin-coating cycles and sintering temperature.

Introduction—The characteristics of ionic conductivity in perovskite-type [1] ceramic oxides were first discovered in 1981 by Iwahara et al. [2]. Since then, ceramic oxides with perovskite structures ($A^{2+}B^{4+}O_3$) have been receiving considerable attention in the solid-state electrochemical systems, such as the development of solid oxide fuel cells (SOFCs) [3,4], gas sensors [5], and hydrogen (H_2) permeable membranes [6-8]. Various doped perovskite ceramics have been investigated including the respective cerates ($SrCeO_3$ [9-11] and $BaCeO_3$ [12-14]) and strontium zirconate ($SrZrO_3$ [11,15]). Evidence of proton conductivity in perovskite materials have been the focus of much research [16-19]. Perovskite ceramic oxide membranes are attractive materials for H_2 separation applications because they provide infinite selectivity toward H_2, require low H_2 chemical potential gradient, and are inexpensive compared to palladium membranes. Moreover, perovskite ceramic oxide membranes are simple and flexible compared to pressure swing adsorption (PSA) process, and do not require external power.

For effective H_2 separation, perovskite ceramic membranes must exhibit both ionic and electronic conductivity in order to achieve high H_2 permeation fluxes suitable for practical applications [20,21]. Also, they must be dense and free of pin holes in order to achieve full H_2 selectivity. At high temperatures, perovskite ceramic oxides exhibit the required ionic and electronic conductivity, as well as high hydrogen diffusivity and solubility, when the *B*-sites are doped with rare earth trivalent cations (M^{3+}). The general formula of doped perovskite ceramic is $AB_xM_{1-x}O_{3-\delta}$, where x (less than 0.1) and δ represent the molar concentrations of cations and oxygen-ion vacancies per perovskite unit cell respectively [13,18]. The doping process creates

the oxygen-ion vacancies (V_o) within the perovskite lattice as means of charge compensation [9,18]. It is possible to avoid the doping mechanism by applying electric potential across the membrane although such a galvanic process is relatively expensive, which limits its practical applications [2,22].

A typical H_2 permeation process in a doped perovskite ceramic oxide system involves three consecutive steps [9,13]: (i) a gas-solid interfacial reaction at high pressure side for the adsorption of H_2 at the membrane surface, where it dissociates into protons and electrons ($H_2 \rightarrow 2H^+ + 2e^-$), (ii) a pressure gradient across the membrane transports the protons through the solid-state membrane lattice, where the protons associate with oxygen sites ($OH_o^{\cdot}$) and hop between adjacent sites [9], and (iii) a solid-gas interfacial reaction at the low pressure side for the protons to re-combine and form H_2 ($2H^+ + 2e^- \rightarrow H_2$). The catalytic activity for oxidation at the solid-gas interfaces can be enhanced through the incorporation of a metallic phase [23]. The scattered H_2-permeation database for the doped proton conducting membranes include Eu or Sm-doped $SrCeO_3$ (disk membrane geometry) [9], Yb-doped $SrCeO_3$ (thin membrane film) [11], Y- doped Ni-Ba(CeZr)O_3 (disk membrane geometry) [23], Tm-doped $SrCeO_3$ (disk membrane geometry) [24], and Y-doped Ni-$BaCeO_3$ (disk membrane geometry) [16].

Some earlier reports have described the synthesis of dense ceramic membranes using polymeric precursors and utilizing both the spin-coating [11] and the sol-gel dip-coating [25-27] techniques on porous and non-porous substrates. Methods for the fabrication of dense disk-type Tb-doped $SrCeO_3$ using citric and oxalic acids have been reported [21,28]. Agarwal and Liu used dip coating with ethylene glycol (EG) and ethylene diamine tetracetic acid to synthesize $BaCe_{0.8}Gd_{0.2}O_{3-\delta}$ thin membrane films [14]. Iglesia et al. used spin-coating with glycolic acid and citric acid to synthesize $SrZr_{0.95}Y_{0.05}O_{3-\delta}$ and $SrCe_{0.95}Yb_{0.05}O_{3-\delta}$ disk and thin film membranes [11]. Kosacki and coworkers [29] employed spin-coating to prepare Gd^{3+} doped CeO_2 thin membrane films using EG as the polymerization agent. Eschenbaum et al. used dip-coating and sol-gel process to prepare Yb-doped $SrZrO_3$ membranes [25]. Sata et al. fabricated and characterized $SrZrO_3$ and $SrCeO_3$ thin films using the pulsed laser ablation technique and Raman spectroscopy [30]. Despite all of these efforts, work is still needed to enhance and produce high quality thin film membranes that are stable with good mechanical strength, free of pin holes (that is, no interconnected cavities through film cross-section), and free of cracks.

The preparation of dense and thin membrane films are sensitive to the synthesis technique and processing route, and are associated with some limitations. Dip coating allows less control over film thickness and quality compared to spin-coating. Thin film membranes require much lower sintering temperatures [31] than disk type membranes for the XRD analysis needed to establish the perovskite structure of the membranes. Also, disk-type membrane geometry is considerably thick (approximately 2 mm), and have low H_2 flux rates [11,24]. In order to increase H_2 permeation rate, it is essential to control the membrane thickness within the submicron to micron range. Since the permeation rate is inversely proportional to the membrane thickness, dense and thin (sub-micron thick) membrane films supported on porous substrates should yield much higher H_2 permeation rates.

Hence, from this perspective, the goal of the present study is aimed to process and characterize doped-strontium cerate ($SrCe_{0.95}Tb_{0.05}O_{3-\delta}$) (SCT) thin film membranes by spin-coating using EG-based polymeric precursor containing Sr, Ce, and Tb ions. Continuous (i.e. unique morphology across film surface) and dense (i.e., permit diffusion of ion-like species only) $SrCe_{0.95}Tb_{0.05}O_{3-\delta}$ membrane thin films having thickness within the range of 0.2 to 2 μm, with no pin-holes or cracks, are reported here. The polymeric precursor and the microstructure of the $SrCe_{0.95}Tb_{0.05}O_{3-\delta}$ membranes are characterized using several techniques including fourier

transform infrared spectroscopy (FTIR), thermogravimetric analysis (TGA), differential thermal analysis (DTA), scanning electron microscopy (SEM), focused ion-beam (FIB) microscopy, atomic force microscopy (AFM), X-ray diffraction (XRD), and X-ray photoelectron spectroscopy (XPS).

Experimental Procedure

Chemicals—Strontium nitrate ($Sr(NO_3)_2$) (99.995%) was purchased from Aldrich Chemical Co. 1.5 N cerium nitrate ($Ce(NO_3)_4.31H_2O$) solution and terbium nitrate ($Tb(NO_3)_3.6H_2O$) (99.9%) were procured from Alfa Aesar. Ethylene glycol (EG, $HOCH_2CH_2OH$) (99%) and nitric acid (HNO_3) were obtained from Fisher Scientific. All chemicals were used as-received without further purifications. Polished 500 to 550 μm silicon (Si) round wafers were purchased from the International Wafer Service Inc.

Synthesis of Polymeric Precursor—To synthesize perovskite ceramic membrane thin films of composition $SrCe_{0.95}Tb_{0.05}O_{3-\delta}$, the respective metal nitrate precursors were quantitatively weighed in definite ratio. The chemicals were then dissolved completely in 25 ml of distilled H_2O containing 40 ml EG (chelating agent) and 10 ml HNO_3 forming a red solution [29,32]. This clear red solution was set on a hot plate and heated at 85 to 90 °C for approximately 3 h to expel water and other volatile materials until it turned into a gelatinous liquid. The heating process polymerized the system and formed a complex mixture between the polymeric precursor and the metal cations.

Spin-Coating and Sintering—A 1 in. silicon substrate was pre-heated at 600 °C for 12 h in air to form a silicon oxide (SiO_2) layer. The oxidized Si-wafer was then affixed to the spin-coater (P6204 Cookson Electronics Equipment) using vacuum. A pipet was used to place few drops of the synthesized polymeric precursor on the surface of the Si/SiO_2 substrate. The spin-coating was conducted at 3000 rpm for 20 s. The viscosity of the polymeric precursor was maintained between 100 to 200 cP in order to obtain high quality films since the precursor viscosity below this range did not wet the surface of the Si/SiO_2 substrate. Also, very viscous precursor resulted in the formation of cracks and deformed films. The spin-coated films were dried on a hot plate at 80 °C for 1 min, and then set on another hot plate at 300 °C for 1 min to remove the organic content. The drying steps were repeated for multiple spin-coating cycles (one to twenty-five). Finally, the spin-coated and dried ceramic films were sintered at 400, 600, 800, and 1000 °C for 4 h to form high quality polycrystalline $SrCe_{0.95}Tb_{0.05}O_{3-\delta}$ membrane films.

Characterization

FTIR and TGA/DTA Analysis—The structural development and reaction mechanism of the polymeric precursor was investigated as a function of heating time and compared to that of pure EG using FTIR (Spectrum 2000, Perkin Elmer). The weight loss and thermal effect of the synthesized precursor were recorded continuously as a function of temperature up to 1000 °C using TGA-DTA (RIS-Diamond, Perkin Elmer). The TGA and DTA analysis were carried out simultaneously on the same sample to monitor the decomposition mechanism of the polymer precursor as it decomposes to its final oxide structure. Three analyses were performed under the same conditions: 18.6 mg of a precursor free of metal ions, 10.8 mg of a $SrCeO_3$ precursor doped with 5 mol% Tb, and 18.6 mg of a $SrCeO_3$ precursor doped with 20 mol% Tb. The samples were placed in a platinum holder with a nitrogen flow rate of 205 $ml.min^{-1}$ and a temperature ramp of 10 °C min^{-1}.

SEM Analysis—The surface morphology and the average particle size of the thin film membranes, processed under different conditions, were analyzed using SEM (JSM-6400F, JEOL, Tokyo, Japan). To avoid any surface charging during the SEM analysis, the ceramic thin film membranes were coated with approximately a 30 nm Au–Pd layer using a sputter coater (K350, Emitech, Ashford, Kent, England).

AFM Analysis—The surface roughness was examined using AFM (Pico SPM, Molecular Imaging Co) over a range of 600 nm. A non contact mode of measurement assembling a magnetic field is used in the analysis. The magnetic mode reflects a cantilever (MAC Levers Type-II) which is excited by a magnetic field with a resonant frequency of about 50 kHz.

FIB Analysis—FIB (FEI FIB 200 TEM, Hillsboro, OR) milling was performed on the Tb-doped $SrCeO_3$ membrane films to estimate the film thickness as a function of temperature and number of coating-cycles. The procedure for the FIB-milling and film thickness measurement has already been described in detail elsewhere [33-35].

XRD Analysis—The crystal structure and purity of the ceramic membrane was determined using Rigaku XRD Technique utilizing Cu Kα X-radiation of wavelength 1.54 Å to confirm the deposition of the perovskite ceramic membrane. The average nanocrystallite size as a function of temperature was calculated using the Scherrer's correlation [36],

$$D = \frac{0.9\lambda}{\beta \cos\theta_\beta} \tag{1}$$

Where, D is the average nanocrystallite size in nm, λ the radiation wavelength (0.154 nm), β the half width at half maximum intensity (radians), and θ_β half the difference between the two extreme diffraction peak angles (radians) where the intensity is zero.

XPS Analysis—The surface chemistry of Tb-doped $SrCeO_3$ membranes spin-coated on the SiO_2/Si substrate was studied using the XPS technique utilizing PHI ESCA spectrometer (5400, Perkin-Elmer), having energy resolution of $\pm$0.1 eV, at a base pressure of 5×10^{-9} torr, using Mg Kα radiation (1253.6 eV). The X-ray power during the analysis was 350 W [37]. Both the survey and the high-resolution narrow-scan spectra were recorded at the pass energies of 44.75 and 35.75 eV, respectively, to achieve the maximum spectral resolution. The binding energy (B.E.) of the Au $4f_{7/2}$ at 84.0$\pm$0.1 eV was used to calibrate the B.E. scale of the spectrometer. Any charging shifts produced by the samples were carefully removed using a B.E. scale referred to C (1s) B.E. of the hydrocarbon part of the adventitious carbon line at 284.6 eV.

Results and Discussion

Mechanism of Thin Film Membrane Formation—The progress of the EG polymerization process, monitored as a function of heating time via FTIR, is presented in Figure 1 [30]. The FTIR spectrum obtained from the pure EG is also provided as a reference (spectra a). In the reference spectrum, the peaks at 2900 cm^{-1} and 1637 cm^{-1} are identified as CH_2 and C=O stretching respectively. A comparison between the FTIR spectra related to the pure EG and EG-based precursors shows that the intensity of the CH_2 stretching decreases while that of the C=O stretching increases with increasing the reaction (heating) time. This suggests that with increasing reaction time more and more CH_2 bonds are oxidized to C=O. In addition, O-H and C-O primary alcohol stretching are observed in Figure 1 at 3395 and 1086 cm^{-1} respectively.

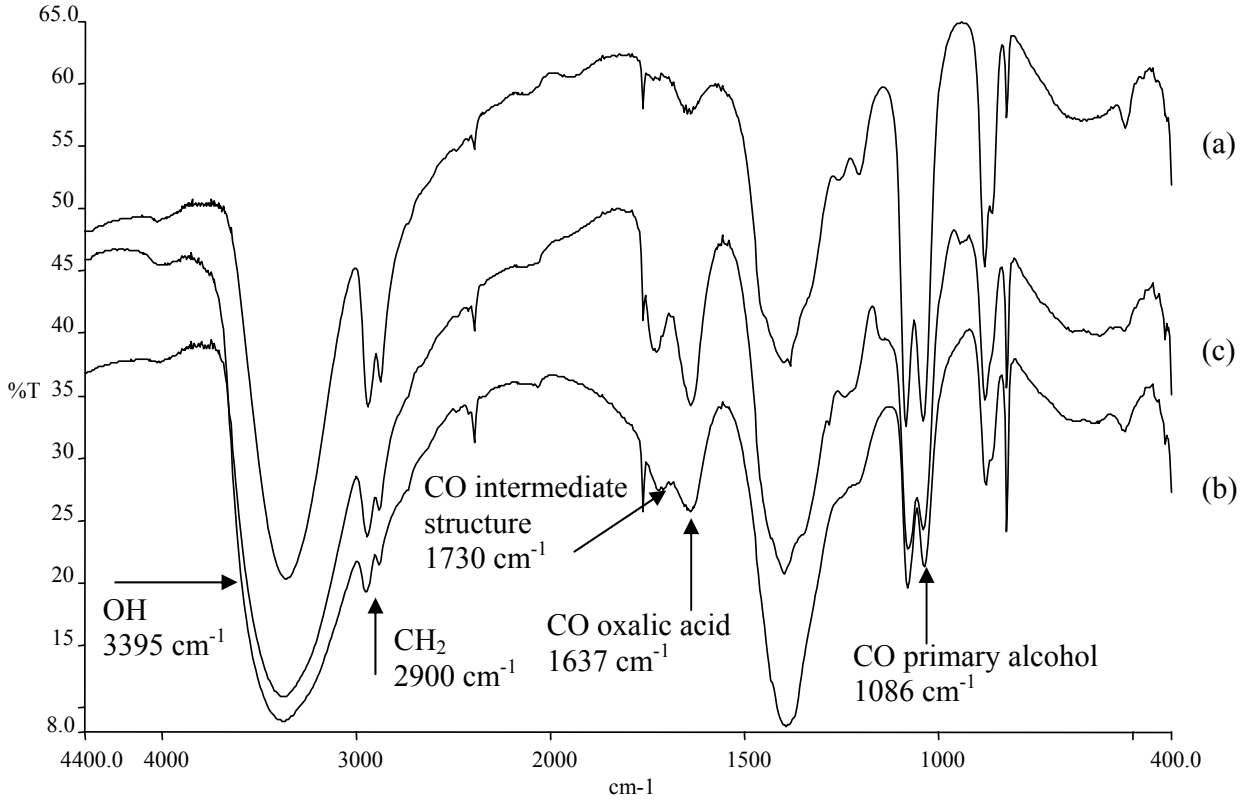

Figure 1. FTIR spectra of the ethylene glycol polymerization process: (a) pure ethylene glycol, (b) intermediate heating time, and (c) final heating time.

The FTIR spectra seems to agree with the proposed oxidation mechanism of EG described by Anderson and coworkers [32] where metal chelated oxalic acid groups get incorporated into the polymer structure by the replacement of two protons from the carboxylic acid functional groups in oxalic acid to form an intermediate ring structure. EG is shown to become oxidized in the presence of heat and a catalyst (HNO_3) to oxalic acid [32], which is primarily responsible for the decrease in the CH_2 stretching intensity and increase in the C=O intensity shown in Figure 1. Interestingly, a new C=O stretch at 1730 cm^{-1} is observed in Figure 1, which is not detected in FTIR spectrum of the pure EG. The intensity of this stretch is also observed to increase with increasing reaction time. As per the reaction mechanism, presented in Figure 1, this new C=O stretch at 1730 cm^{-1} is attributed to the intermediate metal chelated oxalate structure [31].

It is to be noted that heating simultaneously initiates the polymerization of EG; thus, converting it into the final polyester polymer precursor. The modified chemistry of the EG-based precursor ensures that the chelating metal cations remain in the solution throughout the entire polymerization process. Also, it ensures the stability, homogeneity, and uniformity of dispersed metal cations in the liquid medium.

Figure 2 depicts the TGA and DTA decomposition mechanism of a polymer precursor without metal ions (Figure 2a), $SrCeO_3$ polymer precursor doped with 5 mol% Tb (Figure 2b), and $SrCeO_3$ polymer precursor doped with 20 mol% Tb (Figure 2c). The three plots in Figure 2 follow a similar trend where a sharp weight loss takes place followed by a small and gradual

weight loss. In all cases, more than 90% of the total weight loss occurred below 200 °C. At the transition temperature from a sharp to a gradual weight loss, the precursor without metal ions has an endothermic peak, whereas the precursors with metal ions have exothermic peaks. Also, all precursors have endothermic peaks at 100 °C due to the evaporation of excess water.

The TGA profile of the polymer precursor without metal ions (Figure 2a) shows a sharp weight loss up to 165 °C followed by a gradual and small weight loss from 165 to 220 °C. The figure shows that 97% of the total weight loss occurred below 165 °C. At 220 °C the precursor lost all of its weight. The DTA profile in Figure 2a corresponds to three endothermic events and all occurred during the sharp weight loss event. These endothermic events are due to the evaporation of excess water, polymer degradation, and organic burn off.

Figure 2b describes the TGA and DTA profiles of a $SrCeO_3$ polymer precursor doped with 5 mol% Tb. The TGA curve can be classified as a sharp weight loss up to 172 °C and a gradual and small weight loss from 172 to 400 °C. An approximately 1% weight loss occurs above 400 °C and is considered marginal. During the entire TGA process, the precursor lost approximately 95% of its total weight. 90% of the total weight loss occurs below 172 °C and corresponds to two endothermic peaks due to water evaporation and polymer degradation. An exothermic peak occurred at the transition temperature from a sharp weight loss to a gradual weight loss (172 °C) followed with another exothermic peak at 330 °C. The heat evolved in these two exothermic peaks might be due to the ceramic oxide structure as it changes from an amorphous state to a crystalline state. At 400 °C the polymer is degraded and only metal ceramic oxides exist on the Si/SiO_2 substrate.

The trends of the TGA and DTA profiles of the $SrCeO_3$ polymer precursor doped with 20 mol% Tb (Figure 2c) is similar to the precursor doped with 5 mol% Tb. However, the transition temperature from a sharp to a gradual weight loss is shifted to 200 °C and corresponds only to 80% of the total weight loss. In Figures 2b and 2c, only marginal weight loss is observed beyond 400 °C, and no weight loss is observed beyond 600 °C. In Figure 2c, the precursor lost 10% of its total weight during the gradual weight loss process (200-600 °C). At 330 °C, the heat evolved in the precursor with 20 mol% Tb is significantly smaller compared to that with 5 mol% Tb. A sharp endothermic peak at 600 °C accompanied with a slight weight loss is detected in the 20 mol% Tb precursor, which is not observed in the 5 mol% Tb precursor and the precursor without metal ions. The presence of only a small exothermic peak (330 °C) and a strong endothermic peak (660 °C) suggest that Figure 2c has no amorphous to crystalline transition or the film exists either in amorphous or crystalline form throughout this temperature range.

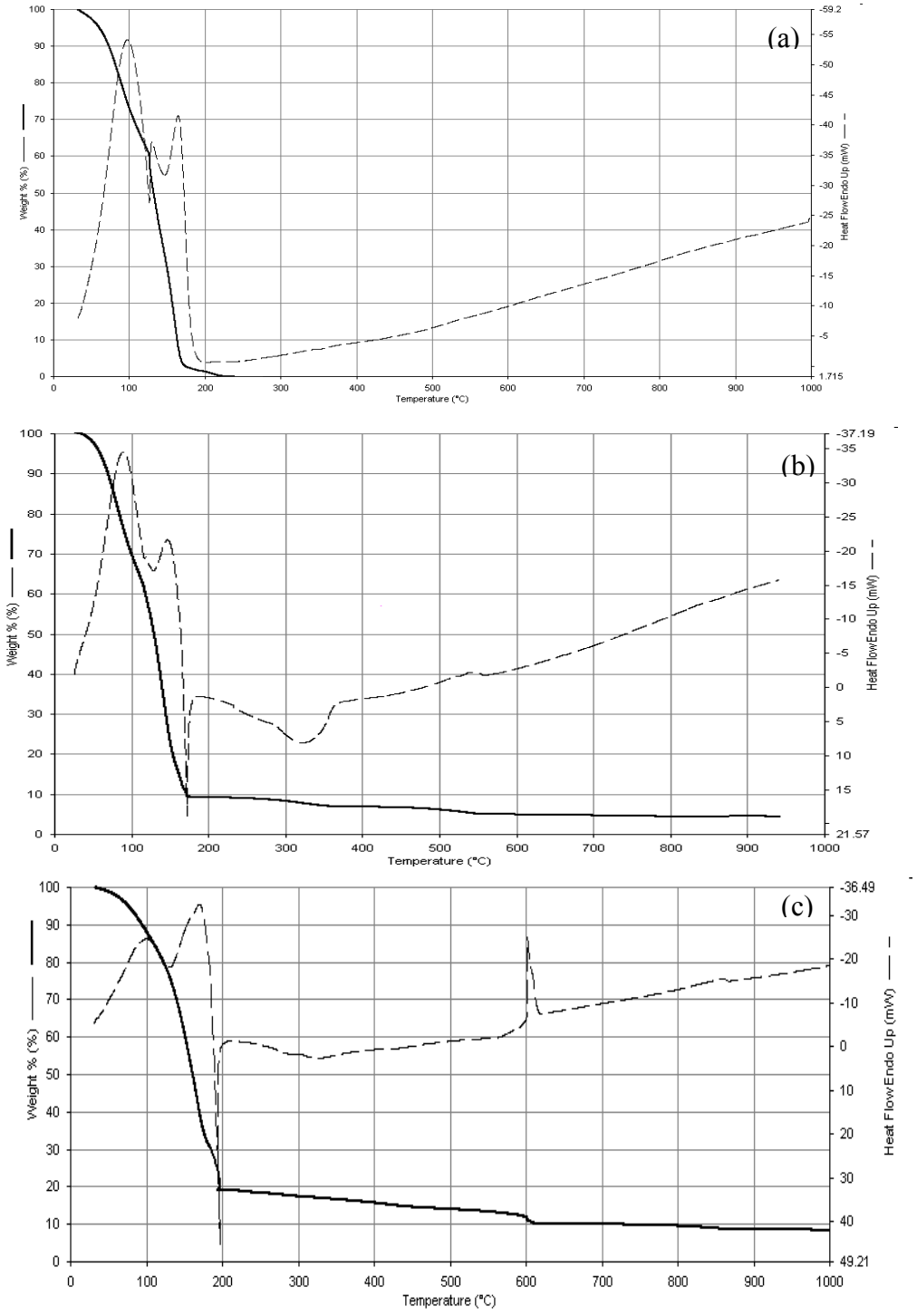

Figure 2. TGA and DTA profiles of synthesized polymer precursor: (a) no metal ions, (b) $SrCeO_3$ with 5 mole% Tb, and (c) $SrCeO_3$ with 20 mole% Tb.

Effect of Number of Spin-Coating Cycles and Calcination Temperature on Surface Morphology and Average Particle Size—Figures 3 shows high magnification SEM images respectively for $SrCe_{0.95}Tb_{0.05}O_{3-\delta}$ film, as a function of the spin-coating cycles, sintered at 400 °C for 4 h. It is noted that the membrane thin film spin-coated for only one cycle (Figure 3a) shows a relatively dense structure at the surface with respect to those processed with more than a single cycle. Moreover, by comparing Figure 3a with Figures 3b-c, it is qualitatively noted that the average particle size decreases with multiple spin-coating cycles. Typically, the average particle size was about 500 nm for the thin film membrane obtained via single-cycle, while for those synthesized using ten and twenty-five spin-coated cycles, the average particle size was approximately 200 nm. Comparison of Figure 3b and 3c, however, reveals that, average surface porosity, morphology, and particle size for the thin film spin-coated membranes (for more than one-cycle) remain qualitatively the same. Thus, multiple spin-coating cycles seemingly increase the extent of surface porosity, but decrease average particle size relative to those prepared by a single coating-cycle.

Figure 4 shows high magnifications SEM images respectively for $SrCe_{0.95}Tb_{0.05}O_{3-\delta}$ as a function of sintering temperature within the range of 400-1000 °C depicting the strong effect of temperature on the $SrCe_{0.95}Tb_{0.05}O_{3-\delta}$ surface morphology. Figures 4d and 4(a-c) show that the surface porosity is reduced significantly as the temperature increases leading to a dense surface structure at 1000 °C. A diffused cluster-like particles form on the surface as the temperature is increased from 400 to 1000 °C. The effect of temperature on the crystallite size will be discussed in Section 3.5.

We observed that multiple spin-coating cycles results in a matrix that is porous only on the surface, but free of any interconnected cavities within the membrane body. In other words, multiple spin-coating generates eventually a membrane that is dense and free of pin holes. It is worth mentioning that dense and pin hole-free structures are need for perovskite-based oxide membranes for the H_2 separation applications. As discussed earlier, the doped perovskite-based oxides, such as $SrCe_{0.95}Tb_{0.05}O_{3-\delta}$, are permeable to H_2 due to simultaneous diffusion of protons and electrons but impermeable to N_2-like molecules as long as the membrane itself is dense and free of pinholes.

Effect of Number of Spin-Coating Cycles and Sintering Temperatures on Membrane Thickness—The cross-sectional FIB images of $SrCe_{0.95}Tb_{0.05}O_{3-\delta}$ membrane thin films synthesized using multiple coating cycles with calcination at 400 and 1000 °C are given in Figures 5a-e and 5f, respectively. As shown in Figure 5a, a membrane with a thickness of 0.18 μm could be synthesized by single coating technique. The membrane film, however, appears to be discontinuous under these processing conditions. With increasing the spin-coating cycles (Figures 5b-f), a dense and continuous membrane having larger film thickness is obtained. Figures 5b-f reveal that with increasing the number of spin-coating cycles, the high porosity is progressively associated with the near surface region, while the bottom layers of the film remain much denser. This suggests that the multiple spin-coating cycles fill in voids associated with the previously deposited layers. Note that the black spots in Figures 5c-e suggest the closed cavities within the membrane. Interestingly, comparison of Figures 5e and 5f reveals that the higher calcination temperature (1000 °C) reduces the bulk porosity due to enhanced diffusion kinetics. However, the effect of the higher calcination temperature on the film thickness is not significant. Overall, it appears that a single-coating cycle results in discontinuous thin film while multiple spin coating cycles provide a dense, pin-hole-free, and continuous thin membrane, which appears to be the best morphology for effective H_2 separation.

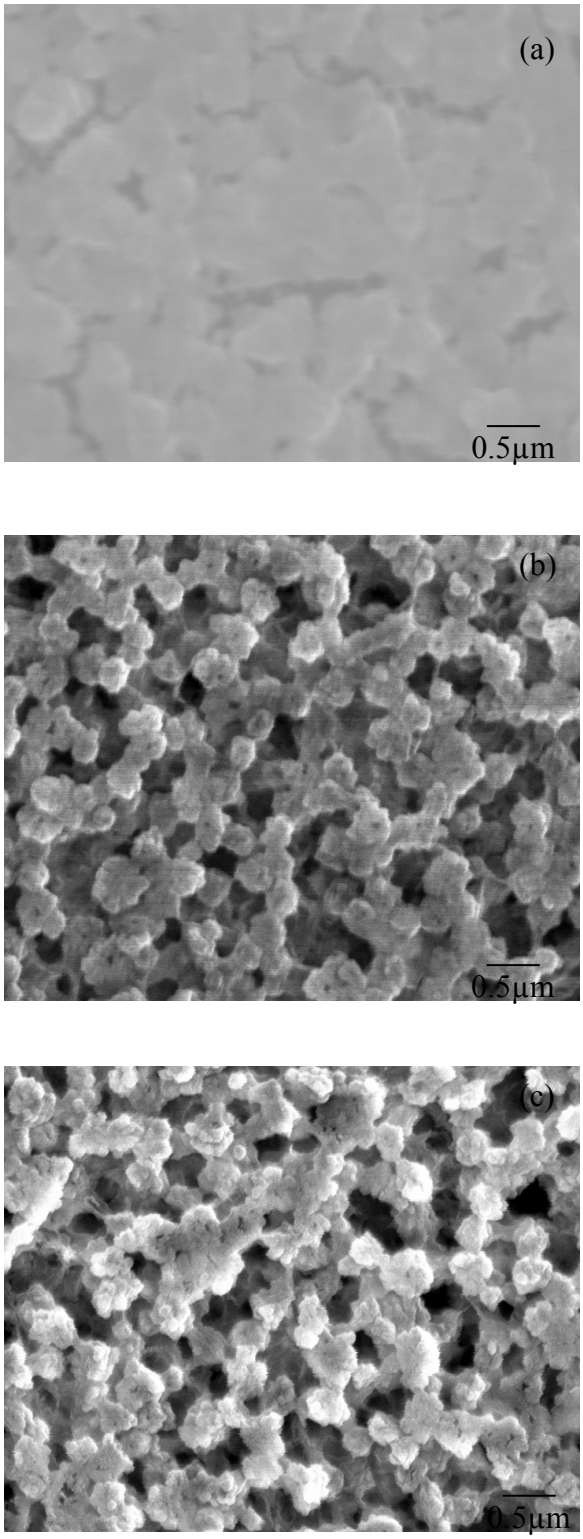

Figure 3. SEM surface morphology images at high magnifications of $SrCe_{0.95}Tb_{0.05}O_{3-\delta}$ after spin-coating at 3000 rpm for 20 s and sintering at 400 °C for 4 h. (a) one spin-coating cycle, (b) 10 spin-coating cycles, and (c) 25 spin-coating cycles.

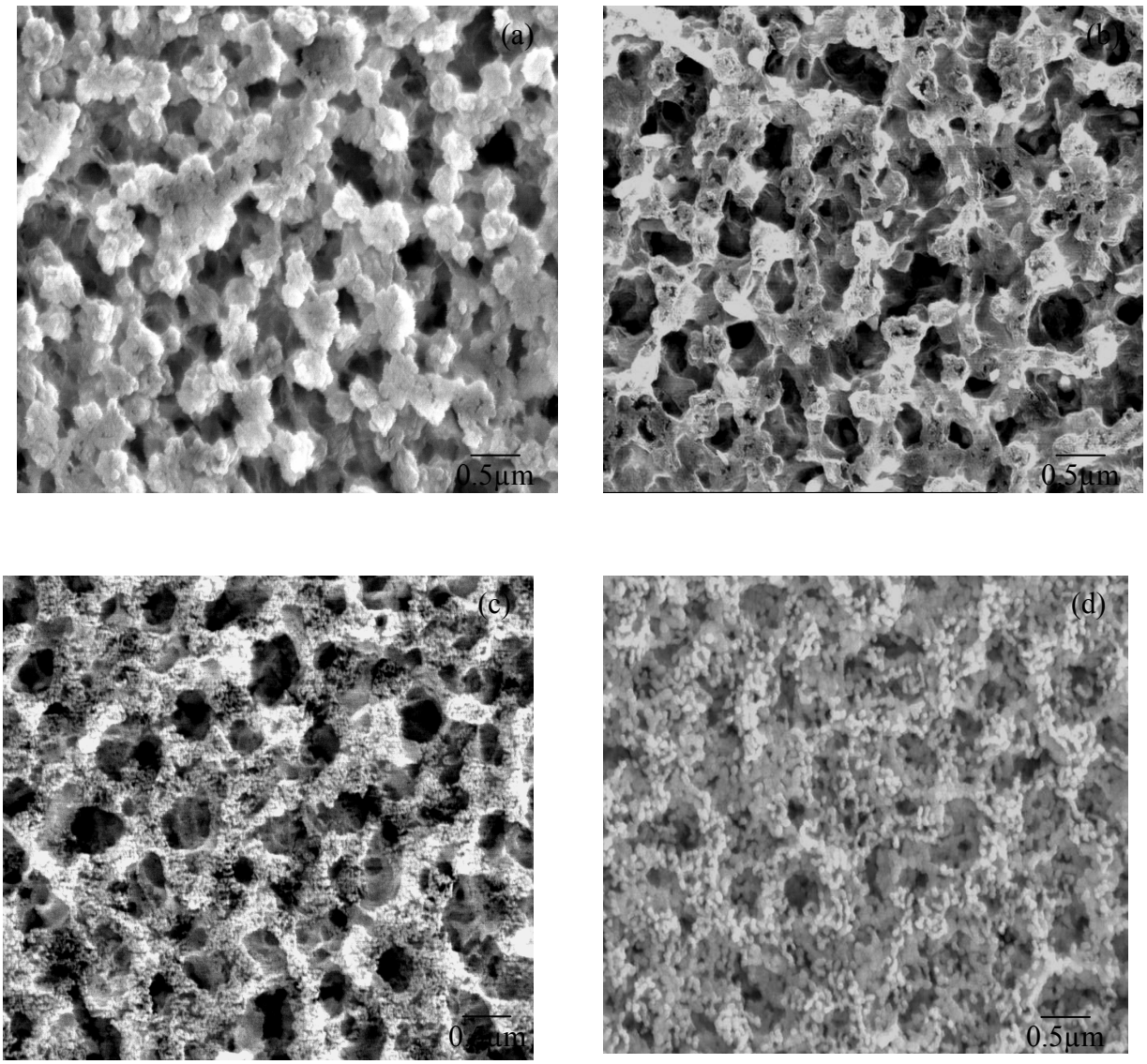

Figure 4. SEM surface morphology images at high magnifications of $SrCe_{0.95}Tb_{0.05}O_{3-\delta}$ after twenty-five spin-coating cycles at 3000 rpm for 20 s and sintering for 4 h at (a) 400 °C, (b) 600 °C, (c) 800 °C, and (d) 1000 °C.

Close inspection of the FIB images in Figure 5 indicate that by coupling the polymeric precursor synthesis with the spin-coating technique, the ceramic membrane thickness can be controlled precisely within a range of 0.2-2.2 μm, which implies the flexibility and advantages of the present technique. Another parameter, in addition to the number of spin coating cycles, that control the thickness of the film is the spin-coating revolution. Increasing the spin-coating revolution, from 3000 rpm to 5000 rpm for instance, can effectively decrease the film thickness. Since H_2 permeability is inversely proportional to film thickness, it is expected that this approach can lead to improved membranes with significantly higher H_2 flux compared with those having disk like geometry. This observation is in agreement with Iglesia and co-workers [19] who demonstrated that spin coated perovskite oxide dense films of 2 μm thickness generating H_2-flux about 500 times greater than those with 1 mm disk configuration at 677 °C.

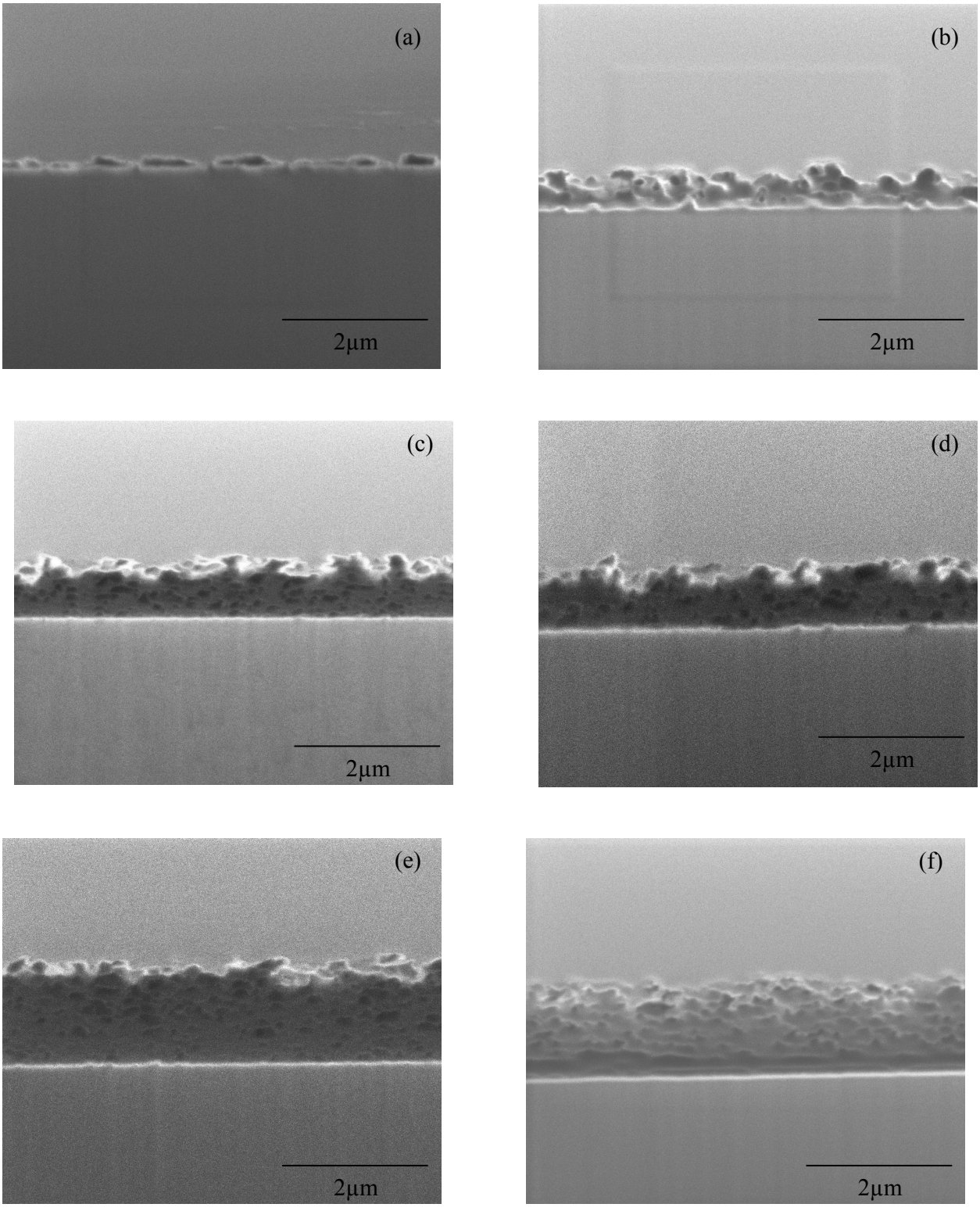

Figure 5. FIB high magnification film thicknesses of $SrCe_{0.95}Tb_{0.05}O_{3-\delta}$ after spin-coating at 3000 rpm for 20 s and sintering for 4 h: (a) 1 spin coating cycle-400 °C, (b) 5 spin coating-cycles-400 °C, (c) 10 spin-coating cycles-400 °C, (d) 15 spin-coating cycles-400 °C, (e) 25 spin-coating cycles-400 °C, and (f) 25 spin-coating cycles-1000 °C.

Surface Roughness of Membrane Thin Film—The surface roughness for the $SrCe_{0.95}Tb_{0.05}O_{3-\delta}$ membrane film, spin-coated ten times at 3000 rpm for 20 s and sintered at 400 °C for 4 h, was examined using AFM. Three-dimensional AFM surface roughness is shown in Figure 6. The AFM image corresponds to approximately 1.2 μm as shown in Figure 5. The apparent roughness of the film surface does not affect the spin-coating technique for producing dense surfaces because the new coating continuously fills the voids left behind in the previously deposited layers. The characteristic properties of the analyzed AFM surface include an average mean height of 1074 nm with maximum and minimum heights of 1302 and 857 nm, respectively. The image exhibits a maximum peak to valley height of 445 nm, and a root-mean-square roughness (or standard deviation) of about 483 °A.

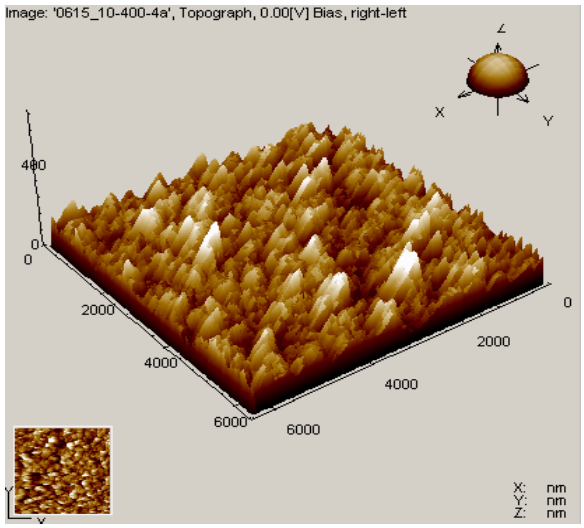

Figure 6. Three dimension AFM images of S $SrCe_{0.95}Tb_{0.05}O_{3-\delta}$ with ten coating-cycles (~1.2 μm) after spin-coating at 3000 rpm for 20 s and sintering for 4 h at 400 °C.

Effect of Calcination Temperature on Nanocrystallite Size—The broad and narrow XRD line traces for the $SrCe_{0.95}Tb_{0.05}O_{3-\delta}$ film obtained with twenty-five spin-coated cycles and sintered at 400-1000 °C, are presented in Figures 7 and 8 respectively. In Figure 7, the presence of XRD pattern strongly suggests the crystalline structure of the thin film membranes. The diffraction in peaks observed in Figure 7 is labeled according to the PDF card (No. 47-1689) of JCPDS-ICDD, which confirms the pervoskite-type crystal structure of these membranes.

In Figure 8, for the narrow scan analysis, the major peak (200) is chosen which shows that, with increasing the calcination temperature, the half width at half maximum intensity (HWHM) of the major peak decreases, which qualitatively suggests that, the nanocrystallite size within the thin film membrane decreases with increasing calcination temperature. The quantitative variation in the nanocrystallite size (*D*), as determined using Eq. 1, as a function of the calcination temperature (*T*) is presented in Figure 9, where the following relationship appears to hold,

$$D = 1.8\, e^{0.04T} \tag{2}$$

As shown in Figure 9, the average nanocrystallite size increases from 8 to 70 nm with increasing calcination temperature within the range of 400 to 0 °C. The increase in the nanocrystallite size results in lower grain boundaries and less defects in the membrane matrix.

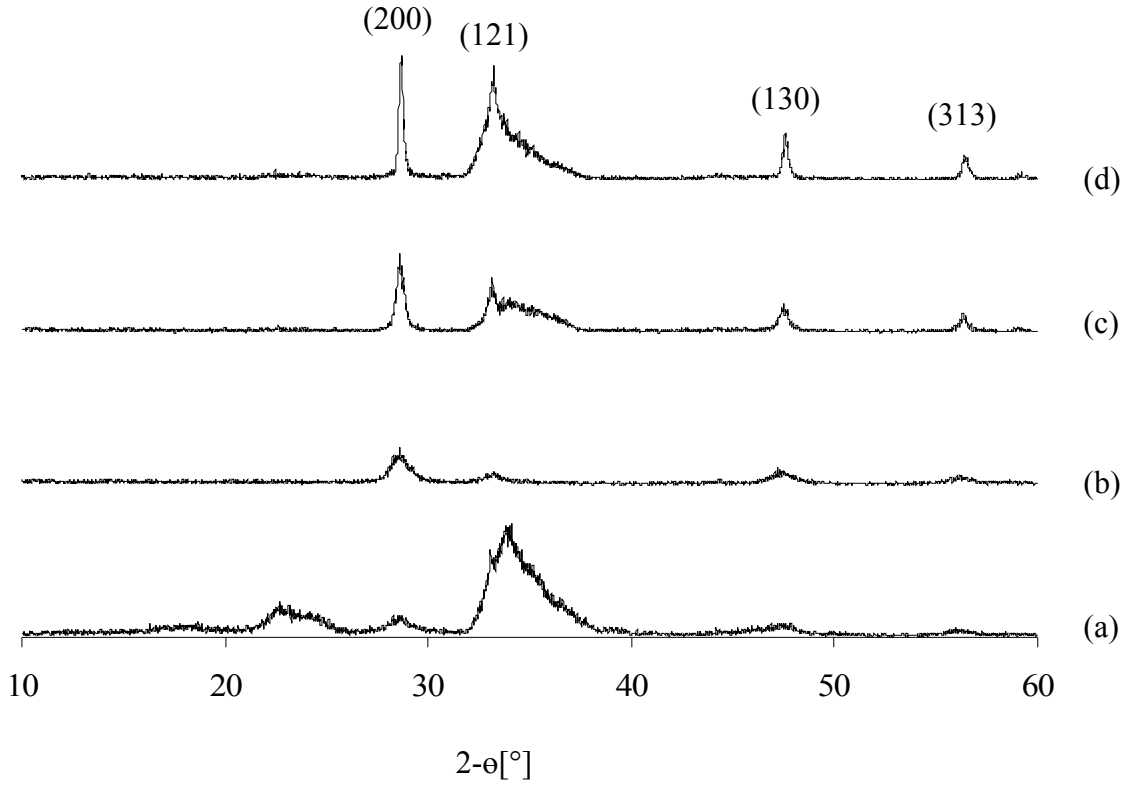

Figure 7. XRD broad scans of 25 spin-coated cycles of $SrCe_{0.95}Tb_{0.05}O_{3-\delta}$ at 3000 rpm for 20 s and sintering for 4 h at: (a) 400 °C, (b) 600 °C, (c) 800 °C, and (d) 1000 °C.

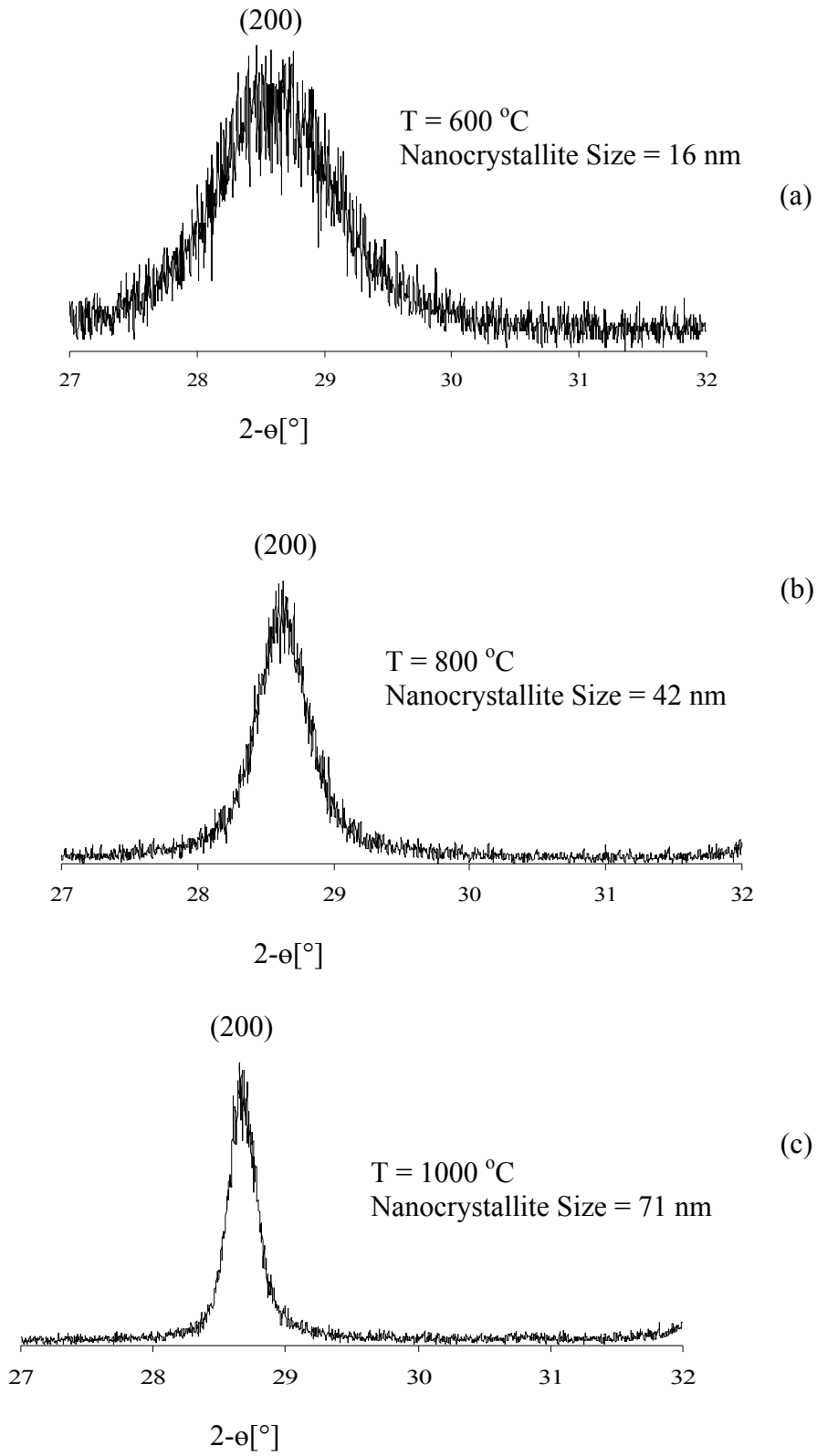

Figure 8. XRD narrow scans of twenty-five spin-coated cycles of $SrCe_{0.95}Tb_{0.05}O_{3-\delta}$ at 3000 rpm for 20 s and sintering for 4 h at (a) 600 °C, (b) 800 °C, and (c) 1000 °C.

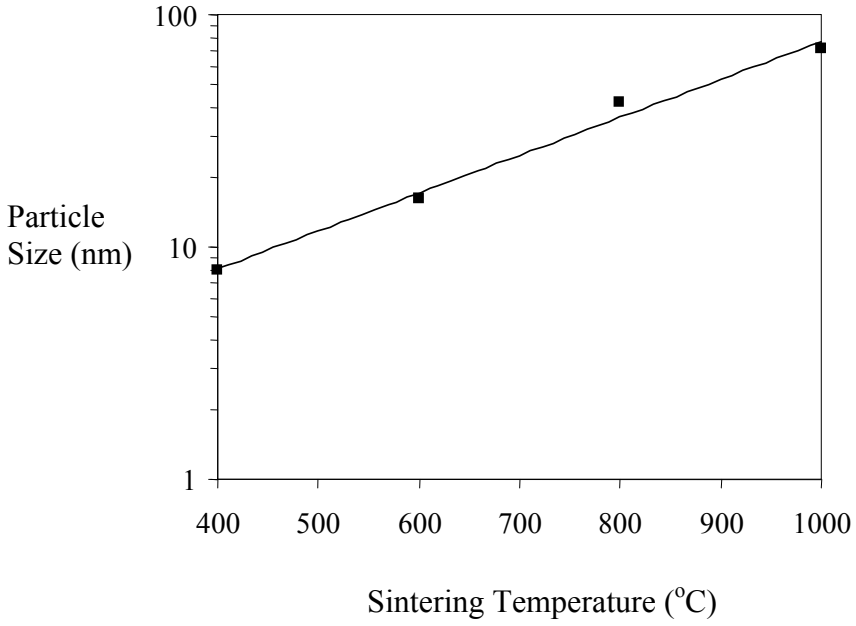

Figure 9. Variation in the particle size as a function of sintering temperature for twenty-five spin-coated cycles of $SrCe_{0.95}Tb_{0.05}O_{3-\delta}$ sintered for 4 h at 400, 600, 800, and 1000 °C.

Surface Chemistry of Membrane Thin Film—Typical XPS broad-scan spectrum within the range of 0-1100 eV B.E. obtained for $SrCe_{0.95}Tb_{0.05}O_{3-\delta}$ thin film, spin-coated twenty-five times and calcined at 400 °C, is presented in Figure 10. The broad-scan analysis indicates the presence of Sr, Ce, O, and Tb as major elements on the thin film membrane surface. The Ce $3d_{5/2}$ and Sr $3d_{5/2}$ B.E. levels of 882.0 and 133.0 eV are observed, which indicate the presence of Ce^{4+} and Sr^{2+} oxidation states within the coating. The broad Ce (3d) peak also suggests the possible presence of Ce^{3+} ions within the membrane thin film which indicates the existence of large number of oxygen-ion vacancies within the membrane thin film. The large oxygen-ion vacancy concentration is very essential for enhancing the H_2 permeation rate through membrane and also reducing its operating temperature.

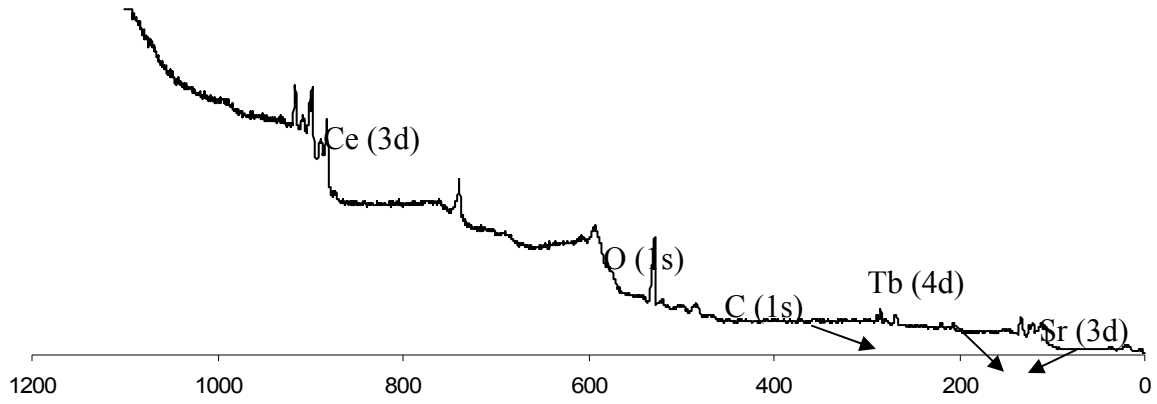

Figure 10. XPS analysis for the 25 spin-coating cycles $SrCe_{0.95}Tb_{0.05}O_{3-\delta}$ film at 3000 rpm for 20 s and sintered at 400 °C for 4 h.

Conclusions

The synthesis and characterization of nanocrystalline $SrCe_{0.95}Tb_{0.05}O_{3-\delta}$ thin film membranes were conducted by combining ethylene glycol chelating process with the spin-coating technique. The mechanism of nanocrystalline $SrCe_{0.95}Tb_{0.05}O_{3-\delta}$ thin film membrane formation via present polymer precursor has been confirmed using the FTIR and DTA/TGA analyses.

The polymeric precursor was deposited on silicone-based substrates and conversed to dense polycrystalline metal oxide films after annealing at 400-1000 °C for 4 h. The ethylene glycol polymerization forms a stable single phase solution between the metal cations and the polymeric network. The synthesis technique described in this work is a simple method to produce pervoskite-type ceramic thin films suitable for various H_2 separation applications.

It was demonstrated that continuous, pin hole-free and crack-free nanocrystalline $SrCe_{0.95}Tb_{0.05}O_{3-\delta}$ thin film membranes having a thickness in the range of 0.2-2 μm with nanocrystallite size (8-70 nm) can be synthesized by controlling the number of spin-coating cycles (1-25) and calcination temperatures (400-1000 °C). The SEM and FIB images show that multiple spin-coating cycles covers the cavities left behind from previous coated layer resulting in a dense membrane matrix. The SEM images demonstrated the strong effect of temperature on the surface morphology of $SrCe_{0.95}Tb_{0.05}O_{3-\delta}$ films

FIB images of $SrCe_{0.95}Tb_{0.05}O_{3-\delta}$ membranes suggest that the film thickness is directly proportional to the number of coating cycles applied. The FIB-milling process along with the spin coating technique provides a precise method for measuring and controlling the membrane film thickness within 0.2 μm. XRD analysis confirmed the perovskite structure of the strontium cerate oxide and showed that the nanocrystallite size increases as the annealing temperature was increased. AFM analysis for a film of about 1.2 μm in thickness spin-coated ten times at 3000 rpm for 20 s and sintered at 400 °C for 4 h shows that the film surface remained rough.

References

[1] F.S. Galaasso, Structure and Properties of Inorganic Solids, Pergamon Press, Oxford, (1970), 1st ed., Chapter 7.

[2] H. Iwahara, T. Esaka, H. Uchida, & N. Maeda, Proton Conduction in Sintered Oxides and its Application to Steam Electrolysis for Hydrogen Production, Solid State Ionics, 3/4, (1981), 359-363.

[3] S. Visco, L. Wang, S. Souza, & L. De Jonghe, Thin-Film Electrolytes for Reduced Temperature Solid Oxide Fuel Cells, Mat. Res. Soc. Symp., 369, (1995), 683-691.

[4] E. Wachsman, & M. Williams, Hydrogen Production From Fossil Fuels With High Temperature Ion Conducting Ceramics, The Electrochemical Society Interface Fall, (2004), 32-36.

[5] H. Fan, S. Lee, C. Yoon, G. Park, J. Choi, & H. Kim, Perovskite Structure Development and Electrical Properties of PZN Based Thion Films, J. European Ceramic Society, 22, (2002),1699-1704.

[6] M. Shah, & R. Drnevich, Integrated Ceramic Membrane System for Hydrogen Production, Proceeding of the 2000 Hydrogen Program Review; NREL/CP-750-28890.

[7] F. Lau, & S. Doong, Coal to Hydrogen: A Novel Membrane Reactor for Direct Extraction, Gas Technology Institute Presentation at GCEP Energy Workshops at Stanford University, April 26-27, 2004.

[8] J. Schwartz, R. Drnevich, P. Apte, & A. Damle, Integrated Ceramic Membrane System for H_2 Production, DOE Annual Merit Review Meeting (Cooperative Agreement: DE-FC36-00G010534), May 19, 2003.

[9] S. Song, E. Wachsman, J. Rhodes, S. Dorris, & U. Balachandran, Hydrogen Permeability of $SrCe_{1-x}M_xO_{3-\delta}$ (x = 0.05, M = Eu, Sm), Solid State Ionics,167, (2004), 99-105.

[10] X. Qi, & Y. Lin, Electrical Conducting Properties of Proton-Conducting Terbium-Doped Strontium Cerate Membrane, Solid State Ionics,120, (1999), 85-93.

[11] S. Hamakawa, L. Li, A. Li, & E. Iglesia, Synthesis and Hydrogen Permeation Properties of Membranes Based on Dense $SrCe_{0.95}Yb_{0.05}O_{3-\delta}$ Thin Films, Solid State Ionics, 48, (2002), 71-81.

[12] R. Slade, & N. Singh, Generation of Charge Carriers and H/D Isotope Effect in Proton-Conducting Doped Barium Cerate Ceramics, J. Mater. Chem., 1(3), (1991), 441-445.

[13] K. Takeuchi, C. Loong, J. Richardson Jr., J. Guan, S. Dorris, & U. Balachandran, The Crystal Structure and Phase Transition in Y-Doped BaCeO3: Their Dependence on Y Concentration and Hydrogen Doping, Solid State Ionics,138, (2000), 63-77.

[14] V. Agarwal, & M. Liu, Preparation of Barium Cerate-Based Thin Films Using a Modified Pechini Process, J. mat. Sci., 32, (1997), 619-625.

[15] J. Muller, K.D. Kreuer, J. Maier, S. Matsuo, & M. Ishigame, A Conductivity and Thermal Gravimetric Analysis of a Y-Doped $SrZrO_3$ Single Crystal, Solid State Ionics, 97, (1997), 421-427.

[16] J. Guan, Ceramic Membranes of Mixed Ionic-Electronic Conductors for Hydrogen Separation, Ph.D. Thesis, Georgia Institute of Technology, (1986).

[17] K.D. Kreuer, Proton-Conducting Oxides, Annual Review Mater. Res., 33, (2003), 333-359.

[18] H. Iwahara, *High Temperature Proton Conductors Based on Perovskite-Type Oxides*, in: Proton Conductors - Solids, Membranes and Gels-Materials and Devices, P. Colomban, Cambridge University Press, Cambridge, 1992, Chapter 8, 122-137.

[19] S. Haile, G. Stanefe, & K. Ryu, Non-Stoichiometry, Grain Boundary Transport and Chemical Stability of Proton Conducting Perovskites, J. Membr. Sci., 36, (2001), 1149-1160.

[20] K.D. Kreuer, On the Development of Proton Conducting Materials for Technological Applications, Solid State Ionics, 97, (1997), 1-15.
[21] D. Dionysiou, X. Qi, Y. Lin, G. Meng, & D. Peng, Preparation and Characterization of Proton Conducting Terbium Doped Strontium Cerate Membranes, J. membr Sci., 154, (1999), 143-153.
[22] F. Garzon, R. Mukundan, & E. Brosha, Enabling Science for Advanced Ceramic Membrane Electrolyzers, Proceeding of the 2002 U.S. DOE Hydrogen Program Review; NREL/CP-610-32405.
[23] C. Zuo, T. Lee, S. Dorris, & U. Balachandran, M. Liu, Composite Membranes for Hydrogen Separation, Abs. 1053, 204th Meeting of the Electrochemical Society (2003).
[24] X. Qi, & Y. Lin, Electrical Conduction and Hydrogen Permeation Through Mixed Proton-Electron Conducting Strontium Cerate Membranes, Solid State Ionics, 130, (2000), 149-156.
[25] J. Eschenbaum, J. Rosenberger, R. Hempelman, D. Nagengast, & A. Weidinger, Thin Films of Proton Conducting $SrZrO_3$-Ceramics Prepared by the Sol-Gel Method. Solid State Ionics, 77, (1995), 222-225.
[26] H. Hwang, A. Towata, M. Awano, & K. Maeda, Sol-Gel Route to Perovskite-Type Sr-Substituted $LaCoO_3$ Thin Films and Effects of Polyethylene Glycol on Microstructure Evolution, Scripta Mater, 44, (2001), 2173-2177.
[27] B. Zhu, K. Rundgren, & B. Mellander, Ceramic Membranes – Potential Uses for Solid State Protonic Conductors, Solid State Ionics, 97, (1997), 385-391.
[28] M.M. Elbaccouch, & A. T-Raissi, Hydrogen Flux in Terbium Doped Strontium Cerate Membrane, in the Proceedings of the 30th International Conference on Advanced Ceramics and Composites, Cocoa Beach, FL, January 22-27, 2006.
[29] T. Suzuki, I. Kosacki, & H. Anderson, Microstructure-Electrical Conductivity Relationships in Nanocrystalline Ceria Thin Films, Solid State Ionics, 151, (2002), 111-121.
[30] N. Sata, H. Matsuta, Y. Akiyama, Y. Chiba, S. Shin, & M. Ishigame, Fabrication of Proton Conducting Thin Films of SrZrO3 and SrCeO3 and Their Fundamental Characterization, Solid State Ionics, 97, (1997), 437-441.
[31] H. Anderson, M. Nasrallah, & C. Chen, Method of Coating a Substrate With a Metal Oxide Film From an Aqueous Solution Comprising a Metal Cation and a Polymerizable Organic Solvent, United States Patent 5,494, 700, April 5, 1994.
[32] C. Chen, M. Nasrallah, & H. Anderson, Synthesis and Characterization of $(CeO_2)_{0.8}$ $(SmO_{1.5})_{0.2}$ Thin Films From Polymeric Precursors, J. Electrochem. Soc.,140 (12), (1993), 3555-3560.
[33] B.I. Prenitzer, L. Giannuzi, K. Newman, S. Brown, R. Irwin, T. Shoftner, & F. Stevie, Transmission Electron Microscope Specimen Preparation of Zn Powders Using the Focused Ion Beam Lift-Out Technique. Mater. Trans. A Physical Metallurgy and Materials Science, 29(9), (1998), 2399-2406.
[34] S. Shukla, S. Seal, J. Akesson, R. Oder, R. Cater, & Z. Rahman, Study of Mechanism of Electroless Copper Coating of Fly-Ash Cenosphere Particles, Applied Surface Science, 181, (2001), 35-50.
[35] J. Akesson, S. Seal, S. Shukla, & Z. Rahman, Copper Plating Process Control by SEM, Advanced Materials & Processes, (2002), 33-35.
[36] B. Cullity, & S. Stock, Elements of X-Ray Diffraction. Prentice-Hall, New Jersey, 2001.
[37] T. Barr, & S. Seal, Nature of the Use of Adventitious Carbon as a Binding Energy Standard, J. Vac. Sci.Technol., 3(3), (1995), 1239-1246.

***Task #3:* Development of Ceramic Oxide Thin Films Using Tape-Casting Process, Mohamed M. Elbaccouch , Clovis Linkous, and Ali T-Raissi (Florida Solar Energy Center)**

Abstract -- The objective of this work is to fabricate a tubular membrane reactor that could be used at high temperatures (above 550 ^{o}C) for hydrogen (H_2) separation and purification. The fabricate tubular membrane support (SrCeO3-NiO) composite was prepared via the tape-casting process and rolling. The tubular reactor is a mixed ionic-electronic conductive system with a doped perovskite structure ($A^{2+}B^{4+}O_3$-doped with a trivalent cation). The reactor consists of a porous $SrCeO_3$-NiO composite support and a dense thin film membrane of $SrCe_{0.95}Y_{0.05}O_{3-\alpha}$.

The support and membrane powders were synthesized by the solid state reaction method. The support material, composed of the ceramic powder, binder, plasticizer, and solvent, was formulated into homogeneously dispersed slurry with uniform structure. The tape-casting process was used to produce a thin film support tape by the shearing action of a doctor blade on the ceramic slurry. After drying, the tape was cut and rolled on a rod producing a tubular geometry. Slow sintering and H_2 atmosphere exposure burned off the organic materials, producing a ceramic composite tube with appreciable porosity.

Introduction -- The objective of this work is to fabricate a tubular membrane reactor that could be used at high temperatures (above 550 ^{o}C) for hydrogen (H_2) separation and purification. The tubular reactor is a mixed ionic-electronic conductive system with a doped perovskite structure ($A^{2+}B^{4+}O_3$-doped with a trivalent cation). The reactor consists of a porous $SrCeO_3$-NiO/or carbon black composite support and a dense thin film membrane of $SrCe_{0.95}Y_{0.05}O_{3-\alpha}$.

The support and membrane powders were synthesized by the solid state reaction method. The support material composed of the ceramic powder, polyvinyl alcohol (as binder), glycerin (as plasticizer), and water (as solvent), was formulated into homogeneously dispersed slurry with uniform structure. The tape-casting technique was used to produce a thin film support by shearing action of a doctor blade on ceramic slurry. After drying, the tape was cut and rolled on a rod producing a tubular geometry. Slow sintering and H_2 atmosphere exposure burned off the organic materials, producing a porous ceramic composite tube.

Experimental

Chemicals -- Strontium carbonate ($SrCO_3$) (99.99%) (metal basis), and cerium (IV) oxide (CeO_2) were obtained from Alfa Aesar. Yittrium (III) oxide (Y_2O_3) (99.999%), nickel (II) oxide (NiO) (97%), and glycerin ($CH_2OHCHOHCH_2OH$) (99.5%) were acquired from Fisher Scientific. Hydrolyzed polyvinyl alcohol (99%) was purchased from Aldrich. Mylar film (3 mil thick, silicone coated) was obtained from Richard E. Mistler, Inc. All chemicals were used as-received without further purification.

Instrumentation -- The perovskite crystal structure and purity of the ceramic powders were determined using Rigaku XRD utilizing Cu Kα, with radiation wavelength of 1.54 Å, rate of 1.2 ^{o}C/min, and 2 θ range of 20 to 80 degrees. Sintering was done in a high temperature furnace (1760 ^{o}C max.) obtained from Micropyretics Heaters International (Model Z18-40). Ball milling machine and 0.25 inch ziconia balls were obtained from U.S. Stoneware.

Results and Discussion

Powder Preparation -- The membrane powders were weighed and mixed to form a stoichiometric mixture representative of $SrCe_{0.95}Y_{0.05}O_{3-\alpha}$ and $SrCeO_3$-NiO. Each powder was ball milled at 85 rpm for 24 h using zirconia balls and polypropylene bottles in ethanol. The slurry was dried in air, sieved to 45 µm, and sintered to 1150 ^oC in air (membrane film) and 1100 ^oC in air (support) for 10 h (ramp 3 ^oC/min). The membrane powder was ball milled again in ethanol for 24 h, dried and sieved to 45 µm, and sintered at 1500 ^oC in air for 10 h (ramp 3 ^oC/min). Figure 1 depicts the XRD spectra of the $SrCe_{0.95}Y_{0.05}O_{3-\alpha}$ powder after each processing step. Figure 1a depicts XRD spectra for the as prepared powder, Figure 1b shows the XRD spectra for the pre-sintered powder at 1150 ^oC in air, and Fig. 1c depicts the XRD spectra for sintered powder at 1500 ^oC in air.

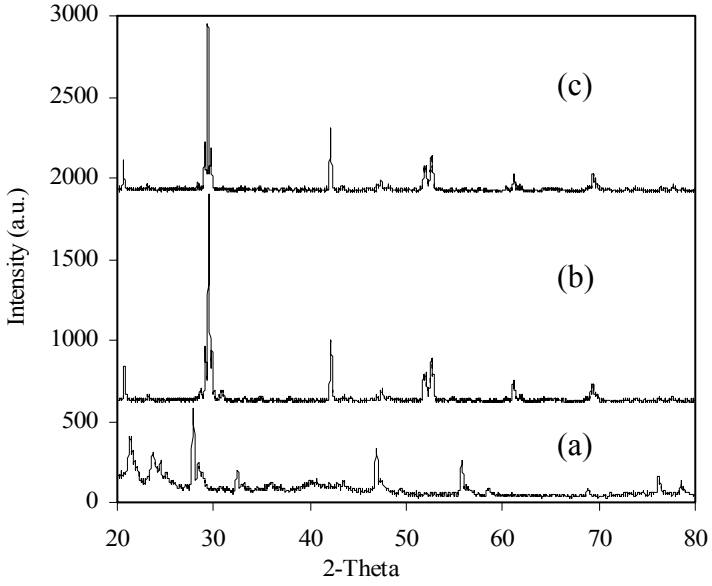

Figure 1. XRD spectra for $SrCe_{0.95}Y_{0.05}O_{3-\alpha}$ powder. a) mixed powder - as is, b) ball milled powder for 24 h and sintered for 10 h at 1150 ^oC, and c) ball milled powder for 24 h and sintered for 10 h at 1500 ^oC.

Figure 2 depicts the XRD spectra of the $SrCeO_3$-NiO powder. The single phase perovskite structure was confirmed by comparing the XRD patterns in Fig. 1 with the standard XRD spectra of $SrCeO_3$. Also, the composite structure of SrCeO3-NiO in Figure 2 was in agreement with the reference $SrCeO_3$ and NiO patterns.

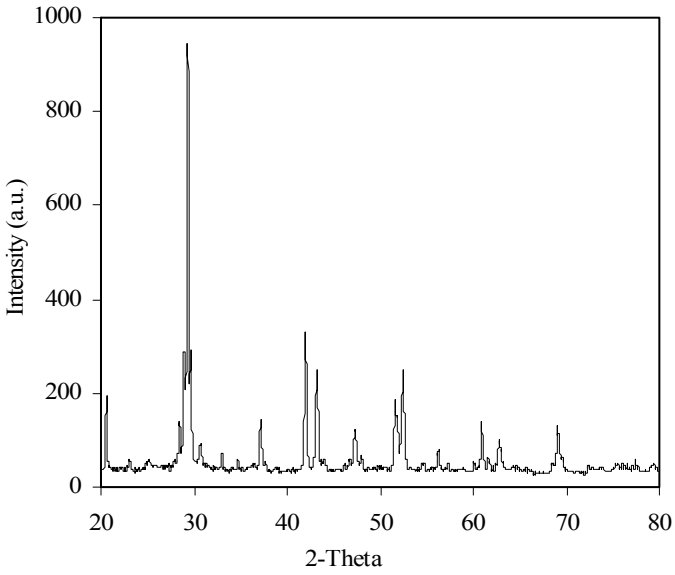

Figure 2. XRD spectra for $SrCeO_3$–NiO composite at 1100 ^oC. The spectra show major perovskite and NiO peaks.

Figure 3 depicts a membrane disk of $SrCe_{0.95}Y_{0.05}O_{3-\alpha}$ sintered at 1150 ^oC for 10 h and then at 1500 ^oC for 10 h using MHI high temperature furnace (1760 ^oC max). The powder was weighed in stoichiometric ratio and ball milled in polypropylene bottle with zirconia balls using a U.S. Stoneware ball milling machine. In stage 1, the powder was ball milled at 90 rpm for 24 h in ethanol. The ethanol was dried over night and the powder was pre-sintered at 1100-1250 C for 10 h. In stage 2, the pre-sintered powder was ball milled at 90 rpm for 24 h in ethanol. The ethanol was dried overnight and the powder was sintered at 1400-1500 ^oC for 10 h.

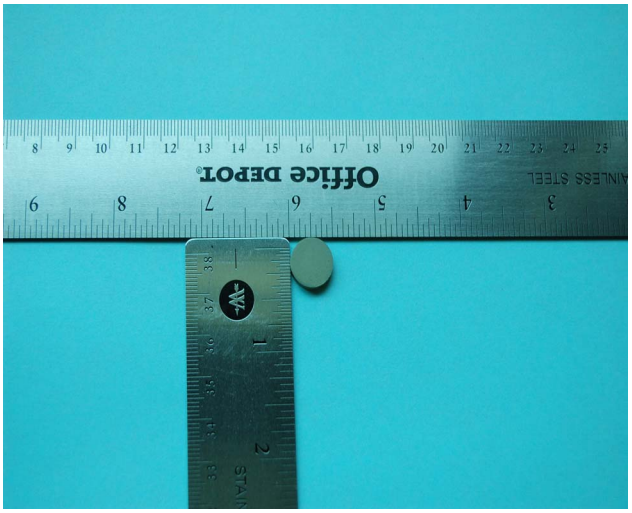

Figure 3. A 2 mm membrane disk of $SrCe_{0.95}Y_{0.05}O_{3-\alpha}$ synthesized by the solid state technique and sintered at 1150 ^oC for 10 h and 1500 ^oC for 10 h.

Tape-Casting Process

Aqueous based Slurry - The conditions employed in preparation of the tape-casting slurry are listed in Table 1 [1]. Tape-casting was done on a stationary-assembled set. The Mylar film was

supported by a clean plate glass [2]. The slurry composite was placed on the Mylar film using the drop-wise method. Doctor blade was used to cast tapes with a thickness of 0.04 inches. The green-tape was air-dried for 24-48 h, then cut and rolled on a rod. The binder gives the green-tape enough strength for it to be removed from the Mylar film without breakage. A schematic diagram of the tape-casting process is given in Figure 4.

Table 1. Conditions for the preparation of the $SrCeO_3$-NiO tape slurry using an aqueous-based solvent.

Metal Precursor	SrCeO3-NiO composite containing 30 wt% NiO
Solvent	18 vol% water with respect to powder composite
Ball mill	5 h, 85 rpm
Additives	Weight ratio of powder composite: binder (polyvinyl alcohol) : plasticizer (glycerin) was 85:10:5
Ball mill	24 h, 85 rpm

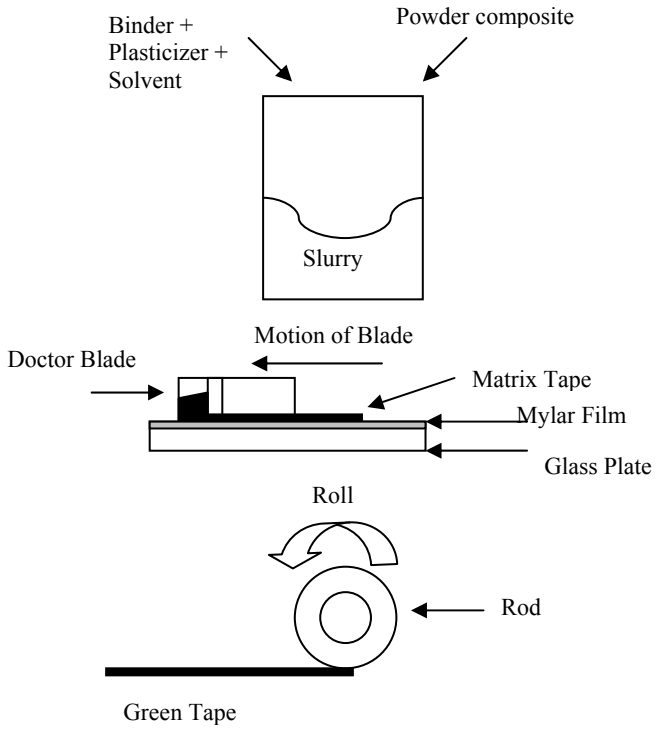

Figure 4. Schematic of the tape-casting process.

Smooth green tapes with good mechanical strength are obtained as shown in Figure 5. The tape has a thickness of less than 0.001 and was cut into different geometry and shapes. It was easier to remove the dried green-tape from a Mylar substrate than a glass substrate. Figure 6 depicts a pre-sintered SrCeO3-NiO tape that was rolled on a rod at 500 ^{o}C in air for 3 h at a

heating rate of 0.5 ^{o}C/min. A significant shrinkage was observed when the tape was sintered at 700 ^{o}C with poor mechanical strength.

Figure 5. An aqueous based-slurry green tape is casted using Mylar film and doctor blade.

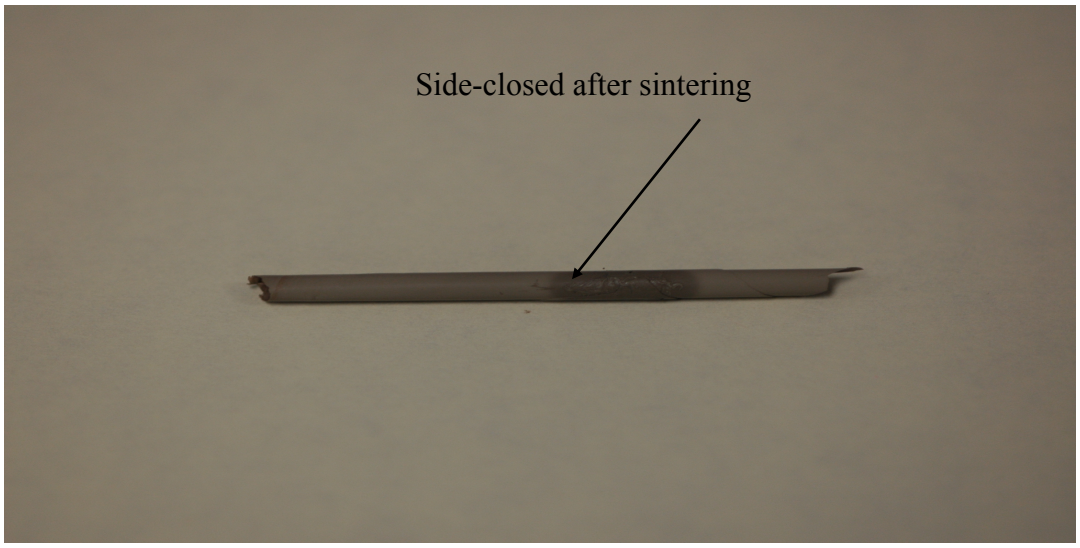

Figure 6. Pre-sintered SrCeO3-NiO tape at 500 ^{o}C for 3 h at 0.5 ^{o}C/min ramp.

Organic-based Slurry - The conditions used in preparing the organic-based tape-casting slurry of SrCeO3-NiO are given in Table 2 [3]. Figures 7 a and b shows a 0.23 inch thick green tape of SrCeO3-NiO and the corresponding SEM morphology.

Table 2. Conditions for the preparation of the $SrCeO_3$-NiO tape Slurry using an organic-based solvent.

	Component	Function	Parameters
Step 1	$SrCeO_3$ + NiO	Powder	Ball mill in ethanol for 24 h & sinter at 1150 °C for 10 h
Step 2	$SrCeO_3$ + NiO	Powder	20.59g; NiO load = 30 wt%
	Solsperse, 20000 MW	Dispersant	0.21g
	Toluene	Solvent	3.60g
	Ethyl Acetate	Solvent	2.24g
	Ethanol	Ball milling solvent, 12 h at 90 rpm	Add to slurry & zirconia balls leaving 25% of silica-based mill jar empty
	Di- Butyl Phthalate $C_{16}H_{22}O_4$	Plasticizer	0.91g
Step 3	Polyvinyl Butyral, 18,000 MW	Binder	1.42g
		Ball mill for 20 h at 90 rpm	

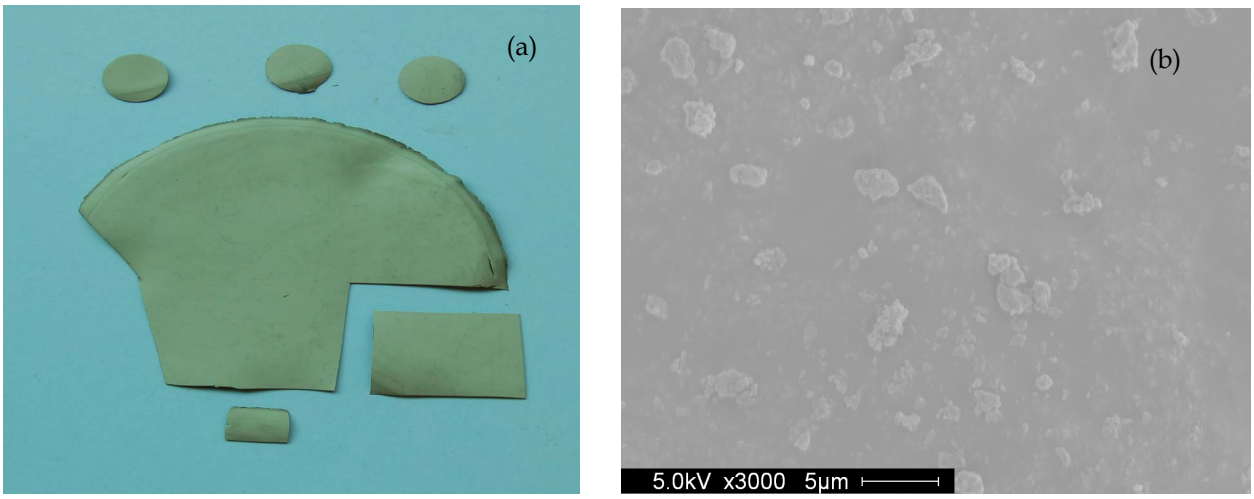

Figure 7. SrCeO3-Nio green tape casted using an organic-based slurry. (a) Green tape cut into different geometry. (b) SEM image of the green tape.

Figure 8 shows SEM surface morphology of a tubular support heated in air at 0.3 C/min to 900 and sintered for 5 h. Approximately 25% shrinkage was observed during the sintering process as the tube was weight before and after sintering. The SEM analysis shows that the sintered tube has no cracks, but it has obvious pinholes due to the low sintering temperature. Higher sintering temperature is needed in order to obtain dense surface.

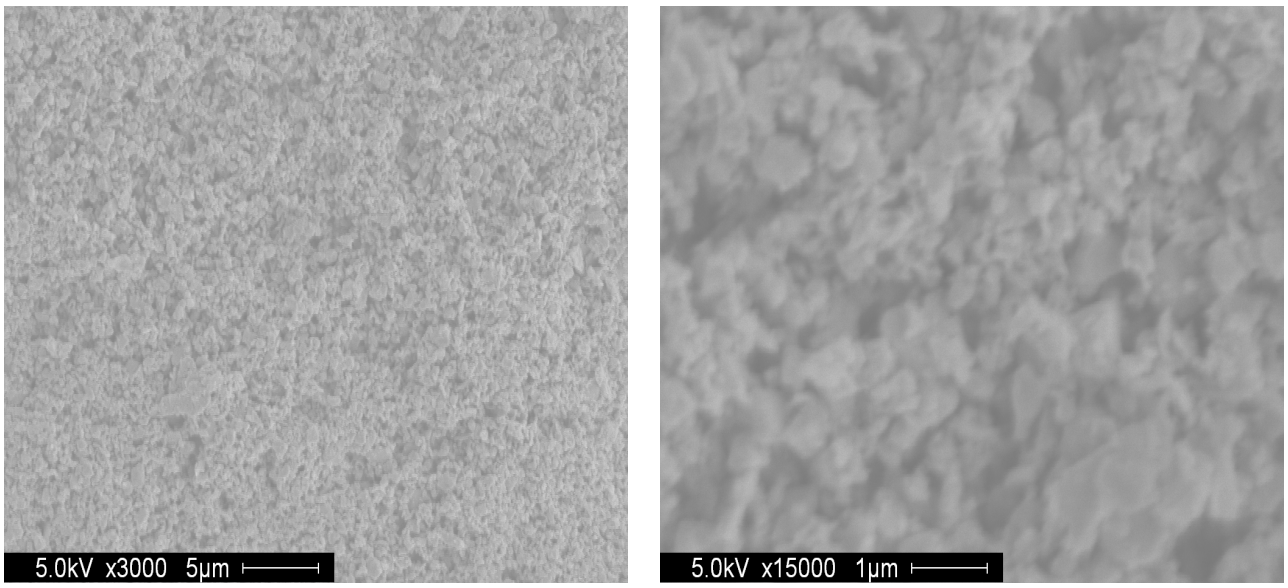

Figure 8. Surface morphology of a tubular support heated in air at 0.3 C/min to 900 and sintered for 5 h.

Figure 9 shows the surface morphology of a tubular support sintered by two stages. In stage one, the tube was heated in air at 1 C/min to 900 C and sintered for 5 h. In stage two, the tube was heated in air at 1 C/min to 1100 and sintered for 5 h. The surface morphology shows an improvement in densification compared to that in Figure 7 due to the higher sintering temperature.

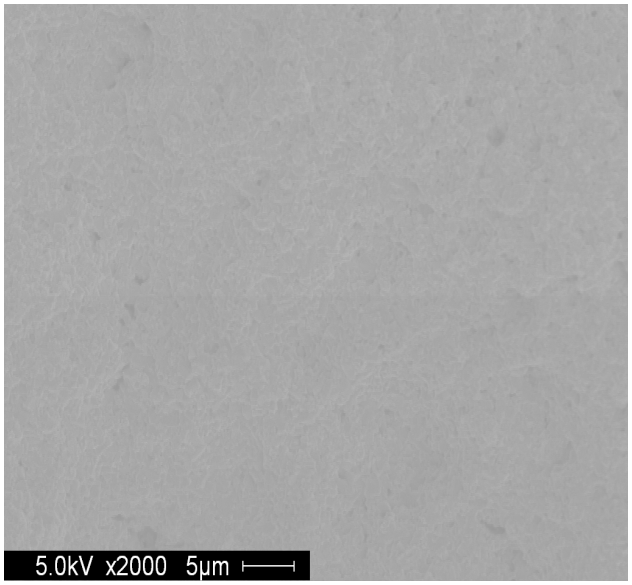

Figure 9. Surface Morphology of Tubular Support: Stage 1: heated in air at 1 ºC/min to 900 ºC & sintered for 5 h. Stage 2: heated in air at 1 ºC/min to 1100 ºC & sintered for 5 h.

Figure 10 shows the surface Morphology of a green tape heated in H_2 at 1 ^{o}C/min to 850 ^{o}C and sintered for 5 h. Significant weight loss was observed due to burning the organic material in hydrogen atmosphere.

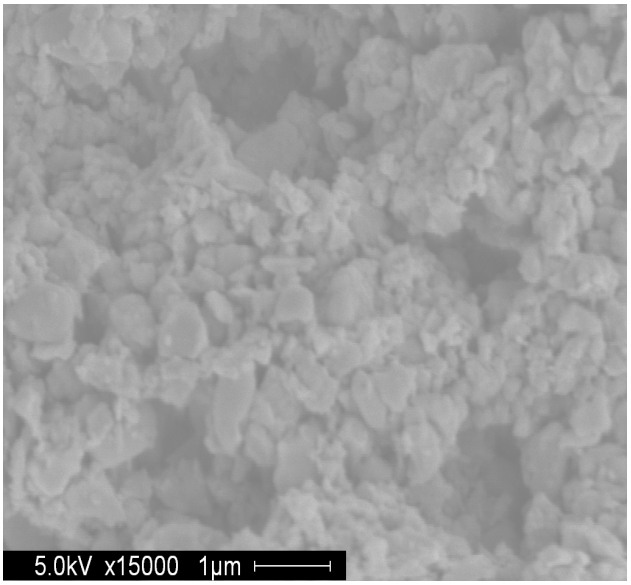

Figure 10. Surface Morphology of a green tape heated in H_2 at 1 ^{o}C/min to 850 ^{o}C & sintered for 5 h.

Figure 11 shows a dense surface Morphology of a green tape obtained by heating in air 0.3 ^{o}C/min to 1400 ^{o}C & sintered for 5 h.

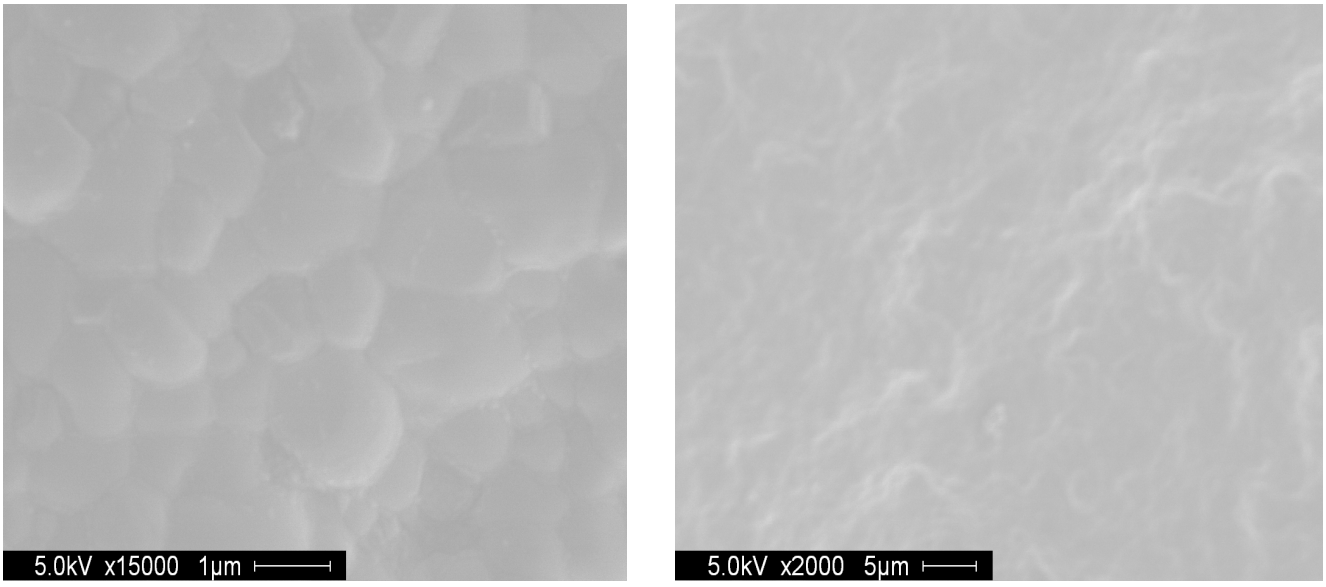

Figure 11. Dense surface morphology of a green tape obtained by heating in air at 0.3 ^{o}C/min to 1400 ^{o}C and sintered for 5 h

Conclusions

Flexible and structurally smooth tapes of $SrCeO_3$-NiO were successfully produced via water-based solvent tape-casting technique. The structure of the membrane film and the supporting tape were confirmed by XRD. Also, a high temperature $SrCeO_3$-NiO tubular support was fabricated using an organic-based solvent and tape-casting process. The aqueous-based formulation produced tapes with good mechanical strength at room temperature, but crumbles when sintering it at high temperatures. The organic-based formulation can be bladed effectively to fabricate support tapes. The fabricated $SrCeO_3$-NiO green support tapes can be cut easily & rolled into tubes & support layers. Dense $SrCeO_3$-NiO surface was produced at 1400 ^oC with good mechanical strength, smooth morphology, and no cracks.

References

[1] Ramanathan, S.; Krishnakumar K. P.; De P. K.; and Banerjee S. *J. mater. Sci.*, **2004**, 39, 3339.
[2] Murphy M. W.; Armstrong T. R.; Smith P. A. *J. Am. Ceram. Soc.*, **1997**, 80(1), 165.
[3] University of Florida mid-term report submitted to the Florida Solar Energy Center, 2006.

Peer Reviewed Publications, Conference Papers, and Patents

1. Elbaccouch M.; Shukla S.; Mohajeri N.; Seal S.; and T-Raissi A. "Microstructural Analysis of Doped-Strontium Cerate Thin Film Membranes Fabricated via Polymer Precursor Technique" *Solid State Ionics*, 178(1-2), 19-28, 2007.
2. Elbaccouch M.; and T-Raissi A. "Development of Ceramic Oxide Thin Film Using the Tape-Casting Process" In the Proceedings of the *234th ACS National Meeting*, Boston, MA, August 19-23, 2007.
3. Shukla S.; Elbaccouch M.; Seal S.; and T-Raissi A. "Effect of Temperature and Spin-Coating Cycles on Microstructure Evolution for Tb-Substituted $SrCeO_3$ Thin Membrane Films" in the Proceedings of the 30*th International Conference on Advanced Ceramics and Composites,* Cocoa Beach, FL, vol. 27, no. 3, pp 285-294, 2006.
4. Elbaccouch M.; and T-Raissi A. "Hydrogen Flux in Terbium Doped Strontium Cerate Membrane" in the Proceedings of the *30th International Conference on Advanced Ceramics and Composites,* Cocoa Beach, FL, vol. 27, no. 4, pp 119-123, 2006.
5. Elbaccouch M.; Shukla S.; Mohajeri N.; Seal S.; and T-Raissi A. "Characterization of Spin-Coated Terbium-Doped Strontium Cerate Thin Film Membranes" in the Proceedings of the *29th International Conference on Advanced Ceramics and Composites*, Cocoa Beach, FL, vol. 26, no.3, pp 219-227, 2005.

September 2007

Compact, Lightweight, and Optimized Fuel Cells for Space and Aircraft Power

J. Fenton, P. Choi, L. Bonville, and R. Kunz
Florida Solar Energy Center

Research Period: June 2005 to February 2008

Abstract

This study was performed to determine techniques for improving proton exchange membrane (PEM) fuel cell performance when operating on dry reactants that are known to harm performance. The use of reactant recirculation, water recirculation, and a cell with a membrane additive were considered. For reactant recirculation, a simple mass balance model was used to determine the membrane inlet relative humidity (RH) for a fuel cell operating on dry reactant gases. Calculations, with cell temperature, cell pressure, reactant stoichiometry and reactant recycle as variables, generated strategies for internally humidifying the stack and for operation under conditions which maximize power density. These calculations showed cathode recycle was much more effective than anode recycle at increasing the membrane inlet relative humidity; but they also showed that, for reasonable total flow rates, the losses due to reduced reactant pressures were much higher than the gains for the increased membrane water content.

In a parallel effort single-cell and multi-cell tests were designed and implemented to demonstrate the operation of a water transport device for the recirculation of water. These tests included internal recirculation of anode and cathode exhaust streams with an internal humidifier that uses a Nafion® membrane as a separator between the exhaust and the inlet gases. Using simple models and this experimental data, the inlet and exit membrane relative humidities were calculated.

Tests were conducted with commercial MEAs as well as with FSEC's thin composite membranes (Nafion – Teflon – Phosphotungstic Acid). Unexpectedly, the performance improvement for anode humidification was much higher than anticipated. The cell performance of the composite membrane was higher than that of commercial Nafion® 112 membranes and MEAs from a commercial source (Ion Power). Synthesis of thin composite membranes and the incorporation of water management strategies using internal humidification improved the performance and reduced the volume of the conceptual fuel cell systems.

Introduction

PEM fuel cells are potentially the most effective energy conversion devices for space applications. Conventional PEM fuel cells use external humidification requiring cumbersome humidification devices, which increase the volume and complexity of the system, making them less valuable for space applications. However, it has proven to be a challenge to achieve efficient fuel cell operation without external humidification of reactant gases.[1,2] The objective of this research is to develop highly efficient and compact fuel cell systems which include effective membrane electrode assemblies and internal water management systems. Some of the many approaches that have been proposed to provide or maintain water content within the MEA without external humidification include the use of i) water absorbing material in the membrane,[3,4] ii) catalyst particles (i.e., Pt) in the membrane,[5] iii) catalyst particles along with water absorbing material,[6] iv) water absorbing materials in flow channels,[7] v) flow channel designs (e.g., counter flow[8] or double path type flow field[9]), vi) additional humidity section within each cell,[10] and vii)

circulation of reactants. Internal humidification by supplying water into fuel cell stack has also been reported.[3] Nevertheless, these approaches have certain drawbacks. For example, the materials added into the membrane can be leached out during fuel cell operation, and a short circuit can occur when using Pt in methods i)-iv). Method v) may cause flooding or increased pressure drop, and stable bonding between the material additive and the bipolar plate can be an issue. Method v) is limited by the rate of water diffusion into dry gas. Method vi) may need to separate inert gases from the reactant gases before the cell which would be more difficult than the external humidification that it replaces.

For highly efficient and durably MEAs, proton exchange membranes require high proton conductivity and stability at the operating conditions of the fuel cell stack. Nafion® is the most commonly used membrane material in proton exchange membrane fuel cells. However, Nafion is expensive and effective only when it has sufficient water. To meet fuel cell requirements, the proton exchange membrane needs to be highly proton conductive, thin for low resistance, compliant to make good contact with the catalyst layers, but rigid enough to maintain contact with the gas diffusion layers, and thermally and mechanically stable. There have been many approaches to improve the conductivity and stability of the membranes. Here we explore improved water management along with organic/inorganic composite membranes as alternatives to the commercial proton conducting membranes. The inorganic materials are expected to help to conduct protons so that reasonable conductivity can be maintained even in low relative humidity conditions.

Background

It is important to develop an efficient and compact fuel cell for space application. In this work, we have investigated the effectiveness of internal humidifier in which the humid gas coming out of the cell provides water vapor and heat to the incoming dry feed gas for the cell (Figure 1).

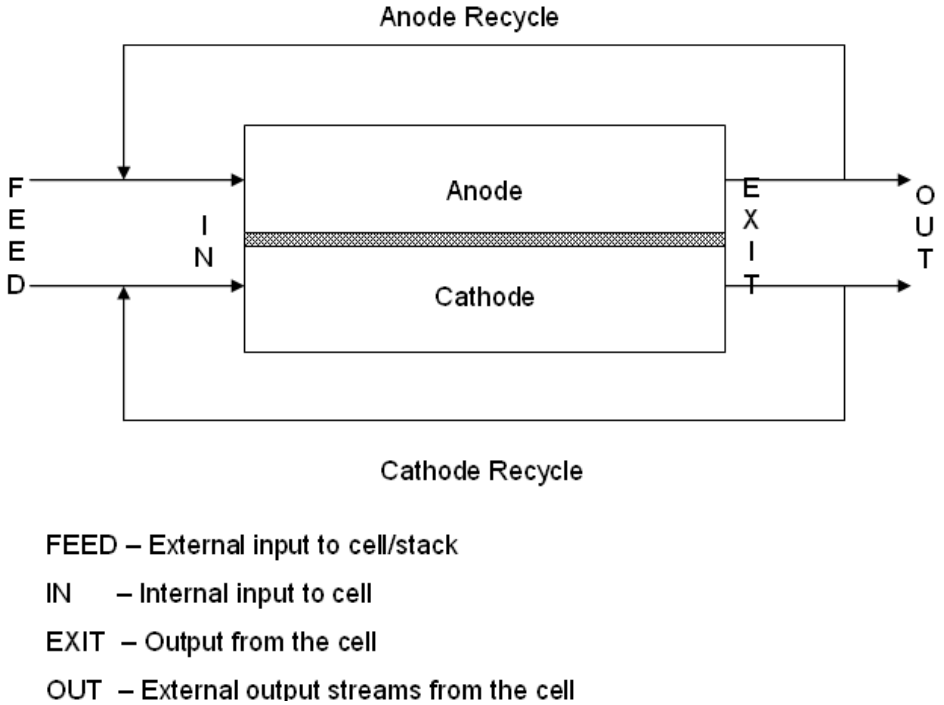

Figure 1. Schematic of internal humidification.

The membrane of a water transport device separates the gases and allows water vapor from the humid gas side to diffuse to the dry feed gas. The permeability of water vapor depends on the type of membrane and concentration gradient across the membrane. The flow pattern design of the bipolar plates, e.g., counter current or co-current flows between two gas streams, affects the concentration gradient through the membrane and, thus, the permeability. Optimum flow pattern and directions were designed to maximize the permeability of water vapor through the membrane.

In the inorganic/organic composite membrane of the fuel cell, a proton exchange membrane is employed as the host membrane and a variety of solid acids are used as functional additives. Some of the functional additives are SiO_2, TiO_2, ZrP, and other solid acids. This type of composite membrane has shown promise in terms of proton conductivity and fuel cell performance. Perfluorosulfonic acid-based organic/inorganic composite membranes with different heteropolyacid (HPA) additives have also been investigated as alternatives to proton conducting membranes.[11-24] Here, we have studied composite membranes with phosphotungstic acid. These membranes have reduced resistance because they are thinner and have increased proton exchange sites from the phosphotungstic acid. These newly developed membranes and MEA's were tested in single cell and multi cell stacks, and the performance of these cells was superior to MEA's with Nafion® 112 and commercial MEAs from Ion Power.

Experimental

Preparation of Composite Membranes

Phosphotungstic acid (PTA) composite membranes were prepared by casting Nafion® solution with the PTA particles and DMF. The cast film was dried and annealed at 150 °C. Then the membrane was immersed in 0.1 M $CsCO_3$ solution to exchange the cation of PTA with Cs, which makes the PTA insoluble.[16,17]

Preparation of MEA

MEAs were prepared by applying both the anode and the cathode catalyst layers directly onto the membranes using a spraying technique. Five wt% solubilized Nafion® (EW1100, supplied by Solution Technology, Inc.) was used as the perfluorosulfonate ionomer within the catalysts. The cathode catalyst was 45.5% Pt/C (Tanaka Kikinzoku Kogyo, Tokyo, Japan) with a Nafion® loading of 32 wt%. The loadings of precious metals were 0.4 ± 0.01 mg/cm^2 and 0.4 ± 0.01 mg/cm^2 for the anode and the cathode, respectively. The heat-treated catalyst-coated membrane was "sandwiched" between two gas diffusion layers to obtain a 25-cm^2 membrane electrode assembly (MEA) for single cell polarization and voltammetry measurements. A single-serpentine pattern graphite flow field was used with an active area of 25 cm^2. Teflon® gaskets were used as seals. They were also used to achieve a sufficient amount of compression on the MEA so that all components established intimate contact to minimize contact losses.

Conductivity Measurement

In-plane membrane conductivity testing was performed following the protocol developed by Bekktech.

Measurement of Water Diffusion through Nafion Membrane

The flux experiment was carried out in a diffusion cell with the active diffusion area of 25 cm^2. Humidified N_2 gas was introduced to one side and dry N_2 gas to the other side of the cell. The effect of the membrane thickness, temperature, and the flow rate of the gases on the water vapor permeation flux was investigated for both co – flow and counter – flow configurations.

Measurement of Gurley Number

Through-plane gas permeability for each gas diffusion layer (GDL) was determined by the Gurley number measurement. A Gurley number apparatus built in our lab (Fig. 2) was used for the measurement with dry nitrogen at room temperature, giving a Gurley number representing gas permeability of each porous GDL. The Gurley number was obtained in [(cm^3/s)/(atm x cm^2)]. It is important to note that the Gurley number measurement gives through-plane gas permeability while performance associated with convection through the GDL is more dependent on in-plane gas permeability. It is assumed in this work that each porous GDL is isotropic making the through-plane permeability applicable to the understanding of the in-plane convection phenomenon. Since the gas permeability values of the three candidate GDLs are very different, even if the in-plane gas permeability is slightly different from the through-plane gas permeability, the difference is not expected to change the trend of convection influence.

Linear and Cyclic Sweep Voltammetry

In addition to polarization tests, two diagnostic tests were used: linear sweep voltammetry (LSV) for determination of hydrogen crossover through the membrane and cyclic sweep voltammetry (CV) for determination of electrochemical surface area (ECA) available for hydrogen adsorption. A Solatron SI1287 Potentiostat (Solartron Analytical, Houston, Texas) was used for these measurements.

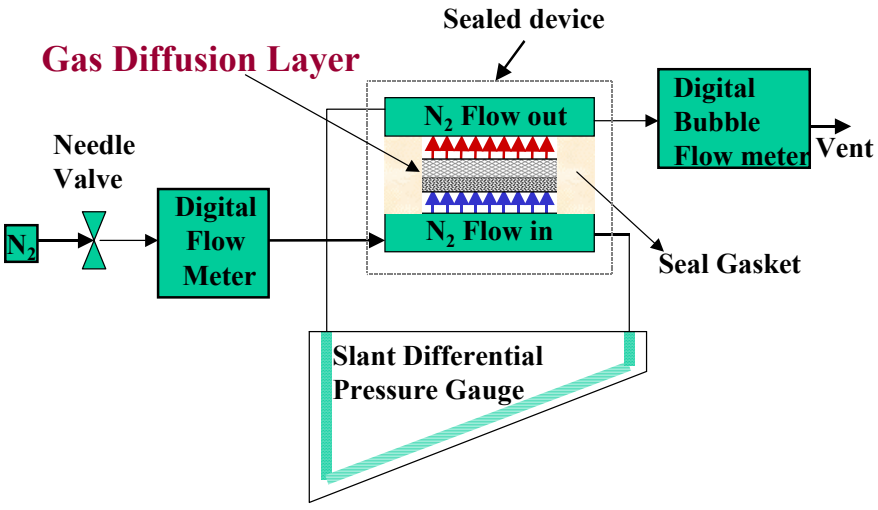

Figure 2. Gurley Number measurement equipment.

For these tests, pure hydrogen was used on the anode and pure nitrogen was used on the cathode with flow rates of 200 cm^3/min. The reference and counter electrode leads were connected to the anode while the working electrode lead was connected to the cathode. For the CV, the sweep rate was 20 mV/sec with a total of 5 cycles and cell potential was scanned from 0.01 to 0.8 V. Additional LSV tests were conducted at the three operating conditions to verify reasonable hydrogen crossover at real operating conditions.

Hydrogen Crossover

Hydrogen crossover was determined using the plateau current density in the LSV at high voltage where the current obtained is limited by hydrogen transport rate through the tested membrane. For the linear sweep voltammetry (LSV), the sweep rate was 4 mV/s and cell potential was scanned from 0.01 to 0.5 V for LSV test.

Fuel Cell Performance Measurements

In measuring polarization curves, current was stepped from zero to the maximum test current density with an increment between 10 and 100 mA/cm^2. Time spent at each current density was 5 min. A 100A Model 890B Scribner load box (Scribner Associates, Southern Pines, NC), which has current interrupt resistance measurement built-in, was used for the polarization measurement. The MEAs, prepared as described above, were tested at atmospheric pressure and different temperatures. The anode and the cathode gas line temperatures were set 10 °C above the cell temperature to ensure no water condensation in the inlet gas lines. Pure hydrogen, certified grade of 99.999%, was the only fuel used. The fuel cell stack was designed by scaling-up the existing fuel cell hardware. The product water in the cells was recycled to internally humidify the stack. Thin polymer membranes are used as a separator between the humidified exit gases and dry inlet gas. Such a humidification scheme does not add significantly to the parasitic loss of the overall system. Figure 3a and 3b shows a single cell running with internal humidifier and a complete four cell stack. The detail anode, cathode, and humidifier drawings are given in Figure 4. The polymer humidifier is incorporated in the stack.

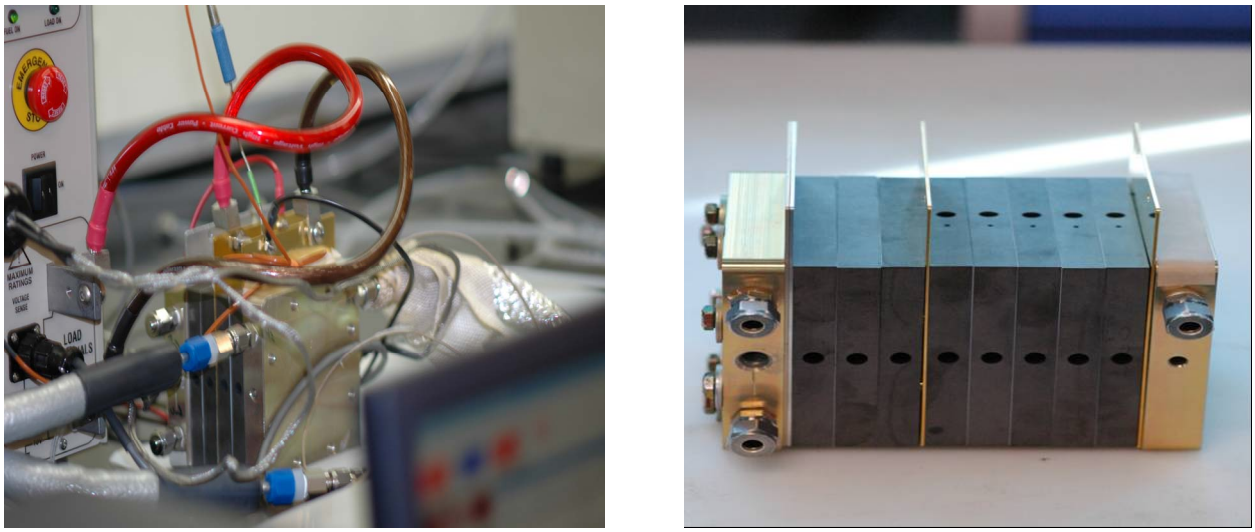

Figure 3. A single cell running with internal humidifier (left) and a four cell stack (right).

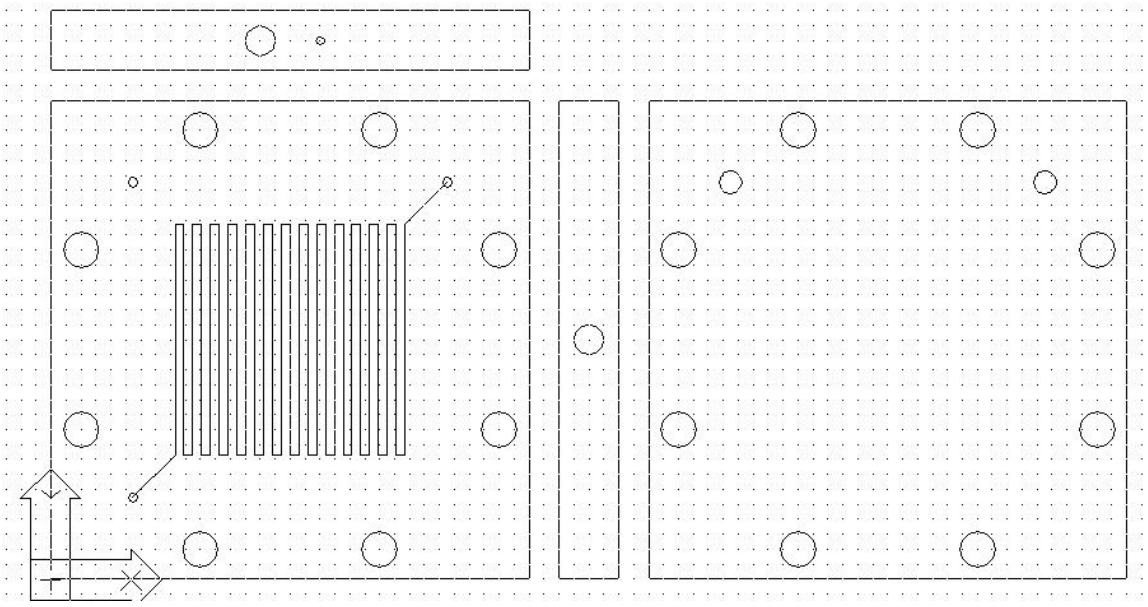

Figure 4a. Anode End Plate Drawing.

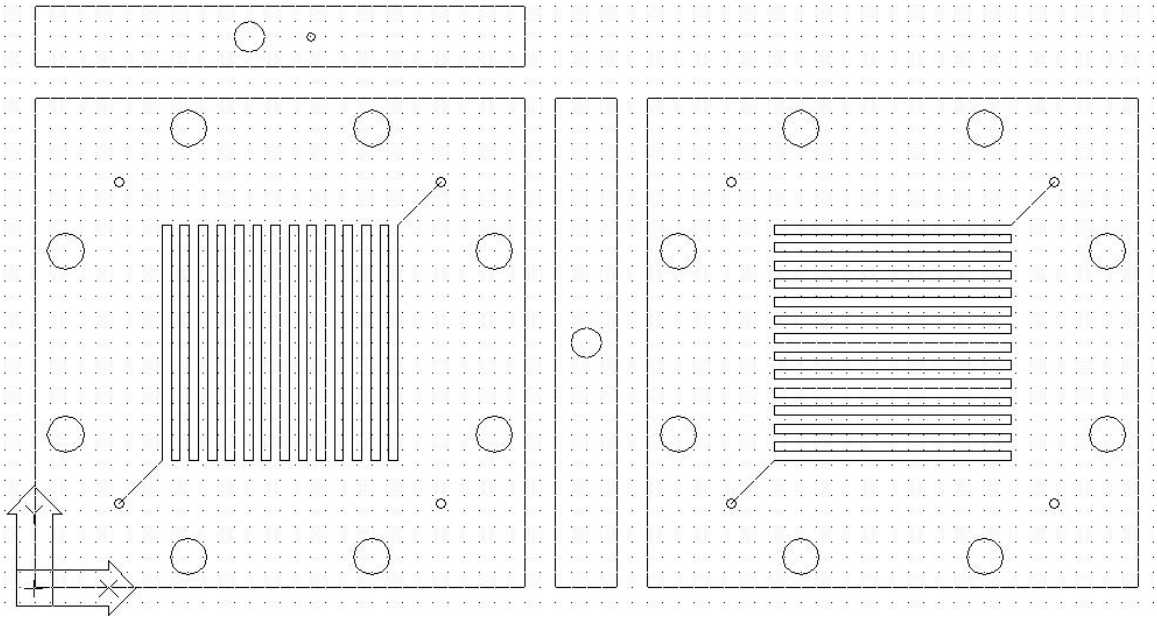

Figure 4b. Bipolar Plate Drawing.

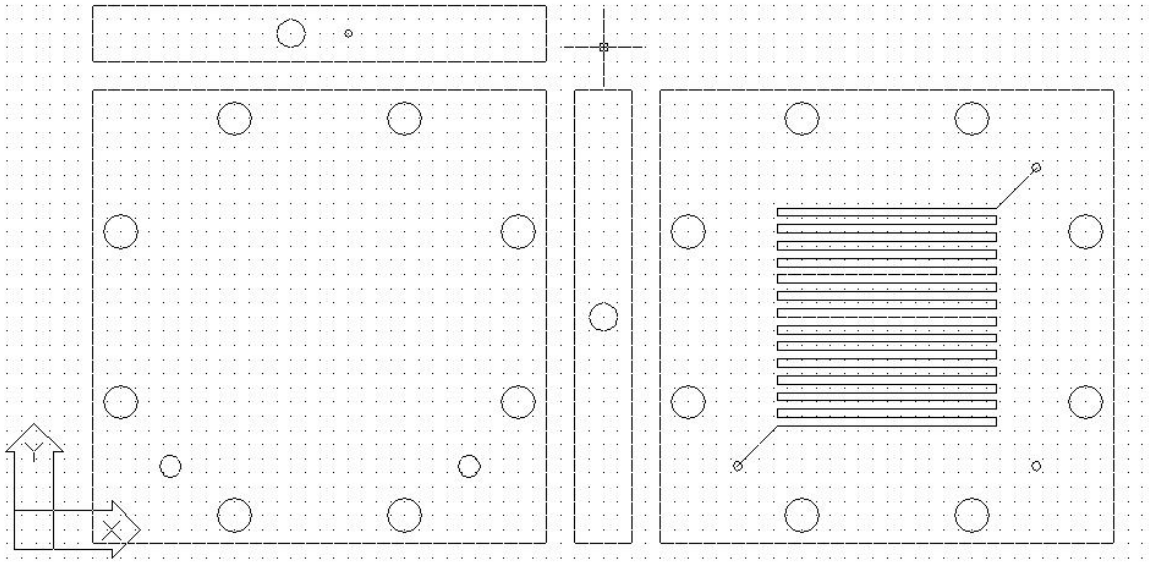

Figure 4c. Cathode End Plate Drawing.

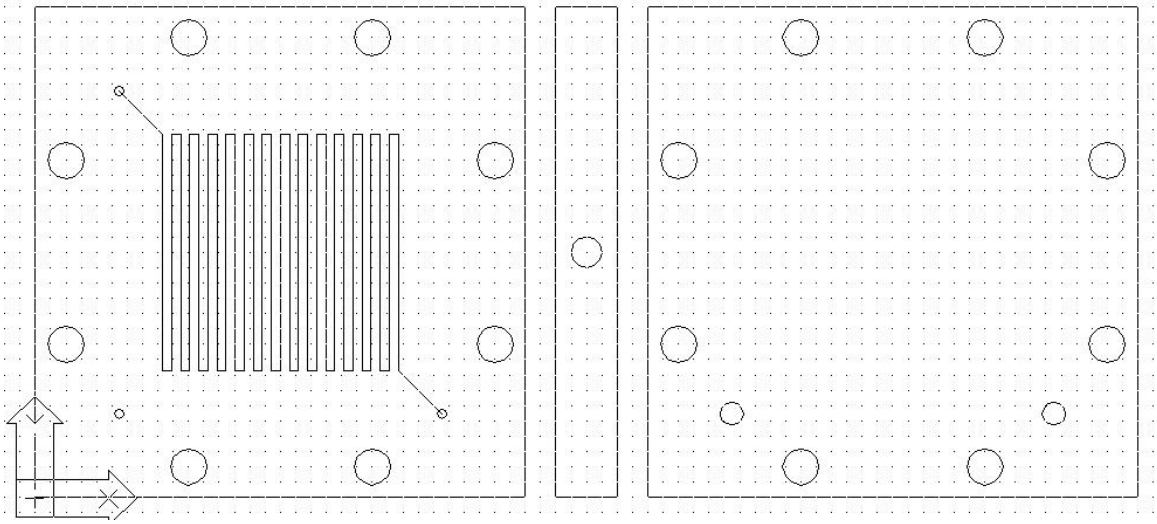

Figure 4d. Humidifier Wet Plate Drawing.

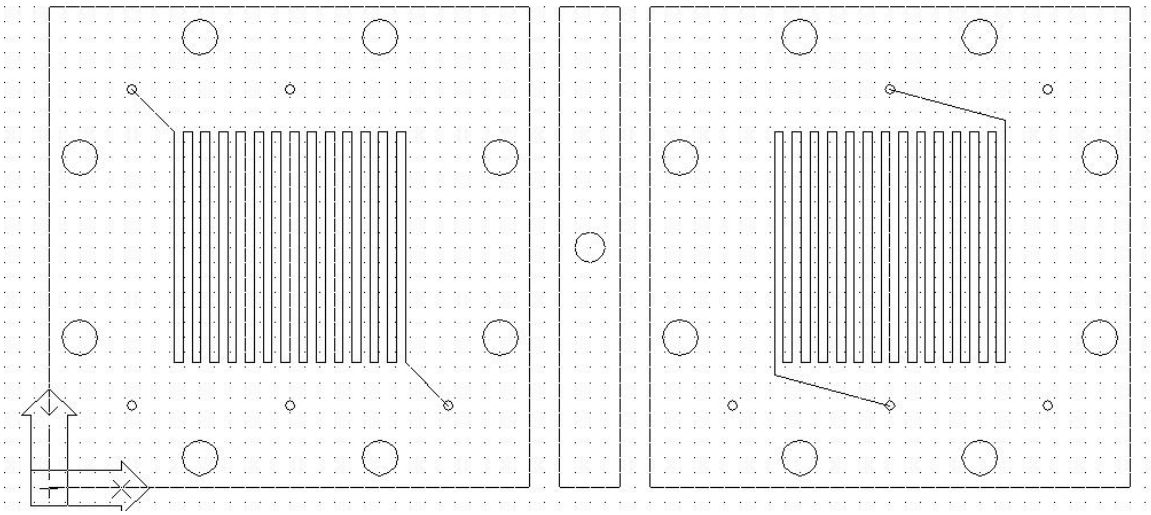

Figure 4e. Humidifier Bipolar Plate Drawing.

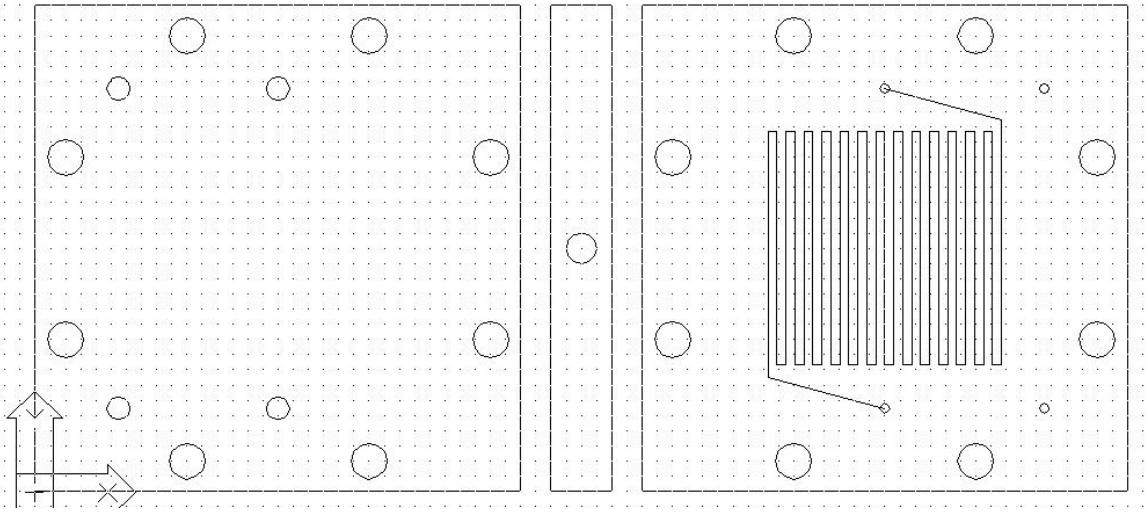

Figure 4f. Humidifier Dry Plate Drawing.

Results and Discussion

Performance of the MEAs

Three types of MEAs were tested in single cells at 80 °C. As shown in Figure 5, an MEA with composite membrane (triangle symbol) demonstrated high performance compared to Nafion 112 (line symbol) and commercial (square symbol) ones. For example, at 0.6 V the current density was 900 mA/cm^2 for MEAs with Nafion 112 and the commercial MEA's, while it was 1300 mA/cm^2 for the composite membrane based MEA. The high fuel cell performance may be attributed to the improved conductivity and lower ohmic resistance of the composite membrane.

Analysis of a Fuel Cell with Internal Humidity Exchanger

Figure 6 shows a fuel cell with the internal humidity exchanger.

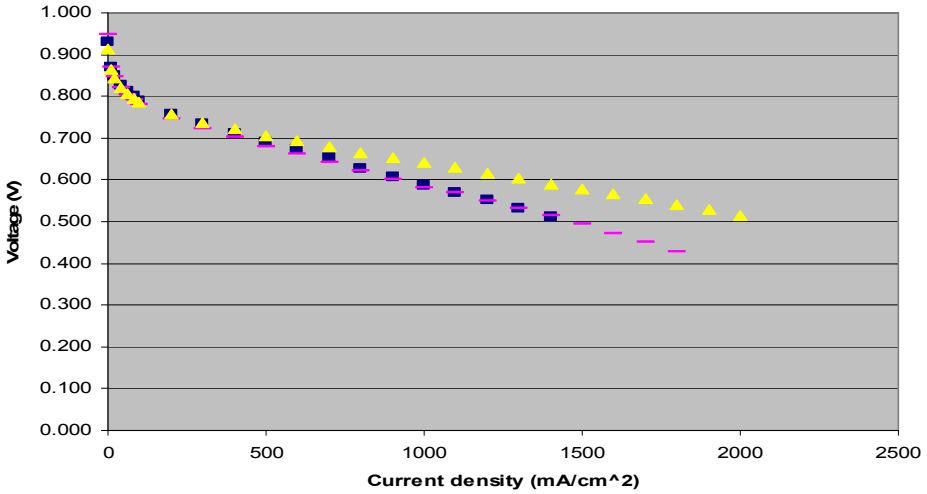

Figure 5. Performance of MEAs at the cell temperature of 80 °C (anode humidifier = 80 °C and cathode humidifier = 73 °C).

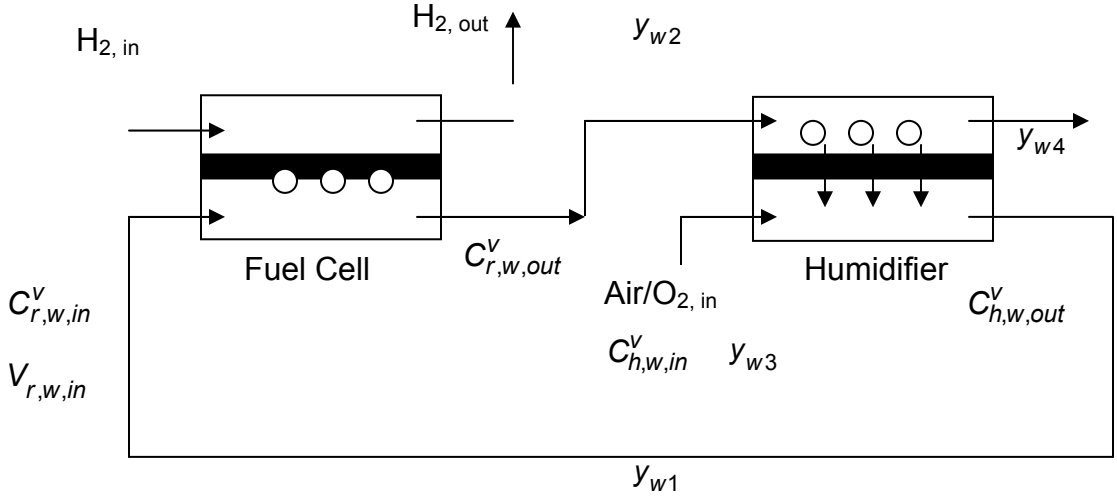

Figure 6. Schematic of the internal humidity incorporated fuel cell.

The basic conservation equations are as follows:

Fuel cell;

$$V_{r,w,in} \cdot C^{v}_{r,w,in} - V_{r,w,out} \cdot C^{v}_{r,w,out} = -r_w \cdot A_r \tag{1}$$

Humidifier (water receiving side);

$$V_{h,wr,in} \cdot C^{v}_{h,wr,in} - V_{h,wr,out} \cdot C^{v}_{h,wr,out} = -N_{w,z} \cdot A \tag{2}$$

Humidifier (water transferring side);

$$V_{h,wt,in} \cdot C^{v}_{h,wt,in} - V_{h,wt,out} \cdot C^{v}_{h,wt,out} = N_{w,z} \cdot A \tag{3}$$

Where V,C,r,N,A_r and A represent flow rate [cm^3/s], concentration [mol/cm^3], rate of water generation [$mol/cm^2/s$], flux [$mol/cm^2/s$], electrochemical area, and geometric area, respectively. The rate of water generation depends on the rate of electrochemical reaction and may be given by

$$r_w = \left(i_0 / n\ F\right) \cdot \left[\exp\left(\beta F\eta \big/ RT \right) - \exp\left(-(1-\beta) F\eta \big/ RT \right) \right] \tag{4}$$

where Butler-Volmer kinetic expression is used for the oxygen reduction reaction. In this equation i_0 is the exchange current density for the oxygen reduction reaction, n is the number of electrons per mole of species, F is the Faraday's constant, β is the transfer coefficient, and η is the overpotential. The electrochemical interface area A_r can be obtained by

$$A_r = \gamma_c \cdot A \tag{5}$$

where γ_c is the roughness factor of the MEA for the oxygen reduction reaction. The superscript v is used to denote the concentration of water in the vapor phase. The concentration of i in the vapor phase can be written as $C_i^v = {y_i P}/{RT_i}$, where y_i is the mole fraction of i in the vapor phase.

The changes of volume with the electrochemical reaction taking place in gas phase can be written as

$$V = V_0 \cdot \left(1 + \frac{y_{A0} \cdot \delta}{S} \right) \tag{6}$$

where y_{A0} is the mole fraction of reacting species, δ is the sum of stoichiometric coefficient for a given reaction, and S is the stoichiometric ratio, i.e., the inverse of conversion.

The flux of water in the humidifier N can be expressed by

$$N_{h,i,z} = -D_i^{e,m} \frac{dC_i^m}{dz} \tag{7}$$

where $D_i^{e,m}$ and C_i^m are the effective diffusion coefficient and concentration of *i* in the membrane, respectively. The concentrations of *i* at the surface of the humid and dry sides of the membrane can be written by $C_i^m = \left(\rho_m / M_m\right) \cdot \lambda_i$, where ρ_m [g/cm^3], M_m [g/mol], and λ_i [mol H_2O/mol SO_3^-] are the density, the molecular weight, and solvent loading of membrane, respectively. The density and molecular weight can be obtained independently and the solvent loading in the membrane depends on the relative humidity of the surrounding. For example, water sorption has been reported to be a function of water activity as[25]

$$\lambda_w = 0.043 + 17.81 * a_w - 39.85 * a_w^2 + 36.0 * a_w^3 \tag{8}$$

where the activity of water is given by

$$a_w = \frac{y_w P}{p^*} \tag{9}$$

where the vapor pressure of water p^* is a function of temperature. Therefore, for a given temperature and pressure condition, the concentration of water at the surface of the membrane C_i^m depends only on the mole fraction of water in the vapor phase.

The diffusion coefficient for the transport of water through the membrane is a function of solvent loading and temperature, e.g.,[26]

$$D_w^e = (1.76 \cdot 10^{-5} + 1.94 \cdot 10^{-4} \cdot \lambda_w) \cdot \exp\left(\frac{-2436}{T}\right) \tag{10}$$

For a given temperature, thus, the diffusion coefficient depends on the mol fraction of water in the vapor phase. The concentration of water vapor coming to the fuel cell, $C_{r,w,in}^v$ in Figure 6, can be obtained as a function of dry feed composition, diffusion flux, and water generation rate at the fuel cell which depends on the temperature, exchange current density and overpotential.

Table 1 shows the flux obtained from the experiment. The humidifier temperature was set to 90 °C. The humid gas was 74 °C (or 90 °C) and the dry gas was 25 °C. The flux increases with concentration gradient through the membrane, i.e., the flux is higher when the humid gas is saturated. The higher the flow rate of the gas in both sides, the higher the flux of water vapor was obtained. The activity of water in the vapor phase in the dry gas side decreases with flow rate in dry N_2 gas. The flux varies with the y-direction of gas flow because the concentration gradient changes with the flow direction. The total flux through the membrane area can be obtained by integrating fluxes over the y-direction. In fuel cells, the relative humidity of gases out of the cell depends on cell temperature and stoichiometry of reactant gases, e.g., as the stoichiometry increases the relative humidity of the exit gas decreases.

Table 1. Water vapor flux through Nafion® 112 membrane

Humid gas (exhaust)	Dry gas (feed)	Flux (mol/cm^2/s)
T = 74 °C (52.7% RH) Flow rate = 0.5 l/min	T = 25 °C Flow rate = 0.5 l/min	3.72×10^{-6}
T = 74 °C (52.7% RH) Flow rate = 1.0 l/min	T = 25 °C Flow rate = 1.0 l/min	4.69×10^{-6}
T = 90 °C (100% RH) Flow rate = 0.5 l/min	T = 25 °C Flow rate = 0.5 l/min	1.01×10^{-5}
T = 90 °C (100%RH) Flow rate = 1.0 l/min	T = 25 °C Flow rate = 1.0 l/min	1.18×10^{-5}

Figures 7 and 8 show results from a simple water balance calculation in the fuel cell. The exit RH from the anode and cathode streams is assumed to be equal. Also, the calculations were done with stoichiometric flow rates and, thus, the results are independent of the current density. Figure 7 shows the exit RH as a function of cathode stoichiometry at different operating pressures. The exit RH is 8 and 18% at cathode stoichiometry of 4 and 1.5, respectively at 150 kPa. At 1.5 cathode stoichiometry the exit RH increases from 12 to 29% with increase in absolute pressure from 100 to 250 kPa.

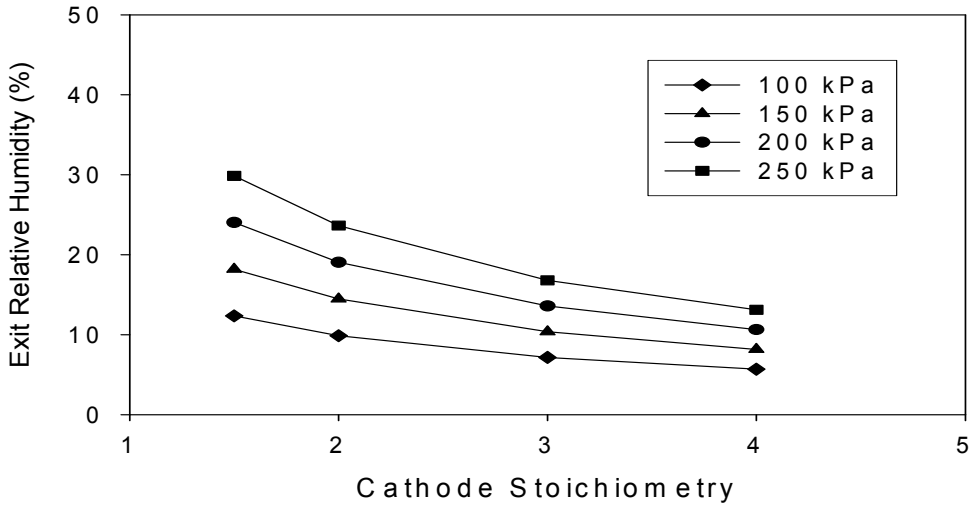

Figure 7. Exit RH calculated as a function of cathode (air) stoichiometry at different operating pressures. The calculations were done with the cell temperature at 120 °C, P_{H2O} Feed = 1.5 kPa and H_2 stoichiometry of 1.3, without recycle.

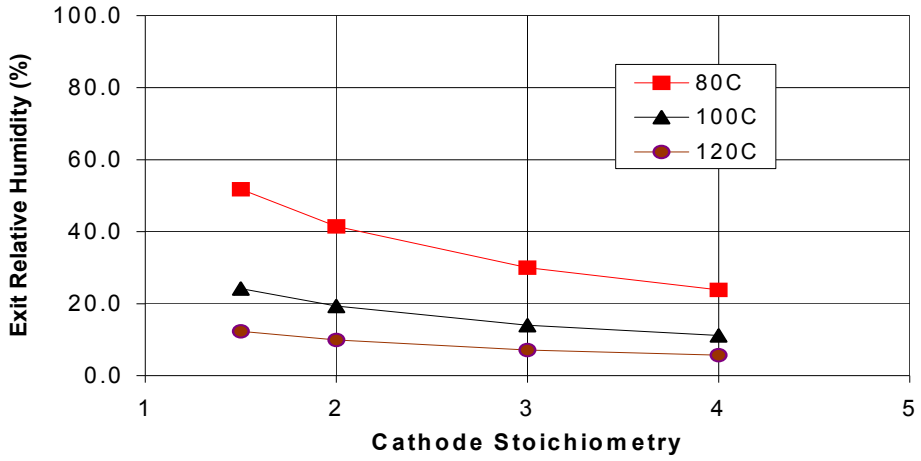

Figure 8. Results from water balance calculations without external humidification to the cell.

Figure 8 shows the effect of cathode air stoichiometry and the cell temperature on the exit RH from the cell. The calculations were done with anode H_2 stoichiometry of 1.3 and atmospheric pressure. At 80 °C the water generated in the cell is enough to bring the exit RH to ~50% at low air stoichiometry. However, at higher temperatures (>100 °C) the exit RH is <25%.The exit relative humidity (%) is plotted as a function of cathode air stoichiometry for three different operating temperatures (80, 100, and 120 °C), atmospheric pressure, and anode H_2 stoichiometry of 1.3.

Figure 9 shows the impact of different recycling strategies on the cathode RH. The conditions used for the calculation were 100 °C, 1.5 atmospheres, 1.3 H_2 stoichiometry, and air stoichiometry of 2. Recycling the anode exhaust stream does not affect the cell RH. Recycling the cathode exhaust stream can increase the exit RH to 40% with 80% recycle. However, recycling the cathode exhaust will also lead to depletion of O_2 in the inlet air stream. Separating the water from the cathode exhaust and recycling can increase the exit RH to ~70%. The exit RH will be 47% with the use of a Nafion® membrane as an internal humidifier using cathode exit gas to humidify the cathode inlet gas (assuming flow rates of dry and humidified gas to the Nafion® humidifier are equal and the exit RH from the humidifier is also equal. This corresponds to 50% of water in the cathode exit stream being recycled). Thus, it can be seen that, depending upon the operating condition, the cell RH can vary significantly even without any external humidification to the cell.

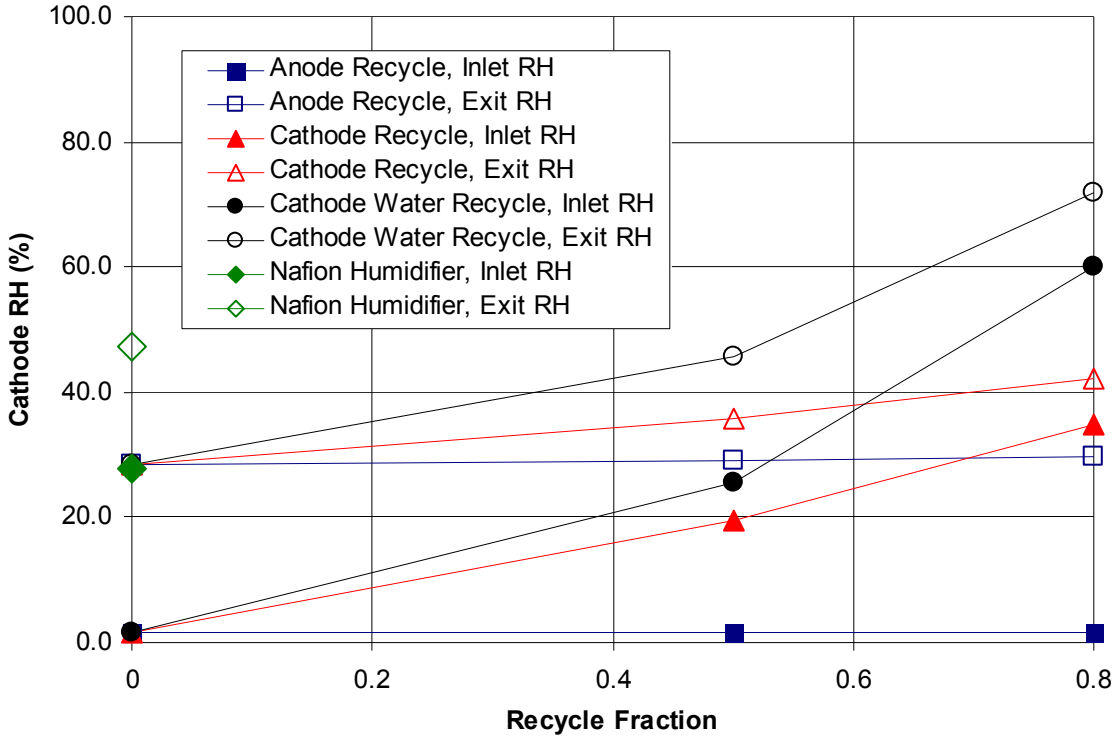

Figure 9. Results from water balance calculations without external humidification to the cell. The cathode RH (both inlet and exit) was plotted as a function of recycle fraction of different exhaust streams. The cell temperature was 100 °C, 1.5 atmosphere, anode H_2 stoichiometry of 1.3, cathode air stoichiometry of 2.0. Also compared was the use of Nafion® for internal water humidification.

The efficiency of the humidifier using a Nafion® membrane will depend upon the water transport (WT) characteristics of the membrane. WT through a Nafion® membrane was investigated in 25 cm^2 fuel cell hardware. The effects of membrane thickness, gas diffusion layer, pinch, gas flow rate, flow direction, and cell temperature were investigated. Water from the anode and cathode exhaust was collected and weighed as a measure of water transport through the membrane. Nitrogen was used as the reactant and the inlet dew point on the anode side was set to 90 °C. Dry N_2 gas was fed to the cathode side. Similar flow rates on both anode and cathode side were used. In a fuel cell, the RH is an important parameter. In this report, however, the data is represented as the percentage of water transported across the membrane. Two to three samples were collected at each condition. The variation in the WT from duplicate samples was <5%. The data shown in this report is the average WT.

Water Transport (WT) = Water collected from cathode exhaust *100/[Water collected from anode exhaust + Water collected from cathode exhaust]

The effect of the following variables was evaluated on the WT through Nafion membrane.

Membrane Thickness - Nafion111, Nafion112

Gas Diffusion Layer - SGL 10BC (hydrophobic microporous layer), Toray (hydrophilic), None

Pinch – 4, 10 mil

Gas Flow Rate – 400, 1000 cm^3/min

Flow Direction – Co-Flow, Counter-Flow

Cell Temperature – 90, 100 °C

Effect of Membrane Thickness—Table 2 shows the effect of membrane thickness on WT. The results from two sets of flow rates are compared. The effect of flow rates is presented in a separate section. The WT through 1 and 2 mil membranes is 43.6 and 31.6% at 400 cm^3/min and 29.4 and 18.6% at 1000 cm^3/min, respectively.

Table 2. Effect of membrane thickness on WT. The build specifications and the operating conditions were SGL 10BC, pinch = 4 mil, cell temperature 100 °C, Anode inlet dew point = 90 °C, Cathode inlet dry, line temperature 110 °C

Membrane Thickness (mil)	Flow Rate (cm^3/min)	WT
1	400	43.6
	1000	29.4
2	400	31.6
	1000	18.6

Effect of Gas Diffusion Layer—Table 3 shows the effect of GDL on WT. The results from two sets of flow rates are compared. The cell without GDL was assembled by sandwiching the membrane between gaskets of 10 mil each. The WT with SGL 10BC and Toray is similar. The WT decreases when the cell is tested without any GDL. In the absence of GDL the reactant may not be distributed across the whole membrane area and the total area available for water transport decreases.

Table 3: Effect of GDL on WT. The build specifications and the operating conditions were Nafion111, pinch = 4 mil, cell temperature 100 °C, Anode inlet dew point = 90 °C, Cathode inlet dry, line temperature 110 °C

Gas Diffusion Layer	Flow Rate (cm^3/min)	WT
SGL 10BC	400	43.6
	1000	29.4
Toray	400	42.8
	1000	31.8
None	400	30.7
	1000	20.1

Effect of Pinch—The contact resistance is not a factor in the design of the Nafion® humidifier. However, the pinch can alter the transport properties through GDL. Table 3 shows the effect of pinch on WT. The results from two sets of flow rates are compared. The effect of flow rates is presented in a separate section. The WT with pinch of 10 and 4 mil is 33.2 and 31.6% at 400 cm^3/min and 20.3 and 18.6% at 1000 cm^3/min, respectively. The WT decreases slightly with the decrease in pinch.

Table 4. Effect of pinch on WT. The build specifications and the operating conditions were SGL 10BC, Nafion112, cell temperature 100 °C, Anode inlet dew point = 90 °C, Cathode inlet dry, line temperature 110 °C

Pinch (mil)	Flow Rate (cm^3/min)	WT
10	400	33.2
	1000	20.3
4	400	31.6
	1000	18.6

Effect of Flow Rate—The contact resistance is not a factor in the design of the Nafion® humidifier. Tables 2, 3, and 4 show that WT through the membrane decreases with increase in flow rate, irrespective of the cell configuration. Compared to 400 cm^3/min, the WT at 1000 cm^3/min decreases by 25 to 40% depending upon the specifications. The WT at higher flow rate can be improved by increasing the area of the membrane used.

Flow Direction—The flow direction can also impact the WT through membrane. The WT should be higher for Counter-Flow because of larger water partial pressure gradient across the membrane. In the fuel cell technology hardware the flow direction in the standard build is shown in Figure 10a. Figure 10b shows the cross counter-flow direction. Table 5 shows the WT for cross co-flow and cross counter-flow direction as shown in Figures 10a and 10b. The WT through the membrane is similar for flow in both directions.

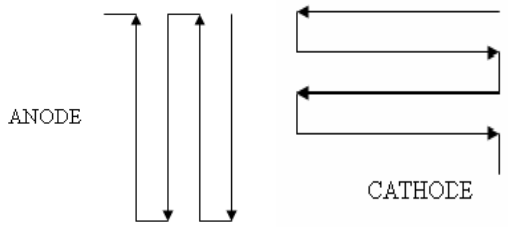

Figure 10a. Flow direction in standard build (cross co-flow).

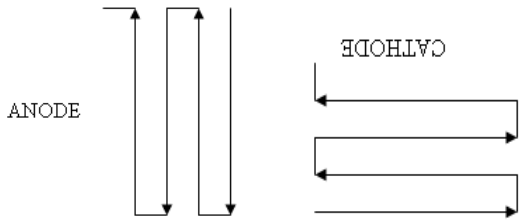

Figure 10b. Flow direction reversed (cross counter-flow).

Table 5. Effect of flow direction on WT. The build specifications and the operating conditions were SGL 10BC, pinch = 4 mil, Nafion111, cell temperature 100 °C, Anode inlet dew point = 90 °C, Cathode inlet dry, line temperature 110 °C.

Flow Direction	Flow Rate (cm^3/min)	WT
Cross Co-Flow	400	43.6
	1000	29.4
Cross Counter-Flow	400	41.8
	1000	27.6

Effect of Cell Temperature—The cell temperature alters the RH gradient across the membrane. Table 6 shows the effect of cell temperature on WT. The decrease in cell temperature (increase in RH gradient) significantly improves the WT across the membrane.

Table 6. Effect of cell temperature on WT. The build specifications and the operating conditions were Toray, pinch = 4 mil, Nafion111, 1000 cm^3/min, Anode inlet dew point = 90 °C, Cathode inlet dry, line temperature 110 °C

Cell Temperature (°C)	WT
90	43.6
100	31.8

The preliminary data was considered to be sufficient to provide the basis for designing the internal humidifier incorporated in the stack.

Gurley Number—It is desirable for fuel cells to operate at a relatively high current density for the highest power output per total system size and weight. The higher the operating current density of the fuel cell, the higher the flux of gas feed needed. This requires the gas diffusion layer to transport reactant gases to the catalyst surfaces at a high rate. The transport aspect of the cathode GDL can be experimentally evaluated under operating conditions where there is low relative humidity. When assembling the cell for Gurley number testing, the total plenum volume on each side has considerable influence on the pressure distribution pattern over the active area on both inlet and outlet sides. Therefore, it is important to employ enough thickness gaskets (spacers) to get relatively uniform pressure distribution, resulting in more meaningful Gurley Numbers. Prior to evaluation of a sample GDL, the system's inherent resistance to gas flow is evaluated by measuring pressure drop across an empty test cell over a range of flow rates. This system resistance to flow is used as a correction in the subsequent measurement of GDL gas flow characteristics. Each of the candidate GDLs consisted of the same macro-porous substrate, but a significantly different micro-porous layer. Even though the micro-porous layer is critical for an effective GDL operation, as mentioned earlier, the third GDL was chosen to be bare macro-porous substrate. The bare paper serves as a control for comparison where the micro-porous layer characteristics are the extreme in permeability of that of the macro-porous layer. An ideal GDL not only has to provide effective oxygen transport by having high limiting current (as shown in this work), but also has to serve as an effective current collector by providing enough electrical conductivity to the catalyst layer to have negligible contact resistances. Polarization curves at constant utilization were collected to examine the overall effects of the GDL and verify whether or not a micro-porous layer on the surface of the GDL is beneficial for the overall fuel cell performance. A parallel analysis of polarization curves with constant utilization showed that when a bare macro-porous substrate was used as a GDL there

were significant ohmic contact losses due to insufficient current collection. Thus a thin micro-porous layer is necessary for effective current collection of the GDL.

Figure 11 shows the measurement of Gurley numbers for various GDLs. 10BB GDL shows relatively high flow rate at a given pressure drop and used in the fuel cell experiment.

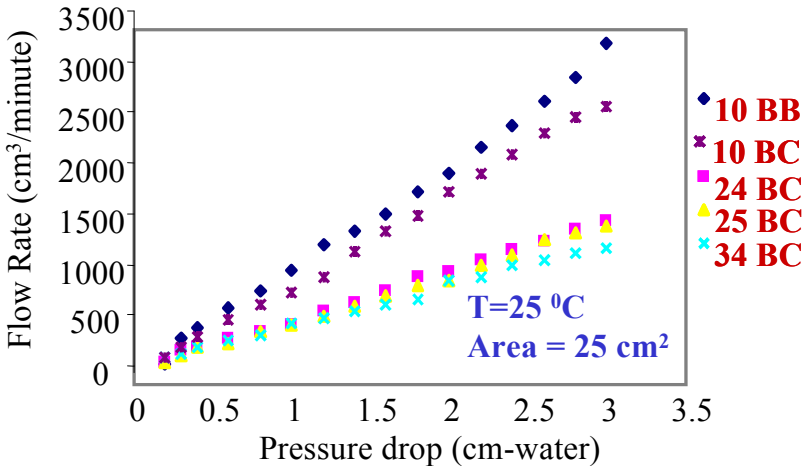

Figure 11. Gurley number results for various gas diffusion layers.

Table 7. Data Summary for Gas Diffusion Layers

Properties	10 BB	10 BC	24 BC	25 BC	34 BC
Thickness (mil)	16.5	15.5	9.3	9.3	3.03
Areal Weight (g/m 2)	125		100	86	133.2
Porosity (%)	84		76	80	80
Permeability (Air) [cm3/(cm2· s)]	3		0.45	0.8	0.8
Electrical Resistivity (through plane) m Ω cm2	< 15		<11	<12	
Gurley Number (cm 3/sec cm2 cm-water)	0.06	0.04	0.012	0.015	0.009

Fuel Cell Performance with Internal Humidifier

Hydrogen Crossover and Cyclic Voltammetry—Figure 12 shows a cyclic voltammogram of an Ion Power MEA. The ECA of the cathode was calculated to be 57 m^2/gmPt. Figure 13 shows the linear sweep voltammetry of the same MEA. The H_2 crossover current density is 2 mA/cm^2.

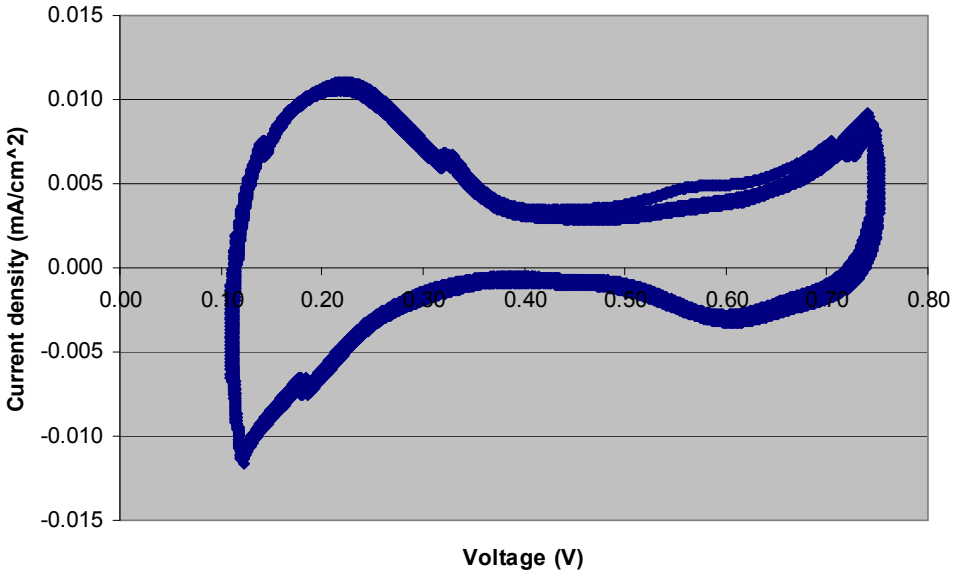

Figure 12. Cyclic voltammogram of an Ion Power MEA at 25 °C, ambient pressure, scan rate 40 mV/s, and H_2 and N_2 flow rates of 200 cm^3/min.

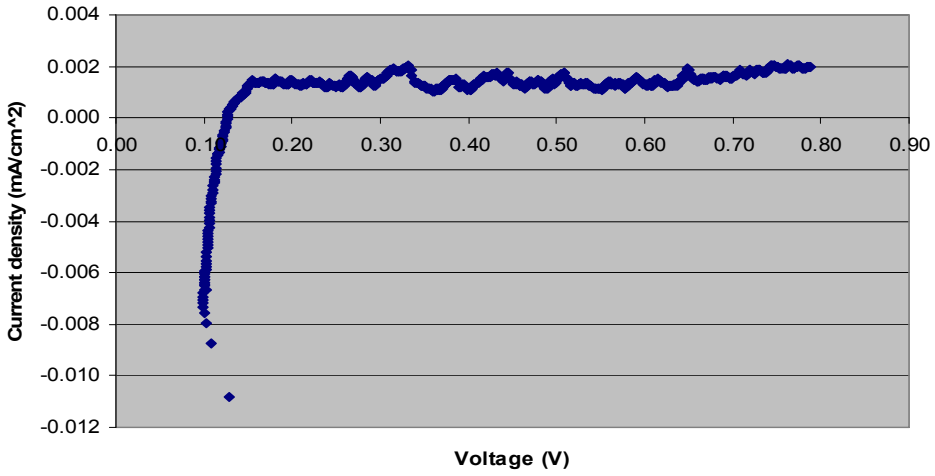

Figure 13. Hydrogen crossover of an IonPower MEA at 25 °C, ambient pressure, scan rate 2 mV/s, and H_2 and N_2 flow rate 200 cm^3/min.

Single Cell Experiment With and Without Internal Humidification—Figure 14 shows the polarization curve of MEAs (IonPower) in a single cell with dry cathode (symbol: diamond), internal humidifier (symbol: square), and external humidification (symbol: triangle) at 80 °C.

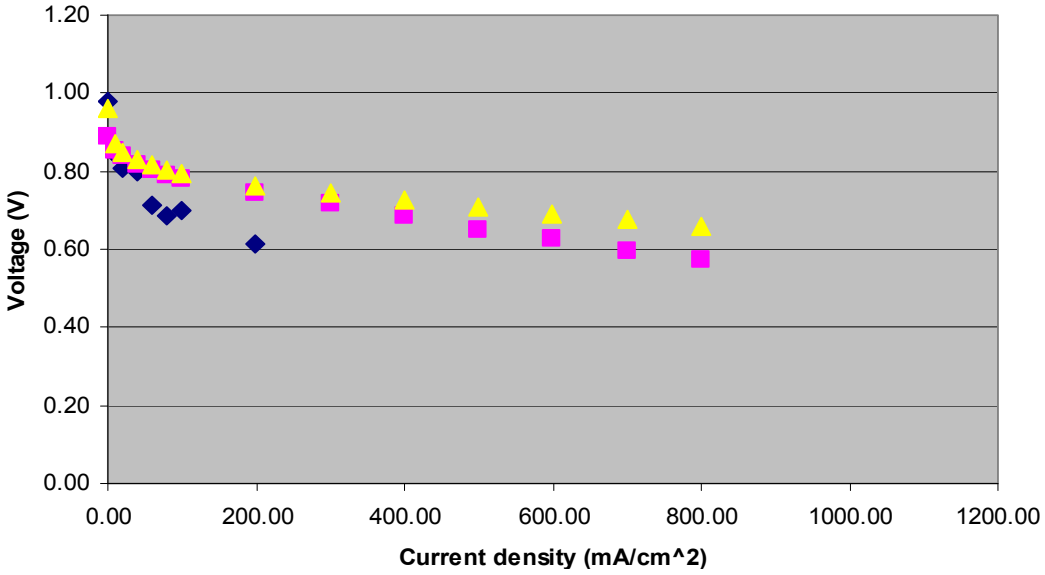

Figure 14. Polarization curves of dry, internal humidity incorporated, and externally humidified cell.

Nafion® 117 was used as humidifier material in this experiment. As can be clearly seen, the performance increased when internal humidifier was incorporated compared to dry feed of the oxidant. Up to 400 mA/cm^2, there is no appreciable difference in the overpotentials of the internal humidity incorporated cell and completely humidified cell. At high current density region, e.g., more than 400 mA/cm^2, the performance of externally humidified cell is better than that of internally humidified system. The Nafion® used for exchanging humidity does transport water effectively. It seems, however, the cathode feed didn't reach an optimum humidification level suggesting that additional internal humidification membrane area or a higher efficiency design is required.

Figure 15 shows the effectiveness of an alternative internal humidifier at different temperatures. For this test, the humidity exchanging material was SPEEK (sulfonated poly ether ether ketone) synthesized in our lab. The sulfonation degree was 60%.

The anode side was fully humidified and the cathode was not externally humidified. In each test, the performance was greater than for dry cathode operation. The performance of internally humidified cell was affected by cell temperature. The lower cell temperature shows higher cell performance. Although higher temperature can increase the kinetics of the oxygen reduction reaction, the results indicates the importance of humidification and the proper water content within the MEAs.

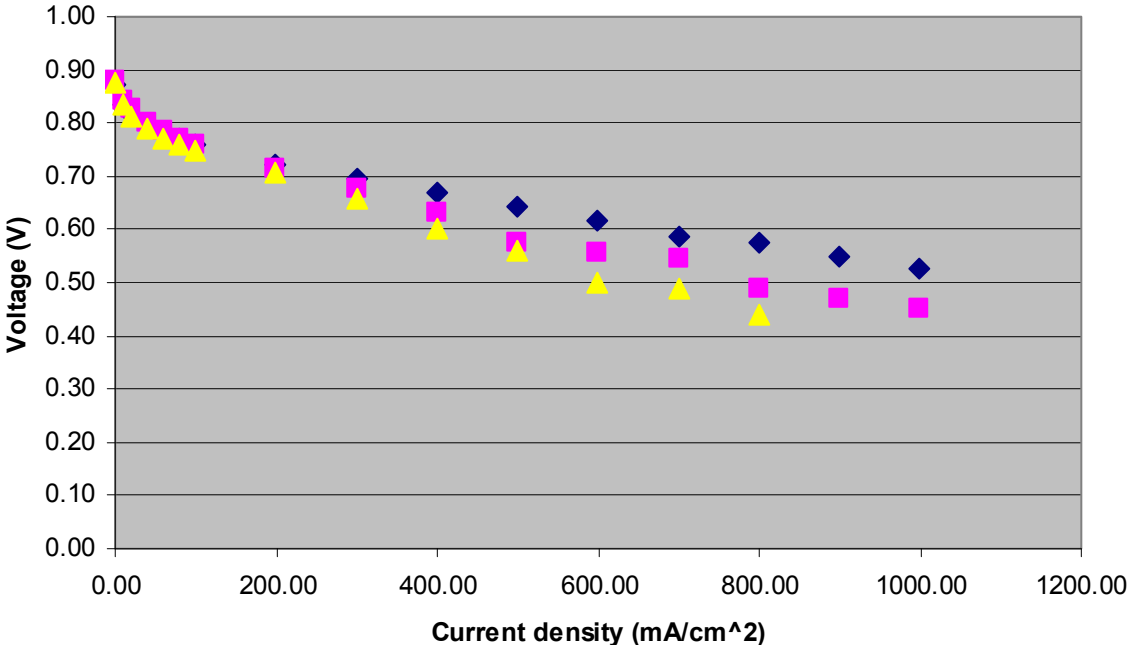

Figure 15. Effectiveness of internal humidifier with cell temperature (60 °C; diamond, 70 °C; square, and 80 °C; triangle).

***Two Cell Stack Experiment*—**Figure 16 shows two-cell stack experiment at 80 °C with no humidification (diamond), internal humidification (square), and external humidification (triangle). It is clear that internal humidification improves the performance of fuel cell compared to dry feed. However, the performance of the internally humidified cell was not close to that of externally humidified one. This may be attributed to the relatively low RH of cathode feed compared to the single cell test and the limited water diffusion through the internal humidifier with the higher flow rates required for the two cell stack.

Figure 17 shows the effect of temperature on the internal humidifier cell stack performance. As the temperature increases, the performance was decreased. This is because the relative humidity in the internal humidifier is higher at lower cell temperature. Under this condition, relative humidity is more important for the cell performance than kinetics at higher temperature. It is also noteworthy that the stoichiometry of the load based feed influences cell performance significantly because it affects the relative humidity of the feed stream.

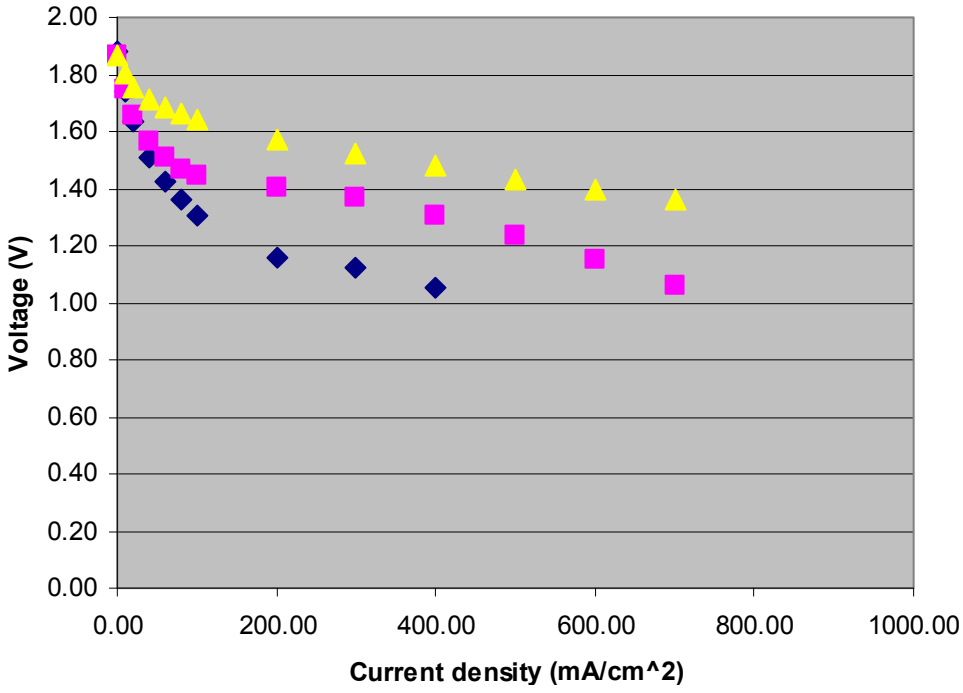

Figure 16. Polarizations of the two-cell stack with no, internal, and external humidifications (stoichiometry of H_2 =1.5, Air = 1.5).

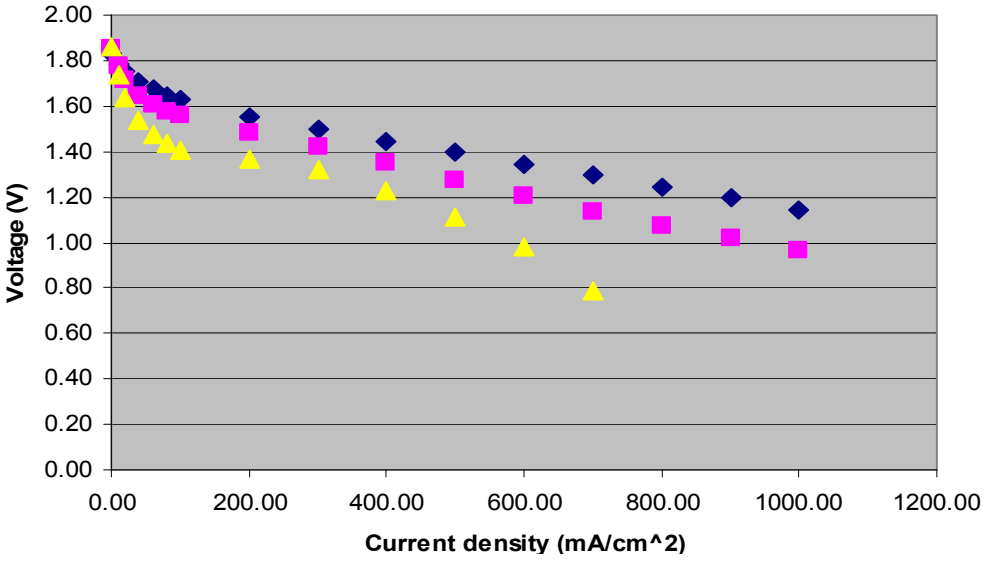

Figure 17. Effect of temperature on the efficiency of internal humidifier (60 °C; diamond, 70 °C; square, and 80 °C; triangle, stoichiometry of H_2 = 2, Air = 3).

Figure 18 shows the effect of anode humidity on the performance of the internal humidifier stack. The temperature of the cathode was kept at 25 °C. As the temperature of anode external humidifier increases, i.e., the relative humidity of anode feed increases, the cell performance increases. This increase in relative humidity at the anode feed stream would increase anode kinetics and increase proton conductivity of the membrane and also increase water content at the cathode catalyst layer by diffusion. Since the overpotential for hydrogen oxidation reaction is low, the effect on the anode electrode itself is small.

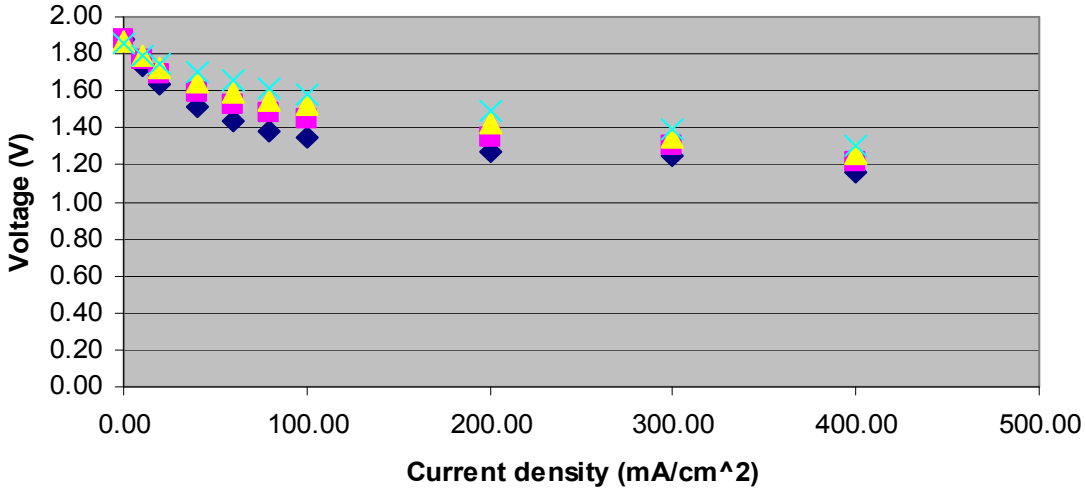

Figure 18. Effect of anode feed saturation temperature on the performance of the internal humidifier (25 °C; diamond, 49 °C; square, 63 °C; triangle, and 74 °C; cross, stoichiometry of H_2 = 1.1, Air = 1.5).

Figure 19 shows the cell resistance measured by current interrupt method during the fuel cell operation.

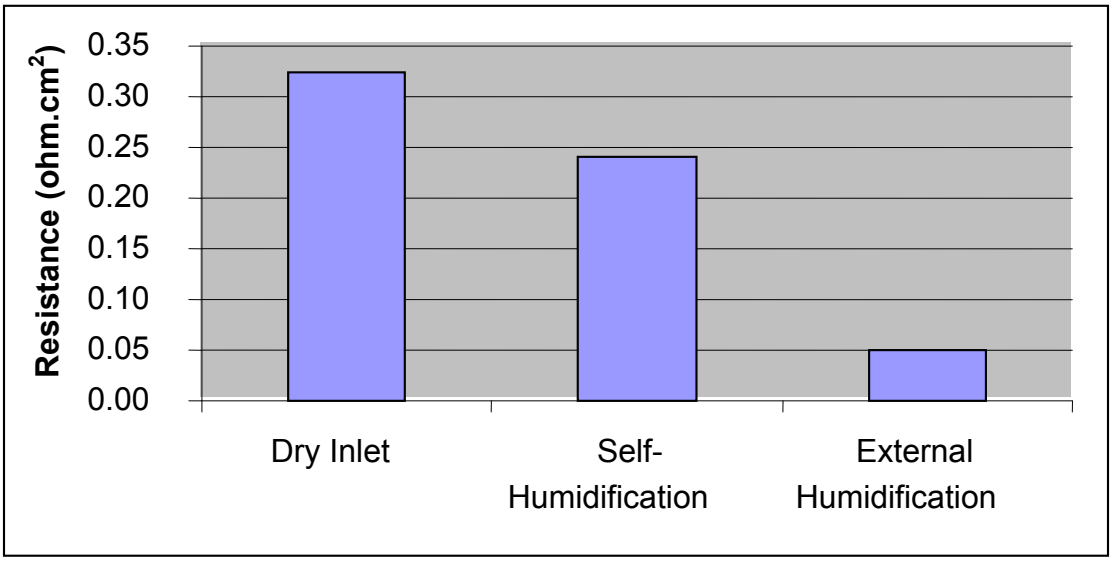

Figure 19. Fuel cell resistance for dry, self, and external humidifications at 80 °C.

The ohmic loss decreased with an increase in relative humidity of feed gas to the cell. The use of humidifier reduced the ohmic resistance.

Four-Cell Stack Experiment—Figure 20 shows the four cell stack experiment with no humidification (diamond), internal humidification (triangle), and external humidification.

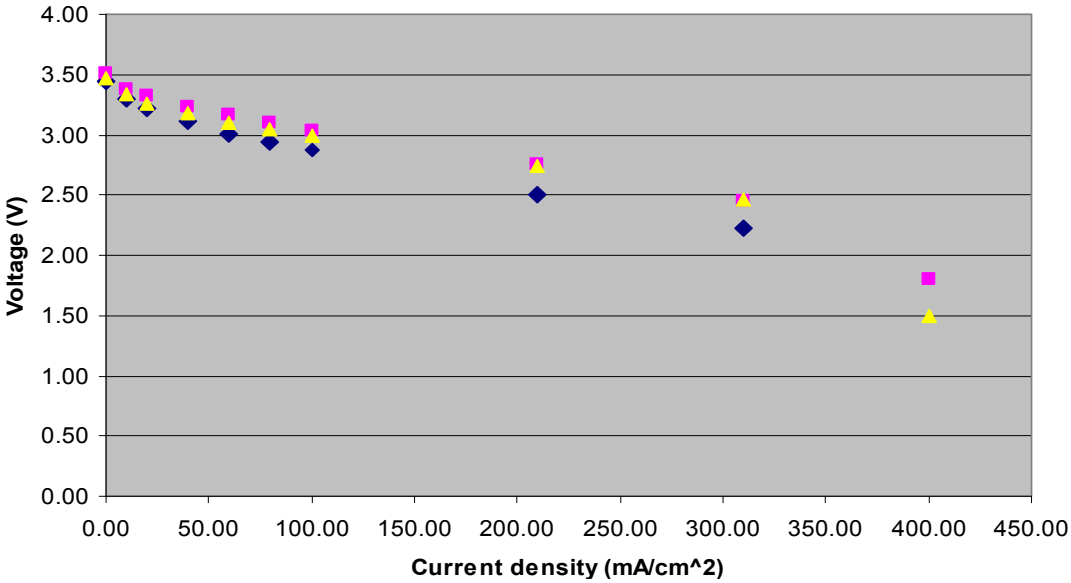

Figure 20. The effect of internal humidification for four-cell stack (cell T = 60 °C, anode T = 25 °C, cathode T = 25 °C).

The operating temperature was 60 °C and the anode was not humidified. The experiment was carried out with two internal humidifier cells and the membrane for the humidifier was Nafion®115. Open circuit voltage was 3.44, 3.46 and 3.51 V for no humidification, internal humidification, and external humidification, respectively. At low current density, where electrode kinetics plays a major role, externally saturated feed provides high voltage, i.e., low overpotential because of high active area for the electrochemical reaction due to the presence of sufficient water. At a current density of 200 to 350 mA/cm^2, the overpotential of the internally humidified cell is close to the externally humidified cell. This may be due to the contribution of water generated within the cell. In this four cell stack experiment, the minimum flow rate required was greater than 1 liter/min for both the anode and cathode, and thus, the load based operation could not be used due to the limitation of flow rate of the system. Although the advantage of utilizing the internal humidifier was not pronounced as much as the case of single cell and two-cell stack, it would improve the performance of fuel cell in the optimized condition.

Conclusions

A simplified and compact fuel cell system with no external humidification has been designed and investigated. A model was developed for the system, which includes a combined analysis of the generation of water in the fuel cell and the diffusion of water from the wet side of humidifier to the dry feed stream. A single cell and stack experiments of the internal humidifier incorporated cell have shown improved performance of fuel cell compared to the dry feed operation. However, the performance was lower than that of externally humidified operation by 20 to 30% in a single cell experiment. Polymer membranes such as Nafion® and SPEEK have

been successfully employed in the fuel cell system to provide the diffusion medium for the transport of water vapor from the humid exhaust gas to the dry feed stream. In order to improve the efficiency of the MEA, new composite membranes using inorganic acid were prepared and tested. The composite membrane showed higher performance, which may be attributed to the improved conductivity and lower ohmic resistance of the membrane

The humidifier may be further improved by increasing the active area of diffusion and reducing the thickness of the membrane. The implementation of an internal humidifier with highly efficient MEAs provides the basis for a new compact fuel cell system for space applications.

Patents, Publications, and Presentations and Students From Research

Publications

1. Choi, V. Mittal, D. Slattery, L. Bonville, R. Kunz, & J. Fenton, Self-humidification of PEM Fuel Cells by Internal Humidity Exchanger: Modeling and Experiment, *To be submitted to the J. Electrochem. Soc*., (2007).

Presentations

1. Pyoungho Choi, Vishal Mittal, Jong Baik, Darlene Slattery, Leonard Bonville, Russell H. Kunz, and James Fenton, Self Humidification of PEM Fuel Cells by Internal Humidity Exchanger, *American Chemical Society*, Boston, MA, August 19-23, 2007.

2. Rohit Agarwal, Nahid Mohajeri, Darlene K. Slattery, Jong Baik, and James M. Fenton, Effects of RH on stabilized Nafion®/Phosphotungstic acid composite membranes during fabrication process, *American Chemical Society*, Boston, MA, August 19-23, 2007.

Students

1. Rohit Agawal (University of Central Florida)

2. Bo Li (University of Central Florida)

References

1. M. V. Williams, H. R. Kunz, and J. M. Fenton, J. Power Sources,135, 122 (2004).

2. W. H. J. Hogarth and J. B. Benziger, J. Power Sources, 159, 968 (2006).

3. M. Watanabe, H. Uchida, Y. Seki, M. Emori, and P. Stonehart, J. Electrochem. Soc., 143, 3847 (1996).

4. S. Arico, V. Baglio, A. Di Blasi, and V. Antonucci, Electrochem. Commun., 5, 862 (2003).

5. S. H. Kwak, T.H. Yang, C.S. Kim, K.H. Yoon, J. Power Sources, 118, 200 (2003).
6. M. Watanabe, Y. Satoh, and C. Shimura, J. Electrochem. Soc., 140, 3190 (1993).

7. S. Ge, X. Li, and I.-M. Hsing, Elecrochim. Acta., 50, 1909 (2005).

8. F. N. Buchi and S. Srinivasan, J. Electrochem. Soc., 144, 2767 (1997).

9. Z. Qi and A. Kaufman, J. Power Sources,135, 122 (2004).

10. M. Santis, D. Schmid, M. Ruge, S. Freunberger, F. N. Buchi, Fuel Cells, 4, 214 (2004).

11. N. Giordano, P. Staiti, S. Hocevar, and A.S. Arico, Electrochim. Acta, 41, 397(1996).

12. S. Malhotra and R. Datta, J. Electrochem. Soc., 144, 23 (1997).

13. B. Tazi and O. Savadogo, Electrochim. Acta, 45, 4329 (2000).

14. B. Tazi and O. Savadogo, J. New Mater. Electrochem. Syst., 4, 187 (2001).

15. V. Ramani, H. R. Kunz, and J. M. Fenton, J. Membrane Science, 232, 31 (2004).

16. V. Ramani, H. R. Kunz, and J. M. Fenton, Electrochim. Acta, 50, 1181 (2005).

17. M. V. Williams, , E. Begg, L. Bonville, H. R. Kunz, and J. M. Fenton, J. Electrochem. Soc., 151, A1173 (2004).

18. M. V. Williams, H. R. Kunz, and J. M. Fenton, J. Electrochem. Soc., 151, A1617 (2004).

19. Y. Song, J. M. Fenton, H.R. Kunz, L. J. Bonville, and M. V. Williams, J. Electrochem. Soc., 152, A539 (2005).

20. Y. Song, Y. Wei, H. Xui, M. Williams, Y. Liu, L. J. Bonville, H. R. Kunz, and J. M. Fenton, J. Power Sources, 141, 250 (2005).

21. Xu, H., Y. Song, H. R. Kunz, and J. M. Fenton, J. Electrochem. Soc. 152, A1828 (2005).

22. Y. Si, R. Jiang, J. –C. Lin, H. R. Kunz, and J. M. Fenton, J. Electrochem. Soc. 151, A1820 (2004).

23. R. Jiang, H. R. Kunz, and J. M. Fenton, J. Electrochem. Soc. 152, A1329 (2005).

24. L. Wang, B.L. Yi, H.M. Zhang, and D.M. Xing, Electrochim. Acta, 52, 5479 (2007).

25. T. A. Zawodzinski, T. E. Springer, J. Davey, R. Jestel, C. Lopez, J. Valerio, and S. Gottesfeld, J. Electrochem. Soc., 140, 1981 (1993).

26. T. V. Nguyen and R. E. White, J. Electrochem. Soc., 140, 2178 (1993).

October 2007

Gas Permeable Chemochromic Compositions for Hydrogen Sensing

N. Mohajeri, N. Muradov, G. Bokerman, and A. T-Raissi
Florida Solar Energy Center

J. Captain
NASA-KSC

B. Peterson
ASRC Aerospace

M. Whitten
University of Central Florida

Research Period: January 2004 to December 2007

Abstract

Safety is always a concern in all applications that utilize hydrogen (H_2) in one form or the other. Hydrogen leaks are invisible and odorless. In addition, blending odorants or additives into hydrogen in a manner similar to natural gas is undesirable for certain applications such as use in proton exchange membrane fuel cells. To facilitate detection of the location of hydrogen leaks, a special chemochromic H_2 sensing material has been researched, developed and patented at the Florida Solar Energy Center (FSEC). The development of the smart paint sensors has been done with close coordination and collaboration with the NASA Kennedy Space Center scientists. The hydrogen leaks are shown by changes in color from white to gray of the sensing material. This sensing material employs titania (TiO_2) supported palladium oxide (PdO) pigments encapsulated within a special silicone matrix. Several batches of PdO H_2 sensing pigments were synthesized using various TiO_2 supports. Hydrogen detection activities were determined by TEM and particle size distribution analysis showed that smaller particles with hemispherical crystalline structure produced faster color change kinetics when exposed to H_2 gas. However, uniformly distributed PdO particles on the TiO_2 surface displayed greater color contrast, quantified by ΔE measurements. XRD analysis indicated that the crystalline phase of TiO_2 had no effect on the chemochromic performance of the pigments in a laboratory environment. Additional development resulted in the formulation of reversible sensors, ones that changed color in the presence of H_2 and reversed to the original color when no H_2 was present. These reversible H_2 sensors were formulated based on isopolycompounds (IPC) of tungsten and molybdenum, heteropolycompounds, HPC, all of which were synthesized and evaluated.

Objectives

The goal of this project was to develop a special powder material that can be applied like paint to the surfaces of cross-county lines at NASA-KSC and used for detecting hydrogen leaks. Operations at KSC require safety and the use of extremely pure hydrogen. The proposed technique provides a visual method to detect and locate possible hydrogen leaks that may occur in the field lines, flanges and joints for hydrogen transport and use. In this report, the results with respect to irreversible and reversible chemochromic hydrogen sensors are presented.

Introduction

One of the future alternatives to current fossil-based transportation fuels is centered on hydrogen (H_2). Currently, H_2 is the primary energy source of today's space exploration projects as rocket propellant. It is also used in fuel cells that generate electrical power. Furthermore, hydrogen is an important industrial commodity produced and used in many industries. For example, it is used for the reduction of metal oxides (e.g., iron ore), ammonia synthesis, production of hydrochloric acid, methanol, higher alcohols, aldehydes and hydrogenation of various petroleum, coal, oil shale and edible oils. One key element in all uses of hydrogen is safety. H_2 is a colorless, odorless gas with a low explosive limit of about 4% in air. Therefore, reliable H_2 sensors are required to detect possible leaks wherever H_2 is produced, stored, or used.

Background

To detect H_2 sensors that consist of a palladium alloy Schottky diode on a silicon substrate are presently used. These sensors are based on metal-oxide-semiconductor (MOS) technology that is used in the semiconductor industry. The gas sensing MOS structures are composed of a hydrogen-sensitive metal (palladium or its alloy) deposited on an oxide adherent to a semiconductor. This hydrogen sensor has been commercialized and exploited in detecting H_2 leaks during pre-launches of space vehicles. Other research groups have also used palladium or the like as a sensing element for detecting H_2.

A hydrogen sensor containing an array of micromachined cantilever beams coated with palladium/nickel has also been reported. Semiconductors (e.g., gallium nitride) with wide band-gap have also been used to make MOS diodes for H_2 detection. One of the concerns for all of these types of sensors using palladium or the like is the requirement of a high operating temperature (greater than 200 °C) and further elevated temperatures (greater than 500 °C) to reactivate the sensing element, bringing about lengthy analysis. Another issue is sensitivity of the sensing element to other compounds commonly found in the atmosphere, including water vapor and various hydrocarbons and reducing gases such as carbon monoxide and hydrogen sulfide.

Although not conventionally used, chemochromic sensors for hydrogen sensing have been disclosed. For example, published U.S. Application No. 20040023595 to Liu et al. discloses a fast response, high sensitivity structure for optical detection of low concentrations of hydrogen gas. This structure is comprised of a substrate, a water-doped WO_3 layer coated on the substrate; and a palladium layer coated on the water-doped WO_3 layer. In related work, U.S. Application No. 20040037740 to Liu et al. discloses a sensor structure for chemochromic optical detection of hydrogen gas comprising of a glass substrate with a vanadium oxide layer coated on the glass substrate and a palladium layer coated on the vanadium oxide layer. Field tests have shown the hydrogen sensors disclosed by Liu et al. lack field stability, have a tendency to crack and peel, and can be washed off by precipitation and/or condensation.

In U.S. Patent No. 5,849,073, Sakamoto discloses a pigment for sensing gas leakage. This pigment is produced by adding one of salts of platinum group metals to a slurry of particulate substrate, neutralizing the resultant mixture to deposit at least one of oxides, hydroxides and hydrated oxides of platinum group metals on the surfaces of the particulate substrate, and if necessary, further adding to said slurry at least one of compounds of aluminum, silicon, titanium, zinc, zirconium, tin, antimony and cerium, neutralizing the resultant mixture to deposit at least one of compounds such as oxides, hydroxides and hydrated oxides of aluminum, silicon, titanium, zinc, zirconium, tin, antimony and cerium, on the particles (something is

missing here, but there is no description of the organic resins revealed in the patent). The resinous composition disclosed is typically quite impervious to gas penetration. Sakamoto requires very thin coatings (typically 2 mils) with relatively high concentrations of active chemochromic compounds. In addition, compositions disclosed by Sakamoto do not show selectivity to hydrogen.

Results and Discussion

The hydrogen (H_2) sensors discussed in this section are comprised of a gas permeable matrix material intermixed and encapsulating with at least one chemochromic pigment. The chemochromic pigment produces a detectable change in color of the overall sensor composition in the presence of H_2 gas.

A wide variety of gas permeable encapsulating matrix materials can be used with the FSEC-developed formulations. Preferred gas permeable polymers generally provide a gas permeability that is at least equal to the gas permeability of low-density polyethylene. The encapsulating matrix materials are preferably cross-linked polymers including silicone rubbers or silicone resins. Such polymers are water resistant which allows sensor composites based on the FSEC formulations to remain useful in wet environment applications despite the water solubility of most pigments. A polysiloxane available in cross linked form that provides higher permeability to gases than other polymers is poly(dimethylsiloxane) rubber or PDMS rubber. PDMS rubber can be prepared using a moisture cure typically referred to as a sealant, or as a high or low consistency pre-form of silicone rubber that is then cured to a rubbery consistency.

The high gas permeability matrix material allows the composition of these sensors to be used in thicker segments and with lower concentrations of the active pigment as compared to previous related sensors while retaining the rate and extent of color change similar to the free pigment. The encapsulating matrix also provides enhanced protection to weather and environmental contaminants, including moisture.

Irreversible Pigments

The irreversible pigment is based on PdO supported on TiO_2.[3] When the pigment is exposed to H_2 gas, PdO is reduced to Pd and this transformation results in color change from beige to dark gray. Figure 1 depicts the application of a chemochromic tape based on the FSEC-developed irreversible hydrogen detecting formulation before leak (at left) and with H_2 leak (at right) at the dark spot.

Figure 1. Irreversible hydrogen sensor before and after leak.

The FSEC sensing pigments were developed as follows.

Pigments Preparation—The HIT-46 pigment was purchased from Ishihara Sangyo Kaisha Ltd. The pigments are based on PdO supported on TiO_2, which undergo a color change when contacted with H_2. Several chemochromic pigments were prepared using different TiO_2 support: Aldrich (mainly, TiO_2, rutile crystalline form) with an average particle size of 1 μm, Fisher Scientific TiO_2, Dupont R103 TiO_2, and P-25 Degussa nanosize TiO_2.

Tape Preparation—The chemochromic H_2 sensing tape was a mixture of 3-wt% of pigment in a silicone matrix. The thickness of the tape was varied during production. Typically, the mixture was spread into thin films (≈2 mils) using a Gardco adjustable film applicator on wax paper.

Transmission Electron Microscopy—A FEI/Philips, Tecnai F30, 300 kV field emission source TEM instrument, equipped with STEM, HAADF detector and XEDS was used to perform TEM bright field high resolution imaging analysis. The software was Tecnai G2 Digital Micrograph (DM) and Tecnai Imaging & Analysis (TIA). The samples were mounted on a micro-grid by placing a few droplet of a methanolic suspension of pigment, followed by air-drying.

X-ray Diffraction (XRD)—The crystalline phase of the TiO_2 particles was analyzed by means of Rigaku XRD using a CuK_α radiation at 40 kV from 20° to 70° at a rate of $2°min^{-1}$ (2θ).

As previously noted, the chemochromic hydrogen sensing tapes are based on a PdO supported on TiO_2 pigment, which are mixed with a silicone matrix and cast as tapes. When the pigment is exposed to H_2 gas, PdO is reduced to Pd and this transformation results in a color change from beige to dark gray.

Since human eye can not quantitatively contrast the extent of color change, we used a calibrated UV spectrometer with a built in algorithm specifically devised for this purpose:

$$\Delta\mathbf{E}^* = \{(L-L')^2 + (a-a')^2 + (b-b')^2\}^{½}$$

Where, L*- Lightness Value, a*- position on red-green axis, and b*- position on yellow-blue axis. The above equation gives a standard measurement with which to compare the color change associated with different samples. The greater the $\Delta\mathbf{E}^*$ value, the greater the color contrast. The chemochromic films were analyzed in this way, both before and after exposure to hydrogen, allowing quantification of the intensity of color change.

Initially, commercially available PdO pigment was evaluated. Figure 2 depicts the ΔE^* values for various weight concentrations (1%, 3%, 6%, 10%) of HIT in sealant cast as films. The ΔE^* value increases as the concentration of the pigment increases to 6 wt%. However, by increasing the amount of the pigment in matrix to 10 wt%, no significant increase on color contrast was observed and as a result 6 wt% seems to be the optimized level with respect to ΔE^*.

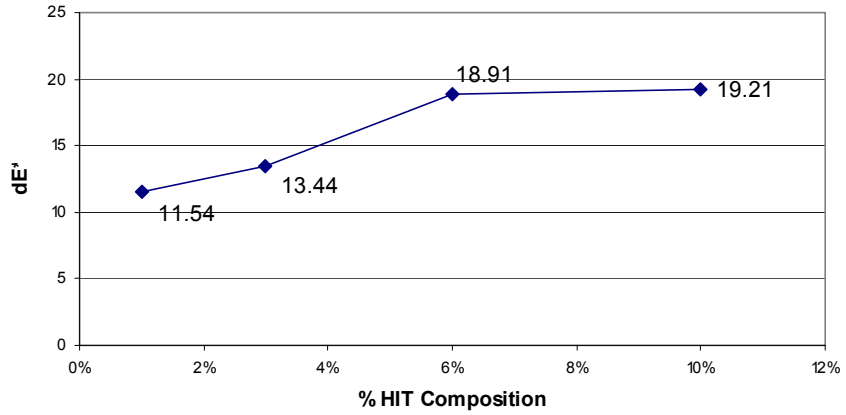

Figure 2. ΔE* values for 1%, 3%, 6%, 10% weight concentration of HIT in sealant cast as films.

In order to enhance the color contrast and increase the rate of the color change, molybdic anhydride (MA), cobalt acetate, and ammonium molybdate (AM) were mixed as color enhancers with HIT using 1:10, 1:5, 1:2, and 1:1 ratios (see Figure 3). With the ammonium molybdate (AM) ranging in AM:HIT ratios from 1:10, 1:5, the time required to complete the color change decreases with increasing concentration of AM (2.5 to 1 min.) while the intensity of the color change also decreased (ΔE* = 19.67 to18.85). The molybdic anhydride/HIT samples react more rapidly (all under one minute) with the intensity increasing with increased concentration of MA (ΔE* = 18.83 for 1:10 ratio of MA:HIT and ΔE* = 24.69 for 1:1 ratio of MA:HIT).

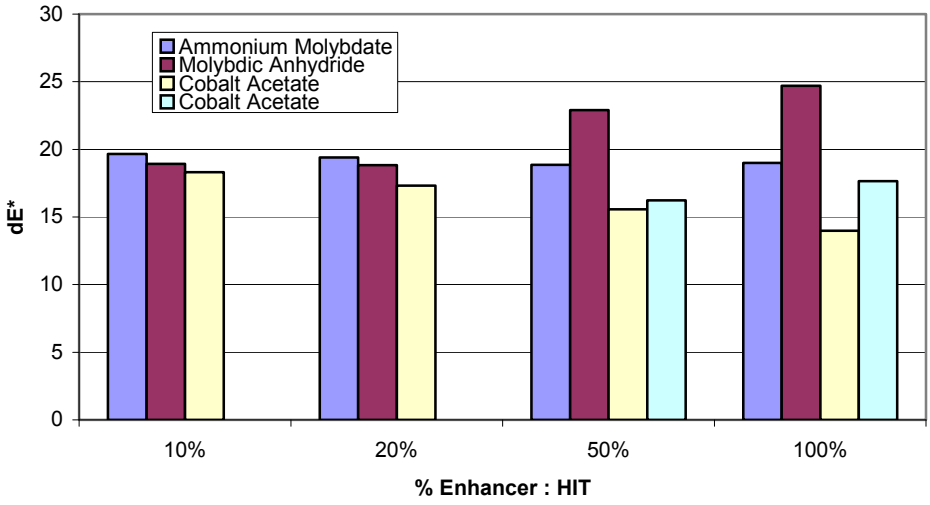

Figure 3. ΔE* values for various weight percentages of color enhancers mixed with HIT in sealant and casted as films.

The cobalt acetate/HIT samples were less impressive. Although they all reacted to completion within about 90 sec, their color change intensities ranged from a high of dE*=18.31 at the lowest ratio to 13.99 at the largest ratio.

Color contrasts measurements, ΔE, of four pigments prepared using four different TiO_2 supports (from Aldrich, Degussa, Fisher Scientifics, and Nanotek) were conducted both as a powder deposited on a glass slide and inside the RTV matrix with a pigment to matrix ratio of 1:10. Samples' colorimetric parameters a*, b*, c*, and L were measured before and after exposure to 100% H_2 gas and then ΔE values were calculated (see Figure 4).

In general, the slides of these four pigments reacted with a greater color change than when tested inside the matrix with Degussa TiO_2 pigment showing the best color contrast. For the samples within the matrix, the Aldrich TiO_2 with a ΔE=29.8 has the best color contrast followed by Degussa TiO_2. It was noted that the Degussa TiO_2 has the fastest response time among all the pigments.

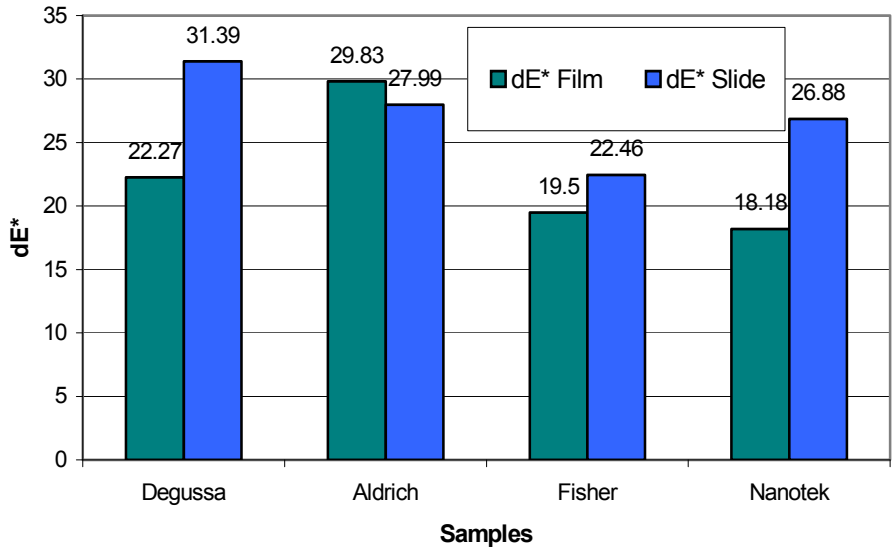

Figure 4. ΔE* values for Aldrich, Degussa, Fisher Scientifics, and Nanotek TiO_2 pigments in sealant in a pigment to sealant ratio of 1:10 casted as films.

Matrix Layering Effect—It has been noted that when a single layer of pigments within silicon matrix is casted as a film, only the one side that is in direct contact with H_2 gas (inner side) changes color and the outer layer's color that should be monitored visually remains unchanged. Since the solubility of O_2 gas in the matrix is almost equal to H_2 gas solubility, the color change phenomenon may be due to having a Pd catalyzed reaction between O_2 and H_2 gases within the middle section of the film. As a result H_2 gas does not reach the outer layer of the film and the color of the pigments remain unchanged. This problem was addressed by providing an extra layer of the virgin silicone matrix as an overcoat. Figure 5, depicts the matrix layering effect with respect to pigments color change when exposed to H_2 gas. Although not clearly shown below, the PdO/TiO_2 pigment is evenly distributed in the silicone throughout the full thickness of the top layer shown. The thickness of the virgin silicone overcoat is equal to or larger than the thickness of top portion containing the pigment.

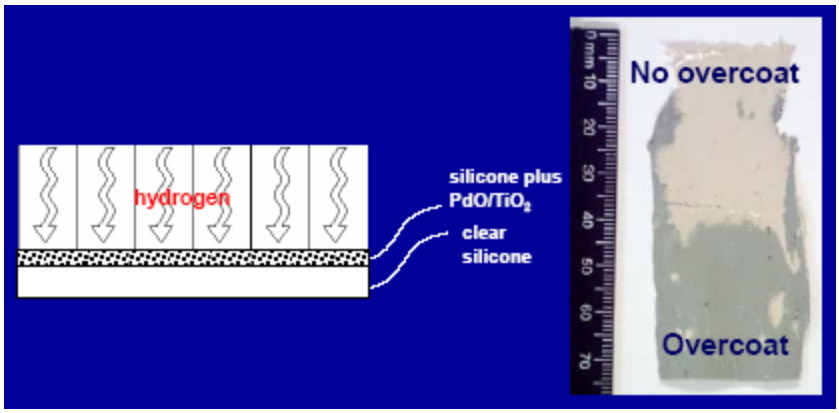

Figure 5. Matrix layering effect for irreversible hydrogen sensor.

***Cryogenic Studies*—**Small amount of HIT pigment (18.6 mg) was placed within the glass U-tube of an Altamira AMI-200 TPD instrument. A flow of 20 ml/min of 10% H_2 in Argon gas was maintained through TPD's U-tube. Sample temperatures within the TPD's U-tube was kept isothermal at –90 °C. Figure 6 depicts the TCD signal detected, which was attributed to the pigment reacting with H_2 gas, and sample color change. Reaction was complete in about 4 minutes.

The effect of matrix at -30 °C (above glass transition temperature of sealant) was studied similarly to pure pigment using the TPD instrument (Figure 7).

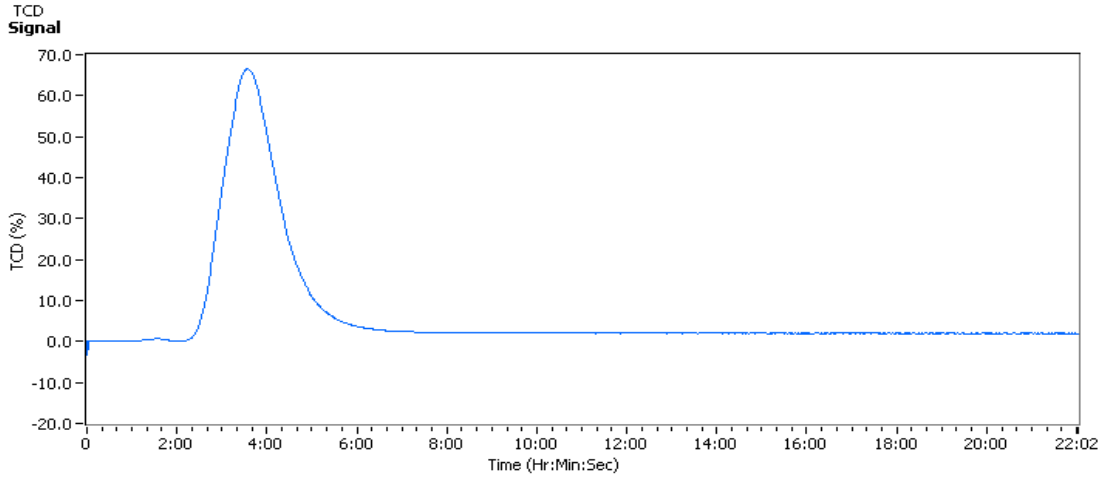

Figure 6. TCD signal vs. time for HIT pigment reacting with H_2 gas at -90 °C.

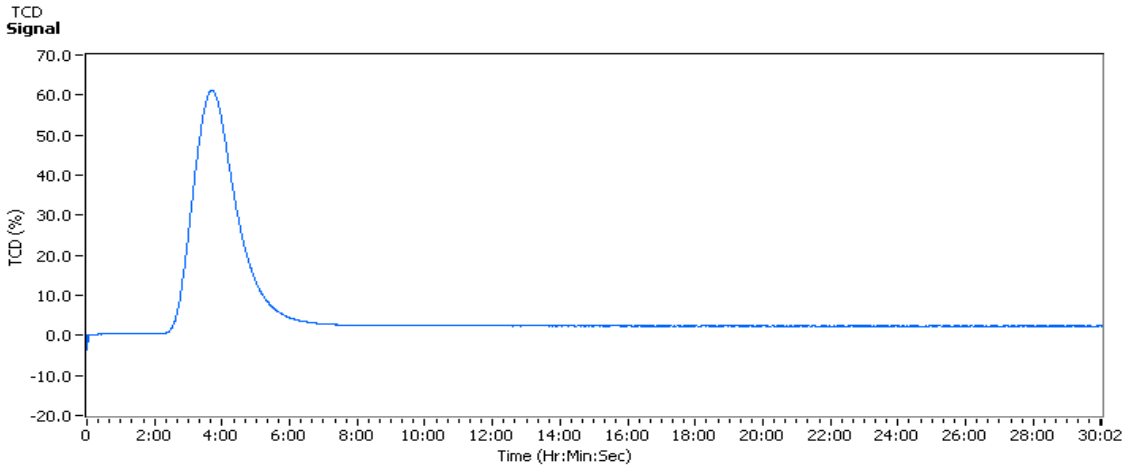

Figure 7. TCD signal vs. time for HIT pigment in matrix reacting with H_2 gas at -30 °C.

Carbon Monoxide Effect—The effect of carbon monoxide was studied using TPD instrument for both the pure form of HIT pigment and one mixed with sealant. A 20 ml/min flow of 25% CO in argon gas was used and the sample temperature was ramped up at a rate of 10 °C/min from -30 °C to 40 °C. For the pure HIT pigment, a TCD signal was detected (Figure 8) as well as sample color change within a range of temperatures from –10 °C to 35 °C, which is attributable to pigment reacting with CO gas and reaction was complete within 6 minutes. However for the matrix, a TCD signal was detected with no color change as a result of pigment reacting with CO gas. To better understand this phenomenon, the pure matrix was loaded in the TPD instrument and the same set of condition with CO gas was applied. A TCD signal was detected which is attributable to dissolution of CO gas in the matrix.

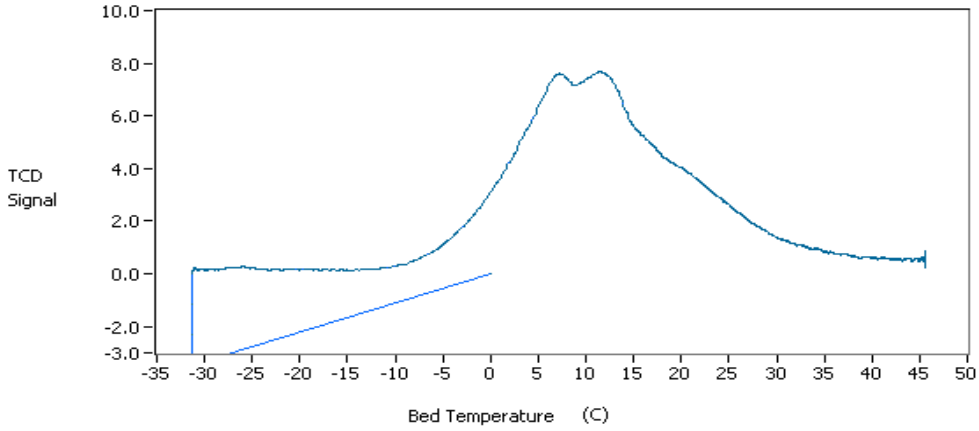

Figure 8- TCD signal vs. temperature for HIT pigment reacting with CO gas.

Hydrazine Effect—Hydrazine is one of the strong reducing agents that can be released into the air during shuttle lunches and as a result its interference with any hydrogen leak detection system is very crucial. The effect of hydrazine on HIT film was studied using the vapors of 17.5% solution of hydrazine in water generated inside the saturator of the TPD instrument. Two pulse chemisorption regiments were used: 50 pulses at 30 °C and 30 pulses at 60 °C. In both cases no reaction or color change was detected.

***TiO_2 Effect*—**The effect of TiO_2 support particles was evaluated by synthesizing four pigments based on Fisher, Dupont R103, Aldrich and Degussa P-25 Titanium dioxides. Each pigment formulation was exposed to hydrogen in an exposure chamber for various lengths of time. Samples were analyzed with a colorimeter to obtain the Δ**E** value for analytical analysis. Results for several of the samples are given in Figures 9 and 10. The original color and final color change can be adjusted by varying the precise makeup of the formulations.

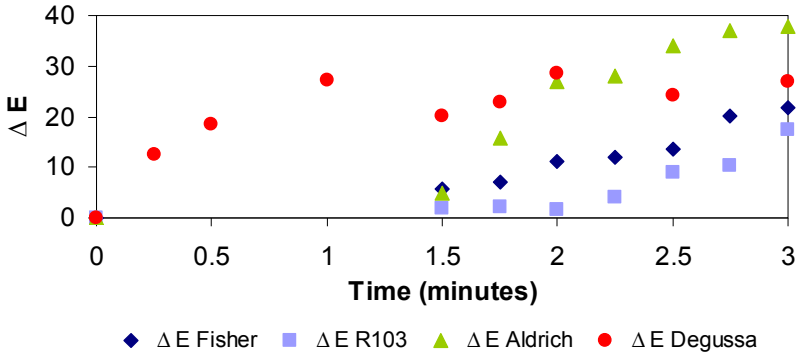

Figure 9. Comparison of Δ**E** vs. hydrogen exposure time for four TiO_2 pigments.

Figure 10. Comparison of pigment formulations exposed to hydrogen.

Characterization of PdO/TiO_2 Particles

Most TiO_2 photocatalysts contain anatase crystalline phase. Anatase titania has a band gap of 3.2 eV while rutile TiO_2 has a band gap of 3.0 eV. Rutile TiO_2 has limited photocatalytic activity. It is known that Degussa P-25 is a mixture of these two phases with an approximate composition of 75% anatase and 25% rutile phase (Figure 11b). Aldrich and DuPont R103 TiO_2 are mainly rutile (Figure 11a). Fisher TiO_2 was the only sample with unknown crystalline phase. The crystal structure of Fisher TiO_2 was characterized using XRD and the diffraction pattern is given in Figure11c. The sharp peaks at 25.3° and 47.9° were attributed to anatase TiO_2. These results indicate that photocatalytic activity of TiO_2 or lack thereof has no effect on the chemochromic activity of TiO_2/PdO pigments in laboratory environment.

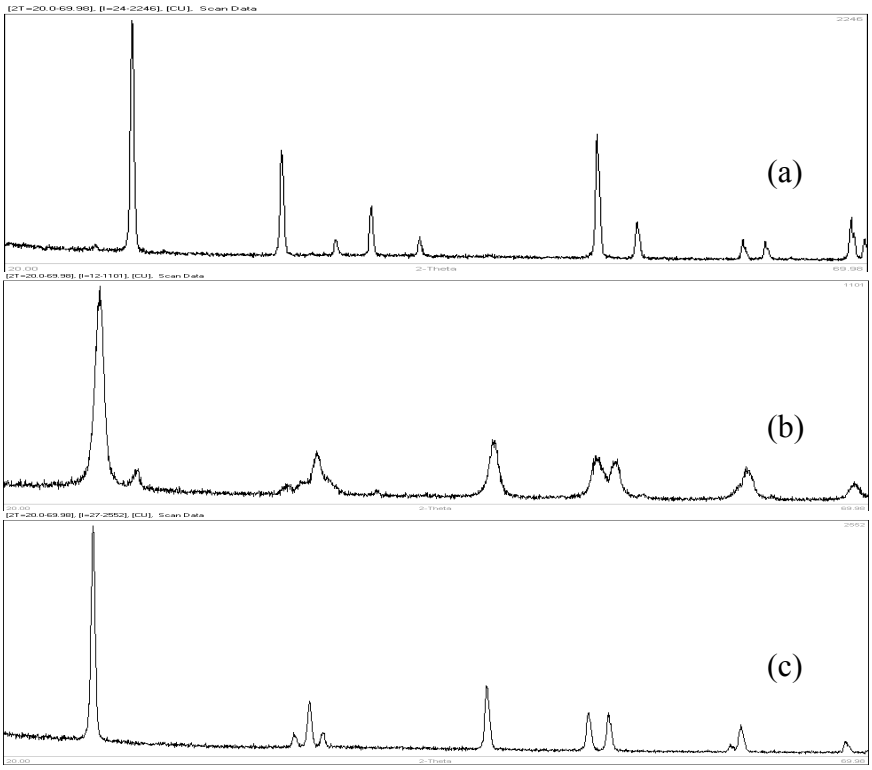

Figure 11. XRD Spectra of TiO_2 supports (a) Aldrich, DuPont R103, (b) Degussa P-25, and (c) Fisher.

Although the TiO_2 support does not change color, it does affect the chemochromic reaction, as variation of the substrate affects the function of the pigment. To gain insight into the size and morphology of the pigments, underlying chemistry and role of the TiO_2 in the coloration reaction, the pigments were analyzed under a transmission electron microscope.

Figure 12 shows TEM images of various PdO/TiO_2 pigments investigated. It can be seen that the TiO_2 particle sizes are different in each case (Table I). Although all pigments have been prepared using the same procedure, it can be seen that PdO particle sizes and their distribution vary. PdO particles are clearly visible as dark areas on the surface of TiO_2 particles. In the case of Degussa P-25 and Aldrich TiO_2, the hemispherical PdO crystallites are well dispersed and strongly attached to the metal oxide support at their flat planes (Figures 12 a & b).

Table 1. Particle size for various TiO_2 supports

TiO_2 Sample	Degussa P-25	Aldrich	Fisher	DuPont R103
Particle size (μm)	0.02-0.04	0.5	0.1-0.5	0.05-0.2

Faster response time of Degussa P-25 based pigments compared to that of Aldrich could be explained in terms of the size and homogeneity of PdO particles and their interaction with TiO_2 surfaces. The PdO particle size for Degussa P-25 is homogenous with an estimated mean diameter of 2.5 nm. On the other hand, the PdO particle size for Aldrich TiO_2 is less homogenous and varied from 2 to 10 nm with an estimated average particle size of 6 nm. Fisher and DuPont R103 supported pigments show similar behavior when exposed to hydrogen. In both cases, PdO particles are spherical and as a result have less interaction with TiO_2 support

surfaces compared to Degussa P-25 and Aldrich supported pigments. PdO particle sizes for Fisher and DuPont R103 pigments are greater than 5 nm.

It is concluded that not only PdO particle size and its distribution on TiO_2 surfaces can affect color change but also the size and particle structure of TiO_2 can influence the sensitivity and extent of color change in irreversible pigments.

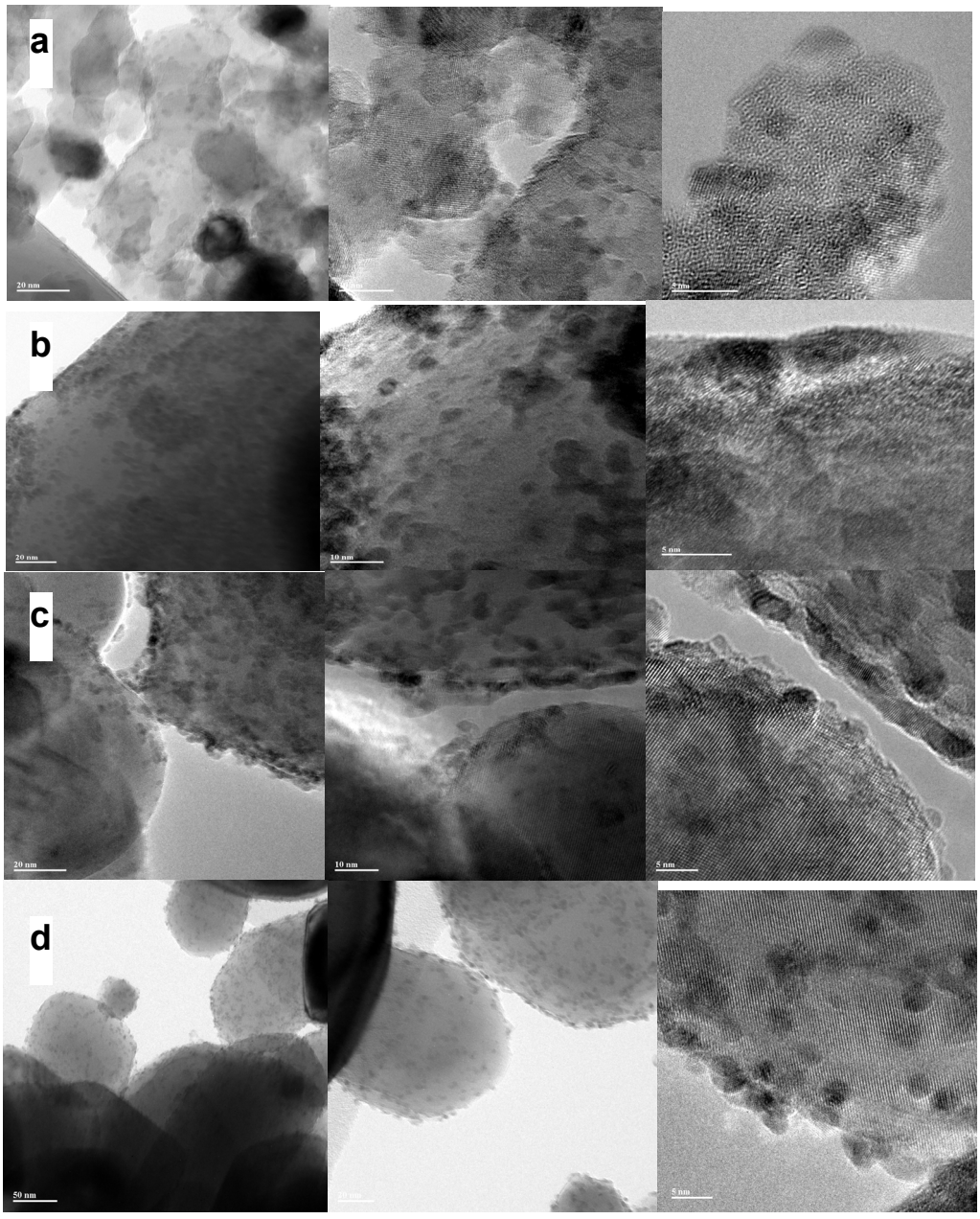

Figure 12. TEM images of a) PdO/Degussa P-25, b) PdO/Aldrich, c) PdO/Fisher, and d) PdO/Dupont R103 TiO_2 pigments.

Reversible Pigments

The color change of the H_2 sensor can be made to be reversible (i.e., the sensor reestablishes its original color after the exposure to H_2 is ceased), by incorporating reversibility enhancing agents. These agents are compounds of transition metals that rapidly change their oxidation state and, subsequently, color in a reducing/oxidizing environment. For reversibility to proceed, it is believed that the sensor composition must allow oxidizing species, such as oxygen, to also permeate to the pigment to regenerate the original color. Cross-linked polymers including silicone rubber (e.g., PDMS rubber), when used in conjunction with the reversibility enhancing agents, have demonstrated reversibility. In such compositions, the original color is reestablished/regenerated generally within 1-30 seconds after exposure of the material to hydrogen has ceased. This behavior was demonstrated with a PDMS rubber encapsulating formulations comprising polyoxo compounds (POC) of W and/or Mo immobilized on a support and doped with small amounts of noble metals. Particular examples of POC of W and Mo include: silico-tungstic acid (STA) $H_4[SiW_{12}O_{40}]$, phospho-tungstic acid (PTA) $H_3[P(W_3O_{10})_4]$), phospho-molybdic acid (PMA) $H_3[P(Mo_3O_{10})_4]$. It should be noted that STA and PTA show very fast kinetics (seconds) for both coloration and bleaching reactions, whereas PMA rapidly acquires color (seconds to minutes), but bleaches very slowly (days). Thus, depending on the particular application, the sensor provides an opportunity to fine-tune the kinetics of bleaching by changing the composition of the H_2 sensor formulation. Various light-colored metal oxides in the form of fine powders (0.01-100 μm) can be used as a support for the POC of W and Mo, e.g., TiO_2, Al_2O_3, SiO_2, ZrO_2, and molecular sieves. Noble metal dopants such as Pt, Pd, Ir, Ru added in small quantities to the sensor formulation are essential for enhancing the kinetics of both coloration and bleaching of POC of W and Mo. Pt is added to the formulation at the level of 0.001-5.0 wt% (of total). The presence of Pt nano-particles (Pt_{np}) significantly accelerates electron transfer from molecular hydrogen to POC, (e.g., STA) resulting in their rapid color change. Without Pt_{np} color change would occur very slowly (hours to days), or may not occur at all. Figure 13 depicts the kinetics of coloration and bleaching using the prepared reversible H_2 sensor.

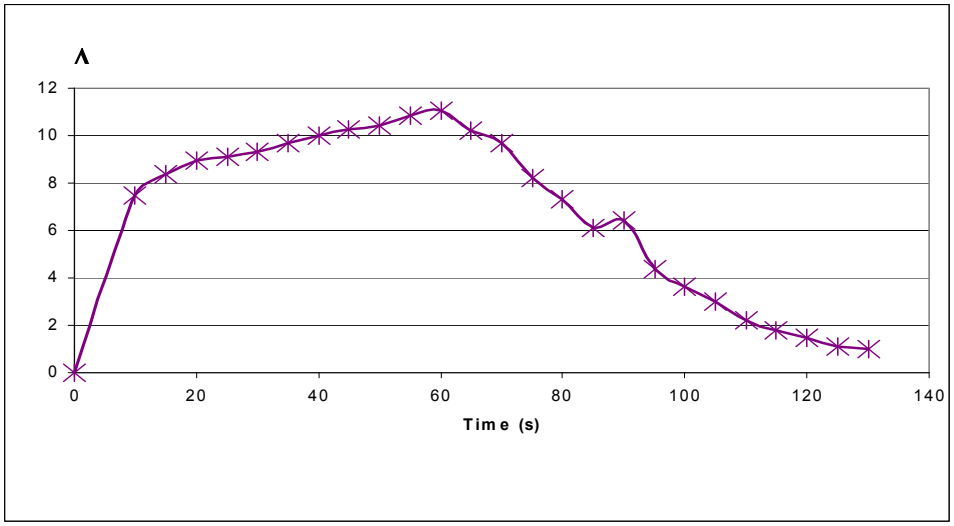

Figure 13. Kinetics of coloration and bleaching using the PDMS-encapsulated STA/Pt/Al_2O_3 reversible H_2 sensor.

Control experiments indicated that reversible H_2 sensors are not sensitive (i.e., do not change color) due to exposure to other reducing gases such as CO, CH_4 and other hydrocarbons. The encapsulation of the reversible chemochromic pigment in the PDMS matrix somewhat slows down the kinetics of both coloration and bleaching processes due to the diffusion limitation of H_2 and O_2 transport through the matrix material.

A series of experiments on synthesis and testing of new formulations acting as reversible H_2 sensors was conducted. In particular, formulations were synthesized based on isopolycompounds (IPC) of tungsten and molybdenum (as opposed to heteropolycompounds, HPC, that were previously used). IPC have a more simple structure than HPC (since they do not contain central atom: Si, P, etc.). Thus, so we reasoned that they demonstrate better long-term stability. IPC of W and Mo form by self-assembling of tungstate $(WO_4)^{2-}$ or molybdate $(MoO_4)^{2-}$ anions in acidic aqueous solutions are described by the following general equation (for tungstate):

$$pH^+ + qWO_4^{2-} \rightarrow [W_qO_y]^{n-} + (4q-y)\ H_2O$$

where p=8q-2y. In aqueous solutions, IPC of W exists as an equilibrium mixture of several polymeric anions, e.g., $[W_7O_{24}]^{6-}$, $[W_{10}O_{32}]^{4-}$, $[W_6O_{19}]^{2-}$, etc. The extent of polymerization is a function of the $H^+/(WO_4)^{2-}$ ratio, ionic strength and temperature. Of particular interest were the hexa- and deca-forms of IPT ($[W_6O_{19}]^{2-}$ and $[W_{10}O_{32}]^{4-}$, respectively) that form at H^+/WO_4^{2-} ratios greater than 1.5.

Synthesized IPC of W and Mo were immobilized on the mixture of activated alumina and Pt (1 wt%)/Al_2O_3. The resulting slurry was left to dry overnight. The resulting solid product was then ground to a fine powder and incorporated in the silicone matrix. The tests with hydrogen exposure indicated that the formulation containing IPC of Mo were not sensitive to H_2. The formulation including IPC of W were sensitive to H_2 and showed good reversibility, but their sensitivity (i.e., the cumulative color change due to H_2 exposure) was about one half of that of the formulation containing HPC of W (e.g., silicotungstic acid). It was concluded that the new formulations containing IPC of W and Mo have insufficient sensitivity to hydrogen in order to be used as reversible pigments.

Another series of experiments was conducted with polyoxometalates (POM) of W and/or Mo deposited on a porous support and doped with small amounts of noble metals, such as colloidal platinum. In this case, the POM-Pt pigments were not encapsulated into the silicone matrix. POM of W and Mo included: silico-tungstic acid (STA) $H_4[SiW_{12}O_{40}]$, phospho-tungstic acid (PTA) $H_3[P(W_3O_{10})_4]$), and phospho-molybdic acid (PMA) $H_3[P(Mo_3O_{10})_4]$. Porous supports included glass and paper filters. The lack of a polymer matrix significantly affected (i.e., increased) the kinetics of coloration and bleaching since H_2 diffusion through the matrix no longer was a limiting factor. STA and PTA showed very fast kinetics (seconds) for both coloration and bleaching reactions, whereas PMA rapidly acquired color (seconds to minutes), but bleached very slowly (hours-to-days). Figure 14 depicts the kinetics of coloration and bleaching for two representative polyoxometalates: STA and PMA supported on a glass filter. For Figure 14, it is clear that STA-silicotungstic acid renders the material a reversible action while PMA- phosphomolybdic acid, makes the system irreversible.

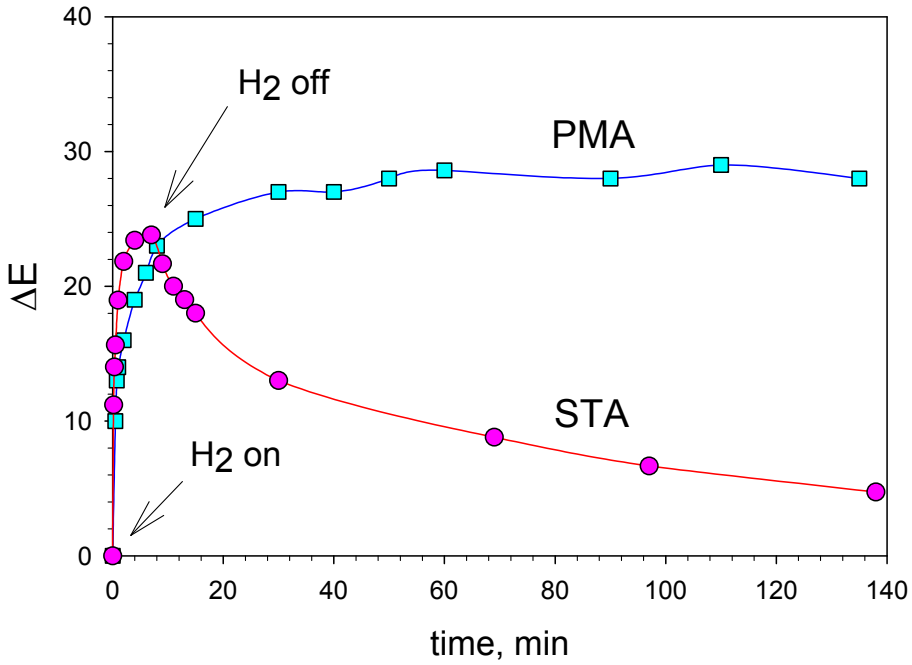

Figure 14. Kinetics of coloration and bleaching for two representative polyoxometalates (or heteropolyacids). STA-silicotungstic acid, renders the material a reversible action; PMA-phosphomolybdic acid, makes the system irreversible.

Thus, depending on the particular application, the reversible sensor provides an opportunity to fine-tune the kinetics of bleaching by changing the composition of the H_2 sensing formulation. The samples with POM-Pt supported on a glass filter showed good sensitivity to H_2 and good stability. In contrast, the POM-Pt samples with a paper filter support were sensitive to H_2, but not stable, especially, when exposed to direct solar light (the samples turned dark over 2-3 days of exposure to day light, or fluorescent bulb light). This could be explained by strong photoredox activity of POM compounds in presence of UV radiation. In this case, POM photooxidize the organic support and are converted to a reduced (colored) form (see details below).

The tentative mechanism of coloration and bleaching is as follows. When $H_4[SiW_{12}O_{40}]/Pt_{np}$ sees H_2, the original white color of the composition changes to dark-blue (within seconds). This is due to electron transfer from hydrogen to hexa-valent W(VI) resulting in the reduced form of the complex W(V) - which has an intense color, according to the reaction (1), where, for the sake of simplicity, W^{6+}= O and W^{5+}- OH moieties represent the original and reduced forms of STA.

$$W^{6+}= O + ½H_2 \rightarrow W^{5+}- OH \text{ (catalyzed by } Pt_{np}) \quad (1)$$

After the cessation of the exposure to hydrogen flow and within a few seconds, the original color of the sensor reappears (for both STA- and PTA-based sensors). The bleaching of the colored sensor can be attributed to the reaction of the reduced form of STA with oxygen from air with the regeneration of the original (oxidized) form of STA as follows:

$$2W^{5+} - OH + ½O_2 \rightarrow 2W^{6+}= O + H_2O \text{ (catalyzed by } Pt_{np})$$

In the presence of organic support and UV radiation POM compounds undergo the following transformation resulting in the reduced (colored) form of POM:

$$W^{6+} = O + OC + h\nu_{UV} \rightarrow W^{5+} - OH + (OC)_{oxidized}$$

Where, OC and $(OC)_{oxidized}$ are original and oxidized organic compound, respectively.

Glass filter cannot be photooxidized by POM (because of its inorganic nature), thus it is more preferred support for POM than paper filter.

In order to make the hydrogen sensing formulation completely irreversible, the composition of the POM compound would need to be changed so that its redox potential shifts to more positive values, thus preventing POM from giving up its electrons to oxygen. This approach can be coupled with the choice of a suitable matrix material that possesses a very low permeability toward oxygen in order to enhance the irreversibility of the H_2 sensing formulation, if so desired.

Field Testing at NASA-KSC

In collaboration with NASA-KSC scientists, field-testing of reversible and irreversible chemochromic hydrogen sensors has been conducted. Test kits of irreversible hydrogen sensor have been prepared and shipped to various NASA centers for evaluation and feedback. Furthermore, studies to uncover the underlying role of TiO_2 support used in irreversible hydrogen sensor have been started. New formulations including other POC and color-enhancing additives have been tested and evaluated in collaboration with NASA researchers. NAS-KSC researchers have applied for a U.S. patent for their efforts in the field testing and matrix development.

Conclusions

Four different chemochromic TiO_2 supported PdO pigments were synthesized and their activity toward hydrogen was measured. Degussa P-25 based pigments yielded the fastest discoloration kinetics toward H_2 gas while the Aldrich titania (mainly rutile crystalline form) based pigments had the greatest ΔE, color contrast, value. The chemochromic activity of the pigments toward hydrogen is a strong function of the PdO particle size and level of PdO dispersion on theTiO_2 support surface. Smaller PdO particles with hemispherical crystalline structure produced faster kinetics when exposed to H_2 gas. However, more uniformly distributed PdO particles on the surface of TiO_2 gave larger color contrast number, ΔE. XRD analyses showed that TiO_2 crystalline phase apparently had no effect on the chemochromic performance of these pigments in laboratory environment.

The color change of the H_2 sensor can be made to be reversible (i.e., the sensor reestablishes its original color after the exposure to H_2 is ceased), by incorporating reversibility-enhancing agents (e.g., the compounds of transition metals that rapidly change their oxidation state and, subsequently, color in a reducing/oxidizing environment). Polyoxometalates (POM) of W and Mo including silico-tungstic acid (STA) $H_4[SiW_{12}O_{40}]$, phospho-tungstic acid (PTA) $H_3[P(W_3O_{10})_4]$), and phospho-molybdic acid (PMA) $H_3[P(Mo_3O_{10})_4]$ were used as reversibility-enhancing agents. POM were doped with small amounts of Pt to catalyze the coloration-bleaching reactions. Two modifications of the reversible pigment were studied: (1) alumina-supported Pt-POM encapsulated in silicone matrix, and (2) Pt-POM supported on porous supports such as glass and paper filters. Both systems performed well during coloration and bleaching stages. The lack of polymer matrix significantly increased the kinetics of coloration and bleaching (since H_2 diffusion through the matrix no longer was a limiting factor). STA and PTA showed very fast

kinetics (seconds-to-minutes) for both coloration and bleaching reactions, whereas PMA rapidly acquired color (seconds-to- minutes), but bleached very slowly (hours-to-days).

Publications

[1] M. Whitten, J. Captain, B. Peterson, S. Trigwell, C. Berger, N. Mohajeri, G. Bokerman, N. Muradov, A. T-Raissi, & J. McPherson, "Chemochromic Hydrogen Detection," Proceedings of SPIE-The International Society for Optical Engineering, (2006).

Patent

U.S. Utility Application No. 11/414,900 "Gas Permeable Chemochromic Composition for Hydrogen Sensing," Gary Bokerman, Nahid Mohajeri, Nazim Muradov, Ali T-Raissi.

Presentations

[1] M. Whitten, J. Captain, B. Peterson, S. Trigwell, C. Berger, N. Mohajeri, G. Bokerman, N. Muradov, A. T-Raissi, & J. McPherson, "Chemochromic Hydrogen Detection," Proceedings of SPIE-The International Society for Optical Engineering, (2006).

[2] N. Mohajeri, A. T-Raissi, G. Bokerman, J. Captain, B. Peterson, S. Trigwell, M. Whitten, & C. Berger, "Effects of PdO Distributions over TiO_2 Particles on its chemochromic behaviors for hydrogen detection," Presented at TMS 2007, February 25-March 1, 2007.

November 2007

Hydrogen Education and Outreach

S. Schleith, P. Hall, A. Henzmann, and D. Block
Florida Solar Energy Center

Research Period: June 2002 to December 2007

Abstract

Education and outreach were extremely important components of the NASA hydrogen research program. These activities have supported four main areas: education of graduate and undergraduate engineering and science students, education for K-12 students and teacher professional development, participation in and offering of seminars and workshops, and a variety of public outreach activities. Each of the university participants have made educational activities a major part of their research program. The educational component has used the topics from the large variety of research projects for graduate student masters and PhD theses. In addition, the projects' results are communicated to local, national and international audiences through publications and presentations by university faculty members and their students. The totals are 222 publications, 196 presentations and the support of 96 students.

The goal of incorporating hydrogen education into K-12 student and teacher programs at FSEC has been successfully accomplished through curriculum development, professional development for teachers and special events for K-12 students. These activities are ongoing and are being continually expanded. Over the course of the grant period, an average 310 teachers per year have participated in hydrogen education training opportunities facilitated by FSEC staff. The teacher opportunities include multi-day institutes, one-day workshops, and half-day experiences. Interest in hydrogen continues to grow amongst teachers, as evidenced by the popularity of the many hydrogen training events held for teachers by FSEC throughout the year. Field trips to the Florida Solar Energy Center are also popular with schools with nearly 800 students with their teachers and 60 parents per year visiting the facility for informal instruction on hydrogen, solar and energy efficiency. The outreach program has been accomplished through the development of a fuel cell short course, publications, presentations, press releases and web site development, as well as personal interaction with the public.

Benefit to NASA

Knowledge and understanding of hydrogen technologies and its uses by NASA are done to assist NASA in the public's understanding of its mission and in gaining agency support. NASA also has a graying of its workforce and the education of science and engineering university students is becoming more critical to NASA's future missions and objectives. Thus, the objectives of this task were to develop and support education and outreach programs.

Graduate and Undergraduate Student Education

Each of the university participants have made educational activities a major part of their research program. The educational component has used the topics from the large variety of research projects for graduate student masters and PhD theses. These same topics are also used by the university students for part-time work. In addition, the projects' results are used for publications and presentations by university faculty members and their students reaching local, national and international audiences. Presented in Table 1 is a listing of the publications,

presentations and students supported by the hydrogen research grant. The totals are impressive with 222 publications, 196 presentations and the support of 96 students. The student statistics are 15 PhD candidates, 23 MS students, 2 postdoctoral fellows, 20 undergraduates and 36 unknown for a total of 96 students.

K-12 Students and Teacher Education

The goal of incorporating hydrogen education into K-12 student and teacher programs at FSEC has been successfully accomplished through curriculum development, professional development for teachers and special events for K-12 students. These activities are ongoing and are being continually expanded.

The hydrogen curriculum materials have been completed, but they are considered to be fluid documents that respond to new research and feedback from teachers. Once the curriculum materials were developed, the main focus was to reach as many teachers as possible. This focus was achieved through various professional development opportunities, providing instruction and hands-on experience with the curriculum content. For every middle or high school teacher that is inspired to teach about hydrogen and renewable energy, approximately 150 students are affected. Over the course of several years, thousands of students are exposed to these topics. Many of these students will someday be our scientists, engineers, teachers and the leaders of tomorrow.

Over the course of the grant period, an average 310 teachers per year have participated in hydrogen education training opportunities facilitated by FSEC staff. Of these teachers, approximately 79 are college students studying to become teachers. The teacher opportunities include multi-day institutes, one-day workshops, and half-day experiences. Interest in hydrogen continues to grow amongst teachers, as evidenced by the popularity of the many hydrogen-training events held for teachers by FSEC throughout the year.

School field trips to the Florida Solar Energy Center are also popular with nearly 800 students and their teachers plus 60 parents per year visiting the facility for informal instruction on hydrogen, solar and energy efficiency. These visit experiences are several hours in length and include hands-on inquiry lessons using equipment, such as fuel cells and photovoltaics, and a tour of the facility and the lab areas. At the culmination of the experience, each teacher receives a packet of materials to further their understanding and support their ongoing exploration of hydrogen and other renewable energy technologies. These materials include background information, resource lists and website addresses. The EnergyWhiz.com website and the K-12 Education section of the FSEC website are useful tools for sharing information about renewable energy, events, and activities. Bookmarks with these websites listed are provided to all K-12 visitors and their teachers. In addition, the U.S. Department of Energy, Office of Energy Efficiency and Renewable Energy included many of the hydrogen curriculum activities developed by FSEC staff in their Get Smart About Energy website and CD. This is an instructional tool with renewable energy lessons for K-12 grades and is available at http://www.eere.energy.gov/education/lessonplans/.

In a closely related activity, the FSEC K-12 educational staff was invited by the U.S. Department of Energy Office of Science to assist with the development of a standardized hydrogen fuel cell workshop for teachers. The standardized workshops will be offered to teachers at the various Regional Science Bowl sites throughout the United States as part of the National Science Bowl program. The Florida Solar Energy Center is one of the designated sites for such offerings and

the resulting training. The first such workshop is being offered at FSEC on January 26, 2008, and is open to all middle school science teachers in Florida.

Another activity of the K-12 educational staff has been the involvement for the past years with the International Youth Fuel Cell Competition (IYFCC) by assisting with the development of the competition events, judging and team recruitment. A summary of various individual educational activities conducted by the educational staff follows.

Curriculum development activities were:

- Hydrogen curriculum activities for K-12 have been incorporated into Solar Matters, Understanding Solar Energy, and Alternative Fuel Matters Curriculum Units.
- The hands-on curriculum unit, High-Energy Hydrogen has been developed for students in grades 3-12 with a supplemental kit of materials that is available on loan to teachers throughout Florida.

Annual activities and events for K-12 students included the following:

- The High School Hydrogen Sprint, as a part of the EnergyWhiz Olympics, held at the Florida Solar Energy Center. In this event student teams design, build and race model-size hydrogen cars.
- Florida Solar Energy Center Middle School Science Bowl held at FSEC – top 8 finalist teams build and race hydrogen fuel cell cars at the EnergyWhiz Olympics. The winning team represents the Southeast Region at the National Middle School Science Bowl in Denver, Colorado.
- Hydrogen fuel cell training for Middle School Science Bowl teams and their teachers. This workshop prepares teams for the National Science Bowl Competition, sponsored by the U.S. Department of Energy Office of Science.
- Exemplary Projects in Energy and Conservation (EPEC) Awards is a program that recognizes outstanding research efforts of 3-12 grade students in the areas of renewable energy and energy conservation.

Professional development for teacher activities has included:

- Two-day summer institute for teachers from west and central Florida schools on hydrogen and renewable energy. Sponsored by Progress Energy, Corp.
- Approximately three teacher in-service opportunities on hydrogen and renewable energy are offered throughout the school year. These are generally over capacity.Hydrogen materials are made available on loan to teachers (fuel cell, curriculum units, etc.)

Presentations on hydrogen at educational conferences have been as follows:

- Florida Association of Science Teachers, November 4, 2005, Orlando, October 12-14, 2006, Gainesville, October 25-27, 2007, Orlando – “Hands-on Hydrogen” presentation, with an average of 30 attendees per session
- International Solar Energy Society World Solar Congress – presentations on Hydrogen education to Education Committee
- Youth Energy Solutions (YES) Summit – April 20, 2006 and December 6, 2007, at the University of Central Florida. This event provides students with a venue to share their research and solutions for the energy problems they face. The December 2007 YES

Summit was expanded to include online video conferencing to encourage more students to participate.
- Southeast BioEnergy Conference, July 31-August 2, 2007. Facilitated a hands-on session for teachers, “Energy Savings with Hydrogen Fuel Cells”.

Education presentations and publications include the following activities:

- Hydrogen presentations given at four schools in west and central Florida. Over 1000 students participated.
- School groups and other tours exposed to fuel cell and hydrogen technology (more than 1200 students and teachers) per year
- Taped interviews for web site regarding renewables, emphasis on hydrogen
- Story in National Hydrogen Association Newsletter regarding EnergyWhiz Olympics
- Exhibits and hydrogen demonstrations at International Solar Energy Society World Solar Congress
- Exhibits and hydrogen demonstrations at Energy Summit at University of Central Florida
- Exhibits and hydrogen demonstrations at Energy Day at the Capitol, Tallahassee
- Exhibits and hydrogen demonstrations at Earth Day at the Capitol, Tallahassee

Short Courses and Seminars

Another major effort directed at graduate students and the technical community was the fuel cell short courses developed and offered for the past three years at the Florida Solar Energy Center. These short courses have taken advantage of using FSEC’s new Integrated Fuel Cell Test Bed (IFCT) facility for the required laboratory experiments. The courses are open to industry, academia and students and have drawn researchers and engineers from such places as NASA, UTC, Giner Electochemical, Lawrence Berkeley National Lab, and Savanah River National Lab. Most attendees were from the US but some came from as far away as Spain and Japan.

The three-day intensive short courses included lecture in the mornings and then hands-on lab training in the afternoon. FSEC’s state-of-the-art laboratories allowed each attendee to obtain real time experience with fuel cell materials, components, testing and performance evaluation. Lecture topics included in the course were:

- Thermodynamics of fuel cells
- Electrochemistry fundamentals
- Electrode kinetics
- Transport phenomena
- Efficiency & sources of loss
- Materials & components
- MEA fabrication
- Diagnostics, performance evaluation & data analysis
- DMFC & CO poisoning
- Challenges & opportunities in fuel cells

Laboratory exercises included

- MEA fabrication & single cell assembly
- Polarization testing & effect of operating conditions
- Fuel crossover & short-circuit by linear sweep voltammetry

- Electrochemical surface area & catalyst utilization by cyclic voltammetry
- Electrochemical impedance spectroscopy
- Effect of impurities on performance
- Data analysis and interpretation

To allow adequate resources, the classes were limited to 18-22 students. This results in three students at each of the test stands during the laboratory exercises. The first year, the course had 20 students, the second year it had 22 and the February 2008 course has 28 students.

Outreach Activities

The outreach work has been accomplished through publications, presentations, press releases and web site development, as well as personal interaction with the public. Already presented in Table 1 are the publications and presentations that have resulted from the research effort.

Another primary outreach activity has been press releases on the NASA work. With regard to press releases, Table 2 presents a listing of the 21 press releases over the past five years. Each press release can be viewed at the FSEC web site or by visiting: http://securedb.fsec.ucf.edu/operation/press_sel. Each of the press releases is emailed to a list that contains 141 media addresses.

In 2006, FSEC launched new web pages for the hydrogen research and development program. This new hydrogen web site contains 34 separate sections and many links to additional sites. Visitors to the site can learn about the element hydrogen, how it can be used as an energy carrier, the research on hydrogen conducted at FSEC, hydrogen education pages and access a hydrogen research database. There is also information on fuel cells and the aspects of these technologies. The new pages include Hydrogen Basics, H2 Economy, H2 in Florida, Hydrogen Q&A, FSEC Research, Production, Storage, Utilization, Fuel Cells, Funded R&D, Analysis, Delivery, Detection/Safety, Patents, Education, Faculty and Staff, Capabilities and Facilities, Resources, Publications, Videos, Related Links and a detailed Hydrogen Database. The pages can be accessed at http://www.fsec.ucf.edu/hydrogen or by clicking on the "hydrogen" button in the menu on the top of the home page at the FSEC website (www.fsec.ucf.edu).

Another web site on hydrogen research has been developed by FSEC. This site is available on the Internet at http://www.hydrogenresearch.org. The site contains detailed research from FSEC and the six participating Florida universities on the individual NASA projects over the life of the program. The site was officially launched March, 2004. The site will serve as a clearinghouse for the latest information on hydrogen research conducted by scientists at the Florida Solar Energy Center, University of Florida, University of Central Florida, Florida State University, University of South Florida, Florida International University and University of West Florida. This research was conducted through the NASA grant. The web site also contains news of upcoming hydrogen and fuel cell events, an extensive list of related informative sites, scientific publications and Florida research and contact information.

Conclusions

The primary objectives of the Hydrogen Education and Outreach task have supported four main areas: education of graduate and undergraduate engineering and science students, education for K-12 students and teacher professional development, participation in and offering of short courses and seminars, and a variety of public outreach activities. The university faculty has

used the topics from the large variety of research projects for graduate student masters and PhD theses. In addition, the project's results are used for publications and presentations by university faculty members and their students to present the results to local, national and international audiences. The totals are 222 publications, 196 presentations and the support of 96 students.

The K-12 student and teacher program activities are successful, ongoing and are being continually expanded. Over the course of the grant period, an average 310 teachers per year have participated in hydrogen education training opportunities facilitated by FSEC staff. The teacher opportunities include multi-day institutes, one-day workshops, and half-day experiences. Interest in hydrogen continues to grow amongst teachers, as evidenced by the popularity of the many hydrogen-training events held for teachers by FSEC throughout the year. Field trips to the Florida Solar Energy Center are also popular with schools with nearly 800 students, their teachers and 60 parents per year visiting the facility for informal instruction on hydrogen, solar and energy efficiency.

The outreach program has been accomplished through short courses, publications, presentations, press releases and web site development, as well as personal interaction with the public. Outreach results in addition to publications and presentations include 21 press releases and the development of two hydrogen web sites.

Table 1- Publications, presentations and students by institution and project.

	Publications	Presentations	Students
Florida Solar Energy Center			
Ammonia-Borane Complex for Hydrogen Storage - Mohajeri, N., T-Raissi, A., Ramasamy, K., Adebiyi, O., Bokerman, G.	9	7	-
Ceramic Membranes of Mixed Ionic-Electronic Conductors for Hydrogen Separation - Elbaccouch, M., T-Raissi, A., Linkous, C., Mohajeri, N.	5	-	-
Compact, Lightweight and Optimized Fuel cells for Space or Aircraft Power - Fenton, J, Choi, P., Bonville, L., Kunz, R.	1	2	2
Gas Permeable Chemochromic Compositions for Hydrogen Sensing - Mohajeri, N., Muradov, N., Bokerman, G., T-Raissi, A., Captain, J., Peterson, B., Whitten, M.	1	2	-
Hydrogen Education and Outreach – Schleith, S., Hall, P., Henzmann, A., Block, D.	-	-	-
Hydrogen Production from Used Lube Oils - T-Raissi, A., Ramasamy, K.	6	2	-
Hydrogen Production via Solar Thermochemical Water Splitting – T-Raissi, A., Huang, C., Muradov, N.	8	8	3
Hydrogen-Powered Aeropropulsion: Compact, Lightweight and Efficient Fuel Cells for Space Power - Linkous, C., Pearman, B., Hall, D., Slattery, D., Baik, J.	2	6	1
Integrated Fuel Cell Test Bed Facility - Slattery, D., Bonville, L., Fowler, R.	-	-	-
Liquid Hydrogen Storage at Kennedy Space Center - Gu, L., Block, D., Bokerman, G., T-Raissi, A., Basarkar, M.	-	-	1
Local Hydrogen Production via Catalytic Reformation of Fossil and Renewable Resources - Muradov, N., Smith, F.	27	17	2
Photoelectrochemical Water Splitting for Hydrogen Production Using Multiple Bandgap Combination of Thin-Film-Photovoltaic-Cells and Photocatalyst – Dhere, N.	13	14	4
System Analysis of Hydrogen Production and Utilization at KSC - T-Raissi, A., Elbaccouch, M., Ramasamy, K., Baik, J.	13	11	-
Zero-Boil-Off Liquid Hydrogen Storage Tanks - Baik, J.	8	9	-
University of Central Florida			
A Reliable, Efficient and Compact Reverse Turbo Brayton Cycle Cryocooler for Storage and Transport of Hydrogen in Spaceport and Space Vehicle Applications - Chow, L., Kapat, J., Chen, Q., An, L., Wu, T. Sundaram, K., Ham, C., Dhere, N.	24	18	10
Development of Cryogenic Shape Memory Actuator Materials for Switches, Seals and Valves - Vaidyanathan, R	12	21	7
Genetic Engineering to Enhance Biological Hydrogen Production - Self, W., Ganyc, D., Halvorsen, L.	1	3	2
Highly Selective Nano-Mems Low Temperature Hydrogen Sensor- Seal, S., Cho, H.	23	25	7
Metal Hydrides for Hydrogen Separation, Recovery and Purification - Hampton, M., Slattery, D.	-	-	-
Wireless Passive Sensors and Systems for Physical Sensors and Hydrogen Sensing Applications - Malocha, D	11	5	9

Florida State University			
Densified LH_2 and LO_2: Transport Properties and Density - Van Sciver, S.	9	6	-
Experimental and Numerical Investigations of Cryogenic Multiphase Flow - Van Sciver, S.	6	5	2
Florida International University			
Improved Hydrogen Yield from Florida Specific Biomass Gasification Using a Pilot Scale Gasification Unit - Srivastava, R	-	-	-
University of South Florida			
Numerical Simulation Model for Thermo-Fluid Analysis of Cryogenic Storage Systems with Zero Boiloff - Rahman, J., Ho, S.	9	7	4
Prototype and Simulation Model for a Magneto-Caloric Refrigerator - Bhansali, S., Rahman, M., Kim, S., Ghirlanda, S., Hernandez, C., Adams, C., Bethala, B., Rosario, S., Sambandam, S.	12	10	4
Smart Porous Metal-Organic Frameworks (MOFs) for Hydrogen Recovery and Storage - Eddaoudi, M., Zaworotko, M., Space, B., Eckert, J., T-Raissi, A., Mohajeri, N.	2	3	7
Surface Acoustic Wave (SAW) Sensors for Hydrogen and Other Gas Detection - Bhethanabotla, V	9	8	9
Thermo Catalytic H2 Production via Oxygen-Free Methane Aromatization - Wolan, J., Stefanakos, E., Kababji, A.	1	-	-
Florida A & M University			
Modeling and Optimization of Fuel Cell systems for Aircraft Applications - Ordonez, J., Lungo, C.	10	7	22
TOTAL =	**222**	**196**	**96**

Table 2. Press Releases on Hydrogen

5/29/2007	EnergyWhiz Olympics at Florida Solar Energy Center-UCF
11/16/2006	Edgewood Junior-Senior High Fuel Cell Team Successful
10/4/2006	Florida Solar Energy Center to Host National Solar Tour - Hydrogen Car to be on Display
9/21/2006	Florida Solar Energy Center Announces the 2007 Short Course in Fuel Cell Technology
4/28/2006	Students Do The Teaching at Unique Energy Summit
9/26/2005	Fuel Cell Technology Course to be held at FSEC
9/14/2005	Florida Solar Energy Center Launches Revamped Hydrogen Web Pages
6/1/2005	Used Automobile Oil May Be a Source of Hydrogen
5/17/2005	Florida Solar Energy Center Announces Winners of EnergyWhiz Olympics
4/20/2005	EnergyWhiz Olympics to be Held at FSEC on Saturday, May 7
12/22/2004	Early Holiday Gifts for Universities as Florida Solar Energy Center Awards $4.85 Million to Continue Hydrogen Research for NASA
7/25/2004	Florida Solar Energy Center Researchers Receive Honor at the 15th World Hydrogen Energy Conference
7/21/2004	Florida Solar Energy Center's Director Emeritus Gives Keynote Speech at American Solar Energy Society Annual Conference
4/1/2004	Florida Solar Energy Center Launches New Hydrogen Research Website
5/12/2003	David Block Receives Space Congress Achievement Award
4/21/2003	Public Invited to EnergyWhiz Olympics on May 3
3/24/2003	Students To Demonstrate Energy Knowledge and Engineering Skills at EnergyWhiz Olympics
10/8/2002	Florida Solar Energy Center's Action Plan for Hydrogen - the Fuel of the Future
7/9/2002	Florida Solar Energy Center Awards Hydrogen Research Contracts to Florida Universities
4/23/2002	Florida Solar Energy Center Kicks Off Hydrogen Research Program
4/5/2002	Florida Solar Energy Center Awarded $5.4 Million from NASA for Hydrogen Research

December 2007

Hydrogen Production From Used Lubricating Oils

A. T-Raissi and K. Ramasamy
Florida Solar Energy Center

Research Period: June 2005 to December 2007

Abstract

Used lubricating oils (lube oils) are generated throughout the U.S. and collected in central locations in many communities. Disposing of these used oils in an improper manner causes environmental degradation. However, used lube oils can be re-used as a lubricant or as an energy source. At the Florida Solar Energy Center, a process has been developed that converts used oils to hydrogen and other valuable low molecular weight hydrocarbons. Used lube oils are a complex mixture of aliphatic and polycyclic hydrocarbons formulated to withstand high service temperatures in internal combustion engines. Both synthetic and mineral oils contain a high concentration of hydrogen (about 13–14 wt%). In this project, lube oil reformation experiments were carried out using several commercially available dehydrogenation catalysts over a range of reactor temperatures, pressures, residence times and steam to carbon ratios. The data giving the experimental results are presented and discussed in this report.

Introduction

Used lubricating oils present a valuable, readily available and cost-effective resource for local production of hydrogen at NASA-KSC. The amount of used lubricating oil available for hydrogen production in Florida amounts to 45 million gallons per year which is available throughout the year without any seasonal fluctuations. It is also available in Florida at a relatively low cost of about 10 cents/gallon delivered.

There are number of re-refining methods to clean the used lubricating oil and reuse it. Even the most advanced lubricant re-refining technology recovers only a portion of the used lube oil available. Re-refining plants employ energy intensive processes such as vacuum flashes, solvent extractions, distillation, demetallization, etc. and produce considerable amount of waste sludge that requires disposal. Thermochemical reformation of used lubricating oils for the production of hydrogen presents a method for reduction of the waste volume headed for the waste disposal facilities.

Background

Used lubricating oil is a very complex mixture of low and high (C_{15}–C_{50}) molecular weight aliphatic and aromatic hydrocarbons [1,2], additives, metals, and various organic and inorganic compounds. The chemical composition of used lubricating oil varies widely and depends on the original crude oil, the processes used during refining, the efficiency and type of engine that utilized the oil, products of gasoline or diesel combustion, the additives added to the fuel and to the original oil, and the length of time that the oil remains in the engine. Used lubricating oil has a density (at 20 °C) of about 0.88 kg/L. Lube oils are designed to withstand very high service temperatures in the internal combustion engines and resist to thermal degradation. In this project, results are presented for several processes used for the extraction of hydrogen from the used oils. The processes used were supercritical water reformation and steam pyrolysis for the production of H_2 and other valuable low molecular weight hydrocarbons.

Elemental analysis of the samples of used and new lubricating oils obtained in Florida is given in Table 1. Note that the analysis shows 13.70 wt% hydrogen content in the used lobe oil tested. This is twice hydrogen available from woody biomass and about three weight percent higher than that of vegetable oils. The high hydrogen content in the used lubricating oil makes it a valuable feedstock for hydrogen production.

Table 1. Elemental analysis of Mobil One™ synthetic oil and a sample of used lubricating oil obtained in Florida.

Elements (wt%)	Lube oil (synthetic)	Lube oil (used)
Hydrogen	13.37	13.70
Carbon	84.35	84.63
Oxygen	2.51	2.17
Sulfur	0.22	0.28
Nitrogen	<0.5	<0.5
H/C (mol/mol)	1.90	1.95

Experimental

Figure 1 depicts a schematic diagram for hydrogen production by thermo catalytic reformation of used lubricating oils. Figure 1 shows the feed and preheat section, a thermocatalytic reactor, product separation section, and a section to conduct product analysis.

In the feed and preheat section, lube oil and water are compressed using two HPLC pumps that deliver a maximum flow rate of 100 mL/min. Water is preheated to a desired temperature using ceramic heaters and mixed with the lube oil. The mixture then enters into the thermocatalytic reactor. The reaction zone is within a tubular reactor constructed from Inconel alloy 600 (for low temperature, high pressure service) and Hastalloy 800T (for high temperature, low pressure service). The volume of catalyst bed within the reactor is adjusted by varying the packing length of the catalyst which allows the residence times within the catalyst bed to be varied. Reactor pressures and temperatures were monitored in real time at the reactor inlet and outlet, and within the catalyst bed. In the posterior section, a series of inline filters trap any char that may be produced in the reactor. Following the product separation stage, the high pressure liquid/gas mixture enters a backpressure regulator, which lowers the pressure to near atmospheric. A condenser is located after the backpressure regulator for separating the liquid and gaseous phases. The exit gas splits into two streams.

An online gas chromatograph equipped with thermal conductivity and flame ionization detectors periodically samples the exit gaseous stream. The sample gas is analyzed for hydrogen, carbon dioxide, carbon monoxide, methane, ethane, ethylene, hexane, pentane and benzene, among others. The exit gas passes through a volumetric bubble flow meter and is vented out. The liquid portion is collected at the bottom of the condenser and periodically sampled for analysis. For safety, the reactor was shielded and several pressure relief valves were installed at strategic locations in the process lines. All the tubes, interconnects and fittings used made of corrosion resistant stainless steel 316.

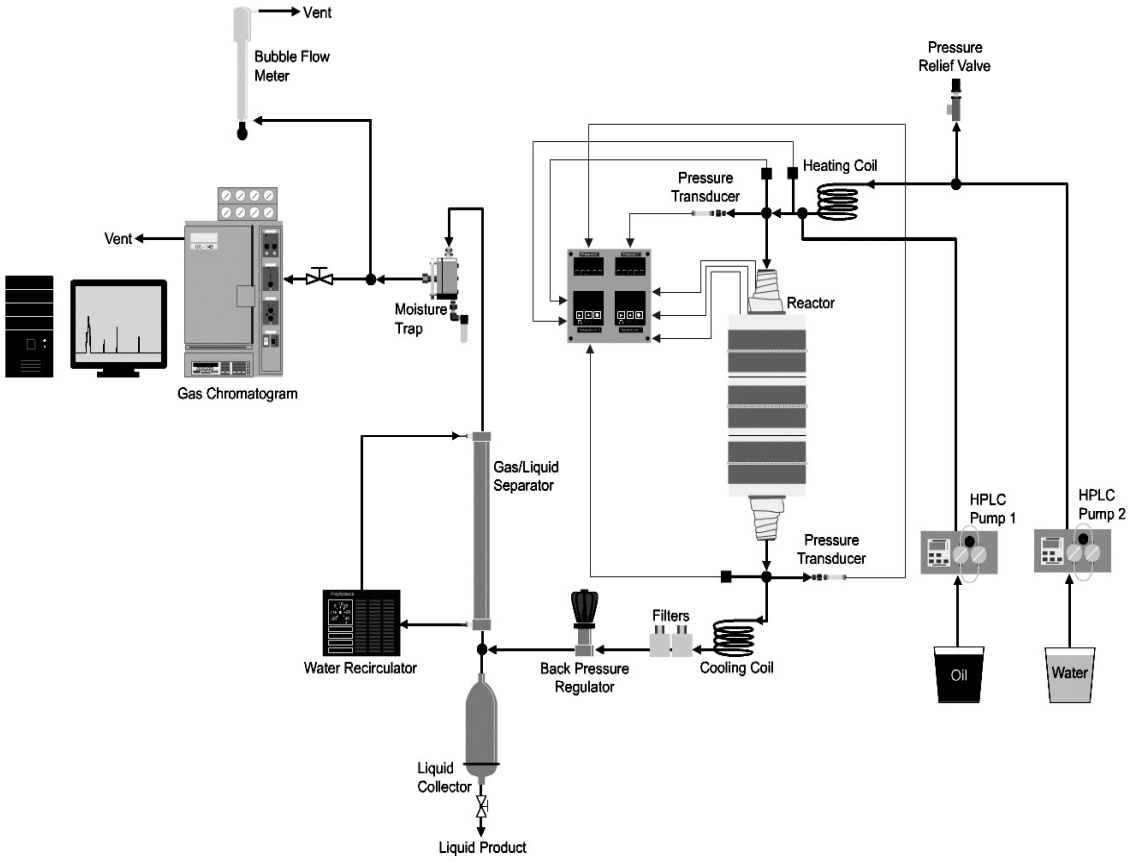

Figure 1. Schematic diagram depicting the experimental setup for the thermocatalytic reformation of used lubricating oils.

Results and Discussion

Supercritical Water Reformation of Lube Oils

The use of supercritical water has several advantages over atmospheric steam. Supercritical fluid is one that is heated above its critical temperature (T_c), and compressed above its critical pressure (P_c). Water becomes a supercritical fluid at temperatures and pressures at or above 374.2 °C and 22.1 MPa, respectively. A key advantage of chemistry in supercritical water is that it becomes possible to vary the properties of the reaction medium such as density, viscosity, and diffusivity by manipulating the pressure and temperature and optimizing the reaction medium without changing the solvent (water). Furthermore, the ion product, or dissociation constant (K_w) for water near the critical point, is about 3 orders of magnitude higher than that of ambient liquid water.

Thus, under certain conditions, near-critical and supercritical water can possess a higher H^+ and OH^- ion concentration than liquid water making dense high temperature water an effective medium for acid- and base catalyzed reactions of organic compounds [3]. However, beyond the critical point, K_w falls precipitously - making it a poor medium for ionic chemistry. According to Antal et al., free-radical mechanisms are favored when the dissociation constant $K_w << 10^{-14}$

(mol kg $^{-1}$)^2 while ionic mechanisms prevail at $K_w > 10^{-14}$ (mol kg $^{-1}$)^2 [4]. Under our experimental conditions (450 °C and 22.06MPa corresponding to a water density of about 0.1 g cm^{-3}), the dissociation constant, calculated using a correlation given by Marshall and Franck [5], was found to be about $K_w = 10^{-22.3}$ (mol kg^{-1})^{2,} which is much less than 10^{-14} (mol kg^{-1})^2. Thus, under our experimental conditions, no siginificant ionic reactions could be expected.

Another advantage of using supercritical water as the reaction medium is that very little energy is required to pressurize water and oil to 22.1 MPa. This will drastically reduce purification and storage costs since most of the energy spent to liquefy hydrogen is for its compression.

A series of steam reforming experiments were carried out at water temperature of 450 °C and 22.06 MPa pressure (corresponding to a water density of about 0.1 g/cm^3) using a commercially available sample of virgin synthetic lubricating oil (Mobil One™). For these experiments, nickel [6] and carbon based catalysts as well as an alkali (KOH) catalyst were used for all of the supercritical water reformation tests. Experiments were conducted for five continuous hours at above supercritical water conditions and the product gas was sampled and analyzed in one hour intervals. The water to oil ratio of four to one was used for all the reforming experiments reported here.

The results produced the following: (1) reformation runs using nickel catalysts yielded higher rate of gas production than the uncatalyzed reaction in the first hour of the run, (2) after 5 hours of continuous operation, the Ni catalysts were completely deactivated and no longer demonstrated catalytic activity, and (3) the rate of gas production from uncatalyzed runs did not change during the 5 hour operation. Analysis of the exit stream indicated that hydrogen and carbon dioxide were the main reaction products with carbon monoxide, methane, ethane and ethylene present in very small quantities.

Figure 2 gives the comparative results depicting the rate of gas production from the supercritical water reformation of virgin Mobil One™ synthetic lube oil in the presence of various dehydrogenation catalysts examined. It can be seen that the nickel catalysts rapidly deactivate in the supercritical water reaction condition. Another observation was that even though the rate of gas production dropped as a function of time, the reaction selectivity toward hydrogen and CO_2 remained unchanged throughout the entire 5 hour period. This means that catalyst deactivation lowers the conversion but does not significantly affect the selectivity of the process toward hydrogen and CO_2 formation.

In the heterogeneous catalytic processes described above, coking occurs and blocks the active sites on the catalyst surface, thus, reducing hydrogen production. Several experiments were conducted using a homogeneous catalyst, potassium hydroxide. The rationale for using a homogeneous catalyst is that all the reactants as well as the catalyst are in a single phase and as such the catalyst should remain active. In addition, homogeneous catalysis has been shown to yield better selectivity and allow easier process modification and optimization. Kruse et al. have shown that alkali salts such as potassium hydroxide (KOH) and potassium carbonate (K_2CO_3) promote gasification of a biomass model compound (pyrocatechol) in supercritical water at temperatures as low as 500 °C [7]. According to these researchers, addition of alkali metal hydroxides increases the yield of hydrogen and carbon dioxide formation and reduces carbon monoxide yield and char formation during the gasification of pyrocatechol in the supercritical water. In their study, KOH was dissolved in the water fed to the reactor, which acted as a catalyst for the reformation reaction in the supercritical water.

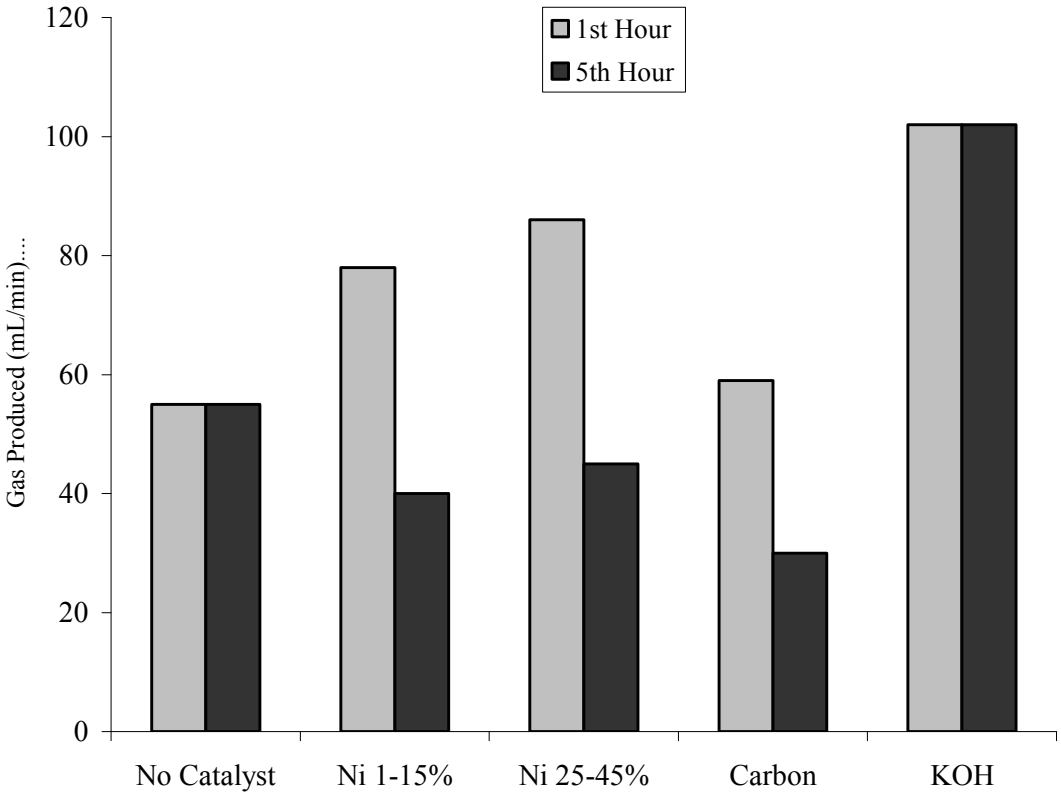

Figure 2. Comparison of alkali catalyst with the carbon and Ni based catalysts during supercritical water reformation of virgin Mobil One™ synthetic lube oil (reaction temperature = 450 °C and pressure = 22.06 MPa corresponding to a water density of about 0.1 g/cm^3).

Addition of alkali metal hydroxides led to the formation of formates, which subsequently decomposed to form hydrogen and carbon dioxide. Formic acid appears to be an intermediate product of the water-gas shift reaction

$$H_2O + CO \longrightarrow HCOOH \longrightarrow H_2 + CO_2$$

Also, Watanabe et al. have demonstrated that sodium hydroxide (NaOH) is an effective catalyst for the gasification of glucose and cellulose in low temperature (400 °C) supercritical water [8]. Unlike biomass model compounds, hydrocarbons are known to be difficult to gasify in supercritical water [9]. According to Watanabe et al., partial oxidation of linear chain and aromatic hydrocarbons in high density (more than 0.25 g/cm^3) and low temperature (400 °C) supercritical water generates hydrogen and carbon monoxide, selectively-but, the yield of hydrogen is low (less than 2% of the hydrogen in feedstock) [10]. More recently, these researchers have studied the catalytic (ZrO_2 and NaOH) partial oxidation of n-hexadecane employing a batch type reactor in supercritical water at 400 °C, water density of 0.52 g/cm^3 (40 MPa pressure), and an O/C ratio of 0.3. The use of these catalysts did not increase n-hexadecane conversion but did promote formation of 1-alkenes and hydrogen [11].

In this project, several experiments were performed at near critical water conditions to determine the effect of KOH catalyst on the lube oil reformation. These results are given in Figure 2 and show the rate of gas production from the KOH catalyzed reformation of lube oil in supercritical water to that of several commercially available heterogeneous catalysts described before. The amount of gas produced in the presence of KOH catalyst at 1 and 5 hours through the runs were, respectively, 15 and 55% higher than those obtained from the Ni and carbon based catalysts. Even though the use of KOH as a catalyst for the reformation of virgin Mobil One™ lube oil increased the rate of total gas generated (with no noticeable degradation of the catalyst activity), the hydrogen yields were still low. The role of water in the hydrothermal reactions (above 200 °C and supercritical water) from the point of view of chemistry and kinetics. A comprehensive review of the role of water in chemical reactions at high temperature water is given by Akiya and Savage [12]. In general, reactions in supercritical water are a combination of hydrolytic and pyrolytic reactions, with the pyrolysis pathway dominating as temperature is increased and the hydrolysis pathway dominating as water density is increased. Furthermore, it is known that for a reactant molecule to be hydrolyzed, it must have a heteroatom bonded to a saturated carbon atom. Molecules with carbon–carbon bonds alone do not show the product slate typical of hydrolysis [13]. In summary, hydrothermolysis of lube oil in near-critical water at a density of 0.1 g/cm^3 results in a relatively low conversion with free-radical chemistry being the primary pathway (pyrolytic path). Water does not appear to be either a reactant (i.e., a means of incorporating oxygen functionalities into the lube oil) or a catalyst. In order to increase the yield of gaseous products and hydrogen, in particular, experiments were conducted at lower reaction pressure and increased reaction temperature. A brief discussion of the results obtained from the low pressure, higher temperature steam reformation and thermal cracking of lube oils follows.

Steam Reformation of Lube Oils

For the steam reformation process, the effect of steam to water feed ratio was investigated. Table 2 depicts the rate of gas produced from steam reformation of virgin Mobil One™ oil for different oil to water feed ratios at 715 °C and 1 atm. The steam to oil ratio of 1 to 0.5 produced as much as 14% more gas than runs with other water to oil feed ratios. Tables 3 and 4 give additional results of steam reformation experiments at the process conditions employed. For the virgin synthetic (Mobile One™) oil, with the steam to oil feed ratio of 2 to 1, the results showed an increase in the gas yield by 11% for the case where the reformation temperature was increased from 715 to 850 °C. For the used oil, increasing the temperature from 750 to 850 °C increased the gas yield by 20%.

Table 2. Rate of gas production from the reformation of lube oil at various water feed and lube oil flow rates at a reformer temperature of 715 °C and 1 atm.

Input synthetic oil[a] (mL/min)	Feed water (mL/min)	Gas produced (mL/min)
0.5	1	255
1	0.5	524
1	1	498
1	2	466
1	3	452

[a]Virgin Mobil One™ Synthetic Oil

The results also indicate that a reformation temperature in the range of 850 °C (at 1 atm) favors high gas yields. Temperature above this level increases the yield of char production with minimal effect on the conversion efficiency. In some cases, the production of char in the reactor lines was excessive resulting in the blockage in the process lines.

Table 3. Volume and product yield of gas produced by the steam reformation of virgin synthetic (Mobil One™) and used lube oils at various reformer temperatures - 1 atm pressure and oil to water feed ratio of 2:1, with and without KOH.

Exp. No.	Catalyst	Temp (°C)	Total volume of gas produced per mL of oil fed, mL	Mass of hydrogen in the product gas/mass of hydrogen in the feed oil	Gas yield wt %
1[a]	None	715	448	0.5761	26.54
2[a]	None	750	461.5	0.5921	27.03
3[a]	0.025M KOH	750	466	0.5600	26.11
4[a]	0.05M KOH	750	482.5	0.6195	27.75
5[a]	0.1M KOH	750	488	0.6269	27.37
6[a]	None	800	488	0.6028	24.64
7[a]	None	850	504	0.5613	22.25
8	None	750	383	0.4601	19.41
9	0.1M KOH	750	363.5	0.4065	19.13
10	None	800	428.5	0.4891	20.38
11	None	850	480	0.5594	22.59
12	0.1M KOH	850	218	0.1318	9.34
13	None	880	500	0.5391	20.96

[a] Virgin Mobil One™ synthetic oil.

Table 4. Composition of gas produced by the steam reformation of virgin synthetic (Mobil One™) and used lube oils at 1 atm, various reformer temperatures, oil to water feed ratio of 2:1, with and without KOH.

Exp. No.	Catalyst	Temp (°C)	Composition of product gas, mL of total							
			H_2	CO	CH_4	CO_2	C_2H_2	C_2H_6	C_2H_4	$>C_3$
1[a]	None	715	58	4.5	157	13.5	4.5	148	45	18
2[a]	None	750	69	5	157	14	-	157	46	14
3[a]	0.025M KOH	750	60	3	136	6	2	183	30	47
4[a]	0.05M KOH	750	67	3	170	4	2	180	34	22
5[a]	0.1M KOH	750	81	3	167	4	2	167	44	31
6[a]	None	800	97.6	2.9	200	2.5	1	135.6	24.4	23.9
7[a]	None	850	124.6	5	194.5	3.5	3	118.9	11	43
8	None	750	50	4	149	-	-	103	31	46
9	0.1M KOH	750	62	4	105	7	11	116	15	44
10	None	800	72.9	4.3	162.8	-[b]	-	111.4	21.4	55.7
11	None	850	91.2	4.8	196.8	-	-	120	19.2	48
12	0.1M KOH	850	64	4	63	11	2	41	4	28
13	None	880	110	5	195	-	-	105	15	70

[a] Virgin Mobil One™ synthetic oil.
[b] Insignificant.

Figures 3 and 4 depict the product gas composition from virgin synthetic (Mobile One™) and used lube oil steam reformation experiments. The result shows that the predominant gases produced were hydrogen, methane, ethylene, ethane and acetylene with very low amounts of carbon monoxide and carbon dioxide. Results from the experiment 3, 4, 5, 9, and 12 (See Tables 3 and 4) imply that, high temperature reformation of lube oil using KOH catalyst doesn't increase total gas yield and has no significant effect on the selectivity toward hydrogen production. As before, addition of alkali metal hydroxides leads to the formation of formates from CO and water, which subsequently decompose to form H_2 and carbon dioxide. Since very little or no CO was produced during high temperature steam reformation, it is clear that KOH does not play a role as catalyst toward increasing the yield of gas generated. Table 5 gives the total amount of hydrogen produced at different reformer temperatures and 1 atm without and in the presence of water. For the same temperature and pressure, the volume and composition of the gas produced were basically same for the experiment runs with and without feed water to the reformer.

The results imply that the addition of feed water during high temperature reformation of lube oil had no appreciable effect on the yield of hydrogen or the amount of gas produced. It appears that, under our experimental conditions, water acts as a heat transfer fluid rather than a reactant. Thus, addition of water does not appear to contribute to the amount of H_2 generated during the reformation process.

Table 5. Total mass of hydrogen produced in one hour for various reformer Input and operating conditions at 1atm.

Lube oil [a] to water feed ratio (mL/min)/(mL/min)	Temp (°C)	Total amount of hydrogen in the feed (g)	Amount of hydrogen in the product gas (g)	Total volume of gas produced (L)	Volumetric rate of liquid product collected (mL/min)
2/1	750	20.46	8.17 (4.1)	55.44 (27.72)	1.66
3/0	750	20.40	12.46 (4.2)	82.8 (27.6)	1.07
2/1	800	20.46	8.32 (4.2)	58.56 (29.28)	1.64
3/0	800	20.40	13.35 (4.5)	89.7 (29.9)	1.05
2/1	850	20.46	7.74 (3.9)	60.48 (30.24)	1.68
3/0	850	20.40	12.02 (4.0)	90 (30)	1.20

[a] Virgin Mobil One™.

( ) Total volume of product gas produced per 1 mL of lube oil fed into the reformer.

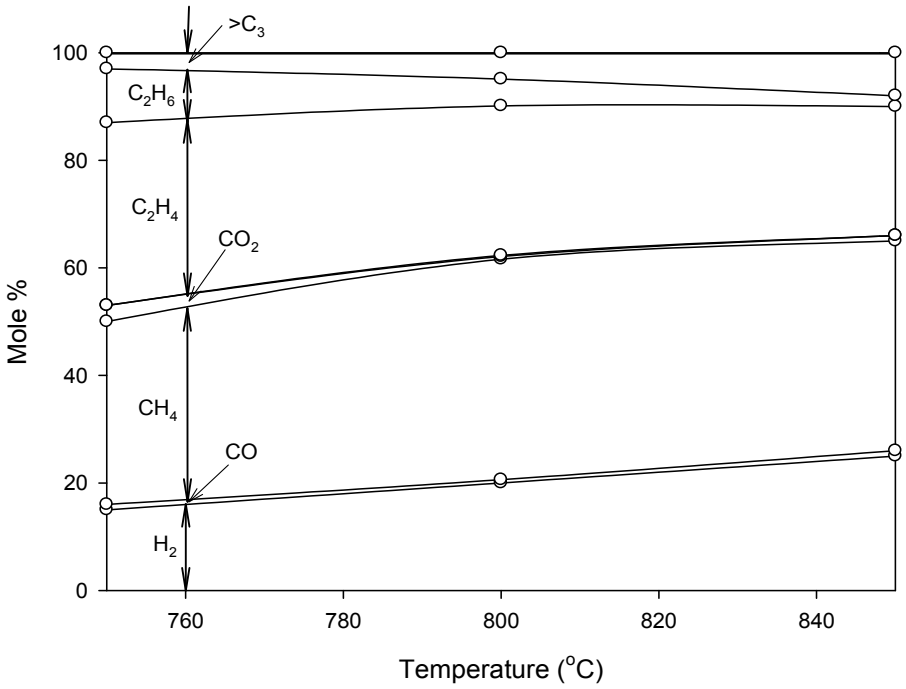

Figure 3. Stacked presentation of the gaseous product from the steam reformation of virgin synthetic lube oil (Mobil One™). Data is open circles and solid lines are spline fit to data points.

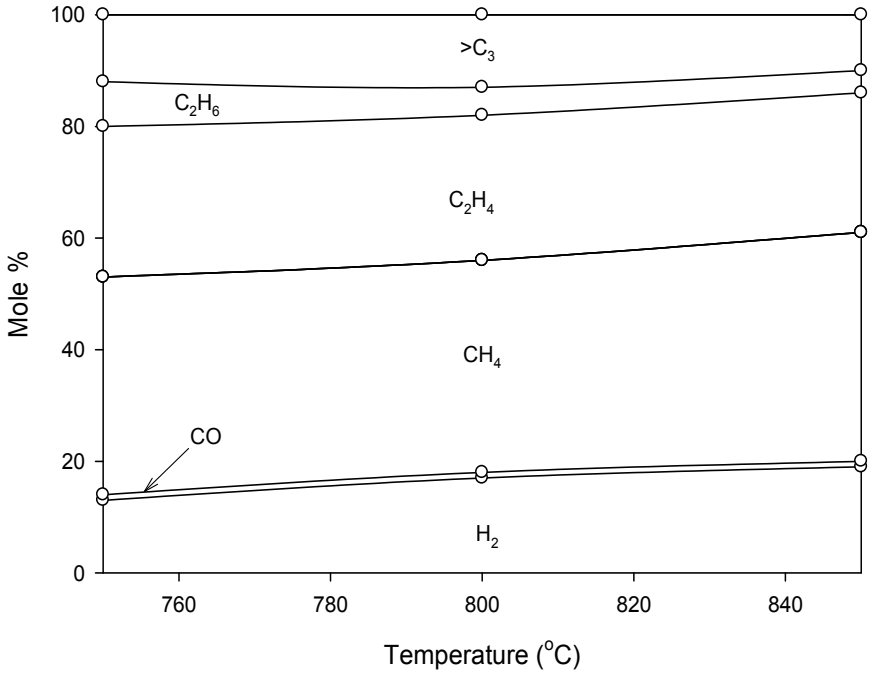

Figure 4. Stacked presentation of the gaseous product from the steam reformation of used lube oil. Data is open circles and solid lines are spline fit to the data points.

Reducing the amount of feed water added to the input stream should lower the amount of disposable waste generated from the process and also reduce the process heat requirement. These results led to the conducting of several experiments involving direct thermolysis of lube oils in the absence of any added water.

Thermolytic Cracking of Lube Oils

Tables 6 and 7 present results on the volume and composition of gas produced from direct thermolytic (no catalyst present) cracking of virgin synthetic (Mobil One™) and used lube oil at a range of temperatures and 1 atm. For the virgin synthetic oil, increasing the reactor temperature from 750 to 850 °C results in 8% increase in the yield of gas produced. For the used oil, increasing the temperature from 750 to 850 °C increases the gas yield by about 29%.

Temperatures above 880 °C increase the yield of char production with minimal effect on the amount of gas produced per unit weight (or volume) of oil fed to the reformer. In some high temperature cases, the extent of char production was so high that resulted in the process lines becoming completely clogged within a short period of time. Similar observations were made at high temperatures during steam assisted reformation experiment described before.

Table 6. Volume of gas produced from the thermolytic (no catalyst present) reformation of virgin synthetic (Mobil One™) and used lube oils at various temperatures and 1 atm.

Exp. No.	Temp (°C)	Total volume (mL) of gas produced per mL of oil fed	Mass of H_2 in the product gas/mass of H_2 in the feed oil	Total gas yield wt %
14[a]	750	460	0.6108	41.2
15[a]	800	498.3	0.6544	41.1
16[a]	850	500	0.5891	35.51
17	800	354	0.4401	28.11
18	850	500	0.6225	37.96
19	880	500	0.5705	31.23

[a] Virgin Mobil One™ synthetic oil.

Table 7. Composition of gas produced from the thermolytic (no catalyst present) reformation of virgin synthetic (Mobil One™) and used lube oils at various temperatures and 1 atm.

Exp. No.	Temp (°C)	Composition of product gas, mL of total							
		H_2	CO	CH_4	CO_2	C_2H_2	C_2H_6	C_2H_4	$>C_3$
14[a]	750	56	2	176	2	1	146	49	28
15[a]	800	91.2	2.5	223.2	2.5	1	127	38.4	12.5
16[a]	850	115	2	220	2	6	102	16	37
17	800	60.2	3.5	148.8	-[b]	3.54	92.1	24.8	21.3
18	850	105	5	230	-	-	115	25	20
19	880	150	5	230	-	-	70	50	30

[a] Virgin Mobil One™ synthetic oil.
[b] Insignificant.

Results obtained from the direct thermolytic reformation of the virgin synthetic (Mobile One™) oil indicate that 58–65% of the total mass of hydrogen in the oil fed into the reformer was converted to hydrogen in the output gas. Likewise, results obtained from the direct thermolysis of the used lube oil show that 40–63% of the total mass of hydrogen in the used oil fed into the reformer was converted to hydrogen in the output gas. Recycling the unconverted liquid at the exit with the fresh feed into the reactor has potential to increase the yield of the gaseous products from the reformer. Figures 5 and 6 depict the product gas composition from thermolytic cracking of the virgin synthetic (Mobile One™) and used lube oil.

The composition of the product gas generated by the thermolytic decomposition of these oils was very close to that obtained from the steam assisted reformation experiments. The main gaseous species generated were H_2, CH_4 and ethylene at 17–30%, 40–45% and 15–25%, respectively. Very small amounts of CO and CO_2 were also generated (0.5–1%). It can be seen that the amount of CO and CO_2 produced by the thermal cracking of lube oils is much less than that normally obtained by conventional steam reformation of methane or hydrocarbons. As noted before, the presence of water does not appear to affect the chemistry in thermolysis of lube oils and only acts as a heat transfer medium.

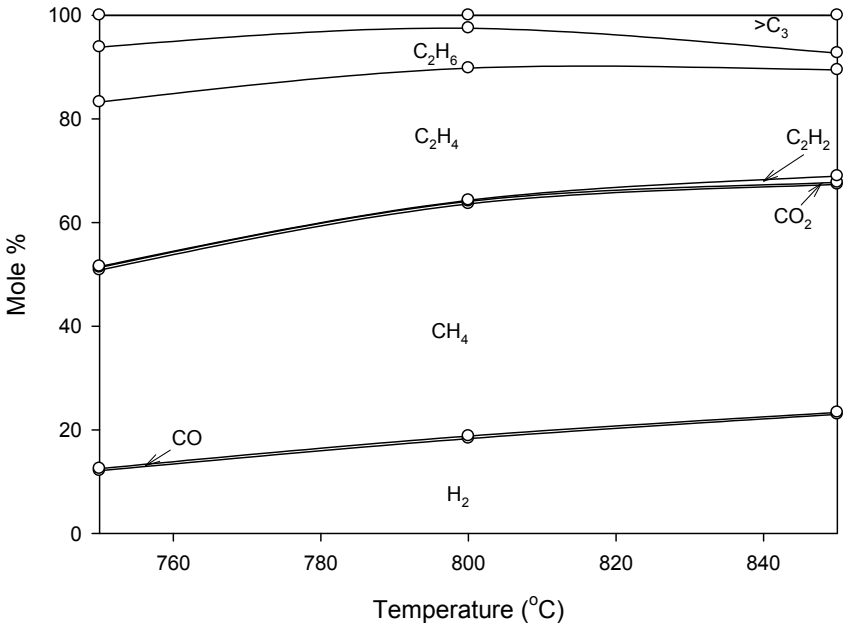

Figure 5. Stacked presentation of the product gas composition from thermal cracking of virgin synthetic lube oil (Mobil One™). Data is open circles and solid lines present spline fit to data.

Gases species other than hydrogen that are produced during pyrolysis of lube oil are low molecular weight hydrocarbons such as CH_4, C_2H_6, C_2H_4, and C_2H_2. These hydrocarbon gases can be reformed easily in a post-reformer to generate additional hydrogen or extracted for use as chemical feedstock.

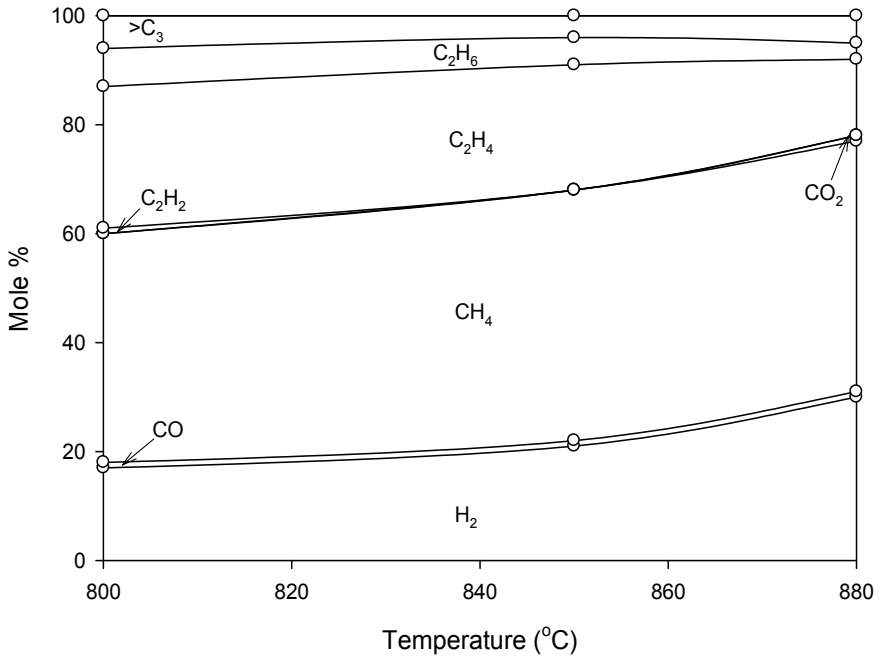

Figure 6. Stacked presentation of the product gas composition from thermal cracking of used lube oil. Data is open circles and solid lines present spline fit to data points.

Conclusions

Hydrogen production from used lube oil via thermal cracking can be an attractive process both environmentally and economically. The project has demonstrated the feasibility of hydrogen production via thermal cracking of lubricating oils—both virgin synthetic oil (Mobile One™) and a sample of used lube oil obtained in Florida.

The performance of several dehydrogenation catalysts—such as nickel, carbon, and an alkali based catalysts—used for the reformation of lube oils and production of hydrogen were investigated. Both nickel and carbon based catalysts performed poorly toward hydrogen production during steam assisted reformation of lube oils because of catalyst deactivation. The amounts of gas produced using KOH catalyst were higher than those obtained from the Ni and carbon based catalysts. Utilizing KOH as a catalyst for the reformation of lube oils increased the total yield of all the gaseous species produced with no noticeable degradation of the catalyst activity and with high selectivity toward hydrogen. However, the hydrogen yields were low. To increase the yield of gaseous products and particularly that of hydrogen, it was necessary to lower the reaction pressure and increase the reaction temperature.

Total gas produced and the yield of hydrogen were significantly higher during both steam assisted reformation and direct thermal cracking of the lube oils at 1atm and reformer temperatures above 715 °C as compared with those obtained by supercritical water reformation (65% of hydrogen contained in oil, compared with only about 5% from supercritical water reformation).

The high temperature, low pressure process also yielded lower concentrations of CO_2 and CO in the output gas (30% compared with only 1% by volume of gas produced by supercritical water reformation). For the same temperature and pressure, the yield and composition of the

gas produced by the steam assisted reformation of lube oils were basically same regardless of whether or not the input stream to the reformer contained water. Results imply that addition of feed water during high temperature reformation of lube oil has no appreciable effect on the yield of hydrogen or the amount of gas produced. Under the experimental conditions of this work, water acted as a heat transfer fluid rather than a reactant. Thus, addition of water did not contribute to the amount of hydrogen generated during the reformation process.

Results obtained from the direct thermolytic reformation of the virgin synthetic (Mobile One™) oil and used oil showed that, respectively, 58–65% and 40–63% of the total mass of hydrogen in the oil fed into the reformer was converted to H_2 in the output gas. Composition of the gaseous species generated by thermal cracking and steam reformation of lube oils were basically the same and included mainly hydrogen, methane and ethylene at 17–30%, 40–45%, and 15–25%, respectively. Under the experimental conditions of this investigation, the presence of water does not appear to affect the chemistry of the thermolysis of lube oils and only acts as a heat transfer medium. Direct thermolysis of lube oils requires less energy and produces about one third less disposable waste materials (compared to that from steam reformation process).

Publications, Presentations and Reports

- Karthikeyan K. Ramasamy, Ali T- Raissi, (2006) “Hydrogen Production from Used Lubricating Oils”, *Catalysis Today* 129 (2007) 365-71.

- Karthikeyan K. Ramasamy, Ali T- Raissi, (2005) “Hydrogen Production from Used Lube Oil” NASA Technical Report, http://hydrogenresearch.org/fr04.htm.

- Karthikeyan K. Ramasamy, Ali T- Raissi, Mohamed Elbaccouch, Nahid Mohajeri (2006) “Hydrogen Production from Used Lube Oil via Supercritical Water Reformation” NASA Technical Report, http://gltrs.grc.nasa.gov/reports/2006/CR-2006-214326.pdf, 138-146.

- Karthikeyan K. Ramasamy, Ali T- Raissi, (2006) “Hydrogen Production from Used Lubricating Oils”, American Chemical Society, Division of Petroleum Chemistry, 51(1), 54-56.

- Karthikeyan K. Ramasamy, Ali. T- Raissi (2005) “Hydrogen Production from Used Lube Oil” NASA Year End Review Meeting, Cocoa, FL.

- Karthikeyan K. Ramasamy, Ali T- Raissi (2004) “Hydrogen Production from Used Lube Oil via Supercritical Water Reformation” NASA Year End Review Meeting, Cocoa, FL.

- Mohamed Elbaccouch, Karthikeyan K. Ramasamy, Jong Baik, Ali T-Raissi (2006) “Aspen Plus™ Plant Design for the Liquid Hydrogen Production by Steam Reforming of Used Automotive Lubricating Oil”, AIChE 2006 Spring National Meeting, Orlando, FL.

- Karthikeyan K. Ramasamy, Ali T- Raissi, Nahid Mohajeri (2007) “Hydrogen Production from Used Lubricating Oils”, American Chemical Society (Florida section) FAME Meeting.

References

[1] R. Kaplan, H. Shan-Tan Lu, J. Alimi, MacMurphey, Environ. Forensics 2, (2001), 231.

[2] W. Bider, et al., Individual sample fuel mixture composition data, Prepared for EPA Office of Solid Waste and Energy Response, Document No. 530-SW-013.

[3] P. Savage, Chem. Rev., 99, (1999), 603–621.

[4] M. Antal Jr., A. Brittain, C. DeAlmeida, S. Ramayya, J. Roy, Supercritical fluids, in: T.G. Squires, M.E. Paulaitis (Eds.), ACS Symposium Series 329, (1987), pp. 77–86.

[5] W. Marshall, E. Franck, J. Phys, Chem. Ref. Data, 10(2), (1981), 295–304.

[6] L. Garcia, R. French, S. Czernik, E. Chornet, Appl. Catal. A: Gen., 201, (2000), 225.

[7] A. Kruse, D. Meier, P. Rimbrecht, M. Schacht, Ind. Eng. Chem. Res., 39, (2000), 4842.

[8] M. Watanabe, H. Inomata, K. Arai, Biomass Bioenergy 22 (2002) 405.

[9] T. Funazukuri, N. Wakao, J. Smith, Fuel 69, (1990), 349.

[10] M. Watanabe, M. Mochiduki, S. Sawamoto, T. Adschiri, K. Arai, & J. Supercrit. Fluids, 20, (2001), 257.

[11] M.Watanabe, H. Inomata, M. Osada, T. Sato, T. Adschiri, & K. Arai, Fuel 82, (5), (2003), 545–552.

[12] N. Akiya, & P. Savage, Chem. Rev., 102, (2002), 2725–2750.

[13] K. Benjamin, P. Savage, & J. Supercrit, Fluids, 31, (2004), 301–311.

December 2007

Hydrogen Production Via Solar Thermochemical Water Splitting

A. T-Raissi, C. Huang, and N. Muradov
Florida Solar Energy Center

Research Period: March 2004 to February 2008

Abstract

This report summarizes project activities related to the development of a new sulfur-family thermochemical cycle for the direct production of hydrogen from solar energy and water. The successful implementation of this technology will enable NASA to produce propellant grade hydrogen and oxygen, in the long term, without consumption of fossil fuels and in an environmentally acceptable manner.

All sulfur-family thermochemical water splitting cycles (TCWSCs) rely on concentration and decomposition of sulfuric acid for the oxygen evolution step of the cycle. The sulfuric acid decomposition step presents serious materials and catalyst deactivation challenges. Platinum based catalysts are currently the most active for the H_2SO_4 decomposition, but they deactivate rapidly. To overcome this difficulty metal sulfate based TCWSCs have been developed. However, the metal sulfate based TCWSCs utilize thermal heat input – thus degrading photonic energy. Based upon FSEC's S-NH_3 TCWSC, a new family of hybrid photo/thermo-chemical water splitting cycles is introduced in this paper that employs the quantum portion of the solar spectrum for the production of hydrogen and the thermal energy (*i.e.* IR) portion of solar radiation for generating oxygen. FSEC's metal sulfate – ammonia (MSO_4-NH_3) hybrid photo/thermochemical water splitting cycles are represented by the following reactions:

$SO_2(g) + 2NH_3(g) + H_2O(l) \rightarrow (NH_4)_2SO_3(aq)$ (chemical absorption, 25 °C)
$(NH_4)_2SO_3(aq) + H_2O \rightarrow (NH_4)_2\ SO_4(aq) + H_2(g)$ (solar photocatalytic, 80 °C)
$x(NH_4)_2SO_4 + M_2O_x \rightarrow 2xNH_3 + M_2(SO_4)_x + xH_2O$ (solar thermocatalytic, 500 °C)
$M_2(SO_4)_x(s) \rightarrow xSO_2(g) + 2MO(s) + (x\text{-}1)O_2(g)$ (solar thermocatalytic, 1100 °C)

Where, M = Zn, Mg, Ca, Ba, Fe, Co, Ni, Mn, Cu.

Chemical equilibrium calculations for the reaction between ZnO and $(NH_4)_2SO_4$ indicate that both $ZnSO_4$ and $ZnO.2ZnSO_4$ can form as the stable reaction products. A series of thermogravimetric/differential thermal analyses/mass spectrometric (TG/DTA/MS) experiments has also been carried out to determine the exact nature of all ZnO + $(NH_4)_2SO_4$ reaction products. Results obtained are summarized and discussed in this final report.

Introduction

Production of hydrogen (H_2) is environmentally acceptable if it is produced from a noncarboneaceous feedstock using a renewable energy source. Hydrogen production by splitting water using solar energy is considered the "Holy Grail" of the hydrogen economy. Water splitting can be accomplished either directly (in a single step) or indirectly (via multiple steps). Direct thermal decomposition of water is an energy intensive process that requires temperatures exceeding 2500 °C. The main obstacle to this approach is that hydrogen and oxygen (O_2) evolving simultaneously in one reactor can readily recombine to form water – *i.e.* by back

reaction. The combination of photovoltaic (PV) cells coupled to water electrolysis often serves as the benchmark solar hydrogen production process by which the performance of other solar based hydrogen generation processes are appraised. PV cell efficiencies vary from 6% for amorphous silicon solar cells to more than 40% for multiple-junction research grade PV cells. Solar cell energy conversion efficiencies for commercially available mono-crystalline silicon PV cells are around 14-16%. The highest efficiency PV cells such as multi-junction cells based on gallium arsenide or indium selenide are still too expensive and not yet economical to use. On the other hand, water electrolysis is a well-developed technology with energy conversion efficiencies in the range of approximately 70-95%, depending on the type of electrolyte used. Therefore the total solar to hydrogen efficiency of a PV-electrolysis system is in the range of 10-15%. We note that the most commonly used PV cells employ only a portion of the solar energy (10 to 12%) while most of the solar thermal heat is unutilized.

Unlike PV-electrolysis, water splitting processes based on the photocatalytic and photoelectrochemical methods provide a single step direct conversion of solar energy into the chemical energy of hydrogen. In the photocatalytic process, a photocatalyst converts the high-energy photons in solar spectrum into electron-hole pairs that promote redox reactions involving water to produce hydrogen and oxygen. In 1998, Khaselev and Turner reported that the hydrogen production efficiency of 12.4% for a monolithic photoelectrochemical-photovoltaic device based on the short-circuit current and the lower heating value of hydrogen [1]. The electrolyte used by Khaselev and Turner was 3 M sulfuric acid aqueous solution and the high cell output could only be maintained for a very short period of time after which the efficiency began to drop precipitously. Licht and co-workers [2] have reported a solar to H_2 energy conversion efficiency of more than 18% using a multi-junction photoelectrode in 1 M $HClO_4$ electrolyte radiated with a lamp equipped with Air Mass 0 (AM0) filter providing a radiant flux of 135 mW/cm^2. However, no information was given by these authors with regard to the lifespan of the photoelectrode used.

Thermodynamically, water splitting requires a minimum of 237.1 kJ per mole of water decomposed at 25 °C and 1 atm – corresponding to 1.229 eV. Considering the prevailing over potentials, water splitting requires upwards of 2.0 V. In a photocatalytic process, this implies the requirement for a wide band gap (greater than 2.0 eV) photocatalyst. There are conflicting requirements for what makes a good photocatalyst for splitting water. In order to utilize large portion of the solar spectrum, a semiconductor with narrow band gap is desirable. However, electron-hole pairs generated by a low band gap semiconductor do not possess sufficient redox potential to allow water splitting. In case of a wide band gap semiconductor such as TiO_2 (band gap energy of 3.0 eV) only a small portion of solar spectrum would be absorbed. Thus, for a semiconductor photocatalyst to be useful for water splitting, it must have several attributes as follows [3]:

its band gap must be wider than about 1.7 eV;
must have a suitable minority band edge and Fermi level that cover both H_2 and O_2 evolution potentials;
be stable in very acidic or very alkaline solutions;
possess high efficiency for conversion of photons to electron-hole pairs; and
electron-hole pairs must be able to rapidly migrate to the semiconductor surface where redox reactions can readily take place thwarting charge recombination.

To date, no such catalyst has been found. Another approach to direct water splitting involves the use of sacrificial reagents – see, for example, the review by Liu and co-workers [4]. The central premise in this approach is that lower potentials would be necessary to evolve hydrogen if a sacrificial reagent is present as opposed to that required for direct unassisted water splitting. Therefore, the efficiency of H_2 or O_2 production from such systems can be significantly higher than direct water splitting. Several redox systems have been extensively investigated including electron donor systems such as: CH_3OH or C_2H_5OH, Na_2EDTA, Na_2SO_3, Na_2S and NaI or KI; as well as the electron scavenger systems, *e.g.* $AgNO_3$ and $Fe(NO_3)_3$. The redox reactions for the photocatalytic production of H_2/O_2 are summarized below:

Photochemical reactions involving electron donors:

$NaSO_3 + H_2O \rightarrow Na_2SO_4 + H_2$ $\quad \Delta E$ = 0.93 V, pH = 10-12 (1)

$Na_2S + H_2O \rightarrow Na_2S_2 + H2$ $\quad \Delta E$ = 0.524 V, pH = 10-12 (2)

$H_2SO_3 + H_2O \rightarrow H_2SO_4 + H_2$ $\quad \Delta E$ = 0.17 V, pH = 1-6 (3)

$CH_3OH(aq) \rightarrow CH_2O(aq) + H_2$ $\quad \Delta E$ = 0.13 V (4)

$NaI + 3H_2O \rightarrow NaIO_3 + 3H_2$ $\quad \Delta E$ = 0.43 V, pH = 10-13 (5)

$(NH_4)_2SO_3+H_2O \rightarrow (NH_4)_2SO_4+H_2$ $\quad \Delta E$ = 0.52 V, pH ~8.0 (6)

Photochemical reactions involving electron acceptors:

$4Ag^+(aq)+2H_2O \rightarrow O_2 + 4H^+(aq) + 4Ag(s)$ $\quad \Delta E$ = 0.42 V (7)

$4Fe^{3+}(aq)+2H_2O \rightarrow O_2 + 4H^+(aq) + 4Fe^{2+}(aq)$ $\quad \Delta E$= 0.46 V (8)

It should be noted that although redox systems utilizing sacrificial reagents require less energy and can be carried out under milder conditions, a reagent is consumed to produce hydrogen (or oxygen) from water. The H_2SO_3-H_2SO_4 system (Reaction 3) can form a closed cycle if the problem with sulfur formation during H_2SO_3 oxidation is mitigated. The only redox pair listed above that can be made to constitute a thermochemical cycle (TCWSC) with overall reaction being water splitting reaction and co-production of hydrogen and oxygen is Reaction (6). In this work, we introduce a solar thermochemical water splitting cycle based on Reaction (6) for the hydrogen formation and an oxygen generation reaction barrowed from the sulfur family cycles. In the new cycle, hydrogen and oxygen production steps employ different but complementing sectors of the solar spectrum in order to maximize the overall TCWSC efficiency.

Efficiency of Thermochemical Water Splitting Cycles

Hydrogen production via thermochemical water splitting cycles (TCWSCs)

Thermochemical water splitting cycles employ two or more chemical reaction steps that taken together form a closed loop with an overall reaction being the splitting of water and co-production of hydrogen and oxygen. Energy is added into one or more steps of the TCWSC. Typically, energy required for splitting water is provided to more than one reaction making up the TCWSC so that each step requires only a portion of the total energy needed to split water ($\Delta H^o_{w,liquid}$= 285.9 kJ/mol and $\Delta H^o_{w,\ gas}$ = 241.83 kJ/mol at 25 °C, 1 atm). Figure 1 depicts a three-step TCWSC in which the total energy (ΔH_w) required is segmented as follows:

$$\Delta H_w = \Delta H_1 + \Delta H_2 + \Delta H_3 \quad (9)$$

Each step requires less energy than that needed for direct water splitting as follows:

$$\Delta H_1 < \Delta H_w;\ \Delta H_2 < \Delta H_{w;}\ \Delta H_3 < \Delta H_{w.} \quad (10)$$

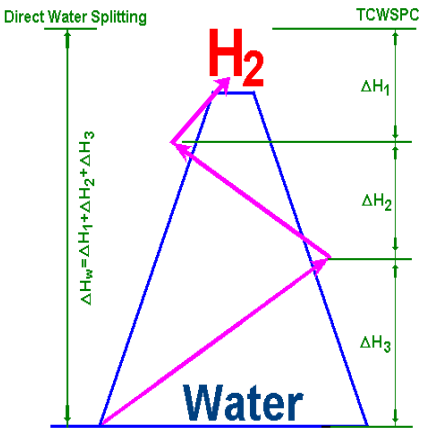

Figure 1. Energetics of TCWSCs.

Clearly, at least two steps are needed to form a TCWSC, namely hydrogen and oxygen evolution steps. In the so called "pseudo TCWSCs", the energy required to perform one of the steps (typically, the oxygen evolving step) exceeds that needed to directly split water (*i.e.* $\Delta H_i > \Delta H_w$). Since more energy than ΔH_w is stored in the products formed from oxygen generation step of the pseudo TCWSCs, hydrogen production step of these cycles can be considerably less energy intensive or even exothermic. Pseudo TCWSCs contain a highly endothermic process for absorbing and storing the solar thermal heat at very high temperatures (above 2000 °C) that require mean solar flux concentration ratios, C_R, of 5000 or higher [5]. Unlike direct thermolysis of water that requires high temperature separation of O_2 from H_2, pseudo TCWSCs typically involve separation of O_2 from a solid product (often an oxide) and as such eliminate the need for oxygen and hydrogen separation. Rapid quenching can also mitigate recombination of the products formed. Figure 2 depicts energetics of pseudo TCWSCs having one step that consumes more energy than ΔH_w. Pseudo TCWSCs fall into three categories: nonmetal oxide, metal/metal oxide and metal oxide/metal oxide cycles [6-8].

Nonmetal oxide cycles

$CO_2(g) = CO(g) + ½O_2$, ΔH = 283.0 kJ/mol, 1700 °C (11)
$CO(g)+H_2O(g)=H_2 + CO_2(g)$, ΔH = -41.2 kJ/mol, 700 °C (12)

$SiO_2 \rightarrow SiO(g) + ½O_2$ 2977 °C (13)
$SiO(g) + H_2O \rightarrow SiO_2 + H_2$ 2656 °C (14)

Reaction (11) requires higher energy than ΔH^o_w = 241.83 kJ/mol.

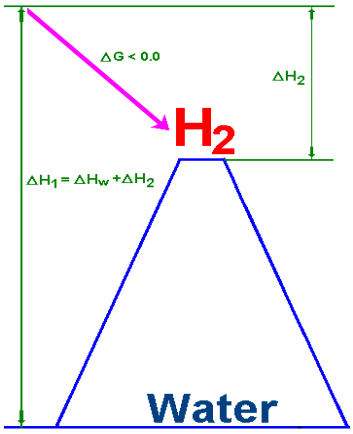

Figure 2. Energetics of pseudo TCWSCs.

Metal/metal oxide TCWSCs

$M_xO_y = x\ M + ½y\ O_2$ (endothermic), $\Delta H^o > \Delta H^o_W$ (15)
$x\ M + y\ H_2O = M_xO_y + y\ H_2$ (exothermic), $\Delta G < 0$ (16)

Where, M represents a metal. Basically, any metal that can reduce water and generate hydrogen can be used in a metal/metal oxide based TCWSC. Examples include: Zn/ZnO, Li/Li_2O, Na/Na_2O, K/K_2O, Mg/MgO, Ca/CaO, Mo/MoO_2, W/WO_3, SiO_2/SiO, Sn/SnO_2, FeO/Fe_3O_4, In_2O_3/In_2O, etc. Some metal and metal oxide based pseudo TCWSCs are given below [8]:

$MoO_2(s) \rightarrow Mo + O_2$ 3713 °C (17)
$Mo + 2H_2O \rightarrow MoO_2(s) + 2H_2$ 1543 °C (18)
$WO_3(s) \rightarrow W + 3/2O_2$ 3910 °C (19)
$W + 3H_2O \rightarrow WO_3(s) + 3H_2$ 884 °C (20)

$SnO_2 \rightarrow Sn + O_2$ 2650 °C (21)
$Sn + 2H_2O \rightarrow SnO_2 + 2H_2$ 600 °C (22)

$ZnO \rightarrow Zn + ½O_2$ 2000 °C (23)
$Zn + H_2O \rightarrow ZnO + H_2$ 1100 °C (24)

Some low temperature metal/metal oxide cycles do not belong to pseudo TCWSCs [8]:

$Hg(g) + H_2O \rightarrow HgO(s) + H_2$ 360 °C (25)
$HgO(s) \rightarrow Hg(g) + ½O_2$ 600 °C (26)

$Cd(s) \rightarrow H_2O \rightarrow CdO(s) + H_2$ (electrolytic, 25 °C) (27)
$CdO(s) \rightarrow Cd(g) + ½O_2$ 1400 °C (28)

These two cycles use heavy metals Hg and Cd and generally viewed as environmentally undesirable cycles.

Metal oxide/metal oxide TCWSCs

$In_2O_3 \rightarrow In_2O + O_2$ 2200 °C (29)
$In_2O + 2H_2O \rightarrow In_2O_3 + 2H_2$ 800 °C (30)

$Fe_3O_4(s) \rightarrow 3FeO(s) + ½O_2$ 2200 °C (31)
$3FeO(s) + H_2O \rightarrow Fe_3O_4(s) + H_2$ 400 °C (32)

$Ni_{0.5}Mn_{0.5}Fe_2O_4 \rightarrow Ni_{0.5}Mn_{0.5}Fe_2O_{4-x} + ½ \text{ x } O_2$ 1100 °C (33)
$Ni_{0.5}Mn_{0.5}Fe_2O_{4-x} + \text{x } H_2O \rightarrow Ni_{0.5}Mn_{0.5}Fe_2O_4 + xH_2$ 600 °C (34)

$MnFe_2O_4 + 3CaO + (1\text{-}x)H_2O \rightarrow Ca_3(Fe, Mn)_3O_{8-x} + (1\text{-}x)H_2$ 1000 °C (35)
$Ca_3(Fe, Mn)_3O_{8-x} \rightarrow MnFe_2O_4 + 3CaO + ½(1\text{-}x)O_2$ 600 °C (36)

TCWSC efficiency

The overall thermal efficiency ($\eta_{overall}$) (or 1st law efficiency) of a TCWSC is defined as the ratio of hydrogen chemical energy to total energy consumed by the cycle.

$$\eta_{overall} = \frac{n \cdot \Delta H^{o}{}_{f}}{\Delta H_{total}} \tag{37}$$

Where n denotes the total mole of H_2 generated by the cycle, ΔH^{o}_{f} is enthalpy of water formation and ΔH_{total} is the total energy input to the cycle to produce *n* moles of hydrogen. If the enthalpy formation of water in liquid state is used (at 298 K, ΔH_f = -68.32 kcal/mol = 285.9 kJ/mol), the efficiency calculated is referred as the high heating value (HHV) efficiency, η(HHV). Some argue that the latent heat of condensation cannot be effectively recovered and prefer using the low heating value (LHV) efficiency η(LHV) in which ΔH^{0}_{f} is the enthalpy of formation of water vapor at 298 K (ΔH^{0}_{f} = -57.41 kcal/mol = 240.2 kJ/mol). The ratio η(HHV)/ η(LHV) = 68.32/54.74 = 1.19. The figure of merit or Carnot efficiency (also, 2nd law efficiency) is defined as:

$$\eta(w) = \frac{n \cdot \Delta G^{0}{}_{f}}{\Delta H_{total}} = \frac{237.2n}{\Delta H_{total}} \tag{38}$$

Where, ΔG^{o}_{f} is to the Gibbs free energy of water formation (237.2 kJ/mol). Since early 1970s, when the concept of TCWSCs was first introduced, numerous methods have been proposed for calculating TCWSC efficiencies [9-11]. Since TCWSCs often contain several reaction steps as well as processes for the material transport and separation, precise determination of the efficiencies has been complicated. Huang and Raissi [12] have shown that efficiency of a TCWSC must be calculated based on a detailed process flowsheet that takes account of material and energy balance as well as precise values of the chemical and physical properties of reactants and products.

Figure 3 depicts a simple flow diagram for a TCWSC. Water is fed into the cycle and hydrogen and oxygen are generated as the only output of the cycle. In addition to the hydrogen and oxygen production steps, there are steps involving separation and recycling thus forming a closed cycle for splitting water into H_2 and O_2. Total energy needed to perform water splitting

includes those required to generate H_2 and O_2 (*i.e.* ΔH_1 and ΔH_2), separate reactants from products (ΔH_S) and recycle reactants (ΔE). Then,

$$\Delta H_{Total} = \Delta H_1 + \Delta H_2 + \Delta H_S + \Delta E \tag{39}$$

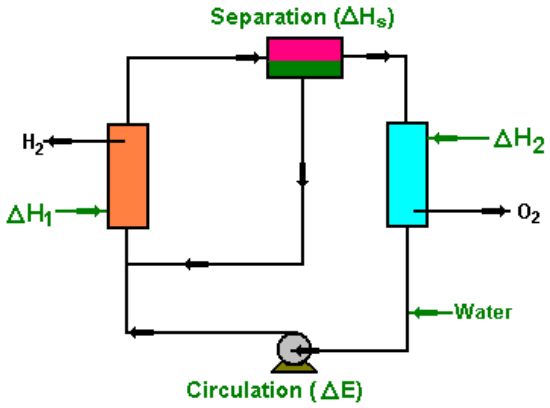

Figure 3. A simple flow diagram depicting TCWSC.

For simplicity, ΔH_S and ΔE may be added to ΔH_1 and ΔH_2 and denoted as $\Delta H(H_2)_{In}$ and $\Delta H(O_2)_{In}$, respectively. Thus, Equation (39) can be written as:

$$\Delta H_{Total} = \Delta H(H_2)_{In} + \Delta H(O_2)_{In} \tag{40}$$

Assuming that the efficiencies for H_2 and O_2 production are $\eta(H_2)$ and $\eta(O_2)$, respectively, we have:

$$\eta(H_2) = \Delta H(H_2)_R / \Delta H(H_2)_{In} \tag{41}$$
$$\eta(O_2) = \Delta H(O_2)_R / \Delta H(O_2)_{In} \tag{42}$$

Where, $\Delta H(H_2)_R$ and $\Delta H(O_2)_R$ denote the amount of energy needed to conduct H_2 and O_2 generation reactions, respectively. Thus, the total energy required for H_2 and O_2 production is

$$\Delta H_{Reaction} = \Delta H(H_2)_R + \Delta H(O_2)_R \tag{43}$$

Assuming that R is the ratio of the energy input into the O_2 and H_2 production steps, $R = \Delta H(O_2)_{In}/\Delta H(H_2)_{In}$, then overall cycle efficiency, $\eta_{Overall}$, is then

$$\begin{aligned}\eta_{Overall} &= \frac{\Delta H_{Reaction}}{\Delta H_{Total}} = \frac{\Delta H(H_2)_R + \Delta H(O_2)_R}{\Delta H(H_2)_{In} + \Delta H(O_2)_{In}} \\ &= \frac{\Delta H(H_2)_R}{\Delta H(H_2)_{In} + \Delta H(O_2)_{In}} + \frac{\Delta H(O_2)_R}{\Delta H(H_2)_{In} + \Delta H(O_2)_{In}} \\ &= \frac{\eta(H_2)}{1+R} + \frac{\eta(O_2)}{1+1/R} = \frac{\eta(H_2) + R \cdot \eta(O_2)}{1+R}\end{aligned} \tag{44}$$

I
n case $\eta(H_2) = \eta(O_2)$, then

$\eta_{Overall} = \eta(H_2) = \eta(O_2) \neq f(R) \equiv$ independent of "R" (45)

In other words, if $\eta(H_2) = \eta(O_2)$, it would not matter how the solar resource is partitioned to supply $\Delta H(H_2)_{In}$ and $\Delta H(O_2)_{In}$ – the cycle efficiency would be the same and equal to $\eta(H_2) = \eta(O_2)$. But, if $\eta(H_2) \neq \eta(O_2)$, Equation (44) implies that, the overall efficiency of the TCWSC ($\eta_{Overall}$) lies between $\eta(H_2)$ (at R= 0) and $\eta(O_2)$ (at R= ∞). Therefore, for the maximum overall cycle efficiency, it is necessary that most of the energy input into the cycle occurs at the more efficient step of the cycle. For example, if $\eta(O_2) > \eta(H_2)$, it is necessary that $\Delta H(O_2)_{In} \gg \Delta H(H_2)_{In}$. Likewise, if $\eta(H_2) > \eta(O_2)$, it is desirable that $\Delta H(H_2)_{In} \gg \Delta H(O_2)_{In}$.

Sulfuric acid/metal sulfate based TCWSCs

The sulfur family cycles are widely studied multi-step TCWSCs. The oxygen producing step in the sulfur family cycles is the decomposition of sulfuric acid or a metal sulfate. The energy input for the decomposition of H_2SO_4, calculated using GTT-Technologies' FactSage™ 5.5 thermochemical analysis software, is only about 80.9% of the total energy required for water splitting (*i.e.* 286 kJ/mol) as follows:

$H_2SO_4 = H_2O + SO_3$ $\Delta H^o 298K$ = 87.1 kJ/mol (46)

$SO_3 = SO_2 + ½O_2$ $\Delta H^o 298K$ = 144.2 kJ/mol (47)

For which the overall reaction is:

$H_2SO_4 = H_2O + SO_2 + ½O_2$ $\Delta H^o 298K$ = 231.3 kJ/mol (48)

The remaining 19.1% of the energy required to split water has to be supplied for the H_2 production step.

Figure 4 depicts the terrestrial solar direct normal spectral irradiance distribution computed using SMARTS version 2.9.2 model with input file from ASTM Standard Table G 173-03[1]

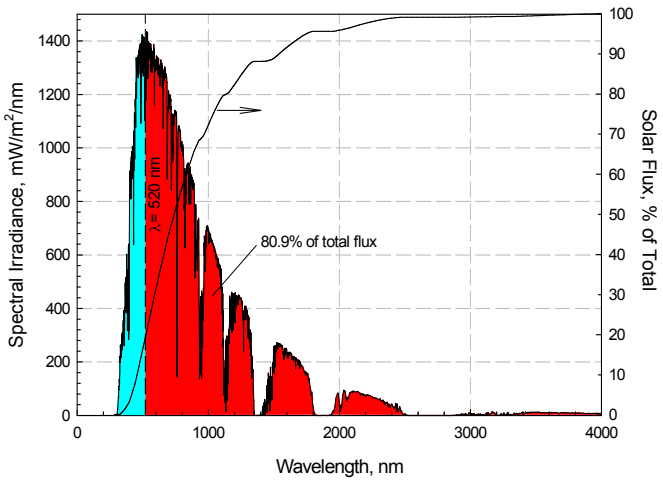

.

Figure 4. Plot of AM 1.5 direct normal spectral solar irradiance computed using SMATRS version 2.9.2 with input file from ASTM Standard Table G 173-03[1].

It can be seen that about 80.9% of the total solar irradiance comprising mostly of thermal energy with wavelengths above 520 nm can be utilized for the decomposition of sulfuric acid in the oxygen generation step of the sulfur-family cycles. The remaining 19.1% of the solar irradiance which consists of photonic energy at wavelengths less than about 520 nm will be used for the hydrogen production step of the cycle. In other words, for optimum overall cycle efficiency, it is necessary that the oxygen production step utilizes 80.9% of the solar irradiance as mostly thermal radiation above a wavelength of approximately 520 nm and the hydrogen generation step consumes the remaining 19.1% of solar resource, at wavelengths shorter than 520 nm – within a photolytic and/or photocatalytic reactor. A suitable photocatalyst for carrying out the hydrogen generation step is cadmium sulfide (CdS) for which the optical absorption edge (λ_{edge}) of the bulk material is at 512 nm making it an ideal photocatalyst for conducting the H_2 generation step of a solar-TCWSC.

Decomposition of sulfuric acid presents an efficient means of generating oxygen via a solar thermochemical water splitting cycle pending the required reaction temperatures can be realizable.

Typically, large-scale solar concentrators utilize parabolic reflectors in the form of trough, tower, or dish systems. These solar concentrators are characterized in terms of their mean flux concentration ratio C_R over an area S_a at the receiving focal plane as follows:

$$C_R = q_s/I \tag{49}$$

Where q_s (W/m^2) refers to the solar flux intercepted by unit area of the receiver at the focal plane and I (W/m^2) is the incident normal beam insolation. C_R is often expressed in units of ‘‘suns’’ when normalized to I = 1000 W/m^2 [13]. The solar flux concentration ratio typically obtained is at the level of 100, 1000, and 10,000 suns for trough, tower, and dish systems, respectively. The most suitable concentrators for applications involving solar thermochemical water splitting cycles are tower and dish systems.

According to Steinfeld [13], there is a temperature, $T_{optimum,}$ for which the TCWSC efficiency is maximum. Assuming a uniform power-flux distribution, $T_{optimum}$ can be determined from the following implicit equation:

$$T^5_{optimum} - (0.75\ T_L)\ T^4_{optimum} - (T_L I C_R / 4\sigma) = 0 \quad (50)$$

Where, T_L is the temperature of the thermal reservoir for heat rejection, usually ambient temperature and σ refers to the Stefan–Boltzmann constant (5.6705×10^{-8} $Wm^{-2}K^{-4}$). In the case that the TCWSC utilizes only a portion of the solar irradiance (say, above λ) for performing the oxygen production step (see Figure 4), we have

$$T^5_{\lambda,\ optimum} - (0.75\ T_L)\ T^4_{\lambda,\ optimum} - (T_L I_\lambda C_R / 4\sigma) = 0 \quad (51)$$

$T_{\lambda,\ optimum}$ refers to the temperature for which the efficiency of oxygen generation step of the solar TCWSC is highest. I_λ (W/m^2) refers to the incident normal beam insolation integrated over wavelength in the range of λ to 4000 nm (see Figure 4).

Figure 5 depicts, the optimum temperatures and maximum achievable efficiencies for the oxygen production step of a sulfur family solar TCWSC as a function of the mean flux concentration ratio at λ= 520 nm. Figure 5 also shows the variation of $T_{optimum}$ vs. λ at constant mean flux concentration ratios in the range of 50 to 10000. The solar insolation values used are taken from Figure (4) for the direct normal spectral irradiance data for the Air Mass 1.5.

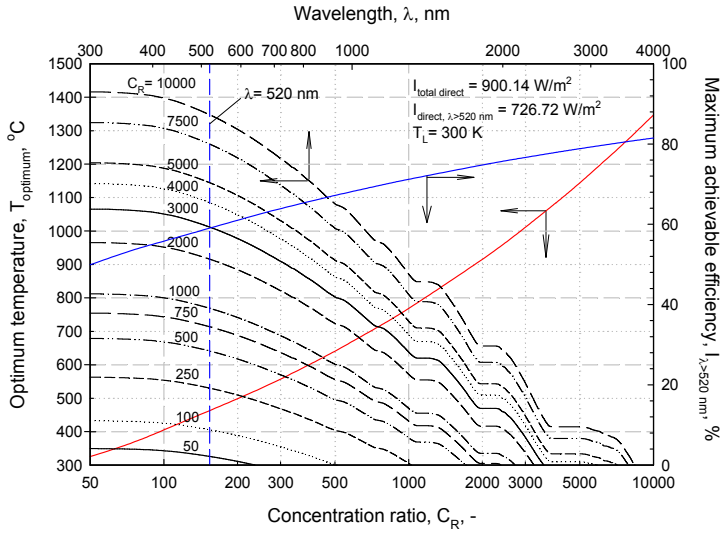

Figure 5. $T_{optimum}$ and maximum achievable efficiencies for oxygen production step of the sulfur- family solar TCWSCs as a function of mean flux concentration ratio, C_R, at λ= 520 nm; and variation of $T_{optimum}$ vs. λ at constant C_R. Direct normal solar irradiance data from Figure (4), AM 1.5.

Results of Figure 5 indicate that $T_{\lambda,\ optimum}$ for the oxygen generation step of the sulfur family TCWSC utilizing solar irradiance at wavelengths above λ= 520 nm varies between 768 °C and 1347 °C for uniform power-flux distribution with concentrations in the range of 1000-10,000. For example, at C_R= 1500, $T_{520nm,\ optimum}$ = 852 °C – giving a maximum theoretical efficiency (or the 1st law efficiency, η_I) of about 73.33%. In other words, the portion of solar energy that could in principle be captured in the form of chemical energy (decomposition of sulfuric acid and generation of oxygen) is 73.33%. In practice, due to various losses, the maximum efficiency will be lower. Therefore, a solar concentrator (of the tower or dish type) with capability to deliver a mean flux concentration ratio C_R of at least 1500 is needed to carry out the sulfuric acid decomposition reaction for oxygen generation requiring temperatures at or above 852 °C.

The exergy efficiency (or the 2nd law efficiency) for the sulfuric acid decomposition step is given by:

$$\eta_{II} = -\acute{n}\Delta G|_{H2O+SO2++0.5O2\rightarrow H2SO4}/C_R I_{\lambda>520nm} \quad (52)$$

Where ΔG refers to the standard Gibbs free energy change for the sulfuric acid decomposition reaction at 298 K and 1 atm (-149.8 kJ/mol). The exergy efficiency is important in determining the merits of any solar thermochemical process. The higher the η_{II}, the lower the required size of the solar installation required for producing a given quantity of product, and lower the plant costs. In the equation above, ń is the molar flow rate of H_2SO_4 consumed which is determined from the definition of the 1st law efficiency as follows:

$$\eta_I = -\acute{n}\Delta H|_{H2O+SO2++0.5O2\rightarrow H2SO4}/C_R I_{\lambda>520nm} \quad (53)$$

In Equation (53), ΔH is the standard enthalpy change for H_2SO_4 decomposition reaction at 298 K and 1 atm (-231.12 kJ/mol). For C_R= 1500, $T_{520nm,\ optimum}$ was calculated to be 1125 K (852 °C) – giving a 1st law efficiency of about η_I = 73.33%. Substituting η_I, ΔH, C_R (=1500) and $I_{\lambda>520nm}$ (=726.72 W/m^2) into the equation (53) gives ń = 3.456 mol/s/m^2. Knowing ń, from equation (52) we have: η_{II} = 47.52%.

Due to high 1st and 2nd law efficiencies of sulfuric acid based cycles, to date, more than 20 sulfuric acid and/or metal sulfate decomposition based TCWSCs have been reported. Despite difficulties that challenge efficient electrolytic oxidation of sulfur dioxide (SO_2), the Westinghouse hybrid cycle still remains as one of the most studied TCWSCs. The Westinghouse cycle is as follows [14]:

$SO_2(g) + 2H_2O(l) = H_2 + H_2SO_4(aq)$ 77 °C (electrolysis) (54)

$H_2SO_4(g) = SO_2(g) + H_2O + ½O_2$ 850 °C (thermolysis) (55)

The Westinghouse cycle has many advantages widely reported and discussed in the literature. However, it is known that the Westinghouse cycle is hampered by the low water solubility of SO_2 and challenges presented by the acidity of the SO_2 electrolytic oxidation process [15]. To date, many efforts have been made to improve the efficiency of the electrolytic process for oxidation of SO_2. Prior work has involved the use of a depolarized electrolyzer as well as addition of a third process step - examples include S-I, S-Br and S-Fe cycles given below:

Ispra Mark 13 sulfur-bromine cycle [16]:

$Br_2(l) + SO_2 + 2H_2O(l) \rightarrow 2HBr(aq) + H_2SO_4(aq)$ 77 °C (56)
$H_2SO_4(g) \rightarrow SO_2(g) + H_2O(g) + ½ O_2$ 850 °C (57)
$2HBr(aq) \rightarrow Br_2(aq) + H_2$ (electrolytic) 77 °C (58)

General Atomics' sulfur-iodine cycle [17]:

$I_2 + SO_2(g) + 2H_2O(l) \rightarrow 2HI(a) + H_2SO_4(aq)$ 100 °C (59)
$H_2SO_4(g) \rightarrow SO_2(g) + H_2O(g) + ½ O_2$ 850 °C (60)
$2HI \rightarrow I_2(g) + H_2$ 450 °C (61)

Sulfur-iron cycle [18]:

$Fe_2(SO_4)_3(aq)+SO_2 + 2H_2O \rightarrow 2FeSO_4(aq)+2H_2SO_4$ 25 °C (62)
$H_2SO_4(l) \rightarrow SO_2(g) + H_2O(g) + ½ O_2$ 850 °C (63)
$2FeSO_4(aq) + H_2SO_4(aq) \rightarrow Fe_2(SO_4)_3(aq) + H_2$ 25 °C (64)

To make the separation of HI for H_2O easier, Sato and co-workers have proposed a nickel-iodine-sulfur version of S-I cycle [19]:

$SO_2(aq) + I_2(aq) + 2H_2O(l) \rightarrow 2H_2SO_4(aq) + 2HI(aq)$ (65)
$2HI(aq)+2H_2SO_4(aq)+2Ni(c) \rightarrow NiI_2(c)+NiSO_4(aq)+2H_2$ (66)
$NiI_2(c) \rightarrow NI(c) + I_2(g)$ (67)
$NiSO_4(c) \rightarrow NiO(c) + SO_3(g)$ (68)
$SO_3(g) \rightarrow SO_2(g) + ½O_2(g)$ (69)
$NiO(c) + H_2(g) \rightarrow Ni(c) + H_2O(g)$ (70)

Others include:

$CO + H_2O \rightarrow CO_2 + H_2$ 550 °C (71)
$CO_2 + SO_2 + H_2O \rightarrow H_2SO_4 + CO$ 500 °C (72)
$H_2SO_4(g) \rightarrow H_2O(g) + SO_2(g) + ½O_2$ 900 °C (73)

$SO_2 + H_2O + I_2 \rightarrow SO_3 + 2HI$ 200 °C (74)
$SO_3 \rightarrow SO_2 + ½O_2$ 900 °C (75)
$2HI \rightarrow H_2 + I_2$ 450 °C (76)

$2FeSO_4 + I_2 + 2H_2O \rightarrow 2Fe(OH)SO_4 + 2HI$ 20 °C (77)
$2HI \rightarrow H_2 + I_2$ 450 °C (78)
$2Fe(OH)SO_4 \rightarrow 2FeSO_4 + H_2O + ½O_2$ 100 °C (79)

$3FeCl_2(s) + 4H_2O \rightarrow Fe_3O_4(s) + 6HCl(g) + H_2$ 650 °C (80)
$Fe_3O_4(s)+Fe_2O_3(s)+6HCl+2SO_2 \rightarrow 3FeCl_2+2FeSO_4+3H_2O$ 100 °C (81)
$2FeSO_4 \rightarrow Fe_2O_3(s) + 2SO_2(g) + ½O_2$ 850 °C (82)

Although these cycles address some of the challenges associated with water splitting, especially with regard to water solubility of SO_2, they have issues of their own. For example, efficient separation of sulfuric acid from reaction products such as HI, HBr or $FeSO_4$ is

challenging. Additionally, the pH of the solutions remains problematic. In fact, this problem becomes more acute due to the generation of other acids such as HI and HBr. For solar driven water splitting, Abanades *et al.* [8] screened 280 TCWSCs. They selected 30 TCWSCs as promising which warrant further investigation. Among them, there were nine metal sulfate based TCWSCs – almost ⅓ of all selected cycles since decomposition of H_2SO_4 or MSO_4 presents an effective method for the heat absorbing step of the TCWSCs. The General Atomics' S-I cycle was not among the selected candidates considered suitable for solar interface by Abanades due to the difficulties in separating HI from water. Several examples of metal sulfate cycles are given below:

$MnSO_4 \rightarrow MnO + SO_2 + ½O_2$	1100 °C	(83)
$MnO + H_2O + SO_2 \rightarrow MnSO_4 + H_2$	250 °C	(84)
$FeSO_4 \rightarrow FeO + SO_2 + ½O_2$	1100 °C	(85)
$FeO + H_2O + SO_2 \rightarrow FeSO_4 + H_2$	250 °C	(86)
$CoSO_4 \rightarrow CoO + SO_2 + ½O_2$	1100 °C	(87)
$CoO + H_2O + SO_2 \rightarrow CoSO_4 + H_2$	250 °C	(88)
$3FeO(s) + H_2O \rightarrow Fe_3O_4(s) + H_2$	200 °C	(89)
$Fe_3O_4(s) + FeSO_4 \rightarrow 3Fe_2O_3(s) + 3SO_2(g) + ½O_2$	800 °C	(90)
$3Fe_2O_3(s) + 3SO_2(g) \rightarrow 3FeSO_4 + 3FeO(s)$	1800 °C	(91)
$3FeO(s) + H_2O \rightarrow Fe_3O_4(s) + H_2$	200 °C	(92)
$Fe_3O_4(s) + 3SO_3 \rightarrow 3FeSO_4(g) + ½O_2$	800 °C	(93)
$FeSO_4 \rightarrow 3FeO(s) + SO_3$	2300 °C	(94)
$Fe_2O_3(s) + 2SO_2(g) + H_2O \rightarrow 2FeSO_4(s) + H_2$	200 °C	(95)
$2FeSO_4(s) \rightarrow 3Fe_2O_3(s) + SO_2(g) + SO_3(g)$	700 °C	(96)
$SO_3(g) \rightarrow SO_2(g) + ½O_2$	2300 °C	(97)
$6Cu(s) + 3H_2O \rightarrow 3Cu_2O(s) + 3H_2$	500 °C	(98)
$Cu_2O(s) + 2SO_2(g) + 1.5O_2 \rightarrow 2CuSO_4$	300 °C	(99)
$2Cu_2O(s) + 2CuSO_4 \rightarrow 6Cu(s) + 2SO_2 + 3O_2$	1750 °C	(100)
$Cu_2O(s) + H_2O(g) \rightarrow Cu(s) + Cu(OH)_2$	1500 °C	(101)
$Cu(OH)_2 + SO_2(g) \rightarrow CuSO_4 + H_2$	100 °C	(102)
$CuSO_4 + Cu(s) \rightarrow Cu_2O(s) + SO_2 + ½O_2$	1500 °C	(103)
$SO_2 + H_2O + BaMoO_4 \rightarrow BaSO_3 + MoO_3 + H_2O$	300 °C	(104)
$BaSO_3 + H_2O \rightarrow BaSO_4 + H_2$		(105)
$BaSO_4(s) + MoO_3(s) \rightarrow BaMoO_4(s) + SO_2(g) + ½O_2$	1300 °C	(106)

The second approach is to introduce a metal oxide as a catalyst to convert low concentration sulfuric acid to metal sulfate which is then decomposed to produce oxygen, sulfur dioxide and metal oxide. Sulfur dioxide and water are sent to acid electrolysis unit for generation of hydrogen and sulfuric acid – closing the cycle. Introducing ZnO into the Westinghouse TCWSC, a new, modified $ZnSO_4$ decomposition based Westinghouse cycle can be written as:

$SO_2(g) + 2H_2O(l) = H_2 + H_2SO_4(aq)$	77 °C (electrolytic)	(107)

H_2SO_4(aq, 50wt%) + ZnO(s) = $ZnSO_4 \cdot H_2O$(s) 80~350 °C (108)
$ZnSO_4 \cdot H_2O$(s) = $ZnSO_4$(s) + H_2O(g) 450 °C (109)
$ZnSO_4$(s) = SO_2(g) + ½O_2 + ZnO(s) 850 °C (110)

Similarly, by adding metal oxide catalysts to the Ispra Mark 13 sulfur-bromine cycle, General Atomics' sulfur-iodine cycle and sulfur-iron cycle (Reactions (56) to (64)), a number of new, modified metal sulfate based TCWSCs can be devised. However, we note that, when energy input for these cycles is solar energy, they can utilize only the thermal energy degrading the photonic portion of solar spectrum to lower grade heat.

At the Florida Solar Energy Center, we have developed a new TCWSC that utilizes the photonic portion of the solar spectrum for the production of hydrogen and the thermal portion of sun light for the generation of oxygen.

Solar Thermochemical S-NH3 Water Splitting Cycle

S-NH_3 Hybrid Cycle

As shown in equation (44), TCWSC efficiency is a function of both hydrogen and oxygen production step efficiencies. The efficiency of any solar driven water splitting cycle depends upon the ability of the cycle to utilize as broad of a range of the solar spectrum as possible – i.e. being able to exploit both the photonic (UV/visible) and thermal components of the solar radiation. Degradation (or thermalization) of the high energy portion of solar radiation to thermal heat, as is the case with purely thermochemical water splitting cycles, can lead to lower overall cycle efficiencies. Thermodynamically, the total energy (ΔH) required to produce H_2 by water splitting is $\Delta H = \Delta G + T\Delta S$. At a given temperature T, a process will be more efficient if it can utilize the photonic energy of solar radiation as Gibbs free energy, ΔG, and the remaining mostly thermal component as $T\Delta S$.

Present technologies for the solar production of H_2 by means of direct water splitting either exclusively use the photonic portion of solar spectrum or thermalize the entire photonic range of the solar spectrum. For example, direct thermal decomposition of water degrades solar photonic energy to lower grade thermal heat, resulting in an exergy loss. Direct thermolysis of water requires temperatures above 2500 °C and in addition, recombination of H_2 and O_2 is a serious issue. Photoelectrochemical (PEC) water splitting has merits over the photovoltaic (PV) plus water electrolysis as it combines photochemical and electrochemical steps into a single process allowing direct H_2 production. However, in the PEC process, only a small portion of the solar spectrum is utilized and the thermal component of sunlight is wasted. Consequently, the PEC energy conversion efficiencies are still at very low levels.

FSEC's hybrid photo/thermo-chemical water splitting cycle employs the quantum portion of the solar spectrum for the production of H_2 and the thermal portion (*i.e.,* IR) portion of solar radiation for O_2 evolution [5,20]. Utilization of the full solar spectrum allows the cycle to reach potentially a higher overall efficiency than is possible with the purely thermochemical water splitting cycles of the past. FSEC's sulfur-ammonia (S-NH_3) hybrid photo/thermochemical cycle is represented by the following four reactions:

SO_2 (g) + $2NH_3$(g) + H_2O(l) → $(NH_4)_2SO_3$(aq) 25 °C (chemical absorption) (111)
$(NH_4)_2SO_3$(aq) + H_2O → $(NH_4)_2SO_4$(aq) + H_2(g) 77 °C (photocatalytic step) (112)

$(NH_4)_2SO_4 \rightarrow 2NH_3(g) + H_2SO_4(g)$ 252 °C (thermocatalytic step) (113)

$H_2SO_4(l) \rightarrow SO_2(g) + H_2O(g) + ½O_2(g)$ 852 °C (thermocatalytic step) (114)

Solar thermal energy is used to drive Reactions (113) and (114) for the production of O_2 via decomposition of ammonium sulfate $(NH_4)_2SO_4$ and sulfuric acid H_2SO_4. Reaction (112) is a photocatalytic process in which SO_3^{2-} ions are oxidized to SO_4^{2-} in the presence of UV-visible light, a photocatalyst and water, generating hydrogen. Figure 6 depicts a schematic diagram of the S-NH_3 cycle showing how the thermal, *i.e.* near infrared (NIR) and infrared (IR), and UV-visible portions of solar radiation are resolved using a spectral splitting mirror. The thermal part of the sunlight is then concentrated into a high temperature thermocatalytic reactor/receiver and used for oxygen production, while the photonic (UV and visible light) portion passes through a coating layer driving the photocatalytic hydrogen generation reaction.

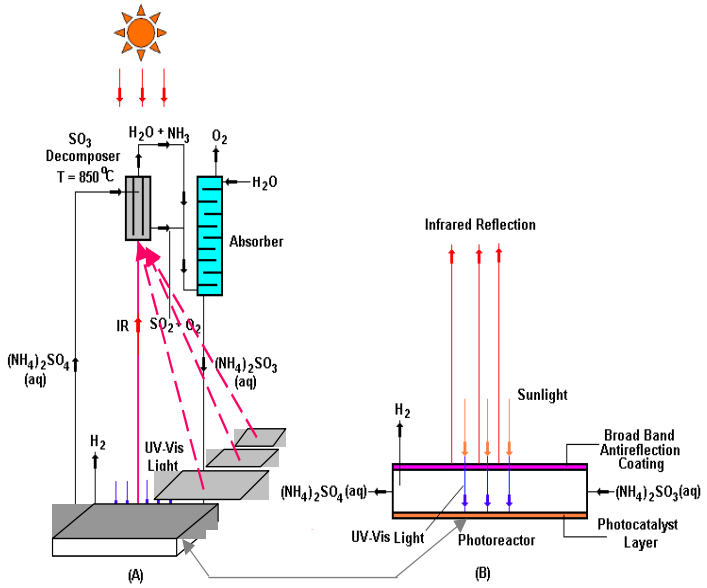

Figure 6. Schematic diagram of S-NH_3 photo-thermochemical water splitting cycle.

Reaction (112) requires approximately 0.52 V potential (vs. NHE) in a 1 M aqueous $(NH_4)_2SO_3$ solution with a pH of 7.8. This potential is about ⅓ of that needed for water splitting (approximately 1.5V). Furthermore, as noted before, Reaction (114) requires 80.9% of the total solar irradiance, comprised of mostly thermal energy with wavelengths above 520 nm. The remaining 19.1% of the solar irradiance, which is photonic energy at wavelengths less than about 520 nm, is then used to carry out the hydrogen production step of the cycle. In the previous section it was shown that this partitioning of solar irradiance was necessary for achieving the highest overall cycle efficiency. In other words, the oxygen production step consumes 80.9% of the solar thermal energy at wavelengths of approximately 520 nm or longer and the H_2 generation step utilizes the remaining 19.1% of solar light having wavelengths shorter than 520 nm. The hydrogen generation step occurs within a photocatalytic reactor. A suitable photocatalyst for carrying out the hydrogen generation step is cadmium sulfide (CdS) with the optical absorption edge (λ_{edge}) of 512 nm for bulk CdS.

Rate of H_2 production for the S-NH_3 TCWSC

Reaction (111) in the S-NH_3 cycle is a chemical adsorption step involving reaction between an acid gas (SO_2) and an alkaline gas (NH_3) to form aqueous $(NH_4)_2SO_3$. Reaction (112) is a photocatalytic hydrogen production step in which photonic energy is converted to the chemical energy of hydrogen. Reaction (112) can occur by either a visible light photocatalytic process or a UV light photolytic route [21,22]. Experimental data obtained to date show it is possible to carry out Reaction (112) with an energy conversion efficiency of about 12% using CdS as the photocatalyst. Figure 7 depicts the rate of H_2 production from an aqueous $(NH_4)_2SO_3$ solution using a 1000 W solar simulator fitted with an AM 1.5 global filter. Data of Figure 7 show that the rate of hydrogen production can be increased substantially by using polymer-stabilized platinum doped CdS.

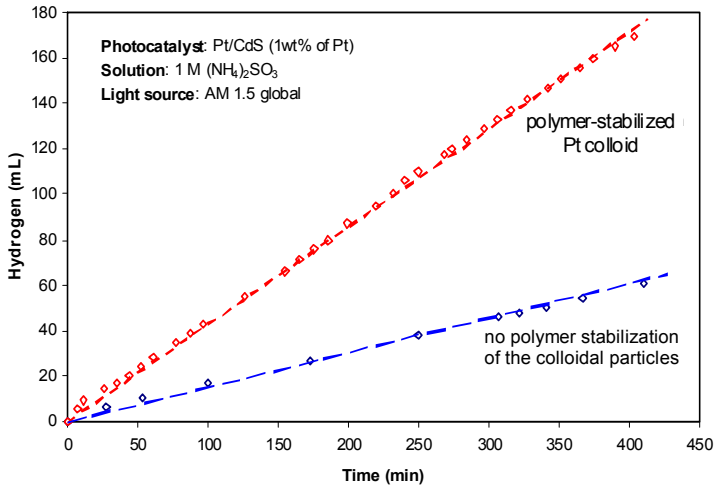

Figure 7. Rate of hydrogen production from aqueous $(NH_4)_2SO_3$ solution (beam area: 33 cm^2, light intensity: ~1.5 kW/m^2, solution pH = 7.5, solution volume = 200 mL, and 0.25 g Pt/CdS photocatalyst).

It should be possible to combine Reactions (113) and (114) into a single step. In fact, Reaction (113) is an intermediate step in which NH_3 is recovered and reacted with SO_2 to form $(NH_4)_2SO_3$ – to be used in the next reaction step.

We employed a Perkin-Elmer Diamond™ TG/DTA system coupled to the Pfeiffer ThermoStar™ benchtop quadrupole mass spectrometer with closed ion source for mass range of 1-300 amu for charting the decomposition of $(NH_4)SO_4$ [23]. Results obtained show that the decomposition of $(NH_4)SO_4$ occurs in two separate and sequential steps – at 250 °C and 340 °C, depending on the heating rate and material of the sample holder used. No sulfur or nitrogen containing gases were detected during the thermolysis process. This suggests that the S-NH_3 cycle as shown below:

$$2(NH_4)_2SO_4(s) = (NH_4)_2S_2O_7(s) + 2NH_3(g) + H_2O(g) \quad (115)$$
$$(NH_4)_2S_2O_7(s) = 2NH_3(g) + H_2S_2O_7(g) \quad (116)$$
$$H_2S_2O_7(g) = H_2SO_4(g) + SO_3(g) \quad (117)$$

can indeed be made to become a closed TCWSC, with the net reaction being that of water splitting:

$$2(NH_4)_2SO_4(s) = H_2SO_4(g) + SO_3(g) + 4NH_3(g) + H_2O(g) \quad (118)$$

Since most of the energy input into the cycle is used in Reaction (117), the overall cycle efficiency is strongly influenced by the efficiency of the H_2SO_4 decomposition step. Thermocatalytic decomposition of H_2SO_4 has been investigated extensively, and very high process efficiencies have been reported. Splitting the solar irradiance so that it can be input to two separate processes eases the requirement for high process efficiency for the photochemical reaction step of the S-NH_3 cycle. We have studied the thermodynamics, kinetics and flowsheeting of all steps involving sulfuric acid concentration and decomposition, and re-circulation of the un-reacted sulfur trioxide [24,25].

As noted in the previous section, for C_R= 1500, at 1125 K (852 °C), a maximum theoretical efficiency (or the 1st law efficiency, η_I) of about 73.33% is achievable for the H_2SO_4 decomposition step. In other words, the portion of the solar energy that could be captured and used to conduct acid decomposition and O_2 generation is about 73.33%. We also note that at temperatures higher than 1000 °C, H_2SO_4 decomposition is no longer kinetically limiting step (*i.e.* there is no need for a catalyst to spur the process to completion). Rather, thermodynamics controls the extent of the conversion.

New MSO_4-NH_3 based solar TCWSCs

Modified cycles

As discussed above, FSEC's S-NH_3 cycle also utilizes decomposition of sulfuric acid as the endothermic step for the absorption of solar thermal heat and production of oxygen. However, high temperature concentration and decomposition of sulfur acid presents daunting materials of construction issues. Like the metal sulfate based TCWSCs, it is possible to modify the S-NH_3 cycle and do without the decomposition of H_2SO_4. There are two ways to accomplish this. The first approach is to decompose ammonium sulfate produced in the hydrogen production step of the S-NH_3 cycle (Reaction (111)) to a metal sulfate in the presence of a metal oxide catalyst. The second approach is to convert ammonium sulfate to metal pyrosulfate (*e.g.* ZnS_2O_7).

If a two valance metal oxide MO (*e.g.* ZnO) is introduced into the S-NH_3 TCWSC, a new family of MSO_4-NH_3 based cycles is devised as follows:

$$SO_2(g) + 2NH_3(g) + H_2O(l) \rightarrow (NH_4)_2SO_3(aq) \quad \text{(chemical absorption, 20 °C)} \quad (119)$$
$$(NH_4)_2SO_3(aq) + H_2O(l) \rightarrow (NH_4)_2\,SO_4(aq) + H_2 \quad \text{(solar photocatalytic, 80 °C)} \quad (120)$$
$$(NH_4)_2SO_4(s) + MO(s) \rightarrow 2NH_3(g) + MSO_4(s) + H_2O(g) \quad \text{(thermocatalytic, 400 °C)} \quad (121)$$
$$MSO_4(s) \rightarrow SO_2(g) + MO(s) + O_2 \quad \text{(solar thermocatalytic, 1100 °C)} \quad (122)$$

Where, M = Zn, Mg, Ca, Ba, Fe, Co, Ni, Mn, Cu and Pb. Oxides Fe_2O_3 and Cu_2O can also be included for by slightly modifying Reactions (121) and (122).

Decomposition of metal sulfates, especially $ZnSO_4$, has been reported by a number of researchers [26-28]. For example, T-Raissi and coworkers [26,27] have given a detailed review of the literature pertaining to the decomposition of $ZnSO_4$. These researchers have also

conducted a series of $ZnSO_4$ decomposition experiments at very rapid heating rates in a concentrating solar simulator. Their findings revealed that $ZnSO_4$ can be completely decomposed into SO_2, O_2 and ZnO. Depending on the magnitude of sample heating rates, a small amount of SO_3 may also be formed. At rapid heating rates (1~2 °C/s) prevailing within concentrating solar furnaces, formation of SO_3 can be minimized, eliminating a need the separation of SO_2 from SO_3.

Unlike the metal sulfate based TCWSCs that employ reaction between sulfuric acid and a metal oxide (*e.g.* Reaction (108)), the new MSO_4-NH_3 cycles rely on the Reaction (121). Reaction (121) was first reported in 1955 by Dugger and coworkers who developed a process for the recovery of ammonia from ammonium sulfate in a two-stage reaction as follows [29]:

$$(NH_4)_2SO_4 + ZnO \rightarrow 2NH_3 + ZnSO_4 + H_2O \quad 400\sim500\ °C \quad (123)$$
$$ZnSO_4(s) \rightarrow SO_2(g) + ZnO(s) + O_2 \quad 800\sim1000\ °C \quad (124)$$

Experimental data show that all the nitrogen is recovered as NH_3, uncontaminated by sulfur oxides, in the low temperature stage. The major sulfur species formed at high temperatures was sulfur dioxide. In another study, Wentworth [30] has reported an ammonia yield of 99.3% by the following reactions involving ammonium hydrogen sulfate and zinc oxide:

$$2NH_4HSO_4(l) + 3ZnO(s) \rightarrow 2NH_3(g) + ZnO{\cdot}2ZnSO_4(s) + 2H_2O(g) \quad 365 \sim 418\ °C \quad (125)$$
$$ZnO{\cdot}2ZnSO_4(s) \rightarrow 2SO_2(g) + 3ZnO(s) + O_2 \quad 800\sim1000\ °C \quad (126)$$

It is therefore clear that Reaction (121) can be the basis of the new MSO_4-NH_3 TCWSCs.

Just as metal oxides can be used as catalysts for converting ammonium sulfate to metal sulfate, metal sulfates can also be employed for converting $(NH_4)_2SO_4$ to ammonium pyrosulfate ($(NH_4)_2S_2O_7$)). Sulfur dioxide and oxygen are products of $NH_4)_2S_2O_7$ decomposition. Thus, a second class of modified S-NH_3 TCWSCs based on the $M_2S_2O_7$-NH_3 can be devised as follows:

$$SO_2(g) + 2NH_3(g) + H_2O(l) \rightarrow (NH_4)_2SO_3(aq) \quad \text{(chemical absorption, 20 °C)} \quad (127)$$
$$(NH_4)_2SO_3(aq) + H_2O \rightarrow (NH_4)_2\ SO_4(aq) + H_2 \quad \text{(solar photocatalytic, 80 °C)} \quad (128)$$
$$(NH_4)_2SO_4(s) + M_2SO_4(s) \rightarrow 2NH_3(g) + M_2S_2O_7(s) + H_2O(g) \quad (400\ °C) \quad (129)$$
$$M_2S_2O_7(s) \rightarrow SO_2(g) + O_2 + M_2SO_4(s) \quad \text{(solar thermocatalytic, 1100 °C)} \quad (130)$$

Where, M = K, Rb, Cs. Reactions (129) and (130) have been described by Wentworth previously [30].

Decomposition of metal oxide and ammonium sulfate mixtures

Reagent grade $(NH_4)_2SO_4$ (Fisher Scientific) and zinc oxide (USP, EM Science) were used without further purification. Deionized water was generated in a two-step purification unit with conductivity of 18.3 MΩ-cm. Tap water was deionized by first passing the liquid through a PRO/RO filtration unit (Labconco) and then through a compact ultra pure water deionization system (Barnstead). As noted before, for the thermal analysis, we used a Perkin Elmer thermogravimetric/ differential thermal analyses (TG/DTA) coupled to a mass spectrometer (Pfeiffer ThermoStar™) with ultra pure grade helium gas (Linde Gas) as a carrier gas. The helium flow rate was set at 150 mL/min, monitored with a rotameter. In some experiments an aluminum sample holder was employed for the measurement of ammonium sulfate decomposition catalyzed by ZnO. The dimensions of the sample holders were: 5.210 mm OD,

4.965 mm high and wall thickness of 0.535 mm. The mixtures of $(NH_4)_2SO_4$ and ZnO were prepared by adding ZnO to aqueous ammonium sulfate solutions and stirring for two hours followed by heating to 50 °C under vacuum until completely dehydrated. Samples from dried mixtures of $(NH_4)_2SO_4$ and ZnO were prepared for the TG/DTA/MS analysis.

Figure 8 depicts the TG/DTA/MS results for ZnO + $(NH_4)_4SO_4$ mixture with molar ratio of ZnO:$(NH_4)_4SO_4$ = 1:1 at a heating rate of 5 °C/min. The MS results show that no O_2, N_2, H_2, HNO_2, NO_2, SO_3 or H_2SO_4 was detectable within temperature range of 50 °C to 600 °C.

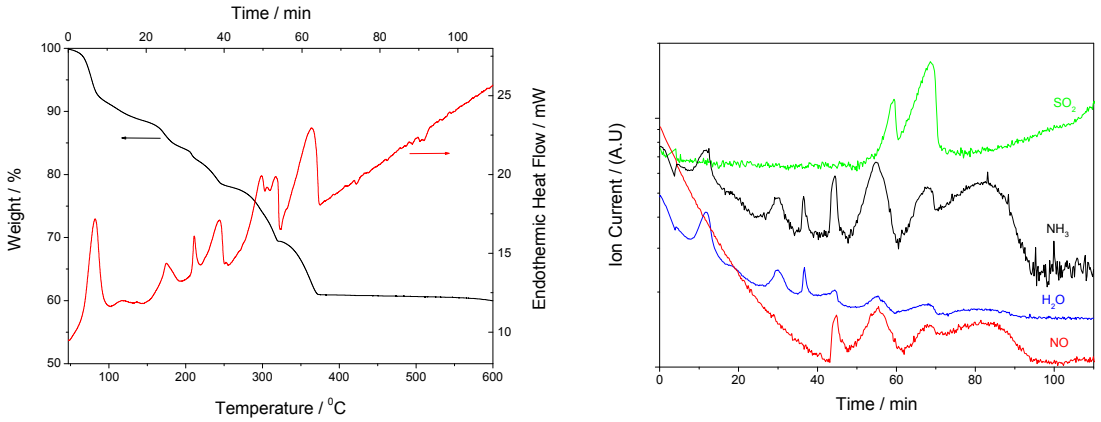

Figure 8. TG/DTA/MS analyses of ZnO + $(NH_4)_2SO_4$ decomposition, mixture molar ratio x= ZnO:$(NH_4)_2SO_4$ = 1:1, heating rate = 5 °C/min.

The main reaction products determined from the MS measurements were NH_3, H_2O, and small amounts of SO_2 and NO. The results indicate that deammoniation and dehydration of the ZnO + $(NH_4)_2SO_4$ mixture is complex and occurs in several successive stages. TG/DTA curves show that NH_3 is released in five or six separate steps evolving at temperatures as low as 50 °C and as high as 500 °C. The heating rate has a significant effect on the temperature at which NH_3 is released.

Figure 9 depicts the TG/DTA/MS results for ZnO + $(NH_4)_4SO_4$ mixture with molar ratio of ZnO:$(NH_4)_4SO_4$ = 1:1 at a heating rate of 20 °C/min. Results of Figure 9 show that when heating rate is increased to 20 °C/min, NH_3 evolves at a higher temperature and the extent of NO and SO_2 formed decreases.

Figure 10 depicts the TG/DTA/MS results for ZnO + $(NH_4)_4SO_4$ mixture with molar ratio of ZnO:$(NH_4)_4SO_4$ = 1:1.5 at a heating rate of 20 °C/min. Results of Figure 10 show that at high heating rates, the extent of SO_2 and NO formed reduced with the SO_2 peak shifting to higher temperatures.

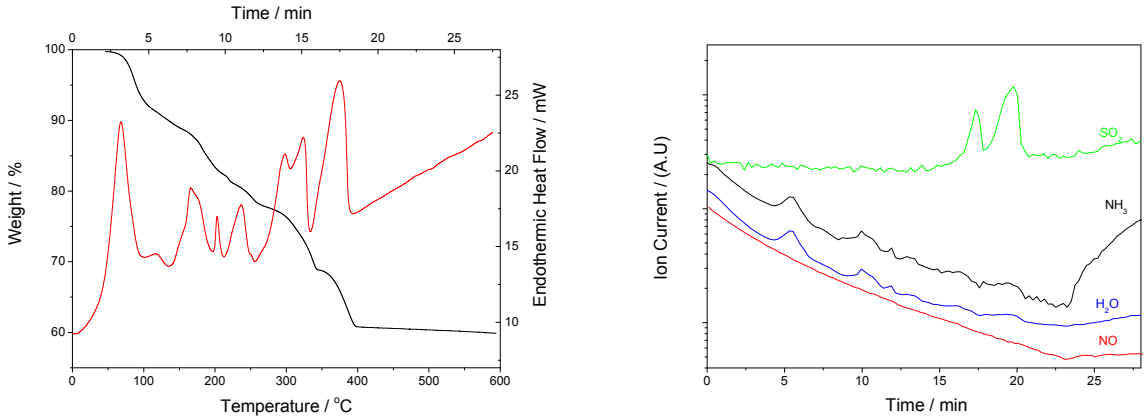

Figure 9. TG/DTA/MS analyses of ZnO + $(NH_4)_2SO_4$ decomposition, mixture molar ratio x= ZnO:$(NH_4)_2SO_4$ = 1:1, heating rate = 20 °C/min.

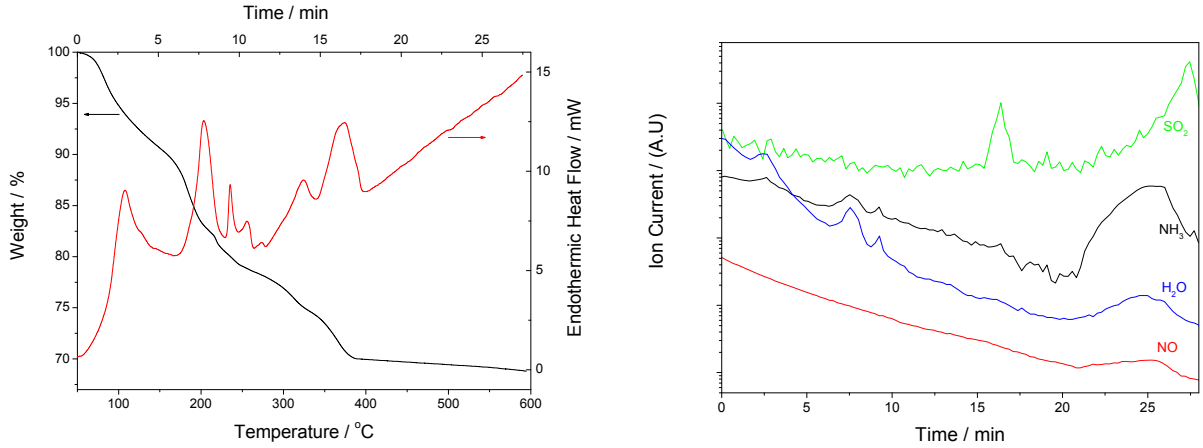

Figure 10. TG/DTA/MS analyses of ZnO + $(NH_4)_2SO_4$ decomposition, mixture molar ratio x= ZnO:$(NH_4)_2SO_4$ = 1.5: 1, heating rate = 20 °C/min.

Figure 10 depicts the TG/DTA/MS results for ZnO + $(NH_4)_4SO_4$ mixture with molar ratio of ZnO:$(NH_4)_4SO_4$ = 1:1.5 at a heating rate of 20 °C/min. Results of Figure 10 show that at high heating rates, the extent of SO_2 and NO formed reduced with the SO_2 peak shifting to higher temperatures.

Release of ammonia from a mixture of ZnO and $(NH_4)_2SO_4$ is accompanied by a series of intermediate reactions as discussed by Dugger et al. [29]:

$(NH_4)_2SO_4(s) = NH_4HSO_4(s) + NH_3(g)$ (131)
$ZnSO_4(s) + xNH_3(g) = ZnSO_4(s)\cdot xNH_3$ (x=1 to 6) (132)
$ZnO(s) + 2ZnSO_4(s) = ZnO\cdot 2ZnSO_4(s)$ (in the presence of excess ZnO) (133)
$NH_4HSO_4(s) + ZnO(s) = ZnSO_4(s) + NH_3(g) + H_2O(g)$ (134)
$ZnSO_4\cdot xNH_3(s) = ZnSO_4(s) + xNH_3(g)$ (135)

We note that by increasing the ratio of ZnO to $(NH_4)_2SO_4$, more ammonia is released at lower temperatures (see Figures 9 and 10). Also, as indicated by the MS data, less SO_2 is released at lower temperatures (300 to 400 °C). By changing the heating method, for example, holding temperature at 200 °C for 45 minutes, both SO_2 and NO peaks are significantly reduced. This is shown in the data of Figure 11.

Conclusions

Any thermochemical water splitting cycle consists of at least two main steps: hydrogen and oxygen production steps. A two-step water splitting cycle can not be efficient if energy requirements for these two steps are significantly different. In this report, we have developed a method for evaluating the overall efficiency of the FSEC developed S-NH_3 and all associated solar thermochemical water splitting cycles. Based on the experimental data presented, we have shown that the S-NH_3 TCWSC attains a high 1st law efficiency by splitting the solar spectrum into two sections and using the shorter wavelength photonic portion for CdS photocatalytic H_2 production and the longer wavelength and IR portions of the sunlight, at a mean concentration ratio of 1500 or above, for the thermocatalytic O_2 production from H_2SO_4 decomposition.

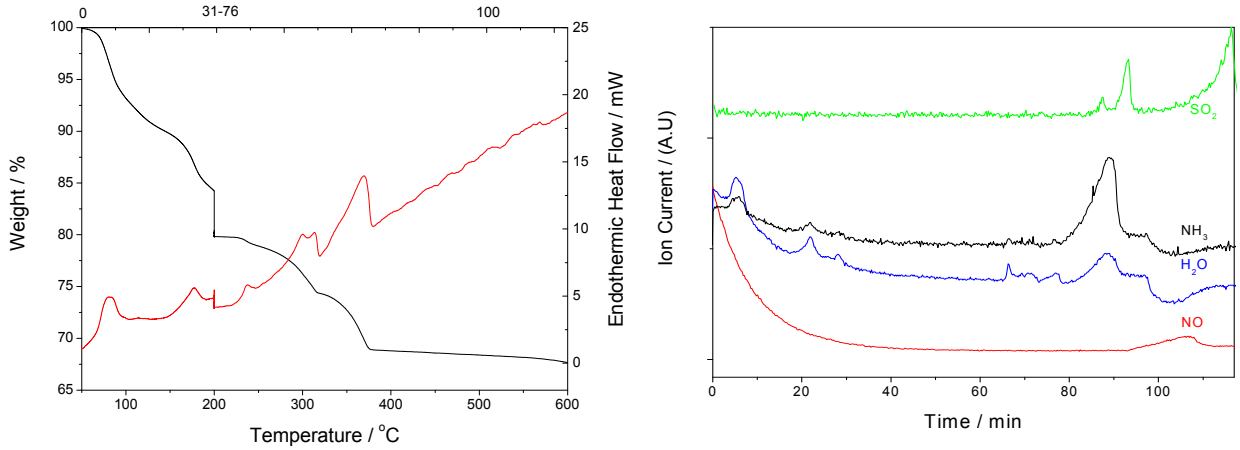

Figure 11. TG/DTA/MS analyses of ZnO + $(NH_4)_2SO_4$ decomposition, mixture molar ratio x= ZnO:$(NH_4)_2SO_4$ = 1.5:1. Samples heated from room temperature to 200 °C at 50 °C/min and held at 200 °C for 45 minutes followed by ramping sample temperature to 600 °C at 10 °C/min.

Due to the materials challenges of sulfuric acid decomposition process, we have devised two new classes of solar driven TCWSCs by modifying the original S-NH_3 cycle that include 12 metal sulfate-ammonia (MSO_4-NH_3) based, and 3 metal pyrosulfate-ammonia ($M_2S_2O_7$-NH_3) based cycles. Our preliminary experimental results of the ammonia released from the ZnO + $(NH_4)SO_4$ mixtures show the feasibility of these new cycles. More experiments are currently underway to determine the reaction mechanisms and the nature of the reaction intermediates and products formed. These experimental and thermodynamic analyses are expected to lead to development of a highly efficient, solar driven water splitting cycle.

Patents, Publications, External Funding Received and Students

Patents Filed

1. Huang, C., T-Raissi, A., Muradov, N. "Water Splitting Non-Carbonaceous Thermochemical Cycle for the Production of Hydrogen," U.S. Utility Patent Application No. 60/694,273, 2006.
2. Huang, C., T-Raissi, A., Muradov, N. "A Thermochemical Cycle for Production of Hydrogen and/or Oxygen via Water Splitting Processes," International Application No. WO 2007/002614; PCT/US 2006/024865.

Publications

1. T-Raissi, A., Muradov, N., Huang, C., & Adebiyi, O. "Hydrogen from Solar via Light-Assisted High-Temperature Water Splitting Cycles," *J. Solar Energy Engineering*, 129, 2, 184-9, May 2007.
2. Huang, C., Mohajeri, N., Muradov, N., & T-Raissi, A., "Solar Thermocatalytic Decomposition of Ammonium Sulfate," *Proc. of Solar 2007,* Cleveland, Ohio, July 7-12, 2007.
3. Huang, C., Olawale, A., Muradov, N.Z., & T-Raissi, A. "UV Light Photolysis of Ammonium Sulfite Aqueous Solution for Hydrogen Production," *Proc. 16th World Hydrogen Energy Conf. (WHEC)*, Lyon, France, 2006.
4. T-Raissi, A., Huang, C., Muradov, N.Z., Olawale, A., & Mohajeri, N. "Production of Hydrogen via Solar Powered Sulfur-Ammonia Thermochemical Water Splitting Cycle," *16th WHEC*, Lyon, France, 2006.
5. Huang, C., & T-Raissi, A. "Analysis of Sulfur-Iodine Thermochemical Cycle for Solar Hydrogen Production. Part I: Decomposition of Sulfuric Acid," *Solar Energy*, 78(5), 632-46, 2005.
6. Huang, C., & T-Raissi, A., "Analysis of Sulfur-Iodine Thermochemical Cycle for Solar Hydrogen Production. Part I - Decomposition of Sulfuric Acid," *Solar Energy,* 78(5), 632-46, 2005.
7. T-Raissi, A., Muradov, N.Z., Huang, C., & Taylor, R.L., Davenport, R.W. "Hydrogen from Solar via Light-Assisted High-Temp. Water-Splitting Cycles," *Int. Solar Energy Conf.*, Orlando, FL, 2005.
8. Huang, C., & T-Raissi, A. "A New Sulfur Ammonia Thermochemical Water Splitting Cycle," *Proc. of the 15th World Hydrogen Energy Conf.,* Yokohama, Japan, 2004.

External Funding Received

"Solar High-Temperature Water-Splitting Cycle with Quantum Boost," a 50%-50% joint FSEC/Science Application International Corp. (SAIC) 4-year program funded by the U.S. Department of Energy, $4.500M (2007-11), T-Raissi, A. (PI), N.Z. Muradov & C. Huang (Co-PIs).

Students & Post-Docs

Olawale Adebiyi (M.S. in Chemical Engineering, Florida Institute of Technology)
Bello Illiassou (M.S. in Chemistry, Florida Institute of Technology)
Dr. Liqun Mao (Laboratory of Special Functional Materials, Henan University, CHINA)

Literature Cited

1. Khaselev O., & Turner J. A., "A Monolithic Photovoltaic-Photoelectrochemical Device for Hydrogen Production via Water Splitting," *Science*, 280(17), 425-7, 1998.
2. Licht, S., Wang, B., Mukerji, S., Soga, T., Umeno, M., & Tributsch, H., "Over 18% Solar Energy Conversion for Generation of Hydrogen Fuel; Theory and Experiment for Efficient Solar Water Splitting," *Int. J. of Hydrogen Energy*, 26, 653-9, 2001.
3. Deutsch, T. G., Koval, C. A., & Turner J. A., "III-V Nitride Epilayers for Photoelectrochemical Water Splitting: GaPN and GaAsPN," *J. Phys. Chem. B*, 110, 25297-307, 2006.
4. Liu, H., Yuan, J., & Shangguan, W., "Photochemical Reduction and Oxidation of Water Including Sacrificial Reagents and Pt/TiO2 Catalyst," *Energy & Fuels*, 20(6), 2289-92, 2006.
5. T-Raissi, A., Muradov, N., Huang, C., & Adebiyi, O., "Hydrogen from Solar via Light-Assisted High-Temperature Water Splitting Cycles," *J. Solar Energy Engineering,* 129, 184-9, 2007.
6. Bilgen, E., Ducarroir, M., Foex, M., Sibieude, F., & Trombe, F., "Use of Solar Energy for Direct and Two-Step Water Decomposition Cycles," *Int. J. Hydrogen Energy,* 2(3), 251-7, 1977.
7. Steinfeld, A., "Solar Hydrogen Production via Two-Step Water Splitting Thermochemical Cycle Based on Zn/ZnO Redox Reaction," *Int. J. Hydrogen Energy,* 27, 611-9, 2002.
8. Abanades, S., Charvin, P., Flamant, G., & Neveu, P., "Screening of Water-Splitting Thermochemical Cycles Potentially Attractive for Hydrogen Production by Concentrated Solar Energy", *Energy*, 31, 2805-22, 2006.
9. Bamberger, C., & Richardson, D., "Hydrogen Production from Water by Thermochemical Cycles," *Cryogenics* 16(4), 197-208, 1976.
10. Bamberger, C., "Hydrogen Production from Water by Thermochemical Cycles; a 1977 update," *Cryogenics* 18(3), 170-83, 1978.
11. Funk, J. , Conger, W., & Carty, R., "Evaluation of Multi-step Thermochemical Processes for the Production of Hydrogen from Water," *The Hydrogen Economy Miami Energy (THEME) Conference,* Miami Beach*,* 457, March 18-20, 1974.
12. Huang, C., & T-Raissi, A., "A Perspective on Thermodynamics and Thermal Efficiency Calculations for Hydrogen Production via Thermochemical Water Splitting Cycles," to appear.
13. Steinfeld, A., "Solar Thermochemical Production of Hydrogen – A Review," *Solar Energy*, 78, 603–15, 2005.
14. Brecher, L., & Spewock, S., et al., "Westinghouse Sulfur Cycle for the Thermochemical Decomposition of Water," *Proceedings of the 1st World Hydrogen Energy Conf.,* 1 9A, 1-16, 1976.
15. Lu, P. "Technological Aspects of Sulfur Dioxide Depolarized Electrolysis for Hydrogen Production," *Int. J. Hydrogen Energy,* 8(10), 773-81, 1983.
16. Beghi, G., "A decade of Research on Thermochemical Water Hydrogen at the Joint Research Center, Ispra," *Int. J. Hydrogen Energy,* 11(12), 761-71, 1986.
17. Besenbruch, G., "General Atomic Sulfur-Iodine Thermochemical Water Splitting Process," *Am. Chem. Soc., Div, Pet, Chem. Preprint*, 271, 48, 1982.
18. Takehara, Z., Nogami, M., & Shimizu, Y., *Int. J. Hydrogen Energy,* 14(4), 233-9. 1989.
19. Sato, S., Shimizu, S., Nakajima, N., & Ikezoe, Y., "A Nickel-Iodine-Sulfur Process for Hydrogen Production," *Int. J. Hydrogen Energy*, 8(1), 15-22, 1983.
20. Huang, C., & T-Raissi, A., "A New Solar-Thermochemcial Water Splitting Cycle for Hydrogen Production," *Proc. 15th World Hydrogen Energy Conf.,* Yokohama, Japan, 2004.

21. Huang, C., Adebiyi, O., Muradov, N., & T-Raissi, A., "UV Light Photolysis of Ammonium Sulfite Aqueous Solution for the Production of Hydrogen," P*roc.16th World Hydrogen Energy Conf.*, Lyon, France, June 13-16, 2006.
22. Huang, C., Adebiyi, O., Muradov, N., & T-Raissi, A., "Production of Hydrogen via a Sulfur-Ammonia Solar Thermochemical Water Splitting Cycle," *Proc. 16th World Hydrogen Energy Conf.*, Lyon, France, June 13-16, 2006.
23. Huang, C., Mohajeri, N., Muradov, N., & T-Raissi, A., "Solar Thermocatalytic Decomposition of Ammonium Sulfate," *Proc. of Solar 2007,* Cleveland, Ohio, July 7 to 12, 2007.
24. Huang, C., & T-Raissi, A., "Analysis of Sulfur-Iodine Thermochemical Cycle for Solar Hydrogen Production. Part I - Decomposition of Sulfuric Acid," *Solar Energy,* 78(5), 632-46, 2005.
25. Huang, C., & T-Raissi, A., "Evaluation of Kinetic Models for the Solar Decomposition of Sulfur Trioxide," to appear.
26. Narayan, R., T-Raissi A., & Antal, Jr., M. J., Ind. Eng. Chem. Res. 27, 1050-8 (1988).
27. T-Raissi, A., Narayan, R., Mok, W., & Antal, Jr., M. J., Ind. Eng. Chem. Res. 28, 355-62 (1989).
28. Krikorian, O., & Shell, P., *Int. J. Hydrogen Energy.* 7(6) 463-9 (1982).
29. Dugger, G., Adams, J., & Bart, R., "Ammonium sulfate decomposition", United States Atomic Energy Commission, RMO-2036 (1955).
30. Wentworth, W., "Thermochemical cycles for energy storage: Thermal decomposition of ZnSO4 systems", Final Topical Report, January 1, 1982-December 31, 1984. Report (1992), (NREL/TP-253-4279; Order No. DE91002144).

December 2007

Hydrogen-Powered Aeropropulsion: Compact, Lightweight, and Efficient Fuel Cells for Space Power

C. Linkous, D. Slattery, J. Baik, B. Pearman, and D. Hall
Florida Solar Energy Center

Research Period: September 2004 to December 2007

Abstract

Various strategies for increasing the specific power (kilowatts of power per kilogram of device weight) of fuel cells were studied. Principally this was done by attempting to increase the fundamental proton conductivity of the electrolyte material in a fuel cell. The effect of temperature was clearly demonstrated, with conductivity values rising on order of 4x in going from room temperature to 100 °C. Another strong effect was the acid electrolyte concentration. Counter to intuition, one could obtain an additional improvement in conductivity by >30% by lowering concentration of the acid from its maximum value to the 4-6 M range. The combined effects can potentially produce a conductivity greater than 5x the ambient concentrated acid value.

Liquid electrolytes must be contained in a porous matrix, however. Hexagonal boron nitride, h-BN, was a strong contender in this regard, due to its chemical inertness and fine particle size. Conductivities as high 0.25 S/cm with a phosphoric acid/BN paste were obtained, some 2.5 times that obtained with conventional solid polymer electrolytes. Boron carbide, BC, and silicon nitride, SiN, gave comparable results. After extensive thermogravimetric and infrared analysis, it was concluded that there was no specific interaction between BN and the various acids tested, including phosphoric and sulfuric acid. Earlier observations of acid retention or specific affinity were determined to be viscosity effects. Therefore, while BN can serve as a stable matrix for proton conductivity, it does not necessarily decrease the vapor pressure and ultimate loss of electrolyte. Mechanical stability of the electrolyte pastes and their ability to withstand differential pressures were also issues.

The use of the FLUENT® computer program as a modeling tool for fuel cell performance was investigated. Its ability to model and visualize the spatial distribution of parameters such as temperature, gas partial pressure, and current density was demonstrated.

Several characterization methods (microphotography, solvent permeation, and conductivity of solvent extract) for monitoring oxidative resistance to peroxide attack on polymer membranes were evaluated. All three techniques showed positive and negative attributes. Microphotography works well, provided the polymer has macroscopic surface features that can be contrasted, and especially well if the membrane possesses substantial color. Permeation of aqueous peroxide solution through the membrane provides a means of monitoring mechanical strength and pore size, although extra care must be taken to ensure uniformity in terms of membrane thickness and density.

Conductivity of the peroxide soaking solution itself was determined to be the best way of comparing rates of membrane degradation among many disparate ionomer materials. Results for sulfonic acids of polystyrene, polymeric perfluoroalkyl ethers, and polyaryletherketones demonstrated that while reaction rates for hydrocarbon-based polymers with peroxide species are not yet as low as their perfluorinated counterparts, they can vary substantially according to

their molecular structure, and point toward the possibility that a nonfluorinated polymer may be developed whose oxidative stability is comparable to Nafion at much lower cost.

Yet another way to improve the conductivity of a proton-conducting electrolyte is to increase the acidity of the acid groups or molecules contained within it. Not all polymeric sulfonic acids are strong acids. This has been found to be the case with the sulfonic acid derivative of a polyaryletherketone known as SPEEK (polyetheretherketone sulfonate). It was attempted to prepare the superacidic α,α-difluoromethanesulfonic acid of SPEEK, starting with monobromination of 2,5-diacetamido-trifluoromethylbenzene. Finding a solvent that would dissolve both the trisubstituted benzene and the BBr_3 brominating agent and remain inert throughout the reaction proved to be a challenge, however.

Introduction

Fuel cells have long been the favored device on manned spacecraft for deriving cabin power [1]. It also is being considered as a substitute for battery power on extraterrestrial land rover vehicles and numerous portable appliances [2]. Having electrochemical devices that rely on or play a part in hydrogen/oxygen/water chemical cycles may also play an important role in synergism with the recycling of biological resources in long-term manned space flight.

However, for fuel cells to play a greater role in the supply of space power, many improvements must be made in terms of size, weight, and fuel efficiency. Efforts in this regard can become complicated, since augmenting one factor must oftentimes be made at the expense of others. Improving volumetric power density points toward operation at higher current densities, yet this action may require increased electrocatalyst loadings and would increase thermal management problems. Improving gravimetric power density would suggest replacing machined metallic and carbon block components with polymeric composites. The result would be lower weight, but also lower electrical conductivity and decreased mechanical stability. Meanwhile, efficiency could be improved by at lowering current density and using more conductive metallic parts. The need to balance the various attributes to optimize performance is obvious.

The effect of temperature can also be complicated. Overpotential effects at the electrodes encourage higher temperature operation, while cooling requirements and thermodynamic voltage favor lower temperature operation. The general effect for fuel cells is that higher temperature favors better performance, due to higher electrolyte conductivity and more easily surmountable overpotentials at anode and cathode. Raising temperature also improves the possibility of operating the fuel cell in a reversible mode, i.e., regenerating the hydrogen fuel by operating the electrochemical cell in an electrolytic mode during periods of excess energy production or collection, and then sending the hydrogen back into the cell to operate in the galvanic mode as a fuel cell.

There are at least 5 fuel cell technologies that can be considered: alkaline (AFC), proton exchange membrane (PEM), phosphoric acid (PAFC), molten carbonate (MCFC), and solid oxide (SOFC) systems, with many variations within each category [2]. Due to its relatively higher gravimetric power density, PEM is the leading candidate for next generation space power fuel cells, as well as for many terrestrial applications.

A fundamental problem for next generation PEM fuel cells is that nearly all PEM's currently run at water saturation; cell pressure must then follow steam curve pressures as temperature rises. By the time cell pressure has risen to 180 °C, the internal pressure of the cell must exceed 10 atm, placing tremendous hydrolytic stress on all the cell components, plus the need for the

cell housing to be massive enough to be able to withstand those pressures. Most proton conductors require water to be effective because the charge carrier is the hydronium ion, H_3O^+. The mechanism proposed for the proton conductivity in these membranes is the Grotthuss mechanism, which involves the transfer of protons between water molecules and the reorientation of these molecules, and the vehicular mechanism, which is the translational motion of the hydronium ions [3]. Managing water content has been a continuing problem in PEM fuel cell development. If too little water is in the cell, the electrolyte membrane dries up and cell resistance rises. If water content becomes too great, the pores of the gas diffusion electrodes flood and mass transport limiting of gaseous fuel and oxidant becomes an issue.

The polymer electrolyte of a PEM fuel cell is currently a major cost factor. The leading PEM electrolyte material (Nafion®) costs>US$800/$m^2$, or some $300/kW, based on calculations by the author. Clearly the electrolyte membrane price must be reduced to compete with internal combustion engines and batteries as power sources. The high cost is mainly related to the perfluorination chemistry that is performed in synthesizing the base polymer.

NASA-GRC is interested in PEM fuel cells with regard to their use in a reversible mode, i.e., the regenerative fuel cell (RFC). NASA is presently focusing on a regenerative PEM fuel cell to support demonstration of a High Altitude Long Endurance (HALE) Solar Electric Aircraft by FY2012. Performance objectives for the RFC include:

- >600 W-hr/kg specific energy,
- >50% round trip efficiency, and
- >1000 hr service life.

In order to advance PEM technology, improvements have to be made on the solid electrolyte about which the cell is designed. Tasks involving fabrication and testing of new electrolyte materials are described with the goal of achieving high performance in terms of

- Temperature stability in excess of 125 °C.
- Proton conductivity in excess of 0.1 Siemens/cm, and
- Reduced dependence on water-saturating conditions (<25% relative humidity).

This project is endeavoring to improve the power density of fuel cells, so that they may be better able to serve as primary and auxiliary power sources on aircraft and ultimately spacecraft. This work is relevant to NASA's Vehicle Systems Program, which has a focus area on New Aircraft Energy Sources. The major objective here is to increase the state-of-the-art fuel cell power density from ~100 W/kg to 1.0 kW/kg and higher. Our approach to improving power density has been to increase the current density of the fuel cell. Current density is frequently limited by electrolyte conductivity, especially for solid electrolytes. Thus we have targeted the ionic conductivity of the electrolyte as a significant barrier in the development of high power density electrochemical devices, including fuel cells. There are two objectives in this regard:

- Establish a cell design algorithm to operate at modest pressures (1-5 atmospheres) and modest differential pressure between anode and cathode compartments.
- Develop a high temperature (200 to 300 °C) proton-conductive solid electrolyte to enable high current density operation at reasonable voltage. The electrolyte conductivity mechanism should negligibly rely on the presence of water.

Successful demonstration of this approach will enable development of a higher current density fuel cell with less water, thus improving the system's specific energy and improving its chances for implementation in a HALE Solar Electric aircraft. It will constitute an advancement of the technology's TRL level from 2 to 4.

Background

Proton Exchange Membrane (PEM) fuel cells are the leading fuel cell technology in applications ranging from vehicular transportation to portable appliances [4]. In order to advance this technology, improvements have to be made on the solid polymeric electrolyte about which the cell is designed. The electrolyte must exhibit high performance in terms of chemical stability and proton conductivity, while maintaining low cost. Some of the current performance standards for PEM electrolytes are listed below:

- Room temperature conductivity: 0.07 S/cm
- Operating temperature: 80 °C
- Conductivity at operating temperature: 0.1 S/cm
- Inlet water vapor partial pressure: 50 kPa
- Area specific resistance: 0.03 Ω/cm^2
- Gas crossover rate: 5 mA/cm^2
- Durability at operating temperature: 2000 h

The application of fuel cells to the NASA space program began in the 1950s as a source of cabin power during flight. The use of fuel cells for propulsion is an extension of that program. The use of fuel cells in terrestrial applications is now an important national technology goal.

The first commercially produced PEM was polystyrene sulfonic acid [5]. Then in the 1960s, DuPont developed an ionomer consisting of a polytetrafluoroethylene backbone with perfluorosulfonic acid side chains [6]. This material, Nafion®, was superior to polystyrene sulfonic acid in terms of conductivity and long term stability. Nafion membranes are currently used as a Na^+ conductor in chlor-alkali cells.

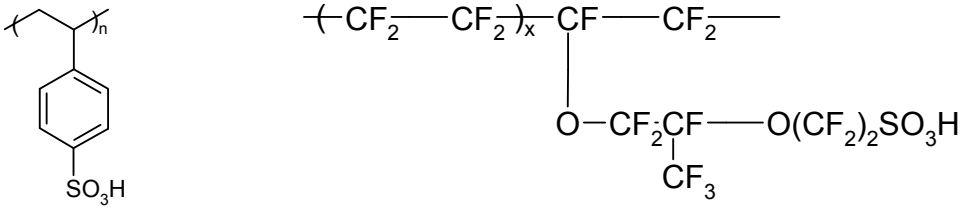

Polystyrene sulfonic acid

Nafion

Figure 1. Structures of some early pem materials.

Most proton conductors, including those discussed above, require water to be effective because the charge carrier is the hydronium ion, H_3O^+. The mechanisms proposed for the proton conductivity in these membranes are the Grotthuss mechanism, which involves the transfer of protons between water molecules and the reorientation of these molecules, and the vehicular mechanism, which is the translational motion of the hydronium ions [3]. Managing water content

has been a continuing problem in PEM fuel cell development. If too little water is in the cell, the electrolyte membrane dries up and cell resistance rises. If water content becomes too great, the pores of the gas diffusion electrodes flood and mass transport limiting of gaseous fuel and oxidant becomes an issue.

There has been some work on PEM's that work in the absence of water. Conductivities have been poor, however. One strategy for water-free PEM's are acid/polymer blends. These consist of a polymer, such as polyvinyl alcohol, with a mineral acid such as sulfuric or phosphoric acid. One example is polyacrylamide doped with sulfuric acid, giving a conductivity of 1.4×10^{-2} S/cm at 100 °C [7].

Most efforts to develop solid state proton conductors have involved hydrated inorganic oxides [8-10]. A less explored avenue would be to consider engineering polymers, those specialized polymers whose structures allow them to be used in applications requiring extremes of temperature and corrosivity [11]. Examples of these polymers are shown below in Figure 2. In nearly all cases, the aromatic polymers are linked together either in a single chain or in a ladder or step-ladder arrangement.

As was mentioned above, another major fuel cell technology is phosphoric acid, or PAFC. While adsorption of phosphate ion on the cathode tends to limit current density for O_2 reduction, the compensating factor is that it can already be operated at higher temperature, in the 180 to 200 °C range [2]. To contain the liquid electrolyte between the electrolyte, a porous matrix, typically silicon carbide, SiC, is used. However, as the fuel cell becomes hotter, the volatility of the acid itself becomes a factor. The ability of SiC to exhibit any capillary force on the acid and lower its vapor pressure is debatable. New approaches to contain phosphoric acid and limit its volatility would be desirable.

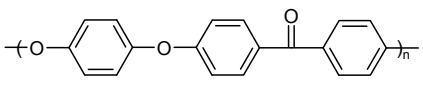

Polyetheretherketone

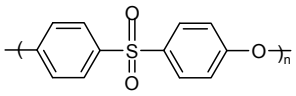

Polyethersulfone

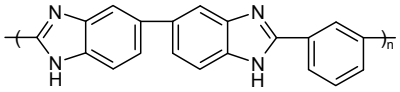

Polybenzimidazole

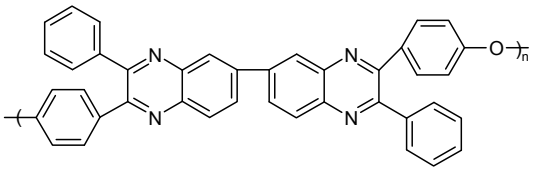

Polyphenylquinoxaline

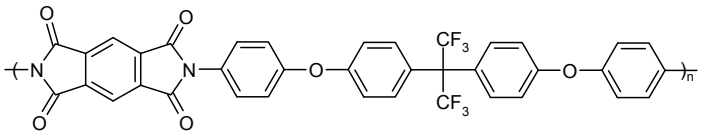

Partially fluorinated polyimide

Figure 2. Molecular structures of high temperature polymers.

Our interest has focused on boron nitride, BN, as a matrix for proton conduction. Boron nitride in hexagonal structure is a white, refractory material that is generally thought to be quite inert [12]. It has found application in refractories industry as a mold-facing and release agent, a crucible material for reactive metal melts, and also as a wall liner in plasma arc devices, and in the semiconductor industry as a solid dopant source. It is structurally and isoelectronically similar to graphite: a = 2.464 Å, c = 6.708 Å; C-C bond length = 1.42 Å; 3.5 Å between sheets; interlayer binding energy = 1.5 kcal/mol. h-BN: a = 2.504 Å, c = 6.660 Å; B-N bond length = 1.446 Å. However, in BN the lattice sheets are stacked directly over one another, alternating between B and N, while for graphite the lattice planes are slightly staggered, so that only one-half of the carbon atoms in a plane are directly overlap carbons in adjacent planes. The lattice structure of BN is shown in Figure 3.

There may be several possible roles that BN could play as part of an electrolyte composite. As an analogue to graphite, it may be able to intercalate molecular species between its lattice planes, providing a two-dimensional framework for proton conduction. BN also has a 50% atomic abundance of nitrogen. Each nitrogen has a lone pair that may act as a proton binding site. This may enable a large density of free protons to participate in the ion transport process. Finally, it may act as an adsorption surface, where it may function as a porous matrix for proton-conducting liquids.

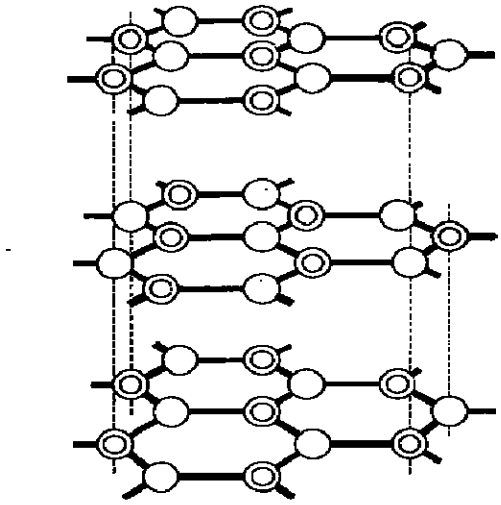

Fig. VI-1: *Layer Arrangement in hexagonal Boron Nitride*

K. Niedenzu and J.W. Dawson, Boron-Nitrogen Compounds, Academic Press, New York, 1965

Figure 3. Crystal structure of hexagonal boron nitride.

Experimental

Monitoring chemical breakdown of a perfluorocarbon ionomer typically involves measuring the fluoride ion content of water effluents or extracts. Since S-PEEK does not possess any fluorine to begin with, other methods needed to be employed. The methods applied in this work are microphotography, solvent permeation, and general conductivity of aqueous extracts.

Microphotography: Ionomer membranes were immersed in 3.5% H_2O_2 solution at various temperatures and let stand. The membranes would periodically be removed, rinsed, and placed under a stereomicroscope with camera attachment. Typically over a matter of days, loss of microstructural integrity could be observed at 100x magnification. Samples could be examined either by reflected or transmitted light.

Solvent permeation: Membrane samples were mounted within a PTFE in-line filter. Temperature was varied by immersing the filter in a water bath. Peroxide solution was placed in the upper half of the filter, filling it and extending up into a 6.4 mm translucent polypropylene feed tube. The tube was connected to an inert gas supply and pressure was applied to the filter. The rate of solution permeation was monitored by measuring the rate of translation of the solution meniscus inside the feed tube. A sudden rise in the rate of permeation was taken as an indication of the mechanical breakdown of the membrane.

Conductivity: Membrane samples were placed in borosilicate glass beakers and exposed to 3.5% H_2O_2 solution at various temperatures. Periodically, aliquots of peroxide solution were removed and placed in a field water analyzer. As the membranes degraded, conductivity would rise from a few parts per million dissolved solids to several thousand. Later, it was found more expedient to measure conductivity by inserting a graphite/epoxy cell probe attached to an Orion conductivity meter directly into the soaking solution. This approach is based on the idea that as

the ionomer is degraded, molecular fragments containing ionic groups are broken away that contribute to a general rise in solution conductivity. It was important to employ graphite electrodes instead of the traditional Pt, because the effervescence due to catalytic peroxide decomposition on the Pt surface was too great to enable stable readings.

The main experimental technique involves conductivity. We assembled an apparatus that includes a PAR potentiostat, oscilloscope, signal generator, and sufficient resistors and connectors to construct a bridge circuit. Early configurations for more resistive electrolytes used a sandwich structure, with probe electrodes mounted on either side of a thin electrolyte. Later, as prototype electrolytes became more conductive, we adopted a side-on configuration, where small connections are attached on the same electrolyte surface, with separation on order of the centimeter. Other techniques that were of value were simple gravimetry, infrared spectrophotometry, and thermogravimetric analysis.

Results and Discussion

Temperature and Concentration Effects on Electrolyte Conductivity

That electrolyte conductivity may be enhanced simply by raising the temperature is shown in Figure 4 below, where conductivity of concentrated (85%) phosphoric acid is shown as a function of temperature. While conductivity is only 0.9 S/cm at 25 °C, it can be nearly quadrupled by heating to 100 °C. Phosphoric acid fuel cells are normally operated at 180 °C, and so the conductivity of the pure acid is nearly 0.7 S/cm. Note however, that in the fuel cell, the acid has been taken up into a SiC matrix, and so the effective conductivity is something less.

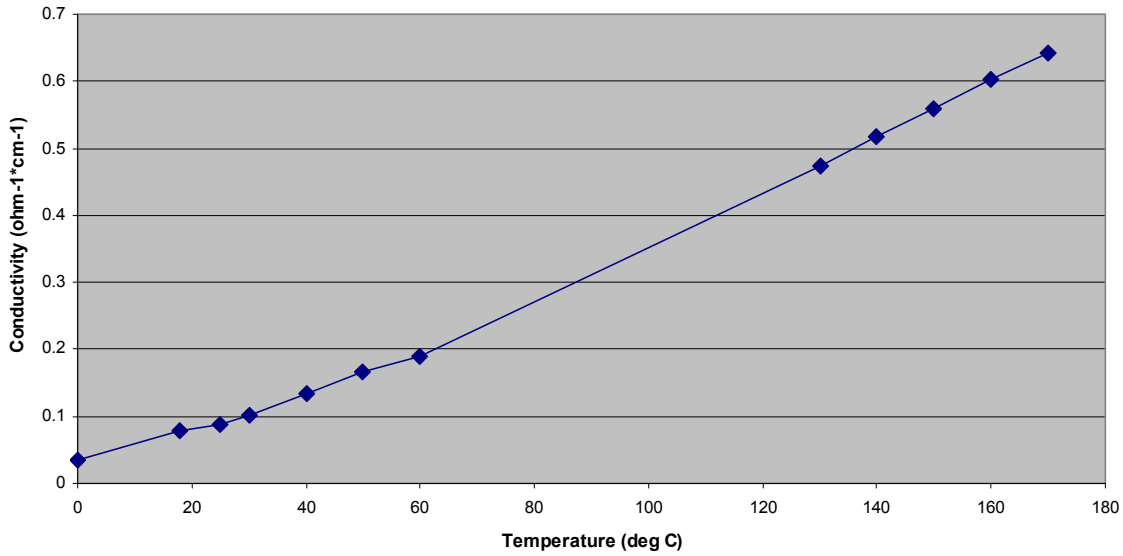

Figure 4. Phosphoric acid conductivity vs. T (85% conc).

Another trend is the effect of acid concentration. General chemical intuition would suggest that conductivity should rise linearly with concentration. However, beyond a certain point, the conductivity peaks and falls. This is due to the fact that at high acid concentration, there is not enough water present to “level” the acid, or accept one or more protons from each acid molecule. This is demonstrated for H_2SO_4 in Figure 5. It is seen that the maximum conductivity occurs at ~4 M concentration, well below the 18+ M found for concentrated (96%) sulfuric. A similar curve can be derived for H_3PO_4, where a peak at ~5.5 M or 45% is observed. The undissociated acid molecules do not contribute to the conductivity, and the amount of water present diminishes as acid concentration rises, so that encountering a maximum in conductivity in the 4-6 M concentration range seems to be a general trend for aqueous acids.

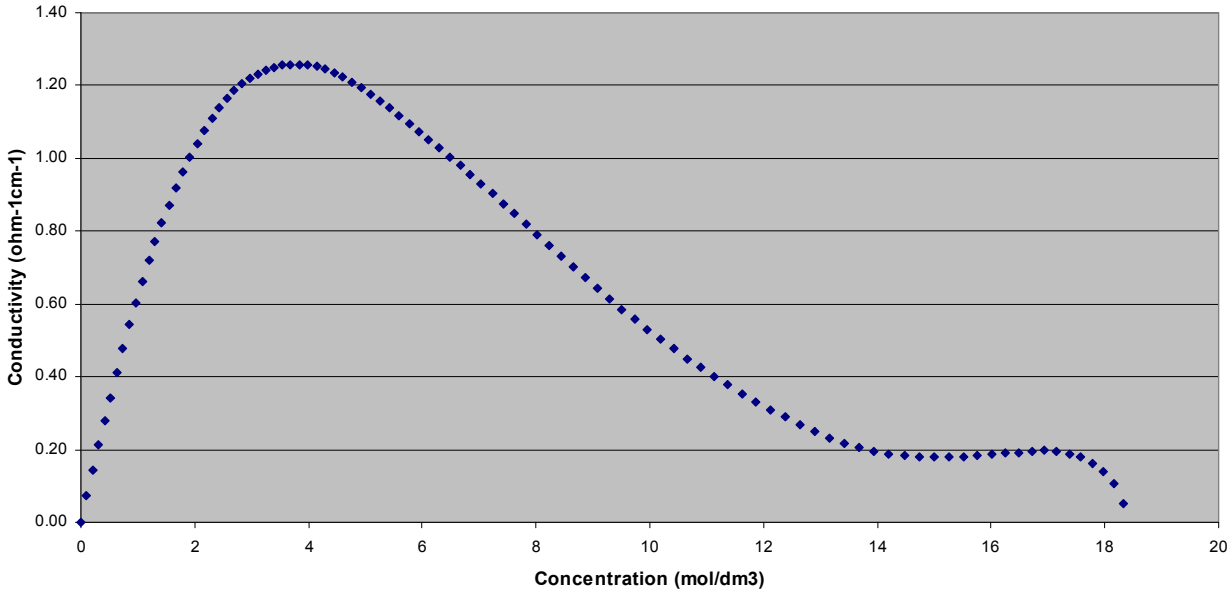

Figure 5. Concentration dependence of sulfuric acid conductivity.

This maximum in conductivity versus concentration effect suggests yet another way to improve fuel cell performance. If the fuel cell is loaded with electrolyte at its maximum conductivity, internal resistance will be even less, and should facilitate maximization of the current density. In Figure 6 below, conductivity versus temperature for H_3PO_4 is plotted once again, but this time at the conductivity maximum concentration of 45%. It is seen that at 100 °C for example, conductivity has increased from 0.35 to 0.48 S/cm, a 38% increase.

This same trend is true for sulfuric acid, except in this case, the conductivity is considerably higher. As seen in Figure 7 below, at 100 °C and concentration of conductivity maximum, the conductivity is greater than 2.5 S/cm, some 25 times greater than what is obtainable with solid polymer electrolytes.

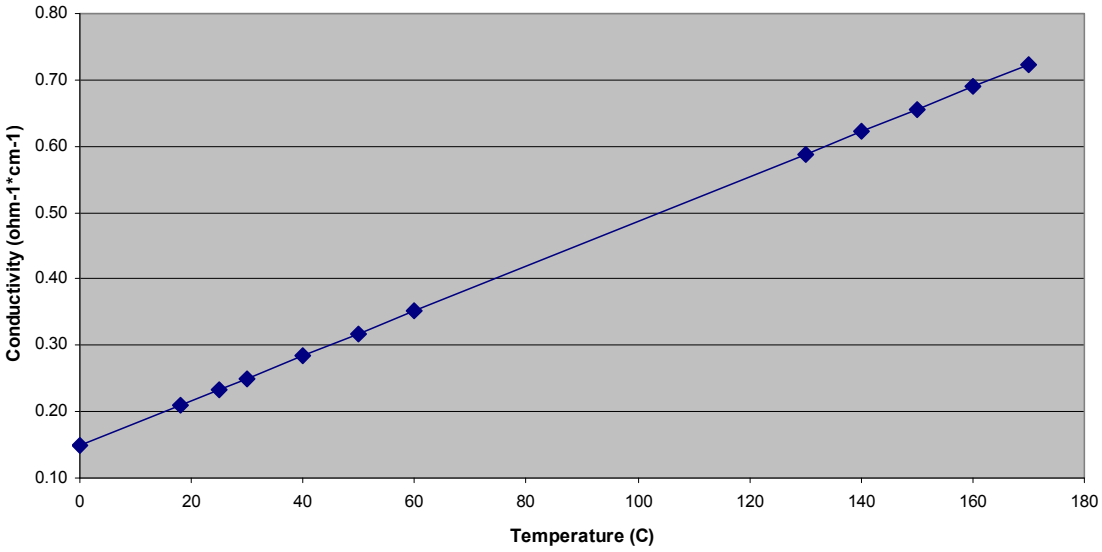

Figure 6. H_3PO_4 conductivity vs. T at optimum concentration (45%).

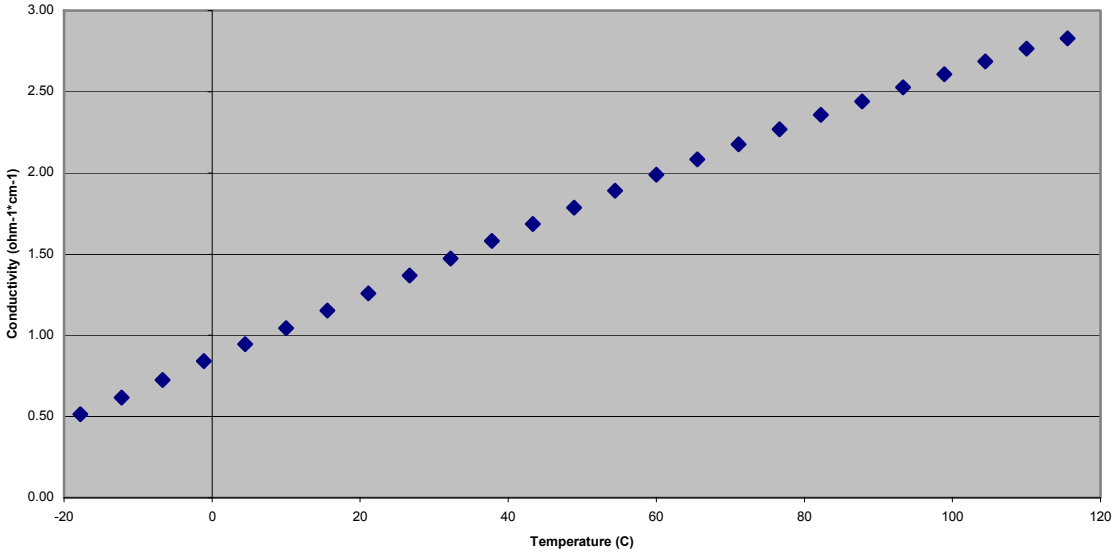

Figure 7. Conductivity vs. T (°C) at concentration of maximum conductivity for sulfuric acid.

Boron Nitride as a Matrix for Phosphoric Acid

As stated previously, to contain a liquid electrolyte between the electrodes in a fuel cell, a matrix of some kind is needed. The following details results of our evaluation of boron nitride, BN, as a matrix material for this application. Pressed pellets of boron nitride powder (~200 mg) were exposed to 50 ml volumes of strong acids at 25 °C for 24 h. After the exposure period, the acid was decanted off, and the disks were extracted with water until the washings were neutral, and then dried in a 120 °C oven and weighed. None of the disks had changed in physical appearance, although mass change in some cases was considerable.

The percent weight change of each BN disk is shown in Table I. In most cases, a slight mass loss corresponding to a fraction of a percent was obtained. However, in a few cases, significant mass increases were noted. Phosphoric acid effected a 36.1% increase in weight, while sulfuric was >40%. Sulfur trioxide was found to contribute to this effect, as a sample exposed to fuming sulfuric acid caused an 87.8% increase, the greatest of any solution tested.

Table 1. Percent weight change of h-BN pressed pellets after 24 h exposure to various mineral acids and NaOH at 25 °C. All acids in concentrated form unless otherwise noted.

Acid	percent weight change
HCl	-0.834, -0.244
HCl (1 week)	-1.50
HCl (3 h, 80 °C)	-2.51
HBr	-0.97
HI	-0.96
H_2SO_4	+40.4, +43.5
H_3PO_4	+36.1
$HClO_4$	-0.995
HNO_3	-0.81
HNO_3 (11% NO_2)	-0.763
H_2SO_4 (30% SO_3)	+88.7
CH_3SO_3H	-0.803
CF_3SO_3H	+0.394, -0.489, -0.687, -1.08, -0.136, -0.238
CF_3COOH	-0.121
NH_4OH	-0.698
NaOH (8.0 M)	+0.054, +5.21, +5.80
H_2O	-0.523, -0.625

At that point, the possibility that the mass increase for sulfuric and phosphoric acid treatments was due to formation of corresponding sulfates and phosphates was considered. Thermogravimetric analysis of the acid-treated powders showed just a general loss of mass starting at ~50 °C and continuing into the 100's of degrees centigrade. This lack of any sharp transitions implies that the acid is largely held in an amorphous way, i.e., a liquid. The temperature ramp was only 1 °C/minute, so that there was ample time for equilibration and phase transition.

A pellet of sulfuric acid-treated BN could be heated at 150 °C and eventually returned to its original mass, so that the acid uptake could be completely reversed. The phosphoric acid-treated sample seemed to hold onto a 20% mass increase, however, so that the possibility of phosphate chemistry remained. X-ray diffraction data implied that there may be the presence of boron phosphate, BPO_4, but was inconclusive.

Infrared spectroscopy was also attempted to ascertain any acid/BN chemistry. Plain BN showed peaks at 1370 and 816 cm^{-1}, consistent with literature values. The acid-treated, oven-dried sample showed broad peaks at 3125.6 cm^{-1} and 2362.8 cm^{-1}, plus bands at 1398, 1088, 922, and 810. 1013.88 and 600 cm^{-1}. However, as shown in Figure 8, thorough rinsing and drying regenerated the BN spectrum.

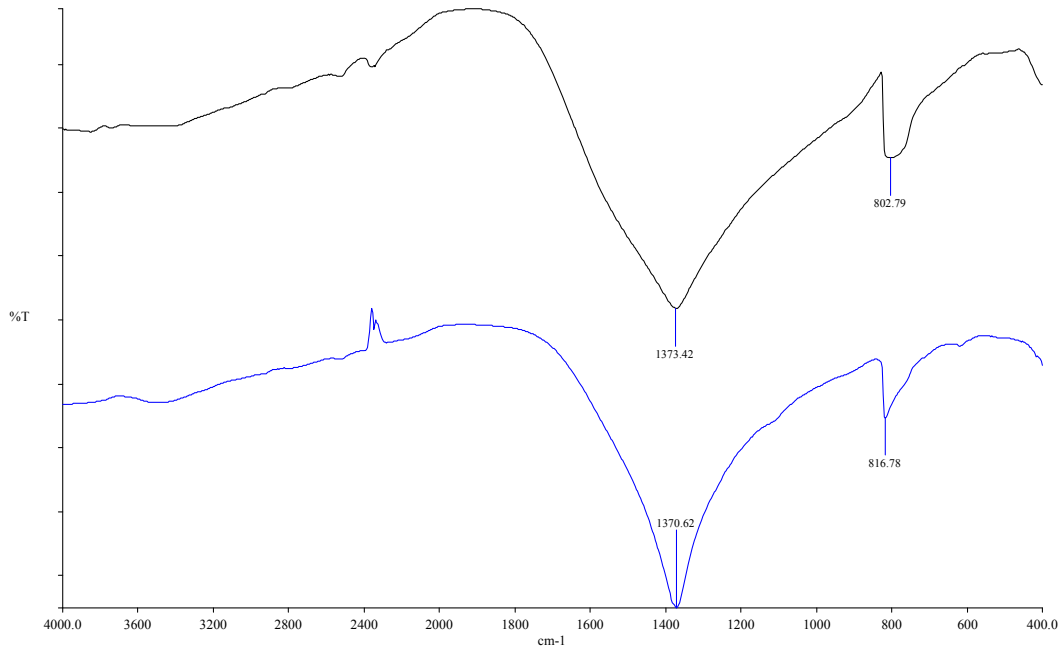

Figure 8. IR spectrum of BN before/after 120 °C H_3PO_4 exposure, rinsing, and drying.

Despite the mass increases noted in Table I above, no obvious evidence of intercalation was seen; the pellets' dimensions remained constant. This was even more evidence that the acid is simply filling the void sites within the pressed powders.

Another telling piece of evidence is demonstrated in Figure 9. Pellets of BN were prepared via pressing powders at various pressures. The idea was that the greater the applied pressure, the higher the density, the lower the void volume, and hence the less acid could be uptaken. Indeed, the amount of acid uptake was found to inversely correlate with the applied pressure used to produce the pellet, i.e., the denser the pellet, the less void volume was available for acid uptake. For both phosphoric and sulfuric acid, the percent weight increase of the pellet after 24 h exposure to concentrated acid was greater as the applied pressure used in making it decreased. This would explain in part the spread of data encountered early on, when these two acids caused exceptional, albeit poorly reproducible, mass increases upon BN exposure.

Thus it was concluded that there was no specific interaction between BN and the two acids, phosphoric and sulfuric. Nevertheless, at the very least, BN has shown itself to be a stable matrix for acid conductivity. Pastes of BN powder slurried in the respective concentrated acid were applied to an electrode surface and examined in an ac voltammetric apparatus. Results for a BN/phosphoric acid paste are shown in Figure 10 below, along with literature data acquired for plain phosphoric acid at the same concentration. The resistivity was quite low, so low in fact that the apparatus had to be modified to make the measurement.

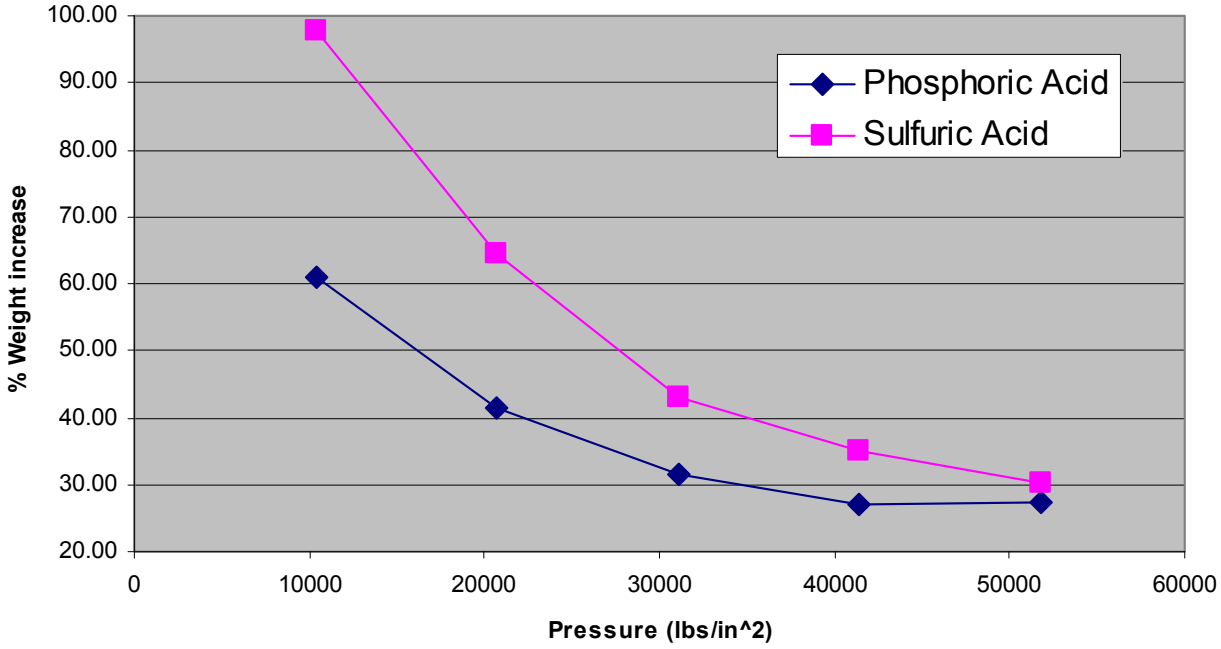

Figure 9. Effect of pressure on acid uptake by BN.

While the conductivity of phosphoric acid is something greater than when it is incorporated into BN at each concentration, the H_3PO_4/BN matrix nevertheless exceeds the 0.1 Siemen/cm threshold that is the benchmark set by DuPont Nafion. Thus while intercalation was not explicitly observed and a porous matrix of BN does not substantially reduce the vapor pressure of H_3PO_4 and other acids, the superior conductivity of acid/water mixtures contributes to higher current density operation and hence should also be considered as a possible fuel cell system for advanced space power.

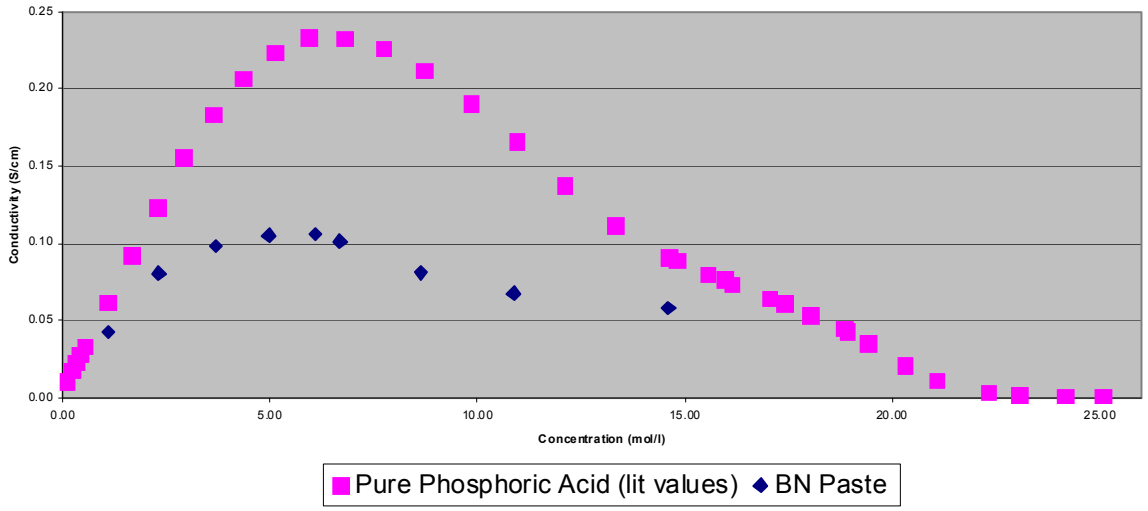

Figure 10. Conductivity versus concentration at 25 °C for H_3PO_4 and H_3PO_4/BN paste. Acid/BN = 3.0

It was still necessary to determine the optimum acid/BN ratio. In Figure 11 below, room temperature conductivity was measured for various phosphoric acid/BN ratios.

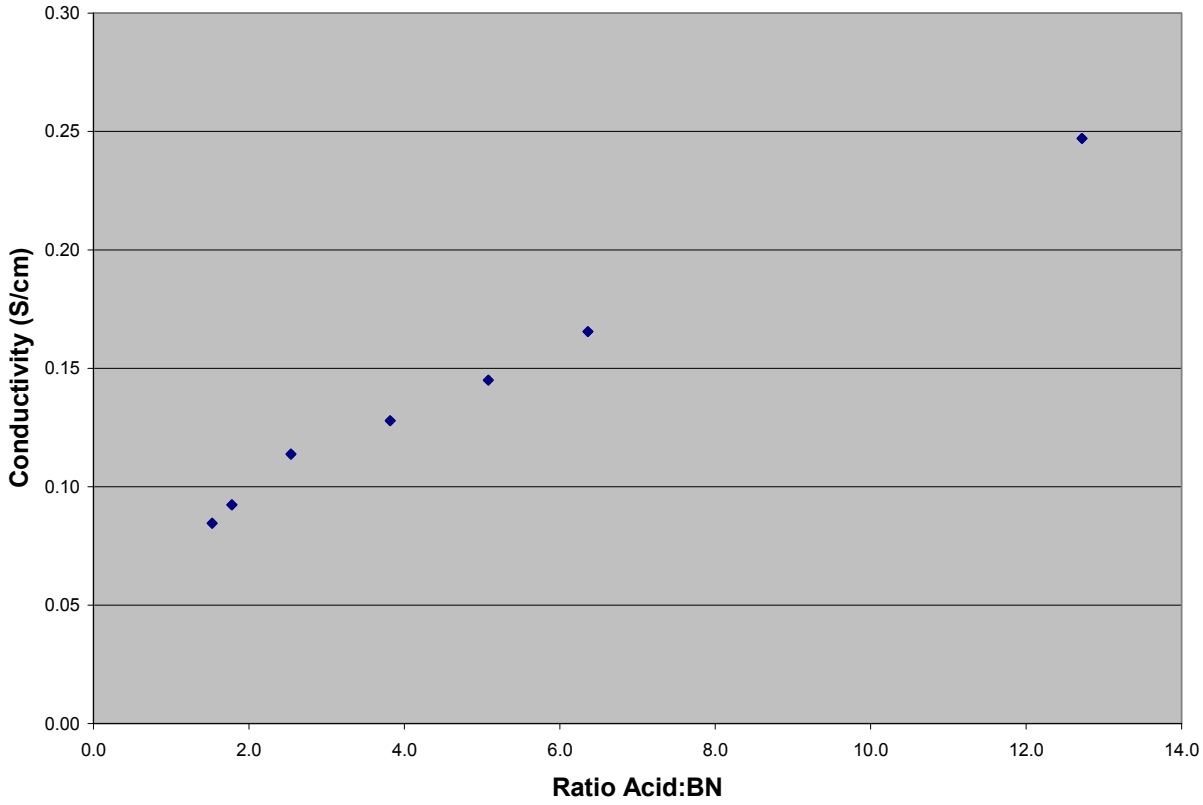

Figure 11. Conductivity vs. H_3PO_4 (42.5%)/BN ratio.

Conductivities as high 0.25 S/cm with a phosphoric acid/BN paste were obtained, some 2.5 times that obtained with conventional solid polymer electrolytes. However, the plot does not reveal the consistency problems that were encountered at the higher acid/BN rations. If the acid/BN ratio went much above 3.0, the paste became too runny and could not be reliably applied between two electrodes without squeezing out around the sides. That constraint would only put phosphoric acid/BN slightly above the 0.1 S/cm benchmark.

Other Acid Matrix Materials

It was known that silicon carbide, SiC, was the most common material for dispersing phosphoric acid in a fuel cell configuration. It was of interest to see if SiC or other inorganic materials could find application as an electrolyte matrix material. In Table II, acid uptake data are shown for SiC, BN, and other materials. One problem was that some of the hard, refractory compounds did not press in pellets very well. This was somewhat alleviated by compounding with Teflon powder. While most materials did not hold up very well in the strong acid environment, boron carbide, BC, and silicon nitride, SiN, nevertheless showed some promise and may serve as substitutes for the BN or SiC.

Table 2. Acid Uptake Data for Various Matrix Materials

Sulfuric Acid		Mass / g					Surface	Area	124.7			Ideal
Boron Oxide	Density g/cm3	Before	After	Mass Increase	% Mass Increase	Date	Height mm	Volume mm3	Mass g	Density g/cm3	% of Ideal Density	Density g/cm3
4	1.40	0.3143	N/A	N/A	N/A	8/16/2005	1.80	224.5	0.3143	1.40	57	2.460
5	1.39	0.3218	N/A	N/A	N/A	until	1.86	231.9	0.3218	1.39	56	
6	1.45	0.3257	N/A	N/A	N/A	8/17/2005	1.80	224.5	0.3257	1.45	59	
Boron Phosphate												
3	N/A	N/A	N/A	N/A	N/A	8/17/2005	1.50	187.1	N/A	N/A	N/A	2.520
5	1.81	0.3394	N/A	N/A	N/A	until	1.50	187.1	0.3394	1.81	72	
6	1.83	0.3495	N/A	N/A	N/A	8/18/2005	1.53	190.8	0.3495	1.83	73	
Aluminium Nitride												
4	1.94	0.5362	N/A	N/A	N/A	8/18/2005	2.22	276.8	0.5362	1.94	59	3.26
5	1.80	0.6536	N/A	N/A	N/A	until	2.91	362.9	0.6536	1.80		
6	1.84	0.4039	N/A	N/A	N/A	8/19/2005	1.76	219.5	0.4039	1.84	56	
Boron Nitride												
2	1.62	0.2051	0.2551	0.05	24.38	8/19/2005	1.09	135.9	0.2051	1.51	66	2.29
						until					0	
						8/20/2005					0	
Fabrication pressure											0	
10000	1.52	0.1852	0.2412	0.056	30.24	8/25/2005	0.98	122.2	0.1852	1.52	66	
8000	1.60	0.2178	0.2944	0.0766	35.17	until	1.09	135.9	0.2178	1.60	70	
6000	1.60	0.2060	0.2945	0.0885	42.96	8/26/2005	1.03	128.4	0.206	1.60	70	
4000	1.65	0.2349	0.3865	0.1516	64.54		1.14	142.2	0.2349	1.65	72	

Table 2. Acid Uptake Data for Various Matrix Materials

2000	1.45	0.1813	0.3587	0.1774	97.85		1.00	124.7	0.1813	1.45	63	
1000	1.36	0.2086	N/A	N/A	N/A		1.23	153.4	0.2086	1.36	59	
Silicon Nitride												
4	1.67	0.2495	0.3304	0.0809	32.42		1.20	149.6	0.2495	1.67	48	3.44
5	1.65	0.2598	0.3495	0.0897	34.53		1.28	159.6	0.2598	1.63	47	
6	1.55	0.2587	0.3387	0.08	30.92		1.34	167.1	0.2587	1.55	45	
Graphite												
4	N/A	N/A	N/A	N/A	N/A	8/22/2005	1.41	175.8	N/A	N/A	N/A	2.16
5	1.44	0.2507	N/A	N/A	N/A	until	1.40	174.6	0.2507	1.44	66	(average)
6	1.48	0.2796	N/A	N/A	N/A	8/23/2005	1.52	189.5	0.2796	1.48	68	Range
7	1.51	0.2528	N/A	N/A	N/A		1.34	167.1	0.2528	1.51	70	2.09 to 2.23
Boron Carbide												
(with Teflon)												
4	1.52	0.2385	0.3527	0.1142	47.88	8/24/2005	1.26	157.1	0.2385	1.52	60	2.51
5	1.34	0.2822	0.4064	0.1242	44.01	until	1.69	210.7	0.2822	1.34	53	
6	1.51	0.3419	0.5067	0.1648	48.20	8/25/2005	1.82	227.0	0.3419	1.51	60	
SiC												
(with Teflon)												
4	2.09	0.3672	N/A	N/A	N/A	8/24/2005	1.41	175.8	0.3672	2.09	65	3.217
5	2.11	0.4601	N/A	N/A	N/A	until	1.75	218.2	0.4601	2.11	66	
6	1.89	0.3819	N/A	N/A	N/A	8/25/2005	1.62	202.0	0.3819	1.89	59	

Simulation of Fuel Cell Performance

Another task under this project was to perform fuel cell simulations that would predict the effect of raising temperature on cell performance. The approach was to generate a family of current-voltage curves as a function of temperature. Numerous factors, such as diffusion coefficient, exchange current density, and electrolyte conductivity, are expected to change according to their theoretical temperature dependence. The FLUENT numerical analysis package with a PEMFC module was utilized. As an initial sample modeling, the PEMFC was limited to a single 10 mm x 20 mm x 200 mm three-dimensional channel. Hydrogen and air (25% O_2) were supplied at 353 K. The operation conditions were chosen to demonstrate the program's capabilities and can later be modified to reflect future design considerations.

The FLUENT program can calculate the spatial distribution of many performance parameters. The temperature contours inside the gas channels above and below the electrode-membrane-electrode lamina are shown in Figure 12. This simple exercise showed that it is difficult to assign a single temperature to the system. In reality, the temperature inside the cell will vary according to the steady-state current density and gas flow at that point. Nevertheless, the input parameters to the current-voltage equations call for an input T, and so couple equations calculate temperature differentials about a base value.

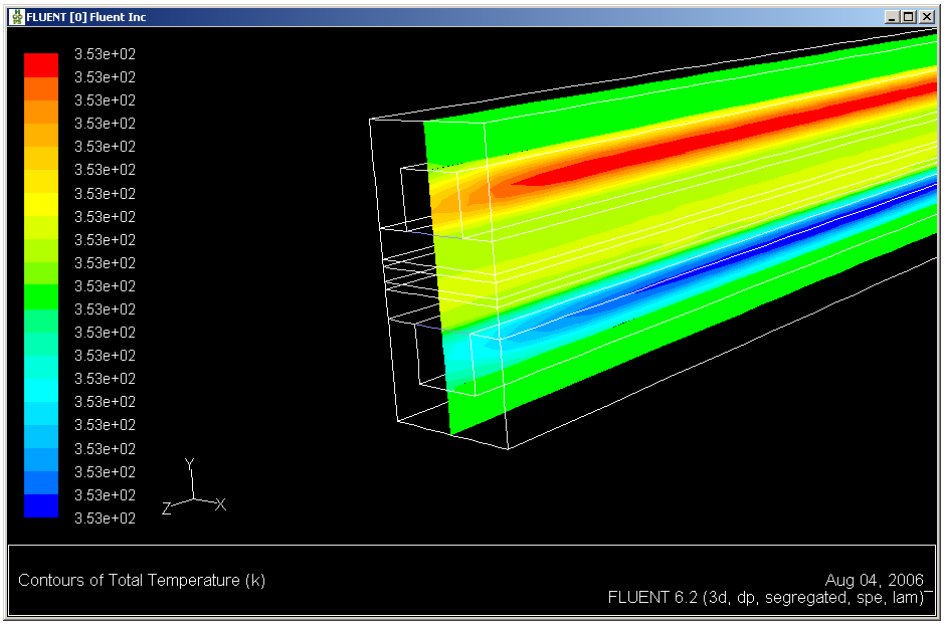

Figure 12. Temperature contours in a simulated single-channel fuel cell cross-section.

Development of Methods for Studying PEM Resistance to Peroxide Oxidation

PEM electrolytes are generally made from organic materials that are susceptible to oxidation by peroxides and other related radical species. This has been identified as a primary failure mechanism of a PEM fuel cell, where the electrolyte loses its mechanical strength due to oxidative depolymerization of the membrane. Several approaches to monitoring that decay process are described below.

Microphotography—Initial work was done on conductive polymer membranes that are known to be susceptible to oxidative attack by peroxides. Neosepta®, a polystyrene-based commercial ion exchange membrane, was found useful for this purpose. Shown in Figure 13 below is a sequence of photographs under 100-fold magnification, where a Neosepta membrane is exposed to hydrogen peroxide solution at 50 °C. This temperature was chosen because it gave a reasonable reaction rate; raising temperature to 80 °C destroyed the Neosepta too quickly to monitor (within 2 days), while at room T, signs of decomposition required more than a month to appear.

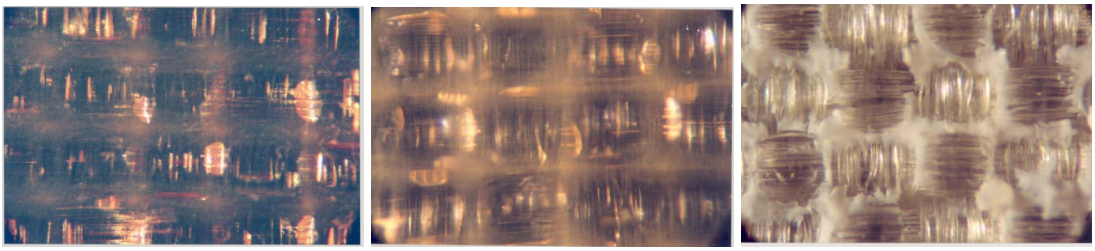

Day 1 Day 3 Day 11

Figure 13. Optical microscope images of neosepta® ion-exchange membrane under action of 3.5% H_2O_2 (100x magnification).

It is seen that, over the course of a few days, the initially dark amber material becomes bleached and fragmented by the peroxide, until finally the fibrous support is exposed, and all that is left of the polymer are a few interstitial clumps.

While these results were informative for the colored, textured surface of Neosepta, it was difficult to resolve surface features on the smooth, solvent-cast SPEEK polymer. This technique was found to be applicable only to those polymers that are impregnated into fillers or reinforcements, where substantial surface features are present to be contrasted. Scanning electron microscopy would of course enable greater magnifications and surface feature resolution, but sample preparation time would be much greater, and would not lend itself to successive examination and reintroduction into the aqueous testing environment.

Solvent Permeation—The rationale behind this approach was that as the membrane degraded, pore size or channel diameter would begin to widen, allowing more and more solvent to pass through per unit time. Gravity-fed experiments required several weeks to acquire measurable volumes of solution of questionable accuracy, so that differential pressures on order of 5 to 10 psi were applied. This modification shortened the experimental trials to a week or less. Heating the in-line filter in a water bath also decreased analysis time.

In a preliminary experiment, 5 psi was applied to a Neosepta membrane while exposed to 3.5% H_2O_2 solution at 50 °C. Breakdown of the membrane occurred after 5 days, in agreement with the microphotographic results, which began to show open gaps in the membrane after that period of time. A subsequent experiment was performed on a 25 μm (1 mil) unsulfonated polystyrene membrane. A total of four trials were run, as shown in Figure 14. Two trials utilized 3.5% H_2O_2 solution, while the other two used only deionized water. All trials were conducted at 80 °C.

The graph clearly shows that the presence of peroxide accelerated the permeation rate through the membrane and eventually its breakdown. The observation that permeation increases even in water after 400 h points to a background failure mechanism likely due to plastic flow of the polymer at 80 °C. The breakdown times for the peroxide tests varied almost by a factor of two. This was due at least in part to the accumulation of O_2 bubbles in the feed tube due to background decomposition of the peroxide, which made accurate volume readings difficult. Multiple tests would be necessary to gather enough statistics to obtain a mean value with reasonable confidence.

Another difficulty with this approach was that measuring a meaningful permeability depended on fabricating a uniform membrane, with no thin spots or pinholes that would yield faster permeation rates. This was quite difficult to achieve via solvent casting of polymer solutions. This technique is better suited to thermoplastic membranes, where hot pressing or rolling can achieve uniformity over wide areas.

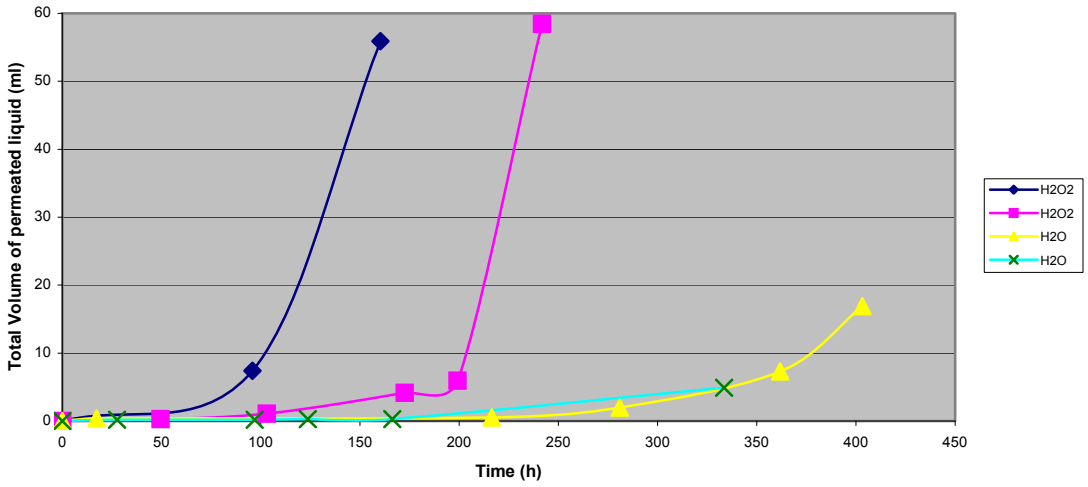

Figure 14. Permeability of 3.5% H_2O_2 solution through a 25 μm polystyrene membrane vs. time at 10 psi differential pressure and 80 °C.

***Conductivity*—**Membrane degradation could be monitored via conductivity of the peroxide soaking solution. As the polymer was being decomposed, ion-containing fragments would be broken off and diffuse into the surrounding peroxide solution. While the identity and species distribution of these fragments has yet to be determined, they all nevertheless would contribute to the conductivity of the solution, and so could be used as an indication of the state of the membrane.

Solution conductivity versus time was measured for a Neosepta membrane in 3.5% hydrogen peroxide at 50 °C. As shown in Figure 15, the initially poorly conductive peroxide solution (75 ppm) became more and more conductive, until after 150 h, when conductivity leveled off at ~3000 ppm. This is in agreement with results obtained by the other two methods.

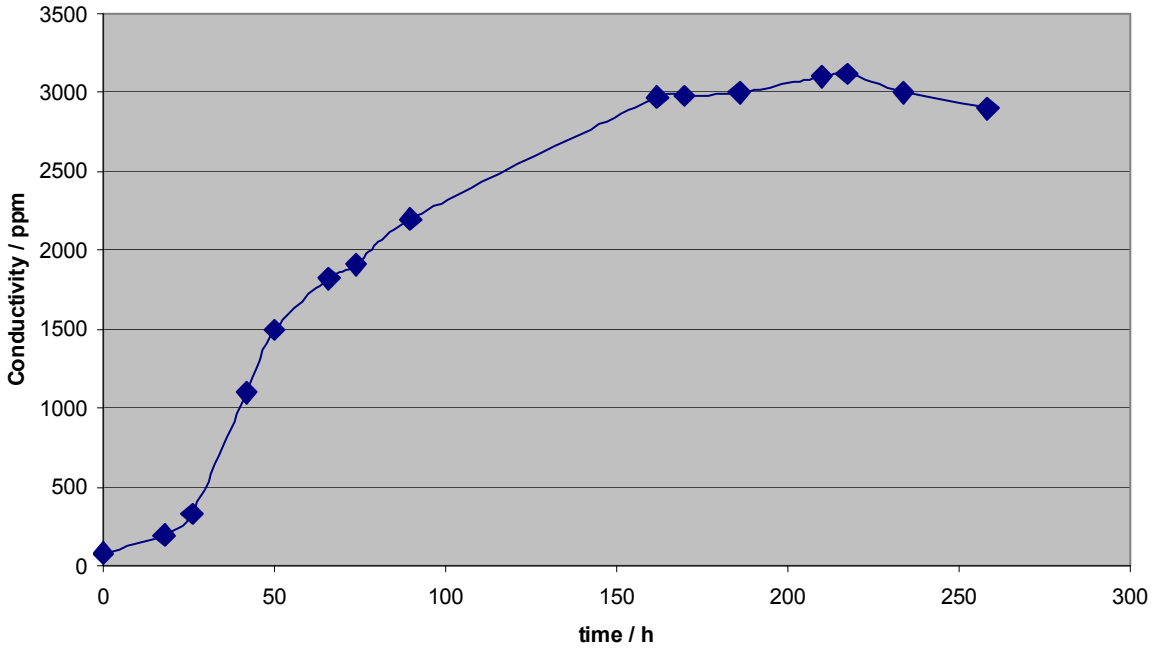

Figure 15. Conductivity of 3.5% peroxide soaking solution versus time in presence of Neosepta® membrane at 50 °C.

This approach was determined to be the best way of comparing rates of membrane degradation among many disparate ionomer materials. Equally sized samples of Neosepta, Nafion, PEEK, and 20% S-PEEK were exposed to 3.5% H_2O_2 solution at 80 °C. These results are shown in Figure 16. The Neosepta polystyrene sulfonate was most susceptible to the action of peroxide, exhibiting increased ion content in the soaking solution almost immediately, and climbing to nearly 2800 μS/cm within 4 days, much more rapidly than was observed at 50 °C with the other techniques. This is due to at least two effects: 1) more rapid reaction kinetics between the polymer and HO• radicals; and 2) more rapid intrinsic decomposition of H_2O_2, resulting in a higher HO• background concentration. The perfluorinated Nafion, as expected, performed much better, showing a more or less linear conductivity rise of only 5.4 μS/cm-h. Nevertheless, a slope of that magnitude would suggest complete deionization or degradation within 40 days, or just over a month, under the solution conditions described above.

Another major finding suggested by this work is that sulfonation greatly increases the susceptibility toward peroxide attack. Slopes for PEEK and PS were more than an order of magnitude less than S-PEEK and Neosepta, respectively. Divinyl benzene-crosslinked polystyrene did not show any improved stability over the uncrosslinked polymer. Of course, it should be noted that conductivity only responds to ionic species; there is a possibility that peroxide attack on the unsulfonated polymers produces a lower proportion of ionic fragments, and so that the degradation rates between sulfonated and unsulfonated polymers are actually much closer than this technique would indicate. Multiple, contrasting techniques may be necessary to fully understand the membrane degradation process.

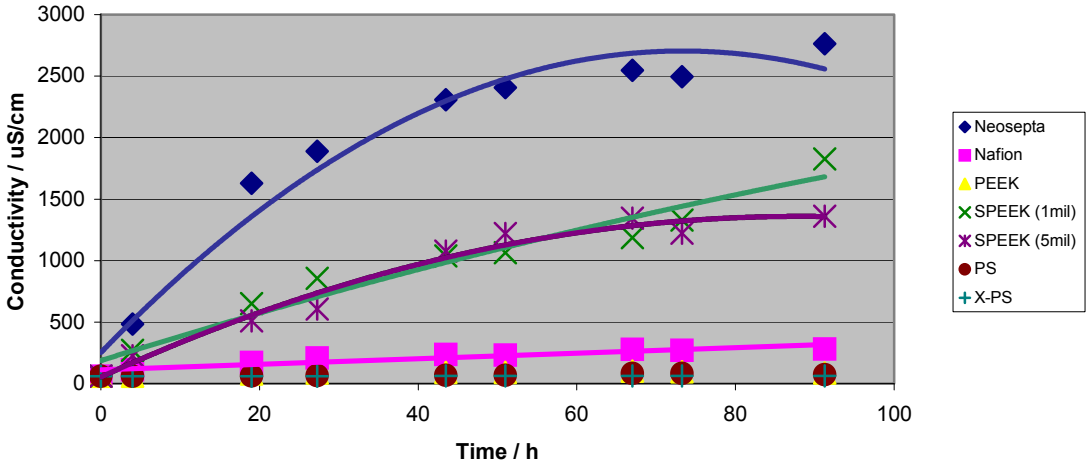

Figure 16. Conductivity of 3.5% peroxide soaking solution as a function of time for various polymer materials at 80 °C.

Intermediate between Neosepta and Nafion was S-PEEK. The results for 25 μm and 125 μm (1 and 5 mil, respectively) membranes were essentially identical. This would lead us to conclude that the peroxide acts as a sort of etchant, continually reacting with newly exposed surface as molecular fragments are scissioned and dissolved away. The rising linear section of the S-PEEK degradation curves indicated a mean rate of 24 μS/cm-h, in comparison with Neosepta at 53 μS/cm-h and Nafion at 5.4 μS/cm-h. These results demonstrate that reaction rates for hydrocarbon-based sulfonic acid polymers with peroxide species can vary substantially according to their molecular structure, and point toward the possibility that a nonfluorinated polymer may be developed whose oxidative stability is comparable to Nafion and other perfluorinated ionomers at much lower cost.

All of the above tests were performed at nearly neutral pH and ambient temperature. They were also performed in the absence of any catalytic species that would hasten peroxide decomposition and hence the background concentration of hydroxyl radicals. As prototype membranes become more and more rugged, the simple H_2O_2 tests described above would have to run for weeks to get a measureable result. A conductivity test on a peroxide solution containing a Neosepta membrane was performed similarly to the above, except that a 1.0 mM concentration of $FeSO_4$ was included. The conductivity vs time curves for identical pieces of Neosepta as a function of initial peroxide concentration are shown in Figure 17. The presence of a catalyst greatly increased the rate of degradation; the timescale of the experiment fell from 10's of hours to 10's of minutes. Interestingly, at the lower concentrations, the rate of reaction followed the initial H_2O_2 concentration in a linear manner, implying that the reaction rate was pseudo first-order with respect to peroxide. However, at the higher concentrations, the degradation rate became independent of peroxide concentration, implying that the rate-determining step had shifted to something that did not involve peroxide or its radicals directly.

The choppiness of the signal for some curves can be related to the instability of the peroxide system. It was discovered early on that the traditional Pt electrode pairs in a conductivity probe would not work in this experiment, as Pt is catalytic for peroxide decomposition, i.e., the Pt surfaces were continuously perturbed by the evolution of O_2 resulting from catalytic peroxide decomposition. Special carbon electrodes were obtained to replace the Pt. The gas evolution

rate was less vigorous, but the electrodes themselves were being attacked by the oxy radicals. Our solution was to keep the conductivity probe out of the reaction breaker except when a measurement was necessary. That way, minimal damage to the electrode occurred, yielding more accurate readings.

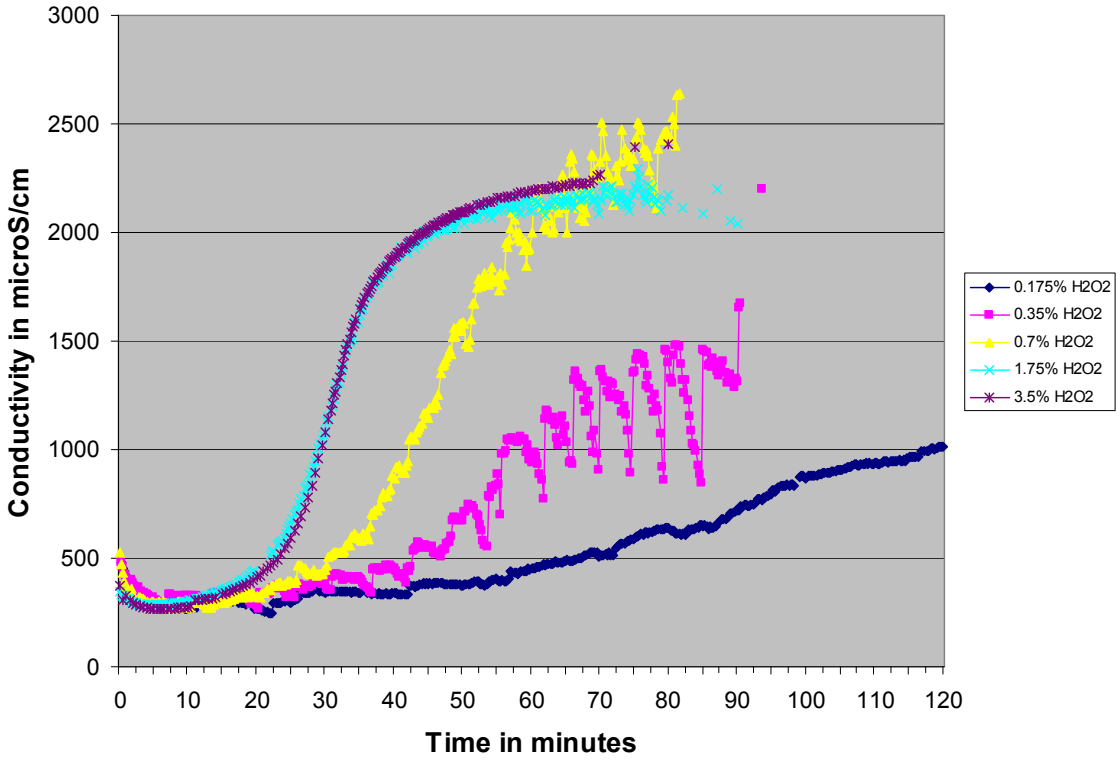

Figure 17. H_2O_2 concentration dependence on Neosepta degradation (1.0 mM $FeSO_4$).

Synthesis of a Fluorosulfonic Acid

Our earlier work on polymer electrolytes showed that not all sulfonic acid polymers are strong acids. Literature values for pK_A's of some aromatic sulfonic acid polymers can be as high as 3, depending on whether there are electron donating groups on the phenyl ring that would destabilize the conjugate base form of the acid [13]. Undissociated acid groups cannot contribute to proton conductivity.

Fluorinated sulfonic acids, such as trifluoromethylsulfonic acid, are classified as "superacids," so called due to their ability to protonate acids which would completely dissociate in aqueous media. Typical pK_A values can be as low as -2 [14]. Our objective then was to synthesize a polymer whose acid groups would be fluorosulfonates. The target polymer was poly(etheretherketone), or PEEK, whose structure is shown below and also in Figure 2. To make fluorosulfonated PEEK, or F-SPEEK, it was decided to make the fluorosulfonic acid monomer first and then polymerize. For the polymerization, the plan was to react sodium salts of hydroquinone and 2,5-dihydroxybenzene-α,α-difluoromethanesulfonicacid, with 4,4'-difluorobenzophenone, as shown in Figure 18 below:

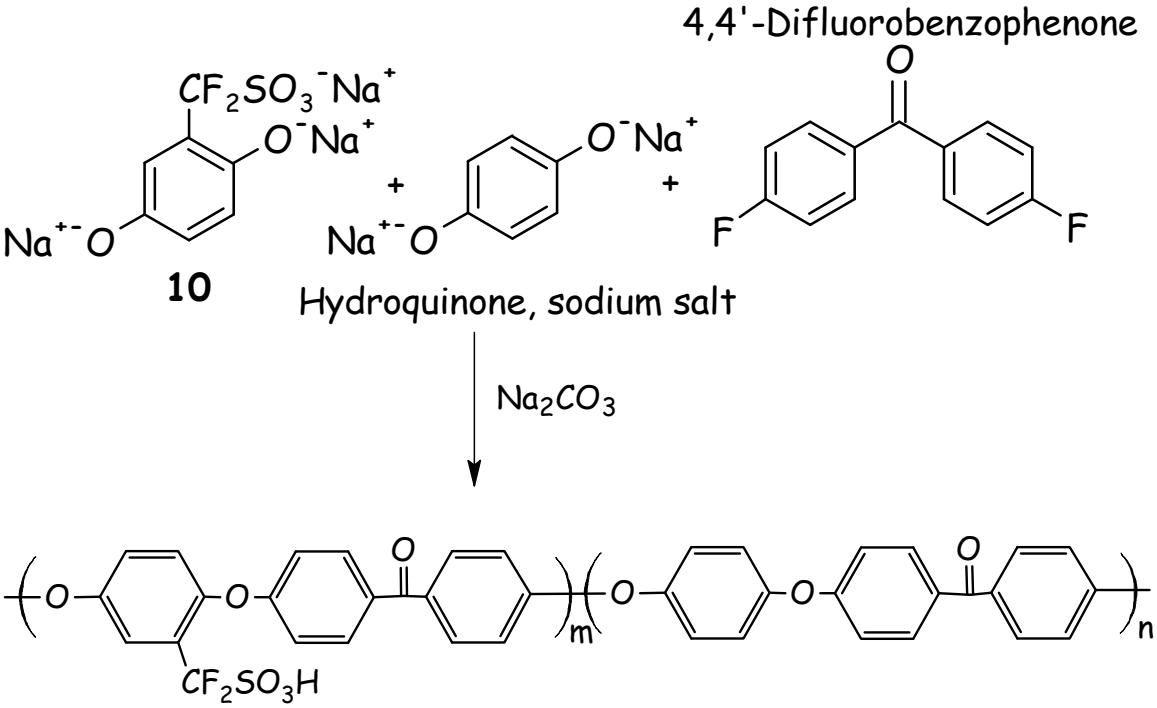

Figure 18. Scheme for preparing the fluorosulfonic acid of PEEK from its three constituent monomers.

However, the first step in the preparation of the acid monomer is to react a trifluoromethylbenzene with boron tribromide, BBr_3, to form the (monobromo-difluoromethyl)benzene. Boron typically behaves like a strong Lewis acid, readily accepting electron donors or electronegative species into its empty sp^3 orbital. Thus any –OH groups on the ring need to be added later after the fluorosulfonic acid has been formed. Our approach to making the dihydroxybenzene fluorosulfonate (**1**) was to start with the diamino-trifluoromethylbenzene (**2**) and convert the amino groups once the fluorosulfonate monomer was formed.

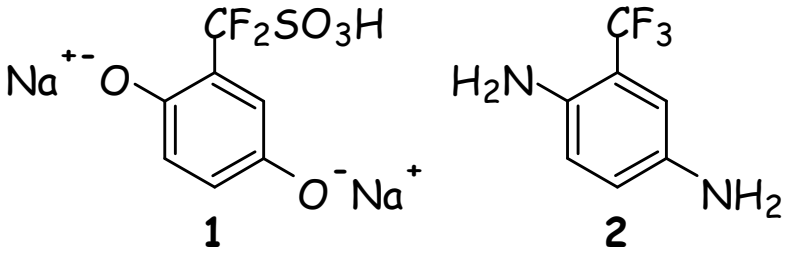

This reaction was attempted, but it soon became apparent that the BBr_3 was reacting with the amino group as well as the trifluoromethyl group. An early reference confirmed that BBr_3 would indeed react with the amine substituents [15], possibly polymerizing the starting material or forming a trimeric species with boron.

Thus it was necessary to even protect the amine from BBr_3. It was conjectured that converting the amine to an amide might confer some degree of protection. Therefore, the first step of the synthesis became making the diacetamide of the diamine by reaction with acetic anhydride. The resulting overall scheme for monomer synthesis is shown in Figure 19.

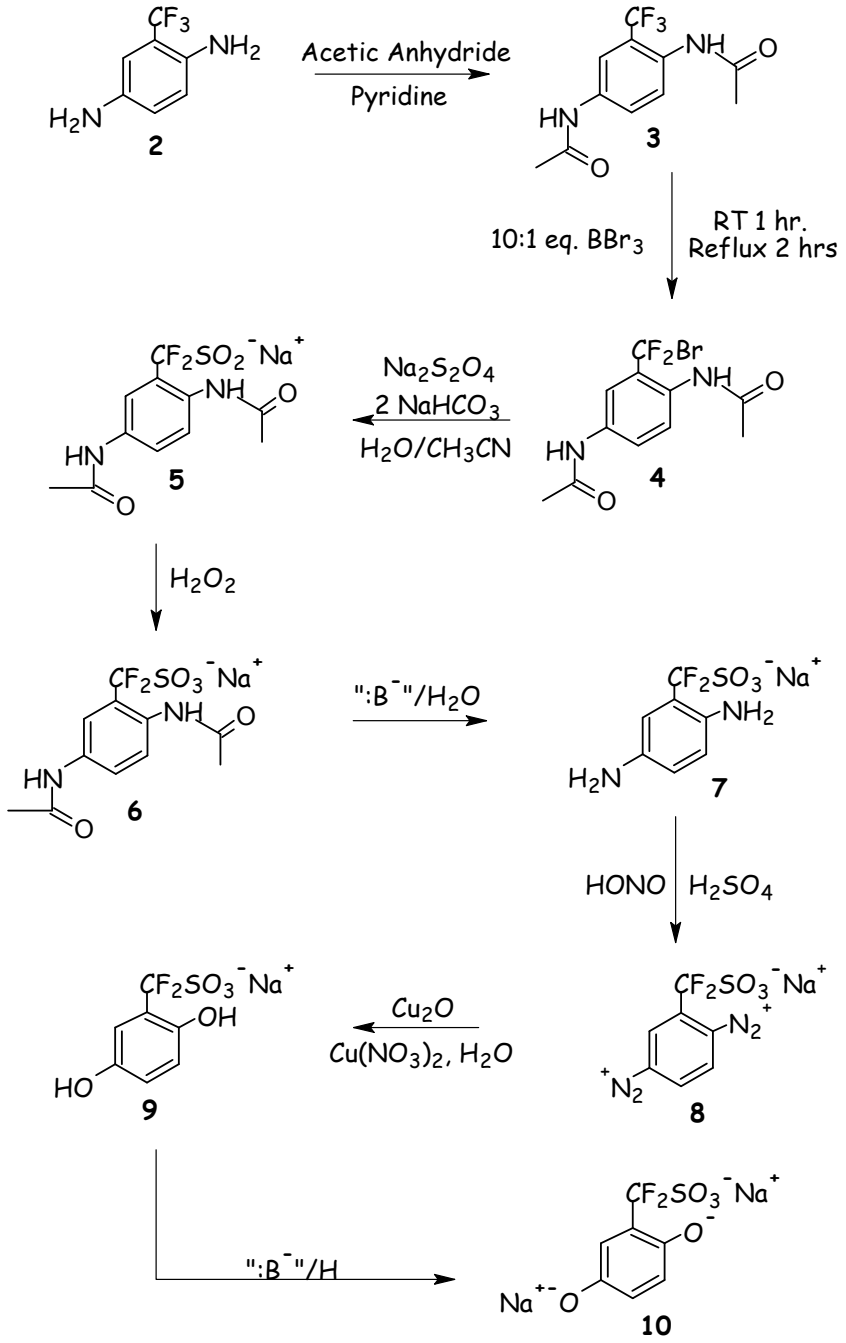

Figure 19. Preparation of the sodium salt of 2,5-dihydroxybenzene-α, α-difluoromethanesulfonic acid.

Synthesis of the acetamide went well with high yield. However, when it came time to react the acetamide with BBr_3, solubility problems ensued. Some of the original amine/BBr_3 efforts used chlorinated hydrocarbons, such as CH_2Cl_2, to run the reaction. The acetamide was insoluble in those solvents. Other solvents, such as o-dichlorobenzene, o-difluorobenzene, tetrahydrofuran, and hexachloropropanone (acetone) were tried instead. In each case, either the acetamide was insoluble or the BBr_3 reacted with it.

Presently, efforts are underway to employ an inert solvent (hexachloroacetone) and introduce the diacetamide as a fine powder slurry and perform a heterogeneous bromination. Work-up of this reaction is in progress.

Conclusions

Means of increasing the proton conductivity of electrolyte materials were investigated. The effect of temperature was clearly demonstrated, with conductivity values rising on order of 4x in going from room temperature to 100 °C. Another strong effect was the acid electrolyte concentration. One could obtain an additional improvements in conductivity by >30% by lowering concentration of the acid from its maximum value to the 4-6 M range. The combined effects can potentially produce a conductivity greater than 5x the ambient concentrated acid value.

Of course, the optimized acid must still be incorporated into a porous matrix. Hexagonal boron nitride, h-BN, is a strong contender in this regard, due to its chemical inertness and fine particle size. Its lubricity also was a positive factor in applying thin dispersions to an electrode surface. Blends of H_3PO_4/BN gave conductivities in excess of those for Nafion® proton exchange membrane at the same temperature.

It was speculated early on that BN may serve as the host for an intercalation compound, where acid species transfer protons between BN lattice planes. However, after extensive thermogravimetric and infrared analysis, it was concluded that there was no specific interaction between BN and the various acids tested, including phosphoric and sulfuric acid. Earlier observations of acid retention or specific affinity were determined to be viscosity effects. Therefore, the role for BN is to serve as a stable matrix for proton-conducting acids. Pastes of BN powder were slurried in concentrated acids, applied to an electrode surface, and examined in an ac voltammetric apparatus. Conductivities as high 0.25 S/cm with a phosphoric acid/BN paste were obtained, some 2.5 times that obtained with conventional solid polymer electrolytes. However, this result does not reveal the consistency problems that were encountered at the higher acid/BN rations. If the acid/BN ratio went much above 3.0, the paste became too runny and could not be reliably applied between two electrodes without squeezing out around the sides. That constraint would only put phosphoric acid/BN slightly above the 0.1 S/cm benchmark at room temperature. Even for the drier formulations, differential pressures of only a few p.s.i. could be maintained without excessive gas permeability.

The FLUENT® computer program was examined as to its fuel cell modeling capability. It was shown that fluid mechanics and electrochemical parameter determination capability was quite good. Parameters such as current density, gas partial pressure, and temperature could be plotted in three-dimensions down the length of a hypothetical gas distribution trough. Expressing these results in two-dimensional graphical cross-section format, could also be done, but would require some intervention into the existing program.

Several characterization methods (microphotography, solvent permeation, and conductivity of solvent extract) for monitoring oxidative resistance to peroxide attack on polymer membranes were evaluated. All three techniques showed positive and negative attributes. Microphotography works well, provided the polymer has macroscopic surface features that can be contrasted, and especially well if the membrane possesses substantial color. Permeation of aqueous peroxide solution through the membrane provides a means of monitoring mechanical strength and pore size, although extra care must be taken to ensure uniformity in terms of membrane thickness and density.

Conductivity of the peroxide soaking solution itself was determined to be the best way of comparing rates of membrane degradation among many disparate ionomer materials. Results for sulfonic acids of polystyrene, polymeric perfluoroalkyl ethers, and polyaryletherketones demonstrated that while reaction rates for hydrocarbon-based polymers with peroxide species are not yet as good as their perfluorinated counterparts, they can vary substantially according to their molecular structure, and point toward the possibility that a nonfluorinated polymer may be developed whose oxidative stability is comparable to Nafion at much lower cost.

Yet another approach to increasing electrolyte conductivity is to increase the acidity of the acid itself. This is especially important for organic polymer solid electrolytes where acid group density is limited. An effort to synthesize the difluoromethanesulfonic acid of PEEK was begun. Instead of directly sulfonating the polymer in a single step, it was necessary to start with a trifluoromethylbenzene monomer and substitute one of the F-atoms with a more labile species, such as Br. The brominating reagent, BBr_3, is quite reactive, and so the oxo-salt groups necessary for eventual polymerization must be added later. It was attempted to reserve those ring positions first with amine groups and then with amide groups, but finding a solvent that would solvate the diacetamide and not react with BBr_3 proved to be a challenge.

Patents, Publications, Presentations and Students

Publications

1. C. Linkous, & S. Rhoden, “Sustainable Fuel Cell Scenarios for the Caribbean,” in Renewables: The Road to Sustainability, Proceedings of SATIS 2007 (Sustainable Applications for Tropical Island States), Caribbean Solar Energy Society, Cape Canaveral, Florida, June 3-6, 2007.

2. C. Linkous, & B. Pearman, “Development of High Performance, Low Cost PEM Electrolytes,” Proceedings of the 16th World Hydrogen Energy Conference, Lyon, France, June 13-16, 2006.

Presentations

1. “Sustainable Fuel Cell Scenarios for the Caribbean,” C. Linkous and S. Rhoden, in Renewables: The Road to Sustainability, SATIS (Sustainable Applications for Tropical Island States) 2007, Caribbean Solar Energy Society, Cape Canaveral, Florida, June 3-6, 2007.

2. “High Temperature Electrolytic Conversion of CO_2 to CO and O_2: A Strategy for *In-Situ* Resource Utilization on Mars,” C. Linkous and M. Elbaccouch, 42nd Space Congress, Canaveral Council of Technical Societies, Cocoa, Florida, April 27-29, 2007.

3. “Development of Procedures for Evaluating Oxy Radical Stability of Proton Exchange Membranes,” C. Linkous, B. Pearman, and D. Hall,” Advances in Materials for Proton Exchange Membrane Fuel Cell Systems 2007, Pacific Grove, CA, February 18-21, 2007.

4. C. Linkous, & B. Pearman, “Development of High Performance, Low Cost PEM Electrolytes,” 16th World Hydrogen Energy Conference, Lyon, France, June 13-16, 2006.

5. B. Pearman, & C. Linkous, “Investigation of Boron Nitride as a Matrix for Acid Fuel Cell Electrolytes,” Materials Research Showcase, University of Central Florida, March 23, 2006.

6. C. Linkous, “Plastics in Fuel Cells – What are the Possibilities?” invited lecture at the Society of the Plastics Industries, Inc., Disney’s Beach and Yacht Club, Orlando, FL, March 9th, 2005.

Students

1. Benjamin P. Pearman, visiting chemistry graduate coop student from University of Bath, England.

References

1. K. Burke, “Fuel Cells for Space Science Applications,” First International Energy Conversion Engineering Conference, American Institute of Aeronautics and Astronautics, Portsmouth, VA, August 17-21, 2003, report # NASA/TM—2003-212730 or AIAA–2003–5938.

2. K. Kordesch & G. Simader, *Fuel Cells and Their Applications*¸ VCH, Weinheim, Germany, (1996).

3. K. Kreuer, *J. Mol. Struct.*, 177, 265 (1998).

4. A. Quade, *Energy Engineering*, 98, 40 (2001).

5. Ref. 2, p. 78.

6. S. Banerjee & D. Curtin, J. *Fluorine Chemistry*, 125, 1211 (2004).

7. J. Lessegues, B. Desbat, O. Trinquet, F. Cruege, and C. Poinsignon, *Solid State Ionics*, 35, 17, (1989).

8. L. Glasser, *Chem. Rev.*, 75, 21 (1975).

9. K.G. Frase & G.C. Farrington, *Ann. Rev. Mater. Sci.*, 14, 279 (1984).

10. P. Staiti, S. Hocevar, & N. Giordano, *Int. J. Hydrogen Energy*, 22, 809 (1997).

11. C. Arnold, Jr., *J. Poly Sci. Macromol. Rev.*, 14, 265 (1979).

12. K. Nidenzu & J.W. Dawson, Boron-Nitrogen Compounds, Academic Press, New York (1965).

13. *CRC Handbook of Chemistry and Physics: 87th Edition;* Lide, David R., ed; Taylor and Francis: New York, 2006.

14. S.J. Sondheimer, N.J. Bunce, M.E. Lemke, and C.A. Fyfe, *Macromolecules*, 19, 339 (1986).

15. R.G. Jones and C.R. Kinney, *J. Chem. Soc.*, 61, 1378 (1939).

December 2007

Integrated Fuel Cell Test Bed Facility

D. Slattery, L. Bonville, and R. Fowler
Florida Solar Energy Center

Research Period: January 2005 to December 2007

Abstract

The objective of the Integrated Fuel Cell Test Bed (IFCT) facility was to create a proving ground and permanent test facility where fuel cell components and systems could be tested and their performance evaluated. The fully integrated test bed facility could also be used for determining figures of merit and performance metrics to include round trip efficiency, specific power (kW/kg), reliability for long duration operation (approximately 1 year), redundancy path development, waste heat/cooling/heating management, turn down effects, transients, and the development of 'expert' systems for the process control.

The specific objective of the IFCT is to focus on fuel cell development in terms of electrochemistry, polymer science and nano-materials. The facility gives researchers the ability to perform hands-on research in membrane and electrode fabrication, electrochemical testing, materials analyses and cell and device operation.

Introduction

Proton exchange membrane fuel cells (PEMFCs) have increasingly received worldwide attention due to their potential use in the hydrogen economy. While fuel cells have long been a part of NASA's program, there are still many problems to be resolved before fuel cells can find widespread usage outside of the space program. Two primary problems are cost and durability. Others include size, weight, and thermal and water management.

To address these issues, researchers worldwide are trying to develop membranes that can function at higher temperatures and lower relative humidity to alleviate the need for large heat exchangers. Others are investigating possible catalysts to replace costly platinum. Additional work is ongoing to develop lower cost, better performing components such as air compressors, water and heat management systems and sensors. These balance of plant components are essential to developing fuel cell systems.

The development of an Integrated Fuel Cell Test Bed (IFCT) facility was conceived as a method to assist researchers at FSEC, within NASA and industry to develop, test and evaluate fuel cell components. The IFCT was to be an all-encompassing facility for fuel cell testing, with instrumentation and data acquisition equipment designed to be flexible and accommodating to the needs of the users. The IFCT was to be a complete and integrated facility equipped with reformers, a hydrogen gas purification unit, provisions for gaseous and/or liquid hydrogen storage, and a 2 kW commercial PEM fuel cell system. Additionally, the IFCT facility was to be set up to test other important hydrogen technologies, e.g., sensors, valves and control systems.

Figure 1. Fuel cell lab component of the integrated fuel cell test bed facility.

Results

An analysis of site requirements was conducted and an appropriate area to be refurbished into the IFCT was selected. Fire Marshal regulations requires that all laboratories must have an air handler system that uses 100% outside, non-recirculated air. As a result, it was necessary to install a separate air handler for the IFCT. This was the single most challenging task, with many set backs before it was finally accomplished.

Instead of a single room as initially visualized, it was determined that two labs would become the backbone of the facility. The first lab was outfitted with two fume hoods, a 6-ft and an 8-ft. Four U-shaped benches were installed and much of the lab is devoted to analytical instrumentation. This incluces an Altimira Thermal Programed Desorption system, a PMI BET Surface Area Analyzer, a Perkin Elmer FT-IR Spectrophotometer, Perkin Elmer Differential Scanning Calorimeter, Dionex High Pressure Liquid Chromatograph, JEOL Gas Chromatograph/Mass Spectrometer/Mass Spectrometer, Shimadzu UV-Vis Spectrophotometer, a Perkin Elmer Thermal Gravimetric/Differential Thermal Analyzer with attached Mass Spectrometer, and a Hiden pct system for analysis of hydrogen storage materials. This 1800 ft^2 laboratory contains instrumentation for material science analysis of fuel cell components.

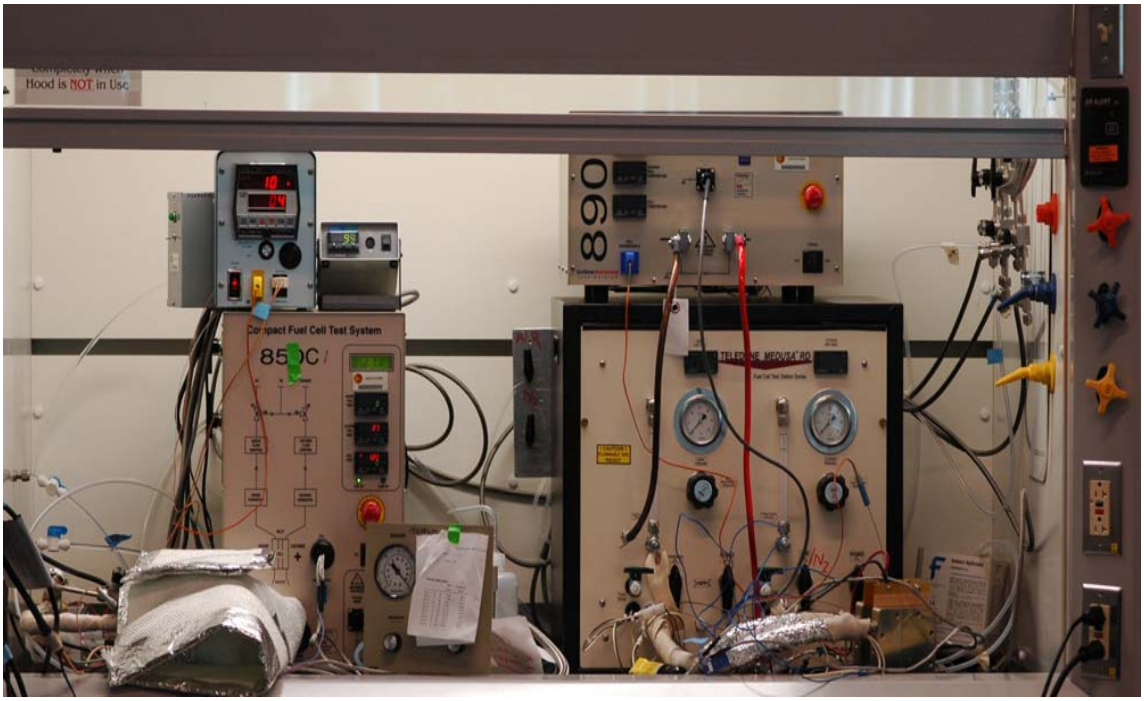

Figure 2. Fuel cell test stands.

The second of the labs is a 1100 ft^2 fuel cell laboratory. This Class B lab has capabilities ranging from those required for membrane electrode assembly fabrication to complete in-situ electrochemical diagnostics. There are three Scribner 850 °C fuel cell test stands, one Teledyne Medusa unit coupled with a Scribner 890 °C, 2 poteniostats, a sonicator and homogenizer for catalyst ink preparation, a screen printer, an enclosure for catalyst spraying, a dry box for membrane fabrication, a hot press under a canopy hood, three extra deep fume hoods (4-ft, 6-ft, and 8-ft), a vacuum oven, and a high temperature oven.

In order to insure safety during operations involving hydrogen, the test stands are permanently located in fume hoods. Additionally, hydrogen sensors shut down the hydrogen in the event a leak is detected.

The laboratory facilities of the IFCT have made it possible to conduct fuel cell short courses the last two years. These courses, open to industry and academia, drew researchers and engineers from such places as NASA, UTC, Giner Electochemical, Lawrence Berkeley National Lab, and Savanah River National Lab. Most attendees were from the US but some came from as far away as Spain and Japan. These three-day intensive courses included lecture in the mornings and then hands-on lab training of fuel cell testing and performance evaluation in the afternoon. Our state-of-the-art laboratories allowed each researcher to obtain real time experience with fuel cell materials and components of current interest to leaders in the industry.

Summary

An Integrated Fuel Cell Test Bed facility was established to create a proving ground and permanent test facility where fuel cell components and systems could be tested and their performance evaluated. This facility is housed with two laboratories and is fully equipped to allow researchers the ability to perform hands-on research in membrane and electrode fabrication, electrochemical testing, materials analyses and cell and device operation.

October 2007

Liquid Hydrogen Storage at Kennedy Space Center

Gu, D. Block, G. Bokerman, Raissi, and M. Basarkar
Florida Solar Energy Center

Research Period: September 2003 to September 2006

Abstract

The objective of this project is to develop a computer model to examine the thermal performance of the Pad B LH_2 tank at the Kennedy Space Center (KSC) and to measure the experimental parameters that are needed for modeling of the granular effects of using glass microspheres as tank insulation. A detailed 3-D model was developed to simulate thermal performance of the tank with a void, a vacuum space without perlite between inner and outer shells. The model was validated against measured data, including boiloff rates, IR images, point temperature and heat flux measurements. A parametric study was performed after validation to investigate which solutions are feasible for future tank renovation. Preliminary recommendations from thermal simulations were provided to KSC. Experimental data from 3M Corp were also sent to KSC to support KSC's model efforts.

The work reported covers tasks performed in FY04 and FY05. The main reason for including all the tasks is that there is continuation among these tasks.

Introduction

The liquid hydrogen and oxygen storage tanks at KSC have served the space launch operations for more than 40 years. Although KSC has two identical liquid hydrogen storage tanks, the current boiloff rate is 750 gal/day for the Pad B tank and 300 gal/day for the Pad A tank. The main cause for the Pad B tank boiloff is a void inside the vacuum space between inner and outer shells generated near the top of the tank, because some perlite used as tank insulation was missing. The void was discovered by IR images taken last summer by a KSC engineer. It is estimated that KSC losses $1 million per year due to liquid hydrogen and oxygen boiloff.

Background

KSC plans to renovate the Pad B tank in the near future. Although there are many possible tank renovation options, the main objective of the present project is to find out which options would be more realistic and economical. For example, one of these options is to add external insulation over the void area. The questions raised are, how large should the coverage area be and what should be the level of the thermal resistance. Thermal simulation can be used to answer these questions. The simulation is a cost-effective way to provide recommendations for KSC to determine which renovation plan is the most feasible. Since the tank geometry is complicated and the void area is required to be simulated, detailed 3-D simulations have to be performed.

In order to use a thermal model with a high confidence level, the model has to be validated against measured data before the evaluation of possible renovation options is undertaken. Although KSC provided measured data of tank boiloff rates and IR images, the data may not be sufficient to validate models. A site visit to obtain more measurements is essential.

Replacement of perlite insulation, currently filled in the vacuum space between the inner and outer spheres of the LH2 tanks, is one of the options for tank renovation. Hollow glass microspheres are the leading candidate for replacing perlite. The microspheres provide improved thermal performance and are significantly stronger particles. While perlite is known to compact with age, the microspheres are expected to remain as free flowing particles. However, their limited use in cryogenic applications has raised questions about particle behaviors.

Granular particles act similar to the familiar solids, liquids and gasses, but have unique behaviors due to the large size of the particle (60 μm for microspheres). The differences result from the elimination of thermodynamics, and interactions between grains are dissipative. Of particular relevance to the insulation application are low reproducibility of behavior, no height dependent pressure head in a cylindrical container, the development of force chains, and jamming. The latter two are illustrated in the following diagrams:

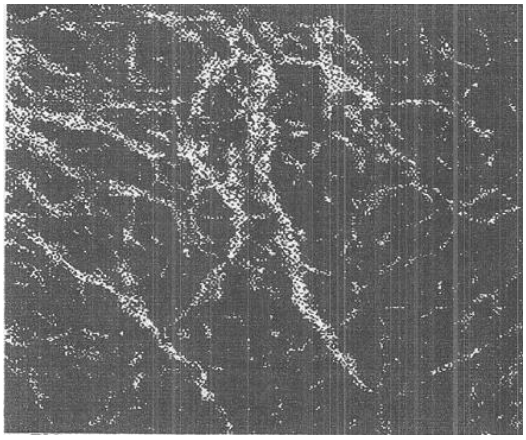

Figure 1. Force chains highlighted for pyrex glass spheres.

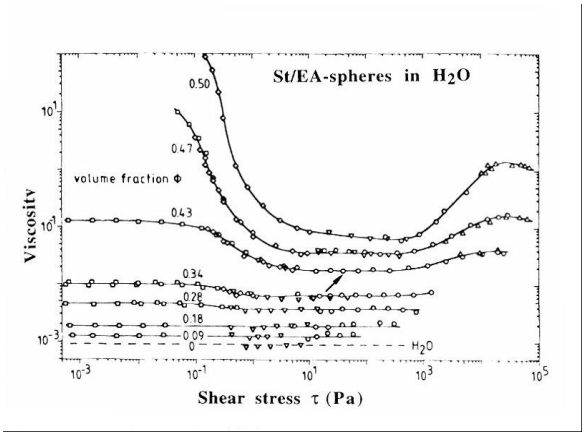

Figure 2. Viscosity vs. shear stress for polystyrene ethylacrylate latex.

The force chains reveal that a small number of particles carry a large portion of the load when stressed, in contrast to an expected averaging process. The second illustration shows the development of a jammed state as the concentration of an emulsion is increased beyond 43%. To achieve flow in these systems a yield stress (to flow) must be exceeded. Since the glass microspheres will have no dilution mechanism, a yield stress is expected.

The latter behavior is presumed to be relevant during LH2 tank thermal cycles. The inner sphere expands and contracts enough during a thermal cycle to change the volume between the inner and outer sphere by 2%. Upon initial cool down a void is created with expected settling of the filler by gravity. When the tank is warmed the particles must return to the void space at the top. The concern is whether the force (yield stress) necessary to break the jammed particles exceeds the crush strength of the microspheres, leading to significant collapse of particles and loss of thermal insulation behavior.

An additional unknown behavior is the impact of the observed expansion of the glass microsphere volume when subjected to cryogenic conditions (Allen et al., Cryogenic Engineering Conference, 2003, C2-C-01). The reported expansion is approximately 5% while the additional space created by contraction of the inner sphere of the tank is only 2%. Large

variations in packing factors (ration of bulk density to true particle density) of microshperes have been reported by 3M (55 to 68%), and may allow for the observed change. If not, the microspheres would be under additional stress.

Results and Discussion

Based on the needs of KSC, the following tasks were performed in the current project:

Task 1: Development of a thermal model of the Pad B LH2 tank based on Mark Berg's data with input from Bob Youngquist at KSC.
Task 2: Delivery of a thermal model of KSC tanks and documentation and training for its use. Bob Youngquist will be the KSC contact.
Task 3: Work with Mark Berg (KSC) and taking high quality IR images of both LH2 tanks.
Task 4: Work with Phil Metzger (KSC) to measure the experimental parameters that are needed for modeling of the granular effects of using glass bubbles as insulation
Task 5: Revisit tanks to map temperature distribution on the outer shell surface and determine the void area
Task 6: Examine the impact of absorptivity and emissivity of the outer shell surface to cover possible void areas
Task 7: Investigate thermal performance of interior vent line embedded inside perlite
Task 8: Examine the thermal impact of other lines and valves under the tanks

Tasks 1-4 were performed in FY04, and Tasks 5 to 8 were performed in FY05.

Site Visit and Data Analysis

IR images taken by Mark Berg (KSC) in the summer of 2003 revealed a cold spot near the top of the tank close to the external vent line. Without perlite insulation in the void area, heat flux increases dramatically, such that cold surface temperatures over the void are expected. The purpose of the site visit was to take high quality images to examine the void area. This was one of tasks in the FY04 project. The visit occurred in the beginning of March 2004. Point temperatures and surface heat fluxes were also measured. The IR images were able to provide information on surface temperature distribution. The point temperature measurements using thermal couple can be used to calibrate IR images in order to provide exact temperature values. The point surface heat flux measurement is able to calculate how thick the insulation level is in the void area.

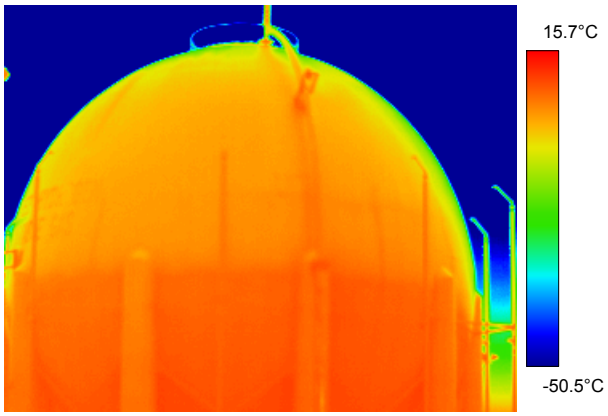

Figure 3. Thermal image of Pad A tank.

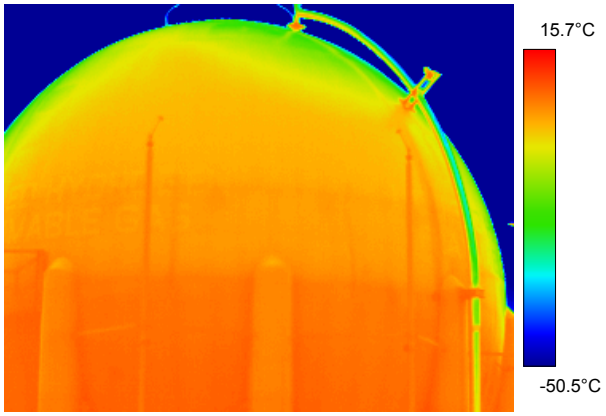

Figure 4. Thermal image of Pad B tank.

Thermal Images of Pad A and B

Thermal images of Pad A and B tanks are shown in Figure 3 and 4, respectively. Since there is no void in the Pad A tank, the color is almost homogenous on the surface, except for edges with green color due to night sky temperature. However, there is an area near the top with green color for the Pad B tank, as shown in Figure 4. That area is where the void is.

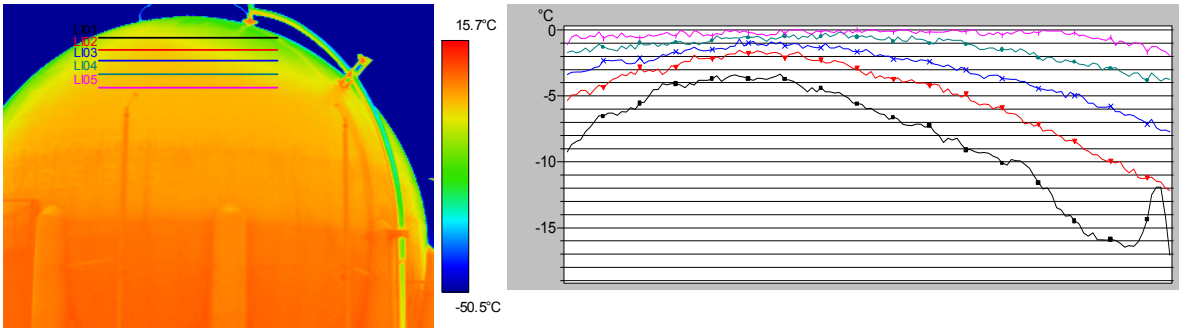

Figure 5. Pad B tank thermal image and associated horizontal surface temperature distribution.

Figure 5 shows an IR image of the Pad B tank and horizontal line surface temperature distribution. Since accuracy of temperature measurement with an IR camera is based on estimation of surface emissivity, the point thermal couple measurement was used to calibrate the thermal images. The calibrated surface emissivity is 0.65 based on the thermal couple point measurements. There are five horizontal lines at the top, which indicate surface temperature distribution. Line 1 near the top edge shows a temperature drop near the right edge at -16 °C, where the void area is.

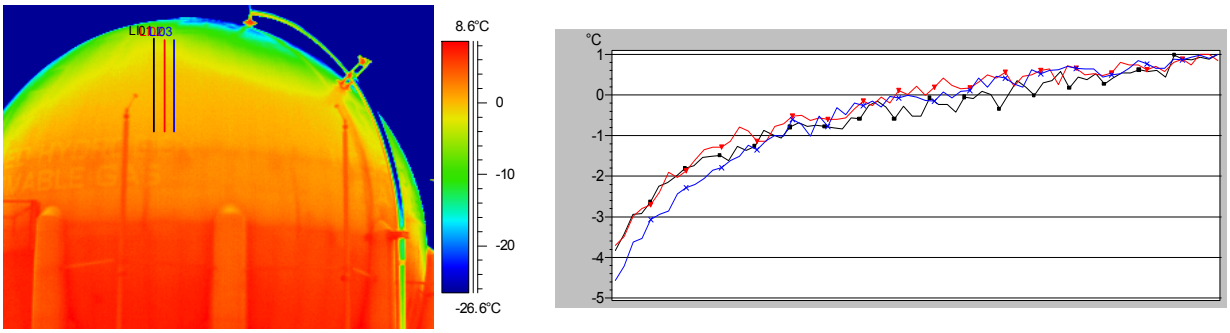

Figure 6. Pad B tank thermal image and associated vertical surface temperature distribution.

Figure 6 shows an IR thermal image of the Pad B tank and its vertical line surface temperature distribution. The IR thermal image is the same as in Figure 5. However, instead of plotting surface temperature horizontally, the surface temperature is plotted vertically using the image processing software.

Heat flux measurements were also performed. The heat flux transducer (HFT) is made by Hy Cal Engineering, Inc. The measurement range is from 0 to 500 Btu/ft^2.h. Any measured values less than 1 or 2 Btu/ft^2.h are considered noise. Since the heat flux with perfect perlite insulation is about 0.07 Btu/ft^2.h, it is beyond the resolution of the HFT. However, the HFT can measure heat flux over the void area and other direct contact areas, such as the manhole, mechanical supports, etc. The following tables list heat flux values in Pad A and B tanks, respectively. The negative sign of heat fluxes indicates the heat flows from outside to inside in the tank.

Table 1. Measured surface heat fluxes in Pad A tank

Location	q (W/m^2)	q (Btu/ft^2.h)
Outside the manhole	-10.50	-3.33
Inside the manhole	-8.08	-2.56
Mechanical supports	-27.56	-8.74

Table 2. Measured surface heat fluxes in Pad B tank

Location	q (W/m^2)	q (Btu/ft^2.h)
Top surface	-27.62	-8.76
Outside the manhole	-14.60	-4.63
Inside the manhole	-11.10	-3.52
Center of the cold spot	-21.17	-6.71
Cold spot	-48.12	-15.26
Outside the cold spot	-64.11	-20.33
Mechanical supports	-5.75	-1.82

Comparing measured surface heat fluxes between the two tanks, the measured values from outside and inside the manhole in the Pad B tank are higher than the ones in the Pad A tank, while the value from mechanical supports are lower than the one in Pad A tank. The main reason is that when the measurement took place in the early morning, the point heat measurement might measure different locations. Since the heat fluxes are heavily dependent on locations, different measured locations would provide different values.

Leaking Valve

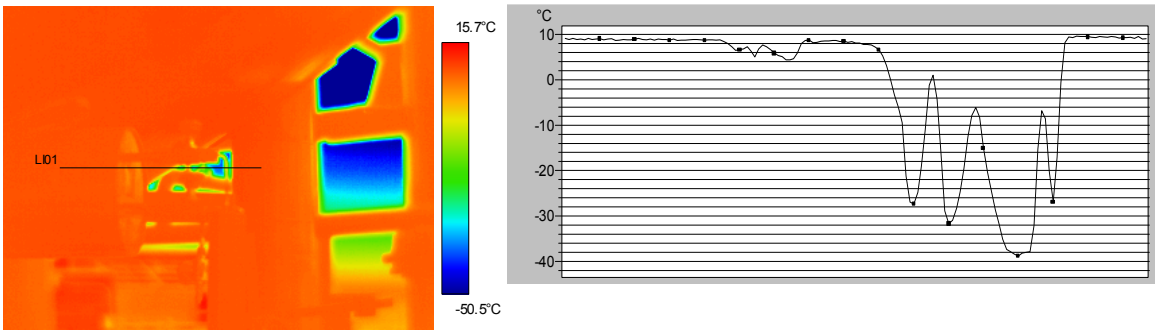

Figure 7. Leaking valve in Pad B tank and associated horizontal surface temperature distribution.

During the site visit, a leaking valve was found near the bottom of the Pad B tank. Ice had formed around the valve and connecting pipes. Figure 7 shows a thermal image with the lowest temperature at -39 °C. Although the leaking valve study is beyond the scope in the present study, the topic of how to reduce heat leaks will be studied in the FY05 project.

1-D Calculation

As mentioned earlier, the HTF can detect any values over the void and other metal connection areas, but cannot detect any heat fluxes over the perfect perlite insulation area, due to HTF resolution and sensitivity. The main purpose of HTF measurement is to determine how much insulation is left in the void area. The effective thermal conductivity in the void area can be calculated when given the heat flux and temperature difference. In order to ensure the measured heat fluxes were valid, 1-D thermal calculation was performed to calculate insulation levels in the void area.

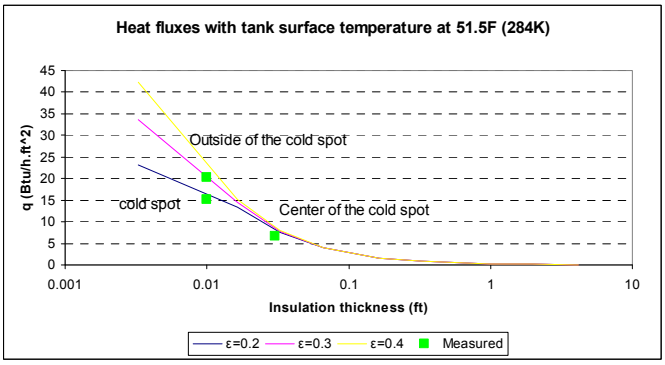

Figure 8. Heat flux comparison between measurement and prediction.

The assumptions used in the 1-D calculation are:

- Heat flux is a function of perlite thickness
- Conduction only inside perlite
- Radiation only between perlite and interior surface of the outer shell

Figure 8 presents comparison of heat flux between measurement and 1-D calculation results at different perlite thickness. The solid lines represent 1-D calculation results based on different internal surface emissivities and thickness of perlite. It should be pointed out that since the interior surface emissivities are unknown, various emissivities were used to cover the possible variation. The green symbol represents the measured heat flux values. The measured values show that the maximum thickness in the void area is less than 0.02 ft, compared to the ideal thickness at more than 4 ft. In other words, there is little perlite left in the void area. Although we did not use non-destructive technology to detect internal perlite levels in the void area, the heat flux measurement did provide equivalent information. The disadvantage is that the heat flux measurement provides point information. In order to determine how large the void area is and how much perlite is left, more point measurements in conjunction with IR images are needed. Because of high conductivity of the carbon steel outer shell, 3-D thermal simulation should be performed to determine the void area based on the boiloff rate.

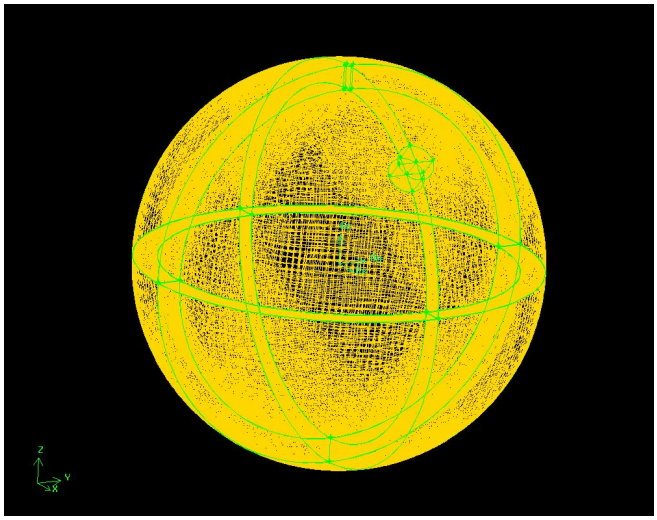

Figure 9. 3-D mesh used in simulations.

From the comparison, the heat flux measurement was successful and measurement goal was reached.

Thermal Model Development

A thermal model was developed with exact geometry (3-D) of the Pad B tank. FLUENT[1], a powerful computational fluid dynamics software, was used to perform thermal simulations. Figure 9 illustrates 3-D mesh used in FLUENT thermal simulations. The model was validated against measured data to ensure that the model provide realistic results before performing a parametric study. The measured data consisted of boiloff rate, IR images, point measurements of surface temperatures and heat fluxes. As mentioned earlier, the point surface temperature measurement was primarily used to calibrate surface emissivity for IR image post-processing.

[1] http://www.fluent.com

The point surface heat flux measurement was used mainly to estimate how much insulation was left in the void area. Unfortunately, due to the limitation of IR images obtained from the site visit, the exact void area was unable to be determined. Thus, one more site visit was proposed as a task in FY05 project. For the time being, the estimation of void area will be a parameter in detailed thermal simulations.

The first model validation was compared to a 300 gal/day boiloff rate of the Pad A tank with perfect insulation. Simulation result indicated a boiloff rate of 270 gal/day. The largest heat loss is from the perlite component. The second and third largest losses are from the access manhole and mechanical supports. Since there are many unknowns in the tank structure and 3-D mesh only covered main components, the simulation result was good enough as a starting point for examination of the thermal performance of the Pad B tank with a known void.

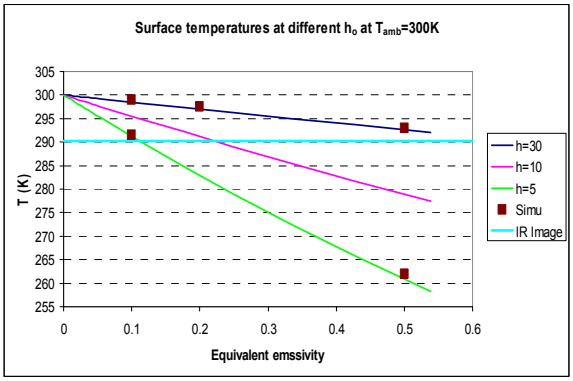

Figure 10. Tank IR image with a cold spot.

By assuming that there was no perlite remaining in the void derived from the heat flux measurement, simulations were performed to calculate surface temperature and boiloff rate caused by the void. Figure 10 is an IR image taken by Mark Berg in the summer of 2003. The dark area is a cold spot near the vent line close to the top of the tank. Figure 11 reveals temperature prediction obtained from the 1-D calculation and the 3-D simulations with different equivalent emissivities of the void surfaces. The solid lines, except for the blue line, represent the surface temperature with various exterior convection conditions. The symbols represent results from the 3-D simulations. The 1-D calculation results compare well with the 3-D simulation results. As long as the void area is large enough, the 1-D calculation can be used to predict surface temperatures, once lateral thermal conduction in the outer shell can be eliminated. The blue line represents measured surface temperature at the cold spot. The simulation agrees well with the actual physical measurement with the exterior convective heat transfer coefficient of 5 $W/m^2.K$ and equivalent interior surface emissivity of 0.1.

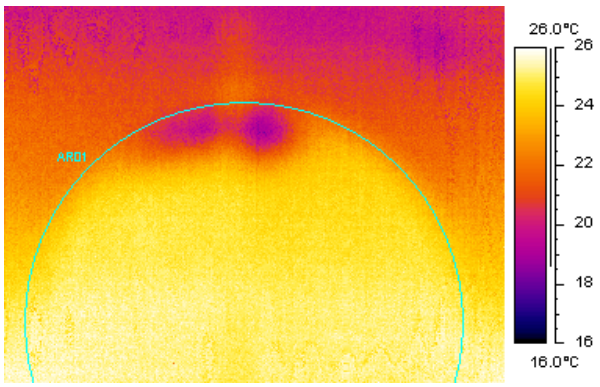

Figure 11. Surface temperature comparison between measurement and prediction.

Since the measurement took place at night, a still air heat transfer at the exterior surface was assumed with h=5 W/m^2.K. Figure 11 also presents a boil off rate at different heat transfer coefficients. The value of 30 W/m^2.K represents day time convective heat transfer caused by heavy winds. The value of 10 W/m^2.K represents convective heat transfer under mild wind condition. It is clear that convective heat transfer is an important factor in boiloff with a void. However, if there is no void in a tank, the impact of convection may be insignificant.

Parametric Study

After model validation, the sensitivity study consists of the following parameters:

- Convective boundary condition at the exterior surface of the outer shell (5 to 30 W/m^2.K)
- Equivalent solar air temperature varies from 35 °F to 125 °F.
- A void with diameter from 2 m to 4 m near the top of the tank
- Equivalent surface emissivity from 0.05 to 0.5 inside the void
- Add an external insulation to cover the void area with double and triple coverage over the possible void area
- A localized area near a single mechanical support was simulated to examine the thermal impact of the single support on boiloff rate.

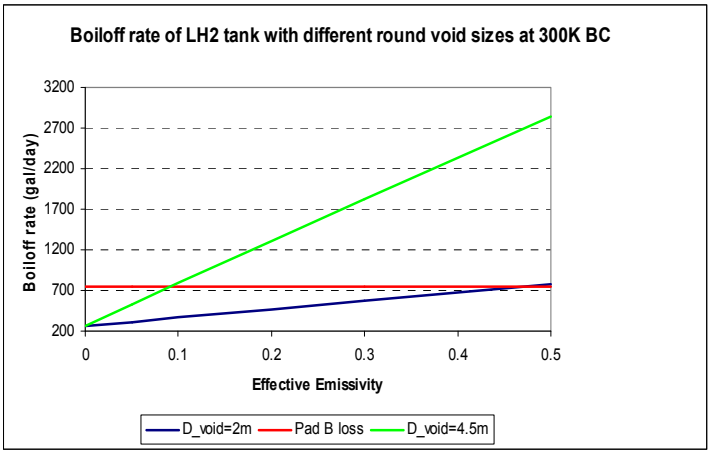

Figure 12. Boiloff rate with two void sizes.

Void Size Impact

As mentioned earlier, we were unable to determine the exact void size from the March visit. However, from the image taken by Mark Berg, the estimated void diameter is about D = 2.5-4 m. That is why we selected a 2 m and 4.5 m void size in order to cover possible void size variations. Figure 12 shows boiloff rates at different interior equivalent emssivities with void sizes at D = 2 m and 4.5 m. The red line represents the Pad B tank boiloff rate. It is observed that it is most likely that the void area is about 4.5 m with effective emissivity of 0.1, which is consistent with the estimation derived from the heat flux measurement.

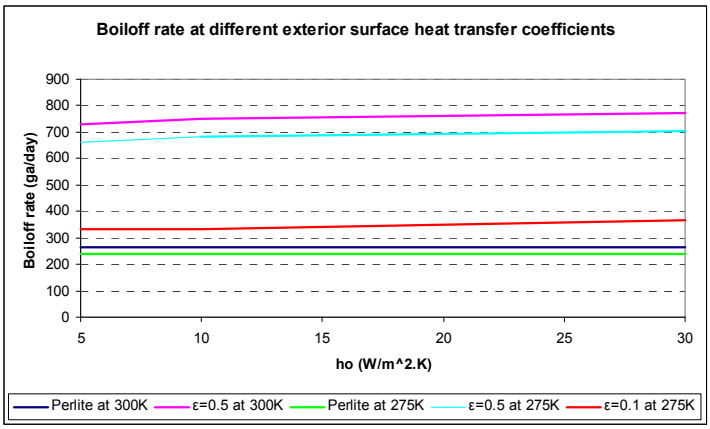

Figure 13. Boiloff rate vs. exterior surface convection.

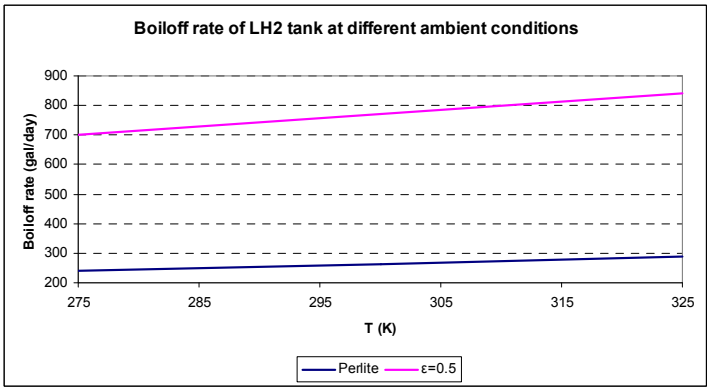

Figure 14. Boiloff rate vs. ambient temperature.

Exterior Surface Convection

Figure 13 shows impact of boiloff rate on exterior surface convection. The dark blue and green lines represent perlite insulation without a void. The boiloff rate remains almost constant with different exterior surface convective rates. The other three lines represent boiloff rates with a void at different interior effective emissivities. The impact of exterior surface convection from still air to heavy wind is 10% at ε = 0.1. Therefore, the exterior surface convection is an important factor in tank boiloff rate with a void.

Ambient Temperature

Figure 14 reveals impact of ambient temperature on boiloff rates with and without a void. The boiloff is proportional to the outdoor temperatures. The slope of the change is based on how large the void is.

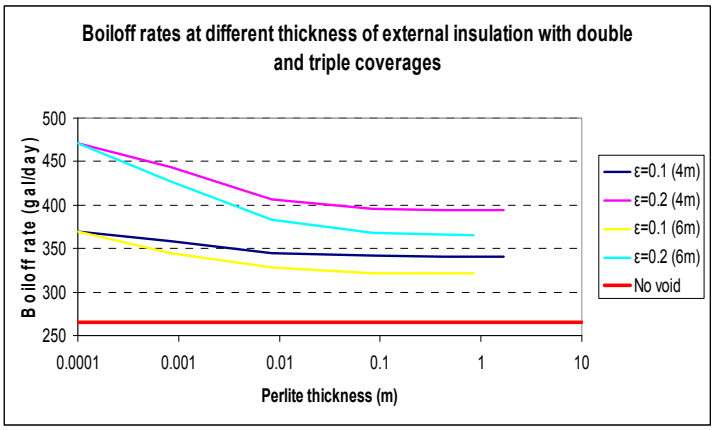

Figure 15. Boiloff rate vs. external insulation.

External insulation

One of possible solutions proposed by Bob Youngquest at KSC was to add insulation over the void area to reduce heat transfer. The present study examined how large the coverage over the void area is and how effective the external insulation is through detailed 3-D simulations.

By assuming the void size to be D = 2 m and the external insulation size to be D = 4 m (double coverage) and 6 m (triple coverage), simulations were performed at different external insulation thickness, equivalent to different insulation levels. For convenience, we assumed that perlite was used as the external insulation material. Figure 15 illustrates boiloff rates at two interior emissivities varying with external insulation thickness. When the external insulation thickness is less than 0.01 m, the boiloff rate drops dramatically. However, the boiloff rate remains almost constant when the external insulation thickness is above 0.01 m. Therefore, the option of increasing external insulation can not reduce the boiloff rate to the level where the tank has no void.

By assuming an interior effective emissivity of ε = 0.1 and 9 times external insulation coverage with infinity insulation level over the void area, a 13% boiloff reduction can be reached, compared to the case with the void and without external insulation. Compared to the case without the void with the same base, the reduction of boiloff rate is 28%. By assuming an interior effective emissivity of ε = 0.2 and keeping 9 times external insulation coverage with infinity insulation level over the void area, a 22% boiloff reduction can be reached, compared to the case with the void and without external insulation. Compared to the case without the void with the same base, the reduction of boiloff rate is 46%. Therefore, external coverage never reaches the boiloff level without the void. This may not be the solution from simulation results.

Single Mechanical Support Investigation

In addition to the above parametric study, thermal impact of a single mechanical support on boiloff losses was examined. This examination was requested by KSC staff. Examination of the thermal impact of a single mechanical support has following reasons:

- There are 40 mechanical supports directly connecting the inner and outer shells in the storage tanks. The supports are made of stainless steel. Since stainless steel has much higher thermal conductivity than perlite, heat losses from mechanical supports may contribute about 20% of the total boiloff loss of the tank from 1-D steady state calculation.

- Although a 3-D model was developed to simulate thermal losses, it is unlikely to use very fine mesh for each mechanical support in the model. A lumped support object was used in the model.

Therefore, a single mechanical support examination with detailed mesh is needed to determine how much total thermal loss is due to both support heat conduction and lateral heat transfer to surrounding perlite. The lateral heat transfer causes higher temperature in the surrounding perlite, so that heat fluxes in the surrounding perlite also increase. That is why we would like to examine total impact, in addition to heat conduction in the support.

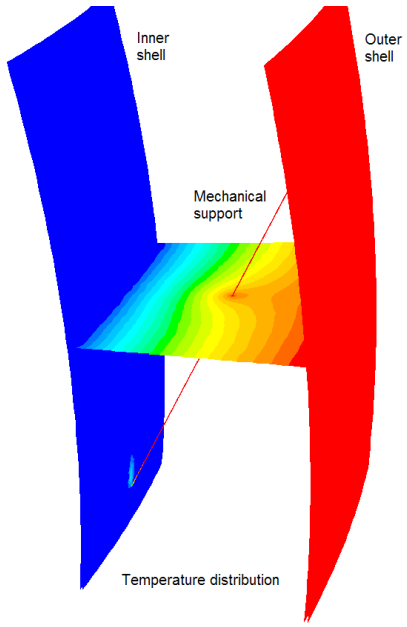

Figure 16. Temperature distribution with a single mechanical support.

A detailed 3-D model was developed. Since 40 mechanical supports are equally distributed at 9° angel. By assuming no heat transfer in the middle surface between two supports, a fortieth of the tank with a certain height was selected as a simulation domain, consisting of inner and outer shells, a mechanical support and surrounding perlite insulation. Figure 16 demonstrates temperature distribution in a mechanical support and surrounding areas. The domain, as shown in the figure, consists of inner and outer shell, a mechanical support, and a cross section area at the tank center. The red color represents the temperature close to ambient temperature about

300 K, and the blue color represents the LH2 temperature about 20 K. Due to higher thermal conduction, the temperature in the mechanical support is very close to the ambient temperature with read, except for a small portion near the inner shell with blue. If there is no mechanical support, the isothermal lines should be parallel to the shells. The isothermal contour lines near the support are not parallel to the shells with the mechanical support. The temperature increase near the support causes heat fluxes to be increased in perlite insulation section. The impact of heat flux increase in the perlite insulation area on boiloff rate was determined by the detailed model simulations.

Following parameters were used to perform a parametric study:

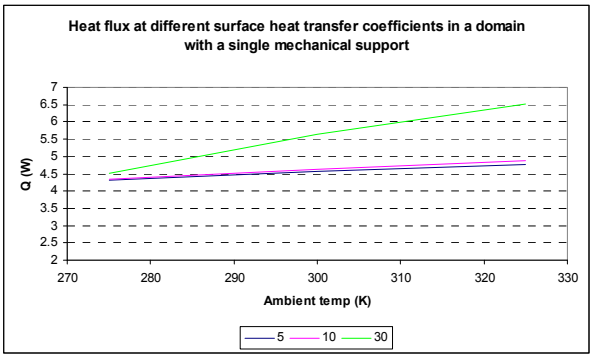

Figure 17. Surface heat transfer impact on heat flux

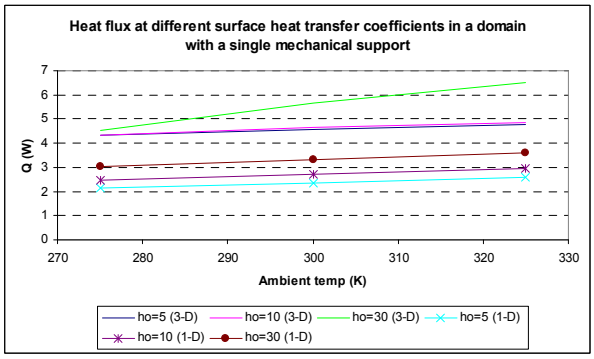

Figure 18. Heat flux comparison with different housing 1-D and 3-D approaches

External surface heat transfer coefficients (h_o): 5, 10, and 30 [W/m^2.K]
Ambient temperature: 275, 300, and 325 [K]

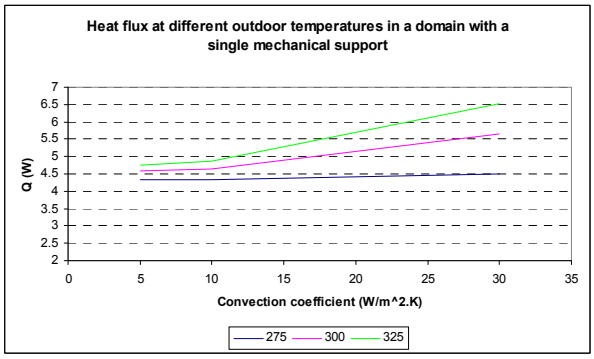

Figure 19. Ambient temperature impact on heat flux.

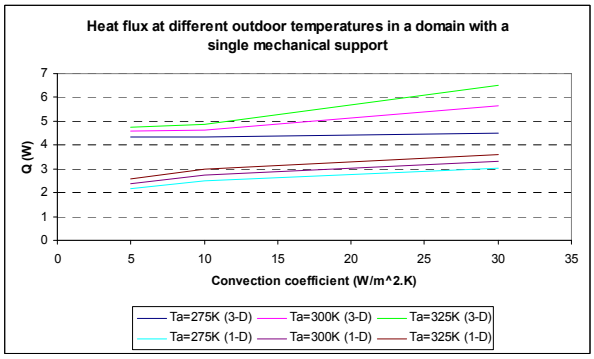

Figure 20. Heat flux comparison with different outdoor T using 1-D and 3-D.

Figure 17 plots the total heat fluxes vs. outdoor temperatures with different surface heat transfer coefficients from 3-D simulations. Although 3 different temperatures were used in the figure, it is clear that heat flux is almost proportional to the outdoor temperature. However, the difference of heat fluxes between h_o=5 and 10 is small, while the difference between h_o=10 and 30 is much larger. Figure 18 plots the same data as shown in Figure 16, and also adds three more lines with symbols calculated using 1-D approach. The amount of heat fluxes using 3-D simulations is much bigger than those obtained using 1-D approach. The ratio is about 1.5-2. Therefore, heat

transfer is much more complicated due to lateral conduction and temperature changer in the surrounding perlite.

Figure 19 plots the total heat fluxes vs. surface heat transfer coefficients with different outdoor temperatures, using the same data plotted in Figure 17. Figure 20 plots the same data as Figure 18. The difference is that surface heat transfer coefficients are used as x-axis.

Therefore, based on detailed 3-D simulation results, the 1-D approach is not good enough to provide accurate boiloff calculation without including lateral heat transfer. The detailed simulations can help the 1-D approach to provide approximated correction coefficients with additional boiloff losses.

Revisit tanks to map temperature distribution on the outer shell surface and determine the void area—This task was supposed to be scheduled this summer after we presented the preliminary simulation results in 2004 June. Unfortunately, due to the very busy schedule of KSC staff, it is expected to be performed in September or October 2004. The objective of this task is to try to map the temperature distribution of a whole tank, and determine possible void area, shape, and insulation levels in the void. This is a very important step. The better we understand tank thermal performance, the better solutions we can recommend to KSC.

Since there is a lack of non-destructive tools to detect how big the void is and how much the perlite level is, it is essential to use conventional and available tools to reach the goal. We proposed making point measurements of temperatures and heat fluxes, in addition to IR images in the last visit. The point measurements did provide valuable validation data for the detailed model. Unfortunately, the visit could not fully meet expectation, although we did obtain valuable information. Therefore, after gaining a greater understanding of tank thermal performance through simulations, we need one final site visit to finalize measurements.

We proposed to coordinate the visit with KSC engineers and scientists. Two IR cameras would be used during the visit. One would be used by a KSC engineer to take images from a crane. The other would be used to take images to determine the location of the KSC engineer from the ground. Since the work has to be performed at night without the effect of wind and solar radiation, it is hard to track where the images are taken. In addition, point temperature and heat flux measurement would be also performed.

Unfortunately, the revisit did not happen, due to very busy schedule of KSC staff. Therefore, we did not perform this task and could not determine how big the void is, and where the void is located exactly. However, we did have data to perform validation from the 2004 visit.

Examine the impact of absorptivity and emissivity of the outer shell surface to cover possible void areas—The objective of this task is to examine possible solutions in the void area to determine how much the boiloff rate can be reduced in relation to surface properties. This can be achieved by applying special paint and aluminum foil at the exterior surface above the void. The question is how effective the paint and foil are and how large the coverage is.

It has already been determined that the greatest amount of boiloff is from the void area. A possible solution is to reduce absorptivity and increase emissivity on the exterior surface in the void area. The possible solution can also be applied to other area with perfect perlite insulation, although it may not be cost-effective at the perfect insulation area.

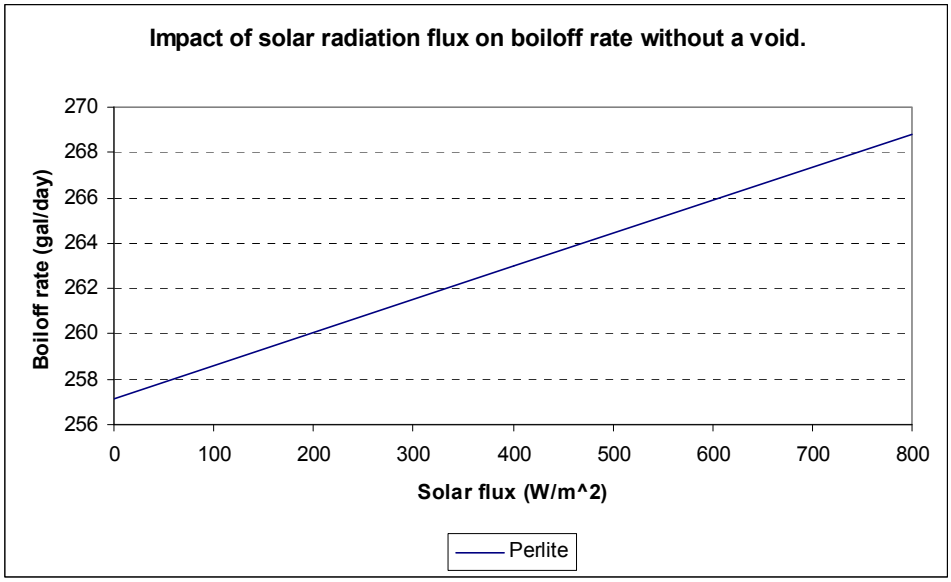

Figure 21. Solar radiation impact on boiloff rate with a perfect tank.

The function absorptivity is to determine how much solar radiation is absorbed by the outer shell. Reducing absorptivity is equivalent to increasing surface reflectivity. The function of emissivity is to determine the impact of radiation exchange between sky temperature and exterior surface temperature.

Before examining absorptivity (α) impact on the tank boiloff rate over a void, it is necessary to investigate the absorptivity impact for a perfect tank without a void. In a summer day with solar radiation at 800 W/m^2, the boiloff rate change is only 4.5% from α = 1.0 to 0.0. The perfect perlite tank insulation protect tank from an external large heat source, solar radiation. Zero solar radiation is equivalent to α = 0.0, while solar radiation at 800 W/m^2 is equivalent to α = 1.0. Figure 21 illustrates boiloff rate change vs. solar radiation. The boiloff rate is proportional to the solar radiation.

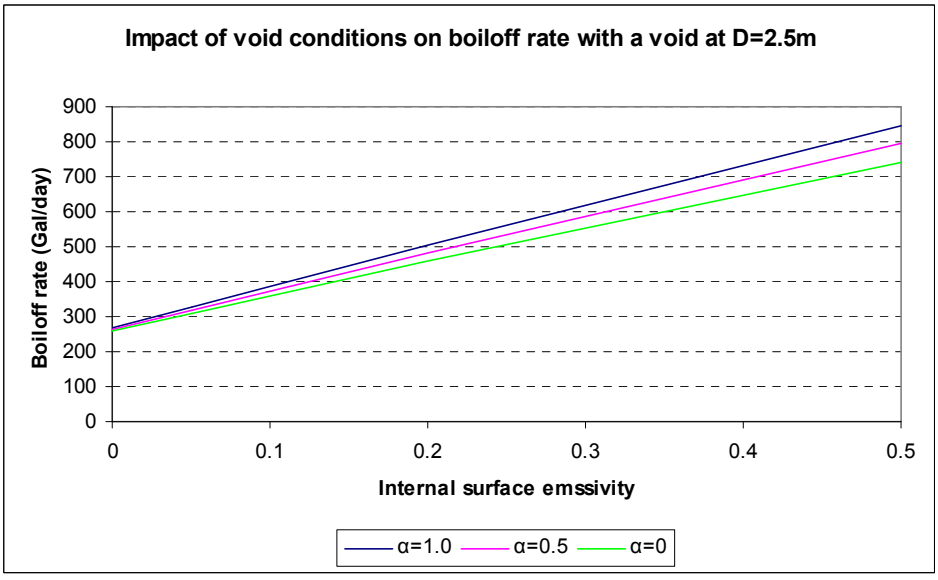

Figure 22. Solar radiation impact on boiloff rate with a void.

However, when a void exists with comparatively higher thermal conductivity, absorptivity makes relatively larger impact compared to the perfect perlite tank. The boiloff rate increase to 11% with a small void (D = 2 m) at internal surface emissivity = 0.2 from α = 0.0 to 1.0. Figure 21 plots the boiloff rate vs. internal emissivity, which is equivalent to how much perflite is missing. It should be pointed out that the boiloff rate change percentage is calculated based on absorptivity change for the storage tank with a void.

Compared to the surface absorptivity over a void, the surface emissivity impact is relatively small. The boiloff rate change is about 2% from ε = 0.45 to 0.9 for the void tank. In addition, sky temperature has an impact on the boiloff rate. For ideal cases, lower absorptivity and high emissivity are expected, because lower absorptivity reduces solar radiation adsorption and higher emissivity increases radiation exchanges between surface and sky. In general, sky temperature in a summer day in Florida varies between 280 and 290 K.

Figure 23 plots boiloff rate vs. internal surface emissivity (equivalent void thermal conductivity) at emissivity = 1 and α = 1.0 with different sky temperatures. The boiloff rate is proportional to the void thermal conductivity. The sky temperature impact is very small, since both lines are very close. Figure 24 plots boiloff rate vs. internal surface emissivity (equivalent void thermal conductivity) at emissivity = 1 and α = 0.0 with different sky temperatures. The boiloff rate is proportional to the void thermal conductivity. The sky temperature impact is very small, since both lines are very close.

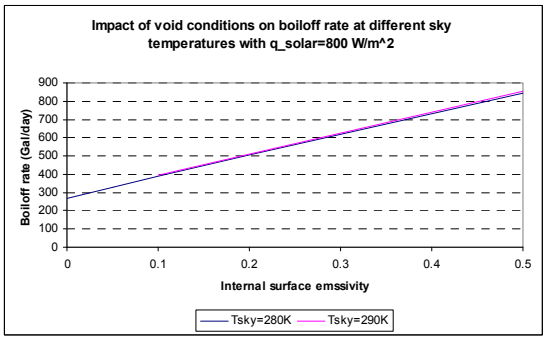

Figure 23. Void condition impact on boiloff rate at α = 1.0 with different sky temperatures.

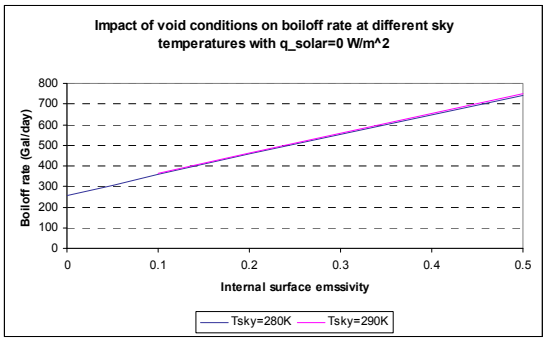

Figure 24. Void condition impact on boiloff rate at α = 0.0 with different sky temperatures.

Following conclusions may be drawn from the above analysis:

- Changing surface absorptivity over a void may reduce boiloff rate
- Changing surface emissivity has little impact
- Sky temperature in Florida climates may have little benefit. Due to humid climates at KSC, the sky temperature is not low enough to have significant cooling impact.
- Changing surface properties may not be a good solution
- The best approach to reduce boiloff rate is to fix the void, so that boiloff rate can be reduced from 750 gal/day to 300 gal/day.

Investigate Thermal Performance of Interior Vent Line Embedded Inside Perlite

The objective of this task is to study the impact of the vent line on boiloff rate. The other reason is that the vent line may be the cause of the void area occurrence during perlite filling, which may be used in task 4 of the FY04 project.

The vent line is made of steel. A part of vent line is embedded inside the perlite with one end of the line connected to a distributor near the top of the LH2 storage area. The other end of the interior line is connected to the outside of the tank near the bottom. The rest of the line is exposed to the outdoors in order to release H2 gas.

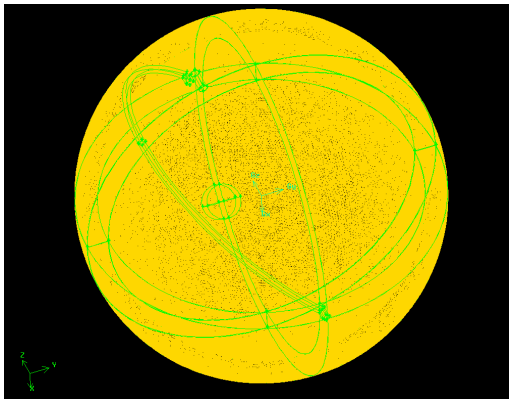

Figure 25. Schematic of vent line mesh used in 3-D simulations.

Although the vent line is cooled by hydrogen gas with boiloff temperature close to LH2, the heat transfer from outdoors through the vent line wall may cause higher temperatures in the vent line. Since the vent line is buried in the perlite insulation, an additional temperature rise in the vent line may cause different thermal performance of the perlite, whose thermal conductivity is heavily dependent on temperature.

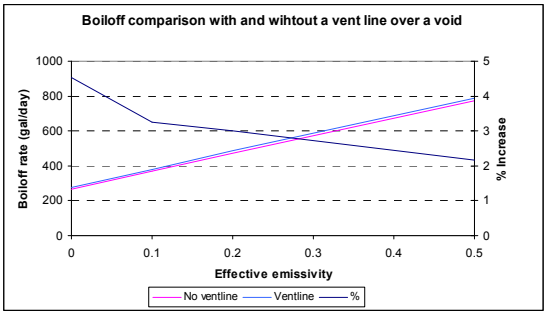

Figure 26. Boiloff rate comparison with and without the vent line.

A vent line was added in the 3-D model with the void tank. The vent line was buried in the middle of perlite insulation and does not pass through the void. Figure 25 shows where the vent line is used in the 3-D model.

Simulation results show that heat transfer rate in the vent line from boiloff gaseous H2 is smaller that the heat transfer from outdoors through the vent line wall. Therefore, the total boiloff rate with the vent line is higher than the boiloff rate without the vent line. However, the difference is small, compared to the total boiloff rate.

Figure 26 plots boiloff rate vs. internal surface effective emissivity with and without the vent line. In order to compare the boiloff rate change, the third line is also plotted to represent the percent change with and without the vent line, labeled in the right Y-axis. It is observed that the absolute

difference of boiloff rate is almost constant, while the boiloff rate percent change with and without the vent line is between 2 and 4.5%.

It may be concluded that the impact of the vent line on boiloff rate may be insignificant, compared to other components, such as mechanical support and manhole. Further investigation was not performed.

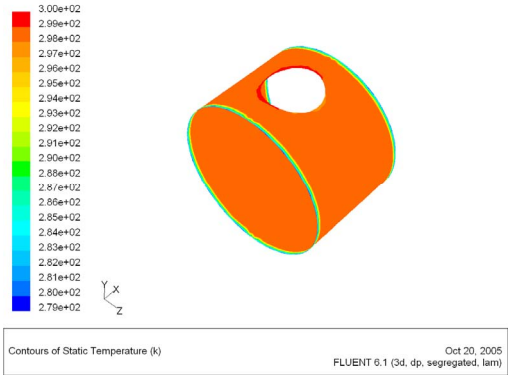

Figure 27. Value temperature contour with insulation at R = 0.

Examine the Thermal Impact of Other Lines and Valves Under the Tanks—The objective of this task is to study the additional impact due to other lines and thermal leak valves. During the tank sit visit in 2004 March, we were informed that the valve under the tank had a leak. The low temperature was detected by an IR camera. We also observed ice around pipes near the leaky valve. The task is to determine the amount of boiloff caused by the leaky valve. Possible solutions, such as adding a well-insulated box to cover the valve, were examined.

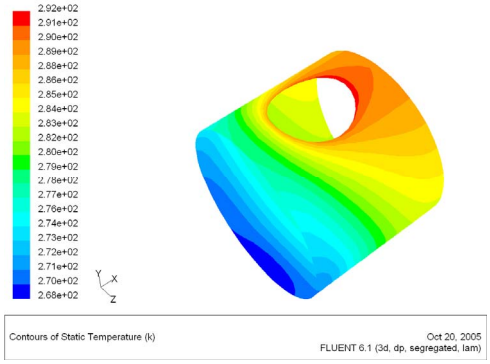

Figure 28. Value temperature contour with insulation at R = 28.

Simulations were performed in order to understand how important the valve insulation level is and how much insulation is needed to avoid ice formed on the valve surfaces. Instead of simulating a whole tank as the above tasks performed, a stand alone valve was simulation with 3-D approach. Following parameters were used in simulations:

- The valve inlet temperature is 20 K
- The outdoor temperature is 300 K
- The inlet gaseous hydrogen flow rate varies from 0.0001 to 1 m/s
- Insulation level varies from R-0 to R-284 [h.ft^2.°F/Btu]

Figures 27 and 28 demonstrate temperature profiles with R = 0 and R = 28, respectively from FLUENT simulations. Red color represents high temperature and blue color represents low temperature. The surface temperature is much higher with R = 28, compared to the case with R = 0. Therefore, insulation is essential to keep heat losses through valves at minimum.

Since temperature profile varies point-by-point, three representative values were selected to determine heat losses: minimum temperature, maximum temperature, and average temperature. Figure 29 plots the average temperature vs. inlet velocity at different valve insulation levels. It is clear that when the valve insulation is above R = 28, the average valve temperature almost remains constant, independent of inlet velocity. Figure 30 illustrates the average temperature vs. valve insulation level at different inlet velocity, using the same data plotted in Figure 29. It should be pointed out that an additional line is plotted in Figure 30 to represent a freezing point (273.15 K). When any temperature is below the freezing point, ice will be formed on the valve surfaces. It is recommended that the valve surface temperature be above the freezing point, so that the minimum valve insulation level should be R = 10. In order to have better insulation to keep heat losses independent of inlet flow rate, R = 30 is recommended.

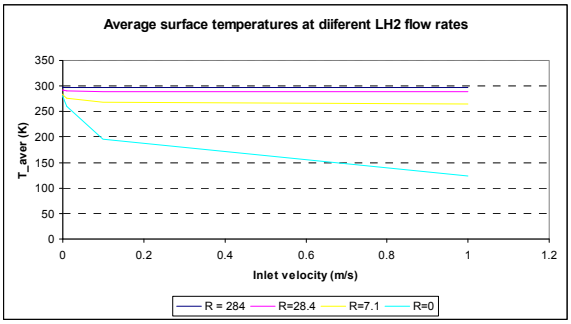

Figure 29. Valve average temperature vs. inlet velocity at different insulation values.

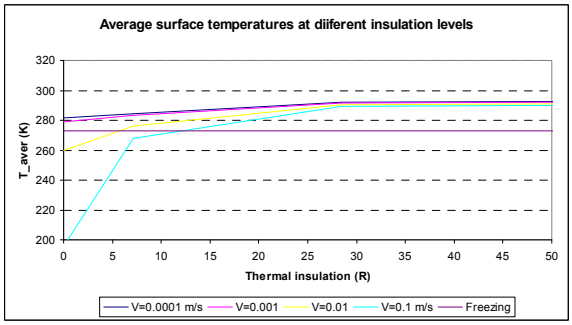

Figure 30. Valve average temperature vs. insulation level at different inlet velocities.

In addition to the leak valve, there are several lines through the perlite, such as the liquid transfer line, liquid fill line and liquid drain line. Although 1-D calculation indicates no large heat transfer occurs along these lines, we would like to perform 3-D simulations to determine how much these lines actually contribute the boiloff. If a large contribution is found, we will perform a parametric study to attempt to find a realistic solution to reducing the boiloff rate caused by the lines.

However, from the previous task study in vent line impact, the boiloff rate change is insignificant with and without the vent line. This conclusion can also be applied to other lines. Hence, it is not necessary to study this any further.

Insulation Experimental Program

Evaluation of Microsphere Crush Strength

Values for the crush strength of glass microspheres have been extensively published by the manufacturer, 3M Corp. These values have been determined by methods to duplicate the typical usage, as a filler in plastic formulations. In this application isostatic conditions apply with

equal stress exerted across the surface area of the particle. The insulation application, however, is a bulk usage where point-to-point contact occurs producing much higher localized stress.

A recent publication (Koopman et al., Scripta Materialia, 50, (5), Mar. 2004, pp. 593-596) served as a guide to expected behavior. A nanoindenter was used in this study, in uniaxial compression, to measure the crush strength of individual glass microspheres. By extrapolation to a bulk application, the crush strength would be expected to be almost a factor of 10 smaller than the isostatic value.

R. W. Hunter of 3M Corp. graciously explored a modification of their quality assurance test to change the particle test from isostatic conditions to point-to-point contact. The test is closely described by ASTM D3102-78 in which the glass microspheres are placed in a rubber balloon along with an agent to prevent direct contact between spheres. This system is then pressurized by liquid or gas and the amount of crushing determined.

Several variations were explored with the elimination of the agent to prevent direct contact between spheres. Gas pressurization of the balloon resulted in measurable crush values. The feasibility results at the usual pressure of 250 psi were significantly below the published isostatic crush strength (>50% vs. published values of <10% crushed). At very modest pressures of 20 psi, no breakage was observed.

An additional effect is the impact of cryogenic temperatures on the strength of the borosilicate glass of the microspheres. While no direct studies were completed, a literature reference on tensile measurements at liquid nitrogen temperatures (H. Hasegawa, et al., Journal of the Ceramic Association, Japan, vol. 82, no. 7, 1974, pp. 387-92) reveals an increase of 1.5-2.3 times the tensile strength at room temperature. Since glass has no directional orientation, crush strength values would be expected to show an improvement as well.

Evaluation of Flow Yield Stress

Thermal Analysis Instruments (F. Mazzeo and M. Taylor) graciously conducted two feasibility studies to find methods to determine the yield stress (to flow) for glass microspheres. The first method explored used a Dynamic Mechanical Analyzer in compressive mode to simulate the expanding internal sphere of the LH2 tanks. Evidence of flow or resistance to flow could not be distinguished by this method.

The second evaluation utilized their AR 2000 Advanced Rheometer equipped with a vane rotor (four paddles at 90°) immersed in a container of glass microspheres. Increasing shear stresses were applied until rotation of the vane occurred. Torque values were determined with the glass microspheres in a loose state and a more compact state achieved by vibrating the container. The resulting yield stress increased by 5X to 10X with two different types of glass microspheres.

K15: Loose vs. Tapped

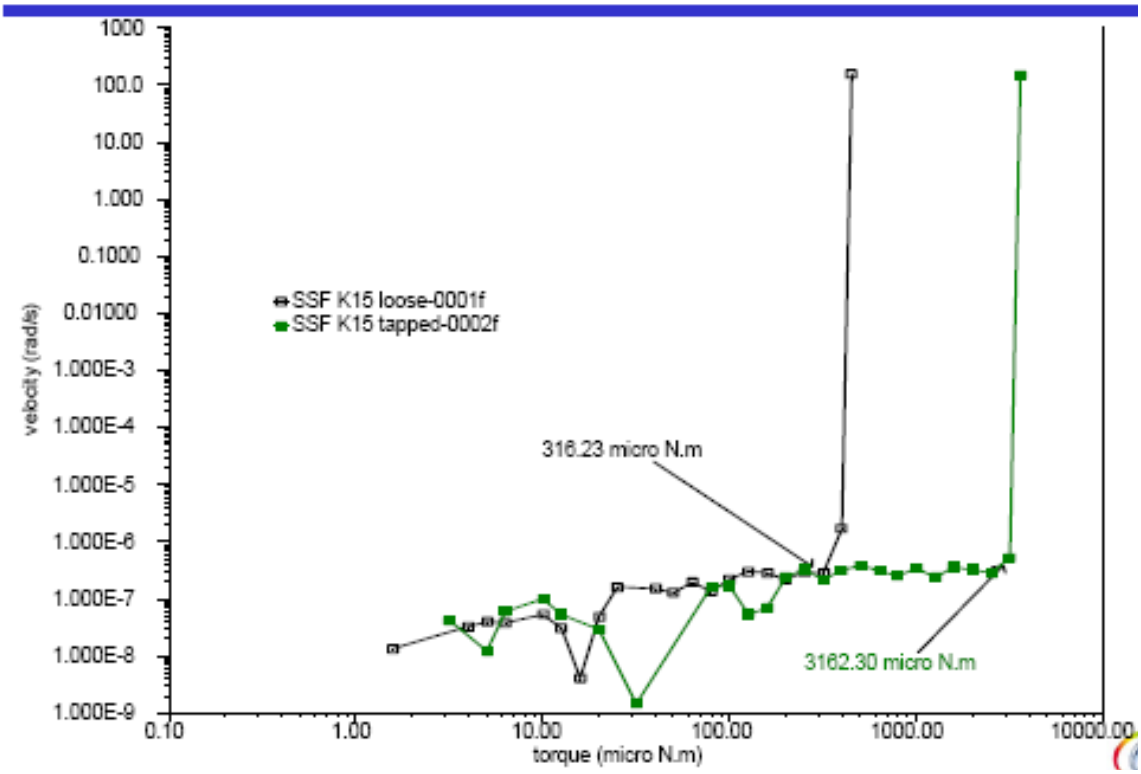

K1: Loose vs. Tapped

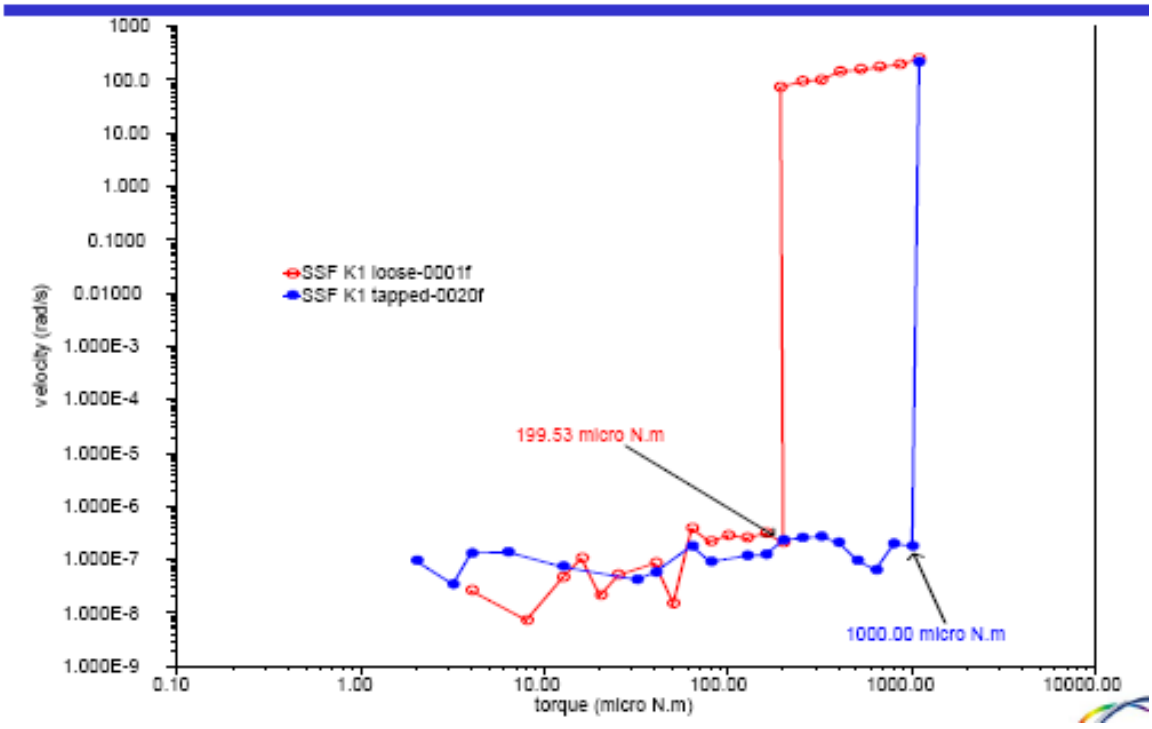

Unfortunately, the determination of traditional rheological parameters with a vane rotor configuration uses an approximation that has not been validated with particle media. Thus the utility is limited to direct comparisons and would be of questionable value in comparing to the previously measured crush strength.

Significant Interactions With NASA Staff

In addition to regular NASA review meetings, we had several meetings to present the work at every critical stage and ensure the work performed at FSEC has the right direction and meets KSC requirements. In addition to our presentations, we had a couple of meetings with KSC staff to discuss the best strategy, both technically and economically, to renovate the storage tanks.

Conclusions and Recommendations

The following conclusions and recommendations may be drawn from the above investigations:

- Simulation results using the 3-D mesh are comparable with measured data on temperature distribution and boiloff rates.
- Heat transfer coefficient at exterior surface plays an important role in determining surface temperature distribution. The cold spot above the void area can be detected by IR images at night only due to still air convection, while not detected during day time due to high convection.
- Boiloff rate is proportional to effective void interior surface equivalent emissivity and ambient conditions.
  - 20% due to ambient (from 275 to 325 K)
  - 40% with 34 ft^2 void at $\varepsilon = 0.5$, 200% with 170 ft^2 void at $\varepsilon = 0.5$
  - 10% from heat convection with a void (5 to 30 $W/m^2.K$)
  - The most important impact on boiloff rate is void size
- External insulation coverage may not be an effective method to reduce boiloff rate
  - 13% boiloff reduction at $\varepsilon = 0.1$ with 9 times external area coverage, compared at 28% without void
  - 22% boiloff reduction at $\varepsilon = 0.2$ with 9 times external area coverage, compared at 46% without void
- The anticipated decrease in microsphere crush strength in point to point contact, and the increase in yield stress to flow when compacted were physically observed and measured. The ability to directly compare the magnitude of one to the other was not possible due to approximations used in the yield stress to flow evaluation. The scope of the project did not allow further refinements to be made.
- The puzzling differences in thermal performance of the Pad A and B liquid hydrogen tanks is best explained by the development of an exposed area of the inner sphere which is not covered by perlite in Pad B. This thermal performance difference was noted immediately upon first usage of the tanks, and is most likely due to less efficient filling of the Pad B tank around the complex hydrogen vent line that is routed between the spheres. As a result of free flowing particulates, small voids may have formed near the pipe supports, then filled with subsequent launch vibrations, leaving more space at the top of the tank. In addition, the thermal contraction of the inner sphere generates a void at the top comprising 2% of the space between the spheres. With Pad B, this combination was significant enough to expose a small portion of the inner sphere. This is very consistent with the observed location of the thermal cost spot. This interpretation of

the thermal performance leads to the conclusion that the filling efficiency of the tank is a key aspect that must be controlled when the refurbishment of the tanks occurs.

- Mechanical support has big influence on boiloff rate. The heat loss consists of heat conduction through the stainless steel support with high thermal conductivity, and lateral heat transfer from surrounding perlite to cause higher temperature distribution. The magnitude from both heat losses is as twice as one with support conduction only.
- Changing surface absorptivity over the void may reduce boiloff rate, while changing surface emissivity over the void has little impact on the boiloff rate.
- Sky temperature in Florida climates may offer little benefit. Due to humid climates at KSC, the sky temperature is not low enough to have significant cooling impact.
- The best approach to reduce boiloff rate is to fix the void, so that boiloff rate can be reduced from 750 gal/day to 300 gal/day, instead of changing surface properties.
- The impact of the vent line on boiloff rate may be insignificant from detailed 3-D simulations, compared to other components, such as mechanical support and manhole.
- It is recommended that the minimum valve insulation level should be R = 10 when the valve surface temperature is above the freezing point. In order to have better insulation to keep heat losses independent of inlet flow rate, R = 30 is recommended.

Local Hydrogen Production via Catalytic Reformation of Fossil and Renewable Feedstocks

N. Muradov and F. Smith
Florida Solar Energy Center

Research Period: June 2002 to December 2007

Abstract

Economical, safety and other factors will potentially necessitate on-site manufacturing of liquid hydrogen at the NASA-KSC site. Currently, liquid hydrogen delivered to NASA-KSC is manufactured by steam methane reforming (SMR). The shortcomings of SMR relate to the production of considerable amounts of CO_2 emissions (which may become a serious problem in a carbon-restricted environment) and ever increasing cost of the natural gas (NG) feedstock. The objective of this project is to develop a process for local production of hydrogen from methane-containing, preferably, renewable feedstocks with minimal environmental impact.

In this project, analytical (AspenPlus™ chemical process simulator) and experimental studies on the development of two novel hydrogen production technologies were conducted, namely: (i) direct reforming of landfill gas (LFG) to syngas and its further processing to H_2, and (ii) catalytic pyrolysis (or decomposition) of methane to hydrogen and carbon. It was estimated that the local resources of LFG would be sufficient for production of 5 tons/day of hydrogen. The advantages of direct reforming of LFG is that it does not require preliminary recovery of methane from LFG, which simplifies the process and reduce the cost of hydrogen production. Efficient and stable catalysts for the direct reforming of LFG were developed and tested. A pilot scale unit with the capacity of 1 SCFM of H_2 was designed, fabricated and operated using CH_4:CO_2=1.3:1 mixture mimicking local (Cocoa) LFG composition. Techno-economic evaluation of the process using AspenPlus™ process simulator was conducted.

The advantage of the methane catalytic pyrolysis process is that it allows producing hydrogen and value-added byproduct: clean carbon without or minimal CO_2 emissions. Comprehensive catalyst and process development studies for the methane pyrolysis reaction were conducted. Since the process is moderately endothermic, the conditions at which the process operates in thermo-neutral regime were determined. Characterization and structural studies of carbon products of the process were conducted. Potential markets for carbon products were evaluated. The technical feasibility of converting citrus waste products (e.g., citrus pulp pellets, CPP) into high purity hydrogen with the yield of 0.55 L of H_2 per gram of CPP was demonstrated. The successful implementation of the above technologies would eliminate the necessity for costly and potentially unsafe transportation of liquid hydrogen from Louisiana-based hydrogen plant to the Central Florida.

Introduction

In view of ever-increasing prices for hydrocarbon fuels and their dwindling resources, it is imperative to find alternative, preferably, renewable sources of energy for power generation and production of transportation fuels, e.g., hydrogen, synthetic hydrocarbons, etc. Biomass-derived methane-containing gases such as landfill gas (LFG), biogas and digester gas are important resources for power generation and production of hydrogen. LFG is generated by natural degradation of municipal solid waste (MSW) by anaerobic microorganisms. Once the gas is

produced, it is collected by a collection system, which typically consists of a series of wells drilled into landfill and connected by pipelines. The advantages of using LFG as a source of energy and a feedstock are three-fold: (i) it is domestic energy resource, which can be used to offset petroleum imports, increasing our energy security, (ii) it can be obtained at little or no cost, thereby helping to decrease the end-use cost, and (iii) if not used, LFG can potentially create even more environmental damage than CO_2 alone, because methane is much more potent greenhouse gas than CO_2. Although the resources of LFG are vast and widely available throughout the country, they are mostly unused. According to a recent study, only small portion (330 out of 2100) landfill sites in the U.S. utilize LFG to generate heat or electricity, and over 500 landfills flare or burn the gas outright [1]. Of particular interest is the possibility of converting LFG (or other BMCG) to ecologically clean fuel-hydrogen. Despite the fact that extensive resources of these methane-containing gases are available, no large-scale commercial hydrogen production process has been implemented yet. In Florida, 59 landfills generate about 1.6mln m^3/day LFG (in methane equivalent) [2], which could yield up to 100,000 tons of hydrogen per year. Location and LFG capacities of landfills within 50 miles from NASA-KSC are shown in the Appendix.

LFG are complex gaseous mixtures containing methane and CO_2 as major components along with small amounts of N_2, H_2, CO, H_2S and a variety of organic components (e.g., non-methane hydrocarbons, alcohols, organic acids, esters) and S-, N-, Si-organic impurities. The composition of LFG varies drastically from one source to another, with methane concentration ranging from 40 to 80 vol.% (the balance being predominantly CO_2). Table 1 shows the composition of Cocoa, FL landfill gas.

Table 1. Composition of Cocoa landfill gas

Composition of Cocoa LFG (v.%):	
Methane	48.3
Carbon dioxide	37.1
Nitrogen	11.3
Oxygen	3.3
Hydrogen	<0.1
Hydrogen sulfide	<0.1
Carbon monoxide	<0.01
Ethylene	<0.01
Ethane	<0.01
Other hydrocarbons	<0.01
Heating value: 488.7 BTU/CF	

In principle, methane could be recovered from LFG using off-the-shelf technologies (e.g., cryogenic absorption, adsorption, membrane separation, etc.), and converted to hydrogen via steam methane reforming (SMR) process. It should be noted, however, that the separation of methane from BMCG is an energy intensive and costly process. Furthermore, in many cases this may not be economically and environmentally advantageous option, especially when the resources are not large enough or the sources are located in remote areas.

The main objective of the present research work is to develop a novel process for direct (i.e., without preliminary recovery of methane) processing of LFG to synthesis gas (or syngas) and further to hydrogen. This option is technologically more simple (since, no CH_4-CO_2 separation stage is required) and feedstock flexible and potentially more cost effective than other approaches. Another objective is to develop a process for catalytic pyrolysis of methane into hydrogen and value-added product carbon with minimal CO_2 emissions.

Background

Since LFG contain CH_4 and CO_2 as two predominant components, they could be processed to syngas according to a well-known reaction called CO_2 reforming of methane (also often called, "dry" reforming). This is a strongly endothermic reaction that is carried out catalytically at the temperature range of 800-950 °C and produces syngas with the H_2:CO molar ratio of 1:1 according to the following chemical equation:

$$CH_4 + CO_2 \rightarrow 2H_2 + 2CO \qquad \Delta H^o = 247 \text{ kJ/mol} \qquad (1)$$

Practical implementation of CO_2-reforming of methane faces several key challenges, both technical and economical. One of the most serious problems hindering the practical application of CO_2-reforming is the deactivation of metal catalysts due to deposition of carbon (or coke). Carbon formation could be attributed to two reactions: methane decomposition and CO disproportionation (or Boudouard reaction) (2):

$$2CO \rightarrow C + CO_2 \qquad \Delta H^o = -86.5 \text{ kJ/mol (CO)} \qquad (2)$$

From the practical viewpoint, it is preferable to operate CO_2-reforming of methane at moderate temperatures maintaining the CH_4:CO_2 ratio close to unity, which would require a catalyst that kinetically inhibits the carbon formation under conditions that are thermodynamically favorable for carbon deposition. The form of carbon deposited on metal surfaces is controlled by the reaction temperature: in the lower temperature range of 350-600 °C, amorphous and filamentous carbons are the predominant forms of carbon, whereas an ordered graphitic structure dominates at the temperatures above 700 °C [3].

With regard to catalytic reforming of LFG, the above technical difficulties are aggravated by two additional factors. The first factor relates to the presence of potentially harmful impurities (S-, N- Si- and halogen-containing compounds) that could easily deactivate catalysts used in the reforming process. In principle, these contaminants could be efficiently removed from LFG before the reforming stage using conventional technologies (e.g., selective adsorbents, scrubbers, etc.) [4]. The second complicating factor is concerned with a feedstock non-uniformity. Due to the fact that in the majority of BMCG sources, methane is the predominant component in the mixture (typically, [CH_4]= 55-65 vol.%), an undesirable and potentially detrimental methane decomposition reaction (2) may occur at the operating temperatures of the reforming process:

Iron-, cobalt- and nickel-based catalysts are known to be particularly active in methane decomposition reaction, and noticeable deposition of carbon on the surface of these catalysts occurs at temperatures as low as 350 °C. The product carbon (or coke) blocks active sites of the catalyst leading to its rapid deactivation. In principle, the deposition of coke could be prevented by: (i) using highly selective catalysts (i.e., catalysts that promote CO_2 reforming of methane, but suppress methane decomposition and/or CO disproportionation reactions), and/or

(ii) adding an oxidizing agent to the CH_4-CO_2 feedstock thus guarding the catalyst against coke formation.

Another technological approach to local hydrogen production explored in this work relates to catalytic pyrolysis of methane into hydrogen and value-added carbon products. In contrast to conventional processes, the significant part of the feedstock carbon will end up in the form of valuable carbon byproducts (activated carbon, pyrolytic graphite, carbon filaments) rather than CO_2. Marketing of carbon byproduct will reduce the net cost of hydrogen production. This approach will significantly expand the resources for local hydrogen production and allow a smooth transition from NG to local renewable feedstocks.

Benefits to NASA

The successful implementation of the above technologies would eliminate the necessity for costly and potentially unsafe transportation of liquid hydrogen from Louisiana-based hydrogen plant to the NASA-KSC site.

This report consists of two main sections:

A. Catalytic reforming of CH_4-CO_2 mixtures followed by water gas shift of syngas and separation of H_2-CO_2 mixture
B. Catalytic pyrolysis of methane to hydrogen-rich gas and value-added carbon products

Experimental

The premixed gaseous mixture with the composition of CH_4- 56.9, and CO_2- 43.1 vol.% (i.e., molar ratio of CH_4:CO_2 =1.32:1) was obtained from Holox Inc. and used as a baseline feedstock in all experiments. This particular CH_4/CO_2 ratio mimics that of the landfill gas produced by the local landfill in Cocoa, Florida. For the sake of simplicity, N_2, O_2, H_2S and other minor impurities were not included in the tested feedstock. Argon (99.999 vol.%) and oxygen (99.5 vol.%) (both from Air Products and Chemicals) were used in the experiments. Steam was produced from deionized water and introduced into the reactor using a precision syringe pump (Cole Palmer) and an evaporator. Ru (0.5 wt.%)/Al_2O_3, Pd (1 wt.%)/Al_2O_3, Pt (0.5 wt.%)/Al_2O_3 catalysts were obtained from Aldrich Chemical Co. Rh (5 wt.%)/Al_2O_3 was purchased from Strem Chemicals. Ir (1 wt.%)/Al_2O_3 and Ni(55-60 wt.%)/kieselguhr were obtained from Alfa Aesar. NiO (1-15 wt.%)/Al_2O_3 and NiO (25-45 wt.%) - Al_2O_3 (45-65 wt.%) - Ca aluminate (3-8 wt.%) were obtained from Süd-Chemie Inc. Fe-Cr-oxide catalyst containing 8-12 wt.% of Cr_2O_3 and small amounts of copper oxide was also obtained from Süd-Chemie Inc. Al_2O_3-supported Co (10 wt.%)-Mo (10 wt.%) oxide catalyst was synthesized according to the procedure described by Richardson [5]. The catalysts were used in the form of 10-18 mesh granules. A catalyst (0.5 g) was placed inside a quartz micro-reactor (O.D. = 1.2 cm) and purged with Ar at 600 °C for 1 hr before the experiments. The reactor temperature was controlled using a type K thermocouple and Love Controls temperature controller. All the experiments were conducted at the atmospheric pressure. The average residence time within the catalyst layer was about 1 s. The amount of carbon on the catalyst surface after the reforming experiments was determined by quantitatively combusting carbon in a stream of oxygen and measuring the amount of CO and CO_2 produced. The gaseous products of the reforming reaction were analyzed gas chromatographically using two SRI- 8610A GC-TCD instruments: the first gas chromatograph used Ar as a carrier gas and a silica gel packed column, and the second one used He and Hayesep D_B column.

Results and Discussion

Description of the Proposed Concept

Figure 1 depicts a simplified schematic diagram of the proposed concept that utilizes NG, LFG and citrus waste. Based on the information provided by the Cocoa landfill facility management we estimated that the LFG resources from the facility would be adequate for the production of about 5 ton/day of hydrogen for the next 50 years. According to the proposed concept, the on-site production of liquid hydrogen could be realized via two technological options (or their combination).

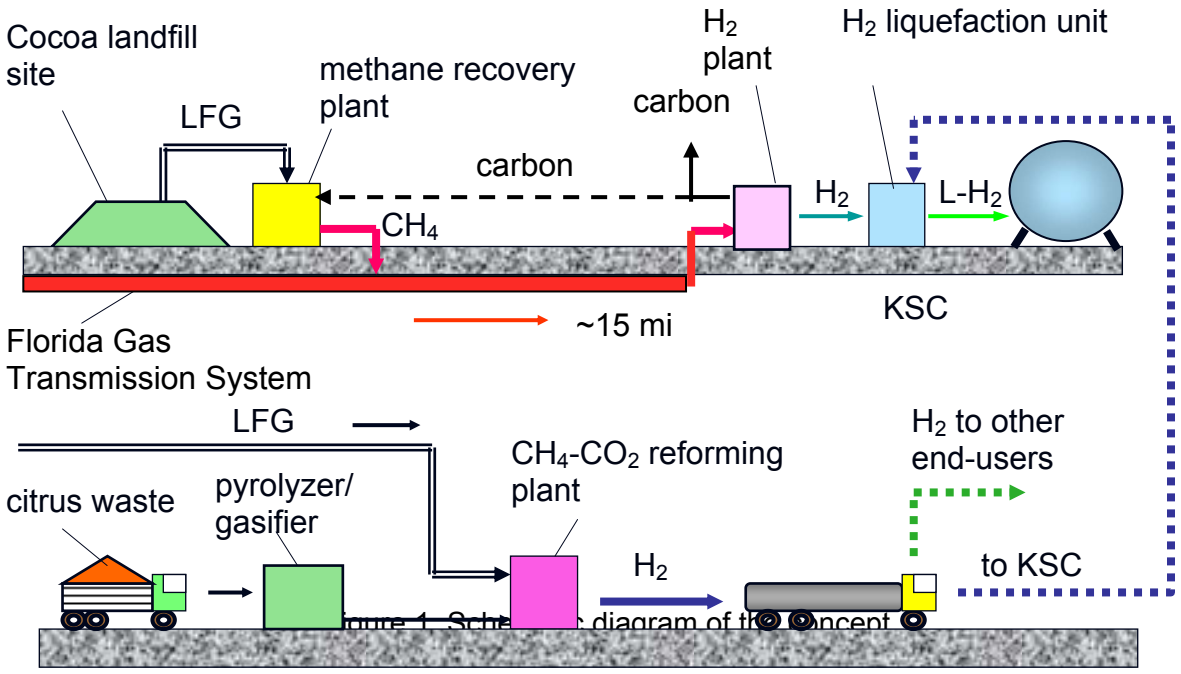

In the Option 1 (upper section of Figure 1), methane is separated from CO_2 at the LFG treatment plant and pumped into the Florida Gas Transmission System (which is in a short distance from the landfill site). Methane (in mixture with NG) is delivered to KSC site (the distance of approximately 15 miles), where it is pyrolyzed into hydrogen and carbon. Hydrogen is liquefied and stored for the use in the Space Shuttle program. Carbon could be marketed, thus reducing the net cost of hydrogen production.

According to the Option 2 (lower section of Figure 2), LFG is purified of sulfurous and siloxane impurities and directly reformed into the synthesis gas (H_2-CO mixture of about equimolar composition). The synthesis gas is further conditioned and purified into hydrogen gas that is directed to a hydrogen liquefaction unit. The advantage of this approach is that it obviates the need for the expensive and energy intensive preliminary CO_2 separation stage. Another advantage relates to the possibility of co-processing of other renewable feedstocks such as biogas, or the producer gas from biomass (e.g., citrus waste) pyrolysis/gasification unit.

Hydrogen Production via Catalytic Reforming of CH_4-CO_2 Mixtures Mimicking LFG

Thermodynamic analysis of CH_4-CO_2 and CH_4-CO_2- O_2 reforming—Aspen Technology's AspenPlus™ chemical process simulation (CPS) platform was used to determine equilibria of CH_4-CO_2 and CH_4-CO_2-O_2 mixtures. The reforming reactions were modeled using a Gibbs reactor minimizing the free energies in order to calculate the conversion rates at given operating conditions. Figure 2 depicts the equilibrium concentrations of reaction products produced from CH_4-CO_2 (1.3°:1 mol/mol) mixture at the temperature range of 300-1000 °C and 1 atm pressure. It is evident from the Figure 2 that H_2/CO molar ratio is greater than 1 and that elemental carbon is present in the mix of products in the entire range of temperatures examined. Both facts point to the contribution of methane decomposition reaction (3). Potentially, carbon product may lay down on the catalyst surface and deactivate it. The production of carbon can be prevented by adding an oxidant, such as CO_2, steam or oxygen, to the reacting mixture. The use of oxygen may present an additional benefit of providing the heat input to the process, namely, it allows arranging the process in a thermoneutral regime.

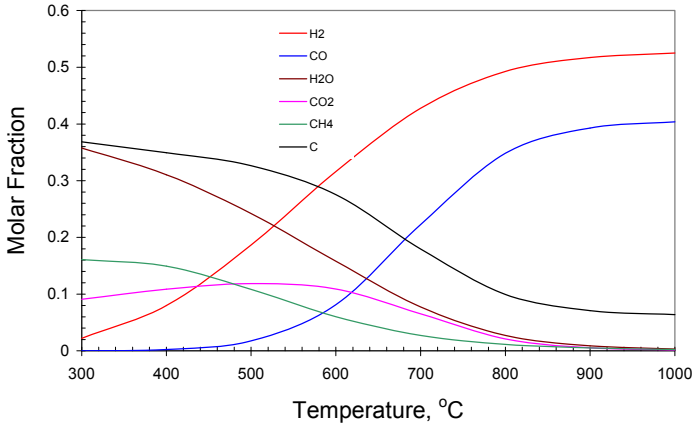

Figure 2. Thermodynamic equilibrium composition of CH_4:CO_2 (1.3°:1 molar) mix.

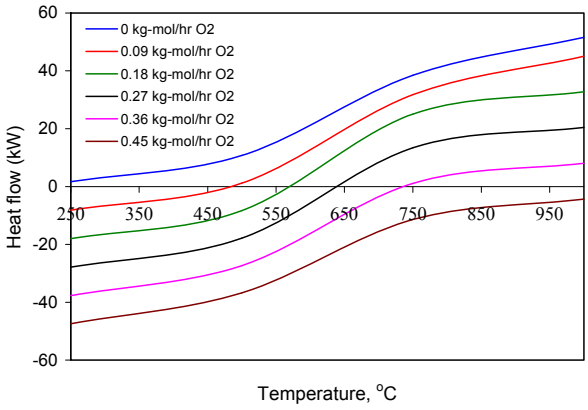

Figure 3. Heat flow as a function of T and amount of O_2. Feedstock: CH_4-0.59 kg-mol/hr, CO_2-0.45 kg-mol/hr (25 °C. 1 atm).

We conducted AspenPlus™ simulation studies to determine the amount of oxygen to be added to the CH_4:CO_2 (1.3:1 molar) mixture in order to carry out the reforming process in an autothermal (or thermoneutral) regime at the practical range of temperatures. Figure 3 depicts the heat flow into the reactor as a function of the amount of oxygen in the feed and the process temperature. Each curve corresponds to a certain amount of O_2 introduced into the reactor; the curves intersect X-axis at a certain temperature corresponding to the conditions of thermo-neutrality. We selected the temperature of 850 °C as a baseline temperature for the CH_4-CO_2 reforming process. The data show that at this temperature and pressure the condition of thermo-neutrality in the reactor can be reached at O_2:CH_4 = 0.675 (mol/mol).

Figures 4 depicts AspenPlus™ thermodynamic equilibrium simulation of the products distribution obtained from the mixture CH_4:CO_2:O_2 = 1.3:1.0:0.9 (molar) as a function of temperature (note, that in this mixture O_2:CH_4 molar ratio is 0.69). The comparison of Figures 4 and 2 indicates that the addition of oxygen diminished the yield of hydrogen and increased the yield of water (which could be expected). Hydrogen yield reaches its maximum at about 720 °C and slightly drops at higher temperatures. CO yield was also reduced, but to a lesser extent compared to H_2. Most importantly, the carbon disappears among the reaction products at temperatures above 700 °C.

Figure 5 depicts molar distribution of products obtained from CH_4-CO_2-O_2 mixture at 850 °C and 1 atm as a function of O_2:CH_4 ratio in the mixture. With the increase in O_2:CH_4 ratio, hydrogen molar fraction monotonously drops from about 0.5 to 0.35, whereas CO fraction reaches maximum at O_2:CH_4 = 0.17 and then drops. CO_2 and H_2O yields monotonously increase with the increase in O_2:CH_4 ratio (in particular, at O_2:CH_4 >0.15). Carbon molar fraction drastically drops to almost zero before O_2:CH_4 ratio reaches 0.3. Methane yield is also reduced with the increase in O_2:CH_4 ratio, and methane practically disappears at the ratio of O_2:CH_4 = 0.6. Thus, it can be concluded that the thermo-neutrality condition for CH_4-CO_2 reforming process can be reached at O_2:CH_4 ≈ 0.7 (at 850 °C, 1 atm); however, at these operational conditions hydrogen yield would drop by almost 30% compared to O_2-free process.

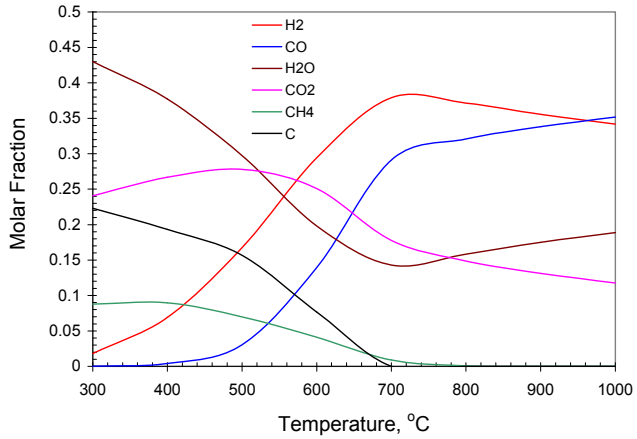

Figure 4. Thermodynamic equilibrium composition of CH_4:CO_2:O_2= 1.3:1.0:0.9 (molar) mixture as a function of temperature at 1 atm.

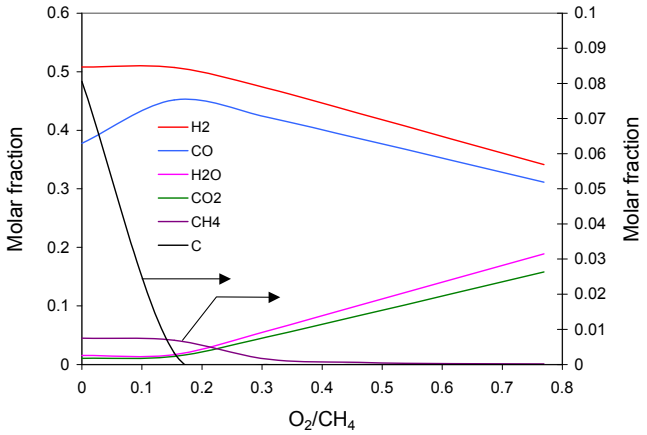

Figure 5. Thermodynamic equilibrium composition of CH_4:CO_2:O_2 = 1.3:1:x (molar) mixture at 850 °C and 1 atm as a function of O_2 to methane molar ratio.

Catalyst Development for Catalytic Reforming of CH_4-CO_2 Mixture—We have conducted a series of experiments on catalytic reformation of CH_4-CO_2 (56.9-43.1 vol.%), which mimicks the composition of LFG). For the sake of simplicity, N_2, H_2S and other minor ingredients of LFG were not included in the tested feedstock. Figure 6 depicts the experimental data for catalytic reformation of CH_4-CO_2 mixture at 850 °C and atmospheric pressure over alumina-supported Ru (left) and Ni (right) catalysts at 850 °C.

It is evident from Figures 6 (left) that Ru-catalyzed process reached a steady state in about an hour with H_2 and CO concentrations being almost equal. In case of Ni-catalyst, the hydrogen yield and CO_2 conversion gradually diminished over the time of the experiment, which points to

the deactivation of the Ni catalyst. The analysis of the catalyst after the reforming reaction indicated the presence of carbon deposits on its surface. Figure 7 summarizes the data on the activity and selectivity of the tested catalysts for CH_4-CO_2 reforming. The measure of activity of the catalysts is determined by the extent of CO_2 conversion during the steady state reforming reaction (using CH_4 conversion for this purpose could be misleading, because CH_4 could also participate in the dissociation reaction). The measure of the catalyst selectivity toward CH_4-CO_2 reforming reaction is determined by the quantity of carbon deposited on the catalyst surface: lesser is the amount of carbon (which is proportional to the methane dissociation yield), higher is the catalyst selectivity for CH_4-CO_2 reforming reaction. It can be seen from the Figure 7 that Ru-, Ir- and Pt-based catalysts demonstrated both high activity and selectivity for CO_2 reforming of methane. Practically no carbon was detected on the surface of these catalysts. On the other hand, Pd- and Rh-catalysts, although featuring high activity in the reforming reaction showed some minor activity in methane decomposition reaction.

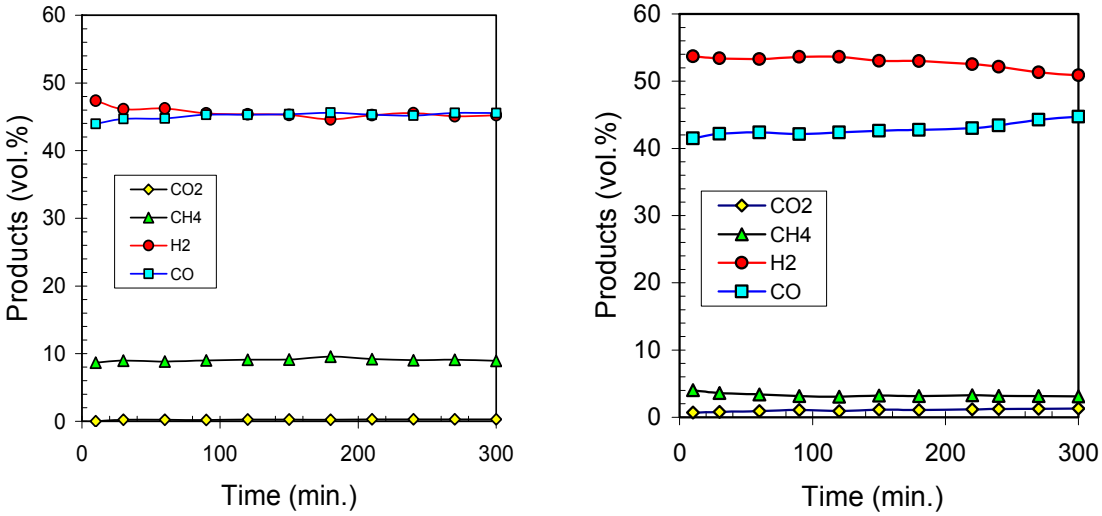

Figure 6. Catalytic reforming of CH_4-CO_2 (56.9-43.1 vol.%) mixture over Ru (0.5 wt.%) /Al_2O_3 (left) and NiO(1-15 wt.%)/Al_2O_3 catalysts at 850 °C.

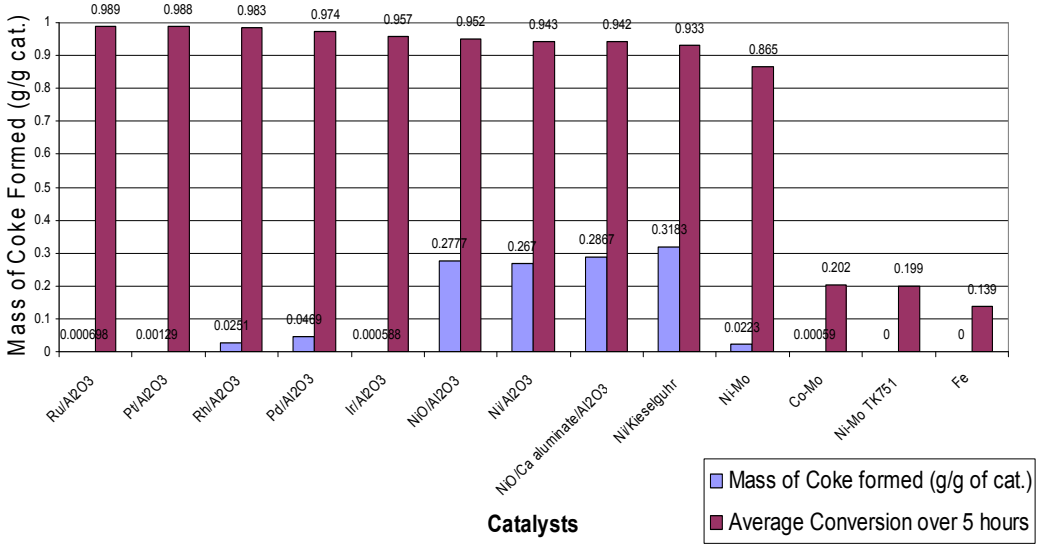

Figure 7. Comparative assessment of different catalysts for catalytic reforming of CH_4-CO_2 mixture.

All Ni-based catalysts were active in both CO_2 reforming and CH_4 decomposition reactions, thus, demonstrating very poor selectivity for CH_4-CO_2 reforming reaction. These catalysts produced significant quantities of carbon deposits, which adversely affected their catalytic activity. For the sake of comparison, we also tested Fe-Cr oxide and Co-Mo oxide catalysts in CH_4-CO_2 reforming reaction (it was reported recently that silica-alumina supported Co catalysts showed high activity in CO_2 reforming of methane [6]). Neither of these catalysts showed adequate catalytic activity for the reforming reaction in operating conditions similar to those of Ni-catalysts. All the transition metal catalysts tested could be arranged according to their activity for CO_2 reforming reaction (at 850 °C) in the following order[1]:

Ru > Pt > Rh > Pd > Ir > Ni >> Co-Mo > Fe-Cr

The order of selectivity toward CO_2 reforming of methane (850 °C) is as follows:

Ru ≈ Ir > Pt > Rh > Pd >> Ni

It is interesting to compare the experimental data for Ru- and Ni-catalyzed reforming reactions with the results of the thermodynamic equilibrium analysis of the CH_4:CO_2=1.3:1 mixture (see Figure 2). It is evident that the simulation data are more consistent with the results of Ni-catalyzed CH_4-CO_2 reforming (particularly, at the onset of the experiment), compared to Ru-catalyzed reaction. This is an indication of high catalytic activity of Ni-catalyst for both CH_4-CO_2 reforming and methane decomposition reactions. In contrast, Ru-catalyst demonstrates high activity only for CH_4-CO_2 reforming reaction and practically no activity for the methane decomposition reaction. From the practical viewpoint, Ru and other noble metal catalysts are rather expensive and unlikely to be used in large-scale commercial production of syngas via catalytic reforming of BMCG. Ni-based catalysts are more affordable and are widely used in commercial hydrogen production units, e.g., steam methane reforming process. Thus, it would be advantageous from practical and economical viewpoints to develop a sustainable process for direct catalytic reforming of BMCG using inexpensive Ni-catalysts.

***Catalytic Reforming of CH_4-CO_2-O_2 Mixtures in Autothermal Regime*—**In this section we studied the effect of adding oxygen to the feedstock. The objectives were twofold:

1) To provide heat input to the reactor
2) To obviate the catalyst deactivation problem.

We conducted a series of experiments on autothermal catalytic reforming of CH_4-CO_2-O_2 mixtures over Ni/alumina catalyst using a bench-scale and a pilot-scale (1 SCFM) units.

Bench-scale experiments were conducted using a quartz reactor (OD = 10 mm). It was found that the addition of oxygen to the feedstock significantly decreased the amount of carbon deposit. Figures 8 and 9 show the effect of oxygen on the amount of carbon deposited on the catalyst surface and the distribution of reforming products. The important conclusion that can be drawn from the Figures 8 and 9 is that carbon practically disappears from the catalyst surface at the molar ratio of O_2:CH_4 ≈ 0.2 and higher. It is interesting to compare the experimental results with the AspenPlus™ simulation data on the reforming of CH_4:CO_2:O_2 mixtures.

[1] It should be noted that this is an apparent (or relative) order of activity (since metal content in the catalysts differs)

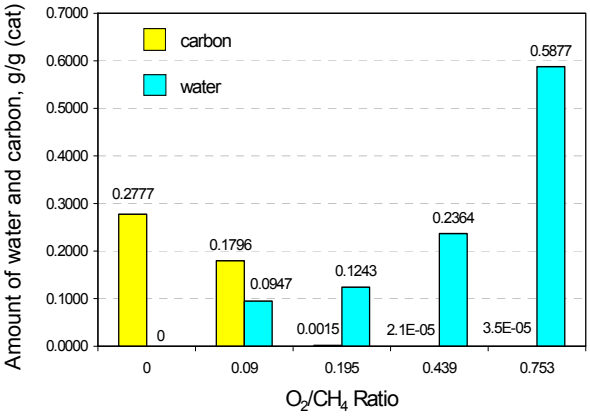

Figure 8. Amounts of carbon and water produced during reforming of CH_4:CO_2:O_2=1.3:1:x (molar) mixture at 850 °C and 1 atm over Ni-catalyst as a function of O_2:CH_4 molar ratio in the feedstock. Time: 5 hrs.

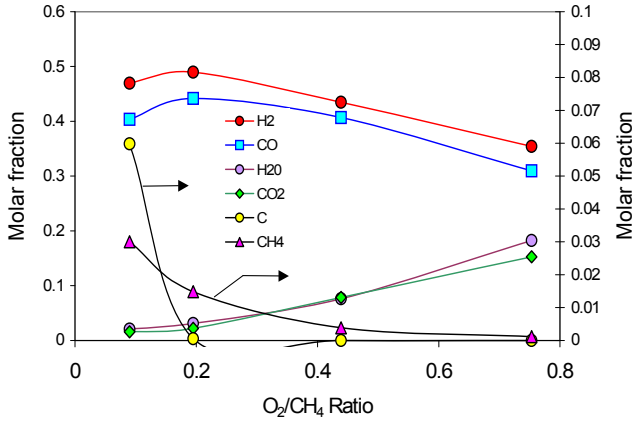

Figure 9. Molar distribution of products of CH_4:CO_2:O_2=1.3:1:x (molar) reforming at 850 °C and 1 atm over Ni-catalyst as a function of O_2:CH_4 ratio in the feedstock.

The comparison of Figures 5 and 9 indicates that there is a good agreement between experimental and predicted values for the molar fractions of the reforming products. Thus the experiments demonstrated that the addition of oxygen to the CH_4-CO_2 feedstock improved long-term stability of Ni-catalyst by preventing carbon build-up on its surface.

Experimental Validation of Catalytic Reforming of CH_4-CO_2 and CH_4-CO_2-O_2 Feedstocks Using Pilot-Scale Unit with the Capacity of 1 SCFM Unit—Figure 10 depicts the schematics of the laboratory scale unit used for hydrogen production via catalytic reforming of CH_4-CO_2-O_2 gaseous mixtures. The experimental unit consists of the following main sub-systems: (i) metering and delivery of gaseous feedstocks, (ii) catalytic reformer, (iii) gas conditioning (including low and high temperature WGS reactors, (iv) hydrogen recovery and purification, and (v) analytical sub-system. Figure 11 shows hydrogen production unit with the capacity of 1 SCFM at FSEC's Hydrogen R&D lab.

In the first series of experiments, we introduced different amounts of oxygen to the reforming reactor along with the CH_4-CO_2 (56.9-43.1 vol.%) feedstock and measured the temperature within the reactor. Initial test was performed to determine the affect of O_2/CH_4 ratio on the internal reactor temperature. It was found that as the ratio of O_2/CH_4 increases, the temperature changes in direct proportionality. This trend shows the endothermic nature of dry reforming reaction, and the relationship between the amount of O_2 necessary for partial oxidation and combustion chemistries and reactor temperature. Thus, the reforming reactor temperature could be controlled by the flow rate of O_2. According to Aspen simulation data (see section 4.2.1), the thermo-neutrality condition could be achieved at O_2/CH_4 ratio of 0.7. It was demonstrated that at the O_2/CH_4=0.7 ratio the reactor temperature can be maintained at the level of 850 °C. It is evident that there is a good agreement between simulation and experimental data.

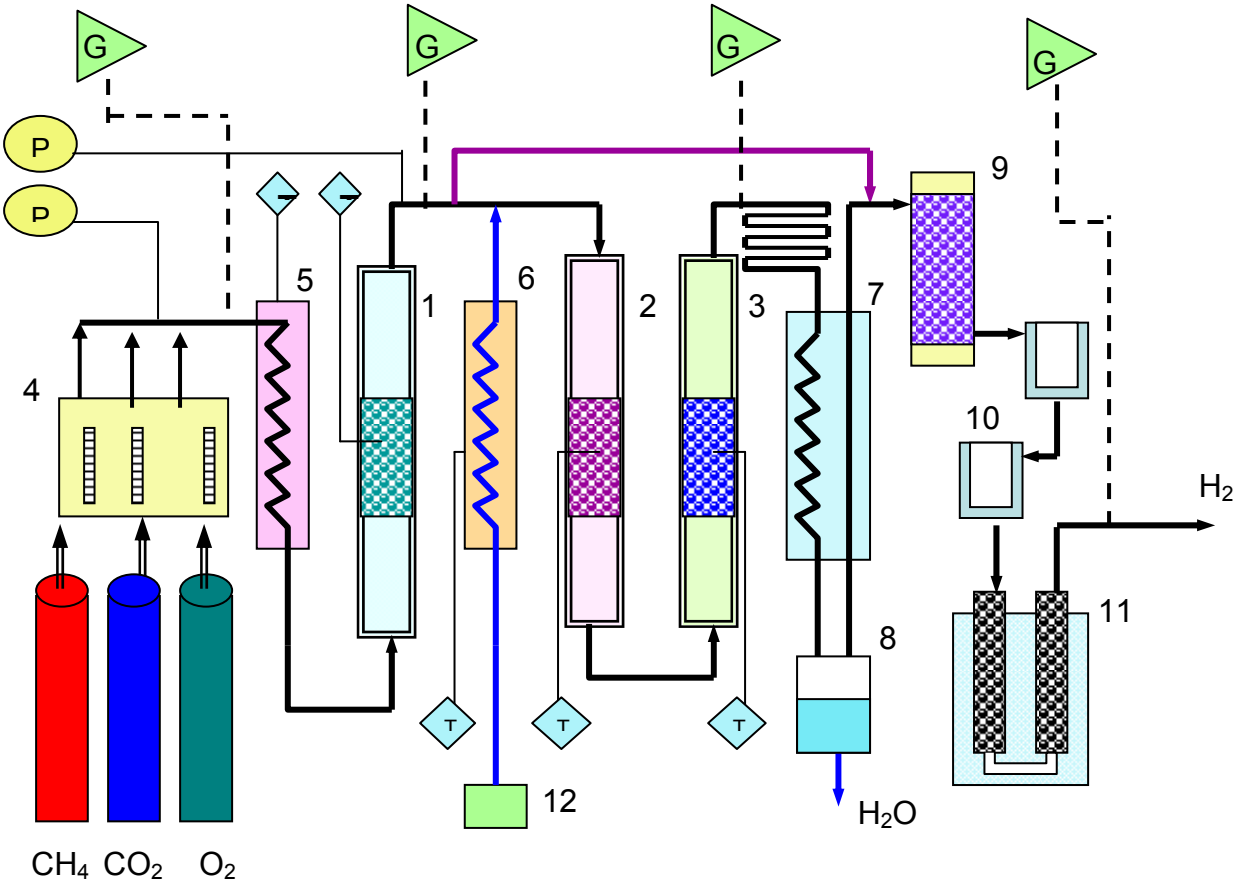

Figure 10. Schematics of experimental unit for H_2 production via catalytic reforming of CH_4-CO_2-O_2 gaseous mixtures (1- reactor (reformer), 2- high temperature WGS reactor, 3- low temperature WGS reactor, 4- gas metering system, 5- pre-heater, 6- steam generator, 7- condenser, 8- water collector, 9- adsorbent, 10- cryo-trap, 11- cryogenic adsorption system, 12- water pump. G denotes points where gas was withdrawn for GC analysis, T- temperature controllers, P- pressure gauges).

Figure 11. Hydrogen production unit with the capacity of 1 SCFM.

The following outlines the results of the initial testing of the pilot scale unit. In the first series of testing experiment the unit was operated at a half capacity. The feed flow rate was 13.5 SLPM; with mole fractions of CH_4, CO_2, and O_2 equal to 0.37, 0.37, and 0.26 respectively. Figure 12 illustrates product concentrations after the reforming reactor over a 7-hr period. The relatively high CO_2 yield may point to excessive combustion of methane occurring in the reformer. Improved mixing before the reactor should obviate this problem and reduce the level of CO_2 in syngas.

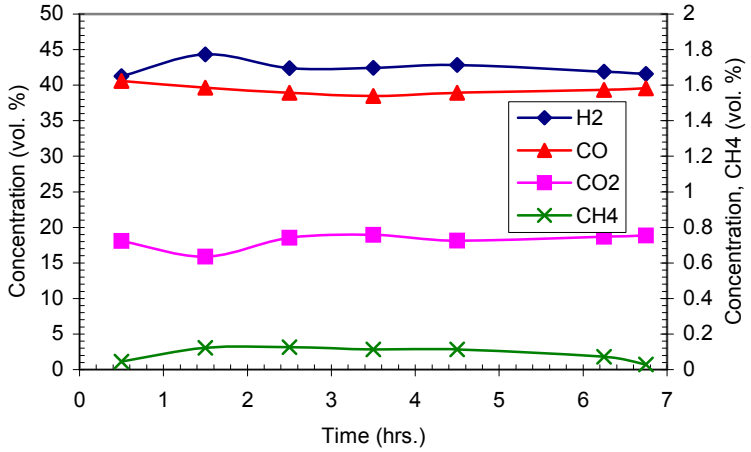

Figure 12. Reforming reactor product poncentrations over a 7-hr period.

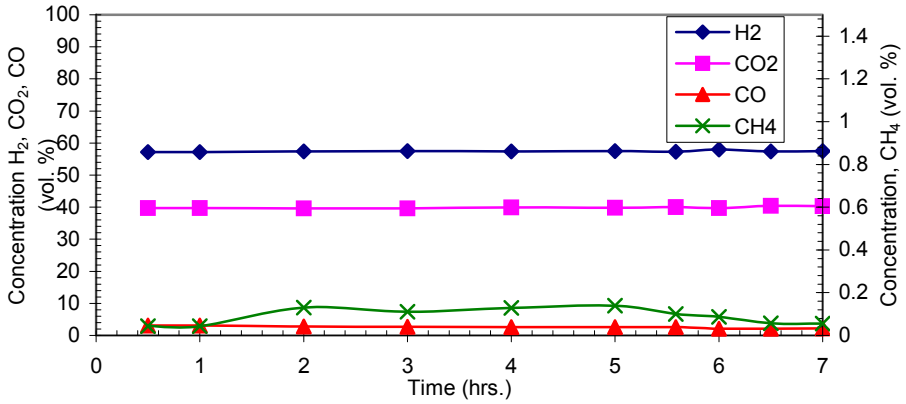

Figure 13. Composition of products of high-temperature water gas shift reaction using the effluent gas after the catalytic reformer as a feedstock.

The syn-gas produced was directed to two-stage WGS reactors. Figure 13 shows product concentrations after WGS. CO concentration decreased from 40% to approximately 2%. This shows that high-temperature WGS (HT-WGS) reactor performs adequately, whereas the low temperature WGS (LT-WGS) reactor still needs to improve its performance. It was found that the performance of LT-WGS reactor could be noticeably improved by adding more steam to the feedstock. A 24% increase in the steam flowrate resulted in 1 vol.% drop in CO concentration after LT-WGS reactor. 1 vol.% may seem to be insignificant, but one should take into consideration that at smaller CO percentages it is increasingly difficult to convert it into CO_2 in the presence of large amounts of CO_2 in the feedstock.

The reforming reactor was operated at the system capacity of 23 SLPM (in H_2 equivalent) (which is close to the unit's full capacity of 1 SCFM). Figure 14 shows the concentration profile of syngas produced over a 13-hr period (i.e., two days of operation). As in the previous experiment the feedstock composition was CH_4-CO_2 (56.9-43.1 vol.%), O_2:CH_4=0.7 (by volume), temperature 850 °C and Ni-catalyst.

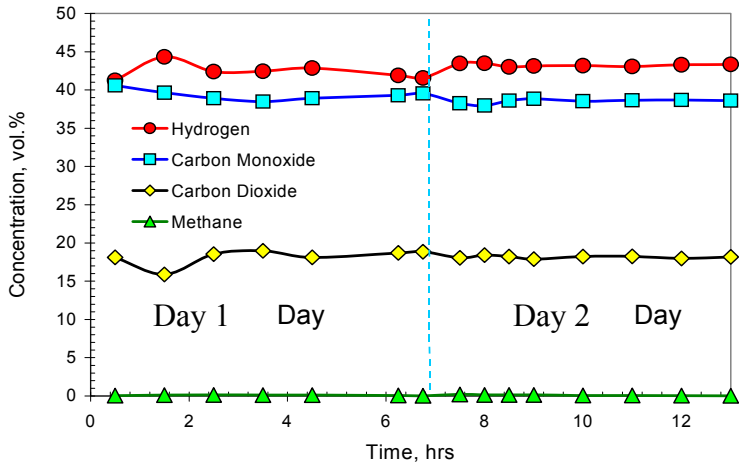

Figure 14. Reforming of CH_4-CO_2-O_2 (1.3 :1 :0.9 mol) at 850 °C over Ni-catalyst.

It is evident that no apparent catalyst deactivation occurred during the two-days long experiment (longer experiments are now in progress). The average concentrations of H_2, CO and CO_2 in the effluent gas (after the reformer) were 43, 39, and 18 vol.%, respectively. Thus, the products composition is in fairly good agreement with the equilibrium composition of the reacting mixture, which is an indication of good activity of the catalyst. Techno-economic evaluation of hydrogen production by catalytic reforming of LFG is included in the Appendix B.

Catalytic Pyrolysis of Methane

Currently, most of the industrial hydrogen production is based on steam methane reforming (SMR) process, which is a source of significant CO_2 emissions into the atmosphere. A typical hydrogen plant with the capacity of one million m^3 of hydrogen per day produces 0.3-0.4 million standard cubic meters of CO_2 per day, which is normally vented into the atmosphere. Different options to mitigate the CO_2 emission problem associated with fossil-based hydrogen production are being actively discussed in the literature (e.g., [7]). One approach that recently attracted the

attention of researchers is CO_2-free production of hydrogen by thermal decomposition (or pyrolysis) of methane [8-10]:

$$CH_4 \rightarrow C + 2H_2 \qquad \Delta H^o = 75.6 \text{ kJ/mole} \qquad (3)$$

Due to very strong C-H bonds methane decomposition occurs at elevated temperatures (>1000 °C). Different transition metal catalysts (e.g., Ni, Fe, Co, Pd) have been used to reduce the maximum temperature of methane thermal decomposition. The major problems associated with the use of metal catalysts relate to a catalyst deactivation (due to blocking of active sites by the carbon deposits) and technical difficulties with catalyst-carbon separation. The use of carbon-based catalysts offers some advantages over metal catalysts due to their availability, durability and low cost. In contrast to metal-based catalysts, carbon catalysts are sulfur resistant and can withstand much higher temperatures (in excess of 1000 °C). Furthermore, there will be no need for the separation of a carbon product from the catalyst. The technical feasibility of using carbon materials as catalysts for methane decomposition reaction is discussed in several publications (e.g., [11]). The concept is based on thermocatalytic decomposition (TCD) of methane over catalytically active carbon particles with the production of hydrogen-rich gas and carbon deposited on the surface of original carbon particles. The data on catalytic activity of a variety of carbon materials of different origin and structure, including a wide range of activated carbons, carbon blacks, micro-crystalline graphites, nanostructured carbons,, toward methane decomposition reaction is reported in [12].

Consideration of Heat Input Options for Methane Pyrolysis Process—Methane decomposition is a moderately endothermic reaction: the thermal energy requirement per mole of hydrogen produced is only 37.8 kJ/mole H_2 compared to 63 kJ/mole for SMR. Less than 10% of the methane heating value is needed to drive the endothermic process. Figure 15 (A, B, and C) illustrates three possible technological concepts of heat supply to the TCD process.

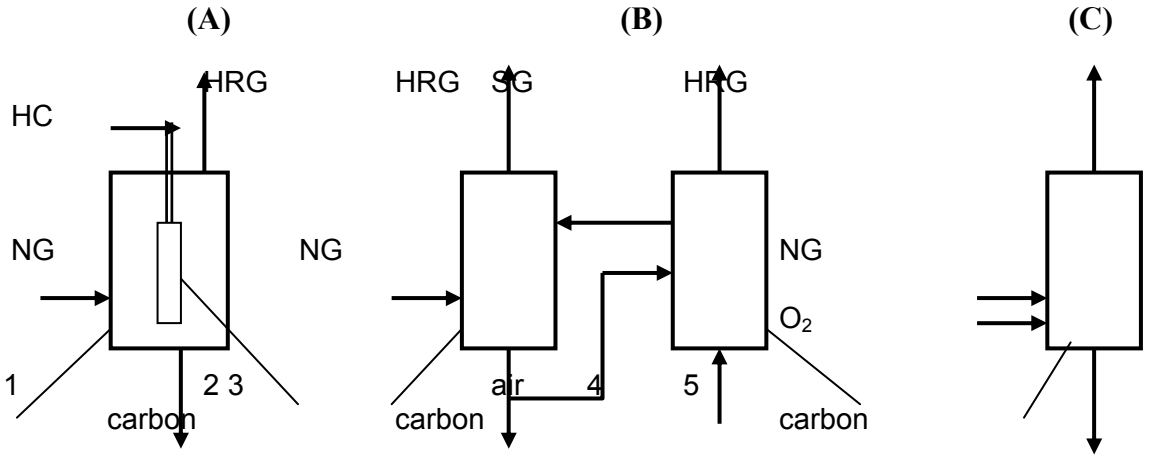

Figure 15. Three process heat input options for catalytic pyrolysis of methane. HRG-Hydrogen-Rich Gas, SG- Stack Gases, HC- Heat Carrier (1- methane decomposition reactor, 2- reactor heater, 3- fluidized bed reactor, 4-catalyst particles heater, 5-autothermal reactor).

According to the option (A) the heat source is located inside the reaction zone. It could be a heat pipe, a heat exchanger or a catalytic burner that uses NG or a portion of hydrogen product as a fuel. In the first two cases the heat source could be located outside the reactor with heat carried to the reactor by a heat carrier, e.g., liquid metals. As an example of this approach, sodium-based heat pipes have been used as a mode of efficient heat transfer in methane steam reformers [13]. In the concept (B), the process heat is introduced to the reactor by means of externally heated catalyst particles acting as a heat carrier (similar to fluid catalytic cracking process widely used in refineries). The process employs two fluid-solids vessels: a reactor and a heater with carbon particles circulating between the vessels in a fluidized state. Catalyst particles are heated (e.g., by burning part of carbon product or by hot combustion gases) and carry the necessary heat to the reactor to achieve NG decomposition. This technological concept has been described in our earlier publications (e.g., [7]).

According to the concept (C), a relatively small amount of oxygen is fed to the reactor along with the methane feedstock to generate necessary heat to carry out the endothermic methane decomposition reaction. One can notice that the concept looks similar to a well-known partial oxidation (POx) process. There is, however, a fundamental disparity between the two processes. In particular, POx process carries out the conversion of methane into synthesis gas and, therefore, it requires relatively large amount of oxygen (normally, $O_2/CH_4 \geq 0.5$). In contrast, the objective of oxygen-assisted methane decomposition is to maximize the yields of both hydrogen and carbon products by introducing oxygen in the quantity just enough to sustain the endothermic methane decomposition reaction. We call this process “autothermal pyrolysis” (ATP) since it involves the combination of an exothermic (methane oxidation) and endothermic (methane pyrolysis) reactions in one apparatus (similar to autothermal reforming, ATR, where methane oxidation is coupled with SMR). It is evident that this approach would use much less oxygen than ATR or POx, since methane decomposition is almost three times less endothermic (per mole of methane) than SMR, and the reaction does not advance to synthesis gas as a final product. As a result, CO_2 emissions from the process would also be significantly less than from ATR and POx. Advantageously, in ATP process most of the feedstock carbon ends up in the form of elemental carbon rather than CO_2. In this paper we explore some process development issues related to the production of hydrogen and carbon by ATP of methane. In particular, we conduct the thermodynamic analysis of ATP of methane in a wide range of temperatures and pressures with O_2/CH_4 ratio as a variable.

Thermodynamic Analysis of Autothermal Pyrolysis of Methane—AspenPlus™ chemical process simulator (CPS) was used to conduct thermodynamic analysis of CH_4-χO_2 system. The reactions involved were modeled using a Gibbs reactor to minimize the free energy in order to calculate thermodynamic parameters of the process at the given operating conditions. Input parameters are: a feed (CH_4-χO_2) composition, inlet pressure and temperature, and reactor temperature and pressure. Peng-Robinson property package was used for the reaction equilibrium calculations. Methane conversion, products yield, pyrolysis gas composition, process enthalpy, entropy and Gibbs energy flows as a function of temperature, pressure and O_2/CH_4 ratio (χ) have been determined. The temperature range of 300÷1200 °C, the pressure range of 0.2÷2.5 MPa and O_2/CH_4 ratio of χ= 0÷1.5 (mol./mol.) were chosen for the thermodynamic analysis of the process. The following Figures illustrate the results of the analysis.

Figure 16 depicts 3D plots of methane conversion as a function of temperature and O_2/CH_4 ratio at two baseline pressures: P = 200 kPa and 2.5 MPa. It is evident from Figure 16 that in both cases methane conversion increases drastically with the increase in both T and χ. For example, at P = 200 kPa, T = 850 °C and relatively low O_2/CH_4 ratios ($\chi \leq 0.2$) methane conversion reaches up to 90%. At P = 2.5 MPa (with the rest of parameters being equal), methane conversion is below 60%, which indicates that the process is not favored by elevated pressures.

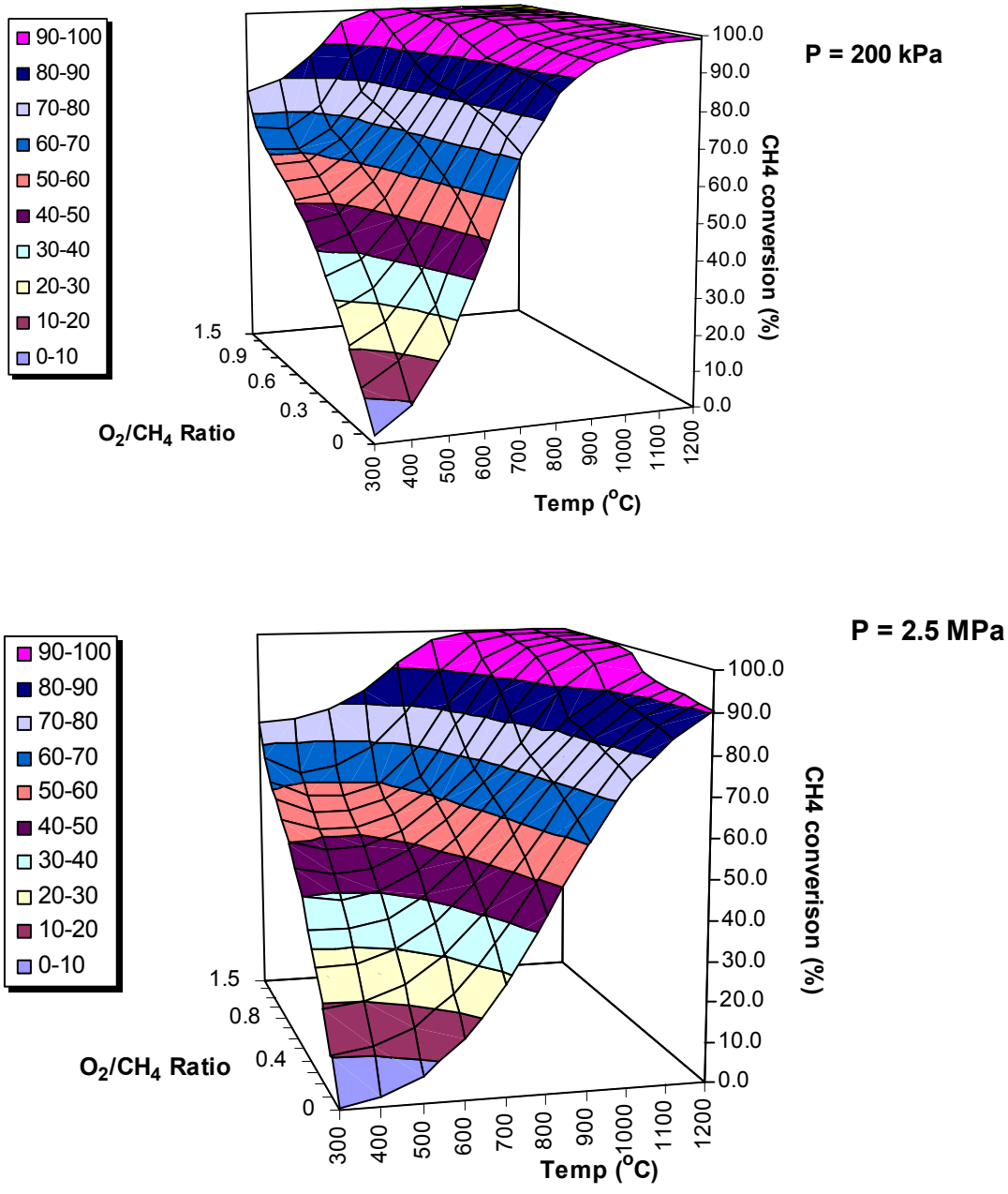

Figure 16. Methane conversion as a function of temperature and O_2/CH_4 ratio at P = 200 kPa and 2.5 MPa.

Figure 17 and 18 depict the temperature dependence of hydrogen and carbon yields at P = 200 kPa and different O_2/CH_4 ratios.

Figure 17 indicates that the hydrogen yield is not appreciably affected by the O_2/CH_4 ratio at $0<\chi<0.5$ in the entire range of temperatures. At $\chi>0.5$ hydrogen yield drops markedly, which is accompanied with the increase in water production yield. In contrast, carbon yield (Figure 18) is quite sensitive to even slight increase in χ value in a whole range of O_2/CH_4 ratios. At $\chi>0.6$ carbon is not present among the reaction products at ≥800 °C.

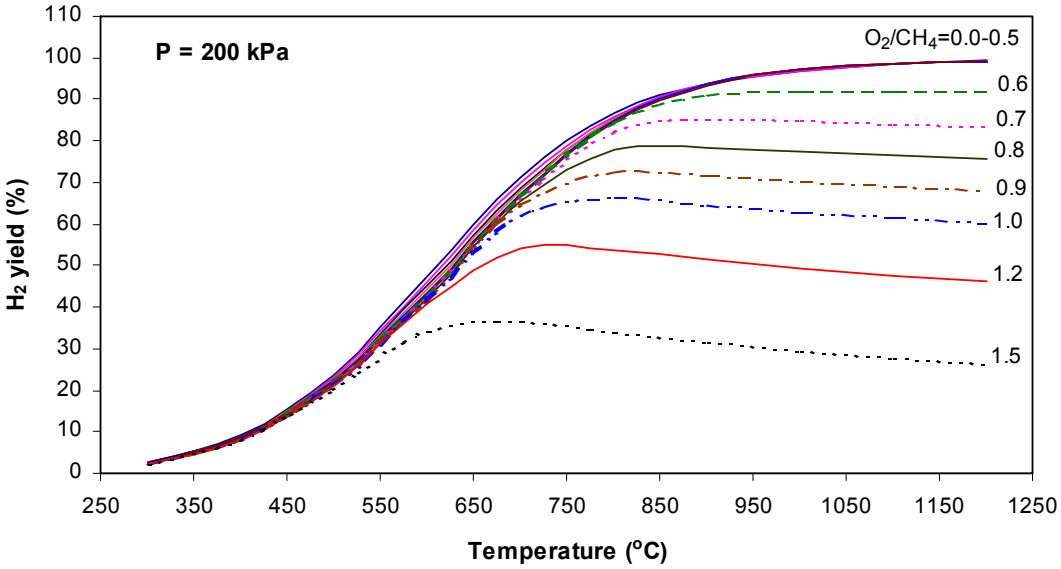

Figure 17. Temperature dependence of hydrogen yield with O_2/CH_4 ratio as a variable at P = 200 kPa.

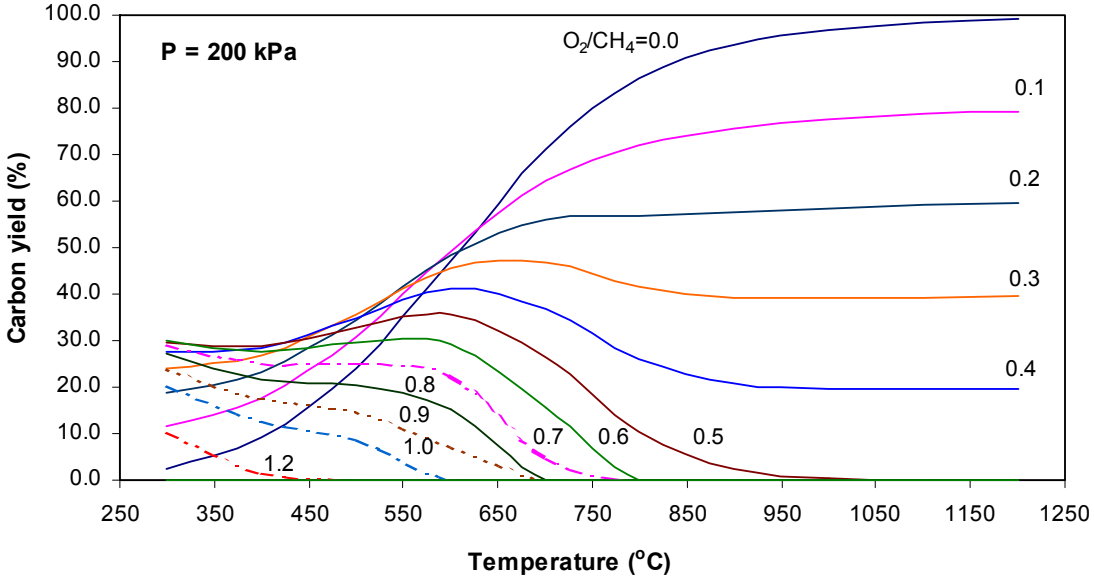

Figure 18. Temperature dependence of carbon yield with O_2/CH_4 ratio as a variable at P = 200 kPa.

Figure 19 depicts the values of total enthalpy flow within the reactor at different temperatures and O_2/CH_4 ratios. The total enthalpy flow rate was calculated as a sum of outlet enthalpies of all products minus sum of inlet enthalpies of CH_4-χO_2 mixtures. A negative enthalpy flow indicates that at the given conditions (χ, T and P) the reactive system produces heat, which obviates the need for the heat input into the reactor. In contrary, positive enthalpy flow indicates that at given conditions a certain amount of thermal energy has to be supplied to the reactor in order to accomplish methane decomposition. It is evident from the Figure 19 that for the practical range of temperatures (600 to 900 °C) and pressures of P = 0.2-2.5 MPa the enthalpy flow is close to zero at O_2/CH_4 ratio of $\chi \approx 0.2$ (which corresponds to an autothermal regime).

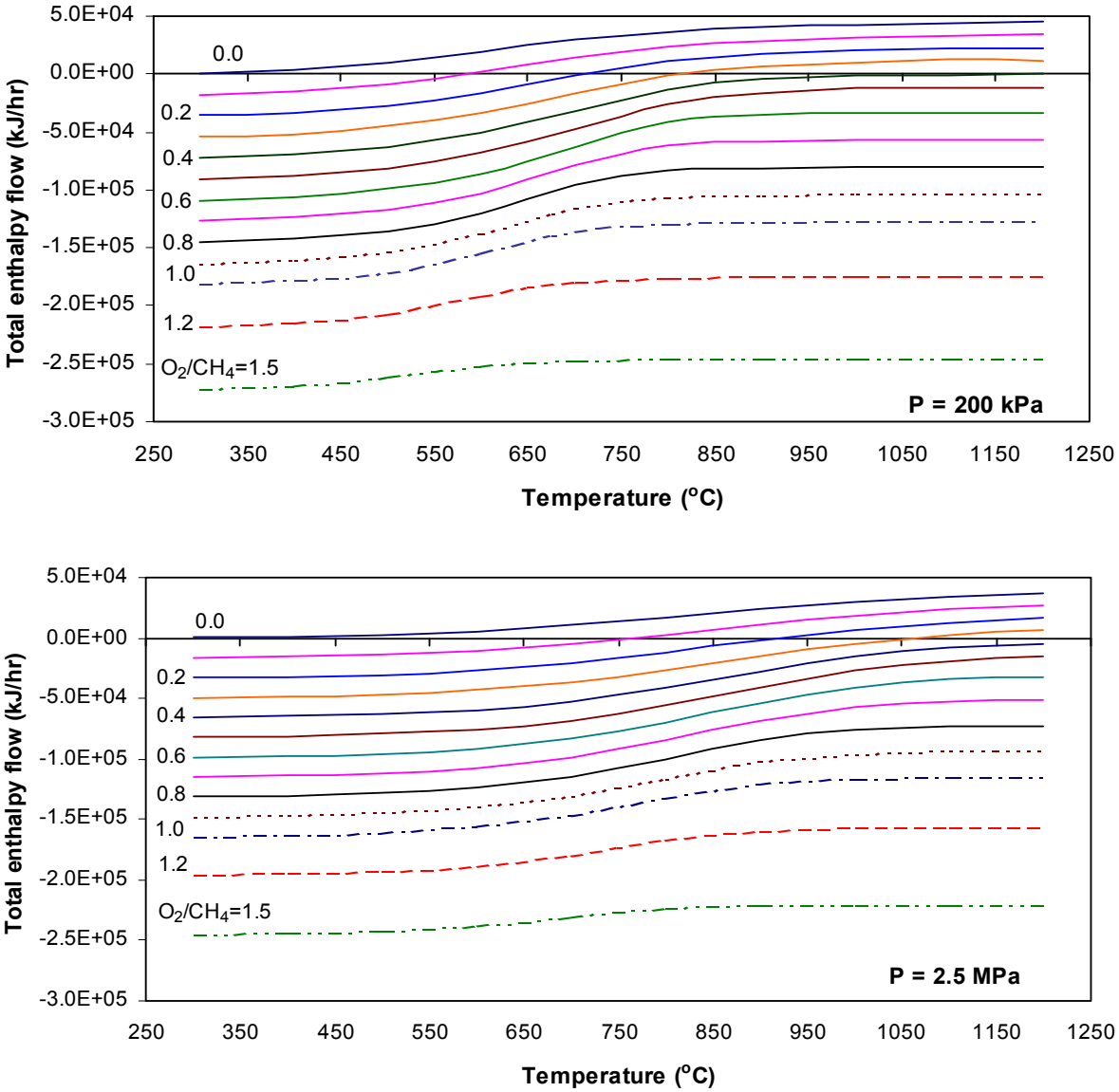

Figure 19. Total enthalpy flow as a function of temperature at P = 200 kPa and 2.5 MPa. enthalpy flow relates to 0.45 kmol/hr of CH_4-χO_2 mixture.

Figure 20 demonstrates methane conversion and the reaction products yields as a function of temperature at P = 200 kPa and $\chi \approx 0.2$. It can be seen that at T>850 °C hydrogen, carbon and CO are major reaction products and their yields are nearly independent of temperature.

The composition of the pyrolysis gas at P = 200 kPa and $\chi \approx 0.2$ is shown in Figure 21. At T>850 °C hydrogen and CO are two main components of the gaseous mixture with the average concentrations of 83 and 17 vol.%, respectively, that are nearly independent of the temperature.

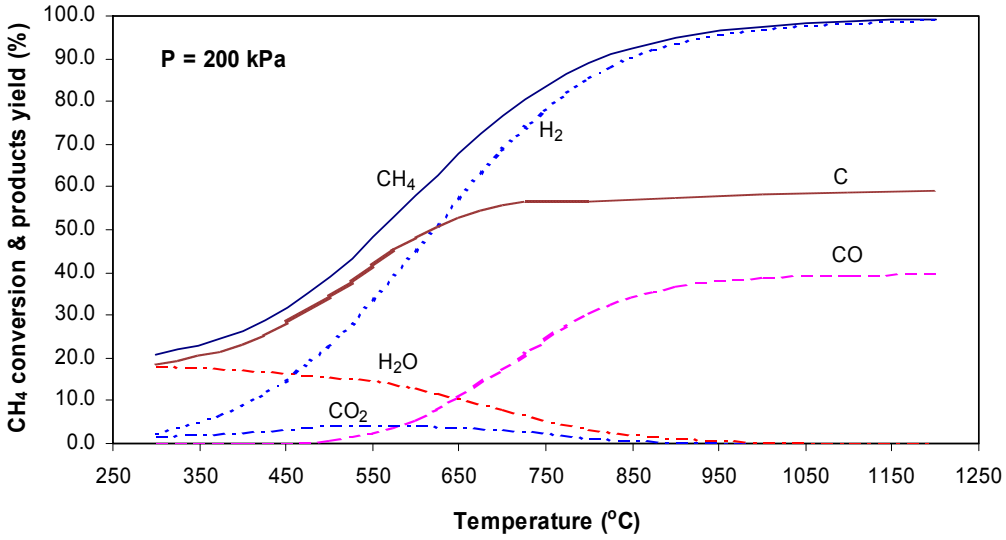

Figure 20. Methane conversion and products yields as a function of temperature at P = 200 kPa and $\chi \approx 0.2$.

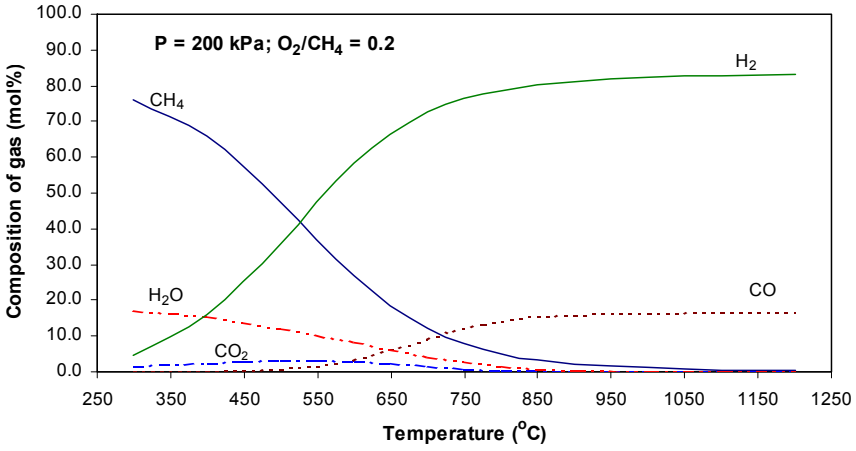

Figure 21. Composition of gaseous product as a function of temperature at P = 200 kPa and $\chi \approx 0.2$.

At T>850 °C and $\chi \approx 0.2$ the composition of the gaseous product of the reaction is consistent with the following stoichiometric equation:

$$CH_4 + 0.2O_2 \rightarrow 0.4\ CO + 0.6C + 2H_2 \quad (4)$$

It is noteworthy that the concentration of hydrogen in the effluent gas is significantly higher than that of the reformate gas after steam reforming of methane (~52 vol.% including water vapor and ~72 vol.% on a dry gas basis [14]). The presence of CO in the gaseous product would require the addition of water-gas shift reactors to the technological chain of the process. At the final stage of the process, high-purity hydrogen (>99.99 vol.%) will be recovered from H_2-CO_2 gaseous mixture using a standard pressure-swing adsorption system. Carbon is a valuable byproduct of the process and, if marketed, it could significantly reduce the cost of hydrogen production. The amount of CO_2 emissions from the process could potentially be as low as 0.17 m^3 CO_2/m^3 H_2, which is 2.5 times less than that from the SMR process (0.43 m^3 CO_2/m^3 H_2) [9].

Experimental Studies of Catalytic Pyrolysis of Methane—The experimental studies on thermocatalytic pyrolysis of methane were conducted using pure (99.99 vol.%) and industrial grade (i.e., pipeline NG) methane. The composition of pipeline natural gas used in the experiments is shown in Table 1.

Table 2. Composition of pipeline NG

Composition of NG, vol.%	
N_2	0.9
CH_4	93.1
C_2H_6	4.1
C_3H_8	0.7
C_4+	0.3
CO_2	0.9
CH_3SH	4 ppm

In this work, we studied inhouse-prepared proprietary metal-doped carbon (MDC) catalysts. It was found that doping with metal increases the catalytic activity and sustainability of the process. Figure 22 depicts the results of methane decomposition at 900 °C in the presence of MDC at the residence time of 1 and 2.2 s using bench-scale unit. It is evident from the Figure 22 that at higher residence time (2.2 s) initial hydrogen concentration in the effluent gas reaches up to 83 vol.%. This however followed by a decrease in hydrogen yield to a quasi-steady level (hydrogen concentration about 60 vol.%). During first hour there was a small amount CO present in the effluent gas, which could be attributed to some residual oxygen in the catalyst. At lower residence time (1 s) (or higher space velocity) the initial concentration of hydrogen in the effluent gas was somewhat lower and the process was not sustainable (i.e., H_2 concentration gradually dropped). This implies that the catalyst needs further improvement in its activity and stability.

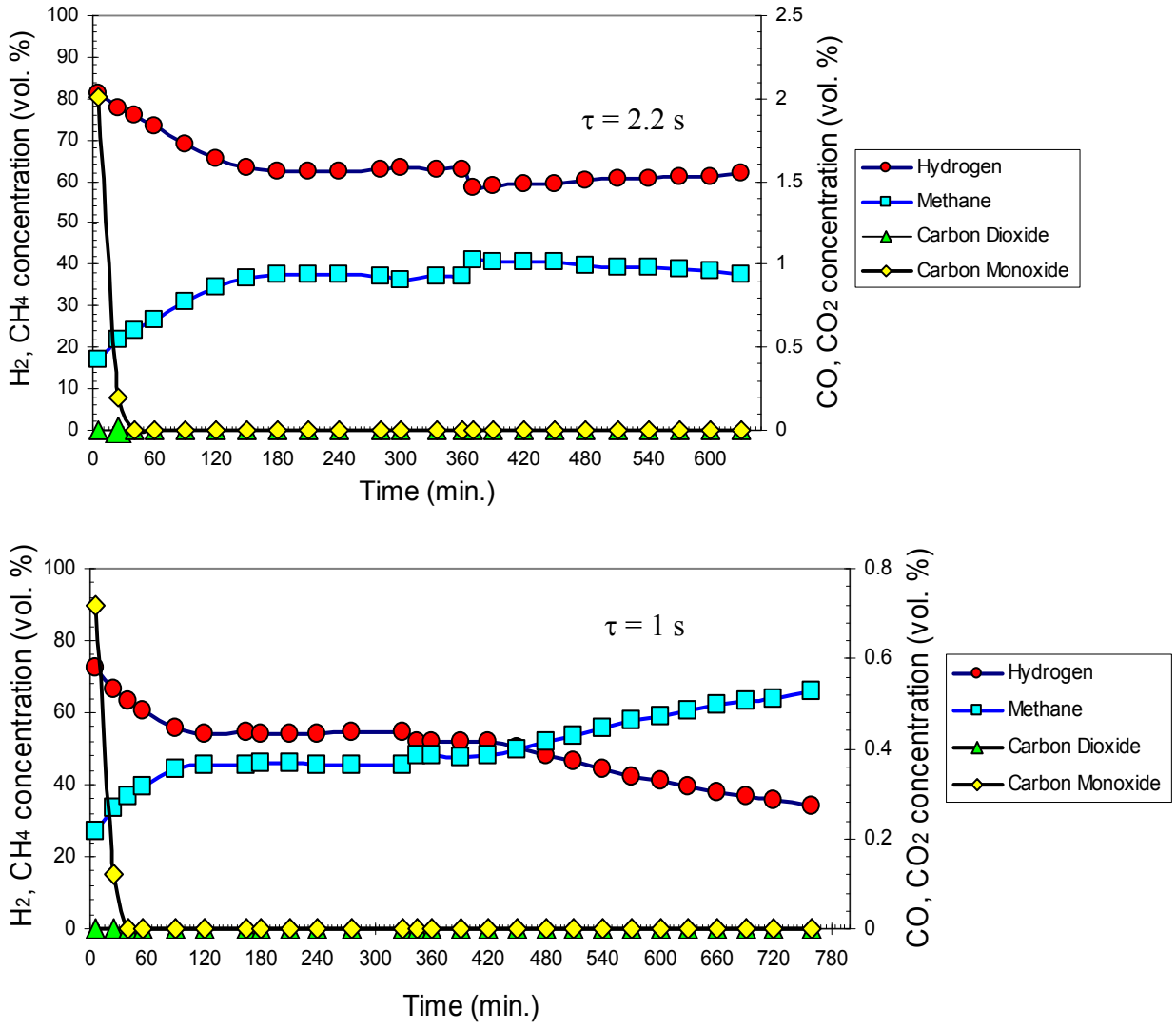

Figure 22. Catalytic pyrolysis of methane over
metal-doped catalyst at 900 °C and residence time of 1 and 2.2 s.

We also conducted high-throughput methane decomposition experiments using pilot-scale unit with maximum capacity of 1 SCFM (see Figure 11) (for this purpose the unit was modified). 180 g of carbon-based catalyst was placed in a two-inch OD Inconel reactor. The catalyst was purged with Ar at 400 °C for 3 hr, and pipeline quality natural gas was preheated to 350 °C and introduced to the reactor. The initial effluent gas consisted of 35 vol.% of H_2 (balance mostly unconverted methane and <1 vol.% C_2 hydrocarbons). CO concentration reached maximum value of 0.5 vol.% at 20 min and over period of 1 hr disappeared. CO_2 concentration reached steady state value of about 0.25 vol.% and stayed at this value throughout the experiment (apparently, this CO_2 was originated from the feedstock, see Table 3). The obtained mixture by composition is close to HYTHANE™ gas.

Autothermal Pyrolysis of Methane—In autothermal pyrolysis (ATP) process a relatively small amount of oxygen is fed into the reactor along with the methane feedstock to generate heat required to accomplish the endothermic methane decomposition reaction. Thus, ATP involves the combination of endothermic (methane decomposition) and exothermic (methane combustion) processes in one reactor (i.e., the process operates in a thermo-neutral regime). This approach may appear similar to the well-known partial oxidation (POx) process. However, there is a difference between the two processes. In particular, POx process is intended for complete conversion of methane into synthesis gas and, therefore, it requires relatively large amount of oxygen (O_2:CH_4 = 0.5 mole/mole). In contrast, the objective of oxygen-assisted methane decomposition is to maximize the yields of both hydrogen and carbon products by introducing oxygen in an amount just enough to sustain the endothermic methane decomposition reaction.

It is evident that the ATP process would use much less oxygen and, consequently, produce less CO_2 emissions than POx or SMR or autothermal methane reforming due to the relatively low endothermicity of methane decomposition reaction (it is almost three times less endothermic than SMR, per mole of H_2) and the fact that it does not produce synthesis-gas as the final product. Advantageously, in the ATP process most of the feedstock carbon ends up in the form of elemental carbon rather than CO_2.

Screening Catalysts for their Catalytic Activity in Methane Decomposition—Performance studies were conducted for six different catalysts under identical conditions. Figure 23 depicts the time dependence of hydrogen production rate at 900 °C for six different cases (in semi-log coordinates). Fe-Cr catalyst exhibited the highest activity (curve 1), however this catalyst tended to disintegrate after several hours at 900 °C. Ni catalyst (curve 2) also exhibited high activity, however, hydrogen production rates gradually decreased as a result of catalyst deactivation caused by carbon deposition. Curve 3 corresponds to oxygen-assisted (χ = 0.2) methane decomposition in the presence of AC (lignite)-supported iron (10 wt.%) catalyst. There is an initial induction period on the kinetic curve, which corresponds to the reduction of iron oxides to the active metallic form of the catalyst. This was followed by relatively steady methane decomposition process (for about 10 hr) with the production of the same assortment of products as in the case of AC catalyst. It is evident that doping carbon catalyst with iron significantly improved the catalyst activity and stability. The positive effect of iron on the reaction is no surprise: high catalytic activity of iron in methane decomposition reaction is well documented (e.g., [8]). On the other hand, alumina- and silica-supported iron-based catalysts are known for their rapid deactivation due to blocking of active sites by carbon deposits. Thus, the combination of iron catalyst with a carbon support ensures better performance through some synergistic action, the nature of which is yet to be understood.

Curve 7 relates to anaerobic methane decomposition (i.e., χ = 0) over AC (lignite). Curve 5 represents oxygen-assisted (χ = 0.2) methane decomposition over the same AC catalyst. It is clear that the addition of oxygen to the system noticeably slowed down the rate of catalyst deactivation. Since the main factors contributing to carbon catalyst deactivation relate to the deposition of catalytically inactive carbon species and the loss of surface area [3], it could be presumed that the presence of small amounts of oxygen promotes methane decomposition by creating more active sites on the catalyst surface and maintaining relatively high surface area. Indeed, BET surface area measurements of carbon samples after the AC (lignite)-catalyzed methane decomposition experiments indicated that the surface area of the carbon product formed in the presence of oxygen (χ = 0.2) is somewhat greater than that of the carbon produced in anaerobic conditions.

Effect of O_2/CH_4 Ratio—Figure 24 depicts distribution of methane decomposition/oxidation products (in molar %) as a function of O_2/CH_4 ratio at 900 °C in the presence of AC-lignite. Hydrogen, carbon and CO are the main products of methane conversion. Minute amounts of ethylene (<0.1 mol.%) were also detected among the reaction products. As expected, hydrogen and carbon yields decrease and H_2O, CO_x yields increase with the increase in O_2/CH_4 ratios in the entire range of χ (due to methane partial combustion). Interestingly, ethylene yield first increases reaching maximum at χ = 0.25 and then decreases.

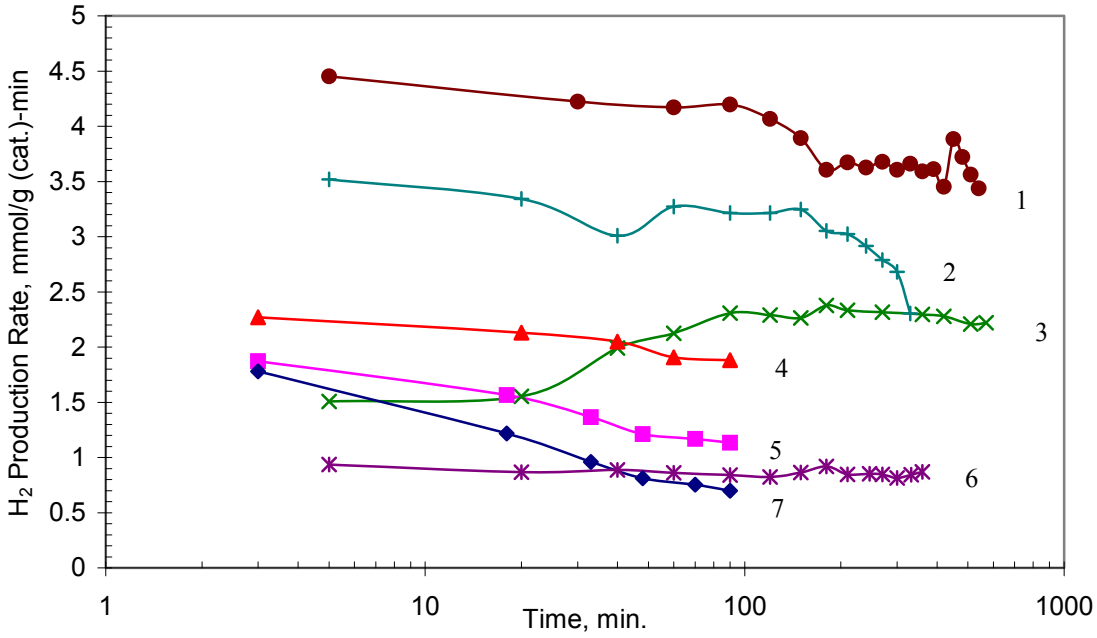

Figure 23. ATP of methane experiments for 6 catalysts (1 – Fe-Cr-oxides, 2 – NiO(1-15wt%)/Al_2O_3, 3 – Fe/AC Lignite, 4 – Fe/AC Peat, 5 – AC Lignite, 6 – Fe/Al_2O_3, 7 – Lignite without O_2 feed (χ =0))

Temperature Dependence—Figure 25 illustrates the temperature dependence of the products yields (in mol.%) at χ =0.2 using AC lignite as a catalyst. It is evident that in the range of 850-1000 °C the CO_x yields remain almost independent of temperature, and the yields of carbon and, particularly, hydrogen steadily increase. The comparison of thermodynamic equilibrium (Figure 26) and experimentally determined (Figure 25) data on products distribution reveals some agreements as well as disparities. In particular, it can be seen that the molar fractions of hydrogen in the products mix on both plots are in fairly good agreement (within less than 10% margin of error), whereas the molar distribution of other products is quite dissimilar. For example, thermodynamic equilibrium data indicate that carbon yield exceeds that of CO, whereas experimental results show an opposite trend (i.e., CO yield is greater than that of carbon). Moreover, at the temperatures above 850 °C the thermodynamic equilibrium values for CO_2 and H_2O are close to zero, which, apparently, is not in agreement with the experimentally determined values. Factors underlying these discrepancies are yet to be determined. One can speculate that the presence of relatively large quantities of carbon (which is both a catalyst and reaction product, at the same time) in the system may hinder formation of carbon and shift the equilibrium in favor of CO.

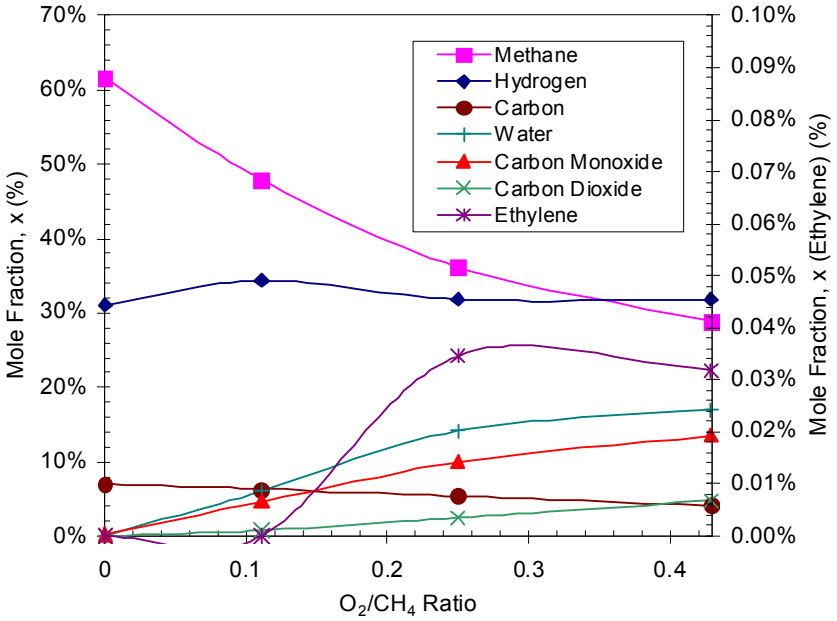

Figure 24. Molar distribution of ATP products as a function of O_2/CH_4 ratio.

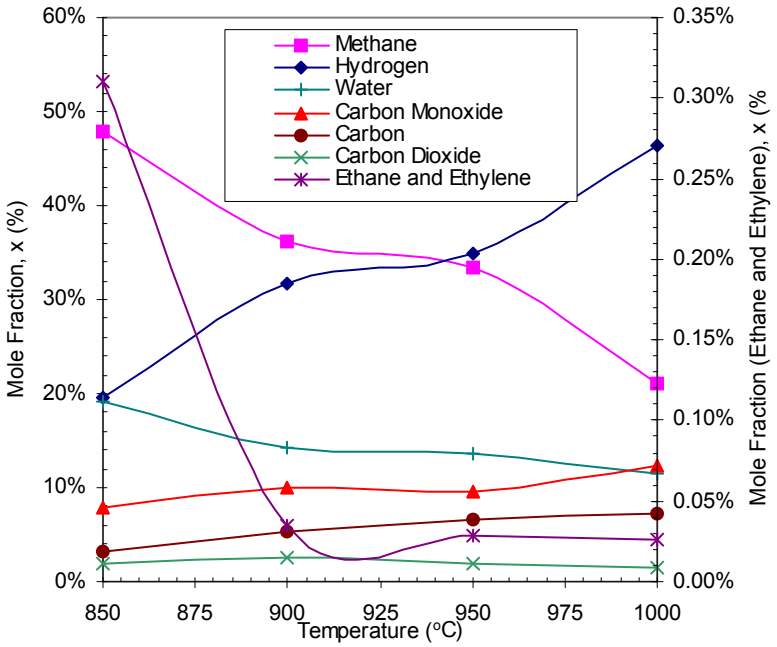

Figure 25. Experimentally determined temperature dependence of the molar fraction of methane decomposition products (O_2/CH_4 = 0.2 (molar), P = 0.1 MPa).

Analysis of Carbon Product—Carbon byproduct of the process could play an important role in reducing the cost of hydrogen production. We have previously reported that depending on the operational parameters of the process (temperature, catalyst, feedstock), carbon could be produced in several modifications: amorphous (i.e., carbon black), turbostratic and filamentous carbon. X-ray diffraction (XRD) studies of carbon samples produced by methane decomposition over carbon catalyst revealed ordering in a "columnar" or stacking direction. The d-spacing (lattice spacing) or spacing between plates is practically uniform, so that the (002) columnar reflection is clearly present.

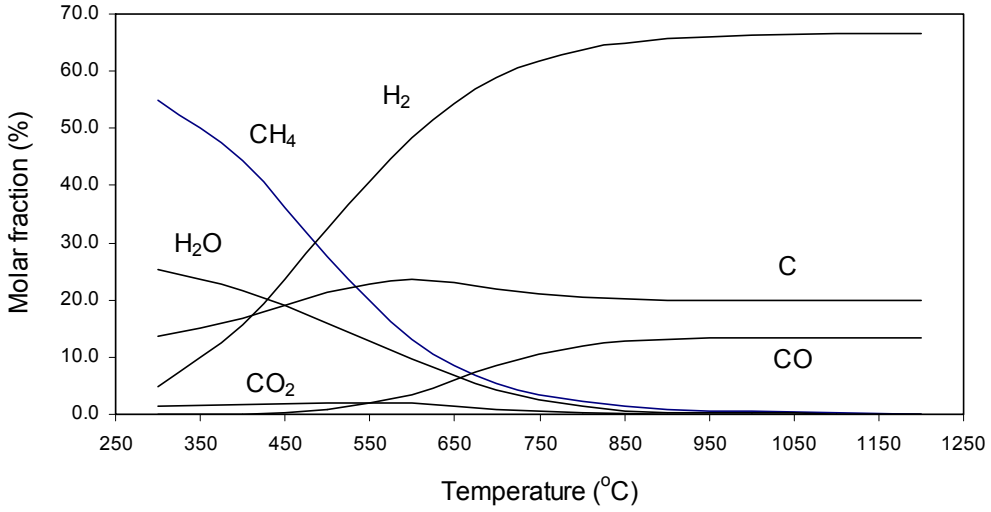

Figure 26. Thermodynamic equilibrium data on molar fraction of methane conversion products as a function of temperature at P = 0.1 MPa and $\chi \approx 0.2$.

Thus, the carbon produced by carbon-catalyzed decomposition of hydrocarbons revealed a graphite-like a-b-c-a type stacking of the carbon ring plates (as opposed to a-b-a-b for pure graphite). The actual d-spacing (d = 3.4948 Å) of this (002) peak is larger than that of the standard graphite structure (d = 3.3480 Å), which indicates that the plates are slightly further apart in the columnar stacking direction. This type of arrangement has been termed in the literature as a turbostratic structure. The Table 3 shows the data on the price and market for carbon products obtained in the process

Table 3. Price, application area and market for carbon products.

	Turbostratic carbon	Pyrolytic graphite	Carbon filaments
Price, $/kg	0.3	1-18	>1000
Application	electrodes, composites	aerospace, N-reactors	composites, electronics
Market	4-5 mln ton	N/A	N/A

Carbon samples were analyzed by scanning (SEM) and transmission (TEM) electron microscopy, XRD and focused ion beam (FIB) materials characterization techniques. Figure 27 depict SEM and TEM images of carbon products obtained by thermocatalytic decomposition of methane in the presence of supported metal catalysts. It is evident that some of these catalysts produce filamentous forms of carbon. Dark spots on the TEM images are nano-size metal catalyst particles. These metal particles are seeds for the growth of carbon nanotubes. The TEM image (A) shows the fine structure of a multi-wall carbon nanotube. It is apparent that the metal catalyst particle (with the diameter of ~10 nm) is wrapped by about 80 carbon graphene layers. The SEM image (B) shows a bunch of carbon nanotubes produced by Fe/alumina catalyzed decomposition of methane. It should be noted that carbon nanotubes and other carbon nano-structures were obtained from non-diluted methane and pipeline quality natural gas using inexpensive sulfur-resistant catalysts. This in contrast to previously reported works where carbon nanotubes were produced from methane-hydrogen mixtures using relatively expensive Ni-based catalysts. Thus, the hydrogen production method developed in this work could be a basis for the production of a value-added byproduct: filamentous carbon, which may significantly improve the commercial potential of the technology.

Figure 27 (C) depict high-resolution transmission electron microscopic (TEM) image of carbon produced by methane decomposition over Fe (10 wt.%)/AC-lignite catalyst. It can be seen that the iron particle (the dark spot) is completely covered by several (about 40 to 50) layers of carbon, which is associated with the substantial deactivation of the catalyst. It is plausible that in the presence of oxygen the iron particle partially catalyzes the oxidation of carbon layers, thus, preventing a buildup of large carbon deposits on its surface (at least, on some portion of the surface). This effect could potentially slow down the rate of the catalyst deactivation and result in better performance (compared to the similar catalyst working in anaerobic conditions). It is also noteworthy that carbon layers around the iron particle are much less ordered compared to the carbon sample from the anaerobic experiment, where carbon layers almost perfectly organized in a parallel pattern. Our earlier studies (e.g., [12]) indicated that disordered carbons (e.g., CB, AC) are catalytically more active in methane decomposition than ordered ones (e.g., graphite). Thus, the presence of disordered carbon species could be another important factor contributing to higher catalytic activity of the carbon-supported iron catalyst.

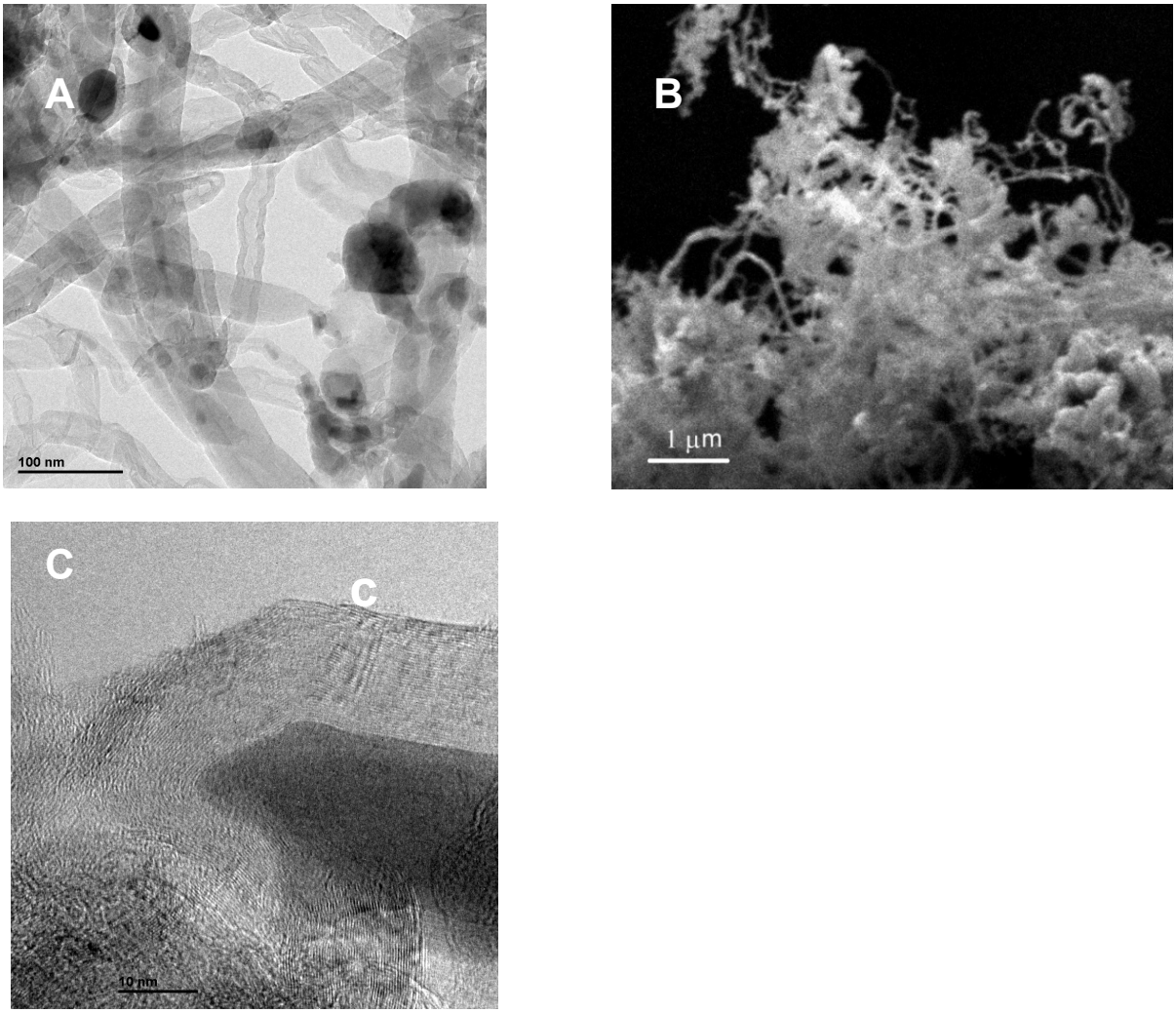

Figure 27. (A) TEM and (B) SEM images of filamentous carbon produced by methane decomposition in presence of Fe (10 wt.%)/alumina catalyst. (C) TEM images of Fe (10 wt.%)/AC-iignite catalyst with carbon deposits produced by methane decomposition.

Production of Hydrogen via Catalytic Processing of Citrus Pulp Pellets

We explored technical feasibility of converting citrus pulp pellets (CPP) into high purity hydrogen. Figure 28 shows the photo of CPP from local citrus processing facility. It was estimated that the Florida citrus industry generates about 1 million tons/yr of citrus waste residue. The citrus peel waste is dried into citrus peel pellets and sold as cattle feed (at approx. $40 to 45/ton). Citrus pulp pellets represent a large resource of inexpensive raw material for the local production of hydrogen.

Figure 28. Citrus pulp pellets.

In the first step, CPP has to be converted into gaseous feedstock suitable for reforming into the SG. There are two options: pyrolysis and gasification of CPP. Figure 29 depicts the schematic diagram of CPP processing into hydrogen. CPP were placed in the pyrolysis reactor and heated to 600-800 °C. In some experiments, a small amount of steam was introduced into the pyrolyzer. The pyrolysis gas produced was directed to the catalytic reformer followed by water gas shift reactor and gas separation unit.

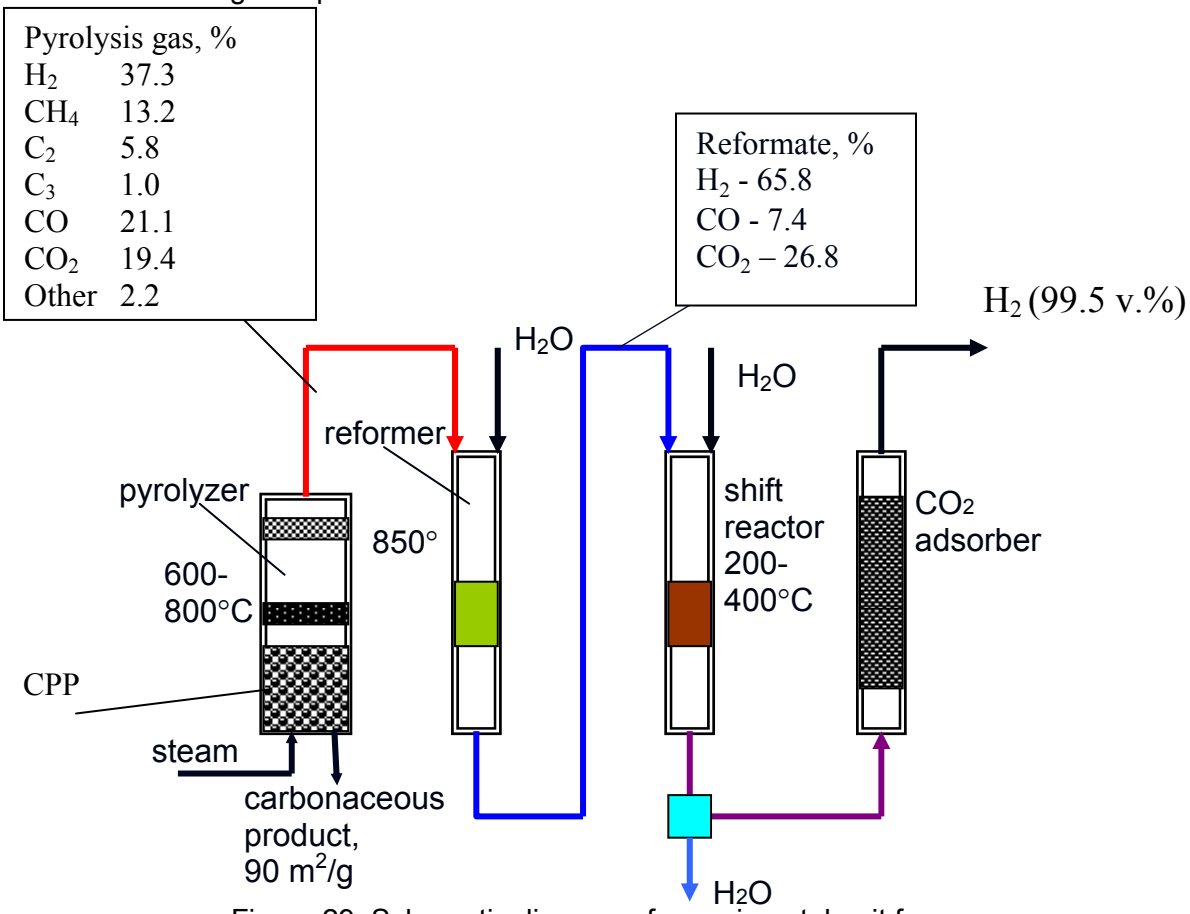

Figure 29. Schematic diagram of experimental unit for hydrogen production from citrus pulp pellets.

We used an activated carbon adsorber at sub-ambient temperature to separate hydrogen from CO_2. A carbonaceous product with the surface area of 90 m^2/g was produced as a byproduct of the process. This carbonaceous product can be upgraded into high-quality activated carbon for environmental applications. These experiments proved that it is technically feasible to process citrus waste products into pure hydrogen with reasonable high yield: 0.55 L of hydrogen per gram of citrus pulp pellets (as received).

Conclusions

The objective of this project is to develop economically viable process for the local production of hydrogen from renewable methane-containing feedstocks with minimal environmental impact. It was estimated that the local resources of LFG would be sufficient for production of 5 tons/day of hydrogen (adequate for up to 8 shuttle launches per year). Analytical (using AspenPlus™ chemical process simulator) and experimental studies on the development of two novel hydrogen production technologies were conducted, namely: (i) direct reforming of landfill gas (LFG) to syngas and its further processing to H_2, and (ii) thermocatalytic decomposition (TCD) of methane to hydrogen and carbon. The advantages of direct reforming of LFG is that it does not require preliminary recovery of methane from LFG, which simplifies the process. The thermodynamic analysis of methane pyrolysis in autothermal regime (in presence of relatively small amounts of oxygen) using AspenPlus™ chemical process simulator was conducted. Methane conversion, products yields, process enthalpy and Gibbs energy flows as a function of temperature, pressure and O_2/CH_4 ratio have been determined. The experimental data were in a fairly good agreement with the simulation results. Efficient and stable catalysts for the direct reforming of LFG were developed and tested. The catalytic activity of a number of commercial and synthesized transition metal catalysts (Ni, Fe, Pt, Pd, Ir, Ru and Rh) were evaluated. Ni-based catalyst was down-selected for further evaluation and the operational conditions for its efficient and stable operation were determined. A pilot scale unit with the capacity of 1 SCFM of H_2 was designed, fabricated and successfully operated using CH_4:CO_2 = 1.3:1 mixture mimicking local (Cocoa) LFG composition. A preliminary economic assessment indicates the cost range of liquid hydrogen product to be $3.00 to $6.00 per kilogram depending upon the production rate and whether or not carbon sequestration is added to the scheme.

The advantage of catalytic pyrolysis of methane process is that it allows producing hydrogen and value-added byproduct: clean carbon without or minimal CO_2 emissions. Comprehensive catalyst and process development studies for the hydrocarbon decomposition reaction were conducted. Since the process is moderately endothermic, the conditions at which the process operates at thermo-neutral regime were determined. Efficient catalysts for methane pyrolysis based on high-surface area carbons and metal-doped carbons have been developed and tested. The technical feasibility of the production of high-value filamentous carbon products (multi-wall carbon nanotubes) from non-diluted methane and pipeline quality NG was demonstrated. Characterization and structural studies of carbon products of the process were conducted using several materials characterization techniques (SEM, TEM, FIB, XRD). Potential markets for carbon products and process economics were evaluated. The technical feasibility of converting citrus waste products (e.g., citrus pulp pellets, CPP) into high purity hydrogen with the yield of 0.55 L H_2 per gram of CPP was demonstrated.

The successful implementation of the above technologies would eliminate the necessity for costly and potentially unsafe transportation of liquid hydrogen from Louisiana-based hydrogen plant to the Central Florida.

Patents, Publications, Presentations, and Students

Patents

1. Muradov, N., *Patent Appl. No. 11/648,453*, Thermocatalytic Process for CO_2 Free Production of Hydrogen and Carbon from Hydrocarbons (2006)
2. Muradov, N., Smith, F., T-Raissi, A., *Patent Appl. No. 11/637,552*, Process for Hydrogen Production via Integrated Processing of Landfill Gas and Biomass (2006)
3. Muradov, N., Smith, F., T-Raissi, A., *Patent Appl. No. 11/431,815*, Process and Apparatus for Hydrogen and Carbon Production via Carbon Aerosol Catalyzed Dissociation of Hydrocarbons (2006)
4. Huang, A. Raissi, N. Muradov, *U.S. Patent Application No. 60/578212 (2004),* "A Method for Zero-emission Liquid Hydrogen Production from Methane and Landfill Gas"

Publications

1. Muradov, N., "Emission-free Reformers for Mobile and Portable Fuel Cell Applications", *Journal of Power Sources,* 5236, 1-5(2003)
2. Muradov, N. "Catalytic Conditioning of Sulfurous Hydrocarbon Fuels for Fuel Cell Applications", *Symposium: Fuel Clean-up Considerations for Fuel Cells, Amer. Chem. Soc. Meeting*, New Orleans, 2003
3. Muradov, N. "On-site Production of Hydrogen from Hydrocarbon Fuels with Minimal Greenhouse Gas Emissions", *Symposium: Hydrogen Energy for the 21st Century, Amer. Chem. Soc. Meeting*, New Orleans, 2003
4. Muradov, N., T-Raissi, A., Robertson, T. "Hydrogen Production via Catalytic Reformation of Low-quality Methane Containing Feedstocks", *Proceedings of HYPOTHESIS Conf.*, Italy, 2003
5. Muradov, N., Smith, F. "Thermocatalytic Hydrogen Production from Natural Gas with Drastically Reduced CO_2 Emissions", *Proc. HYPOTHESIS Conf.*, Italy, 2003
6. Muradov, N., Huang, C., T-Raissi, A., Smith, F. "Hydrogen Production from Natural Gas with Reduced CO_2 Emissions", *Proc. XV World Hydrogen Energy Conf.*, Yokohama, Japan, 2004
7. Muradov, N., T-Raissi, A., Smith, F., Elbaccouch, M. "Hydrogen Production via Catalytic Reformation of Landfill Gas and Biogas", *Proc. XV World Hydrogen Energy Conf.*, Yokohama, Japan, 2004
8. Huang, C., Muradov, N., T-Raissi, A. "Analysis of Liquid Hydrogen Production from Methane and Landfill Gas", *Proc. XV World Hydrogen Energy Conf.*, Yokohama, Japan, 2004
9. Muradov, N., Smith, F., T-Raissi, A. "Catalytic Properties of Carbons in Methane Decomposition Reaction", *Proceedings of International Symposium on Carbon for Catalysis*, Lausanne, Switzerland, 2004
10. Muradov, N., Smith, F., T-Raissi, A. "Thermocatalytic Hydrogen Production from Natural Gas with Drastically Reduced CO_2 Emissions", *Hydrogen Power Theoretical and Engineering Solutions,* Eds. M. Marini, G. Spazzafumo, SG Editoriali, Padova, Italy, 2004, pp. 87-95 (peer reviewed)
11. Muradov, N., T-Raissi, A., Robertson, T. "Hydrogen Production via Catalytic Reformation of Low-quality Methane Containing Feedstocks", *Hydrogen Power Theoretical and Engineering Solutions,* Eds. M. Marini, G. Spazzafumo, SG Editoriali, Padova, Italy, 2004, pp. 191-199
12. Muradov, N., Smith, F., T-Raissi, A. Catalytic Activity of Carbons for Methane Decomposition Reaction", *Catalysis Today, v. 102-103 (2005) 225-233*
13. Muradov, N., Veziroglu, N., "From Hydrocarbon to Hydrogen-Carbon to Hydrogen Economy", *International Journal of Hydrogen Energy,* v.30 (3), pp. 225-237 (2005)

14. Muradov, N., Chen Z., Smith F., "Modeling TCD of Methane in Fluidized Bed of Carbon Particles", *International Journal of Hydrogen Energy, 30, 1149-1158 (2005)*
15. Muradov, N., Smith, F., Huang, C. T-Raissi, "Autothermal Catalytic Pyrolysis of Methane as a New Route to Hydrogen Production with Reduced CO_2 Emission", *2nd European Hydrogen Energy Conf*., Saragossa, Spain, 2005
16. Muradov, N., Smith, F., T-Raissi, A. "Hydrogen Generators for Portable and Back-up Power Applications", *Abstracts of 2nd Annual Florida Tech-Transfer Conf., Orlando, FL, May 18-19, 2005*
17. Muradov, N., Smith, F., T-Raissi, A. "Catalytic Dissociation of Hydrocarbons: a Route to CO_2-free Hydrogen", *Proc. XV Annual Saudi-Japanese Symposium "Catalysts in Petroleum Refining and Petrochemicals", Dhahran, Saudi Arabia, November, 2005*
18. Muradov, N., Smith, F., T-Raissi, A. "Autothermal catalytic pyrolysis of methane as a new route to hydrogen production with reduced CO_2 emissions", *Catalysis Today, 116, 281-288, 2006*
19. Muradov, N., Smith, F., T-Raissi, A., Catalysis of Methane Dissociation by Carbon Materials, *Proc. Intern. Symp. Carbon in Catalysis*, Saint Petersburg, Russia, 2006
20. Muradov, N., Smith, F., T-Raissi, A. "Decentralized Production of Hydrogen from Hydrocarbons without CO_2 Emission", *Proc. XVI World Energy Conf., Lyon, France, 2006.*
21. Muradov, N., Smith, F., Elbaccouch, M., T-Raissi, A. "Hydrogen Production via Catalytic Processing of Renewable Feedstocks", *Proc. XVI World Energy Conf., Lyon, France, 2006*
22. Muradov, N., Rahman, Z., Synthesis and Characterization of Radially-Alligned Carbon Filaments, *J. Nanoscience and Nanotechnology*, submitted for publication
23. Muradov, N., Chapter 2: Hydrogen Production from Hydrocarbons, in book *Hydrogen Production, Storage and Utilization,* Fransis and Taylor Publ., 2007
24. Smith, F., Muradov, N., Raissi, A. Production of Hydrogen via Autothermal Dry Reforming of Landfill Gas, Proc. ACS (Florida section) FAME Meeting, 2007
25. Muradov, N., Smith, F., Catalytic Reforming of Landfill Gas to Syngas, *Appl. Catal,* submitted for publication, 2007
26. Muradov, N., CO_2-free Production of Hydrogen: Vision of Hydrogen-Carbon Economy, *Dutch Hydrogen Dialogue Meeting*, Amsterdam, March, 2007
27. Muradov, N., Veziroglu, N., CO_2-free Fossil Hydrogen: Vision of Hydrogen-Carbon Economy, *Proc. Intern. Hydrogen Energy Conf. and Exhibition,* Istanbul, Turkey, 2007

Presentations

1. Muradov, N. "Catalytic Conditioning of Sulfurous Hydrocarbon Fuels for Fuel Cell Applications", *Symposium: Fuel Clean-up Considerations for Fuel Cells, Amer. Chem. Soc. Meeting*, New Orleans, 2003
2. Muradov, N. "On-site Production of Hydrogen from Hydrocarbon Fuels with Minimal Greenhouse Gas Emissions", *Symposium: Hydrogen Energy for the 21st Century, Amer. Chem. Soc. Meeting*, New Orleans, 2003
3. Muradov, N., Huang, C., T-Raissi, A., Smith, F. "Hydrogen Production from Natural Gas with Reduced CO_2 Emissions", *Proc. XV World Hydrogen Energy Conf*., Yokohama, Japan, 2004
4. Muradov, N., T-Raissi, A., Smith, F., Elbaccouch, M. "Hydrogen Production via Catalytic Reformation of Landfill Gas and Biogas", *Proc. XV World Hydrogen Energy Conf*., Yokohama, Japan, 2004
5. Huang, C., Muradov, N., T-Raissi, A. "Analysis of Liquid Hydrogen Production from Methane and Landfill Gas", *Proc. XV World Hydrogen Energy Conf*., Yokohama, Japan, 2004
6. Muradov, N., Smith, F., T-Raissi, A. "Catalytic Properties of Carbons in Methane Decomposition Reaction", *Proceedings of International Symposium on Carbon for Catalysis*, Lausanne, Switzerland, 2004

7. Muradov, N., Smith, F., T-Raissi, A. “Thermocatalytic Hydrogen Production from Natural Gas with Drastically Reduced CO_2 Emissions”, *Hydrogen Power Theoretical and Engineering Solutions,* Italy, 2004
8. Muradov, N., T-Raissi, A., Robertson, T. “Hydrogen Production via Catalytic Reformation of Low-quality Methane Containing Feedstocks”, *Hydrogen Power Theoretical and Engineering Solutions,* Italy, 2004
9. Muradov, N., Smith, F., Huang, C. T-Raissi, “Autothermal Catalytic Pyrolysis of Methane as a New Route to Hydrogen Production with Reduced CO_2 Emission”, *2nd European Hydrogen Energy Conf*., Saragossa, Spain, 2005
10. Muradov, N., Smith, F., T-Raissi, A. “Hydrogen Generators for Portable and Back-up Power Applications”, *Abstracts of 2nd Annual Florida Tech-Transfer Conf., Orlando, FL, May 18-19, 2005*
11. Muradov, N., Smith, F., T-Raissi, A. “Catalytic Dissociation of Hydrocarbons: a Route to CO_2-free Hydrogen”, *XV Annual Saudi-Japanese Symposium “Catalysts in Petroleum Refining and Petrochemicals”, Dhahran, Saudi Arabia, November, 2005*
12. Muradov, N., Smith, F., T-Raissi, A., Catalysis of Methane Dissociation by Carbon Materials, *Intern. Symp. Carbon in Catalysis*, Saint Petersburg, Russia, 2006
13. Muradov, N., Smith, F., T-Raissi, A. “Decentralized Production of Hydrogen from Hydrocarbons without CO_2 Emission”, *XVI World Energy Conf., Lyon, France, 2006*
14. Muradov, N., Smith, F., Elbaccouch, M., T-Raissi, A. “Hydrogen Production via Catalytic Processing of Renewable Feedstocks”, *XVI World Energy Conf., Lyon, France, 2006*
15. Smith, F., Muradov, N., Raissi, A. Production of Hydrogen via Autothermal Dry Reforming of Landfill Gas, Proc. ACS (Florida section) FAME Meeting, 2007
16. Muradov, N., CO_2-free Production of Hydrogen: Vision of Hydrogen-Carbon Economy, *Dutch Hydrogen Dialogue Meeting*, Amsterdam, March, 2007
17. Muradov, N., Veziroglu, N., CO_2-free Fossil Hydrogen: Vision of Hydrogen-Carbon Economy, *Intern. Hydrogen Energy Conf. and Exhibition,* Istanbul, Turkey, 2007

Students

Franklyn Smith (Florida Institute of Technology)
Neal Atmaram (Vilanova University)

References

[1] J. Keating: Cheaper energy by going to waste. Distributed Energy, January/February (2004) 22-26.

[2] Landfill Gas-to-Energy Project Opportunities. EPA 430-K-99-007 (1999).

[3] Y. Hu, E. Ruckenstein, Advances in Catalysis, 48, (2004) 297-345.

[4] H. Henz et al, Gas Production, in Ullmann’s Encyclopedia of Industrial Chemistry, Wiley-VCH Verlag GmbH & Co. KgaA, 2002.

[5] J. Richardson, Principles of Catalyst Development, Plenum Press, NY, 1989.

[6] K. Mondal, V. Choudhary, U. Joshi, Appl. Catal. A: General, 316 (2007) 47-52.

[7] N. Muradov: Hydrogen via methane decomposition: an application to decarbonization of fossil fuels. Int. J. Hydrogen Energy 2001; 26:1165

[8] N. Muradov: How to produce hydrogen from fossil fuels without CO_2 emission. Int. J. Hydrogen Energy 1993; 18: 211

[9] M. Steinberg: Fossil fuel decarbonization technology for mitigating global warming. Int. J. Hydrogen Energy 1999; 24: 771,

[10] L. Fulcheri, Y. Schwob: From methane to hydrogen, carbon black and water. Int. J. Hydrogen Energy 1995; 20: 197.

[11] N. Muradov: CO_2-free Production of hydrogen by catalytic pyrolysis of hydrocarbon fuel. Energy & Fuels 1998; 12:41

[12] N. Muradov: Catalysis of methane decomposition over elemental carbon. Catalysis Commun. 2001; 2: 89

[13] James Richardson: A gas-fired heat pipe reformer for small scale hydrogen production, Natural Gas Conversion IV, Studies in Surface Science and Catalysis, vol. 107, Eds. M.de Pontes et al., 1997, Elsevier, Oxford

[14] Ullmann's Encyclopedia of Industrial Chemistry, vol. A-13, VCH, 1985

Appendix A

Location and Resources of LFG in Central Florida within 50 miles from NASA-KSC

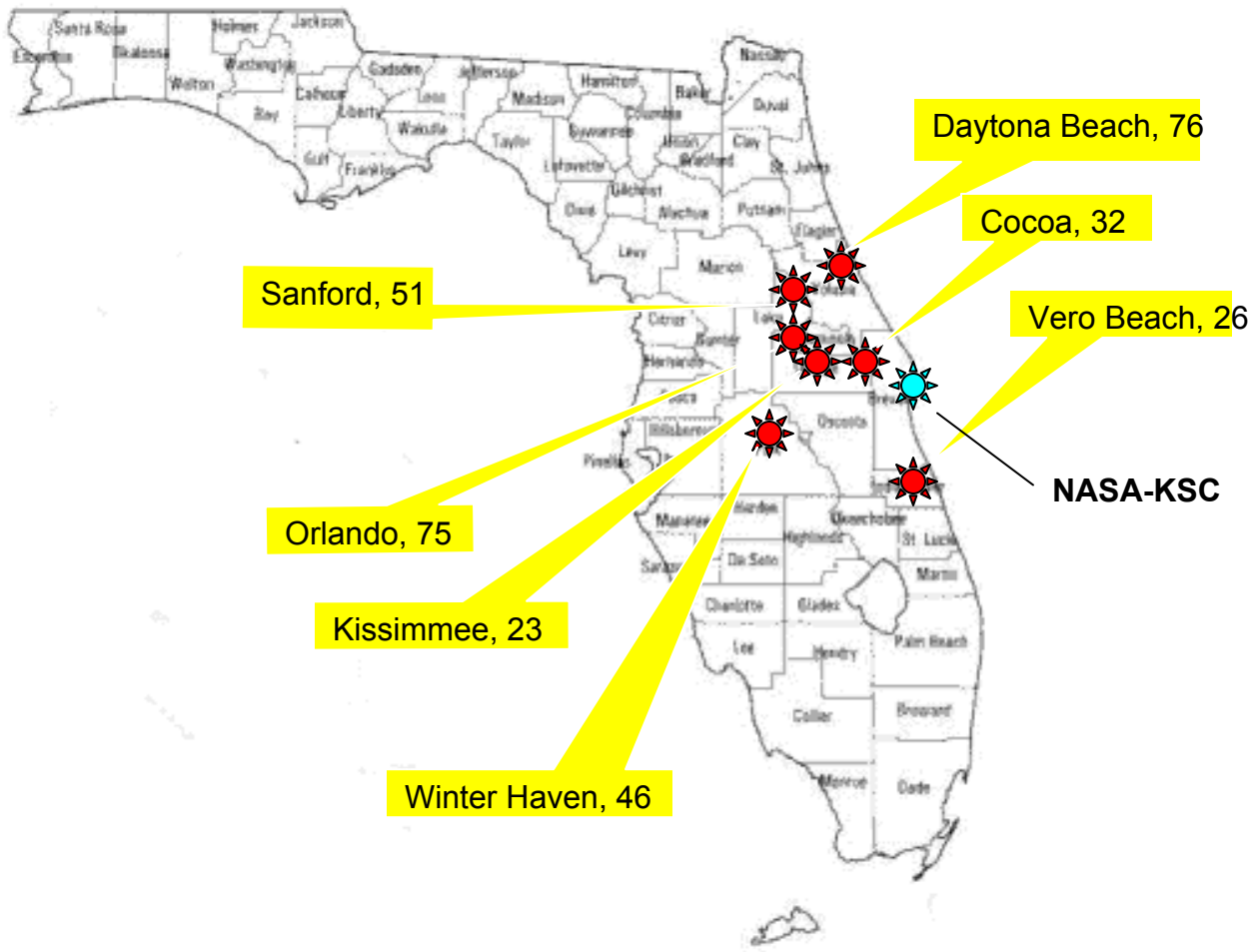

Figure A-1. Location and Resources of LFG in Central Florida within 50 Miles from NASA-KSC

The capacities of landfill sites are shown in MMbtu/hr.

Appendix B

Technoeconomic Assessment of Hydrogen Production from Landfill Gas

Input Data and Assumptions—Capital cost estimation was performed using the Icarus Process Estimator™ (IPE™), part of the Aspen Engineering Suite of programs. Individual process components are mapped into IPE™; process simulation results are transferred from Aspen Plus™ in order to size the equipment. Components in the Aspen Plus spreadsheet are equated to equipment types and then priced for the next largest size. All pricing data comes from actual industry data. Engineering, procurement and construction costs are added to the project. This procedure was performed for simulations producing from less than one ton per day of hydrogen to twenty tons per day of hydrogen in order to determine economy of scale for all three scenarios. IPE™ provides operating cost estimates as well.

In order to determine total production cost of hydrogen for KSC's use, liquefaction capital cost estimates were added [*Syed MT et al. An Economic Analysis of Three Hydrogen Liquefaction Systems. International Journal of Hydrogen Energy 1998,23, 565*] along with power costs assuming an electricity rate average of $0.052/kWh [*Bossel U, Eliasson B and Taylor G. The Future of the Hydrogen Economy: Bright or Bleak? 2003*]. Actual landfill gas cost was assumed to be $1.42/GJ (in NG equivalent); no actual cost data for the LFG was found in the literature. Compressor power requirement cost was added at the same rate. Total production cost was calculated assuming a plant lifetime of twenty years, and a discount rate of 6% was used to calculate present value of operating and maintenance.

For oxygen costs in the oxygen-fired dry reforming and autothermal reforming cases, a current KSC gate purchase price of $650/ton was assumed [*Bain A. NASA Kennedy Space Center Base Center Hydrogen Operations. FSEC-UCF report for NASA FSEC-CR-1359-02, October 2002*]. In addition, evaporator capital cost was added and amortized. In reality, this scenario would not be likely to be considered; oxygen firing would only occur if there were a cheap local source of oxygen available. After analysis, however, this scenario becomes even less attractive. No great improvement in process efficiency is realized for the standard reforming case, and the autothermal case is not an economical fit with PSA purification.

In addition, carbon sequestration costs were estimated in order to account for possible environmental impact of the proposed technology. Carbon sequestration for this type of production facility would in fact result in a net decrease in greenhouse gas emissions compared to the release of LFG directly to the atmosphere. To include this cost, additional capital cost estimation for CO_2 compression equipment is included along with the corresponding power cost at the $0.052/kWh rate. For sequestration, an average of Department of Energy cost estimates utilizing currently available technology are used [*Office of Fossil Energy, DOE website, http://www.fossil.energy.gov/coal_power/sequestration/index.shtml*].

For this study, a range of one to seven shuttle launches per year at KSC was analyzed. Costs were calculated as detailed above for the broad range of production rates (<1 to 20 tons per day) and a regression analysis was performed to give an approximate cost of hydrogen on a per kilogram basis. This procedure was performed for three separate cases: gaseous hydrogen production without carbon sequestration, liquid hydrogen production without carbon sequestration, and liquid hydrogen production with carbon sequestration.

Results of Analysis—Figures B1-B3 depict cost results for this analysis. One launch at KSC requires, on the average, approximately 0.8 tpd of hydrogen averaged over the period of one year. This is only an estimate, however; actual hydrogen demand is not a linear function of number of shuttle launches because of the base annual requirements [*Bain A. NASA KSC Base Center Hydrogen Operations. FSEC-UCF report for NASA FSEC-CR-1359-02, October 2002*].

Figure B1 shows the case where gaseous hydrogen is produced. Clearly, the unit cost of gaseous hydrogen produced drops as plant capacity is increased. The air-fired reforming process is more cost effective on a per kilogram (of gas) basis than an oxygen-fired process; the autothermal case is less economically attractive because of hydrogen losses in PSA offgas and high oxygen cost.

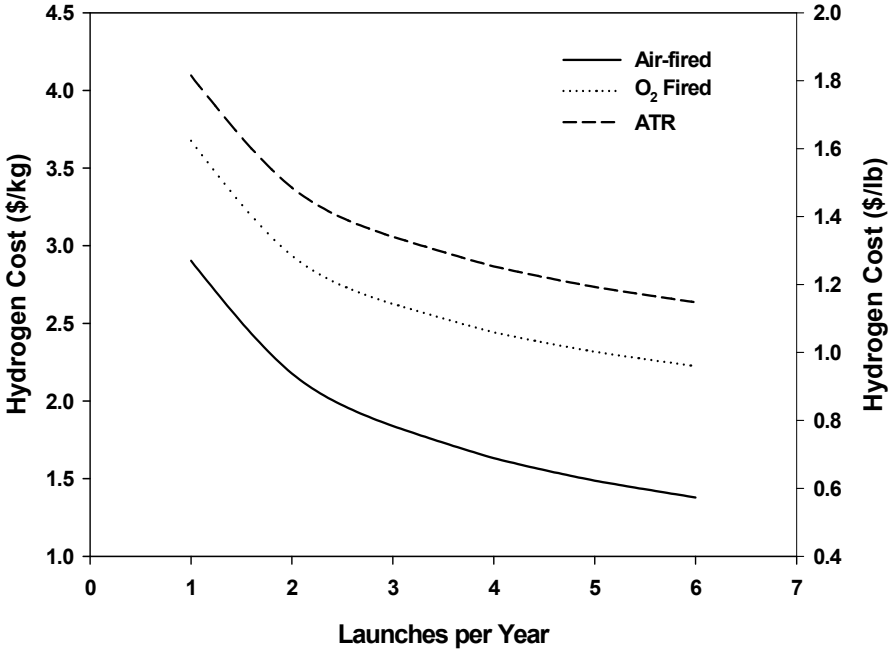

Figure B1. Cost of gaseous hydrogen production by dry reforming of LFG (1 launch/year = 725 kg H_2/day, LFG Cost = $1.42/GJ).

In case of liquid hydrogen production (Figure B2) the trend is identical, provided, liquefaction costs will be equal for all three scenarios. In Figure B3, that presents the analysis of liquid hydrogen production by the autothermal process the hydrogen cost approaches that of the oxygen-fired reformer. This is due to the lack of carbon sequestration for the flue gas needed in the standard reforming cases. All of the CO_2 present in the process exists in the actual process stream and is separated out in the PSA unit. These preliminary results indicate that, for greater than two launches per year, local liquid hydrogen production via catalytic reforming of LFG with air used for combustion appears to be cost competitive with the option of liquid hydrogen delivery from Louisiana. When greenhouse gas sequestration is accounted for, the break-even number of launches is driven up to four. At a lower range of launches, the processes requiring oxygen are not economical when compared to the current KSC purchase price of liquid hydrogen.

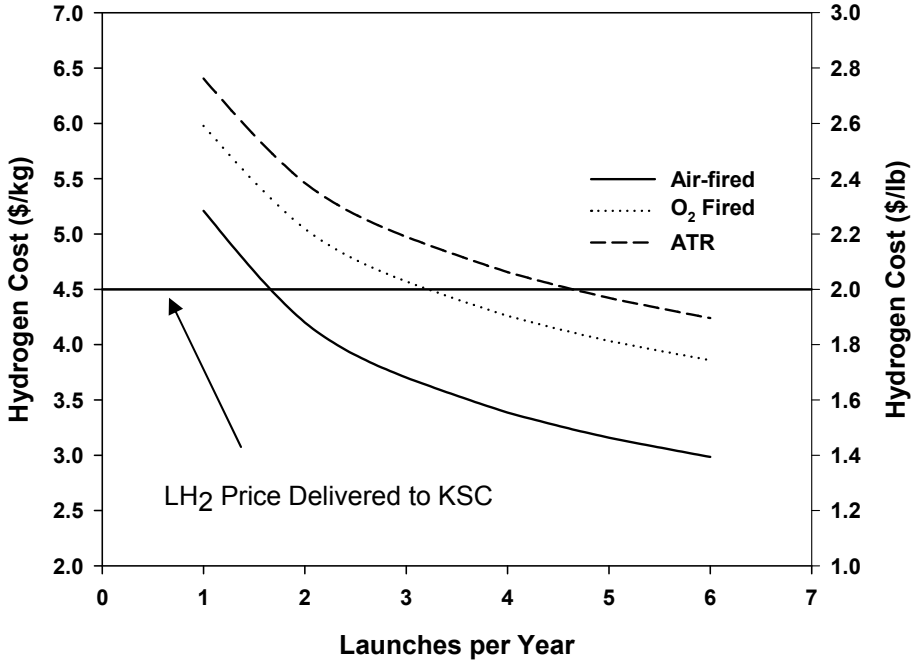

Figure B2. Cost of liquid hydrogen production by dry reforming of LFG.

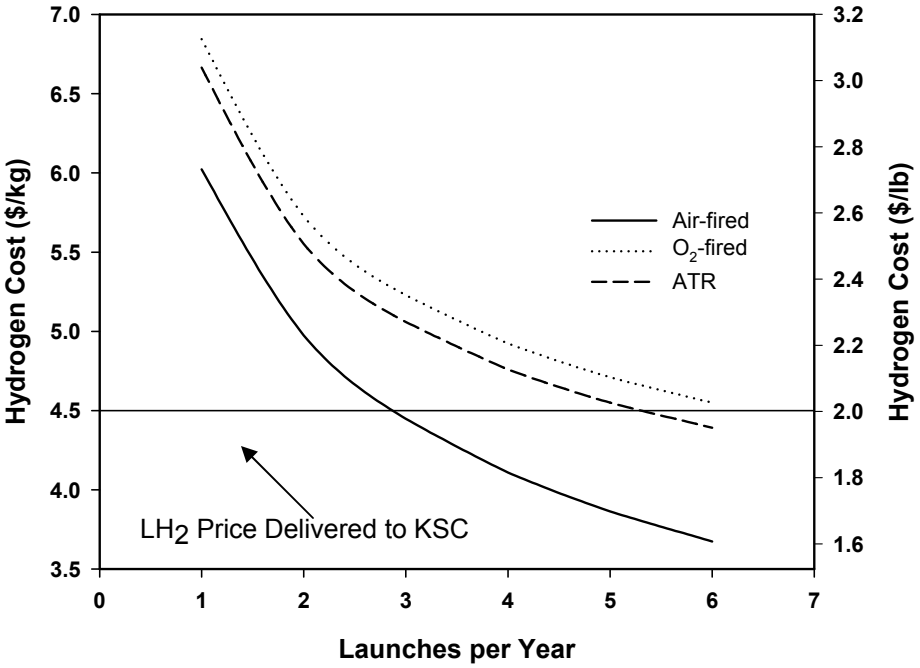

Figure B3. Cost of liquid hydrogen production with carbon dioxide sequestration.

Summary of Appendix B—This study identifies catalytic reforming of landfill gas as a technically and economically viable process for on-site hydrogen production at NASA-KSC. Experimental verification of hydrogen production from CH_4-CO_2 mixtures mimicking LFG using commercial catalysts was demonstrated. The composition of the reforming gas is in good agreement with the thermodynamic equilibrium data, which is an indication of high catalytic activity and near optimal operational conditions. Three scenarios distinguished by the mode of heat input to the process were modeled and compared. The reforming using an external heat input and using air for combustion results in an overall first law efficiency of approximately 60%. This scenario is particularly advantageous because PSA produces hydrogen with very purity , and the PSA offgas can be used in the combustor. A preliminary economic assessment indicates the cost range of liquid hydrogen product to be $3.00 to $6.00 per kilogram depending upon the production rate and whether or not carbon sequestration is added to the scheme. Hydrogen production options with external heat input and O_2 for combustion, and autothermal reforming were economically less attractive; the liquid hydrogen cost was estimated to be in the range of $3.75 to $7.00 per kilogram.

November 2007

Photoelectrochemical Water Splitting for Hydrogen Production Using Multiple Bandgap Combination of Thin-Film-Photovoltaic-Cells and Photocatalyst

N. Dhere
Florida Solar Energy Center

Research Period: July 2002 to September 2006

Abstract

One of the NASA research activities was to identify, characterize, and simulate a series of technologies that could be used for hydrogen production at NASA Kennedy Space Center (NASA-KSC) using locally available sources. This project examined the production of hydrogen from solar energy. To produce hydrogen by water splitting, the operating voltage of conventional photovoltaic (PV) cells cannot supply the overvoltage required. Thus, the objective of this project was to research and develop photoelectrochemical (PEC) cells that can supply the required voltage for water splitting by constructing a multiple bandgap tandem PV cell and a photocatalyst that can be activated by infrared (IR) photons transmitted through the PV cell. The proposed concept is different from conventional PEC water splitting using multiple band gap combinations. The advantages for this PEC cell concept is that the PV cells are not in contact with the electrolyte solution, thus reducing the problems of corrosion and the photocatalyst is not grown directly over the PV cell as is the case with solid-state tandem PV cells.

Background

From the literature, research in the U.S. has been carried out to increase the PEC solar-to-hydrogen efficiencies by using amorphous silicone cells (a-Si:H) and by careful design considerations that include an integrated multijunction photoelectrode comprised of a low-cost semiconductor, catalytic films, and protective thin films deposited on low-cost substrates. To meet the cost and performance goals, efforts have been concentrated on development of a "Hybrid Photoelectrode" (HPE), which incorporates low-cost metal-oxide (such as Fe_2O_3 and WO_3) and photovoltaic-grade semiconductor thin films (such as CIGS and a:Si:H). Along with the a:Si:H hybrid photoelectrode, III-V semiconductors are also being studied for efficient PEC water splitting [1-11].

For a GaAs/GaInP2 system, the calculated solar-to-hydrogen conversion efficiency of over 16% has been achieved [1]. GaAs-based cells are expensive as well as fragile and have a bulk single crystalline substrate. These cells are suitable for solar concentrator type applications where high efficiency is of paramount importance, but for a practical cost effective application, they will not be the choice. They also are not applicable in areas with large amounts of diffuse solar radiation such as Florida. In another study, Licht et al. presented the concept of using multiple bandgap tandem cells for PEC water splitting [12-14]. His work has shown a PEC solar-to-hydrogen generation using illuminated AlGaAs/Si, RuO_2/Pt black setup achieved an efficiency of 18.3% [13].

Thus, the research conducted by this project was to base the PEC process on development of lower cost $CuIn_{1-x}Ga_xS_2$ (CIGS2) polycrystalline-thin film solar cells. CIGS2 thin film solar cells have following advantages over III-V based and a-Si:H solar cells:

1. They cost considerably less because they utilize cheaper and more robust soda-lime glass substrate.
2. As semiconductors, they are 100-200 times thinner when compared to silicon cells.
3. Large area depositions and integral interconnects can be achieved more easily.
4. The polycrystalline-thin film cells do not suffer from intrinsic degradation mechanisms such as the Staebler-Wronski effect as a-Si:H cells do.
5. Efficiencies of polycrystalline thin film cells are 50-80% higher than the efficiencies of a-Si:H triple junction cells.

Experimental Technique

The PEC work carried out by this project is presented in this section. FSEC has developed very good facilities for the preparation of CIGS2 solar cells and photoelectrochemical cells [20-22]. The CIGS2 thin films were prepared in two steps. Step one involved the deposition of CuGa-In metallic precursors using DC magnetron sputtering on glass substrate. Step two involved the sulfurization of metallic precursors in dilute (8%) H_2S at ambient temperatures. After the films were prepared, the material properties of the CIGS2 thin films were studied using scanning electron microscopy (SEM) for morphology, X-ray diffraction (XRD) for crystallographic structure and Auger electron spectroscopy (AES) for variations of elemental composition with depth in conjunction with ion etching. Next, excess copper at segregating at the surface as cuprous sulfide was etched away to obtain near stoichiometric CIGS2 thin films. CIGS2 thin film cells were completed by the deposition of n-type CdS layer using chemical bath deposition. Finally, the deposition of ZnO/ZnO:Al bilayer window using RF magnetron sputtering and the depositing of Cr/Ag front contact fingers using thermal evaporation through metal masks was done.

Experimental Results

In the first series of experiments that were carried out highly uniform CuGa-In metallic precursors were deposited on a 10 cm x 15 cm molybdenum coated glass substrate. CIGS2 thin films were prepared with a copper excess composition of 1 to 1.4 by using a modified sulfurization cycle to achieve optimum characteristics of the CIGS2 films. The thin films were then analyzed by SEM for morphology, XRD for crystallographic structure and AES analysis for the variation of composition with regard to thickness of the film. SEM micrographs of the films are shown in Figure 1. Figure 1a is unetched, 1b is etched, x5500, 1c is etched, x30000 and 1d is a cross-section SEM. The cross-section SEM was done by cleaving the thin-film sample from the glass side.

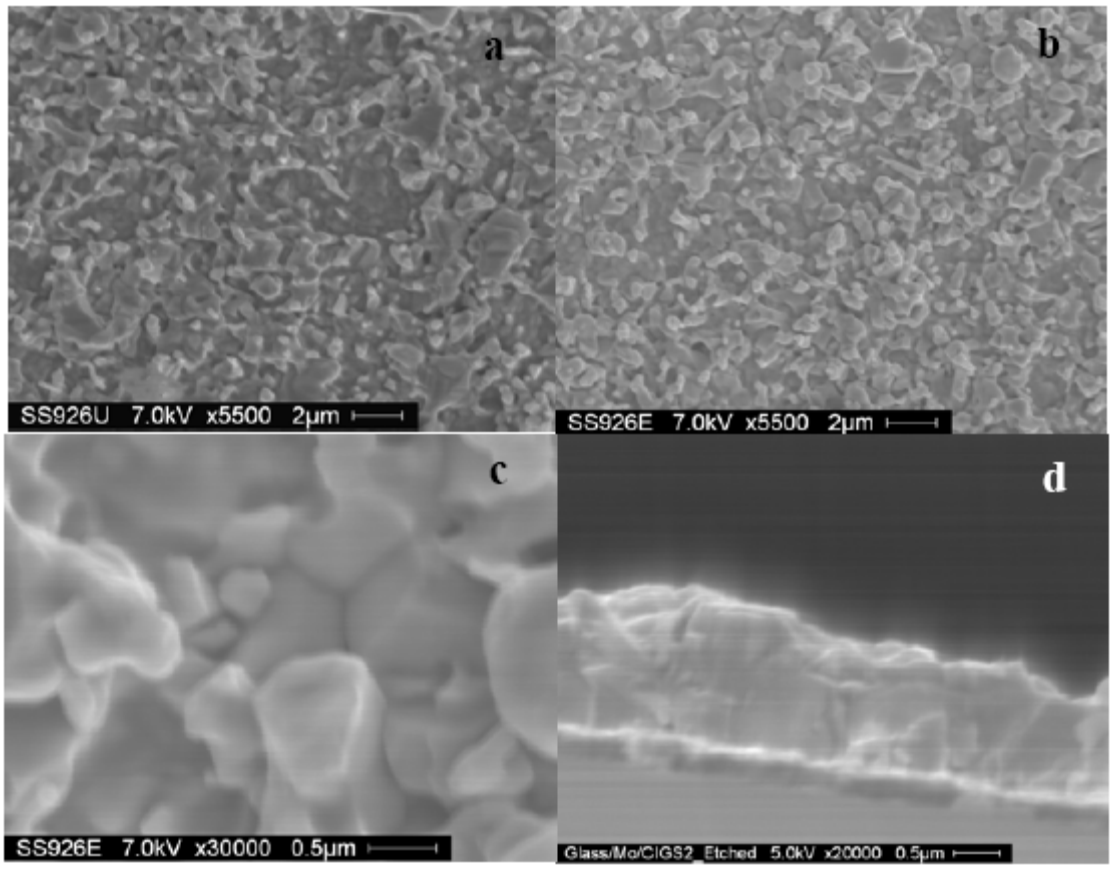

Figure 1. SEM micrographs of (a) unetched x5500, (b) etched x5500, (c) etched x30000 and (d) cross-section of etched CIGS2 thin film with copper excess composition of 1 to 1.4, x20000.

In Figure 2, XRD patterns of etched CIGS2 thin film show (101), (112), (103), (200), (220), (312), (400), (316) and (424) reflections of crystalline chalcopyrite CIGS2 and reflections from molybdenum. The strongest reflection was from (112) plane at 2θ = 27.92°. The lattice parameters were calculated as = 5.52 Å and c = 11.04 Å. The molybdenum reflection was observed at 2θ which is equal to 40.4°. The measured intensity ratio of (112)/(220/204), for these films was 2.74, thus, showing a preferred {112} orientation.

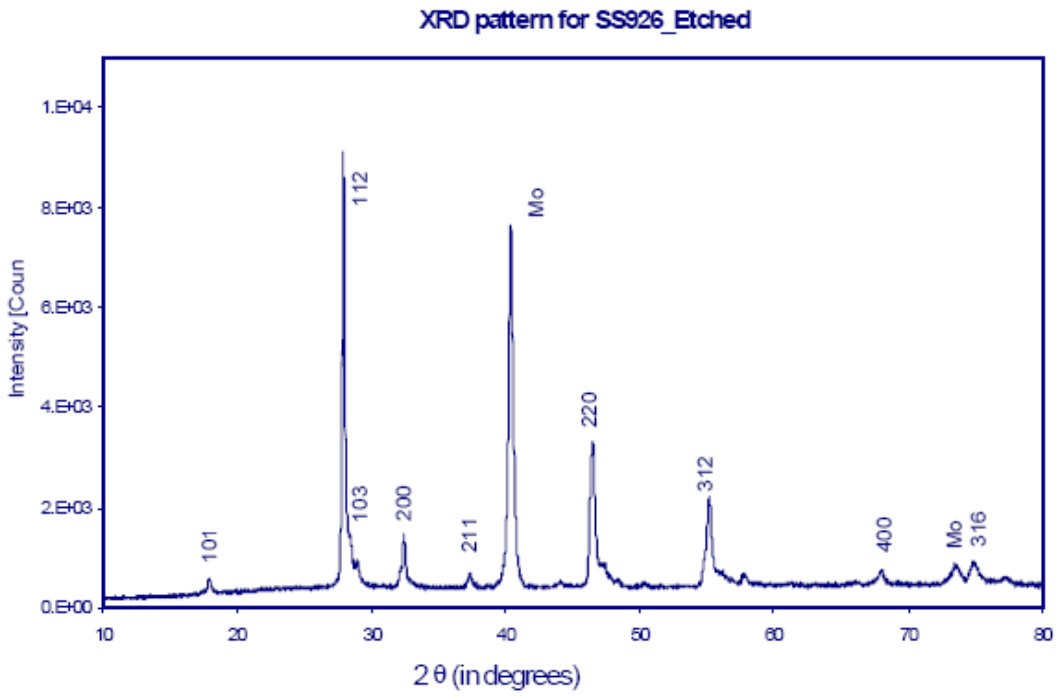

Figure 2. XRD pattern of etched CIGS2 thin film with copper excess composition of 1 to 1.4.

Figure 3 shows the AES profile of etched CIGS2 thin film. The results show that copper and sulfur signals are constant through the CIGS2 thickness, that gallium is increasing towards the back contact and indium is decreasing (being replaced by gallium).

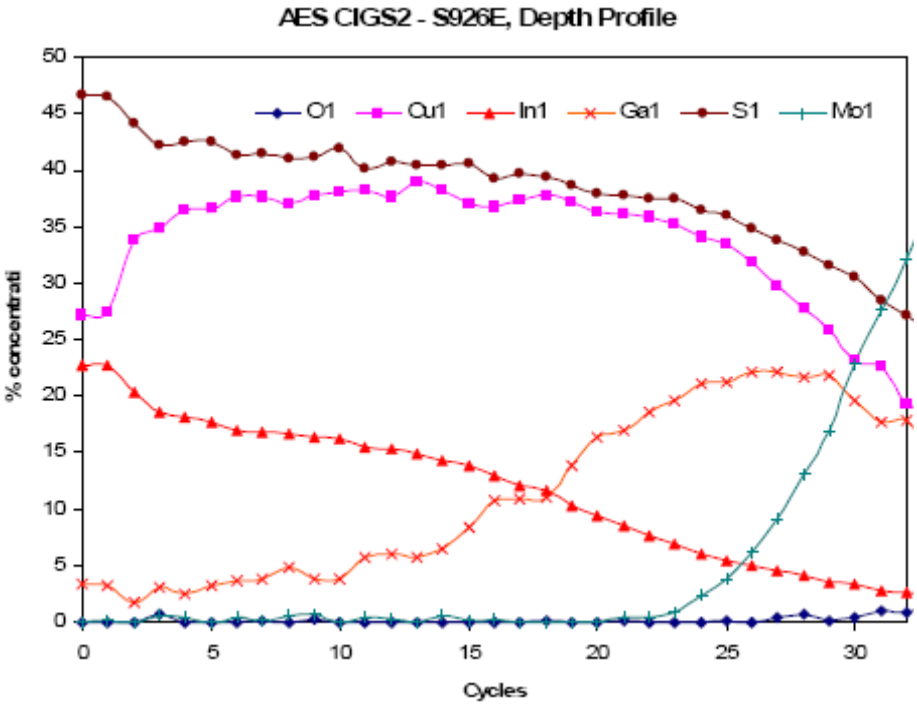

Figure 3. AES depth profile of etched CIGS2 thin film with copper excess composition.

The CIGS2 thin film solar cells were completed by the depositions of (1) CdS by CBD, (2) the ZnO/ZnO:Al window bilayer using RF magnetron sputtering and (3) the Cr/Ag front contact fingers by thermal evaporation.

With the cells completed, I-V measurements were done to understand the diode characteristics and to evaluate their performance. From the I-V measurements, the shunt resistance, R_p, was calculated using the nine point differential of change in voltage divided by the change in current at near-zero voltage, i.e. near the short circuit current density J_{sc} value. The series resistance was calculated in the similar manner at near-zero values current i.e. near the open circuit voltage, V_{oc}. Routine I-V measurements were carried out at FSEC PV Materials Lab. Selected samples were then sent to the National Renewable Energy Laboratory (NREL) for the deposition of MgF_2 antireflection coating and additional I-V measurements. Figure 4 shows the I-V measurement and resulting characteristics of the CIGS2/CdS thin film cell. The measured results at NREL were done for an air mass (AM) 1.5 conditions. The photovoltaic conversion efficiency obtained from these measurements was 11.99% with an open circuit voltage of 830 mV (see Figure 4). Band alignement measurements were also performed in order to measure band-offsets between CIGS2 and CdS and results from this study were used for improvement in the solar cell and PEC cell performance [23].

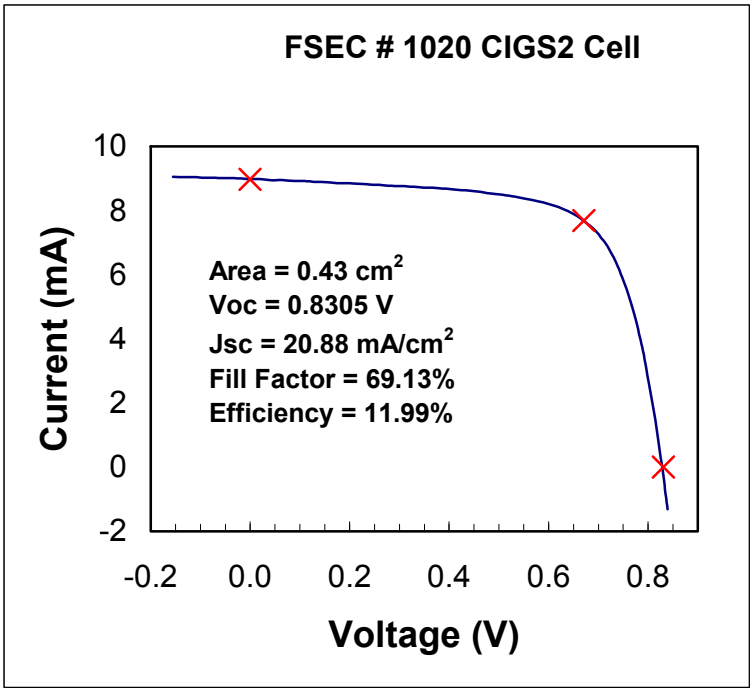

Figure 4. I-V characteristics of CIGS2/CdS thin film cell measured at NREL for AM 1.5 condition.

The 11.99% efficiency and open circuit voltage of 830.5 mV were the highest for a selenium free CIGS2/CdS thin film solar cells, prepared using sulfurization technique [15,18]. The same cell was sent to NASA Glenn Research Center (NASA GRC) for the I-V measurements at AM 0 conditions (space applications). Table 1 presents these cell performance results.

Table 1. Cell parameters from I-V measurements carried done at NASA GRC for AM 0 conditions

Cell	Voc (mV)	Jsc (mA/cm^2)	Fill Factor (%)	Efficiency (AM0)
SS1020-1	827.08	24.13	68	9.93
SS1020-2	824.14	23.76	68	9.75
SS1020-3	825.13	24.40	68.6	10.1
SS1020-4	825.69	24.00	69.1	10.01
SS1020-5	827.52	25.00	67.7	10.25
SS1020-6	825.37	24.56	63.5	9.41
SS1020-7	822.37	24.57	67.1	9.92
SS1020-8	819.96	24.31	67.5	9.84
SS1020-9	814.83	25.23	64.7	9.73

The next stage of the research was to prepare and characterize the cell's transparent conducting back layer. The materials chosen for this layer were ZnTe:Cu for superstrate type CdS/CdTe cells and ITO/MoS2 for substrate type CIGS2/CdS cells. Transparent and conducting ZnTe:Cu films were grown using a hot wall vacuum evaporation (HWVE) on 10 cm x 10 cm glass substrate. Deposition parameters were optimized to obtain a highly stoichiometric 5000 Á thick ZnTe film.

Various experiments were carried out by doping ZnTe film with Cu and Cu_2Te for comparison of their optical properties in the near IR region. The ZnTe:Cu thin films were obtained by doping ZnTe with 2-3% copper and annealing at 300 °C for 30 minutes. The substrate temperature was 300 °C, the hot wall temperature was 350 °C, and the deposition time was 10 minutes. These films were characterized using optical transmittance spectroscopy and X-ray diffraction (XRD) for their structure. Figure 5 presents the optical spectroscopy measurements which shows that the ZnTe film doped with Cu_2Te has better transparency (~80-90 % near IR region) as compared to films doped with Cu (~60-65 % near IR region). Thus, ZnTe was deposited to obtain a CdS/CdTe PEC cell. Figure 6 shows the XRD pattern of ZnTe:Cu film. The figure shows (111), (222) planes, indicating a highly textured growth in 111 direction.

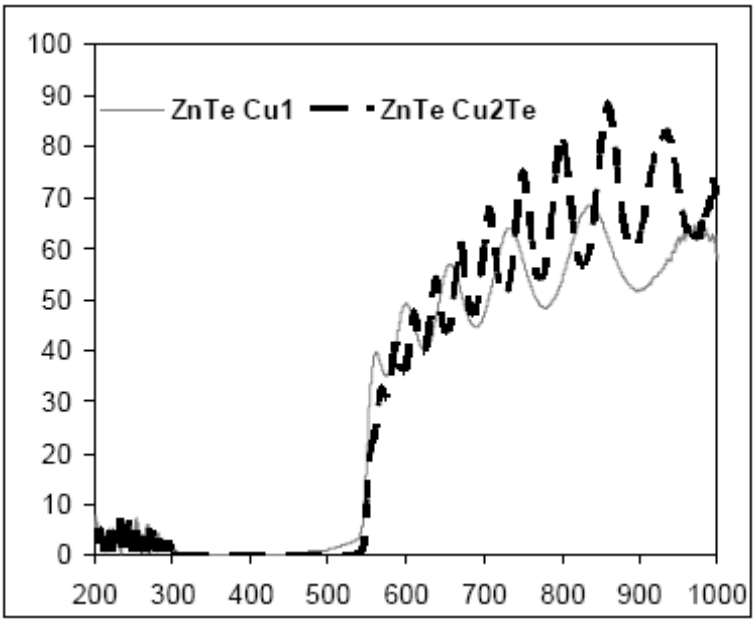

Figure 5. Optical transmittance spectroscopy plot for ZnTe doped with copper and with Cu_2Te.

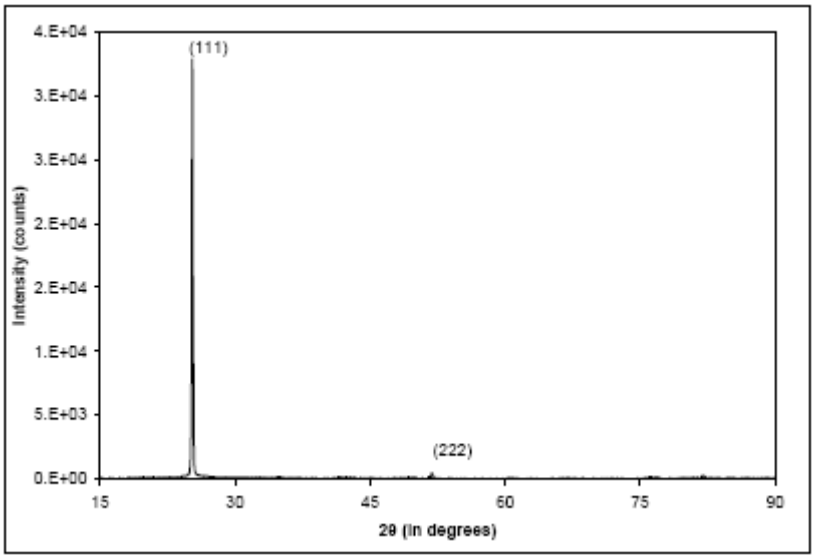

Figure 6. XRD pattern of ZnTe:Cu film deposited on glass using HWVE technique.

Another series of thin film cells were made using the SnO_2:F/CdS/CdTe samples procured from First Solar. For these cells, ZnTe:Cu was deposited giving thin films with optimized parameters. The completed cell had the configuration, SnO_2:F/CdS/CdTe/ZnTe:Cu/ZnO:Al/Ni-Al. The transparent conducting back layer of ITO/MoS2 for the substrate type CIGS2/CdS thin film PV cells was prepared and characterized.

Following the above, the photoanode and electrolyte for the photoelectrochemical (PEC) cell were prepared and characterized. The bandgap of the photoelectrode has a critical impact on the energy conversion of photons. Only photons of energy equal or higher than bandgap may be absorbed and used for conversion. In addition, in a heterojunction (CIGS2/CdS) device, the semiconductor with smallest bandgap determines the maximum cell efficiency. In the proposed two-cell PEC setup shown in Figures 7 and 8, CIGS2 has the smaller band gap of approximately ~1.5-1.7 eV. Therefore, photons of energy greater than1.5-1.7 eV are absorbed by the PV cell.

A two cell PEC using GIGS2 and CdTe set up is shown in Figure 7 and was developed during the first phase. This set-up uses a pH10 (NaOH + buffer) to liberate the hydrogen and oxygen at calculated efficiency of 5%.

During earlier work platinum foil (Pt) was used for oxygen evolution. However, Pt is a poor oxygen electrocatalyst. Therefore, the oxygen overpotential was reduced by utilizing a ruthenium oxide (RuO_2) electrode. Based on experiments with various electrolytes, suitable electrolytes with high electrolytic conductivity were prepared. A photocatalyst based on ruthenium sulfide (RuS_2) was employed for use in combination with the GaAs/GaAlAs cell. RuS_2 has a direct band gap of 1.3 eV and recent studies have shown that the bandgap of RuS_2 can be reduced to 1.1 eV by addition of 1% iron (Fe) or by sputter-deposition of a thin RuS_2 layer.

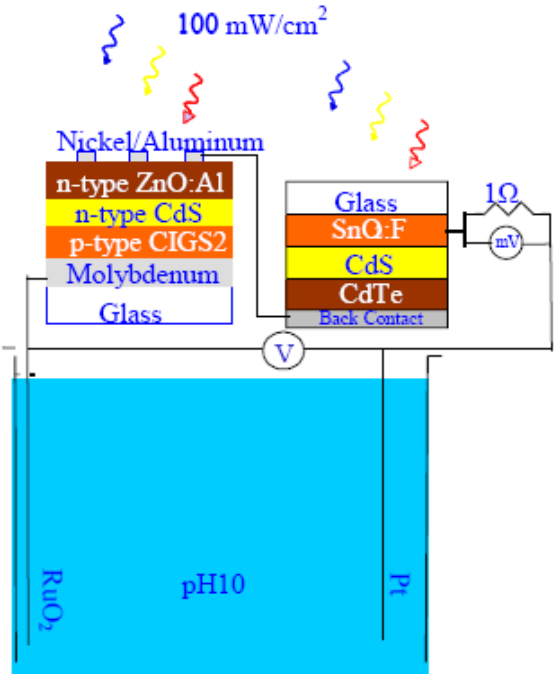

Figure 7. Two cell PEC setup with metallic back contact.

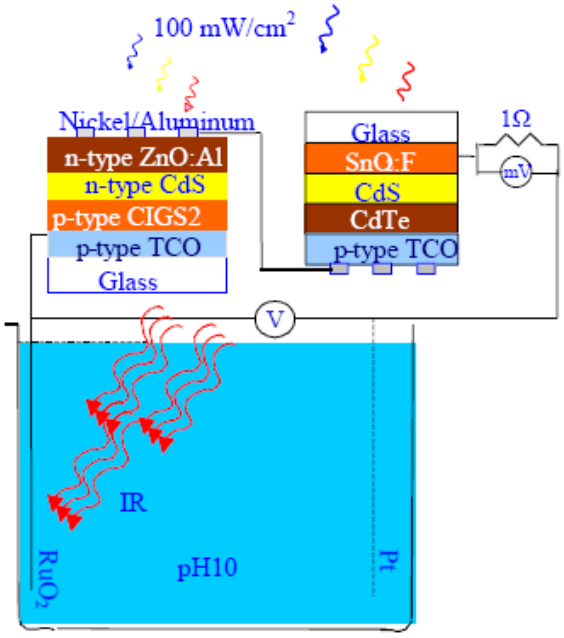

Figure 8. Two-Cell PEC setup with p-type TCO back contact.

Since there is a reasonably good match between photons above 1.5 eV and those between 1.1 to 1.5 eV, an efficient multiple bandgap combination of a thin film photovoltaic cell and a thin-film photocatalyst for water splitting can be developed [19,24,25]. Therefore, the work concentrated on developing an efficient photoanode for oxygen evolution. Experiments were carried out to analyze the performance of RuS_2, RuO_2, and Pt photoanodes for oxygen evolution. RuS_2 electrodes were prepared at 350 °C, 425 °C, and 475 °C and tested for their performance. The RuS_2 electrodes prepared at 350 °C showed better performance than those prepared at 425 °C and 475 °C. Table 2 presents the values of photo current for RuS_2, RuO_2 and Pt. The results shows RuS_2 and, RuO_2 have better performance than Pt.

Table 2. Comparison of photocurrents from RuS_2, RuO_2, and Pt.

Photoanode	Electrolyte	Photocurrent
RuS_2 (@ 350 °C	pH12	7mA @ 1.25V
RuO_2	pH10	3.6mA @ 1.27V
Pt	pH12	1.56mA @ 1.3V

A detailed literature search was then done on p-type transparent conducting oxides (TCO). Transparent and conducting layers such as zinc oxide, tin oxide and cadmium stannate are routinely used as n-type window layers in CIGS, CIGSeS, CIGS2, and CdTe cells. The non-existence of p type transparent conducting oxides has been postulated to originate from the general electronic characteristic of a strong localization of the upper edge of the valance band in oxide ions. Recently, thin films of p-type TCO have been prepared by modification of the energy band structure to reduce the localization behavior. To reduce the localization, cationic species such as Cu^+ were selected for the p-layer. The Cu^+ species has a closed shell, whose energy is almost comparable to those of the 2p levels of oxygen anions. The crystal structure with tetragonal coordination has been chosen to enhance the covalency in the bonding between cation and oxide ion and the dimension of crosslinking of Cu ions has been lowered. The delafossite-type compound $CuAlO_2$ exhibits p-type conductivity and mild transparency. The delafossite structure is characterized by layers of Al-O octahedral separated by layers of linearly coordinated Cu in the +1 state. Experimental work has shown $CuAlO_2$ to be a small polaron conductor with a low mobility. Other cuprous delafossite materials that are flexible with respect to chemical composition and cation size have been studied.

Several compounds of the general formula $CuMO_2$ have been considered. These are M equal to Ga, Y, Sc, and In. The gallium and yttrium compounds have been reported in the literature to have similar bulk electrical properties to $CuAlO_2$. However, due to the larger cation size relative to aluminum, these materials have a higher propensity for doping on the M3+ site as well as incorporating oxygen interstitials, leading to higher hole concentrations. Both the gallium and yttrium compounds have been synthesized by a standard solid-state reaction at high temperature in a controlled atmosphere. The electrical properties of the scandium compound have been reported with a conductivity of 30 S cm^{-1}, which is low compared to ITO. However, it is several orders of magnitude greater than other reported p-type TCO's. The work, mostly carried out in Japan demonstrates that the delafossite structure has merit for displaying p-type TCO behavior.

Understandably, the properties of the p-type transparent and conducting oxides are considerably inferior to those of their n-type counterparts, but it is still an area of enormous opportunity. Successes will be slow in coming, but the work must be pursued. So far, p-type electric conduction has been obtained in transparent thin films of $CuAlO_2$, $CuGaO_2$, NiO, ZnO, $SrCu_2O_2$, and In_2O_3-Ag_2O layers prepared by laser ablation, RF magnetron sputtering, pulse-

laser deposition, and chemical vapor deposition. The best reported conductivity of p type transparent conducting oxides has been in the range 1-10 S cm^{-1} with a transmissivity of >20%. P-type electrical conductivity on ZnO thin films has been achieved by co-doping method using Ga (donor) and N (acceptor) as dopants [16,17]. These films have a resistivity of 2 Ω-cm and hole concentration of 4 x 10^{19} cm^{-3} at room temperature.

Photoanodes for better oxygen evolution were prepared and characterized. For example, 1% Fe was incorporated into RuS_2 which improves the bandgap to 1.1 eV from 1.3 eV enabling further reduction of the overpotential required for oxygen evolution. These photoanodes were characterized with XRD for their structure and SIMS for the depth composition. Figures 9a and 9b show the XRD pattern of RuS_2 and $Ru_{0.99}Fe_{0.01}S_2$ respectively.

Figures 10(a) and 10(b) show the SIMS depth profiles for RuS_2 and $Ru_{0.99}Fe_{0.01}S_2$ on Ti substrate.

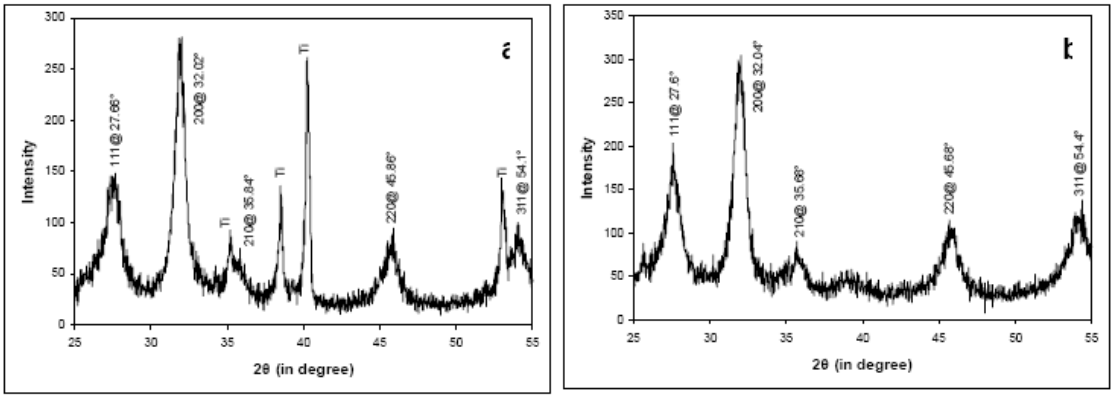

Figure 9. (a) XRD pattern of RuS_2, (b) XRD pattern of $Ru_{0.99}Fe_{0.01}S_2$.

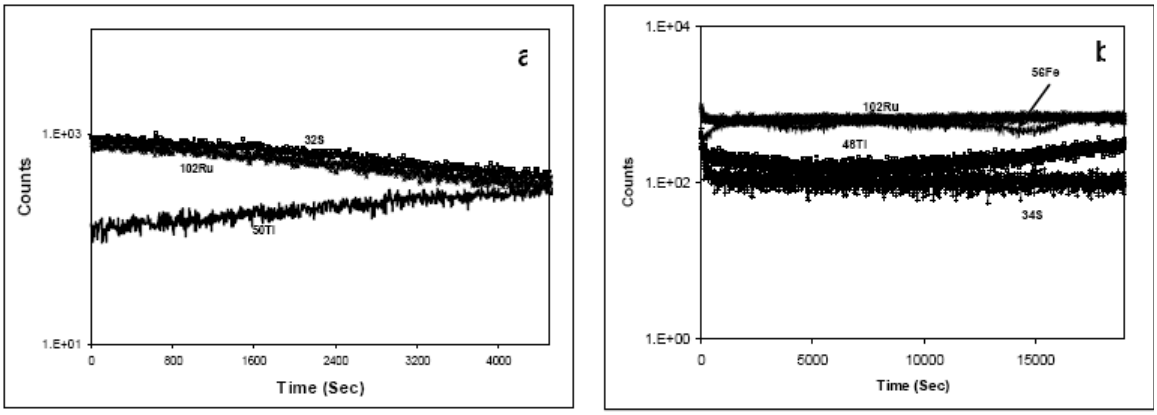

Figure 10(a) SIMS depth profile of RuS_2, (b) SIMS depth profile of $Ru_{0.99}Fe_{0.01}S_2$.

PEC Efficiency Calculations

This section presents the PEC calculations from the PV cells and photoanodes that were developed. For the calculations, two CIGS2/CdS thin film solar cells were used in series with the RuS_2 anode for oxygen generation and platinum for hydrogen generation. Figure 11 shows the I-V characteristic of two CIGS2 thin film solar cells with copper excess composition 1 to 1.4, connected in series and illuminated with AM1.5 illumination (100 mW/cm^2). The figure also shows the variation of current with voltage of PEC cell having a RuS_2 anode in dark for oxygen and platinum cathode for hydrogen. Maximum power from this PEC setup is obtained at the crossover point of the cell I-V curve and the anode I-V curve.

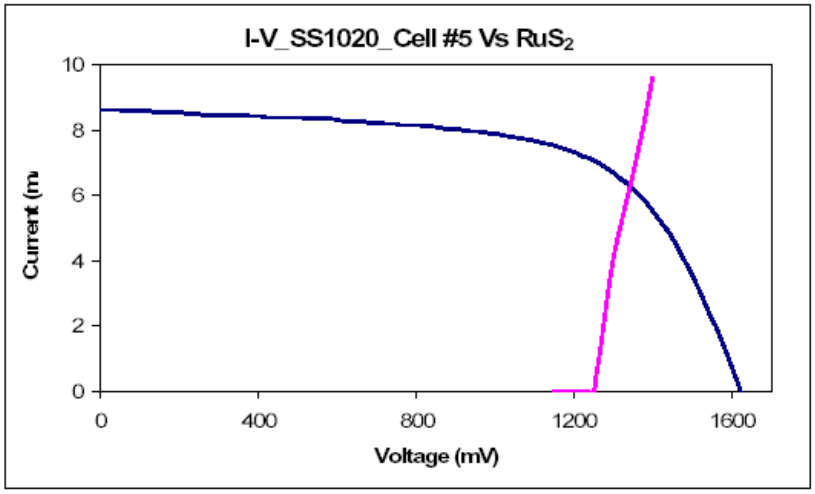

Figure 11. I-V characteristic of two CIGS2/CdS thin film solar cells illuminated with AM1.5 illumination along with the I-V of PEC cell having RuS_2 anode in dark and platinum.

In theory, an ideal PEC systems will operate at a short-circuit condition. Thus, the efficiency can be calculated using power out divided by power in and assuming 100% photocurrent efficiency. From Figure 11, this calculation gives the following result:

Crossover point = 6.3 mA @ 1.343 V
Power input = 100 mW/cm^2
Electrical Power output = 6.3 x 1.343 = 8.46 mW, Total area of two cells = 0.882 cm^2
Hydrogen Power output = 6.3 x 1.229 = 7.743 mW, Total area of two cells = 0.882 cm^2
where the lower heating value of hydrogen is 1.229 watts/A.
PEC efficiency = 8.78%

In another experiment, CIGS2 cells were prepared on glass with a transparent conducting back contact. For this case, the PEC setup is as shown in Figure 8. For this case, two CIGS2 cells were employed instead of using CIGS2 and CdTe cells. The efficiency of the CIGS2 cells as measured at NREL was 5.95%. Connecting the two CIGS2 thin-film solar cells in series with a RuS_2 anode and a platinum cathode gives a total area of the two CIGS2 cells of 0.862 cm^2. When the cells were illuminated at 100 mW/cm^2 under with AM1.5 conditions, a PEC efficiency of 2.99% was obtained. It is noted that this PEC efficiency obtained using back contact TCO layers, as shown in the Figure 8, is lower than that obtained using conventional opaque back contacts, as shown in Figure 7. This lower value is because of the lower operating voltage of the

PV cells. The PEC efficiency can be improved when the back contacts are further optimized to obtain a more optimum operating voltage. In addition, higher efficiencies can be attainable because of the increase in the oxygen evolution using the IR photons incident on the photoanode.

Discussions

The results obtained from this research shows that PEC systems require an optimum trade off between efficiency and economics. Thin film solar cells have the potential of costs as low as $1/Wp by the year 2015 [estimation of U. S. DOE]. The PV cells chosen for this application were superstrate type CdTe and substrate type CIGS2 thin film solar cells.
During the course of this study, conditions under which an oxygen photocatalyst can be improved were probed. New photoanodes RuS_2 and $Ru_{0.99}Fe_{0.01}S_2$ were introduced, both of which had better anode characteristics than RuO_2. The bandgap of RuS_2 is 1.3 eV and the addition of 1% of iron into RuS_2 ($Ru_{0.99}Fe_{0.01}S_2$), reduces its bandgap to 1.1 eV.

Conclusions

Photoelectrochemical water splitting was studied for hydrogen generation using a multiple bandgap combination of thin-film photovoltaic cells and photocatalysts. The research has developed P-type transparent and conducting layers, CIGS2 and CdTe thin film cells with transparent and conducting back contacts, suitable electrolytes with high conductivity and ruthenium oxide, ruthenium sulfide and ruthenium-iron sulfide photoanodes. Over the course of this study, the photovoltaic efficiency of conventional CIGS2 cells was enhanced to 11.99%. with an open circuit voltage of 830 mV. The calculated PEC efficiency for this configuration was 8.78%.

In another experiment, the PEC hydrogen generation efficiency using two CIGS2 thin-film solar cells on transparent and conducting back contacts, connected in series with a RuS_2 anode and a platinum cathode under AM1.5 illumination. The PEC efficiency was calculated as 2.99%. This efficiency is lower than the CIGS2 and CdTe cycle because of the lower operating voltage of the CIGS2 pair. This efficiency can be improved by optimization of the operating voltage and increasing of the efficiency the photoanode for oxygen evoluation.

Patents, Publications, Presentations, and Students from Research

As a result of the research there were 9 technical papers, 4 graduate student theses and 14 presentations. The research supported 1 Ph.D and 3 M.S students.

Publications

1. U. S. Avachat, A. H. Jahagirdar and N. G. Dhere, “Multiple bandgap combination of thin film photovoltaic cell and photoanode for efficient hydrogen and oxygen generation by water splitting”, Solar Cells & Solar Energy Materials, 91 (2007), 1488–1491.

2. G. Braunstein, A. Muraviev, H. Saxena, N. Dhere, V. Richter, and R. Kalish, “P-Type Doping of Zinc Oxide by Arsenic Ion Implantation”, Applied Physics Letters, Vol. 87, p. 192103, (2005).

3. N. G. Dhere, V. S. Gade, A. A. Kadam, A. H. Jahagirdar, S. S. Kulkarni and S. M. Bet, “Development of CIGS2 thin film solar cells”, Materials Science and Engineering B, 116, (2005), pp. 303-309.

4. N. G. Dhere , A. A. Kadam, A. H. Jahagirdar, S. S. Kulkarni, L. Weinhardt, D. Groß, C. Heske and E. Umbach, “Spectroscopic Analysis Of CIGS2/CdS Thin Film Solar Cell Heterojunctions On Stainless Steel Foil”, Journal of Physics and Chemistry of Solids, 66, (2005), pp. 1872-1875.

5. O. Hamad, G. Braunstein, H. P. Patil and N. G. Dhere, “Effect of thermal treatment in oxygen, nitrogen, and air atmospheres on the electrical transport properties of zinc oxide thin films”, Thin Solid Films, 489, (2005), pp. 303-309.
6. N. G. Dhere, A. H. Jahagirdar, “Photoelectrochemical Water Splitting for Hydrogen Production using Multiple Bandgap Combination of Photovoltaic Cell and Thin-Film-Photocatalyst”, Thin Solid Films, 480-481, (2005), pp. 462-465.

7. N. G. Dhere, A. A. Kadam, S. S. Kulkarni, S. M. Bet and A. H. Jahagirdar, “Large Area CIGS2 Thin Film Solar Cells on Foils: Nucleus of a Pilot Plant”, Solar Energy Journal, 77, (2004), pp. 697-703.

8. N. G. Dhere, V. S. Gade, A. A. Kadam, A. H. Jahagirdar, S. S. Kulkarni and S. M. Bet, “Development of CIGS2 Thin Film Solar Cells” Materials Science and Engineering B, 116, (2004), pp. 303-309.

9. A. H. Jahagirdar, A. A. Kadam, N. G. Dhere, “CIGSS Thin Films for Photoelectrochemical Water Splitting Using Multiple Bandgap Combination of Thin Film Photovoltaic Cell and Photocatalyst: Clean and Renewable Hydrogen Source”, Proceedings CD of the 2005 Solar World Congress, Orlando, August 6-12, 2005, Article 1470.

Graduated Students

Anant H. Jahagirdar, Ph.D.
Anil Pai, M.S.
Upendra S. Avachat, M.S.
Vinay V. Hadagali, M.S.

References

1. O. Khaselev, A. Bansal and J. A. Turner, International Journal of Hydrogen Energy, Volume 26, Issue 2, February 2001, p. 127.

2. O. Khaselev and J. A. Turner, J. Electrochem. Soc. 133 (1998), p. 3335.

3. A. J. Nozik In: F. Cardon, W. P. Gomes and W. Dekeyser, Editors, Photovoltaic and Photoelectrochemical Solar Energy Conversion, Plenum Publ., New York (1981), p. 263.

4. R. S. Nicholson and I. Shain, J. Anal. Chem. 36 (1964), p. 706.

5. W. R. Heineman, P. T. Kissinger, American Laboratory, 1982, p. 29.

6. E. L. Miller, R. E. Rocheleau and X. M. Deng , International Journal of Hydrogen Energy, Volume 28, Issue 6, June 2003, p. 615.

7. O. Khaselev and J. A. Turner, Science 280 (1998), p. 425.

8. J. A. Turner, Science 285 (1999), p. 687.

9. R. E. Rocheleau, E. L. Miller and A. Misra, Energy Fuels 12 (1998), p. 3.

10. S. U. M. Khan and J. Akikusa, J. Phys. Chem. B 103 (1999), p. 7184.
11. C. Santato, M. Ulmann and J. Augustynski, J. Phys. Chem. B 105 (2001), p. 936.
12. S. Licht, J. Phys. Chem. B 105 (2001), p. 6281.

13. S. Licht, B. Wang, S. Mukerji, T. Soga, M. Umeno and H. Tributsch, J. Phys. Chem. B 104 (2000), p. 8920.

14. S. Licht, S. Ghosha, H. Tributsch and S. Fiechter, Sol. Energy Mater. Sol. Cells 70 (2002), p. 471.

15. A. H. Jahagirdar and N. G. Dhere, Solar Energy Materials and Solar Cells Volume 91, Issues 15-16, 22 September 2007, p. 1488.

16. G. Braunstein, A. Muraviev, H. Saxena, N. Dhere, V. Richter, and R. Kalish, Applied Physics Letters, Vol. 87, p. 192103, (2005).

17. O. Hamad, G. Braunstein, H. P. Patil and N. G. Dhere , Thin Solid Films, 489, (2005), p. 303.

18. A. H. Jahagirdar, A. A. Kadam and N.G. Dhere, Proc. 4th World Photovoltaic Solar Energy Conference, Hawaii, (2006), pp. 557-559.

19. U. S. Avachat, A. H. Jahagirdar and N. G. Dhere, Solar Energy Materials and Solar Cells, 91 (2007) p. 1488.

20. N. G. Dhere, V. S. Gade, A. A. Kadam, A. H. Jahagirdar, S. S. Kulkarni and S.Bet, Materials Science and Engineering B, 116, (2005), p. 303.

21. N. G. Dhere, A. A. Kadam, S. S. Kulkarni, S. M. Bet and A. H. Jahagirdar, Solar Energy Journal, 77, (2004), p. 697.

22. N. G. Dhere, V. S. Gade, A. A. Kadam, A. H. Jahagirdar, S. S. Kulkarni and S. M. Bet, Materials Science and Engineering B, 116, (2004), p. 303.

23. N. G. Dhere , A. A. Kadam, A. H. Jahagirdar, S. S. Kulkarni, L. Weinhardt, D. Groß, C. Heske and E. Umbach, Journal of Physics and Chemistry of Solids, 66, (2005), p. 1872.

24. N. G. Dhere, A. H. Jahagirdar, Thin Solid Films, 480-481, (2005), pp. 462-465.

25. A. H. Jahagirdar, A. A. Kadam, N. G. Dhere, Proceedings of the 2005 Solar World Congress, Orlando, August 6-12, 2005, Article 1470.

October 2007

System Analysis of Hydrogen Production and Utilization at KSC

A. T-Raissi, M. Elbaccouch, K. Ramasamy, and J. Baik
Florida Solar Energy Center

Research Period: January 2003 to December 2007

Summary

The objectives of this project are to identify, characterize, and simulate a technology for hydrogen production for the National Aeronautics and Space Administration - John F. Kennedy Space Center (NASA-KSC) from locally available sources. This activity will establish a baseline for the future procurement and use of hydrogen propellants at NASA-KSC. Chemical Process Simulators (CPS) are used to generate highly detailed and accurate process models for use in chemical plant designs. Aspen Technology's Aspen Plus is among the most widely used CPS platforms by leading companies in the process industries. The approach of the project is to generate gaseous and liquid hydrogen, under steady state conditions, sufficient for several NASA space shuttle mission.

The followings are the major tasks of the project:

Task #1: Chemical Process Simulation of Used Oil for the Liquid Hydrogen Production.

Task #2: Aspen Plus Process Model for the Production of Gaseous Hydrogen via Steam Gasification of Bagasse.

Introduction

Task #1

The objective of this work is to simulate an economically viable process for the production of liquid hydrogen by steam reforming used automotive lubricating oil. The simulation is carried out using Aspen Plus™, Aspen Adsim™, and Aspen Icarus™ chemical process simulators. The reformer is simulated as a Gibbs reactor to reform the large oil molecules. A water-gas shift unit, simulated as an equilibrium reactor, is used to enhance the production of hydrogen. A flash separator is used to remove excess water from the product stream. The off-gas is burned with air in a combustor and the generated energy is used to heat the processing units. Aspen Adsim™ is incorporated to simulate the adsorption process of the pressure swing adsorption (PSA). A hydrogen liquefaction unit, simulated as a Claude densifier cycle, is used to produce liquid hydrogen. Aspen-Icarus™ is utilized to develop a detailed capital costs breakdown for the plant.

Task #2

The objective of this task is to simulate a chemical plant for the production of hydrogen from bagasse using Aspen Plus Chemical Process Simulator with no heat generation. The goal of the simulation is to design and optimize the performance of a directly heated gasification system that converts bagasse into gaseous hydrogen. The Aspen model consists of four sections: 1) a dryer section to partially dry the bagasse, 2) a gasifier consists mainly of a bagasse combustion zone, and a gasification zone to volatilize the bagasse feedstock, 3) a gas clean up section to

purify the hydrogen product, and 4) a pressure swing adsorption unit to recover the hydrogen at desired purity levels. A fraction of the bagasse was used as a fuel and directed into combustor reactors to fire up the plant. The temperatures of the combustor reactors in the gasifier section were set at 1550 °C, and the generated heat was used to heat up the plant's reactors and flow streams. All other process units operate adiabatically. 900 $kg.hr^{-1}$ of bagasse was used as the feed stock of the plant to produce 17.4 $kg.hr^{-1}$ ultra pure hydrogen product.

Project Results

Task #1: Chemical Process Simulation of Used Oil for the Liquid Hydrogen Product in Mohamed, M. Elbaccouch, Ali T-Raissi, Karthik K. Ramasamy, and Jong Baik (Florida Solar Energy Center)

Abstract

The objective of this work is to simulate an economically viable process for the production of liquid hydrogen by steam reforming used automotive lubricating oil. The simulation is carried out using Aspen Plus™, Aspen Adsim™, and Aspen Icarus™ chemical process simulators. The reformer is simulated as a Gibbs reactor to reform the large oil molecules. A water-gas shift unit, simulated as an equilibrium reactor, is used to enhance the production of hydrogen. A flash separator is used to remove excess water from the product stream. The off-gas is burned with air in a combustor and the generated energy is used to heat the processing units. Aspen Adsim™ is incorporated to simulate the adsorption process of the pressure swing adsorption (PSA). A hydrogen liquefaction unit, simulated as a Claude densifier cycle, is used to produce liquid hydrogen. Aspen-Icarus™ is utilized to develop a detailed capital costs breakdown for the plant.

Introduction

Millions of gallons of used lubricating oil are available throughout the year in the United States at approximately 10 cents per gallon of delivered cost. Used lubricating oil is a high volume resource with a high energy density that can be converted into a valuable energy source. Elemental analysis of virgin synthetic and used lubricating oil contains 13.4 and 13.7 wt% hydrogen respectively. Calculations have shown that one gallon of used automotive lubricating oil produces approximately 1.38 kg of hydrogen via steam reformation process. Used lubricating oil has an approximate density of 0.88 g/ml at 20 °C and consists typically of 73-80 wt% aliphatic hydrocarbons, 11-15% monoaromatic hydrocarbon, 2-5% diaromatic hydrocarbons, and 4-8% polyaromatic hydrocarbons. The goal of this project is simulate a chemical plant for the production of liquid hydrogen from used lubricating oil.

Process Model Simulation

Aspen Plus™ Design—Figure 1 shows the Aspen Plus™ flowsheet of the steam reformation of used automotive lubricating oil to produce pure liquid hydrogen. Table 1 describes the various unit operations in the Aspen model. The goal of the simulation is to produce 12.5 kg/h of liquid hydrogen at a reformer temperature of 850 °C and a volumetric flow rate ratio of used oil-to-water of 2-to-1. The process consists of a Gibbs reactor for the thermal reforming of used oil with water followed by cyclone and filter units to remove carbon from the main product stream. The product stream is directed to a water-gas shift reactor to produce more hydrogen ($CO + H_2O = CO_2 + H_2$) [5]. The product stream is then introduced to a flash separator to remove

excess water. A pressure swing adsorption (PSA) unit recovers pure hydrogen from the product stream. A combustor converts the off-gas into energy which is used to heat the processing units. The pure gaseous hydrogen stream is directed to a Claude cycle where it is converted to liquid hydrogen. All of the unit operations in the plant run adiabatically utilizing the exothermic heat of the plant.

The Gibbs reactor minimizes the total Gibbs free energy of the feed streams to the reactor assuming that all of the components defined in the simulation in the component specification sheet are viable products [2]. The Gibbs reactor reforms the complex oil mixture by braking down the oil into simple hydrocarbon molecules, such as H_2, H_2O, CO, CO_2, CH_4, etc. 15 mol% of the pure hydrogen produced from the PSA is recycled in order to meet the 70 mol% hydrogen requirements in the feed stream to the PSA [5, 6].

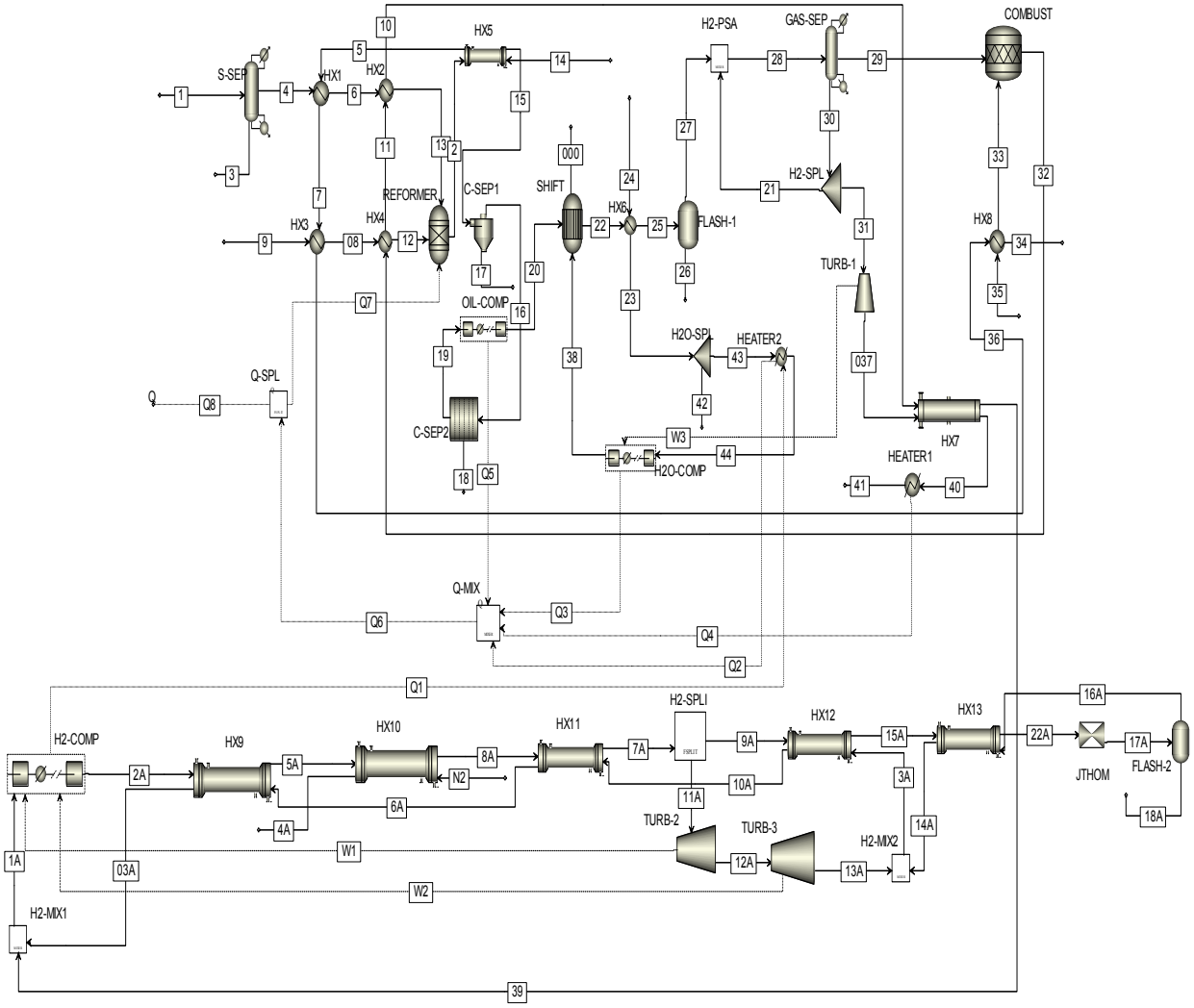

Figure 1. Aspen Plus[tm] flowsheet of the steam reformation of used automotive lubricating oil to produce liquid hydrogen.

Table 1. Specifications of the unit operations given in Figure 1.

Unit Operation	Description
S-sep	C_8H_6S separator
Reformer	Gibbs reactor at 850 °C and 1 atm
C-sep1	Cyclone for solid carbon removal
C-sep2	Filter for solid carbon removal
Oil-comp	Used oil Micro compressor with 67 °C inter cooler
H_2O-comp	Water vapor compressor with 217 °C inter cooler
H_2-comp	H_2 gas compressor with 27 °C inter cooler
Shift	Equilibrium reactor for water-gas shift reaction at 280 °C
Flash-1	Flash reactor to remove excess water prior to PSA
Flash-2	Flash reactor for liquid H_2 production
H_2-PSA	H_2 mixer in the PSA unit specifies
Gas-sep	Separator to separate H_2 from off-gas in the PSA unit
H_2-spl	Splitter to recycle gaseous H_2 to generate 70 mol% H_2 in stream 28 (PSA)
H_2O-spl	Adjust the correct flow of water to HX6
Combust	Combustor to burn the off-gas and generate energy for the plant
Turb-1;2;3	Turbine
Q-mix	Mixer for the heat generated from the micro compressors
Q-spl	Heat splitter to run the reformer
H_2-Mix1;2	H_2 mixer in the liquefaction plant
Jthom	Joule Thomson valve
H_2-spl	Splits 50% H_2 in the Calude cycle
Heater1;2	Heater
HX	Heat exchangers

Claude Cycle Design—The gaseous hydrogen stream produced from the PSA unit is directed to a Claude cycle hydrogen liquefaction unit shown schematically in Figure 2. Most of the large scale hydrogen liquefaction plants are based on the Claude cycle or its modifications. The hydrogen liquefaction unit uses liquid nitrogen pre-cooled Claude cycle with an isentropic expander and an isenthalpic expansion valve. A multi-stage hydrogen compressor with intercoolers produces 23.5 atm of high pressure gas while the temperature remains at room temperature, and the liquid nitrogen bath cools the compressed gas down near 77 K [7]. Some of the compressed gas is routed to the expander, and then it gets colder by experiencing isentropic expansion process. The expanded gas helps to cool the counter flow high pressure gas in the heat exchanger. After the high pressure gas gets colder through the coldest heat exchanger, the cold gas experiences isenthalpic expansion process over the Joule-Thompson (JT) expansion valve. The expansion valve generates 20.3 K of liquid-vapor mixture of hydrogen at 1 atm. The liquefied hydrogen is separated to storage tanks and only the saturated vapor goes back to the liquefaction cycle. The same amount of makeup gas as the liquefied hydrogen is supplied to the liquefaction cycle to complete the cycle.

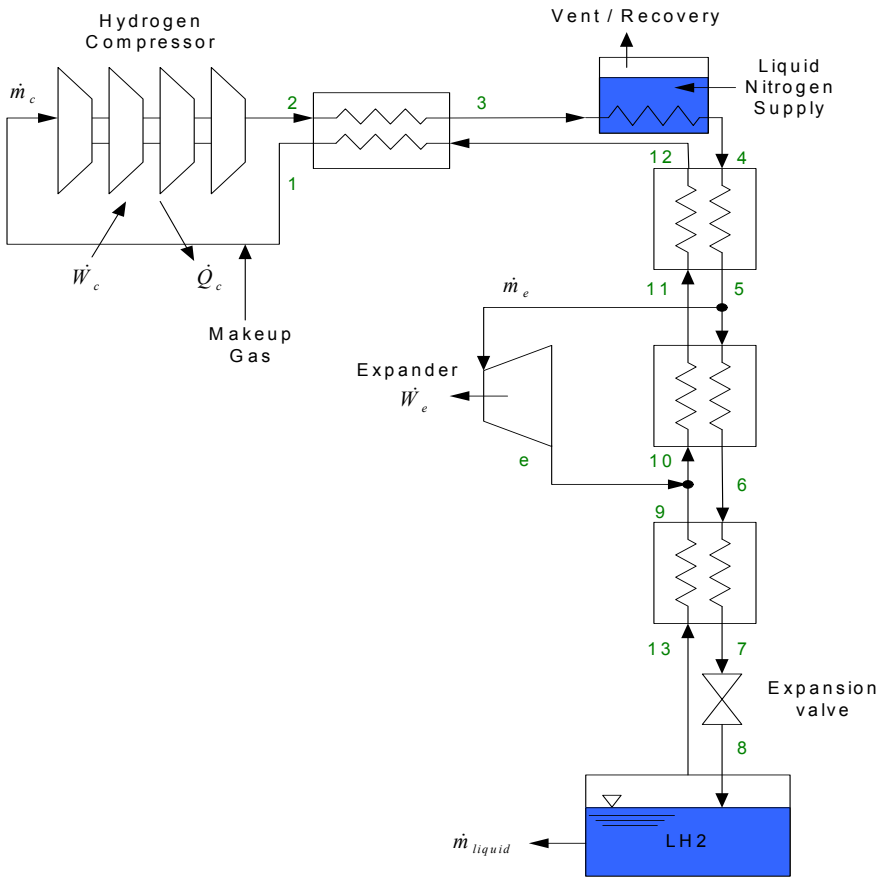

Figure 2. Schematic diagram of the Aspen Plus™ Claude Cycle Hydrogen Densifier.

Pressure Swing Adsorption (PSA) Design—The pressure swing adsorption (PSA) is widely used for hydrogen recovery processes (+0.99%) in petroleum refinery, ethylene plants, and reformer off-gas. Aspen Adsim™ is a gas phase adsorption process suitable for the PSA simulation. Aspen Adsim™ simulates preferential adsorption of components (i.e., CH_4, CO, CO_2, NOx, etc) in multiple beds for hydrogen recovery. As shown in Figure 3, one bed is in an adsorption step, while the others in pressurization, depressurization, and purging steps.

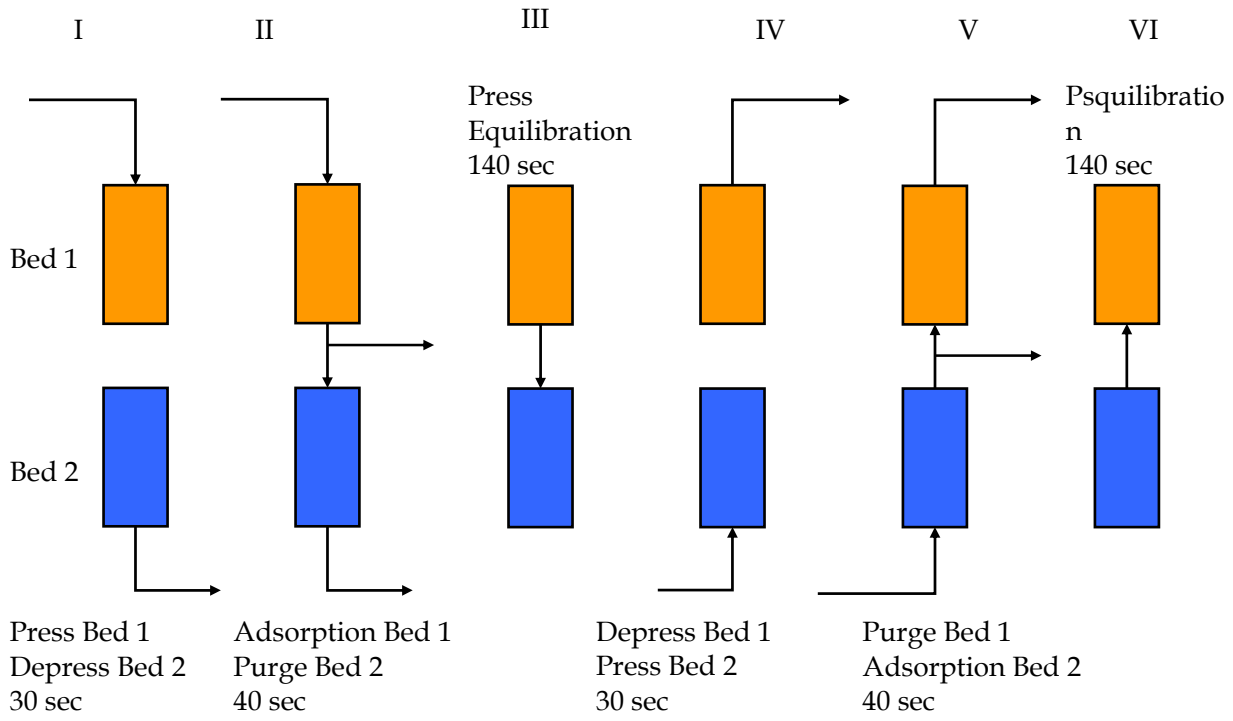

Figure 3. Cycle steps of the two-bed pressure swing adsorption process in Aspen Adsim™.

Results and Discussions

Gaseous Hydrogen Production—The Aspen Plus™ flowsheet for the liquid hydrogen production by steam reforming used automotive lubricating oil (Figure 1) consists of a gaseous hydrogen production section simulated using the Peng Robinson with Boston-Mathias alpha function (PR-BM) equation of state, and a liquid hydrogen production section simulated using the Benedict Webb Rubin-Lee Starling (BWR-LS) equation of state. The plant was simulated at a reformer temperature and pressure of 850 °C and 1 atm respectively. Also, the volumetric flow rate ratio of used oil-to-water was maintained at 2-to-1. 1.43 L/min of used oil and 0.715 L/min of water were introduced to the plant at ambient conditions to produce 12.5 kg/h of liquid Hydrogen. It should be noted that the plant produces carbon due to the restricted reformer temperature and used oil-to-water volumetric flow ratio. The used oil components and composition are published elsewhere [8].

The streams mole fractions, molar flow rates, temperatures, and pressures are given in Tables 2. The sulfur in the used oil feed stream was represented as benzothiophen, and separated before introducing the feed stream to the reformer. The off-gas stream, contained mostly hydrogen and methane, was burned in a combustor to produce the required heat to run the plant. The reformer product stream was fed to a cyclone and a filter to remove solid carbon before introducing the product stream to the water-gas-shift reactor. The carbon molar composition and processing parameters are given in Table 3.

Table 2. Stream balance and composition for liquid H_2 production from used oil at reformer temperature of 850 °C and water-to-used oil volumetric flow ratio of 1-To-2

Stream	Mole fraction						Mole flow (kmol/h)	vapor fraction	Temp (°C)	Press (atm)
	H_2	CO	CO_2	CH_4	H_2O	S				
0	0.000	0.000	0.000	0.000	0.000	0.000	0.000	0.000	na	na
1	0.000	0.000	0.000	0.000	0.000	0.0932	0.635	0.000	25	0.99
1a	1.000	0.000	0.000	0.000	0.000	0.000	31.844	1.000	16	1.0
2	0.708	0.261	0.00500	0.0130	0.0140	0.000	7.564	1.000	850	1.0
2a	1.000	0.000	0.000	0.000	0.000	0.000	31.844	1.000	27	23.5
03a	1.000	0.000	0.000	0.000	0.000	0.000	25.664	1.000	13	1.0
3	0.000	0.000	0.000	0.000	0.000	0.000	0.0590	0.000	25	0.99
3a	1.000	0.000	0.000	0.000	0.000	0.000	25.664	1.000	-238	1.0
4	0.000	0.000	0.000	0.000	0.000	0.000	0.576	0.000	25	0.99
4a	0.000	0.000	0.000	0.000	0.000	0.000	7.139	1.000	-155	1.0
5	0.000	0.000	0.000	0.000	1.000	0.000	40.000	0.000	94	1.0
5a	1.000	0.000	0.000	0.000	0.000	0.000	31.844	1.000	-143	23.5
6	0.000	0.000	0.000	0.000	0.000	0.000	0.576	0.000	60	0.99
6a	1.000	0.000	0.000	0.000	0.000	0.000	25.664	1.000	-202	1.0
7	0.000	0.000	0.000	0.000	1.000	0.000	40.000	0.000	93	1.0
7a	1.000	0.000	0.000	0.000	0.000	0.000	31.844	1.000	-200	23.5
0-8	0.000	0.000	0.000	0.000	1.000	0.000	2.020	0.000	60	0.99
8a	1.000	0.000	0.000	0.000	0.000	0.000	31.844	1.000	-195	23.5
9	0.000	0.000	0.000	0.000	1.000	0.000	2.020	0.000	25	0.99
9a	1.000	0.000	0.000	0.000	0.000	0.000	15.922	1.000	-200	23.5
10	trace	0.000	0.166	0.000	0.105	0.000	12.663	1.000	521	1.0
10a	1.000	0.000	0.000	0.000	0.000	0.000	25.664	1.000	-208	1.0
11	trace	0.000	0.166	0.000	0.105	0.000	12.663	1.000	599	1.0
11a	1.000	0.000	0.000	0.000	0.000	0.000	15.922	1.000	-200	23.5
12	0.000	0.000	0.000	0.000	1.000	0.000	2.020	1.000	600	0.99
12a	1.000	0.000	0.000	0.000	0.000	0.000	15.922	1.000	-221	6.0
13	0.000	0.000	0.000	0.000	0.000	0.000	0.576	0.863	200	0.99
13a	1.000	0.000	0.000	0.000	0.000	0.000	15.922	1.000	-239	1.0
14	0.000	0.000	0.000	0.000	1.000	0.000	40.000	0.000	25	1.0
14a	1.000	0.000	0.000	0.000	0.000	0.000	9.743	1.000	-236	1.0
15	0.708	0.261	0.005	0.013	0.014	0.000	7.564	1.000	80	1.0
15a	1.000	0.000	0.000	0.000	0.000	0.000	15.922	1.000	-234	23.5
16	0.708	0.261	0.005	0.013	0.014	0.000	7.564	1.000	80	1.0
16a	1.000	0.000	0.000	0.000	0.000	0.000	9.743	1.000	-253	1.0
17	0.000	0.000	0.000	0.000	0.000	0.000	0.000	0.000	80	1.0
17a	1.000	0.000	0.000	0.000	0.000	0.000	15.922	0.720	-253	1.0
18	0.000	0.000	0.000	0.000	0.000	0.000	0.000	0.000	80	0.98
18a	1.000	0.000	0.000	0.000	0.000	0.000	6.179	0.000	-253	1.0
19	0.708	0.261	0.005	0.013	0.014	0.000	7.564	1.000	80	0.98

20	0.708	0.261	0.005	0.013	0.014	0.000	7.564	1.000	67	20.0
21	1.000	0.000	0.000	0.000	0.000	0.000	0.126	1.000	26	19.2
22	0.415	0.002	0.112	0.006	0.465	0.000	17.564	1.000	280	20.0
22a	1.000	0.000	0.000	0.000	0.000	0.000	15.922	1.000	-237	23.5
23	0.000	0.000	0.000	0.000	1.000	0.000	17.000	0.575	101	1.0
24	0.000	0.000	0.000	0.000	1.000	0.000	17.000	0.000	25	1.0

Table 2 (continued)

Stream	Mole fraction						Mole flow (kmol/h)	Vapor fraction	Temp (C)	Press (atm)
	H_2	CO	CO_2	CH_4	H_2O	S				
25	0.415	0.002	0.112	0.006	0.465	0.000	17.564	0.536	26	20.0
26	trace	trace	trace	trace	1.000	0.000	8.150	0.000	26	17.7
27	0.775	0.004	0.209	0.011	0.002	0.000	9.415	1.000	26	17.7
28	0.778	0.003	0.207	0.011	0.002	0.000	9.541	1.000	26	19.2
29	0.344	0.01	0.609	0.031	0.005	0.000	3.236	1.000	26	19.2
30	1.000	0.000	0.000	0.000	0.000	0.000	6.305	1.000	26	19.2
31	1.000	0.000	0.000	0.000	0.000	0.000	6.179	1.000	26	19.2
32	trace	0.000	0.166	0.000	0.105	0.000	12.663	1.000	870	1.0
33	0.000	0.000	0.000	0.000	0.000	0.000	10.000	1.000	77	1.0
34	0.000	0.000	0.000	0.000	1.000	0.000	40.000	0.000	86	1.0
35	0.000	0.000	0.000	0.000	0.000	0.000	10.000	1.000	25	1.0
36	0.000	0.000	0.000	0.000	1.000	0.000	40.000	0.000	91	1.0
0-37	1.000	0.000	0.000	0.000	0.000	0.000	6.179	1.000	-124	1.0
38	0.000	0.000	0.000	0.000	1.000	0.000	10.000	1.000	217	20.0
39	1.000	0.000	0.000	0.000	0.000	0.000	6.179	1.000	27	1.0
40	trace	0.000	0.166	0.000	0.105	0.000	12.663	1.000	462	1.0
41	trace	0.000	0.166	0.000	0.105	0.000	12.663	1.000	50	1.0
42	0.000	0.000	0.000	0.000	1.000	0.000	7.000	0.575	101	1.0
43	0.000	0.000	0.000	0.000	1.000	0.000	10.000	0.575	101	1.0
44	0.000	0.000	0.000	0.000	1.000	0.000	10.000	1.000	101	1.0
N2	0.000	0.000	0.000	0.000	0.000	0.000	7.139	0.000	-196	1.0

Table 3. Carbon balance at specification given in Table 2

Stream	Mole fraction	Mole flow (kmol/h)	Solid fraction	Temp (°C)	Press (atm)
2	1.000	2.581	1.000	850	1.0
15	1.000	2.581	1.000	80	1.0
16	1.000	0.440	1.000	80	1.0
17	1.000	2.142	1.000	80	1.0
18	1.000	0.440	1.000	80	0.98

As shown in Figure 4, the hydrogen flow rate is monitored as a function of the major unit operations of the plant. Most of the hydrogen was produced in the reformer, and the water-gas-shift reactor enhances the hydrogen production. Insignificant amount of hydrogen was lost in the flash reactor placed before the PSA section. The PSA consists of mixer, a separator, and a splitter. The feed stream to the PSA (stream 27) consists of mostly of H_2, CH_4, and CO_2. The separator separates the hydrogen from the off-gas, and the splitter recycles part of the hydrogen to the mixer in order to maintain 70 mol% of hydrogen in stream 28. Also, Figure 4 shows the temperature flow throughout the plant.

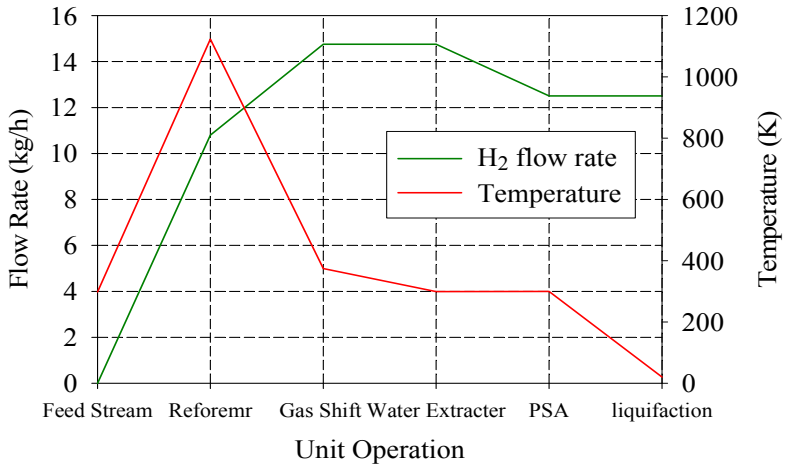

Figure 4. Flow rate of H_2 as a function of the major unit operations of the plant.

Figure 5 and Table 4 depict the reformer major products as a function of temperature on dry basis. The reformer temperature and pressure were varied from 750-900 °C, and 1 atm respectively, while the volumetric flow rate ratio of used oil-to-water ratio was held at 2-to-1.

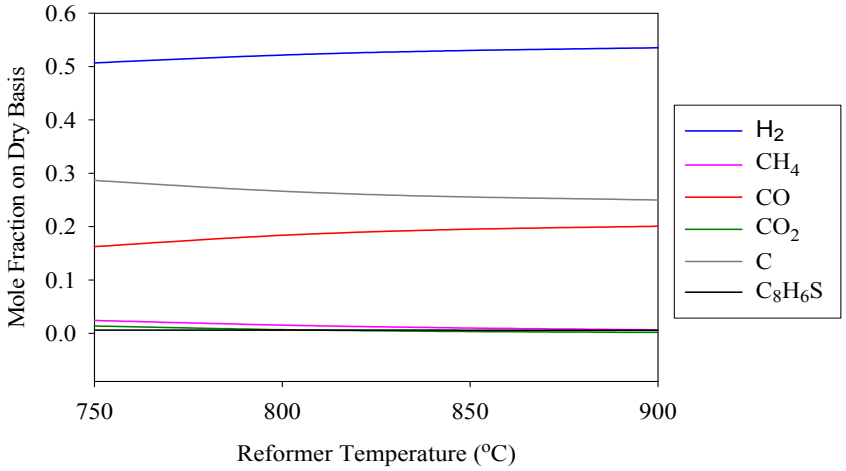

Figure 5. Reformer product as a function of temperature on dry basis.

Table 4. Reformer products as a function of temperature on dry basis

	750 °C	750 °C	800 °C	800 °C	850 °C	850 °C	900 °C	900 °C
	kmol/h	mol fract	kmol/h	mol fract	kmol/h	mol fract	kmol/h	mol fract
C8H6S	0.0414	0.00620	0.0414	0.00600	0.0410	0.00580	0.0410	0.00570
H2	3.412	0.507	3.619	0.522	3.746	0.530	3.823	0.535
CO2	0.0926	0.0138	0.0480	0.00690	0.0240	0.00340	0.0120	0.00170
CO	1.093	0.162	1.275	0.184	1.379	0.195	1.434	0.201
CH4	0.163	0.0243	0.107	0.0154	0.0700	0.00990	0.0470	0.00660
C	1.929	0.287	1.848	0.2663	1.805	0.256	1.786	0.250
total	6.731	1.000	6.938	1.000	7.065	1.000	7.143	1.000

Liquid Hydrogen Production—Figure 6 represents the thermodynamic calculations of the Claude cycle simulated in Aspen Plus™. The figure shows the Calude cycle cooling sequence as a function of temperature and entropy. A series of heat exchangers reduce the temperature of the system coupled with an expansion engine and a JT expansion valve. The cycle is optimized by manipulating the discharge pressure and the split ratio at the expansion engine. Aspen plus™ results show that the mass of hydrogen liquefied to hydrogen compressed is 6.2/32.4 = 0.19, and the split ratio through the expander is 50%. Table 5 has the temperature, pressure, and efficiency parameters of the cycle's heat exchangers.

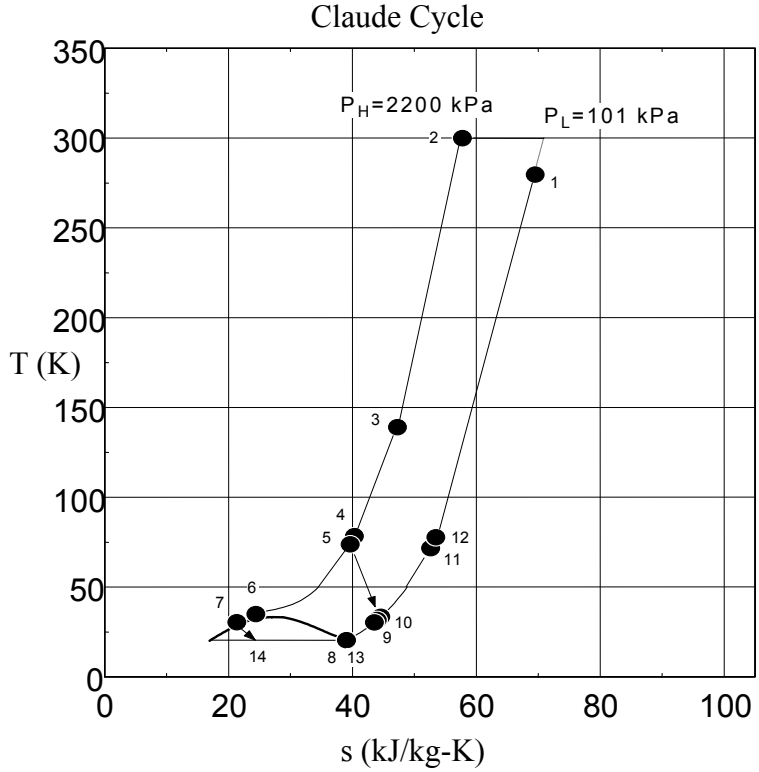

Figure 6. Claude Cycle thermodynamic analysis.

Table 5. Processing parameters of the heat exchangers in Claude Cycle of the liquefaction plant

Block	HX9	HX10	HX11	HX12	HX13
H_2 $kmol^{-1}$	32.4	32.4	32.4	16.2	16.2
T in (K)	300	130	78.0	73.3	38.9
T out (K)	130	78.0	73.3	38.9	36.1
P (atm)	23.5	23.5	23.5	23.5	23.5
Efficiency	0.94	0.98	0.49	0.91	0.91

Plant Efficiency—The efficiency of the plant is calculated according to equation 1.

$$\text{Efficiency} = \frac{\text{net.H}_2\,\text{produced, kW} + \text{heat, kW}}{\text{Fuel, kW}} \tag{1}$$

The plant produces 12.5 kg/h liquid hydrogen and a surplus 61 kW of heat. The volumetric flow rate of used oil is 1.43 L/min or the equivalent energy of 799 kW. The energy requirement for the three compressors in the gaseous and liquid hydrogen sections of the plant is 160 kW. Equation 2 is used to calculate the amount of heat needed for the Carnot engine [9].

$$\frac{W}{Q_H} = \frac{T_H - T_C}{T_H} \tag{2}$$

Where W is the work needed by the compressors, Q_H is the heat reservoir at T_H, and Q_C is the heat reservoir at T_C. T_H is assumed to be the flame temperature of H_2 (2045 °C), and T_C is assumed to be 50 °C. From equation 2, QH is found to be 164 kW, and the equivalent flow rate of hydrogen that needs to be burned is 4.9 kg/h. The efficiency of the plant, calculated using equation 1, is 39%.

Pressure Swing Adsorption—Figure 7 depicts the Aspen Adsim™ flowsheet of the two-bed PSA system with zeolite adsorbent. The PSA has ten-cycles of six-steps and 420 s per cycle (Figure 3). Each cycle has multiple steps of adsorption, desorption, purging, and equilibration. Figure 8 a and b depicts an Aspen Adsim™ dynamic run. The mole fraction of hydrogen in the product stream in Figure 8a is 0.9776.

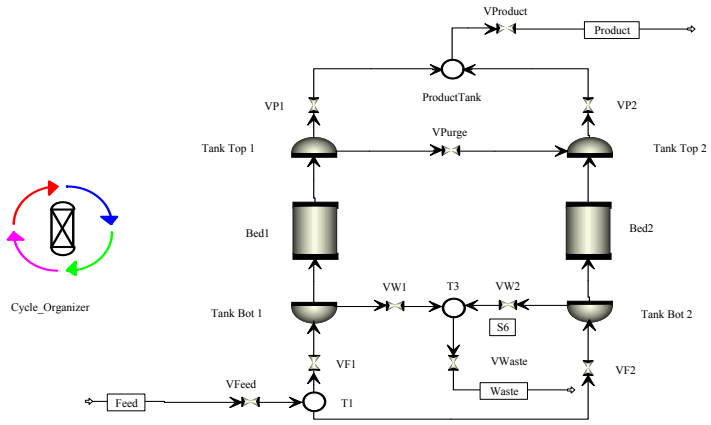

Figure 7. Aspen Adsim™ flowsheet of the pressure swing adsorption.

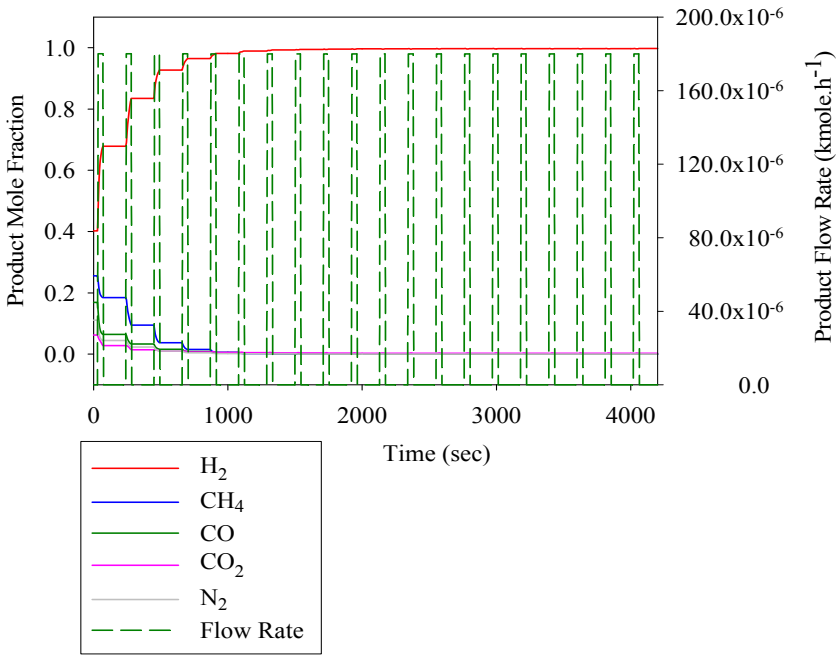

a

a

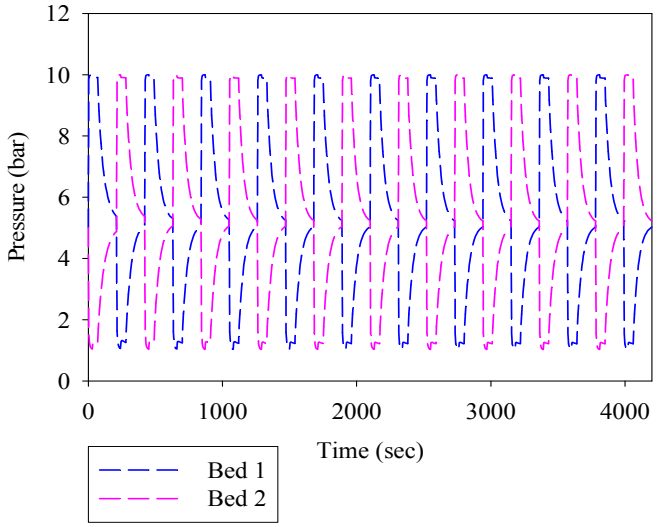

Figure 8. Aspen Adsim™ dynamic results of the two-bed pressure swing adsorption system a) Product stream composition b) Pressure profile of the two-beds.

Process Economics—The initial capital costs of the liquid hydrogen plant are given in Figure 9-11. The capital costs is divided into direct field costs, indirect filed costs, and non-field costs. The initial capital costs of the plant are estimated to be $8.2MM. The material costs breakdown for the direct field costs is $3.2M, and the labor costs breakdown for the direct field costs with 63.6MM total. The indirect field costs and non-field costs are estimated to be $1.0MM and $3.4MM respectively.

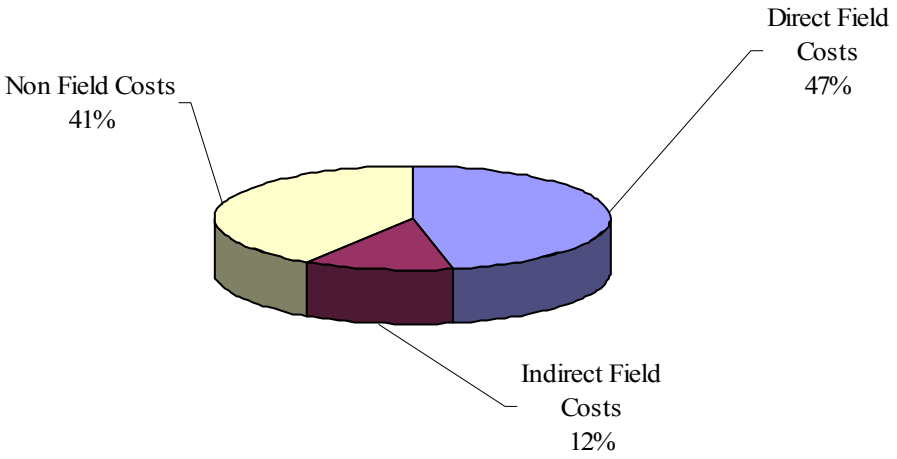

Figure 9. Capital costs breakdown of the hydrogen plant with $8.2MM total.

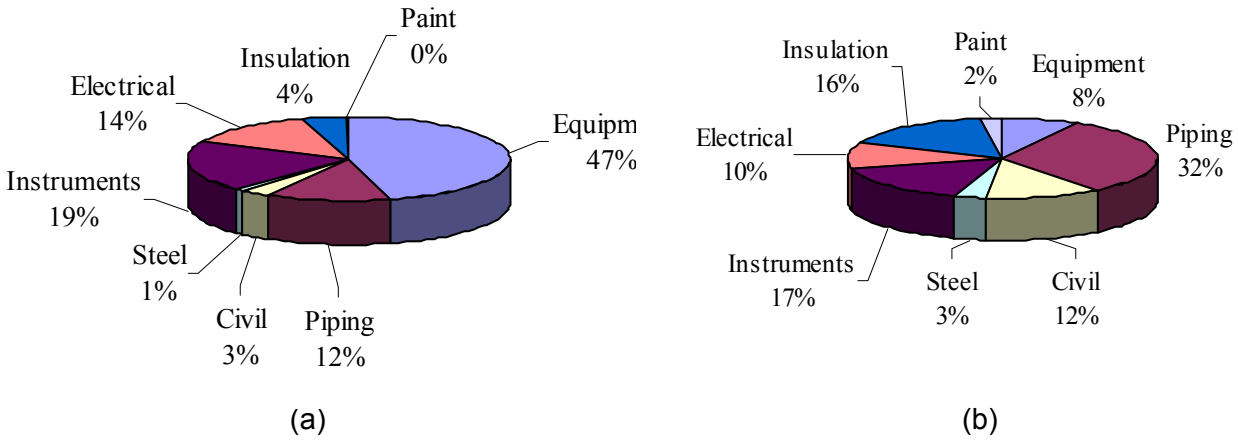

Figure 10. a) Material costs breakdown for the direct field costs with $3.2MM total. b) Labor costs breakdown for the direct field costs with 63.6MM total.

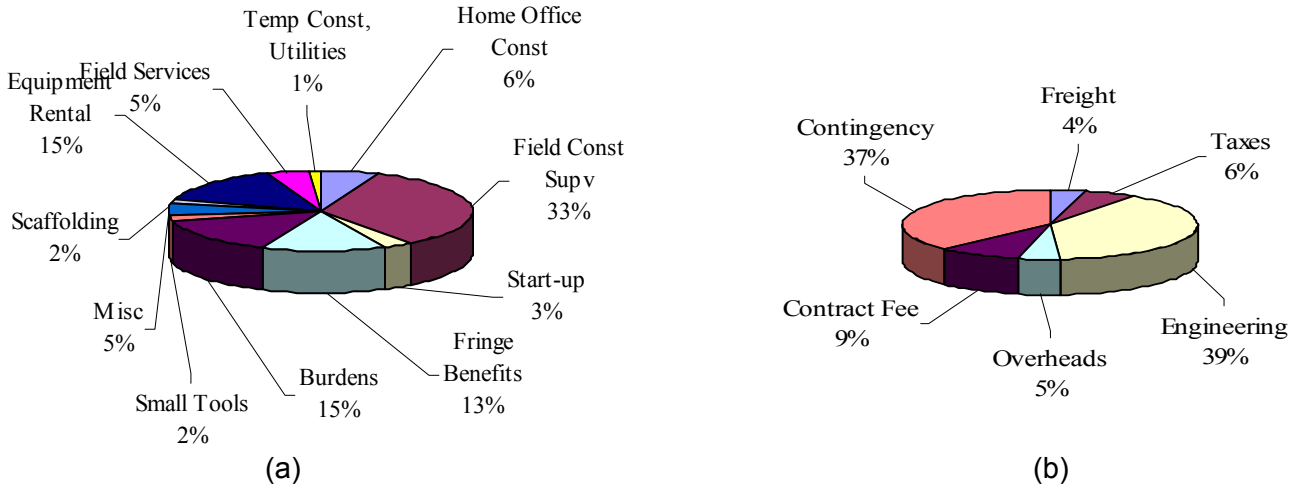

Figure 11. a) Indirect field costs breakdown with $1.0MM total.
b) Non field costs breakdown with $3.4MM total.

Conclusions

This study utilizes Aspen Plus™ and Aspen Adsim™ to design a plant for the production of liquid hydrogen by the steam reformation of used lube oil. The temperature of the reformer was held constant at 850 °C and the volumetric flow rate ratio of used oil-to-water was maintained at 2-to-1. 1.43 L/min of used oil and 0.715 L/min of water were used to produce 12.5 $kg.h^{-1}$ of liquid hydrogen. Most of the hydrogen was produced within the reformer. The plant generated its energy by burning the off-gas stream with air and heating/cooling the processing streams in heat exchangers. A Claude cycle was used to simulate the hydrogen liquefaction process and integrated with the gaseous hydrogen section of the plant. The mass of hydrogen liquefied to hydrogen compressed was 6.2/32.4 = 0.19, and the split ratio through the expander was 50%. The efficiency of the plant was found to be 39%. Aspen Adsim™ is used to develop a two-bed PSA system for the hydrogen recovery from a mixture containing CH_4, CO, CO_2, and NO_2. The mole fraction of hydrogen in the PSA product stream was 0.9766.

References

[1] Used Mineral-Based Crankcase Oil, Chemical and Physical Information. http://www.atsdr.cdc.gov/toxprofiles/tp102-c3.pdf.

[2] Elbaccouch M., & T-Raissi A. Aspen Plus Process Model for the Production of Gaseous Hydrogen via Bagasse Gasification. In the Proceedings of the *15th World Hydrogen Energy Conference*, Yokohama, Japan, 2004.

[3] Muradov, N, T-Raissi, A., & Robertson, T. Hydrogen Production via Catalytic Reformation of Low-Quality Methane Containing Feedstocks. Presentation at the *Hydrogen Power Theoretical and Engineering Solutions International Symposium (HYPOTHESIS)*, Porte Conte, Italy, 2003.

[4] Bain A. NASA Kennedy Space Center Base Center Hydrogen Operations. Florida Solar energy Cente, University of Central Florida, FSEC- CR-1359-02, October 2002.

[5] Skolnik, E,, & Putsche, V. Hydrogen Implementation Agreement, Task 11: Integrated Systems, Final Report of Subtask B: Analysis Tools. International Energy Agency, 1999.

[6] Ruthven, D. Principles of Adsorption and Adsorption Processes. John Wiley & Sons, New York, 1984.

[7] Klaus, D., Timmerhaus, K., & Flynn TM. *Cryogenic Process Engineering,* Plenum Press, New York, 1989.

[8] T-Raissi, A., Elbaccouch, M., Mohajeri, N., Ramasamy, K., Solanki, A., Muradov, N., & Block, D. NASA-Hydrogen Research at Florida Universities, Mid-Year Review Meeting, Task IV-A, System Analysis of Hydrogen Production & Utilization at KSC, http://www.hydrogenresearch.org/home.htm, Tallahassee, FL, March 30, 2004.

[9] Smith, J., & Van Ness, H. Introduction to Chemical Engineering Thermodynamics, 4th ed., 1987, McGraw-Hill, Inc.

Task#2: Aspen Plus Plant Design for Gaseous Hydrogen Production by Steam Gasification of Bagasse

Abstract

This work presents a process design for the production of gaseous hydrogen (H_2) from bagasse using Aspen Plus chemical process simulator (CPS). The goal of the simulation was to model performance of a gasifier that converts bagasse into gaseous H_2. The Aspen plant consists of four sections: 1) a dryer section to partially dry the bagasse, 2) a gasification section to volatilize the bagasse feedstock, 3) a gas clean-up and conditioning section to purify H_2, and 4) a pressure swing adsorption (PSA) unit to recover pure gaseous H_2. The simulation was thermo-neutral in that all of the reactors in the flowsheet operated adiabatically with zero heat duty except the compressor. The adiabatic process was simulated with minimum destruction of green bagasse by utilizing a combustor in the dryer section to combust the off-gas and a portion of the partially dried bagasse, and a second combustor in the gasifier section to burn a fraction of the carbon in the partially dried bagasse. 900 kg/h of green bagasse was used as the feedstock for the plant to produce 36.90 kmol/h of gaseous H_2 with an overall efficiency of 78%.
Key words: Hydrogen; Bagasse; Aspen Plus; Gasifier; Gibbs; PSA.

Introduction

The objective of this paper was to design a directly heated steam gasification plant for converting bagasse into gaseous hydrogen (H_2) using Aspen Plus chemical process simulator (CPS). The approach was to generate gaseous H_2 under steady state conditions adiabatically without producing excess heat. The H_2 production process modeled contains drying, gasification, clean-up and conditioning, and pressure swing absorption (PSA) sections. Aspen Plus is a widely used CPS platform capable of generating highly detailed and accurate process models for use in chemical plant designs.

In planning a H_2 production system, the mass of H_2 contained in the feedstock, determined from the ultimate and proximate analysis of the fuel, is a key consideration. H_2 is present in biomass (e.g., wood, sugarcane bagasse, peanut shells, orange peels, etc.), organic waste (e.g., municipal solid waste), landfill gas, and fossil fuels (i.e., petroleum, and natural gas). Methods for producing H_2 include thermochemical (e.g., gasification, pyrolysis), and biological schemes. The potential U.S. biomass resource for energy production is estimated to be the energy equivalent of seven million barrels of oil per day [1]. Of that, about 40% is produced from biomass waste and the remaining is attributed to 80 million acres of excess agricultural crops. Bagasse is the matted fiber residue that remains after crushing and extracting the juice from the cane and consists mainly of cellulose, hemicellulose, and lignin [2]. In the U.S., sugar cane is produced in Hawaii, Florida, Texas, Louisiana, and Puerto Rico.

The most straightforward method for producing H_2 from biomass material is by gasification. The directly heated gasifiers include, fixed-bed updraft, fixed-bed downdraft, and fluidized bed reactors [3]. At steady state, within a typical gasifier, three zones can be identified, namely: drying, gasification, and combustion zones. Typically, biomass feedstock is fed from the top of the gasifier, while ash and char are withdrawn from the bottom, below the combustion zone. Air or oxygen and steam are introduced into the combustion zone to provide the necessary energy for drying, pyrolysis and gasification of the feedstock to mostly H_2, CO, CO_2, N_2, H_2O, CH_4, and tar. In the updraft gasifier, the hot gases flow upward and withdrawn from the top of the gasifier to be cleaned and conditioned. In the fixed-bed gasifiers, the drying zone is located at the top below the feed hopper. A good design is one that results in minimal heat loss from the gasifier and produces a clean gas with minimal tar and unreacted char.

Aspen Plus has been used for analysis of biomass gasification process by several investigators. Kinoshita and Turn used Aspen Plus CPS to analyze steam reforming of bio-oil into H_2 [4]. The complex bio-oil compound was modeled as dextrose ($C_6H_{12}O_6$), and Gibbs reactors were used to carry out the gasification process. Dellepiane et al. used Aspen Plus to simulate and analyze an electric power generation from bagasse and barbojo gasification [5]. Their process generated electricity from molten carbonate fuel cells operated with H_2 produced from gasification of bagasse and barbojo. The fuel cell was modeled in Fortran and integrated into the Aspen Plus code as a user-defined module. Mansaray et al. employed Aspen Plus™ code with Gibbs reactors to construct a flowsheet for predicting the performance of a fluidized bed rice husk gasifier under various process conditions [6]. Mathieu and Dubuisson used Aspen Plus to evaluate the process parameters for a wood fired gasifier by minimizing the Gibbs free energy [7]. The International Energy Agency (IEA) modules described by Skolnik and Putsche used Aspen Plus to produce H_2 by wood gasification using two Gibbs reactors (one for homogeneous and the other for heterogeneous reactions) [8]. Bowen used Aspen Technology's HYSYS CPS to flowsheet H_2 production by gasification of bagasse, grass, and nutshell used in proton exchange membrane (PEM) fuel cells [9]. Still, others have used Aspen Plus to evaluate the technical and economic feasibility of producing H_2 by reforming syngas from indirectly heated biomass gasifiers [10,11]. In most of these simulations, the feedstock is modeled using the ultimate and proximate analysis of the biomass feedstock. This work presents an adiabatic Aspen model for gaseous H_2 production from bagasse with high efficiency and minimum destruction of bagasse. The model is divided into four interconnected sections and depicts industrial processing parameters producing gaseous H_2 with relatively high yield.

Process Design

Figure 1. depicts an overall schematic of the gaseous H_2 production plant. Green bagasse was partially dried, and steam directed to the gasification zone of the gasifier. The process was divided into a dryer, gasifier, clean-up and conditioning, and PSA sections. The dryer was modeled in three segments: a stoichiometric reactor, heat exchanger, and a flash reactor. The gasification section consisted of four zones: a combustor, heat exchanger, Gibbs reactor, and an ash separator. The combustor was used to burn a fraction of the carbon in the partially dried bagasse to heat the gasification zone. The heat exchanger was used to reduce the temperature of the combustion gases before they entered into the Gibbs reactor. Ash was separated from the producer gas in a solid-gas separator before entering the clean-up and conditioning section of the plant. The clean-up section consisted of a reformer, compressor, water pumps, high and low temperature water-gas shift reactors, and a flash reactor. H_2 was recovered in the PSA section of the plant. The high and low temperature water-gas shift reactors and the PSA units operated at 20 bars while all other unit operations operated at 1 bar. With the exception to the work required by the compressor, all other units of the plant operated in adiabatic mode with zero heat duty. The off-gas stream and a portion of the partially dried bagasse were combusted in the dryer section to provide energy to other unit operations via heat exchangers.

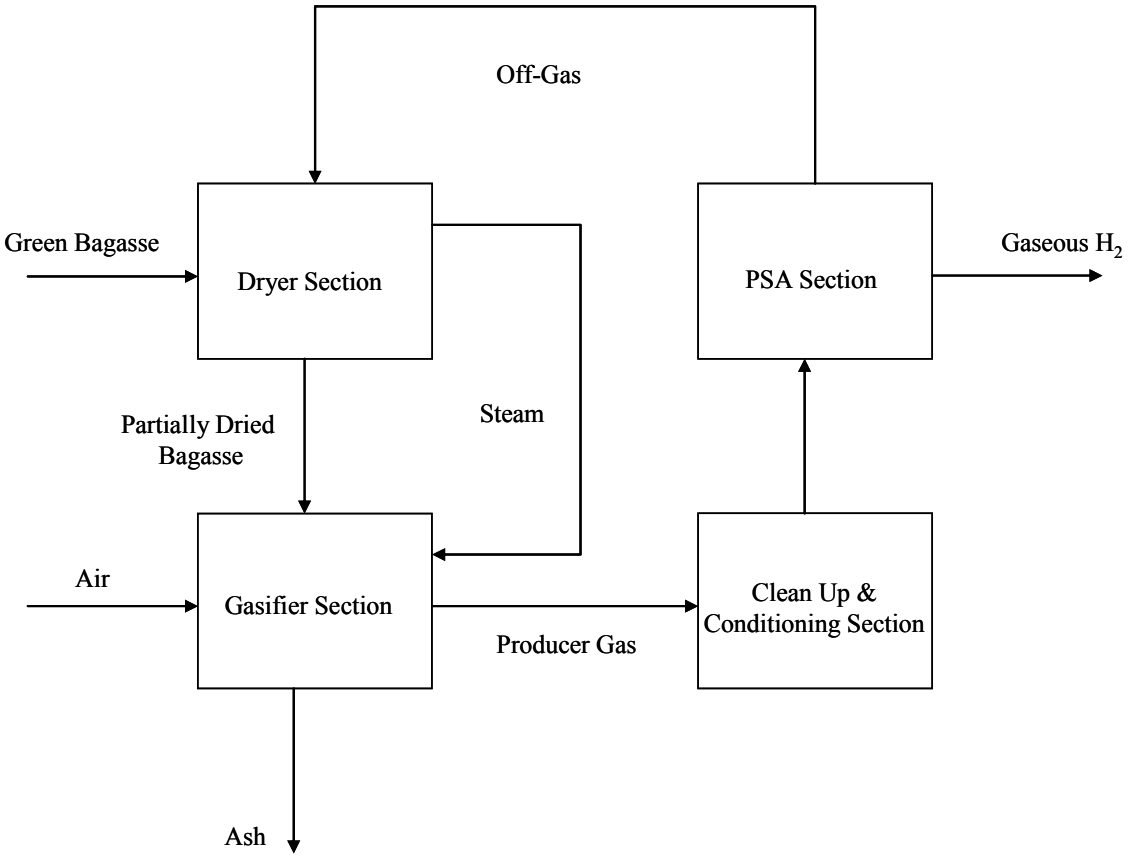

Figure 1. Schematic of the gaseous hydrogen production process design.

Process Evaluation

One of the objectives of this paper is to calculate the modules exergy destruction ($\varepsilon_{dis,m}$), total exergy destruction ($\varepsilon_{dis,total}$), Carnot efficiency (η_{Carnot}), and exergy efficiency (η_{ε}) of the gaseous hydrogen producing process. The lower heating value (*LHV*) is the amount of heat released by combusting a substance, initially at 25 °C, and returning the temperature of the combustion products to 150 °C without recovering the latent heat of vaporization of water. Thus, the *LHV* is equal to the higher heating value of (*HHV*) minus the vaporization enthalpy of the exhaust water at 25 °C (2.44 MJ/kg or 44 kJ/mol of water). Prins et al, reported that the HHV could be predicted within 1.45% standard deviation from the experimentally determined values for a wide range of biomass according to the following correlations,

$$HHV = 0.3491\,Z_C + 1.1783\,Z_H - 0.1034\,Z_O - 0.0151\,Z_N + 0.1005\,Z_S - 0.0211\,Z_A \tag{1}$$

Exergy is the maximum amount of reversible work that can be obtained form a process in order to reach equilibrium with the surroundings at a referenced temperature (T_o = 298 K) and atmospheric pressure. The chemical exergy of the feed bagasse to the process can be correlated using the following equation [2],

$$\varepsilon_{bagasse} = \beta\, LHV_{bagasse} \tag{2}$$

where,

$$\beta = \frac{1.0414 + 0.0177\frac{H}{C} - 0.3328\frac{O}{C}\left[1 + 0.0537\frac{H}{C}\right]}{1 - 0.4021\frac{O}{C}} \qquad 0.5 \le \frac{O}{C} \le 2 \tag{3}$$

The exergy destruction ($\varepsilon_{dis,m}$) (i.e., irreversible loss) of a module (*m*) is equal to the irreversible exergy within the boundary of module. It is given by the Guoy-Stodola theorem as the product of the reference temperature and entropy generation.

$$\varepsilon_{dis,m} = T_O\, S_{gen,m} \tag{4}$$

where,

$$S_{gen,m} = \Delta S_m - \frac{W_m + \Delta H_m}{T_O} \tag{5}$$

By performing mass and energy balances for each module in the process, one can calculate ΔS_m, and ΔH_m for each module as the difference between the entropy and enthalpy of the outlet streams and the entropy and enthalpy of the inlet streams respectively. The total exergy destruction of the process is the sum of the exergy destruction of each module,

$$\varepsilon_{dis,total} = \sum_m \varepsilon_{dis,m} \tag{6}$$

The carnot efficiency (η_{Carnot}) of the plant is calculated according to equation 7,

$$\eta_{Carnot} = \frac{n\,LHV_{H2,\,produced} + Q_{heat} - W_{Carnot}}{N\,LHV_{greenbagasse}} \tag{7}$$

Where, Q_{heat} is the useful heat produced by the plant (assuming 50% heat recovery), and Q_{carnot} is the thermal energy equivalent to the compression work (assuming 50% efficiency), which is calculated from the Carnot equation [12],

$$\frac{W_{Carnot}}{Q_H} = \frac{T_H - T_C}{T_H} \tag{8}$$

Where, W_{Carnot} is the work done by the compressors, Q_H is the high temperature heat reservoir at T_H, and T_C is the low temperature heat reservoir at Q_C. T_H and T_C were assumed to be 2045 °C (adiabatic flame temperature for H_2) and 50 °C, respectively.

The exergy efficiency (η_ε) of the process is calculated according to equation 9,

$$\eta_\varepsilon = \frac{n\,LHV_{\varepsilon\,H2} + Q_{\varepsilon\,heat} - W_\varepsilon}{N\,LHV_{\varepsilon\,greenbagasse}} \tag{9}$$

Results and Discussion

Aspen Plus Flowsheet

Figure 2 depicts the Aspen Plus design for the production of gaseous H_2 by steam gasification of bagasse. A description of the major unit operations and their specifications are given in Table 1. 900 kg/h of green bagasse was fed into the plant to generate 36.90 kmol/h of gaseous H_2. The model assumes that the gasifier does not produce tar. Also, the residence time in the Gibbs reactor was assumed to be long enough to allow complete approach to equilibrium.

Stream class (MIXCINC) was defined in the flowsheet by characterizing the components as substreams (MIXED), conventional inert solid substreams (CISOLID), and non conventional substreams (NC). MIXED substreams were assigned to conventional components that reach vapor-liquid-solid phase equilibrium (i.e., H_2). CISOLID substreams were assigned to components that can participate in solid chemical equilibrium in Gibbs reactor (i.e., carbon). NC substreams were component attributes assigned to the bagasse and ash in the flowsheet. Table 2 depicts the material flow, temperature, and pressure balance of the process design. The plant was modeled using the Peng-Robinson equation of state with Boston-Mathias modification.

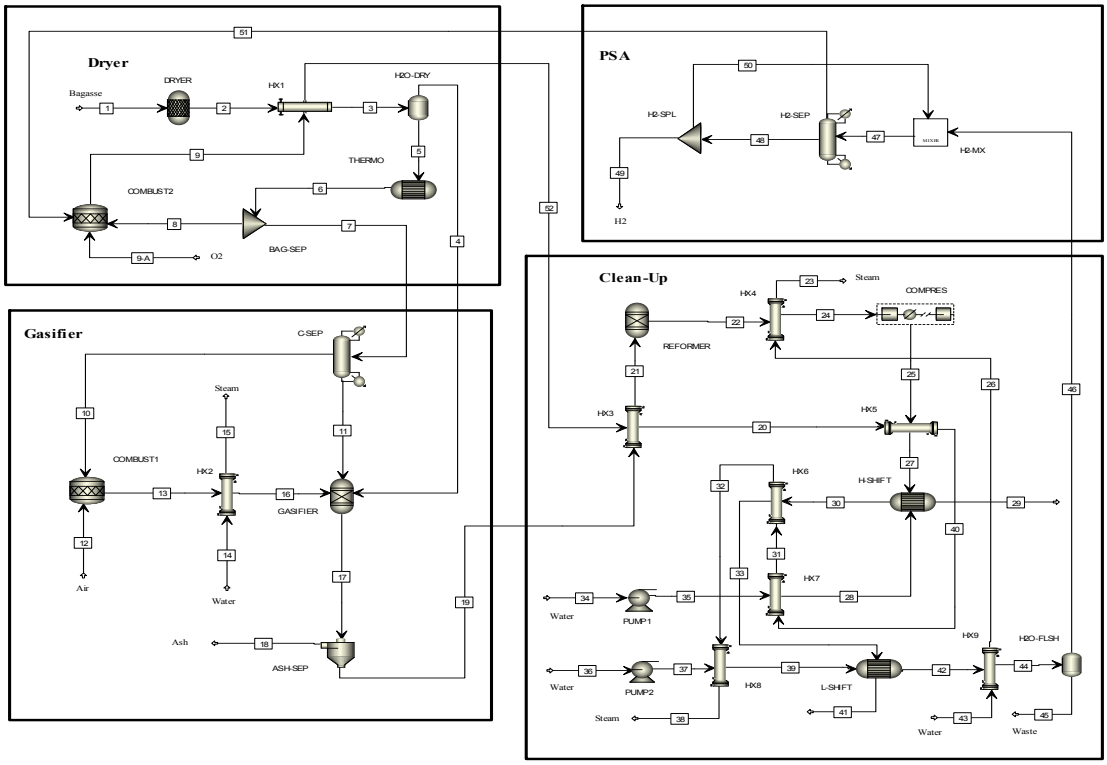

Figure. 2. Aspen Plus flowsheet for the production of H_2 via steam gasification of bagasse.

Table 1. Unit operations specifications and descriptions

Unit Operation*	Description
Dryer Section	
Dryer	Stoichiometric reactor (110 °C, 1 bar) – reduces bagasse moisture from 30 to 15 wt%
Hx1	Heat exchanger to dry bagasse
H_2O-Dry	Flash reactor – separates steam at 110 °C and feed it to gasifier
Yield	Yield reactor – define material flow of bagasse
Bag-Spl	Split 2% of bagasse and feed it to Combust2
Combust2	Stoichiometric reactor (1480 °C, 1 bar) - combust off-gas & 2% of dried bagasse
Gasifier Section	
C-Sep	Separate 3.5% of carbon and ash in bagasse & direct it to Combust1 & and balance to gasifier
Combust1	Stoichiometric reactor (1146 °C, 1 bar) – burn 3.5% of carbon in bagasse with air
Hx2	Heat exchanger - reduces temperature of combustor product stream to 450 °C.
Gasifier	Gibbs reactor (735 °C, 1 bar)
Ash-sep	Separates ash from producer gas stream
Clean Up Section	
Hx3	Reduces temperature of producer gas stream from 735 °C to 990 °C
Reformer	Gibbs reactor (908 °C, 1 bar)
Hx4	Reduces temperature of reformer product stream to 105 °C
Compres	4 stages compressor with intercooler (160 °C, 20 bar, 278 kW work duty, 250 kW cooling duty)
Hx5	Raises temperature of water-gas shift reactor inlet stream to 308 °C
H-Shift	Equilibrium reactor – high water-gas shift reactor (315 °C, 20 bar)
Hx6	Raises temperature of H-Shift outlet stream to 375 °C
Pump1	Pumps 12 kmol/h water at 25 °C and 20 bar to H-Shift
Hx7	Raises temperature of water inlet stream to H-Shift to 155 °C
L-Shift	Equilibrium reactor – low water-gas shift reactor (209 °C, 20 bar)
Pump2	Pumps 17 kmol/h water at 25 °C and 20 bar to H-Shift
Hx8	Raises temperature of water inlet stream to H-Shift to 180 °C
Hx9	Reduces temperature of L-Shift to 35 °C and 20 bar
H_2O-Flsh	Flash reactor – removes water from PSA inlet stream at 35 °C & 20 bar
PSA Section	
H2-SEP	pressure swing adsorption – recover 85% of gaseous H_2
H2-Mx & H_2-Spl	mixer & splitter - specify 70 mol% H_2 in PSA (stream 50).

Table 2. Material flow rate, temperature, and pressure balance

	H_2O	C	H_2	N2	S	O_2	CO_2	CO	CH_4	H_2S	Total	bagasse	ash	T	P	Phase
	kmol/h	kmol/h	kmol/h	kmol/h	kmol/h	kmol/h	kmol/h	kmol/h	kmol/h	kmol/h	kmol/h	kg/h	kg/h	°C	bar	
1	0.00	0.00	0.00	0.00	0.00	0.00	0.00	0.00	0.00	0.00	0.00	900.00	0.00	25	1	S
2	8.82	0.00	0.00	0.00	0.00	0.00	0.00	0.00	0.00	0.00	8.82	900.00	0.00	32	1	S
3	8.82	0.00	0.00	0.00	0.00	0.00	0.00	0.00	0.00	0.00	8.82	741.18	0.00	110	1	S+V
4	8.82	0.00	0.00	0.00	0.00	0.00	0.00	0.00	0.00	0.00	8.82	0.00	0.00	110	1	V
5	0.00	0.00	0.00	0.00	0.00	0.00	0.00	0.00	0.00	0.00	0.00	741.18	0.00	110	1	S
6	6.17	24.33	18.31	0.04	0.01	7.66	0.00	0.00	0.00	0.00	56.53	0.00	54.18	110	1	S+V
7	6.05	23.84	17.95	0.04	0.01	7.51	0.00	0.00	0.00	0.00	55.39	0.00	54.18	110	1	S+V
8	0.12	0.49	0.37	0.00	0.00	0.15	0.00	0.00	0.00	0.00	1.13	0.00	0.00	110	1	S+V
9	11.08	0.00	0.00	5.52	0.00	2.09	24.33	0.00	0.00	0.01	43.02	0.00	0.00	1480	1	V
9-A	0.00	0.00	0.00	0.00	0.00	8.00	0.00	0.00	0.00	0.00	8.00	0.00	0.00	25	1	V
10	0.00	0.83	0.00	0.00	0.00	0.00	0.00	0.00	0.00	0.00	0.83	0.00	54.18	110	1	S
11	6.05	23.01	17.95	0.04	0.01	7.51	0.00	0.00	0.00	0.00	54.56	0.00	0.00	110	1	S+V
12	0.00	0.00	0.00	5.48	0.00	1.46	0.00	0.00	0.00	0.00	6.93	0.00	0.00	25	1	V
13	0.00	0.00	0.00	5.48	0.00	0.62	0.83	0.00	0.00	0.00	6.93	0.00	54.18	1146	1	S+V
14	2.78	0.00	0.00	0.00	0.00	0.00	0.00	0.00	0.00	0.00	2.78	0.00	0.00	25	1	L
15	2.78	0.00	0.00	0.00	0.00	0.00	0.00	0.00	0.00	0.00	2.78	0.00	0.00	894	1	V
16	0.00	0.00	0.00	5.48	0.00	0.62	0.83	0.00	0.00	0.00	6.93	0.00	54.18	450	1	S+V
17	4.85	0.00	26.74	5.52	1.4E-12	2.4E-20	4.70	18.55	0.60	0.010	60.97	0.00	54.18	735	1	S+V
18	0.00	0.00	0.00	0.00	0.00	0.00	0.00	0.00	0.00	0.00	0.00	0.00	54.18	735	1	S
19	4.85	0.00	26.74	5.52	1.4E-12	2.4E-20	4.70	18.55	0.60	0.010	60.97	0.00	0.00	735	1	V
20	11.08	0.00	0.00	5.52	2.0E-04	2.09	24.33	0.00	0.00	0.010	43.02	0.00	0.00	986	1	V
21	4.85	0.00	26.74	5.52	1.4E-12	2.4E-20	4.70	18.55	0.60	0.010	60.97	0.00	0.00	990	1	V
22	5.66	0.00	27.12	5.52	3.1E-10	1.9E-16	3.30	20.53	0.011	0.010	62.15	0.00	0.00	908	1	V
23	190.00	0.00	0.00	0.00	0.00	0.00	0.00	0.00	0.00	0.00	190.00	0.00	0.00	101	1	L+V
24	5.66	0.00	27.12	5.52	3.1E-10	1.9E-16	3.30	20.53	0.011	0.010	62.15	0.00	0.00	105	1	V
25	5.66	0.00	27.12	5.52	3.1E-10	1.9E-16	3.30	20.53	0.011	0.010	62.15	0.00	0.00	160	20	V
26	190.00	0.00	0.00	0.00	0.00	0.00	0.00	0.00	0.00	0.00	190.00	0.00	0.00	101	1	L
27	5.66	0.00	27.12	5.52	3.1E-10	1.9E-16	3.30	20.53	0.011	0.010	62.15	0.00	0.00	308	20	V
28	12.00	0.00	0.00	0.00	0.00	0.00	0.00	0.00	0.00	0.00	12.00	0.00	0.00	155	20	L
30	3.47	0.00	41.31	5.52	3.1E-10	0.00	17.49	6.34	0.011	0.010	74.15	0.00	0.00	315	20	V

Strm	H_2O	C	H_2	N_2	S	O_2	CO_2	CO	CH_4	H_2S	Total	bagasse	ash	T	P	Phase
	kmol/h	kmol/h	kmol/h	kmol/h	kmol/h	kmol/h	kmol/h	kmol/h	kmol/h	kmol/h	kmol/h	kg/h	kg/h	°C	bar	
31	11.08	0.00	0.00	5.52	0.0002	2.09	24.33	0.00	0.00	0.010	43.02	0.00	0.00	788	1	V
32	11.08	0.00	0.00	5.52	0.0002	2.09	24.33	0.00	0.00	0.010	43.02	0.00	0.00	713	1	V
33	3.47	0.00	41.31	5.52	3.E-10	0.000	17.492	6.34	0.011	0.010	74.15	0.00	0.00	375	20	V
34	12.00	0.00	0.00	0.00	0.00	0.00	0.00	0.00	0.00	0.00	12.00	0.00	0.00	25	1	L
35	12.00	0.00	0.00	0.00	0.00	0.00	0.00	0.00	0.00	0.00	12.00	0.00	0.00	25	20	L
36	17.00	0.00	0.00	0.00	0.00	0.00	0.00	0.00	0.00	0.00	17.00	0.00	0.00	25	1	L
37	17.00	0.00	0.00	0.00	0.00	0.00	0.00	0.00	0.00	0.00	17.00	0.00	0.00	25	20	L
38	11.08	0.00	0.00	5.52	0.0002	2.09	24.326	0.00	0.00	0.010	43.02	0.00	0.00	603	1	V
39	17.00	0.00	0.00	0.00	0.00	0.00	0.00	0.00	0.00	0.00	17.00	0.00	0.00	180	20	L
40	11.08	0.00	0.00	5.52	0.0002	2.09	24.326	0.00	0.00	0.010	43.02	0.00	0.00	851	1	V
42	14.53	0.00	47.25	5.52	3E-10	0.00	23.431	0.40	0.011	0.010	91.15	0.00	0.00	209	20	V
43	190.00	0.00	0.00	0.00	0.00	0.00	0.00	0.00	0.00	0.00	190.00	0.00	0.00	25	1	L
44	14.53	0.00	47.25	5.52	3E-10	0.00	23.431	0.399	0.011	0.010	91.15	0.00	0.00	35	20	L+V
45	14.32	0.00	0.00	0.00	3E-10	0.00	0.0012	1E-07	0.00	0.00	14.32	0.00	0.00	35	20	L
46	0.21	0.00	47.25	5.52	2E-19	0.00	23.43	0.40	0.011	0.010	76.83	0.00	0.00	35	20	V
47	0.21	0.00	69.00	5.52	2E-19	0.00	23.43	0.40	0.011	0.010	98.58	0.00	0.00	34	17	V
48	0.00	0.00	58.65	0.00	0.00	0.00	0.00	0.00	0.00	0.00	58.65	0.00	0.00	34	17	V
49	0.00	0.00	36.90	0.00	0.00	0.00	0.00	0.00	0.00	0.00	36.90	0.00	0.00	34	17	V
50	0.00	0.00	21.76	0.00	0.00	0.00	0.00	0.00	0.00	0.00	21.76	0.00	0.00	34	17	V
51	0.21	0.00	10.35	5.52	0.00	0.00	23.430	0.40	0.011	0.010	39.93	0.00	0.00	34	17	V
52	11.08	0.00	0.00	5.52	0.0002	2.09	24.326	0.00	0.00	0.010	43.02	0.00	0.00	1238	1	V

Dryer Section—The input stream to the plant was 900 kg/h of bagasse containing 30% by weight (wt) moisture (stream 1). The dryer section operated adiabatically at 110 °C and 1 bar in order to reduce the moisture content of the bagasse to 15 wt% (stream 5). The extracted steam (8.8 kmol/h, stream 4) was directed at 110 °C and 1 bar to the gasification zone. The dryer section was modeled in three segments, a stoichiometric reactor (Dryer), heat exchanger (HX1), and a flash separator (H_2O-Dry). Bagasse composition was represented by its proxanal, ultanal, and sulfanal analysis, as shown in Table 3 [12,13]. The partially dried bagasse was directed to a Yield reactor where a mass balance on wet basis was performed using the ultimate and proximate analysis of bagasse (stream 5) to arrive at the equivalent concentration of the species: H_2, H_2O, O_2, S, etc. (stream 6). 2 wt% of the partially dried bagasse (stream8) was burned with the PSA off-gas stream (stream 51) in a combustor (combust2) in order to drive the drying process in HX1. The flow rate of H_2 in the dryer section product stream (stream 7) was 17.95 kmol/h at 110 °C and 1 bar.

Gasification Section—The gasifier volatilizes bagasse with steam assuming that all of the components defined in the component specification sheet of the CPS are viable products. Then, the flowsheet minimizes the total Gibbs free energy of the feed stream that enters the Gibbs reactor. Unlike calculations of Mansaray et al. [6], Mathieu and Dubuisson [7], and Skolnik and Putsche [8], the chemical equilibrium calculations for the Gibbs free energy in this work are not restricted by the reactions.

The gasifier was modeled adiabatically and divided into four zones: a carbon separator, a Gibbs reactor, heat exchanger, combustor, and an ash separator. 3.5 wt% of the carbon in the partially dried bagasse (stream 10) was burned with air in a stoichiometric reactor (combust1) and the product (stream 13) was directed to the gasifier to derive bagasse pyrolysis and gasification

reactions. The temperature of the combustor product stream (stream 13) was reduced from 1146 to 450 °C before entering the gasifier zone. The ash in the producer gas stream (stream 17) at 735 °C and 1 bar was separated (stream 18) before it entered into the clean-up and conditioning section of the plant (stream 19). The total flow rate of stream 19 was 60.97 kmol/h at 735 °C and 1 bar of which 26.74 kmol/h was H_2.

Table 3. Ultanal, proxanal, and sulfanal analysis of bagasse

	Wt%	Proxanal	wt%	Sulfanal	wt%
Ash	8.61	Moisture	30	Pyritic	0
C	46.38	Fixed Carbon	12.14	Sulfate	0.05
H	5.86	Volatile Material	79.26	Organic	0
N	0.19	Ash	8.6		
Cl	0.01				
S	0.05				
O	38.9				

Clean Up Section—The clean-up section consisted of a reformer modeled as a Gibbs reactor (reformer), high and low temperature water-gas shift reactors modeled as equilibrium reactors (H-shift and L-shift), a water separator modeled as a flash separator (H_2O-flash), water pumps (pump1 and pump2), and an isentropic compressor (compress). The inlet stream to the clean-up section (stream 19) was heated from 735 to 990 °C via HX3. The reformer operated adiabatically at 908 °C and 1 bar utilizing water to enhance H_2 production ($CH_4+H_2O = CO+3H_2$). The reformat (stream 24) was compressed isentropically in a four stage compressor with intercooling at 20 bar producing a gas stream at 160 °C (stream 25). Make-up water (streams 34 and 36) was pumped at 20 bar to derive the adiabatic high and low temperature shift reactors at 315 and 209 °C respectively. In the water-gas shift rector, carbon monoxide reacts with water to produce H_2 ($CO + H_2O = CO_2 + H_2$). The compressed product gas exiting shift reactor (stream 42) was cooled in HX9 and excess water removed using an adiabatic flash separator before it entered the PSA section (stream 46). The total flow rate of stream 46 was 76.83 kmol/h at 35 °C and 20 bar of which 47.25 kmol/h was gaseous H_2.

PSA Section—PSA is widely used for H_2 recovery providing gas purities greater than 99.999%. The PSA has the capability of preferential adsorption-desorption of the components in multiple beds to allow full H_2 recovery. While one bed operates in adsorption mode, others undergo pressurization, depressurization, or purging. In this work, the PSA section was treated as a 'black box' due to the unsteady-state nature of the process and the inability of Aspen Plus to handle adsorption in solid materials. The PSA section was modeled as a separator where 85 wt% of H_2 was recovered while the balance left the process via off-gas stream to the dryer section of the plant. A recycle stream (stream 50) specifies 70 mol% of H_2 in H_2-MX. Stream 46 enters the PSA section at 35 C and 20 bar to produce 36.90 kmol/h gaseous H_2 at 34 C and 17 bar (stream 49), and 39.93 kmol/h off-gas at 34 °C and 17 bar (stream 51).

Effect of Unit Operation Parameters on H_2 Production—H_2 content in the inlet stream to the gasification section was 17.95 kmol/h at 110 °C and 1 bar (stream 7) while that in the producer gas was 26.74 kmol/h at 735 °C and 1 bar (stream 19). A marginal flow of H_2 was generated by the reformer at 908 °C and 1 bar (27.12 kmol/h, stream 22). H_2 content in the high and low temperature water-gas shift reactors were 41.31 kmol/h at 315 °C and 20 bar (stream 30), and

47.25 kmol/h at 209 °C and 20 bar (stream 42) respectively. Figure 3 depicts H_2 flow rates and temperatures in the dryer, gasifier, reformer, high and low temperature water-gas shift reactors, and PSA. The figure shows that the gasifier and water-gas shift reactors strongly influence the extent of H_2 production. H_2 flow rate in the low temperature water-gas shift reactor is higher than that in the PSA because only 85% of H_2 was recovered as pure H_2 while the balance was directed to the off-gas stream. Also, a fraction of H_2 had to be recycled in order to specify 70 mol% H_2 in the PSA separator. The reaction in the reformer was endothermic favoring high temperatures while reactions in the water-gas shift reactors were slightly exothermic.

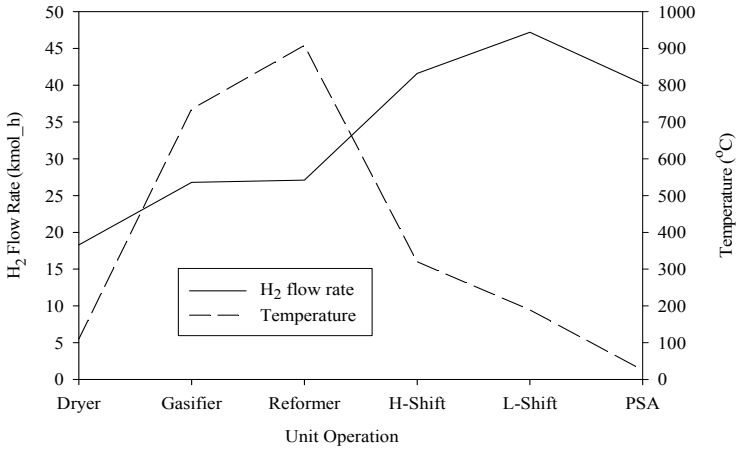

Figure. 3. H_2 flow rate and temperature in the gasifier, reformer, high & low water-gas shift reactors, and PSA.

Effect of Gasifier Temperature on H_2 Production—Figure 4 depicts the effect of the gasifier temperature on the flow rate of the products (on dry basis). Also, the figure depicts the heat duty of the gasification zone as a function of temperature. The figure shows that the gasifier zone operates with zero heat duty at 735 °C. The figure shows that a small amount of CH_4 is produced while H_2 generation remains constant from 715 to 965 °C. Furthermore, yield of CO decreases slightly at elevated temperatures.

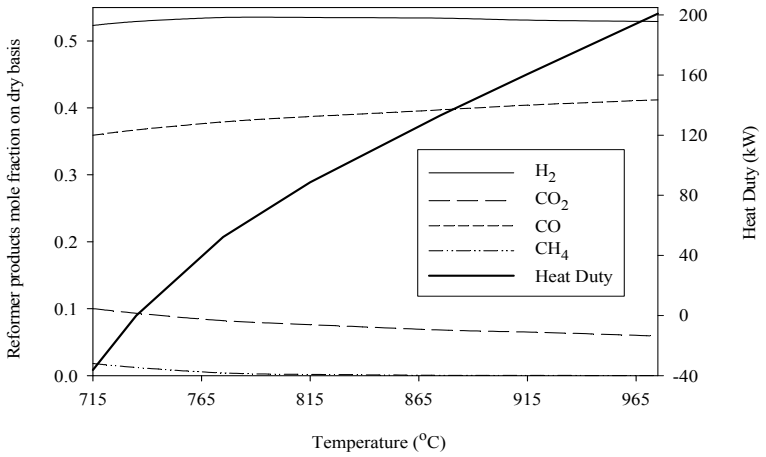

Figure 4. Effect of temperature and heat duty on the concentration of major gasifier products (on dry basis).

Plant Efficiency—900 kg/h of wet bagasse was partially dried to produce 36.90 kmol/h of gaseous H_2. The efficiency (η) of the gaseous hydrogen plant was found to be 78%, calculated according to equation 7. The plant produced 36.90 kmol/h of gaseous H_2–equivalent to 2481 kW. The compression work (W) of the plant was 278 kW-equivalent to 285 kW of heat (Q_H), which was calculated according to the Carnot equation 8. Equation 8 gives Q_H equals to 285 kW. Also, the cooling duty of the compressor was 125 kW (assuming 50% heat recovery).

Conclusions

Gaseous H_2 production by steam gasification of bagasse was flowsheeted using Aspen Plus CPS. The aim of the simulation was to perform a system-level analysis and determine the effects due to the unit operations employed on the performance of the H_2 production plant. The simulation consists of a drying, gasification, cleaning and conditioning, and PSA sections. The unit operations used in the flowsheet operate within a range of parameters typical of similar industrial processes.

The simulation was carried out for 900 kg/h of wet bagasse to produce 36.90 kmol/h of gaseous H_2. Results indicate a plant efficiency of 78% which was calculated by dividing the *LHV* of net gaseous H_2 produced by the *LHV* of the bagasse feed stream on dry basis. 3.5 wt% of the carbon in the partially dried bagasse was needed to heat the adiabatic gasifier, and only 2 wt% of the partially dried bagasse was combusted along with the off-gas stream to provide energy to the plant..

The ultimate and proximate analysis were used to characterize the bagasse feed composition in the dryer section where 15 wt% of the moisture in bagasse was removed. The adiabatic gasification zone operates at 735 °C and 1 bar with no carbon lay down. The adiabatic reformer converted most of the methane to H_2 at 908 °C and 1 bar. The high and low water gas shift reactors operated adiabatically at 315 °C and 20 bar, and 209 °C and 20 bar, respectively. The water-gas shift reactors were effective in reducing the CO molar flow in the product streams and increasing the rate of H_2 production. The gaseous H2 recovery in the PSA section was 85% and the feed stream to the PSA was maintained at 70 mol% H_2 by recycling a portion of the pure H_2 recovered.

Nomenclature

$LHV_{bagasse}$	lower heating value of green bagasse (MJ/kg)
$HHV_{bagasse}$	higher heating value of bagasse (MJ/kg)
Zc	weight fraction of carbon in bagasse on dry basis
Z_H	weight fraction of hydrogen in bagasse on dry basis
Z_O	weight fraction of oxygen in bagasse on dry basis
Z_N	weight fraction of nitrogen in bagasse on dry basis
Z_S	weight fraction of sulfur in bagasse on dry basis
Z_A	weight fraction of ash in bagasse on dry basis
T_O	298 K
ε	chemical exergy of bagasse (MJ/kg)
β	ratio of bagasse chemical exergy and bagasse lower heating value

C	mole fraction of carbon in bagasse on dry basis
H	mole fraction of hydrogen in bagasse on dry basis
O	mole fraction of carbon in bagasse on dry basis
m	module
$\varepsilon_{dis,m}$	exergy destruction per module
$S_{gen,m}$	entropy generation per module
ΔS	entropy outlet streams minus entropy of inlet streams for a module m (xyz)
W	compression work of a module
ΔH	enthalpy p outlet streams minus enthalpy of inlet streams for a module m (xyz)

Publications

1. Huang, C., & T-Raissi, A. “Analyses of One-Step Liquid Hydrogen Production from Methane and Landfill Gas,” *J. Power Sources,* 173 (2007) 950–8.
2. Ramasamy, K., & T-Raissi, A. “Hydrogen Production from Used Lubricating Oils,” *Catalysis Today* 129 (2007) 365-71.
3. Ramasamy, K., & T-Raissi, A. “Hydrogen Production from Used Lubricating Oil,” Final Report to NASA-GRC, May, 2006.
4. Ramasamy, K., & T-Raissi, A. “Hydrogen Production from Used Lubricating Oil,” *Pre-Prints of the 231st ACS National Meeting*, Atlanta, GA, March 26-30, 2006.
5. Elbaccouch M., Ramassamy K., Baik J., & T-Raissi A. “Aspen Plus Process Design for the Liquid Hydrogen Production by Steam Reforming of Used Automotive Lubricating Oil,” *Proc. of the AICHE Spring National Meeting*, Orlando, FL, April 23-27, 2006.
6. Ramasamy, K., & T- Raissi, A. “Hydrogen Production from Used Lubricating Oils,” *ACS Division of Petroleum Chemistry,* 51(1), 54-6, 2006.
7. Elbaccouch M., Ramassamy K., Baik J., & T-Raissi A. “Systems Analysis of Hydrogen Production and Utilization at KSC,” NASA Progress Report, January-May, 2006.
8. Ramasamy, K., & T-Raissi, A. “Hydrogen Production from Used Lube oil via Supercritical Water Reformation,” Annual Report to NASA-GRC, April 2005.
9. Elbaccouch, M., & T-Raissi, A. “Aspen Plus Process Model for the Production of Gaseous Hydrogen via Bagasse Gasification,” *Proc. of the 15th World Hydrogen Energy Conference*, Yokohama, Japan, 2004.
10. T-Raissi, A., et al. “Task IV-A, System Analysis of Hydrogen Production and Utilization at KSC,” Final Contract Report on NASA NAG3-2751, Jan. 2004.
11. Huang, C., & T-Raissi, A. “Task IV-B, Analysis of Alternate Hydrogen Production Processes - Liquid Hydrogen Production via Hydrogen Sulfide Methane Reformation,” Final Contract Report NASA NAG3-2751, January 2004.
12. T-Raissi, A., et al. “Task IV-2, System Analysis of Hydrogen Production and Utilization at KSC,” Interim Contract Report NASA NAG3-2751, January 2003.
13. Huang, C., & T-Raissi, A. “Task IV-6, Analysis of Alternative Hydrogen Production Processes,” Interim Contract Report NASA NAG3-2751, Jan. 2003.

Presentations

1. Elbaccouch M.; Ramassamy K.K.; Baik J.; T-Raissi A. “Aspen Plus Process Design for the Liquid Hydrogen Production by Steam Reforming of Used Automotive Lubricating Oil,” at the AICHE Spring National Meeting, Orlando, FL, April 23-27, 2006.
2. Mohajeri, N. “Hydrogen Production from Used Lubricating Oil,” at the 231st ACS National Meeting, Atlanta, GA, March 26-30, 2006.
3. T-Raissi, A. “System Analysis,” NASA Mid-year Hydrogen Program Review, Florida Solar Energy Center, Cocoa, Nov. 3-4, 2004.
4. T-Raissi, A. “Analysis of Hydrogen Production and Use at the NASA Kennedy Space Center - An Energy System Integration Perspective,” SCAQMD Conference “*Hydrogen - Fueling the Clean Air Future*” Session: *“Integrated Energy Systems and Safety,”* held at Palm Desert, CA, August 17, 2004.
5. T-Raissi, A. “Aspen Plus Process Model for the Production of Gaseous Hydrogen via Bagasse Gasification,” at the *15th WHEC*, Yokohama, Japan, July 2004.
6. T-Raissi, A. “System Analysis of H_2 Production at KSC,” at the NASA Hydrogen Review Meeting at Orlando, FL, March 30, 2004.
7. T-Raissi, A. “System Analysis of H_2 Production at KSC,” at the NASA Hydrogen Review Meeting at Gainesville, FL, August. 14, 2003.
8. T-Raissi, A. “System Analysis of H_2 Production and Utilization at KSC,” at the NASA Hydrogen Review Meeting at Tampa, FL, Jan. 15, 2003.
9. T-Raissi, A. “Analysis of Alternate Hydrogen Production Processes,” at the NASA Hydrogen Review Meeting at Tampa, FL, Jan. 15, 2003.
10. T-Raissi, A. “Cryogenics Tasks, NASA KSC Update and System Analysis, and Analysis of Alternate Hydrogen Production Processes,” at the NASA-GRC Program Review Meeting, Cleveland, OH, Sept. 3-4, 2002.
11. T-Raissi, A. “System Analysis of H_2 Production Concepts - Overall System Analysis,” at the NASA-Hydrogen Research at Florida Universities Program Review Meeting held at FSEC, July 16-17, 2002.

References

[1] Course manual on hydrogen fuel cell engines and related technologies, U.S. Department of Energy, Manual 2: Hydrogen Use, 2001.

[2] E. Hugot, Handbook of Cane Sugar Engineering. Elsevier, New York, N.Y., 1972.

[3] R.P.S. Da Silva, Catalytic Indirectly Heated Gasification of Bagasse. Dissertation – University of Florida, 1997.

[4] C. Kinoshita, & S. Turn, Production of Hydrogen from Bio-Oil Using CaO as a CO_2 Sorbent, Int J Hydrogen Energy 28 (10) (2003) 1065-1071.

[5] D. Dellepiane, B. Bosio, & E. Arato, Clean Energy from Sugarcane Waste: Feasibility Study of an Innovative Application of Bagasse and Barbojo. J. of Power Sources, 122(1) (2003) 47-56.

[6] K. Mansaray, A. Al-Taweel, A. Ghaly, & F. Hamdullahpur, V.I. Ugursal, Mathematical Modeling of a Fluidized Bed Rice Husk Gasifier: Part I – Model Development. Energy Sources 22(1) (2000) 83-98.

[7] P. Mathieu, & R. Dubuisson, Performance Analysis of a Biomass Gasifier. Energy Conversion and Management 43(9-12) (2002) 1291-1299.

[8] E. Skolnik, & V. Putsche, International Energy Agency Hydrogen Implementing Agreement Task 11: Integrated Systems, Final Report of Subtask B: Analysis Tools, 1999.

[9] D. Bowen, A Technoeconomic Assessment of Hydrogen Production by Gasification of Biomass. Poster presentation at the U.S. DOE Hydrogen, Fuel Cells and Infrastructure Merit Review and Peer Evaluation, Berkeley, CA, May 19-22, 2003.

[10] M. Mann, Technical and Economic Assessment of Producing Hydrogen by Reforming Syngas from the Battelle Indirectly Heated Biomass Gasifier. Technical Report: National Renewable Energy Laboratory, TP-431-8143, August, 1995, at: www.eere.energy.gov/hydrogen andfuelcells/pdfs/29964.pdf

[11] R. Craig, & M. Mann, Cost and Performance Analysis of Biomass-based Integrated Gasification Combined-cycle (BIGCC) Power Systems. Technical Report: National Renewable Energy Laboratory, Prepared under Task No. BP611717, October 1996.

[12] J. Smith, & H. Van Ness, Introduction to Chemical Engineering Thermodynamics, fourth ed., McGraw-Hill, New York, 1987, pp. 140-148.

[13] Siemens Westinghouse Power Co. Hawaiian Biomass Gasification Commercialization Project-Technology Verification Phase. Report to the U.S. DOE under Contract No DE-FC36-96GO10150, March 1999.

[14] R. Trenka, Preliminary Operational Experiments from the Biomass Gasification Facility (BGF) in Paia, Hawaii. Proceedings of the 7th National Bioenergy Conference, vol. 1, September 15-20, 1996.

Zero-Boil-Off Liquid Hydrogen Storage Tanks

J. Baik
Florida Solar Energy Center

Research Period: September 2003 to September 2006

Abstract

Using densified liquid hydrogen as a cryogenic propellant for launch vehicle applications can reduce fuel tank volumes, decrease vapor pressures, and improve cooling capacity over the normal boiling point propellant. A densified liquid hydrogen test bed has been developed using Gifford-McMahon cryocooler to refrigerate hydrogen inside the 150 liter storage tank at the Florida Solar Energy Center (FSEC). The test bed has an integrated refrigeration and storage system with multiple capabilities including hydrogen liquefaction, densification, and zero-boil-off (ZBO) storage test. The test bed has successfully demonstrated hydrogen liquefaction and densification processes at 16.5 K followed by long term ZBO liquid hydrogen storage. This report contains the design considerations, the detailed system descriptions, and the results obtained during initial hydrogen liquefaction, densification and ZBO storage tests.

Introduction

The Florida Solar Energy Center and NASA Kennedy Space Center have performed collaborative research processes for increasing the density of cryogenic propellants for launch vehicle applications. Technologies that provide for the densification, conditioning, transfer and storage of cryogenic propellants can reduce gross lift-off weight of a launch vehicle by up to 20% or increase its payload capacity [1]. By using densified propellants, one can expect reduced external tank volumes, decreased vapor pressures, and increased enthalpy gain before boil off. NASA Kennedy Space Center has years of experience handling cryogenic propellants, but all with saturated liquids. This work focuses on using existing cryogenic technology to densify hydrogen, and developing a test bed where densified propellant handling techniques can be researched. Various research efforts for the development of densified propellants technology in NASA are reviewed in previous report by the same author [2-3].

FSEC and NASA KSC have designed the hydrogen densification system, and Cryogenic Technical Services (CTS) of Longmont, Colorado fabricated and delivered it to the FSEC in late 2003. In addition to the test bed, various data acquisition systems, power and water utility lines, emergency hydrogen vent line and remote alarm system were prepared to start running the system in safe environment. As a preliminary densification test, a nitrogen liquefaction and densification test was performed to exercise subatmospheric operating condition for subcooled cryogen. Then, the hydrogen densification test bed successfully demonstrated hydrogen liquefaction and densification as well as ZBO storage test. This report includes the test bed design considerations, the detailed system descriptions, major experimental results of the hydrogen densification and ZBO storage test, and future research plans will be also discussed later.

Hydrogen Densification Test Bed

Design Considerations

To achieve demonstration goals of hydrogen liquefaction, densification and ZBO storage test with limited cryocooler cooling power available, various thermal and mechanical design considerations were required at the initial design stage. The volume of inner storage vessel was limited to 150 liter by the facility safety regulation code. The aspect ratio of the vessel was optimized by vessel material, operating temperature, thermal analysis of heat conduction and radiation heat transfer from ambient. Heat pipe technology was selected to extend the cold head of cryocooler down to the bottom of storage vessel. Operating temperature, pressure and thermodynamic properties of working fluid in the heat pipe can provide heat pipe design parameters such as material choices and dimensions. A couple of bundles of copper braids at the bottom of the heat pipe were considered to increase surface area so that more efficient heat exchange between hydrogen and heat sink can be expected. Pressure build-up unit (PBU) was employed to control internal vessel pressure by evaporating stored liquid hydrogen without any vent loss. It also allows self-pressurization of the system in a short period of time to drain and/or transfer stored liquid hydrogen to other storage tanks and applications. The top plate of the vessel and its dewar necks were designed to maximize reconfiguration flexibility with flanged connections on the cryocooler interface and the outer vessel. This design allows full access to reveal components such as the cryocooler cold head, heat pipe, and copper braids structures out of the vessel when repairs and future modifications are needed. Thermal insulation design was one of the most important issues to minimize heat loads on the system. Sophisticated design efforts in dewar necks, inner vessel support, baffles, instrumentation lines, fluid supply and drain lines, valves, and appropriate use of multilayer insulations minimized heat loads on the cryocooler.

System Descriptions

The hydrogen densification test bed consists of cryocooler, helium compressor for cryocooler, 150 liter double-walled vacuum jacketed cryostat, LN_2 precooler bath, vacuum pump system, gas supply and vent lines, vacuum jacketed liquid hydrogen supply and drain line, and data acquisition system. Figure 1 depicts various components of the test bed.

The cryocooler constitutes the heart of the hydrogen densification test bed. Cryomech AL-330 single-stage Gifford-McMahon(G-M) cryocooler was selected and installed on the top of the storage vessel. It has an expected cooling capacity of 40 W at 20 K and 25 W at 15 K [4]. The water-cooled type helium compressor uses 7 kW of power and provides 2 MPa of helium gas to the G-M cryocooler. The cryostat has been designed to store 150 liter of densified liquid hydrogen in its inner stainless steel tank with additional ullage space. To minimize convective heat transfer between inner vessel and outer jacket, a combination of mechanical and turbo molecular vacuum pumps generates 10^{-6} torr of high vacuum. Total loss including radiation, conduction through the support structure and instrumentation lines is estimated to less than 8.3 W at 15 K. Table 1 shows the detail of heat loads estimation on the cryocooler.

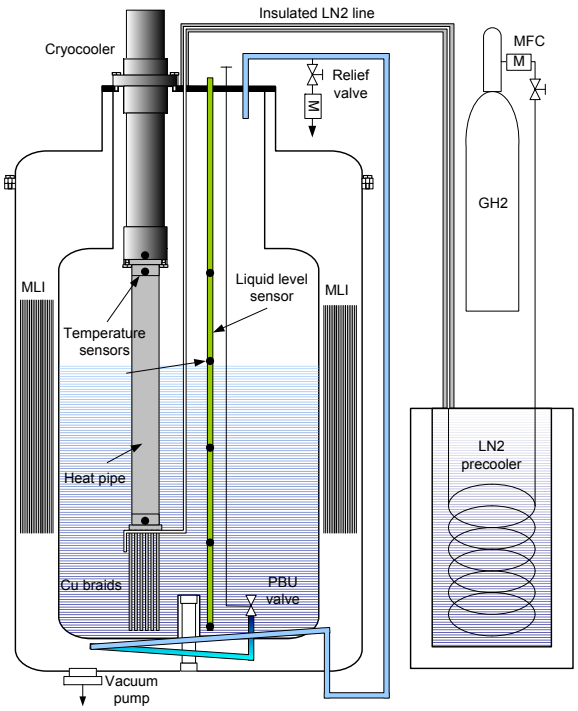

Figure 1. A 150 liter liquid hydrogen densification and zero-boil-off storage system at FSEC.

TABLE 1. Heat loads estimation on the cryocooler at 15 K

Component	Heat Load
MLI	2.2 W
Instruments	2.7 W
Support	0.3 W
PBU line	0.1 W
Other lines	3 W
Total	**8.3 W**

The entire assembly is designed to be easily modified, if needed, with flanged connections on the cryocooler interface and the outer jacket. Since the cold head of the cryocooler is not long enough to reach the bottom of the storage tank, a heat pipe is used. The heat pipe is located at the bottom of the cold head and extends the cryocooler cold head to the bottom of the inner vessel. This pipe uses hydrogen gas as working fluid. Three silicon diode temperature sensors are installed on the cryocooler cold head, top and bottom end of the heat pipe, respectively. A gas supply line is wrapped around the bottom of the heat pipe so that supplied gas can be precooled, liquefied and densified at heat pipe temperature. Also, more than 2,500 pieces of thin copper braids per bundle are attached to the bottom of the heat pipe to increase the contact surface between heat pipe and fluids.

One capacitance-type liquid level sensor (AMI, Model 185) is installed to measure liquid level in the storage tank. Also, five calibrated silicon diode sensors are installed on a 0.75 m long fiber glass tube along the vertical axis of the storage tank to provide vertical temperature profiles in the tank.

A pressure build-up (PBU) unit controls internal pressure by evaporation of stored liquid without any vent loss. The PBU unit consists of a cryogenic valve, a pressure regulator and evaporation coils at the bottom of cryostat. Opening the PBU valve allows stored cryogenic liquid to be evaporated in the PBU coil by exchanging heat with ambient temperature. It results in an increase of storage tank pressure without imposing any external pressure.

A vacuum-jacketed cryogenic liquid transfer line mounted on the top flange supplies cryogen to the storage tank or drains liquid out of the storage tank. Using an additional gas supply line and the PBU unit, one can easily transfer cryogenic liquid into or out of the storage tank. An adjustable relief valve, a rupture disk and a manual venting valve are installed in the gas supply line, PBU coil and manual vent manifold for operational safety and emergency vent process. The relief valve and the rupture disk are set to 412(= 45 psig) and 446 kPa (= 50 psig), respectively to prevent the system from over-pressurization. FIGURE 2 depicts various system components installed at the top and bottom of the heat pipe area, and detailed configurations of each component are listed Table 2.

TABLE 2. Summary of system configurations

Component	Material	Dimension (OD x H or L)
Inner vessel	SA 240 304	0.51 m x 0.91 m
Outer vessel	SA 240 304	0.61 m x 1.14 m
Heat pipe	SA 269 304	0.07 m x 0.68 m
Support	G-10/11	35 mm x 159 mm
Braids	C110(ETP) copper cable	0.254 mm x 178 mm x 2500 strands x 6 bundles
Insulation	MLI	40-45 layers

In the test bed, various sensors are installed to study the thermo-physical behavior of densified hydrogen. Three pressure transducers measure the inner storage vessel, annular vacuum space and heat pipe pressure. Low and high vacuum gauges depict the pressures of the mechanical and turbo molecular vacuum pumps. Two mass flow meters installed at gas supply and vent lines measure the rate of liquefaction and heat leak rate. Eight temperature sensors measure the liquid level stored in the tank, cryocooler cold head temperature and heat pipe temperatures. Signals from these instruments are sent to National Instrument Field Point data acquisition modules. A Labview 7 Real-time module performs all the real-time data processing, display and storage of the data on a PC. All data acquisition Field Point modules can be monitored and controlled by intranet and internet network connections from any remote location.

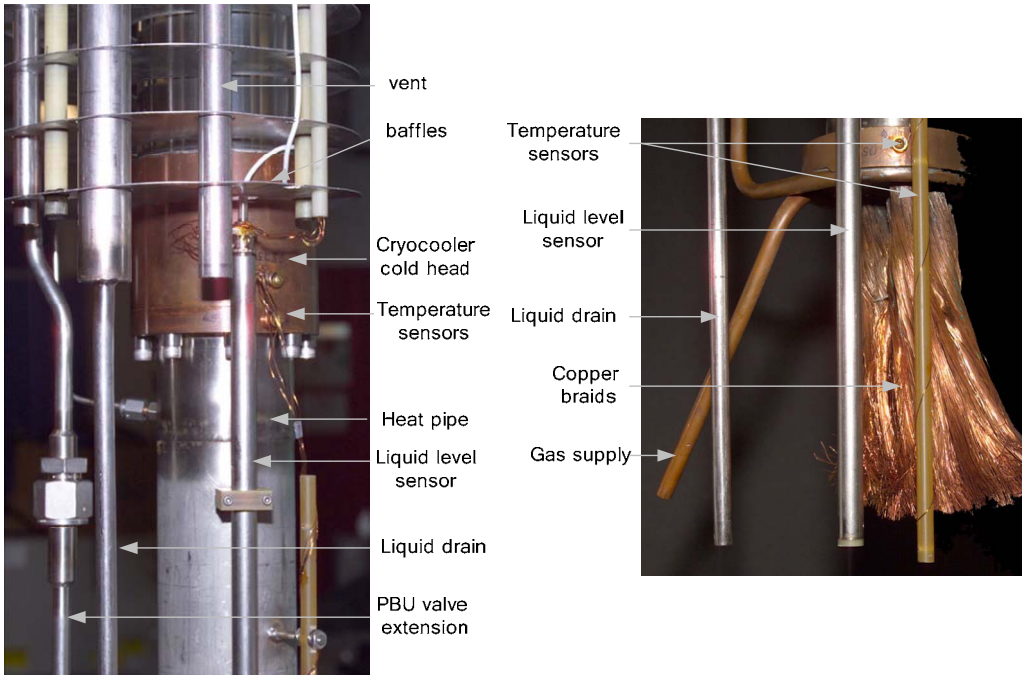

Figure 2. Component arrangements at the top and bottom of the heat pipe in detail.

Test Descriptions

The test bed needs multiple purge processes to remove any impurity through the entire system before the cryocooler starts. The heat pipe, the inner vessel and every flow path in the system has to be purged by 200 kPa dry nitrogen gas, and evacuated to 10^{-4} torr of high vacuum. The test starts with a chill down process using LN_2 to cool the inner vessel to save cool-down time, as opposed to using the cryocooler refrigeration power. At the start of the test, all valves on the system are closed, and a portable 160 liter LN_2 dewar is connected to the liquid fill & drain line. LN_2 supply begins while the system manual vent valve is opened. The LN_2 supplied through a vacuum jacketed transfer line cools the inner vessel and the heat pipe down to about 77 K in a short period of time. After the inner vessel pressure becomes stable, the LN_2 stored is drained to LN_2 precooler bath for future use to precool ambient hydrogen gas.

Once LN_2 is drained, the system experiences multiple purge processes again to remove the liquid nitrogen and residual cold nitrogen gas using gaseous helium and vacuum pump. After the purge process, the heat pipe is charged with hydrogen gas up to pre-determined pressure or mass. The amount of hydrogen charged in the heat pipe is obtained from pressure-volume-temperature relations of hydrogen and mass conservations. In this test, 5.6 g of hydrogen which corresponds to 20 mm liquid level of 16 K densified liquid hydrogen in the heat pipe is charged. After the heat pipe is charged with required amount of gas hydrogen, the cryocooler starts its operation. Within an hour, the lower heat pipe temperature completes its cooldown to ~15 K. The temperature differences between the cold head and the heat pipe end is approximately 0.7 K, which is very efficient considering there is thermal contact resistance between the top of the pipe and the cold head, and thermal resistance down the length of the pipe. The inner vessel pressure remains below 10^{-5} torr because of cryopumping effect on the cold head and the heat pipe surfaces. The cold head temperature often shows temperature oscillations of a magnitude near 1.5 K, which are damped out by the thermal mass of the heat pipe.

Hydrogen gas at room temperature is slowly introduced into the vessel through the LN_2 precooler bath, and its mass flow rate and pressure increases are recorded. The introduced gaseous hydrogen flows through the coiled copper tube soldered at the bottom of the heat pipe, releases heat to the lower heat pipe, and then becomes cold gaseous and/or liquid hydrogen. Also, the copper braids soldered at the bottom of the heat pipe enhance heat transfer between the lower heat pipe and hydrogen. The temperature and pressure profiles are driven by the mass flow rate into the vessel, since the enthalpy from the warm gas introduces the energy in the system while the cryocooler tries to remove this thermal energy. Accurate control of the mass flow rate of gaseous hydrogen is important to maintain the inner vessel pressure below 273.7 kPa (= 25 psig) for safe operation.

Results and Discussions

Hydrogen Liquefaction and Densification Test

The cryocooler refrigerates hydrogen gas, and in turn, the natural convection effect of the cold gas cools the inner storage vessel until it becomes sufficiently cold enough to store liquid hydrogen. For initial liquefaction and densification tests, a total of 13.7 m^3 or 1.13 kg of gaseous hydrogen was introduced into the tank. Figure 3 shows temperature variations of the cold head and densified hydrogen in the inner vessel when the system becomes close to a steady-state densification condition of 16.5 K at the saturation pressure of 26 kPa (= 3.8 psia). Figure 3 indicates that the densified liquid hydrogen is stored up to the ‘bottom’ sensor of the inner vessel, and the remainder is cold gaseous hydrogen. The measured thermodynamic properties

allow us to estimate the state of the hydrogen inside, and the quality of the stored hydrogen is found to be 4.8%, or a total liquid mass of 1.075 kg. It is converted to about 14.4 liter of 16.5 K densified liquid hydrogen. The density of the saturated liquid at 16.5 K is 74.7 kg/m^3, and an increase of 5.6% over the NBP of hydrogen. Table 3 summarizes overall densification test results, when LN_2 precooler bath was used and not used. The initial test results indicate that actual heat load on the cryocooler was less than 8.3 W.

ZBO Liquid Hydrogen Storage Test

The ZBO storage test was performed with the 14.4 L densified liquid hydrogen stored in the tank by turning the cryocooler on and off. Figure 4 shows the pressure and temperature changes during the ZBO storage test. After the cryocooler was turned off, the pressure was increased to 207 kPa (= 30 psia) within 7 hrs, and the densified liquid hydrogen at the bottom of the tank found another equilibrium state at elevated pressure. After the cryocooler was turned on again, the temperatures and pressure were recovered to previous conditions within ~1 and 8 hrs, respectively. In the ZBO test, it is demonstrated that the system can be maintained at least 8~9 hrs without the cryocooler operation before the relief valve starts to releases boil-off gas, and 1 hr/day of the cryocooler operation can provide enough refrigeration power to maintain the densified liquid hydrogen for a long time without any boil-off loss. The ZBO storage test was repeated once a day for a week to show the system reliability. When several Hurricanes hit the state of Florida in late 2004, the test bed and researchers successfully exercised the emergency draining and the system evacuation procedure which is a part of predocumented facility evacuation routines.

Table 3. Comparison between densification rate estimations and test results.

Cold head temperature	**Cooling power**	**Densification rate without LN_2 precooling**	**Densification rate with LN_2 precooling**
15 K	25 W	4.9 liter/day	17 liter/day
16.5 K, estimation	30 W	6.5 liter/day	23 liter/day
16.5 K, measured	30 W	***~7.2 liter/day***	***~25 liter/day***
20K	40 W	10 liter/day	36 liter/day

*15K, 16.5 K estimation, and 20 K operations are estimated based on 8.3W of heat load on the cryocooler.

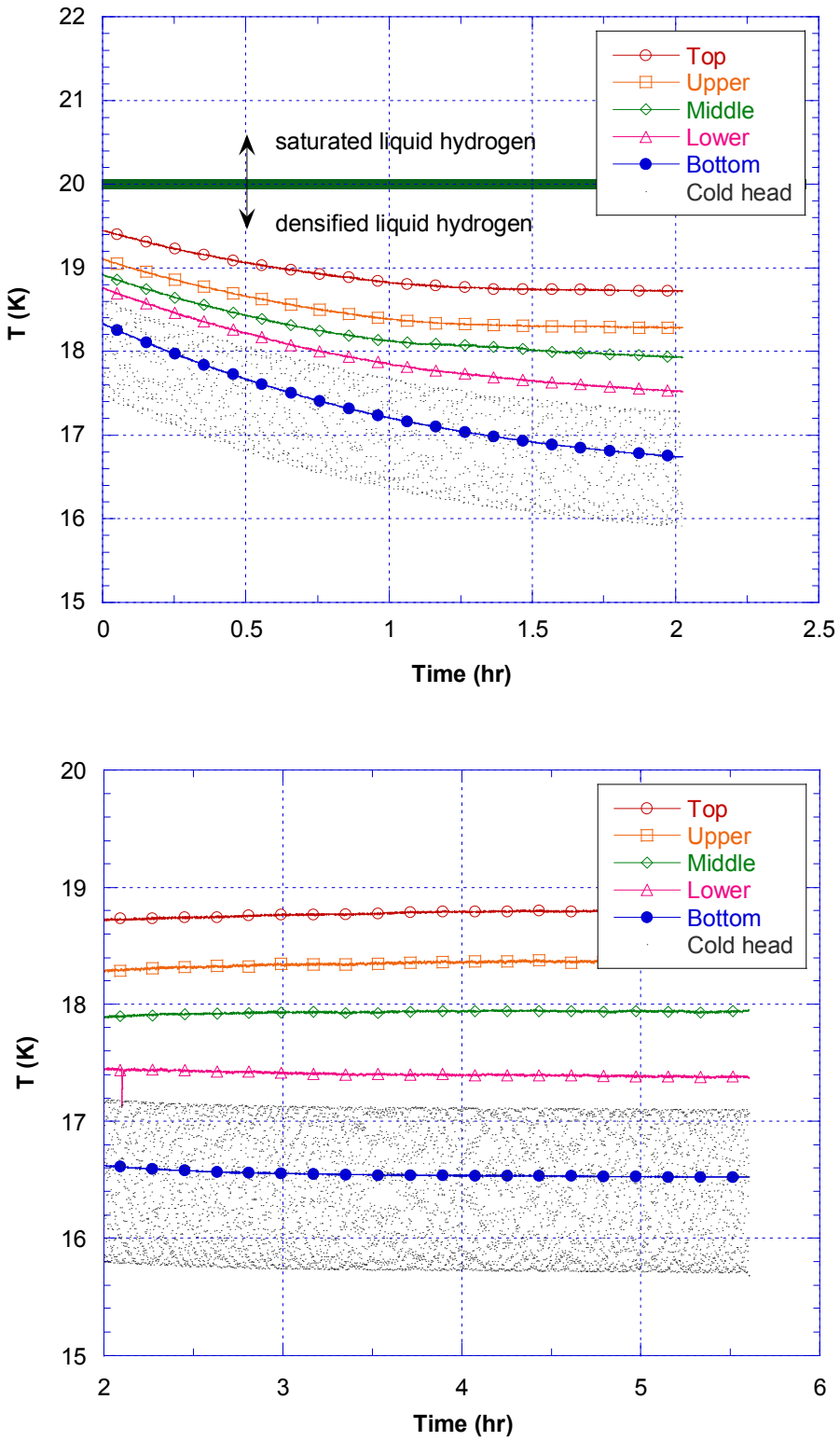

Figure 3. Temperature changes of the cold head and densified hydrogen during the densification test.

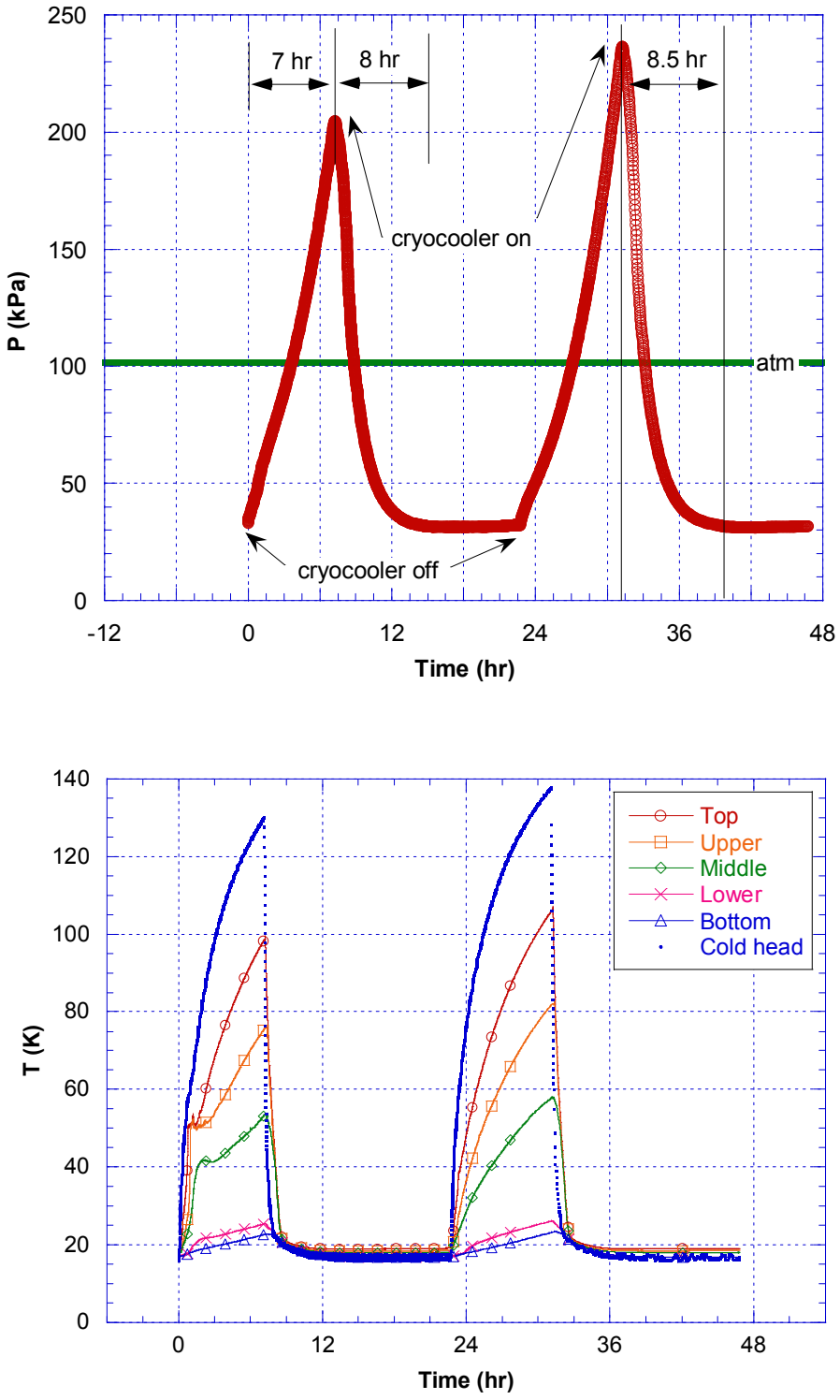

Figure 4. Pressure and temperature changes during ZBO storage test.

Figure 5. The densified hydrogen testing field facility at FSEC.

Conclusions

Researchers at the Florida Solar Energy Center and NASA KSC have developed a hydrogen densification test bed to investigate hydrogen densification and ZBO liquid hydrogen storage technology. The test bed successfully performed 7.2~25 liter/day of 16.5 K densified liquid hydrogen demonstration from ambient gaseous hydrogen using a G-M cryocooler. A series of ZBO storage tests proved that the system can store densified liquid hydrogen without any boil-off loss by ~1 hr/day of the cryocooler operation.

FSEC has constructed and instrumented a densified hydrogen testing field facility that combines hydrogen production, purification, storage, and application test sites as shown in Figure 5. At the facility, the hydrogen densification test bed can be integrated with a fuel cell backup power system to demonstrate a self-sustained densified liquid hydrogen storage technology. This facility allows for the handling of larger quantities of liquid hydrogen than the current laboratory so that advanced handling techniques such as pressure control, thermal stratification, and recovery of chill down losses can be investigated. To increase hydrogen liquefaction rate and remove inherent conversion heat during long-term storage, in-line type ortho-to-para hydrogen converter can be integrated at the LN_2 bath. Development of vapor-cooled-shield (VCS) structure combined with in-line type para-to-ortho hydrogen converter in the storage tank can extend storage time before boil-off. The endothermic process of para-to-ortho hydrogen conversion through the VCS can reduce heat leak into the inner storage tank. Figure 6 shows the schematic of it.

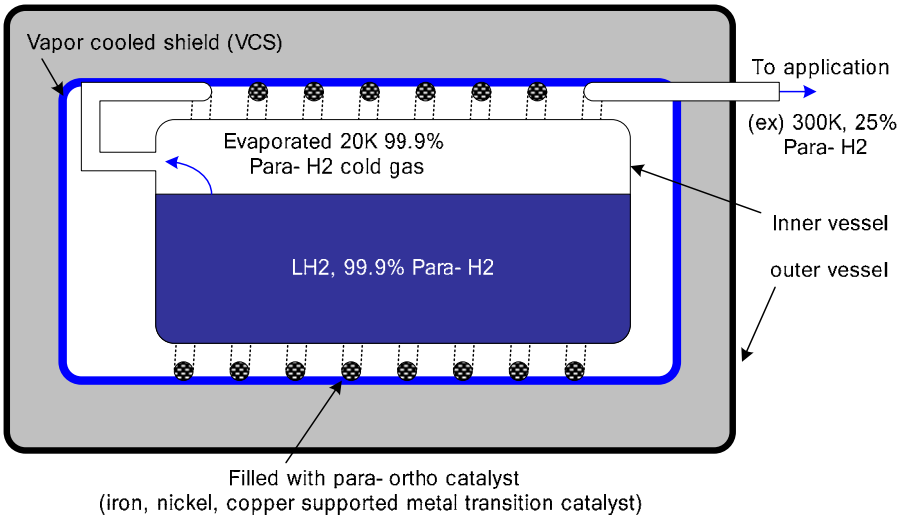

Figure 6. A schematic diagram of vapor cooled shield combined with in-line para-to-ortho hydrogen converter for ZBO storage tank.

Publications

1. J. Baik and W. Notardonato. “Initial Test Results of Laboratory Scale Hydrogen Liquefaction and Densification System,” *Advances in Cryogenic Engineering*, vol. 51B, 1530-7, AIP, Melville, New York, 2006.
2. J. Baik, “R&D Processes for Increasing the Fluid Density of Cryogenic Liquids,” 2004 Project Final Report for NASA Hydrogen Research in Florida Universities, March 2005.
3. J. Baik, “Experimental Design and Evaluation of Zero Boil-off of Cryogenic Systems,” 2004 Annual Report for NASA Hydrogen Research in Florida Universities, March 2005.
4. J. Baik, H. Chang, and W. Notardonato. “Two-stage Refrigeration for Subcooling Liquid Hydrogen and Oxygen as Densified Propellants,” *Cryocoolers*, vol. 13, 711-8, Springer, 2005.
5. J. Baik and H. Chang. “Hydrogen Research Activities in NASA and Department of Energy in USA,” The Korea Institute of Applied Superconductivity and Cryogenics, vol. 7, no.1, 28–33, 2005.
6. J. Baik, A. T-Raissi, and D. Block. “R&D Processes for Increasing Density of Cryogenic Propellants at FSEC,” *Cryogenics*, vol. 44, 451–8, 2004.
7. W. Notardonato and J. Baik, “Operational Testing of Densified Hydrogen Using G-M Refrigeration,” *Advances in Cryogenic Engineering*, vol. 49A, 64–71, 2004.
8. J. Baik, H. Chang, and W. Notardonato. “Thermodynamic Cycle Analysis of a Two-stage Reverse Brayton Refrigeration System for Subcooling Liquid Hydrogen and Oxygen as Densified Propellants,” *Proc. Society of Air-Conditioning and Refrigerating Engineers of Korea, Refrigeration Division*, 131–4, 2004.

Presentations

1. J. Baik and W. Notardonato, “Initial Test Results of Laboratory Scale Hydrogen Liquefaction and Densification System,” 2005 Cryogenic Engineering Conference & International Cryogenic Materials Conf., Keystone, CO, August 29–September 2, 2005.
2. J. Baik, “ZBO Liquid Hydrogen Storage,” NASA Hydrogen Review Meeting, University of Florida, Gainesville, May 10–11, 2005.
3. J. Baik, “ZBO Liquid Hydrogen Storage,” NASA Hydrogen Review Meeting, FSEC, Cocoa, November 1–4, 2005.
4. J. Baik, H. Chang, and W. Notardonato, “Two-stage Refrigeration for Subcooling Liquid Hydrogen and Oxygen as Densified Propellants,” 13th International Cryocooler Conference, March 29–April 1, 2004, New Orleans, Louisiana.
5. J. Baik, H. Chang, and W. Notardonato, “Thermodynamic Cycle Analysis of a Two-stage Reverse Brayton Refrigeration System for Subcooling Liquid Hydrogen and Oxygen as Densified Propellants,” The Society of Air-Conditioning and Refrigerating Engineers of Korea 2004 Conference, 2004.
6. J. Baik, “R&D Processes for Increasing the Fluid Density of Cryogenic Liquids,” NASA Hydrogen Review Meeting, FSEC, November 2004.
7. J. Baik “Experimental Design and Evaluation of Zero Boil-off of Cryogenic Systems,” NASA Hydrogen Review Meeting, FSEC, November 2004.
8. J. Baik and A. T-Raissi, “R&D Processes for Increasing Density of Cryogenic Propellants,” 2003 Cryogenic Engineering Conference and International Cryogenic Materials Conference, Anchorage, Alaska, September 22–26, 2003.
9. W. Notardonato, J. Baik, and G. Macintosh, “Operational Testing of Densified Hydrogen Using GM Refrigeration,” 2003 Cryogenic Engineering Conference and International Cryogenic Materials Conference, Anchorage, Alaska, September 22–26, 2003.

References

1. Tomsik, T. M. (2000). Recent advances and applications in cryogenic propellant densification technology. NASA/TM, 41, 2000–2099.

2. Notardonato, W. U., Baik, J. H., and McIntosh, G. E. (2004). Operational testing of densified hydrogen using GM refrigeration in advances in cryogenic engineering 49A, 64–71.

3. Baik, J. H., and Raissi A. T. (2004, June-August). R & D process for increasing density of cryogenic propellants at FSEC. Cryogenics, 44(6–8), 451–458.

4. Cryomech. (2003). AL330 Operation Manual.

December 2007

Final Reports for University of Central Florida

- A Reliable, Efficient and Compact Reverse Turbo Brayton Cycle Cryocooler for Storage and Transport of Hydrogen in Spaceport and Space Vehicle Applications - Chow, L., Kapat, J., Chen, Q., An, L., Wu, T., Sundaram, K., Ham, C., Dhere, N.
- Development of Cryogenic Shape Memory Actuator Materials for Switches, Seals and Valves - Vaidyanathan, R.
- Genetic Engineering to Enhance Biological Hydrogen Production - Self, W., Ganyc, D., Halvorsen, L.
- Highly Selective Nano-Mems Low Temperature Hydrogen Sensor - Seal, S., Cho, H.
- Metal Hydrides for Hydrogen Separation, Recovery and Purification - Hampton, M., Slattery, D.
- Wireless Passive Sensors and Systems for Physical Sensors and Hydrogen Sensing Applications - Malocha, D.

A Reliable, Efficient and Compact Reverse Turbo Brayton Cycle (RTBC) Cryocooler for Storage and Transport of Hydrogen in Spaceport and Space Vehicle Applications

L. Chow, J. Kapat, Q. Chen, L. An, T. Wu, and K. B. Sundaram
University of Central Florida

C. Ham
Florida Space Institute

N. Dhere
Florida Solar Energy Center

Research Period: July 2002 to September 2007

Summary

This report presents a summary of the activities and results of the research project on the development and testing of key components of a reliable, efficient and compact RTBC cryocooler conducted over a five-year period by University of Central Florida (UCF) for the U.S. National Aeronautics and Space Administration (NASA). The R&D activities under this program cover the design and thermodynamics of a high efficient cryocooler and development of a highly efficient, compact, reliable, high-speed and light-weight integrated compressor/motor setup for the cryocooler. Suggestions for improvement in the integrated compressor/motor setup were provided in addition to heat exchanger (HEX) design and friction and wear reduction techniques that help in the betterment of the system performance. Possible applications of the designed cryocooler for future NASA needs have also been addressed.

Introduction

In the last four decades, we have witnessed tremendous developments in the field of cryogenics, which led to numerous newer applications for cryocoolers. Spaceport operations of the near future are one of the prominent applications for usage of large quantities of cryogenic propellants. Efficient storage and transfer of these fluids is necessary for reducing the launch costs. In addition, for future manned and unmanned deep space missions and other missions to Mars, NASA is planning for extended cryogenic propellant storage durations of the order of several months as opposed to a few days or weeks. There would be boil-off of propellant in the transfer lines and in the propellant storage tanks in space due to heat leak.

The key objective of this project is to design a reliable, compact, lightweight, affordable and highly efficient in their class cryocooler for distributed cooling of liquid hydrogen systems for spaceport applications and to develop an appropriate integrated compressor/motor system for the said cryocooler. The overall work accomplished in the project is categorized under the following individual performance tasks in accordance with the project objective:

Task 1: Cryocooler Overall System Evaluation and Design
Task 2: Design and Fabrication of Miniature Centrifugal Compressor
Task 3: Miniature Centrifugal Compressor Design Verification by Numerical Simulation and Testing (with appropriate scaling)

Task 4: Design, Fabrication and Testing of a High-speed, High-efficiency Permanent Magnet Synchronous Motor (PMSM)
Task 5: Integration and Preliminary Testing of the Motor/Compressor Assembly
Task 6: Overall System Optimization – Systematic Testing of the Motor/Compressor Assembly, Evaluation, and Possible Design Changes
Task 7: 5.4 kW Permanent Magnet Synchronous Motor – Design
Task 8: Two-stage Centrifugal Compressor – Design
Task 9: Extended Activities in the Aspects of Friction, Wear Mitigation and HEX Design
Task 10: Evaluation of Application of Current Effort to Other NASA Applications

Background

Recent improvements in cryocoolers (insulation, motor/control, compressor and anti-friction coating technologies) paved a way for their application in zero boil-off (ZBO) storage of cryogenic propellants in space. NASA Glenn Research Center, Ames Research Center and Marshall Space Flight Center have cooperatively developed a concept for ZBO in space applications and the success of this concept primarily depends on the performance of its key component, the cryocooler. Various cryocoolers were developed and tested for this attempt. With joint effort by US Air Force, NASA and Northrop Grumman, a flight-like 10 W, 95 K pulse tube cryocooler for liquid oxygen and liquid methane storage has been developed and weighs around 4 kg [1]. Similar developments include a three-step Stirling cryocooler with 120 mW of cooling power at 20 K, a split Stirling two-step cryocooler with 0.45 W of cooling power at 30 K and a sorption cooler having a cooling capacity of 1.6 W at 20 K. All of these previous attempts of flight cryocoolers have cooling capacities less than 2 W at liquid hydrogen temperature [2]. There are commercially available cryocoolers that have higher cooling powers but their weight restricts their possible usage for in-space applications. Cryomech, Inc. uses a GM cycle for cooling and can remove 40 W of heat at 20 K but the weight of the unit is 143 kg or more [3]. Our proposed cryocooler uses a reverse turbo Brayton cycle (RTBC) with an estimated weight of about 22 kg has a heat removal rate of 20-30 W at 18 K, which makes it attractive and ideal for its application of ZBO in space. Creare, Inc. uses a two-step reverse turbo Brayton cycle for its cryocooler concept but the cooling power of that cryocooler is aimed to be only 250 mW at 18 K and has a projected mass of about 27 kg [4]. For many NASA space missions, cooling capacities much higher than 2 W are estimated to be required. This effort of developing a light weight, compact and higher cooling capacity cryocooler is highly beneficial for these applications. The goal of this project is to develop a reverse turbo Brayton cycle cryocooler for zero boil-off of cryogenic propellants. Key focus was on the development of an integrated motor/compressor designed for use in the cryocooler. This cryocooler will be capable of extracting a few tens of watts (20-30 W) of heat at liquid hydrogen temperature (~18 K).

All the previous attempts of cryocoolers by NASA for ZBO of cryogenic propellants in space have cooling powers of less than 2 W at liquid hydrogen temperature. These versions of flight-like cryocoolers would be more appropriate for cooling of sensors and super conducting materials in a spacecraft. The cryocooler designed under this project with a few tens of watts of cooling power at liquid hydrogen temperature would be ideal for ZBO of cryogenic propellants in NASA's future robotic missions to Mars and for other human space missions.

Work Accomplished

Task 1: Cryocooler Overall System Evaluation and Design

The primary application of the cryogenic system for spaceport and space vehicle applications is a liquid hydrogen cooler, which is designed to liquefy hydrogen gas at atmospheric pressure and maintain the liquid hydrogen below 19 K. According to the application requirements, the liquid hydrogen cryocooler should be able to start up at room temperature and cool down the gaseous hydrogen continuously to its boiling point (~19 K) and keep it at this temperature. It includes two processes: cool-down process and stable refrigerating process. A two-step RTBC (reverse turbo-Brayton cycle) cryocooler is proposed for this purpose and is shown in figure 1.

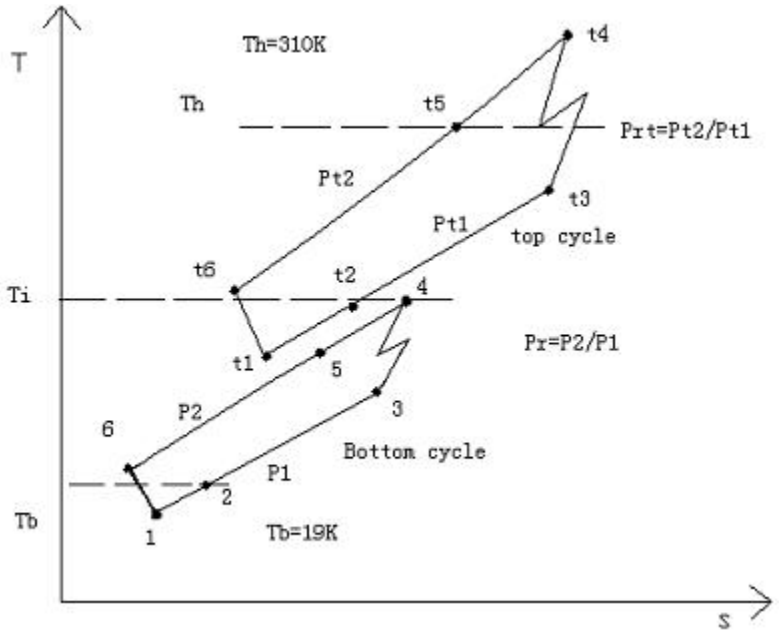

Figure 1. System scheme of the two-step RTBC cryocooler

The major advantages of the two-step RTBC cryocooler are: a) top step can be separately started up to cool down the gaseous hydrogen and its container to liquid nitrogen temperature, which is a relatively efficient cooling process that can save power and have rapid cooling ability; b) top cycle can use neon as working fluid, which is better than Helium in the cryogenic system. Neon is relatively easy to compress by a dynamic compressor and its larger molecules provide for easy sealing; c) separated two steps also give versatility to system development and operation. The top and bottom steps can be separately developed and freely combined. One top step machine can also drive multiple bottom steps; d) bottom Helium cycle works in cryogenic temperature, which can reduce its compressor's rotational speed for the same pressure rise.

The two-step scheme also has some major technical difficulties, which finally forced us to switch to a single-step system. These drawbacks include: a) inter-cycle heat exchange will be very troublesome because heat exchange between gases need large surface area and possibly large pressure loss. The heat that must be exchanged could be up to 1 kW, which may include the heat generated by the motor; b) two different working fluids cause inter-leakage problem; c) coupled cycle steps need complicated control system in operation; d) the top step need to cool down the motor of bottom step which is an extra cost of the two-step structure and will bring down its performance. Figure 2 shows the thermodynamic scheme of the single-step RTBC cryocooler.

The conclusion is, although the two-step scheme is better for the cool-down process, it shows lower overall coefficient of performance (COP), larger size and inconvenient operation. After carefully evaluating the cost and development difficulties, the one-step scheme proves to be advantageous. Table 1 shows the comparison of the two types of schemes.

Table 1. Hydrogen cryocooler scheme comparison

	Two-step	*One step*
Cooling power (W)	20	20
Overall COP	0.0045	0.005
Working fluid pressure ratio	Neon 3.3; Helium 2.7	Helium 2.8

The major finding is that with proper optimization of several parameters such as the pressure ratios of the top and bottom cycles, immediate cycle temperature, compressor intercooling, etc., the overall system coefficient of performance (COP) can be as high as 0.012 compared to 0.005 as stated in the original proposal.

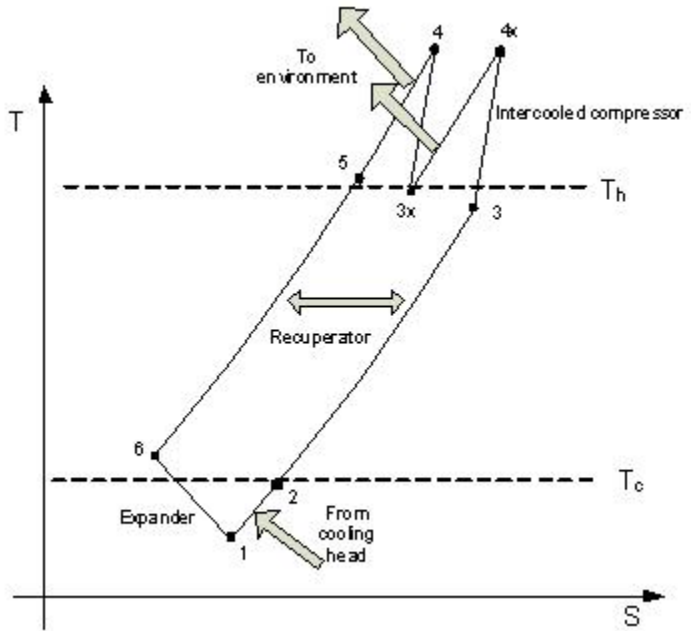

Figure 2. System scheme of the one-step RTBC cryocooler

Task 2: Design and Fabrication of Miniature Centrifugal Compressor

The initial focus in this task was on the development of a smaller Helium compressor for the cryocooler. Higher speeds can achieve the required pressure ratio but high-speed bearing is always a problem. To keep the speed below 200,000 rpm, the compressor was designed to have four stages. Since our centrifugal compressor design is novel and untested, the project plan was to design, fabricate and test one of the stages to establish a knowledge base for future similar designs.

Concept of four-stage Helium compressor for the RTBC cryocooler—As shown in figure 3, there will be four impellers, two on each side of the motor. There will be an intercooler between the second and the third stages to reduce the power input.

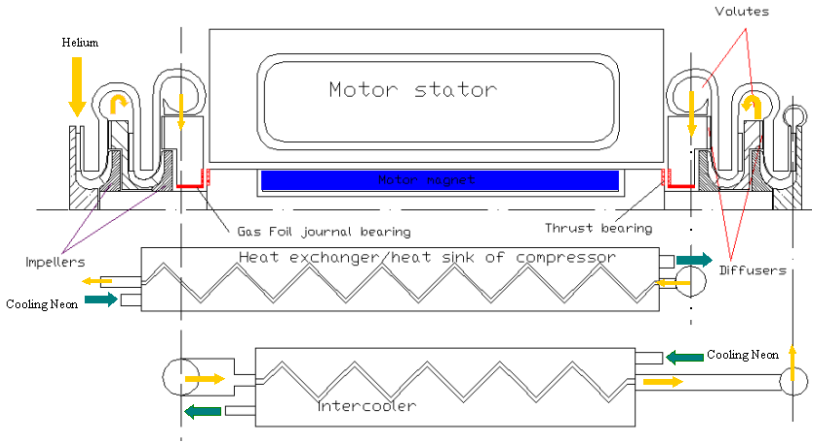

Figure 3. Schematic of the four-stage helium compressor

This symmetric layout design (two impellers on either side of the motor; figure 4) will balance the axial forces and reduces the footprint of the system. It requires a much-complicated mechanical design. The rotational parts include the rotor of the motor and the impellers mounted on it. The rotor of the motor is a hollow cylinder in which the magnet will be inserted (figure 5).

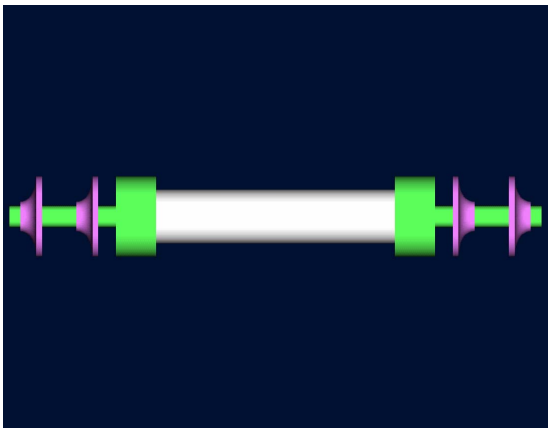

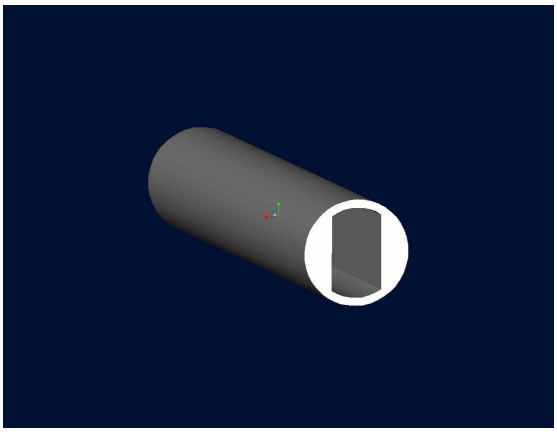

Figure 4. Complete assembly (concept figure) Figure 5. Rotor of the motor

The primary area of concern is that extreme care must be taken to make sure the magnet, which is solid but brittle, is strong enough to sustain the large stress when it rotates at 200,000 rpm. One solution is to inflict a pre-stress in it before inserting it into the main shaft.

Figure 6 shows how the impellers, diffusers and volutes would be assembled together. Due to the symmetric design, it is enough to focus on one side of the assembly. After Helium flowing in axially and getting compressed in the first stage, it needs to be turned to get compressed in the second stage. So the first diffuser will also be used as a Helium flow guider for the flow between the two stages. Every part, excluding the end gas guider, will be split into two portions, an upper

one and a lower one, for final assembly. The reason being, after the rotational portion is assembled and balanced; it should not be dissembled again. Another problem area would be to split the stator of the motor and the windings in it to two portions. One solution is to wind the stator after assembly. The compressor assembly may require more components that are not shown in figure 6. They include the heat recuperator, the carbon rings, the bearing assembly and a sealing device. The footprint can be around 7“ length X 3.5” diameter. It will provide the power to compress Helium. The motor will provide 1000 W of output power to the compressor by spinning at 200,000 rpm.

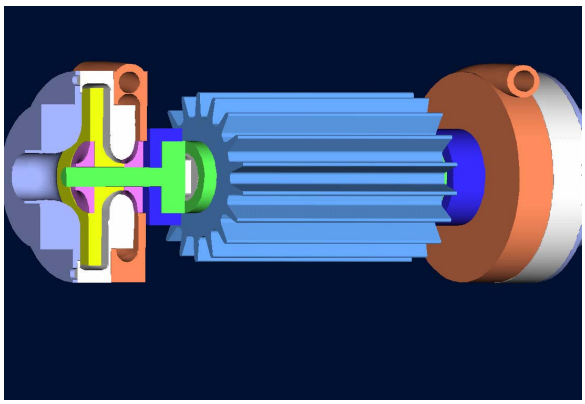

Figure 6. 3D Model of the four-stage centrifugal compressor
(Partial half-sectional view)

In order to avoid the complications involved in a multistage-compressor design, a high rotational speed is a must. Even then, we still have to design a two-stage compressor with intercooler to increase its performance. Accordingly, a new design with two-stages was proposed as an alternative and is shown in figure 7. The two-stage compressor with an intercooler is designed to have a pressure ratio of 2.8.

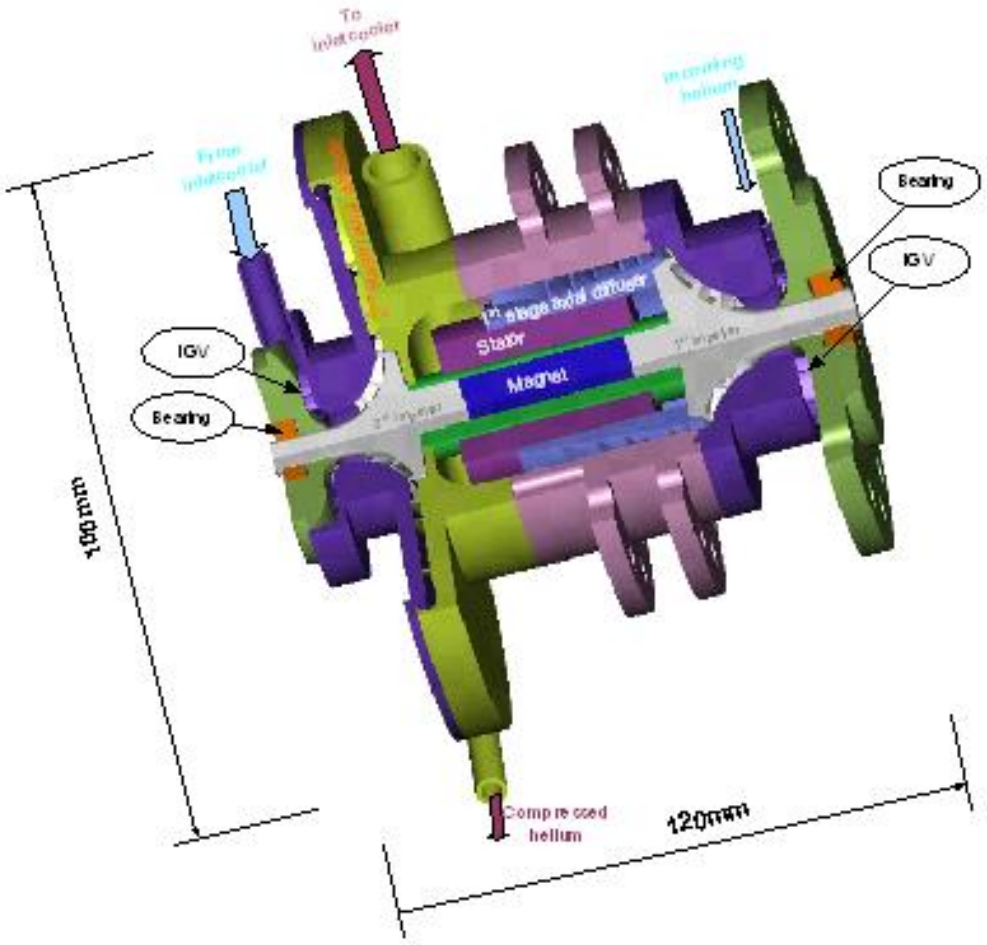

Figure 7. Two-stage compressor solid model

The hydrogen RTBC cryocooler with this Helium compressor will have the following performance characteristics as shown in Table 2.

Table 2. Helium compressor specifications

Stages	2
Intercooler power (W)	630
Mass flow rate (g/s)	4.6
Compression power (W)	3780
Stage efficiency	0.67
Rotation speed (rpm)	313,000
Inlet condition	300K, 2 atm

Since the design speed of this compressor is 313,000 rpm and requires non-contact bearings for support as mentioned before, it is impossible to test it with commercial off-the-shelf bearings. Non-contact bearings are complicated to design, manufacture and test and are very costly. Therefore, it required a trade-off between dealing with high-speed bearing issues and dealing with more number of stages. Geometric scaling was used to get over this conflicting situation and is explained below.

The similarity principle followed in geometric scaling of centrifugal compressors can be expressed as:

$$\underbrace{pr_{tt}, \eta_{tt}, \frac{\hat{P}}{\rho_{00} N^3 D^5}}_{Performance\ Variables} = f\left\{ \underbrace{\frac{\dot{m}\sqrt{RT_{00}}}{p_{00} D^2 \sqrt{\gamma}}, \frac{ND}{\sqrt{\gamma RT_{00}}}, \frac{ND^2}{\nu}, \gamma}_{Similarity\ Variables} \right\}$$

Where,
pr_{tt} = total-to-total pressure ratio
η_{tt} = total-to-total efficiency
$\frac{\hat{P}}{\rho_{00} N^3 D^5}$ = dimensionless power
$\frac{\dot{m}\sqrt{RT_{00}}}{p_{00} D^2 \sqrt{\gamma}}$ = dimensionless mass flow rate
$\frac{ND}{\sqrt{\gamma RT_{00}}}$ = ratio of impeller blade tip speed to the speed of sound
$\frac{ND^2}{\nu}$ = Reynolds number and, γ = specific heat ratio

This equation predicts the performance of a new compressor if it comes from scaling of an existing compressor. It also predicts the performance of a compressor if we change its inlet conditions or working fluid. Using the above equation, it was found that performance of the Helium compressor could be predicted by testing it with air at a much lower speed. Table 3 compares the stage performance when we switch gas from Helium to air.

Table 3. Stage performance for different gases

	Helium	Air
Rotating speed (rpm)	313,000	108,000
Mass flow rate (g/s)	4.6	10.6
Inlet temperature(K)	300	300
Inlet pressure (atm)	2	1
Impeller diameter(cm)	4.8	4.8
Gas specific heat ratio	1.67	1.4
Gas constant (J/kg*K)	2079	286
Compression power (W)	2370	823
Pressure ratio	1.7	1.55

Therefore, a single-stage compressor was developed and tested to validate the concept of our compressor design. Several of the concepts that were implemented in the one stage compressor can be directly applied to the two-stage compressor, once the data is retrieved after testing. This would also provide a strong knowledge base in the design, development and testing of mesoscale centrifugal compressors, which enables for easy development of similar sized (with respect to power and speed) compressors in future. Detailed design (and slightly modified version of the design mentioned above) of the two-stage compressor was dealt under Task 8 and it includes all the experience that we gained through testing the single-stage compressor.

Design and fabrication of a single-stage compressor—The single-stage centrifugal air compressor design was started based on the design parameter values from Table 3. All the parts were designed in 3-D CAD software (figure 8) and modeled using a stereolithography process (figure 9). This allowed for a visual aid to the machine shop for a thorough understanding of the desired shape. The simplest parts of the compressor (ones that can be turned on a lathe) were machined first followed by intricate parts. The fabrication of the parts with blades (impeller, inlet guide vane (IGV), and diffuser) required the use of a five-axis machine with the ability of simultaneous movement. However, the impeller was cast due to its intricate blade design and for cost savings.

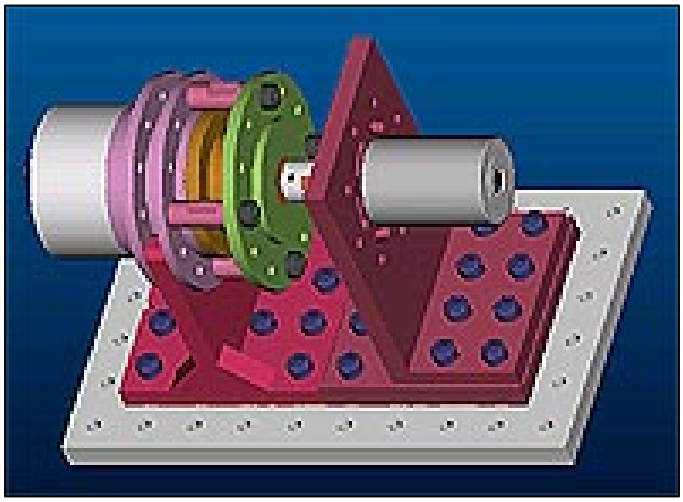

Figure 8. 3D CAD model of single-stage air compressor

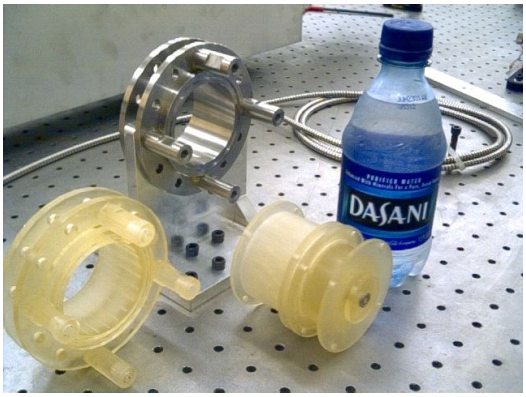

Figure 9. Prototypes of single-stage air compressor assembly (Impeller, IGV and diffuser) and housing

Using the ‘iges’ file, the diffuser and the inlet guide vane were machined on a four-axis CNC mill. The impeller, due to its intricate design of the blades, was cast in 356A Aluminum. All the machined components are shown in figure 10. The top cap to the impeller was also machined using the ‘iges’ file (figure 11), in which the curved portion of the top cap was determined from the file.

Since an ‘iges’ file does not give the required surface finish, additional finishing work was completed on the surface of the diffuser and the inlet guide vane. When all of the parts were machined, the compressor was ready for assembly. The impeller was balanced before assembly. Some additional turning on a lathe was done on the impeller to true the part for balancing.

The compressor was then integrated with the motor designed and developed simultaneously and the assembly was then instrumented for testing. The equipment needed for the compressor testing process included a mass flow meter, pressure transducers, and thermocouples to measure the temperatures of the flow at inlet and exit. The determination of the direction of the flow at exit was also performed, which aided in the calculation of the compressor efficiency. Complete details of compressor testing are elucidated under Task 5.

Impeller Inlet Guide Vane Diffuser

Figure 10. Fabricated components of single-stage centrifugal compressor

Figure 11. Impeller Top Cap

Task 3: Miniature Centrifugal Compressor Design Verification by Numerical Simulation

Detailed CFD simulation of the one-stage centrifugal compressor was performed to validate the design numerically. Analysis of the inlet guide vane section was first completed. Fully structured mesh of IGV is created in the commercial preprocessor GAMBIT® (figure 12), and then solved by using a commercial fluid flow code FLUENT®. The results (figure 13) show that pressure loss through IGV is about 5000 Pa. As expected, IGV creates an acceptable flow angle at the eye of

impeller. However, certain amount of reverse flow was still found to exist in spite of careful design. This reverse flow was assumed to be eliminated by the interaction of IGV and impeller, which was simulated and is detailed in the next paragraph.

IGV and impeller interaction was simulated using the 3D integrated geometry from CAD as shown in figure 14. A ‘mixing plane model’ with unstructured grid (figure 15) was used. Results are shown in figure 16. It was found that the separation, which existed in IGV simulation, would be eliminated by the interaction.

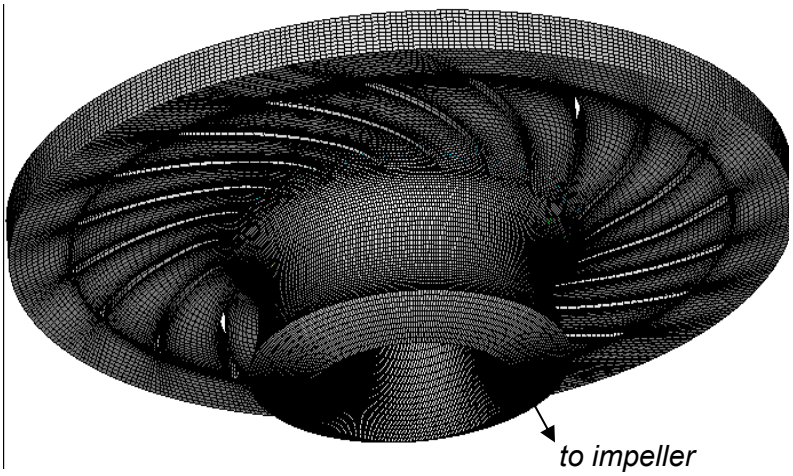

Figure 12. IGV fully structured 3D grid

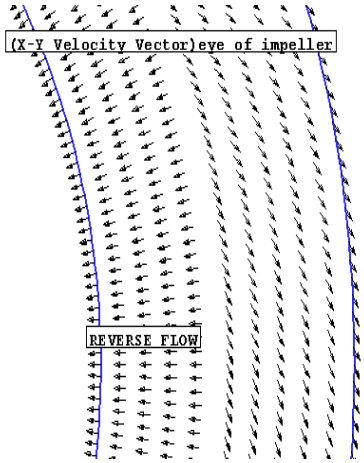

Figure 13. Swirling flow creates an incident flow angle to the eye of impeller reducing power input.

The second stage of CFD simulation included simulation of the impeller and the diffuser. Since the nature of the problem is periodically repeating and to make simulation possible for the existed computer resources and time scale, only one pass of impeller and diffuser was included (cyclic boundary, see figure 17). Meshing such geometry will take more time. A ‘sliding mesh technique’ was used to predict this rotor-stator interaction. Also, for this model, meshes were created in cell zones independently (for diffuser and impeller). The grid interface was positioned with fluid cells on both sides (not on the edge of any part of rotor and stator).

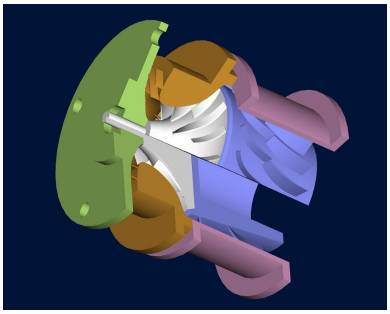

Figure 14. Design geometry

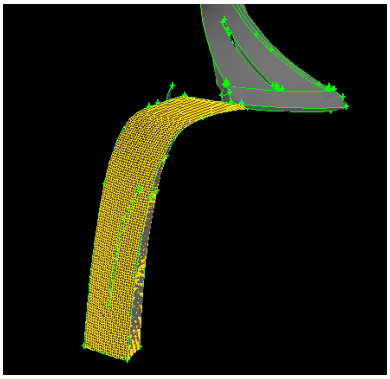

Figure 15. Partial mesh created for the study of IGV and impeller interaction

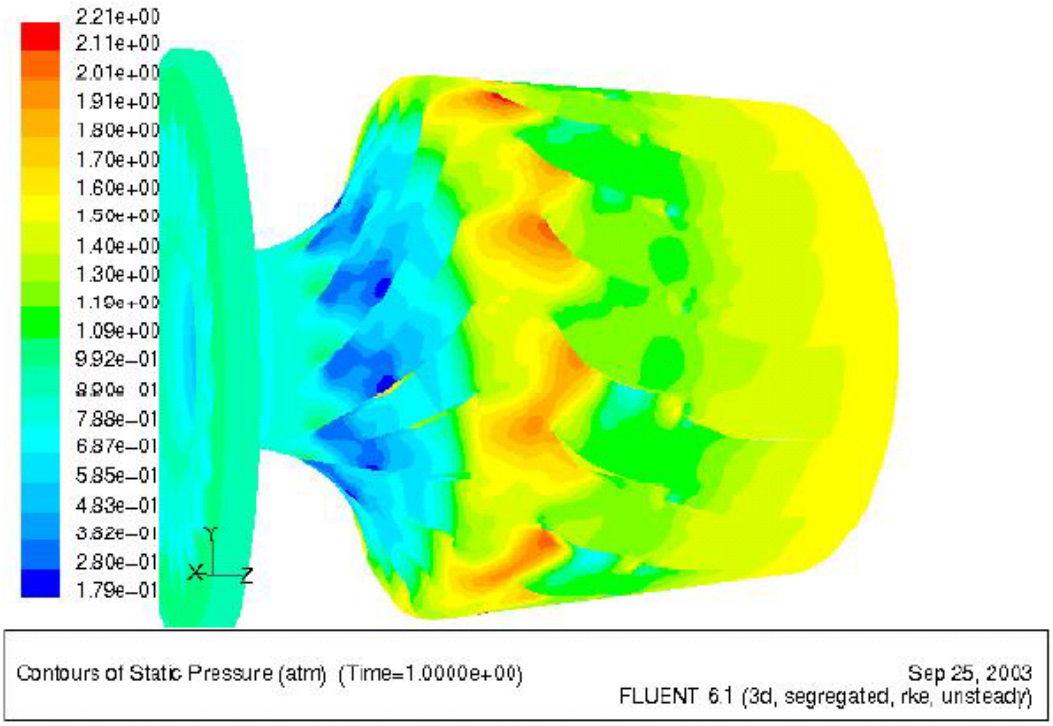

Figure 16. Simulation of IGV and impeller interaction

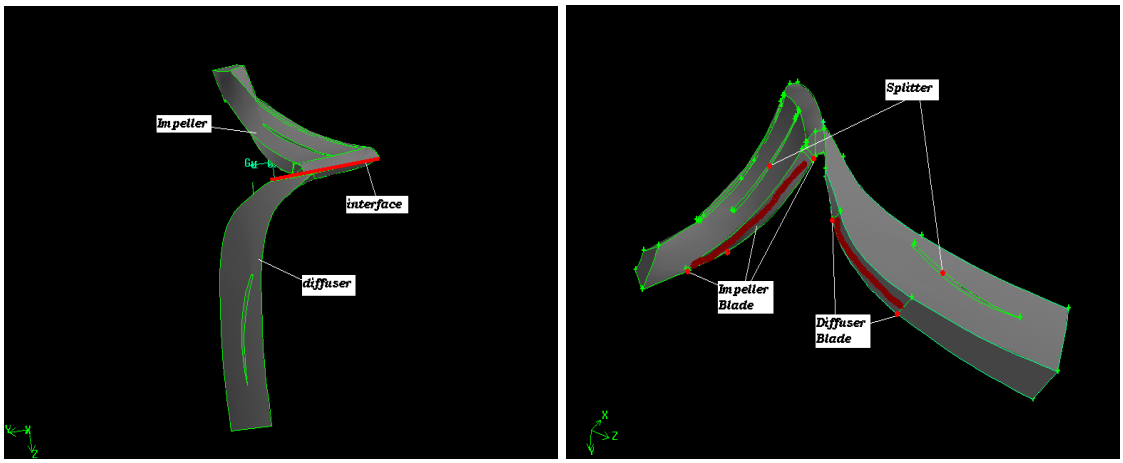

Figure 17. Model for impeller and diffuser Interaction

After the preliminary testing of the compressor assembly, it was found that the designed pressure rise was not achieved at the off-design-points. This under-performance was thought to be possible at the design point. With simulation analysis, we figured out that a flow separation occurs at the first blade rows (figure 18). This separation severely reduces the diffuser performance and wastes most of the kinetic energy of the flow from impeller.

Table 4 shows the thermodynamic status at a series of stations and component efficiencies. We can see that the old diffuser's efficiency is as low as 0.086, and that there is almost no pressure rise in the diffuser (1.278 to 1.3 atm). Depending on the simulation results, we redesigned the

diffuser and ran the simulation again. Figure 18 shows the comparison between old and new diffusers. The flow separation is eliminated in the new design. Table 4 shows that the diffuser efficiency is improved to 0.748 and there is much more pressure recovered in the diffuser (1.302 to 1.5 atm).

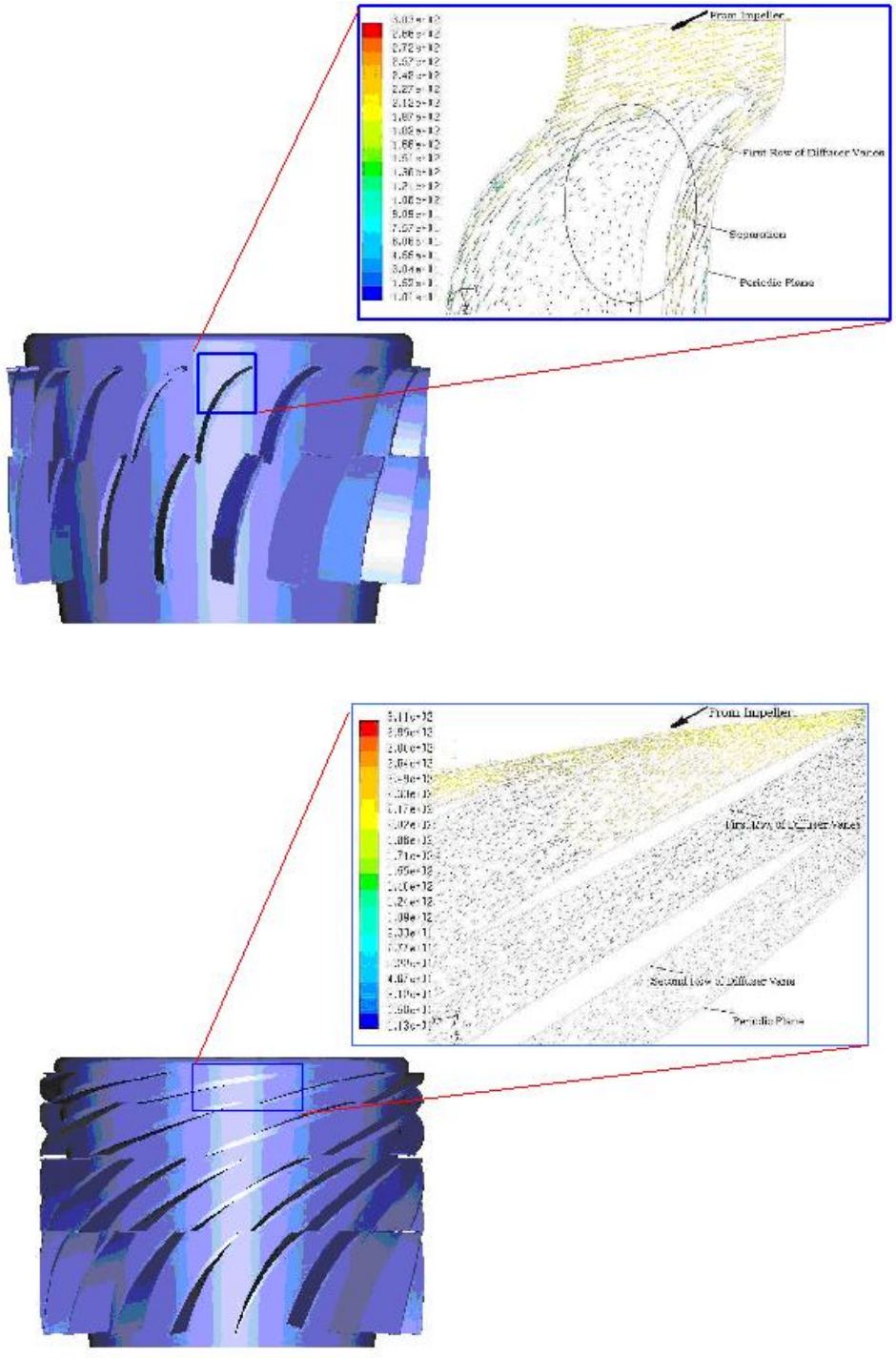

Figure 18. Old and New Diffuser Flow Fields using CFD Simulation

Table 4. Simulation Data for Old and New Diffuser Designs

		Old Diffuser	New Diffuser
Static Pressure (atm)	P00S	0.955	0.994
	P01S	0.862	0.879
	P02S	1.278	1.307
	P03S	1.3	1.5
Total Pressure (atm)	P00O	1	1
	P01O	0.978	0.975
	P02O	1.564	1.595
	P03O	1.302	1.501
Static Temperature (K)	T00S	297.55	297.45
	T01S	287.38	289.17
	T02S	329.9	330.84
	T03S	249.85	351.08
Total Temperature (K)	T00O	298	298
	T01O	297.88	297.86
	T02O	349.4	350.43
	T03O	350.01	350.5
Mass Flow rate (g/s)		15.97	15.7
N (rpm)		108000	108000
Efficiency		0.4487239	0.698388
IGV-Efficiency		0.7634409	0.782609
Impeller Efficiency		0.8300031	0.855529
Diffuser Efficiency		0.0859476	0.748759

(00- inlet of IGV; 01-inlet of impeller; 02-outlet of impeller; 03-outlet of diffuser)

CFD simulation was also used to validate the scaling of the two-stage Helium compressor and the performance is plotted in figure 19. The performance curves of air, neon, and Helium at design condition are in a very close region. Helium and neon results have almost the same values of efficiency at the same pressure ratio. CFD results thus verify the dimensional analysis.

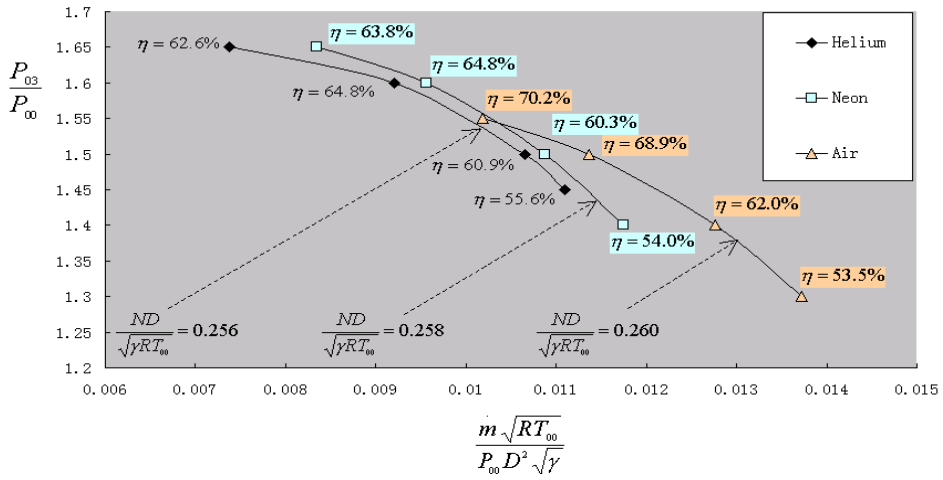

Figure 19. Performance of the compressor at design speed (with Air, Neon, and Helium)

Task 4: Design, Fabrication and Testing of a High-Speed, High-Efficiency Permanent Magnet Synchronous Motor (PMSM)

This part of the report summarizes the work involving the preliminary design, simulation, fabrication and testing of the high-speed permanent magnet synchronous motor (PMSM) for running the single-stage air compressor.

Over the project span, the research has been primarily concentrated in two areas; high-speed permanent magnet synchronous motor development and orealizing a high-efficient open-loop motor control system. An FEM software (Ansoft®) has been acquired which facilitated the motor/generator design. At the same time, knowledge on building open loop motor control using commercially available motors has been achieved. It was determined that the use of inverter output filter is promising in increasing power transfer efficiency.

Different types of motors can be considered for this application like:

1) *Induction motor* (IM) is a low cost option, but the efficiency is low at high speed and at smaller size due to the higher iron loss in the rotor.
2) *Switched reluctance motor* (SRM) has very high reliability, but the iron loss is very critical at high speed, so the efficiency is low.
3) *Wound-field synchronous motor* is generally used in high power application. But it is not good for high-speed application since the mechanical contact of the slip rings and brushes are not reliable at high speed.
4) *Permanent magnet synchronous motor* (PMSM) has very high efficiency since there is no exciting copper loss in the rotor. Also, by using high energy density permanent magnet Nd-Fe-B, the power density can also be very high.
5) *Brushless DC motor* (BLDC) can also have as high power density as PMSM, but since the large harmonics will introduce very large iron loss at high speed, the efficiency will reduce significantly at high speed.

Considering the efficiency and the volume of these different options, we selected PMSM as our preliminary design. The motor specifications considered are shown in Table 5. The motor efficiency was intended to be kept as high as possible.

Table 5. Motor design considerations

Output Shaft Power	2000 W
Shaft Speed	200,000 rpm
Shaft Diameter	14 mm
Max. Length	100 mm
Max. Outer Diameter	44 mm

Even though the single-stage air compressor was required to rotate at a speed of 108,000 rpm, the motor with no load was designed to rotate at 200,000 rpm. This was done because with load from the compressor, the motor speed of rotation could lower to have an high efficiency. For super-high speed applications, a 2-pole configuration is preferred. Low electrical frequency can reduce switching loss of the controller. The advantage of 2-pole is that it can have lowest electrical frequency (3.33 kHz @ 200,000 rpm) for the same speed and so the iron loss in the rotor and the switching loss in the control board can be reduced. A slotless stator was chosen. The slotless stator can greatly reduce the torque ripple, so the iron loss in the rotor and stator can also be reduced. The number of turns per phase and the pitch factor were considered based on the requirements such as dc supply voltage, shaft speed and desired back-EMF. The designed PMSM (figures 20 and 21) consisted of a hollow shaft with a magnet inside it. The direction of flux flow is radial. An obround shape was chosen for the magnet to prevent it from slipping inside the shaft while rotating. Two plugs of same material as that of the shaft were designed to support the magnet at the center from two sides. The bearings were mounted on the plugs.

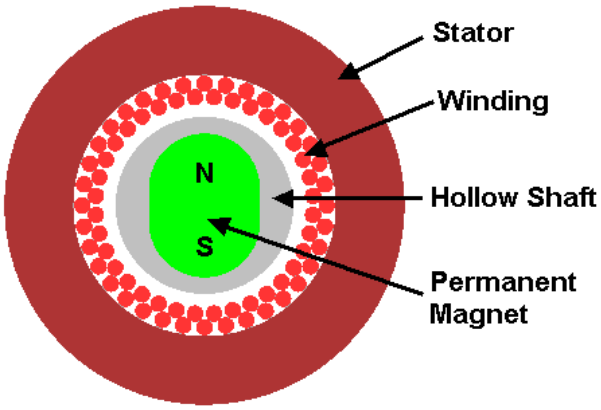

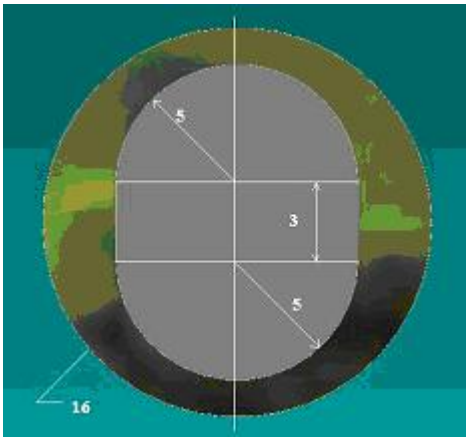

Figure 20. Cross-section of the designed PMSM Figure 21. Dimensions of the hollow shaft

The materials were carefully selected for cryogenic and super-high speed application. Neodymium-iron-boron (Nd-Fe-B), which has the highest energy product compared to other types of permanent magnets, is widely used in electrical machines and other applications. However, when the temperature is below 140 K, Nd-Fe-B will change from a uniaxial material to an easy-cone anisotropy material, which makes the magnet to easily get demagnetized. Therefore, Nd-Fe-B is generally not considered for applications below 140 K, although operations at 60~64 K has been reported. Samarium Cobalt (SmCo) also has very high energy product. It is very stable at low temperatures and has very low temperature coefficient of coercivity and remanence. The Curie temperature and operating temperature of SmCo are also very high. So while inserting the permanent magnet into the shaft, we can heat the shaft to very

high temperature without affecting the performance of SmCo. Therefore, for 77 K application, SmCo was chosen as the permanent magnet in our design.

Copper was used for the winding. The copper dc loss is greatly reduced at low temperature due to increased conductivity. However, the eddy current loss of the winding due to proximity effect will increase because it is inversely proportional to the conductivity. Thus, multi-strand Litz-wire has been used to reduce the eddy current loss. The Litz-wire was constructed using 75 strands of AWG 36 (0.125 mm diameter), coated with heavy 200 °C polyesterimide and overcoated with polyamide-imide to meet IEC MW 35. After that, it was further wrapped with sofimide to withstand temperatures down to 77 K. The constructed Litz-wire was tested at 77 K, and the results show that it can survive at 77 K without any insulation problems.

The motor stator was made of laminated silicon steel. The magnetic properties of the silicon steel are relatively insensitive to the temperature changes. However, since the conductivity of silicon steel will increase with the decrease in temperature, the eddy current loss will increase when temperature decreases. To reduce eddy current loss, thin laminations are required. 0.127 mm (0.005 in) non-oriented silicon steel that is available in the market was used. The conventional epoxy adhesive (Magna-Tac E645) was used to bond the laminations.

The selection of the shaft material was based on certain major factors like, 1) the shaft material should be non-magnetic and must have high yield strength to withstand the centrifugal stress developed in the shaft-magnet system while operating at 77 K and 200,000 rpm. 2) The assembly of the shaft and magnet should be done such that the magnet is at interference fit while operating at 77 K and 200,000 rpm. An unequal expansion-contraction in shaft and magnet at 77 K as well as an expansion of the shaft due to centrifugal force while rotating at 200,000 rpm may cause the magnet to be loose fit and cause mechanical failure. 3) The shaft material should be machineable. The materials taken into consideration were Titanium, Inconel and MP35N. All these materials have high yield strength at 77 K. However, the density of Titanium is less compared to the other considered materials and is fairly machineable. The coefficient of thermal expansion of Titanium is almost the same as that of magnet material SmCo. Thermal conductivity of Titanium is more than other metals considered. The material used for shaft was commercially available Titanium 6 Al -4 V. This material possesses a yield strength of 1400 MPa at 77 K.

Some key dimensions of the designed PMSM are shown in Table 6, the Litz-wire is twisted with one-inch pitch.

Table 6. Motor design specifications

Gap length	0.5 mm
Stator inner diameter	25.5mm
Stator outer diameter	36 mm
Motor active length	25.4 mm
Litz-wire size	1.78 mm x 2.27 mm
Litz-wire configuration	50 strands @AWG 30
Winding pitch	10/15
Shaft diameter	16 mm

The rotating shaft will also be subjected to stress due to centrifugal force while operating at 200,000 rpm. Centrifugal stress analysis was done using FEM software at the operating speed. The shaft was observed to expand more than the magnet and would result in a clearance fit. A high risk of crumbling of the magnet while shuddering inside the shaft prevails. Thus, interference fit was required. It was calculated that heating the shaft to 400 °C and cooling the magnet to liquid nitrogen temperature would produce the necessary clearance to insert the magnet in the shaft. On cooling, the required interference fit would be established. Residual stresses arising due to this process of assembling were calculated. The magnet was tested for failure by compressive stress due to interference fit between the shaft and magnet. The centrifugal stress and residual compressive stress would contribute to the total stress developed while the shaft is in operation. The shaft was tested for pure shear with Maximum Shear Stress theory. The maximum bending stress is given by $\sigma_{max} = M/Z$, where Z = section modulus. The maximum total stress observed was 852 MPa (figure 22). This value was much less than the yield strength of Titanium grade that was used to build the shaft.

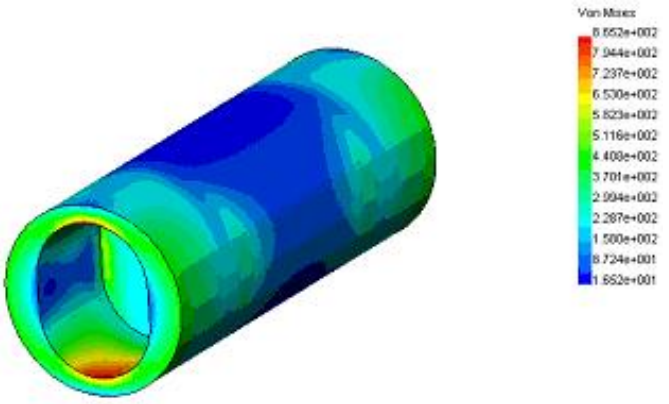

Figure 22. Stress in the shaft and magnet assembly

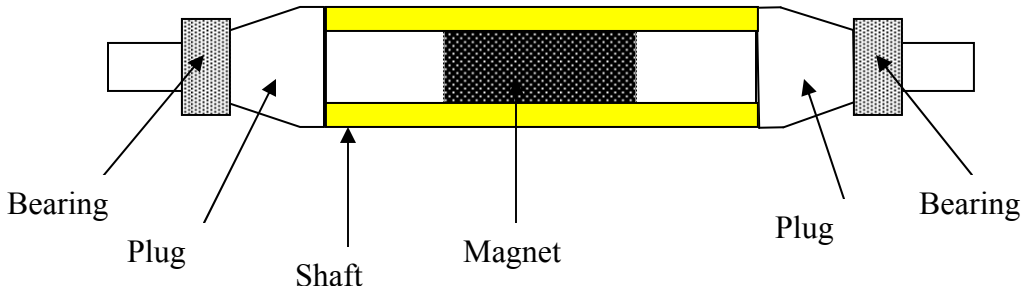

Figure 23. Conceptual design of the rotor

The conceptual design for the rotor system can be seen in figure 23. The magnet had to be assembled inside the shaft. The two plugs were used to house the bearings. One side of the plug had the same section as that of the shaft. Flexible couplers could have been used on a separate component to house the bearings, but the rotor system critical speed would go down. The plugs were press fit on to the shaft, which acted like a rigid coupler.

The air gap flux densities in normal and tangential directions are shown in the figure 24. The corresponding harmonics analysis of the flux density in normal direction shows that the

dominated harmonics is the 3rd harmonics, which is still very low compared to that of slot structure.

The no-load back-EMF was simulated by using 2-D transient time-stepping solver with motion (figure 25). The FFT analysis shows that the normalized 3rd harmonics of back EMF is less than half that of the normalized 3rd harmonics of air gap flux density in normal direction. This improvement is due to the short-pitch winding.

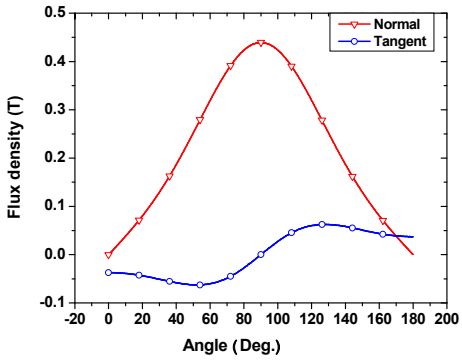

Figure 24. Air gap flux density in normal and tangential directions

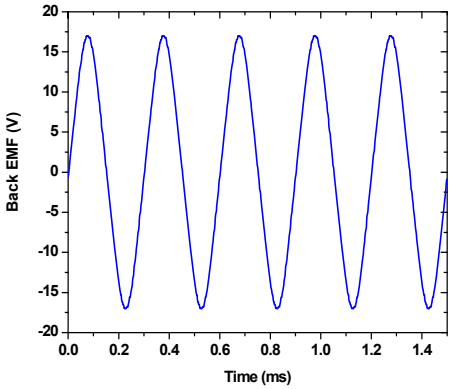

Figure 25. No-load back EMF

The torque was simulated by applying field-oriented current. When there are no harmonics in the field oriented current, the simulated results showed that the torque ripple can almost be ignored.

Eddy current losses of the winding were simulated for both solid wire and multi-strand Litz-wire cases. If solid wire is used instead of multi-strand Litz-wire, the eddy current density can be larger than 2,000 A/mm^2 when the rotor is rotating at 200,000 rpm and the operating

temperature is 77 K. Such a large eddy current is mainly due to the super-high speed and extremely low copper resistivity at 77 K. So solid wire is not practical for the cryogenic motor with slotless structure and rotating at super-high speed. The eddy current was found to greatly reduce after using multi-strand Litz-wire. The simulation and analysis results (table 5) show that the motor efficiency is about 89.9% when running at room temperature, and 91.8% when running at 77 K. Table 7 shows the simulated loss of the designed PMSM that was designed to work at cryogenic temperatures. The controller efficiency was projected at about 95% and so the projected efficiency of the PMSM was about 91.9%.

To further reduce the control loss, soft switching technology was investigated. One of the main losses of the control part was from voltage source inverter. The traditional hard switching inverter will be hard to meet our performance targets even with the improved devices because of switching loss and dv/dt induced problems. Soft switching uses resonance to clamp current or voltage to zero to create zero voltage switching (ZVS) or zero current switching (ZCS) conditions. This would significantly reduce the device switching loss and lower dv/dt problem. But to realize soft switching in inverters is considerably more complex. This is primarily because inverters require bi-directional power flow between the dc bus and the ac output, and typically have two distinct operating frequencies, one associated with modulation and the other with the fundamental output frequency. Further, soft switching operation is required over a much wider range of load conditions. With soft switching, it can decrease total loss on inverters by about 50% according to the literature. That would help a lot to realize the target (95% efficiency) and so soft-switching technology was used for the controller.

Table 7. Simulated and estimated losses of PMSM

	@ RT	*@77K*
Copper DC loss (W)	71.3	7.5
Copper AC loss (W)	1.4	12.8
Stator iron loss (W)	4.2	9.85
Bearing loss (W)	30	
Windage loss (W)	6.3	
Low pass filters loss (W)	11	
Controller loss (W)	100	
Total loss (W)	224.2	177.5
Efficiency	89.9%	91.8%

Rotordynamic analysis was done prior to fabrication. Two models were considered. The first model was based on our initial conceptual design. Figure 26 is a schematic of the FE rotordynamics model with 9 elements and 40 degrees of freedom. The upper half of the model shows the mass distribution while the lower half shows the stiffness distribution. The mass distribution shows the magnet counted for the mass, but not for the stiffness. The rigid body modes are quite sensitive to both bearing stiffness and bearing span. Ball bearing stiffness can vary widely depending on preload, operating internal clearance, etc. In this case, the bearing stiffness can vary anywhere from 10000 to 200000 lb/in, resulting in fairly large variations in the first rigid body mode (~155,000 to ~250,000 rpm). Ball bearings have very little damping and hence operation near these modes results in very large transmitted forces. Generally, the 1st bending critical speed is kept at least 30% higher than the highest operating speed.

The 1st bending mode strain energy in the shaft represents nearly 94% of the total energy, with 6% of the strain energy due to motion at the bearings (figure 27). However, even this motion at the bearings will transmit large forces. The curves in the critical speed map represent the first

two rigid body modes and the first bending mode on the top. As the bearing stiffness increases, the critical speed goes higher.

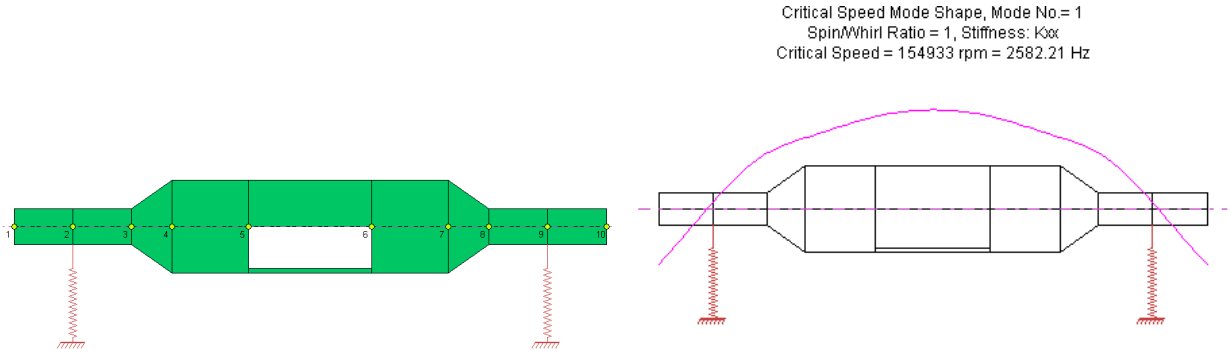

Figure 26. Rotordynamic analysis of motor shaft for Model 1

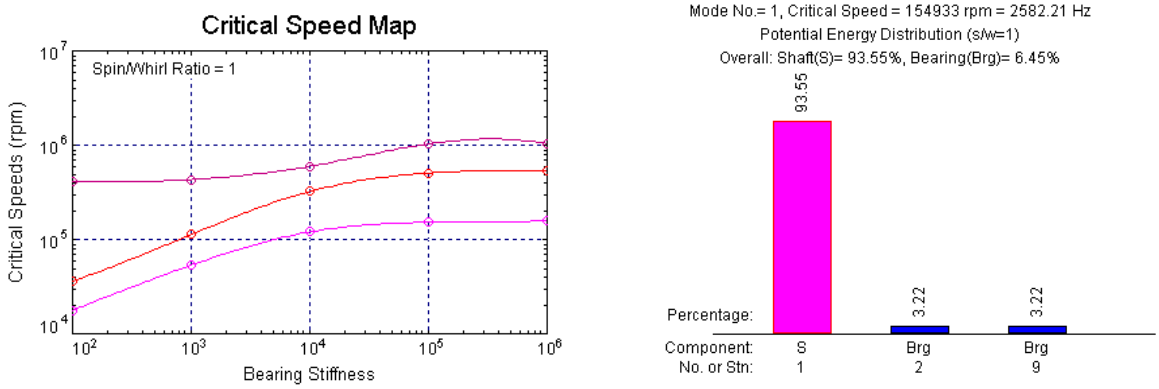

Figure 27. Critical speed map and strain energy distribution for Model 1

The second model shown in figure 28 represents a modification of first model in which an attempt has been made to increase the first rigid body mode. The above model has a slightly smaller bearing span (by 14 mm) compared model 1. It is, however, noted that this results in considerable changes in the critical speed locations. The first mode increases considerably, to around 250,000 rpm.

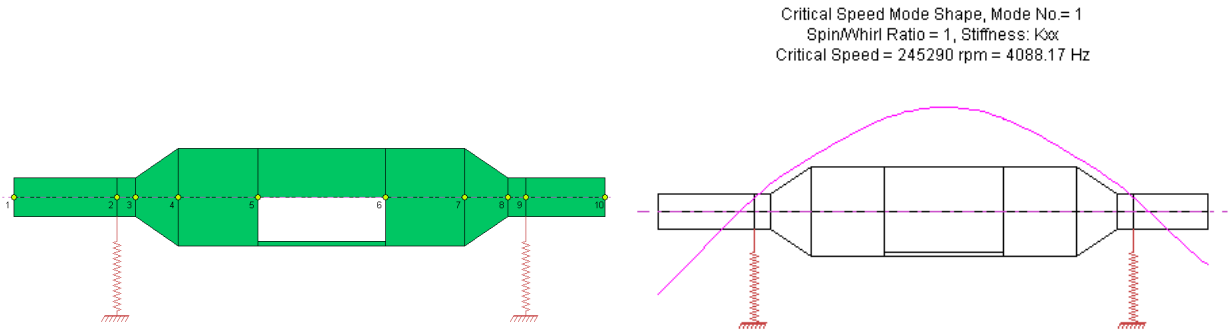

Figure 28. Rotordynamic analysis of motor shaft for Model 2

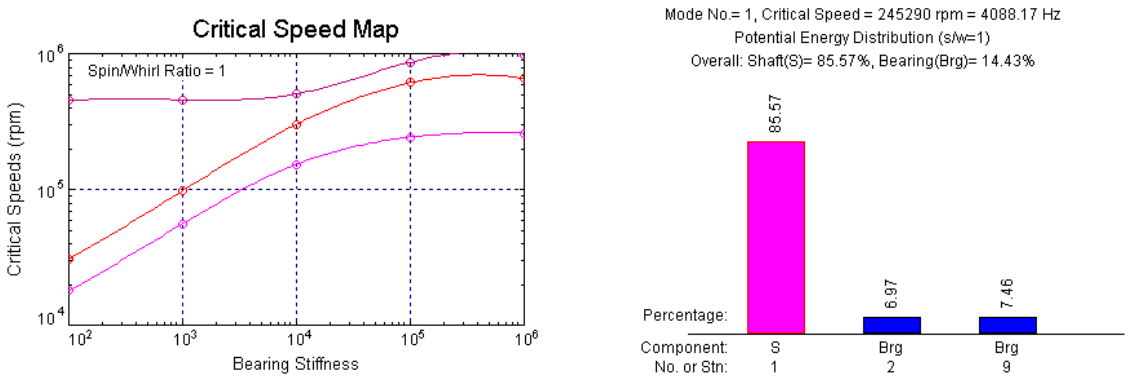

Figure 29. Critical speed map and strain energy distribution for Model 2

For the 1st mode (bending mode) strain energy in the shaft represents about 86% of the total energy, with 14% of the strain energy due motion at the bearings (figure 29). It can be observed that the bearing stiffness has to be around 100,000 lb/in to get the 1st mode above 200,000 rpm. Different kinds of bearings were pursued for the application and high-speed ball bearings were selected. Compared to a steel ball bearing, ceramic ball bearings have less frictional loss and higher speed capabilities, since ceramic balls are lighter than steel balls and so ceramic ball bearings were the final choice. To further reduce the frictional loss in the bearings, smaller bore size bearing was considered (0.25” inner diameter x 0.5” outer diameter x 0.1875” width). These bearings can spin up to 300,000~500,000 rpm.

The lubrication is also a very critical issue for such high-speed bearings. The DN (product of diameter of a shaft in mm and its speed of rotation in rpm) number of the bearing (about 9 mm mean diameter) rotating at 200,000 rpm is approximately 1,800,000. Most of the low speed greases are not shear stable at this speed and the thickener would be damaged to the point that would generate high torque, oil separation, and high heat resulting in a short life. Also, high base oil viscosity of the low speed grease will most likely result in ball skidding, heat, and failure. High-speed grease (Kluberspeed BF 72-22) was selected to lubricate the bearings. BF 72-22 has very low viscosity (22 cSt at 40 °C) and is shear stable at 1,800,000 DN. This grease is designed for high-speed bearings and would provide optimum protection. Friction loss would be minimal once the bearing grease has been run-in.

The fabrication of the rotor of the PMSM was based on the second rotordynamic model as discussed above. The components of the PMSM were then fabricated and are shown in figures 30, 31, and 32. The rotor of the motor was fabricated out of Titanium 6Al-4V as planned. The shaft was machined by EDM process. It included two caps that housed the bearings and supported the magnet inside the shaft. These parts were machined partly by EDM and regular machining process.

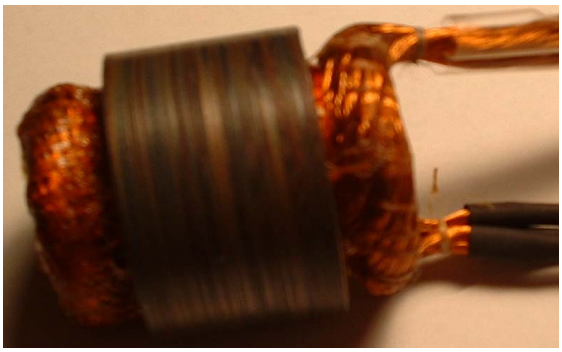

Figure 30. Hollow shaft and magnet Figure 31. Stator and winding

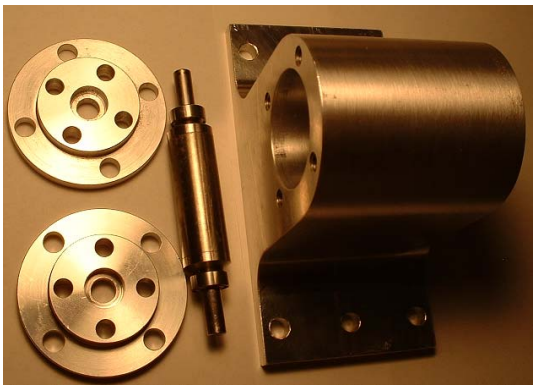

Figure 32. Casing, caps and the assembled shaft

The assembly process involved heating the Titanium shaft with simultaneous cooling of the magnet to achieve a specified clearance between them and shrink fit the magnet inside the shaft. The two caps that hold the magnet and house the bearings have interference fit with the main shaft. The bearings have the fit with the housing as specified by the bearings manufacturer. The housing is air-cooled. The fixture in figure 33 was used to assemble the shaft and magnet. The heated shaft was placed on it as shown. The magnet was dropped inside the shaft and was located by the projected part from the fixture base.

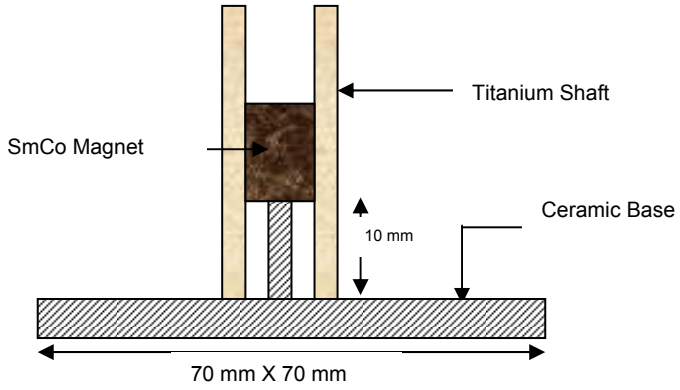

Figure 33. Fixture schematic to assemble the shaft and magnet

The controller design for the motor was based on TI Digital Signal Processor TMSLF2407A. It includes hardware and software parts. Hardware is mainly to provide suitable drive power to the motor. Software is to produce the control signals based on space vector PWM to obtain good performance. Several optimal approaches were considered to improve the efficiency and performance of the controller.

On the hardware side, various new chosen components were employed to improve controller dynamic characteristics and provide higher efficiency. Firstly, power dissipation in MOSFETs is a main concern of controller system efficiency. The total power loss includes resistive power loss and power loss in switching. Resistive power loss will increase a lot if MOSFET drain to rain on resistance (R_{ds} (on)) is high when load current is huge. The MOSFET used namely, FDP047AN08A0, has an R_{ds} (on) of 4.7 mΩ, which is less than one-tenth of the most common MOSFETs. The gate drive current was increased to 2A, which was a ten fold increase compared to the prior similar controller designed for the project. This was done to reduce conduction and switching losses. Secondly, the total gate charge of the MOSFET was only 92nC, which was small enough to make sure that transistors were switched on/off correctly. Thirdly, high-speed optocoupler HCPL 2631 (10 M bit/s) replaced HCPL 2531 (1 M bit/s), which was fast enough for our high switching frequency need and will lower SVPWM signal distortion.

The drive chip is an important component in the controller system, which critically affects the dynamic characteristics. Well-known IR 2110 was used for this controller. The hardware circuit is shown in figure 34.

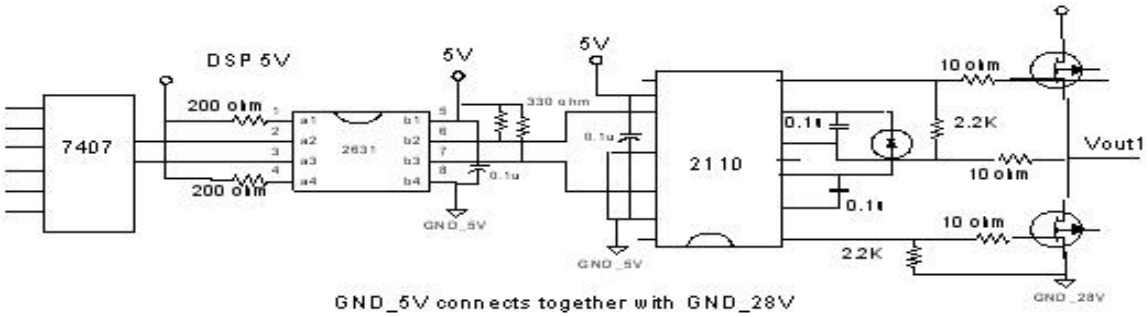

Figure 34. 2000 W PMSM motor controller hardware circuit schematic
(Only one phase shown in this figure because of symmetry of the other two phases)

On the software side, constant volts/Hertz method was employed to produce controlling voltage responding to frequency because of its easiness to realize and advantage at middle to high speed applications. The purpose of constant V/f control is to generate required phase voltage Vs* which is maintained proportional to the frequency so that the stator flux remains constant. This permits for nearly maximum available torque per ampere of the stator current and fast transient response for the V/f control. As a result, higher efficiency and better performance can be permitted. For normal motor system, constant V/f control is a linear control because stator resistance is small compared with motor inductance and can be neglected. However, because of the compact size requirement of the 2000W PMSM motor, the stator resistance effect cannot be neglected anymore. An optimal volts/Hertz control was proposed based on system simulation and analysis. System simulation results provided optimal V/f control as shown in figures 35 and 36.

Test results showed that the proposed optimal V/f control method improved system performance and efficiency. In space vector PWM method, voltage modulation index, m, was chosen less than 0.952 to avoid over-modulation. In addition, a switching frequency was carefully chosen to realize higher speed and better performance.

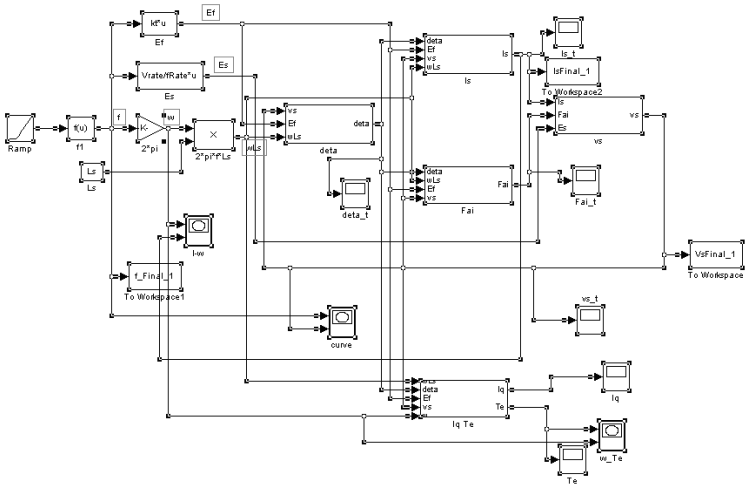

Figure 35. Optimal V/f control simulation

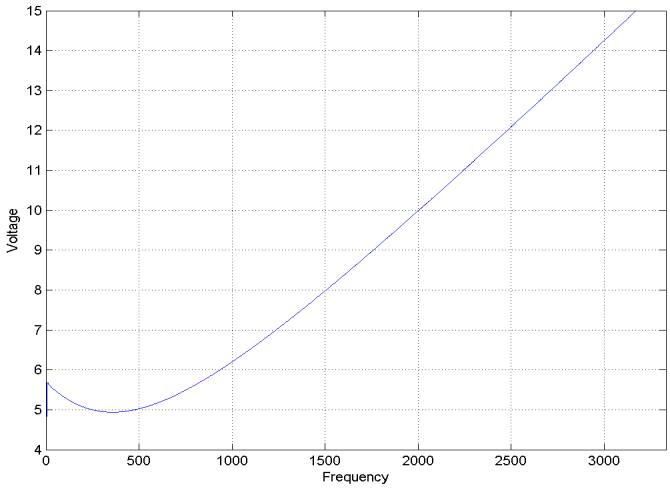

Figure 36. Proposed optimal V/f curve for the super high-speed motor

After building the appropriate controller and completing the motor fabrication, a free spin test was first performed (figure 37). The motor ran very smoothly below 130,000 rpm. We expected the free spin loss at 200,000 rpm to be about 184 W if it was well adjusted. And the projected efficiency at 200,000 rpm with 2000 W output was around 90%.

When the speed was above 140,000 rpm, the losses increased greatly. One reason of large loss was that the pre-load was not applied in this prototype. Preload can help to avoid skidding of the bearing balls to reduce noise and vibration. There are two basic methods of preloading: solid preloading and spring preloading. Solid preload can be obtained by mechanically locking all of the rings in position while under a reasonable axial load. The advantages of solid preload are simple structure and high stiffness. The disadvantage is high variation in preload under temperature variation, and that the preload can reduce with wear. Spring preload can be applied

using coil springs. An advantage of spring preload is that it maintains consistent preload with temperature variation. The disadvantages are that the designs are more complex and normally have lower stiffness. If the applied preload is insufficient, fretting corrosion can occur. This happens because of vibration causing the balls to resonate and abrade on the raceways. Therefore, obtaining the correct preload is very important. The cap was modified to consider spring preload (figure 38). Four springs were used inside the cap to provide adjustable axial preload. The motor was tested again with the modified cap.

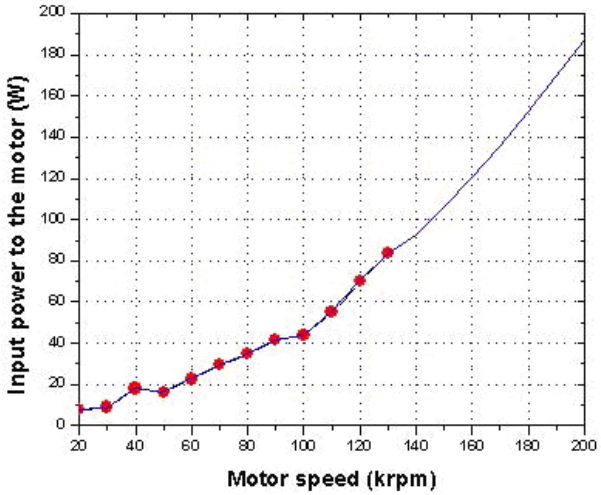

Figure 37. Motor free spin test curve

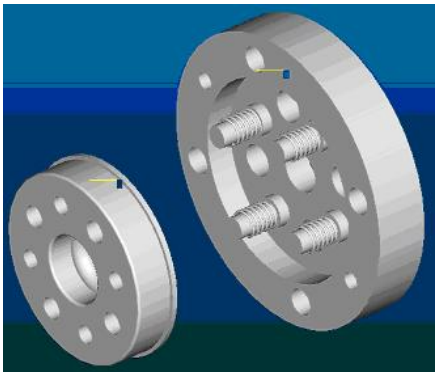

Figure 38. Modified motor cap considering spring preload

With the modified cap, the motor was spun to 200,000 rpm successfully with no load. As projected, the loss was less than 10% of the total input power. Figure 39 shows the tested input power versus free spin motor speed. It shows that total input power to the controller is less than 190 W when the motor was spun at 200,000 rpm without any load applied. The controller input power is the summation of controller loss, bearing loss, windage loss, copper loss, and the iron loss in the rotor and stator.

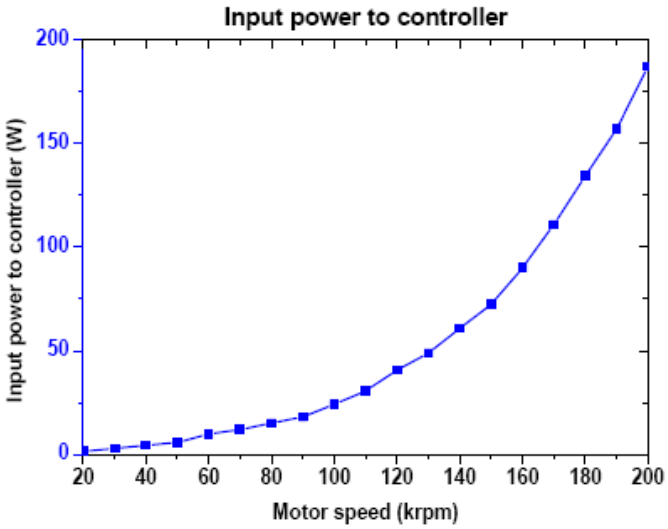

Figure 39. PMSM no load test results

The motor was then coupled with a generator to perform the load test. An integrated single shaft design (figure 40) was used to avoid a coupler since it was found that mechanical couplers posed a lot of problems when performing a preliminary compressor test with the developed motor (details are mentioned under Task 5). When coupled with a generator, the PMSM was found to stably rotate to speeds up to 120,000 rpm, which is still more than the required speed of 108,000 rpm of the single-stage air compressor. Figure 41 shows the assembled motor/generator system. Figure 42 shows the efficiency vs. motor speed for an average torque of 0.05 N.m. It can be seen that the efficiency is above 92% at high speeds.

Figure 40. Integrated motor/generator shaft

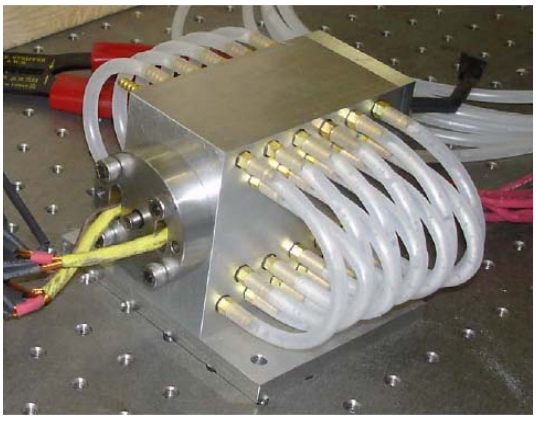

Figure 41. Integrated motor/generator test setup

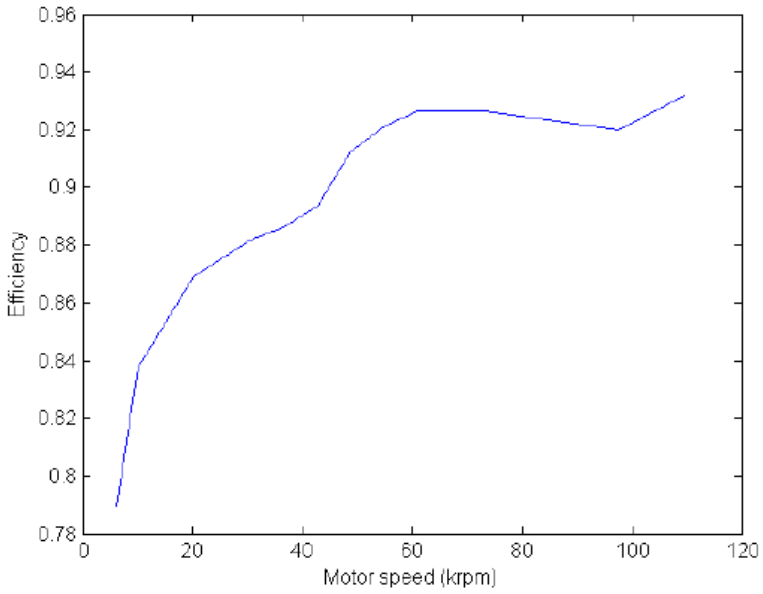

Figure 42. PMSM efficiency vs. speed for the load test

Task 5: Integration and Preliminary Testing of the Motor/Compressor Assembly

As mentioned in the geometric scaling details of Task 2, the single-stage centrifugal air compressor was designed to rotate at 108,000 rpm and provide a pressure ratio of 1.55. The single stage compressor was intended to be tested at 120,000 rpm. Components required for the integration of PMSM motor-single stage compressor assembly were developed and fabricated based on their individual 3D CAD models.

Figure 43 shows the schematic of the test setup. The critical component in testing is the coupler to couple motor shaft to the compressor shaft. A custom designed high-speed helical coupler® (figure 44) was manufactured under collaboration with Heli-cal, Inc. This coupler can handle a torque of 0.75 lb-in, allowing misalignments of 0.01” parallel, 0.05” axial and angular tending towards 0°. This coupler was designed to transmit power between compressor and the motor assembly when rotating at speeds up to 108,000 rpm.

For preliminary testing, another similar coupler manufactured by WM Berg, Inc. was used. This coupler (figure 45) is built in disc couplings style. The hub and the center were made of aluminum alloy, rivets and washer of brass and discs of stainless steel.

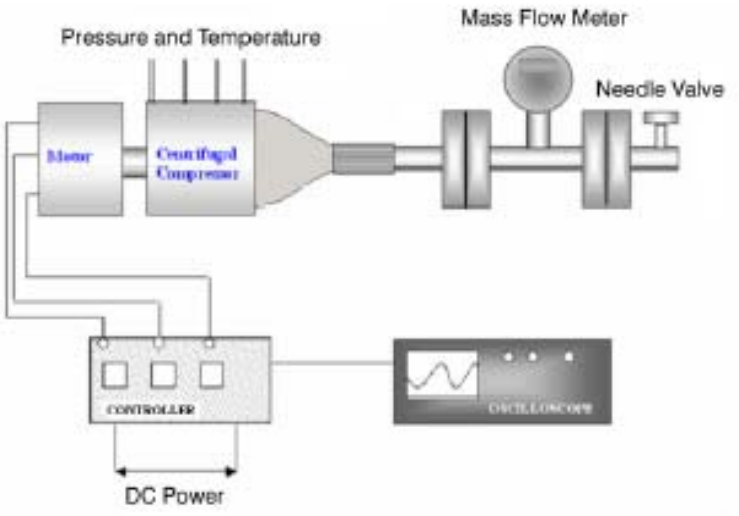

Figure 43. Schematic of the single-stage centrifugal air compressor test setup

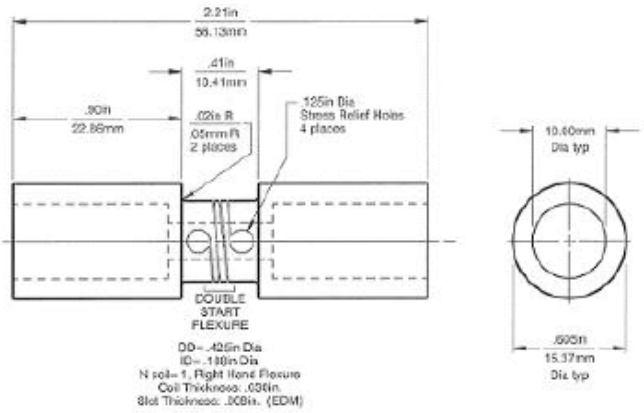

Figure 44. CAD drawing of Heli-cal, Inc. coupler

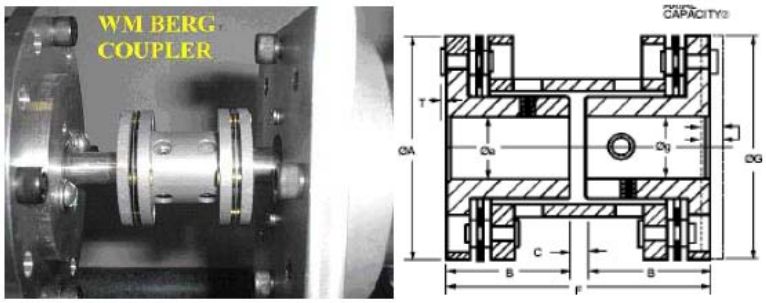

Figure 45. WM Berg, Inc. coupler – left; CAD drawing – right

Figure 46 shows the coupler integrated motor/compressor test assembly. Preliminary test results are shown in figure 47 plotted as gauge pressure vs. shaft rotational speed. It can be observed that the highest speed reached was about 90,000 rpm. Due to the coupler failure, we could not reach speeds beyond this point. However, from the graph, it appeared that on proper extrapolation, we were on the right track to the design point.

In order to tackle the coupler problem, laser alignment was considered. But the equipment used for laser alignment procedure was larger compared to our system and so hindered its usage.

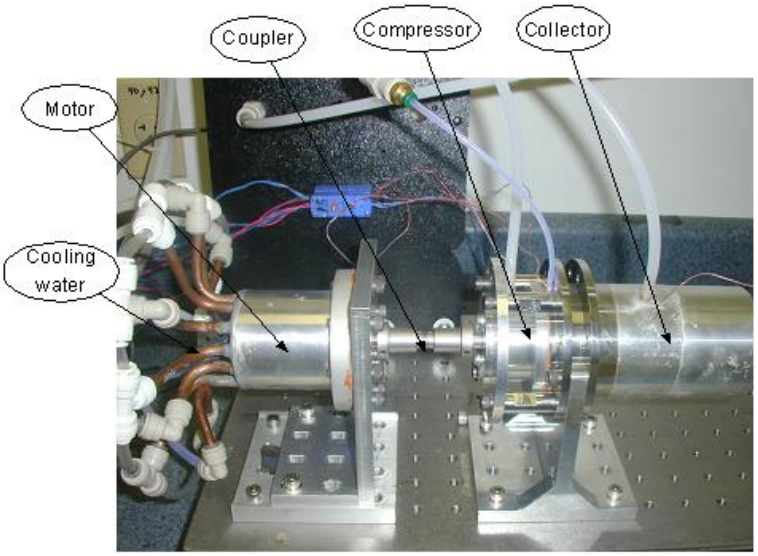

Figure 46. Compressor/motor test rig

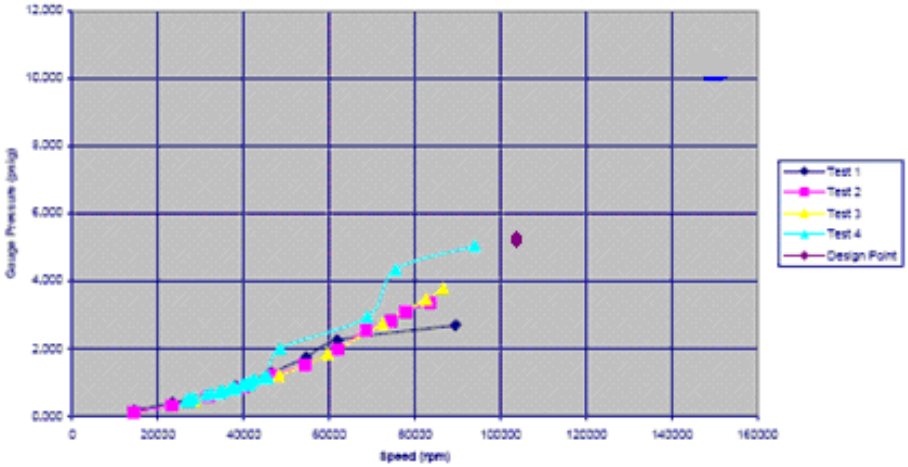

Figure 47. Integrated (using coupler) compressor/motor test results

The use of ‘translational stages’ then became an option in order to resolve this problem. Translational stages offer control of motion, ranging with fair accuracy. The motor side of the test assembly was chosen for modification depending on its structural simplicity compared to the compressor side. Modifications were made on the motor side and re-fabricated to match the translational stages to build up a system. This system provides control of motion in X-Y-Z directions (figure 48). The base for the compressor side was re-fabricated. But it was found that the system could reach a maximum speed of only 92,000 rpm (figure 49).

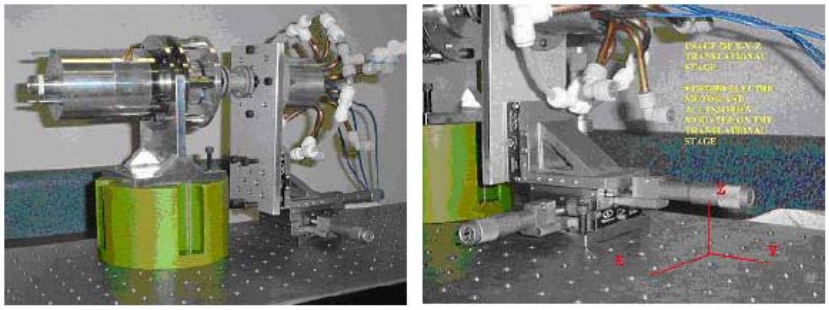

Figure 48. Translational stages for motor/compressor assembly alignment

In figure 49, we can see that the designed pressure rise is not achieved at the off-design-points. As mentioned in Task 3, the poor pressure rise performance was found to be because of flow separation in the diffuser.

It was found that the key issue that prevented the setup to go over 92,000 rpm was rotordynamics. The conclusion is that high-speed designs must eliminate the use of coupler. Even though translational stages solved the alignment problem of the coupler, the stiffness of the coupler affected the overall structural stiffness and caused rotordynamic problems.

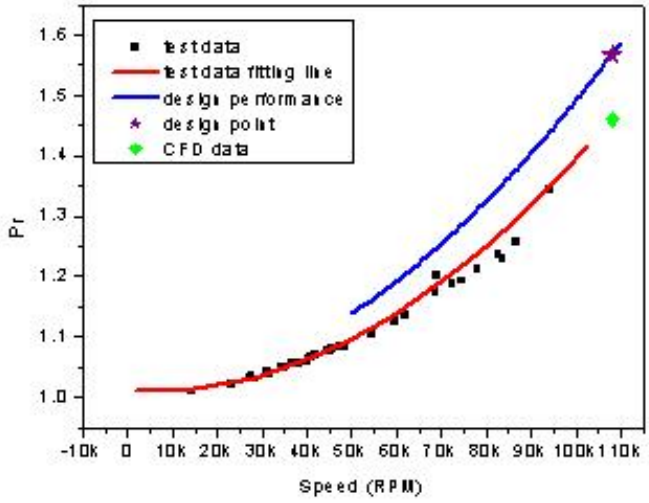

Figure 49. Compressor pressure rise performance

Therefore, a new motor/compressor integrated single shaft design was done. The difficulty of coupling did not arise in this new design. Figure 50 shows the solid model of the new test rig section with its components, which was done first to observe any difficulties that might arise during actual integration. Distinguishable features of this modified assembly are described below.

1) Single Rotor design – Eliminates the usage of coupler and improves the rotating stability.
2) Spring-preloaded bearing system – A structure to control the preload on ceramic ball bearings and enhance their performance at high speeds.
3) Closed gas passage structure – A closed gas passage that facilitates testing of the compressor with various gases at arbitrary inlet conditions.

4) Precision impeller tip clearance control – A thread-scale structure was designed to measure and control the tip clearance.

The components were fabricated at various machine shops and are detailed below.

Rotor Structure – Figure 51 shows the fabricated components of the rotor structure. The titanium plug and titanium shaft were machined by EDM process and were welded together by Electron Beam Welding. The aluminum plug was fabricated by EDM process and was welded to aluminum impeller. The two sets were then assembled by a metal bonding adhesive.

Bearing Loader – This part (figure 52) was used to support and preload the ceramic ball bearings. The preload with was applied with the help of springs.

Gas Passage and Inlet Guide Vane – The gas enclosure was fabricated to house the inlet guide vane and also to input various gases for testing with the help of a 1/16” NPT connection as shown in figure 53.

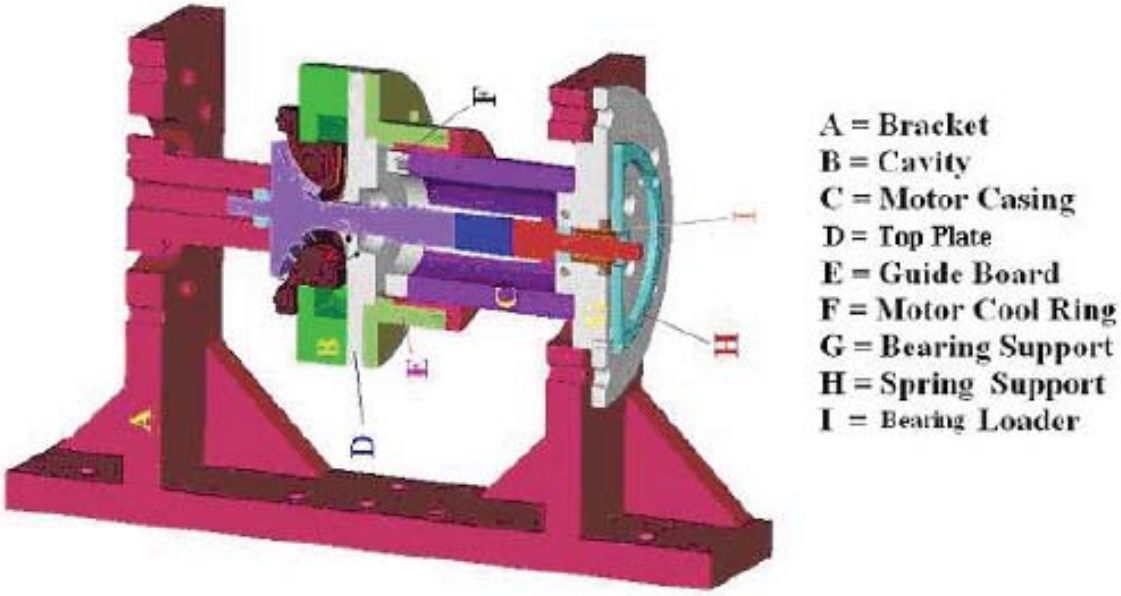

Figure 50. Solid model of the test rig

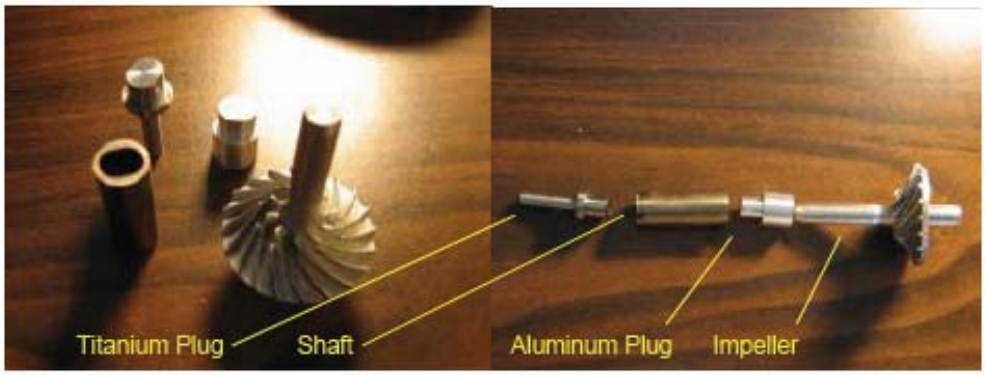

Figure 51. Rotor structure

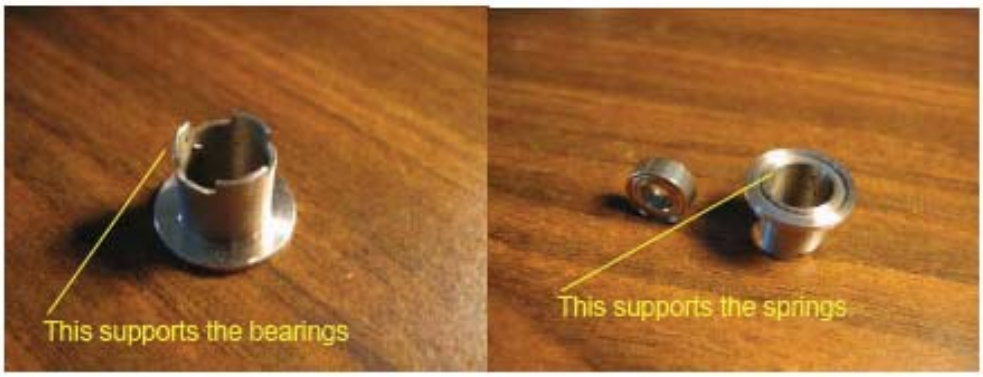

Figure 52. Bearing loader

Top Plate – This plate (figure 54) was fabricated with the contour of the IGV blades and was used to close the compressor chamber.

The instrumentation needed for the compressor testing process included a mass flow meter, pressure transducers, thermocouples to measure the temperatures of the flow at inlet and exit and the temperature of the bearings.

Figure 53. Gas passage and IGV

Figure 54. Top plate

The integrated compressor – motor rotor was mounted on a structure as shown in figure 55.

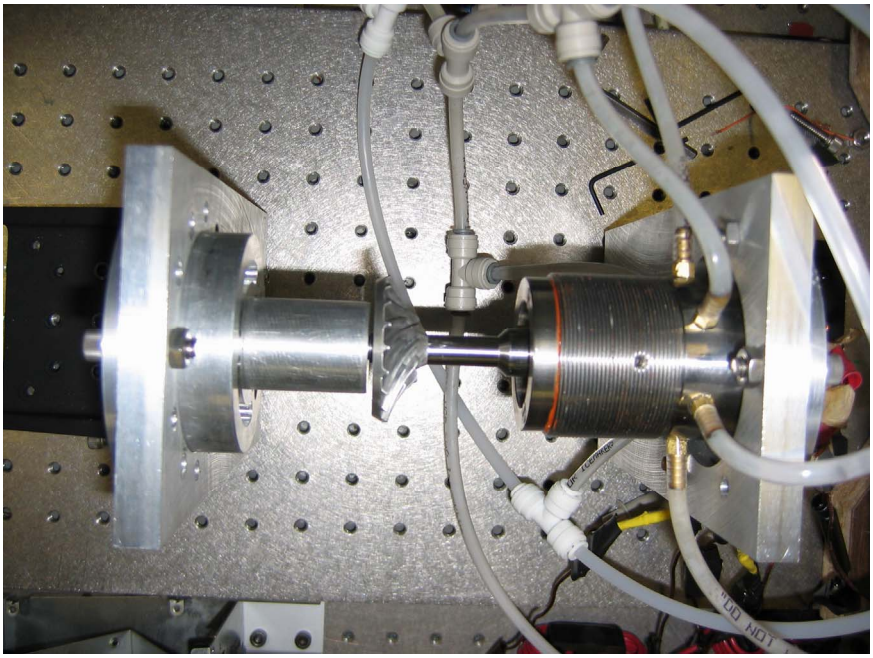

Figure 55. Single shaft integrated compressor/motor test setup

Stator of the motor was housed inside the motor cooling jacket. The cooling jacket was cooled with water. Part of the rotor and stator can be seen in figure 56.

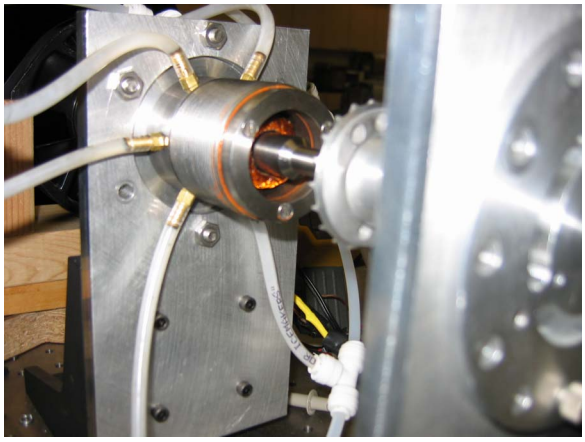

Figure 56. Stator and rotor housed inside the cooling jacket

The motor control software installed in a computer was used to control the DSP board (figure 57) connected through an emulator. The DSP board was connected to the controller, which supplied power to the stator of the motor by a low pass filter.

Figure 57. Emulator, DSP board and controller board

Temperatures and pressures were measured at various places in the experimental setup to get sufficient and accurate data. This helped for better optimization of the performance parameters and thus enabled for an easy and successful implementation of Task 6. An Innova-Vortex® mass flow meter was used for mass flow rate measurements. Setra P- Transducers® supported by multimeters were used for pressure measurements. Figure 58 shows the accessories used in the test setup.

The rotor was run up to a speed of 100,000 rpm. Because of some problems with the bearings used and the shaft balancing issues, it was not possible to stably run the rotor at this speed for enough time so that data can be collected sufficiently to evaluate the compressor performance. From a preliminary analysis, it was realized that the problem is with the bearing radial play provided (0.0002 in) and the maximum interference fit specified by the manufacturer (0.0002 in). Since both the values were the same, the bearing did not provide any provision for thermal and centrifugal growth of the shaft. Since it is customary to provide a tight interference fit between high speed rotating shafts and bearings, a value of 0.0002 in. was chosen with the presumption that it provides good rigidity (when the motor alone was tested to 200,000 rpm under Task 4 of the project, the fit provided was lower than 0.0002 in. because of short length of the shaft and a different material used, which does not need enough rigidity from the bearings). So for the next test, a fit of 0.0000 in. was provided, so that there existed some radial play even after the fit.

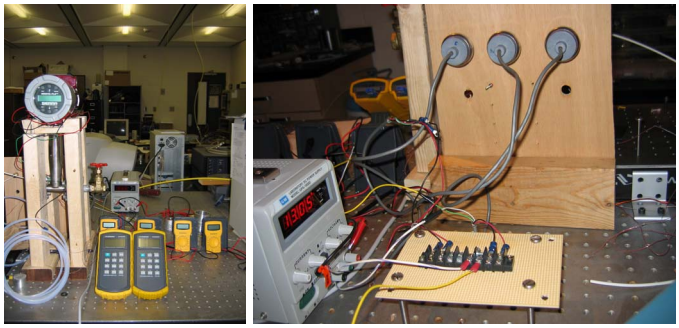

Figure 58. Mass flow meter, thermocouple units, pressure transducers and multimeters

Even though the three-piece rotor was better aligned compared to using a mechanical coupler, the structural rigidity was still not satisfactory because of the condition that three pieces must exist in the same plane in all the axes. A new rotor was again machined out of two pieces with a hope to improve rigidity and rotor instability issues. This time, the impeller on the rotor comprised a single piece and plug comprised the other. Magnet was inserted into the rotor and was contained inside with the help of plug.

To confirm that the bearing friction due to misfit was important for not allowing the tests to be successful after 100,000 rpm, for the next test, we devised a way to measure how much power the bearings were consuming for which it was important to precisely know the input power to the motor. Since we know the efficiencies of the controller, motor and the compressor, the power consumed by the bearings can be found by knowing the input power exactly. But the major difficulty we had in measuring input power to the motor accurately was that the current input to motor was AC current and the motor had a power factor, which depends on the working conditions and DC power supply. The voltage between lines is only a couple of volts so it was difficult to find an appropriate power meter. This problem was resolved using an oscilloscope and a differential probe. The differential probe can measure the voltage between two points without the risk of introducing a shortage between lines (which may cause burning of motor or controller). The output is a sinusoidal wave of the voltage and current on each phase, which can be displayed on the oscilloscope. By measuring the phase difference and the wave amplitude, the power input into the motor can be accurately measured. Figure 59 shows a typical voltage-current measurement at 30,000 rpm and 20 V DC output.

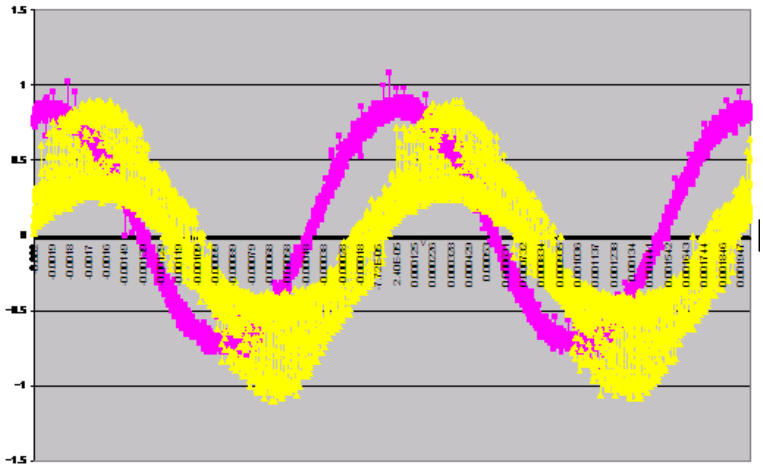

Figure 59. Voltage (pink) – current (yellow) wave form at 30,000 rpm; phase angle is 51°

With change of the DC output from 20 to 15 V, we can find that the power factor has changed (figure 60), although speed is kept the same.

From figure 60, we can see that if more power is supplied to the controller, the motor is still running at the same speed, but the power factor has changed. When more current goes into system, the loss goes up. The power is wasted on heating up the connection lines, controller chips and motor windings. Because the controller was open-looped, it could not adjust the output power of the DC power supply to the needs of the motor. Therefore, the power factor was manually adjusted to make it close to unity and the voltage current wave form for such a configuration is shown in figure 61.

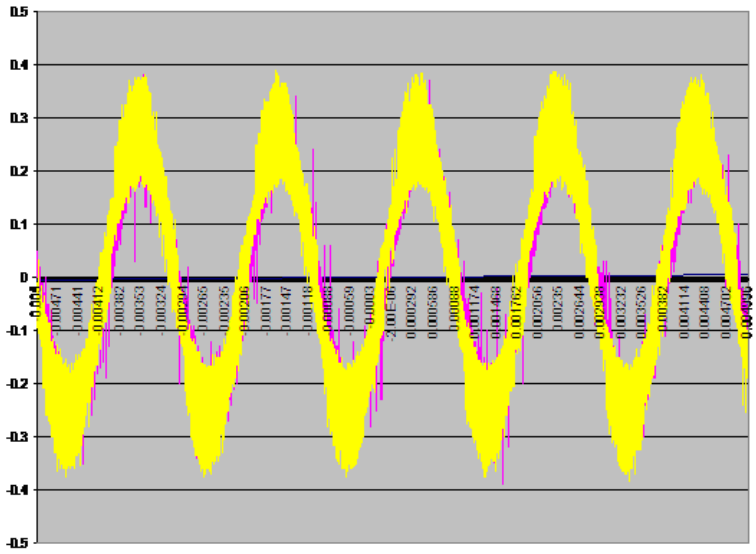

Figure 60. Voltage – current wave form at 30,000 rpm; phase angle is 6°

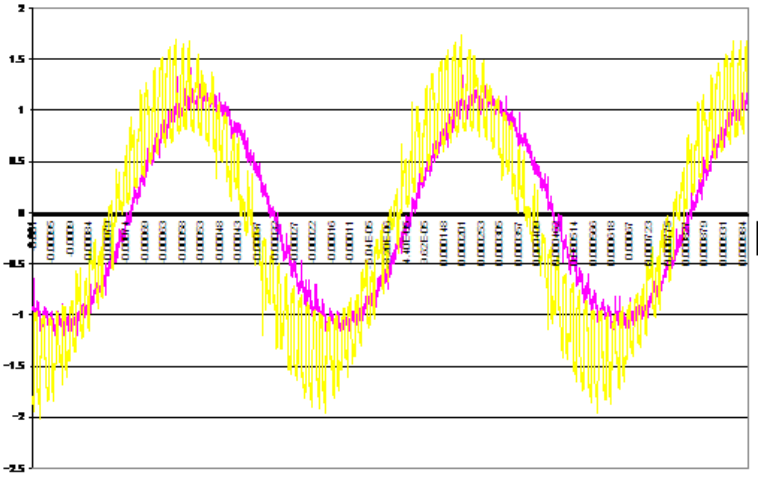

Figure 61. Voltage – current wave form at 76,300 rpm; phase angle is 30°

Another significant area of interest of the failure diagnosis was the rotor instability. Instability of the magnet integrated rotor can be classified under two categories namely; rotordynamic instability (rigid body modes and critical speeds) and aerodynamic instability (compressor choke/stall). Rotordynamic instability can be prevented by having a high rigid design for the rotor, which pushes the rigid body modes and critical speeds to a higher limit. Hence, as mentioned before, a two-piece shaft was used for the next test.

As far as aerodynamic instability is concerned, it was found difficult to avoid it completely since the impeller design, working fluid, and pressure ratio were already decided and optimized for the specific application of ZBO of cryogenic propellants. In case, the developed miniature integrated motor-compressor design was intended to use for some other application like storage of

methane, the optimization for the same design can be done such that it gives minimum aerodynamic instability.

After resolving the bearing fit, rigidity and power measurement issues, the compressor has been spun successfully to a speed of about 110,000 rpm. Three zones of instability were encountered during spin-up at,

Zone 1: 33,000 – 37,000 rpm
Zone 2: 41,000 – 45,000 rpm
Zone 3: 63,000 – 66,000 rpm

After passing these zones, the rotor was found to stably rotate until 110,000 rpm (the design speed is 108,000 rpm as mentioned in Task 2). The compressor performance was measured up to a speed of 96,800 rpm and the results are shown in figure 62. CFD results are plotted on the same figure for comparison. The tip clearance was 5% the blade height, or 125 microns.

Table 8 lists all the related losses and power consumptions at two speeds with motor loss, bearing loss and windage loss based on theoretical calculation.

Table 8. Power distribution of the compressor performance test

Speed (rpm)	Input power to motor (W)	Motor loss (W)	Bearing loss (W)	Windage loss (W)	Compressor consumption (W)
30800	27	3	5	5	14
76300	323	33	15	35	240

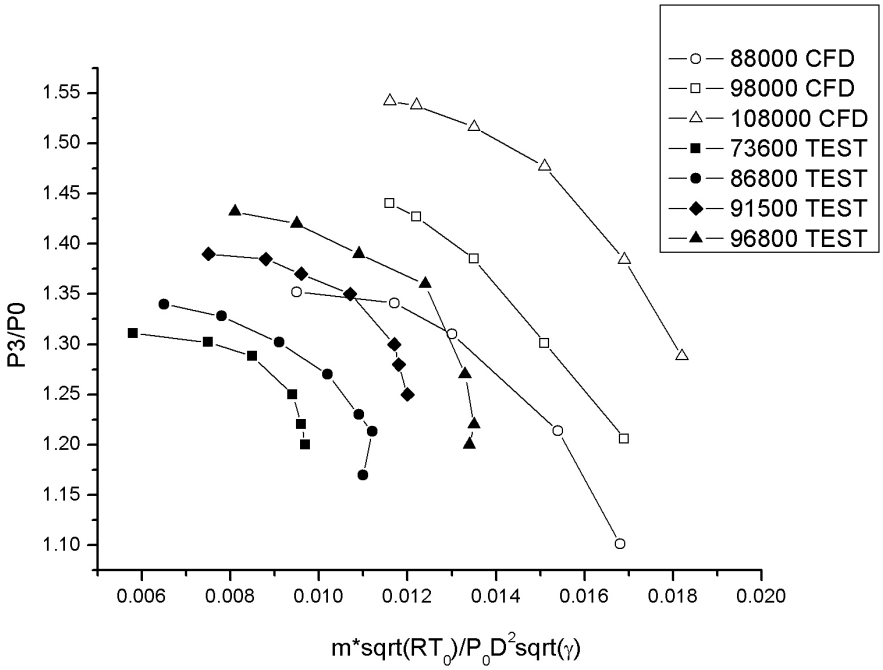

Figure 62. Compressor performance chart

Where,
P3/P0 – the non-dimensional pressure at the exit of the diffuser (pressure ratio of the compressor); and m*sqrt(RT0)/P0)D^2sqrt(γ) – the non-dimensional mass flow rate with 'T0', 'P0' as the inlet temperature and pressure to the inlet guide vane (here, ambient conditions), 'D' is the impeller diameter and 'γ' is the ratio of specific heats (here, of air), 'R' is the universal gas constant and 'm' is the mass flow rate measured at the diffuser exit.

From figure 62, it can be observed that there is a small deviation of the performance curves between experimental and CFD results. The location of test curves to the left of the simulation curves indicates that there was some leakage of gas/air before the mass flow meter at the diffuser exit. We suspected this leakage to be at the impeller tip since there was no accurate impeller tip gap control in our experiments.

Task 6: Overall System Optimization

Our efforts in the last five tasks have successfully proved our integrated compressor/motor concept and design through preliminary testing. But we still had difficulty in spinning the compressor for long durations. We suspected this problem can be either because the rotor is not balanced perfectly enough or the bearing is not tuned properly and assembled for this speed.

As a part of design optimization, we continued our efforts on testing by mainly focusing on three major improvements:

1. Investigating the problem of selecting an appropriate bearing outer ring-housing fit,
2. Enhancing the heat spreading area around bearings to avoid their possible overheating,
3. Using acceleration sensor(s) to identify the rotor vibration and thus address the rotor instability problem.

After implementing the above, we have solved many speed-related problems and successfully spun the compressor to 108,300 rpm. In our previous diagnosis of the test results (Task 5), we found that tip leakage might be a significant factor for the reduced dimensionless mass flow rate and pressure ratio in the obtained compressor performance chart. Therefore, in further tests we also measured the performance by varying the tip gap. At a fine tip gap (gap = 5% of the blade height), we found that the compressor gave a good pressure rise (figure 63), although it was still a bit lower than what we expected at this speed (design pressure ratio = 1.55). If the tip clearance was increased, the pressure rise dropped dramatically from 1.53 to 1.48 and hence deterioration in the performance was observed (figure 64).

This proves the correctness of our past analysis that tip gap plays a very important role in miniature centrifugal compressor performance, especially in achieving the required pressure rise. It will also have an effect on the flow rate, but not as apparent as on the pressure rise. A tip gap effect on the performance at the design speed can be clearly seen in figure 65, where x-axis represents the dimensionless mass flow rate and y-axis represents the pressure ratio in all the three figures.

Efforts in testing have been made to lower the tip gap but it was found that our current test rig design does not favor that. This is because when the high speed flow passes through compressor at the exit, it exerts a backward reaction force on the test rig, which makes the impeller move backward along with the rig. This makes the impeller touch the shroud and hence small tip gaps completely disappear. This will have a negative impact on the compressor

performance with impeller blades rubbing against the shroud at high speeds. Although it may be theoretically possible to have an initial tip gap sufficient so that it compensates for the backward movement of the impeller towards the shroud, it is very unlikely to dynamically predict during the experiment the backward reaction force on the impeller. Hence, a precise tip gap control is not possible in the current test rig design. Care in this aspect must be observed during future rig designs for high speed centrifugal compressor testing.

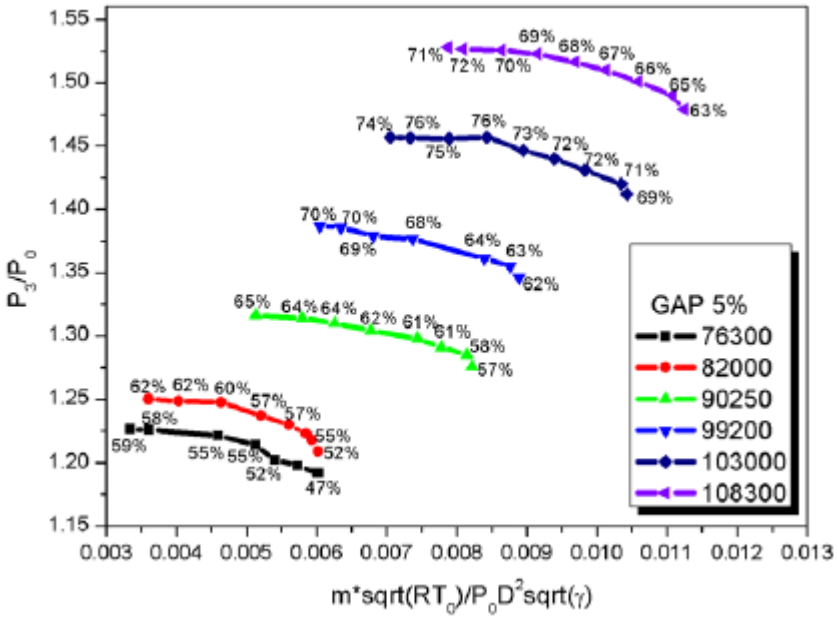

Figure 63. Compressor performance chart at a tip gap of 5% of impeller blade height

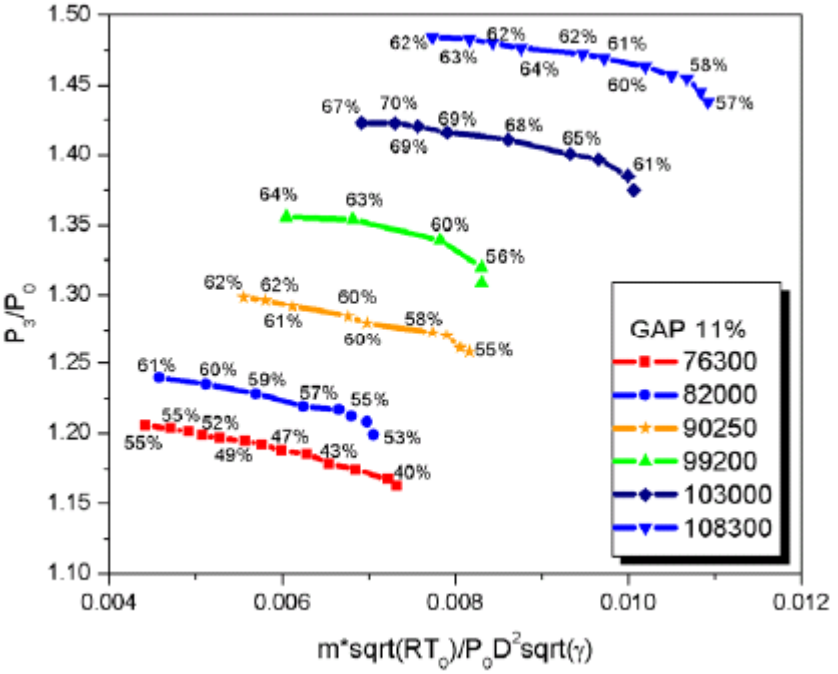

Figure 64. Compressor performance chart at a tip gap of 11% of impeller blade height

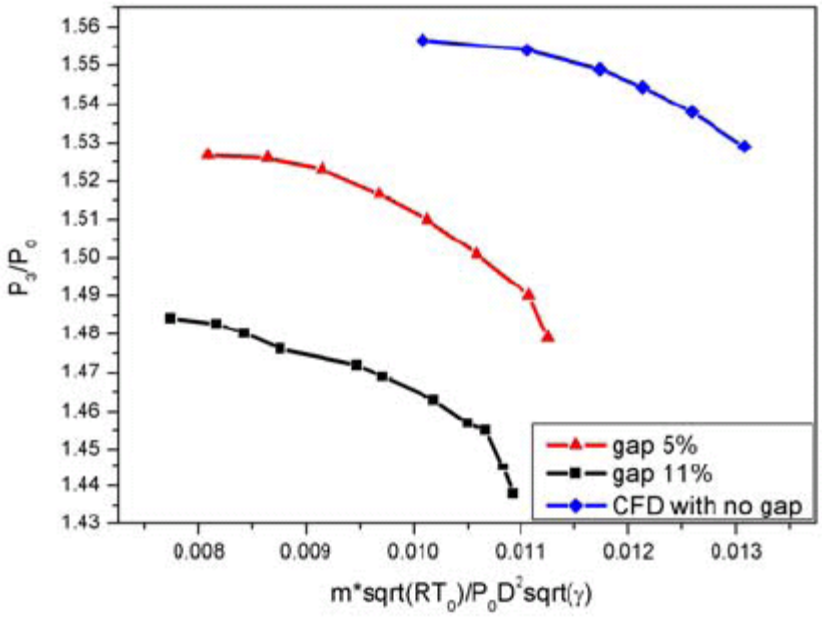

Figure 65. Compressor performance variation with tip gap at 108,300 rpm

Task 7: 5.4 kW PMSM Design

This part summarizes the design of a 313,000 rpm permanent magnet synchronous motor with 5.4 kW shaft output power. This motor would be useful in driving the two-stage helium compressor (as mentioned in Task 2 and as detailed in Task 8). The design work included analytical analysis, numerical simulation, mechanical design, components selection, thermal design, rotordynamic analysis, optimization, and final verification. Figure 66 shows the designed rotor structure. Table 9 shows the optimized key dimensions of the PMSM design. This new 5.4 kW, 313,000 rpm PMSM design is adopted from the already developed 2 kW, 200,000 rpm PMSM since the 200,000 rpm PMSM design was very successful and it has been demonstrated through testing that this kind of structure is ideal for super high-speed motor design. The same low loss ceramic ball bearings will be used. Based on manufacturer's report, these bearings can run up to 500,000 rpm. Since no slip between magnet and the shaft inner surface was found in our previous motor/generator test, round permanent magnet will be used to reduce machining cost and increase assembling feasibility. High energy density permanent magnet of Samarium-Cobalt (SmCo) will be used in the design. SmCo can work at high temperatures, which will prevent it to get demagnetized when the operating temperatures go high during testing. 240 strands of Litz-wire will be used to reduce eddy current loss and ohmic loss in the stator winding. Shaft diameter will be increased to meet the new rotordynamic requirements.

(a)

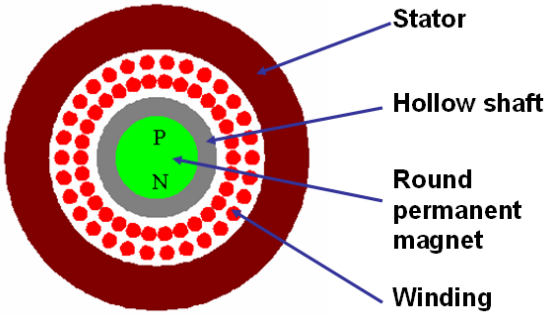

(b)

Figure 66. (a) Integrated rotor, and (b) the cross-section of 5.4 kW PMSM

Table 9. Optimized dimensions of the 313,000 rpm PMSM design

Physical gap length	1 mm
Stator inner diameter	32 mm
Stator outer diameter	48 mm
Motor active length	36 mm (35.8 mm)
Litz-wire	240 strands @AWG 36
Turns/phase/pole	5
Winding pitch	12/15
Shaft diameter	17 mm
PM diameter	13 mm
Shaft thickness	2 mm
Permanent magnet	SmCo 2:17-31

More extensive FEM simulations with rotation, including eddy current loss in the permanent magnet and stainless steel shaft were performed and the simulation results are shown in Table 10. The PMSM simulation also included a connection with external rectifier circuit. Figure 67 shows the simulated eddy current distribution in the shaft and permanent magnet, when the PMSM is working as a generator and rotating at 313,000 rpm with 5.4 kW of rectified DC output power. The simulated eddy current loss is found to be 20 W as shown in Table 10.

Table 10. Simulated and/or calculated PMSM parameters and losses

Back peak EMF (V)	64.1
Nominal phase current (A)	40.5
Required minimum DC bus (V)	112
Torque (N.m)	0.165
Output Power (W)	5400
Copper DC loss (W)	42
Copper AC loss (W)	16
Stator iron loss (W)	25.8
Rotor eddy current loss (W)	20
Bearing loss (W)	210
Windage loss (W)	44.6
Low pass filters loss (W)	7
Total loss (W)	365.4
Efficiency (%)	93.7

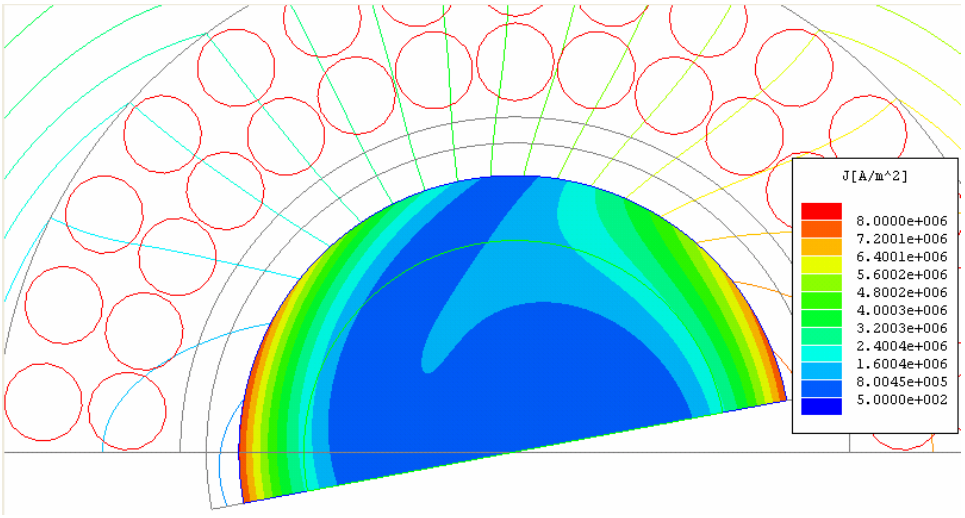

Figure 67. Simulated rotor Eddy current when rotating at 313,000 rpm

Detailed thermal/cooling system design and rotordynamic analyses are reported under Task 8.

The controller design for the 5.4 kW PMSM is based on space vector PWM method and switch mode method to realize high efficiency real-time control and power supply. Figure 68 shows the block chart of the proposed controller for this design.

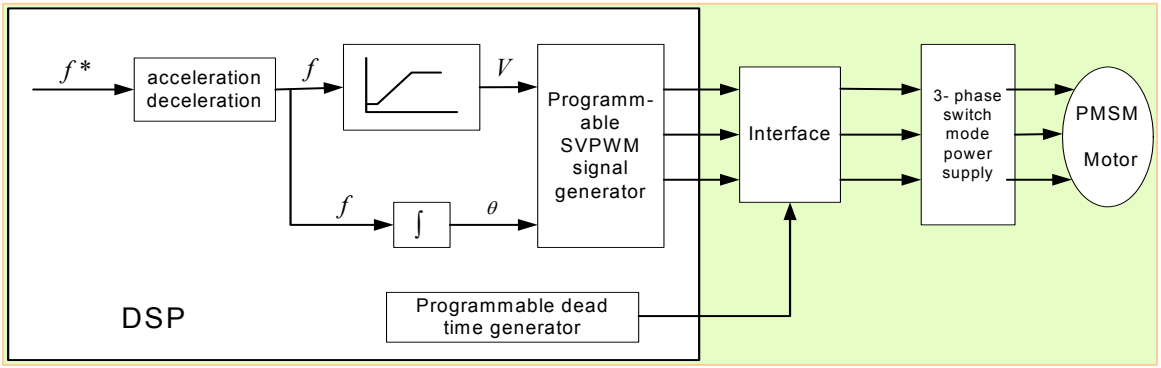

Figure 68. Block diagram of the proposed controller design

Task 8: Two-Stage Centrifugal Compressor Design

The structure and design of the 313,000 rpm two-stage miniature Helium centrifugal compressor incorporated the proven aerodynamic design of its scaled version, the 108,000 rpm single-stage air compressor.

Due to the current limitation of bearing selection, the same ceramic ball bearings will be used (as mentioned in the 5.4 kW PMSM design section). The ¼ in. ball bearing is rated higher than 300,000 rpm, while it limits the shaft size. With the use of bearing support at both sides, the radial IGV, radial impeller and axial diffuser design will be used to minimize the overall system size. Manufacturability is another issue that needs to be considered in this design. A base-cover structure to ease manufacturing and assembling will be used as is the case with single-stage compressor assembly. Some components, including second stage diffuser, compressor end-board and motor cooling jacket may also be split for easy assembling. The overall cross-sectional drawing of the two-stage compressor/motor assembly is shown in figure 69. Based on the ease of manufacturability, one of the two similar configurations (figure 70) will be considered for the rotor. The second configuration will not have a tie-shaft structure but has threading on the plug projection.

Alignment for such a high-speed rotating machine is a big issue. The base will be machined from a single stainless steel block to ensure the perfect alignment of the bearing holes. All other stationary components will be installed in the base to ensure the relative positional accuracy. Left side bearing has an adjustable axial spring loader to ensure stable running at high speeds.

An FEA model was built for this integral shaft system to perform rotordynamic simulation accurately. The rotordynamic equation of motion for a coupled, flexible rotor/casing system with conventional bearings is: $[M]\{\ddot{q}\}+[C]\{\dot{q}\}+[K]\{q\}=\{f\}$, where *q* represents the physical coordinate degrees of freedom, *f* represents external forces, M represents mass matrix, K represents the bearing stiffness matrix, and C represents damping matrix. The simulated results for the structure with two impellers are shown in Table 11. The rigid body modes were found to lie well below the nominal operating speed of 313,000 rpm. The first bending mode is found to be much higher than the operating speed. So there is enough room for a safe operation.

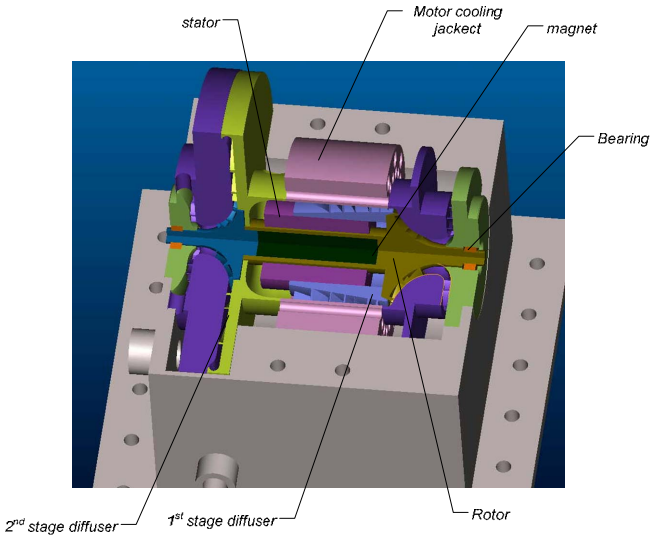

Figure 69. Solid model of the compressor/motor assembly

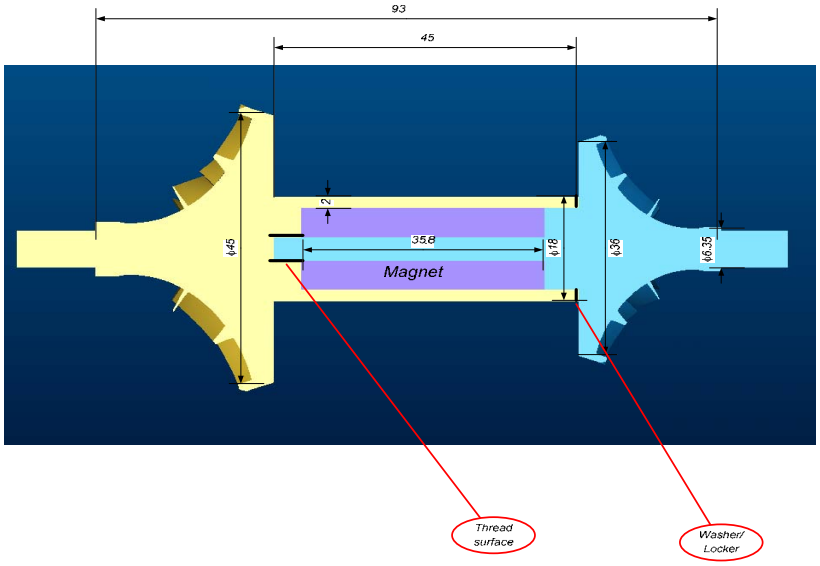

Figure 70. Rotor design for two-stage helium compressor

Table 11. Simulated critical speed for the rotor structure with two impellers

Shaft Material	*Titanium*	*Stainless Steel*
1st rigid body mode (rpm)	44609	35153
2nd rigid body mode (rpm)	92813	72150
1st bending mode (rpm)	508389	512075

Thermal management forms a necessary aspect in this design because the motor will generate 5.4 kW shaft power at full load. Supposing it has an efficiency of 0.9 (including controller efficiency), the heat generated will be higher than half-a-kW. Because of small size, it is imperative to have an efficient cooling system design to transfer this heat and to guarantee the safe and efficient running of motor. An aluminum water cooling jacket is designed to handle this problem. Simulation shows that with water speed in the jacket as 2 m/s and inlet water

temperature as 20 °C, the inner surface of the water jacket can be below 60 °C at full load (figure 71). This will ensure the temperature in winding and magnet is less than 100 °C. This water jacket can also be such that it can be split into two half pieces axially for an easy installation.

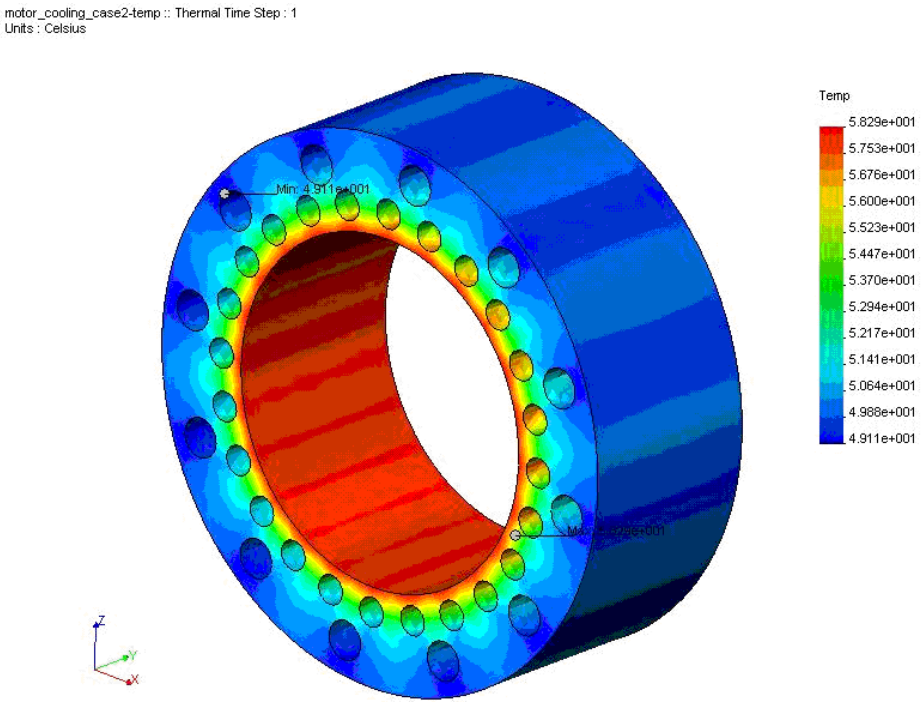

Figure 71. Thermal management of the rotor – water jacket simulation

A possible improvement could be to use an axial IGV with tiltable vanes to ensure perfect aerodynamics in the compressor.

Task 9: Extended Activities in the Aspects of Friction, Wear Mitigation and Heat Exchanger Design

This task is categorized under three major extended activities comprising of characterization of tribological coatings, preliminary design of non-contact bearings and heat exchanger design and fabrication for cryocoolers.

Friction and Wear Mitigation Coatings **(**PI: Dr. Neelkanth Dhere, FSEC**) –** The goal of this subtask was to develop tribological coatings having extremely high hardness, low coefficient of friction, and high durability at temperatures lower than 60 K. These coatings are very useful in reducing the frictional heat losses in high-speed turbine, bearings and compressor for the RTBC cryocooler.

Under this subtask, a number of titanium nitride (TiN), molybdenum disulphide (MoS_2) films were deposited by DC and RF magnetron sputtering on glass, aluminum and Si-wafer substrates respectively and the film parameters were optimized. Also, bilayer coatings of TiN/MoS_2 were deposited on the above substrates. Good adhesion, thickness uniformity and stoichiometry of TiN and MoS_2 coatings on glass and aluminum substrates were verified by peel test, Dektak Profilometry and energy dispersive spectroscopy (EDS) respectively.

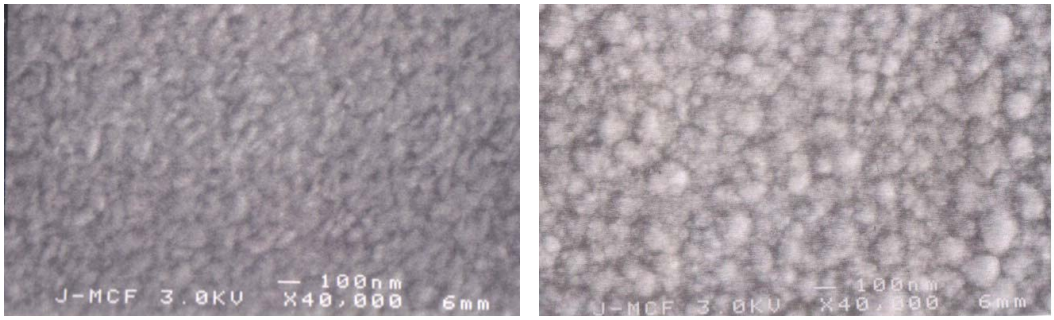

(a) (b)

Figure 72: Scanning electron microscopy (SEM) images of (a) TiN and (b) MoS_2 coatings

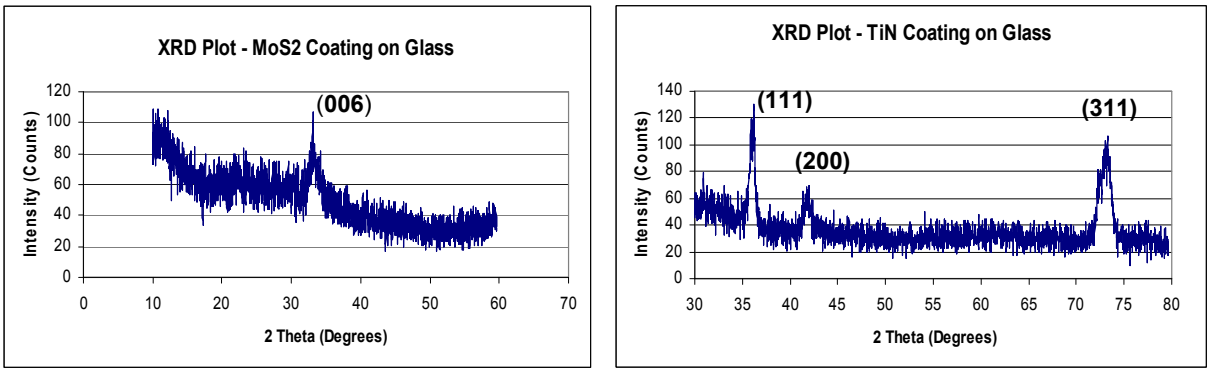

Figure 73: XRD patterns of MoS_2 and TiN coating

SEM images showed that the grains are nanocrystalline in nature for both TiN and MoS_2 coatings (figure 72). EDS analysis also have shown good stoichiometric ratio of N and Ti (Atomic Percent N:Ti = 52.91:47.09). X-ray Diffraction (XRD) patterns provided in figure 73 also show that both TiN and MoS_2 coating are nanocrystalline in nature as can be seen by the broad nature of peaks.

The coefficient of friction and wear measurements on TiN/MoS_2 bilayer coating on Si wafer were carried out on the “Tytron™ 250 MicroForce Testing Equipment” with the assistance of Dr. Quanfang Chen and his colleagues at UCF. These measurements require the film to be deposited on three 0.9 mm diameter bumps on 1 cm x 1 cm silicon wafer to minimize the contact area between two rubbing samples and providing more accurate coefficient of friction and wear measurements. Photolithography method was used to carry out masking and etching to define the bumps on the Si wafer. TiN/MoS_2 films were deposited using the optimized parameters on 1 cm x 1 cm silicon wafers with and without these bumps. Number of measurements were carried out and the average coefficient of friction for the TiN/MoS_2 Bilayer coating on Si wafer with 1 N normal load was = 0.045.

The coefficient of friction tests were also carried out by ball-on-disc method on TiN and bilayer coating of TiN/MoS_2 on aluminum substrates with the assistance of Dr. Gregory Sawyer and his colleagues at University of Florida (UF). A number of friction tests were carried out at room temperature by the ball-on-disc method. The results are provided in Table 12.

Table 12: Coefficient of friction measurements on TiN and TiN/ MoS_2 coatings on aluminum substrate by ball-on-disc method

Substrate	Tribological Coating	Coating Pair	Force (gm)	Speed (rpm)	Average COF
Aluminum	TiN/MoS_2	3/16 diam alumina ball	66.3	605	0.205
Aluminum	TiN	3/16 diam alumina ball	27.4	42	0.143

Microhardness and coefficient of friction tests were also carried out at room temperature on TiN and TiN/ MoS_2 coatings on glass and aluminum substrates with the help of Dr. Arun Kumar and colleagues at University of South Florida (USF). The microhardness measurements were carried out on TiN coating on a glass substrate with a MTS microhardness tester using a Berkovich diamond tip and the results obtained were: average hardness = 24.90 GPa and average elastic modulus = 256.60 GPa.

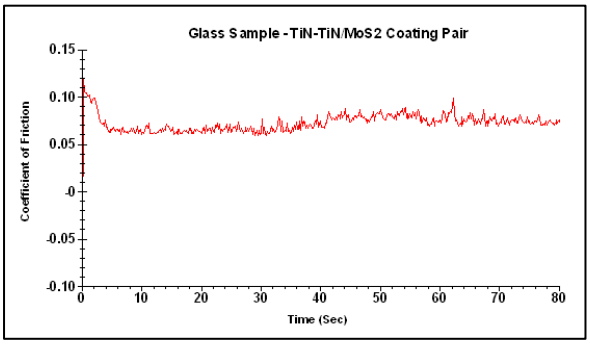

Figure 74: Graph showing coefficient of friction variation with time for Sample ID 4

A number of friction measurements were carried out. Table 2 shows values of coefficient of friction for TiN and TiN/MoS_2 coatings on glass and aluminum substrates with various coating pairs at USF by ball-on-disc method. Figure 74 shows the coefficient of friction graph for Sample Id 4.

Table 13: Coefficient of friction measurements on TiN and TiN/ MoS_2 coatings on aluminum and glass substrate by ball-on-disc method

Sample ID	Substrate	Tribological Coating	Coating Pair	Force (gm)	Average COF
1	Aluminum	TiN	TiN coated Steel Ball	50	0.21
2	Aluminum	TiN / MoS_2	Steel Ball	50	0.16
3	Aluminum	TiN / MoS_2	TiN coated Steel Ball	50	0.15
4	Glass	TiN / MoS2	TiN coated Steel Ball	50	0.08
5	Glass	TiN / MoS_2	TiN / MoS_2 coated Steel Ball	50	0.15
6	Glass	TiN / MoS_2	Steel Ball	50	0.19

Literature search of friction behavior and wear resistance of high hardness coatings under cryogenic temperatures has shown that diamond-like-carbon (DLC) and nitrides of high-melting-point metals (e.g., TiN, ZrN) are potential candidates for cryogenic applications. These coatings are known to have coefficient of friction less than 0.1 at room temperature. However, cryogenic environment leads to increase in the coefficient of friction. At cryogenic temperatures, DLC coatings have shown lower coefficient of friction and good wear resistance as compared to hard coatings of nitrides. Based on literature search, microwave assisted chemical vapor deposition (MWCVD) technique was chosen for preparation of DLC coatings. Design and drawings of MWCVD system were prepared. The MWCVD system was installed and initial deposition and characterization of diamond-like-carbon (DLC) coatings was carried out.

Preliminary Design of Non-contact Bearings – As seen in Tasks 4 and 5 of this project, ceramic ball bearing loss was one of the considerable losses in reducing the system efficiency in addition to causing rotordynamic instabilities because of proper installation and fit problems. Non-contact bearings provide for friction-free and oil-free operation and are a proven technology [5]. Usage of these bearings will drastically lower the power losses due to friction in bearings in addition to contributing for better rotordynamic stability. The problem with non-contact bearings is that they are not available commercially for any specific application and their design involves complex fluid-structure interaction issues. Hence, they are very expensive and only a basic design suggestion of these bearings is provided below.

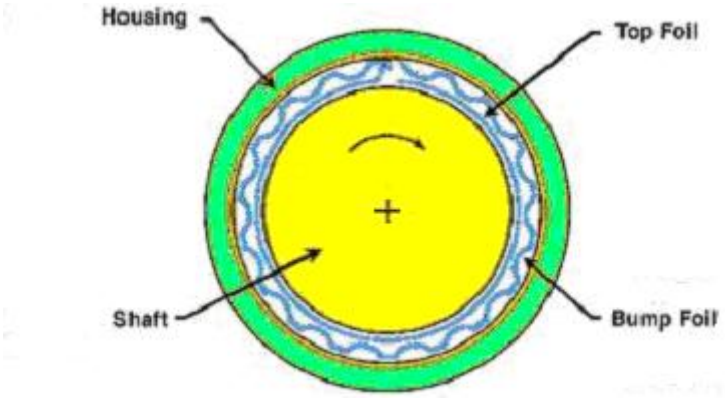

Figure 75. Bump gas foil bearing – conceptual design [5]

Various types of non-contact bearings exist like hydrostatic, hydrodynamic, magnetic, foil, flexure-pivot etc., but only a specific type is chosen here for illustration purposes. The conceptual design (figure 75) consists of a single continuous leaf-foil that would envelope the entire shaft circumference. It will be supported by bump foils as shown in the figure that provide the required compliancy, and optimized structural stiffness and coulomb damping. The structure that acts as a back up to the top foil could be of any shape and is usually decided by the requirements of a particular bearing system like load bearing capacity, operational speed (above or below a critical speed) etc.

The bearing is based on the working principle that as the shaft starts rotating, it drags in air/gas and a thin film of it is formed between the shaft and the top foil. This creates high pressure and the shaft gets lifted-off avoiding a contact. The hydrodynamic pressure that would be generated will be a result of the convergent wedging action between the top foil and the rotating shaft. The gas film in usual cases would be of the order of a few tens of microns and in some cases like magnetic recording applications, it is of the order of 2.5 microns. Since sizes in the current case are mesoscaled and since foils provide support to the shaft in addition to gas, the flow can be assumed to be in continuum regime. The compliant foil surface accommodates itself to centrifugal forces, shocks and thermal expansion of the rotor.

During start-up and stop operations, there would be contact between the top foil and shaft that generates heat. Coating the friction surfaces with tribological coatings (mentioned under the previous subtask) would minimize friction and is an established technology.

Basing on the factors like room temperature testing and fabrication feasibility at meso-scale, Titanium 6-4 can be used for fabricating both the foils and the bearing housing. Inconel 600 can be used for fabricating the foils in case of extreme temperature operations.

Some basic design parameters were developed to prove the design is enabling. The bearing number for the bearing was found to be 0.113, which shows that it has a non-dimensional

stiffness value of about 0.06. Figure 76 shows the bearing stiffness plotted against the bump foil thickness. The plot shows that as the bump foil thickness increases, the bearing becomes stiffer and linearly. But since most of the compliancy is expected from foils for this design, bump foil thickness must be an optimized low value in the plot. The bearing load capacity coefficient (∂) for the bearing is 0.254, which is a good value considering the fact that the application involves low loads (∂ = 1 is a very good value).

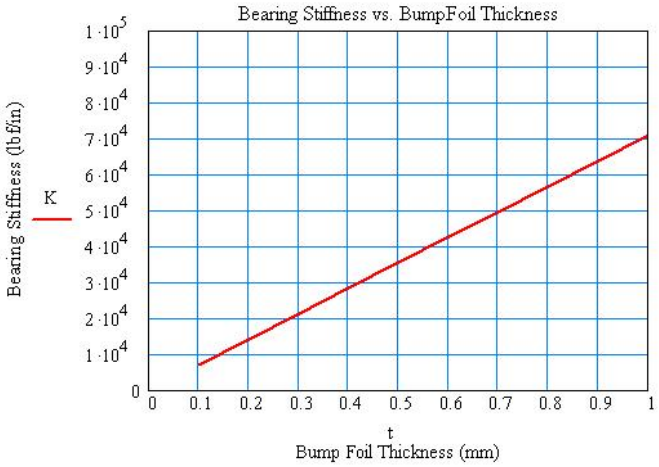

Figure 76. Bearing stiffness vs. foil thickness

Key preliminary design parameters for the bearing were considered as follows for illustration purposes:

R = rotor radius (D/2) = 5 mm
N = angular speed of the rotor in radians per second = 20,940
L = bearing axial length = 10 mm
P_a = ambient pressure = 2 atm
C = radial clearance between the shaft and the bearing = 0.01 mm
K = bearing steady-state stiffness
E = elastic modulus of the foil material = 30 X 10^6 psi
t = bump foil thickness = 0.02 mm = top foil thickness
p = bump pitch = 1.587 mm
$2l_0$ = bump foil length = 1.058 mm
n = number of bumps = 20
D_b = bearing inner diameter = 10.2 mm
h = bump height = 0.03 mm
(Assumptions: Perturbation load: 20 psi; Working fluid: Air for testing purposes)

Figures 77 and 78 show the preliminary design. For easy assembly in future designs, a split-type design can be considered. The foils can be spot-welded to the housing, which is a combination of two symmetrical pieces and can be joined by axial sliding or using nuts and bolts.

For this preliminary design, the steady-state stiffness value is used from experiments conducted by NASA and Mohawk Innovative Technologies, Inc. that used different sized bearings. All the dimensions are scaled linearly and approximately from a commercially available Foster-Miller Technologies, Inc. second-generation foil bearing design and so there will be a small degree of error. However, this design error can be eliminated by proven detailed design methods.

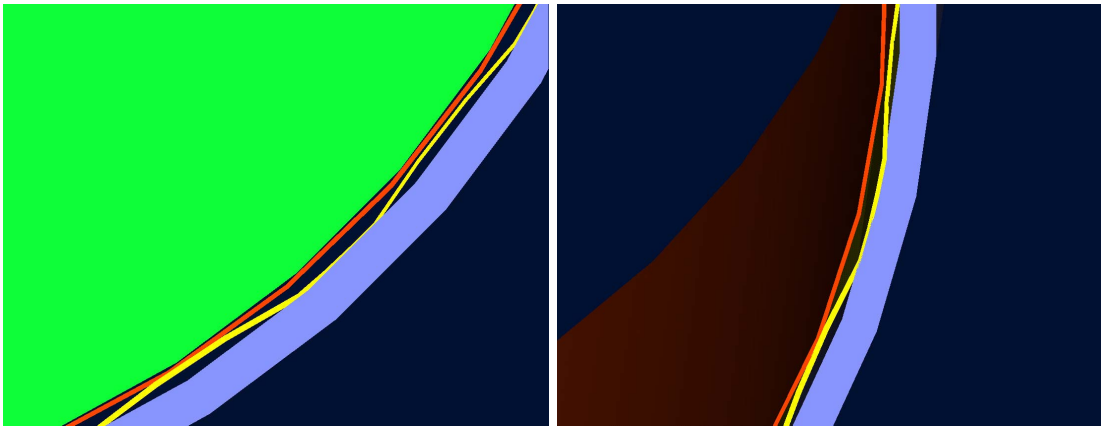

Figure 77. Bump foil (yellow), top foil (red), shaft (green) and bearing housing (purple)

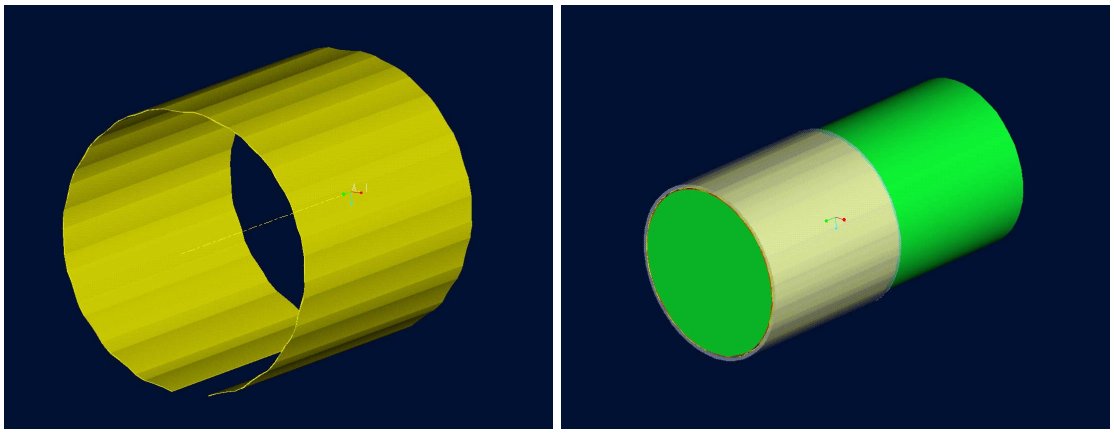

Figure 78. Bump foil structure (left) and complete assembly (right)

High Effectiveness Microchannel Heat Exchanger – Design and Fabrication Feasibility **(**with funding from NASA KSC – Dr. William Notardonato and Mr. George Haddad**) –** A key component that decides the COP of any cryocooler is a heat exchanger. A high effective heat exchanger design is a must to have a high system COP and hence is suggested for the RTBC cryocooler. The design was a generalized one for use in any mesoscale system a like JT cryocooler. The design was based on past development work undertaken at UCF, where designs of highly effective counterflow heat exchangers have been developed. Researchers at UCF have shown through detailed analysis that in compact heat exchangers that aim to have effectiveness approaching or in excess of 0.97, axial conduction through the heat exchanger material must be minimized [7,8]. Based on this analysis, three alternative designs were proposed and an application for patent disclosure for the selected design is currently being considered. The schematic of the proposed heat exchanger is shown in figure 79. Samples of the recuperative heat exchanger were manufactured by American Technical Ceramics out of a polymer-derived ceramic (LTCC-Low Temperature Co-Fire Ceramic) by micro casting. The individual flow ducts have dimensions around 140 microns diameter with the thickness of intervening walls around 150 microns. These dimensions were derived by performing both the mechanical stress and heat transfer rate calculations keeping in mind the commercial manufacturability feasibility. As thickness of parts produced by micro casting is limited to around 1 mm, many of these layers (around 40 for the current samples, one of which is shown in figure 80) were bonded together to produce the required overall length. The final version of this heat exchanger with an overall length of about 10 cm is very compact when compared to some of the smallest commercially available heat exchangers being used for similar applications. Table 14 shows the comparison with Creare, Inc. heat exchangers intended for similar application.

Table 14. HEXs comparison

HEX (Cooling Load)	*Length, mm*	*Size*	*Weight, kg*
UCF HEX (20 W)	100	30X30 mm^2	0.24
Creare, Inc. SPHX (7 W) [5]	560	90 mm dia.	7.7
Creare, Inc. RFHX (200 mW) [6]	120	210 mm dia.	5.1

A light source is used to pass light from bottom of the heat exchanger sample and a digital camera aided by a microscope is used to capture it from the top. Any channel, if it is not a see-through type, could thus be identified. Figure 81 shows the throughness of the microchannels thus observed and hence successful fabrication. Dimensions of the fabricated microchannels and distance between any two of those could be seen in the same figure.

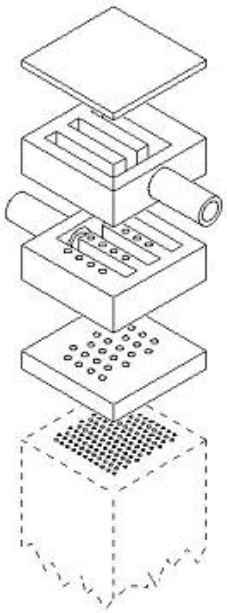

Figure 79. Schematic of the HEX

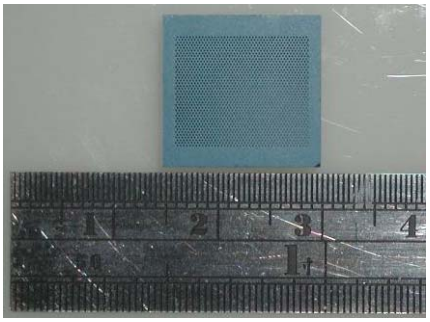

Figure 80. A sample of UCF counter-flow microchannel heat recuperator with regeneration

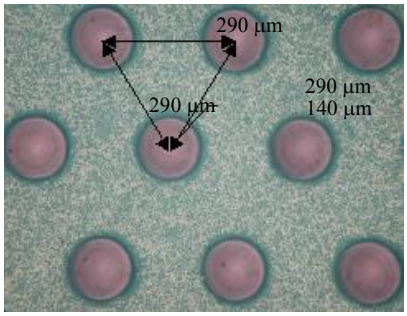

Figure 81. Digital camera image showing the throughness and dimensions of the circular microchannels

Task 10: Evaluation of Current Application to Other NASA Applications

This task focused on the evaluation of application of the technology developed over the course of this project to potential NASA applications like missions to Mars involving storage of methane and LOX and ISRU on Moon for LOX management. ISRU propellant liquefaction requires highly reliable refrigeration systems that provide a few hundred watts of cooling and the UCF developed RTBC with features like high reliability, light-weight and high cooling power would be optimal. Focus was on analyzing the applicability of overall cryocooler design and the same will be reported below.

UCF Neon working fluid cryocooler for LOX applications (figure 82):

Compressor inlet temperature (T1): 300 K
Cold head outlet temperature (T6): 80 K
Compressor efficiency: 65%
Turbine efficiency: 75%
Recuperator effectiveness: 0.985
Compressor inlet pressure: 100 kPa

Cold head inlet temperature (T4): 70.75 K
Turbine inlet temperature (T5): 83.30 K
Compression power: 663.75 W
Turbine power: 56.64 W
Pressure loss in recuperator – Included
COP: 0.093
COP/Carnot-COP: 0.217 (where Carnot-COP= 90/(300-90))
Cooling power: 56.51 W

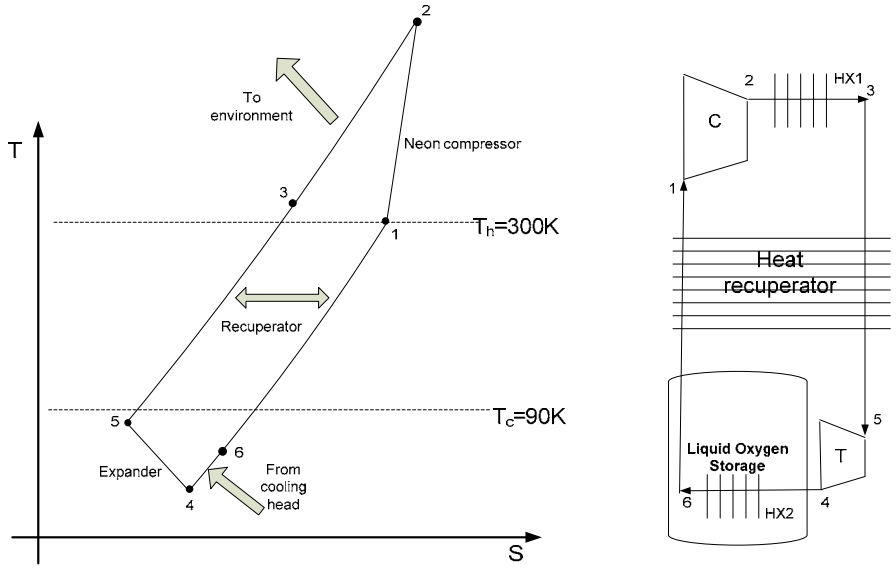

Figure 82. Schematic of neon cryocooler for LOX

From the above results, we can observe that the developed RTBC cryocooler (20-30 W cooling power at liquid hydrogen temperature; refer Task 1) with neon as the working fluid can provide a few tens of watts of cooling power for LOX applications, still preserving the COP for the new cold-end temperature.

UCF Neon working fluid cryocooler for CH_4 applications (figure 83):

Compressor inlet temperature (T1): 300 K
Cold head outlet temperature (T6): 101 K
Compressor efficiency: 65%
Turbine efficiency: 75%
Recuperator effectiveness: 0.985
Compressor inlet pressure: 100 kPa
Cold head inlet temperature (T4): 89.14 K
Turbine inlet temperature (T5): 104 K
Compression power: 663.75 W
Turbine power: 72.5 W
Pressure loss in recuperator – Included
COP: 0.122
COP/Carnot-COP: 0.209 (where Carnot-COP= 111/(300-111))
Cooling power: 72.33 W

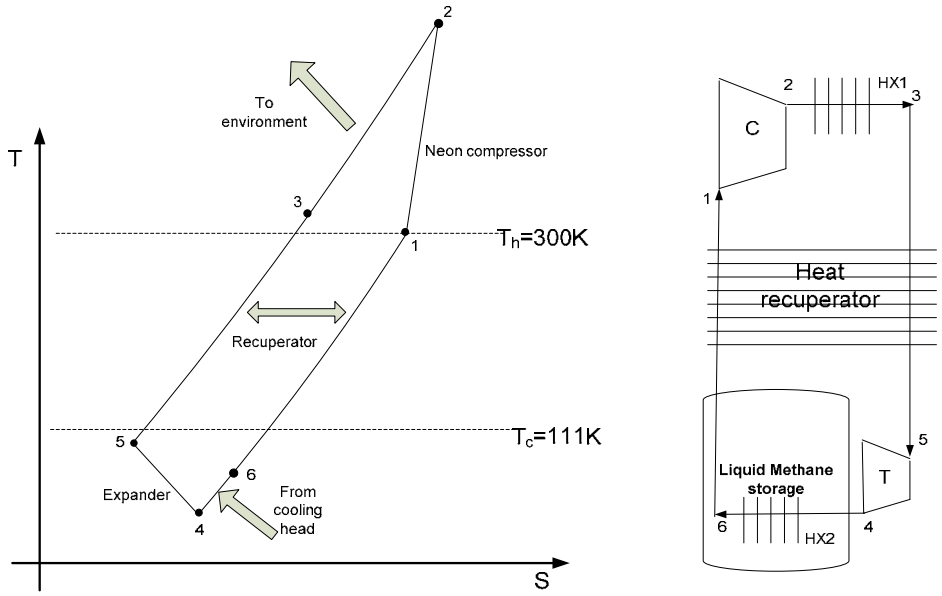

Figure 83. Schematic of neon cryocooler for liquid CH_4

From the above results, we can observe that the developed RTBC cryocooler with neon as the working fluid can provide a few tens of watts of cooling power for liquid methane applications, still preserving the COP for the new cold-end temperature.

Therefore, the developed cryocooler technology under this project was found to have a high COP in its class even when applied to other similar NASA applications.

Conclusions

An innovative design of a reverse turbo Brayton cycle cryocooler for application in zero boil-off of cryogenic propellants in space is presented and it has been shown that a reasonably high COP is possible even at mesoscale through proper optimization at the component level. Design, simulation, fabrication and testing of a high-efficient, super high-speed centrifugal compressor and a motor for driving the compressor were discussed. Many conclusions were drawn from this research like:

1) It is possible to support high speed machinery (integrated compressor/motor system) on off-the-shelf bearings with proper balancing, alignment and aerodynamic optimization.
2) It is not advisable to use a mechanical coupler for high-speed rotating machinery.
3) Less the number of rotating parts in conjunction, better is the design for high rigidity and rotordynamic stability.
4) Tip gap plays a very important role in deciding the performance of a mesoscale centrifugal compressor.
5) A proper diffuser design (without flow separation) is a must for realizing high compressor efficiency.
6) A high effectiveness HEX design is a key enabling technology for a high system COP.

Patents, Publications and Students from Research

Patents

1. "Miniature High Speed Compressor Having Embedded Permanent Magnet Motor," U.S. Patent Application No. 11/752,021, May 22, 2007.

Publications

1. Lei Zhou, Dipjyoti Acharya, Jayanta Kapat, Louis Chow, Nagaraj Arakere, "Aerodynamics Performance Tests of a High-Speed Miniature Centrifugal Compressor," Proceedings of ASME Energy Sustainability Conference, Long Beach, CA, June 27-30, 2007.

2. Dipjyoti Acharya, Lei Zhou, Liping Zheng, Thomas Wu, Jay Kapat, Louis Chow, "Mechanical and Rotordynamic Design, Fabrication and Testing of a High-Speed Miniature Cryocooler Motor," Proceedings of ASME Turbo Expo, Montreal, Canada, May 14-17, 2007.

3. Limei Zhao, Chan Ham, Liping Zheng, Thomas Wu, Kalpathy Sundaram, Jay Kapat and Louis Chow, "A Highly Efficient 200000 rpm Permanent Magnet Motor System," IEEE Transactions on Magnetics, vol. 43, no. 6, pp. 2528-2530, June, 2007.

4. L. Zhao, C. Ham, L. Zheng, T.Wu, K. Sundaram, J. Kapat and L. Chow, "A Highly Efficient 200000 rpm Motor System for Cryogenic Applications," 10th Joint MMM/Intermag Conference, Baltimore, MD, January, 2007.

5. Limei Zhao, Chan H. Ham, Thomas X. Wu, Liping Zheng, Hubert P. Seigneur, Kalpathy B. Sundaram, Jay Kapat , Jay Vaidya and Louis Chow, "Development of A Super High Speed Permanent Magnet Synchronous Motor (PMSM) Controller and Analysis of The Experimental Results", Journal of Systemics, Cybernetics and Informatics, 3, No.1, 2006.

6. L. Zhao, C. Ham, T.X. Wu, L. Zheng, K. Sundaram, J. Kapat and L. Chow, "A New Design Approach of an Ultra-High speed Permanent Magnet Synchronous Motor (PMSM) System," Proceedings of the IEEE INTERMAG 2006, May 8-12, 2006.

7. L. Zhao, C.H. Ham, Q. Han, T.X. Wu, L. Zheng, K.B. Sundaram, J. Kapat and L. Chow, "Design of Optimal Digital Controller for Stable Super-High-Speed Permanent-Magnet Synchronous Motor," IEE Proc.-Electrical Power Applications, vol. 153, no. 2, pp. 213-218, March, 2006.

8. Liping Zheng, Thomas Wu, Dipjyoti Acharya, Kalpathy Sundaram, Jay Vaidya, Limei Zhao, Lei Zhou, Lei Zhou, Chan Ham, Nagaraj Arakere, Jayanta Kapat, Louis Chow, "Design of a Super High-Speed Cryogenic Permanent Magnet Synchronous Motor," IEEE Transactions on Magnetics, vol. 41, no. 10, pp. 3823-3825, October, 2005.

9. Liping Zheng, Thomas Wu, Jay Vaidya, Muhammad Sarwar, Kalpathy Sundaram, Chan Ham, Hubert Seigneur, Limei Zhao, Neil Vanasse, Alex Canale, Jay Kapat, Louis Chow, "Design of a Super-High Speed Axial-Flux Permanent Magnet Synchronous Motor," Electromotion, vol. 12, no. 1, pp. 9-17, Jan-Mar, 2005.

10. Liping Zheng, Thomas Wu, Dipjyoti Acharya, Kalpathy Sundaram, Jay Vaidya, Limei Zhao, Lei Zhou, Krishna-Murty Kota, Chan Ham, Nagaraj Arakere, Jayanta Kapat, Louis Chow, "Design of a Super-High Speed Permanent Magnet Synchronous Motor for Cryogenic Applications," IEEE International Electric Machines and Drives Conference, San Antonio, TX, May, 2005.

11. Liping Zheng, Thomas Wu, Kalpathy Sundaram, Jay Vaidya, Limei Zhao, Dipjyoti Acharya, Chan Ham, Jayanta Kapat, Louis Chow, “Analysis and Test of a High-Speed Axial Flux Permanent Magnet Synchronous Motor,” IEEE International Electric Machines and Drives Conference, San Antonio, TX, May, 2005.

12. Liping Zheng, Thomas Wu, Dipjyoti Acharya, Kalpathy Sundaram, Jay Vaidya, Limei Zhao, Chan Ham, Nagaraj Arakere, Jayanta Kapat, Louis Chow, “Super-High Speed Cryogenic PMSM Design,” IEEE International Magnetics Conference, pp. 1961-1962, April 4-8, 2005.

13. Xiaoyi Li, Lei Zhou, Jay Kapat and L.C. Chow, “Use of Inlet Guide Vanes for a Miniature Centifugal Compressor,” Turbo Expo 2005, Reno, NV, June 6-9, 2005.

14. Liping Zheng, Thomas X. Wu, Jay Vaidya, Dipjyoti Acharya, Krishna Murty, Limei Zhao, Chan H. Ham, Kalpathy B. Sundaram, Jay Kapat and Louis Chow, “Design and Simulation of a Cryogenic Electrical Motor,” *IEEE AP-S International Symposium and USNC/URSI National Radio Science Meeting*, Monterey, CA, June 20-26, 2004.

15. Limei Zhao, Chan H. Ham, Thomas X. Wu, Liping Zheng, Hubert P. Seigneur, Kalpathy B. Sundaram, Jay Kapat, Jay Vaidya and Louis Chow, “Development of A Super High Speed Permanent Magnet Synchronous Motor (PMSM) Controller and Analysis of The Experimental Results”, Proceedings of The 8th World Multi-conference on Systemics, Cybernetics and Informatics, Volume VIII, pp. 268-271, July 18-21, 2004.

16. Chen Ham, Limei Zhao, Thomas X. Wu, Liping Zheng, Hubert P. Seigneur, Kalpathy B. Sundaram, Jay Kapat , Jay Vaidya and Louis Chow, “Development of a New V/f control for a Super High-Speed Permanent Magnet Synchronous Motor (PMSM)”, Proceedings of The 8th World Multi-conference on Systemics, Cybernetics and Informatics, Volume VIII, pp. 312-315, July 18-21, 2004.
17. Limei Zhao, Chan H. Ham, Thomas X. Wu, Liping Zheng, Kalpathy B. Sundaram, Jay Kapat, Jay Vaidya and Louis Chow, “A DSP-Based Super High Speed PMSM Controller Development and Optimization”, Proceedings of 11th Digital Signal Processing Workshop & 3rd Signal Processing Education Workshop (IEEE DSP2004), ISBN: 0-7803-8435-0.

18. Limei Zhao, Chan H. Ham, Thomas X. Wu, Liping Zheng, Kalpathy B. Sundaram, Jay Kapat, Jay Vaidya and Louis Chow, “Design of An Optimal V/f Control for A Super High Speed Permanent Magnet Synchronous Motor,” Proceedings of the 30th Annual Conference of the IEEE Industrial Electronics Society (IECON 2004).

19. Limei Zhao, Chan H. Ham, Thomas X. Wu, Liping Zheng, Kalpathy B. Sundaram, Jay Kapat , Jay Vaidya and Louis Chow, “A New Design Approach of A Super High-Speed Permanent Magnet Synchronous Motor,” IEEE 49th Conference on Magnetism and Magnetic Materials (MMM 2004), Jacksonville, FL, November 7-11, 2004.

20. William Notardonato, George Haddad, K.V. Krishna-Murty, Jinying Zhu, Jayanta Kapat, Louis Chow. “Miniature Joule Thomson (JT) Cryocoolers for Propellant Management”. Proceedings of ASME International Mechanical Engineering Congress and Exposition, Anaheim, CA, November 13-19, 2004.

21. Louis C. Chow, Jayanta S. Kapat, Krishna M. Kota, “Mesoscopic Energy Systems”, Annual Review of Heat Transfer, vol. 14, pp. 475-509, 2005.

22. L. An, Q. Chen, J. Cho, L. Chow, N. Dhere, C. Ham, J. Kapat, K.B. Sundaram, T. Wu, K. Finney, X.Y. Li, K.V. Krishna-Murty, A. Pai, H. Seigneur, L. Zhao, L. Zheng, L. Zhou. “Two-Stage Cryocooler Development for Liquid Hydrogen Systems”. Presented at Annual Joint

Symposium of the Florida Society of Microscopy and the Florida Chapter of the American Vacuum Society, Orlando, FL, March 17-20, 2003.L. An, Q. Chen, J. Cho, L.C. Chow, N.G. Dhere, C.H. Ham, J.S. Kapat, K.B. Sundaram,
T. Wu, K. Finney, G. Haddad, X. Li, K.V. Krishna-Murty, W. Notardonato, A. Pai, H. Seigneur, J. Vaidya, L. Zhao, L. Zheng, L. Zhou. “Two-Stage Cryocooler Development for Liquid Hydrogen Systems”. Presented at Space Cryogenics Workshop, Anchorage, AK, September 18-19, 2003.

24. Liping Zheng, Thomas X. Wu, Jay Vaidya, Krishna-Murty, Limei Zhao, Chan H. Ham, Kalpathy B. Sundaram, Jay Kapat and Louis Chow, "Design of a Super-high Speed PMSM for Cryocooler Application," *Space Cryogenics Workshop 2003*, Girdwood, Alaska, Sept.18-19, 2003.

Students from Research (mentioned in the order of graduation date)

1. Hubert Seigner, M.S. Thesis, Open-Loop Control of a Super High Speed Minaturized PMSM Using the TMS320LF2405 Digital Signal Processor, Spring 2003.

2. Kevin Finney, M.S. Thesis, The Development, Fabrication, and Testing of a Miniature Centrifugal Compressor, Fall 2003.

3. Lei Zhou, Ph.D. Dissertation, A Miniature Reverse Brayton Cycle Cryocooler and its Key Components: High Effectiveness Heat Recuperator and Miniature Centrifugal Compressor, Summer 2004.

4. Xiaoyi Li, Ph.D. Dissertation, Topic: CFD Analysis of a Miniature Centrifugal Compressor, August 2005.

5. Limei Zhao, Ph.D. Dissertation, Topic: Super High Speed Motor Control Design and Implementation, December 2005.

6. Liping Zheng, Ph.D. Dissertation, Topic: Super High Speed Motor Design, Fabrication and Testing, December 2005.

7. Dipjyoti Acharya, M.S. Thesis, Topic: Design and Performance Evaluation of an Integrated Miniature Single Stage Centrifugal Compressor and Permanent Magnet Synchronous Motor, August 2006.

Three additional graduate students worked on the project, but have not completed their degrees.

References

[1] Hastings LJ, Plachta DW, Salerno L, Kittel P, “An Overview of NASA Efforts on Zero Boil-off Storage of Cryogenic Propellants,” *Cryogenics* 41, 833-839, 2002.

[2] Donabedian M, Curran DGT, Glaister DS, Davis T, Tomlinson BJ, “An Overview of the Performance and Maturity of Long-Life Cryocoolers for Space Applications,” Aerospace Reports No. TOR-98 (1057)-3, Revision A, April 30, 2000.

[3] http://www.cryomech.com/AL330%20page.htm

[4] Ross RG Jr., Boyle RF, Key RW and D.R.Coulter, NASA Advanced Cryocooler Technology Development Program, NGST-ARTL-001944, July 31, 2002.

[5] http://www.nasa.gov/centers/glenn/about/fs14grc.html

[6] Nellis, G., Dolan, F., McCormick, J., Swift, W., Sixsmith, H., Gibbon, J., and Castles, S., "Reverse Brayton Cryocooler for NICMOS," *Cryocoolers*, 10, pp. 431-438, 1999.

[7] McCormick, J., Nellis, G., Sixsmith, H., Zagarola, M., Gibbon, J., Izenson, M., and Swift, W., "Advanced Developments for Low Temperature Turbo-Brayton Cryocoolers," *Cryocoolers*, 11, pp. 481-488, 2001.

[8] Carman, B., Kapat, J., Chow, L., An, L., "Impact of a Ceramic Microchannel Heat Exchanger on a Micro Turbine," Proceedings of ASME Turbo Expo, Amsterdam, The Netherlands, 2002.

[9] Zhou, L., Kapat, J., Chow, L., Li, X., "Design of a High Effectiveness Micro Heat Exchanger for Mars Applications," SAE Transactions – *Journal of Aerospace*, 109-1, pp. 875-882, 2000.

September 2007

Development of Cryogenic Shape Memory Actuator Materials for Switches, Seals and Valves

R. Vaidyanathan
University of Central Florida

Research Period: July 2002 to October 2007

Abstract

Shape memory alloy actuators are widely recognized as having the following advantages for space-related applications: (i) high power/weight and stroke length/weight ratios (ii) integration of sensor and actuator in a single element (iii) clean, debris-less, spark-free operation and (iv) ability to function in zero-gravity environments with small, controlled accelerations. The goal of this project was to lower the operating temperature range of shape memory alloys in order for them to be used in hydrogen related technologies. The emphasis is on the R-phase transformation in NiTiFe alloys and the approach used includes arc melting followed by thermo-mechanical treatments, SEM, TEM, DSC, dilatometry, indentation and incorporation of shape memory alloy actuator elements in prototype thermal switches. The immediate benefit to NASA is the development of a shape memory thermal conduction switch for application in cryogenic liquefaction, densification and zero boil-off systems. This can extended to include the potential use of shape memory alloy actuator elements for cryogenic seals, valves, fluid-line repair, self-healing gaskets, and even to ambient debris-less separation and latch/release mechanisms.

Introduction and Background

Shape memory alloys (SMAs) when deformed can produce strains as high as 8%. Heating results in a phase transformation and associated recovery of all the accumulated strain, a phenomenon known as shape memory. This strain recovery can occur against large forces, resulting in their use as actuators [1]. This principle is schematically illustrated in Figure 1a. When the SMA element is exposed to an increase in temperature, it undergoes a phase transformation. Associated with this phase transformation is a shape change which constitutes the actuator displacement and can occur against large forces. Once the temperature returns to the initial level, the new phase is no longer stable and reverts to the original phase. This original phase deforms easily and hence an external force (e.g., bias spring) can be used to construct an SMA actuator switch (as shown in Figure 1b).

SMA actuators are particularly advantageous for space applications in that:

i They integrate sensory and actuation functions. The SMA element inherently senses a change in temperature and actuates by undergoing a shape change as a result of a phase transformation. Consequently, the need for external electronic sensors and control is eliminated.

ii They function in a clean, debris-less, spark-free manner. The shape change that is responsible for the actuator displacement is again an inherent material property. It is not associated with moving parts that require lubrication or electrical signals with a potential to spark.

iii They have high power/weight and stroke length/weight ratios. The operating range includes strain and stress limits of 8% and 700 MPa, respectively, depending on the number of required cycles.

iv They posses the ability to function in zero-gravity environments with small, controlled accelerations. The displacement strains are a result of a thermally-induced phase transformation which can be controlled by the heat transfer rate (e.g., appropriate insulation).

Even though a wide range of alloys are found to exhibit the shape memory effect, NiTi alloys are of particular interest owing to the best combination of material properties coupled with substantial strain recovery (up to 8%) associated with the phase transformation. In NiTi, the phase transformation usually occurs in a single step from the high temperature austenite (B2, cubic) phase to the low temperature martensite (B19', monoclinic) phase or vice versa. However, under certain conditions [2] the phase transformation proceeds through an intermediate trigonal phase known as the R-phase. The formation of the R-phase and the subsequent suppression in the formation of the monoclinic phase (while cooling or on the application of stress) is attributed to the presence of defects in the form of dislocations, precipitates, and/or impurity elements. Despite its unique properties, such as a recoverable strain of approximately 8%, the B2 to B19' phase transformation in the NiTi system has various short comings - these being inferior fatigue life and the large hysteresis when compared to the R-phase transformation. This limits the application of the B2 to B19' transformation to thermal actuators that operate within a narrow temperature range. The B2 to R-phase transformation exhibits good fatigue life and reduced hysteresis but the transformation only yields a small recoverable strain of approximately 1%. By optimizing the design of an R-phase actuator (such as by using the shape memory element in the form of a helical spring), this issue can be overcome. In NiTi, the R-phase can be introduced by:

i annealing below the recrystallization temperature immediately after cold-working resulting in a high density of rearranged dislocations [3,4];

ii ageing at lower temperatures (573-773 K) in Ni-rich NiTi alloys to form Ni_4Ti_3 precipitates which facilitate the formation of the R-phase due to internal stress contributed by precipitates [3-5];

iii addition of a ternary element, such as Fe, Co, Al [4,6]; and

iv by thermal cycling [7-9].

Of the different ways to obtain the R-phase transformation, addition of a ternary element (Fe, in our case) was chosen for the following reasons:

i It is well known that a shift in 1 at.% Ni can alter the transformation temperatures by 100 °C The addition of a ternary element reduces the sensitivity of transformation temperature to composition. [1,10]

ii The addition of Fe lowers the R-phase transformation temperature. [11]

Previously, NiTiFe based SMA couplings were widely used to connect titanium hydraulic tubing in Grumman F-14 aircrafts. Given the operating temperature of these aircrafts, the couplings were deformed and stored in liquid nitrogen (77 K). At the time of application, a coupling was

introduced to join two tubes at room temperature. The increase in temperature resulted in a phase transformation (at around 120 K) and the shape change associated with the phase transformation decreased the coupling diameter. This decrease in diameter exerted a stress on the tubes and resulted in a secure joint. More than 100,000 couplings were successfully employed. The deployment of a large number of NiTiFe SMA couplings validated the reliability and the manufacturability of the alloys.

The goal of this project was to lower the operating temperature range of shape memory alloys in order for them to be used in hydrogen related technologies. The immediate benefit to NASA KSC is the development of a shape memory thermal conduction switch for application in cryogenic liquefaction, densification and zero boil-off systems. This is being extended to include the potential use of shape memory alloy actuator elements for cryogenic seals, valves, fluid-line repair, self-healing gaskets, and even to ambient debris-less separation and latch/release mechanisms. There has been no systematic research that evaluates the role played by the ternary addition of Fe in a Ni-rich or Ti-rich NiTiFe system. Although there have been numerous published articles on the R-phase transformation in NiTi based alloys, very few address the R-phase transformation in the NiTiFe system and the influence of thermo-mechanical treatments on the formation of the R-phase in such a system. The present work seeks to address these issues through a systematic approach of processing-structure-property correlation studies in the NiTiFe system. It is worth mentioning that such an alloy development study requires NiTiFe alloys of various compositions to be fabricated and thermo-mechanically processed. This was achieved using the arc melting route. Arc melting has several advantages, prominent among them are:

i. It facilitates the melting of small quantities of alloys with varying composition.

ii. It is economical owing to the high cost of raw materials and

iii. It eliminates contamination from carbon, as is the case with induction melting.

While thermo-mechanical properties of the alloys were studied using a differential scanning calorimeter (DSC), a dilatometer, an instrumented indenter and a dynamic mechanical analyzer (DMA), microstructural analyses were done using scanning and transmission electron microscopes (i.e., SEM and TEM) and energy dispersive X-ray spectroscopy was used for quantitative chemical analysis.

Based on the aforementioned objectives, there is an obvious need for better understanding the microscopic mechanisms concerning the R-phase transformation. This necessitates associated characterization techniques for the investigation of microscopic mechanisms under the influence of phase transformations and external stresses, which act on the actuator as a result of temperature changes and application of bias forces, respectively. Among available advanced techniques, *in situ* neutron diffraction during loading at changing temperatures is uniquely suited to following the texture, strain and phase fraction evolution in a bulk polycrystalline sample [12-16]. Neutron diffraction measurements have previously been performed during *in situ* loading at ambient and high temperatures, but not at low temperatures. For this purpose, a low temperature loading capability for *in situ* neutron diffraction measurements was implemented on the Spectrometer for Materials Research at Temperature and Stress (SMARTS) at Los Alamos National Laboratory, with capabilities as low as 90 K. With the new capability, *in situ* neutron diffraction measurements during loading were carried out at 216 K and 92 K to study associated deformation mechanisms. *In situ* neutron diffraction measurements during constrained recovery

were performed that simulated and evaluated the performance of NiTiFe alloys as actuator elements.

Lastly, efforts were focused on the engineering development of a shape memory alloy based cryogenic thermal conduction switch. Such a switch can control the liquid methane temperature and pressure in a zero boil-off system by allowing on demand heat transfer between two reservoirs kept at separate temperatures in an efficient and autonomous manner. It would also support methane liquefaction for future Mar's missions in addition to fulfilling immediate requirements at NASA-Kennedy Space Center.

Experimental

As part of this project, leveraging synergistic funding from the University of Central Florida and the National Science Foundation, the following processing and characterization capabilities were commissioned.

1. An arc melting furnace with a vertical vacuum quench facility (Figure 2a)

2. A differential scanning calorimeter with a liquid nitrogen cooling capability (Figure 2b)

3. A dilatometer with a liquid helium cooling capability (Figure 3a)

4. A dynamic mechanical analyzer with a liquid nitrogen cooling capability (Figure 3b)

5. A cryogenic cooling and loading capability during neutron diffraction, which was implemented at Los Alamos National Laboratory. (Figure 4)

Results

Alloy Development

NiTiFe alloys with varying compositions were fabricated and thermo-mechanically processed to assess structure-property correlations in these alloys. From the equilibrium phase diagram of the binary Ni-Ti system, the primary phase field of the intermetallic phase NiTi exists between a Ni:Ti ratio of 0.96 on the Ti-rich side and 1.32 on the Ni-rich side at 1373 K (in at.%) [11]. With the objective of lowering the R-phase transformation temperature, emphasis was placed on understanding the role of Fe addition on selected Ni:Ti ratios, starting at 0.96, continuing till 1.3. Fe was added in steps of 1 at.% from 0 to 5 at.%. Ni:Ti ratios falling outside the single phase region of NiTi, on both the Ti-rich and the Ni-rich sides, were also investigated. The compositions studied in this work can be divided into four regions based on the equilibrium binary Ni-Ti phase diagram. Table 1 lists the Ni:Ti ratios in the four regions. Ternary phases are reported to be absent in the NiTiFe system at the compositions considered in this study [18,19]. Table 2 lists the nominal compositions of all the alloys that were melted along with the choice starting material (powder or slug).

The starting materials for several initial attempts of the fabrication of NiTiFe alloys were fine powders of Ni, Ti and Fe. Owing to the high surface to volume ratio, the powders possessed excessive oxygen even before they were melted and the oxides inhibited the phase transformation in the system. Following this, high purity slugs of Ni, Ti (99.999% pure) and high purity Fe (99.99% pure) rod were used to fabricate NiTiFe shape memory alloys. The alloys were flipped and remelted 15 times to ensure homogeneity in the melt and subsequently

subjected to DSC and dilatometric testing (Figure 5). A selected summary of results of the various alloys fabricated in Table 2 is presented here from DSC, dilatometry, indentation, SEM, TEM and DMA studies (Figure 6 through Figure 9).

Region I (Ni:Ti < 0.96)

i. Addition of Fe supersedes the influence of Ni:Ti ratio in governing the R-phase transformation. However, at Fe contents greater than around 5 at.%, the system does not exhibit any phase transformation to temperatures as low as 103 K. It is speculated that the first order B2 to R-phase transformation is substituted by a second order B2 to incommensurate phase and an incommensurate to commensurate phase transformation [20,21].

ii. A high density of dislocations impede the R-phase transformation in a representative $Ni_{46.8}Ti_{50}Fe_{3.2}$ alloy. Annealing at appropriate temperatures can annihilate dislocations, reducing the dislocation density and reducing the transformation interval range. The reduced transformation interval range is important for the engineering applications of NiTiFe alloys. Additionally, a homogeneous distribution of dislocations results in a reduced transformation interval range.

iii. In Ti-rich alloys, the R-phase transformation is not influenced by aging. This is due to the presence of a vertical boundary on the Ti-rich side of the NiTi equilibrium phase diagram.

Region II (Ni:Ti between 0.96 to 1.00)

i. The R-phase transformation in this region was seen in alloys having a Ni:Ti ratio of 0.96 (at.%) with 1, 2 and 3 at.% Fe. However, alloys with higher Fe content failed to exhibit the R-phase transformation. A possible reason could be the presence of Ti_2Ni precipitates, which stabilizes as the Fe content increases thereby inhibiting the martensitic phase transformation.

ii. Addition of Fe to NiTi in this region is more efficient in lowering the R-phase to B19' transformation as opposed to the B2 to R-phase transformation.

Region III (Ni:Ti between 1.0 and 1.32)

i. Ni-rich NiTiFe alloys exhibit the R-phase transformation only after thermo-mechanical treatments. Additionally, the alloys are homogenized as a result of thermo-mechanical processing.

ii. Ni-rich alloys lower the R-phase transformation temperatures more efficiently than Ti-rich alloys for comparable Fe contents.

iii. As the Fe content increases, multiple heat treatments are needed to observe the R-phase transformation in NiTiFe alloys in this region.

iv. The equilibrium phase precipitate, Ni_3Ti, largely influences the R-phase transformation in the NiTiFe system in this region. However, with increasing Ni and Fe contents the transformation interval also widens.

Region IV (Ni:Ti greater than 1.32)

i. In this two-phase region, the NiTi matrix has equiatomic composition and exhibits the phase transformation at ambient temperatures. The phase transformation is inhibited as the volume of Ni_3Ti precipitates increase. Furthermore, the R-phase transformation with wide transformation intervals, is seen in alloys with around 2 at.% Fe. Workability of the alloys in this region become extremely difficult owing to the presence of hard Ni_3Ti precipitates.

Neutron Diffraction Measurements at Los Alamos National Laboratory

As previously mentioned, neutron diffraction measurements were conducted on the Spectrometer for Materials Research at Temperature and Stress (SMARTS), a third generation neutron diffractometer at Los Alamos National Laboratory. A novel cryogenic capability was implemented on SMARTS that can vary temperatures between 300 K and 90 K, while collecting neutron diffraction spectra *in situ* during loading. This experimental setup has expanded the capabilities of the SMARTS diffractometer to perform *in situ* neutron diffraction measurements from ambient and high temperatures to cryogenic temperatures. The deformation behaviors of a representative $Ni_{46.8}Ti_{50}Fe_{3.2}$ shape memory alloy was studied for the first time at 92 K using this capability.

The scientific study encompassed three aspects of the behavior of NiTiFe:

i. In order to study deformation mechanisms in the R-phase in NiTiFe, measurements were performed at a constant temperature of 92 K under external loading.

ii. With the objective of examining NiTiFe in cyclic, low-stroke, actuator applications (such as in cryogenic thermal switches), a NiTiFe sample was strained to 1% at 92 K and subsequently heated to full strain recovery under a constant external load.

iii. With the objective of examining NiTiFe in one-time, high-stroke, actuator applications (such as in safety valves), a NiTiFe sample was strained to approximately 5% at 92 K and subsequently heated to full strain recovery under a constant external load.

Neutron diffraction spectra were recorded at suitable stress and time intervals during these experiments, which assisted in the monitoring of the phase-specific strain, texture and phase fraction evolution. The results are summarized in the following.

i. The room temperature cubic B2 phase transformed to the trigonal R-phase during cooling. During the transformation, the $\{110\}_{B2}$ peak split into $\{112\}_R$ and $\{300\}_R$, respectively. This was due to the unit cell elongation in the <111> crystallographic direction of the B2 phase associated with the formation of the R-phase. A very similar splitting was observed for the $\{210\}_{B2}$ peak to $\{303\}_R$ and $\{411\}_R$, respectively. The splitting increased with cooling and was evident while comparing the diffraction patterns obtained at 92 K with that at 216 K. (Figure 10)

ii. When loaded at 92 K, the emergence of a stress-induced B19' phase was noticed at a low stress of 68 MPa, with strain redistribution among lattice planes in the R-phase. Bulk of the R-phase transformed to the B19' phase at approximately 5% strain and the transformed B19' phase was stabilized during unloading to a holding load of 8 MPa. This behavior was attributed to the fact that the B19’ phase is stabilized at a temperature

lower than the reverse transformation temperature of the B19' phase to the R-phase, arising from the thermal hysteresis. (Figure 11)

iii. The estimated elastic modulus of lattice planes varied between 92.9 GPa for {111} planes to 113.8 GPa for {322} planes. This was in good agreement with the measured macroscopic elastic modulus of 90.9 GPa. The lack of twinning in the R-phase below 68 MPa was consistent with this agreement between macroscopic and microscopic measurements.

iv. The base-centered orthorhombic B33 phase was experimentally identified for the first time in NiTi based alloys. The orthorhombic B33 phase was observed while identifying a diffraction peak shifting between the $\{111\}_R$ and $\{100\}_{B19'}$ peaks in the diffraction spectra collected during loading. During cooling to 92 K in the no-load condition (nominal holding stress of 8 MPa), $Ni_{46.8}Ti_{50}Fe_{3.2}$ consisted primarily of the R-phase with approximately 17 vol.% monoclinic phase and approximately 12 vol.% orthorhombic phase. It was inferred that orthorhombic martensite was formed in stress-free areas, while monoclinic martensite formed in areas that experienced internal stresses. Upon loading, the R-phase underwent a stress-induced transformation to monoclinic B19' phase. Since the orthorhombic B33 was unstable under stress, certain planes of B33 phase gradually distorted at higher applied stresses. This distortion was viewed as a change in the monoclinic angle from $\gamma = 107°$ to $\gamma = 97°$. The tilting of the $\{021\}_{B33}$ planes was observed in the diffraction spectra, which started at approximately 114 MPa and finished at approximately 210 MPa.

v. Given an existing ambiguity in the published literature as to whether the trigonal R-phase belongs to the *P*3 or $P\bar{3}$ space groups, Rietveld analyses were separately carried out incorporating the symmetries associated with both space groups and the impact of this choice evaluated. No statistical differences in the refinement quality were noted for structure, strain and phase fraction analyses between the choice of *P*3 or $P\bar{3}$ space groups. The accuracy of the refinement for strain determination was confirmed by comparing single peak fitting and Rietveld approaches which resulted in comparable results for the three sets of diffraction patterns considered. The accuracy of the texture and phase fraction determination was confirmed from visual inspection of raw spectra. For texture analyses, the choice of the $P\bar{3}$ space group resulted in unrealistically high texture indices (when compared to qualitative analyses). This was attributed to the heterogeneous strain in the diffracting volume resulting in a loss of the center of symmetry. (Figure 12)

vi. The neutron diffraction spectra acquired *in situ* during uniaxial compression loading of $Ni_{46.8}Ti_{50}Fe_{3.2}$ at 92 K, were subjected to the Rietveld method using GSAS for quantitative determination of phase fractions, textures, and strains of the respective phases. The neutron diffraction spectra collected under the no-load condition (nominal holding stress of 8 MPa), $Ni_{46.8}Ti_{50}Fe_{3.2}$ consisted primarily of the trigonal R-phase with approximately 17 vol. % monoclinic B19' phase and approximately 12 vol. % orthorhombic B33 phase. Upon loading, at a stress lower than 100 MPa, the trigonal R-phase underwent a stress-induced transformation to the monoclinic B19' phase. The volume fraction of the orthorhombic B33 phase remained constant, until distortion to monoclinic B19' phase. The bulk of the R-phase was transformed to the B19' phase at the maximum load of 425 MPa and the transformed B19' phase was stabilized during unloading to a holding load of 8 MPa. During loading, the texture of the R-phase increased while that of the

B19' decreased. This was attributed to the preferential transformation and stress assisted detwinning. The lattice strains obtained through single peak fitting and the Rietveld method suggested that the R-phase carried the load until 68 MPa. Upon further loading, the bulk of the load was transferred to the evolving B19' phase. The discrepancy between the macroscopic and microscopic strains was attributed to detwinning. Additionally, the magnitude of the anisotropic strains (with isotropic strains remaining constant) in the B33 orthorhombic phase suggested a shearing type mechanism associated with a cooperative movement of atoms.

vii. Neutron diffraction spectra was acquired *in situ* during two constrained recovery experiments performed on $Ni_{46.8}Ti_{50}Fe_{3.2}$ samples, i.e., from B19' phase to R-phase and R-phase to B2 phase. The neutron diffraction spectra, representative of bulk measurements, were subjected to the Rietveld method using GSAS for quantitative determination of phase fractions and textures of the respective phases. The bulk recovery in strain for the first experiment recorded approximately 4% strain recovery between 150 K and 170 K, with a strain recovery of approximately 2% that took place between 160 K and 162 K. The Rietveld refinements suggested the volume fractions of the B19' phase and the R-phase at 160 K to be 83.3 vol.% and 16.7 vol.%, respectively and at 162 K to be 46.3 vol.% and 53.7 vol.%, respectively. The texture evolution exhibit a preferential transformation of the B19' phase to the R-phase. The bulk recovery in strain for the second experiment recorded approximately 1% strain recovery between 231 K and 243 K, with a preferential transformation from the R to the B2 phase. (Figure 13 and Figure 14)

Development of NiTiFe Shape Memory Alloy based Thermal Conduction Switch Prototypes

The objective was to design, construct and test an SMA thermal conduction switch (actuator) to facilitate thermal conduction of approximately 8 watts between two liquid reservoirs held at 118 K and 92 K. Such a switch would control the liquid methane temperature and pressure in a zero boil-off system by allowing on demand heat transfer between two reservoirs kept at separate temperatures in an efficient and autonomous manner. It would also support methane liquefaction for future Mar's missions in addition to fulfilling immediate requirements at NASA-Kennedy Space Center. Gas gap and liquid gap thermal switches that rely on convective heat transfer between two surfaces are currently being used as cryogenic range thermal switches. The sensors and active controls in such systems make them further complicated and expensive, yet less efficient than the proposed switch. Other systems using conduction bands make use of mechanical means to generate sufficient thermal contact and may not be reliable. SMA thermal switches have the potential to limit these problems.

Version I

The first prototype proof-of-concept switch which used a commercially available NiTi alloy and operated between an ice-water mixture (273 K) and hot water (338 K) is shown in Figure 15. In this prototype, four NiTi SMA helical springs act against two bias springs for actuation. The SMA springs are contained inside oxygen free copper cylinders, which also act as the thermal conduction path between the dewars. Connected to the moving plate are four pistons, each placed inside the cylinders. The SMA springs exert force on pistons for actuation.

Version II

The implementation of the concept in a working prototype at cryogenic temperatures needed to address issues such as: (i) hysteresis of the SMA element; (ii) the developing temperature gradient over the length of the SMA element when the switch is in the closed condition; (iii) contact resistance for efficient and reliable heat transfer, as the switch is expected to work in vacuum conditions; (iv) and contact force generated by the SMA element. A second prototype (Figure 16) was arrived at after considering the aforementioned issues, by positioning both the SMA element and the bias spring on the same side, using insulation at one end of the element, using indium foil between the mating surfaces and by controlling the phase transformation. The design consists of a stationary plate (fixed copper contact) on the methane side, three rods for support and heat transfer, three SMA helical compression springs concentric to the support rods, three spring seats that keep the SMA springs in position and also insulate them from the stationary plate, a bias extension spring placed in between the SMA springs with bias spring holders on both ends, a moving plate (moving copper contact) for actuation, and three bushings fixed to the moving plate for easy sliding on the support rods. The two ends of the bias spring were made straight due to dimensional constraints and for ease of adjustment of the distance between the two plates (stationary and moving plates). The bias spring holders were devised to adjust the length of the bias spring, with two set screws securing the ends of the bias spring. All the materials for the final design were selected keeping in mind issues of low-temperature embrittlement and thermal conductivity. These materials included oxygen free pure Cu for the stationary and moving plates, Be-Cu alloys for the support rods and bushings, austenitic stainless steels containing more than 7% Ni for the bias spring, brass for the bias spring holders and polytetrafluoroethylene (Teflon) for the spring seats. Indium foil and Apiezon® N grease were used to enhance the thermal conductivity between mating parts.

Version III

The third prototype of the switch (Figure 17) used SMA strips instead of SMA helical spring. Furthermore, NiTi was replaced by NiTiFe that is characterized by operation in the low temperature range as well as by the presence of the R-phase. The mechanical operation of the low-hysteresis switch is dependent on a force balance between the buckling of the NiTiFe strips and the bias spring. In order to ensure proper switch actuation, consideration must be given to the force balance between the bias spring and the SMA elements. The spring must not be excessively stiff that it prevents movement of the SMA strips as they undergo phase transformation, but it must be stiff enough to overcome the rigidity of the SMA elements when they are in the R-phase. The force generated by the bias spring in maximum extension was calculated to be 20.7 N. Since there are three strips in this configuration, this is equivalent to a force of 6.9 N per strip. The force required to buckle a single SMA strip was calculated using the Euler equation for buckling of slender columns, and was found to be 5.37 N. Therefore the force imparted by the bias spring is adequate to cause buckling of the strips while they are in the R-phase. To help achieve maximum displacement of the switch during actuation and obtain the appropriate bending stiffness, the strips were installed in a pre-buckled configuration. Pre-buckling the strips also provided the advantage of being able to control the direction of the buckle (inward or outward), which helped ensure symmetrical movement of the switch against buckling instabilities.

Version IV

A fourth prototype (Figure 18) was made by modifying version II by using NiTiFe as the SMA element in order that significant stroke coupled with low thermal hysteresis can be achieved.

Conclusions

This project has made theoretical as well as applied contributions to understanding and using R-phase transformations in the ternary NiTiFe shape memory alloy system. Applied aspects include alloy development by recourse to arc melting followed by thermomechanical processing and a range of characterization techniques that include SEM, TEM, DSC, dilatometry, DMA, and indentation. The alloys were also used in prototype thermal conduction switches. Theoretical aspects include *in situ* neutron diffraction measurements during loading and cooling at Los Alamos National Laboratory. Valuable information on deformation mechanisms were thus obtained.

The immediate benefit to NASA is the development of a shape memory thermal conduction switch for application in cryogenic liquefaction, densification and zero boil-off systems. This can easily be extended to include the potential use of shape memory alloy actuator elements for cryogenic seals, valves, fluid-line repair, self-healing gaskets for hyrdrogen-related technologies and even to ambient debris-less separation and latch/release mechanisms.

Various aspects of this project benefited from concurrent synergistic funded efforts from the National Science Foundation (a CAREER award), UCF-UF's Space Research Initiative (SRI), NASA KSC and Arctic Slope Regional Corporation (ASRC). A new project funded by NASA has just been initiated at UCF that leverages the knowledge and experience gained from this project for application to NiTiPt and NiTiPd alloys. Another separate project from ASRC is also expected to use NiTiFe springs in a convection-based heat-pipe type thermal switch.

Patents

1. Hitch Release Mechanism; application filed November 2007

2. Shape Memory Thermal Conduction Switch; application to be filed January 2008

3. A Shape Memory Phase Transformation for Large Shape Change; to be disclosed January 2008

4. Shape Memory Thermal Conduction Switch with Reduced Thermal Gradients; to be disclosed January 2008

Publications

1. V.B. Krishnan, R.M. Manjeri, B. Clausen, D.W. Brown and R. Vaidyanathan, "Analysis of Neutron Diffraction Spectra Acquired *in situ* during Mechanical Loading of Shape Memory NiTiFe at Low Temperatures", Mat Sci Eng A (2007, accepted, in press)

2. V.B. Krishnan, C. Bewerse, W.U. Notardonato and R. Vaidyanathan, "A Thermal Conduction Switch based on Low Hysteresis NiTiFe Shape Memory Alloy Helical Springs", Advances in Cryogenic Engineering, American Institute of Physics, (2007, accepted, in press)

3. J.L. Lemanski, V.B. Krishnan, R. Mahadevan Manjeri, W.U. Notardonato and R. Vaidyanathan, "A Low Hysteresis NiTiFe Shape Memory Alloy Based Thermal Conduction Switch", Advances in Cryogenic Engineering, American Institute of Physics, (2006) 52A 3-10.

4. C.R. Rathod, B.C. Clausen, M.A.M. Bourke and R. Vaidyanathan, “A Neutron Diffraction Investigation of Hysteresis Reduction and Increase in Linearity in the Stress-Strain Response of Superelastic NiTi”, Appl Phys Lett 88 (2006), 201919-3.

5. S. Rajagopalan, A.L. Little, M.A.M. Bourke and R. Vaidyanathan, “Elastic Modulus of B19’ Shape Memory NiTi from *in situ* Neutron Diffraction during Loading, Instrumented Nanoindentation and Extensometry”, Appl Phys Lett 86 (2005) 081901-3.

6. V. Livescu, T.R. Woodruff, B. Clausen, T. Sisneros, M.A.M. Bourke, W.U. Notardonato and R. Vaidyanathan, “Design and Rationale for an *in situ* Cryogenic Deformation Capability at a Neutron Source”, Advances in Cryogenic Engineering, American Institute of Physics, (2004) 50A 83-89.

7. C.R. Rathod, V. Livescu, B. Clausen, M.A.M. Bourke, W.U. Notardonato, M. Femminineo and R. Vaidyanathan, “Neutron Diffraction Characterization of Residual Strain in Welded INCONEL 718 for NASA Space Shuttle Flow Liners”, Advances in Cryogenic Engineering, American Institute of Physics, (2004) 50A 167-175.

8. V.B. Krishnan, J.D. Singh, T.R. Woodruff, W.U. Notardonato and R. Vaidyanathan, “A Shape Memory Alloy Based Cryogenic Thermal Conduction Switch”, Advances in Cryogenic Engineering, American Institute of Physics, (2004) 50A 26-33.

9. C.R. Rathod, S. Rajagopalan and R. Vaidyanathan, “Mechanical Characterization of Shape Memory Alloys using Diffraction and Instrumented Indentation”, Shape Memory and Superelastic Technologies, International Organization on Shape Memory and Superelastic Technology, (2004) 331-339.

10. R.M. Manjeri and R. Vaidyanathan, “On the Formation of the R-phase in NiTiFe Alloys”, to be submitted to Metallurgical and Materials Transactions A.

11. V.B. Krishnan, D.W. Brown, B. Clausen, M.A.M. Bourke and R. Vaidyanathan, “Cryogenic Deformation of NiTiFe Alloys”, to be submitted to Nature.

12. V.B. Krishnan, D.W. Brown, B. Clausen, M.A.M. Bourke and R. Vaidyanathan, “Neutron Diffraction Studies of Deformation of the R phase in NiTiFe Alloys”, to be submitted to Acta Materialia.

Presentations

Invited

1. R. Vaidyanathan, “Insights into the Deformation of Shape Memory Alloys from Instrumented Indentation and *in situ* Neutron Diffraction”, TMS 2007 Annual Meeting, Orlando, FL, February 25-March 1, 2007.

2. R. Vaidyanathan, “Neutron Diffraction Studies of Deformation in NiTiFe Shape Memory Alloys at Cryogenic Temperatures”, THERMEC 2006, International Conference on Processing and Manufacturing of Advanced Materials, July 4-8, 2006, Vancouver, Canada.

3. R. Vaidyanathan, “Deformation Studies in Shape Memory Alloys using Neutron Diffraction and Nanoindentation”, plenary lecture at ESOMAT 2006, Bochum, Germany, September 10-15, 2006.

4. R. Vaidyanathan, “Neutron, Synchrotron X-ray Diffraction and Instrumented Indentation Studies of Deformation in Shape Memory Alloys”, Japan Institute of Metals Meeting, Tokyo, Japan, March 21-23, 2006 (TMS/JIM Young Leader International Scholar Lecture)

5. R. Vaidyanathan, “Deformation in Shape Memory Alloys”, 3rd International Conference on Stress Evaluation By Neutron and Synchrotron Radiation, Santa Fe, NM, October 17-19, 2005.

6. R. Vaidyanathan, “Neutron Diffraction Studies of Deformation in Shape Memory Alloys”, National Science Foundation ANSWER Workshop, Knoxville, TN, November 16-20, 2003.

7. R. Vaidyanathan, “Internal Stress Measurements in Shape Memory Alloys”, TMS 2003 Annual Meeting, San Diego, CA, March 2-6, 2003.

Contributed

8. V.B. Krishnan, B. Clausen, M.A.M. Bourke and R. Vaidyanathan, “Low Temperature Behavior of Shape Memory NiTiFe”, TMS 2007 Annual Meeting, Orlando, FL, February 25-March 1, 2007.

9. R. Mahadevan Manjeri, M.D. Nandiraju, C. Bewerse and R. Vaidyanathan, “On the Formation of the R-phase in NiTiFe Shape Memory Alloys”, TMS 2007 Annual Meeting, Orlando, FL, February 25-March 1, 2007.

10. R. Vaidyanathan, “NiTiFe Alloys for Low Temperature Thermal Switches: Alloy Development and Prototype Testing”, Shape Memory and Superelastic Technologies 2006 Conference, Asilomar, CA, May 7-11, 2006.

11. R. Mahadevan Manjeri and R. Vaidyanathan, “Characterization of NiTiFe Shape Memory Alloys”, FLAVS/FSM Meeting, Orlando, FL, March 13-14, 2006 **(honorable mention)**.

12. R. Vaidyanathan, “Neutron Diffraction Studies of Deformation in NiTiFe Shape Memory Alloys at 90 K”, TMS 2006 Annual Meeting, San Antonio, TX, March 12-16, 2006.

13. V.B. Krishnan, S. Shmalo, T.R. Woodruff, B. Clausen, T. Sisneros, D.W. Brown, M.A.M. Bourke and R. Vaidyanathan, “Cryogenic Neutron Diffraction Measurements during Loading and Heating in NiTiFe Shape Memory Alloys”, 7th Los Alamos National Laboratory LUG Meeting, Los Alamos, NM, September 11-13, 2005.

14. S. Shmalo, V.B. Krishnan, T.R. Woodruff, C.R. Rathod, B. Clausen, M.A.M. Bourke, R. Vaidyanathan “Deformation Mechanisms in NiTiFe Shape Memory Alloys at 90K”, 7th Los Alamos National Laboratory LUG Meeting, Los Alamos, NM, September 11-13, 2005 (first prize).

15. R. Vaidyanathan, S. Shmalo, C.R. Rathod, B. Clausen and M.A.M. Bourke, “Low Temperature Deformation Studies in Shape Memory Alloys using the SMARTS Spectrometer at Los Alamos National Laboratory”, Cryogenic Engineering Conference and the International Cryogenic Materials Conference, Keystone, CO, August 29 - September 2, 2005.

16. J. Lemanski, V.B. Krishnan, R. Mahadevan Manjeri, W. Notardonato and R. Vaidyanathan, “A Low Hysteresis NiTiFe Shape Memory Alloy based Thermal Conduction Switch”, Cryogenic Engineering Conference and the International Cryogenic Materials Conference, Keystone, CO, August 29 - September 2, 2005.

17. S. Shmalo, C.R. Rathod, T. Woodruff, V. Livescu, B. Clausen, M.A.M. Bourke, W. Notardonato and R. Vaidyanathan, “Neutron Diffraction Investigation of NiTiFe Shape Memory Alloys during Mechanical Loading at Cryogenic Temperatures”, TMS 2005 Annual Meeting, San Francisco, CA, February 14-18, 2005.

18. V.B. Krishnan, J. Singh, T. Woodruff, W. Notardonato and R. Vaidyanathan, “A Shape Memory Alloy Based Cryogenic Thermal Conduction Switch: Design, Construction and Materials Development”, 41st Space Congress, Cape Canaveral, FL April 27-30, 2004.

19. V.B. Krishnan, J. Singh, T. Woodruff, W. Notardonato and R. Vaidyanathan, “A Shape Memory Alloy based Cryogenic Thermal Conduction Switch: Design, Construction and Materials Development”, Cryogenic Engineering Conference and the International Cryogenic Materials Conference, Anchorage, AK, September 22-26, 2003.

20. M.A.M. Bourke, V. Livescu, B. Clausen, T. Sisneros, W. Notardonato, T.R. Woodruff, R. Vaidyanathan, “Deformation Mechanisms at Cryogenic Temperatures - Insights from Neutron Diffraction Measurements”, Cryogenic Engineering Conference and International Cryogenic Materials Conference, Anchorage, AK, September 22-26, 2003.

21. R. Vaidyanathan and S. Rajagopalan, “Mechanical Characterization of Shape Memory Alloys using Diffraction and Instrumented Indentation”, International Conference on Shape Memory and Superelastic Technologies, Pacific Grove, CA, May 4-8, 2003.

Students

1. R.M. Manjeri, “Formation of the R-phase in NiTiFe Shape Memory Alloys”, PhD, expected to graduate in December 2008.

2. V.B. Krishnan, “Low Temperature NiTiFe Shape Memory Alloys: Actuator Engineering and Investigation of Deformation Mechanisms using *in situ* Neutron Diffraction at Los Alamos National Laboratory”, PhD, graduated December 2007.

3. N.M. Diwakar, “Commissioning of a Dynamic Mechanical Analyzer for the Characterization of Low Temperature NiTiFe Shape Memory Alloys”, MS, graduated Fall 2006.

4. J.L. Lemanski, “Cryogenic Shape Memory Alloy Actuators for Spaceport Technologies: Material Characterization and Prototype Testing”, MS, graduated April 2005 (awarded best thesis award in the College of Engineering and Computer Science).

5. J. Singh, “Commissioning of an Arc Melting/Vacuum Quench Furnace Facility for Fabrication of Ni-Ti-Fe Shape Memory Alloys, and their Characterization”, MS, graduated December 2004.

6. V.B. Krishnan, “Design, Fabrication and Testing of a Shape Memory Alloy based Cryogenic Thermal Conduction Switch”, MS, graduated March 2004 (awarded best thesis award in the College of Engineering and Computer Science).

7. C. Bewerse, undergraduate student.

References

1. K. Otsuka and C.M. Wayman, eds., *Shape Memory Materials*, Cambridge University Press, UK, 1998.

2. M. Fremond and S. Miyazaki, *Shape Memory Alloys*, Springer Wien New York, 1996, pp. 71-142.

3. S. Miyazaki, Y. Ohmi, K. Otsuka and Y. Suzuki; J. De Phys. 43 12 1982 C4-255

4. W.B. Cross, A.H. Kariotis and F.J. Stimler; NASA CR-1433, September 1969

5. T. Saburi, T. Tatsumi and S. Nenno; J. de Phys. 43 12 1982 C4-26

6. M. Matsumoto and T. Honma; JIM International symposium (Kobe) 1976 199-204

7. C.M. Wayman, L. Cornelis and K. Shimizu; Scripta Mater. 6 1972 115

8. F.E. Wang, B.F DeSavage, W.J. Buehler and W.R. Hosler; J. Appl. Phys., 39 (1968), 2166.

9. T. Tadaki, Y. Nakata and K. Shimizu; Trans. JIM, 28 (1987), 883.

10. L. M. Wang, L. H. Liu, H. Yang, L.Y. Wang and G. Q. Xiu, Mater. Sci. Forum 394-395 (2002) 297.

11. K. Otsuka and X. Ren, Progress in Mater. Sci., 50 (2005) 511.

12. M.A.M. Bourke, D.C. Dunand, and E. Ustundag, Appl. Phys. A, 74 (2002) S1707.

13. M. A. M. Bourke, R. Vaidyanathan, and D. C. Dunand, Appl. Phys. Lett., 69 (1996) 2477.

14. R. Vaidyanathan, M. A. M. Bourke and D. C. Dunand, J. Appl. Phys. 86 (1999) 3020.

15. R. Vaidyanathan, M. A. M. Bourke and D. C. Dunand, Acta. Mater. 47 (1999) 3353.

16. R. Vaidyanathan, D. C. Dunand, and U. Ramamurty, Mater. Sci. Eng., A, 289 (2000) 208.

17. M.A.M. Bourke, D. C. Dunand, and E. Ustundag, Appl. Phys. A, 74 (2002) S1707.

18. G. Cacciamamani, J. De Keyzer, R. Ferro, U. E. Klotz, J. Lacaze and P. Wollants; Intermetallics 14 (2006) 1312-1325.

19. P. Riani, G. Cacciamamani, Y. Thebaut and J. Lacaze, Intermetallics (2006) 1226-1230.

20. Mi. S. Choi, T. Fukuda, T. Kakeshita and H. Mori; Phil. Mag, 86, 1, 67, 2006.

21. Mi. S. Choi, T. Fukuda, T. Kakeshita and H. Mori; Script. Mater., 53, 869, 2005.

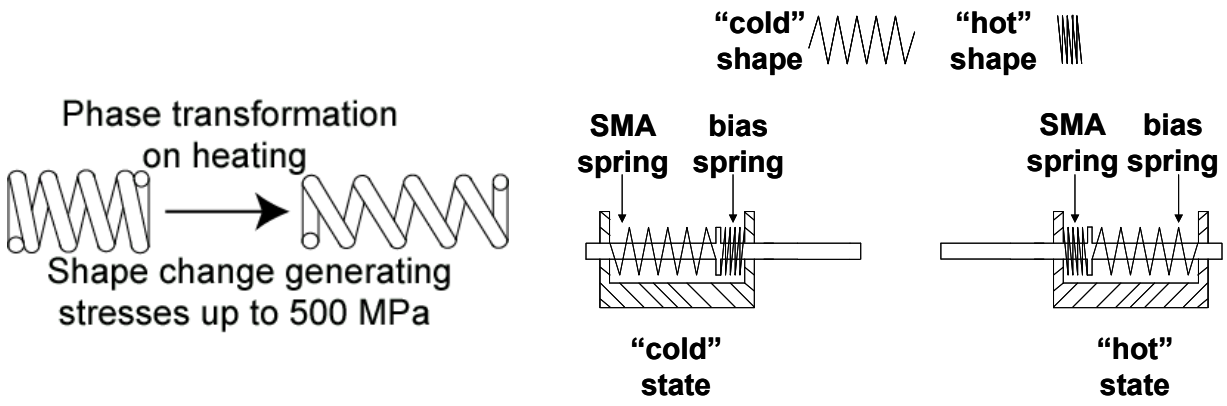

(a) (b)

Figure 1: (a) Schematic of the shape memory effect. (b) A simple switch based on this effect.

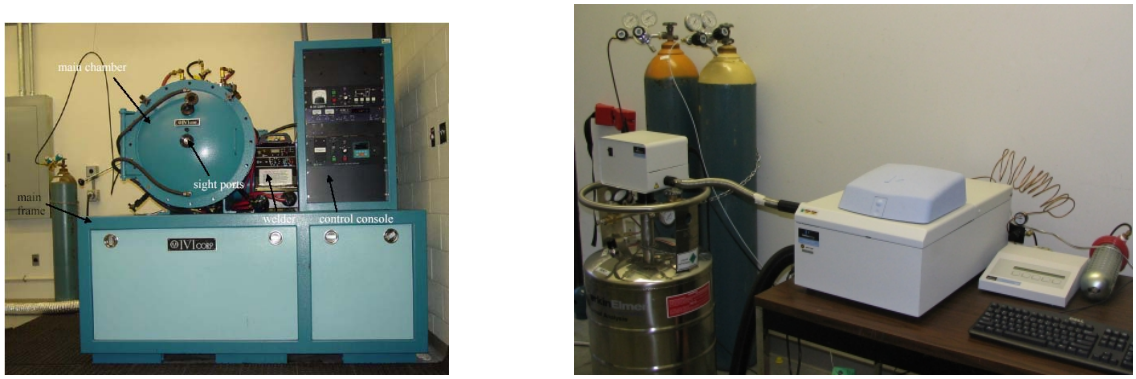

(a) (b)

Figure 2: (a) Arc melting/thermal treatment facility. (b) Differential Scanning Calorimeter with liquid nitrogen cooling capability.

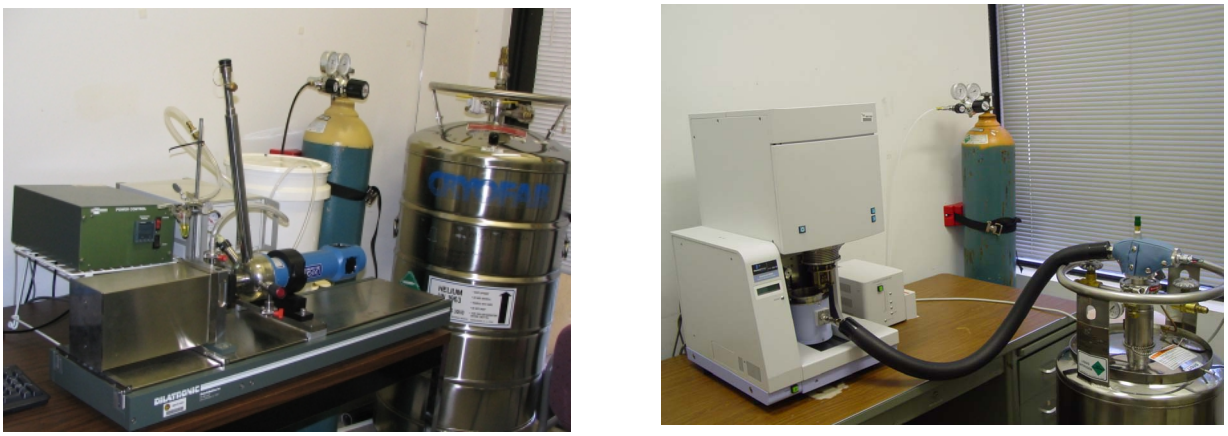

(a) (b)

Figure 3: (a) Dilatometer with liquid helium cooling capability (b) Dynamic Mechanical Analyzer with liquid nitrogen cooling capability

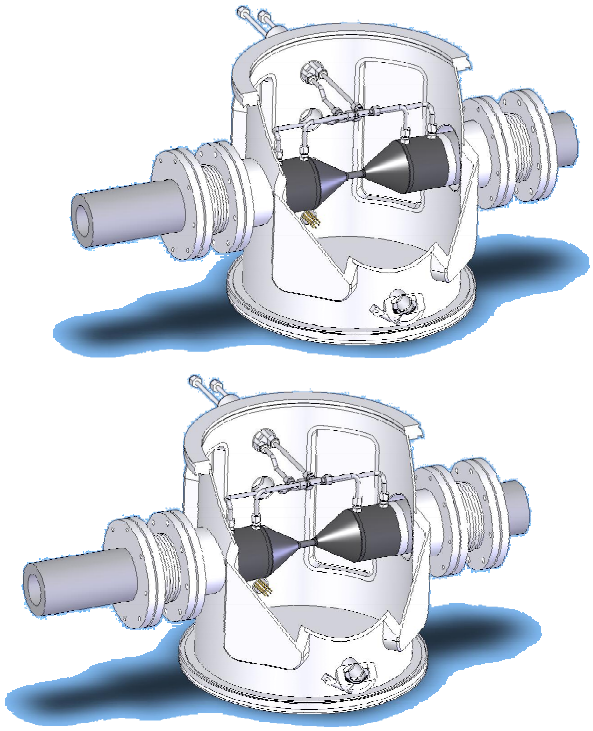

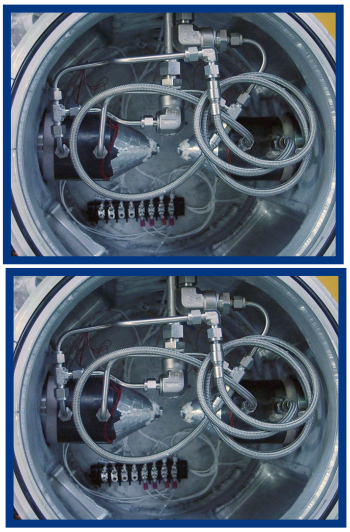

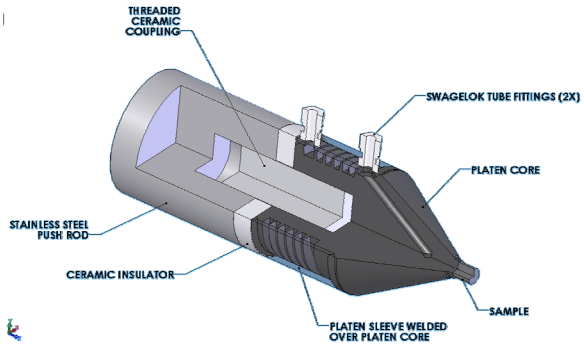

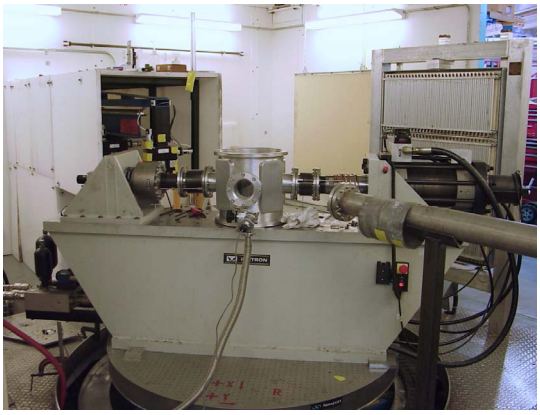

Figure 4: Design and implementation of a cryogenic loading capability at Los Alamos National Laboratory

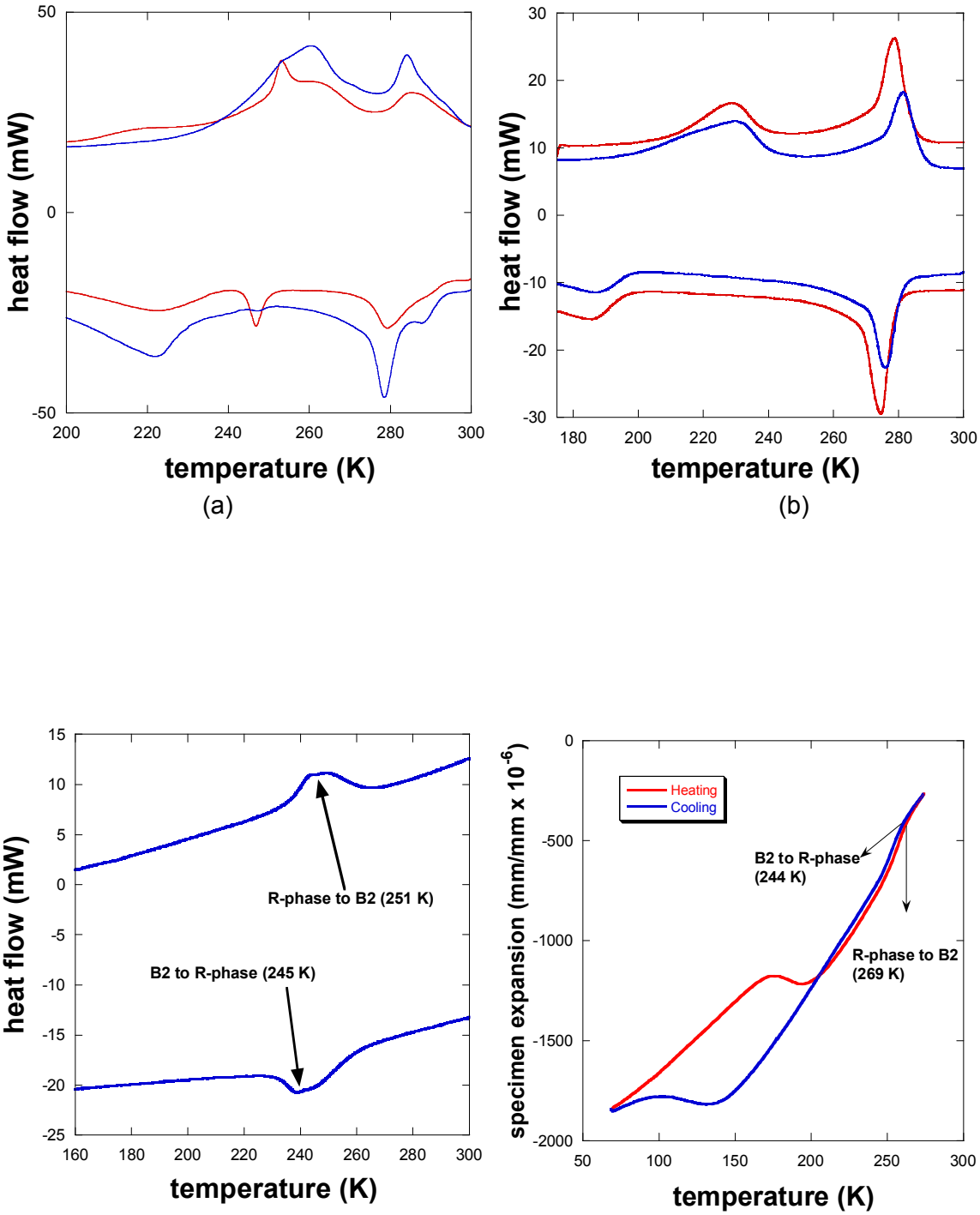

Figure 5: Results from a $Ni_{47.5}Ti_{49.5}Fe_3$ alloy in the as-fabricated condition. A button flipped (a) 9 times and (b) flipped 15 times during arc-melting. The specimens in (a) and (b) were taken from diametrically opposite ends (25 mm apart) of the button sample. Transformation temperatures as measured in (c) a DSC and (d) a dilatometer. The DSC sample was 2 x 2 x 2 mm and the dilatometer sample was 2 x 2 x 25 mm. The DSC and dilatometry results are from $Ni_{46.1}Ti_{51}Fe_{2.9}$ that had been solutionized at 1173 K for 24 hours and furnace cooled.

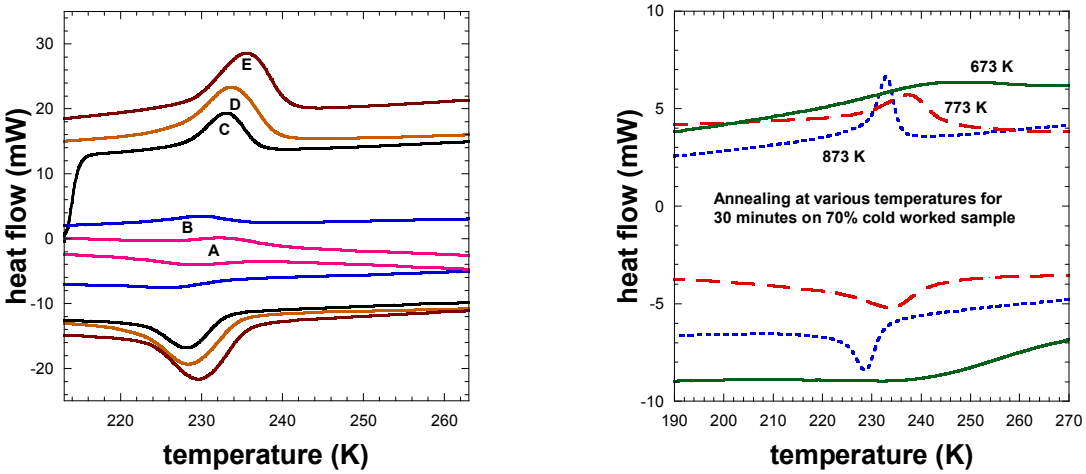

Figure 6: DSC curves of $Ni_{46.8}Ti_{50}Fe_{3.2}$ (a) with different heat treatments. A - as melted; B - solutionized at 1123 K for 24 h and furnace cooled; C - solutionized at 1123 K for 24 h and furnace cooled, aged at 923 K for 30 min; D - solutionized at 1123 K for 24 h and furnace cooled, aged at 723 K for 30 min; E - solutionized at 1123 K for 1 hr. and furnace cooled. (b) 70% cold worked and annealed at selected temperatures for 30 minutes.

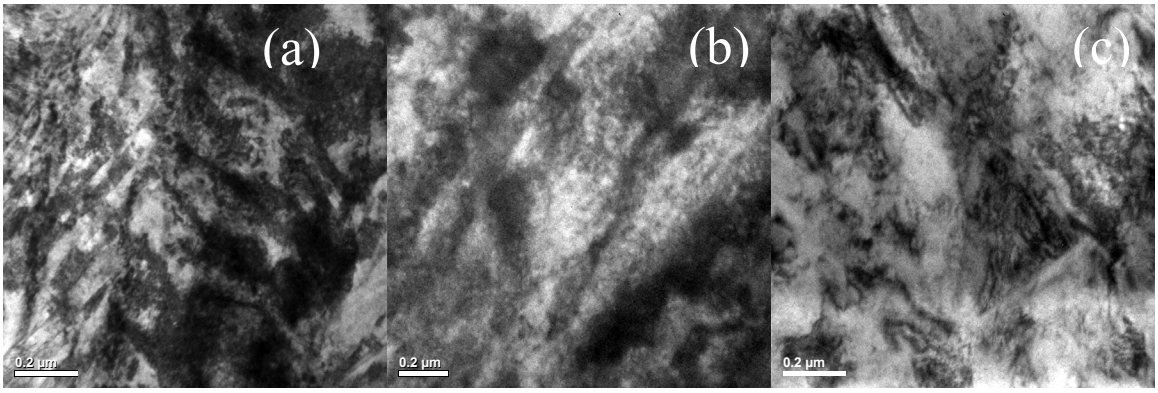

Figure 7: Bright field images of 70% cold worked $Ni_{46.8}Ti_{50}Fe_{3.2}$ annealed for 30 minutes at (a) 673 K, (b) 773 K, and (c) 873 K.

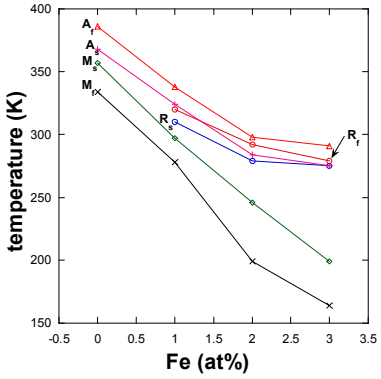

Figure 8: Variation of transformation temperatures with Fe addition. The results are from as-fabricated Ti-rich NiTiFe alloys with a Ni:Ti ratio of 0.96 (at%).

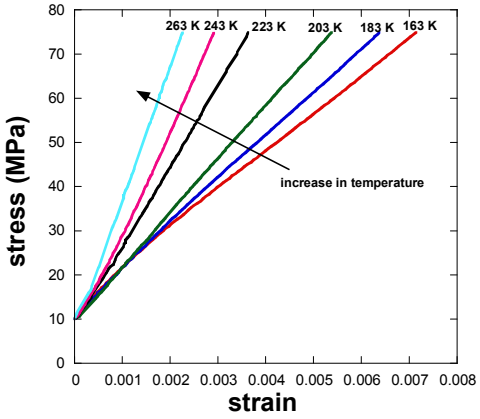

Figure 9: Stress-strain response of $Ni_{46.8}Ti_{50}Fe_{3.2}$ (solutionized at 1123 K for 1 hr and furnace cooled) as a function of temperature.

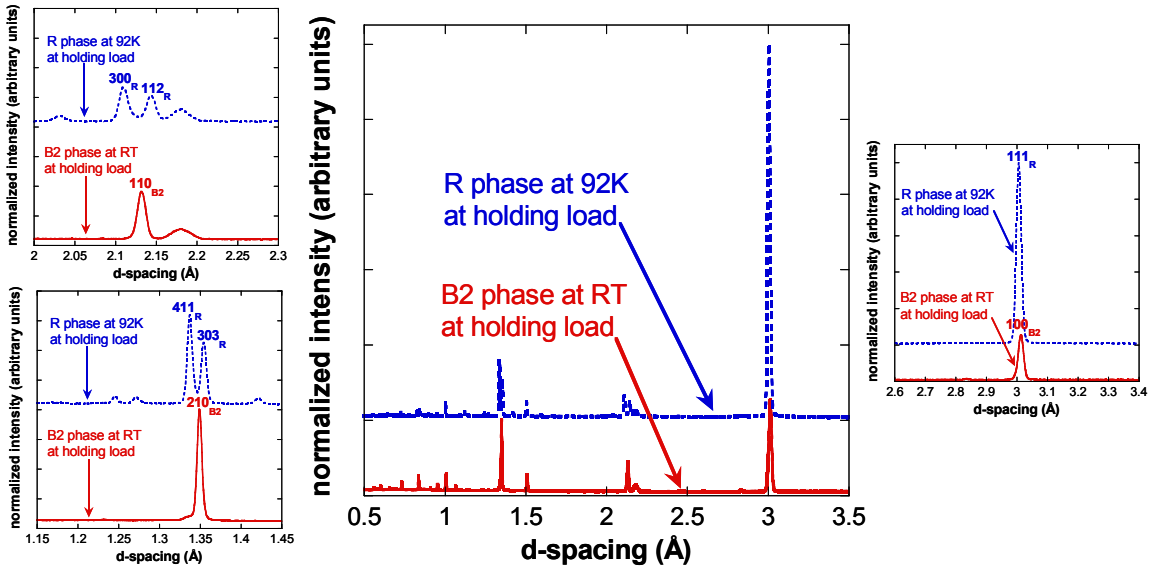

Figure 10: Comparison of diffraction patterns obtained at room temperature and at 92 K, in the no-load condition (nominal holding stress of 8 MPa).

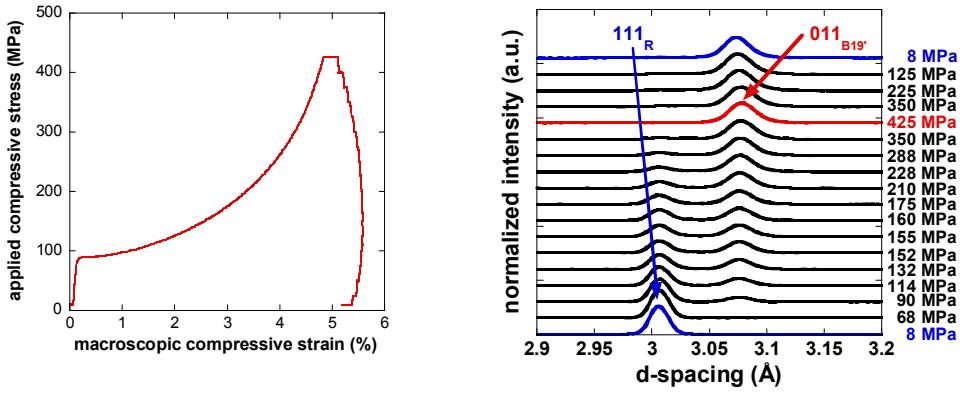

(a)

Figure 11: (a) Macroscopic stress-strain curve obtained *ex situ* at 92 K. (b) Stress-induced transformation from R-phase to B19' phase during loading at 92 K.

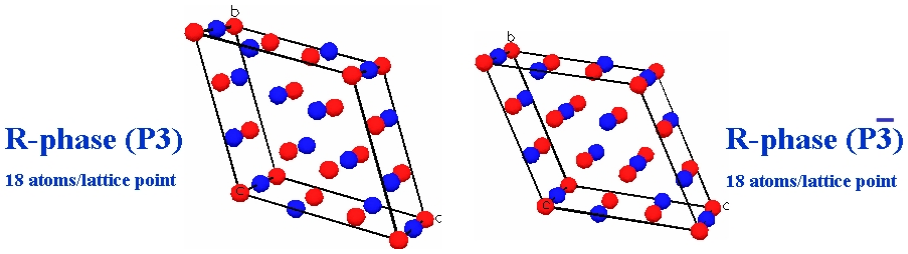

Figure 12: R-phase unit cell - *P*3 space group (left) and $P\bar{3}$ space group (right).

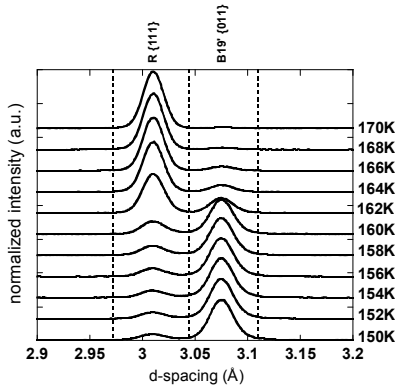

Figure 13: Constrained recovery of the R-phase from the B19' phase during heating of 5% strained $Ni_{46.8}Ti_{50}Fe_{3.2}$ from 150 K to 170 K.

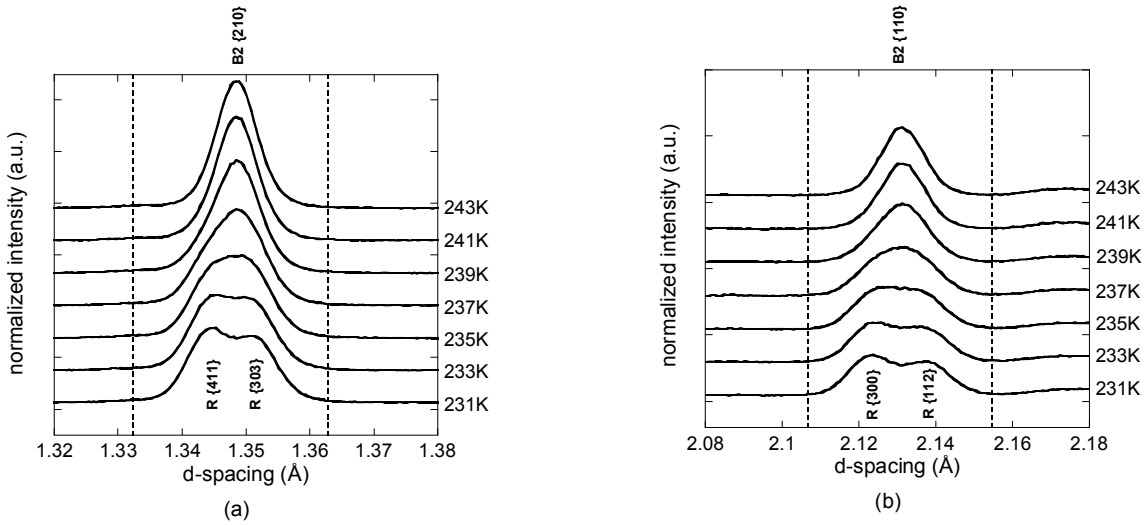

Figure 14: Constrained recovery of the B2 phase from the R-phase during heating of the 1% strained $Ni_{46.8}Ti_{50}Fe_{3.2}$ sample from 231 K to 243 K, (a) showing R{411} and R{303} combining to form B2{210} and (b) showing R{300} and R{112} combining to form B2{110}.

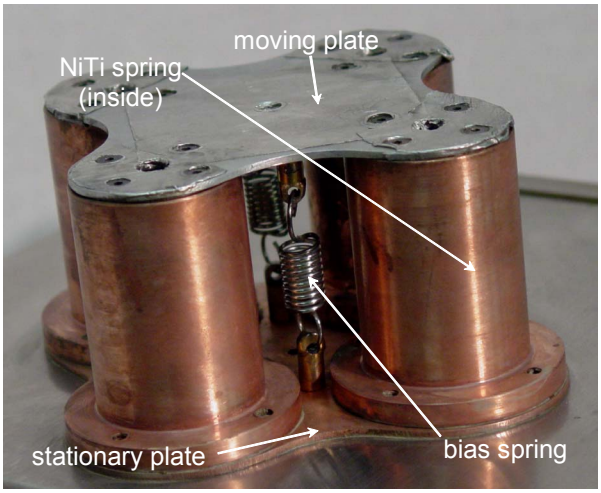

Figure 15: The first prototype of the switch that operated between an ice-water mixture and hot water.

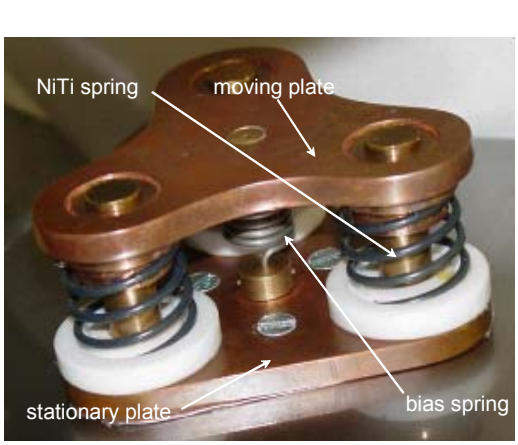

(b)

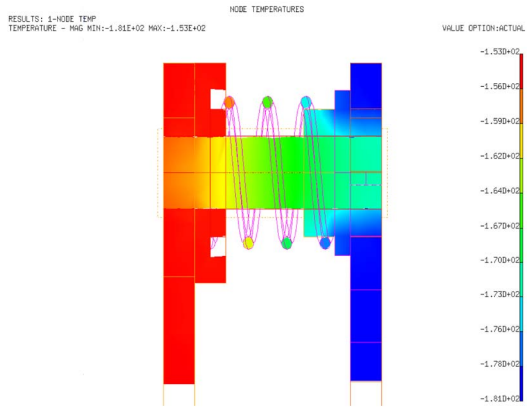

(a)

Figure 16: (a) The second prototype of the switch using NiTi elements in the form of helical springs for low-temperature actuation. (b) The temperature profile of the heat transfer cross-section obtained from steady state finite element analysis using I-DEAS.

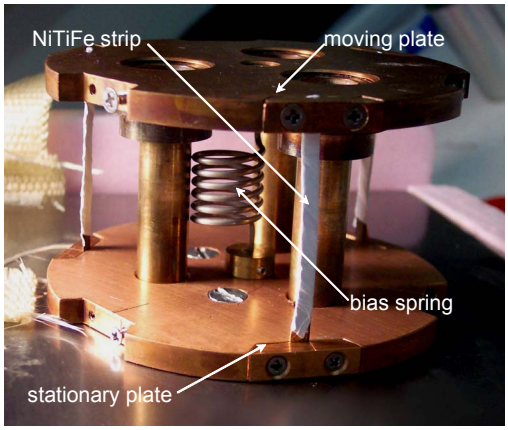

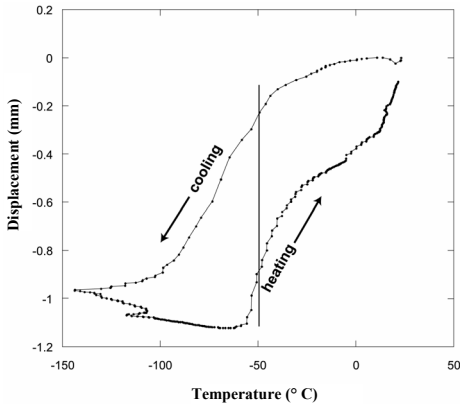

(a) (b)

Figure 17: (a) The third prototype of the switch using NiTiFe elements in the form of strips for low-temperature actuation. (b) Switch performance between 77 K and room temperature.

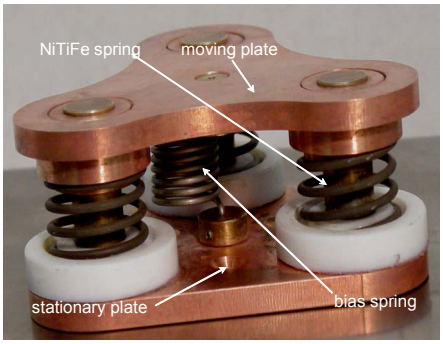

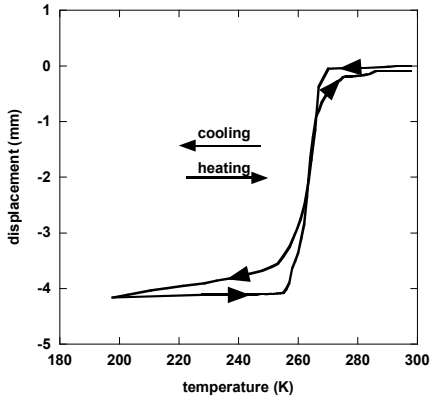

Figure 18: (a) The fourth prototype of the switch using NiTiFe elements in the form of helical springs for low-temperature actuation. (b) Switch performance between 200 K and room temperature.

Table 1: Ni:Ti ratios from the four regions in the binary Ni-Ti equilibrium phase diagram.

Region	Ni:Ti ratio (at%)
I	$x < 0.96$
II	$0.96 \leq x < 1.00$
III	$1.00 < x \leq 1.32$
IV	$x > 1.32$

Table 2: Nominal compositions of the arc-melted NiTiFe alloys.

Starting Material	Atomic percentage			Ni:Ti ratio
	Ti	Ni	Fe	
Slug	50	49	1	0.98
Slug	50	47	3	0.94
Slug	50	46	4	0.92
Slug	50	45	5	0.90
Slug	50	44	6	0.88
Slug	50.5	48.5	1	0.96
Slug	50	48	2	0.96
Slug	49.5	47.5	3	0.96
Slug	49	47	4	0.96
Slug	48.5	46.5	5	0.96
Slug	48.5	50.5	1	1.04
Slug	48	50	2	1.04
Slug	47.5	49.5	3	1.04
Slug	47	49	4	1.04
Slug	46.6	48.4	5	1.04
Slug	46	52	2	1.13
Slug	45.5	51.5	3	1.13
Slug	42.6	55.4	2	1.30
Slug	42.1	54.9	3	1.30
Slug	40	58	2	1.45
Slug	39.6	57.4	3	1.45
Slug	37.7	60.3	2	1.60
Slug	37.3	59.7	3	1.60
Slug	51	49	0	0.96
Slug	49	51	0	1.04
Slug	40.8	59.2	0	1.45
Slug	38.5	61.5	0	1.60
Powder	48.5	49	2.5	1.01
Powder	46.1	51	2.9	1.10
Powder	46	50.9	3.1	1.10
Powder	50.9	46	3.1	0.90
Powder	50	46.8	3.2	0.93
Powder	46.8	50	3.2	1.06
Powder	48.4	48.4	3.2	1.00
Powder	48.6	48	3.4	0.98

Genetic Engineering to Enhance Biological Hydrogen Production

W. Self, D. Ganyc, and L. Halvorsen
University of Central Florida

Research Period: June 2005 to September 2007

Abstract

Bacteria produce hydrogen by catalyzing the reduction of protons with electrons using enzymes termed hydrogenases. The reducing potential (electrons) for hydrogen production is primarily derived from the oxidation of sugars (and other carbon sources). Large quantities of plant biomass go unutilized as waste products in the agriculture community each year. These waste products are typically turned into the soil at which time endogenous soil bacteria catalyze the conversion of organic polymers such as cellulose (sugars) into organic acids, H_2 and CO_2. Much of this hydrogen is then converted to methane by methanogens, yielding a potent greenhouse gas. We aim to genetically engineer metabolic pathways in bacteria to enhance the hydrogen yield generated from oxidation of the polymers (sugars). Using engineered bacteria we can then couple fermentation of sugars derived from biomass to hydrogen that can be used to support our ever increasing energy needs. We will first demonstrate that genetic engineering of metabolic pathways can enhance hydrogen production in the model system of Escherichia coli. We will build upon this by implementing a similar strategy in a hydrogen producing microbe that can efficienty degrade plant biomass, Erwinia chrysanthemi. Optimization of high level expression of the formate hydrogenlyase (FHL) complex will be accomplished in order to determine whether this approach is feasible for long term hydrogen production from plant biomass. This will ensure that this engineered system will be useful in the near term for hydrogen production from plant biomass.

Introduction

Importance to NASA

Conversion of lignocellulosic biomass to hydrogen, and potentially other fuels, can be a vital part of NASA's goal of deep space exploration. Hydrogen is utilized as a primary fuel source on current space shuttle missions. Efficient production of hydrogen from a renewable source is a fundamental need for near term hydrogen production. More importantly hydrogen production will be key to long term space exploration. Recent NASA directives include mission to the Moon as well as Mars and one of the limitations to these missions is long-term fuel supplies. The ability to recharge fuel cells on exploration missions, such as the moon and mars, will require novel technologies to supply renewable sources of hydrogen for long space journeys and outposts on the moon and mars. These renewable sources can be achieved using biological sources. The development of biological catalysts that can convert any form of biomass to hydrogen (and other potential fuels such as ethanol) thus has great significance for long term exploration of space within the current NASA directives. It is unlikely that near term developments in this field would suffice to produce hydrogen in quantities that could fuel the launch of the space shuttle or similar vehicle. However, small scale biofermentors will be needed in space exploration – the next phase of NASA's mission in the 21st century.

Objectives

The tasks of this proposal are as follows:

Task 1. Genetically engineer an E. coli strain that will increase H2 production by increasing the protein components of formate hydrogenase lyase enzyme complex.

Task 2. Determine the increase in formate dehydrogenase levels (FDH-H), H2 production, and FHL activity in the engineered strains.

Task 3. Increase H_2 production (FHL activity) in *Erwinia* strains by introducing mutant transcriptional activators of the FHL regulon.

Task 4. Determine H_2 production by wild type and mutant (engineered) strains of *Erwinia chrysanthemi* when cultivated on plant biomass.

Background

Long Term Potential for Hydrogen Derived from Biomass

Recent surges in energy prices have focused attention on alternate sources of energy, with an emphasis being placed on ethanol and hydrogen. Ethanol use to reduce reliance on petroleum based fuels has efficacy as a short term solution (20), however hydrogen can be seen as a long term solution to our energy needs. Hydrogen production and storage is still far too costly to compete with fossil fuels, so novel technologies to produce, store and distribute hydrogen are at the forefront of this expanding field (36). Biological production of hydrogen, sometimes termed biohydrogen, could serve as one source of this clean and environmentally friendly fuel in the next century (2). Enzymes that catalyze the reduction of protons to form H_2 are classified into two major categories; NiFe and Fe only hydrogenases (35). Both CN and CO ligands are unusual cofactors that have been discovered in recent years, and the enzymes which catalyze the biosynthesis of these cofactors are products of the hyp gene cluster in E. coli (3, 22, 24). In addition to metal and organic cofactors within the hydrogenase subunits, physiological electron donors such as ferredoxin or selenium-dependent formate dehydrogenases also require extensive post-translational modification (insertion of FeS clusters) for activity. Maturation of these cofactors and the need for alternate amino acids such as selenocysteine are likely to be a key stumbling block behind any attempts to use metabolic engineering to increase any cell's capacity to produce hydrogen.

Escherichia Coli as a Model System for Hydrogenases

One of the best model systems for the study of NiFe hydrogenases is Escherichia coli. E. coli produces three separate hydrogenase enzymes, termed HYD1, HYD2 and HYD3 encoded by the hya, hyb, and hyc operons, respectively (27). Of these HYD3 is the predominant enzyme producing hydrogen in anaerobically grown cultures fermenting glucose or other sugars as a carbon source. HYD3 is part of the formate hydrogenlyase enzyme complex (FHL). FHL is composed of a selenium dependent formate dehydrogenase (FDH-H), electron carrier proteins (FeS cluster rich proteins) encoded by the hyc operon, and HYD3, encoded by hycE and hycG (26). In the absence of active FDH-H, no hydrogen is produced by the complex and HYD3 has not been shown to use alternate electron donors for hydrogen production. The FHL system has been used as a good model not only for defining the genetics and biochemistry for NiFe

hydrogenase maturation (3), but also for determining the means by which bacteria produce selenoproteins (32).

Selenium is Needed for E. Coli Hydrogen Production

Selenium is required in the form of selenocysteine in the three different formate dehydrogenase isoenzymes in E. coli (27). The incorporation of selenium into the polypeptide requires a specific elongation factor, SelB, which binds to a stem loop structure within the mRNA termed a SECIS element (8, 15) to facilitate read through of the UGA codon. A special tRNA, encoded by the selC gene, is first charged with serine and subsequently converted to selenocysteine by the product of the selA gene, selenocysteine synthase (15). Prior to this ligation to tRNA selenium must first be activated to selenophosphate by the selenophosphate synthetase (SelD, (7)). Since FDH-H requires selenocysteine for activity (9), each of these genes is required for FHL activity. Indeed these genes were discovered in a mutation screen to identify E. coli strains that lacked FDH-H activity, and all sel mutants do not produce hydrogen (15). Because of the complexity of the selenoprotein synthesis machinery, high level expression of selenoproteins is limited by the level of expression of these genes (1). Increased gene copy number by carrying $selAB^{+}$ and $selC^{+}$ on a low copy plasmid has been shown to improve expression of mammalian selenoenzymes in E. coli (1).

Coordinated Regulation Makes FHL System Attractive for Bioengineering

Although the FHL system is a large macromolecular complex with several metalloproteins, the transcriptional regulation of all the genes encoding components of the complex and enzymes involved in cofactor biosynthesis and insertion are under the control of the FhlA regulon (11). FhlA is a σ54-dependent transcriptional activator that responds to the cytosolic level of formate and binds to and activates transcription of hyc and hyp operon and the fdhF gene (encoding FDH-H). This global regulation is needed for concomitant upregulation of all the gene products needed for HYD3 synthesis in response to formate, the physiological electron donor for FHL complex. Mutant FhlA proteins have been described that eliminated formate dependence and also resulted in significantly increased expression of hyc operon (16, 30, 31). These mutants have large in-frame deletions within the N-terminal sensor domain which has been implicated in the binding of formate (12, 30). One of these mutant FhlA protein alleles, FhlA165, has also been shown to be capable of activating transcription of an apparently silent hydrogenase operon, hyf (29). A similar mutant activator has also been shown to be resistant to the anti-activator protein HycA, encoded by the first gene in the hyc operon (16). Although it is well established that increasing levels of HycA protein can reduce expression of hyc and fdhF gene, the molecular mechanism is not yet established. Nonetheless since FhlA is a single activator, one can envision the use of mutant activators that upregulate FHL complex as a straightforward means to increase the hydrogen production potential of E. coli.

Indeed a recent study demonstrated that by expressing FhlA from its native promoter in a medium copy vector significant increases in FHL activity and hydrogen production were achieved (37). Since mutant FhlA proteins have been described that can activate transcription of hyc operon to higher levels, we investigated whether these mutant FhlA alleles would improve on the level of hydrogen that can be generated from E. coli. To our surprise this combination revealed an interesting requirement for selenoprotein synthesis in transcriptional regulation of genes encoding components of the FHL system, and the results obtained highlight some of the limitations for metabolic engineering to increase hydrogenase levels.

Lignocellulosic Biomass as a Source of Hydrogen – Rationale for Choosing Erwinia

One of the key limitations in the conversion of lignocellulosic biomass to energy is the inability to degrade this recalcitrant biopolymer. Instead of trying to reconstitute the lignocellulosic enzymes for release of sugars, the aims of this research are to harness the natural biomass degrading capabilities from soft rot pathogens, while engineering these bacteria to produce useful fuels. For proof of principle we have chosen hydrogen as a fuel of interest, since certain strains of Erwinia have been reported to produce gas under anaerobic conditions. One key limitation of the E. coli model described above appears to be the efficient production of formate dehydrogenase, a selenoenzyme, which is the primary electron donor to the Ni-Fe hydrogenase in the FHL system (11, 19). Fortunately, many bacteria express a cysteine dependent FDH enzyme and so such limitation (i.e. the need for the unusual amino acid selenocysteine) may not exist in certain poorly studied organisms.

We sought out organisms that did not require selenium. One of these bacteria, Erwinia chrysanthemi, appears to express only a cysteine dependent FDH enzyme (based on genome sequence analysis). More importantly, this organism is well established to degrade plant biomass efficiently. E. chrysanthemi expresses cellulases and pectin lyases that can degrade plant biomass (10, 17). This bacteria is a also a close relative (gram negative enterobacteriaceae) of E. coli and also has been reported to produce hydrogen, although this property has never been explored for its biotechnological applications. In addition this strain can be easily manipulated at the genetic level (5, 6), allowing for efficient genetic engineering to alter flux through metabolic pathways. Based on genome sequence analysis (complete unannotated genome sequence is available from the Sanger center and the University of Wisconsin) we have identified the genes encoding hydrogenases (hyf, hyb) as well as a sulfur dependent formate dehydrogenase (FDH-H).

Experimental Details

Bacterial Strains and Plasmids

The bacterial strains and plasmids used in this study are listed in Table 1. All strains are derivatives of E. coli K-12. Erwinia chrysanthemi was obtained from ATCC and two strains were obtained from Dr. James Preston (University of Florida, Dept. of Microbiology and Cell Science).

Media, Growth Conditions and Materials

The medium used for growth of strains (E. coli and E. chrysanthemi) for all experiments is a modified Luria broth that consists of 1.0% tryptone, 0.5% yeast extract, 0.5% NaCl, 50 μM sodium molybdate, 50 μM nickel chloride, 36 μM ferrous sulfate and 0.5 μM sodium selenite. All cultures were grown in 12 x 75 mm screw cap test tubes under anaerobic conditions. Antibiotics, when necessary, were at the following concentrations: ampicillin, 100 μg/mL; chloramphenicol, 50 μg/mL (plates), 10 μg/mL (liquid); kanamycin, 50 μg/mL.

Biochemicals were purchased from Sigma Chemical Co. (St. Louis, MO) or Fisher Scientific (Atlanta, GA) and were of the highest grade available. Restriction endonucleases and DNA modifying enzymes were purchased from New England Biolabs (Boston, MA).

Construction of Plasmids Carrying E. Coli fhlA165 Allele

The fhlA165 mutant allele was first transferred from plasmid pWS165 (30), which is a pACYC184 derivative, to medium copy vector. This was accomplished by subcloning a 1.7 kb NheI-ClaI fragment into pWS3 (Self, W. T., Doctoral dissertation) at the same restriction sites, functionally replacing the wild type fhlA gene within this plasmid with the fhlA165 allele. The resulting plasmid (pWTS33) carries fhlA165 transcribed from its native promoter in a medium copy vector, and a chloramphenicol cassette (BsaAI-BstYI from pACYC184). Removal of the Cm^R cassette was accomplished by digesting pWTS33 with MscI to yield pDG1. This plasmid remains as medium copy vector since it still contains the rop region. To generate a high copy vector carrying fhlA165, pWTS33 was digested with MscI-BsaAI which removes both Cm^R and the rop region. This resulting plasmid was designated pDG2.

FHL Activities

FHL activities were determined using whole cells essentially as previously described (13), with minor modifications. Briefly, cells were cultured in modified L-broth with metal salts (see above) in tightly sealed 12 x 75 mm culture tubes. A 5% inoculum (overnight culture in same medium) was used and cells were harvested at mid-logarithmic phase (4-6 hours after inoculation) by centrifugation at 5000 x *g* and resuspended in buffer A (50 mM Na/K phosphate buffer, pH 5.8, 1.0 mM GSH and 100 µg/mL chloramphenicol). The optical density of the cell suspension was determined using an Agilent 8453 UV-visible spectrophotometer (Agilent Technologies, Palo Alto, CA). Cell suspensions were diluted to an optical density of 2.0 ($A_{600\ nm}$), and 2.0 mL of this suspension was transferred to a 128 mL septum-sealed glass bottle. These transfers were performed in a Coy Labs anaerobic chamber (Coy Labs, Grass Lake, MI) under an atmosphere of 99% nitrogen, 1% hydrogen. Formate was added via a gastight syringe to a final concentration of 40 mM, and hydrogen production was detected by gas chromatography.

Hydrogen Detection by Gas Chromatography

Hydrogen was detected using a Hewlett Packard 5890 series II gas chromatograph by thermal conductivity detector (TCD) after separation on a Molecular Sieve capillary column (19091-MS4, Agilent Technologies, Palo Alto, CA). The column was run at a flow rate of 3.0 mL/minute using argon as the carrier. Injector, column and detector temperatures were 80, 25, and 180 °C, respectively. A standard curve was generated using pure hydrogen.

Real Time RT-PCR Analysis

Samples (7 mL) were harvested during mid-logarithmic growth (4-6 hours) by centrifugation (5000 x *g*) and cells were subsequently washed with diethylpyrocarbonate (DEPC) treated phosphate buffered saline (PBS). Total RNA was isolated utilizing the ChargeSwitch Total RNA Cell kit (Invitrogen, Carlsbad, CA) and quantified by UV-visible spectrophotometry at 260 nm using an Agilent 8453 UV-visible spectrophotometer. cDNA was generated with 0.5 µg of purified RNA utilizing the iScript cDNA synthesis kit (BioRad, Hercules, CA).

Real-time PCR amplification was performed utilizing a BioRad i-Cycler. Oligonucleotides used in PCR reactions are listed in Table 1. Amplification of the transcripts for gapA were used as an internal standard (23). BioRad iQ SYBR green supermix was utilized for real-time PCR amplification with primers at a concentration of 200 nM each. cDNA was diluted 1:10 in sterile H_2O before addition to the reaction mix. Amplification of each of the targets was optimized and were as follows: fdhF - 95.0 °C for 3 min; subsequent 40 cycles of 95.0 °C for 10 s, 59.6 °C for

45 s; hycC - 95.0 °C for 3 min; subsequent 40 cycles of 95.0 °C for 10 s, 55.5 °C for 45 s; fhlA - 95.0 °C for 3 min; subsequent 40 cycles of 95.0 °C for 10 s, 54.9 °C for 45 s; gapA - 95.0 °C for 3 min; subsequent 40 cycles of 95.0 °C for 10 s, 58.3 °C for 45 s. Melt curve analysis was performed to confirm the presence of a single product in each case, and this was also confirmed by agarose gel electrophoresis. Efficiency of amplification for each target gene was calculated utilizing a 10-fold dilution series of control cDNA. Relative expression of each target gene was calculated according to the Pfaffl method described previously (21).

Reporter Gene Fusion Studies

Expression of hyc operon was determined using a hyc-lacZ fusion carried by the plasmid pHYC1 (Table 1). This construct contains a hyc promoter fusion that has been previously described (28). ß-Galactosidase activity (expressed as nmol min^{-1} mg^{-1} cell protein) was determined with chloroform-sodium dodecyl sulfate-permeabilized cells as described by Miller (1972), using o-nitrophenyl-ß-D-galactopyranoside (ONPG) as substrate. Cells were cultured in modified Luria broth with metal salts under anaerobic conditions and harvested in late exponential phase.

^{75}Se Labeling Studies

For identification of selenoproteins 10 µCi of ^{75}Se (University of Missouri, Columbia, Missouri), in the form of sodium selenite (50 nM), was added to each 9 mL culture (12 x 75 mm test tubes). Cells were harvested by centrifugation for 5 minutes at 5000 x *g* , washed once with buffer A (50 mM tricine, pH 7.5, 0.1 mM benzamidine, 1.0 mM dithiothreitol), and resuspended in buffer A. Cells were lysed by sonication using a sonic dismembranator model 100 (Fisher Scientific, Atlanta, GA) for 10 seconds at a power output of 12 watts, and the resultant crude cell extracts were clarified by centrifugation at 13,500 x *g* for 10 minutes at 4 °C. Protein concentration was determined by Bradford assay (4) using bovine serum albumin (Pierce, Rockford, IL) as a standard. Selenoproteins were identified by separating cell extracts using SDS-PAGE, and radioisotope-labeled proteins were detected by phosphorimage analysis (Molecular Dynamics).

Experimental Results and Discussion

Increased Gene Dosage of fhlA165 Results in High Levels of hyc and fdhF mRNA

We first analyzed the changes in expression of hyc-lacZ when fhlA165 was carried in a wild type strain by either a medium copy (pBR322 type) vector or a high copy vector (lacking the rop region of the plasmid). These results are summarized in Table 2. The native FhlA protein, expressed from chromosomal fhlA gene, activated expression of hyc promoter to give about 900 units of β-galactosidase activity. With plasmid pDG1, the expression of hyc-lacZ increased by 50% to give almost 1500 units, and further increased nearly three fold to 2500 units when pDG2 was present. This shows that expression of hyc operon can be increased as much as three fold by increasing the gene dosage of the fhlA165 mutant allele driven from its native promoter.

To determine whether hyc expression increased with this mutant allele present in a hycA mutant, we again determined expression using a hyc-lacZ fusion. Mutation in hycA alone increased expression by about 50% (Table 2). This is expected based on earlier findings that HycA acts as an anti-activator to counteract the FhlA protein (26). In stark contrast the fhlA165

allele was unable to activate hyc-lacZ even to parent levels in the hycA mutant strain. This result was quite unexpected, as it would be anticipated based on current knowledge of the regulation of the genes encoding FHL complex that these strains would have exhibit far higher levels of hyc-lacZ expression than even the parent MC4100 strain. Although we were successful in increasing the level of FHL in the wild type strain, further experiments were carried out to try and identify the cause of this decrease in hyc expression in the hycA mutant strain.

Presence of FhlA165 Mutant Allele Nearly Eliminates FHL Activity in a hycA Mutant Strain

To determine whether expression of FhlA165 in a hycA mutant strain would affect hydrogen production, we carried out FHL specific activity assays on these strains and these results are shown in Table 3. As expected, HD701 produced higher FHL activity than wild type MC4100. Likewise MC4100 carrying pDG1 or pDG2 also exhibited higher levels of FHL activity, more than 50% higher with fhlA165 present via a high copy plasmid. However formate dependent hydrogen formation was nearly abolished in a hycA mutant carrying either pDG1 or pDG2. Although this corroborates the data obtained using hyc-lacZ fusions, the reason for this reduction in FHL complex synthesis was unclear. Given that the FHL complex require a selenium dependent FDH-H and that components of the selenoprotein synthesis pathway have been shown to be limiting for the overexpression of selenoenzymes (1), we investigated whether limitations in selenoprotein synthesis might be occurring under these conditions.

Expression of Mutant Allele FhlA165 Reduces FDH-H Levels in hycA Mutant Strain

To determine if the presence of FhlA165 in a hycA mutant is affecting selenoprotein synthesis, we followed incorporation of radioactive selenium into formate dehydrogenases. In cells grown anaerobically in modified Luria broth (see materials and methods for details) containing glucose as a carbon source the only selenoprotein that is expressed is FDH-H (27). We quantified the level of FDH-H after separation of cell extracts using SDS-PAGE and autoradiography. The level of FDH-H increased significantly in a wild type strain carrying fhlA165 either from pDG1 or pDG2 (Figure 1). Based on phosphorimage analysis the level of FDH-H was approximately two-fold higher. A slightly higher level of FDH-H was produced in hycA mutant (HD701), but was significantly reduced to nearly undetectable levels when pDG1 or pDG2 are present (Figure 1). This suggested that the presence of FhlA165 in a hycA mutant may be reducing the ability of the cell to produce selenoproteins.

fdhF mRNA Levels are Significantly Reduced When Activated by FhlA165 in a hycA Mutant

We utilized semi-quantitative real time RT-PCR to determine the level of both hyc and fdhF mRNA in both wild type and hycA mutant strains. In the wild type strain the level of fdhF mRNA increased by more than 18-fold when FhlA165 was produced from pDG1, and by more than 28-fold from pDG2 (Figure 2A). This clearly shows that high gene dosage does indeed improve the capacity of the cell to produce these transcripts that encode the FHL components. The absence of the anti-activator protein HycA (HD701) also increased fdhF mRNA levels significantly, but when FhlA165 was present the level of this mRNA decreased to nearly undetectable levels (Figure 2A).

A similar pattern of regulation was observed when hyc mRNA levels were analyzed (Figure 2B). The level of hyc mRNA increased as high as 80-fold in the wild type strain with high copy plasmid carrying the fhlA165 allele. It should be noted that even though this high level of mRNA can be made, under these same conditions only a three-fold increase in active FHL complex is

formed (Table 2). Taken together these data suggest that limitations in formation of NiFe cluster, incorporation of CO and CN ligands, and/or synthesis of selenoenzyme FDH-H is limiting the synthesis of FHL complex. The absence of the HycA anti-activator increased hyc mRNA to 16-fold higher levels, but this was significantly reduced with FhlA165 present. The level of hyc mRNA was still higher than in MC4100 (Figure 2B) demonstrating that the apparent lack of FHL complex produced under these conditions indeed lies in production of FDH-H and not HYD3. These results led us to determine whether increases in the cell's capacity to produce active selenoproteins could lead to an increase in fdhF mRNA levels and subsequent synthesis of active FDH-H.

Increasing the Capacity to Make Seleno Proteins Reverses the Inhibitory Action of FhlA165 in a hycA Mutant Strain

Increases in copy number of selAB$^+$ and selC$^+$ have been shown to improve the efficiency of translating mRNAs encoding selenoproteins in E. coli (1). We evaluated the impact of having the plasmid pSUABC on FDH-H synthesis, again using radiolabeled selenium. The presence of pSUABC alone in MC4100 increased FDH-H levels two-fold (Figure 3). The combination of pSUABC and pDG1 or pDG2 also increased FDH-H levels as high as four-fold based on phosphorimage analysis. In contrast the level of FDH-H was increased by only 50% when pSUABC was carried in the hycA mutant strain, a somewhat surprising result. Nonetheless the presence of selAB$^+$ and selC$^+$ via pSUABC did restore the synthesis of FDH-H in HD701 carrying pDG1 or pDG2 (Figure 3). This clearly demonstrates that the lack of expression and production of FHL components, when FhlA165 is used as the activator in a hycA mutant, is tied to selenoprotein synthesis.

FHL activity assays also confirmed that the presence of pSUABC was able to increase FHL complex formation in HD701 carrying pDG1 or pDG2 (Table 4). Although the level of FDH-H has increased nearly 4-fold in the wild type strain carrying pSUABC and pDG2, the level of FHL activity is not significantly higher than in the absence of pSUABC (Table 2). This indicates that synthesis of FDH-H is not limiting in a wild type strain but that a significant physiological change has occurred when HycA is not longer present (Table 2).

We also confirmed that the level of hyc and fdhF mRNA concurrently increased under these conditions by real time RT-PCR (Figure 4). The level of both fdhF and hyc mRNA were comparable in both MC4100 and HD701 when activated by FhlA165. However the highest gene dosage of fhlA165 (pDG2) did cause a lower level of mRNA in both cases relative to medium copy plasmid (pDG1, Figure 4). Although the results in Figures 3 and 4 clearly show that increasing selenoprotein synthesis capacity can 'complement' for the conditions imposed in our experiment, the molecular mechanism for this result was still not resolved. Since it seemed that both hyc and fdhF were coordinately affected, we decided to investigate whether this phenomenon might be due to a decrease in expression of fhlA (and fhlA165).

fhlA Gene Expression is Greatly Reduced by the Presence of FhlA165 in hycA Mutant

Although there is no evidence that expression of fhlA is regulated at the transcriptional level, we determined whether the observed effects on FHL complex production might be due to changes in the synthesis of fhlA or fhlA165. For this analysis oligonucleotides that amplify both chromosomally derived fhlA mRNA and plasmid derived fhlA165 transcripts were used and the results are summarized in Figure 5. As expected the level of mRNA encoding FhlA proteins was elevated if pDG1 or pDG2 is present in MC4100 (Figure 5). This is likely due solely to gene dosage as pDG2 is equivalent to pUC19-based vectors, thus exhibiting as much as a 1000-fold

increase in mRNA. These results also show that increased gene dosage indeed can increase these transcripts, likely removing the possibility that expression of fhlA requires an as yet unidentified activator beyond σ-70 RNA polymerase. In contrast, the level of mRNAs encoding FhlA proteins drastically decreased in HD701 if pDG1 or pDG2 were present. This result suggests that the entire phenotypic change to shutdown FHL complex formation is tied to lack of expression of fhlA and fhlA165. In support of this hypothesis the presence of pSUABC restored fhlA expression in HD701, and thus the apparent need for increased selenoprotein synthesis manifests itself in the regulation of fhlA gene transcription or perhaps mRNA stability.

Identification and Analysis of Erwinia Chrysanthemi Formate Hydrogen Lyase Complex

Erwinia chrysanthemi is known to produce hydrogen gas under fermentative conditions. BLAST alignment of E. coli FHL complex genes reveled a cluster of homologues genes located between residues 1,670,761 and 1,688,542 on the E. chrysanthemi chromosome. All of the open reading frames (ORFs) in this region were identified and translated into their corresponding amino acid sequences. The protein sequences were blasted against all non-redundant GenBank CDS translations, PDB, SwissProt, PIR, and PRF (excluding environmental samples from WGS projects) using the NCBI blastp 2.2.17 [41, 42] algorithm. Gene names were assigned based on their E. coli K-12 homologs having the highest bit score (Table 1). The function of the query protein was assigned based on the closest homologues protein, according to score, in the results set regardless of its species of origin (Table 1).

This cluster of genes apparently codes for all the necessary components of an FHL complex likely represents the E. chrysanthemi version of the E. coli formate regulon (Figure 6). Notably absent is the presence of a gene coding for a HycA-like protein which would serve to down-regulate transcription of the other genes. There is also the absence of a gene encoding a selenocysteine containing formate dehydrogenase-like enzyme. The E. chrysanthemi counterpart appears to a cysteine based dehydrogenase and is clustered in cis with the other genes of the regulon rather than in trans (Figure 6).

Conclusions

Our manipulations with the regulatory systems of the FHL complex have inadvertently revealed a link between selenoprotein synthesis and the regulation of the FhlA transcriptional activator. It would appear that E. coli has some type of sensory mechanism that monitors the intracellular levels of available selenocysteine. This mechanism is in turn able to modulate the amount of selenocysteine requiring enzymes being transcribed by directly affecting the expression of the fhlA protein. Based on past research we fully expected the highest amount of FHL complex activity with the combined expression of fhlA165 along with a hycA mutant background, we instead observed just the opposite. The combination of these two mutations results in a phenotype having no detectable FHL complex activity. However, the fact that increasing the capacity for selenoenzyme synthesis, by transforming into these same cells the pSUABC plasmid, fully recovers this phenotype provides strong evidence that selenoprotein synthesis is involved.

It is known that if selenium is limiting there will be insufficient charged Sec-tRNA^{Sec} available for translating ribosomes thus resulting in premature termination of protein synthesis [cite 15]. However, if the demand for charged Sec-tRNA^{Sec} was so great that the normal pools of Sec-tRNA^{Sec} and SelB were woefully inadequate, the same situation would occur even if selenium were not limiting. An excess of selenoprotein mRNA does inhibit selenoprotein synthesis by overwhelming the necessary trans-acting factors [26, 43]. Since the efficiency of Sec insertion in

E. coli is approximately only 4% compared to the other amino acids (34), it is reasonable to assume that the glut of fdhF mRNA would shut down selenoprotein synthesis. This does not explain the near total lack of selenated-tRNAs and non-specific incorporation into other proteins. We propose that this is due to general inhibition of protein synthesis. This is evidenced by the fact that the fhlA165^{+} ΔhycA strains grow at less than half the rate of their counterparts (see grow curve). In mammals, mRNAs are rapidly degraded by nonsense mediated decay (NMD), but despite the fact that many mammalian selenoprotein mRNAs should make good substrates for NMD (33), many show resistance to NMD even if selenium is limiting (14). Because of the similarities in the mechanism of selenoprotein biosynthesis across all three domains of life, it is not unlikely that selenoprotein mRNAs might resist NMD mechanisms in bacteria. So the problem of excess selenoprotein mRNA is exacerbated by the fact that it probably degrades much slower than other mRNAs. This excess of mRNA poses a significant problem; as ribosomes attempt to translate them they will stall at the UGA codon without the proper complex of sec-tRNA^{Sec} and SelB bound to the SECIS. Ribosomes are known to undergo a long translational pause once the UGA/stop codon arrives in the A site (34) even when a complete sec-tRNA^{Sec} and SelB complex is present. If one or more elements are missing, the ribosome could be stalled for a long time, during which it is not making other cellular proteins. Eventually though, despite these translational inefficiencies, the stalled ribosome will dissociate from the selenoprotein mRNA. The product then, in this case fdhF, is an incomplete protein whose translation was prematurely truncated at the point at which selenocysteine should have been added to the chain. In is very unlikely that a complex metalloenzyme would fold at all correctly under these circumstances. A build up of these misfolded proteins is almost certain to induce a stress response. This may explain why we observe an up regulation of genes to combat oxidative stress in these cells when, because they are fermenting and not respiring, there shouldn't be ROS or RNS to combat. The increase in katG transcription is part of a more general stress response triggered by misfolded proteins. However, a run away buildup of unfinished peptides due to an unregulated constitutive activator would be expected to kill the cells, yet they still grow, if not very well.

The mRNA levels of fhlA/fhlA165 is decreased under these conditions, and this regulation lies at the heart of the problem. The mechanism by which fhlA mRNA expression is being reduced is not clear but it is most likely caused by the oxidative stress response. This is based on increased levels of both katG and oxyS mRNA (data not shown) when pDG1 or pDG2 is present in a hycA mutant. oxyS, a small RNA whose transcription is also controlled by OxyR, is induced under oxidative stress, and it is well established that oxyS is an interfering RNA that is known to interact with and sequester the activity of fhlA by forming a so-called "kissing complex" of paired complimentary regions [47-49]. However, this effect occurs post translationally and so cannot account for the down regulation of fhlA transcription. It may be that the production of selenoproteins is suppressed during a stress response. Since production of fhlA is necessary for the transcription of fdhF, it would be the natural target for such a mechanism. The fact that OxyS, itself a stress response protein, is know to sequester lends support to this hypothesis.

Further work is needed to complete the engineering of Erwinia strains for hydrogen production. Funding for this continuation of the studies begun here will be sought from a variety of sources including NSF and DOE in programs focused on biomass and energy research.

Appendix A – Data Tables and Figures

Table 1. E. coli strains, plasmids and oligonucleotides used in this study

Strains, plasmids or oligonucleotides	Relevant genotype or sequence	Source
Bacterial Strains		
MC4100	wild type	CGSC #6152
HD701	ΔhycA	August Böck (18, 26)
PMD23	ΔhypF	K. T. Shanmugam
Plasmids		
pHYC1	pBR322 – hycP1-lacZ	(28)
pWS165	pACYC184 – fhlA165 Cm^R	(30)
pWTS33	pBR322 – fhlA165 Cm^R	This study
pDG1	pWTS33 – fhlA165 Cm^S	This study
pDG2	pDG1 – Δrop region (high copy)	This study
pSUABC	pACYC184 – $selAB^+$ $selC^+$	Elias Arnér (1)
Oligonucleotides		
gapA-fwd	5'-TATGACTGGTCCGTCTAAAGACAA-3'	(23)
gapA-rev	5'-GGTTTTCTGAGTAGCGGTAGTAGC-3'	(23)
fdhF-fwd	5'-GCTCGAACATCGCGCTGTTG-3'	This study
fdhF-rev	5'-GCCGCCTGACGAATCTCACT-3'	This study
hycC-fwd	5'-CTCCATCGCCATGTTAGTCG-3'	This study
hycC-rev	5'-GAGAACGTGACGCCATAGA-3'	This study
fhlA-fwd	5'-TGGAGTTACAGCCGAAGTTG-3'	This study
fhlA-rev	5'-ACGTTCAGGCGGTAATAGAG-3'	This study

Table 2. Expression of Φ(hycP1-lacZ) in the presence of fhlA165 allele carried on medium or high copy vector

Strain	Relevant genotype	β-galactosidase activity
MC4100	wild type	920
MC4100 pDG1	pfhlA165 (medium)	1460
MC4100 pDG2	pfhlA165 (high)	2500
HD701	ΔhycA	1430
HD701 pDG1	ΔhycA pfhlA165 (medium)	510
HD701 pDG2	ΔhycA pfhlA165 (high)	510

All strains carry Φ(hycP1-lacZ) via pHYC1 (28). Cultures were grown in modified Luria broth with supplemental metal salts (see methods) under anaerobic conditions. β-galactosidase activity is expressed as nmol min^{-1} mg^{-1} cell protein.

Table 3. FHL activities of E. coli strains with fhlA165 carried in either medium or high copy vector

Strain	Relevant Genotype	FHL Activity*
MC4100	wild type	2290 ± 170
MC4100 (pDG1)	fhlA165^{+} (medium)	2970 ± 662
MC4100 (pDG2)	fhlA165^{+} (high)	3260 ± 310
HD701	hycA	2790 ± 190
HD701 (pDG1)	hycA fhlA165^{+} (medium)	60 ± 10
HD701 (pDG2)	hycA fhlA165^{+} (high)	ND

*FHL activities are given as nmol min^{-1} mg^{-1} cell protein. ND = activity not detectable. Copy number of plasmid carrying fhlA165 allele is indicated within the relevant genotype.

Table 4. FHL activities of E. coli strains carrying fhlA165 as well as pSUABC (selAB$^+$selC$^+$)

Strain	Relevant Genotype	FHL Activity*
MC4100 pSUABC	selAB$^+$ selC$^+$	2020 ± 419
MC4100 pSUABC / pDG1	fhlA165$^+$ (medium) selAB$^+$ selC$^+$ (25)	3230 + 82
MC4100 pSUABC/pDG2	fhlA165$^+$ (high) selAB$^+$ selC$^+$ (25)	3300 ± 240
HD701 pSUABC	ΔhycA selAB$^+$ selC$^+$	2190 ± 410
HD701 (pDG1) pSUABC	hycA fhlA165$^+$ (medium) selAB$^+$ selC$^+$ (25)	2890 ± 760
HD701 (pDG2) pSUABC	hycA fhlA165$^+$ (high) selAB$^+$ selC$^+$ (25)	3069 ± 180

*FHL activities are given as nmol min^{-1} mg^{-1} cell protein. Copy number of plasmid carrying fhlA165 or sel genes is indicated within the relevant genotype.

Table 1 Analysis of the E. chrysanthemi FHL complex genes by sequence homology

Size (residues)	Closest *E. coli K-12* homologues			Closest homologues		
	Gene name	Percent Identity	Description	Organism	Percent Identity	Description
726	*fhlA*	51%	DNA-binding transcriptional activator	*Yersinia frederiksenii*	61%	transcriptional regulator containing GAF, AAA-type ATPase, and DNA binding domains
723	*fdhF*	67%	formate dehydrogenase-H, selenopolypeptide subunit	*Yersinia frederiksenii*	85%	anaerobic dehydrogenase
181	*hydN*	50%	fused predicted oxidoreductase: FeS binding subunit/NAD/FAD-binding subunit	*Yersinia enterocolitica subsp. Enterocolitica*	70%	4Fe-4S ferrodoxin
163	*yieF*	27%	chromate reductase, Class I, flavoprotein	*Marinomonas sp.*	40%	putative transcriptional regulator
165	*hycI*	62%	protease involved in processing C-terminal end of HycE	*Yersinia bercovieri*	67%	Ni,Fe-hydrogenase maturation factor
133	*hyfJ*	53%	predicted processing element hydrogenase 4	*Yersinia enterocolitica subsp. enterocolitica*	66%	hydrogenase-4 component J
264	*hyfI*	69%	hydrogenase 4, Fe-S subunit	*Yersinia frederiksenii*	78%	Ni,Fe-hydrogenase III small subunit
190	*hycF*	53%	formate hydrogen lyase complex iron-sulfur protein	*Yersinia intermedia*	71%	formate hydrogenlyase subunit 6 / NADH:ubiquinone oxidoreductase 23 kD subunit (chain I)
490	*hyfG*	77%	hydrogenase 4, subunit	*Yersinia frederiksenii*	82%	Ni,Fe-hydrogenase III large subunit
559	*hyfF*	72%	hydrogenase 4, membrane subunit	*Yersinia enterocolitica subsp. Enterocolitica*	72%	hydrogenase-4 component F
217	*hyfE*	63%	hydrogenase 4, membrane subunit	*Yersinia intermedia*	78%	hydrogenase 4 membrane component E
480	*hyfD*	70%	hydrogenase 4, membrane subunit	*Yersinia bercovieri*	77%	NADH:ubiquinone oxidoreductase subunit 5 (chain L) / Multisubunit Na+/H+ antiporter, MnhA subunit
316	*hyfC*	65%	hydrogenase 4, membrane subunit	*Yersinia intermedia*	74%	formate hydrogenlyase subunit 4
680	*hyfB*	60%	hydrogenase 4, membrane subunit	*Yersinia frederikseni*	74%	formate hydrogenlyase subunit 3 / Multisubunit Na+/H+ antiporter, MnhD subunit
227	*hyfA*	51%	hydrogenase 4, 4Fe-4S subunit	*Yersinia mollaretii*	71%	Fe-S cluster-containing hydrogenase components

Figure Legend.

Figure 1. Analysis of FDH-H levels using ^{75}Se labeling. Wild type and hycA mutant strains were cultured in a modified Luria broth supplemented with metal salts under anaerobic conditions. The presence or plasmids pDG1 or pDG2 is indicated above the appropriate lane of the gel. Synthesis of FDH-H was followed under these growth conditions by the addition of 10 μCi of selenium in the form of selenite to each culture. - μg of cell extract was separated using 12% SDS-PAGE followed by drying and exposing the gel to phosphoimage analysis.

Figure 2. Real time RT-PCR analysis of fdhF and hyc mRNA levels. Strains were cultivated in modified Luria broth under anaerobic conditions with glucose as a carbon source. The fold changes in mRNA levels were calculated using a previously described method (21). Efficiency of amplification for each target mRNA was quantified by serial dilution of control cDNA. gapA was used as an internal standard using previously described oligonucleotides (23).

Figure 3. Increase in selAB and selC gene copy number rescues FDH-H synthesis in HD701 carrying pDG1 or pDG2. Analysis of FDH-H levels in anaerobic cultures as indicated in Figure 1. - μg of protein from clarified cell extracts was loaded in each lane. The presence or absence of pSUABC is indicated by a +/- symbol below the phophorimage.

Figure 4. fdhF and hyc mRNA levels increase in response to the presence of pSUABC. Strains were cultivated in modified Luria broth under anaerobic conditions with glucose as a carbon source. Semi-quantitative mRNA analysis was carried out as described in Figure 2 and in Materials and Methods section.

Figure 5. Evidence that transcriptional regulation of fhlA is tied to selenoprotein synthesis. Relative changes in fhlA mRNA were determined using gapA as an internal standard as described in Figure 1.

Figure 6. Cluster of genes apparently responsible for hydrogen production in Erwinia chrysanthemi. Genes are annotated as described in Table 5.

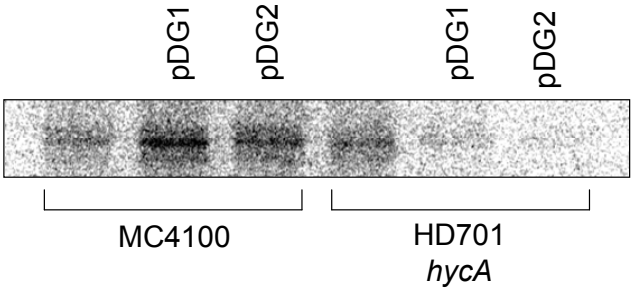

Figure 1

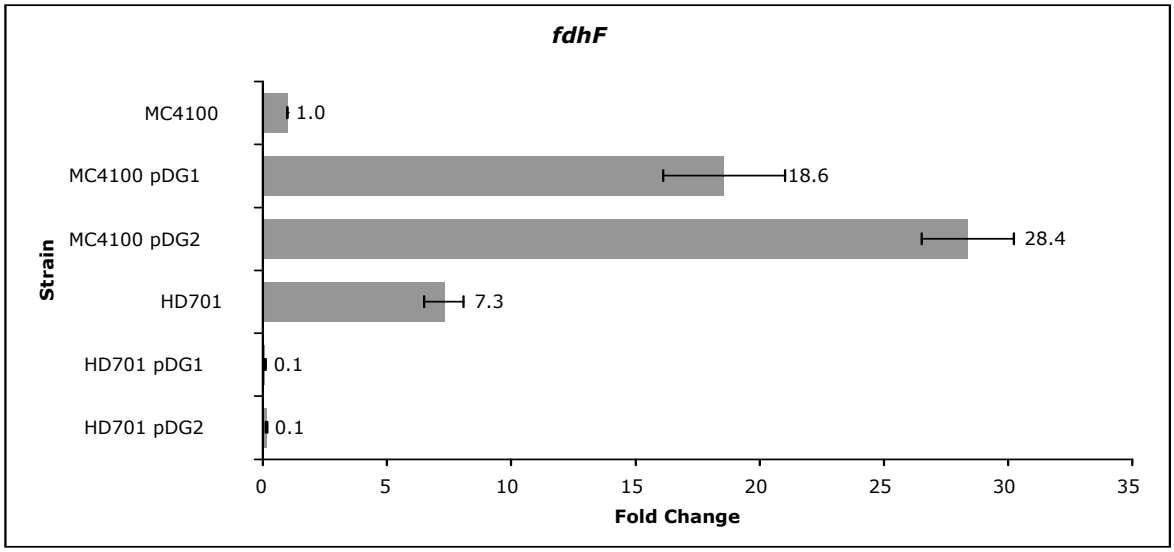
fdhF
MC4100
MC4100 pDG1
MC4100 pDG2
HD701
HD701 pDG1
HD701 pDG2
Strain
1.0
18.6
28.4
7.3
0.1
0.1
0
5
10
15
20
25
30
35
Fold Change

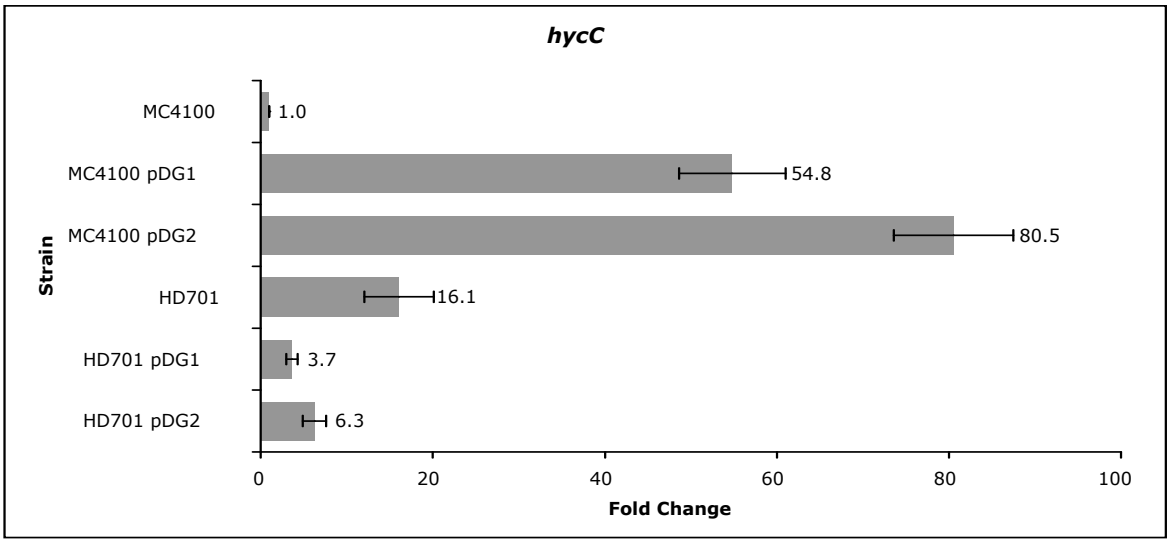
hycC
MC4100
MC4100 pDG1
MC4100 pDG2
HD701
HD701 pDG1
HD701 pDG2
Strain
1.0
54.8
80.5
16.1
3.7
6.3
0
20
40
60
80
100
Fold Change

Figure 2

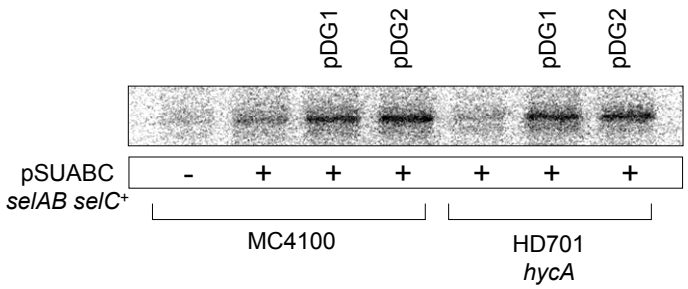

Figure 3

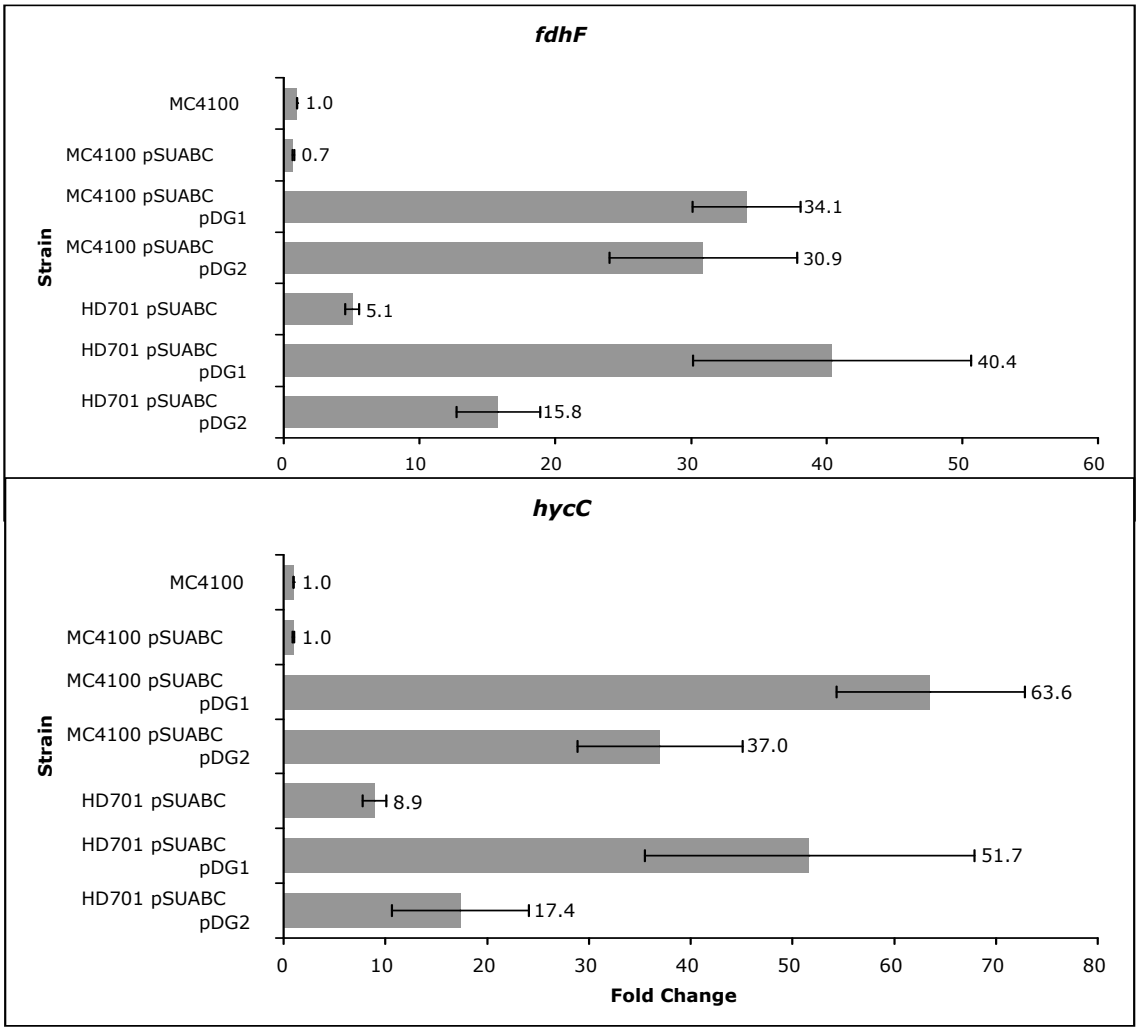
fdhF
MC4100
MC4100 pSUABC
MC4100 pSUABC pDG1
MC4100 pSUABC pDG2
HD701 pSUABC
HD701 pSUABC pDG1
HD701 pSUABC pDG2
Strain
1.0
0.7
34.1
30.9
5.1
40.4
15.8
0
10
20
30
40
50
60
hycC
MC4100
MC4100 pSUABC
MC4100 pSUABC pDG1
MC4100 pSUABC pDG2
HD701 pSUABC
HD701 pSUABC pDG1
HD701 pSUABC pDG2
Strain
1.0
1.0
63.6
37.0
8.9
51.7
17.4
0
10
20
30
40
50
60
70
80
Fold Change

Figure 4

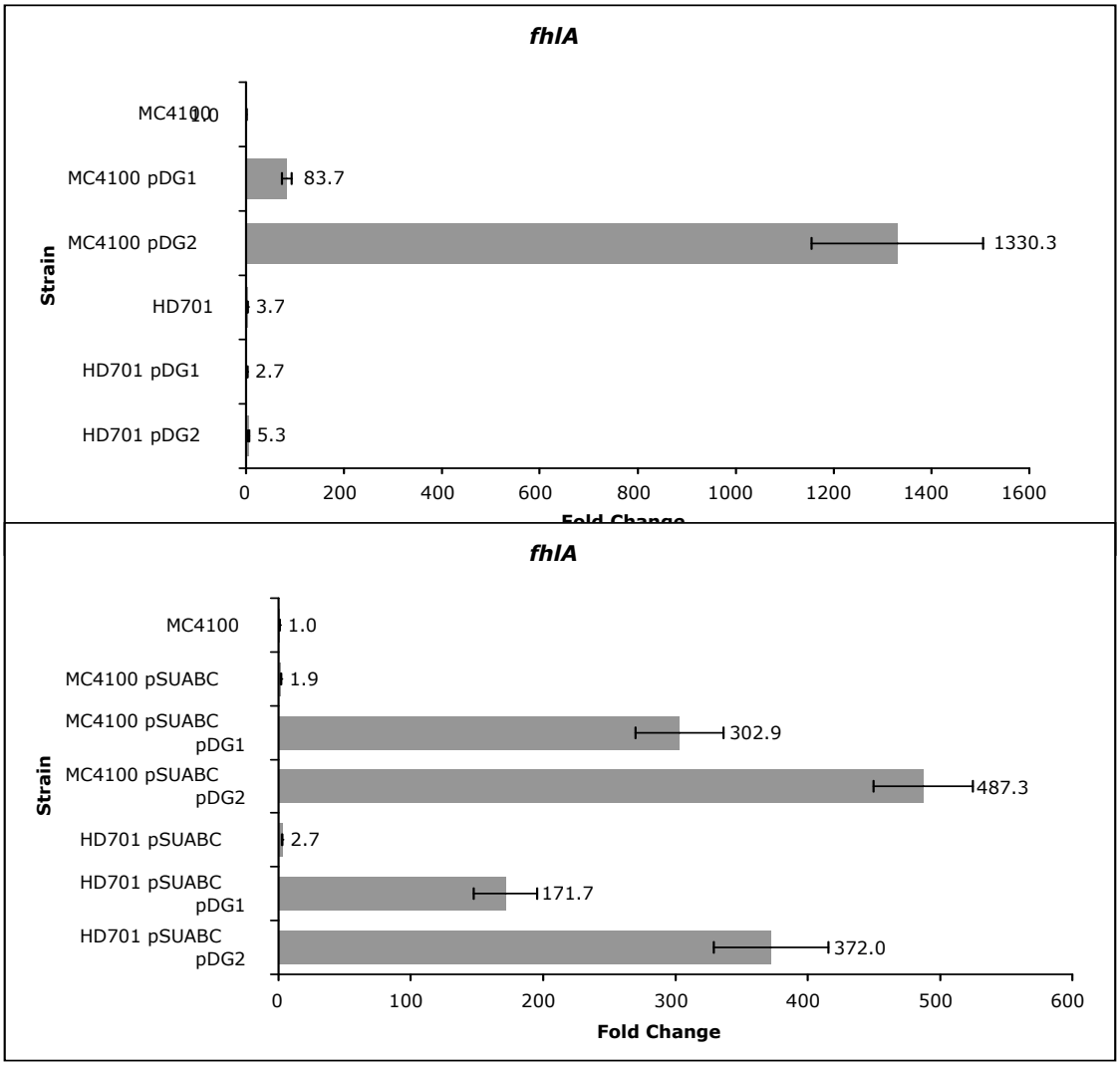
fhlA
MC4100
MC4100 pDG1
MC4100 pDG2
HD701
HD701 pDG1
HD701 pDG2
1.0
83.7
1330.3
3.7
2.7
5.3
Strain
0
200
400
600
800
1000
1200
1400
1600
fhlA
MC4100
MC4100 pSUABC
MC4100 pSUABC pDG1
MC4100 pSUABC pDG2
HD701 pSUABC
HD701 pSUABC pDG1
HD701 pSUABC pDG2
1.0
1.9
302.9
487.3
2.7
171.7
372.0
Strain
0
100
200
300
400
500
600
Fold Change

Figure 5

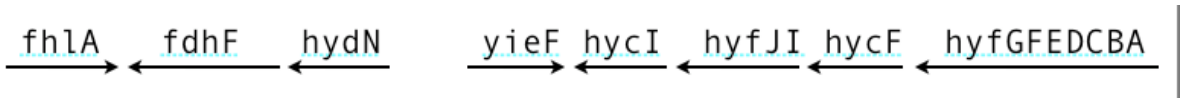

Figure 6

References

1. Arner, E. S., H. Sarioglu, F. Lottspeich, A. Holmgren, and A. Bock. 1999. High-level expression in Escherichia coli of selenocysteine-containing rat thioredoxin reductase utilizing gene fusions with engineered bacterial-type SECIS elements and co-expression with the selA, selB and selC genes. J Mol Biol 292:1003-16.
2. Benemann, J. 1996. Hydrogen biotechnology: progress and prospects. Nat Biotechnol 14:1101-3.
3. Blokesch, M., A. Paschos, E. Theodoratou, A. Bauer, M. Hube, S. Huth, and A. Bock. 2002. Metal insertion into NiFe-hydrogenases. Biochem Soc Trans 30:674-80.
4. Bradford, M. M. 1976. A rapid and sensitive method for the quantitation of microgram quantities of protein utilizing the principle of protein-dye binding. Anal Biochem 72:248-54.
5. Chatterjee, A. K. 1980. Acceptance by Erwinia spp. of R plasmid R68.45 and its ability to mobilize the chromosome of Erwinia chrysanthemi. J Bacteriol 142:111-9.
6. Chatterjee, A. K., and M. A. Brown. 1980. Generalized transduction in the enterobacterial phytopathogen Erwinia chrysanthemi. J Bacteriol 143:1444-9.
7. Ehrenreich, A., K. Forchhammer, P. Tormay, B. Veprek, and A. Bock. 1992. Selenoprotein synthesis in E. coli. Purification and characterisation of the enzyme catalysing selenium activation. Eur J Biochem 206:767-73.
8. Forchhammer, K., W. Leinfelder, and A. Bock. 1989. Identification of a novel translation factor necessary for the incorporation of selenocysteine into protein. Nature 342:453-6.
9. Gladyshev, V. N., S. V. Khangulov, M. J. Axley, and T. C. Stadtman. 1994. Coordination of selenium to molybdenum in formate dehydrogenase H from Escherichia coli. Proc Natl Acad Sci U S A 91:7708-11.
10. He, S. Y., C. Schoedel, A. K. Chatterjee, and A. Collmer. 1991. Extracellular secretion of pectate lyase by the Erwinia chrysanthemi out pathway is dependent upon Sec-mediated export across the inner membrane. J Bacteriol 173:4310-7.
11. Hopper, S., M. Babst, V. Schlensog, H. M. Fischer, H. Hennecke, and A. Bock. 1994. Regulated expression in vitro of genes coding for formate hydrogenlyase components of Escherichia coli. J Biol Chem 269:19597-604.
12. Korsa, I., and A. Bock. 1997. Characterization of fhlA mutations resulting in ligand-independent transcriptional activation and ATP hydrolysis. J Bacteriol 179:41-5.
13. Lee, J. H., P. Patel, P. Sankar, and K. T. Shanmugam. 1985. Isolation and characterization of mutant strains of Escherichia coli altered in H2 metabolism. J Bacteriol 162:344-52.
14. Lei, X. G., J. K. Evenson, K. M. Thompson, and R. A. Sunde. 1995. Glutathione peroxidase and phospholipid hydroperoxide glutathione peroxidase are differentially regulated in rats by dietary selenium. J Nutr 125:1438-46.
15. Leinfelder, W., K. Forchhammer, F. Zinoni, G. Sawers, M. A. Mandrand-Berthelot, and A. Bock. 1988. Escherichia coli genes whose products are involved in selenium metabolism. J Bacteriol 170:540-6.
16. Leonhartsberger, S., A. Ehrenreich, and A. Bock. 2000. Analysis of the domain structure and the DNA binding site of the transcriptional activator FhlA. Eur J Biochem 267:3672-84.
17. Liu, Y., G. Jiang, Y. Cui, A. Mukherjee, W. L. Ma, and A. K. Chatterjee. 1999. kdgREcc negatively regulates genes for pectinases, cellulase, protease, HarpinEcc, and a global RNA regulator in Erwinia carotovora subsp. carotovora. J Bacteriol 181:2411-21.
18. Lloyd, J. R., G. H. Thomas, J. A. Finlay, J. A. Cole, and L. E. Macaskie. 1999. Microbial reduction of technetium by Escherichia coli and Desulfovibrio desulfuricans: enhancement via the use of high-activity strains and effect of process parameters. Biotechnol Bioeng 66:122-30.

19. Maupin, J. A., and K. T. Shanmugam. 1990. Genetic regulation of formate hydrogenlyase of Escherichia coli: role of the fhlA gene product as a transcriptional activator for a new regulatory gene, fhlB. J Bacteriol 172:4798-806.
20. Morrow, W. R., W. M. Griffin, and H. S. Matthews. 2006. Modeling switchgrass derived cellulosic ethanol distribution in the United States. Environ Sci Technol 40:2877-86.
21. Pfaffl, M. W. 2001. A new mathematical model for relative quantification in real-time RT-PCR. Nucleic Acids Res 29:e45.
22. Reissmann, S., E. Hochleitner, H. Wang, A. Paschos, F. Lottspeich, R. S. Glass, and A. Bock. 2003. Taming of a poison: biosynthesis of the NiFe-hydrogenase cyanide ligands. Science 299:1067-70.
23. Robbins-Manke, J. L., Z. Z. Zdraveski, M. Marinus, and J. M. Essigmann. 2005. Analysis of global gene expression and double-strand-break formation in DNA adenine methyltransferase- and mismatch repair-deficient Escherichia coli. J Bacteriol 187:7027-37.
24. Roseboom, W., M. Blokesch, A. Bock, and S. P. Albracht. 2005. The biosynthetic routes for carbon monoxide and cyanide in the Ni-Fe active site of hydrogenases are different. FEBS Lett 579:469-72.
25. Rosentel, J. K., F. Healy, J. A. Maupin-Furlow, J. H. Lee, and K. T. Shanmugam. 1995. Molybdate and regulation of mod (molybdate transport), fdhF, and hyc (formate hydrogenlyase) operons in Escherichia coli. J Bacteriol 177:4857-64.
26. Sauter, M., R. Bohm, and A. Bock. 1992. Mutational analysis of the operon (hyc) determining hydrogenase 3 formation in Escherichia coli. Mol Microbiol 6:1523-32.
27. Sawers, G. 1994. The hydrogenases and formate dehydrogenases of Escherichia coli. Antonie Van Leeuwenhoek 66:57-88.
28. Self, W. T., A. M. Grunden, A. Hasona, and K. T. Shanmugam. 1999. Transcriptional regulation of molybdoenzyme synthesis in Escherichia coli in response to molybdenum: ModE-molybdate, a repressor of the modABCD (molybdate transport) operon is a secondary transcriptional activator for the hyc and nar operons. Microbiology 145 (Pt 1):41-55.
29. Self, W. T., A. Hasona, and K. T. Shanmugam. 2004. Expression and regulation of a silent operon, hyf, coding for hydrogenase 4 isoenzyme in Escherichia coli. J Bacteriol 186:580-7.
30. Self, W. T., A. Hasona, and K. T. Shanmugam. 2001. N-terminal truncations in the FhlA protein result in formate- and MoeA-independent expression of the hyc (formate hydrogenlyase) operon of Escherichia coli. Microbiology 147:3093-104.
31. Self, W. T., and K. T. Shanmugam. 2000. Isolation and characterization of mutated FhlA proteins which activate transcription of the hyc operon (formate hydrogenlyase) of Escherichia coli in the absence of molybdate(1). FEMS Microbiol Lett 184:47-52.
32. Stadtman, T. C. 1996. Selenocysteine. Annu Rev Biochem 65:83-100.
33. Sun, X., P. M. Moriarty, and L. E. Maquat. 2000. Nonsense-mediated decay of glutathione peroxidase 1 mRNA in the cytoplasm depends on intron position. Embo J 19:4734-44.
34. Suppmann, S., B. C. Persson, and A. Bock. 1999. Dynamics and efficiency in vivo of UGA-directed selenocysteine insertion at the ribosome. Embo J 18:2284-93.
35. Vignais, P. M., and A. Colbeau. 2004. Molecular biology of microbial hydrogenases. Curr Issues Mol Biol 6:159-88.
36. Woodward, J., M. Orr, K. Cordray, and E. Greenbaum. 2000. Enzymatic production of biohydrogen. Nature 405:1014-5.
37. Yoshida, A., T. Nishimura, H. Kawaguchi, M. Inui, and H. Yukawa. 2005. Enhanced hydrogen production from formic acid by formate hydrogen lyase-overexpressing Escherichia coli strains. Appl Environ Microbiol 71:6762-8.

Highly Selective Nano-Mems Low Temperature Hydrogen Sensor

S. Seal and H. Cho
University of Central Florida

Research Period: September 2002 to September 2007

Abstract

We have developed the sol-gel derived nanocrystalline indium oxide (In_2O_3)-doped tin oxide (SnO_2) sensor, in the form of thin film/nanowires/nanofibers, for room temperature hydrogen (H_2) sensing application, for NASA, under the atmospheric conditions existing on the surface of the Earth. The nanocrystalline thin film sensor is incorporated into the microelectromechanical system (MEMS) device to achieve high H_2 sensitivity and selectivity with minimum detection and recovery time at room temperature. Effect of various test parameters such as the air pressure, the H_2 concentration as well as the MEMS design parameters such as the finger spacing and the number of fingers on the room temperature H_2 sensing characteristics of the present sensor has been evaluated. The present nano-micro integrated sensor shows giant room temperature H_2 sensitivity ($S=10^3$-10^5) with high selectivity over carbon monoxide (CO). The current H_2 detection and recovery time at room temperature lie within the range of 10 to 250 sec and 10 to 200 sec respectively. New technological solutions for further reducing the response and the recovery time of the present nano-micro integrated sensor have been proposed. Nano-micro integrated sensor prototype has been successfully developed.

Introduction

Hydrogen (H_2) is the most abundant element in the universe and one of the most abundant on Earth. Due to the rapid consumption of the fossil fuels, much attention has been paid towards H_2 as an economical non-conventional energy source for the diversified industrial applications. For example, solid oxide fuel cell (SOFC) technology uses gaseous H_2 for the generation of power and heat. H_2 powered cars and buses are already in normal transit service in some of U.S. cities12. Liquid H_2 has been used by NASA for launching the space-shuttles. As summarized in Figure 1. H_2 also finds applications in electronic, metallurgical, pharmaceutical, nuclear fuel, food and beverages, as well as glass and ceramic industries. Every day, millions of pounds of H_2 are used by hundreds of industries around the world. Due to the realization of the potential use of H_2 energy further interest has grown into the production of large quantity of different forms of H_2, the enhancement of H_2 storage capacity, and the development of safe transportation system for H_2.[345]

Depending on the quantities required, H_2 can be transported by road tanker or pipeline. North America alone has at least 700 km H_2 pipeline system. Pipelines for liquid H_2 have also been built by NASA for direct delivery of H_2 to the space vehicle at the launch pad. However, due to its very small size, H_2 is the most susceptible for the leakage through the pipelines; typically about 1 to 3% of H_2 in the existing systems is always lost, mostly through the joints in the pipes. If handled carelessly, H_2 is as dangerous for transport, storage and use as many other fuels. As a result, safety remains a top priority in all the aspects of H_2 energy and has been the prime motivation for the present work.

In the recent years, nanotechnology has emerged as an attractive field for the development of novel materials having unusual properties, which have provided different pathways to solve many unresolved issues in various other fields. We strongly believe that the application of

nanotechnology to H_2 sensors would help in advancing the science and the technology related to the development of sensor materials.

Background

Different experimental (metal-oxide-semiconductor (MOS)-based, catalytic resistor, acoustic wave and pyroelectric) 678 and commercial sensors (catalytic combustion, electrochemical, semiconductor, and thermal conductivity)[9101112] based on different principles are currently available but with major drawbacks as outlined in Figure 1. The very low sensitivity of these sensors at room temperature to low concentrations of H_2 has been invariable associated with the poor response and recovery time, which insists further investigation in these areas. In addition to this, the poor H_2 selectivity, which is a severe problem at room temperature, has been another major but pending issue, which needs to be delved in great detail. Particularly, attention must be paid in improving the H_2 selectivity by a novel approach without sacrificing the room temperature H_2 sensitivity and the response and recovery time of the sensor. Moreover, many of the experimental as well as commercially available sensors use the nanocrystalline materials, which are susceptible to changes in their physical properties (such as nanocrystallite size) if operated at highly temperature, which may reduce the potential life of the sensor. Such sensors, hence, must be operated at lower temperatures, where further research is still awaited. The commercially available sensor devices are claimed to sense H_2 at room temperature within the concentration limits of 200 ppm-2%, which large enough for any practical application. Response time quoted for these sensor devices is less than 10 sec, but it is related to high H_2 concentration as high as 90% and not for ppm-level H_2 concentration. Although the sensor devices are claimed to operate at room temperature, the recovery time often is associated with higher temperature (70 °C). Moreover, the room temperature H_2 sensitivity values for these devices are often not quoted. In addition to this, there are only few manufacturers, which guarantee the cross-sensitivity to other poisonous gases. No claims are made regarding the suitability of these sensor-devices for sensing H_2 on other planetary conditions, which is an essential requirement for NASA. It is suggested that, the commercial sensors currently available in the market are designed only to meet the atmospheric conditions on the earth's surface. Modifying the sensor material properties to meet the NASA's over all requirements is imperative. Various forms of sensors such as thin films, random network of nanowires and Nanotubes, as well as aligned or single nanowires of semiconductor oxides have been developed for the H_2 sensing application. The maximum H_2 sensitivity at room temperature has been reported for the thin film form of the sensor with the response and the recovery time in few minutes. On the other hand, a single nanowire type sensor exhibits the response time in few seconds but with extremely low H_2 sensitivity. The random network of nanowires, having large porous structure, may be a good choice for selecting the appropriate form of the sensor, which may compromise the H_2 sensitivity to some extent for improving the response time. Recently, the single-walled carbon nanotubes (SWCNTs) and multi-walled carbon nanotubes (MWCNTs) have been synthesized and utilized for the H_2 (and other gases as well) sensing application. Three different forms of carbon nanotubes such as single, parallely aligned and random network have been investigated for the gas sensing. Comparison reveals that, relative to the semiconductor oxides gas sensors, the carbon nanotubes exhibit very low gas sensitivity (<2) and high detection time (5 to 2700 sec). Moreover, the recovery time associated with the carbon nanotubes based gas sensor has been few hours.

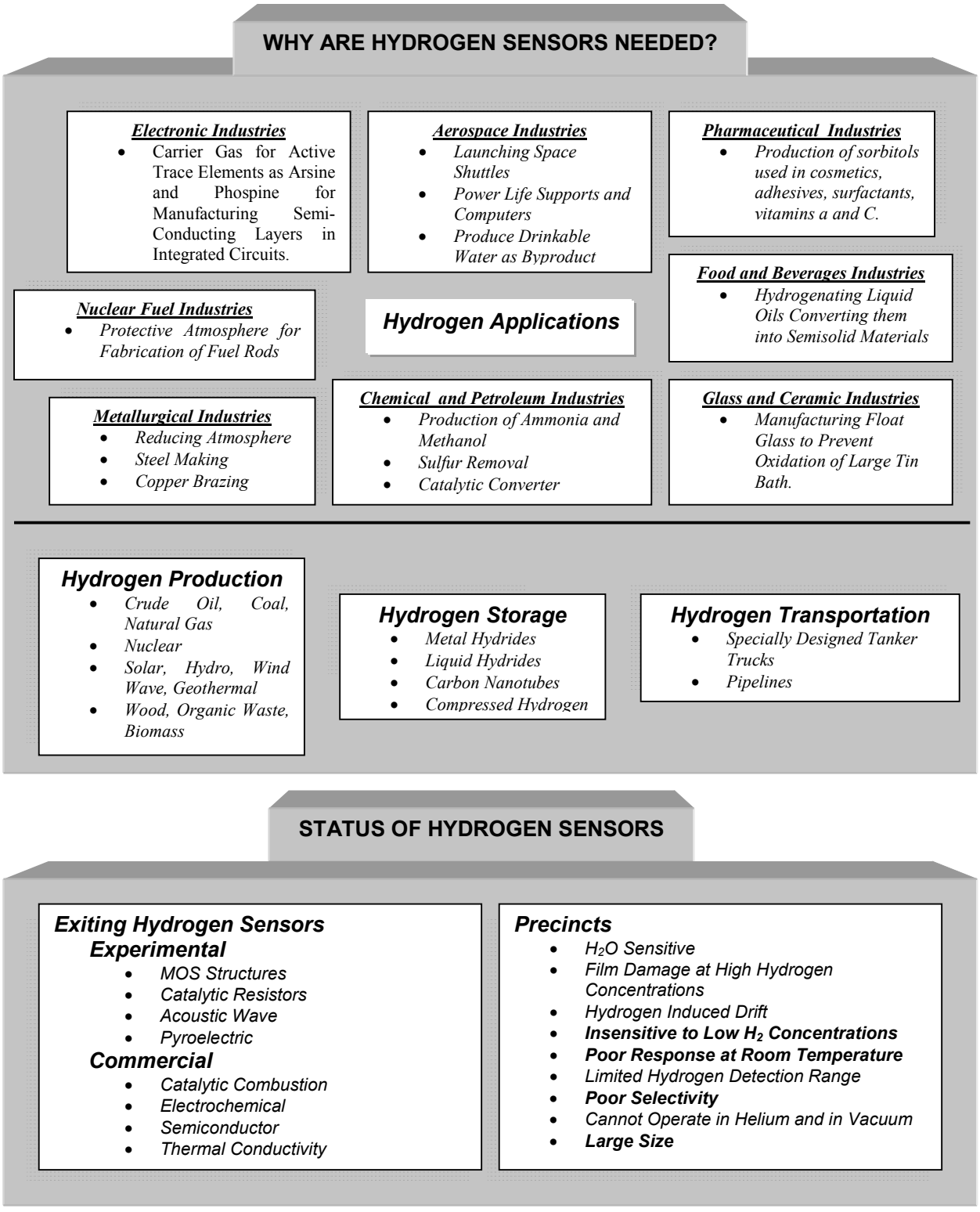

Figure 1: Charts summarizing the need for an immediate development of hydrogen sensors based on innovative approaches for overcoming the limitations of the current sensor technology and meeting the requirements of the hydrogen based industries.

Experimental

Development and Optimization of Nanostructures

In present work, sol-gel derived nanocrystalline thin films were developed for gas sensing application. Surface adsorbed oxygen ions (O^- or O^-_2) govern the overall gas sensing properties of the nanomaterials. Considering this facts Indium doped tin oxide nanostructures are developed and optimized. In process of synthesis first tin-isopropoxide solution in iso-propanol and toluene, corresponding to the concentration of 0.23 M of tin-isopropoxide, was used with the addition of different amount of amount of indium (III)-isopropoxide used to obtain In doped SnO_2. Figure 2 shows the various steps involved in the nanostructure synthesis for room temperature hydrogen detection.

Pre-screening of Nanomaterials for Sensor Application

Fourier transform infrared (FTIR) spectrometry is a powerful technique to characterize the very first atomic layer of a material. The importance is that the surface chemical species generated during the nanostructured material synthesis process and/or generated by surrounding contaminants can be identified as well as reactive sites in a non destructive manner. These surface groups and the reactive sites can be modified in situ by controlled adsorption of molecules while the resulting modifications of the surface properties can be continuously followed in the same cell by FTIR spectroscopy[13]. At the same time, independently from fundamental vibrational studies, some semiconducting properties can be deduced from the infrared spectra. Diffuse reflection spectroscopy is a very sensitive method for detecting changes at the surface of rough materials in the IR region. It is particularly effective for powders with a high surface area (nanomaterials). This makes diffuse reflectance a valuable tool for catalysis, oxidation, and photochemical studies. However, measurements for these applications must be obtained in a carefully controlled environment. The variations of the infrared energy transmitted by a sample are related to the variations of the electrical conductivity of this sample according to the Drude-Zener theory as:

$$\Delta\sigma = \Delta A \varepsilon_0 cn / z$$

Where, $\Delta\sigma$ = Change in electrical conductivity of the nanoparticles after exposure to H_2.

ΔA = Change is absorption of the sample after exposure to H_2.

c = velocity of light,

n = refractive index of the material

z = sample depth.

Therefore; the FTIR spectrometry allows the simultaneous study of the electrical conductivity variations and the surface chemical species perturbations under various gaseous environments.

In present work Fourier Transform Infrared Spectrometer (Model: Spectrum I) of Perkin Elmer Inc having analyzed range from 7800 to 450 cm-I with a 4 cm^{-1} resolution is used. Figure 1 shows the set up build at SNF Lab for performing in-situ characterization of nanopowders. The

Praying Mantis is the first generally available diffuse reflection (DRIFTS) attachment for FTIR and remains the forerunner in the field. It incorporates two 6:1, 90° off-axis ellipsoids which form a highly efficient diffuse reflection illumination and collection system. This unique configuration deflects the specular reflectance away from the collecting ellipsoid, minimizing the associated spectral distortions. The Praying Mantis can be configured to study materials and reactions in controlled environments. High temperature, low pressure reaction chamber (HVC-DRP) for operation from high vacuum
(10^{-6} torr) to two or three atmospheres and at high temperatures (up to 600 °C under vacuum). DRIFTS reaction chamber feature a sample cup that is part of a temperature-controlled sample stage. The reaction chamber also features three gas ports for evacuating, pressurizing or flowing gas through the sample. To evacuate the diffuse reflectance reaction chamber, compact, a low-noise level PDC Vacuum Pump with a minimum pumping speed of 1.4m^3/hr is used.

Designing Microelectromechanical Systems (MEMS) Device

The steps involved in the MEMS device fabrication process are described schematically in Figure 4. A 3 in. silicon (Si) wafer is utilized, which is oxidized at higher temperature to produce an insulating silica (SiO_2) layer. During the fabrication, chromium (Cr, 10 to 20 nm) and gold (Au, 150 to 200 nm) thin films are deposited by thermal evaporation technique. Four interdigitated and one resistive temperature sensor are patterned on the substrate using the photolithography and the wet chemical etching techniques,

Integration with Microelectrochemical Devices (MEMs)

The MEMS devices were designed with the different number of fingers (8 and 20) and different finger spacing (10 and 20 μm). For integration of nanostructures tin-isopropoxide solution in iso-propanol and toluene, was used with the addition of calculated amount of indium (III)-isopropoxide to obtain the thin films of SnO_2-6.5 mol% In_2O_3 via a sol-gel dip-coating process.
The dried gel films were sputtered with a thin Pt-layer for 10 sec using a sputter-coater. The coated-MEMS devices were dried at 150 °C for 15 to 30 min in air. The dip-coating, the sputtering, and the drying processes were repeated to obtain a desired film thickness. Finally, the Pt-sputtered dried gel films were fired at 400 °C in air for 1 h and utilized for the characterization and H_2 sensing tests.

The coated and calcined MEMS devices were wire-bonded to an integrated circuit chip and installed in the 32 pin socket assembly, which was in turn placed centered over the sensor test-board designed using the LPKF CircuitCAM 4.0 software and cut using the LPKF Boardmaster 4.0 software on a single-sided copper clad prototype boards.

Thus, in the “nano-micro” integrated sensor device, the term “nano” indicates the nanocrystalline SnO_2-based sensor materials and the term “micro” refers the electrode distance of 20 to 50 μm. Comparison shows that, in the “nano-micro” integrated sensor device, the electrode distance is much smaller (20 to 50 μm) relative to that (1 cm) in the “nano-macro” integrated sensor device.
Figure 5 shows the Nano-Micro integrated H Sensor.

H_2 Sensing Test Bed Development and Testing Procedures

The photographs of the sensor test-bed facility developed at NASA/UCF are shown in Figure 6. It consists of a 50 L chamber, which houses the H_2 sensor device. The test-chamber is connected to the turbo-pumps through throttle valves for maintaining a desired air-pressure

level during the H_2 sensing tests. The test-chamber is also connected to gas cylinders through the respective mass flow controllers (MFCs), which allow blowing a specific amount of H_2 gas into the test-chamber. The sensor resistance during the H_2 gas sensing tests is measured, using a constant-current (100 nA) source multimeter via four probe technique. The sensor test-results are acquired by the data acquisition system for further data analysis. H_2 sensing tests were conducted in the dynamic test condition at room temperature (22 °C with the relative humidity of 35 to 50%). In this type of sensor-testing, the air-pressure within the test-chamber was reduced and maintained at a desired level. A mixture of appropriate amounts of nitrogen (N_2 and H_2 was admitted into the test-chamber through the respective mass-flow-controllers. The N_2 (15000 ppm) was used as a carrier-gas. The amount of H_2 in ppm was calculated using the ratio of number of moles of H_2 admitted into the test-chamber per minute to the total number of moles of gas molecules (that is, the summation of number of moles of N_2, H_2, and air) within the test-chamber. Thus, in the dynamic test condition, a desired amount of H_2 was continuously blown into the test-chamber per minute and simultaneously pumped out of the test-chamber throughout the test-duration. Thus, the dynamic test condition simulates the condition, which may be encountered in an actual service application, for example, H_2 leakage through a pipe line.

Nanowires/Nanofibers Sensor Material Development

Two different techniques, electrospinning and thermal evaporation, have been utilized to synthesize the nanocrystalline SnO_2-based nanowires/nanofibers. In the electrospinning, tin (II) chloride ($SnCl_2$) precursor was dissolved completely in a highly concentrated polymeric solution, which was then taken in a syringe placed on a syringe pump, which fed the syringe tip with the polymeric solution at a constant speed. A Cu plate covered with Al-foil was placed in front of the syringe at a distance of 10 cm and a high voltage (15 kV) was applied in between the Cu-plate and the syringe tip. The polymer fibers were drawn from the syringe tip, which were subsequently deposited on the Al foil (or the Si-SiO_2 substrate). Since, the polymer fibers contain the Sn-precursor, low temperature calcination temperature burnt off the polymer leaving behind the inorganic SnO_2-based nanowires/nanofibers. In the thermal evaporation technique, Figure 3, a high temperature furnace was utilized. The Sn-precursor powder and the Si-SiO_2 substrate (with Pt catalyst) were taken into the Al_2O_3 crucible, which was placed in the center of the furnace. Argon (Ar) gas was blown continuously into the furnace. The furnace was ramped to 900 °C, held at that temperature for 5 h, then cooled naturally to room temperature.

Results and Discussion

H_2 Sensing Test Results for "Nano-Micro" Integrated Sensor Device

Typical results of a cyclic sensor-test, conducted at room temperature (22 °C) and 50 torr air pressure for 900 ppm H_2 without the UV-exposure is presented in Fig. 11. The response time is kept constant to 3600 sec for the three cycles. A very high value of room temperature H_2 sensitivity as high as 110×10^3 has been observed for 900 ppm H_2, which, is much higher than those reported under any processing and test conditions for the SnO_2-based sensors. Moreover, this room temperature H_2 sensitivity value, observed for the "nano-micro" integrated sensor device is two orders of magnitude larger than that observed for "nano-macro" integrated sensor device, Fig. 6. For the constant response time of 300 to 350 sec, the "nano-micro" integrated sensor device exhibits the room temperature H_2 sensitivity of 150 to 200 with the recovery time of 150 to 200 sec, Fig. 12, which are much lower than those associated with the "nano-macro" integrated sensor device. A major reduction in the response time from 540 min to 300 to

350 sec, and that of the recovery time from 60 min to 150 to 200 sec has been successfully achieved by using the “nano-micro” integrated sensor device. (Note: Other significant results obtained using the “nano-micro” integrated sensor device could be found in the published articles). Thus, we are successfully accomplished the task of developing room temperature hydrogen sensor with very high sensitivity. New approaches for reducing the response time from 300 to 350 sec to less than 60 sec are discussed below.

Development of Theoretical Model

A new constitutive equation for the gas sensitivity of the semiconductor oxides based thin film sensors has been derived by the authors, which can satisfactorily explain the variation in the gas sensitivity as a function of number of critical parameters such as the nanocrystallite size, the film thickness, the gas concentration, the operating temperature, and the surface-adsorbed oxygen-ion concentration. The developed constitutive equation for the gas sensitivity is of the form,

$$S = \frac{1}{D} \bullet \sqrt{\frac{4\varepsilon_r \varepsilon_o k}{q^2}} \bullet \frac{\sqrt{T}}{n_b^{1.5}} \bullet A_2 C^n \bullet \exp\left[\frac{q^2}{2\varepsilon_r \varepsilon_o k} \bullet \frac{\left[O^-\right]^2}{V_o T} \right] \quad (1)$$

where, S is the gas sensitivity, $\varepsilon_r\varepsilon_o$ permittivity of the sensor, k the Boltzmman’s constant, q the electronic charge, T the operating temperature, C the gas concentration, n the gas exponent, A_2 a constant, $[O^-]$ the surface-adsorbed oxygen-ion concentration, and V_o the oxygen-ion vacancy concentration. (Note: The details regarding the model assumptions, its predictions, and the comparison with the experimental results could be obtained in the published articles). Thus, successful accomplishment of this task leads us to predict gas sensing behavior of any material based on materials property.

Sensing H_2 at Higher Air-Pressures at Room Temperature

Typical variation in the room temperature H_2 sensitivity as a function of response time for different air-pressures within the range of 50 to 600 torr is presented in Fig. 13. Within investigated air-pressure range, the air-pressure has almost no effect on the room temperature H_2 sensitivity, and the response and the recovery time. The present “nano-micro” integrated sensor device is, hence, suitable for applications involving variation in the air-pressure.

Demonstrating H_2 Selectivity Over CO at Room Temperature

The present “nano-micro” integrated sensor device is almost insensitive to CO at room temperature, Fig. 14. However, it exhibits very high room temperature H_2 sensitivity under similar test conditions. The “nano-micro” integrated sensor device is, hence, highly selective over CO at room temperature. Thus, the Task 1.4. has been partly successfully demonstrated in the third year of the project.

Sensing H_2 in He Environment at Room Temperature

The “nano-micro” integrated sensor device successfully sensed H_2 at room temperature in the He environment, Fig. 15. The room temperature H_2 sensitivity of 11 and 26 are observed without and with the UV-radiation exposure respectively, Fig. 15(a). Although, the total response time is kept constant at 3600 sec, the same data plotted as a variation in the slope of the resistance-time graphs as a function of test-duration results in the response time of 200 to 250 sec only, Fig. 15(b), which is indicated by the sudden rise in the graph as observed after an introduction of H_2 into the test-chamber. Thus, the Task 1.5 has been successfully accomplished in the third year of the project.

Development of Modified MEMS Devices

The design for the modified MEMS device is shown in Fig. 17, where for the constant electrode distance of 20 μm, the numbers of electrodes are varied within the range of 8 to 20. Such modified MEMS devices have also been fabricated for varying electrode distances within the range of 1-50 μm. Also, Length of the electrodes have been varied to understand the impact of these parameters on the gas sensing properties such as sensitivity and response time. It has been found that length as well as number of fingers did not interfere in the gas sensing properties of the sensor. But electrode spacing plays keys role in the overall gas sensing properties. Small gap between the electrodes leads to faster response of the gas sensor device. This is due to the fact that the less distance required for the free carriers to reach to electrode and scattering centers are minimal. But at the same time smaller electrode spacing causes decrease in sensitivity. This is due to the fact that less surface area available for the hydrogen reaction and this results in less free carrier concentration density.

Development of “1D-Micro” Integrated Sensor Device

Since, the response time of the “nano-micro” integrated sensor device is 300 to 350 sec at room temperature, “1D-micro” integrated sensor device has been developed, Fig. 10. It consists of highly porous network of nanofibers SnO_2 fibers (synthesized via thermal evaporation technique). Integration of 1-D nanostructures with the MEMS is a rigorous task. In present situation the contact pads were fabricated on the top of TNW grown on Si/SiO_2 substrate by thermal evaporation. A shadow mask was used to form the contact pattern. The shadow mask was made out of thick polyamide tape. The shape of the contact pad was cut out on the polyamide tape. Metallization was performed at a high vacuum of $3x10^{-5}$ torr. The sensor, with the fabricated Au contact pads, was mounted on a ceramic package. The sensor contacts were connected to the package contacts and the conductivity was test deposited on the MEMS device. Four interdigitated Au electrode configurations covered with SnO_2-based fibers can be seen in Fig. 16(a). Two Au electrodes short circuited with semiconductor SnO_2-based fibers are seen in Fig. 16(b). Such highly porous network of SnO_2-based fibers, Fig. 16(c), would allow very fast H_2 circulation through out the sensor, which was anticipated to reduce the response time below 60 sec at room temperature.

Prototype Sensor Development:

A hand-held size prototype instrument was developed using a room temperature hydrogen microsensor. The instrument was designed to generate a warning signal and display a concentration level on exposure to hydrogen leak at room temperature. The sensor was designed and fabricated integrating indium oxide (In_2O_3) doped polycrystalline tin dioxide (SnO_2) nanoparticles with intedigitated microelectrodes then fully-packaged into a portable instrument with a measurement circuit and a display unit. The instrument demonstrated early detection of hydrogen leak at normal environmental conditions without any heated activation of the sensor surface. The whole system consists of a micro control unit (MCU, ATmega48V), a LCD, a piezo buzzer, a positive voltage regulator (SPX3819) and a step-up DC/DC converter (HT7737). The values of resistances at different concentrations (400 ppm and 900 ppm) were tabulated and "written" into the micro control unit (MCU, ATmega48V) of the instrument for calibration. In the calibration process, the MCU generates a "data base" of resistance versus concentration based on the recorded values. The DC/DC converter together with the positive voltage regulator provides the suitable driving voltage to the H_2 sensor, MCU and piezo buzzer. In operation, the MCU transfers the signals (resistances) obtained from the sensor to signals of the concentration by comparing resistances with the data base generated in the calibration step. Converted signals are sent to the display circuitry for LCD and piezo buzzer for alarm signals. Figure 15 shows the measurement, display and buzzer circuitry on a PCB with the H_2 sensor. Figure 16 exhibits a fully packaged portable H_2 instrument with a wire-boned H_2 sensor chip inside. Testing of the instrument was carried out at room temperature without inclusion of any heating element for sensor activation. Upon exposure to the hydrogen gas blown over the instrument at room temperature, within a minute, the instrument generated a warning alarm signal and displayed concentration level in 0.01 up to 0.99, in which the numerical value of 1.00 corresponds to LFL (lower flammable limit) of hydrogen gas.

Comparison of Different Forms of Sensors

The room temperature H_2 sensitivity and the response time of different forms (single nanobelt/single nanowire/random network of nanowires/network of nanotubes/nano thin films) of semiconductor oxides are compared in Table 1. It is seen that maximum room temperature H_2 sensitivity is shown by thin film sensor and minimum response time is obtained using single nanowire/nanobelt sensor. Thus, there is trade-off between the H_2 sensitivity and the response time in choosing the appropriate form of sensor. The random network of nanowires appears to be an optimum solution to achieve moderately high sensitivity with minimum response time.

Table 1. Typical gas sensing results reported recently for the various forms of semiconductor oxides.

Sensor Material	Sensor Form	Synthesis Method	Operating Temperature (^oC)	Gas (Amount)	Sensitivity (R_{air}/R_{gas})	Response Time (Sec)
SnO_2	Single Nanobelt	Vapor Phase Evaporation	200	C_2H_5OH (250 ppm)	2	Few Seconds
				NO_2 (0.5 ppm)	30	
SnO_2/Pd	Single Nanowire	Thermal Evaporation	200	H_2 (?)	2.5	2.5
Pd	Single Nanowires	Electrochemical Deposition	25	H_2 (5 %)	3.5	75 (mSec)
In_2O_3	Random Network of Nanowires	Carbothermal Reduction	370	C_2H_5OH (1000 ppm)	30	10
ZnO	Random Network of Nanowires	Thermal Evaporation	300	C_2H_5OH (200 ppm)	50	15
TiO_2	Nanotubes Array	Anodization	290	H_2 (1000 ppm)	10000	200
In_2O_3-SnO_2 (Current Work)	*Thin Film*	*Sol-Gel*	*25*	*H_2 (900 ppm)*	*10000-100000*	*10*

References

[1] J. M. Ogden, M.M. Steinbugler, and T.G. Kreutz, J Power Sources 79, 143 (1999)
[2] J.M. Ogden, Phys. Today 55, 69 (2002)
[3] L. Schlapbach, MRS Bull. 27, 675 (2002)
[4] R.S. Irani MRS Bull. 27, 680 (2002)
[5] A. Domashenko, A. Golovscheko, Yu. Gorbatsky, V. Nelidov, and B. Skorodumov, Int. J. Hydrogen Energ. 27, 753 (2002)
[6] W.-C. Liu, H.-J. Pan, H.-I. Chen, K.-W. Lin, S.-Y. Cheng, and K.-H.Yu, *IEEE Transactions on Electron Devices* 48, 1938 (2001).
[7] P. Liu, S.-H. Lee, H. M. Cheong, C. E. Tracy, J. R. Pitts, and R. D.Smith, *J. Electrochem. Soc.* 149, H76 (2002).
[8] F. Favier, E. C. Walter, M. P. Zach, T. Benter, and R. M. Penner,*Science* 293, 2227 (2001)
[9] W. P. Jakubik, M. W. Urbanczyk, S. Kochowski, and J. Bodzenta,*Sensors and Actuators B* 82, 265 (2002).
[10] D. R. Baselt, B. Fruhberger, E. Klaassen, S. Cemalovic, C. L.Britton Jr., S. V. Patel, T. E. Mlsna, D. McCorkle, and B. Warmack,*Sensors and Actuators B* 88, 120 (2003).
[11] Y. Zhang, S. Asahina, S. Yoshihara, and T. Shirakashi, *J. Electrochem.Soc.* 149, H179 (2002).
[12] I. Simon and M. Arndt, *Sens. Actuators B* 97–98, 104 (2002).
[13] M.-I. Baraton and L. Merhari, J. Euro. Ceramic Soc., 24,1399 (2004).

LIST OF PUBLICATIONS

Journal Articles

1. S. Deshpande, A. Karakoti, G.Londe, H.J. Cho and S.Seal, “Room temperature hydrogen detection using 1-D nanostructured tin oxide sensor”, J. Nanosci. Nanotech. (In press).

2. S. Deshpande S,P. Zhang, N. Posey, H.J. Cho and S.Seal, “Electrode architecture in tuning room temperature sensing kinetics of nano-micro-integrated hydrogen sensor”, Applied Physics Lett 90 (7) 073118 (2007).

3. C. Drake, S.Deshpande and S.Seal, “Determination of free carrier density and space charge layer variation in nanocrystalline In3+ doped tin oxides using Fourier transform infrared spectroscopy”, Applied Physics Lett, 89 (14) 143116 (2006).

4. C. Drake, J. Bernard, A. Amalu and S. Seal, J. Appl. Phys. (2007).

5. S. Shukla, P. Zhang, H. J. Cho, S. Seal, “Room temperature hydrogen response kinetics of nano-micro-integrated doped tin oxide sensor”, Sens Actuators B 120 (2): 573-583 (2007).

6. S. Shukla, V. Venkatachalapathy and S. Seal, “Thermal evaporation processing of nano and submicron tin oxide rods”, J Phys. Chem B 110 (23): 11210-11216 (2006).

7. Z. Rahman, S. Shukla, and S. Seal, “State-of-the-Art In-Situ Site Selective FIB for TEM Sample Preparation” (in preparation).

8. S. Shukla and S. Seal, “Electrospinning of Hydroxypropyl Cellulose Polymer Fibers and Their Application in Synthesis of Nano and Submicron Tin Oxide Fibers”, Polymer (submitted).

9. S. Shukla, L. Ludwig, H.J. Cho, C. Drake, and S. Seal, “Hydrogen Discriminating Room Temperature Micro-Sensor Based on Nanocrystalline Doped-Tin Oxide” J. Appl. Phys. 98 (10)104306 (2005).

10. S. Shukla, A. Rajnikant, L. Ludwig, H.J. Cho, and S. Seal, “Air-Pressure Effect on Room Temperature Hydrogen Sensing Characteristics of Tin Oxide Based Micro-Sensor”, J. Nanosci. Nanotech. 5 (11) 1864-1874 (2005).

11. S. Shukla and S. Seal, “Nanocrystalline Semiconductor Tin Oxide as Hydrogen Sensor”, In: “Encyclopedia of Sensors”, Edited by C. Grimes, E. Dickey, and M. Pishko, American Scientific Publishers (in press).

12. M. Meyyappan, S. Shukla, and S. Seal, “Novel One Dimensional Nanostructures”, Interface 14 (2) 41-45 (2005).

13. S. Shukla, R. Agrawal, L. Ludwig, H.J. Cho, and S. Seal, “Effect of Ultraviolet Radiation on Room Temperature Hydrogen Sensitivity of Nanocrystalline Sol-Gel-Doped Tin Oxide MEMS Sensor”, J. Appl. Phys. 97, 054307-054319 (2005).

14. S. Shukla and S. Seal, “Sol-Gel Derived Nanocrystalline Semiconductor Oxide Thin Film Gas Sensors”, In: “Encyclopedia of Nanoscience and Nanotechnology”, Edited by H.S. Nalwa, American Scientific Publishers, Vol. 10, pp. 27-42 (2004).

15. S. Shukla and S. Seal, “Theoretical Model for Film Thickness Dependent Gas Sensitivity Variation in Nanocrystalline Tin Oxide Sensor”, Sens. Letts. 2(3/4), 260-264 (2004).

16. S. Shukla and S. Seal, “Constitutive Equation for Gas Sensitivity of Nanocrystalline Tin Oxide Sensor”, Sens. Letts. 2(2) 125-130 (2004).

17. S. Shukla and S. Seal, “Theoretical Model for Nanocrystallite Size Dependent Gas Sensitivity Enhancement in Nanocrystalline Tin Oxide Sensor”, Sens. Letts. 2 (1) 73-77 (2004).

18. S. Shukla, S. Seal, L. Ludwig, and C. Parrish, “Inverse-Catalyst-Effect Observed for Nanocrystalline Doped-Tin Oxide Sensor at Lower Operating Temperatures”, Sens. Actuators B 104, 223-231 (2004).

19. S. Shukla, S. Seal, L. Ludwig, and C. Parrish, “Nanocrystalline Indium Oxide-Doped Tin Oxide Thin Film as Low Temperature Hydrogen Sensor ”, Sens. Actuators B 97 (2-3) 256-265 (2004)

20. S. Shukla and S. Seal, “Room Temperature Gas Sensitivity of Nanocrystalline Pure Tin Oxide”, J. Nanosci. Nanotech. 4 (1/2) 141-145 (2004).

21. S. Shukla, S. Seal, P. Nguyen, H. Ng, and M. Meyyappan, “Transmission Electron Microscopy Sample Preparation of Nanocrystalline Tin Oxide Fibers Sensor Using Focused Ion-Beam Milling”, Sens. Letts. 1 (1) 75-78 (2003).

22. S. Shukla, S. Patil, S. Kuiry, S. Seal, L. Ludwig, and C. Parrish, “Synthesis and Characterization of Sol-Gel Derived Nanocrystalline Tin Oxide Thin Film as a Hydrogen Gas Sensor”, Sens. Actuators B 76, 343-353 (2003).

23. S. Seal and S. Shukla, “Nanocrystalline SnO Gas Sensor in View of Surface Reactions and Modifications”, JOM 54 (9) 35-38, 60 (2002)

Conference Proceedings Articles/Presentations/Posters

1. S. Deshpande, A. Karakoti, G. Londe, H.J. Cho and S. Seal, “ Room Temeprature hydrogen detection using 1- D nanostructured Tin Oxide sensor” In American Vacuum Society, October 16-20, San Francisco, California (2006).

2. S. Shukla, C. Drake, L. Ludwig, H.J. Cho, and S. Seal, “Air-Pressure Effect on Room Temperature Hydrogen Sensitivity of Semiconductor Tin Oxide based Thin Film Micro-Sensor”, (Oral Presentation) In: ASM International Surface Engineering Congress and Exhibition, August 1-3, St. Paul, Minnesota (2005).

3. S. Shukla, C. Drake, L. Ludwig, H.J. Cho, and S. Seal, “Air-Pressure Effect on Room Temperature Hydrogen Sensitivity of Semiconductor Tin Oxide ased Thin Film Micro-Sensor”, (Article) In: Proceedings of ASM International Surface Engineering Congress and Exhibition, August 1-3, St. Paul, Minnesota (2005).

4. P. Zhang, S. Shukla, L. Ludwig, H.J. Cho, and S. Seal, “A Room Temperature Hydrogen Sensor with High Sensitivity and Selectivity using Nanocrystalline Semiconductor Particles”, (Article) In: Proceedings of IMECE2005 2005 ASME International Mechanical Engineering Congress and Exposition November 5-11, 2005, Orlando, Florida USA (in review).

5. S. Shukla, R. Agrawal, J. Duarte, H.J. Cho, And S. Seal, “Photo-Deactivated Room Temperature Hydrogen Gas Sensitivity of Nanocrystalline Doped-Tin Oxide Sensor” (Article) In: Conference Proceedings of 29th Annual Cocoa Beach Conference and Exposition on Advanced Ceramics and Composites, Cocoa Beach, Florida (in press).

6. S. Shukla, L. Ludwig, R. Agrawal, H.J. Cho, and S. Seal, “Room Temperature Hydrogen Gas Sensitivity of Nanocrystalline Doped-Tin Oxide Sensor Incorporated into MEMS Device” (Article) In: Semiconductor Oxide Gas Sensing Symposium A, MRS 04 Fall Meeting, Edited by S. Seal, M. Baraton, N. Muryama, and C. Parish, MRS Proceedings ISBN No. 1-55899-776-8, Pittsburgh, PA, Vol. 828, pp. 51-57 (2005).

7. S. Shukla, L. Ludwig, and S. Seal, “A Novel Theoretical Model for Semiconductor Oxides Gas Sensors” (Article) In: Semiconductor Oxide Gas Sensing Symposium A, MRS 04 Fall Meeting, Edited by S. Seal, M. Baraton, N. Muryama, and C. Parish, MRS Proceedings ISBN No. 1-55899-776-8, Pittsburgh, PA, Vol. 828, pp. 161-167 (2005).

8. S. Shukla, L. Ludwig, R. Agrawal, J. Duarte, H.J. Cho, and S. Seal, “Room Temperature Hydrogen Sensitivity of Nanocrystalline Doped-Tin Oxide Sensor under UV-Light” (Oral Presentation) In: TMS 134th Annual Meeting and Exhibition, San Francisco, California (2005).

9. S. Shukla and S. Seal, “Novel Single Crystal Model for Semiconductor Oxides Thin Film Gas Sensors” (Oral Presentation) In: TMS 134th Annual Meeting and Exhibition, San Francisco, California (2005).

10. S. Shukla, R. Agrawal, L. Ludwig, H.J. Cho, and S. Seal, “Nano-Micro Integrated Highly Sensitive Room Temperature Hydrogen Detector” (Oral Presentation) In: Applied Surface Analysis, Annual Joint Symposium of Florida Chapter of the AVS and Florida Society for Microscopy, Orlando, FL (2005).

11. S. Shukla, L. Ludwig, R. Agrawal, J. Duarte, H.J. Cho, and S. Seal, “Photo-Deactivated Room Temperature Hydrogen Gas Sensitivity of Nanocrystalline Doped-Tin Oxide Sensor” (Oral Presentation) In: 29th Annual Cocoa Beach Conference and Exposition on Advanced Ceramics and Composites, Cocoa Beach, Florida (2005).

12. S. Shukla and S. Seal, “Constitutive Equation for Semiconductor Oxides Thin Film Gas Sensors” (Oral Presentation) In: 29th Annual Cocoa Beach Conference and Exposition on Advanced Ceramics and Composites, Cocoa Beach, Florida (2005).

13. S. Shukla, L. Ludwig, R. Agrawal, H.J. Cho, and S. Seal, “Room Temperature Hydrogen Gas Sensitivity of Nanocrystalline Doped-Tin Oxide Sensor Incorporated into MEMS Device” (Oral Presentation) In: MRS Fall Meeting, Boston, Massachusetts (2004).

14. S. Shukla, L. Ludwig, and S. Seal, “A Novel Theoretical Model for Semiconductor Oxides Gas Sensors” (Oral Presentation) In: MRS Fall Meeting, Massachusetts (2004).

15. S. Shukla, S. Seal, R. Agrawal, J. Duarte, G. Alvero, H.J. Cho, L. Ludwig, C. Parish, and M. Meyyappan, “Highly Selective Nano-MEMS Low Temperature Hydrogen Sensor” (Oral Presentation) In: NASA Hydrogen Research at Florida Universities-Review Meeting, Florida Solar Energy Center (FSEC), Cocoa, Florida (2004).

A. Rajnikant, S. Shukla, S. Seal, and H. J. Cho, “A Nanoparticle Based Microsensor For Room Temperature Hydrogen Sensor” (Oral Presentation) In: 3rd IEEE Conference on Sensors, Vienna, Austria, (2004).

16. S. Seal, S. Shukla, R. Agrawal, J. Duarte, G. Alvero, H.J. Cho, L. Ludwig, C. Parrish, and M. Meyyappan, ‘Challenges and Solutions For a Room Temperature Hydrogen Sensor Based on Nanotechnology” (Oral Presentation) In: NASA’s Nanotechnology in Space Exploration, National Nanotechnology Initiative Grand Challenge Workshop Series, Palo Alto, CA (2004).

17. S. Shukla, J. Duarte, S. Seal, and C. Parrish, Nanostructured Functional Hydrogen Separation Membrane for Space Applications” (Oral Presentation) In: Florida Space Grant Consortium (FSGC) STD Awardees Meeting, Center for Space Education, Kennedy Space Center (KSC), Florida (2004).

18. S. Shukla, S. Seal, L. Ludwig, and C. Parish, “Development of Low Temperature Hydrogen Sensor Based on Nanocrystalline Doped Tin Oxide” (Oral Presentation) In: Florida Chapter of the American Vacuum Society and Florida Society for Microscopy-Annual Symposium, Orlando, Florida (2004).

19. S. Shukla, S. Seal, L. Ludwig, and C. Parish, “Low Temperature Hydrogen Sensing Behavior of Nanocrystalline Doped Tin Oxide Sensor” (Oral Presentation) In: 28th Annual Cocoa Beach Conference and Exposition on Advanced Ceramics and Composites, Cocoa Beach, Florida (2004).

20. S. Shukla, S. Seal, L. Ludwig, and C. Parish, “Modeling and Sensing Hydrogen at Lower Operating Temperatures using Nanocrystalline Tin Oxide Thin Films” (Oral Presentation) 204th Meeting of The Electrochemical Society, Co-sponsored in Part by the Electronics Division of The American Ceramic Society, Orlando Florida (2003).

21. S. Shukla, S. Patil, S. Kuiry, S. Seal, Ludwig, and C. Parish, “Sol-Gel Derived Nanocrystalline Tin Oxide Based Hydrogen Gas Sensor” (Oral Presentation) In: TMS 132nd Annual Meeting and Exhibition, San Diego, California (2003).

22. S. Shukla, S. Patil, S. Kuiry, S. Seal, Ludwig, and C. Parish, “Room Temperature Hydrogen Gas Sensor Based on Nanocrystalline Tin Oxide Thin Film” (Oral Presentation) In: 27th Annual Cocoa Beach Conference and Exposition on Advanced Ceramics and Composites, Cocoa Beach, Florida (2003).

23. S. Shukla, S. Patil, S. Kuiry, S. Seal, Ludwig, and C. Parish, “Development of Nanocrystalline Hydrogen Gas Sensors” (Oral Presentation) NASA Hydrogen Research at Florida Universities-Midterm Review Meeting, Tampa, Florida (2003).

24. S. Shukla, S. Patil, S. Kuiry, S. Seal, Ludwig, and C. Parish, “Room Temperature Hydrogen Gas Sensor Based on Doped Metal Oxide Semiconductor Thin Film” (Poster Presentation) Florida Chapter of the American Vacuum Society and Florida Society for Microscopy-Annual Symposium, Orlando, Florida (2003).

25. S. Patil, S. Shukla, S. Kuiry, L. Ludwig, C. Parish, and S. Seal, “Nanocrystalline Oxide Thin Films For Oxygen Sensor” (Poster Presentation, Honorable Mention) In: Florida Chapter of the American Vacuum Society and Florida Society for Microscopy-Annual Symposium, Orlando, Florida (2003).

October 2007

Metal Hydrides for Hydrogen Separation, Recovery and Purification

M. Hampton
University of Central Florida

D. Slattery
Florida Solar Energy Center

Research Period: June 2003 to September 2006

Abstract

Hydrogen absorption properties of $LaNi_5$ and $LaNi_5Al_x$ intermetallics prepared by mechanical alloying have been investigated as a function of alloy preparation parameters and alloy composition in the range of 0.9 to 33.3 at.% Al in $LaNi_5Al_x$. $LaNi_5$ and its aluminum added derivatives, powdered by mechanical alloying, did not readily interact with H_2. Activation has been achieved by thermal treatment of the powdered samples. Interactions were rapid at 193 K and 5 atm. H_2 pressure. Hydrogen capacity was reduced slightly with the addition of Al, however the time of completion of the reaction was unaffected. Formation of $LaNi_4Al$ has been verified by X-ray diffraction analysis. $LaNi_5$ was tested to selectively react with H_2 in a stream of H_2-He and it retained H_2, producing pure He.

Introduction

Lanthanum nickel, $LaNi_5$ has long been studied as a possible hydrogen storage material. Unfortunately, because of its high mass, the weight content of hydrogen is extremely low, making the material unsuitable for automotive purposes. However, the material forms a hydride at room temperature, or lower, with good kinetics. This makes $LaNi_5$ an excellent candidate for applications that require rapid uptake under mild conditions. One such use is for the recovery of hydrogen that is lost during the purging of transfer lines, or is lost due to boil-off during the storage of liquid hydrogen.

At NASA's Kennedy Space Center, KSC, hydrogen is used for the space shuttle and other launch vehicles. As a result, huge quantities of liquid hydrogen are transported, transferred and stored at KSC. During the transfer of the hydrogen from the trucks to the storage dewars, significant quantities of hydrogen are lost during the cooldown of the transfer lines and from flash evaporation as the high pressure cryogenic liquid enters the low pressure dewars. Additionally, during storage, hydrogen is constantly lost because of boil off. Recovery of this lost hydrogen could lead to substantial savings.

In addition to the hydrogen that is lost due to transfer operations and boil off, NASA also loses hydrogen during purge operations. Prior to filling lines with liquid hydrogen, they must be precooled with liquid helium. After an operation, the residual hydrogen is purged, again with helium, in order to safe the systems. Both the hydrogen and helium in these operations is currently not recovered, leading to additional losses.

It was the loss of this hydrogen and helium that led to the study described here. $LaNi_5$ absorbs hydrogen rapidly, reversibly and selectively. As a result, it is capable of not only absorbing hydrogen as it vaporizes during transfer operations, but also is potentially useful for separating hydrogen from the helium purge gas. Selective removal of the hydrogen would allow recovery of helium, in high purity, for future use.

Background

Hydriding alloys of the AB_5 type are suitable materials for hydrogen storage applications because of their large hydrogen capacity, easy activation and rapid hydriding/dehydriding rates. One of those representative compounds that has been extensively studied is $LaNi_5$.[1, 2] It has been used as an electrode in nickel metal hydride batteries and as an absorber for gaseous hydrogen. $LaNi_5$ rapidly reaches equilibrium with hydrogen, even at low pressures and temperatures, and the hydriding and dehydriding processes are reversible at H_2 partial pressures close to atmospheric.[3]

Hydriding alloys are of great interest due to the simplicity of tailoring the hydriding properties by a variety of methods. One common method is the partial substitution of one metal for another. For example, the substitution of Ge, Zn or Al for the Ni in $LaNi_5$ was reported to have increased the cycle life of the hydride with a slight decrease in hydrogen capacity.[4,5,6] Partial substitution of La by rare earth metals, however, deteriorated the hydriding properties and cycle life.[7] Another option to manipulate the characteristics is to change the sample preparation method. Laboratory scale possibilities include melting, annealing or mechanical alloying, or a combination of several techniques.[8] Further treatment after alloying is also necessary for $LaNi_5$ to readily react with hydrogen.

Hydrogen absorbing alloys reported previously were prepared by arc melting the elements, which were analyzed after size reduction and several hydriding-dehydriding cycles for activation. For example, $LaNi_{5-x}Al_x$ samples, prepared by arc melting followed by annealing and size reduction, were activated by hydriding in pure hydrogen gas at 17 atm and dehydriding at 363 K three times.[6]

Mechanical alloying is a low temperature activation method and has been reported to activate FeTi, Mg_2Ni and $LaNi_5$, which are inert to hydrogen prior to milling. For FeTi, milling is believed to give rise to Fe rich clusters on the surface and the generation of new surfaces by cracking.[9] $LaNi_5$ has been formed from elemental La and Ni via milling at room temperature, and partially substituted $La_{0.5}Zr_{0.5}Ni_5$ has been synthesized from an equimolar mixture of $LaNi_5$ and $ZrNi_5$.[10]

In the present study, we had an interest in being able to selectively remove hydrogen from a hydrogen-helium stream, such as is generated when helium is used to purge a system that has carried hydrogen. The particular application was for NASA, which uses liquid helium to precool systems that are going to be filled with liquid hydrogen and then purges residual hydrogen with helium after a procedure. Currently, these purge gases, a hydrogen-helium mixture, are vented, resulting in a loss of millions of dollars of resources. The ability to selectively remove and capture the hydrogen would also allow the helium to be reclaimed for further use.

Experimental

Sample Preparation

Sample preparation involved the ball milling of $LaNi_5$ that had been pre-alloyed by the manufacturer. Al and $LaNi_5$ were mechanically alloyed in changing proportions using a high energy ball mill. Al content is presented as mole percentages, varying between approximately 0.9 and 33.3% of the total number of atoms in $LaNi_5Al_x$. The results of the effect of the addition of Al to $LaNi_5$ on hydriding capacity and rate was analyzed by differential scanning calorimetry at 293 K and 5 atm initial H_2 pressure. $LaNi_5$ (99.9%, REacton) and Al (99.5%, -325 mesh) were obtained from Alfa Aesar and stored under the Ar atmosphere of a Labconco glove box. The mechanical activation of $LaNi_5$ and $LaNi_5Al_x$ was done by ball milling in a high energy Spex

8000M Mixer/Mill. A 50-mL tungsten carbide grinding vial obtained from Spex Certi Prep Inc., Metuchen, NJ, was used with two 11.11 mm tungsten carbide balls as the high energy ball milling medium. The milling canisters were loaded and unloaded in the glove box to avoid contact with air and moisture. $LaNi_5$ samples were ball milled with the following durations and ball to powder ratios, respectively: 10 minutes, 10:1; 10 minutes, 1:1; 30 minutes, 1:1.

Approximately 200 mg of the milled powder was utilized for hydrogen uptake analysis. $LaNi_5Al_x$ samples were ball milled for 10 minutes with 10:1 ball to powder ratio and analyzed for hydrogen uptake, followed by elemental analysis. Five $LaNi_5$ samples were milled for 3, 6, 10, 15, and 30 minutes with a ball to powder ratio of 10:1 for x-ray diffraction studies.

$LaNi_5$ samples for use in the large scale U-tube reactor were prepared using a 50-mL stainless steel grinding vial with two 12.70 mm stainless steel balls. Samples were milled for 30 minutes with a ball-to-powder ratio (BPR) of 1.7:1.

Equipment

Hydriding and dehydriding characteristics of sample materials were determined using a SETARAM DSC-111 Differential Scanning Calorimeter. The DSC furnace was fitted with sample and reference cells made from 1/4 in. Hastelloy C-22 seamless tubing. The cells were connected to inlet and exit valves, with quick disconnects for easy access. The inlet and exit valves were needle and globe valves, respectively. The inlet valves were connected to hydrogen and helium cylinders and the exit valves opened to the atmosphere. All components and fittings were made of 316 stainless steel. Pressure was monitored with two Omega type PX602 pressure transducers with a range up to 13.6 atm. Pressure data were acquired with a Dell 4200 PC using LabView software with a National Instruments board. Thermal data were directly transferred to the PC from the DSC and analyzed using Setsoft 2000 software. The amount of hydrogen absorbed or released was calculated and graphed using SigmaPlot software. Sample boats for the DSC were made from 316 stainless steel. The samples loaded into the boat were placed into a hollow glass tube that was sealed at both ends with plastic caps and then transferred from the glove box to the DSC to prevent exposure of the samples to air. Sample cell volume was determined by a water displacement method. Lateral heat loss compensation curves were previously determined.

A U-tube reactor was constructed from a seamless stainless steel pipe, 1 ft long, 1 in. O.D., that was bent into a U-shape to contain samples as large as 300 g. The reactor was fitted with 0.5 μ pore size inline filters and needle valves on each end. The downstream valve was connected to a three neck flask for effluent gas collection. The compositional analysis of the effluent gas was done with a Buck Scientific type 910 gas chromatograph fitted with a Hayesep DB 100/120, 30 ft, 1/8 in. O.D. stainless steel column obtained from Alltech. The GC utilized a TCD detector and the carrier gas was argon. Sample injection was done with a gas tight 100 μL syringe. The GC was connected to a Dell GX110 PC and the data was recorded using PeakSimple chromatography software.

Thermal Activation

In the DSC, samples were activated with a thermal cycle following milling. This was done by placing the sample in the DSC in a hydrogen atmosphere at approximately 5 atm, and heating the furnace to 150 °C, followed by cooling to ambient temperature. During this activation step, samples were hydrided to some extent, if not completely. Therefore, these samples were heated up to 150 °C under a minimal flow of argon to ensure no hydrogen was left in the sample.

For study in the U-tube reactor, samples were ball milled in stainless steel vials with lower ball to powder ratios and longer milling times. Approximately 200 grams of milled alloy were placed in a Pyrex petri dish that was then transferred into a 2 L capacity Parr pressure reactor for activation. Samples were heated to 250 °C under a hydrogen pressure of approximately 20 atm. After the system reached equilibrium, it was allowed to cool under hydrogen pressure. After cooling, the system was vented and heated to remove absorbed hydrogen.

Hydriding Procedure

Activated samples for hydriding trials in the DSC were prepared by loading 100 to 300 mg of sample into sample boats under an argon atmosphere in the glove box. The boats were transferred to the DSC after the furnace temperature had been adjusted to between 20 to 25 °C. The boat was loaded into the cell under a minimal hydrogen flow, which limited air exposure of the samples and avoided blowing the samples out of the boat. After inserting the boat, the exit valves were closed, the system was adjusted to the desired pressure and then the upstream valves and the hydrogen source cylinder valve were closed.

The U-tube reactor was used to determine hydriding characteristics via continuous operation. The U-tube was disconnected from the rest of the structure by the quick disconnects and filled with approximately 200 g of sample under an argon atmosphere in the glove box. The rest of the structure was then assembled on both ends and the reactor was removed from the glove box. After purging the reactor with argon, a hydrogen/helium mixture was allowed to flow through the reactor. At the same time, samples were injected into the GC continuously with appropriate one minute intervals, determined by the start and end of a hydrogen-helium peak pair. The flow rate through the reactor was monitored with a Fisher Scientific digital flow meter.

Dehydriding was accomplished by heating the reactor to 150 °C under argon flow. The exit stream was analyzed for hydrogen using the GC. As soon as no hydrogen was detected in the stream, the system was allowed cool to room temperature.

Sample Characterization and Analysis

A Rigaku Multiflex x-ray diffractometer using Cu-Kα radiation, was employed to characterize $LaNi_5$+Al samples. Analysis was done over a 2θ range of 20 to 80°. The slit width and scanning speed, respectively, were 0.020 mm and 2.400 degrees per minute. The x-ray generator voltage and current were set to 40 kV and 30 mA, respectively. Samples were supported on a metal sample holder whose bottom was closed by scotch tape and the sample was filled above it. Data were analyzed with Jade analysis software.

Elemental analysis of $LaNi_5$ and Al doped $LaNi_5$ was done by flame emission spectroscopy using a Varian Inc. SpectrAA10 spectrometer. Lanthanum, nickel, and aluminum were determined at 441.7, 341.5, and 396.1 nanometers, respectively. An acetylene/nitrous oxide flame was used with a slit width of 0.2 nm for all elements. Lanthanum standards were prepared by making dilutions from a stock solution of La_2O_3 dissolved in HNO_3. Nickel and aluminum stock solutions were prepared by dissolving pure elements in 1:1 HNO_3 and then standards were prepared by making appropriate dilutions. The interference of Ni on Al determination and of Al on the determination of La were accounted for by matching the concentrations of the interferences in the standards to those of samples.

Results and Discussion

During ball milling, it was noted that a significant amount of material always coated the grinding media and the walls of the vial. Because Al was the more malleable component of the two and, therefore, more likely to stick to the media and walls, elemental analysis was run after the samples had been ball milled and used for hydrogen uptake. The composition of $LaNi_5Al_x$ samples initially and after ball milling are given in Table 1. The mole% Al after milling was less than originally placed in the milling jar for all samples except for Sample 4. Apparently, during milling the aluminum did coat the milling media and was depleted from the bulk. The increase of Al content in Sample 4 is assumed to be the result of non-homogeneity of the milled product; the sample taken for analysis may not have been representative of the whole.

Table 1. Aluminum content of free powder in milling jar

	Mole% Al	
Sample	Initial mixture	After milling
1	0.87	0.77
2	5.26	4.74
3	14.29	12.00
4	33.33	47.31

$LaNi_5$ samples, prepared with various milling conditions, were reacted with H_2 at 293 K and 5 atm H_2. None of the samples showed activity towards hydrogen in the DSC after only ball milling. However, ball milling followed by a single thermal activation cycle resulted in a material that readily reacted with hydrogen. The hydrogen uptake reaction was observed to be rapid in all cases, reaching completion within 10 min. On the other hand, the total hydrogen absorption capacity was affected by changes in milling settings. The results are listed in Table 2. When the ball to powder ratio was decreased, a decrease in hydrogen capacity was observed. This effect is believed to be a consequence of the reduced number of collisions between milling media and the particles, resulting in relatively less stress being induced in the particles. This resulted in less activation of the sample. Furthermore, the degree of activation of the sample was independent of the material from which the milling jar and media were made. This indicates that contamination with iron is not a factor in the activation of the samples.

Table 2. Effects of various milling parameters on hydrogen capacity

Milling vial	SS[1]	WC[2]	WC	WC	WC
Milling time, min	30	Non milled	10	10	30
Ball to powder ratio	1.7:1	n/a	10:1	1:1	1:1
% H absorbed (wt%)	0.76	0	1.06	0.54	0.66

[1] Stainless steel
[2] Tungsten carbide

Using the DSC, reactions between the samples shown in Figure 1 and hydrogen were carried out at 293 K and 5 atm H_2. The weight percent of H absorbed by the $LaNi_5Al_x$ samples is listed in Table 3 and the uptake curves are given in Figure 1. The dependence of percent hydrogen absorbed on Al content in LaNi5 is given in Figure 2. The observed amount of H_2 absorbed remained constant at low Al content, and then decreased as Al content increased.

Table 3. Percent H uptake values for different amounts of Al in $LaNi_5$

Mole% Al	0	0.77	4.74	12.00	47.31
Average wt% H absorbed	1.04	1.05	0.95	0.87	0.68
Maximum wt% H absorbed	1.09	1.13	0.98	0.92	0.69

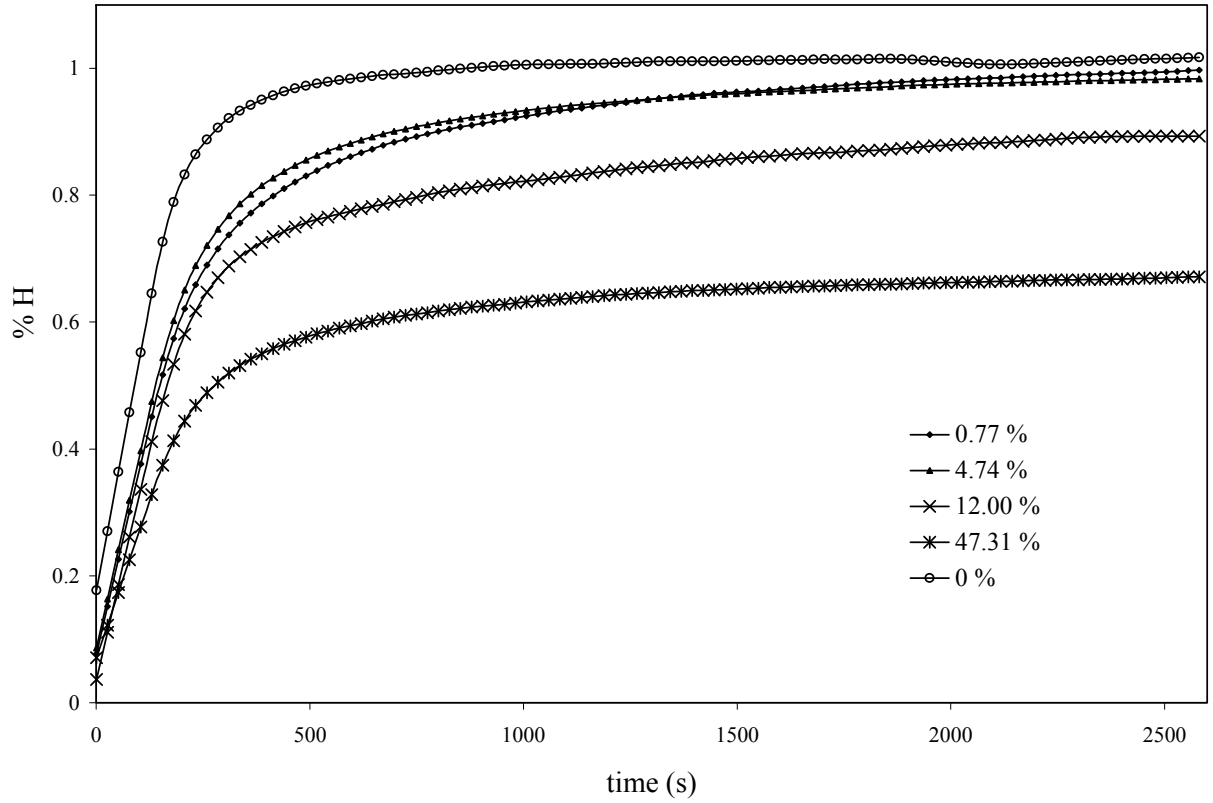

Figure 1. Hydrogen uptake curves for $LaNi_5$ samples with various amounts of Al.

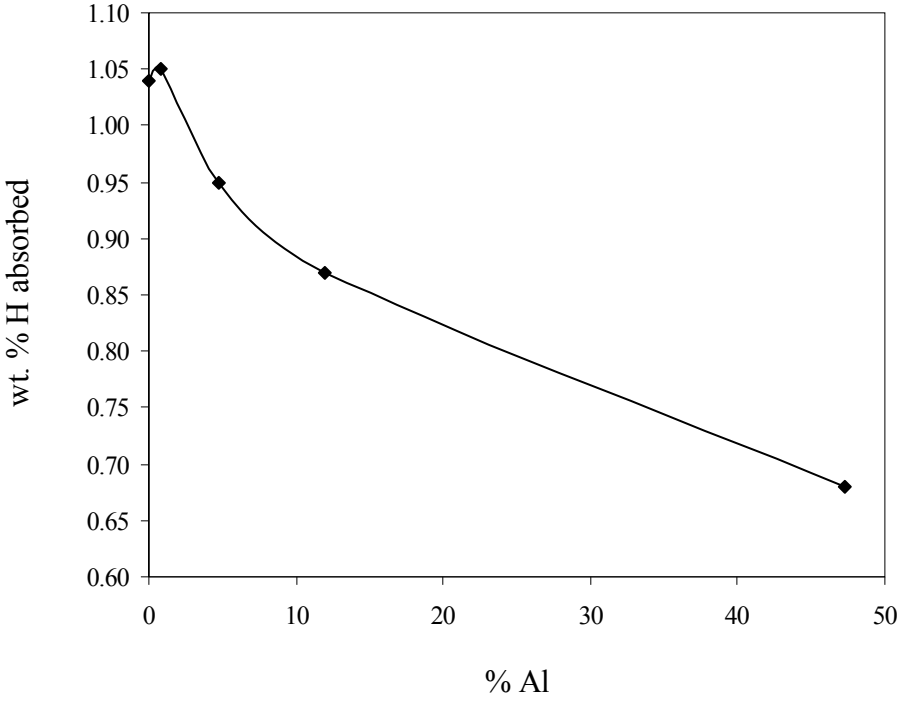

Figure 2. Hydrogen capacity as a function of Al in $LaNi_5$.

Four consecutive x-ray diffraction spectra were obtained for a $LaNi_5$ sample, Figure 3. The spectra were not consistent with each other, yet the elemental analysis proved that the composition of the sample was $LaNi_5$. The inconsistencies may indicate that the $LaNi_5$ from Alfa Aesar was not in its normal crystalline form and the energy from the x-ray beam was inducing changes in the crystal phase.

After grinding $LaNi_5$ with a mortar and pestle in the glove box, three consecutive XRD scans yielded peaks that were consistent with the reported peak positions of $LaNi_5$. However, the relative intensity of the observed peaks did not match with the reported ratios, and inconsistencies within the spectra were observed.

Five more $LaNi_5$ samples were prepared by ball milling in the Spex8000M for 3, 6, 10, 15, and 30 min, respectively. The XRD spectra of the samples are given in Figure 4. As reference, the XRD spectrum of non-milled $LaNi_5$ that most closely matches the expected spectrum is included. The relative intensities of the peaks were observed to approach the reported ratios for $LaNi_5$ as milling duration was increased. This suggests that the normal phase of $LaNi_5$, a $CaCu_5$ phase was formed as the milling proceeded. In contrast, the peaks were observed to lose intensity and broaden, which suggested the formation of an amorphous phase, but the broadening effect could be because of particle size reduction.

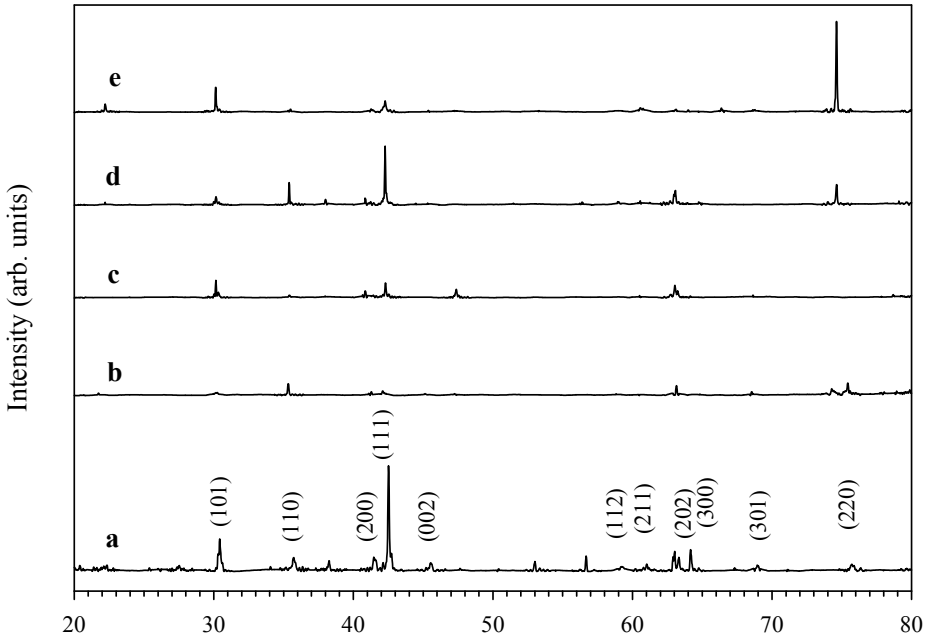

[a]$LaNi_5$ (reference), [b, c, d, e]non-milled sample

Figure 3. XRD spectra of $LaNi_5$.

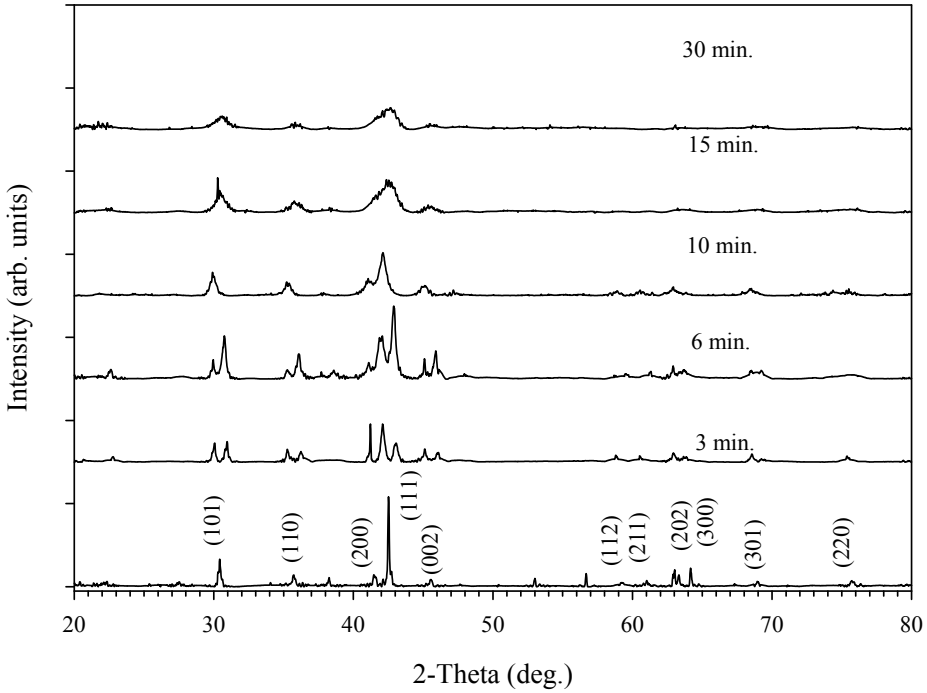

Figure 4. XRD spectra of LaNi5 milled for various times.

Samples of $LaNi_5$ mixed with 5.26, 14.29, and 33.33 mole% Al were examined with x-ray diffractometry. The spectrum of $LaNi_5$ with 33 mole% Al is given in Figure 5. The Bragg peak for $LaNi_5$ at 42.5° was identified; as were peaks for Al. However, the intensities of other $LaNi_5$ reflections were not strong enough to be identified.

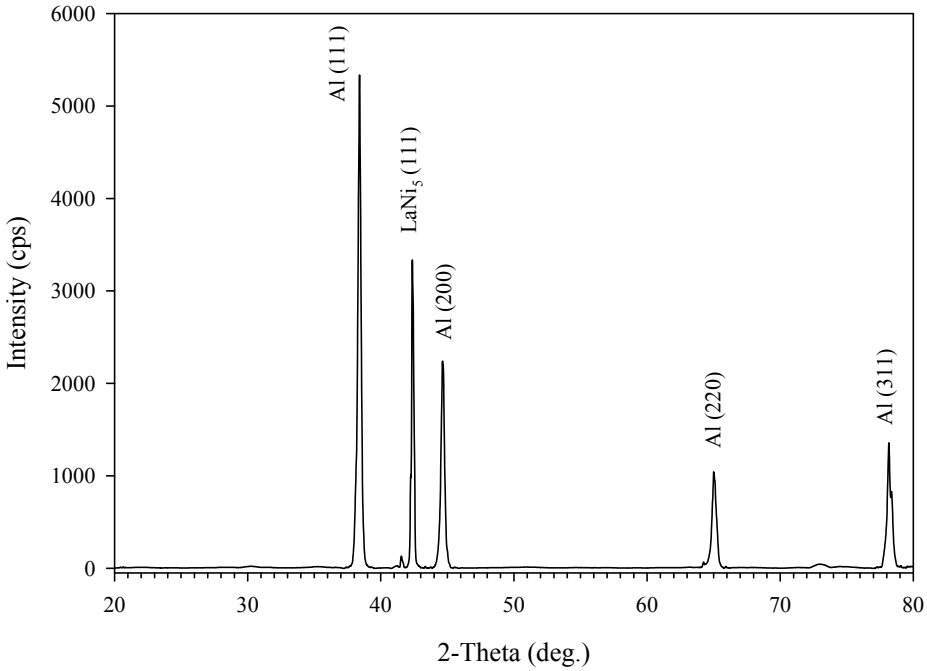

Figure 5. XRD spectrum of non-milled $LaNi_5$ with 33 mole% Al.

In the XRD spectra of the milled samples, Figure 6, the intensity of the Al Bragg peak at 38.5° increased with the increased Al content; however, its intensity was less than the Bragg peak of $LaNi_5$. The angle of the Bragg peaks also changed from 42.5 to 42.0°. This suggests the formation of $LaNi_4Al$ for which the angle of the Bragg peak is at 42.0°. The formation of $LaNi_4Al$ would lead to the release of free Ni through $LaNi_5 + Al \rightarrow LaNi_4Al + Ni$. The formation of Ni could not be verified because the Bragg peak for Ni, at 45.5°, coincides with one of the lines of $LaNi_5$. However, for $LaNi_4Al$, a reflection expected at 44.5° was observed for $LaNi_5$ milled with Al, also suggesting the formation of $LaNi_4Al$ by ball milling. This peak is indicated with an arrow in the figure.

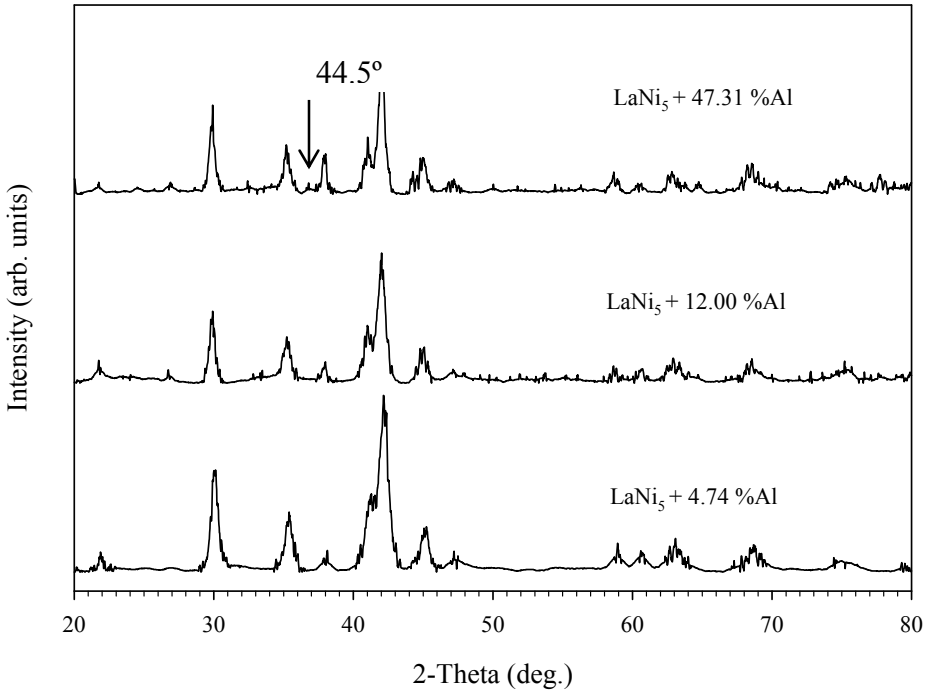

Figure 6. XRD spectra of milled $LaNi_5$ containing Al.

In order to determine the ability to selectively absorb hydrogen, the U-tube was filled with approximately 190 g of $LaNi_5$ and then the flow of 2% (v/v) H_2:He at about 9 atm was fed into it. The flow out of the reactor was restricted to about 200 $mL.min^{-1}$ by a pressure relief valve. The valve maintained the pressure within the reactor, while allowing a slow flow. The gas chromatogram of multiple injections is given in Figure 7. The single peaks over the first 20 min were assigned to helium as a result of their retention time and are shown as empty circles in the figure. Hydrogen was not observed in the effluent because it was captured by $LaNi_5$. When $LaNi_5$ became saturated with H_2, peaks at the retention time for hydrogen began to appear in the gas chromatograms of samples (filled circles). The percent hydrogen values in the effluent were calculated using peak area ratios of H_2 and He. The breakthrough curve is plotted as a function of time, Figure 8.

The $LaNi_5$ in the U-tube reactor successfully removed the hydrogen from the H_2-He stream and allowed the passage of pure He. The amount of hydrogen retained in the reactor at the time of saturation was calculated from material balance as follows. The amount of helium leaving the system was calculated using flow rate and time, V_{He} (mL) = flow rate ($mL.min^{-1}$) x time (min), which was equal to the amount of He that entered the system. Since the composition of the entering gas mixture was known, the amount of H_2 entered was calculated using $V_{Hydrogen} = V_{He}$ x (20/80) and converted to the weight percent hydrogen in the $LaNi_5$.

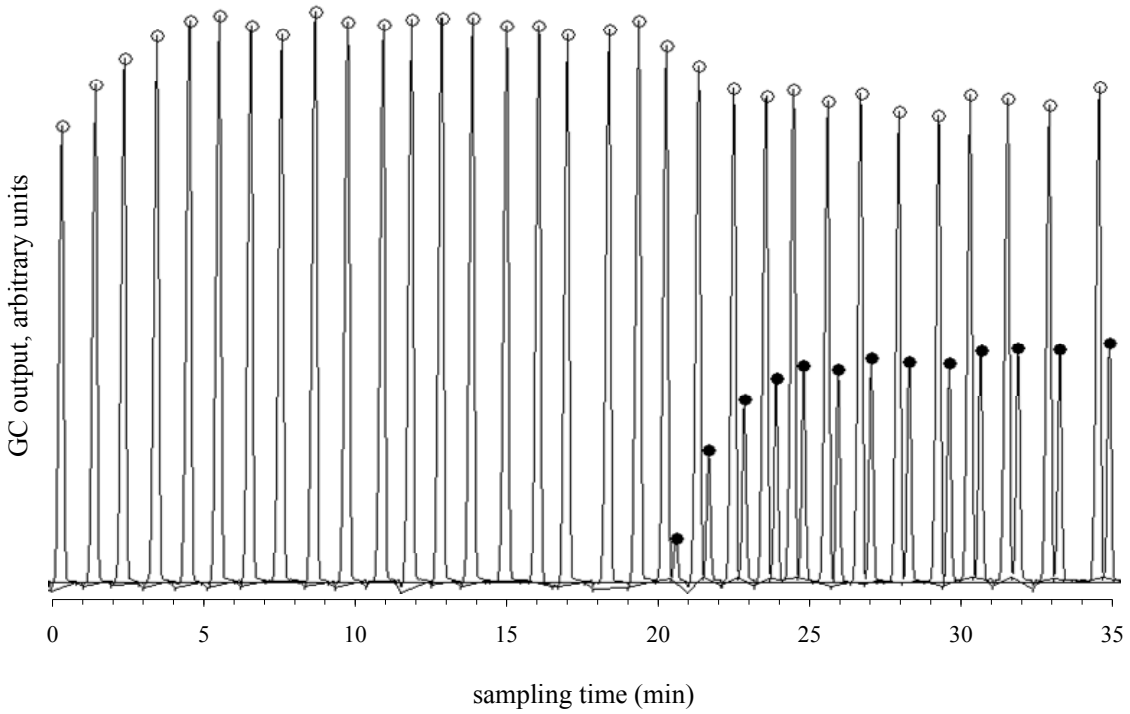

Figure 7. Chromatograms for hydrogen absorption in the U-tube reactor.

The average percent hydrogen absorbed in four trials with the same feed pressure was calculated as 0.041%. The low percent hydrogen of $LaNi_5$ was possibly due to the low pressure of H_2. To increase the hydrogen absorption in the continuous system, a higher partial pressure of H_2 would be useful. However, in this experiment, the absorption characteristics of the absorbing material were sufficient to remove the hydrogen from the feed stream to levels below the limit of detection of the gas chromatograph.

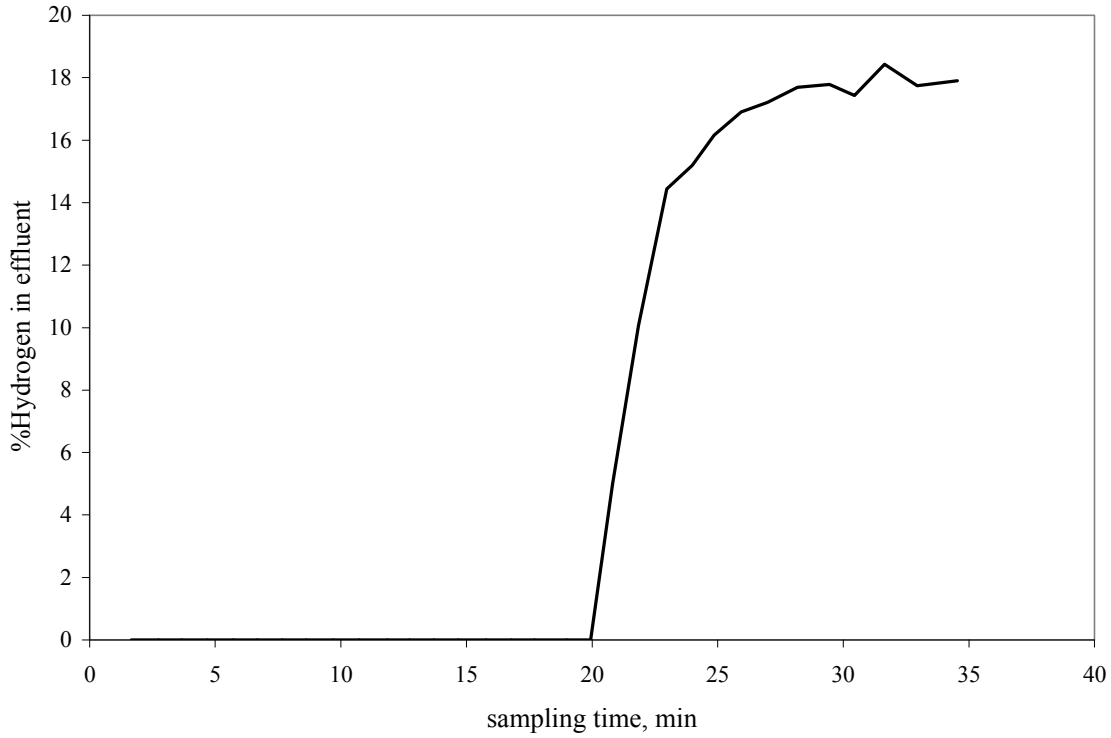

Figure 8. Effluent gas composition as percent hydrogen (v/v).

Conclusions and Recommendations

The alloy, $LaNi_5$, was shown to have the kinetics and capacity needed to remove hydrogen from a flowing stream of hydrogen and helium, thus allowing purification of both gases. Addition of aluminum to the alloy up to a level of 47 mole% provided for an improvement in the kinetics of hydrogen absorption without significantly reducing capacity. This incorporation of aluminum into the lanthanum nickel alloy will enormously reduce the weight and cost of the alloy required to purify hydrogen and helium at KSC.

In addition to being used to purify helium and hydrogen, $LaNi_5$ could also be used to capture the hydrogen currently lost to boil-off. While the hydrogen recovered could not be used for shuttle functions because of the requirement for liquid hydrogen, it could be used for other functions at the space center, such as fueling automobiles or buses.

It is recommended that a system based on lanthanum, nickel, aluminum alloy be implemented at KSC for the purification of hydrogen and helium and the recovery of boil-off hydrogen. Such systems will allow for conservation of resources as well as taxpayer dollars.

References

[1] Van Vucht, J.H.N.; Kuijpers, F.A.; Bruning, H.C.A.M. Philips Research Reports, 1970, 25, 133-140.

[2] Tanaka, S.; Clewley, J.D.; Flanagan, T.B. *Journal of the Less Common Metals*, 1997, 56, 137-139.

[3] Boser, O. *Journal of the Less Common Metals*, 1976, 46, 91-99.

[4] Bowman, Jr., R.C.; Luo, C.H.; Ahn, C.C.; Witham, C.K.; Fultz, B. *Journal of Alloys and Compounds*, 1995, 217, 185-192.

[5] Witham, C.; Bowman Jr., R.C.; Fultz, B. *Journal of Alloys and Compounds*, 1997, 254, 574-578.

[6] Nishimura, K.; Sato, K.; Nakamura, Y.; Inazumi, C.; Oguro, K.; Uehara, I.; Fujitani, S.; Yonezu, I. *Journal of Alloys and Compounds*, 1998, 268, 207-210.

[7]Brundle, C.R., *Physical Review Letters*, 1978, 40, 972-975.

[8] Percheron-Guegan, A.; Welter, J-M. *Preparation of Intermetallics and Hydrides*, in *Hydrogen in Intermetallic Compounds I*, L. Schlapbach, Editor. 1992, Springer-Verlag: Heidelberg.

[9] Aoyagi, H.; Aoki, K.; Masumoto, T. *Journal of Alloys and Compou*nds, 1995, 231, 804-809.

[10] Msika, E.; Latroche, M.; Cuevas, F.; Percheron-Guegan, A. *Materials Science and Engineering B*, 2004, 108(1-2), 91-95.

Wireless Passive Sensors and Systems for Physical Sensors and Hydrogen Sensing Applications

D. Malocha
University of Central Florida

Research Period: July 2005 to September 2007

Abstract

This research proposes the development of passive, wireless surface acoustic wave (SAW) multi-sensor systems for NASA application to gauging systems and for remote hydrogen sensing. The proposed SAW sensors are passive, wireless, small and lightweight. SAW devices have no fundamental limitation in material or physical principle for wide temperature operation; from cryogenic temperatures to 1000 °C (with appropriate substrate material), making them ideal for use in cryogenic applications, space vehicles, robots, structures in space, or in hostile environments. It is believed that many of the commercially available SAW materials will operate at cryogenic temperatures, and at high temperatures materials from the langasite family will work and are available. These wide operating temperature ranges are very attractive for space applications. The proposed SAW sensor can be encoded which provides security and close proximity multi-sensor operation. Finally, the proposed SAW sensor is totally passive, which means there are no batteries or other source for a spark or ignition; critical for the hydrogen environment. The SAW device can be accessed remotely without external connections, removing cabling and interconnects to a sensor array.

The objective of this research is to build new and novel SAW wireless-passive sensors, to research the SAW components operation at cryogenic temperatures, to build new devices and test fixtures for hydrogen gas sensing, and to develop measurement and test procedures. The device embodiment presented uses orthogonal frequency coded (OFC) SAW reflective structures to encode the signal and to send back the sensor information. The encoding technique is similar to multi-tone CDMA in terms of its implementation, where a transducer or reflector is built with the desired code. The applications are for a wide range of NASA ground and aerospace needs, which include temperature sensing in harsh environments of space or ground-based operations, liquid level sensing for hydrogen, oxygen, nitrogen or other cryogenic liquids, and hydrogen gas sensing. The research effort demonstrates that SAW devices can operate at cryogenic temperatures, that various device embodiments can be used for sensing temperature and gas, and that the devices can survive even under extreme temperatures. A RF 250 MHz transceiver system has been built for sensor interrogation, which shows the feasibility of a software-radio approach for data acquisition, post processing and sensor data extraction.

Introduction

The objective is to develop a passive, wireless SAW tagged-sensor for use in hydrogen liquid and gas sensing, to show that the device can operate as a temperature sensor over wide temperature ranges, and to expand the operation of the SAW OFC technology. The objectives of this research are:

1. To investigate the use of SAW technology based piezoelectric materials. We proposed to apply the SAW OFC approach to cryogenic temperature sensors. To our knowledge, SAW cryogenic sensing has never been done, however, there appears to be no fundamental problem in working at low temperatures with SAW materials. There may be issues in developing the materials and interfaces to work at these temperatures. The first

approach was to use lithium niobate substrates and our standard thin film process and determine if there are material compatibility issues. Both ebeam and sputtering is available at UCF which provides a wealth of material choices. Materials issues were resolved, devices were tested at cryogenic temperatures and results evaluated. The first prototypes were evaluated at approximately 250 MHz which is a reasonable RF frequency for prototype testing.

2. Demonstrated the feasibility of high frequency OFC SAW sensors above 500 MHz.

3. A hydrogen gas sensor was explored using an OFC sensor tag configuration as previously discussed. The hydrogen sensing was accomplished by using a palladium film in one delay area between the transducer and one grating. If hydrogen gas is present and absorbed, the differential delay will change depending on the quantity of gas absorbed.

4. To understand the coding of the devices for RF tagging in a multi-sensor environment. The study of code collision and separation was studied.

5. To understand the thin film sensitivity to the hydrogen exposure. The desired effect is to have a room temperature reversible hydrogen sensor. Research explored the thin film approaches, developed thin film models, and experiments were performed.

6. A transceiver system capable of interrogating the SAW sensor-tags and extract the sensor temperature information was designed, built and measured SAW OFC tags.

7. Submission of conference presentations and articles, and peer reviewed publication, of results are listed. Submission of other proposals to federal agencies and industry occurred which has furthered the technology.

Experimental

SAW OFC Device

A dual delay line OFC SAW device was designed and fabricated using the SAW design capabilities, the UCF mask pattern generator and the fabrication facilities in the UCF Advanced Microelectronics Facility (AMF). The device was simulated using a COM model and verified by experiment using devices fabricated on YZ LiNbO3. The designed center frequency was 250 MHz, and seven chips were implemented using seven frequencies which occupied a 25% fractional bandwidth. Each chip was approximately 100 ns long resulting in a bit length of roughly 700 ns. The free space delays, $\tau 1$ and $\tau 2$, were approximately 0.65 μs and 1.5 μs. The resulting device length was approximately 1 cm. The transceiver was then simulated using the predicted and experimental responses of the sensor. Figure 1 shows a schematic of the device and the actual time domain responses, theoretical and experimental. Figure 2 shows the correlated compressed pulses from a transceiver simulation using the predicted and experimental SAW responses. There is excellent agreement between prediction and experiment. Also note the time ambiguity of the compressed pulses. Each pulse is approximately $0.28 \bullet \tau c$ long. This corresponds to a processing gain of 49 which is seven times greater than that of a seven chip PN sequence using a single frequency carrier. As a result, the OFC system has increased range and sensitivity when compared with conventional single frequency pulse implementations. To verify general operation and tests at room temperature, the fabricated wafer was placed on a temperature controlled RF probe for near room

temperature measurements. The SAW temperature sensor results are shown in Figure 3. This plot compares the YZ LiNbO3 sensor with thermocouple measurements. The results are presented using the SAW sensor device and the temperature-controlled chuck output. The device was tested between 10 and 180 °C increments. Overall, there is good agreement between the sensor and thermocouple.

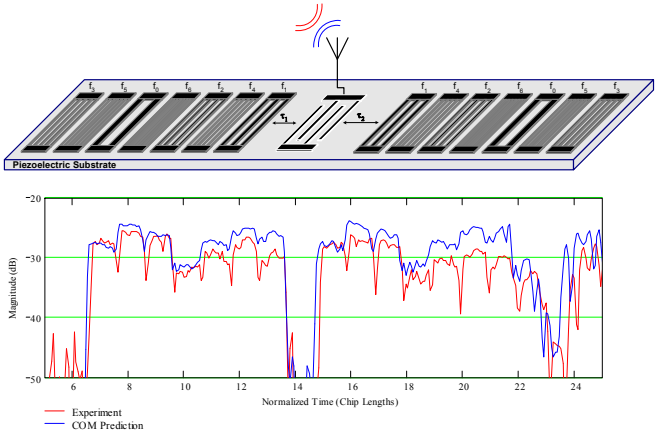

Figure 1. OFC SAW sensor schematic drawing and corresponding measured impulse response received from reflector grating. Experimental data – lower trace (red), COM model – upper trace (blue).

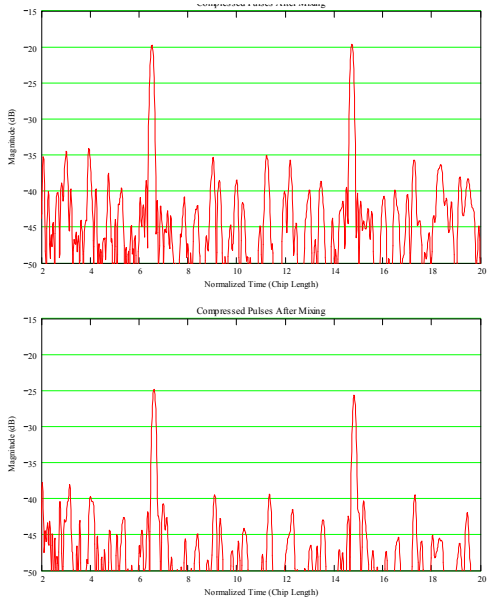

Figure 2. OFC SAW sensor compressed pulses using COM model (above) and experimental device on YZ $LiNbO_3$ (below).

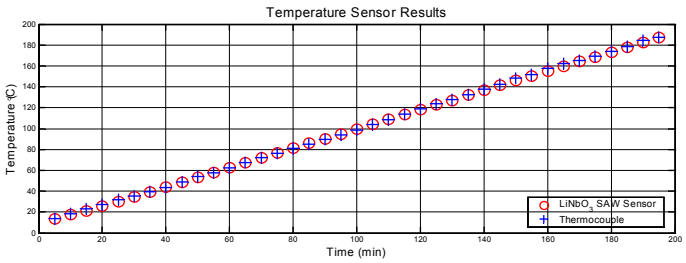

Figure 3. Seven chip OFC SAW temperature sensor tested between 10 and 180 °C and compared to thermocouple measurements.

Cryogenic Testing of SAW OFC Temperature Sensor

The OFC SAW sensor device was diced from the wafer, packaged and bonded. A cold finger was created using a copper rod and liquid nitrogen-filled Dewar. The temperature of liquid nitrogen is approximately 77 °K which is well above that of hydrogen. However, liquid nitrogen is inert and readily available and was chosen as a good first step in reaching the liquid hydrogen temperature range. A vacuum chamber was designed and built and fixtured to sit atop the Dewar. The vacuum was used to eliminate condensation on the surface of the SAW device and RF cabling. Figure 4 shows a picture of the test setup with the liquid nitrogen Dewar, vacuum chamber, and test apparatus. Swept frequency device measurements using an automatic network analyzer and thermocouple measurements of the SAW sensor were taken every minute. For these first tests, the device was hard-wired to test just the SAW OFC sensor operation. The measurement data were then applied to a simulated transceiver using Matlab® software. The matched filtering process yields two compressed pulses. The time separation between pulses is proportional to the sensor temperature. A second order polynomial curve fit was generated using the pulse separation data. The second order curve was then used to estimate the material temperature coefficient and is shown in the figure 5. The SAW sensor continued to operate as expected over the entire temperature range. Note the minimum temperature reached is approximately -170 °C, which is about 30 °C higher than that of liquid nitrogen. This is due to ambient temperature losses at the vacuum chamber, and is unavoidable using the current test equipment. Next, the extracted temperature coefficient and pulse separation data were used to predict the sensor temperature. The results were compared with thermocouple measurements and are shown in Figure 5.

Figure 4 Cryogenic temperature experimental setup.

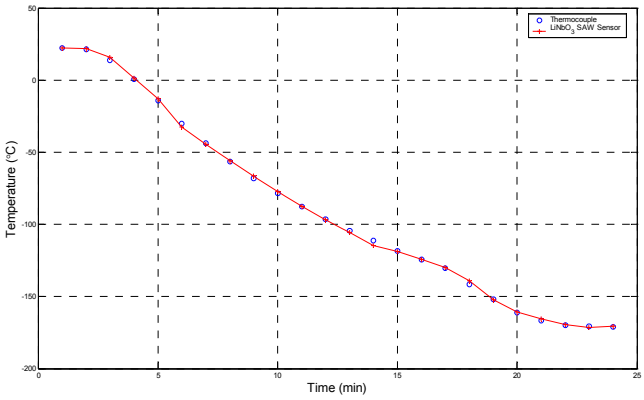

Figure 5 Measured temperature from SAW OFC sensor (solid) and thermocouple measurement (points). Scale: Vertical: +90 to -200 °C, Horizontal: Relative time (min), 0 to 30 minutes.

OFC SAW High Frequency Device Experiments

We have successfully fabricated and tested OFC devices at 1 and 1.5 GHz. The motivation for higher frequency operation is that at these frequencies the antenna size will be significantly smaller and easier to design. Figures 6 and 7 show the COM model predicted and experimental time domain and frequency domain responses of the 1.5 GHz device, respectively. The attenuation observed in the latter chips in the time domain response is due to bulk mode and propagation losses. Various modifications to the device design are being investigated to eliminate or minimize this loss significantly. These results demonstrate that high frequency devices can be successfully designed for use with OFC SAW sensors.

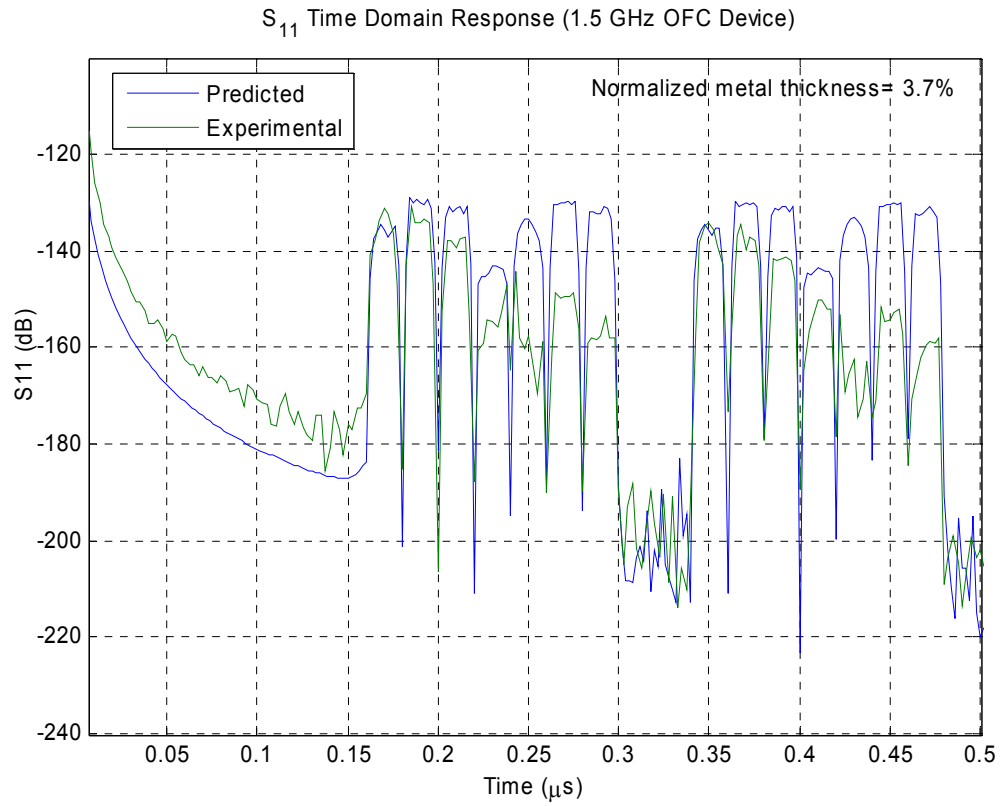

Figure 6. Time Domain S11 response of 1.5 GHz OFC sensor.

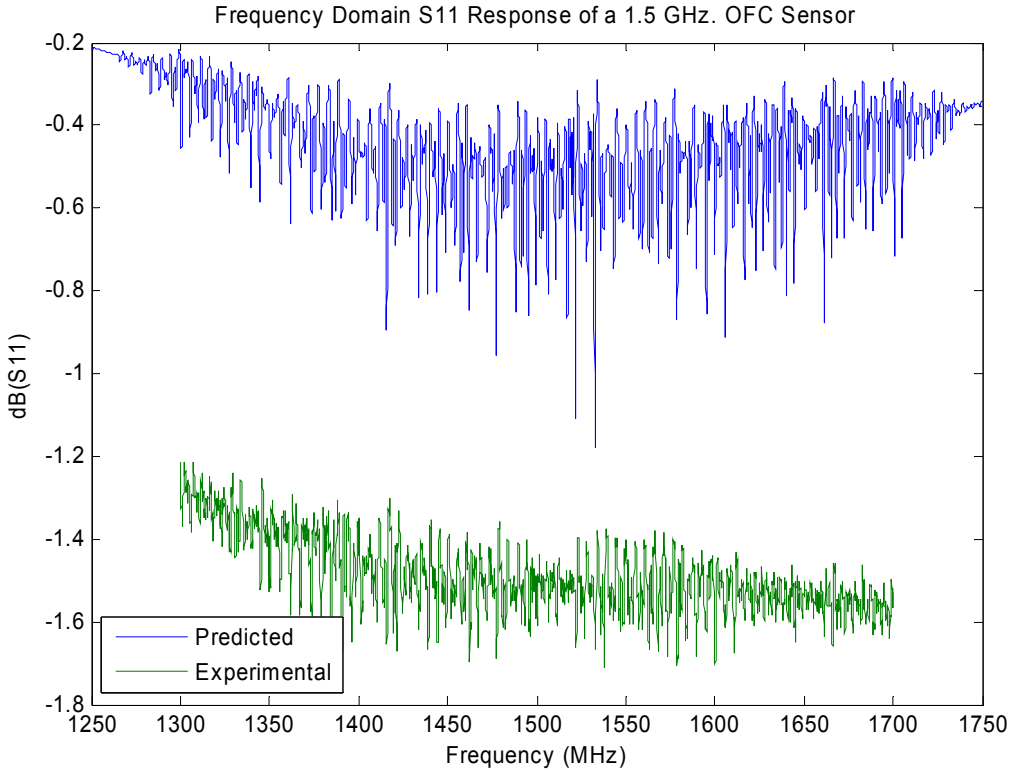

Figure 7. Frequency Domain S11 response of 1.5 GHz OFC sensor.

Hydrogen Gas Sensing Using SAW Devices

SAW Hydrogen Sensing with Pd Films on OFC SAW Sensor – First Experiments

Thin Palladium films of varying thicknesses (45A^{o}, 80A^{o} and 120A^{o}) were deposited in one of the delay paths of an OFC device at a center frequency of 250 MHz, similar to the initial devices used for temperature sensing. The other delay path was used as a reference in order to eliminate temperature effects. The devices were then probed in a probe station. The probe station chamber was filled with a mixture of 3% hydrogen and nitrogen for testing and during the "off" cycle the chamber was purged with nitrogen. The actual device layout is shown if figure 8, where the transducer is being probed and the palladium film is depicted to the right of the transducer, with two reflector banks, one on either side of the device. The compressed pulse shifts for both delay paths of a device with a 45A^{o} palladium film are shown in figure 9. The blue curve is the compressed pulse shift for the delay path with palladium and shows a shift of roughly 80 picoseconds when the hydrogen is turned on, and a slow recovery when the hydrogen is turned off. The green curve is the compressed pulse shift for the delay path without palladium and is fairly stable during the entire experiment.

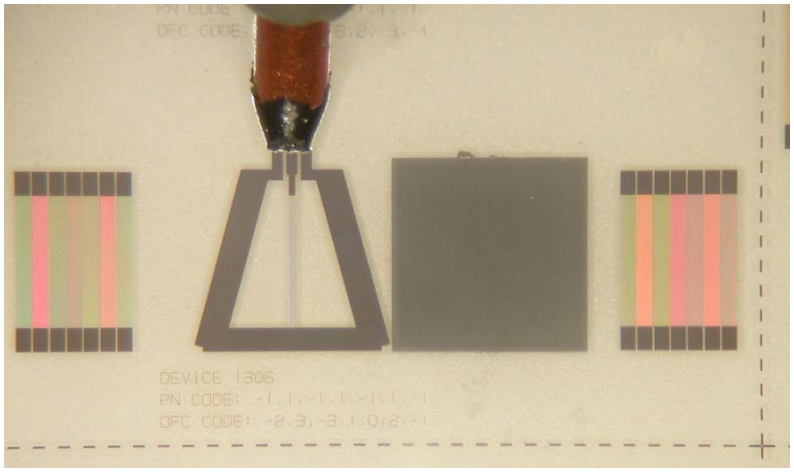

Figure 8: A 250 MHz OFC device with Pd film (Solid dark electrode) in the delay path.

These initial tests are very promising since it shows that the devices are sensitive to hydrogen gas. The test setup needs modification since the RF probe test station uses a very large chamber which yields no good control when introducing the gas, purging, measuring time delays, etc.

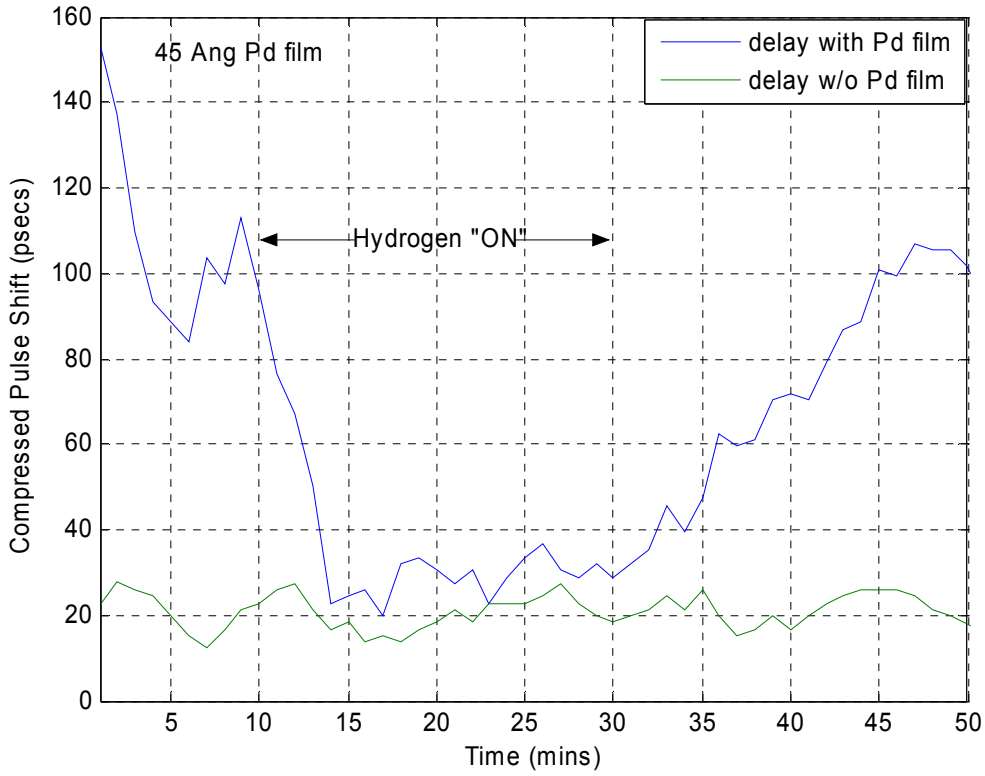

Figure 9. Compressed Pulse Shift for Device with 45A^{o} film in Delay Path.

Work in Collaboration with FSEC for SAW Hydrogen Gas Sensing

Discussions were conducted with FSEC to determine if a proprietary, chemical which has been developed for visually seeing hydrogen exposure would also be applicable to the SAW sensor. FSEC prepared a proprietary chemical (tungsten oxo-complex) which was applied on one side of the delay path of a 250 MHz OFC device. This chemical has a response time on the order of seconds, and using it on OFC SAW sensor could allow for wireless sensing of hydrogen with very quick response times.

For the first attempt the chemical was mixed in a ratio of 1gram of chemical in a 5 mL solution of DI water and methanol in a 1:1 ratio, (i.e., 2.5 mL of DI water and 2.5 mL of methanol). This was done so that the evaporation rate off of the surface of the device would be much faster than if the solution was prepared in DI water. The solution was then spun onto a wafer yielding a thin film in one of the delay paths. Once the solution had evaporated leaving behind crystals of the chemical, the device was tested. It was observed that the presence of the chemical on the surface of the device had damped the wave so that no response was observed. Since the SAW has a component of particle motion normal to the surface, the presence of the chemical damped the SAW due to heavy coupling.

Successive attempts were made to obtain an operational device by reducing the concentration by half (i.e., using 0.5 grams of chemical instead of 1 gram) and dropping a very small amount of solution on the delay path. Pt was also deposited in the delay path, since it can be used as a catalyst in the chemical reaction. However, the presence of the FSEC chemical on the surface of the device continued to damp the SAW. Thus far, these experiments have been

unsuccessful. Finally, It has also been observed that the device is highly hygroscopic, making it challenging to isolate the effects of moisture from the presence of hydrogen. The mechanism for detecting hydrogen is to measure a change in delay due to mass loading or a change in the stiffness parameters. If water absorption is significant, then it will be impossible to separate humidity effects from hydrogen gas presence. This approach was abandoned since it was not making progress, and it seemed unlikely that success would be achieved, toward a successful SAW hydrogen sensor at this time.

Background Research on Palladium Thin films

Palladium (Pd) Nano-thickness Films

Palladium (Pd) is an appropriate material for hydrogen sensing because it selectively absorbs hydrogen gas and ultra-thin films of Pd that are deposited on glass may form nanoclusters[1],[2]. When exposed to hydrogen, these films exhibit a sharp change in resistivity primarily due to hydrogen-induced lattice expansion (HILE)[2]. HILE is responsible for swelling of Pd nanoclusters consequently creating more conductive pathways and lowering the resistivity of the film. This behavior is most pronounced for films that are between 2 to 5 nm thick. The majority of the effort focused on Pd nano-thin films as discussed in the following sections.

Platinum Indium Tin Oxide (Pt/In_2O_3-SnO_2) Films

Platinum indium tin oxide (Pt/In_2O_3-SnO_2) films can also be used for hydrogen sensing since platinum absorbs hydrogen and exhibits a change in it electrical properties. The film absorbs hydrogen molecules at the surface then dissociates them into protons and electrons. These protons form water molecules in a reaction with absorbed oxygen ions and the electrons contribute to an enhanced electrical conductivity of the film[3]. These type films have been produced by Drs. Seal and Cho's groups at UCF. A small effort was conducted to study their films for possible use in the SAW sensors.

Palladium Nano-thin Film Efforts

Palladium Thin Film Resistivity Model

Research was conducted on Pd thin films ranging from approximately 1.5 to 100 nm in thickness to determine resistivity versus thickness, develop a model, and to study the Pd films reaction to hydrogen gas exposure. Using deposited and measured Pd thin films at UCF, and previously published data (by Argonne National Labs [2]), resistivity versus film thickness plots were obtained. Based on these plots, a model was developed, which predicts the film resistivity versus film thickness over the ultra-thin to thick film regime (1.5 to 100 nm). A comparison of the predicted versus measured data will be presented. In addition, the Pd films were exposed to 2% hydrogen gas and the change in sheet resistances was measured.

The data from Argonne Labs (Fig. 10) represents Pd films that were grown on polished glass slides at a rate of 0.01 nm per second, in a ~10^{-6} torr vacuum chamber. The Pd was vaporized with a Polaron evaporator and its thickness was observed with the use of a crystal monitor [2]. The electrical and mechanical properties of ultra thin films (1.5 to 10 nm) are dependent upon various conditions of the growth environment, most notably, deposition rate, chamber vacuum, and the topology and temperature of the material on which the film is being grown. Thus, in order to grow comparable films, it was desired to replicate, as close as possible, the environmental conditions during Argonne Labs' film growth. The films from UCF were grown on polished ST quartz wafers using approximately the same growth rate and vacuum conditions as

Argonne Labs'. The Pd at UCF was vaporized using a concentrated electron beam and it thickness monitored using a crystal monitor. UCF grew films on polished quartz wafers as opposed to polished glass slides because quartz is a known piezoelectric material which is frequently used to construct SAW devices. Also, quartz wafers have a highly polished, optical-polish finish, and are very smooth and flat. Bare glass slides have little to no control on surface polish quality. Thus it is desirable to determine the baseline behavior of Pd thin films on quartz substrates. The resistivity of the films for Argonne Labs was monitored *in situ* (during film growth). UCF does not yet have this capability, thus the film resistivity was measured after removal from the chamber using a four point probe and DC probing. The measurement accuracy of four point and DC probing decreases below 8 nm and it is fairly difficult to characterize ultra thin films using these methods. This issue is apparent in the experimental results plot (Fig. 10), which shows some scatter in the UCF data due to thickness measurement precision and accuracy, and thin film resistivity measurement accuracy.

E.H. Sondheimer derived a model for the electrical resistivity of metals as a function of film thickness, based on the mean free path of electrons in an infinitely thick medium (Eq. 1) [4]. The mean free path is defined as the average distance an electron travels before it collides with the lattice of the medium.

$$\rho_{thin} = \frac{\rho_\infty \cdot 4 \cdot \lambda_\infty}{3 \cdot t\left(\ln\left(\frac{\lambda_\infty}{t}\right) + .4228\right)} \quad \text{(a)} \qquad \rho_{thick} = \rho_\infty \cdot \left(1 + \frac{3}{8} \cdot \frac{\lambda_\infty}{t}\right) \quad \text{(b)}$$

Equation 1: (a) Sondheimer's approximation for thin films (b) Sondheimer's approximation for thick films; where t is the film thickness, ρ_∞ is the resistivity of an infinitely thick metal and λ_∞ is the mean free electron path in an infinitely thick film. When compared to the raw data, Sondheimer's approximations showed poor agreement for films that were below 8 nm thick (Fig. 10).

It was desired to develop a thin film resistivity model which would be valid over the entire film range of interest. It was apparent by looking at the data that the current equation forms would not work. A modification and extension of the equation included an exponential component to Sondheimer's thick film approximation which would provide a fit in the nano-thin film regime and is given in Eq. 2.

$$\rho = \rho_\infty \cdot \left[1 + \frac{3 \cdot \lambda_\infty}{8 \cdot t} \cdot \left[1 + B \cdot e^{-A \cdot (t - t_c)}\right]\right]$$

Equation 2: UCF's amended Sondheimer Relation resistivity equation, where A and B are constants determined by curve fitting; the critical thickness, t_c, is the approximate thickness that the measured data and the Sondheimer's approximations disagree.

There are a few data points that deviate from the model below 10nm; these deviations are due to possible errors in measurement and/or variations in the growth environment of the film. Even with these deviations, the UCF model shows fairly good agreement with the measured data.

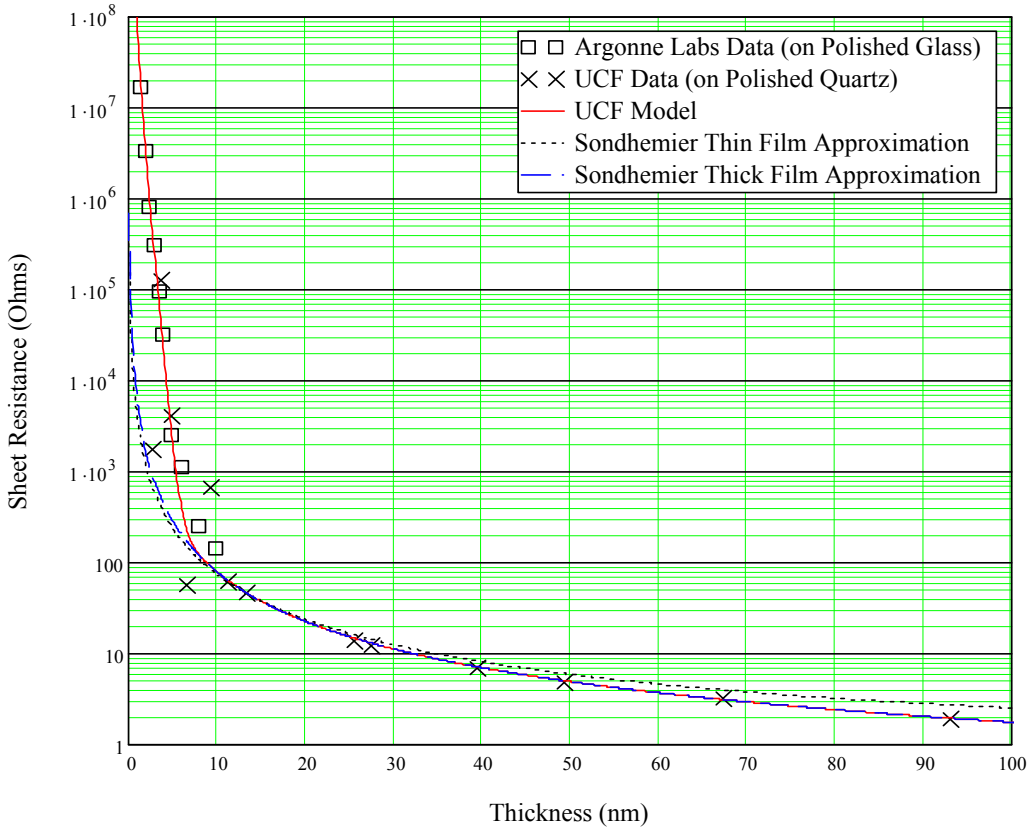

Figure 10. Pd sheet resistance vs. film thickness theoretical and experimental comparison.

Hydrogen Exposure of Ultra- Thin Pd Films

Ultra thin films are extremely difficult to measure so they were placed on electrode structures with large probe pads for easy nondestructive probing. The most useful structure in the experiments was the inter-digitated resistor (IDR) pattern (Fig. 11). When a film is deposited on the fingers of this structure, rows of parallel resistors are created, thus lowering the overall resistance of a film. The IDR bus bars and fingers are constructed of an approximately 5 nm thick titanium adhesion film and 150 nm aluminum film. Approximately 4 nm of Pd were deposited on the fingers of the IDR presented.

Several different methods were attempted to measure film sheet resistance. The method that was reproducible was to use a voltage source and current meter to extract the IDR resistance, both with and without exposure to 2% hydrogen gas; results are shown in Fig. 12. Prior to hydrogen exposure the Pd film current versus voltage test was performed in order to determine the resistance of the film (i.e., Resistance = Voltage/Current). The voltage source was varied from 1 to 8 V in one volt increments and the corresponding current output was recorded at each interval. The contact resistance and system DC resistance was measured and compensated. The measured data shows a nonlinear current-voltage relationship (Fig. 13a). This suggests that the Pd film resistance is voltage dependent when the interdigitated structure is placed beneath it (Fig. 13b). The reported resistance needs to indicate the applied voltage for the measurement. This was an unexpected result. The effect may be due to field assisted tunneling of the nano-structured films, or some other phenomenon. This result was discovered at the end of the contract and further research is warranted to determine the mechanism(s). The change in resistance is very dramatic as the applied field is increased.

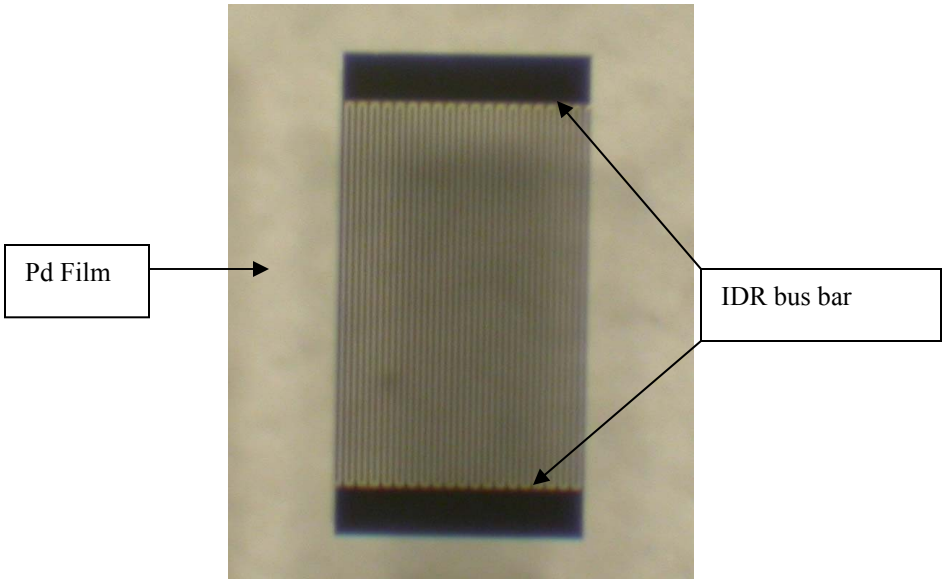

Figure 11. Interdigitated Resistor (IDR) with 4nm film. The Pd film is the grey shadow covering the IDR electrodes.

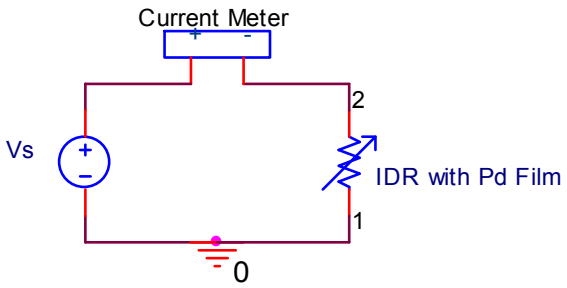

Figure 12. Measurement configuration for DC probing of Pd film.

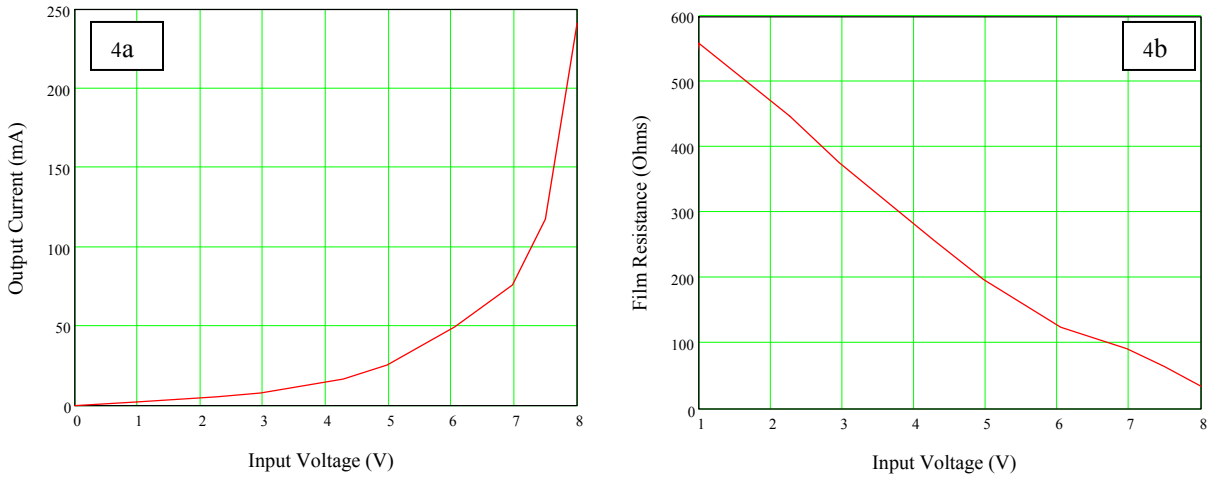

Figure 13. (a) Current vs. voltage relationship of Pd ultra-thin film with an IDR beneath it (b) Resistance vs. voltage relation ship of ultra-thin Pd film with an IDR beneath it.

Using the same measurement configuration depicted in figure 12, the source voltage was set to a constant voltage and the Pd film was exposed to 2% hydrogen gas and the current was recorded. The hydrogen gas was cycled on and off repeatedly and the current change from each cycle was recorded. This cycling was performed at source voltages of three, four and five volts in order to observe the amount of change in film resistivity as a function of the applied potential; the results are presented in figures 14 to 17. The graphs show a rapid increase in current when the film is exposed to 2% hydrogen gas and a fairly rapid decrease in current flow when the hydrogen is removed. The mean rise and falls times are approximately 1.5 and 15 sec, respectively. The rise time is defined as the amount of time required for the current to reach 90% of the maximum change after H_2 is applied to the film. The fall time is defined as the time required for the current to reach within 10% of its value prior to the cycle. The mean percentage change in the current through the Pd film during each cycle is voltage dependent as is expected from the voltage dependent resistance of the film (Table 1). Figures 14 to 17 show an increase in current through the film after the first cycle and several successive cycles; in each case after the last cycles was performed the current through the film returned to its initial value. The amount of time to return to the final value is voltage dependent (Table 1).

The results of the cycling experiments indicate that there is a reversible change in the electrical resistivity of an approximately 4 nm thick Pd film due to the presence of 2% hydrogen. This room temperature reversibility suggests that the IDR with Pd film may be implemented as a reusable hydrogen sensor. Previous reports on hydrogen sensing using Pd films on a bare substrate do not show reversibility without temperature annealing the film to remove the hydrogen[5]. Furthermore, this data suggests that the creation of a SAW hydrogen sensor using Pd ultra-thin films is feasible.

Table 1. Source voltage compared to the amount of time required for the system current to return to its initial value.

Vs	Amount of Time to Return to Initial Current Value Before Any Cycling was Performed	Average Percentage Change in Current During Cycling
3V	5 minutes	29.7%
4V	16 minutes	35.3%
5V	90 minutes	89.61%

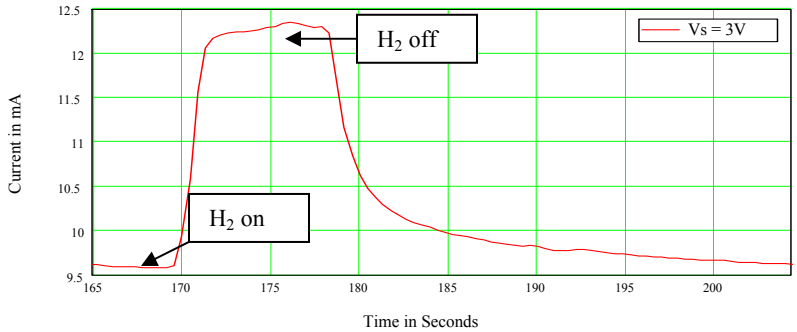

Figure 14. Close-up of the one cycle of the Pd film response to 2% H_2 gas.

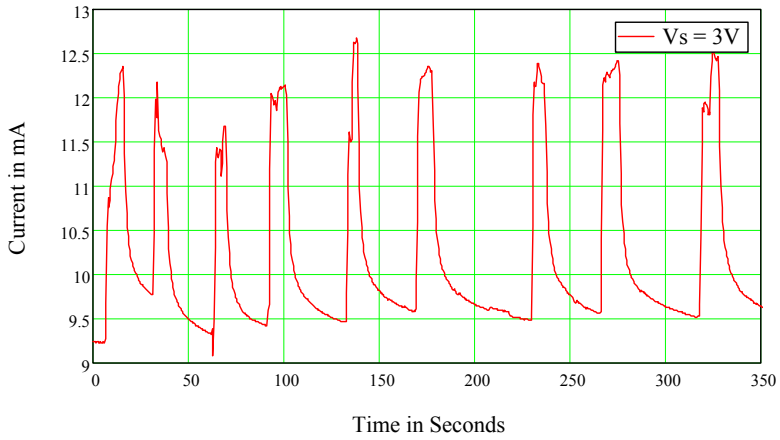

Figure 15: Repeated cycles of 2% H_2 gas with source voltage = 3V.

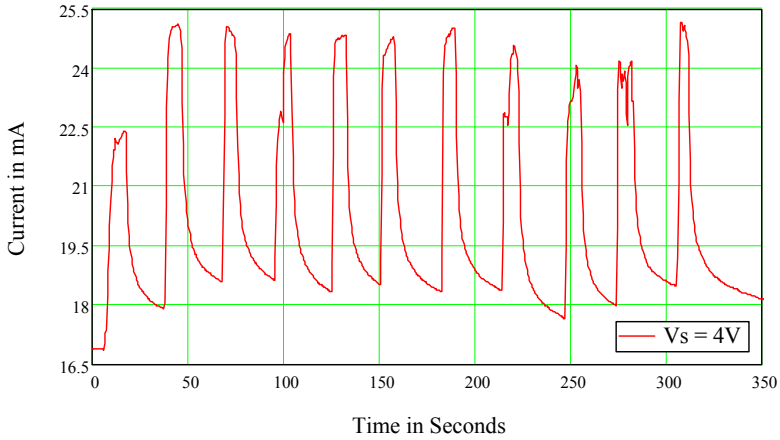

Figure 16: Repeated cycles of 2% H_2 gas with source voltage = 4V.

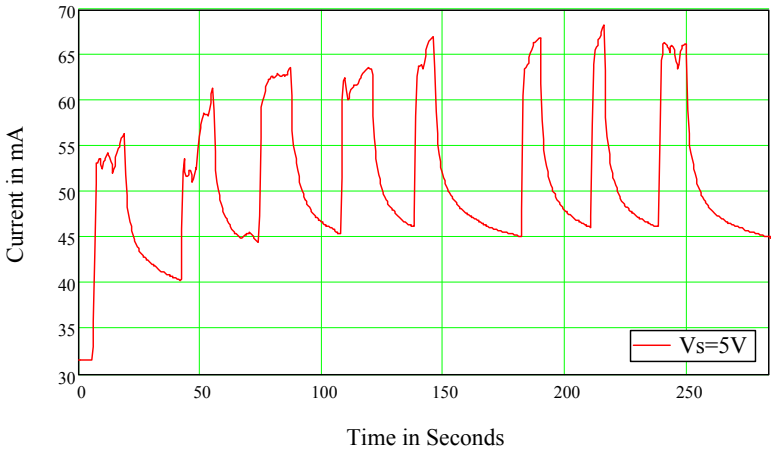

Figure 17: Repeated cycles of 2% H_2 gas with source voltage = 5V.

Platinum Indium Tin Oxide (Pt/In_2O_3-SnO_2) Films

UCF obtained a silicon wafer coated with Pt/In_2O_3-SnO_2 film form Drs. Seal's and Cho's research group at UCF in order to evaluate its response to 2% hydrogen gas loading via the same experimental setup depicted in figure 12, and to determine if this could also be integrated into a SAW sensor. They had reported large changes in resistivity when exposed to hydrogen, but the starting resistance value is also very large. The application technique is somewhat tricky and may not be applicable to SAW application due to the chemistry, heating and chemical PH. Unfortunately the results were inconclusive based on several attempts and further research in the future is warranted.

Palladium Thin Films on SAW Delay Line

The IDR shown in figure 9 was placed in the delay path of a SAW delay line fabricated on ST quartz (Fig. 18). Ideally, the velocity and/or amplitude of a surface wave between the input and output transducer should be altered by the IDR and Pd film. The amount of change in the velocity of the surface wave should be proportional to the electrical and mechanical loading on the substrate as a result of the IDR Pd structure. Additionally, the velocity change is dependent upon the electro-acoustic coupling coefficient, k^2, of the piezoelectric material (Eq. 3)[6].

$$\Delta v = \frac{k^2 \cdot v}{2}$$

Equation 3: Approximate relationship between electro-acoustic coupling coefficient and the change in surfac wave velocity in a piezoelectric material.

The coupling coefficient of the piezoelectric substrate examined here (ST Quartz) is low (0.17%), thus, it may be difficult to observe any changes in velocity from this delay path [6]. The delay line shown in figure 18 was connected to a vector network analyzer (VNA) and the S parameters were measured before and after the Pd film was applied. The film was then exposed to 2% H_2 gas and the S parameters were measured again. In doing these measurements the change in delay and/or amplitude may be observed in order to determine the behavior of the SAW beneath the IDR with and without a Pd film and H_2 gas exposure. An examination of the data shows no measurable change in wave amplitude or delay in the three cases (Fig. 19). This suggests that the low coupling coefficient of ST quartz may be a problem. To address this issue, a similar device will be fabricated on YZ lithium niobate (LN) where the coupling coefficient is approximately 25 times that of ST quartz. It is not known if the same growth mechanisms for the nano-thin film will exist on the LN as on quartz. Given the fact that the early work on the Pd thin film on LN did show a change in SAW delay with hydrogen exposure, we are optimistic. Also, only this one experiment was performed since the Pd thin film effect was discovered near the very end of the program.

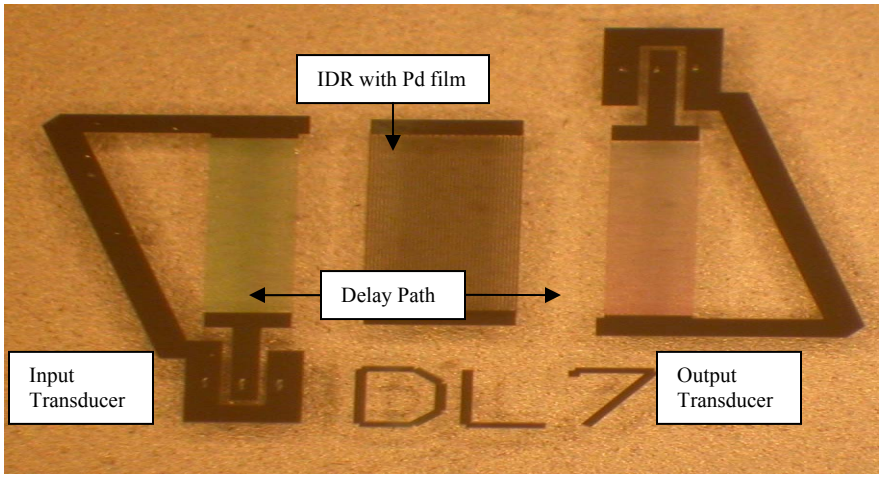

Figure 18. Pd thin film on IDR in SAW delay path.

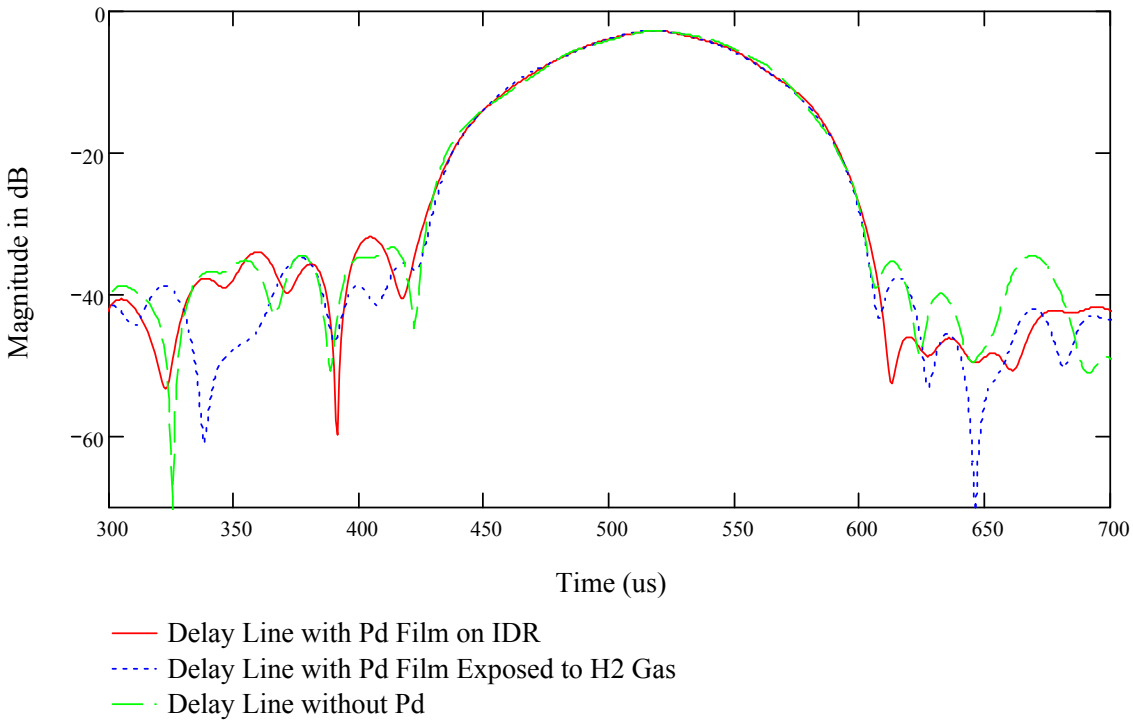

Figure 19. Comparison of peak delay for the SAW delay line with and without Pd film when exposed to 2% H_2 gas.

Multi-Sensor Code Collision Research

PN OFC Coding

After some preliminary studying, it was determined that the reception of the coded responses from multiple sensors could be difficult to separate. Since this is key to the device platform, efforts were begun to study the effects and to find possible solutions. First, UCF completed a preliminary evaluation of PN and OFC coding approaches. The goal of this effort was to study the interactions of multiple codes in a realistic sensor environment. The evaluation approach used consisted of modeling ideal OFC signals in a simulated multi-sensor environment. Each OFC "bit" is equivalent to a sensor, with an embedded PN-OFC code. Seven or more "bits" with different codes were considered. Multiple bits with random delays were generated, and the OFC autocorrelation of one code (with itself) and the cross correlation with the other 6 codes is simulated. Initial MathCAD simulations show that the code sequence is important in minimizing the cross-correlation sidelobes, as was expected. An example of the distortion effects which can be obtained is shown in the two figures below. Figure 20 shows the autocorrelation of the 3rd bit (3rd sensor) in the multiple sensor environment. The autocorrelation sidelobes are not optimum, but are acceptable. Figure 21 shows a comparison of the optimal autocorrelation (3rd bit or sensor only) and the entire correlation simulated using the signal received from all 7 bits (7 sensors) utilizing a different time delay than was used in Figure 20. For this particular example, it is clear that the received signal at the expected correlation time position is smaller than the sum of the cross-correlation sidelobes, which would produce an error. This effect is a function of the random delay between bits and the actual PN-OFC code sequences. Simulations were conducted to understand these effects, to try to determine a methodology for code sequence choices, and to bound the problem for real world OFC sensor system implementation.

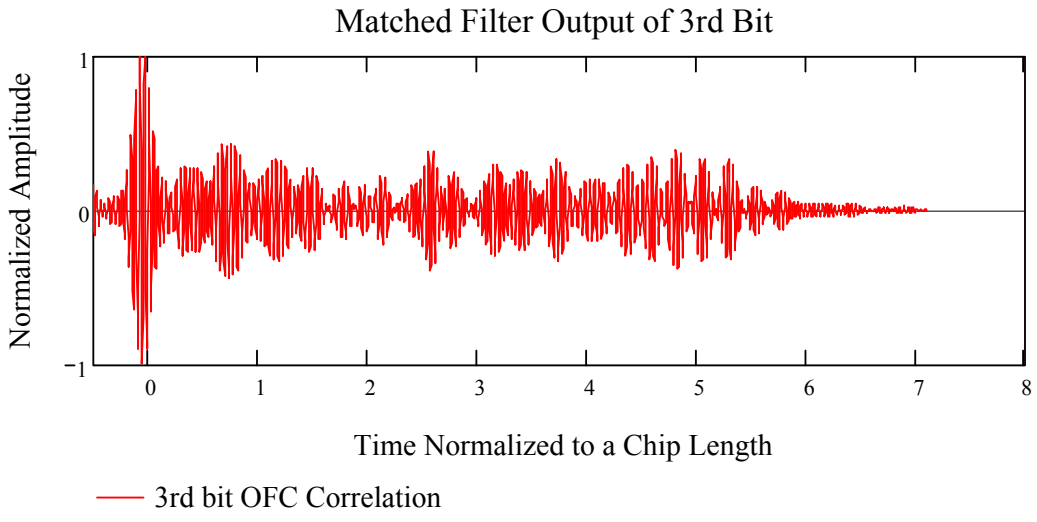

Figure 20. Matched Filter output for the 3rd Bit with time delay.

Initial evaluations showed that the use of PN coding and maximal sequences such as Barker codes and Gold codes are not useful for improving the sidelobe behavior of the auto- and cross-correlations of different codes, nor for increasing the number of useful unique codes. As an alternate approach, shuffling of the reflector frequency chips in an optimized fashion was considered. The goal of this optimization is to find different codes that provide good cross-correlation behavior and will therefore work well together in a multisensor system. Once a method for determining optimum codes has been established, it can be used to select good code sets.

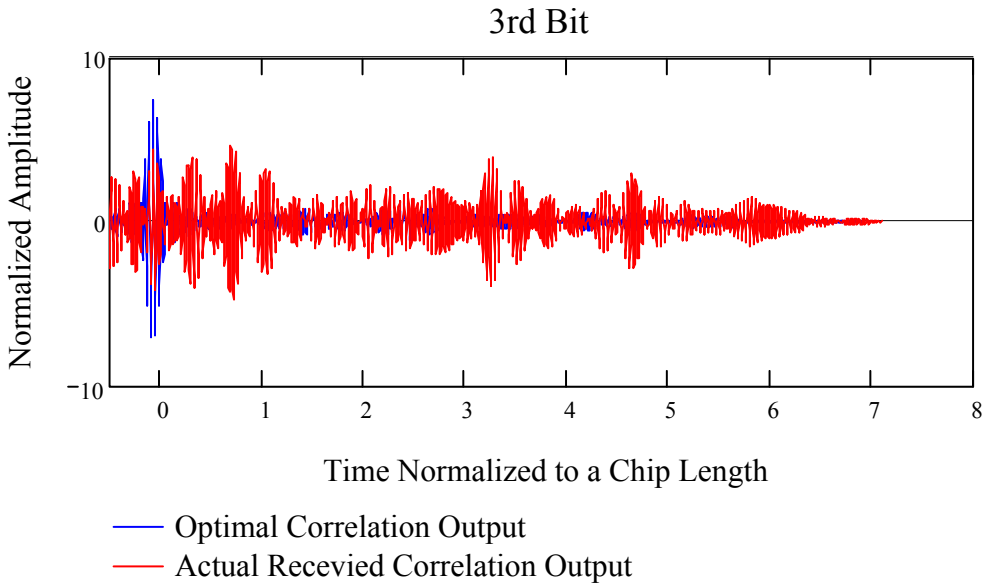

Figure 21. Comparison of Ideal output with output received from multiple bit system.

The first code shuffling criterion considered was ordering of chips in such a fashion that no two chips that are sequential in frequency occur sequentially in time in a given device. By keeping chips of close frequencies separate in time, it was thought that interference between any two codes could be minimized. Finding multiple codes that meet this criterion proved difficult, and thus UCF decided to analyze sets of codes based on correlation criteria instead.

The autocorrelation of each possible chip sequences for Nc (number of chips) using Nf different frequencies was created. For example all 7! (i.e., 5040) possible chip sequences were created for Nc=7, and Nf=7. The autocorrelation was performed on each sequence followed by the evaluation of the sidelobe levels. A maximum sidelobe level criteria was implemented which allowed for different numbers of codes to be outputted, based on user input. This evaluation method allows for outputs using different Nc's as well as different Nf's with the allowance of one or more Nf to be repeated. This initial step allowed for the narrowing of sequence possibilities. The set of code sequences created can now be manipulated and used as an initial set for the next phase of optimization, or it can be used as a set in and of itself. While this analysis provided initial narrowing of possibilities by elimination codes with poor autocorrelation sidelobe behavior, it does not take into account how these codes will interact with each other, which requires consideration of the cross correlation of various codes.

Code sets meeting the autocorrelation requirements were then used as input sets for cross correlation studies, with the goal of achieving low cross correlation studies, with the goal of achieving low cross correlation response sidelobes. A computer program was developed that takes each code selected and correlates it with all other selected codes. It then checks the sidelobe levels versus the criteria created. When the sidelobe of the cross correlation of the two codes is above the pre-set maximum acceptable level, the code being crossed with is discarded. This step is repeated for each of the different codes until at the end you are left with a set of codes that work well with the initially selected code. This set of codes work well with the one code they were created for but not necessarily with the others. It is necessary to compare all such sets of codes to obtain a set of codes that are common therefore work well with all other codes being considered. This set of codes will work together in a system in such a way that all cross correlations have sidelobes that remain below the preset target sidelobe maximum. This can be done with any number of codes desired, however due to computer run time limitations, only code sets with no more than two chips occurring at the same time positions were considered.

Once cross correlation of codes with no PN coding was evaluated, interaction of codes with PN superposition was considered. The program developed by UCF allows the user to input the set of codes they will be using in their system and the program gives the PN sequence that will give the smallest sidelobes for each code. The addition of code shuffling and subsequent PN coding produced slightly better results than previously obtained. However, implementing just this code selectivity was not able to create perfect reception, even from a small number of total tags. It also become quite evident that no amount of code shuffling or PN sequence generation optimization will be able to eliminate all errors once a large number of bits are introduced. Figure 22 shows a comparison of a system simulation with and without using the optimization. The simulation was run 100 times, meaning 100 different time delays implemented for every bit within the different systems. This creates for example 500 different bits that could be in error for a 5 bit system run 100 times. All simulations were performed in this manner.

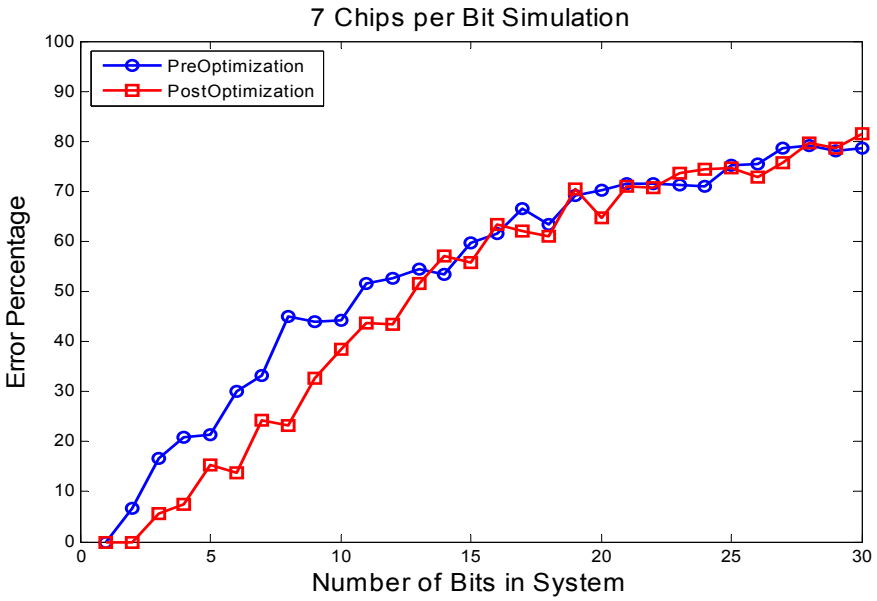

Figure 22. Comparison of error rates for pre and post optimization.

The additional of chips in each associated bit was surmised would logically add additional diversity therefore creating better performance. This was examined and found to be true as can be seen in the figure below. Observing these results which were taken before optimization we see that the amount of errors increases rapidly. The simulation was run using random time delays causing offsets in the tags. Each error was created when the matched filter output peak was not within 5ns of the random time delay associated with that tag. It also very plain that the 12 chips per bit greatly outperforms the other system simulations implemented and any additional chips would likely follow the same pattern.

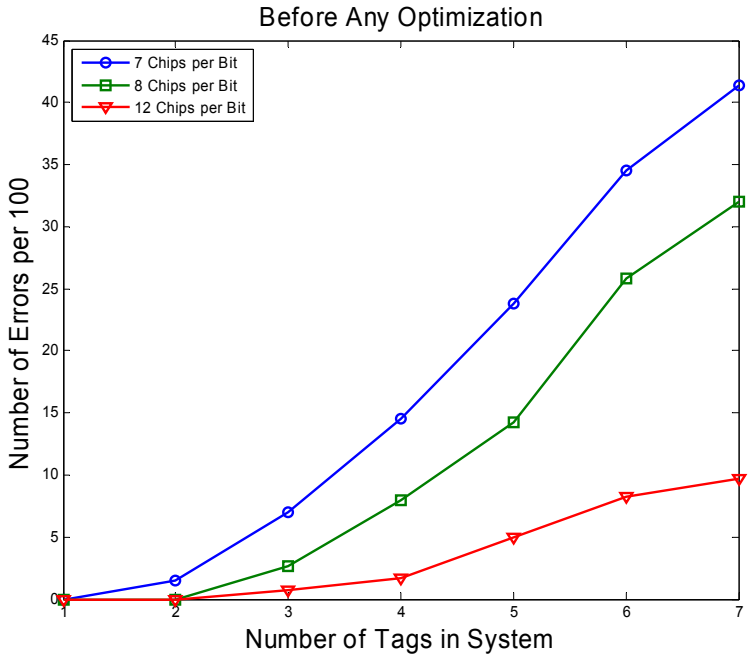

Figure 23. Errors versus number of tags in system.

Quadrature Modulation Technique

Use of quadrature modulation (QM) with parallel OFC tracks was considered, with the intent of adding additional energy to the mainlobe in order to improve performance. Implementing QM using the same OFC code in each track with one track in phase and one in quadrature did increase the main lobe energy, but also added energy to the sidelobes, not resulting in any improvement in performance. Use of QM with different OFC codes in the two tracks produced slight improvements, but not as much as was anticipated. These results were due mainly to the fact that the number of codes introduced was now double what it had been. This was thought to give a more noise like signal thus not affecting our bit or tag of interest but this was not the case. QM with a half-chip offset in the two tracks was also considered with little to no improvement over the optimized system. The half chip offset was to be implemented using a integer number of half cycles on the reflector banks. The half cycle allowed for the canceling of some of the signal creating a TDMA like signal with zeros instead of ones or minus ones being transmitted. This additional zero was thought to give us greater diversity as well without any additional reflector length or phase alteration. The signal however was difficult to separate in this form creating more problems than it canceled. The results of two different quadrature simulations are seen in Figure 24, one using a 1/4f0 delay between the tracks and the other Tau/2. The 1/4f0 slightly improves on the previously optimized code while the Tau/2 clearly does not.

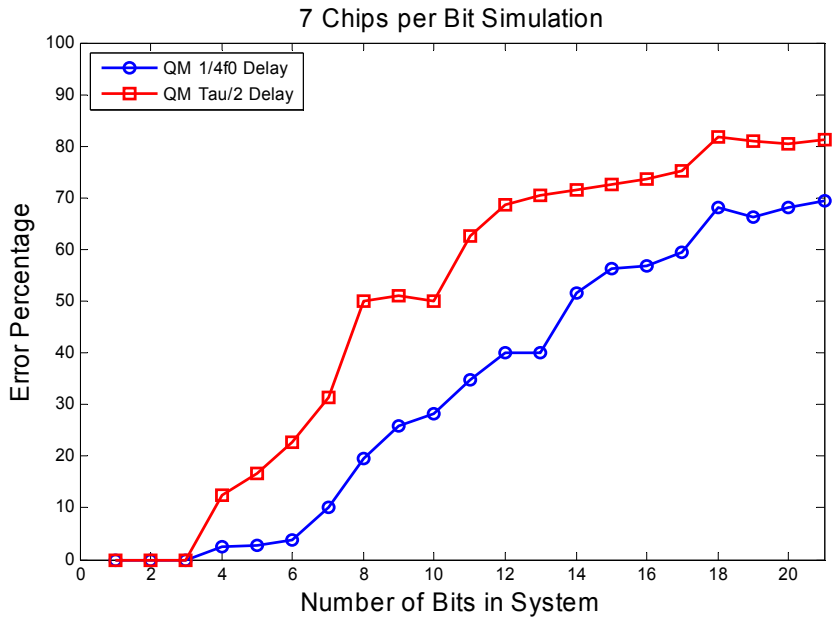

Figure 24. Comparison of two different QM techniques; 1/4f0 time delay and Tau/2.

Parallel Tracks Initial Findings

The utilization of separate tracks was implemented with the use of inphase and quadrature as seen previously in the QM technique. The use of separate tracks for this technique does not attempt to create any unique phase relationship between the two or more tracks but rather equally spaces them on the substrate. The system utilizes a configuration similar to that depicted in Figure 25.

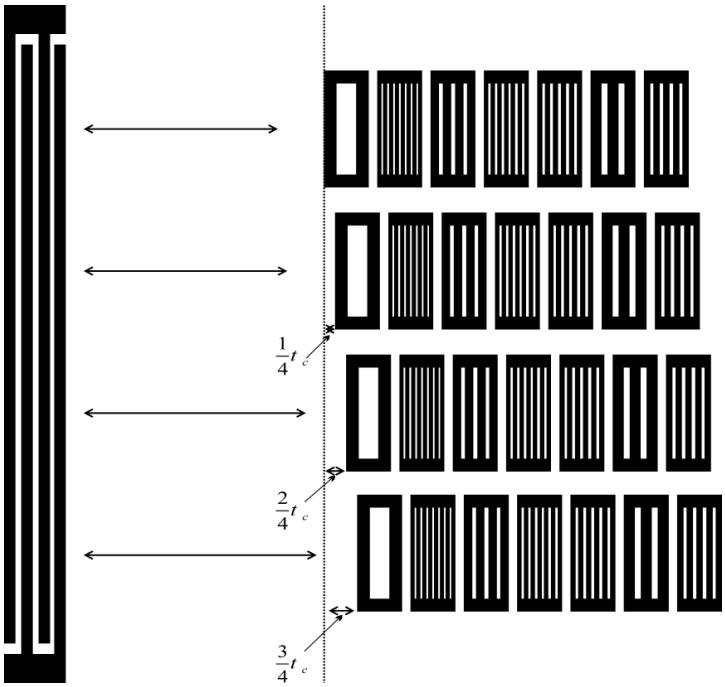

Figure 25. Parallel tracks spacing configurations.

The system performance was measured for such a configuration with the results seen below. It is evident that multiple tracks did provide better error performance as compared to previous single track systems.

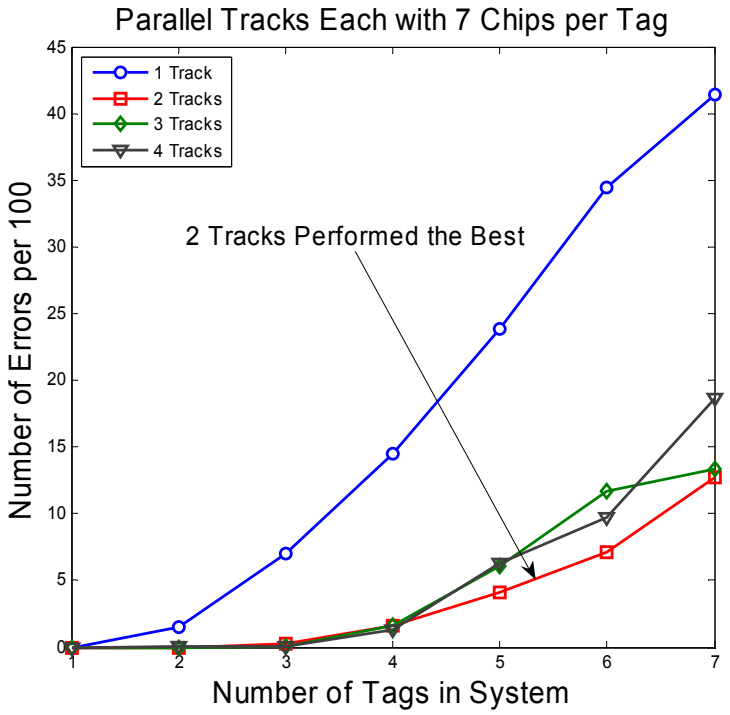

Figure 26. Error performance for 7 Chips per Bit with parallel tracks.

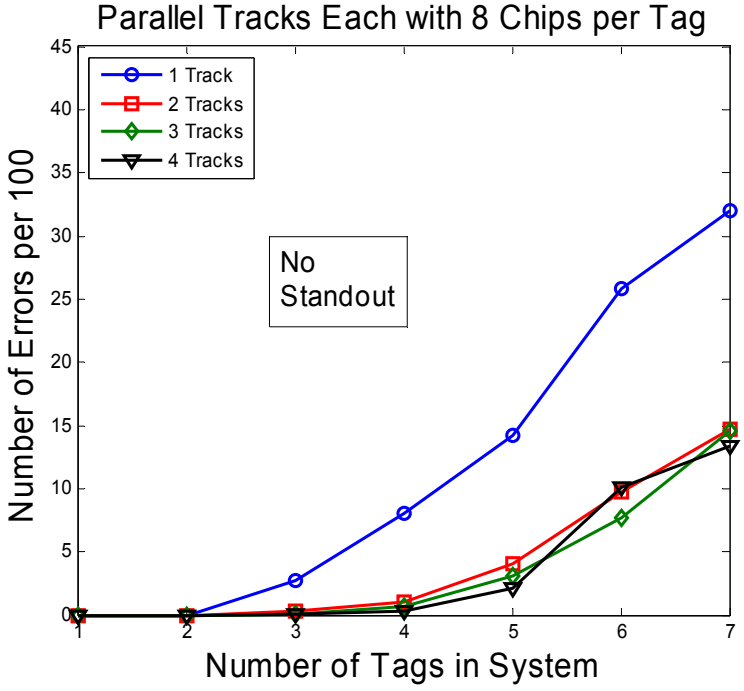

Figure 27. Error performance for 8 chips per bit parallel tracks.

These simulations utilized the same criterion based error assignments as with the 7, 8, and 12 bit figure seen earlier. This allowed the comparison of the 1 track error rate with the multiple tracks. Clearly the multiple track wins out hands down however further investigation is needed into creating better codes and PN sequences.

The evaluation of the error percentages allows for a certain level of information to be obtained by a cursory glance. The histograms given below allow for further investigation of the errors. These represent how far away from the expected value the errors appear. The four graphs represent benchmark points in the system evaluation.

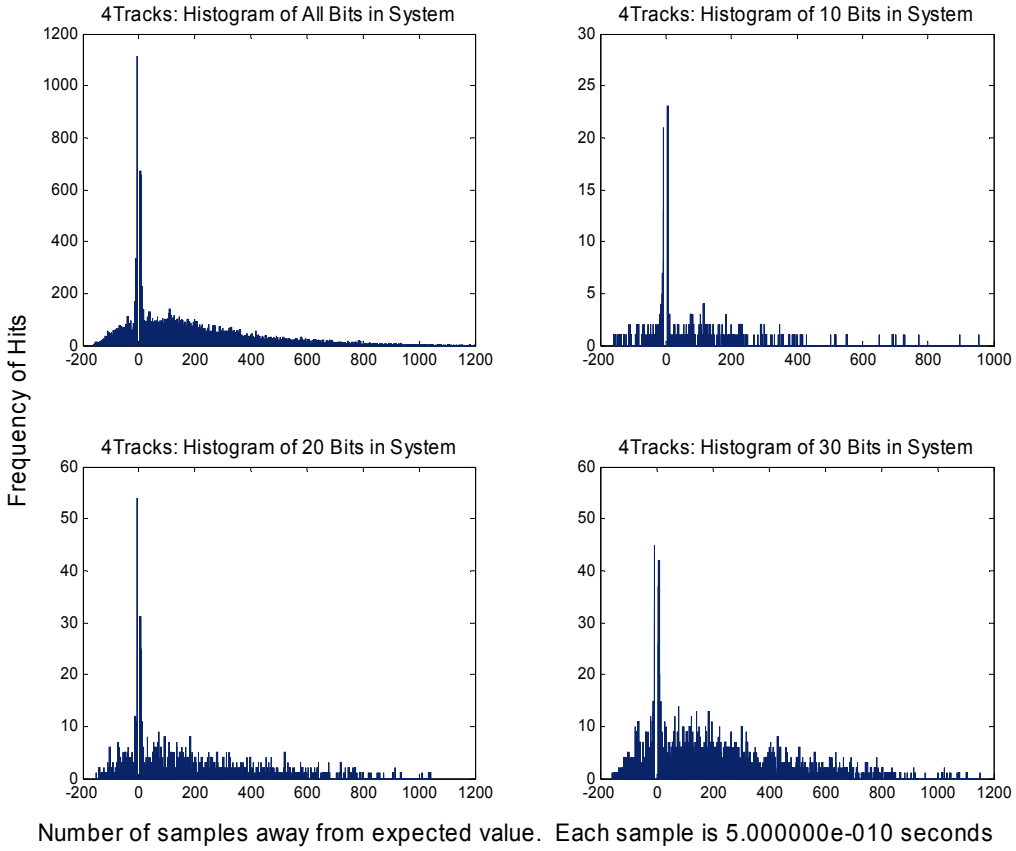

Figure 28. Histogram representations of the different benchmark error investigations.

Little discernable difference between the different track numbers and even number of bits in system doesn't allow for this implementation to be singled out as the most effective. Much needs to be looked at in this system to more thoroughly understand it. Work into the observation of correlation peaks to observe the difference when different PN codes were used on the different tracks as well as the use of Tau over 2 with an integer number of cycles giving the possibility of a TDMA like system was also looked into as to its viability. The observation of a TDMA like signal prompted investigation into a planned TDMA signal.

Tri-level Coding, One Zero Minus One

In order to minimize crosscorrelation sidelobes and the minimize the code collision effects, a tri-level coding approach was introduced which allows amplitudes/phases of -1,0,1 values. Zero amplitude eliminates any energy at chip position and can also be thought of as pulse-position-modulation (PPM).

First steps involved the use of a possible time division multiplex or pulse position modulation scheme was the determination of how the sequences would be chosen while still employing the orthogonality and pseudo noise sequences that were used previously. This presented itself with the use of a one, zero or minus-one for the possible multiplier to the chip signal. Each chip location would have the possibility of being multiplied by one, zero, or minus one creating a gap in the time domain, Tau_c long. With this idea in mind, sets of possible sequences were created and simulated in the system format. The results for using 4 frequencies and 5 frequencies can be viewed below.

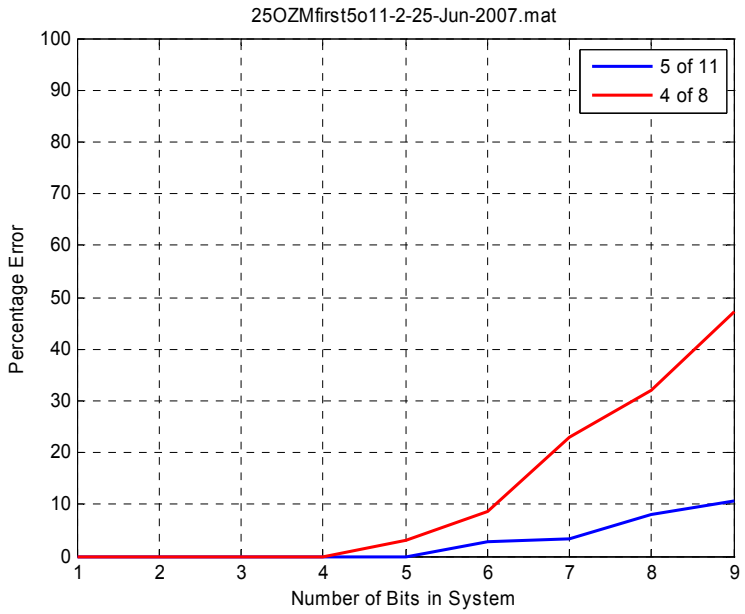

Figure 29. Error percentage versus number of nits for use of 4 of 8 and 5 of 11 chip slots.

It is clear that the 5 frequencies performs superior in this scenario. While this is clearly the best error rate that we have seen at mere 10% with 9 tags simultaneously in the system, a further step was taken by creating an additional space between each of the chip lengths to verify the reduction in collision which yields better performance. The results are seen below in Figure 30. It is clear that the performance of this method is much better than any utilized previously. An error percentage of a only 1.9% error with 9 tags in the system and 0 elsewhere was established.

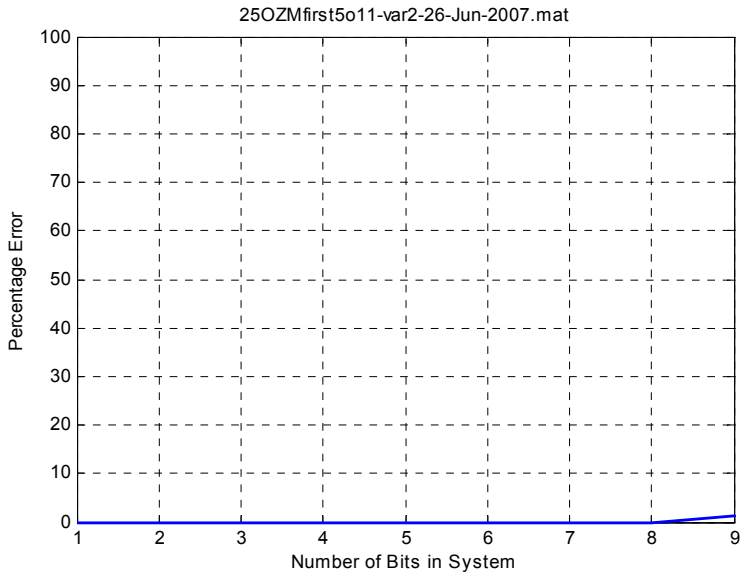

Figure 30. Use of 5 of 11 slot-frequencies, with an additional slot between each chip.

Data acquisition System—Design 1

In order to first research the devices, an automatic network analyzer (ANA) is used in place of the transceiver. The device scattering (S-) parameters are obtained. Using this data, a software simulation can be developed which studies the device. Further simulation tools are developed for simulating the receiver system, using real, measured device data, but simulating the interrogator system in software. A data acquisition system is ultimately necessary to interrogate, receive and process the SAW OFC sensor-tag information. The UCF approach is to use a transmitter which can interrogate the SAW device with either an impulse, or a chirp input. This allows for a relatively short time burst interrogator that allows for a high interrogation rate, or allows for multi-time integration in a synchronized receiver. The UCF transceiver design concept is shown in the block diagram in Figure 31.

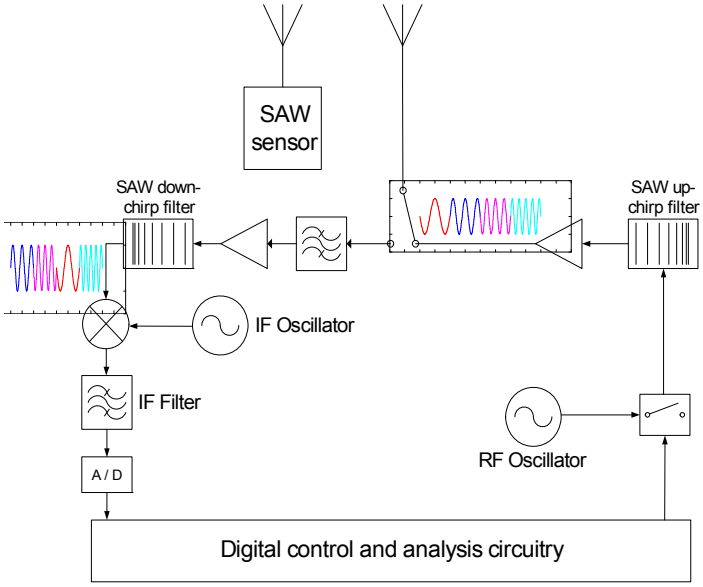

Figure 31 SAW transceiver block diagram.

The system first designed is shown in Figure 32. The system operates asynchronously and uses external generators, and the outputs are sent to a digital oscilloscope. The digital oscilloscope acts as the A/D converter and allows visual confirmation of acquisition and also allows data to be stored for post processing in the computer. The purpose of this first system was to show feasibility and proof of concept. The system can be used with either wired or wireless devices. Both types of devices were successfully demonstrated with the system. It was possible to demonstrate data acquisition, synchronous acquisition with multiple sweeps and post processing correlation.

A number of issues were addressed in obtaining an operational first system which included interfering images, triggering, and RF feedthrough in double balanced mixers (DBM), transmission lines, signal sources, etc. As an example, a matched filter consisting of two SAW devices was used to demonstrate system operation. The oscilloscope trace in Figure 33 shows the correlated output of the SAW matched filters, verifying proper system operation and data acquisition.

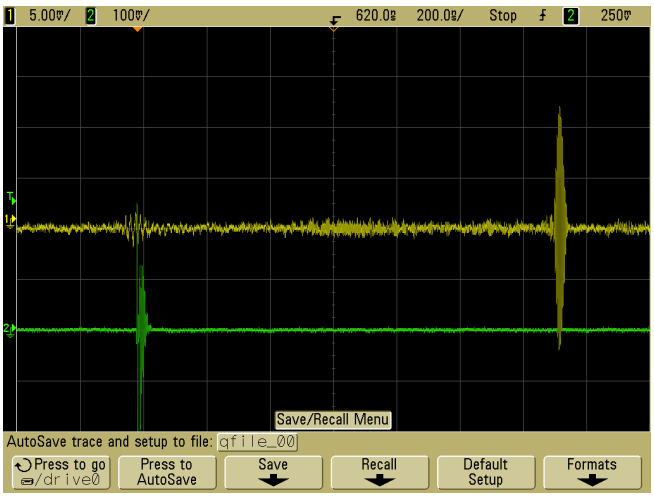

Figure 33. System correlation responses.

A high speed digital to analog converter card for a computer (CompuScope 82G w/ 8GS onboard memory by GaGe Applied) was purchased and successfully introduced into the system to interrogate a SAW band-pass filter using the system. The output of a single OFC device was however too low for the A/D card. An ongoing detailed analysis of power levels throughout the system ultimately resolved this problem. Due to minimum input levels to the A/D card, the card was not able clearly obtain a SAW device correlation peak. Attempts to fix this problem by simply adding amplifiers into the system resulted in either saturation of other amplifiers or amplification of noise above the threshold for detection due to the noise in amplifiers.

Also an approach with a single local oscillator (LO) frequency was examined. Using a LO frequency slightly below the lowest frequency of interest of the SAW device resulted in significant roll-off at high frequencies due to the finite time width of the interrogation pulse. Using a LO frequency equal to the center frequency of the OFC showed more promising results. The results of all these efforts allowed a design for a second RF transceiver with A/D acquisition and post processing to proceed.

Data Acquisition System—Design 2

The final approach undertaken was to use a master clock to generate a single frequency source to control the pulse and sine wave generators. This approach allows synchronization throughout the system and will allow multiple interrogation pulses to be synchronously be generated and the received outputs to be synchronously integrated at the receiver. A signal from a 50 MHz voltage controlled oscillator (VCO) is used to generate a 50 MHz CW signal that acts as a master clock for the entire system. The clock controls the pulse generator trigger, the CW signal is multiplied by four which is used as the 200 MHz carrier for the interrogator pulse, and the 200 and 50 MHz signals are then mixed to produce a 250 MHz sine wave which is used to mix the signal back down to a near-zero-IF in the receiver. Figure 34 shows the block diagram of the system which was implemented.

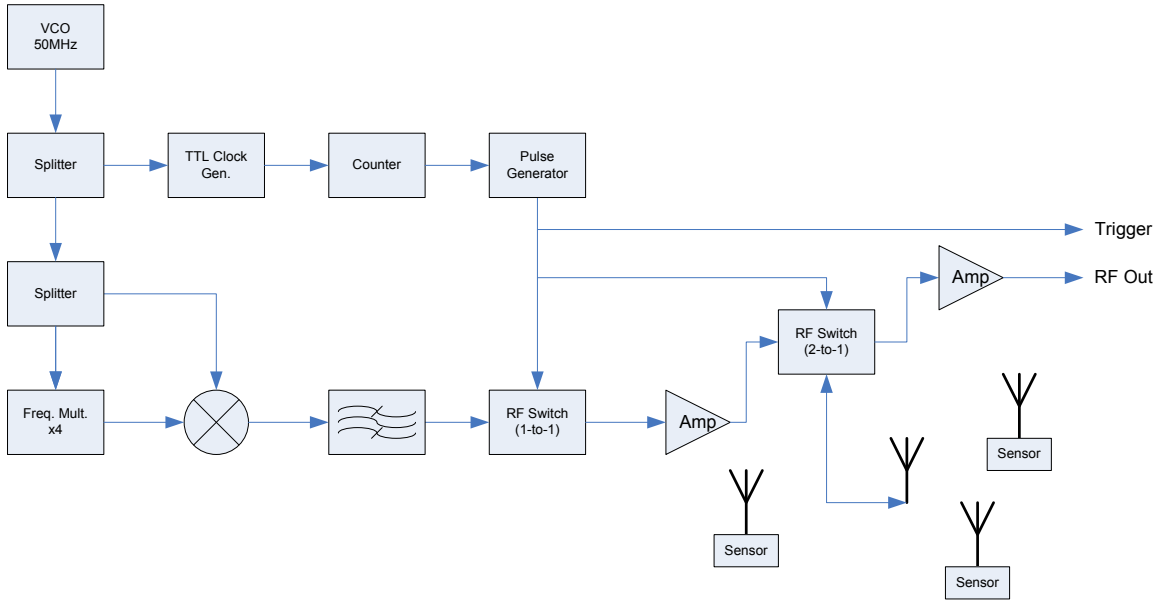

Figure 34. Final SAW sensor transceiver block diagram.

This system was implemented with commercially available discrete surface mount RF and IF IC chips, as shown in the system photograph in Figure 35. A large, high gain amplifier is visible in black. The actual SAW device, seen on the left of the photo, is hard-wired into the system since antennas at 250 MHz are large, difficult to characterize in the current system, and narrowband. This will need to be configured for exact operation in the future.

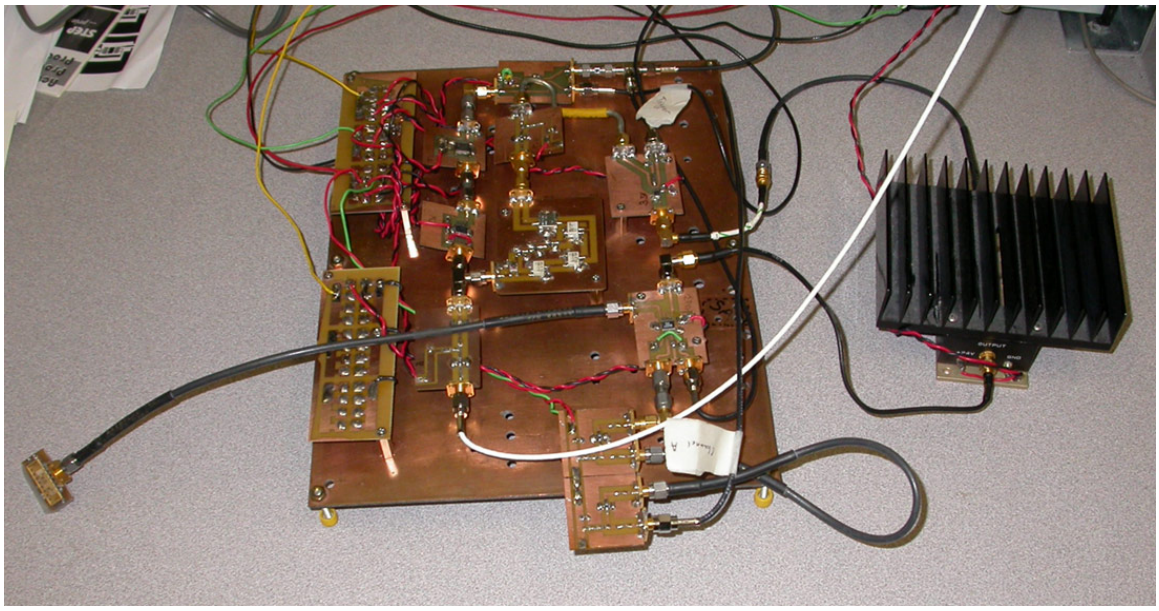

Figure 35. Final SAW transceiver system.

Figure 36 shows the interrogation sine burst at the output of the RF switch. It is noted that the sine burst does not have a square envelope which was designed. This is due to harmonic generation by the frequency multipliers which is leaking through. This will be removed in the future revisions, but at this point this signal was deemed sufficient to demonstrate the system.

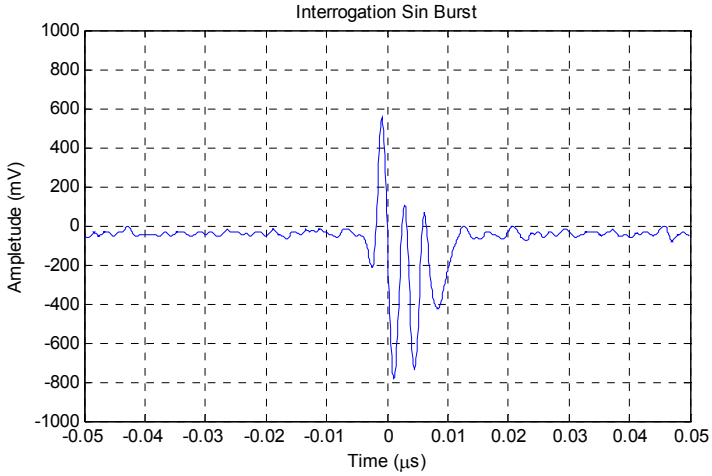

Figure 36. Measured transmitter interrogation pulse.

Initially, the system was connected to a digital oscilloscope to verify operation, to debug the system, and to record the data for further processing. As an example, Figures 37 and 38 show correlation peaks from a SAW OFC device. Recorded data was correlated with two sensors having differing OFC codes to verify that the correlation and cross correlation of the devices, and to test system operation.

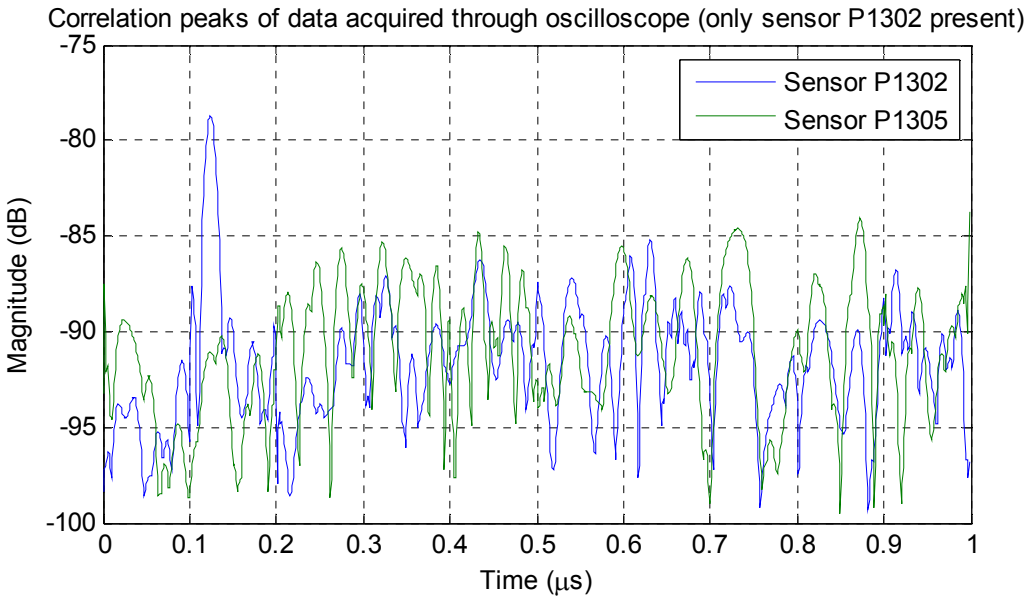

Figure 37. Measured SAW sensor correlation peak from oscilloscope.

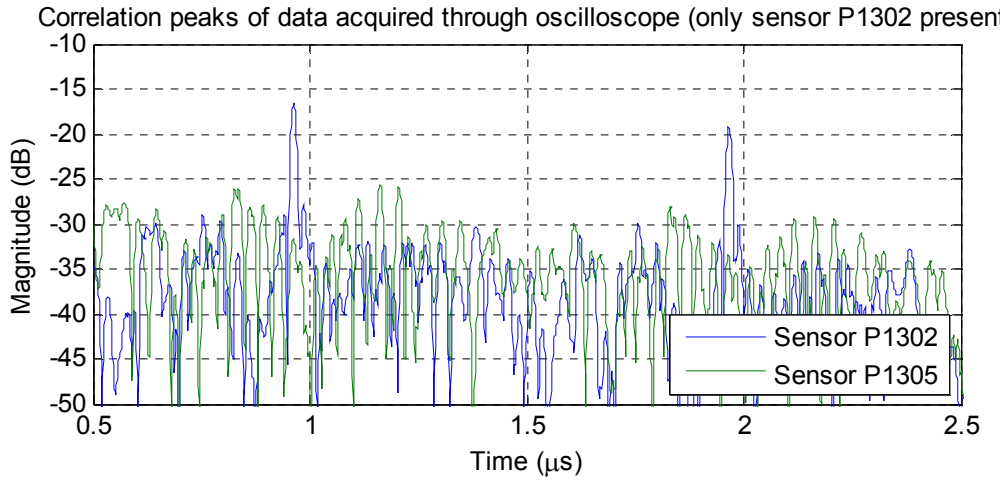

Figure 38. Measured SAW sensor correlation peaks from oscilloscope, two peaks due to the double sided SAW reflector banks.

The final simulation was to connect the input from the RF section into a computer which had a 2 GHz analog to digital card (ADC) on board. On initial testing, multiple correlation peaks were observed and they appeared to be non-stationary. This seems to be due to the A/D card and trigger signal interaction. It was determined that the mis-triggering was within ±10 data points. It was further determined that if the system is stationary over the multiple sweep times of a few microseconds, the trigger problem can be solved in software. Figure 39 shows the mis-trigger jitter effect and then the software processed trigger jitter; showing a much more stable trigger. Software re-triggering minimizes mis-triggering to ±1 data sample point. Software retriggering brings mis-triggering down to ±1 data points. The SAW OFC differential mode device was "pinged" by the transmitter and then received and processed. The two correlation peaks are visible which corresponds to the device operating in a differential delay mode. The existence and visual confirmation of the pulses indicates that the transceiver system has acquired the SAW sensor tags and has identified the tag sensor correctly.

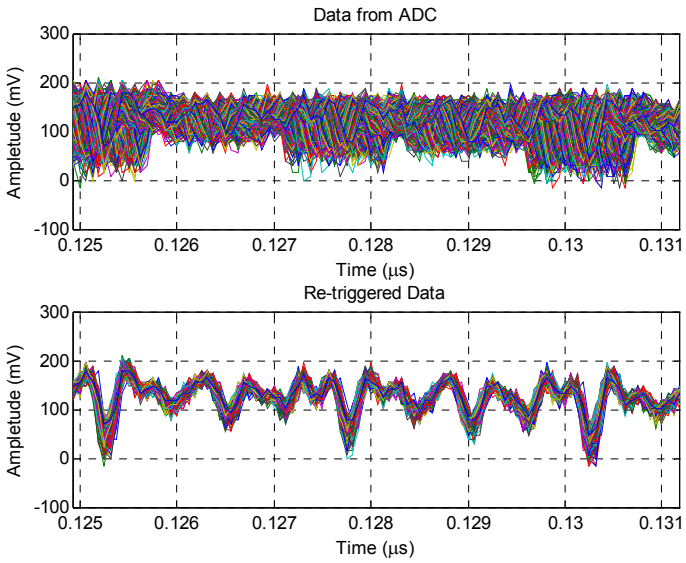

Figure 39. Upper trace shows the measured trigger stability from multiple sweeps which does not allow synchronous operation. Lower trace shows the software enhancement which reduces the trigger jitter to an uncertainty of about 2 samples.

Once the data had been properly triggered, a total of 128 data sweeps were averaged and processed for each temperature measurement. This provides a processing gain of 128 and enhances the signal to noise ratio by over 20 dB.

There are two ways to extract the temperature from the raw data sets. The first method is to maximize the correlation peak by dithering the matched filter's center frequency. Since the SAW device's absolute frequency is temperature dependent, the use of an adaptive filter which changes the matched filter's frequency response to match that of the sensor, is an effective way to directly determine the device temperature. The devices were fabricated on Y-cut, Z-propagating lithium niobate (LN), and for LN the temperature coefficient of frequency (TCF) is approximately $-96\ {}^{ppm}/_{\circ C}$. This allows for a direct conversion from the devices room temperature nominal frequency to the current device frequency. To first order the TCF is linear with velocity, frequency, propagation time, etc.

Each sensors coded matched filter can be correlated against the acquired signal, and the largest correlation peak essentially defines the frequency shift and its extracted temperature. Figure 40 shows an example search for the best temperature compensation factor.

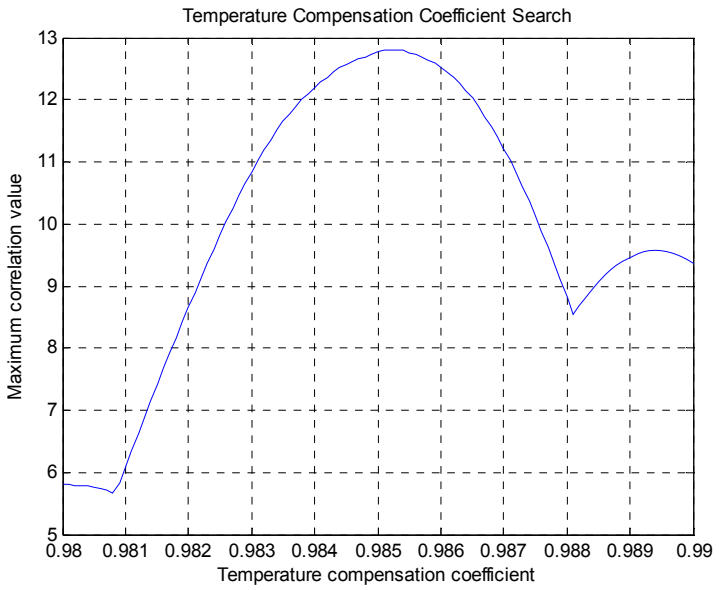

Figure 40. A temperature compensation coefficient is determined based on the temperature coefficient of the YZ lithium niobate crystal.

A single SAW OFC sensor was then taken and heated from approximately room temperature (24 °C) to approximately 100 °C on a simple hot plate and then cooled down again. Figure 41 shows plots of the thermocouple recorded temperature versus the temperature extracted from the sensor using the frequency (temperature) compensation coefficient. The data looks remarkably close, assuming some thermal lag as well as thermal offset due to the proximity of the thermocouple to the actual SAW substrate. This is the first demonstration of the SAW transceiver system in operation and demonstrates the complete SAW OFC device and transceiver system. Further work is certainly needed and by eliminating spurious responses, trigger jitter, and RF system induced noise, a smooth temperature curve is expected. One main advantage of using a temperature compensation factor is that a single sensor can be simultaneously used for measuring two different parameters, one of which is temperature and another one could be pressure, torque, gas, etc.

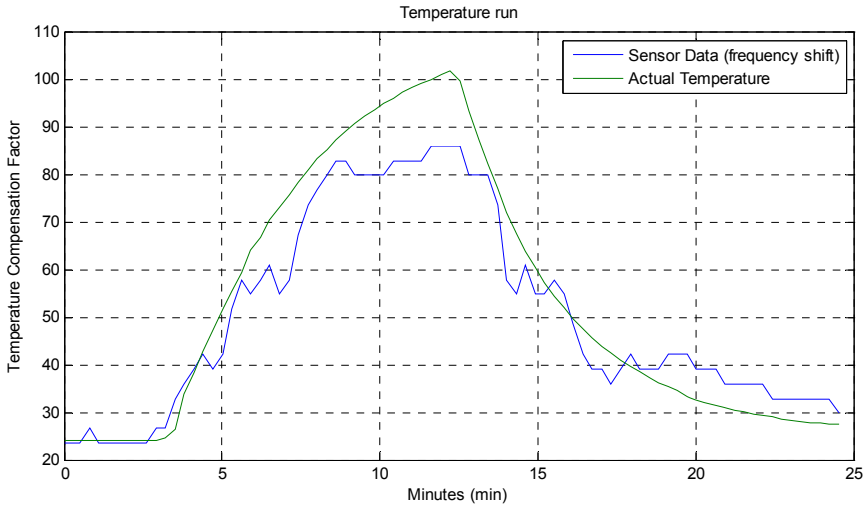

Figure 41. Thermocouple and SAW sensor temperature measurement made on a hot plate versus time. This is the first successful transceiver demonstration for SAW OFC sensors using an adaptive filter approach.

The relevant data is located in given bands of time, dependent on the SAW OFC differential device's delays and the short, free-space propagation delay. For the given SAW sensors, the correlation peaks are located around 1 μs and 1 μs, ±0.2 μs depending on the temperature dynamic range spatial delay offsets. Figure 42 shows a close-up of the measured test correlation peaks over the expected time range from the SAW sensor.

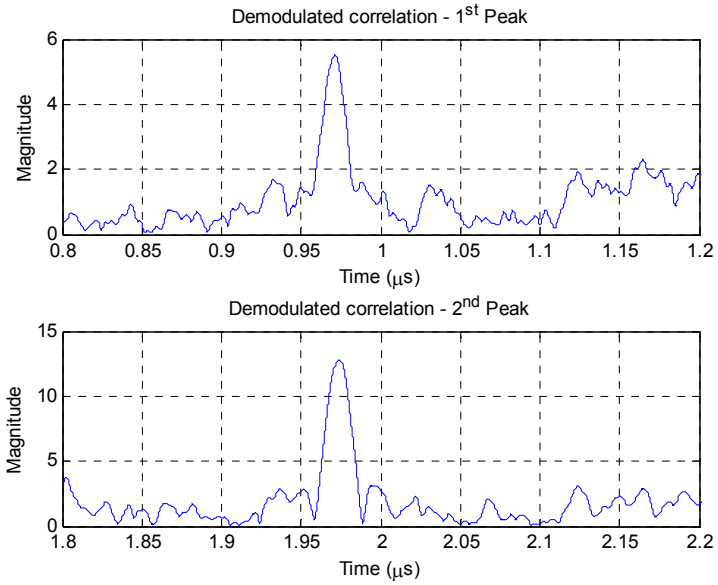

Figure 42. Example of the correlation peaks obtained by the transceiver when examining the received signal from both reflective banks of the OFC device.

As a second method when a SAW sensor is used for temperature only, a differential delay between the peaks can be used to determine the temperature. Figure 43 shows the plot of the thermocouple temperature and the temperature acquired using the SAW device's differential delay between correlation peaks.

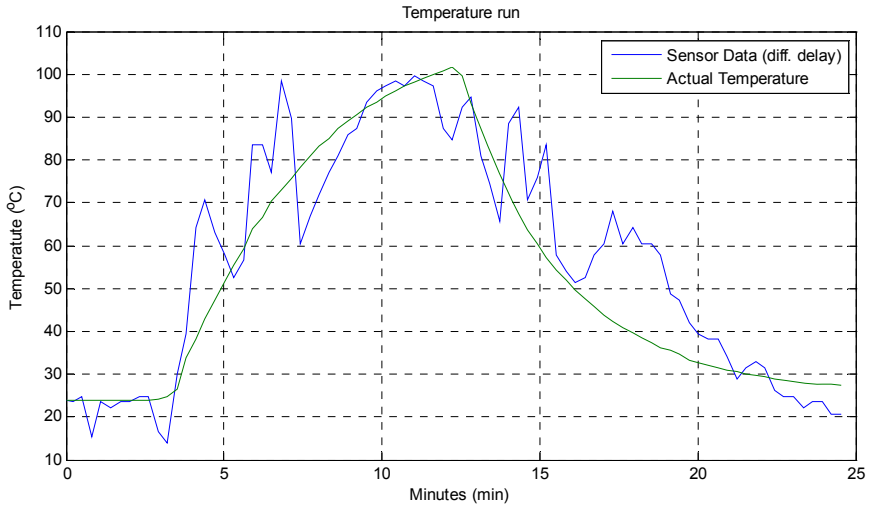

Figure 43. Thermocouple and SAW sensor temperature measurement made on a hot plate versus time. This is the first successful transceiver demonstration for SAW OFC sensors using the differential time delay between two reflector banks on the same OFC SAW sensor.

While the extracted temperature follows the thermocouple temperature curve, the error is bigger then that obtained when the TCF compensation coefficient was used. It can also be noted that there seems to be a correlation between the amount of error and the actual temperature of the sensor. For example, when the temperature is around 45 °C on both heating-up and cooling-down slopes, the extracted temperature is higher than the actual temperature. Similarly this is noticed around 65 °C. This suggests that the error may be deterministic and can be eliminated at the software level.

The advantages of the processing gain of a spread spectrum system can be visually seen when examining the signal (even an averaged one) in time or frequency domains; the desired signal from the sensor cannot be visually identified. Figure 44 shows a typical example averaged signal (128 sweeps) in time and frequency domain.

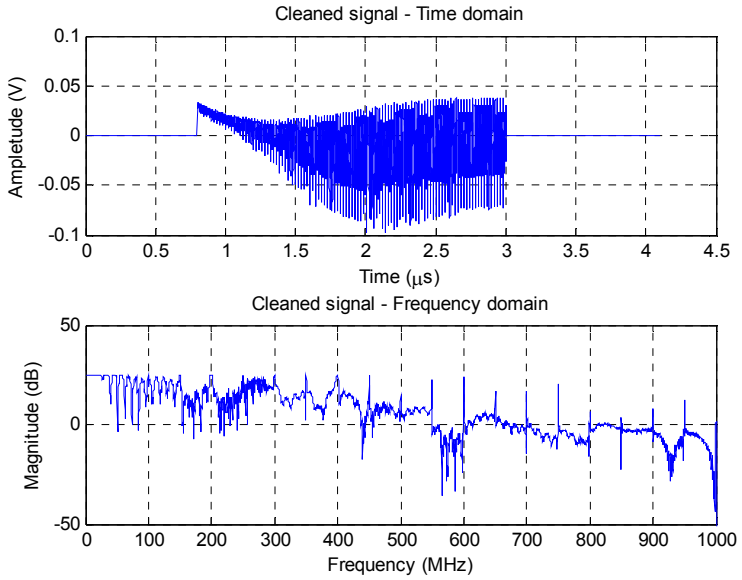

Figure 44. The advantages of the SAW OFC spread spectrum system can be demonstrated by the plots in this figure. Upper trace is the time domain and the lower trace is the frequency domain response of the received signal which includes all system feedthrough and spurious modes, plus the desired SAW sensor response. Despite the desired signal being buried in the noise, the processing gain of the spread spectrum system can extract the correlation peaks, as shown in Figure 42.

In conclusion, a SAW OFC sensor transceiver system has been designed, fabricated, and tested, and provides a proof-of-concept system for the measurement of a wireless passive SAW sensor system. The current system was completed at the very end of this program and only initial data and tests could be conducted. Further work is required to optimize the transceiver system, to eliminate spurious signals, to optimize the trigger, and to integrate antennas.

Results and Discussion

- We have demonstrated that the OFC SAW device concept is viable and can be used for wireless, passive sensing. The approach allows for individual device tagging, secure communications and demonstrated performance as an integrated sensor.
- Devices have been successfully designed, analyzed, fabricated and tested at 250 MHz, 500 MHz and 1.5 GHz. Prototype devices at lower frequencies allow easier device fabrication and testing. Higher frequency devices are advantageous in order to reduce the antenna to a very reasonable size. We have shown that the devices do operate over a wide range of frequencies and can be successfully fabricated.
- We have demonstrated wireless temperature sensing around room temperature using a 250 MHz SAW OFC sensor. Data is extracted from the device and then software is used to simulate a complete transceiver system.
- We have successfully demonstrated cryogenic temperature sensing to approximately 100 °K using a SAW OFC sensor using a differential delay line measurement. This first device test was conducted with a wired device to eliminate a large antenna and all antenna effects. Further testing in a completely wireless mode is required.

- An OFC SAW device was designed, fabricated and tested on YZ lithium niobate and used a Pd thin film as a hydrogen film sensor. The initial experiment showed that the device did respond by a change in propagation delay to 2% hydrogen gas presence. Further work is required to build an experimental test set and to make more precise measurements.
- Collaborative work was conducted with FSEC to determine if their proprietary hydrogen chemical film sensor could be integrated into the SAW OFC sensor. Initial results were negative, but further experiments are warranted.
- Collision effects and coding in a multi-sensor environment was studied and approaches to minimizing the effects obtained.
- A SAW sensor transceiver prototype system was designed and built using commercially available parts. The system confirms the feasibility of the transceiver approach and SAW OFC sensors were successfully tested and temperature extracted.
- The work has resulted in six accepted proposals to continue these efforts in the SAW sensor area using OFC devices.
- Multiple publications have been accepted and presented at international symposia.
- Several graduate student fellowships have been obtained to work in similar technology areas.

Conclusions

The use of OFC SAW sensor technology has been shown to be a viable platform for passive, wireless sensor systems. The results of this research have demonstrated the use of the devices as room temperature and cryogenic temperature sensors. Initial work is very promising for the use of Pd thin films as a possible reversible room temperature sensor. New methods of the coding devices have been studied which will lead to lower collision effects in a multi-sensor system environment. Higher frequency devices have been demonstrated which will reduce the required antenna size and should increase range. The study of the nano-thin films of Pd on polished quartz have shown room temperature reversibility, which may lead to other sensor embodiments not studied in this contract.

We believe that SAW sensor technology will ultimately be adopted for many NASA applications. We have had contacts from NASA for inflatable space habitats, ground based support, antenna temperature sensing, aeronautics, and health safety monitoring. Since the devices have such a broad range of possible sensing applications, if a single platform can be developed, there will be an enormous number of possible applications. The OFC SAW device approach offers lower loss, coding and security compared to many other sensor approaches. The SAW devices are rugged, can work at temperature extremes, and are radiation hard. Although we have made great progress, more research is required to make these a viable commercial product.

Because of this effort, a number of NASA STTR proposals and contracts were submitted and won. Nine students have been funded from this program which will increase the engineering workforce within the US. Publications were submitted and presentations made at NASA and international symposium. Because of all these efforts, collaboration is now established between our UCF group and NASA KSC, JSC, Langley, and Glenn. It is certainly our judgment that this has been an extremely fruitful program.

Other NASA Synergistic Contracts, Grants and Collaborations

1. STTR Phase II, NNK05OB31C, “Passive, Wireless Multi-Sensor Temperature and Pressure Sensing System Using Acoustic Wave Devices”, May 2005-May 2007, UCF as RI.
2. STTR Phase I, NNK06OM24C, “Passive Wireless Hydrogen Gas Sensors Using Orthogonal Frequency Coded Acoustic Wave Devices”, Jan. 2006-Jan. 2007, UCF as RI.
3. STTR Phase I, NNK06OM23C, “Passive Wireless Cryogenic Liquid Sensors Using Orthogonal Frequency Coded Acoustic Wave Devices”, Jan. 2006-Jan. 2007, UCF as RI.
4. STTR Phase II, NNK07EA39C, “Passive Wireless Hydrogen Gas Sensors Using Orthogonal Frequency Coded Acoustic Wave Devices”, Aug 2007-Jan. 2009, UCF as RI.
5. STTR Phase II, NNK07EA38C, “Passive Wireless Cryogenic Liquid Sensors Using Orthogonal Frequency Coded Acoustic Wave Devices”, Aug 2007-Jan. 2009, UCF as RI.
6. NASA, Johnson Space Center, “900 MHz OFC SAW Device Development”, Aug.-Oct. 2007.
7. NASA Graduate Student Research Program, Rick Puccio, 2004 - 2006.
8. NASA Graduate Student Research Program, Nancy Saldanha, 2005 - 2007.
9. NASA Graduate Student Research Program, Daniel Gallagher, 2007 - .
10. Florida Space Grant Consortium Fellowship, Nick Kozlovski, 2007 - .
11. NASA Harriett Jenkins Fellowship, Erica Wells, 2006 - .
12. NASA Team on Passive Wireless Sensor-Tag System, Johnson Space Center, June 2007- .

Patents, Publications Presentations and Students From Research

Patents

Four OFC SAW patents are in filing process and have been submitted to the patent office. These were conceived prior to this contract start but this contract aided in further confirmation of the claims made.

1. Weighted Reflectors for OFC Coding, Malocha and Puccio, Utility patent.
2. Orthogonal Frequency Coding for Communications and Sensors, Malocha and Puccio, in US patent office.
3. OFC SAW Sensor Using Multiple Antennas, Malocha, in US patent office.
4. Delayed Offset Multi-Track OFC Sensors and Tags, Malocha and Puccio, in US patent office.

UCF SAW OFC Sensor Relevant Publications and Presentations

1. B.H. Fisher and D.C. Malocha, “Cryogenic Liquid Level Sensing using SAW Devices”, Joint European Frequency and Time Forum and IEEE International Frequency Control Symposium, May 2007, Geneva, CH, in print.

2. N. Kozlovski and D.C. Malocha, “SAW Phononic Reflector Structures”, Joint European Frequency and Time Forum and IEEE International Frequency Control Symposium, May 2007, Geneva, CH, in print.

3. D.C. Malocha, “Passive, Wireless, Orthogonal Frequency Coded SAW Devices for Tagging and Sensors”, CANEUS NASA Fly-by-Wireless Conference, April 2007, Dallas, TX, presentation.

4. D.C. Malocha, “Passive, Wireless, SAW Device Platform for Tagging and Sensors”, IEEE/NASA Space Applications of Wireless and RFID 2007 Symposium, Galveston, TX, May 2007, presentation only.

5. D.C. Malocha, “SAW Ultra Wide Band Communications and Correlators”, IEEE/NASA Space Applications of Wireless and RFID 2007 Symposium, Galveston, TX, May 2007, presentation only.
6. Puccio, and N. Saldanha, ”Passive, Wireless, Orthogonal Frequency Coded SAW Sensors and Tags-Design and Systems”, 3rd International Symposium on Acoustic Wave Devices for Future Mobile Communication Systems Proceedings, pp. 47-56, March 2007, Invited.
7. Puccio, D.; Malocha, D.C.; Saldanha, N.; Gallagher, D.R.; Hines, J.H., ”Orthogonal frequency coding for SAW tagging and sensors”, IEEE Transactions on Ultrasonics, Ferroelectrics and Frequency Control, Volume 53, Issue 2, Feb. 2006 Page(s):377 – 384.
8. N. Saldanha, D. Puccio, and D.C. Malocha, “Experimental Measurements and Modeling of Aluminum Gratings on YZ $LiNbO_3$ for OFC SAW Sensor”, IEEE 2006 International Frequency Control Symposium Proceedings, pp. 368-373.
9. D.C. Malocha, D. Puccio, and N. Lobo, “Reflector Design for Orthogonal Frequency Coded Devices”, IEEE 2006 International Ultrasonics Symposium Proceedings, pp. 820-823.
10. D.C. Malocha, D. Puccio and N. Saldanha, “Orthogonal Frequency Coded Surface Acoustic Wave Passive Remote Sensing” 2006 SPIE Defense and Security Symposium Proceedings, pp: 62220D 1-10.
11. D. Puccio, D.C. Malocha, and N. Saldanha, “Implementation of Orthogonal Frequency Coded SAW Devices Using Apodized Reflectors”, IEEE 2005 International Frequency Control Symposium Proceeding, pp. 892-896.
12. N. Saldanha, D. Puccio, M. Pereira da Cunha, and D.C. Malocha, “Experimental and Predicted TCD and SAW Parameters on LGT [0, 132, Ψ] Substrates”, IEEE 2005 International Ultrasonics Symposium Proceedings”, pp. 918-921.
13. D. Puccio, D.C. Malocha, and N. Saldanha, “Multiple Access SAW Sensors using Orthogonal Frequency Coding”, 2005 IEEE Sensors Conference Proceedings, pp. 723-726.
14. D. C. Malocha, D. Puccio and N. Saldanha, “Spread Spectrum Techniques and Applications to SAW Sensor Device Platforms”, 2005 Electro-Chemical Society Symposium, October 2005, presentation only.
15. D.C. Malocha, D. Puccio and D. Gallagher, “Orthogonal Frequency Coding for SAW Device Applications”, IEEE 2004 International Ultrasonics Symposium Proceeding, pp 1082-1086.
16. D. Puccio, DC. Malocha, D. Gallagher, and J. Hines, “SAW Sensors Using Orthogonal Frequency Coding” IEEE 2004 International Frequency Control Symposium Proceeding, pp. 307-314.

Students involved in Research

1. Derrick Puccio, PhD, EE, 2006
2. Nancy Saldanha, PhD, EE, in progress
3. Nick Kozlovski, PhD, EE, in progress
4. Brian Fisher, PhD, EE in progress
5. Daniel Gallagher, MS, EE, 2007
6. Daniel Gallagher, PhD, EE, in progress
7. Matt Pavlina, PhD, EE, in progress
8. Mike Roller, MS, MMAE, in progress
9. Bianco Santos, UG, EE, 2007

Referenced Publications

[1] A. D'Amico, A. Palma, and E. Verona, "Hydrogen Sensor Using a Palladium Coated Surface Acoustic Wave Delay-Line," *IEEE Ultrasonics Symposium*, pp. 308-311, 1982.

[2] T. Xu, M. P. Zach, Z. L. Xiao, D. Rosenmann, U. Welp, W. K. Kwok, and G. W. Crabtree, "Self-assembled monolayer-enhanced hydrogen sensing with ultrathin palladium films," *Applied Physics Letters*, vol. 86, pp. 203104, 2005.

[3] A. Rajnikant, S. Shukla, L. Ludwig, M. Anjum, H. J. Cho, and S. Seal, "A nanoparticle-based microsensor for room temperature hydrogen detection," *Proceedings of IEEE Sensors*, pp. 395-398 vol.1, 2004.

[4] R. W. Berry, P. M. Hall, and M. T. Harris, Thin Film Technology. New York: Van Nostrand Reinhold, 1968.

[5] Z. Zhao and M. A. Carpenter, "Annealing enhanced hydrogen absorption in nanocrystalline Pd/Au sensing films," Journal of Applied Physics, vol. 97, pp. 124301, 2005.

[6] D. P. Morgan, "Surface Acoustic Wave Devices and Applications," IEEE Ultrasonics, vol. 11, pp. 121-131, 1973.

November 2007

Final Reports for Florida State University

- Densified LH_2 and LO_2: Transport Properties and Density - Van Sciver, S.
- Experimental and Numerical Investigations of Cryogenic Multiphase Flow - Van Sciver, S., Hussaini, Y., Justak, J.

Densified LH_2 and LO_2: Transport Properties and Density

S. Van Sciver
Florida State University

June 2002 to September 2007

Summary

Precision measurements of the transport properties and density of subcooled liquid oxygen and hydrogen have been completed. This experimental effort initially focused on the development of three new measuring instruments. The first instrument is for measurements of the thermal conductivity (k) and dielectric coefficient (κ) of subcooled liquids. The measuring device consists of a guarded parallel plate cell contained in a liquid filled copper can that is cooled to the desired operating temperature with a two-stage Giffiord McMahon cryocooler. This device was used for subcooled liquid oxygen measurements of k of between 55 and 81 K and κ between 55 and 91 K, both for pressures to 1 MPa. The precision of the resulting thermal conductivity values is better than $\pm$0.3%, while that of the dielectric coefficient values are to within $\pm$0.005%. The instrument was then modified to make measurements on subcooled liquid hydrogen. In this case, both sets of measurements were made between 15 and 23 K for pressures up to 1 MPa. The hydrogen k values resulting from this work have a precision of better than $\pm$1.8% and the κ values are within $\pm$0.001%. The dielectric coefficient results for both fluids were correlated with the liquid density using the Clausius-Mossatti relation.

The second instrument developed under this program is a capillary tube viscometer. This instrument consists of a precision dimension capillary tube connecting two reservoirs in a copper cylinder, which is cooled with a two stage pulse tube cryocooler. Measurements of the kinematic viscosity (ν) of subcooled liquid oxygen were made between 55 and 90 K for pressures to 1 MPa. The results have a precision of better than $\pm$1%. The instrument was then modified to make measurements on subcooled liquid hydrogen. Some preliminary data were obtained; however, we were unable to complete the measurements because the instrument failed due to hydrogen embrittlement of the capillary tube.

Finally, an dedicated ortho-para converter was developed under this program to supply equilibrium hydrogen to both experiments. This stand-alone device was used to convert up to about one liter of liquid normal hydrogen (75%(o); 25%(p)) to equilibrium liquid hydrogen at 20 K (99.8% (p); 0.2% (o)) for supplying the measuring instruments.

Introduction

The overall objective of this experimental program was to produce precision measured values for the thermal conductivity, viscosity and density of subcooled LO_2 and LH_2. The region of primary interest was subcooled liquid below the normal boiling point (56 to 93 K for LO_2 and 14 to 20 K for LH_2 for pressures up to 0.7 MPa), where available data is either scarce or non-existent. A measurement precision of better than $\pm$1% was the goal, which required considerable effort to refine measurement technique. A longer term goal was to establish facilities through this program that can be used to investigate transport in other cryogenic fluids of interest to the broader engineering community. No other similar facilities are currently in operation in the US.

Access to accurate property data is an essential component to engineering design. Many of the new propulsion systems under development by NASA and elsewhere for future space exploration will utilize densified fuels such as subcooled LH_2 or LO_2. However, there are very few experimental data available on the properties of these fluids and until we initiated our program, there was almost no effort to remedy this situation. Thus, our program's main goal was to provide this basic engineering data for a variety of future NASA projects. Three couples research tasks were carried out.

Sub-Task 1: Thermal Conductivity of Subcooled O_2 and H_2

The thermal conductivity of liquid oxygen and hydrogen have been studied extensively; however, available data, which are needed when calculating heat transport processes such as temperature distribution in storage vessels do not extend below about 77 K in the case of oxygen and are very few below 20 K for hydrogen [1-3]. We were therefore tasked with the development of a precision thermal conductivity apparatus and to use that apparatus to perform precision measurements. The results of these measurements were to be compared with the available experimental data in the literature and from Refprop, a NIST standard reference database code [4].

The Thermal Conductivity Apparatus

The design of the thermal conductivity apparatus is based on the guarded, horizontal flat-plate calorimeter concept of Roder and Diller [5]. A schematic of the calorimeter is given in Figs. 1.1 and 1.2. The hot plate is formed by sandwiching a film heater with 100 Ω resistance between two 76.6 mm diameter copper discs with 6.4 mm thickness. Discs are bolted together using #0 to 80 stainless steel screws. This construction, however, caused a temperature difference between the upper and the lower parts of the hot plate when the heater is energized. A platinum resistance thermometer [6] is inserted in each disk through 2.0 mm diameter radial holes that extends from the side to about 4 mm beyond the center. The center of the radial hole is 1.7 mm below the surface of the discs that is in contact with the liquid.

The hot plate is attached to the first thermal guard, and first thermal guard is attached to the second thermal guard each using three 2-mm-diameter G-10 supports and secured with epoxy. The assembly process is done on a thick glass surface to ensure that the components are at the same plane. Both guards are made of copper, and the inner diameter of the first guard is 80.0 mm. In addition to a film heater that is sandwiched between the guard body and a copper disc, each guard also has a wire heater wrapped around the body. The first thermal guard has two platinum resistance thermometers: one at the center of the top, inserted similar to the hot plate thermometers, and the second one is on the side of the guard. The second thermal guard has only one platinum resistance thermometer at the center of the top. This whole assembly is supported by three pieces of silica glass on the copper cold plate. The cold plate is placed at the bottom of the measurement cell and electrically insulated from it by means of a piece of Kapton® tape. The cold plate has a platinum resistance thermometer installed similar to those in the hot plate.

The cooling power is provided by a two-stage model GB-37 Gifford-McMahan cryocooler by Cryomech [7], which enables the experiments over a very broad temperature range. The temperature of the cell is controlled a pair of silicon diodes and a film heater installed on the thermal link between the cryocooler stage and the measurement cell, Fig. 1.2.

High purity gaseous oxygen or hydrogen is condensed inside cell and pressurized up to 1 MPa during the measurements using helium gas. The solubility of helium in liquid oxygen is very small, less than 0.04 mole-percent in the range of the experiments [8]. The purity of the gases used for the measurements is 99.996% and contain the following [9]: moisture <1 ppm, methane <0.5 ppm, carbon monoxide <1 ppm, carbon dioxide <1 ppm, argon <20 ppm, nitrogen <10 ppm. A cold trap at 77 K is utilized to minimize the impurities; however, some trace amount of nitrogen may still be present together with oxygen in the experimental cell. For the hydrogen experiments, the normal hydrogen gas (25% p – 75% o) is first converted to equilibrium hydrogen (99.8% p – 0.2% o) is an external o-p converter [10] and then transferred to the experimental cell.

Temperature, Pressure, and Capacitance Measurements

The temperature is measured at six different locations using platinum resistance thermometers. These thermometers were calibrated by the manufacturer against The International Temperature Scale of 1990 (ITS-90) [6]. The resistance of each thermometer is monitored using a Lakeshore model 370 A/C resistance bridge operating at 13.7 Hz, and a model 3716L low resistance scanner board. The A/C bridge has an accuracy of $\pm 0.03\%$ and a resolution of 40 $\mu\Omega$ in the operating range (20 Ω resistance range and 316 μA current).

Pressure in the measurement cell is measured by an MKS model 221D differential pressure gage, which has a resolution of 200 Pa and an accuracy of 0.5% of the read value. The gage is calibrated in our laboratory against a calibrated US Gauge series 1400 Solfrunt 6 in. test gage [11].

The capacitance measurement to determine the gap between the calorimeter plated is performed using an Andeen-Hagerling model 2550A capacitance bridge. The bridge has an accuracy of 5 ppm, and a resolution of 0.1 attofarad (10^{-7} pF) at its 1 kHz operating frequency. The error in the cell constant caused by the accuracy of the capacitance bridge is about 5×10^{-4}%, which does not cause any measurable error in the thermal conductivity.

Experimental Details

In order to measure the thermal conductivity, a known amount of heat is supplied to the hot plate. The exact amount of heat is determined by multiplying the current going into the heater and the voltage drop along the heater. Both quantities are monitored constantly. Throughout the experiments the nominal value of the heating power was of order 0.5 W with a standard deviation of less than 10^{-5} W.

During the measurements the temperature of the upper section of the hot plate is matched by both thermal guards to make sure that all heat generated by the hot plate heater goes to the cold plate. However, a small temperature difference between the hot plate upper and lower parts had to be taken into account.

The working equation of the calorimeter is given by the following:

$$k = \frac{Q}{\frac{A}{d}\Delta T - \frac{A^*}{d^*}\Delta T^*} \tag{1.1}$$

In the above equation, k is the thermal conductivity of the liquid in W/m-K, Q is the heat applied to the hot plate heater in W, ΔT is the temperature difference between the hot plate lower part and the cold plate in K, A/d (termed as the cell constant) is the ratio of the hot plate area to the gap between the hot plate and the cold plate in m, A^*/d^* is the ratio of the hot plate lower part circumferential area to the gap between the hot plate and the first thermal guard in meters and ΔT^* is the temperature difference between the hot plate lower part and the first thermal guard.

The cell constant (A/d) is determined from a capacitance measurement by using the hot plate, cold plate and the thermal guards assembly as a three-terminal capacitor. However, the capacitance measurement needed to be corrected for the fringing effects around the edges of the capacitor plates [12]. Consequently, the cell constant was obtained from the following:

$$\frac{\pi R^2}{d} = \frac{C}{\varepsilon_0} - R\left(\log\frac{8\pi R}{5d}\right) \tag{1.2}$$

where, C is the measured capacitance of the cell in pF, ε_0 (=8.85 pF/m) is the permittivity of free space, R and d are the radius of the hot plate and the gap between the hot and cold plates in meters, respectively. The second term on the right hand side is due to fringe effects.

Results and Discussion

Oxygen—Our measured values of thermal conductivity for compressed liquid oxygen are given in Table 1.1 and Fig. 1.3 along with the measurement uncertainties. The errors shown in the table are the standard error values (standard deviation of the mean), and are calculated by taking the ratio of the standard deviation of the samples to the square root of the number of samples [13]. The thermal conductivity values are calculated from the working equation of the calorimeter, Eq. (1). The effect of the correction due to heat load from the thermal guard to the cold plate is less than 3.5%. Overall, the percentage error in these thermal conductivity measurements is less than 0.24%.

Hydrogen—Our measured values of the thermal conductivity for subcooled liquid hydrogen are given in Table 1.2 and a sample shown in Fig. 1.4. The thermal conductivity values are also calculated from the calorimeter working equation. T_{mean} is the average of the two temperatures used in this same equation. δP, δT, and δk are the ratio of the samples standard deviation to the number of samples square root [13]. Overall, the percentage error in these thermal conductivity measurements is less than 1.8%.

Summary

We have performed high precision thermal conductivity measurements of subcooled liquid oxygen in the temperature range of from 55 to 81 K and pressures up to 1 MPa. The precision of the measurements is better than 0.3% and there is a good agreement between our results and existing data as well as transport properties software. We have also performed thermal conductivity measurement of subcooled liquid hydrogen in the temperature range from 15 K to 23 K and pressures up to 1 MPa. The precision of our measurements is better than $\pm$1.8%. Results compare favorably to existing data when uncertainties are taken into account.

Publications

1. “Thermal Conductivity Measurements of Subcooled Oxygen Below 80 K” T. Kucukomeroglu, D. Celik, and S.W. Van Sciver, Advances in Cryogenic Engineering Vol. 49, 1123 (2004).
2. “Thermal Conductivity of Subcooled Liquid Oxygen”, D. Celik, and S.W. Van Sciver, Cryogenics Vol. 45, 620 (2005).
3. “Ortho and Para Hydrogen Concentration Determination Based on Vapor Pressure”, S.R. Lydzinski, D. Celik, A. Hemmati and S.W. Van Sciver, Advances in Cryogenic Engineering, Vol. 51A, 475 (2006).
4. “Thermal conductivity of subcooled liquid hydrogen”, T.M. Charignon, D. Celik, A. Hemmati, and S.W. Van Sciver, Advances in Cryogenic Engineering, Vol. 53 (accepted).

This work produced no patents or theses.

References

[1] Verkin, BI, Handbook of Properties of Condensed Phases of Hydrogen and Oxygen, Hemisphere Publishing Co., New York, Chapters 3 and 4, 1991.

[2] Roder, HM, The Thermal Conductivity of Oxygen, Journal of Research of the National Bureau of Standards 1982; 87(4):279-305.

[3] Jacobsen RT, Leachman JW, Penoncello SG, and Lemmon EW. “Current Status of Transport Properties of hydrogen”, 16th Symposium on Thermophysical Properties, Boulder-CO-USA, July 30-August 4, 2006.

[4] Lemmon, E.W. et al., Refprop, NIST Standard Reference Database 23, v 7.0, Beta Version, 2002.

[5] Roder, HM and Diller DE, Thermal Conductivity of Gaseous and Liquid Hydrogen, The Journal of Chemical Physics 1970;52(11):5928-5949.

[6] Information from the supplier, Lake Shore Cryotronics, Inc., 575 McCorcle Boulevard, Westerville, OH 43082.

[7] Information from the supplier, Cryomech, 113 Falso Dr., Syracuse, New York 13211, USA.

[8] Sinor, JE and Kurata, F, Solubility of Helium in Liquid Argon, Oxygen and Carbon Monoxide, Journal of Chemical Engineering Data 1966;11(4):537-539.

[9] Information from the supplier, Airgas South, 945 Yulee St., Tallahassee, FL 32304.

[10] Lydzinski, S.R. Celik, D. Hemmati A. and Van Sciver S.W. “Ortho and Para Hydrogen Concentration Determination Based on Vapor Pressure”, Advances in Cryogenic Engineering, Vol. 51A, 475 (2006).

[11] Information from the supplier, US Gauge, 820 Pennsylvania Blvd., Feasterville, PA 19053.

[12] Landau, LD and Lifshitz, EM, Electrodynamics of Continuous Media, 2nd Ed., Butterworth-Heinemann, Oxford, 1984, p. 19.

[13] Taylor, JR, An Introduction to Error Analysis, 2nd ed., University Science Books, Sausalito, 1997, p. 102.

[14] Laesecke, A, et al., Transport Properties of Fluid Oxygen, Journal of Physical Chemistry Reference Data 1990;19(5):1089-1122.

[15] Weber, LA, P-V-T, Thermodynamic and Related Properties of Oxygen from the Triple Point to 300 K at Pressures to 33 MN/m^2, Journal Of Research of the National Bureau of Standards-A. Physics and Chemistry 1970;74A(1):93-129.

Sub-Task 2: Dielectric Coefficient and Density Measurements

To our best knowledge, dielectric coefficient of liquid oxygen has only been measured either along the liquid-vapor saturation curve [1] or above 100 K for compressed fluid [2]. In addition for the case of subcooled liquid equilibrium hydrogen, the dielectric coefficient of has not been measured to very high accuracy and precision [3]. Such data are critical input to correlative property data base codes such as REFPROP [4].

Here we report the dielectric coefficients measured for liquid oxygen below 95 K and for liquid hydrogen below 23 K both at pressures up to 1 MPa. The results are combined with the previously published data for liquid along the liquid-vapor saturation line to express the fluid density in terms of the dielectric coefficient embedded in the Clausius-Mossotti relation. This expression covers both the liquid and the gaseous state.

The Dielectric Coefficient Apparatus

The schematic of the parallel plate capacitor used for the dielectric coefficient measurements is given in Fig. 2.1. The 76.58 mm diameter capacitor plates are placed inside G-10 insulating assemblies. These assemblies are resurfaced on a lathe and then polished on a granite flattop to ensure that the insulator and capacitor surfaces are in the same plane. These two plate-insulator assemblies are then joined with stainless steel bolts. The gap between the plates is maintained by brass washers made out of shim stock with 305 μm thickness. In order to eliminate stray capacitance between the signal carrying wires, the cores of the two separate co-axial cables are soldered to the backside of the plates near the center. The shields of these cables are then soldered to the main shield that surrounds the whole assembly. The room temperature vacuum capacitance of the capacitor is measured to be 142.9213 pF with a standard error of 0.00040 pF. The capacitor is placed inside the same experimental cell as was used for the thermal conductivity experiments.

Experimental Method

The dielectric coefficient is determined from the ratio of the capacitance of a three-terminal, flat plate capacitor when it is filled with liquid to that when the capacitor is in vacuum at the same temperature. However, since the design involves dissimilar materials with different thermal

expansion coefficients, the capacitor needs to be first calibrated over the operating temperature range.

The calibration of the evacuated capacitor is performed in the temperature range of approximately 47 to 97 K for the oxygen measurements and 14 to 25 K. To minimize hysteresis effects, all the experimental data are taken right after the calibration, without cycling to room temperature. Later, the vacuum capacitances are fit to fifth order polynomials, which are used to calculate the dielectric coefficient.

Liquid oxygen in the experimental cell is pressurized using an external supply of 99.994% pure helium gas. The solubility of helium gas in liquid oxygen is negligible being less than 0.04 mole-percent in the range of the experiments [5]. Liquid hydrogen in the experimental cell is pressurized through a capillary connected to the experimental cell using an external supply of 99.999% ultra high purity hydrogen gas. The thermal gradient between the liquid temperature and the saturation temperature at the operating pressure occurs in the capillary and contributes a negligible heat load to the experiment. In this case, we chose not to pressurize the experiment with pure helium gas since it may lead to helium going into solution contaminating the pure hydrogen and therefore affecting the measured dielectric coefficient [5].

Results and Discussion

Oxygen—To our best knowledge, ours are the first measurements of the dielectric coefficient of subcooled liquid oxygen. To obtain a correlation for the density of liquid oxygen we used the appropriate correlation reported in the literature [6]. We then compared our results to the Clausius-Mossotti relation reported in [3] for compressed fluid:

$$\frac{1}{\rho}\left(\frac{\kappa-1}{\kappa+2}\right) = B_1 + B_2\rho + B_3\rho^2 + B_4 T \qquad (2.1)$$

In Eq. (2.1) ρ is in g/cm^3 and the constants are: B_1 = 0.12378 cm^3/g, B_2 = 0.00029 cm^6/g^2, B_3 = -0.00126 cm^9/g^3 and B_4 = -0.67x10^{-6} cm^3/g-K. Equation (3) was originally derived for compressed fluid based on experimental data above 100 K and pressures up to 33 MPa. The difference between the experimental data and the computed values of the Calusius-Mossotti function was said to be less than 0.03%.

The calculated values of densities from Eq. (2.2) using our experimentally obtained dielectric coefficients are given in Table 2.1. Also included in the table are the densities obtained from Ref. 6 for comparison purposes. The difference between the two density values is better than 2.7%. This trend in the difference between the experimental and the calculated values suggested to us that Eq. (2.1) may not be valid for compressed liquid below 100 K. In an attempt to derive a new expression for the Clausius-Mossotti relation that better represents the data in the compressed liquid region, the numerical values of the Clausius-Mossotti relation, left hand side of Eq. (2.1), based on our measurements of the dielectric coefficient and the density are plotted in Fig. 6. Also included in the figure are the experimental values for the compressed fluid and the saturated liquid from Refs. [1,2]. The fit to all the data is given by the following equation:

$$\frac{1}{\rho}\left(\frac{\kappa-1}{\kappa+2}\right) = C_1 + C_2\rho + C_3\rho^2 + C_4\rho^3 \qquad (2.2)$$

The constants in Eq. (2.2) are as follows: C_1 = 0.1236200706314 cm^3/g, C_2 = 2.573931688499x10^{-4} cm^6/g^2, C_3 = -1.121799380394x10^{-3} cm^9/g^3 and C_4 = -3.067102196955x10^{-5} cm^{12}/g^4 and ρ is in g/cm^3. Equation (2.1) reproduces the experimental values of the dielectric coefficient to better than 0.002% in the compressed liquid region, better than 0.005% for the saturated liquid except near the critical point, and better than 0.01% in the compressed gas region. Similarly, compared Eq. (2.2) predicts the density of oxygen to better than 0.005% in the compressed liquid region, better than 0.08% in the compressed gas region and better than 0.03% for the saturated liquid, except near the critical point.

Hydrogen—Measurements of the dielectric coefficient for pressurized liquid hydrogen are given in Table 2.2 and Fig. X. We believe that these data are the highest precision dielectric coefficient measurements for subcooled liquid hydrogen ever reported. In an attempt to quantify the accuracy of our results, a comparison was performed against other measurements reported in the literature. Since the present study does not include direct measurement of the density, it was necessary to first derive the density from the appropriate Clausius-Mossotti relation [2]. This form of relation (Eq. (1) below) was originally derived for compressed oxygen fluid based on experimental data above 100 K and pressures up to 33 MPa. The coefficients in Eq. (5) for liquid hydrogen are obtained from a fit to data reported in [2]. When fit to our data points as in Fig. 3, Eq. (5) gives a density in good agreement with the general trend of the published values for the dielectric coefficient [2,3].

$$\frac{1}{\rho}\left(\frac{\kappa-1}{\kappa+2}\right) = A_1 + A_2\rho + A_3\rho^2 + A_4 T \qquad (2.3)$$

Where: A_1 = 0.99871727 cm^3/g, A_2 = 0.27819534 cm^6/g^2, A_3 = -2.55377631 cm^9/g^3, A_4 = -1.976 $\times$ 10^{-5} $cm^3/(g\ K)$, ρ is in g/cm^3 and T is in K.

For hydrogen, the calculated values of densities from Eq. (2.3) using our experimental data points are given in Table 2.2. Also included in the table are the densities obtained from a fit to previous data [1,2]. For hydrogen, the difference between the computed and experimental density values is less than 0.01%.

The small difference between the previous data and the calculated values suggests that Eq. (1) is a good fit for compressed liquid hydrogen between 15 and 23 K. Furthermore, the very small difference between density calculated with our data points and older studies suggests a very high accuracy of our measurements.

In an attempt to derive a new expression to cover both the gas and liquid region that is only a function of the density through the Clausius-Mossotti relation, a fit to all hydrogen data is made in the form,

$$\frac{1}{\rho}\left(\frac{\kappa-1}{\kappa+2}\right) = B_1 + B_2\rho + B_3\rho^2 + B_4\rho^3 + B_5\rho^4 \tag{2.4}$$

The constants in Eq. (2.4) are as follows: B_1 = 1.0034244 cm^3/g, B_2 = 0.2008675 cm^6/g^2, B_3 = -6.0813334 cm^9/g^3, B_4 = 86.307704 cm^{12}/g^4, B_5 = -499.9523344 cm^{13}/g^5 and ρ is in g/cm^3. Measurements of the dielectric coefficient obtained in this research, as well for other data from the literature [1,2], are plotted in Fig. 4. The agreement between the data and Eq. (2.4) is very good with the equation reproducing the experimental values of the dielectric coefficient to better than 0.02% in the Ref. [1], better than 0.007% in the Ref. [2] and better than 0.001% in this research.

Overall, the density in subcooled liquid hydrogen is strongly dependent of the temperature and only slightly dependent of the pressure. Therefore, to cast the data in a more useful form, we propose a simplified state equation for this region as [13],

$$\begin{aligned} \ln(\rho) &= b_0(P) + b_1(P)T^{\frac{9}{4}} \\ b_0(P) &= C_1 + C_2 P \\ b_1(P) &= C_3 + C_4 P \end{aligned} \tag{2.5}$$

The constants in Eq. (2.5) are given without units as follows: C_1 = -2.532955, C_2 = 3.588795 $\times$ 10^{-2}, C_3 = -1.694709$\times$ 10^{-4}, C_4 = 2.248987 $\times$ 10^{-5}, and ρ is in g/cm^3, T is in K, and P in MPa. Equation (2.5) reproduces the experimental values of the density to better than 0.05% in the compressed liquid region studied in this research.

Summary

We have performed high resolution dielectric coefficient measurements of liquid oxygen, and developed a correlation for the density in terms of the dielectric coefficient based on these new data and existing data of other researchers. This correlation should be useful with better than 0.1% reproducibility in the subcooled liquid region up to at least 1 MPa pressure, in the gaseous region up to 33 MPa and 300 K, as well as for the saturated liquid. We have also performed high resolution dielectric coefficient measurement of equilibrium subcooled liquid hydrogen. In this case, we produced two correlations for the density in terms of the dielectric coefficient in the form of the Clausius-Mossotti relation that are based on our new data and published data of other researchers. The second correlation should be accurate to better than 0.001% in the subcooled liquid region up to at least 1 MPa pressure and better than 0.02% in the gaseous region up to 20 MPa and 100 K. Finally, a new state equation for the density is proposed that should be useful for computing the density directly from the temperature and pressure. The accuracy of this expression is better than 0.05% between 15 and 23 K up to 1 MPa.

Dielectric Coefficient Measurement Publications

1. “Dielectric Coefficient and Density of Subcooled Liquid Oxygen”, D. Celik, and S. W. Van Sciver, Cryogenics Vol. 45, 356 (2005).

2. “Dielectric Coefficient and Density of Subcooled Liquid Hydrogen,” T. Charignon, D. Celik, A. Hemmati and S.W. Van Sciver, Cryogenics Vol. 47, 252 (2007).

This work produced no patents or theses.

References

[1] Younglove, B.A., Measurements of the Dielectric Constant of Saturated Liquid Oxygen, Advances in Cryogenic Engineering, ed. by Timmerhaus, K.D., New York-London: Plenum Press, 1970; v. 15, pp. 70-75.

[2] Younglove, B.A., Dielectric Constant of Compressed Gaseous and Liquid Oxygen, Journal of Research of the National Bureau of Standards-A. Physics and Chemistry 1972; 76A(1):37-40.

[3] Stewart JW, Dielectric polarizability of fluid *para*-hydrogen, J. Chem. Phys. 1964; 40(11): 3297-3305.

[4] Lemmon EW, McLinden MO and Huber ML, REFPROP, Reference Fluid Thermodynamic and Transport Properties, NIST Standard Reference Database 23, Version 7.0 (2002).

[5] Sinor, J.E. and Kurata, F., “Solubility of Helium in Liquid Argon, Oxygen and Carbon Monoxide”, J of Chemical Engineering Data 1966; 11(4):537-539.

[6] Weber, L.A., P-V-T, Thermodynamic and Related Properties of Oxygen from the Triple Point to 300 K at Pressures to 33 MN/m^2, Journal Of Research of the National Bureau of Standards-A. Physics and Chemistry 1970; 74A(1):93-129.

Sub-Task 3: Kinematic Viscosity Measurements

We successfully measured the absolute dynamic viscosity of subcooled liquid oxygen over the desired the pressure and temperature domains; however, we were less successful with the subcooled liquid hydrogen measurements as is discussed below. Published viscosity data and correlations for subcooled liquid oxygen are not complete nor precise in the domain of interest pressures up to 1.0 MPa and from 55 to 90 K, respectively [1-3]. Similarly, viscosity data for subcooled liquid hydrogen below 23 K are inaccurate [1]. The goal of the present work was to acquire viscosity data for these two fluids with an uncertainty of 1% at a 95% confidence level. The instrument used for these measurements is a pressurized gravitational capillary (PGC) viscometer specifically designed for subcooled liquefied gases [4].

Experimental Method

Shown in Fig. 3.1 is a schematic of the PGC viscometer instrument. The two measurement reservoirs of equal heights are connected at their bottom ends with a hydraulically

communicating coiled capillary. A liquid level difference is initially created between the two reservoirs using high purity helium gas from an external supply to temporarily drive liquid from a third supply reservoir. The resulting pressure gradient along the capillary induces liquid flow. Helium gas is then used to pressurize equally the two reservoirs to reach the subcooled liquid state. The solubility of helium gas in liquid oxygen is negligible; however, for the hydrogen measurements, this issue is of concern. Each of the two reservoirs holds a co-axial capacitive sensor that measures liquid level to high precision. The kinematic viscosity of the liquid is derived from a corrected form of the Hagen-Poiseuille equation using measurements of the level difference as a function of time.

The PGC viscometer cell consists of a copper cylindrical block of diameter of 177.8 mm, a height of 152.4 mm, and an approximate mass of 30.4 kg, containing three reservoirs, each with a diameter of 34.93 mm and a depth of 127.0 mm. The coiled capillary is an electroformed nickel tube with a radius of 253.36±0.5 μm and length of 955.0±0.5 mm. The ends of the capillary pass through holes in the bottom end of the cylindrical block, into the bottom of the sending and receiving reservoirs, so that those two reservoirs hydraulically communicate through the capillary. Cooling power is supplied by a two-stage pulse tube cryorefrigerator (PT 810) from Cryomech, Inc. A Lake Shore Cryotronics Model 340 temperature controller is used to select and stabilize the viscometer cell temperature. The viscometer cell temperature is controlled within a ±1 mK using two matched Model PT-103-14D platinum resistor sensors.

The sending reservoir and receiving reservoir have the same height and cross-section at both capillary ends with $h = z_1 - z_2$ corresponding liquid-level difference. The corrected form of the Hagen-Poiseuille equation is given by Eq. 3.1, after including the volumetric flow rate due to mass conservation and the pressure drop driving the flow.

$$\frac{\mu}{\rho} = \frac{r^4 g}{4LR^2} \frac{\Phi(h)t}{\ln[h(0)/h(t)]} \tag{3.1}$$

The factor Φ(h) in the kinematic viscosity, given by Eq. 3.2 below, includes the kinetic energy and end corrections, adjusted by the coefficients *m* and *n*, respectively, with the values by Kestin et al. [5].

$$\Phi(h) = \frac{1 + \left[1 - \frac{m}{4g}\left(\frac{R}{r}\right)^4 \frac{1}{\tau^2} \frac{h(0) - h(t)}{\ln[h(0)/h(t)]}\right]^{1/2}}{2[1 + n(r/L)]} \tag{3.2}$$

$$m = m_0 + \frac{8n}{N_{\mathrm{Re}}}, \tag{3.3}$$

$$m_0 = 1.17 \pm 0.03, n = 0.69 \pm 0.004, 0.5 \le N_{\mathrm{Re}} \le 100 .$$

The Reynolds number, given by Eq. 3.4 below, is on the order of 10 in this work, and thus, a fixed value of *m* = 1.50 was adopted for expedience.

$$N_{\mathrm{Re}} = \frac{2\rho v r}{\mu} \tag{3.4}$$

Where $v = -\frac{1}{2}\left(\frac{R}{r}\right)^2 \frac{dh}{dt}$ is the fluid velocity. The time constant for the level difference decay, τ in the correction factor $\Phi(h)$, given by Eq. 3.5 below, is a first-approximation requiring an estimate of the kinematic viscosity, yielding an iterative calculation for the kinematic viscosity.

$$\tau = \frac{4\mu L R^2}{\rho r^4 g} \tag{3.5}$$

The Weber equation-of-state for high-density liquid oxygen was used to determine the mass density, and thus calculate the dynamic viscosity [6].

Results and Discussion

Oxygen—Presented in Table 3.1 are the absolute dynamic viscosity measurements for subcooled liquid oxygen at the temperatures and pressures given. In the table, N is the number of repeated data points at each state (i.e., at each T, P pair). The mean was calculated of the repeated data points after applying Eq. 3.1 to each of them, to give a measurement at each state. The column labeled $2 \bullet \sigma_\mu$ is twice (i.e., a coverage factor of 2) the standard deviation of the measurements, to give a 95% confidence level. The measurements were repeated at the highest pressure (1.0 MPa), at three different temperatures (60.0, 70.0, and 80.0 K), demonstrating their excellent repeatability.

The dynamic viscosity measurements in the present work are interpreted using the chemical reaction rate theory of viscosity by Eyring [7]. The flow is thus considered a unimolecular chemical reaction with the elementary process being a molecule passing from one equilibrium position to another in the liquid over an energy barrier. The resulting rate equation is Eq. 3.6, where E is the barrier energy, and ***R*** is the universal gas constant. The factor A includes a weak pressure dependence [8].

$$\mu = \mathrm{A}\, \mathrm{e}^{\mathrm{E}/\boldsymbol{R}\mathrm{T}} \tag{3.6}$$

The result of this fit is shown in Fig. 3.2 showing excellent agreement with the data. A similar kinetic and hole theory of viscosity by Frenkel corroborates the chemical reaction rate theory of viscosity by Eyring [8]. This fit, which is within ±2% provides a useful form to estimating the viscosity values.

Hydrogen—We encountered a severe technical challenge when attempting to use the PGC to measure the viscosity of subcooled liquid hydrogen. Mainly, we found that after a short time the liquid hydrogen embrittled the nickel capillary tube, which would result in cracking and leaking of the tube. As a result, we were only able to obtain for a few sets of data at different parameters (T, p). A sample of the successful runs where reasonable results were obtained is given in Table 3.2, which compares our measured values with those obtained from the database code, REFPROP [1]. For these cases, the relative error becomes larger as temperature decreases. This is probably a real deviation between data as REFPROP extrapolates hydrogen viscosity

values from higher temperature since there are no published viscosity measurements at these low temperatures. REFPROP suggests an uncertainty of between 4 and 15% in this region.

Conclusions

New absolute dynamic viscosity measurements of subcooled liquid oxygen were acquired in the pressure and temperature domains from 0.15 to 1.0 MPa and from 55 to 90 K, respectively. They were acquired using a pressurized gravitational capillary (PGC) viscometer specifically designed for subcooled liquefied gases.

The measurements are correlated to the Arrhenius-Eyring rate equation ($\mu = Ae^{E/\boldsymbol{R}T}$) and interpreted with respect to the chemical reaction rate theory. The Arrhenius-Eyring plot fit parameters reproduce the dynamic viscosity measurements with only a 2% RMS error, which is remarkable considering just two parameters are involved.

Unfortunately, we were not able to obtain many data points for the viscosity of subcooled liquid hydrogen due to technical challenges. Further work is recommended to develop a capillary tube that is resistant to hydrogen embrittlement, thus allowing these measurements to be completed.

References

[1] Lemmon, E. W., McLinden, M. O., Huber, M. L., NIST Standard Reference Database 23: Reference Fluid Thermodynamic and Transport Properties – REFPROP, Vers. 7.0, National Institute of Standards and Technology, Standard Reference Data Program, Gaithersburg, Maryland (2002).

[2] Lemmon, E. W., Jacobsen, R. T., Int. J. Thermophys., Vol. 25, No. 1, pp. 21–69 (2004).

[3] Laesecke, A., Krauss, R., Stephan, K., Wagner, W., J. Phys. Chem. Ref. Data, Vol. 19, No. 5, pp. 1089–1122 (1990).

[4] Hilton, D. K., Van Sciver, S. W., Rev. Sci. Instrum., Vol. 78, 033906 (2007).

[5] Kestin, J., Sokolov, M., Wakeham, W., Appl. Sci. Res., Vol. 27, pp. 241–264 (1973).

[6] Weber, L. A., J. Res. NBS – A., Vol. 74A, No. 1, pp. 93–129 (1970).

[7] Hirschfelder, J. O., Curtiss, C. F., Bird, R. B., Molecular Theory of Gases and Liquids, John-Wiley, New York (1954).

[8] Frenkel, J., Kinetic Theory of Liquids, Oxford University, London (1946).

Viscosity Measurement Publications

1. “Pressurized Gravitational Capillary Viscometer for Subcooled Liquefied Gases”, D. K. Hilton and S. W. Van Sciver, Reviews of Sci. Instrum. 78, 033906 (2007).

2. “Absolute Dynamic Viscosity Measurements of Subcooled Liquid Oxygen from 0.15 MPa to 1.0 MPa, D. K. Hilton and S. W. Van Sciver, Cryogenics, (accepted).

3. “Measurement of the Kinematic Viscosity of Subcooled Liquid Hydrogen”, A. Hemmati, D. K. Hilton and S. W. Van Sciver, Internal report – NHMFL Cryogenics group (2007).

This work produced no patents or theses.

Table 1.1. Thermal conductivity values for subcooled liquid oxygen

Pressure (MPa)	T (K)	k (W/m-K)	δP (MPa)	δT (K)	δk (W/m-K)
1.0002	55.9486	0.19990	0.00015	0.00062	0.000090
1.0003	60.1572	0.19472	0.00014	0.00056	0.000065
0.9998	65.5879	0.18754	0.00002	0.00038	0.000055
0.9993	71.3274	0.17966	0.00051	0.00050	0.000035
1.0022	75.6650	0.17340	0.00005	0.00044	0.000038
1.0002	80.6776	0.16640	0.00030	0.00024	0.000034
0.7500	55.9423	0.19966	0.00010	0.00150	0.000015
0.7493	58.8036	0.19616	0.00052	0.00078	0.000044
0.7496	70.7689	0.18018	0.00003	0.00043	0.000022
0.7503	75.3548	0.17357	0.00008	0.00071	0.000021
0.7498	80.6889	0.16614	0.00015	0.00077	0.000047
0.5002	56.5024	0.19880	0.00013	0.00017	0.000026
0.5002	60.1102	0.19435	0.00020	0.00130	0.000031
0.5020	71.1511	0.17942	0.00017	0.00025	0.000030
0.5003	75.1652	0.17370	0.00018	0.00036	0.000025
0.5003	80.6849	0.16587	0.00011	0.00050	0.000032
0.2503	55.4962	0.19979	0.00011	0.00120	0.000020
0.2507	60.7846	0.19325	0.00002	0.00045	0.000021
0.2498	71.1504	0.17920	0.00002	0.00012	0.000023
0.2506	75.1497	0.17345	0.00016	0.00043	0.000022
0.2504	80.5935	0.16576	0.00022	0.00035	0.000036

Table 1.2. Thermal conductivity values for equilibrium subcooled liquid hydrogen

P (MPa)	T_{mean} (K)	k (mW/m.K)	δP (MPa)	δT_{mean} (K)	δk (mW/m.K)	Δk (mW/m.K)
0.2475	15.0314	84.0095	0.00004	0.0003	0.0791	1.5065
0.2466	17.0423	99.7379	0.00008	0.0004	0.0892	1.3501
0.2460	19.1066	102.5436	0.00012	0.0005	0.1309	1.1660
0.2483	21.0890	102.2769	0.00008	0.0004	0.1135	1.1657
0.2518	23.1068	100.1525	0.00013	0.0003	0.1040	1.1303
0.5048	15.0177	84.0429	0.00017	0.0009	0.1807	1.5076
0.4998	17.0434	100.3853	0.00011	0.0003	0.0928	1.3627
0.4983	19.0839	103.2783	0.00013	0.0005	0.1471	1.1768
0.5000	21.0725	103.3041	0.00006	0.0004	0.0796	1.1780
0.2518	23.1068	100.1525	0.00013	0.0003	0.1040	1.1303
0.7508	15.0451	84.3801	0.00005	0.0003	0.1034	1.5173
0.7524	17.0612	100.9285	0.00004	0.0003	0.0396	1.3748
0.7473	19.0875	103.9432	0.00008	0.0004	0.0538	1.1869
0.7505	21.0611	104.0534	0.00004	0.0004	0.1120	1.1896
0.7514	23.0528	102.6045	0.00006	0.0005	0.1477	1.1684
1.0024	17.0511	101.3064	0.00002	0.0002	0.0467	1.3822
0.9990	19.0895	104.7119	0.00006	0.0005	0.0778	1.1986
1.0017	21.0699	105.0580	0.00002	0.0002	0.0519	1.2046
1.0000	23.0883	103.3222	0.00009	0.0006	0.0787	1.1791

Table 2.1. Comparison of densities for liquid oxygen

P(MPa)	T(K)	ρ_1 (g/cm^3) (Eq. 1)	ρ_2 (g/cm^3) (Eq. 2)	$\left(\frac{\rho_2 - \rho_1}{\rho_1}\right)(\%)$
1.0009	91.3143	1.137.4	1.1261	-1.02
1.0004	80.9962	1.1873	1.1744	-1.10
1.0009	76.0108	1.2106	1.1965	-1.18
1.0008	71.1396	1.2330	1.2182	-1.21
1.0006	66.3230	1.2547	1.2391	-1.26
1.0000	61.4184	1.2766	1.2599	-1.32
1.0002	55.3595	1.3033	1.2848	-1.44
0.7500	91.2206	1.1373	1.1220	-1.36
0.7501	80.9956	1.1869	1.1699	-1.45
0.7502	75.9912	1.2103	1.1922	-1.52
0.7501	71.1366	1.2326	1.2139	-1.54
0.7505	66.3159	1.2544	1.2349	-1.58
0.7501	61.4294	1.2763	1.2556	-1.64
0.7502	55.3757	1.3029	1.2798	-1.81
0.5009	91.1579	1.1370	1.1179	-1.71
0.5000	80.9859	1.1865	1.1656	-1.80
0.5001	75.9960	1.2099	1.1879	-1.85
0.5001	71.1449	1.2322	1.2096	-1.87
0.5003	66.3229	1.2541	1.2306	-1.91
0.5001	61.4335	1.2759	1.2513	-1.97
0.5003	55.3400	1.3028	1.2752	-2.17
0.2508	91.1400	1.1365	1.1137	-2.05
0.2504	80.9780	1.1861	1.1610	-2.16
0.2502	75.9905	1.2095	1.1834	-2.21
0.2501	71.1249	1.2319	1.2052	-2.22
0.2501	66.3119	1.2538	1.2263	-2.24
0.2502	61.4223	1.2757	1.2468	-2.32
0.2502	55.3402	1.3025	1.2687	-2.67

Table 2.2. Comparison of the density computed from the Clausius-Mossatti relation for liquid hydrogen

P (MPa)	T (K)	ρ_l(g/cm^3) (Eq. (1))	$\rho_{fit\ [2,\ 3]}$ (g/cm^3)	$(\rho_{fit}-\rho_1)/\rho_1$ (%)
1.0000	23.0014	0.06942	0.06942	-0.001
1.0001	21.0034	0.07164	0.07164	0.002
0.9994	18.9381	0.07372	0.07372	0.004
0.9998	16.9945	0.07553	0.07553	0.005
0.9986	15.1199	0.07704	0.07704	0.005
0.7502	23.0039	0.06837	0.06837	-0.002
0.7495	20.9682	0.07070	0.07070	0.002
0.7503	18.9471	0.07278	0.07279	0.005
0.7503	16.9874	0.07463	0.07463	0.006
0.7499	15.0544	0.07621	0.07622	0.007
0.5001	23.0065	0.06731	0.06731	-0.002
0.4994	21.0058	0.06967	0.06967	0.003
0.5003	18.9270	0.07187	0.07187	0.006
0.5004	17.0153	0.07371	0.07372	0.008
0.4996	15.0670	0.07533	0.07533	0.009
0.2490	23.0116	0.06624	0.06624	-0.003
0.2487	20.9643	0.06871	0.06872	0.003
0.2493	18.9391	0.07091	0.07092	0.006
0.2499	17.0524	0.07275	0.07275	0.009
0.2486	15.1126	0.07441	0.07442	0.010

Table 3.1. Subcooled LO_2 Dynamic Viscosity vs. Temperature and Pressure.

T [K]	P [kPa]	μ [μPa•s]	2•σ_μ [μPa•s]	ρ [kg/m^3][6,7]	N [-]
55.000	152.3	799.3	1.5	1303.9	283
59.999	153.7	588.4	1.0	1281.7	143
64.999	153.9	459.2	1.2	1259.3	257
69.999	153.5	373.1	1.1	1236.7	245
74.999	154.4	311.9	1.1	1213.7	329
77.353	155.3	284.9	2.1	1202.7	72
80.001	156.8	254.7	1.2	1190.3	226
84.999	157.8	233.0	2.5	1166.3	163
90.187	153.7	196.7	1.4	1140.7	307
54.991	309.0	809.7	2.3	1304.1	183
90.186	305.7	193.2	0.48	1141.4	117
55.984	508.6	816.2	2.4	1300.0	305
60.000	515.7	595.3	0.71	1281.7	154
65.000	515.9	464.0	0.75	1259.3	384
70.000	515.9	375.5	0.50	1236.7	302
74.999	515.8	312.6	1.5	1213.7	118
77.353	515.5	296.2	2.2	1202.7	300
79.998	517.6	264.9	1.9	1190.3	508
84.999	517.9	228.6	1.3	1166.3	421
90.188	518.9	195.6	1.3	1140.7	149
54.998	810.6	814.9	1.1	1303.7	81
60.001	810.5	599.4	2.3	1281.7	93
65.000	811.3	467.0	0.62	1259.3	109
69.993	810.8	378.3	1.8	1236.7	190
75.000	811.0	312.5	1.2	1213.7	138
77.353	811.2	288.2	0.93	1202.7	136
79.999	811.8	265.8	0.66	1190.3	135
84.996	812.2	227.1	1.1	1166.3	293
90.187	811.1	198.0	0.72	1140.7	142
55.000	1013.7	813.7	2.4	1303.7	415
59.997	1013.8	602.9	1.4	1281.7	90
60.003	1014.4	599.5	1.4	1281.7	395
64.990	1014.7	465.3	0.65	1259.4	424
69.997	1015.1	375.7	0.42	1236.7	207
69.992	1014.1	372.9	1.4	1236.7	475
75.001	1014.7	295.7	8.0	1213.7	284
77.354	1014.5	291.0	0.83	1202.7	523
79.995	1016.5	265.7	1.1	1190.3	222
79.987	1014.3	262.8	0.60	1190.3	347
85.001	1017.3	228.5	1.4	1166.3	264
90.187	1020.8	198.8	0.75	1140.7	245

Table 3.2. Comparison of hydrogen viscosity results to those obtained using REFPROP. REFPROP quotes an uncertainty in viscosity of between 4 and 15% in this range. N is the number of points used.

	T (K)	***p(kPa)***	***ν (m^2/s)***	***ν(REFPROP) (m^2/s)***	***% relative error***
Mean	14.9999	110.1136	3.2347E-07	2.9383E-07	10.087%
σ	0.0035	0.0475	3.39E-11		
N	89	89	89		
Mean	16.0000	102.7645	2.8342E-07	2.6454E-07	7.136%
σ	0.002491	0.0673	9.65E-11		
N	156	156	156		
Mean	17.9998	115.9044	2.3330E-07	2.2183E-07	5.173%
σ	0.0019	0.0391	1.08E-10		
N	86	86	86		

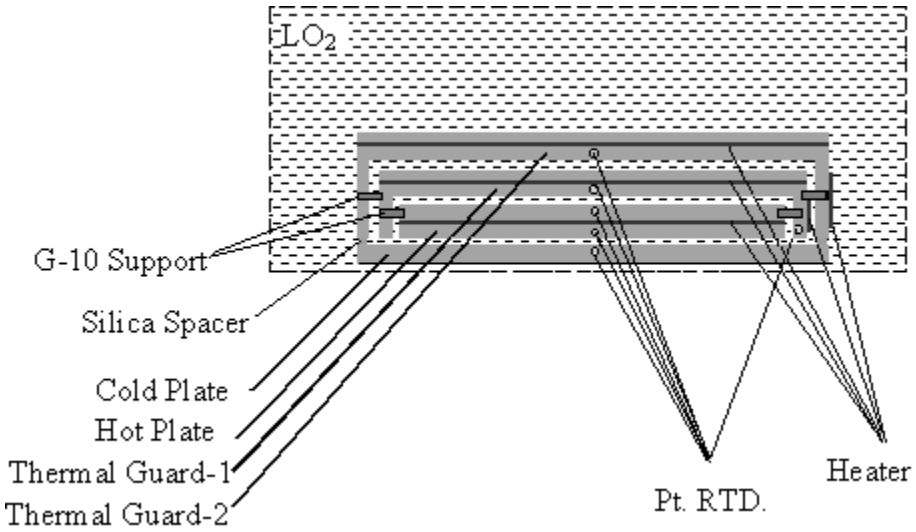

Figure 1.1. The schematic of the guarded, flat plate calorimeter.

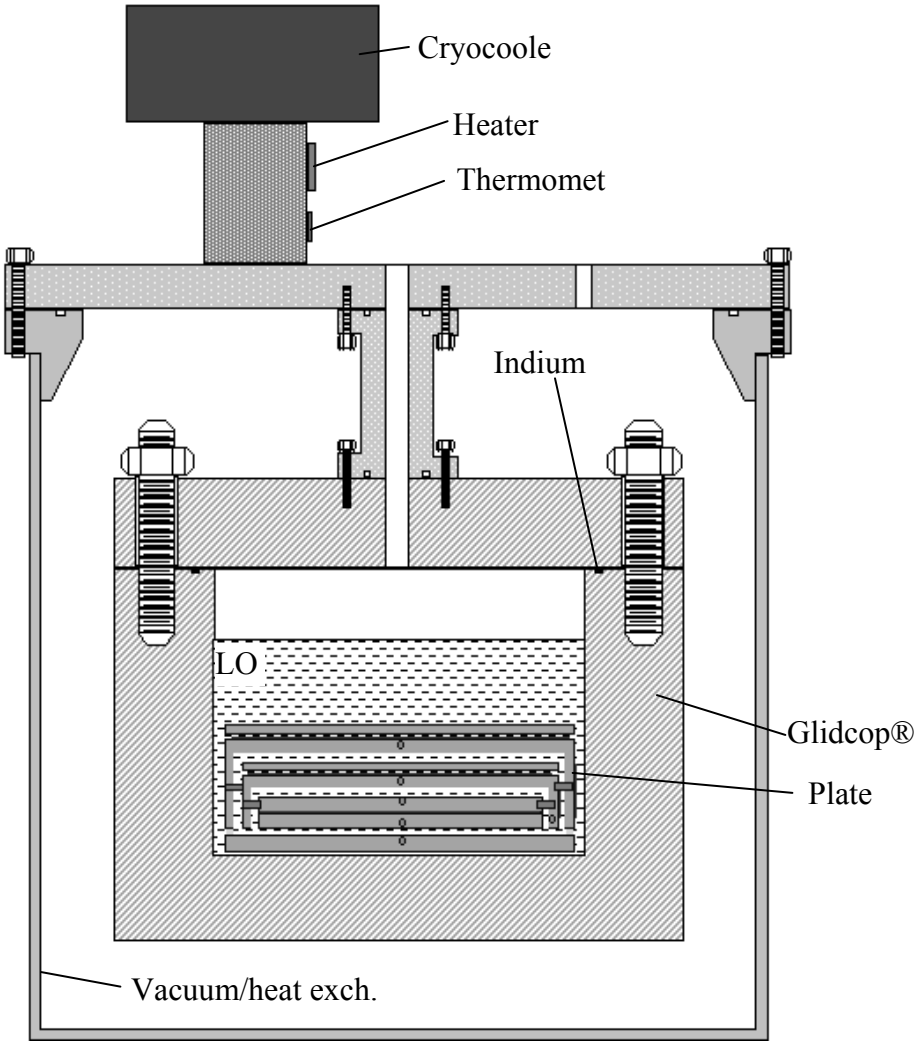

Figure. 1.2 The schematic of the experimental cell.

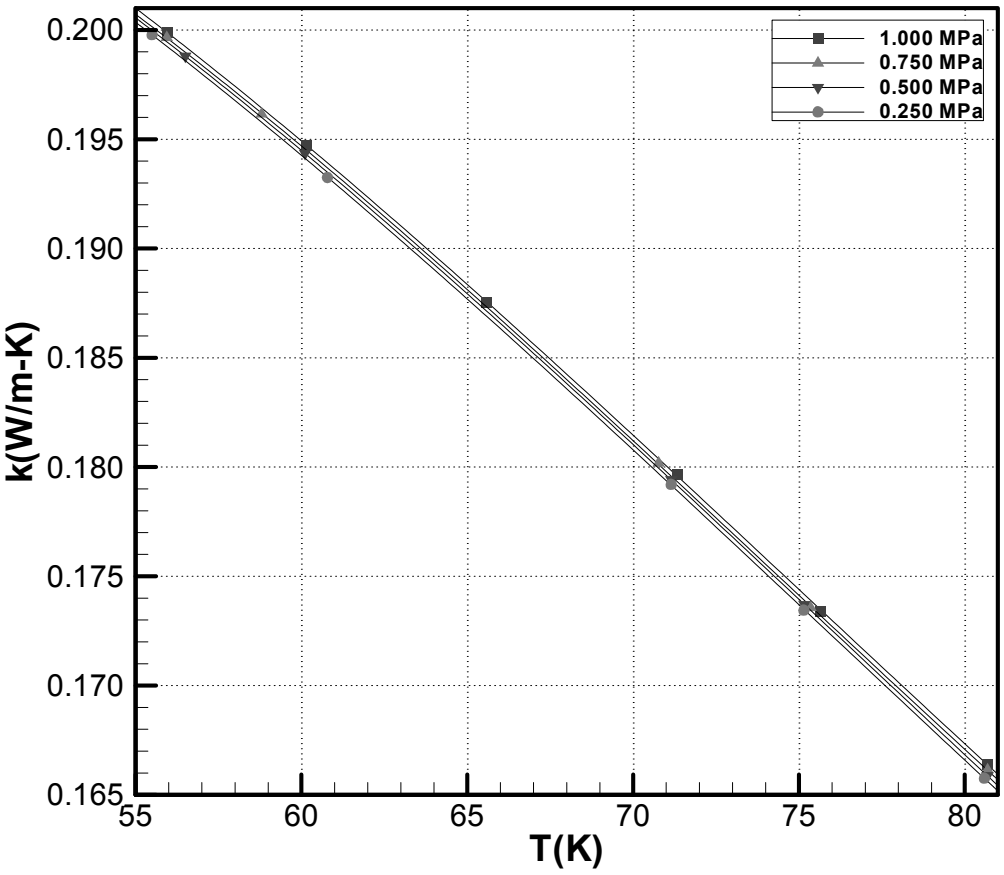

Figure 1.3. Oxygen thermal conductivity measurements at constant pressures (lines are curve fits to experimental results).

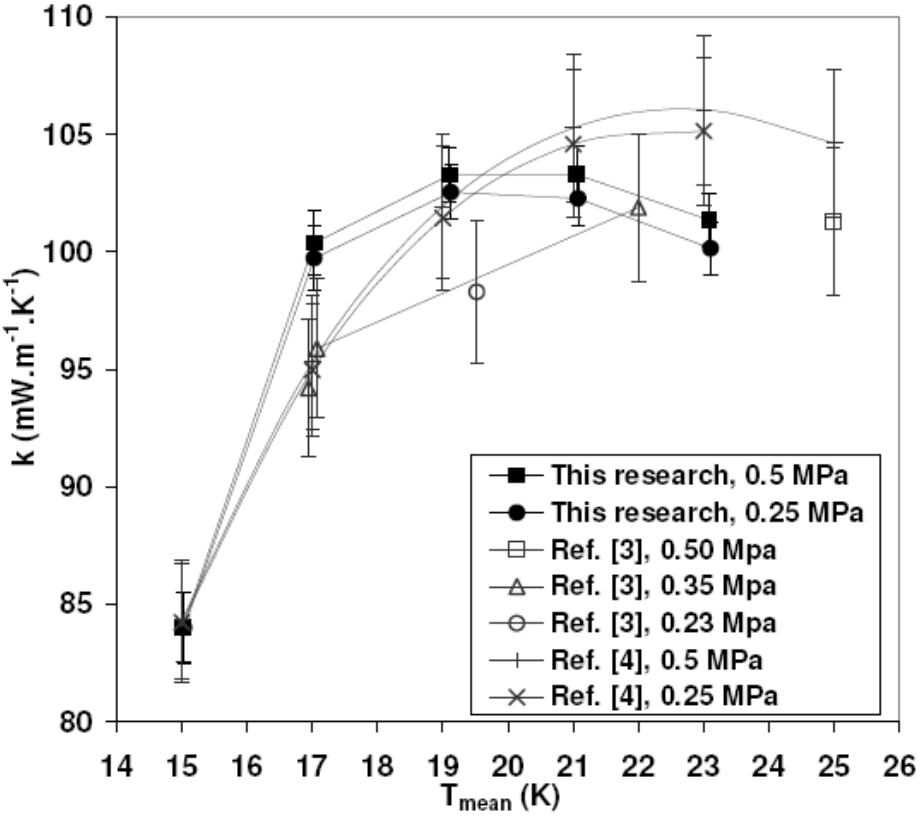

Figure 1.4. Hydrogen thermal conductivity measurements at constant pressures.

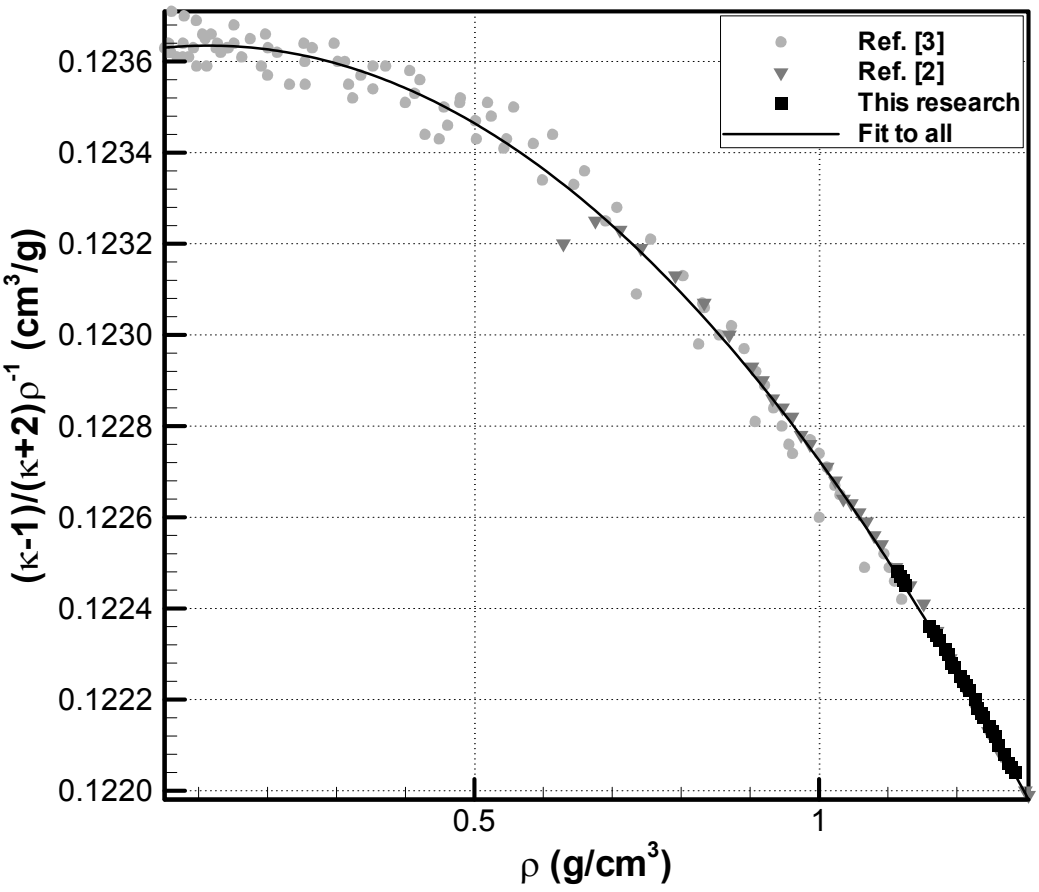

Figure 2.1. Clausius-Mossotti relation for oxygen.

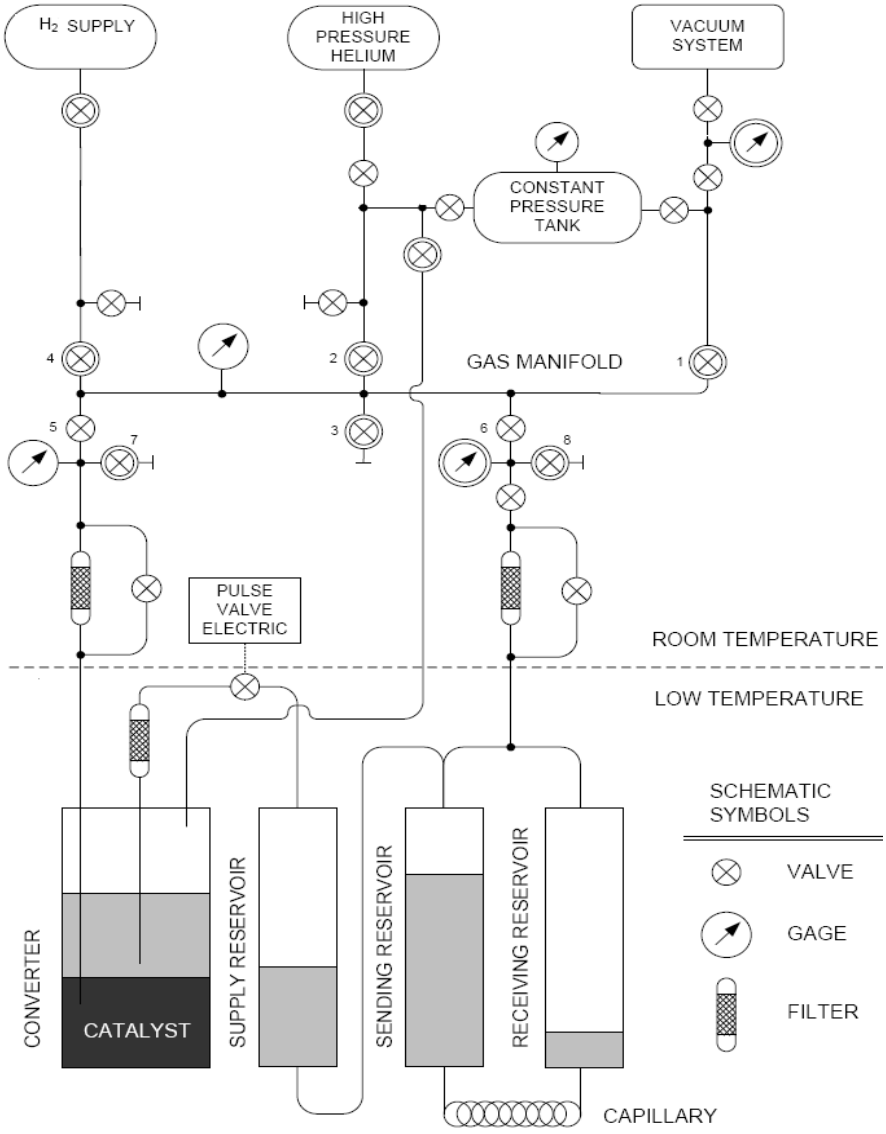

Figure 3.1. Schematic of the PGC viscometer instrument.

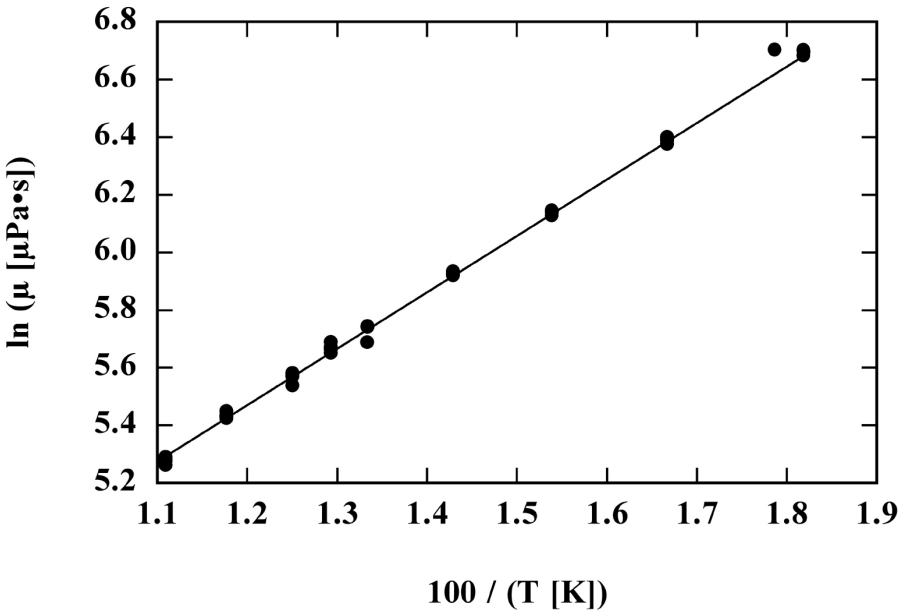

Figure 3.2. Arrhenius-Eyring correlation plots for subcooled LO_2 dynamic viscosity vs. reciprocal of temperature.

Experimental and Numerical Investigations of Cryogenic Multiphase Flow

S. Van Sciver and Y. Hussaini
Florida State University

J. F. Justak
Advanced Technology Group

Research Period: June 2002 to December 2005

Summary

The purpose of this project was to experimentally measure and model solid hydrogen particle mass flow in liquid helium, two phase liquid/vapor flow or solid/liquid hydrogen flow for fluid handling systems of interest to NASA. This project was a joint effort between the Cryogenics group at Florida State University (FSU), members of the School of Computational Sciences (SCS) at FSU and the Advanced Technology Group (a small business in Stewart, FL). The work focused on three main subtasks: 1) building an experimental test facility to produce and measure cryogenic multiphase flows; 2) performing robust modeling efforts to simulate the dynamic phenomena in cryogenic multi-phase flows; and 3) to develop prototype mass flow sensors for measurements in two phase cryogenic flows. The mass flow sensors were tested in liquid nitrogen and liquid helium using the experimental multiphase flow facility at FSU.

Introduction

Advanced propulsion systems for future spaceflights may require delivery of a variety of hydrogen fluid systems including two phase liquid/vapor flow, densified liquid, hydrogen slush or possibly solid hydrogen in a liquid helium carrier. To this end, the understanding of two phase flow phenomena in cryogenic fluid systems is of critical interest to NASA for developing fluid management systems both under earth and microgravity conditions. The issues of most significant interest in two-phase flow systems are the ability to predict the flow regime and independently measure the mass flow rate of the individual phases. Since these issues are primarily of an empirical nature depending on many factors in the fluid system, proper characterization depends on a combination of experimental investigation coupled with numerical simulation. To address these technical issues of multiphase flow in cryogenic hydrogen delivery systems, Florida State University has organized a research team consisting of the FSU Cryogenics Group led by the PI at the National High Magnetic Field Laboratory, a computational group at the FSU School of Computational Sciences and a small business (Advanced Technology Group).

The first objective of this program was to investigate the dynamics of the two phase system consisting of solid hydrogen in liquid helium (sH_2/LHe). To implement such a fluid system, a better understanding of the flow regimes, anticipated pressure drop and heat transfer characteristics is needed. As organized, the Cryogenics group at FSU was tasked with developing an experimental facility to study the flow dynamics and flow regimes; the FSU computational group was responsible for simulating the various processes involved in the production and flow of solid H_2 particles in liquid helium; and the Advanced Technology Group was to develop optical techniques for measurement of solid hydrogen mass and multiphase flow regimes.

Two phase flow in cryogenic fluids has long been of interest to NASA as these flow states commonly occur in fluid handling systems both on earth as well as in space. Although there has been considerable engineering work done on two phase flow, the vast majority of this work has involved water/steam or water/air flows. By contrast, much less work has been done on cryogenic two phase flows, leaving a considerable uncertainty when it comes to prediction of fluid handling system performance.

Characterization of multiphase flow requires knowledge of more parameters than for single phase (liquid or vapor) flows. While in the latter case, a flow can be fully characterized by its local thermodynamic variables (T, p, and ρ) along with the system dimensions and mass flow rate, a two phase flow is usually more complex. In addition to the thermodynamic variables of both phases and the system configuration, one also needs to know the relative volume or area fraction of the two fluids (α = void fraction = A_v/A) and the flow quality (χ = flow quality = vapor mass flow rate/total mass flow rate). Also, the void fraction and flow quality depend strongly on the particular flow regime that may be present in the two phase flow. The flow regime generally depends on many factors (fluid velocity, channel orientation with respect to gravity and flow quality). Unfortunately, there is insufficient data on cryogenic two phase flows to be able to confidently design a system for application. Further, although there are many proposed techniques, there still is no reliable and accurate technique for measuring the total flow rate or flow quality of a cryogenic two phase flow.

Sub-Task 1: Experimental measurements of multiphase flow

Two Phase Flow Experimental Facility—Figure 1.1 shows the FSU cryogenic flow visualization facility, which was developed for two phase flow experiments. This facility, which has an overall length of 5 m, includes two visualization ports, one at the midpoint and a second one 1 m down stream. Flow channels within the facility are suspended in a vacuum environment and surrounded by thermal radiation shields cooled by LN_2 and LHe natural circulation loops. The end stacks contain metal bellows pumps, each with a volume displacement of one liter and controlled by linear stepper motors. These components can force the liquid cryogens to flow in either direction at precisely controllable volume flow rates up to 0.3 liters/s.

The experimental channel, designed to allow visualization measurements, is shown in Figs. 1.1 and schematically in Fig. 1.2. The channel has a square cross-section, 32 mm x 32 mm measured inside and a total length of 2.2 m, with two optical ports aligned to those on the flow facility and mounted with vacuum tight optical windows.

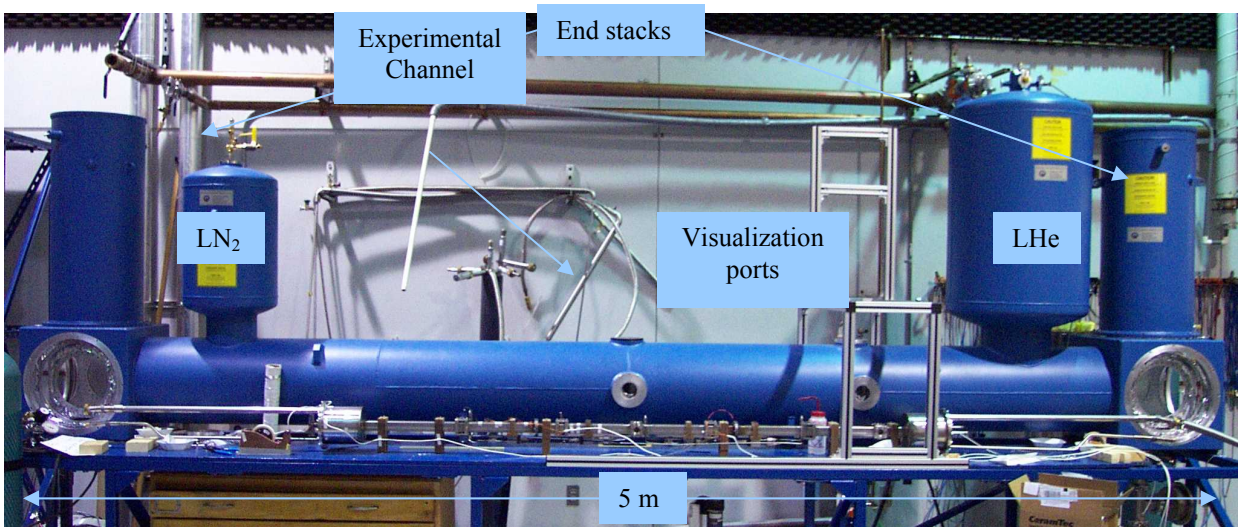

Figure 1.1. FSU Cryogenic flow visualization facility.

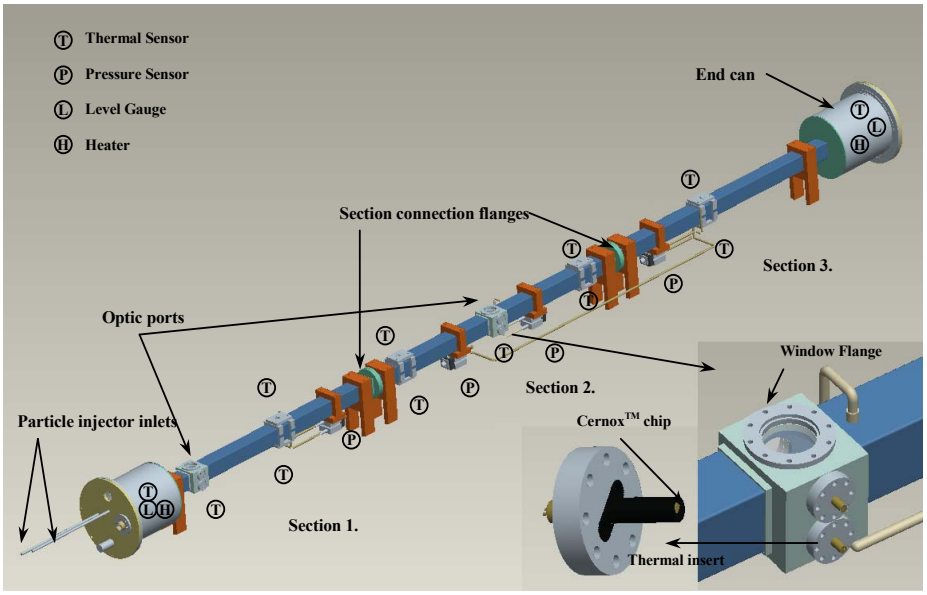

Figure 1.2. Experimental channel configuration.

The channel contains temperature, pressure and liquid level sensors. With the thermal insert shown in Figure 1.2, the temperature sensor can directly measure the temperature of the fluid in the channel. There are six pairs of temperature sensors at different locations in the channel, with each pair being placed top and bottom of the channel inner wall for monitoring both the vapor and liquid phase. The end cans contain calibrated temperature sensors, which provide a standard for *in situ* calibration of the other sensors.

The channel is also equipped with four differential pressure sensors. As shown in Fig. 2, one pressure transducer is used to measure the pressure loss along the channel. These pressure taps are connected 0.3 m from either end of the channel to avoid entrance effect corrections to the measured pressure drop. The entrance length is calculated according to the maximum Reynolds number 1 x 10^5 expected in the experiment. The other three pressure transducers located along the channel measure the difference in pressure between top and bottom to determine the hydrostatic head of the liquid cryogen.

The capacitive liquid level gauges are located at each of the end cans to the channel. These gauges use the difference in dielectric constant for the vapor and the liquid to make a device, which has an output directly proportional to the liquid level in the gauge. In this configuration, the level difference can be measured to within $\pm$0.1 mm. The experimental apparatus can circulate either LN_2 or LHe. Measurements of pressure drop and heat transfer in the two-phase liquid/vapor flow can be made, while monitoring the flow regime at the access points.

The two phase flow facility is also capable of studying flows consisting of a mixture of solid hydrogen particles (sH_2-p) and LHe. To support these measurements, we have developed the capability to inject sH_2 particles into liquid helium [1]. This work is experimental confirmation of the numerical simulations conducted by our computational group (see below). Of particular interest is a measurement of the relative motion of the suspended particles as it depends on particle size, concentration and background LHe flow rate. In addition to video imaging, particle image velocimetry (PIV) techniques can also be used to quantitatively visualize the velocity field in the flow.

This work produced no patents or theses.

Sub-Task 2: Mass Flow Meter Development

Fluid Optical Quality Sensor (FOQS)—As part of this program, Advanced Technologies Group (ATG) developed a Fluid Optical Quality Sensor (FOQS) for cryogenic fluids. This unit was tested in the FSU cryogenic flow visualization facility, described above. Current point sensor technology is incapable of determining high pressure, high flow rate cryogenic fluid quality and has proven to be inaccurate in attempting to rapidly measure cryogen depletion. The capability to measure cryogen depletion instantaneously is critical when operating cryogenic turbo-machinery. The Fluid Optical Quality Sensor (FOQS) provides a means of measuring fluid quality for a wide range of flow systems.

Advanced Technologies Group's FOQS utilizes the optical properties of the fluid being analyzed to determine mass flow rate, and quality of the flow. Two techniques are combined in the sensor: an optical absorption/scatter and acousto-optic signal processing. The basic principle of the quality measurement is the accurate determination of light attenuation due to a change in refractance in a liquid flow environment and the optical absorption coefficient. The device uses an innovative technique to create a plane-of-light (POL) within the propellant fluid line. As the fluid passes through the plane, specific wavelengths of light indicative of the fluid will be absorbed. The POL intensity is continuously monitored and any alteration of transmittance due to non-uniformity of the media flowing through the plane is recorded. In the least complex form, this method determines when two-phase flow is present. As a gas bubble passes through the POL, signal attenuation occurs.

An acousto-optic interaction occurs in all optical media when an acoustic wave and a laser beam are present. When an acoustic wave is launched into the optical medium, it generates a refractive index wave that behaves like a sinusoidal grating. The incident laser beam passing through this grating will diffract the laser beam with its angular position being linearly proportional to the acoustic frequency. If the acoustic wave is traveling in a moving fluid, the

fluid velocity will affect the frequency of the traveling wave, relative to a stationary sensor. This frequency shift changes the angle of diffraction. Hence, the fluid velocity can be determined from the diffraction angle. To the best of our knowledge, the acousto-optic interaction has never been attempted in a cryogenic liquid [2].

Laminar Two Phase Flow Meter—As an alternative approach to two phase mass flow metering, the FSU cryogenics group has developed a sensor based on laminar flow in the two fluid components. The sensor consists of 30 thin parallel channels in the space between G-10 printed circuit board spacers in a stainless steel housing. The flow within the channels is assumed to be laminar, so that the pressure drop is proportional to the mass flow rate. The two phase flow is also assumed to be stratified, with the liquid on the bottom, a condition that has been previously confirmed with a similar channel containing water/air two phase flow. The liquid level within each of the parallel channels can be measured at seven equally spaced locations along the channel using capacitive level gauges bonded to the G-10 channel walls. A schematic of the two phase flow sensor assembly is given in Figure 2.1 and a photograph of the partially assembled unit showing the parallel G-10 plates in the stainless steel housing in Figure 2.2.

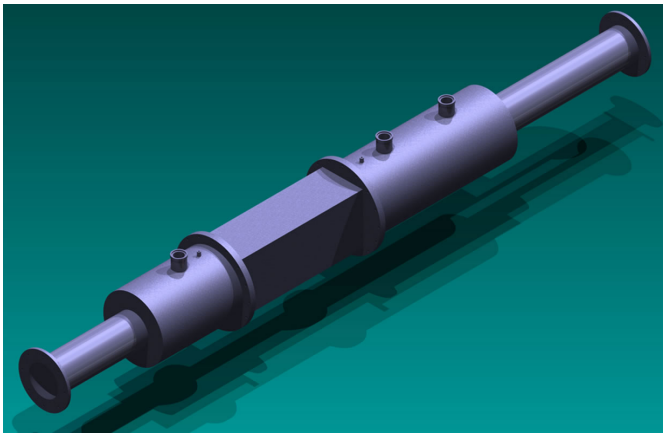

Figure 2.1: Schematic of the laminar two phase flow sensor. The overall length of this unit is

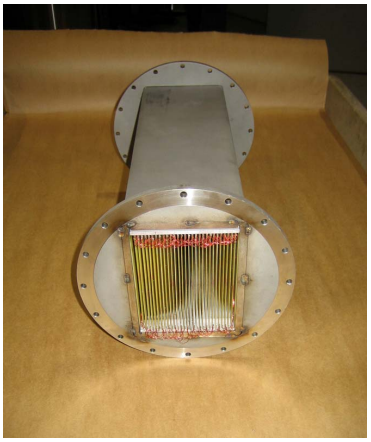

Figure 2.2: Photograph of the partially assembled flow sensor.

The principle of operation for the laminar two phase flow meter is as follows. With a mixture of liquid and vapor passing through the sensor, the void fraction (A_v/A) can be measured at seven locations along the channels providing information about the location of the liquid-vapor interface versus position. Since the flow is laminar, the pressure gradient along the sensor is directly proportional to the fluid velocity. By measuring the pressure drop and integrating the dynamic equations for the two phases, one can infer the individual fluid mass flow rates and thus determine the total mass flow rate through the sensor.

Experimental testing of this two phase flow meter provided preliminary results that confirmed the operating principle [3]. However, more work is needed to fully confirm that this device can measure two phase cryogenic flows to sufficient accuracy to be useful to applications.

This work produced no patents and one MS thesis [3].

Sub-Task 3: Numerical Modeling of Multiphase Flows

The numerical simulation program has involved a synergistic approach with the experiments to study the production of hydrogen particles of uniform size and shape, their storage in the LHe carrier, and the multi-phase flow characteristics of the slurry comprising sH_2 in LHe. The simulations are first validated by the experiments followed by a simulation-based parametric study to guide future experiments. For the purpose of simulations, physical models have been developed for the complex phase change phenomena involving simultaneous vaporization/condensation of helium and solidification of hydrogen droplets. Computational models have also been developed based on appropriate numerical algorithms to solve the governing equations for multiphase flow.

Simulations have been performed on the phase change phenomena that occur during the generation of sH_2 in LHe, which include vaporization and re-condensation of helium around a hydrogen droplet and solidification of the droplet in helium. As these phenomena are extremely complex, they have been separately studied. In a single-fluid, two-phase mixture framework, the simulation of vaporization and condensation involves a vapor-liquid exchange model that accounts for mass and energy transfers due to phase changes between liquid and vapor helium. The model separately predicts the helium vapor flow field resulting from the phase change and the motion of the hydrogen droplet and the solidification evolution of hydrogen particles of various diameters.

Liquid hydrogen droplet formation has also been addressed within the context of the incompressible Navier-Stokes equations for multiphase flows with the surface-tension model properly incorporated. These governing equations are discretized on a dynamic grid to accommodate a vibration of the generator orifice. In view of the extreme complexity of the problem, the problem has been limited to the incipient stage of droplet generation when the effects of phase change may be negligible. Numerically predicted droplet shapes show satisfactory agreement with the photographs of LH_2 droplets generate in experiments. Parametric studies have been carried out to characterize the influence of injection velocity, nozzle vibration frequency and amplitude on the droplet shape. The computational model provides a definitive qualitative picture of the evolution of a droplet shape as a function of the operating parameters [4].

Finally, in order to study the flow characteristics of liquid helium (carrying sH_2 containing atomic species), a three-dimensional two-phase mixture model along with a two-equation mixture turbulence model has been developed. Numerical results show that turbulence is required to keep the sH_2 in suspension, which otherwise form a sliding layer of particles on top of the helium layer, Fig. 3.1. The sH_2-p concentration profiles in the slurry system are functions of particle size, flow velocity, and influx volume fraction of hydrogen particles [5].

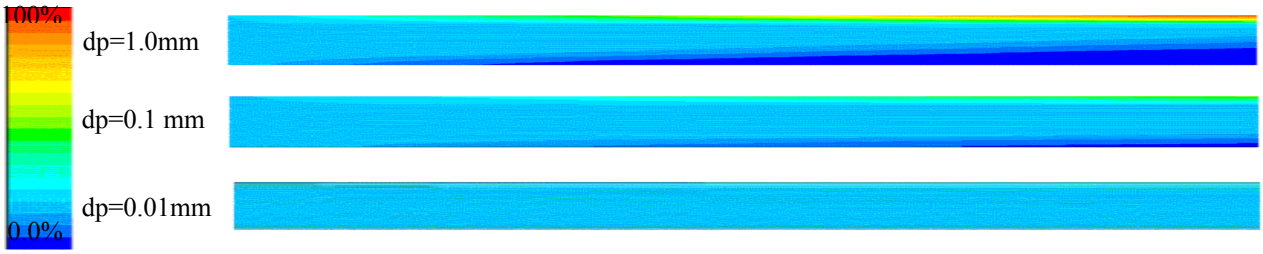

Figure 3.1: Slurry flow model showing hydrogen particle concentration vs. particle size.

This work produced no patents or theses.

Publications

1. T. Xu and S. W. Van Sciver "H_2/D_2 Particle Seeding and injection system for PIV Measurement of He II", Advances in Cryogenic Engineering, Vol. 51A, 1685 (2006)
2. D. M. Kocak, J. F. Justak, F. M. Caimi and S. W. Van Sciver, A cryogenic mass flow sensor , Advances in Cryogenic Engineering, Vol. 51A, 281 (2006)
3. R. H. Ashmore, "Two Phase Flowmeter: A Proof of Concept", Masters Thesis, Florida State University, 2006
4. J. Xu, D. Celik, M.Y. Hussaini, and S.W. Van Sciver, "Numerical Studies of Liquid Hydrogen Droplet Generation from a Vibrating Orifice", Physics of Fluids Vol. 17, 082103 (2005)
5. B. Unlusu, J. Xu, M. Hussaini, D. Celik and S. Van Sciver, "Investigation of Hydrogen Droplet Solidification in Cryogenic Helium", Journal of Thermophysics and Heat Transfer, Vol. 22, 83 (2008)

November 2007

Final Report for Florida International University

- Improved Hydrogen Yield from Florida Specific Biomass Gasification Using a Pilot Scale Gasification Unit - Srivastava, R.

Improved Hydrogen Yield From Florida Specific Biomass Gasification Using a Pilot Scale Gasification Unit

R. Srivastava
Florida International University

Research Period: July 2002 to September 2007

Abstract

Concerns about the depletion of fossil fuel reserves, energy security, and pollution caused by continuously increasing energy demands make biomass and hydrogen attractive alternative energy sources. Recently, there has been an increasing interest in taking the necessary steps to move towards a hydrogen-based economy. NASA and Kennedy Space Center (KSC) and the Cape Canaveral Air Force Station (CCAFS) in particular, have been exploring options to locally produce the hydrogen. Local production of hydrogen is necessitated by economic, transportation safety, and energy security considerations.

Hydrogen is currently derived from nonrenewable resources by steam reforming in which fossil fuels, primarily natural gas, react with steam at high pressures and temperatures in the presence of a nickel-based catalyst. In principle, hydrogen can also be generated from renewable resources such as biomass through thermochemical or biological pathways. Gasification (thermochemical methodology) yields fuel gas that makes a wide array of power options viable, including traditional internal combustion engines and fuel cells.

During the earliest phase of this project, citrus peels in Central Florida and sugarcane bagasse were identified as promising local biomass resources in Florida due to their overabundance and favorable market value. The farmland acreage dedicated to citrus almost exceeds 800,000 acres. The citrus industry generates more than 1 million tons/year of citrus waste residue (dry basis). The undertaken research has focused on utilizing biomass residue from citrus juice production to co-produce hydrogen and heat. Hydrogen can then be used to generate electricity and additional heat.

The pilot-scale gasification system was designed using mostly off-the-shelf components. This report assesses the technical and economic potential of producing hydrogen from citrus peel fed biomass gasifier. The report also includes information on the feedstock preparation, feedstock handling, feedstock performance, hydrogen yields and potential problems identified during the pilot scale experiments.

Background

Concerns about the depletion of fossil fuel reserves, energy security, and pollution caused by continuously increasing energy demands make biomass and hydrogen attractive alternative energy sources that require further development towards commercialization. The nation's reliance on imported oil and the continued volatility in the Middle-East necessitate the development of alternative energy sources. NASA's KSC is one of the primary users of hydrogen in the state of Florida. Hydrogen is used as rocket fuel and in the fuel cells for spacecrafts. The KSC spaceport hydrogen requirements vary due to fluctuations in launch activities, program changes and other technical and weather related factors. This historically has had an adverse effect on the hydrogen procurement costs from commercial off-site locations. In addition, quiescent storage tank boil-off and losses due to transfer operations add

to the operational expenses. Coupled with this is manpower costs associated with tanker offloading and concerns with transportation safety and production disruptions. Local production of hydrogen will alleviate some of the concerns related to transportation safety and energy security.

Hydrogen is currently derived from nonrenewable resources using steam reforming in which fossil fuels, primarily natural gas, react with steam at high pressures and temperatures in the presence of a nickel-based catalyst. Another possible pathway for hydrogen generation is through gasification of renewable resources. Among the available renewable resources, biomass holds special promise as future fuel and feedstock. Biomass is eco-friendly, locally available in abundance and hence an excellent distributed energy source. Sustainable exploitation of biomass for generating energy has a potential to act as a catalyst for overall sustainable development. In order to increase the share of biomass (obtained preferably from bio-residues) in the country's energy resource portfolio, new power generation systems need to be developed to provide high-energy efficiency and clean environmental performance.

In Florida, almost 800,000 acres are planted with citrus trees. The Florida citrus industry processes more than 80% of the citrus crop into juice products. Fortunately, citrus processing plants are concentrated in a relatively small area within a radius of approximately 100 miles and sufficiently close to KSC. Figure 1 shows a map of the citrus processing facilities in Florida. During citrus juice processing, approximately one half of the fruit weight is left behind as waste. The Florida industry generates more than 1 million tons/year of citrus waste residue on a dry basis. This residue cannot be disposed of in landfills due to its large volume. To dispose the citrus waste stream, the peel waste is dried into citrus peel pellets and sold as cattle feed to Europe. The value of citrus peel pellets has been declining over the last five years and is currently at approximately $29-45/ton, while the production costs range from $50-65/ton, depending on fuel cost for drying. The reasons for the decline in value are the abundance of other commodities available for use in cattle feed formulations, the low protein content of citrus peel compared to other feedstock, and temporarily, the lingering effect of the "mad cow" disease on European cattle operations. As a result, the disposition of the citrus peel as cattle feed is a losing venture and the Florida Citrus Processors Association is very keen on finding alternate uses for the citrus peel. Citrus peel and similar co-products represent a large reservoir of inexpensive raw material for the production of energy (combined electricity and heat). As a bio-based product, it has the potential to provide a distributed energy generation source particularly in the rural areas. We envision that the proposed citrus peel-based power plant in central Florida will serve as a prototype for other biomass based power plants elsewhere in the country.

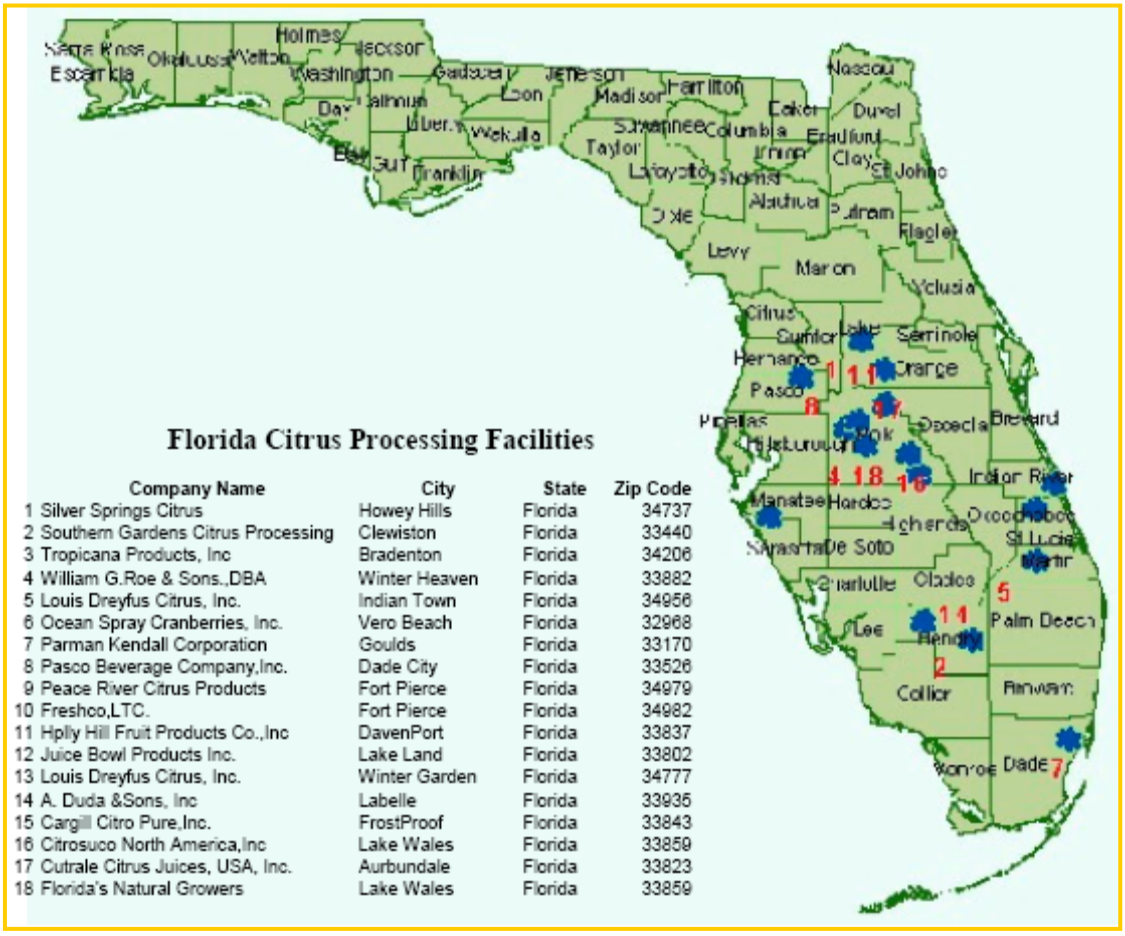

Figure 1. Florida citrus processing facilities.

Objective and Benefits to NASA

The primary objectives of the project were to:

a) Design, fabricate, and operate a pilot-scale biomass gasification unit for the production of hydrogen-rich gas from local Florida biomass resources, such as citrus peel.
b) Validate its performance, efficiency, economics, and reliability as a sustainable hydrogen source.
c) To identify the economic and technical barriers associated with biomass gasification.

Successful demonstration of biomass gasification for hydrogen generation using local resources would:

- Help local economy by developing a market for the citrus peel, a waste byproduct of citrus processing.
- Bring a new generation of small-scale biomass residue power plants much closer to technical and economic reality.
- Data from the project would ascertain the viability of a biomass gasification plant to address the long-term hydrogen needs of KSC and CCAFS. Local production of hydrogen would secure a renewable and environmentally friendly fuel for the spaceport operations.
- Create jobs associated with power generation.

Overview of Biomass Gasification

Gasification is a two-step process in which a solid fuel (biomass or coal) is thermochemically converted to a low- or medium-energy-content gas. A highly critical factor in the high-energy efficiency of the gasification process is that of the gasifier (primary reformer). Four main gasification stages occur at the same time in different parts of the gasifier as shown in Figure 2.

Drying

Biomass fuels consist of moisture ranging from 5 to 35%. At the temperature above 100 °C, the water is removed and converted into steam. Biomass does not experience any kind of decomposition in the drying stage.

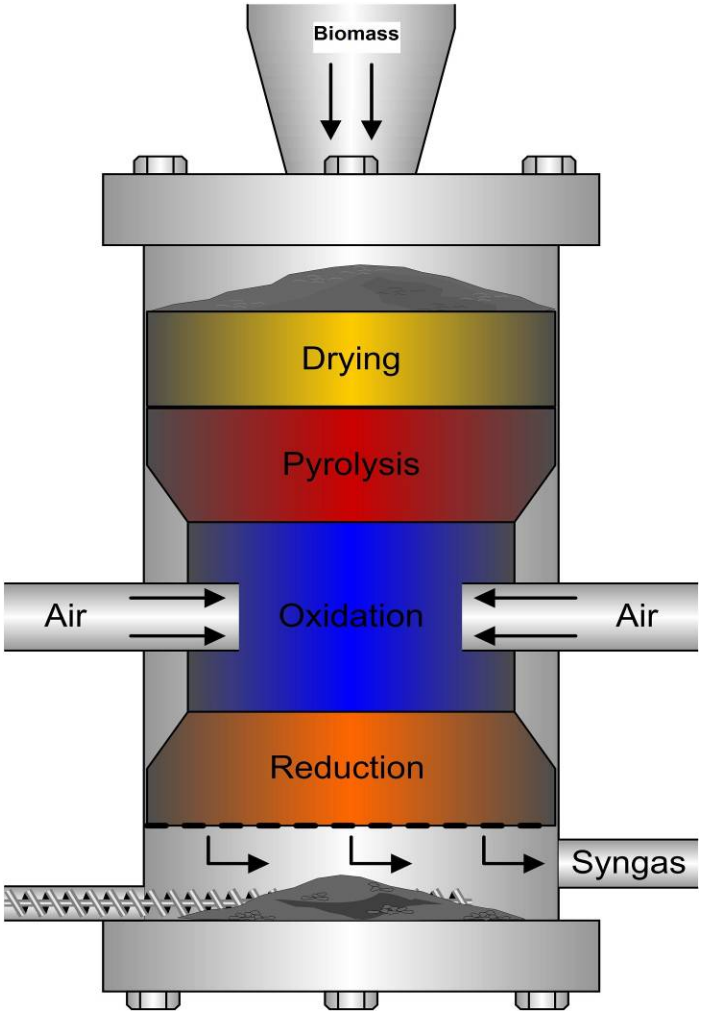

Figure 2. Biomass gasification basics.

Pyrolysis

Pyrolysis is the thermal decomposition of biomass in the absence of oxygen. Pyrolysis involves release of three kinds of products: solid (char), liquid (oil) and gases (CO, H_2, and N). The ratio of products is influenced by the chemical composition of biomass fuels and the operating conditions. The heating value of gas produced during the pyrolysis process is low (3.5 to 8.9 MJ/m^3). The dissociated and volatile components of the fuel are vaporized at temperatures as low as 600 °C (1100 °F). Included in the volatile vapors are hydrocarbon gases, hydrogen, carbon monoxide, carbon dioxide, tar, and water vapor. Because biomass fuels tend to have more volatile components (70 to 86% on a dry basis) than coal (30%), pyrolysis plays a larger role in biomass gasification than in coal gasification. Gas phase thermal cracking of the volatiles occurs, reducing the levels of tar. Char (fixed carbon) and ash are the pyrolysis byproducts that are not vaporized.

Oxidation

The combustion takes place at temperature ranging from 700 to 2000 °C. Heterogenous reaction takes place between oxygen in the air and solid carbonized fuel, producing carbon dioxide as follows.

$$C + O_2 = CO_2$$

Hydrogen in fuel reacts with oxygen in the air blast, producing steam.

$$H_2 + ½\ O_2 = H_2O$$

Reduction

In the reduction zone, a number of high temperature chemical reactions take place in the absence of oxygen. The principal reactions that take place are:

$$CO_2 + C = 2CO$$

$$C + H_2O = CO + H_2$$

$$CO_2 + H_2 = CO + H_2O$$

$$C + 2H_2 = CH_4$$

The main reactions show that heat is required during the reduction process. Hence, the temperature of gas goes down during this stage. If complete gasification takes place, all the carbon is burned or reduced to carbon monoxide, a combustible gas and some other mineral matter is vaporized. The remains are ash and some char (unburned carbon).

Gasification coupled with water-gas shift is the most widely practiced process route for biomass to hydrogen. Thermal, steam and partial oxidation gasification technologies are under development around the world. Feedstocks include both dedicated crops and agricultural and forest product residues of hardwood, softwood and herbaceous species.

When any fuel is completely burned, all of its potential energy, or heating value (designated HP) in units of Btu/lb, is released as sensible (“can be felt”) heat (designated HS) that can be

recovered for immediate use in a boiler, for example. In most established gasification processes, a fuel (wood or coal) is partially burned, leaving some gaseous products, while releasing a smaller amount of sensible heat, carried by the high temperature product gases. An established use for simple gasification is to pass the hot product gases directly to a closely coupled boiler or gas turbine, to do useful work, like generating electricity. Here the overall efficiency is defined as HP of product gases + HS carried by gases)/(HP of fuel). For a well-designed system, the overall efficiency may approach that of a well-designed solid fueled boiler. The advantage of such designs is to use efficient gas-fired boilers or turbines with solid fuels.

When steam is injected into such a gasifier, it reacts with the burning of solid fuel, to produce more of the gaseous product, the primary reaction being carbon (C) plus water (H_2O), yielding hydrogen (H_2) and carbon monoxide (CO). This reaction is endothermic, consuming part of the sensible heat of combustion, HS, in effect converting it to more fuel value, HP, in the product gas. The sensible heat consumed in these reactions is a heat of reaction (designated HR), which reduces the overall efficiency, as a price paid for a richer fuel or syngas product. Overall thermal efficiencies of gasifiers are in the range of 50 to 75%. “Directly heated” is defined as that in which air or oxygen is used to burn part of the fuel to provide the heat of reaction, HR.

As with coal gasification, biomass may be gasified using a variety of methods, primarily indirect and direct gasification. Thermal gasification is essentially high severity pyrolysis although steam is generally present. Indirect gasification as exemplified by the Battelle-Columbus Laboratories and Future Energy Resources Corporation (BCL/FERCO) gasifier uses a medium such as sand to transfer heat from the char combustor to the gasification vessel (Spath and Mann, 1998).

Biomass + Energy $\rightarrow$ CO + H_2 + CH_4 + ….

By including oxygen in the reaction gas the separate supply of energy is not required, but the product gas is diluted with carbon dioxide and, if air is used to provide the oxygen, then nitrogen is also present. Examples of this are GTI (formerly IGT) High Pressure Oxygen-Blown Gasifier, as well as the circulating fluid bed by TPS Termiska.

Biomass + $O_2 \rightarrow$ CO + H_2 **+** CO_2 + Energy

All of these gasifier examples require significant gas conditioning, including the removal of tars and inorganic impurities and the conversion of CO to H_2 by the water-gas shift reaction:
$CO + H_2O \rightarrow CO_2 + H_2$

Pyrolysis to hydrogen and carbon is being explored as a viable technology for carbon sequestration although most work is applied to natural gas pyrolysis. Biomass or biomass derived intermediates could be processed in this way.

Biomass Resource Assessment

The improvement in efficiency, its reduced environmental impact, and the capacity to generate hydrogen from renewable resources combine to make hydrogen an attractive choice for future energy development. Among the renewable resources, biomass offers several attractive attributes as a primary feedstock for hydrogen production. Biomass is currently used as a fuel for heat or electricity in most parts of the world, at a wide range of scales. Biomass most attractive applications are those where supply and collection systems have been established to provide raw material for a primary product (i.e., food or fiber) and power production has played a secondary role. These situations often provide large quantities of fiber material at attractive

prices and producing renewable hydrogen from this type of resource would be a logical first choice. Under scenarios of a favorable regulatory environment or reduced availability of fossil resources, systems dedicated to the production of biomass to supply hydrogen from production facilities are also likely.

Hydrogen production from a typical biomass material has a theoretical yield of 16.5% on a mass basis when steam is used as the oxidizer in a simplified, two-reaction mechanism. At this theoretical yield, the energy content of 165 g hydrogen is roughly equal to that of the initial kilogram of biomass feedstock.

A key element in planning a biomass to hydrogen facility is to locate a plant that will have ready access to adequate feedstock supplies.

Feedstock Cost and Availability

Information regarding the sizes and geographic locations of processing facilities and feedstock costs were determined for citrus pellets.

Table 1. Feedstock cost and availability.

Feedstock Availability			
Feedstock	**Tons/Day**	**US $/Ton**	**US $/GJ**
Citrus Pellets	500	$29-$40	$1.63-$2.25

Feedstock Handling

The supply of biomass of the right quality, size, and moisture content was a key to the operation and feasibility of FIU's gasification unit. The citrus pellets were manually screened using sieves having ¼ in. mesh size for uniformity (Fig. 3).

Figure 3. Citrus pellets.

Overview of FIU's Gasification Unit

Pilot Plant Location

The FIU's Pilot-scale gasification unit was located at the Applied Research Center at Florida International University in Miami, Florida. Its physical location is 10555 West Flagler Street, Miami, Florida 33174 (Fig. 4).

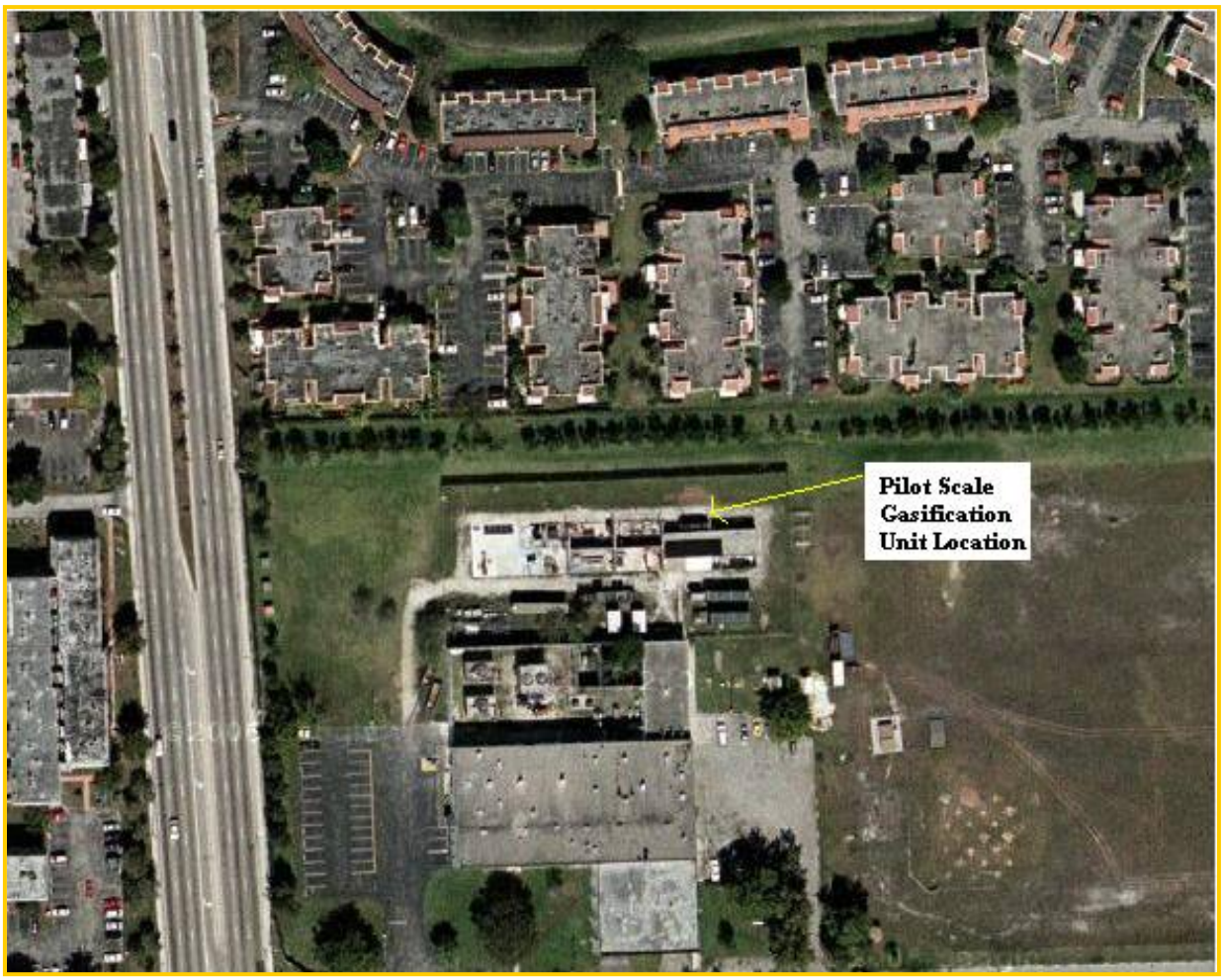

Figure 4. FIU's gasification unit location.

Gasifier Specifications

The gasifier used for this project was procured from Community Power Corporation (CPC), a firm located in Littleton, CO. The gasifier is a downdraft unit, fully automated system that has the ability to convert a variety of woody biomass residues into syngas. The resulting gas can then be used in place of liquid and gaseous fossil fuels such as gasoline, diesel, natural gas, propane, etc. to operate engine generators, boilers, dryers, chillers, etc. Table 2 describes the gasifier specifications and Table presents the gasifer construction details.

Table 2. Gasifier specifications

	System	Components	Specifications
1	Gas Production Module	Gasifier	Converts 1 kg of feedstock to 2.8 m^3 of producer gas (PG) and 1kWe (electricity) and 2 kWt (thermal)
2	Gas Cleanup Module	Fine Dry Filter Pre-heat system Ash removal auger	Passive cleaning, bag house filter system removes particulate down to 0.7 μm while maintaining constant low dP of less than 3. At startup, heats interior surfaces to eliminate condensation Particulates are removed by automatic auger system and deposited in storage bin which is cleaned daily before the operation.
3	Maintenance	Gasifier Heat Exchanger Feedstock handling Overall Maintenance	Daily clean grate (1 hr), Daily clean out tubes (1 hr) Daily: 20 min Daily: (2 hr) Gasifier requires daily maintenance of 2 hr for every 4 hr run
4	Gas Quality & Emissions	Producer Gas Gasifier Filtered Gas Emissions System level Ash	Typical composition:CO_2, H_2, CH_4, CO_2, N_2 Typical energy content ~135 Btu/cf <25 ppm tars, <10 ppm particulate Meets Florida Air Resource Board Standards (8% below NOx, 99% below CO, 97%THC No toxic or harmful effluents (liquid or solid), no condensate Non-hazardous
5	Total weight	All components	8,000 lb (3.6 metric tons) Deployed in one 40 cu ft standard container

Table 3. Gasifier construction details

Type	Fixed bed downdraft
Material construction	304 Stainless steel
Diameter	6 in.
Height	40 in.
Footprint	24 x 24 in.
Gross weight	250 lb
Fuel moisture specifications	0–15% MC
Fuel size specifications	Pelletized orange peels
Feed gate	Solenoid butterfly valve
Fuel level control	Infrared level sensor
Char air injection design	Multiple layers of fixed injectors on a central tree
Char air control	Single char air blower
Bed temperature monitoring	High temperature K rated thermocouples
Bed pressure monitoring	Pressure transducer
Bed uniformity control	Vibrator mounted to char air tree
Grate design	Reciprocating positive displacement
Gas flow measurement	Venturi flow meter
Gas production rate	>30 Nm^3/hr
Power consumption	<100 W average

FIU Gasification System Description & Operation

The FIU gasifier unit was designed to be used with pelletized fuel and deliver a stream of producer gas to a flare up to 30 SCHM. Detailed system schematic is shown in Figure 5.

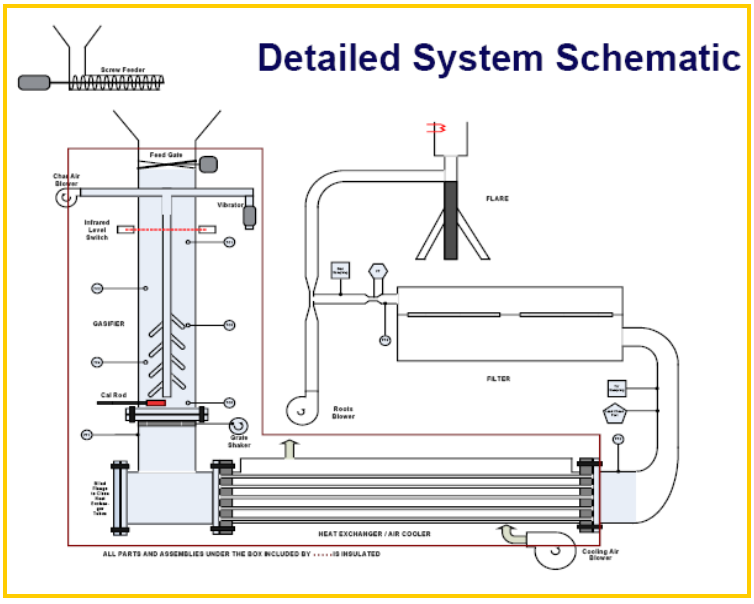

Figure 5. Detailed system schematic of the pilot-scale FIU gasifier.

The process unit comprised of six main parts:

1. An Automated Feed System
2. Downdraft Gasifier
3. Shell and Tube Heat Exchanger
4. Box Filter
5. Air Blower
6. Flare

The control system and the cooling air blower comprised the rest of the unit.

Feeder

The feeder subsystem (Fig. 6) was a simple horizontal auger mechanism, driven by a 3 rpm AC motor that advanced the pellets when sensors at the top of the gasifier indicated that the feed level was getting too low. The level sensors consisted of an IR transmitter/receiver pair and relied on a clear line of sight in order to function.

Figure 6. Feeder.

Gasifier

The gasifier (Fig. 7) was a two stage fixed bed downdraft gasifier and consisted of a heavily insulated combustion chamber that housed the char bed and contained the combustion reactions while the unit was in operation. Typical temperatures in the char bed ranged from 700 °C to over 1000 °C. Inside the inner cylinder of the gasifier, five thermocouples were placed (Gasifier Thermo Couples (GTC) 1 – (GTC) 5) to measure critical temperatures throughout the bed. A cal rod at the grate on the bottom of the gasifier was used to light the char.

Figure 7. Gasifier.

In the center of the gasifier was a long metal tube connected to the gasifier by four connection rods. This metal tube was called the “Char Air Tree” (Fig. 8). The char air tree was used to inject air into the char bed in order to get an extra amount of heat that was used to “crack” the tar molecules and produce cleaner gas.

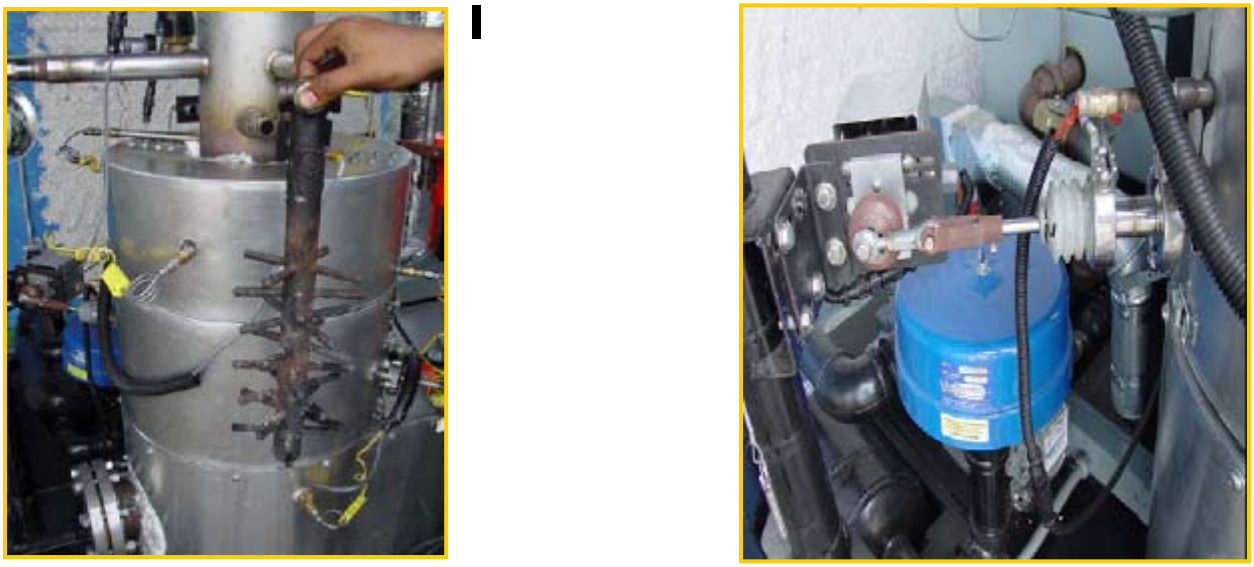

Figure 8. Char Air Tree (Left) and Grate Shaker (Right).

Figure 9. Char Air Blower (Left) and Vibrator (Right).

Citrus peels were fed through the top of the gasifier and converted to char and then char ash within the central core of the gasifier. Char and char ash were supported by a grate that was vibrated periodically to clear the buildup. Some of the ash also got entrained in the exiting gas and was cleaned downstream of the gasifier.

Heat Exchanger

A shell and tube heat exchanger (Fig. 10) was used to cool the gas further less than 100 °C for use of baghouse filter to clean the gas of its particulates.

Figure 10. Heat Exchanger.


Figure 11. Top of Heat Exchanger (Left) and Bottom of Heat Exchanger (Right).

Large char particles were removed before entering the heat exchanger. Fines were carried through the heat exchanger, and in process most of the residual tars were condensed and absorbed into the fines that were removed later using the fines filter. The gas-cooling blower located near the filter regulated this outlet temperature automatically and exhausted the clean, hot air out of the system. The heat exchanger was accessible from the top and bottom for periodic cleaning operations (Fig. 11). Details of the heat exchanger are presented in Table 4.

Table 4. Heat exchanger details

Type	Gas to air
Construction	Tube and shell, dual pass
Material construction	304 Stainless steel
Length	4 ft
Height	20 in.
Width	20 in.
Gross weight	300 lb
Blower size	1/3 HP
Power consumption	<500 W

Filter

The filter (Fig. 12) was used to collect any tar aerosols and fine char particles still in the gas stream. It consisted of a simple insulated enclosure with two internal paper filters. Details of the filter are shown in Table 5.

Figure 12. Filter Box.

Table 5. Filter details

Type	Insulated Baghouse
Bag construction	Teflon coated woven polyester
Bag configuration	Pleated construction
Cake removal	Manual shaker
Safety filters	None
Char and ash collection	Manual cleanout port
Char and ash storage	30 gallon drum
Diameter	25 in.
Height	40 in.
Gross weight	150 lb
Filter dP control	dP display and alarm only; non-automated
Power consumption	None
Particulate removal performance	<25 ppm clean glass
Maintenance requirements	Periodic bag replacement
Bag life	>500 hr

Blower

A Roots Blower was used to maintain a desired gas flow rate through the system. The Roots blower was designed as an air blower only. The system utilized an eductor to induce a vacuum on the rest of the system. An inline venturi flow meter was used to calculate the system gas flow rate in SCMH (standard cubic meters per hour @ 0 °C, 1 atm).

Flare

A flare was used to burn the product gas from our system. The flare used a hot surface igniter to automatically keep the flare lit.

Control System

The control system for the FIU gasification unit consisted of a National Instruments Compact Field Point PAC (programmable automation controller). The PAC (Fig. 13) consisted of an embedded control module, an 8-channel analog input module, a 16-channel digital output module, and an 8-channel PWM module. The control system was connected to a computer via a LAN connection. All incoming data from the input modules was collected and stored in the control system's control module's internal memory. The data was then viewed using a spreadsheet program like Microsoft Excel.

Figure 13. National Instruments Compact Field Point PAC.

The control program was written in LabView VI code (Fig. 14), from National Instruments. The program included automatic control algorithms that control the different devices in the system. The program also monitored system status and alerted the operator when a control parameter went out of the desired limits and take any necessary action based on the severity of the undesirable operating conditions.

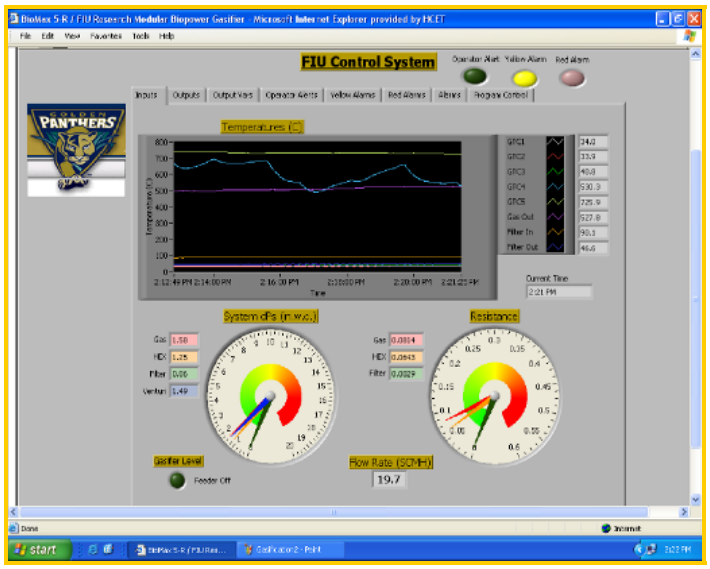

Figure 14. Labview program.

The control programs broke up control failures into 3 categories–Operator alerts, Yellow alarms, and Red alarms. An operator alert would simply display the value that had gone out of range on the Alarms page of the control program. An operator would try and alleviate the problem or simply shut the system down and perform the required maintenance after the system had cooled. A Yellow alarm would alert the operator the same way an operator alert did, but a yellow alarm forces the system to perform a controlled shutdown if the problem was not fixed within the pre-programmed time limit. A Red alarm would also alert the operator in the same fashion that the operator alert and yellow alarm did, however a red alarm would force the system into an emergency shutdown if the problem did not go away within the pre-programmed time limit.

Experiments and Results

The research was focused on the biomass gasification testing in a pilot-scale gasifier of 10 to 100 KW range. Effort was directed towards maximizing the hydrogen yield in the synthesis gas, which is the product of chemical conversion of biomass involving partial oxidation of the feedstock.

Ultimate and Proximate Analysis of the Citrus Pellets

The citrus peels pellets were obtained from Citrus World Inc. in Lake Wales, FL. Citrus World, Inc. is one of the largest producers of citrus products in the US. The citrus pellets had approximately 14% (wt) moisture content. The ultimate composition is shown in Table 6. The peels showed an equivalent amount of hydrogen that was present in wood chips. The ultimate analysis showed trace amounts of sulfur that may have to be dealt on the downstream side of the gasifier.

Table 6. Ultimate analysis of the citrus peels pellets

Elements	Wt (%)	Method Used
Carbon	38.80	ASTM D 5291
Hydrogen	6.71	ASTM D 5291
Nitrogen	0.91	ASTM D 5291
Oxygen	43.86	ASTM D 5291
Sulphur	0.052	ASTM D 5291
Ash	9.67	ASTM D 1552

Elemental Analysis of Ash

The elemental analysis (Table 7) on ash revealed the following metals. Sodium, Potassium, Calcium, Magnesium, and Silicon were the major elements found in ash.

Table 7. Elemental analysis of ash

Element	(mg/kg)	Elements	(mg/kg)
Sodium	126.1	Barium	4.610
Manganese	5.211	Boron	7.227
Nickel	2.544	Chromium	1.570
Copper	2.830	Magnesium	1926
Potassium	7025	Silicon	44.11
Calcium	17090	Rubidium	2.168
Iron	62.80	Vanadium	8.224
Aluminum	58.32	Zinc	7.526

Gasification Experimental Results

Gasification experiments were conducted at 500, 550, 600, 650, 700, 750, 800, 850, and 900 °C, respectively. At the start of the batch experiments, approximately 4.53 kg of dried citrus peels was loaded into the gasification chamber. The furnace temperature was then increased to the desired setting by the control program. Outgases from the gasifier were monitored continuously using Portable Gas Analyzer.

The initial gas composition at the outgas port of the gasifier was similar to that of the air. As the temperature rose, major air components, such as O_2 and Ar, disappeared and were replaced with gasification products primarily H_2, CO, CO_2, higher hydrocarbons, and water. We typically observed high gas outflow at around 550 to 600 °C. The outflow rate remained high for about 30 to 40 min and gradually decreased as the mass spectrum of outgases become less complex.

Three different gas compositions (ambient air, steam and oxygen) were analyzed and audited for energy. No hydrogen was observed for temperature below 550 °C. Higher hydrogen yields were obtained at higher temperatures.

Detailed data for exit gas composition (% vol) for citrus peel with stoichiometric amounts of air, with stoichiometric amounts of air and 20% (wt) steam and with stoichiometric amounts of air and oxygen are presented in Tabless 8, 9, and 10, respectively.

Table 8. Exit gas composition (% vol) for citrus peel with stoichiometric amounts of air

Temp (°C)	O_2 (% vol)	CO (% vol)	CO_2 (% vol)	CH_4 (% vol)	H_2 (% vol)
500	0.70	3.89	7.92	0.36	10.63
550	0.30	5.89	9.64	0.78	11.65
600	0.10	7.61	11.84	1.36	13.45
650	0.10	8.93	12.29	2.54	14.23
700	0.10	9.56	12.80	4.69	14.89
750	0.20	10.80	13.10	4.89	15.01
800	0.10	11.20	13.56	5.12	15.89
850	0.10	11.56	13.89	5.35	16.49
900	0.10	11.83	14.01	5.41	16.89

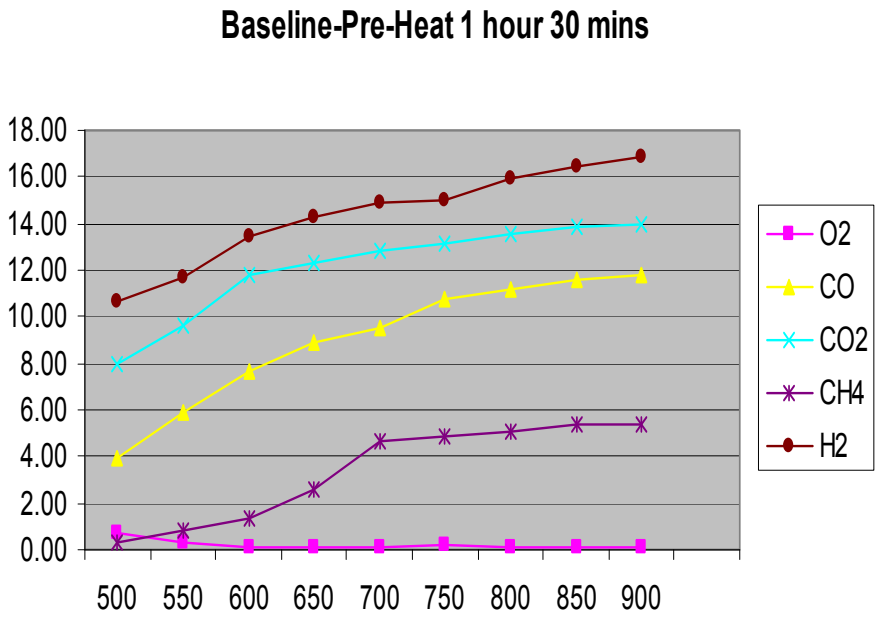

Table 9. Exit gas composition (% vol) for citrus peel with stoichiometric amounts of air and 20% (wt) steam

Temp (°C)	O_2 (% vol)	CO (% vol)	CO_2 (% vol)	CH_4 (% vol)	H_2 (% vol)
500	0.10	8.90	9.89	1.10	12.16
550	0.10	9.52	10.16	1.32	12.89
600	0.10	9.69	11.45	1.58	13.18
650	0.20	10.28	12.87	2.79	14.02
700	0.10	10.89	13.57	3.49	15.89
750	0.20	11.14	13.96	4.12	16.51
800	0.10	11.23	14.23	4.89	16.89
850	0.10	11.56	15.10	5.01	17.10
900	0.20	11.89	15.38	5.29	17.80

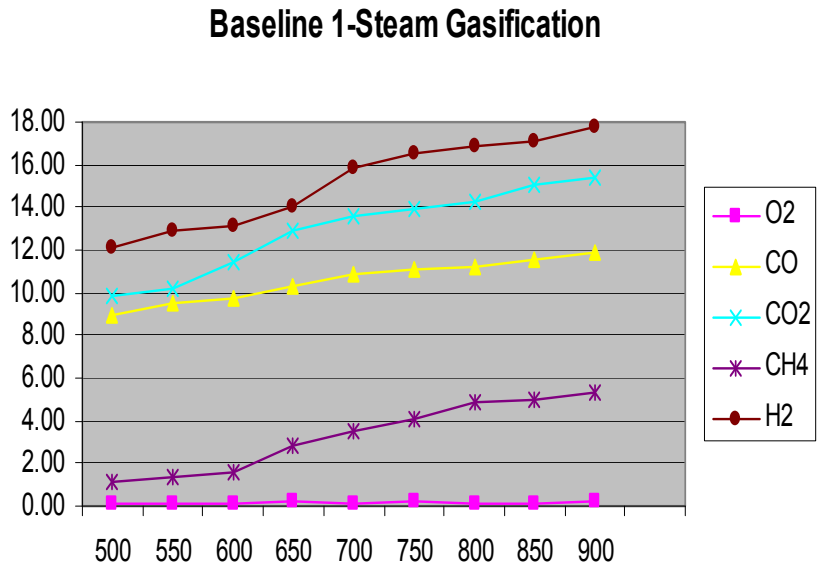

Table 10. Exit gas composition (% vol) for citrus peel with stoichiometric amounts of air and oxygen

Temp (°C)	O_2 (% vol)	CO (% vol)	CO_2 (% vol)	CH_4 (% vol)	H_2 (% vol)
500	0.10	7.89	8.30	0.19	10.89
550	0.00	9.80	9.10	2.14	12.70
600	0.00	10.10	10.30	3.77	14.80
650	0.00	10.80	10.40	3.82	22.20
700	0.00	11.50	11.89	4.92	23.10
750	0.00	11.20	13.20	5.13	28.20
800	0.00	17.80	13.60	7.89	29.20
850	0.00	19.10	15.20	9.98	29.90
900	0.00	24.10	15.68	10.10	31.10

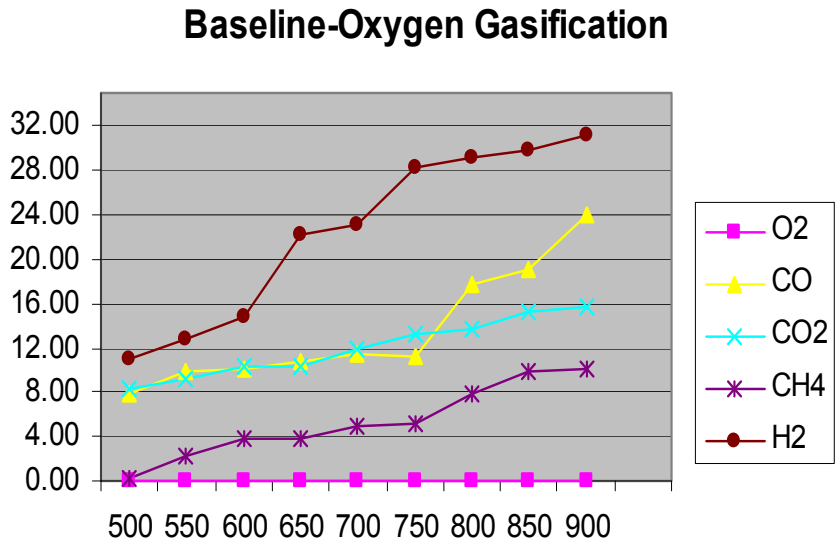

Average Hydrogen Yield

Table 11 shows the typical average hydrogen yield obtained from the three different gas compositions–air, air and 20% steam and air and oxygen—at a temperature of 900 °C. The results show the largest hydrogen output is the air and oxygen case.

Table 11. Average hydrogen yield for three gas compositions at 900 °C

	O_2 (% vol)	CO (% vol)	CO_2 (% vol)	CH_4 (% vol)	H_2 (% vol)
Air	0.10	11.83	14.01	5.41	**16.89**
Steam	0.20	11.89	15.38	5.29	**17.80**
Oxygen	0.00	24.10	15.68	10.10	**31.10**

Energy Audit of Biomass Gasification Unit

Energy Input

The process consisted of two sub processes, the first being the pre-heating of the biomass to a predefined temperature and the latter being the gasification of the biomass to obtain the flue gases.

The energy utilized in the pre heating stage was given as follows:

The power utilized during this process: 0.0426 KW
Operation time of the pre-heating stage: 90 min
Energy utilized during this operation: 0.6394 KWH

The energy utilized during the gasification stage was as follows:

The power utilized during this process: 0.4330743 KW
Operation time of the gasification stage: 50 min
Energy utilized during this second stage: 0.360895 KWH

On a daily basis:

Amount of Biomass burnt: 0.13 T/d

Hence, Total amount of energy utilized daily: 10.564 KWH/d

Energy Output

The energy output was calculated using the heating values of the flue gases: Three cases were considered.

Case 1: Biomass Gasification (without any Oxygen or Steam usage)

Flow rate of flow gases from the gasifier unit: 20 m^3/hr = 450 m^3/d

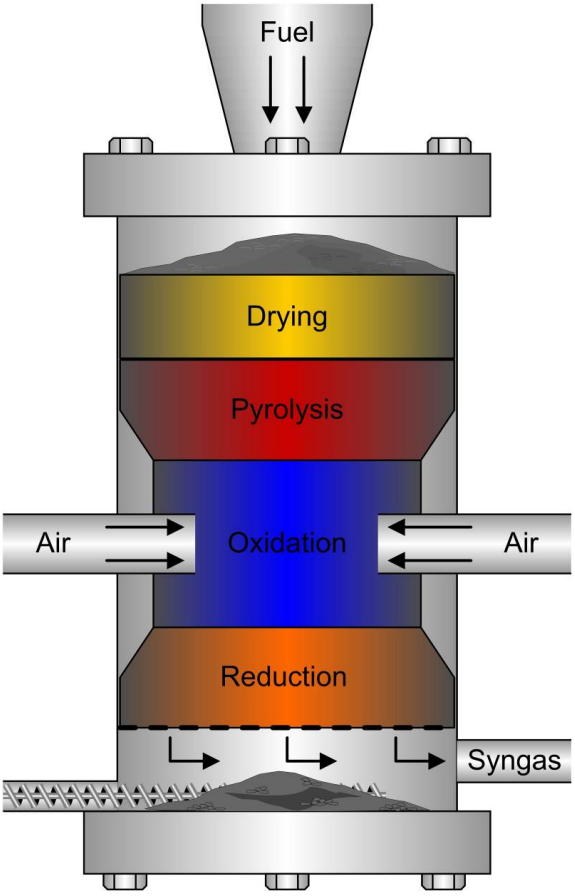

Figure 15. Biomass Gasification with Air.

Composition of the flue gases was given as follows:

	O_2	CO	CO_2	CH_4	H_2
Vol%	0.13	11.80	14.23	5.35	16.49
Flow rate(m^3/d)	0.56	53.3	64.2	24	74.1

Temperature of the flue gases coming out: 900 °C

The heat energy processed by the flue gases was sapped out before calculating the net heating value of the flue gases.

The heat energy extracted from the flue gases:

Heat Energy: $\sum mCp$ * (900 – 35) = 582 * (865) = 503 MJ/d = 140 KWH/d

The Energy obtained from the flue gases was as follows:

Compound	Heating Value (KJ/m^3)
CO	4074
CH_4	11605
H_2	3450

Total Output Energy of the flue gas:
(0.1180*450*13625) + (0.0535*450*39820) + (0.1649*450*13000)
= 752 MJ/d = 209 KWH/d
Energy Output: 209 + 140 = 349 KWH/d
Case 2: Steam Gasification (Steam usage)

Flow rate of flow gases from the gasifier unit: 20 m^3/hr = 450 m^3/d

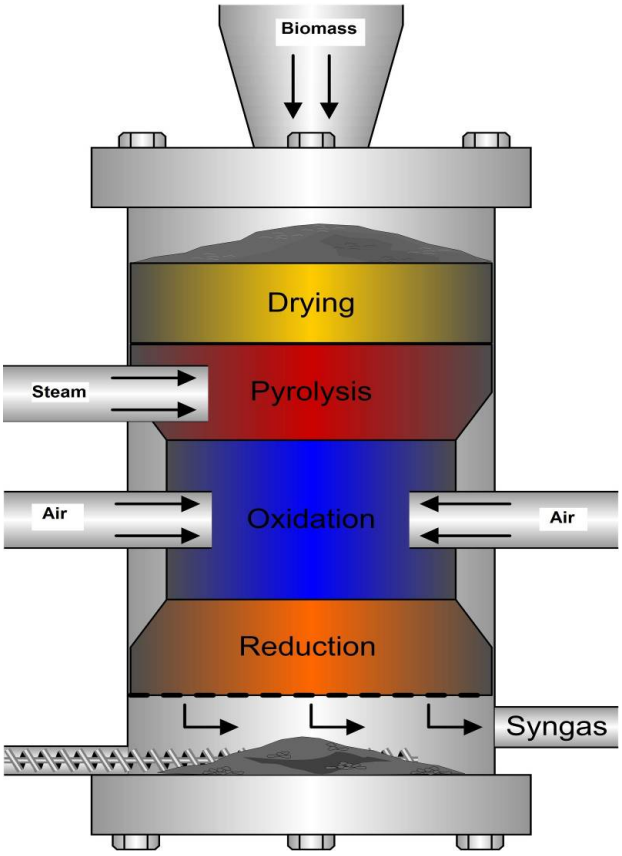

Figure 16. Biomass Gasification via steam.

Composition of the flue gases was given as follows:

	O_2	CO	CO_2	CH_4	H_2
Vol%	0.20	11.74	15.10	5.89	17.80
Flow rate(m^3/d)	0.88	53	68.1	26.5	80.1

Temperature of the flue gases coming out: 900 °C

The heat energy processed by the flue gases was sapped out before calculating the net heating value of the flue gases.

The heat energy extracted from the flue gases:

Heat Energy: $\sum mCp$ * (900 – 35) = 584 * (865) = 505 MJ/d = 140.3 KWH/d

The Energy obtained from the flue gases is as follows:

Compound	Heating Value (KJ/m^3)
CO	4074
CH_4	11605
H_2	3450

Total Output Energy of the flue gas:
= (0.1174*450*4074) + (0.0589*450*11605) + (0.1780 *450*3450)
= 799 MJ/d = 222 KWH/d
Energy Output: 222 + 140.3 = 362.3 KWH/d

Case 3: Oxygen Gasification

Flow rate of flow gases from the gasifier unit: 20 m^3/hr = 450 m^3/d

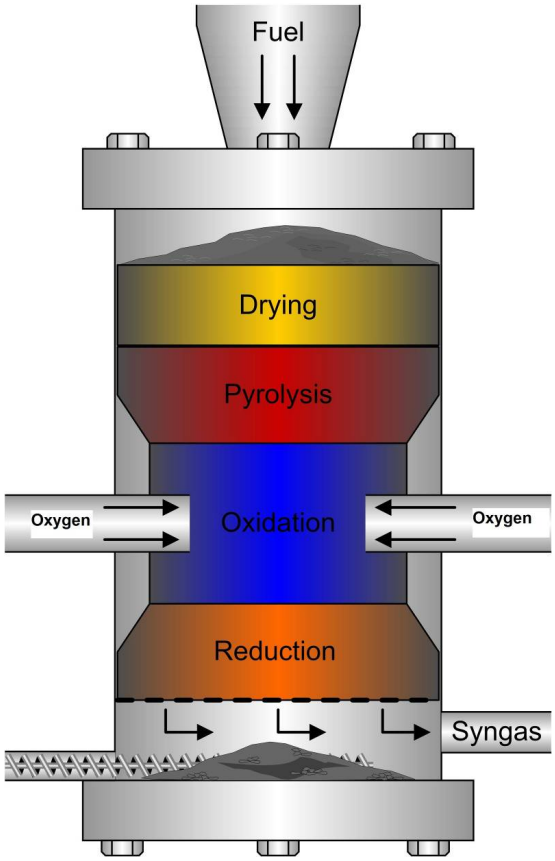

Figure 17. Biomass gasification via partial oxidation.

Composition of the flue gases was given as follows:

	O_2	CO	CO_2	CH_4	H_2
Vol%	0.20	24.30	13.6	10.10	29.90
Flow rate(m^3/d)	0.88	109.4	61.2	45.5	134.5

Temperature of the flue gases coming out: 900 °C

The heat energy processed by the flue gases was sapped out before calculating the net heating value of the flue gases.

The heat energy extracted from the flue gases:

Heat Energy: $\sum mCp$ * (900 – 35) = 624 * (865) = 540 KJ/d = 150 KWH/d

The Energy obtained from the flue gases was as follows:

Compound	Heating Value (KJ/m^3)
CO	13625
CH_4	39820
H_2	13000

Total Output Energy of the flume gas:
= (0.243*450*4074) + (0.101*450*11605) + (0.299 *450*3450)
= 1437 MJ/d = 399 KWH/d
Energy Output: 399 + 150 = 549 KWH/d

Table 12 summarizes the energy results for the above three cases.

Table 12. Energy results

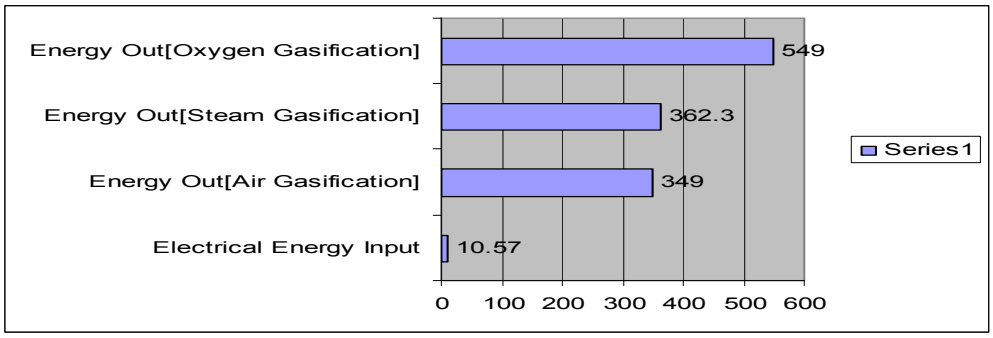

Typical Operation Yields and Efficiencies

The operation results gave the following yields and efficiencies:

- 1 kg of feed (dry basis) yielded 1 KWhr equivalent of Producer Gas.
- 1 kg of feed yielded 3 Nm^3 of gas with 17% H_2, 6% CH_4, 12% CO, 15% CO_2 and 0% O_2.
- Overall gasification efficiency was 50% (considering LHV of feed to LHV of Gas Output).

Hydrogen Cost Estimate

The purpose of this section was to provide capital cost estimates of various systems and components comprising the biomass gasification-based power generation facility. The costs presented here are only preliminary estimates. They do not have the benefit of a detailed estimate due to the evaluation nature of the study.

The approach had been to rely on historical data as much as possible with adjustments and extrapolations for differences in size, capacity, and implementation timing.

Plant capital cost comprised of two components:

Capital Cost = Direct Cost + Indirect Cost.

The direct cost of the system referred to all the costs that can be directly allocated to the system under consideration.
Direct Cost = installed equipment cost
+ support facilities applicable to the installed equipment.

Installed cost = Cost of the Equipment
+ cost of shipment
+ cost of installed labor
+ cost of material associated with field installation.

Indirect cost referred to all the cost that cannot be directly attributed to any specific system or equipment. These costs were generally expressed as fixed percentages of total direct cost of the total plant. Table 13 below gives an overview of the hydrogen gas cost estimate.

Table 13. Hydrogen cost estimates

Data	Air Gasification	Steam Gasification	Oxygen Gasification
Capital Cost $/GJ	5.03	5.03	5.03
Operational Cost $/GJ	0.95	0.88	0.56
Biomass Fuel Cost S/GJ	1.63	1.63	1.63
Hydrogen Production $/GJ	7.61	7.54	7.22
GJ/ton (dry biomass)	17.84	17.84	17.84
GJ per ton of H_2	143.49	143.49	143.49
Tons of dry biomass/yr	131400	131400	131400
Tons of H_2/yr	9287.8	10039	16846
Biomass Input/yr [103 GJ]	3255.8	3255.8	3255.8
H_2 Output/yr [103 GJ]	1332.7	1441	2417
Efficiency of H_2 production	0.41	0.44	0.74
Cost of H_2 in $/GJ	**7.61**	**7.54**	**7.25**

Conclusion

Hydrogen is a valuable fuel that can provide sustainable energy for fuel energy consuming systems. The majority of hydrogen is produced by steam methane reforming of natural gas where average prices of $5.50 to $7.50 per gigajoule can be realized for larger facilities. This is the least expensive way to produce hydrogen, but it relies on a non-renewable, fossil fuel.

Biomass gasification represents an alternative means to produce hydrogen. This study evaluated hydrogen production by gasification of citrus pellets and the economics of hydrogen production by gasification of citrus pellets show that hydrogen can be produced economically at an average $7.54/GJ for 10 to 100 KW range pilot scale gasification unit. Previous literature studies have cited that hydrogen prices from $6 to $10/GJ can be realized.

With the growing environmental concern over the release of CO_2 from the burning of fossil fuel and the elevated public concern towards global warming and climate changes, biomass gasification technology has the potential of generating clean energy and significantly reducing carbon dioxide emissions.

As technology improves, natural gas prices increase, and government incentive programs evolve, biomass gasification will present an economical way to produce hydrogen for use in energy consuming systems.

However, there are still some obstacles that must be overcome before biomass gasification can replace or compete in this market. Future research in the following areas is warranted:

• Hot Gas Clean Up: Evaluate an economical way to clean syngas at reforming temperatures.

• Hydrogen Infrastructure: Develop a strategy to pursue the transition into a hydrogen economy; Improve hydrogen delivery technologies; and Develop codes and standards for hydrogen storage to ease the public's fear of hydrogen as a fuel.

Appendix A presents a variety of biomass energy related units.

References

Aznar, M.P.; Caballero, M.A.; Gil, J.; Olivares, A. and Corella, J. (1997). Hydrogen by Biomass Gasification with Steam-O2 Mixtures and Steam Reforming and Co-Shift Catalytic Beds Downstream of the Gasifier. *Making a Business from Biomass in Energy, Environment Chemicals, Fibers and Materials, Proceedings of the 3rd Biomass Conference of the Americas, Vol. I*, Montreal, Quebec, Canada, August 24-29, 1997, Ed R.P. Overend and E. Chornet: pp. 859-860.

Abedi, J., Yeboah, Y.D., Realff, M., McGee, D., Howard, J., and Bota, K.B., (2001) An Integrated Approach to Hydrogen Production from Agricultural Residue for use in Urban Transportation, *Proceedings of the 2001 U.S. DOE Hydrogen Program Review* (NREL/CP 570-30535).

Bakhshi, N. N.; Dalai, A. K., and Srinivas, S. T. (1999). Conversion of Various Biomass-derived Chars to Hydrogen/High Btu Gas by Gasification with Steam. *Proceedings of the 4th Biomass Conference of the Americas, Oakland, CA, August 29-September 2, 1999*: pp. 985-990.

Caglar, A., and Demirbas, A. (2001) Hydrogen . Rich Gaseous Products from Tea Waste by Pyrolysis. *Energy Sources 23* pp. 739-746.

Chaudhari, S. T.; Bej, S. K.; Bakhshi, N. N.; Dalai, A. K (2001) Steam Gasification of Biomass-Derived Char for the Production of Carbon Monoxide-Rich Synthesis Gas. *Energy and Fuels 15* pp. 736-742.

Chaudhari, S. T.; Ferdous, D.; Dalai, A. K.; Bej, S. K.; Thring, R. W., and Bakhshi, N. N. (2000). Pyrolysis and Steam Gasification of Westvaco Kraft Lignin for the Production of Hydrogen and Medium Btu Gas. Abstracts - *Progress in Thermochemical Biomass Conversion, Tyrol, Austria, 17-22 September*.

Cox, J. L.; Tonkovich, A. Y.; Elliott, D. C.; Baker, E. G., and Hoffman, E. J. (1995). Hydrogen from Biomass: A Fresh Approach. *Proceedings of the Second Biomass Conference of the Americas*, (NREL/CP-200-8098; CONF-9508104) August, Portland, Oregon: pp. 657-675.

Demirbas, A.; Karshoglu, S., and Ayas, A. (1996). Hydrogen Resources Conversion of Black Liquor to Hydrogen Rich Gaseous Products. *Fuel Science and Technology International*;14(3):pp. 451-463.

Demirbas, A.; Caglar, A. (1998). Catalytic Steam Reforming of Biomass and Heavy Oil Residues to Hydrogen*. Energy Edu. Sci. Technol.*1:pp. 45-52.

Dermirbas, A. (2002) (Turkey). Yields of Hydrogen-Rich Gaseous Products via Pyrolysis from Selected Biomass Samples. *Fuel* 80:pp. 1885-1891.

Dihu, R. J. and Patel, J. G. (1983). U-Gas Process for Production of Hydrogen from Coal. *Int. J. Hydrogen Energy*; 8, (3):pp. 175-182.

García, L.; Sánchez, J.L.; Salvador, M.L.; Bilbao, R., and Arauzo J. (1996). Hydrogen-rich Gas from Steam Gasification of Biomass Using Coprecipitated Nickel-alumina Catalysts. *Bioenergy .96. The Seventh National Bioenergy Conference*:pp. 859-865.

García, L.; Salvador, M.L.; Arauzo J. and Bilbao, R. (1997). Steam Gasification of Biomass in Fluidized Bed Using a Ni-Al Coprecipitated Catalyst. *Making a Business from Biomass in Energy, Environment Chemicals, Fibers and Materials, Proceedings of the 3rd Biomass Conference of the Americas, Vol. I*, Montreal, Quebec, Canada, August 24-29, Eds. R.P. Overend and E. Chornet:pp. 373-382.

Gallin-Ast. (1999). Method and Apparatus for Production of Hydrogen, Particularly High-Purity Hydrogen, During Gasification of Biomass. *Offenlegungsschrift, Hannelore Germany, Patent No. DE-197-34-259191*:pp. 2-6.

Gas Technology Institute (2002). Techno-Economic Analysis of Hydrogen Production by Gasification of Biomass.

Hauserman, W.B. and Timpe, R.C. (1992). Catalytic Gasification of Wood for Hydrogen and Methane Production. *Energy & Environmental Research Center,* University of North Dakota:pp. 1-38.

Hauserman, W.B. (1992). High Yield Hydrogen Production by Catalytic Gasification of Coal or Biomass. *Hydrogen Energy Progress IX, Proceedings of the 9th World Hydrogen EnergyConference*:pp. 63-72.

Hauserman, W.B. (1994a). Relating Catalytic Coal or Biomass Gasification Mechanisms to Plant Capital Cost Components. *Hydrogen Energy Progress X, Proceedings of the 10th World Hydrogen Energy Conference,* Cocoa Beach, FL, 20-24 June, Vol. 1:pp. 471-479.

Hauserman, W.B. (1997). Relating Catalytic Coal or Biomass Gasification Mechanisms to Plant Capital Cost Components. *Int. J. Hydrogen Energy*; 22, (4):pp. 409-414.

Hayashi, J.I.; Tomioka, Y.; Shimada, T.; Takahashi, H.; Kumagai, H.; Chiba, T. (1998). Rapid Steam Reforming of Volatiles from Flash Pyrolysis of Coal. *Hydrogen Energy Progress XII, Proceedings of the 12th World Hydrogen Energy Conference*:pp. 669-678.

Hirano, A.; Hon-Nami, K.; Kunito, S.; Hada, M.; Ogushi, T. (1998). Temperature Effect on Continuous Gasification of Microalgal Biomass: Theoretical Yield of Methanol Production and its Energy Balance. *Catalysis Today* 45:pp. 399-404.

Hofbauer, H., Rauch, R., Foscolo, P., Matera, D. Hydrogen-rich Gas from Biomass Steam Gasification. (2000) *1st World Conference on Biomass for Energy and Industry,* Sevilla, Spain, June 2000*,* pp. 1999-2001.

Kubiak, H.; Papamichalis, A., and van Heek, K. H. (1996). Production of Hydrogen by Allothermal Gasification of Biomass. *Hydrogen Energy Progress XI, Proceedings of the 11th World Hydrogen Energy Conference*; Vol. 1:pp. 621-629.

Lobachyov, K.V. and Richter, H.J. (1998). An Advanced Integrated Biomass Gasification and Molten Fuel Cell Power System. *Energy Convers. Manage. 39*:pp. 1931-1943.

McKinley, K.R.; Browne, S.H.; Neill, D.R; Seki, A., and Takahashi, P.K. (1990). Hydrogen Fuel from Renewable Resources. *Energy Sources*; 12:pp. 105-110.

Midilli, A., Dogru, M., Howarth, C.R., Ayhan, T. (2001). Hydrogen Production from Hazelnut Shell by Applying Air-Blown Downdraft Gasification Technology. *Int. J. Hydrogen Energy* 26(1):pp. 29-37.

Milne, Thomas A.; Carolyn C. Elam, Robert J. Evans (2002). Hydrogen from Biomass

Padro,Gregoire,C.E. and Putsche, V. (1999). Survey of the Economics of Hydrogen Technologies.

Pasternak, A. D.; Richardson, J. H.; Rogers, R. S.; Thorsness, C. B., and Wallman, H. (1994). MSW to Hydrogen. *Proceedings of the 1994 U.S. DOE Hydrogen Program Review* Livermore, CA, April 18-21 1994 (NREL/CP-470-6431):pp. 433-450.

Rabah, M.A. and Eldighidy, S.M. (1986). Low-Cost Hydrogen Production from Waste, *Hydrogen Energy Progress VI, Proceedings of the 6th World Hydrogen Energy Conference*, Vienna, Austria:pp. 1362-1370.

Rapagna, F.P. U. (1996). Hydrogen from Biomass by Steam Gasification. *Hydrogen Energy Progress XI, Proceedings of the 11th World Hydrogen Energy Conference,* Stuttgart, Germany, 23-28 June; Vol. 1:pp. 907-912.

Rapagna, S., and Foscolo, P. U. (1998). Catalytic Gasification of Biomass to Produce Hydrogen Rich Gas. *Int. J. Hydrogen Energy*; 23, (7):pp. 551-557.

Richardson, J. H.; Rogers, R. S.; Thorsness, C. B., and Wallman, P. H. (1995). Conversion of Municipal Solid Waste to Hydrogen. *Proceedings of the 1995 U.S. DOE Hydrogen Program Review,* Coral Gables, FL, April 18-21, 1995; Vol. 2(NREL/CP-430-20036):pp. 731-755.

Rogers, III R. (1994). Hydrogen Production by Gasification of Municipal Solid Waste. Lawrence Livermore National Laboratory(UCRL-ID-117603).

Saha, R. K.; Gupta, B. R. and Sen, P. (1982). Production of Hydrogen in an Autothermal Fluidised Gasifier. *Hydrogen Energy Progress IV, Proceedings of the 4th World Hydrogen Energy Conference,* Pasadena, CA, 13-17 June 1982; 1:pp. 69-77.

Saha, R.K.; Gupta, B.R. and Sen, P. (1984). Production of Hydrogen in an Autothermal Fluidized Gasifier. *Int. J. Hydrogen Energy*; 9, (6):pp. 483-486.

Soo, S.L., Gibbs, R.T., Ma, K.T. (1978). A Steam Process for Producing Hydrogen from Coal. *Hydrogen Energy System II*, *Proceedings 2nd World Hydrogen Energy Conference*, Zurich, Switzerland, Pergamon Press:pp. 957-998.

Spath, P.; A. Aden, T. Eggeman, M. Ringer, B. Wallace, J. Jechura (2005). Biomass to Hydrogen Production Detailed Design and Economics using the Battelle-Columbus Laboratory Indirectly-Heated Gasifier.

Srinivas, S. T.; Dalai, A. K., and Bakhshi, N. N. (1998). Potential of Producing Hydrogen and High Btu Gas from Steam Gasification of Biomass-derived Chars. *Canadian Society for Chemical Engineering Conference, London, Canada, 4-7 Oct*; CONF-981052(ISBN 0-920804-32-2).

Timpe, R. C.; Hauserman, W. B.; Kulas, R. W., and Young B.C. (1996). Hydrogen Production from Fossil Fuels and Other Regionally Available Feedstocks. *Hydrogen Energy Progress XI, Proceedings of the 11th World Hydrogen Energy Conference,* Stuttgart, Germany, 23-28 June; Vol. 1:pp. 489-498.

TSS Consultants (2004). Gridley Ethanol Demonstration Project Utilizing Biomass Gasification Technology: Pilot Plant Gasifier and Syngas Conversion Testing.

Turn, S.; Kinoshita, C.; Zhang, Z.; Ishimura, D., and Zhou, J. (1998). An Experimental nvestigation of Hydrogen Production from Biomass Gasification. *Int. J. Hydrogen Energy*; 23, (8):pp. 641-648.

Van Bibber, L.; Shuster, E.; Haslbeck, J.; Rutkowski, M.; Olson, S.; Kramer, S. (2007). Baseline Technical and Economic Assessment of a Commercial Scale Fischer-Tropsch Liquids Facility.

Walcher, G.; Girges, S., and Wanartner, S. (1996). Hydrogen Project Bad Brückenau. *Hydrogen Energy Progress XI, Proceedings of the 11th World Hydrogen Energy Conference*; Vol. 1:pp. 413-418.

Wallman, P. H.; Richardson, J. H.; Thorsness, C. B.; Laninger, T.F.; Klein, J.D.; Winter, J.K. and Robin, A.M. (1996). Hydrogen Production from Municipal Solid Waste. *Proceedings of the 1996 U.S. DOE Hydrogen Program Review*, Miami, FL, 1-3 May 1996; NREL/CP-430- 21968(UCRL-JC-124574; CONF-9605195-2):pp. 481-498.

Wallman, P. H. and Thorsness, C. B. (1997). Hydrogen Production from Wastes. *Proceedings of the 1997 U.S. DOE Hydrogen Program Review,* Herndon, VA, May 21-23, 1997:pp. 165-176.

Wallman, P. H.; Thorsness, C. B., and Winter, J. D. (1998). Hydrogen Production from Wastes. *Energy*; 23, (4):pp. 271-278.

Weber, S. L.; Sealock, L. J.; Mudge, L. K; Rboertus, R. J., and Mitchell, D. H. (1980).

Gasification of Biomass in the Presence of Multiple Catalysts for the Direct Production of Specific Products. *AIAA Paper Symp Pap. Energy From Biomass and Wastes 4,* Lake Buena, Vista, FL, Jan 21-25*,A*:pp. 351-367.

Williams, L.D. (1980). Application of Centrifugal Separation to the Production of Hydrogen from Coal. *Applied Energy 6*:pp. 63-70.

Zhou, J.; Ishimura, D.M., and Kinoshita, C.M. (1999). Effects of Injecting Steam on Catalytic Reforming of Gasified Biomass. *Fourth Biomass Conference of the Americas,* Oakland, CA, 29 Aug- 2 Sep: pp. 991-997.

APPENDIX A—Biomass Related Energy Units

Areas and crop yields

- 1.0 hectare = 10,000 m^2 (an area 100 m x 100 m, or 328 x 328 ft) = 2.47 acres
- 1.0 km^2 = 100 hectares = 247 acres
- 1.0 acre = 0.405 hectares
- 1.0 US ton/acre = 2.24 t/ha
- 1 metric ton/hectare = 0.446 ton/acre
- 100 g/m^2 = 1.0 ton/hectare = 892 lb/acre
    - for example, a “target” bioenergy crop yield might be: 5.0 US tons/acre (10,000 lb/acre) = 11.2 tons/hectare (1120 g/m^2)

Biomass energy

- **Cord:** a stack of wood comprising 128 cubic feet (3.62 m^3); standard dimensions are 4 x 4 x 8 feet, including air space and bark. One cord contains approx. 1.2 U.S. tons (oven-dry) = 2400 lb = 1089 kg
    - 1.0 metric ton **wood** = 1.4 cm (solid wood, not stacked)
    - Energy content of **wood fuel** (HHV, bone dry) = 18-22 GJ/t (7,600-9,600 Btu/lb)
    - Energy content of **wood fuel** (air dry, 20% moisture) = about 15 GJ/t (6,400 Btu/lb)
- Energy content of **agricultural residues** (range due to moisture content) = 10-17 GJ/t (4,300-7,300 Btu/lb)
- Metric ton **charcoal** = 30 GJ (= 12,800 Btu/lb) (but usually derived from 6-12 t air-dry wood, i.e., 90-180 GJ original energy content)
- Metric ton **ethanol** = 7.94 petroleum barrels = 1262 liters
    - ethanol energy content (LHV) = 11,500 Btu/lb = 75,700 Btu/gallon = 26.7 GJ/t = 21.1 MJ/liter. HHV for ethanol = 84,000 Btu/gallon = 89 MJ/gallon = 23.4 MJ/liter
    - ethanol density (average) = 0.79 g/ml (= metric tons/m^3)
- Metric ton **biodiesel** = 37.8 GJ (33.3 - 35.7 MJ/liter)
    - biodiesel density (average) = 0.88 g/ml (= metric tons/m^3)

Fossil fuels

- **Barrel of oil** equivalent (boe) = approx. 6.1 GJ (5.8 million Btu), equivalent to 1,700 kWh. “Petroleum barrel” is a liquid measure equal to 42 U.S. gallons (35 Imperial gallons or 159 liters); about 7.2 barrels oil are equivalent to one ton of oil (metric) = 42-45 GJ.
- **Gasoline:** US gallon = 115,000 Btu = 121 MJ = 32 MJ/liter (LHV). HHV = 125,000 Btu/gallon = 132 MJ/gallon = 35 MJ/liter
    - Metric ton gasoline = 8.53 barrels = 1356 liter = 43.5 GJ/t (LHV); 47.3 GJ/t (HHV)
    - gasoline density (average) = 0.73 g/ml (= metric tons/m^3)

- **Petro-diesel** = 130,500 Btu/gallon (36.4 MJ/liter or 42.8 GJ/t)
    - petro-diesel density (average) = 0.84 g/ml (= metric tons/m^3)
- Note that the energy content (heating value) of petroleum products per unit mass is fairly constant, but their density differs significantly – hence the energy content of a liter, gallon, etc. varies between gasoline, diesel, and kerosene.
- Metric ton **coal** = 27-30 GJ (bituminous/anthracite); 15-19 GJ (lignite/sub-bituminous) (the above ranges are equivalent to 11,500-13,000 Btu/lb and 6,500-8,200 Btu/lb).
    - Note that the energy content (heating value) per unit mass varies greatly between different "ranks" of coal. "Typical" coal (rank not specified) usually means bituminous coal, the most common fuel for power plants (27 GJ/t).
- **Natural gas:** HHV = 1027 Btu/ft^3 = 38.3 MJ/m^3; LHV = 930 Btu/ft^3 = 34.6 MJ/m^3

Carbon content of fossil fuels and bioenergy feedstocks

- **coal** (average) = 25.4 metric tons carbon per terajoule (TJ)
    - 1.0 metric ton **coal** = 746 kg carbon
- **oil** (average) = 19.9 metric tons carbon/TJ
- 1.0 US gallon **gasoline** (0.833 Imperial gallon, 3.79 liter) = 2.42 kg carbon
- 1.0 US gallon **diesel/fuel oil** (0.833 Imperial gallon, 3.79 liter) = 2.77 kg carbon
- **natural gas (methane)** = 14.4 metric tons carbon/TJ
- 1.0 cubic meter **natural gas (methane)** = 0.49 kg carbon
- carbon content of **bioenergy feedstocks:** approx. 50% for woody crops or wood waste; approx. 45% for graminaceous (grass) crops or agricultural residues

November 2007

Final Reports for University of South Florida

- Numerical Simulation Model for Thermo-Fluid Analysis of Cryogenic Storage Systems With Zero Boiloff - Rahman, J., Ho, S.
- Prototype and Simulation Model for a Magneto-Caloric Refrigerator - Bhansali, S., Rahman, M., Kim, S., Ghirlanda, S., Hernandez, C., Adams, C., Bethala, B., Rosario, S., Sambandam, S.
- Smart Porous Metal-Organic Frameworks (MOFs) for Hydrogen Recovery and Storage - Eddaoudi, M., Zaworotko, M., Space, B., Eckert, J., T-Raissi, A., Mohajeri, N.
- Surface Acoustic Wave (SAW) Sensors for Hydrogen and Other Gas Detection - Bhethanbotla, V.
- Thermo Catalytic H_2 Production via Oxygen-Free Methane Aromatization - Wolan, J., Stefanakos, E., Kababji, A.

Numerical Simulation Model for Thermo-Fluid Analysis of Cryogenic Storage Systems With Zero Boiloff

M. Rahman and S. Ho
University of South Florida

Research Period: September 2002 to September 2007

Summary

This report presents a study of fluid flow and heat transfer in a cryogenic storage tank for liquid hydrogen using a three-dimensional model for numerical simulation. The model includes a tank with cylindrical wall and oblate spheroidal top and bottom, a heat pipe located along the axis of the tank, and a pump-nozzle unit that collects fluid at the suction inlet and discharges at its nozzle face onto the cool tip (evaporator) of the heat pipe in order to prevent the fluid to boil off. A steady state condition was assumed. Simulations with different normal speeds of fluid discharged at the nozzle face were run for a parametric analysis. Typical distributions of velocity and temperature are presented. Average speed and maximum temperature for each case are evaluated for assessing mixing and boiling effects, respectively. Simulations using an axi-symmetric model, which represents the case of an array of many pump-nozzle units installed around the heat pipe, were also carried out with the same fluid discharge speeds as those of the three-dimensional cases for comparison. For both models, the results show that as the normal fluid speed at the nozzle increases, the average fluid speed increases whereas the maximum temperature decreases. It is also found that with the same fluid speed discharged normally from the nozzle face the axi-symmetric model gives higher average speed and higher maximum temperature compared to the three-dimensional model.

Introduction

Hydrogen has been well recognized as a powerful and clean energy fuel for a few decades, especially for space applications such as the Centaur upper stage rocket [1]. Although hydrogen has many advantages over most conventional fuels, efficient storing of hydrogen is difficult because of its very low density [2]. Besides several new devising storage methods (carbon nanotubes, carbon fullerenes, and hydrides), conventional methods in which hydrogen is stored as a compressed gas or as a cryogenic liquid are still two primary storage techniques used in the industry. Liquid storage of hydrogen has a very significant advantage over gaseous or chemical storage because of its much lower storage volume and ease of regeneration of the fuel with its demand. Conventional cryogenic storage tanks suffer loss of hydrogen due to boil-off of the cryogen induced by heat leak to the tank from the surrounding environment. In order to keep the inner pressure within the structural limits of the tank, the stored fluid needs to be periodically vented. The Zero Boil-Off (ZBO) concept has evolved as an innovative means of storage tank pressure control by a synergistic application of passive insulation, active heat removal, and forced mixing within the tank. The goal is that the fuel can be stored for a very long time with almost no loss.

In recent years, a number of efforts have been done towards the guidelines of building cryogenic storage systems, especially with the ZBO concept. Hasting et al. [3] presented an overview of the efforts in the development of the ZBO storage systems at NASA, showing that a

ZBO system has mass advantage over passive storage. Kittel [4] suggested an alternative approach for the long term storage of cryogenic propellants using a re-liquefier that uses the propellant vapor as the working fluid. Salerno and Kittel [5] presented the proposed Mars reference mission and the concomitant cryogenic fluid management technology with a combination of both active and passive technologies to satisfy a wide range of requirements. Hofmann [6] presented a theory of boil-off gas-cooled shields for cryogenic storage vessels using an analytical method to determine the effectiveness of intermediate refrigeration. Haberbusch et al. [7] developed a design tool for thermally zero boil-off densified cryogen storage system for space. The model predicted that a ZBO densified liquid hydrogen storage system minimizes the overall storage system mass and volume for nearly the same input power for cooling. Kamiya et al. [8-9] consecutively presented the development of a large experimental apparatus to measure the thermal conductance of various insulations and used that for the testing of insulation structures. Mukka and Rahman [10-11] used computational fluid dynamics (CFD) simulation to study the fluid flow and heat transfer in a cryogenic liquid hydrogen storage tank of displacement type where cool fluid enters the tank at one end, mixes with hot fluid inside, and exits at the other end.

Rahman and Ho [12] studied the fluid flow and heat transfer in a closed ZBO cryogenic storage tank with a heat pipe and an array of many pump-nozzle units surrounding it as an artificial circulatory system. The numerical simulations were done using an axi-symmetric model because of the nearly axi-symmetric nature of the problem. It was found that the normal speed at the nozzle and several dimension parameters significantly affect the mixing, cooling, and boiling of the fluid inside the tank and those can be used to optimize the performance of the cryogenic system. This paper presents a parametric analysis for the fluid flow and heat transfer, focusing on the effect of the normal speed at the nozzle face, in a similar storage tank with only one pump-nozzle unit. Although it costs more computing resources, a three-dimensional model is employed since the axi-symmetry is now no longer the case. Besides, axi-symmetric simulations with the same parameters as their three-dimensional counterparts were also computed for relative comparison.

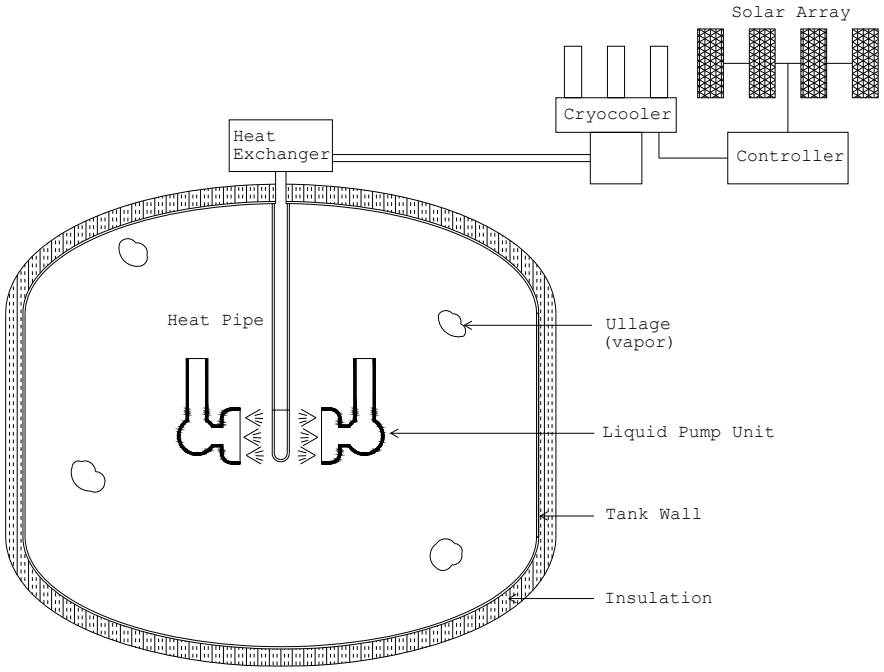

Figure 1. Schematic of the cryogenic storage system for hydrogen with heat pipe.

The study considered a cylindrical tank with elliptical top and bottom as shown in Fig. 1. The tank wall is made of aluminum and a multi-layered blanket of cryogenic insulation (MLI) has been attached on the top of the aluminum. The tank is connected to a cryocooler via a heat pipe to dissipate the heat leak through the insulation and tank wall into the fluid within the tank. The condenser section of the heat pipe dissipates heat to the cryocooler while the evaporator section picks up heat from the fluid within the tank. The hot fluid is directed to the heat pipe using a fluid circulation system within the tank. This system consists of a pump, a spray head for discharge of fluid and a collector tube network feeding to the pump. Different heat pipe sizes, different locations of hot fluid collection and discharge, and different discharge velocities were investigated to put together an optimum design for the ZBO hydrogen storage system. Equations governing the conservation of mass, momentum, and energy were solved in the fluid region. The steady-state velocity and temperature distributions were computed. The numerical simulation results presented here will be very useful to analyze the effects of each design parameter and to optimize the design of ZBO systems for specific applications.

Nomenclature

A-C	=	dimension parameters, m
C_p	=	specific heat of fluid, J/(kg.K)
D-H	=	dimension parameters, m
k	=	thermal conductivity of fluid, W/(m.K)
L-N	=	dimension parameters, m
P	=	dimension parameter, m
p	=	pressure, Pa
R	=	dimension parameter, m
T	=	temperature, K
$\mathbf{u}$	=	velocity vector, m/s
u_x	=	velocity component in x direction, m/s
u_y	=	velocity component in y direction, m/s
u_z	=	velocity component in z direction, m/s
V	=	normal fluid speed discharged at nozzle face, m/s
μ	=	effective viscosity of fluid, kg/(m.s)
μ_0	=	laminar viscosity, kg/(m.s)
μ_t	=	eddy (turbulent) viscosity, kg/(m.s)
ρ	=	density of fluid, kg/m^3

Mathematical Model

To describe the fluid flow and heat transfer of liquid hydrogen in the tank, it is necessary to determine the distributions of velocity and temperature in the entire computational domain by solving the governing equations for the conservation of mass, momentum, and energy. For a steady incompressible flow, the equation for the conservation of mass can be written as

$$\nabla \cdot \mathbf{u} = 0 \tag{1}$$

Considering the microgravity condition where the gravitational force and the buoyancy effects are negligible, the equation for the conservation of momentum can be written as

$$\rho \mathbf{u} \cdot \nabla \mathbf{u} = -\nabla p + \mu \nabla^2 \mathbf{u} \tag{2}$$

For modeling the turbulent flow, the effective viscosity is defined as the sum of the laminar and eddy viscosities, where the eddy viscosity is computed by using the mixing length model [13].

$$\mu = \mu_0 + \mu_t \tag{3}$$

Assuming that there is no heat generation and viscous dissipation and pressure work are negligible, the equation for the conservation of energy can be written as

$$\rho C_p \mathbf{u} \cdot \nabla T = k \nabla^2 T \tag{4}$$

To completely define the problem, appropriate boundary conditions are required on all boundaries of the computational domain. The relevant boundary conditions for fluid velocity are: prescribed velocity on the nozzle face, zero normal velocity on the symmetry plane, and zero velocity on all fluid-solid interfaces. The boundary conditions for temperature/heat flux are: prescribed heat flux on the heated surfaces of the wall, zero heat flux on the adiabatic section of the heat pipe and the symmetry plane, constant temperature on the evaporator section (the cool tip) of the heat pipe, and prescribed heat flux on the wall of the pump body. This latest heat flux represents the effect of heat generation at the pump-motor assembly. For simplification, all the prescribed parameters are assumed to be constant and uniformly distributed. The solution of Eqs. (1-4) associated with their boundary conditions gives the distributions of velocity components, pressure, and temperature.

Numerical Solution Procedure

A three-dimensional model of the storage tank is presented in Fig. 2a in half-cut view to show the heat pipe and the pump-nozzle unit inside. The fluid inside the tank is enclosed by a cylindrical side wall, a top and a bottom both in oblate spheroidal surface shape; all of which are referred as “wall.” The heat pipe is modeled as a cylindrical rod with a rounded end installed along the axis of the tank and attached to the top. The heat pipe has two sections: the green one is the cool tip (evaporator), where the constant low temperature boundary condition is applied, and the blue one is the adiabatic section of the heat pipe. The pump-nozzle unit, modeled as the copper-color solid in Fig. 2a, includes a spherical pump body, a vertical cylindrical suction tube, a horizontal cylindrical outlet tube, and a shower type nozzle. The flat face of the nozzle facing the cool tip (evaporator) of the heat pipe has many small exit holes for spraying the fluid out onto the heat pipe. The spraying flow is considered normally and uniformly distributed on the nozzle face. Figure 2b shows the essential dimensions for the system. These essential dimensions are denoted in general form as the capital letters A-H, L-N, P, and R. For this study, the numerical values of the parametric dimensions are fixed and given in Table 1. The Cartesian coordinate system for three-dimensional model is also given in Fig. 2b where the *z* direction lies along the axis of the tank and the x direction is on the symmetry plane that cuts the pump-nozzle unit into two identical halves (the plane that half-cut the tank as shown in Fig. 2a). The *y* direction is perpendicular to both *x* and *z* axes, i.e. perpendicular to the paper plane.

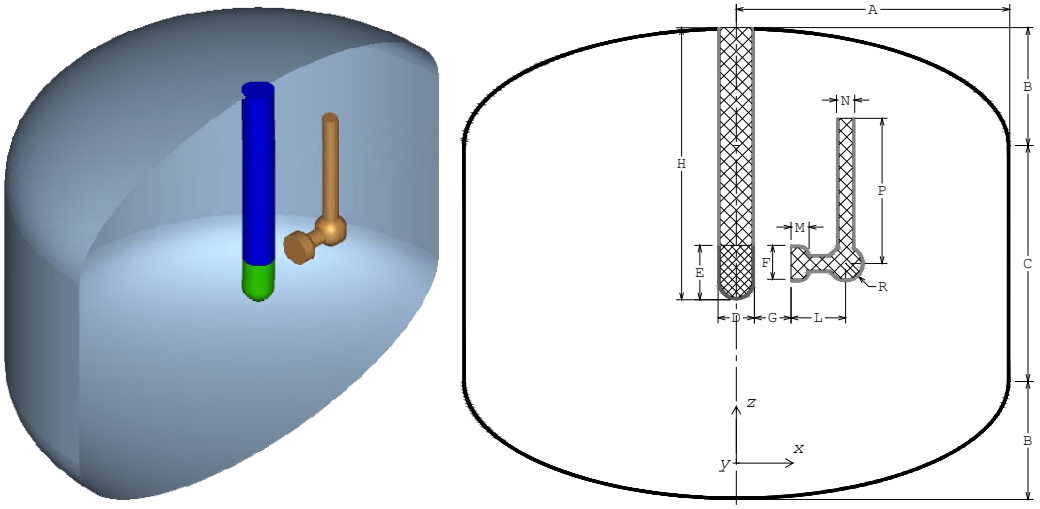

a) Three-dimensional model. b) Essential dimensions.

Figure 2. Liquid hydrogen cryogenic storage tank with single set of heat pipe and pump-nozzle unit.

Table 1. Numerical values of dimensions in Figure 2b.

Length, m	A	B	C	D	E	F	G	H	L	M	N	P	R
	1.50	0.65	1.30	0.20	0.30	0.20	0.20	1.50	0.30	0.10	0.10	0.80	0.10

Due to its symmetry, the computational domain is taken as a half of the tank including the heat pipe and the pump-nozzle unit. For solving the governing equations numerically by using the finite element method, the computational domain needs to be discretized into small elements. A mesh of hexahedral elements was generated as shown partly in Fig. 3 focusing on the region around the heat pipe tip and the pump-nozzle unit where highly irregular geometry is located. The mesh has layers of more regular elements of finer size assigned along the solid surfaces where high rates of momentum and heat transfer exist to increase accuracy of the solution. For a three-dimensional domain of irregular shape as this is, it is easier to generate a mesh of tetrahedral elements but the number of elements will be very large, yielding to more computing resources required, sometimes may exceed the available resources or even become impractical. The hexahedral-element mesh, on the other hand, usually takes longer to generate, but can reduce the number of elements significantly, thus reduces computing resources needed, and gives greater control over the irregular geometry. For the three-dimensional model of this study, the hexahedral mesh was generated with about 39000 elements. Once the mesh had been built, velocity components, pressure, and temperature were approximated for each element by using the Galerkin procedure [14], which led to a set of algebraic equations that defined the discretized continuum. Eight-node hexahedral elements were used.

The boundary conditions in details are given in Table 2. The constant fluid properties, given in SI units, were taken at reference temperature of 20 K as follows: ρ = 71.10 [kg/m^3], μ_0 = 13.59E-6 [kg/(m.s)], C_p = 9530 [J/(kg.K)], k = 0.09844 [W/(m.K)].

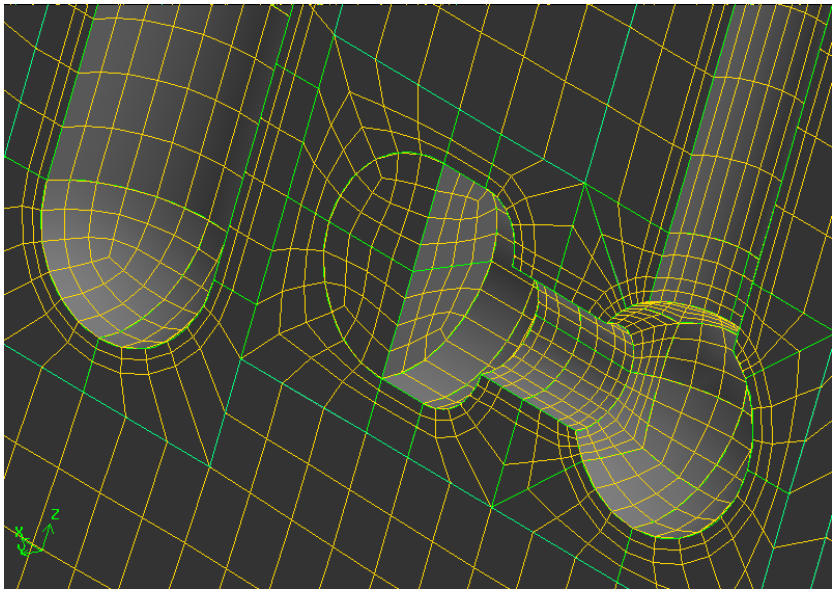

Figure 3. Three-dimensional hexahedral-element mesh.

The governing equations Eq. (1) to Eq. (4) along with the associated boundary conditions were solved using the finite element method. Since fully coupled algorithms are not applicable due to large number of elements and equations solved for this problem are three-dimensional, the segregated algorithm was used to solve the nonlinear system of equations. The convergence criterion of relative errors of the solutions was used. The relative error criterion is reached when the relative error of the solution at an iteration to the previous one is less than a tolerance. The tolerance for the three-dimensional simulations was set at 0.0001.

Table 2. Boundary conditions.

#	Entity	Velocity, m/s	Temperature, K	Heat flux, W/m^2	Notes
1	Wall	0	-	2	-
2	Symmetry plane	$u_y = 0$	-	0	-
3	Heat pipe insulated section	0	-	0	-
4	Heat pipe cool-tip section	0	18	-	-
5	Suction inlet	$u_x = u_y = 0$	-	-	-
6	Suction tube wall	0	-	0	-
7	Pump body wall	0	-	0.01	-
8	Exit tube and nozzle wall	0	-	0	-
9	Nozzle face	u_x = -V, $u_y = u_z = 0$	-	-	*See Table 3*

Axi-symmetric simulations were also carried out for comparison. For axi-symmetric model, the right half of the model on Fig. 2b with the same dimensions is used. In this case, the *z* (axial) direction remains the same whereas the *r* (radial) direction is coincident to the *x* direction. The geometric dimensions and the boundary conditions applied are the same as for three-

dimensional simulations. Details of the simulations for the axi-symmetric model were presented in a previous paper by the authors [12].

Ten simulations were carried out to investigate the effects of the discharging fluid speed at the nozzle, ranging from 0.01 m/s to 0.05 m/s, five three-dimensional simulations and five axi-symmetric counterparts. The simulation cases with related parameters are given in Table 3.

Table 3. Simulation cases.

Computational model	Three-dimensional (half volume)					Axi-symmetric				
Simulation number	1	2	3	4	5	6	7	8	9	10
Normal speed at nozzle, V, m/s	0.01	0.02	0.03	0.04	0.05	0.01	0.02	0.03	0.04	0.05

Discussion of Results

Figure 4 shows the velocity vector field for the basic case (simulation 1). The color of the velocity vector represents the magnitude of velocity (speed). The pump creates a pressure difference that drives the fluid in the tank towards the inlet of the suction tube. The fluid enters the suction tube of the pump and move towards the nozzle. In the nozzle, the flow expands to fill the hollow space inside, thus reducing speed, and then exiting through many tiny holes on the nozzle face. After being discharged from the nozzle, the flow spreads into many streams spraying on the cool tip (evaporator section) of the heat pipe. We can roughly distinguish three groups of streams moving in three main directions. The first group sweeps along the cylindrical part of the cool tip of the heat pipe, then the heat pipe adiabatic section, until it reaches the top, sweeps along a short portion on the top before being collected again at the suction tube inlet. The second group moves down along the tip of the heat pipe, wraps around the spherical part of the heat pipe then moves towards the bottom and creates a strong circulation in the region on the left below the heat pipe. The third group of streams is the main part which wraps around the side of the cylindrical part of the heat pipe towards the open space on the left side of the heat pipe. In the absence of any obstacle, this group of streams reaches the wall of the tank and sweeps through part of it (the streams, although seem unlikely, touch the side wall of the tank at the position of 90° from the axis of the nozzle, or the position at the middle of the half wall) before returning to the pump side and being collected at the suction tube inlet. The velocity pattern can only be observed clearly in the region around suction tube inlet, the nozzle and the heat pipe; in other regions fluid speeds are very small. At the nozzle face, the fluid speed is 0.01 m/s as assigned by its boundary condition. At the inlet of the suction tube, the fluid speed is about 0.04 m/s to 0.05 m/s which is consistent with the estimated average speed of 0.04 m/s there, based on cross-sectional area ratio and continuity condition. The fluid speed around the cool tip of the heat pipe is about 50% to 60% of the discharge speed at the nozzle face.

Figure 5 shows the distribution of temperature on the wall of the tank and the symmetry plane for the basic case (simulation 1). For the problem at hand in which the fluid is heated up by heat flux applied on the tank wall, the temperature on the wall is always higher than that of the fluid inside and its pattern is of interest. The temperature pattern on the symmetry plane, on the other hand, somehow reflects the velocity pattern and its effect on temperature. A part of the tank wall on the left of the heat pipe is kept at a lower temperature since the third group of streams splash and spread on it with an incoming flow cooled on the tip of the heat pipe. This part extends up to half of the tank wall on the left side. The second group of streams moves down to the left cools

down a part of the bottom but the circulation is confined in a small region preventing the cool fluid to spread further to the right, leaving the part of the tank wall on the right of the heat pipe at higher temperature. The fluid region next to this part of the tank wall shows the pattern of diffusive heat transfer, confirming the absence of any strong convective heat transfer in this region. The first group of streams does not show any significant effect. There is also a unique high temperature spot right above the inlet of the suction tube which can be explained as follows: as the fluid is being collected at the inlet of the suction tube, the flows would sweep through the wall nearby but since they bend towards the inlet, there is no flow sweeping through that area and it behaves like a stagnant region.

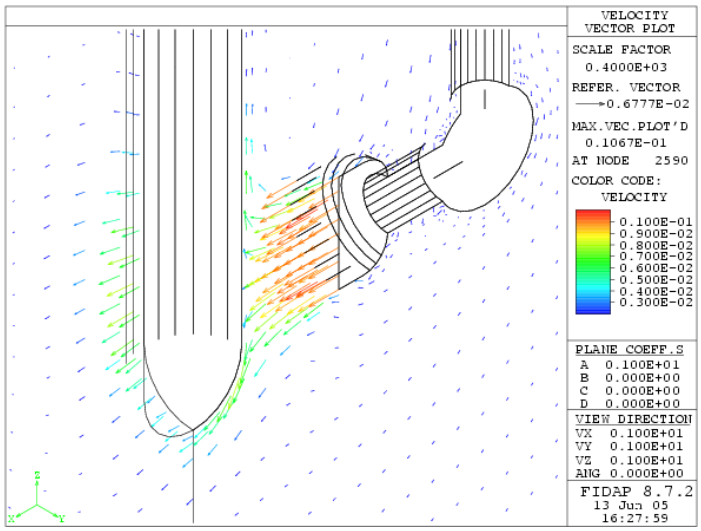

Figure 4. Velocity vector field, m/s, simulation 1.

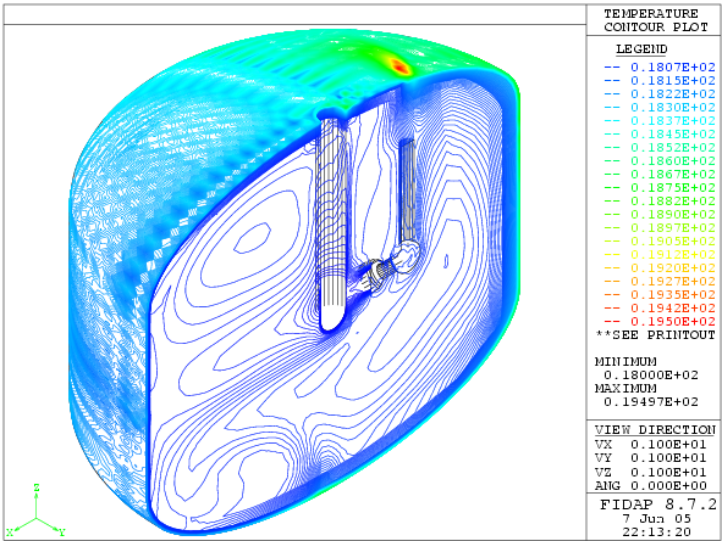

Figure 5. Temperature, K, simulation 1.

Figure 6 presents a comparison of the temperature distribution pattern on the symmetry plane for simulation 1, Fig. 6a, as the typical case for three-dimensional simulations, and simulation 6, Fig. 6b, as the typical case for axi-symmetric simulations. Figure 6b was created by putting together a temperature distribution plot of simulation 6 with its mirror image. Boundary conditions and dimensions are also the same for the two models. Both simulations have the fluid speed at the nozzle face of V = 0.01 m/s. However, the flow rates at the nozzle face are different due to different total nozzle face area (for the axi-symmetric model, the actual nozzle face is a cylindrical surface which has the area of 12 times of the area of the nozzle face of the three-dimensional model, a flat circle). Also note that Fig. 6a only shows temperature distribution on the symmetry plane of the three-dimensional model whereas the plot in Fig. 6b can be of any cross-section through the axis of the tank. In Fig. 6a, heat diffusion dominates in the region on the right and under the pump-nozzle unit with a clear temperature gradient from the tank wall where as the rest has lower temperature due to convection heat transfer as discussed previously. In Fig. 6b, the temperature distribution for the axi-symmetric model is totally different. Temperature is distributed more uniformly since the larger flow rate from the nozzle yields better mixing over the entire region. Due to the axi-symmetry of the model, the fluid flow discharged from the nozzle face after spraying on the cool tip of the heat pipe can only flow in two directions: going up along the heat pipe up to the top of the tank or going down along the axis of the tank in an axi-symmetric manner (annular flow wrapping around the heat pipe). Low temperature fluid is confined in a small region next to the heat pipe, especially the portion right under the spherical tip. Overall temperature is higher than that for the three-dimensional model.

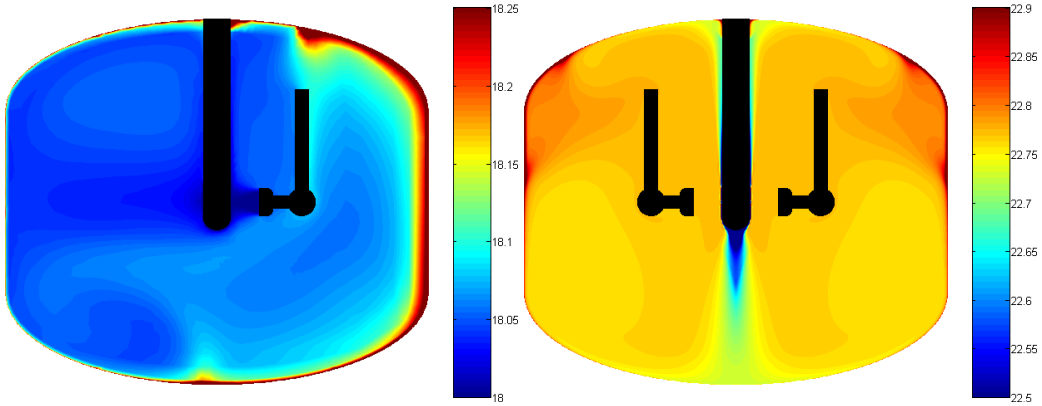

a) Three-dimensional model. b) Axi-symmetric model.

Figure 6. Comparison of temperature distribution pattern on symmetric plane, K.

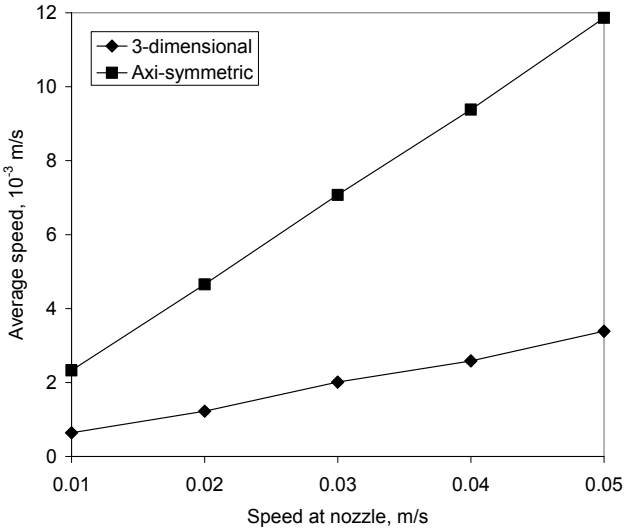

Figure 7. Effect of fluid speed at nozzle face on average speed.

Average speed, taken over the entire computational domain, can be used as a parameter for assessing the mixing effectiveness, which plays a role in leveling the temperature difference in the fluid. Figure 7 shows how the fluid speed at nozzle face affects the mixing effectiveness. As the speed at nozzle increases, the average speed also increases linearly for both three-dimensional and axi-symmetric models. The rate of increasing average speed for the axi-symmetric model is much higher than that for the three-dimensional model (about 4 to 5 times), meaning that the axi-symmetric model has better performance in mixing effectiveness. The value of average speed for axi-symmetric model (ranging in about 0.002 to 0.012 m/s) is always higher than that for three-dimensional model (ranging in about 0.001 to 0.003 m/s) as expected because of higher flow rate from the nozzle as discussed above.

The leveling of temperature difference itself can be assessed by observing the maximum-to-average temperature difference, which is convenient for comparison between models (e.g., three-dimensional model vs. axi-symmetric model) despite different temperature ranges. Figure 8 shows the dependency of the maximum-average temperature difference on the fluid speed at the nozzle face. As the speed at the nozzle increases, the temperature difference decreases for both models with much higher drop rate (about 4 to 8 times) for three-dimensional model (from 1.4 K to 0.6 K) compared to that for the axi-symmetric model (from 0.4 K to 0.3 K). This means that the three-dimensional model is more sensitive to the increasing of the speed at nozzle but the higher values of temperature difference confirms that the axi-symmetric model gives better mixing effectiveness.

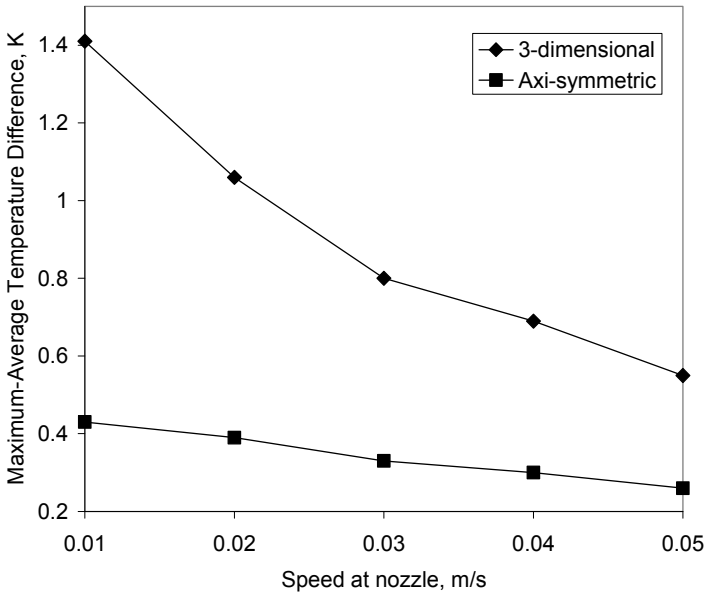

Figure 8. Effect of fluid speed at nozzle face on maximum-average temperature.

For a Zero Boil-Off (ZBO) system, the maximum temperature is the most important parameter indicating if evaporation can happen, or zero-boiling-off effectiveness. Figure 9 shows the maximum temperature as a function of fluid speed at the nozzle for both models. As the speed at nozzle increases, the maximum temperature decreases nonlinearly but monotonously, this yields an important conclusion that increasing the fluid speed discharged at the nozzle face improves the zero-boiling-off effectiveness. The maximum temperature in the three-dimensional model is always much lower than that in the axi-symmetric model, meaning that it has better performance in zero-boiling-off effectiveness. This is an interesting observation: the use of one pump-nozzle unit (with three-dimensional model) gives better zero-boiling-off effectiveness than the use of “infinite” number of pump-nozzle units (axi-symmetric model). It is also found that a system that has higher mixing effectiveness also has lower zero-boiling-off effectiveness, and vice versa. For a ZBO cryogenic system like the system being considered in this study, the zero-boiling-off effectiveness always takes higher priority.

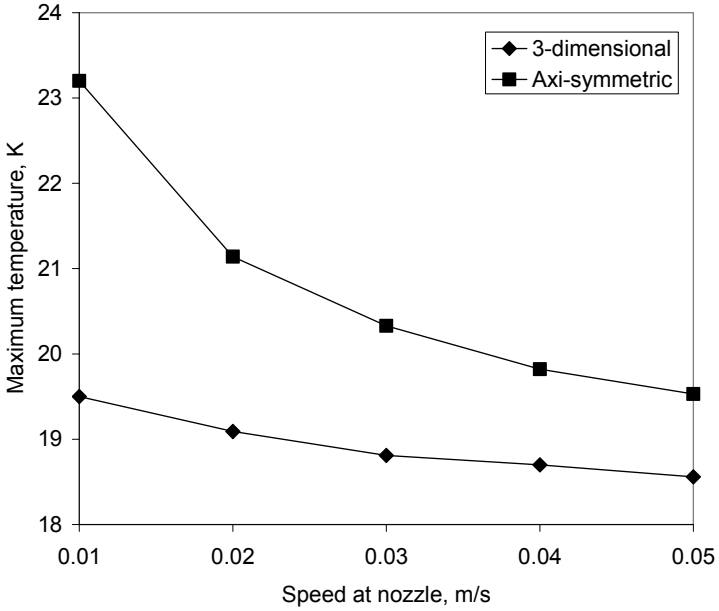

Figure 9. Effect of fluid speed at nozzle face on maximum temperature.

Conclusions

The numerical simulations give better understanding of the fluid flow and heat transfer phenomena needed for the design of a cryogenic storage tank for liquid hydrogen. The results from the simulations for both models show that the increasing of the fluid speed discharged at the nozzle face improves both mixing effectiveness (increase average speed, decrease maximum-average temperature difference) and zero-boiling-off effectiveness (decrease maximum temperature). In all cases, the axi-symmetric modeling and simulation, with its advantage of less computing resources required, can be used to give conservative predictions for the maximum temperature (with the correction margin of 1-4 K) in a tank with single pump-nozzle unit, instead of using expensive three-dimensional modeling and simulation. These guidelines are very useful in designing cryogenic storage systems. This suggests that numerical modeling and simulation can be satisfactorily used in the design of these systems to obtain good predictions over a wide range of design alternatives and operating conditions. It is also found that the use of a single pump-nozzle unit in the tank, as simulated in the three-dimensional model, results in better zero-boiling-off performance than the use of an array of many (infinite) pump-nozzle units, as simulated in the axi-symmetric model. This may be happening because the fluid in a real three-dimensional flow can move in all directions and through the gaps between pump-nozzle units to connect different parts of the tank whereas the nature of the axi-symmetric model is to separate the fluid into regions blocked by solid walls.

References

1. Dawson, V., & Bowles, M. (2004). Taming liquid hydrogen: The centaur upper stage rocket 1958-2002. Kennedy Space Center, FL: National Aeronautics and Space Administration (NASA).

2. Colozza, A. (2002). Hydrogen storage for aircraft applications overview. Kennedy Space Center, FL: National Aeronautics and Space Administration (NASA).

3. Hastings, L., Plachta, D., Salerno, L., & Kittel, P. (2002). An overview of NASA efforts on zero boiloff storage of cryogenics propellants. Cryogenics, 41, 833-839.

4. Kittel, P. (2002). Propellant preservation using re-liquefiers. Cryogenics, 41, 841-844.

5. Salerno, L., & Kittel, P. (1999). Cryogenics and the human exploration of mars. Cryogenics, 39, 381-388.

6. Hofmann, A. (2004). Theory of boil-off gas cooled shields for cryogenic storage vessels. Cryogenics, 44, 159-165.

7. Haberbusch, M., Stochl, R., & Culler, A. (2004). Thermally optimized zero boil-off densified cryogen storage system for space. Cryogenics, 44, 485-491.

8. Kamiya, S., Onishi, K., Kawagoe, E., & Nishigaki, K. (2000). A large experimental apparatus for measuring thermal conductance of LH_2 storage tank insulations. Cryogenics, 40, 35-44.

9. Kamiya, S., Onishi, K., Kawagoe, E., & Nishigaki, K. (2001). Thermal test of the insulation structure for LH_2 tank by using the large experimental apparatus. Cryogenics, 41, 737-748.

10. Mukka S., & Rahman, M. (2004, February). Analysis of fluid flow and heat transfer in a liquid hydrogen storage vessel for space applications. Proceedings of the Space Technology and Applications International Forum (AIP), Albuquerque, New Mexico.

11. Mukka S., & Rahman, M. (2004, August). Computation of fluid circulation in a cryogenic storage vessel. Proceedings of the AIAA 2nd International Energy Conversion Engineering Conference, Providence, Rhode Island.

12. Rahman, M., & Ho, S. (2005, March). Zero boil-off cryogenic storage of hydrogen. Proceedings of the 2005 NHA Hydrogen Conference, Washington, D.C.

13. Kays, W., & Crawford, M. (1993). Convective heat and mass transfer (3rd Edition). New York: McGraw Hill.

14. Fletcher, C. (1984). Computational galerkin methods. New York: Springer-Verlag.

October 2007

Prototype and Simulation Model for a Magneto-Caloric Refrigerator

S. Bhansali, M. Rahman, S. Kim, S. Ghirlanda,
C. Hernandez, C. Adams, B. Bethala, L. Rosario, and S. Sambandam
University of South Florida

Research Period: September 2002 to September 2007

Summary

Hydrogen liquefaction is necessary technology for satellite and space craft. The magnetocaloric refrigeration of this project is being explored as a highest efficient pathway for cooling hydrogen for storage and liquefaction. The miniaturization technology of refrigeration system is a key technology for future pico satellite and space device. Realizing micro cryo-coolers that can operate at low temperature with high cooling capacity, and in a small size has been a challenge. This research makes a development of micro-cooling device which has compact size. The information about cooling test procedure and experimental setup will reduce the time to commercialize the product and application to space device. The technology to synthesize the magnetocaloric material enlarges the variety application area and is applicable to Si based micro structure device. Analysis technology of the refrigerator system will guide to design the system and change the parameter.

Introduction

Micro cryo-cooling has been a subject of intense research and development in the recent past. Low temperature coolers have been used for decades to reduce cooling temperatures down to the cryogenic range for a variety of applications. Thus, realizing micro cryo-coolers that can operate at low temperature with high cooling capacity, and in a small size has been a challenge. This research focuses on development of micro-cooling technology based on the magnetocaloric effect. Magnetocaloric refrigeration is being explored as an efficient pathway for cooling hydrogen for storage.

The objective of this research is to establish the feasibility of reduced magnetic field based active magnetic refrigeration (AMR) cycle as a liquefaction technology for hydrogen. The research aims to design, fabricate and validate a magnetocaloric microcooler capable of operating in the temperature range from 77 to 20 K.

This process is environmentally friendly and requires that magnetocaloric materials be exposed to an alternating magnetic field. Analysis and experimentation have positioned the investigators to both (a) demonstrate the feasibility of magnetocaloric refrigeration and (b) experimentally validate the critical parameters required for design of scalable cooling systems. Simulation of cooling hydrogen from 77 to 20 K suggests a multi-stage GdSiGe based magnetocaloric refrigeration system.

Thermodynamic analysis was carried out for a magnetic refrigeration system for near room temperature application using Gd as the magnetic material. The conceptual design and analysis of a magnetic refrigeration system near hydrogen liquefaction temperature was established based on two prototypes with circular and trapezoidal microchannels. In aspect of fabrication, the microfabrication processes and fabrication of trapezoidal flow channels in silicon was developed and tested. The experimental setup was accomplished to test the magnetocaloric

effect directly. The temperature change of GdSiGe by the magnetic field variation was measured and analyzed using temperature sensor. The magnetocaloric material (GdSiGe) was sputtered into wafer to make different forms with optimal properties, and the processes to synthesize the multiple phase formations, phase stability and interface stability in thin film GdSiGe synthesis are obtained. The several barrier layers are tested and verified to make optimal barrier structure.

Analysis of fluid flow and heat transfer in microchannels with rectangular and square cross section was carried out. When subjected to the magnetic field, heat transfer processes during the heat up and cool down phases of a magnetic material were studied. The application of the magnetic field was simulated by using the concept of volumetric heat source distributed uniformly over the entire solid material. The strength of the source was calculated from energy balance during magnetization of the material. Equations governing the conservation of mass, momentum, and energy were solved in the fluid region. In the solid region, heat conduction equation with heat generation was solved. From the simulation results, plots of Nusselt number and heat transfer coefficient were obtained over the length of the channel. A thorough investigation for velocity and temperature distributions was performed by varying channel aspect ratio, Reynolds number, and heat generation rate in the substrate. It was found that the peripheral average heat transfer coefficient and Nusselt number is larger near the entrance and decreases downstream because of the development of the thermal boundary layer. With the increase in Reynolds number, the outlet temperature decreased and the average Nusselt number increased. An analysis of a magnetic refrigeration cycle was carried out. The system consists of heat exchangers and beds of magnetic materials operating near room temperature. The beds are periodically magnetized and demagnetized and the working fluid flows are arranged to meet the cycle requirements. Sensitivity analysis has been performed. Cooling power, magnetic field, and temperature span trends are simulated. The cooling and heating effects were estimated based on the magnetocaloric effect of gadolinium. Findings indicate that the higher the magnetic field is the higher the cooling power with the same temperature span. It was also observed that the cooling power decreases with the increase in the temperature span for various magnetic fields. COP versus temperature span was also considered. The trend indicates that COPactual/COPCarnot decreases with an increase in the temperature span. These trends agreed with those shown by experimental data.

A simple analysis of a thermal system that represents a magnetic refrigerator illustrates insights about exergetic efficiency using thermodynamics second law. Simulations showed contribution to the availability destroyed by the system. Analysis using various working fluids was also performed. R-134a showed a better performance. Results can draw designer attention toward improvement of the magnetic refrigerator components where the most availability is being destroyed and quantify the extent to which modification of one component can affect the performance of the magnetic refrigerator. A comparison of exergetic efficiency of components between a magnetic and commercial refrigerator was also executed.

Results and Discussion

Deposit and Caracterize MCE Thin Films

Attempts have been made to synthesize and stabilize $Gd_5Si_2Ge_2$ phase in thin film form. Previous work established the formation of required precursor phases for forming the $Gd_5Si_2Ge_2$ phase by annealing. A high temperature annealing has also led to the formation of $Gd_5Si_2Ge_2$ phase, however in small volume fraction. To improve the content of this phase and stabilize it, further work has been progressed by depositing GdSiGe thin films and annealing in vacuum.

Our earlier work used Pt as barrier layer between GdSiGe and Si. Results showed Pt acts as barrier at low temperatures (700 °C), however, at higher temperatures (1150 °C) leads to the formation of silicide phases in the film. Alternatively SiO_2, and Si_3N_4 were considered attractive materials for diffusion barrier layers for this fabrication. Both of the materials are compatible with Si processing and routinely used as diffusion barriers in Si at temperatures greater 1000 °C. As past studies had found the GdSiGe alloy to be highly reactive with oxygen, Si_3N_4 was selected as the diffusion barrier material based on past work from literature that suggests silicon nitride is thermally stable at high temperatures till 1600 °C.

Films of 300 nm Si_3N_4/ Si were deposited using PECVD at 300 °C. 100 nm thick GdSiGe was deposited on these films by sputtering. The films were vacuum annealed at temperatures up to 1150 °C. The films were then studied to determine the phase and surface morphology using XRD, and SEM. The stability of Si_3N_4 as a barrier layer was studied using SIMS. PECVD silicon nitride was deposited on the wafer by flow of precursors in gases SiH_4 :NH_3 : He: N_2 in the ratio 10: 4: 800: 200, at a pressure of 120 Pa, and R.F. power 50 W. Next GdSiGe films were deposited on the substrate using a custom DC/RF-magnetron sputtering system (designed in-house). For sputtering, the vacuum chamber was pumped down to a base pressure of $1.5x10^{-4}$ Pa using a cryopump. For sputtering, the argon was flown in at 30 sccm to purge the chamber and a throttle valve was used to maintain the pressure. For the deposition process, the chamber pressure was maintained at 5 Pa by throttling the valve. Sputtering was done at RF power of 150 W. The targets were cleaned by pre-sputtering to remove any surface oxides that may have formed on the target. Pre-sputtering was carried out for 10 min. The substrate was rotated during deposition to obtain uniform thickness over the wafer. The 100 nm thickness of the deposited GdSiGe thin films was confirmed by the surface profilometer. Next the films were vacuum annealed at $1x10^{-4}$ Pa in the temperature range 700 to 1150 °C. The structure and morphology of the films were analyzed by x-ray diffraction (Philips model X'pert Pro) and SEM (Hitachi model S800). The compositional gradient of the film and the interface was studied by secondary ion mass spectrometry.

A critical element in establishing an effective diffusion barrier is to have a high quality Si_3N_4 film that is not porous. Figure 1(a) schematically illustrate the process used to evaluate the porosity of the nitride. As shown in the figure, the Si_3N_4 coated substrate was immersed in KOH solution for 30 min to evaluate the quality of the film. The solution was maintained at 80 °C. KOH attacks Si about 300 times faster than PECVD Si_3N_4. Any pinhole in the nitride leads the etchant to the Si surface, resulting in significant pitting of the underlying substrate. Next, the substrate nitride was stripped using phosphoric acid and the surface of silicon was examined using optical microscope. Figure 1(b) shows an optical micrograph of the silicon surface. It can be seen the surface of the wafer is intact and without pitting. This confirms that silicon nitride films are not porous and free from pinholes. Figure 1(c) shows a pitted etched surface of silicon for comparison.

Figure 1(a). Process for testing the porosity of silicon nitride thin film, (b) Smooth surface of silicon nitride, (c) Etched pitted surface.

GdSiGe films were deposited on to silicon nitride films and vacuum annealed with an aim of developing the magnetocaloric $Gd_5Si_2Ge_2$ phase in thin film form. Due to the strong affinity of the material with oxygen, generally it is has been difficult to keep the bulk material oxygen free during annealing. The traditional approach in annealing this material is to wrap it in Ta foil and put in an evacuated quartz ampule. These samples were instead directly placed in a vacuum furnace without any passivation. Figure 2 shows the XRD patterns of (100 nm GdSiGe/300 nm Si_3N_4/ Si) films annealed at different temperatures for 1 hr.

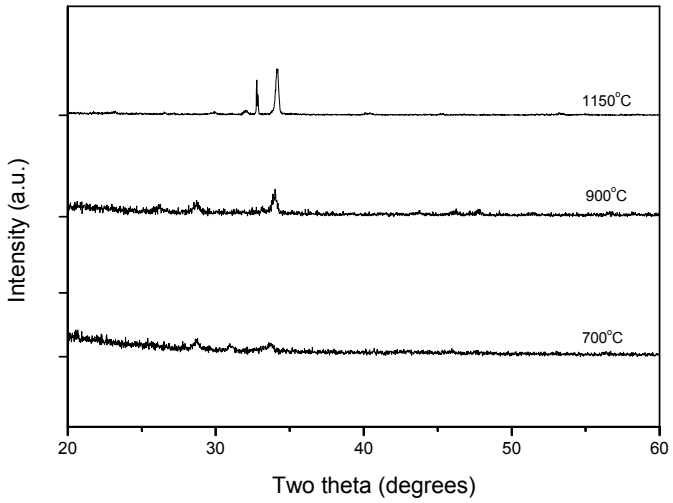

Figure 2. XRD profiles of films annealed at different temperatures.

Annealing at 700 °C resulted in the formation of $GdSi_2$ phase. Increasing annealing temperature enhanced the formation of $GdSi_2$ phase at 900 °C. At 1150 °C, the $Gd_5Si_2Ge_2$ phase started forming along with even higher level of crystallization of $GdSi_2$. The crystallization studies suggest that optimizing the time of annealing at 1150 °C could result in the stoichiometric film.

Figure 3 shows the morphological changes in the structure of the film with the change in annealing temperature. Figure 3 is the SEM of the sputtered film. Figure 3(a), (b), (c) show the surface morphology of the films after annealing at 700, 900, and 1150 °C respectively. At lower temperatures (700 °C) surface of the films are smooth with no noticeable texturing, reflecting very little presence of the crystalline phase as evidenced in the XRD. Increasing to 900 °C,

results in a film that is textured. The increased texture of the film can be attributed to the formation of the crystalline phase in the film. Increasing the annealing temperature to 1150 °C has resulted in significant texturing in the film, the texturing is the reflection of increased crystallinity in the film that was evidenced by XRD.

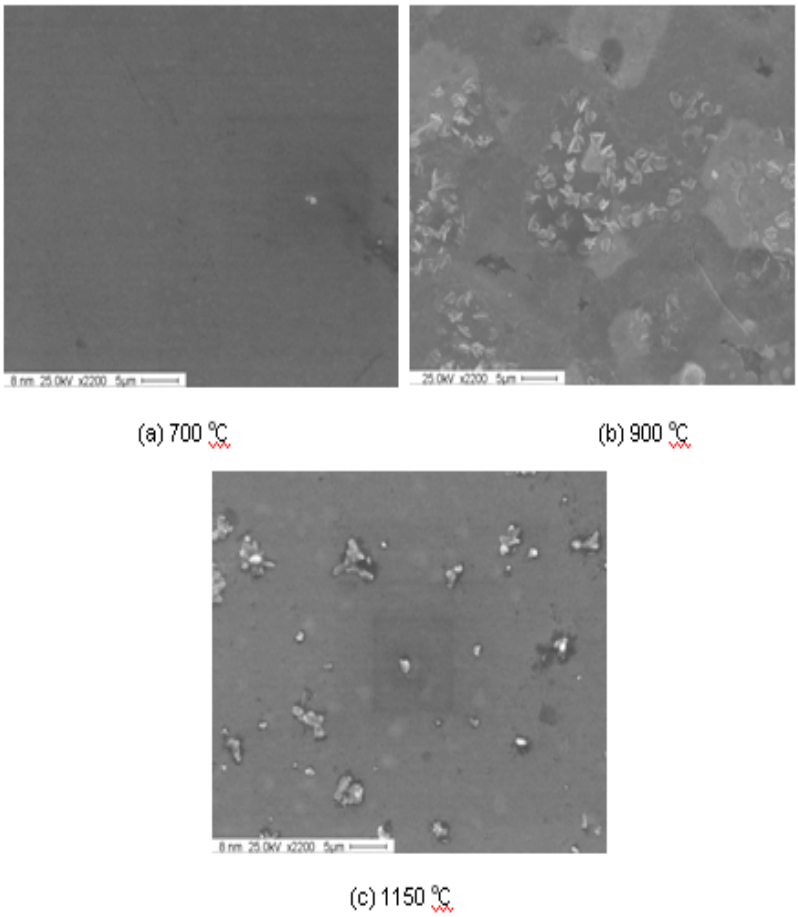

Figure 3. Scanning electron micrographs of thin films annealed at different temperatures.

It can be seen in the XRDs that at low temperatures the alloy forms a Si rich phase and no Ge-based phase can be seen. When annealed at 1150 °C though the desired GdSiGe phase appears, the crystalline phases are Si rich and Ge deficient. To understand the distribution of the materials and to ensure the stability of the interface, ,the elemental composition of the as deposited and annealed film was studied by SIMS depth profiling Figure 4(a) shows the distribution of different elements along the depth of the film for an as-grown sample. For the first 600 sec (equivalent to 100 nm of the film) stable high counts of Gd, Si and Ge (102 to 103 counts per sec) can be seen, confirming that the the deposited film has the three elements consistently distributed across the film thickness. At 600 sec the Gd and Ge signals drop while the Si, SiN and N signals rise, confirming the presence of Si_3N_4. The interface between the alloy and Si_3N_4 is sharp. The signals for the SiN are stable till about 2100 sec indicating the uniformity of the Si_3N_4 barrier after which the beam looks at bulk Si. The profiles show peaks at the

interfaces due to multiple charge exchanges. Silicon nitride layer is also stable and homogenous with sharp interface with Si substrate.

Figure 4(b) shows the SIMS profile of this sample after annealing at 1150 °C the temperature at which the desired phase is formed. It can be seen that the elemental profile is totally redistributed. Based on Figure 4(a), the thickness of the GdSiGe layer in the annealed sample (Figure 4(b)) corresponds to approximately 600sec of sputter time. The SIMS profile shows that the diffusion barrier has totally broken down and is absent. It shows an enrichment of Gd with signal strength of 104 counts per sec compared to 103 counts per sec in as-grown sample. Si is also observed to be enriched and Ge is significantly depleted compared to Figure 4(a). The nitrogen in the sample and the consequent nitride profile is also diffused. The nitrogen seems to be moving to the surface faster than the bulk. Gd appears to be diffused through silicon nitride layer into Si substrate along with Ge. The significant enrichment of the surface in Gd and Si explains the formation of $GdSi_2$ phase in the sample. The Ge fixation (possibly near the original interface) shows the small crystalline peak.

Although silicon nitride is expected to be stable till 1600 °C, the results confirm that PECVD deposited Si_3N_4 is unstable as a diffusion barrier in GdSiGe alloy system. A potential contributor to the decomposition of this layer could be hydrogen in the nitride film. It is well known that hydrogen gets chemically fixed in silicon nitride films during growth and can have up to 10% hydrogen. Hydrogen in the nitride films exhibit deleterious effects and are prone to being unstable when subjected to high temperature treatment. The presence of hydrogen in the film results in dangling Si and N bonds in the film. Generally these bonds can be terminated by annealing of the film that causes its densification too. In our experiments, the nitride films were not annealed. We hypothesize that the annealing of the GdSiGe/SiN/Si stack resulted in the dangling bonds interacting with the elements in the thin film (primarily Ge) and thus compromised the diffusion barrier. Tests are underway to confirm the role of hydrogen in the failure of the diffusion barrier. Alternatively other possible diffusion barriers such as TiN, TaN are being studied.

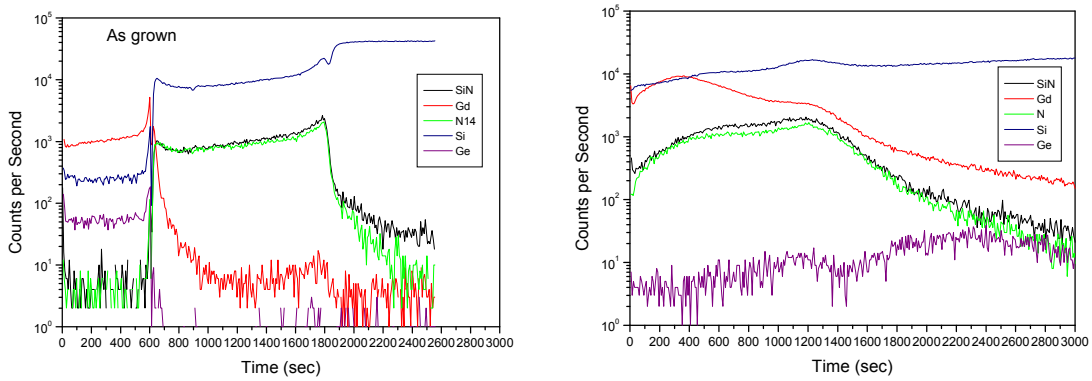

Figure 4(a) SIMS depth profiling of as-deposited film on SiN/Si,
(b) SIMS depth profiling of thin films annealed at 1150 °C.

Fabrication of a Micro Cooling Channel Prototype

We have fabricated the microcooler with trapezoidal microchannels. Eight microchannels, each 300 μm wide, 150 μm deep and around 1 in. long have been fabricated in a 1x1 in. area on 2 in. silicon wafer. Each channel would contain 762 x 106 μm^3 of fluid. For effective cooling

capacity the distance between the channels was set as 2700 μm. This ensured that at least 3000 μm of $Gd_5Si_2Ge_2$ (1350 μm on each side + 300 μm in direct contact with the fluid) would be dedicated for cooling each channel. The structure of the trapezoidal channel and the fabricated microchannels is shown in Figure 5.

A 250 μm thick silicon wafer was used for the fabrication. A 3000Å thick oxide was thermally grown on the wafer. Positive photoresist S1813 was used to pattern the inlet and outlet ports using lithographic technique (UV exposure – 17 sec). The oxide was then removed using Buffered oxide etch (BOE) for 25 min. The photoresist was then stripped off and it was then followed by wet etching in TMAH @ 85 °C for 100 μm. Wet etching of Si (100) wafer leads to a side wall angle of 54.74° leading to a trapezoidal shape. S1813 was spun again and the channels were then patterned, followed by BOE and wet etching for 150 μm. The combined etching of 250 μm formed the inlet and outlet ports (holes). This process flow has the advantage that it requires a single oxidation step. The fabrication procedure of the microchannels is schematically illustrated in Figure 6.

The temperature of the heat transfer fluid is measured at the inlet and outlet by in-situ temperature sensors. The temperature sensing principle is based on the phenomena of resistivity change of bulk Si with temperature. In order to fabricate a sensor with high resolution and sensitivity, the resistivity of silicon was increased by addition of deep impurities. The resistivity can be increased by controlled co-doping of Si with a deep donor (DD) and a deep acceptor (DA). Almost all transition metals are known to introduce a pair of DD and DA in the Si bandgap.

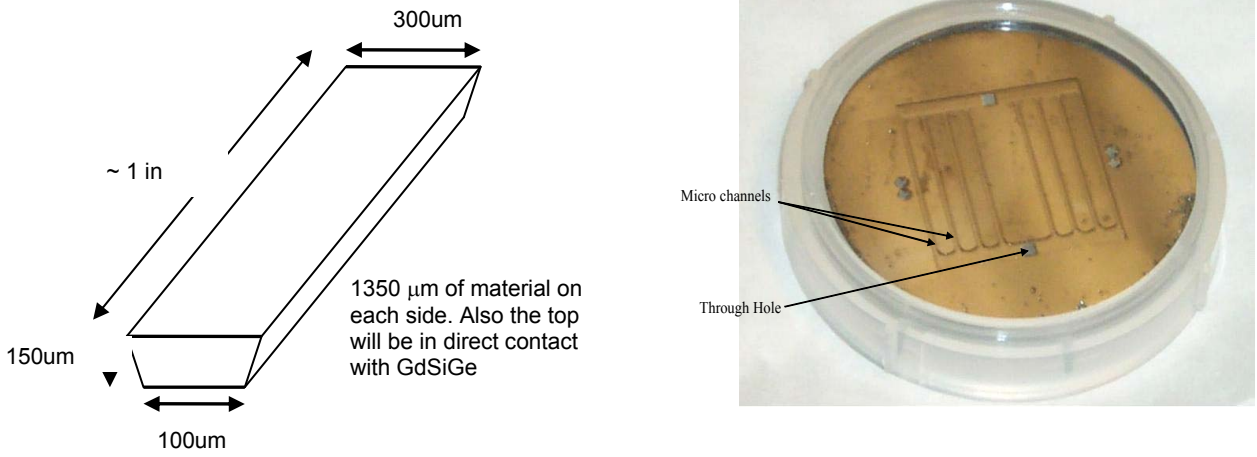

Figure 5. Dimension of unit channel and fabricated microchannels.

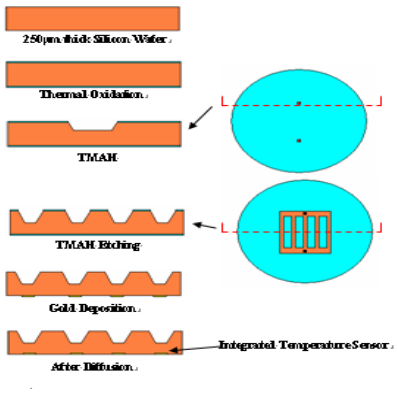

Figure 6. Process flow of the fabrication of the microchannels with integrated temperature sensors.

Au was used as the deep impurity in the fabrication of the temperature sensor. Au dissolves substituionally and diffuses interstitially in silicon at temperatures above 800 °C, also known as the kick-out mechanism. It introduces two impurity levels in silicon, an acceptor level 0.54 ev below Ec and a donor level 0.35 ev above Ev.

250 Å of Au was deposited on specific areas of the channels using a shadow mask. It was then diffused at high temperatures in an oxygen rich environment in an open tube furnace. Au diffusion modified the properties of silicon resulting in a high resolution temperature sensor.

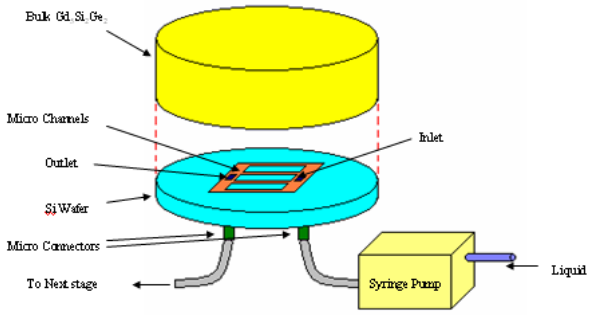

Figure 7. Schematic of the microcooler system.

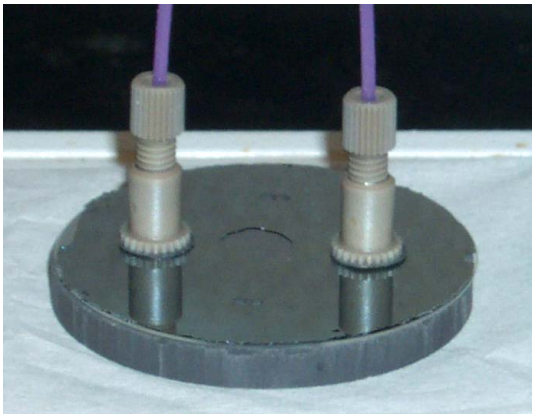

Figure 8. Photograph of Microfabricated prototype.

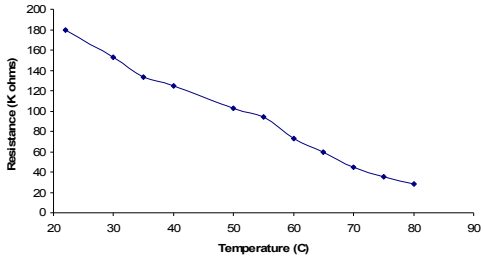

Figure 9. Output characteristics of temperature.

The schematic of the microcooler system is shown in Figure 7 and the fabricated prototype in Figure 8. Table 1 shows the complete process flow.

Table 1. Process flow for fabrication.

Step	Process name	Details
1	Wafer Cleaning	RCA Standard clean on 250 μm thick Si (100) wafer
2	Oxidation	3000 Å thermal oxide
3	Positive photoresist (S1813) spin	3000 rpm , 30 sec
4	Lithographic patterning (Ports)	UV exposure–17 sec Developed in MF319–25 sec Hard Bake–110 °C for 60 sec
5	Oxide Patterning	BOE - 25 mins @ Room temperature
6	Wet Etching	TMAH etching @ 85 °C for 100 μm
7	Positive photoresist (S1813) spin	3000 rpm , 30 sec
8	Lithographic patterning (Microchannels)	UV exposure – 17 sec Developed in MF319 – 25 sec Hard Bake – 110 °C for 60 sec
9	Oxide Patterning	BOE - 25 mins @ Room temperature
10	Wet Etching	TMAH etching @ 85 °C for 150 μm
11	Oxide removal	BOE - 25 mins @ Room temperature
12	Gold Deposition	250 Å of gold deposited on selective areas using shadow mask
13	Gold Diffusion	Open tube furnace @ 1000 °C
14	Gold etch	Removal of surface gold (after diffusion)
15	Positive photoresist (S1813) spin	3000 rpm, 30 sec
16	Lithographic patterning (Ohmic contacts)	UV exposure–17 sec Developed in MF319–25 sec Hard Bake–110 °C for 60 sec
17	Deposition	100Å Cr/1500Å Au
18	Lift-off	Wafer kept in acetone for 4 hr
19	$Gd_5Si_2Ge_2$ Bonding	CrystalbondTM 509: Heat to120 °C and gradual cooling till room temperature
20	Microconnectors	N-333 microconnector-Placed in oven @121 °C for 95 min

Gd5Si2Ge2 bulk material has been synthesized by high temperature alloying process and the powdered. To make the cooling disk, the powder has been compacted by cold press and sintered at 800 °C. The magnetic and magnetocaloric properties of the disk has been studied and is shown in the figure below.

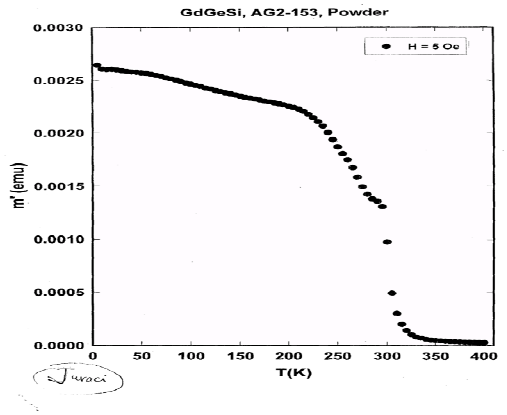

Figure 10. Dependence of magnetization on temperature.

Figure 10 shows the dependence of magnetization on temperature. Figure 10 shows a transition from paramagnetic to ferromagnetic at 276 K. The change in magnetic entropy has been studied and plotted in the following Figure 11. The characteristics in the Figure 11 indicate sharp transitions at 260 and 276 K.

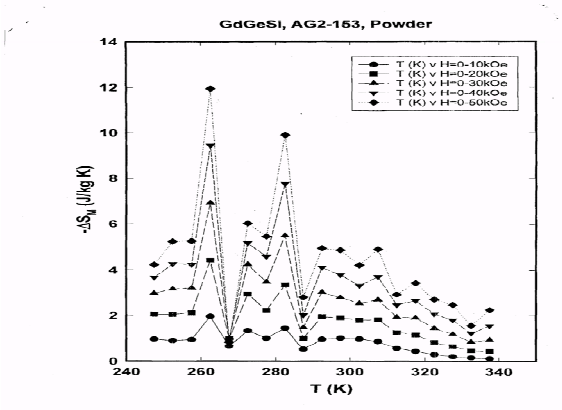

Figure 11. Dependence of magnetizatic entropy with temperature.

A 5mm thick $Gd_5Si_2Ge_2$ disc has been bonded to the open end of the channels using Crystalbond-509TM. This adhesive was chosen as it can be easily stripped, hence allowing the use a single $Gd_5Si_2Ge_2$ block for many wafers. The adhesive was crushed and dissolved in acetone to facilitate application of a thin layer. The adhesive was then heated to 120 °C and the Si wafer (with microchannels) was bonded to the $Gd_5Si_2Ge_2$ block and allowed to cool to room temperature. For transfer of fluid through the microchannels, nanoprtTM assemblies N-333 were connected to the inlet and outlet ports.

Figure 12 shows the experimental setup for refrigeration test, and Table 2 is the specification of the microchannels and refrigerator system.

Table 2. Cooler specification.

Microcooler channel size (WxHxL)	300 μmx150 μmx1 in.
Channel material	Si (100) wafer, 250 μm thickness
MCE material	$Gd_5Si_2Ge_2$ (AMES Lab)
MCE block	2 in. dia x 1/4 in. thickness
Temp sensor	Diffusion Au @950 °C
Testing temp	~276K
Electromagentic field	1~2 Tesla

The testing is done using a V-3700-1 series electromagnet with a capability of 1.5T. The electromagnet is driven by a V-FR2900 power supply. The distance between the poles determines the maximum achievable field. The $Gd_5Si_2Ge_2$ block is placed between the poles with the poles as close as possible to generate a high magnetic field. The temperature of the block is measured using a dual thermocouple with traceable computer output. The setup is shown in Figure 13.

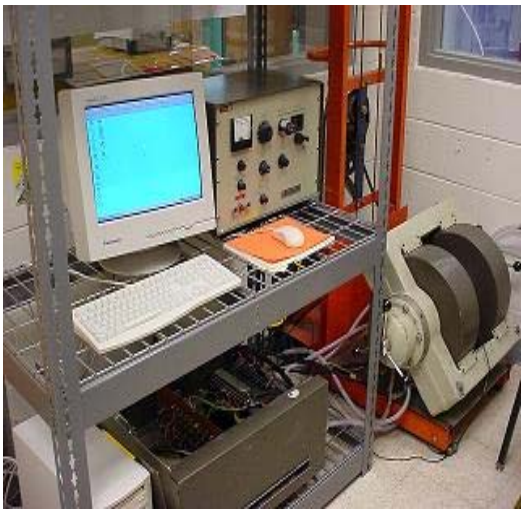

Figure 12. Experimental setup for refrigeration test.

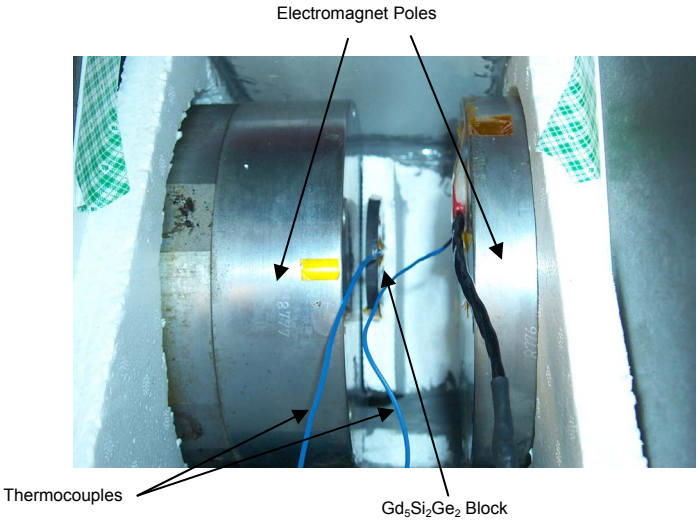

Figure 13. Temperature measurement by changing the magnetic field at the $Gd_5Si_2Ge_2$.

To test the affect of magnetic field on $Gd_5Si_2Ge_2$ block, the temperature of the surrounding was varied from very low temperatures to near room temperature. The low temperatures were achieved by surrounding the setup with liquid nitrogen. The maximum magnetic filed of 1.2T (due to the distance between the poles) was applied during the testing. The thermocouple used is capable of connecting to a computer and log the readings. The testing was done at various temperatures by applying the magnetic field and observing the temperature change of the $Gd_5Si_2Ge_2$ block. It was observed that on the application of magnetic field the temperature of $Gd_5Si_2Ge_2$ block rises till it reaches a saturation point. Figure 14 shows the characteristics at various temperatures.

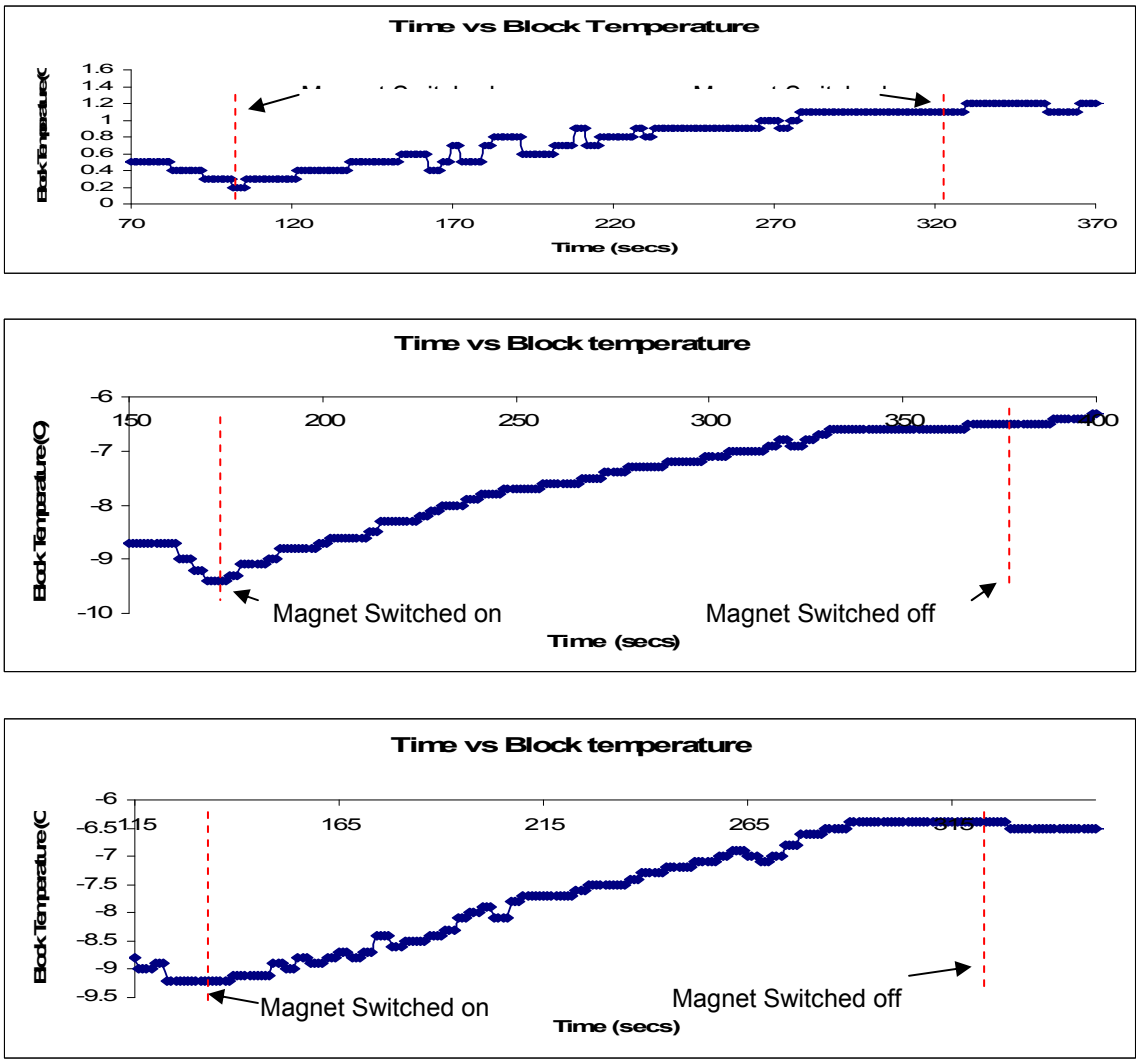

Figure 14. Response characteristics at various temperatures.

The temperature change of the $Gd_5Si_2Ge_2$ block is dependent on the ambient temperature as seen from the above graphs. It was observed that the lower the ambient temperature more the change in temperature as shown in Figure 15.

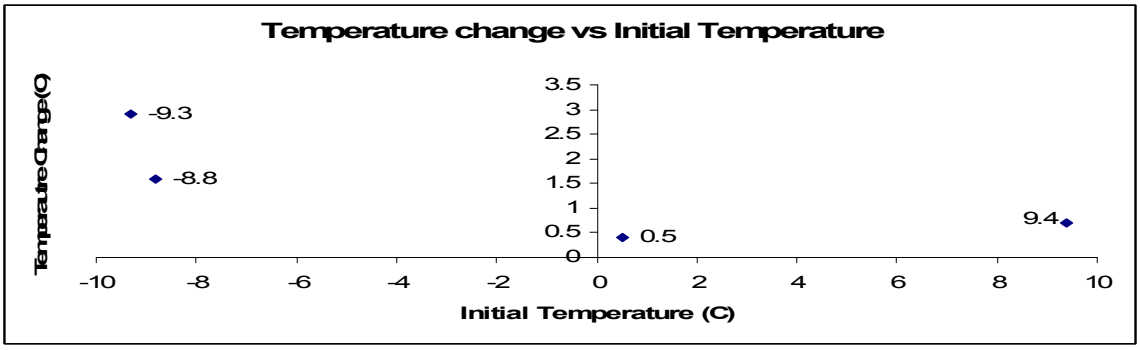

Figure 15. Initial temperature vs. temperature change.

Modeling of Magnetic Cooler Heat Exchanger for Periodic Heating and Cooling (magnetization and demagnetization)

The transient heating and cooling process, when the heat exchanger is exposed to the fluctuating magnetic field was studied. The volumetric heat source was turned on and off for certain period of time and the variations of temperature and Nusselt number was studied. The results computed were for Gadolinium substrate and water as the working fluid. The parameters were calculated at different sections along the length of the channel for different time intervals.

Figure 16 shows the variation of volumetric heat generation rate with time. When a magnetic field of 5T is applied to the microchannel heat exchanger, 6.4E8 W/m^3 of heat is generated and the magnetic material heats up. When the magnetic field is removed, the material cools down. The negative heat generation rate of -6.4E8 W/m^3 shows the condition when the magnetic field of 5T is removed.

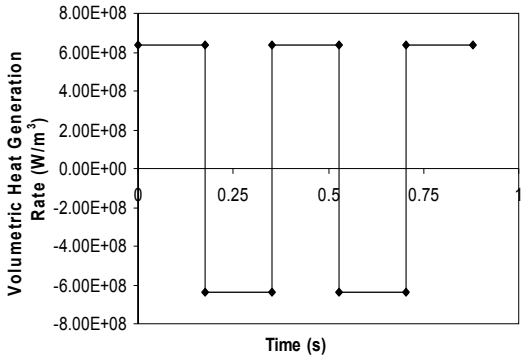

Figure 16. Variation of volumetric heat generation rate with time.

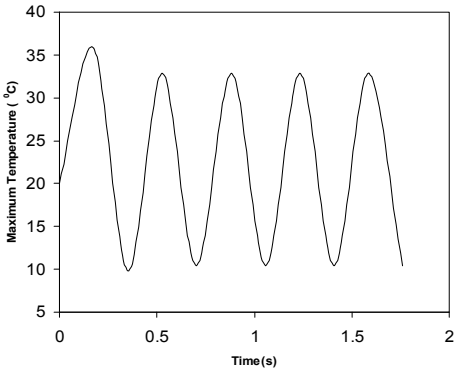

Figure 17. Variation of maximum temperature in the substrate (Re=1600, Bc=0.05 cm, Hc=0.1 cm, g0=6.4E8 W/m^3).

Figure 17 shows the variation of maximum temperature in the substrate with time for heating and cooling cycles. Reynolds number is 1600. The maximum temperature in the microchannel is found in the solid region at the outlet edge of the channel. A sinusoidal behavior of the temperature is seen for the heating and cooling cycles. After a small time period the maximum temperature maintains fluctuations between 330 °C and 100 °C.

Figure 18 shows the variation of peripheral average interface temperature with time at different locations along the length of the channel for Re=1600. During the heating phase as the fluid passes along the length of the channel it gains heat. The solid-fluid interface temperature increases as the fluid moves downstream due to the development of thermal boundary layer starting with the entrance section as the leading edge. During the cooling phase the solid-fluid interface temperature decreases. Fluid cools down as the heat is taken out from the fluid. The highest values of interface temperature are seen near the outlet of the channel.

Figure 19 shows the variation of interfacial heat flux in the channel with time at different sections of the channel for Re=1600 and dimensions of 0.05*0.1 cm. Interface heat flux also shows a sinusoidal behavior and it shows higher values near the entrance of the channel. During the cool down phase, the heat flux near the entrance also becomes lower. This is because of larger transport rate at the leading edge of the thermal boundary layer that develops starting at the entrance section.

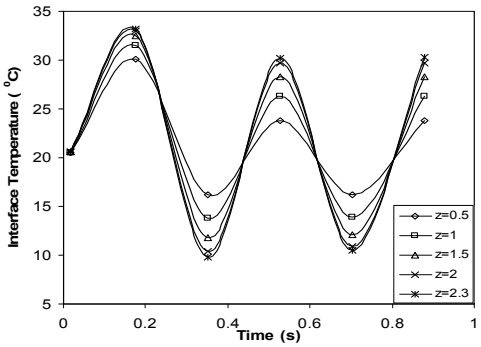

Figure 18. Variation of interface temperature with time at different sections in the rectangular channel (Re=1600, Bc=0.05 cm, Hc=0.1 cm, g0=6.4E8 W/m^3).

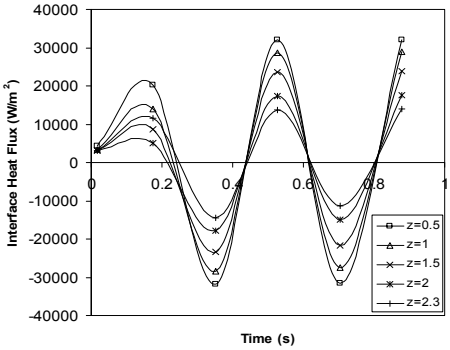

Figure 19. Variation of interface heat flux with time at different sections in the rectangular channel (Re=1600, Bc=0.05 cm, Hc=0.1 cm, g0=6.4E8 W/m^3).

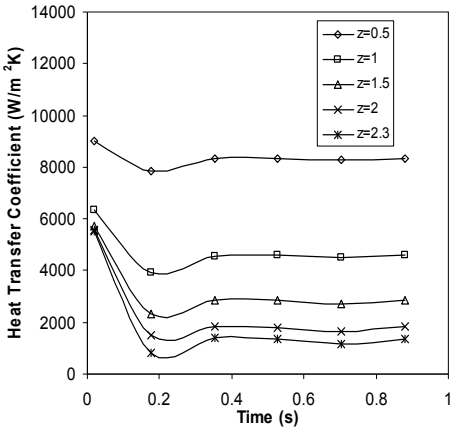

Figure 20. Variation of heat transfer coefficient with time at different sections in the rectangular channel (Re=1600, Bc=0.05 cm, Hc=0.1 cm, g0=6.4E8 W/m^3).

Figure 20 shows the variation of heat transfer coefficient with time at different locations along the length of the channel for Re=1600 and dimensions of 0.05*0.1 cm. After 0.2 sec heat transfer coefficient remains almost constant for further heating and cooling cycles. Heat transfer coefficient decreases along the channel length. Fluid gets heated as it passes through the channel. The temperature difference between fluid and solid decreases as one moves along the length of the channel. Thermal boundary layer grows until fully developed flow is established. Therefore, the heat transfer coefficient is higher at the entrance and decreases downstream. The variation is larger at the entrance because of the rapid development of thermal boundary layer near the leading edge.

Figure 21 shows variation of Nusselt number with Fourier number at different locations along the length of the channel for Re=1600 and dimensions of 0.05*0.1 cm. The trends are analogous to that seen for the variation of heat transfer coefficient presented in Figure 20.

Figure 22 shows the interface temperature variation for heating and cooling cycles. The heat generation rate is 12.8E8 W/m^3 and the channel dimensions are 0.05*0.1 cm. As compared to Figure 18, it is seen that the interface temperature variation increases as the heat generation rate is doubled. The increase is seen in all locations within the channel. Figure 23 shows the Nusselt number variation for g0 = 12.8E8 W/m^3 and channel dimensions of 0.05*0.1 cm. It may be noted that at all locations, the Nusselt number is highest at the beginning of the transient, decreases rapidly with time and undershoots before settling to a constant value for that location. The undershoot is caused by rapid distribution of heat between solid and fluid as they both store and release thermal energy at different rate until settling for a periodic equilibrium condition.

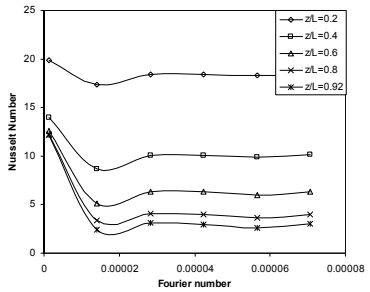

Figure 21. Variation of Nusselt number with time at different sections in the rectangular channel (Re=1600, Bc=0.05 cm, Hc=0.1 cm, g0= 6.4E8 W/m^3).

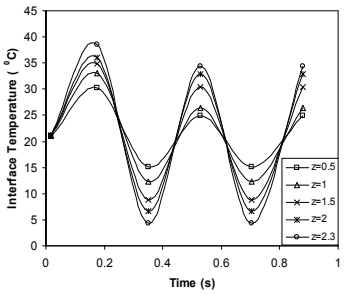

Figure 22. Variation of interface temperature with time at different sections in the rectangular channel with double heat generation rate (g0= 12.8E8 W/m^3, Re=1600, Bc=0.05 cm, Hc=0.1 cm).

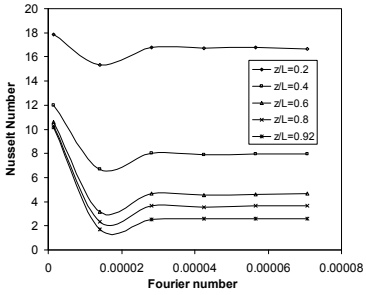

Figure 23. Variation of Nusselt number with time at different sections in the rectangular channel with double heat generation rate (g0= 12.8E8 W/m^3, Re=1600, Bc=0.05 cm, Hc=0.1 cm).

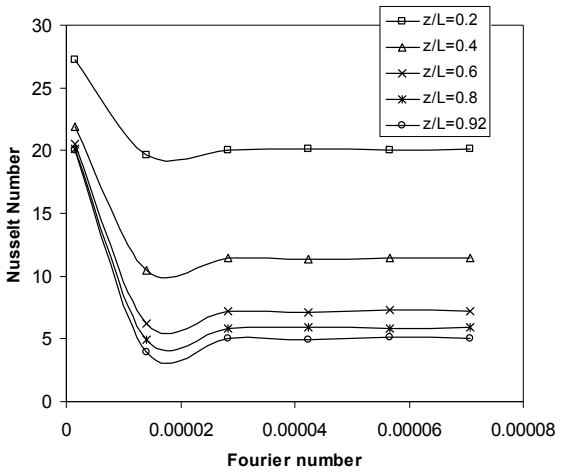

Figure 24. Variation of Nusselt number with time at different sections in a square channel (Re=1600, Bc=0.1 cm, Hc=0.1 cm, g0=6.4E8 W/m^3).

Figure 24 shows the variation of Nusselt number with Fourier number at different locations along the length of the channel. Reynolds number of the fluid is 1600 and channel dimensions are 0.1x0.1 cm. As compared to a rectangular channel with dimensions of 0.05x0.1 cm, more amount of fluid is passing through this square channel. Therefore, the values of interface temperature are lower than that of the rectangular channel and consequently the Nusselt number is higher.

Thermodynamic Analysis of the Magnetic Refrigeration Cycle for Hydrogen Liquefaction

The above model allows a quantitative analysis of the thermodynamic cycle for a magnetic refrigerator. Sensitivity analysis has been performed using gadolinium metal as the magnetic material and water as the working fluid. Cooling power, temperature span, and coefficient of performance are analyzed by simulations. Calculations have been carried out for the proposed model operating at near room temperature in a magnetic field between 1 and 5 T and using 3 kg of Gd spheres packed in two identical magnetocaloric beds. The other parameters are the lowest working fluid temperature of 273 K limited by the freezing temperature and the temperature at the hot heat exchanger limited by the ambient temperature. The temperature span was varied over small range. The primary objective of these calculations was to observe the effect of the variation of the temperature span on the system performance.

Figure 25 shows the cooling power as a function of the magnetic field. The cooling power was evaluated from the magnetization data. A temperature spans of 10, 15, and 20 K were considered in this case. As can be seen for an increase in the magnetic field, there is an increase in the cooling capacity. When the applied field is increased, the cooling load increases because the increased adiabatic temperature change from the higher field produces more cooling. Figure 26 presents cooling power as a function of temperature span for various magnetic fields. In this case it can be observed that the cooling power decreases with an increase in the temperature span. This result is expected because the system is working on a higher temperature range causing a decrease in the cooling capacity. It may be also noticed that the sensitivity of the temperature span is higher at larger values of the magnetic field.

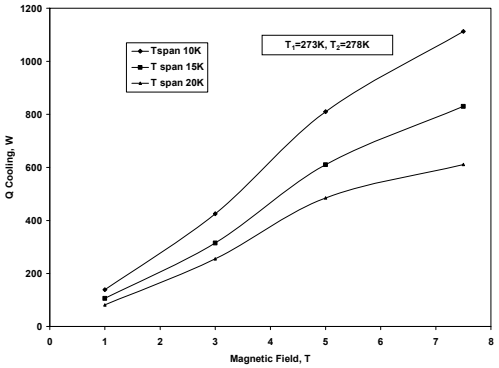

Figure 25. Cooling power vs. magnetic field for various temperature spans.

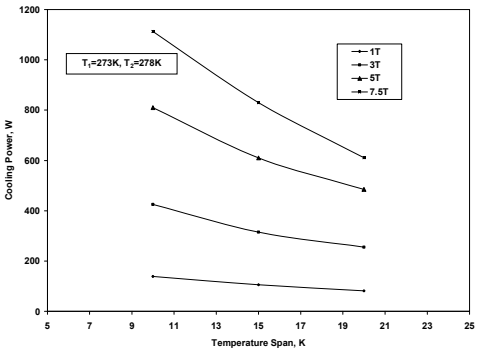

Figure 26. Cooling power vs. temperature span for various magnetic fields.

Figure 27 shows the coefficient of performance (COP) dependence on temperature span for various magnetic fields. The COP ranges from about two to eleven, which compares favorably with commercial vapor cycle refrigerators. The Carnot cycle, which is completely reversible, is a perfect model for a refrigeration cycle operating between two fixed temperatures. The Carnot limit to the COP of a refrigerator is the maximum coefficient of performance that may be attained by a refrigerating machine. Figure 28 presents the ratio of COPactual/COPCarnot vs. temperature span for 3T, 5T, and 7.5T magnetic fields. COPactual is the coefficient of performance predicted by present model under the same working conditions. No refrigerating cycle may have a coefficient of performance higher than that for a reversible cycle operating between the same temperature limits. The ratio of COPactual/COPCarnot is presented as a percentage of the Carnot cycle performing in a similar temperature range. The percentage of Carnot COP is less than 35% as is generally true for most real refrigerators. As expected the ratio of COPactual/COPCarnot drops with increasing temperature span. When the magnetic field is increased the tendency of the ratio decreases. These trends agreed with those shown by experimental data. Figure 29 presents predicted and experimental ratios of COPactual/ COPCarnot vs. Temperature span for 5T magnetic field. The experimental data used is that presented by Zimm et al. As can be seen there is a reasonably good agreement between predictions by the proposed model and those from the experimental data. Figure 30 shows the behavior of the ratio of COPactual/COPCarnot with the temperature span for various working fluids under a 5T magnetic field. As can be seen R134a and Ammonia exhibit better efficiency than that showed by water as the working fluid. R134a shows ratio higher than 35% over the entire temperature span. Figures 31 and 32 present cooling power and COP dependence on temperature span for R-134a. Vineyard presented a complete study about alternative refrigerants for a household refrigerator. He tested various viable refrigerants including pure and mixture refrigerants. Table 3 compares results for coefficient of performance between present model and commercial refrigerators as presented by Vineyard. It can be seen that magnetic refrigerator provides significantly higher coefficient of performance compared to vapor compression refrigerator of the same capacity. Therefore, magnetic refrigeration has a great potential to reduce operating cost and maintenance cost when compared to the conventional method of compressor based refrigeration.

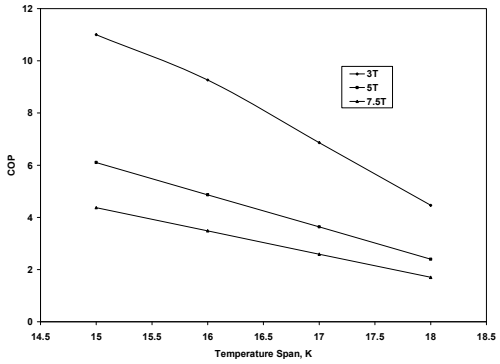

Figure 27. COP vs. temperature span for different magnetic fields.

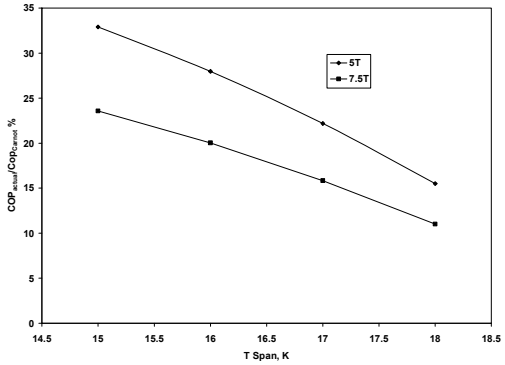

Figure 28. COPactual/COPCarnot vs. temperature span for various magnetic fields.

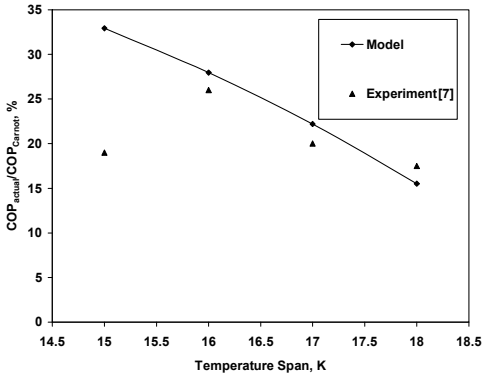

Figure 29. Predicted and experimental COPactual/ COPCarnot vs. temperature span for 5T magnetic field.

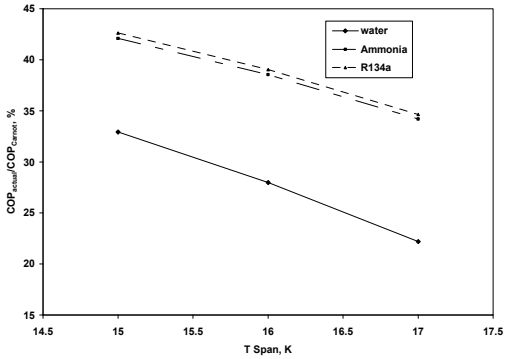

Figure 30. COPactual/COPCarnot vs. temperature span for various fluids with a 5T magnetic field.

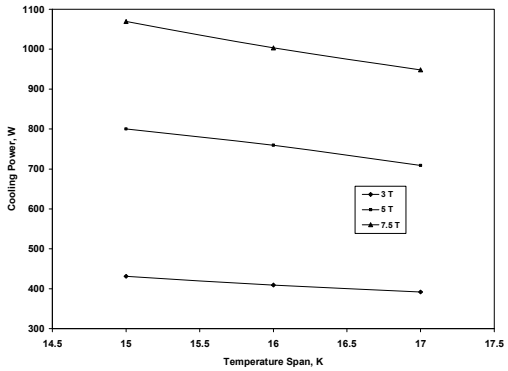

Figure 31. Cooling power vs. Temperature span for different magnetic fields with R-134a.

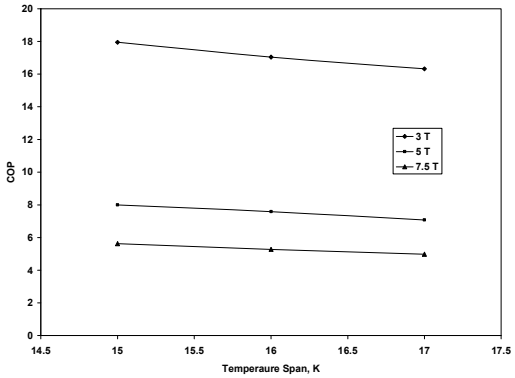

Figure 32. COP vs. temperature span for different magnetic fields and R-134a.

Table 3. COP comparison between this model and commercial refrigerators

COP (Typical 18 ft3 refrigerator)		
Magnetic Refrigerator	Commercial Vapor Cycle Refrigerators	
N/A	Refrigerant R134a	Refrigerant R22
11	2.26	2.29

In recent years, exergy analysis and availability analysis have been applied to thermal systems by a number of investigators for analyzing and evaluating system thermodynamic performance, as well as system technologies. Thermodynamic second law analysis in conjunction with first law analysis gives a bonus to the consideration of the quality of energy over the quantity involved in a refrigeration system and can lead the way to improve the system's performance. Recent developments in magnetic refrigeration have demonstrated that it exhibits a great potential by showing a very high efficiency when compared to commercial vapor cycle refrigerators. This part of this investigation considers second law simulations for magnetic refrigerators so that potentials for component improvement can be analyzed to reduce system irreversibility The aim of this section is to demonstrate through modeling the contribution of each magnetic refrigerator component to the availability destroyed by the system using second law analysis. A simple thermodynamic model to represent a magnetic refrigerator is considered. The system consists of heat exchangers and beds of magnetic materials. The analysis considered that the system operates near room temperature in a magnetic field between 1 and 7.5T and uses 3 kg of gadolinium (Gd) spheres packed in two magnetocaloric beds. The heat transfer fluid is water. The beds are periodically magnetized and demagnetized and the fluid flows are arranged to meet the cycle requirements. A second law analysis of each component is performed to determine the component potential to the overall system efficiency. Other working fluids are also considered. Properties, entropy, and exergy of the working fluids are calculated to examine the second law efficiencies under different operating conditions. Parametric analysis of the magnetic refrigeration system is done to study effects on the exergetic efficiency of the system. Magnetic refrigerator exergy efficiency is compared to that for commercial refrigerators.

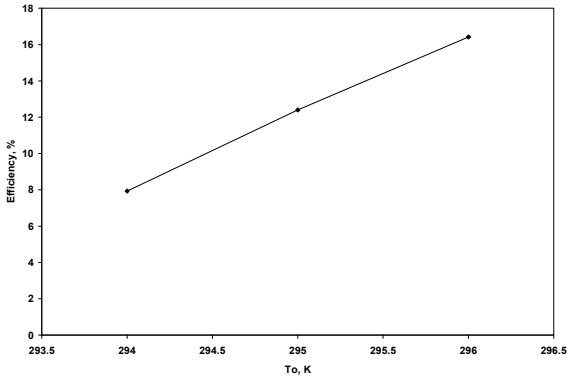

Figure 33. Efficiency vs. To.

Effect of the reference temperature on the exergetic efficiency of the heat exchanger is illustrated in Figure 33. The exergetic efficiency of the heat exchanger increases as the reference temperature increases. This can be explained because any increment in the reference temperature generates less exergy losses in the heat exchanger. This contributes positively to the exergetic efficiency of the heat exchanger.

Figure 34 shows the exergetic efficiency dependency on the temperature of the incoming air. The analysis was performed with a range of temperature about 300 K for the incoming air to the heat exchanger. As can be seen when the incoming air temperature increases there is a decrease in the exergetic efficiency for the heat exchanger. This can be explained that when the incoming air temperature is increase there is an increase in the exergy losses for the heat exchanger. The heat exchanger is required to work under more severe conditions and therefore becoming more inefficient.

In Figure 35 a similar analysis was performed but studying the incidence of the exiting condition of the air from the heat exchanger. A similar trend was found, observing a decrease in exergetic efficiency with an increase in the exiting condition of the air.

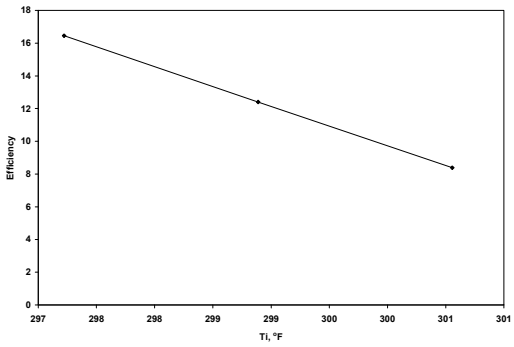

Figure 34. Efficiency vs. incoming air temperature.

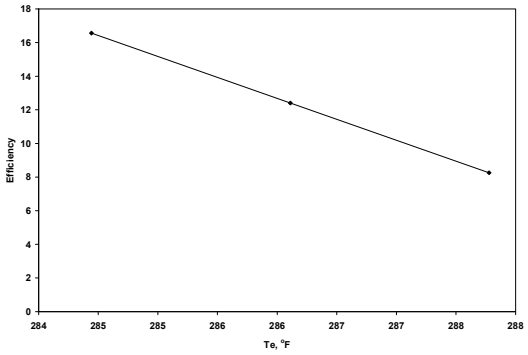

Figure 35. Efficiency vs. exiting air temperature.

Figure 36 irreversibility, in normalized terms, is presented as an equivalent power input per unit capacity for the magnetic refrigerator. Even though, the magnetic refrigerator does not use any input power, equivalent power figure is used for comparison purposes. This equivalent power has a meaning of a theoretical power that could be used as an input of the magnetic refrigerator. Reversibility of the Carnot refrigerator is also shown in Figure 36. The overall height of the bar graph is simply the inverse of the actual COP, reflecting the total irreversibility which is the sum of all irreversibility refrigerator components. The inverse of COP shows the amount of work necessary to provide a unit cooling capacity for a particular system.

Figure 37 shows the effect of using a different working fluid for the magnetic refrigerator. In this case a comparison in the refrigerator performance is executed using the second law with various working fluids. Water, Ammonia and R-134a are the three working fluids that are used. The R-134a shows less total availability destroyed.

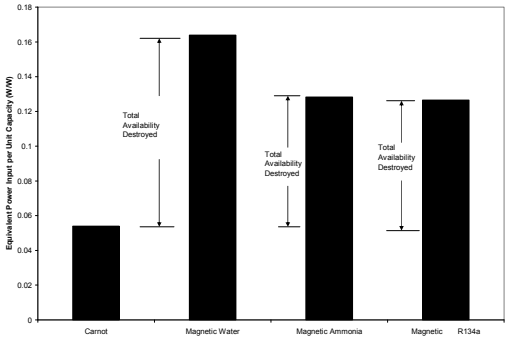

Figure 36. Availability destruction in the magnetic refrigerator.

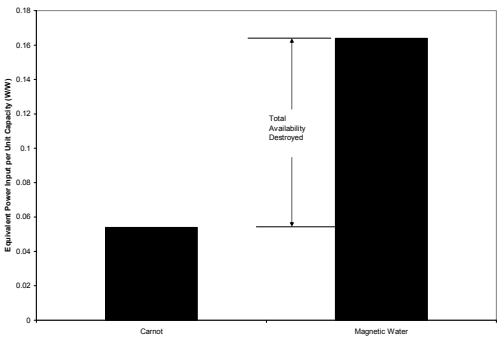

Figure 37. Effect of working fluid.

Figure 38 provides a greater insight into the fate of the availability lost from the cooling water. Note how little of the cooling water availability loss was actually transferred to the incoming air passing over the heat exchanger; the remainder was destroyed immediately. Ultimately, the availability transferred to the air is also destroyed as the exiting air from the heat exchanger mixes with the surroundings.

Figure 39 quantifies the irreversibility associated with the magnetic bed. This figure provides more detailed insights into the fate of the available energy transferred from the magnetic material; about half of it is transferred to the working fluid (water).

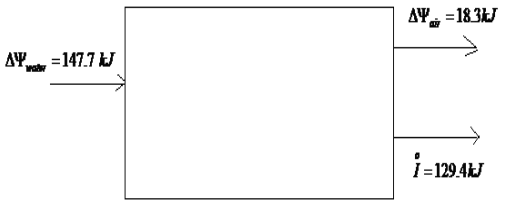

Figure 38. Heat exchanger irreversibility.

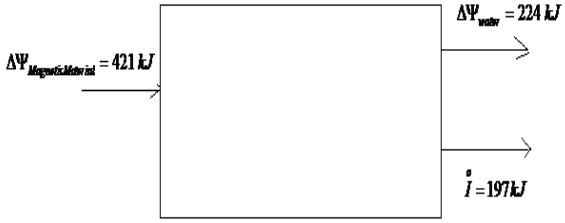

Figure 39. Magnetic bed irreversibility.

Table 4 compares results for exergetic efficiency of magnetic refrigerator components with commercial refrigerator components presented by Bridges et al. This table shows similar order of magnitude in efficiencies.

Table 4. Exergetic efficiency for refrigerator components.

Component	Efficiency [%]	Refrigerator
Evaporator	48.38	Commercial
Condenser	27.8	Commercial
Heat exchanger	12.4	Magnetic
Magnetic bed	53.19	Magnetic

Smart Porous Metal-Organic Frameworks (MOFs) for Hydrogen Recovery and Storage

M. Eddaoudi, M. Zaworotko, and B. Space
University of South Florida

J. Eckert
Los Alamos National Laboratory

A. T-Raissi and Nahid Mohajeri
Florida Solar Energy Center

Research Period: January 2005 to November 2006

Abstract

"What could we do with layered structures with just the right layers? What would the properties of materials be if we could really arrange the atoms the way we want them? They would be very interesting to investigate theoretically. I can't see exactly what would happen, but I can hardly doubt that when we have some control of the arrangement of things on a small scale we will get an enormously greater range of possible properties that substances can have, and of different things that we can do – Richard P. Feynman, December 29, 1959."

Synthesis of novel materials from molecular building blocks (MBBs) offers an opportunity to address Feynman's vision since new nanostructures can be accessed *via* "bottom-up" approaches. Recently, applications of rigid MBBs have led to the development of a wide range of metal-organic frameworks with large accessible 3-D pores decorated with adjustable periodic organic and inorganic moieties suitable for hydrogen uptake. Better hydrogen storage materials would have far-reaching impact -- for example, aerospace technology of the future will depend on the ability to store hydrogen efficiently. For example, during Shuttle operation, more LH2 is consumed on the ground than is used to launch Shuttle into the orbit. If terrestrial LH2 losses and boil off at KSC could be reduced (or eliminated), NASA's STS fuel bill can be lowered by more than 50%.

This challenge can be met by developing novel H_2 storage materials that are safer and more effective for NASA-KSC's ground operations. Our strategy and approach involve the development of tunable porous metal-organic frameworks for H_2 storage. The results of this project provide a basis for developing selected metal-organic frameworks as high-capacity hydrogen storage materials for onsite H_2 recovery, purification and storage.

Introduction

Recent advances in the fast growing field of microporous metal organic frameworks (MOFs) have led to numerous practical and conceptual developments. Specifically, the chemistry of MOFs has provided a range of low-cost porous crystalline materials assembled from MBB's that exhibit high stability, tunable properties, and porosity. Most recently, systematic studies of MOFs have indicated that increasing the number of benzene rings in the scaffold of a MOF greatly improves the amount of hydrogen uptake. Furthermore, Inelastic Neutron Scattering (INS) studies suggest that MOFs can contain several types of hydrogen binding sites ranging from organic components to the metal constituents of the framework Preliminary studies have

from organic components to the metal constituents of the framework Preliminary studies have demonstrated that MOFs have the ability to store larger amounts of non-cryogenic hydrogen than amorphous porous carbon and inorganic zeolites. Further, the facile tunability of the MOF constituents and pore size has reinforced the belief that materials with superior H_2 storage capacity are achievable.
In order to meet the needs of NASA to reduce or eliminate terrestrial LH_2 losses and boil off at KSC, a program to synthesize rigid porous (neutral or anionic) MOFs with augmented and tunable sorption sites for H_2 storage is pursued.

General Objectives of the Project

1. Synthesize and characterize viable porous MOFs for H_2 storage.

2. Develop a better understanding of the interactions between sorbed hydrogen with the organic and inorganic constituents of the sorbent MOF by means of inelastic neutron scattering (INS) (to characterize the hydrogen-MOF interactions) and computational studies (to interpret the data and predict novel structures).

3. Synergistically combine the outcomes of objectives 1 and 2 to construct made-to-order cost-effective MOFs that exhibit superior hydrogen storage capacity.

Background

Synthesis of Metal Organic Frameworks (MOFs)

Metal-carboxylate polyhedral frameworks and molecules -- Professor Zaworotko leads one of the first groups to have applied the principles of self-assembly to the design and isolation of nanoscale molecular structures that are based upon metal-carboxylate building blocks. Recently, such networks have attracted much interest for their properties such as porosity, H_2 storage and magnetism. Though a myriad of crystalline porous carboxylate based MOFs have been synthesized and structurally characterized they remain unexplored for their potential as H_2 storage media. Fig. 1A illustrates the prototypal small rhombihexahedron, which can be regarded as a structure that is generated by linking (angular carboxylates) molecular squares (dimetaltetracarboxylate paddlewheel clusters) at their vertices. The nature of these structures, which we have termed nanoballs, is such that they are simple and inexpensive to prepare, they are modular, contain windows and nanoscale cavities decorated with adjustable open metal sites suitable for H_2 sorption and they can be fused to generate networks (Figure 1B).

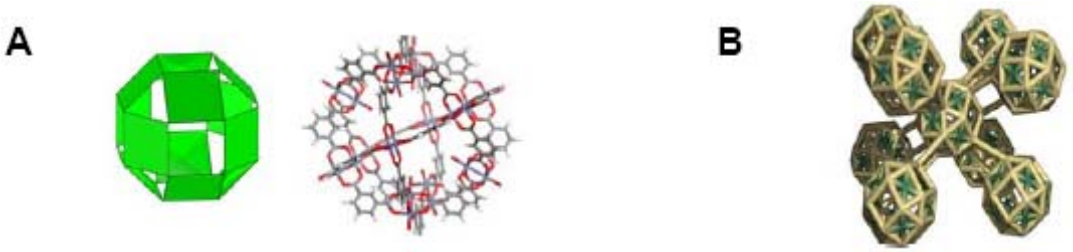

Figure 1. A) The prototypal “nanoball”, a molecular small rhombihexahedron, B) BCC crystal structure of fused nanoballs.

Metal-bipyridyl Networks - Metal-bipyridyl networks have been extensively studied for over a decade and they exemplify the "node-and-spacer" approach for design of MOFs. Several examples of the types of networks that can be generated by simply reacting a transition metal with an appropriate quantity of 4,4'-bipyridyl (or related ligand) are illustrated schematically in Fig. 2, and we were among the first groups to report the synthesis and structure of such compounds.

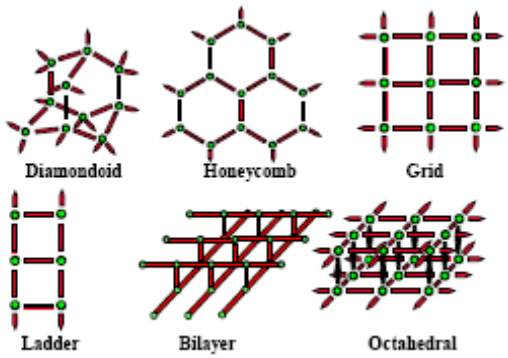

Figure 2. Node-and-spacer representation of several common networks.

These networks include the "bilayer" structure, one of the first metal-organic structures shown to exhibit permanent porosity; grid, diamondoid and octahedral metal-organics are also capable of sustaining porosity. The degree of porosity in such structures is exemplified by [Ni(4,4'-dipyridylethane)$_2$(NO_3)$_2$], which exhibits channels that represent ca. 50% of the volume of the crystal structure.

Porous Anionic Metal-Organic Frameworks -- Hydrogen sorption sites in neutral frameworks are restricted to the organic and inorganic constituents decorating the walls of the pores and thus a large portion of the void space remains unavailable for H_2 uptake. Ability to decorate the pores with additional sorption sites for H_2 will significantly increase the amount of stored H_2 per unit volume making MOFs extremely promising as a storage medium. On the other hand, inorganic porous anionic frameworks, zeolites, have limited hydrogen sorption capacity due to restricted number of extra-framework sorption sites and enlarging their cavities is not typically feasible. Until now, few porous anionic MOFs were known. We have demonstrated the ability to synthesize porous zeolite-like net anionic metal-organic frameworks with extra-large cavities that will permit, for the first time, the combination of intra-framework organic and inorganic H_2 sorption sites (MOFs) and extra-frameworks inorganic ones (zeolites) into a unique complete system. Organic and inorganic additional hydrogen sorption sites are generated by tunable facile ionic exchange.

Synthesis of Zeolite-like Metal-organic Frameworks (ZMOFs) -- Three porous anionic zeolite-*like* metal-organic frameworks (ZMOFs) with extra-large cavities have been synthesized. The ZMOFs were assembled from tetrahedral secondary building units and ditopic organic linkers (4,5-imidazoledicarboxylate, ImDC) having the commensurate angles (Fig. 3C). The cavity volume of the first *rho*-ZMOF (Fig. 3E) is 8 times larger than its rho zeolite analogues (2.96 nm *vs.* 1.4 nm) and contains 48 monovalent cations suitable for H_2 sorption. Different organic and cations have been already successfully introduced in those large cavities by ionic exchange.

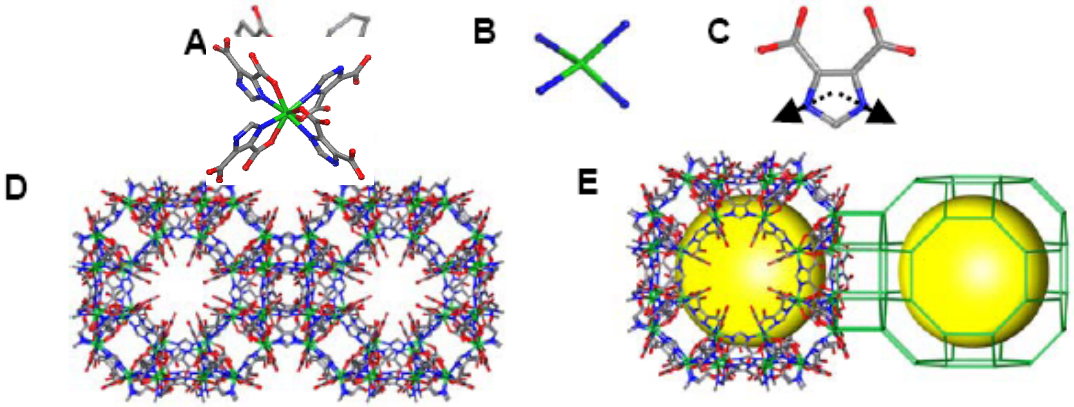

Figure 3. Single-crystal structure of *rho*-ZMOF. (A) eight-coordinated molecular building blocks (MBBs), which can be viewed as a 4-connected node (B), (C) showing the angle in ImDC ligand, linked to indium forming an 8-coordinated cluster (A), (D) a fragment of the porous *rho*-ZMOF. (E) The accessible extra-large α-cavity is illustrated as a yellow sphere.

MOFs with zeolite-like topology based on the assembly of 8- and 4-coordinated SBUs - It is also possible to synthesize zeolite-*like* frameworks based on double four-member rings (d4r) by assembling pre-synthesized *in situ* d4r SBUs (cube-like) with four-connected organic building blocks. Synthetic pathways and experimental conditions have been identified for the *in situ* preparation of eight-coordinated SBUs, namely the anionic $[In(CO_2)_8]^{5-}$

These structures are porous and offer systems where the impact of the framework charge on the hydrogen sorption properties can be explored. *These systems offer the possibility to tune the pore dimension and functionality by utilizing expanded linkers thus possibly increasing the H_2 uptake by augmenting sorption sites on the network.* In addition, for anionic ZMOFs, different cations (Na^+, Li^+, Mg^{2+}…) were introduced by facile ionic exchange.

Relevance to NASA

This project dealt with the design, synthesis, and development of novel tunable porous materials which can store adequate hydrogen and/or reduce the boil off of LH_2. Better hydrogen storage materials would have far-reaching impact -- for example, aerospace technology of the future will depend on the ability to store hydrogen efficiently. For example, during shuttle operation, more LH_2 is consumed on the ground than is used to launch the shuttle into the orbit. If terrestrial LH_2 losses and boil off at KSC could be reduced (or eliminated), NASA's STS fuel bill could be lowered by more than 50%. This challenge can be met by developing novel H_2 storage materials that are safer and more effective for NASA-KSC's ground operations. Our strategy and approach involved the development of tunable porous metal-organic frameworks (MOFs) for H_2 storage.

The results of this project can provide a basis for developing selected metal-organic frameworks as high-capacity hydrogen storage materials for onsite H_2 recovery, purification and storage. In addition, these materials have potential applications in H_2 powered aeropropulsion, especially unmanned aerial vehicles (UAVs) - HALE and solar-powered stratospheric platform airships.

Experimental

Synthesis

All chemicals were used as received from the respective chemical company. Programmable ovens were used to control the heating and cooling rates of the solvothermal reactions in 20 mL scintillation vials.

Hydrogen Sorption Measurements & Modeling

Gravimetric and Volumetric Sorption Measurements -- Gravimetric and volumetric H_2 sorption isotherms were measured for MOFs proposed in this project. The volumetric sorption apparatus was used to measure H_2 uptakes at 77K and derive the energetics of the adsorption processes.

Inelastic Neutron Scattering (INS) Measurements --The INS experiments observe the rotational ground state splitting of the sorbed H_2 molecule, which is an extraordinarily sensitive measure of the guest-host interaction at the sorption site. We can thereby deduce information on the H_2 sorption sites and their interaction energies with the cationic or other framework species. No other experimental technique can provide this level of detail regarding the sorbed H_2 interaction with the host material, especially when combined with computational methods detailed below. The INS measurements were carried out on the Quasielastic Neutron Spectrometer (QENS) at the Intense Pulsed Neutron Source (IPNS) of Argonne National Laboratory (ANL). The combined use of inelastic neutron scattering and computational studies help in developing an understanding of the interactions during hydrogen sorption for different intra-framework and extra-framework cations.

Computational Studies -- To gain a deeper understanding of the factors that control H_2 adsorption in our new and proposed MOFs, the atomistic simulations of extant and proposed MOFs was pursued to identify and refine candidate hydrogen sorption sites and sorption interaction mechanisms. Extended ensemble molecular dynamics and Grand Canonical Monte Carlo (GCMC) simulations were performed. These techniques permit the calculation of relevant observables like sorption isotherms and gas diffusion coefficients while providing a full picture of the structure and dynamics of the process including detailed thermodynamic data. Molecular dynamics methods provide structure and dynamics directly while the GCMC simulations are performed at a fixed chemical potential with variable hydrogen loading and can thus determine equilibrium hydrogen sorption capacities. The theoretical methods provide molecularly detailed insight that cannot be achieved experimentally while still making direct connection with experimental observables (this serves to validate the theoretical models). The connection with INS experiments is established by analyzing the rotational potential experienced by the sorbed H_2 molecule at each likely binding site, and calculating the associated rotational energy levels of the quantum rotator. The resulting transitions can then be directly compared with the INS experimental results. As such, the simulations are critical in rationally designing better MOFs and in discovering design principles that can then be tested experimentally – *the experiments then spur new molecular simulations in the iterative design and evaluation process.*[2]

The theoretical methods require accurate potential energy interaction models for and between the MOF and H_2. A force field has been developed, building on existing potential models that

enables us, for example, to predict adsorption isotherms for these systems. The approach is similar to the one used to develop computational models for halocarbons in zeolites, with the additional complication that appropriate force field terms must be added to describe the direct binding of dihydrogen to metals.[2]

Results and Discussion

MOFs Based on Metal-Nitrogen Ligands

MOFs based on metal-nitrogen ligands were synthesized and tested for their hydrogen sorption uptake at 77K. The tested MOFs based on metal-nitrogen ligands showed low hydrogen sorption uptake, below **0.8 %** per weight, of the fully evacuated porous material. The low uptake can be attributed to the flexibility of MOFs based on flaccid single-metal ion and nitrogen coordination bonds.

MOFs Based on Metal-Carboxylate Ligands

Novel porous MOFs based on metal-carboxylate ligands were synthesized and fully characterized. The hydrogen sorption uptake at 77 K on two compounds showed the highest uptake compared to all reported crystalline porous materials in the open literature at the time of their synthesis. The first MOF (ME087, Fig. 4) can store at atmospheric pressure and 77K up to **2.6%** of hydrogen per weight (28mg of H_2/ g of MOF, Figure 5).

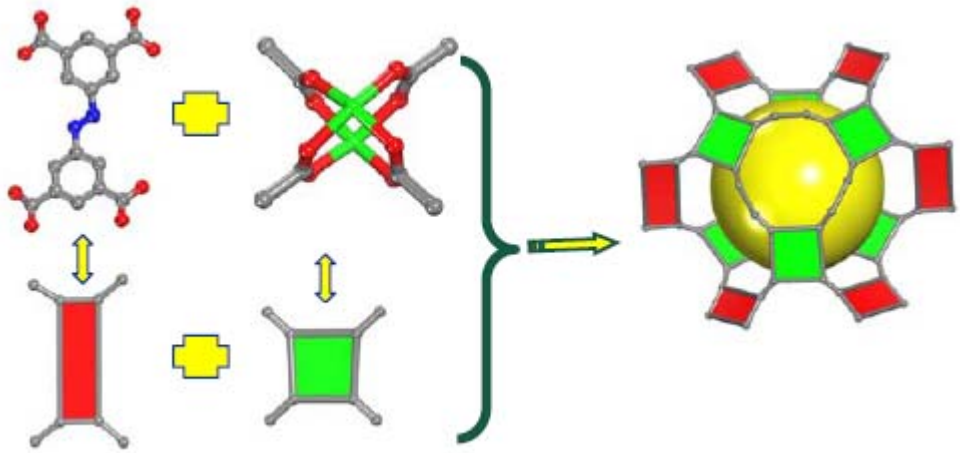

Figure 4. The structure of ME087 constructed from 4-connected building blocks (green, copper; gray, carbon; red, oxygen; blue, nitrogen).

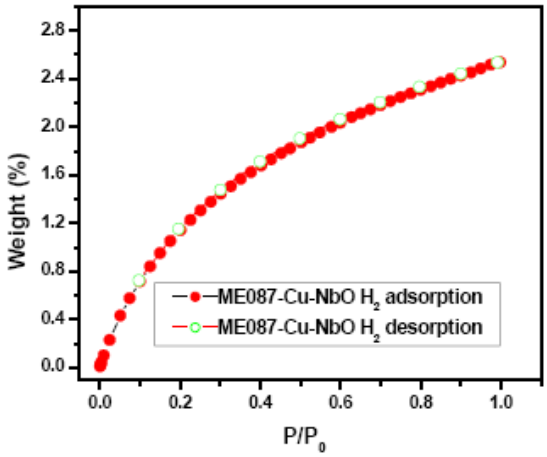

Figure 5. The hydrogen sorption isotherm @ 77K on ME087. Maximum uptake is 2.6% per weight.

Another MOF (ME080, Fig. 6) can store at atmospheric pressure and 77K up to **2.8%** of hydrogen per weight (28mg of H_2/ g of MOF, Fig. 7). The isosteric heats adsorption for ME080 were evaluated by performing hydrogen sorption at two different temperatures specifically 87K and 77K and estimated to be Q_{st} = 6.5 kJ/mol.[1]

.

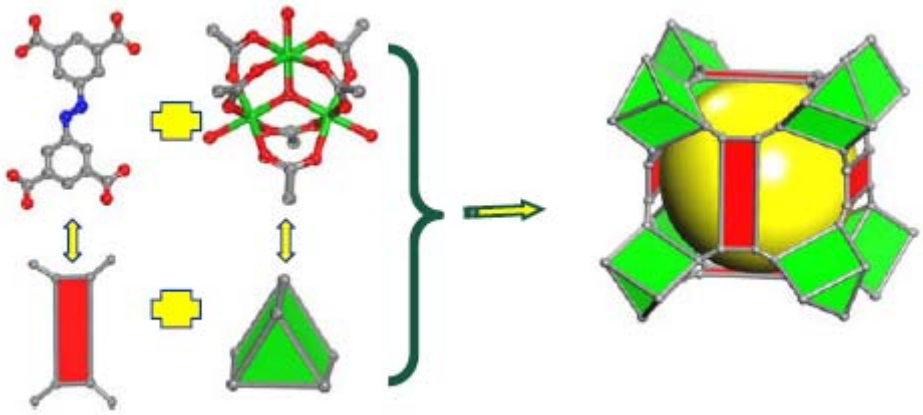

Figure 6. The structure of ME080 constructed from 4-connected and 6-connected building blocks (green, indium; gray, carbon; red, oxygen; blue, nitrogen).

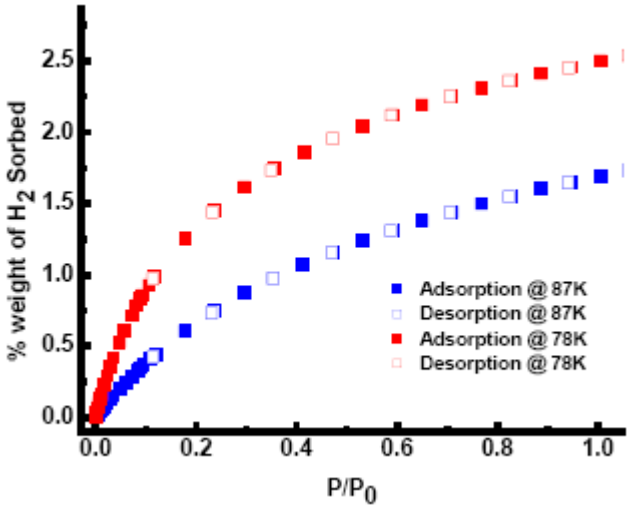

Figure 7. The hydrogen sorption isotherm @ 77K and 87K on ME080. Maximum uptake is 2.8% per weight at atmospheric pressure and 77K.

Recently, we have also discovered that metal-organic polyhedra, specifically metal-organic cubes (MOCs), may serve as candidates for hydrogen storage (up to 2.15 wt. % H_2 at 77K). The MOCs are composed of the same starting materials as the *rho*-ZMOF (Fig. 8), although there are several different packing arrangements of the cubes (Fig. 9) to give an array of crystal structures with varying hydrogen sorption.

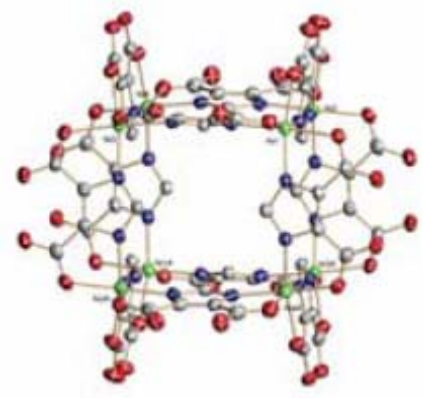

Figure 8. Structure of the $[M_8(HImDC)_{12}]^{8-}$ cube (MOC-1) showing 30% probability ellipsoids.

Reactions between 4,5-dicyanoimidazole (4,5-DCIm) and $In(NO_3)_3 \cdot 5H_2O$ have lead to the synthesis of two forms of MOCs, namely MOC-2 and MOC-3, that have different packing modes, based on the different experimental conditions/guest molecules that lead to the formation of the two compounds. For each cube, there are twelve independent ImDC ligands, generated *in situ*, that coordinate to eight In^{3+} ions with octahedral geometry, through N-, O-hetero-chelation.

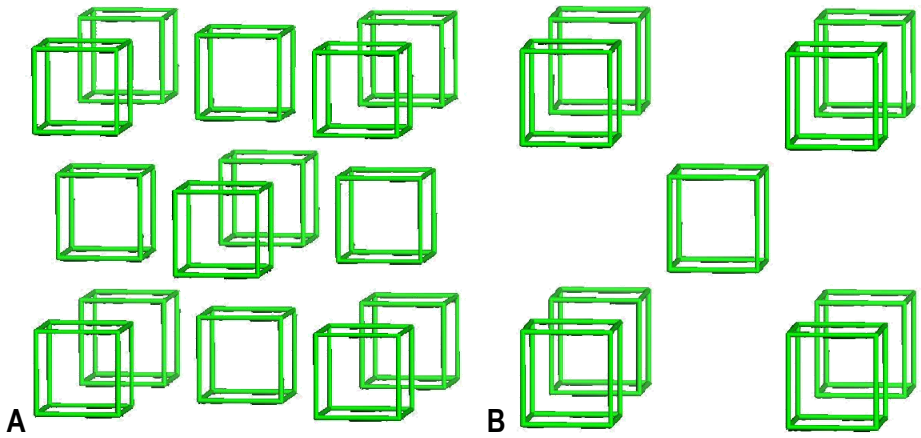

Figure 9. (A) FCC packing mode in MOC-3; (B) BCC packing mode in MOC-2.

In the case of MOC-3, the imidazole-based ligand is singly protonated, intramolecular O-H···H hydrogen bonding interactions existing between the carboxyl groups on each ligand (2.815Å), giving rise to an overall neutral MOC. Since there are no other guest molecules present to balance the assembly, the packing efficiency is higher than in the case of MOC-2, namely cubic closed-packed, or face-centered cubic (FCC), in an ABCABC fashion arrangement as seen in Fig. 9A. The cubes are connected edge to egde *via* weak intermolecular interactions, C-O···O (3.824 Å).

In the case of MOC-3, the N_2 uptake at 77K reveals an estimated Langmuir surface area of 584 $m^2 \cdot g^{-1}$ and a pore volume of 0.2129 $cm^3 \cdot g^{-1}$; also, an approximate value of 0.95 % weight H_2 was noted for studies at 77K. From the hydrogen adsorption isotherms measured at 77K and 87K, the isosteric heat of adsorption was determined to have a value of 7.2 kJ/mol. As expected, the more efficient packing encountered in MOC-3 leads to lower values of the amounts of gas adsorbed compared to MOC-2.

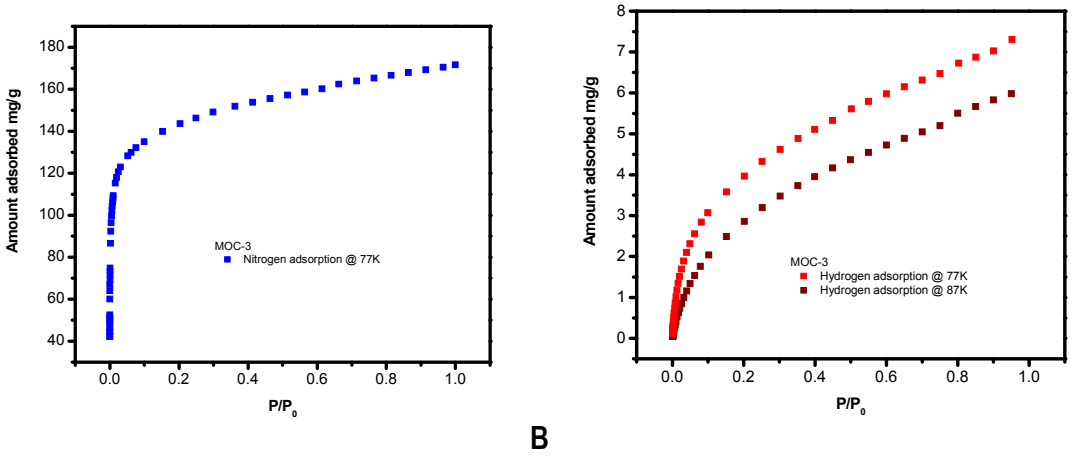

Figure 10. (A) Nitrogen adsorption isotherm for MOC-3 @ 77K; (B) Hydrogen adsorption isotherm for MOC-3 @ 77K and 87K.

In the case of MOC-2, the organic ligand is doubly protonated, intramolecular O-H···H hydrogen bonding interactions existing between the carboxylic groups on each individual ligand (2.707 Å). Therefore, deprotonation occurs only for the N-H on the imidazole ring, giving rise to an overall 12^+ charged structure. The charged framework is balanced by 12 nitrate ions, which are statistically distributed in-between the cubes. The crystal structure (Fig. 11A) reveals that the cationic cubes are connected vertex to vertex via intermolecular C-O···H hydrogen bonding (2.707Å), to generate a 3D framework that resembles the zeolite ACO topology (Fig. 11B), the packing mode being in a body-centered cubic (BCC) fashion.

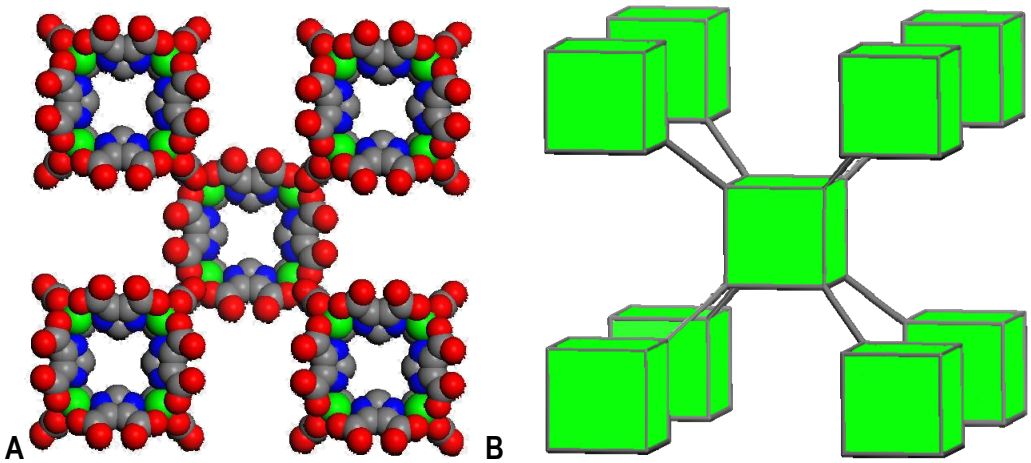

Figure 11. (A) Hydrogen bonding at the vertices of MOC-2 results in a 3D framework, which, (B) when the cubes are connected, results in a network with a zeolite-*like* topology (*pcb*, zeolite ACO).

In the case of MOC-2, the N_2 adsorption/desorption studies at 77K revealed a reversible type I isotherm (Fig. 12A), characteristic to microporous materials. The apparent estimated Langmuir surface area being 1420 $m^2 \cdot g^{-1}$ and a pore volume of 0.5145 $cm^3 \cdot g^{-1}$. Hydrogen storage investigations revealed that the MOC-2 stores approximately 1.9 % weight H_2 when the sample was outgassed at 25˚C (Fig. 12B). By raising the degassing temperature to 135˚C, there is an increase in the amount of hydrogen adsorbed to approximately 2.15 % weight H_2. It can be speculated that at higher temperatures more space is available, since some of the guests may be removed and potentially favor the gas diffusion. All isotherms show no hysteresis upon desorption. The isosteric heat of adsorption, Q_{st}, was calculated from the hydrogen adsorption isotherms measured at 77K and 87K, having a value around 6.5kJ/mol, for the sample outgassed at 135˚C.

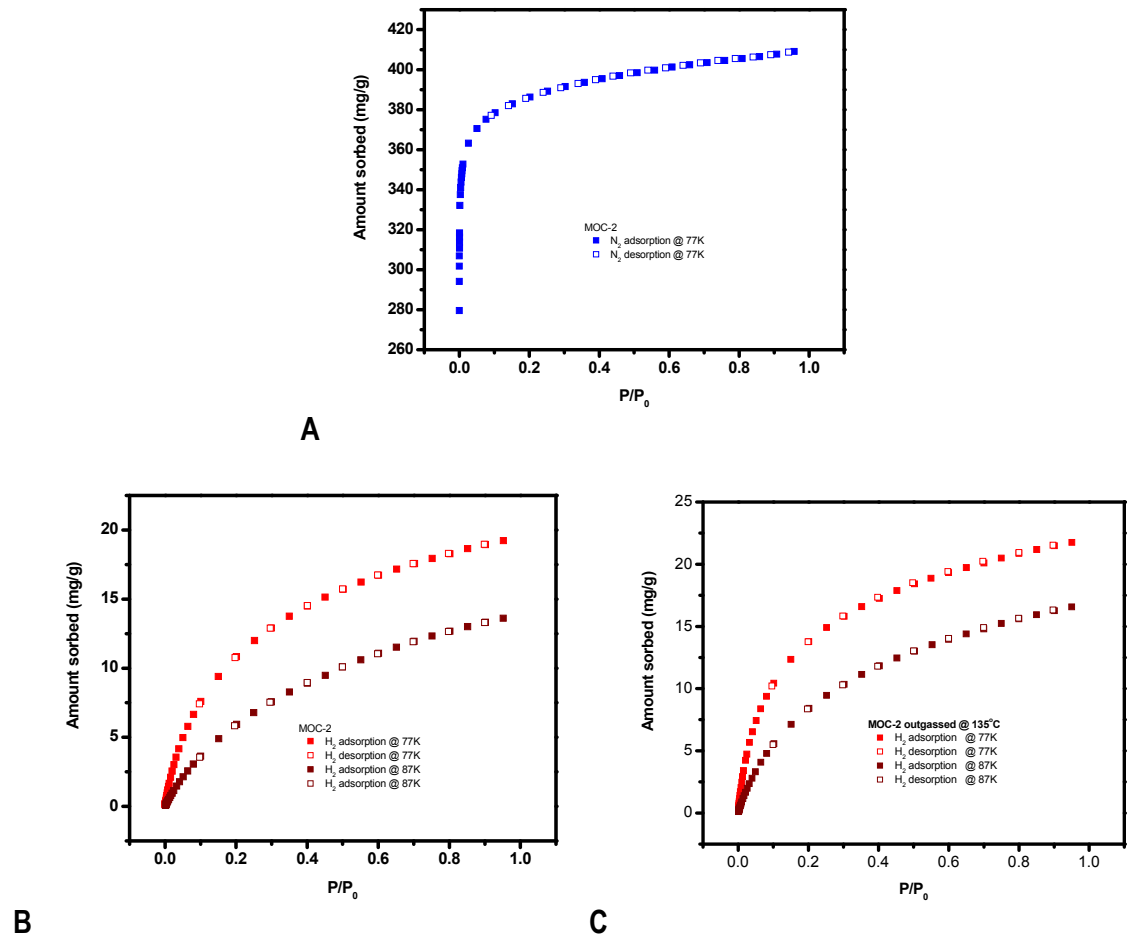

Figure 12. (A) Nitrogen sorption isotherm for MOC-2 at 77K; (B) Hydrogen sorption isotherm for MOC-2 at 77K and 87K (sample outgassed at 25˚C); (C) Hydrogen sorption isotherm for MOC-2 at 77K and 87K (sample outgassed at 135˚C).

Based on the experimental values that we obtained, we can state that, to the best of our knowledge, MOC-2 exhibits the highest porosity amongst all molecular metal-organic polyhedra reported to date, and one of the highest values amidst the hydrogen uptake for metal-organic frameworks. MOC-2's excellent capabilities in terms of adsorption properties can be attributed to the stability of the compound while maintaining its efficient packing mode even upon dessolvation, as indicated by the sorption isotherms. Further studies are necessary to analyze in depth the dependence between the temperature at which the sample is degassed and the enhancement of the gas adsorption.

Synthesis and Characterization of Zeolite-like MOFs (ZMOFs)

Three types of zeolite-*like* MOFs (*rho*-ZMOF, *sod*-ZMOF, and *usf*-ZMOF) were synthesized and fully characterized. Their surface area and pore volume were evaluated from the nitrogen sorption isotherms at 77K. The hydrogen sorption capacity for the as-synthesized *rho*-ZMOF and *sod*-ZMOF and their cation exchanged derivatives were evaluated at 77K. The *rho*-ZMOFs show an uptake of H_2 at atmospheric pressures and 77K of up to ~1.2% per weight (Fig. 13B).

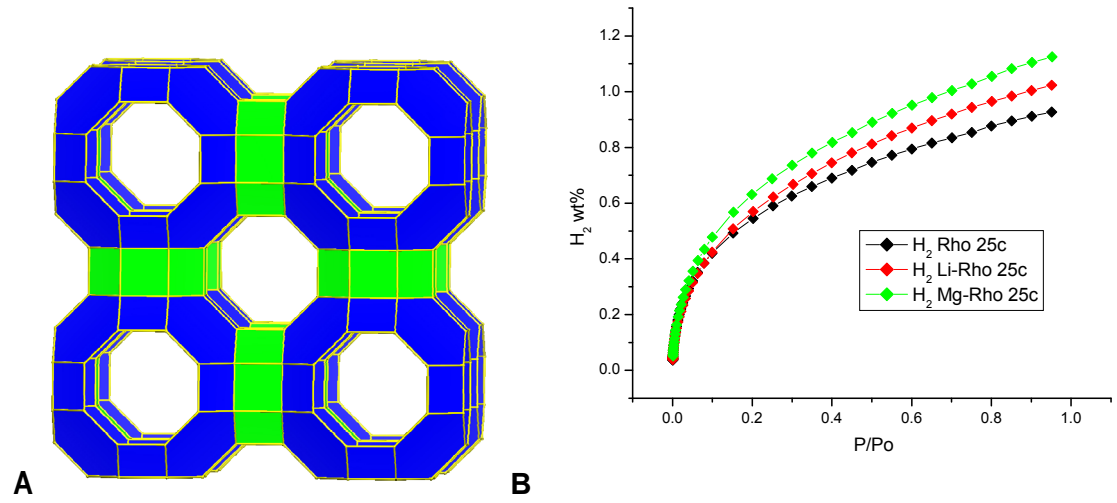

Figure 13. (A) Illustration of *rho*-ZMOF with the eight-member windows open; (B) The hydrogen sorption isotherms @ 77K on DMA-*rho*-ZMOF, Li-*rho*-ZMOF, and Mg-*rho*-ZMOF (all outgassed @ 25°C). Maximum uptake is 1.2% per weight at atmospheric pressure and 77K.

As synthesized *rho*-ZMOF (DMA-*rho*-ZMOF, where DMA indicates the dimethylammonium cations generated *in situ*) can easily undergo ion exchange; the cavities (and cation within) are accessible through eight-membered ring windows, as indicated in Fig. 13A. The DMA molecules were exchanged with lithium and magnesium cations. The three compounds were then washed with a volatile solvent (acetonitrile) to remove any residual water or ethanol molecules and excess metal salt. The isotherms of hydrogen recorded after complete outgassing of the materials @ 25°C under vacuum. It was found that the Mg-*rho*-ZMOF can store more H_2 molecules per indium at 1atm than Li-*rho*-ZMOF, and Li-*rho*-ZMOF can store more than DMA-*rho*-ZMOF (Fig. 13B).

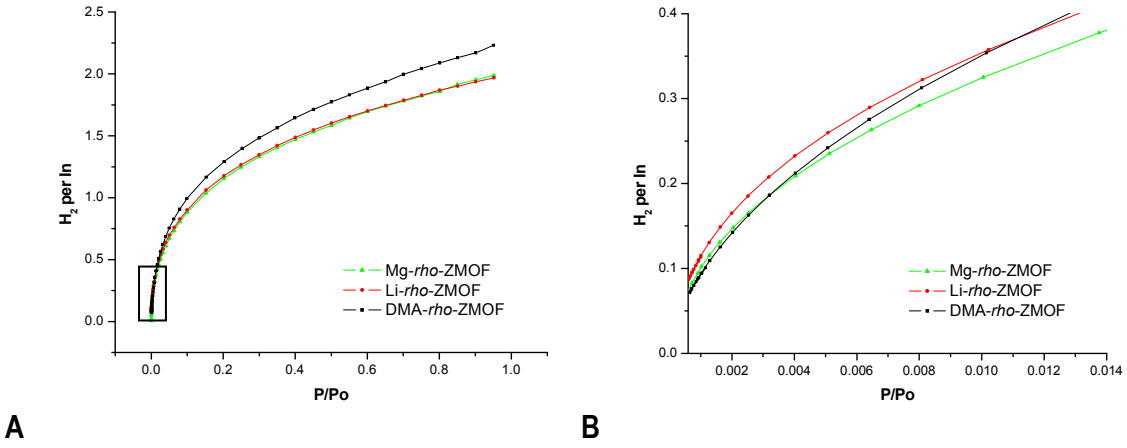

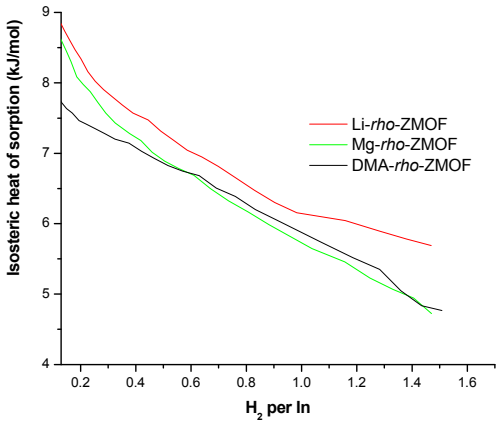

C

Figure 14. (A) The hydrogen sorption isotherms @ 77K on DMA-*rho*-ZMOF, Li-*rho*-ZMOF, and Mg-*rho*-ZMOF(all outgassed @ 115°C), *x* axis is listed as H_2 per In to help determine loadings for INS studies; (B) An enlarged view of the boxed region in (A) for the hydrogen isotherms at low pressures; (C) The isosteric heats of adsorption for all three compounds.

In order to eliminate most guest water molecules, which is necessary for INS studies, the compounds were also outgassed at 115°C. The resultant sorption studies (Table 1) indicate that now the parent framework can store more H_2 molecules per indium at 1atm than the cation exchanged materials, Li-*rho*-ZMOF and Mg-*rho*-ZMOF (2.23, 1.99, 1.97 respectively). However, at pressures below 0.02 atm, the phenomenon is inverted, the Li-*rho*-ZMOF and Mg-*rho*-ZMOF isotherms seem to be sharper than the parent compound isotherm. Indeed, the highest heats of adsorption value calculated was for Li-*rho*-ZMOF (9.1 kJ/mol); the heat calculated for Mg-*rho*-ZMOF was 9 kJ/mol, and for the parent DMA-*rho*-ZMOF the heat was lower than both exchanged frameworks: 8.3 kJ/mol.

Table 1. Sorption data on *rho*-ZMOFs after outgassing @ 115°C.

	DMA-*rho*-ZMOF	**Mg-*rho*-ZMOF**	**Li-*rho*-ZMOF**
H_2 Gravimetric uptake wt%	0.951	0.912	0.914
H_2 Volumetric uptake kg/m^3	11.966	10.731	10.558
Density g/cm^3	1.259	1.176	1.154
Surface area m^2/g	~850	~850	~850
H_2 molecules / In at 0.95 atm:	2.23	1.99	1.97
Heat of sorption kJ/mol Lowest coverage	8.3033	9.0	9.1170

Several studies on inorganic zeolites showed that the lithium or magnesium cations are not very accessible to hydrogen molecules; nevertheless, for *rho*-ZMOFs the heats of adsorption calculation, along with the isotherm at low pressures, demonstrate the fact that Mg^{2+} and Li^{+} are

responsible for higher H_2-extra-framework cations interactions. The high diffusibility of cations in inorganic zeolites is known, which potentially results in cations interacting with the framework, blocking some potential hydrogen interaction sites present in the DMA framework (DMA, an organic molecule, has minimal interaction with the framework). This results in higher enthalpy over the entire pressure range for Li-*rho*-ZMOF and Mg-*rho*-ZMOF, but at the same time the capacity in wt% or H_2/In is lower at atmospheric pressures as compared to DMA-*rho*-ZMOF.

Table 2. Sorption data on *sod*-ZMOFs after outgassing @ 115°C.

	HIm-*sod*-ZMOF	**Mg-*sod*-ZMOF**	**Li-*sod*-ZMOF**
H_2 Gravimetric uptake wt%	1.02	1.11	0.635
H_2 Volumetric uptake kg/m^3	17.09	16.517	9.3
Density g/cm^3	1.676	1.482	1.464
Surface area m^2/g	539.6	540	319.1
H_2 molecules / In at 0.95 atm:	2.49	2.41	1.35
Heat of sorption kJ/mol Lowest coverage	8.156	8.034	8.31

As synthesized *sod*-ZMOF (HIm-*rho*-ZMOF, where HIm indicates the protonated imidazole cations generated *in situ*) can also easily undergo ion exchange. The HIm molecules were exchanged with lithium and magnesium cations. The three compounds were then washed with a volatile solvent (acetonitrile) to remove any residual water or ethanol molecules and excess metal salt. The isotherms of hydrogen recorded after complete outgassing of the materials @ 115°C under vacuum. The results are listed in Table 2, and INS studies are pending.

Inelastic Neutron Scattering Studies

We submitted three proposals to carry out experiments at ANL a nd both of them were granted with full access to QENS instrument for three full weeks. Since January 2005, we visited the IPNS facility four times and we were able to test five samples namely ME080, MOC-2, and *rho*-ZMOFs (as-synthesized and Li^+ and Mg^{2+} exchanged).

ME080 (2.8% per weight at 78K) - There appear to be as many as three sets of bands corresponding to 0-1 transitions for weakly bound H_2. The corresponding 1-2 transitions are evidently contained in a broad band at low frequency near 3 meV. A well-defined peak at 25.5 meV may possibly be attributed as the 0-2 transition for H_2 at a site with much higher barrier, which would likely be the vacant In coordination site. The corresponding 0-1 transition would according to our model be attributed to a broad intensity maximum at 4.8 meV if the molecule were physisorbed at the In site. This assignment is supported by the fact that the intensities of the respective peaks does not increase with further hydrogen loading, i.e. that all the vacant In sites are filled at the lowest loading ($1H_2$/In) we used. We can make some inferences about the nature of the binding sites from our study of the dependence of the INS spectra on H_2 loading. The principal effect of going to three molecules hydrogen per In is to increase intensities of the strong bands around 12.8 and 14 meV, i.e. increasing the population of the sites associated with the respective set of rotational transitions.[1]

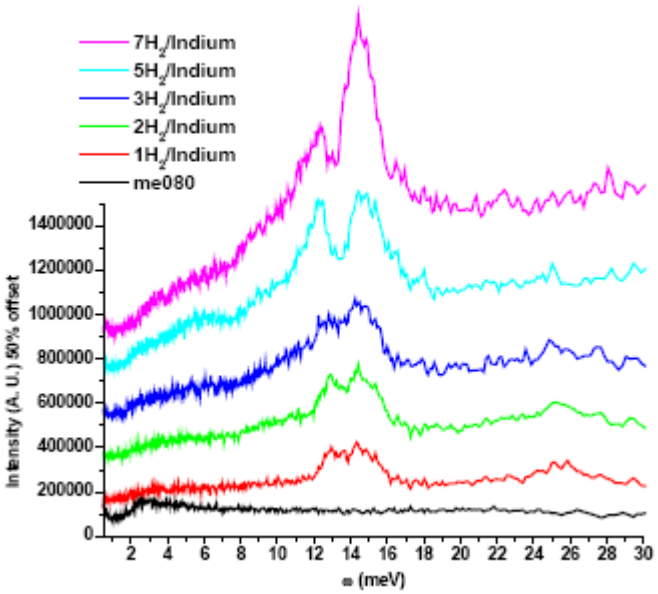

Figure 15. INS spectra of ME080 at different loadings of H_2.

We observe a remarkable effect when the loading is further increased to 5 H_2/In, which corresponds to saturation at 77Kand 1 atm of H_2. A pronounced increase in intensity at lower energies signals to occupation of as many as three new binding sites with stronger interactions at these higher loadings. This is in contrast to what has been observed previously in MOF's, where it is mainly sites with weak guest/host interaction that are populated at the highest loadings. We may speculate that at these loadings in ME080 sites with some steric hindrance become available upon dynamic interactions (*i.e. pushing and shoving*.) between the H_2 molecules.[1]

MOC-2 (2.15% per weight at 77K) -- Preliminary data: The three INS spectra with the "blank" run subtracted are shown in Fig. 16. The features in this spectrum are all rather broad when compared with those in MOF-5, for example, which indicates the presence of a rather substantial adsorption site heterogeneity. The identifiable peaks in the INS spectra were assigned on the basis of the same model previously used by us[1]. We also note that there is a very broad "background" underlying the INS spectra, which increases in intensity as a function of hydrogen loading. This part of the spectrum is likely to arise from random, or non-specific site adsorption of H_2 on interior surfaces lined by O atoms, as has been observed in many cases for H_2 in zeolites. At the lowest loading of 1 H_2/In the INS spectrum consists of strong peaks at 11 meV and 14 meV, where the former is accompanied by weaker shoulders at 10 and at 11.7 meV. Under the assumption that these transitions are between the two lowest levels of the hindered rotor ("0-1"), we can assign both the 0-2 and 1-2 transitions from the experimental spectrum for four separate binding sites.

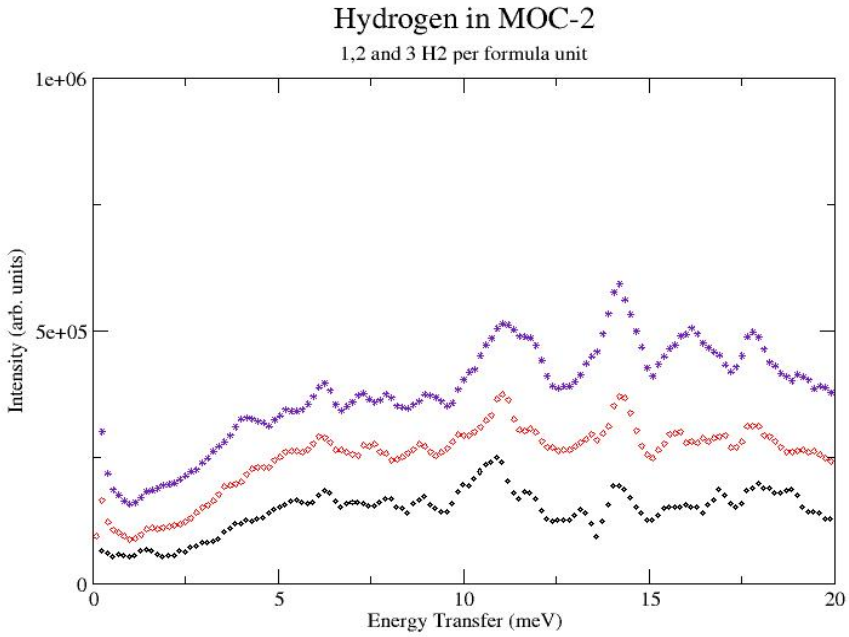

Figure 16. INS spectra of MOC-2 at different loadings of H_2.

In analogy with previous work, we attribute the main peak at 11 meV along with the low- and high energy shoulders to binding sites around the octahedral In cluster. The InO_3N_3 octahedron may be viewed as having four different binding sites on the eight triangular faces faces with, respectively, OOO, NNN, NOO and ONN atoms in the corners. However, not all of these faces can be occupied by a hydrogen molecule, namely those facing the inaccessible small cavity, and the one with three O atoms which form H-bonds with neighboring cubes. We may assume that the binding energies for the remaining available sites on the octahedraon are sufficiently similar for the transitions of hydrogen on all these can be assigned to this band between 10 and 12 meV. We note that these sites appear to bind hydrogen slightly more strongly than those around the In carboxylate trimer building block in ME080 (0-1 transition at 12.8 meV)[1], except for the open binding site on the In in the latter material. Peaks associated with hydrogen sorbed at such a site are indeed absent in MOC-2, as the In is fully coordinated in this case.

The broad band at 14 meV falls into the energy range we have previously assigned to binding sites around organic linking groups. When the hydrogen loading is increased to 2 and 3 H_2 per formula unit, we observe mainly increases in intensity of existing bands, i.e. changes in the occupancy of the sites described above. It therefore appears that most of the available binding sites for hydrogen in this material have at least partial occupancy at the lowest loading used. The reason for this is that the binding energies at the various sites do not differ to a great extent, so that sole occupancy of the most attractive site by the hydrogen molecules cannot be achieved as the temperature is lowered, and the molecules lose kinetic energy. This type of multiple site occupancy at low hydrogen loading has, in fact, been commonly observed in other related porous materials.

Close inspection of the intensity changes in the band centered at 11 meV reveals that much of the increase as a function of loading is in the shoulders of this peak. Both the hydrogen molecules already present on the faces of the octahedron and those added at higher loadings

may rearrange and this produce increases in intensities in different parts of this band. We also note that many of these sites may not be accessible as the highest total loading in this material at 1 bar is far below (4.6 H_2) the value of 8 H_2/In that could, in principle, be possible. It is instructive to refer the loading dependence of the INS spectra to the measured adsorption isotherms and corresponding isosteric heats of adsorption. In the steep portion of the isotherms more cluster sites are being filled up to the region between 1 or 2 H_2/In where the slope of the isotherms decreases, at which point more sites on the link are becoming occupied with the result that the average value of Q_{st} for the system decreases.

We may conclude that overall high capacity of this material has its origin in the large number of relatively strong binding sites about the octahedral In cluster combined with small pore sizes, and that the ratio of the number of sites around the cluster to that of the weaker sites around the imidazole must be higher than that in comparable systems. This is borne out by the intensity changes in the INS spectra where we find a continuous increase in cluster site occupation along with those on the imidazole to the highest loadings used.

rho-ZMOFs (1.2% per weight at 77K) -- Preliminary data: the most important feature of this class of material is the fact that the mean energy of 5 meV for the rotational 0-1 transition for hydrogen in this material is considerably lower than what has been observed for *ALL* metal-organic neutral framework compounds studied to date by this technique as well as for all carbon materials (e.g., activated carbons, SWNT's, carbon fibers). This indicates that the binding of hydrogen in the present ANIONIC metal-organic framework compound is significantly enhanced by the interaction of the H_2 molecule with the ionic framework, and the electrostatic field in the cavity.

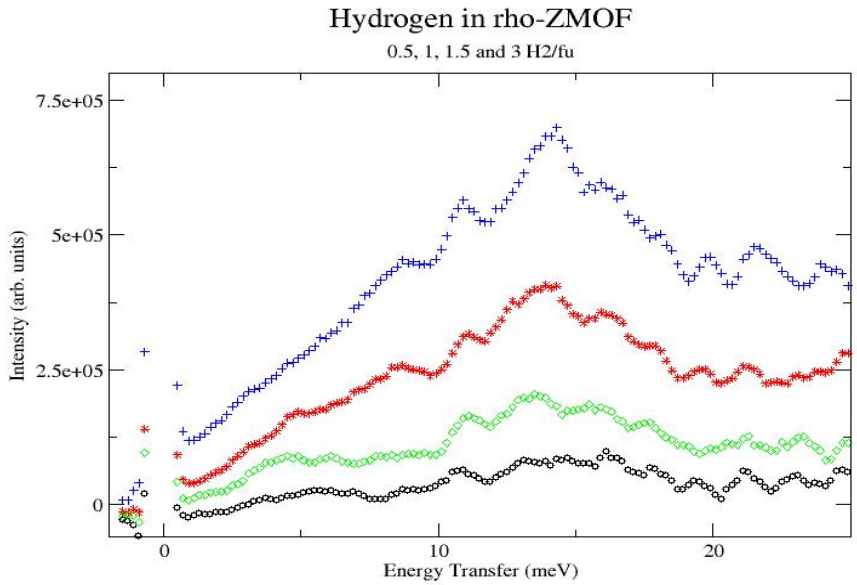

Figure 17. INS spectra of DMA-*rho*-ZMOF at different loadings of H_2.

The INS spectra for each sample with the "blank" run subtracted are shown in Figs. 17-19. Peaks in the INS spectra were assigned on the basis of the same model previously used by us[1], namely that of a hindered rotor with two angular degrees of freedom in a simple double-minimum potential. In the absence of a barrier to rotation the lowest transition is that between para- and ortho H_2 and it occurs at 14.7 meV (or 119 cm^{-1}, = 2B).

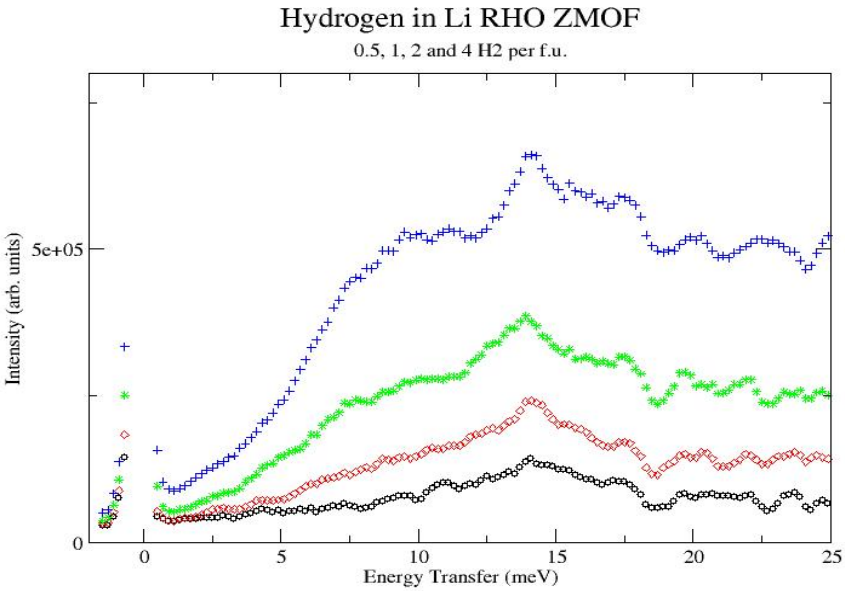

Figure 18. INS spectra of Li-*rho*-ZMOF at different loadings of H_2.

The interaction of the sorbed hydrogen molecule with the host material gives rise to a barrier to rotation which in turn partially lifts the degeneracy of the J=1 level. The lowest transition frequency for the hindered rotor (between the J=0 and the J=1, m_J=0 states, which we subsequently refer to as the "0-1" transition) decreases approximately exponentially with increasing barrier height (rotational tunnel splitting) and is thereby extraordinarily sensitive to small differences in barrier height.

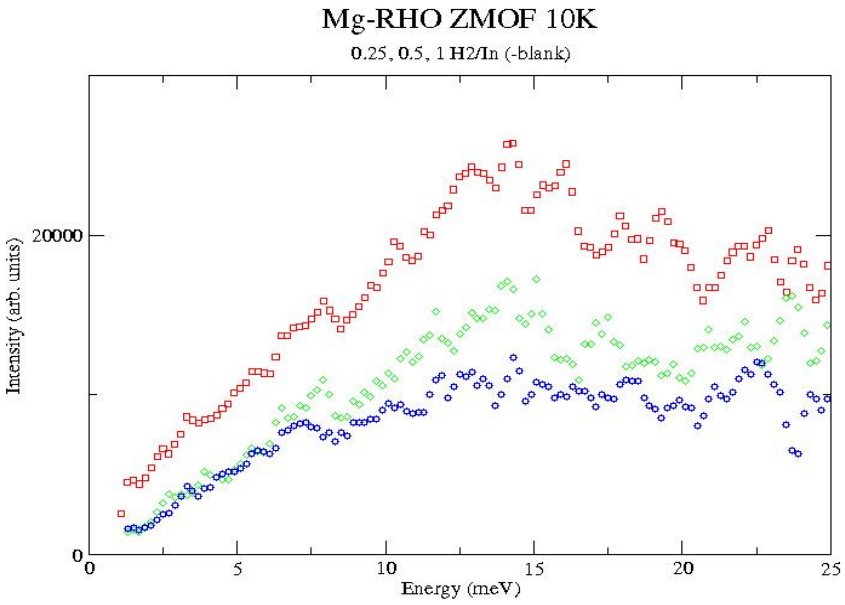

Figure 19. INS spectra of Mg-*rho*-ZMOF at different loadings of H_2.

Our results on hydrogen sorbed in *rho*-ZMOFs clearly demonstrate the importance of having a charged framework to strengthen the interaction of adsorbed hydrogen with the host material. This approach is crucial to the effort to lower pressures of sorbed hydrogen storage systems at room temperature to a point where these may be considered practical provided that the capacity is sufficiently high.

Computational Studies on Selected MOFs

To model a novel MOF material, we established a structure and force field to begin our sorption studies. A candidate MOF was chosen with a known crystal structure and experimentally demonstrated large hydrogen storage capacity. The crystal structure positions were used for initial coordinates of the simulations. The crystal lattice was treated as rigid and dihydrogen was treated explicitly. In order to obtain a reliable electrostatic potential surface, a representative segment of the MOF (shown in Figure 20) was chosen and *ab initio* calculations were performed using the GAMESS package.[2]

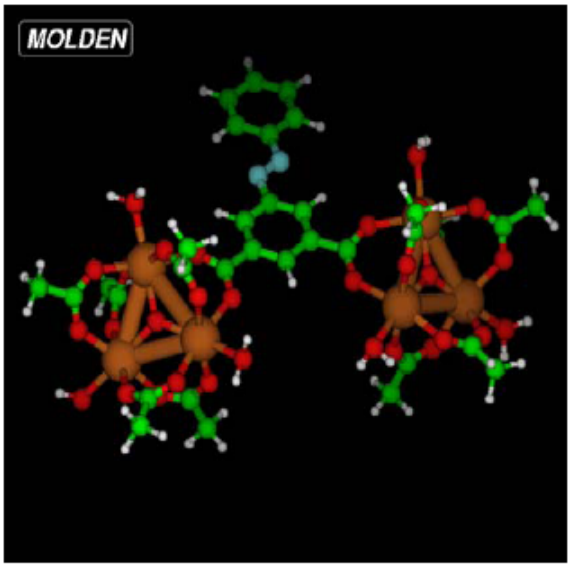

Figure 20. A small representative segment of the MOF studied. Green=carbon, red=oxygen, white=hydrogen, blue=nitrogen, and brown=indium.

A 6-31G*/SBKJC basis sets was used that handles the Indium ions using a semi-relativistic (ECP) pseudopotential and the standard 6-31G* basis set for all other atoms. The 6-31G* basis was chosen for its over estimation of the (gas phase) charges (fit to reproduce the electrostatic potential surface); using over polarized charges accounts, on average, for condensed phase polarization effects. In testing, both the SBKJC and LANL2DZ basis sets were employed in treating indium and gave very similar results. The charges used in MD were the result of averaging the derived charges of chemically equivalent atoms from the fragment in Figure 20. To complete the force field, intermolecular (repulsive and dispersion) parameters were taken from the AMBER forcefield where available and then from Jorgensen's OPLS database.[2]

Intermolecular gas-framework interactions, following Garberoglio, et al., Lennard-Jones parameters calculated via Lorentz-Bethelot mixing rules. With a complete force field in hand we have begun microcanoncial molecular dynamics (MD) simulations to determine important hydrogen-MOF interaction sites. We plan to proceed to also calculate sorption isotherms using extended ensemble, Grand Canonical Monte Carlo simulations. Simulations will be conducted

as a function of temperature to probe the underlying potential energy landscape that controls hydrogen sorption. Using the insights gained from the MD simulations we will then proceed to suggest potential chemical modifications to increase sorption capacity.[2]

Patents, Publications, Presentations and Students from Research

PIs of this proposal intend to pursue the proposed research in this project. A proposal submitted to the DOE (October 4, 2006) was declined, but a second has been funded by the DOE (DE0FG02-07ER4670).

See references for publications.

References

1. Y. Liu, J. F. Eubank, A. J. Cairns, J. Eckert, V. Ch. Kravtsov, R. Luebke and M. Eddaoudi "Assembly of metal-organic frameworks based on indium trimer building blocks: A novel porous MOF with unprecedented *soc* topology and high hydrogen storage", *Angew. Chem. Int. Ed.* **2007**, *46*, 1-7.

2. Belof, J. L.; Stern, A. C.; Eddaoudi, M.; Space, B. "On the mechanism of hydrogen storage in a metal-organic framework material", *J. Am. Chem. Soc.*; (Article); **2007**; *129*(49); 15202-15210.

October 2007

Surface Acoustic Wave (SAW) Sensors for Hydrogen and Other Gas Detection

V. Bhethanabotla
University of South Florida

Research Period: September 2002 to September 2007

Summary

Sensitive, selective, fast-responding, low-power, and robust sensors for hydrogen and other gases are necessary for safety of the shuttle mission, space exploration and terrestrial applications such as in the hydrogen fuel economy and chemical process monitoring. Acoustic wave devices have been known for the past decade or so in sensor applications, and are capable of meeting the above requirements, as well as are capable of providing passive, wireless, operation. To achieve these goals however, advances in device fabrication, wireless communication, packaging and sensing materials are necessary. This research has focused on advances in sensing nanomaterials and novel devices to achieve hydrogen and organic vapor sensors at room temperature that have been demonstrated to be superior in sensitivity, response-time and robustness in comparison to existing technologies. Future research along these lines is being conducted to yield commercially viable sensors.

Background

Design, construction and testing of inexpensive, solid-state sensors that respond sensitively, selectively, and rapidly to hydrogen and other gases is the motivation for this research. Specifically, such sensors for hydrogen detection are of interest to NASA, and to the hydrogen-based economy that holds current promise for automotive transportation and other terrestrial uses.

To achieve the specific objective of such a hydrogen sensor, our research took an approach that combines the somewhat developed surface acoustic wave (SAW) transducer technology (Ballantine *et al.,* 1997) with nanomaterial sensing layers. Solid-state SAW devices are mass produced in current cell phone, TV and other radio frequency uses, and a suitably designed hydrogen sensor can be similarly produced inexpensively. They also lend themselves to wireless interrogation, and a passive, non-power consuming SAW sensor that can be wirelessly interrogated for gas concentration is a distinct possibility in the near future.

Nanomaterials hold the promise of producing sensing materials for SAW devices that can lead to enhanced selectivity, sensitivity and speed of response. While there is substantial recent literature lending support to these assertions, we only point to the relevant ones for hydrogen sensing. Thus, Penner and co-workers have demonstrated Pd nanowire hydrogen sensors that showed milli-second to second response times (Walter *et al.*, 2002, Favier *et al.,* 2001), and Dai and co-workers have demonstrated similarly effective hydrogen sensors with Pd-coated single walled carbon nanotubes (SWNTs) (Kong *et al.*, 2001). Lowering the limits of detection, development of more robust fabrication processes than are possible in these nano-sized devices, improving and achieving selectivity, and transferability of the techniques to sensors for other gases were our motivations to utilize these nanomaterials in our SAW-based sensors, starting from the groundwork laid by these recent researchers.

Most hydrogen sensors utilize the enormous capacity of Pd to absorb hydrogen, however, several issues of reaction kinetics, mechanical stability, and reversibility are present with Pd-based hydrogen sensors. Metal oxides have been utilized as successful alternatives, which have required high (400+ ºC) temperatures for effective operation, which in turn requires higher power to operate.

Our approach is to leverage the mass, electroacoustic and elastic response mechanisms of SAW devices (Ballantine *et al.*, 1997), with the advantages afforded by the nanomaterials of Pd-alloys as sensing layers. We aimed to construct field devices in using suitably designed high frequency SAW devices. We also aimed to understand the mechanisms by which the nanomaterials worked, utilizing electronic structure and molecular dynamics simulations, and macroscopic sensor response modeling utilizing electrical equivalent circuits, mechanical perturbations methods, and finite element techniques. The final result is superior sensors for hydrogen and other gases and vapors.

Results and Discussion

The first year was primarily spent in setting up the laboratory, hiring students, and designing devices and experiments. Given that the funding was only 60,000 dollars, a lot of bootstrapping was done, and accomplishments were (a) the design and fabrication of a 100 MHz SAW delay-line device, (b) construction of an RF test-bed, and (c) some development towards the synthesis of nanomaterial Pd by physical vapor deposition and electrochemical techniques. Pd is the chosen material for hydrogen absorption, and it was and is our favored material for hydrogen sensing. Related research on hydrocarbon and other organic vapor sensors was started at that time, again, bootstrapping from other resources. Results for the three years of this project are described below, in a topical fashion and in a somewhat chronological order.

Device Fabrication

200 MHz SAW devices on Y-Z lithium niobate were designed, and successfully fabricated by optical lithography, using standard etching process. The 200 MHz SAW sensors are dual-delay line devices with 50 finger pairs. Figure 1 shows optical micrographs of the inter-digital transducers (IDTs) on the 200 MHz SAW sensor. Electron beam lithography was utilized in fabricating the 900 MHz device shown in Figure 1. The sub-micron (about 350 nm) line-widths required for this device necessitated electron-beam lithography, which is suitable for a university environment that avoids expensive sub-micron mask fabrications.

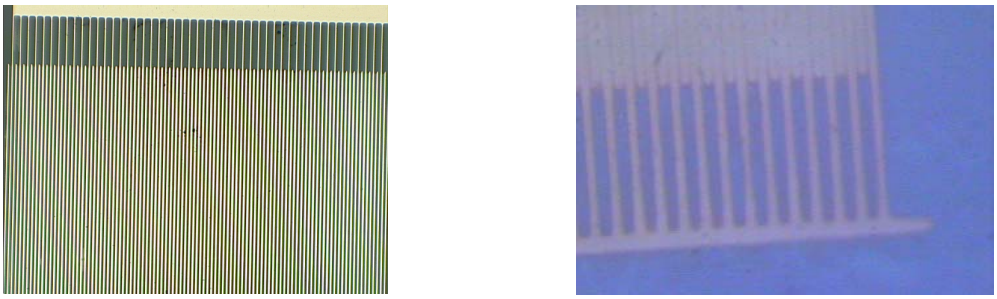

Figure 1. Optical micrograph of fabricated 200 MHz (left) and 900 MHz (right) IDTs.

To expand the research to other gas and organic vapor detection, high frequency (about 100 MHz) thickness shear mode resonators were fabricated by etching the central portion of quartz blank by chemical methods. The concept and devices are shown in Figures 2.

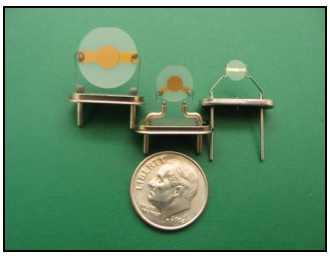

Figure 2. Milled TSM device schematic, showing the thinned-down central quartz blank, and comparison of 10, 20 and 100 MHz devices.

Radio Frequency Test-bed with Gas and Organic Vapor Dilution Systems

A fully instrumented and automated radio-frequency test bed (Figure 3) has been designed and fabricated at the Sensor Research Laboratory (SRL) to test SAW sensors. Two dilution systems consisting of arrays of mass-flow controllers (MKS 1479A series) to (i) achieve gas concentrations of a few volume percent to ppm range, and (ii) multiple organic vapors concentrations of low volume to high ppm ranges using vapor bubblers have also been constructed. The target analytes (e.g. hydrogen gas or hydrocarbon vapor) are mixed with an inert or other gas mixture (nitrogen or contaminated nitrogen, for example) to get the desired concentration. Solenoid valves are used to select specific gas flow lines. The gases go through the mixing chamber to the temperature controlled test cell, where the SAW device is placed. The two-port radio-frequency measurements are done by an S-parameter Vector Network Analyzer. An RF switch is used to switch between the two delay-lines. We have interfaced an Agilent 4294A impedance analyzer for impedance spectroscopy studies to characterize these micro- and nano-structured materials *in-situ*, and a Keithley 2010 digital multi-meter primarily for 4-point resistivity measurements. A Dell PC uses PCI bus data acquisition and GPIB to communicate with the instrumentation via a Labview interface. The set-up permits us to analyze high-speed and long-term response characteristics at sub/supra ambient temperatures, and pressures, with and without contaminants.

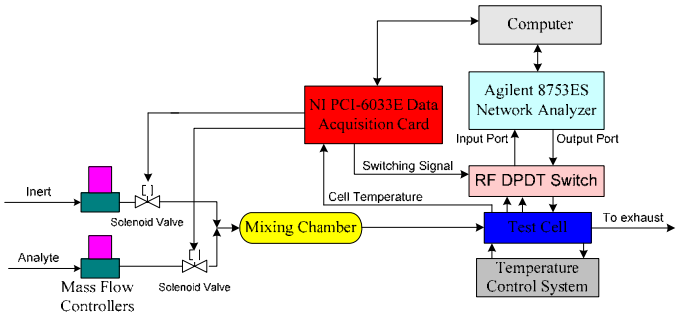

Figure 3. Schematic of gas dilution test-bed.

Test Results for Hydrogen Sensors

Figure 4 shows the reproducible room temperature response of the 200 MHz SAW device after a sensing bi-layer of 115 nm hydrogen-phthalocyanine (by e-beam evaporation) and 200 nm nanocrystalline Pd (by sputtering, grain size of 32 nm determined by XRD and AFM) were deposited. The nanocrystalline Pd reduced the response time to order of a few seconds, a significant improvement over existing Pd based hydrogen sensors, where the response times are in order of hundreds of seconds. Figure 4 includes the transport delay of about 20 seconds, and therefore, the sensing film actually begins to respond in the sub-second range. Furthermore, an anomalous behavior is seen. The center lobe peak frequency increases with hydrogen concentration, contrary to what has been previously reported by others with micro-crystalline Pd (Jakubik *et al.*, 2003), and needs to be understood.

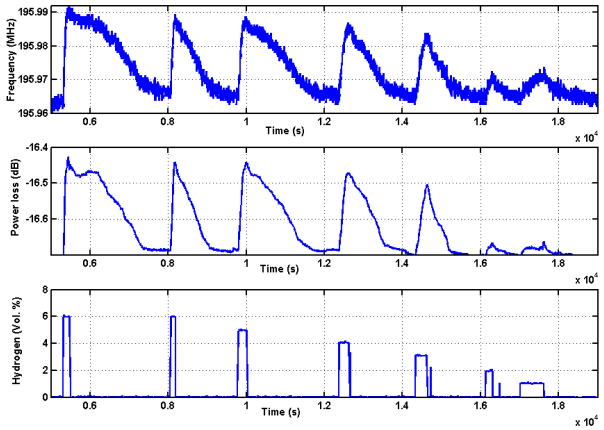

Figure 4. Response of 200 MHz hydrogen SAW sensor at 24C.

Oscillator Circuit Design and Testing for 200 MHz SAW Sensors

We fabricated a conventional feedback radio-frequency oscillator circuit (Figure 5) consisting of (a) an amplifier (MAN-1LN), (b) a low-pass filter (PLP-200), (c) a directional coupler (TDC-10-1), (d) the device under test, i.e., the SAW sensor, (e) a (variable) phase shifter, and (f) an (variable) attenuator. Two oscillator circuit layouts were laid next to each other on a printed circuit board, for the dual-delay line SAW sensors. The dual-delay line configuration is addressed later in this section.

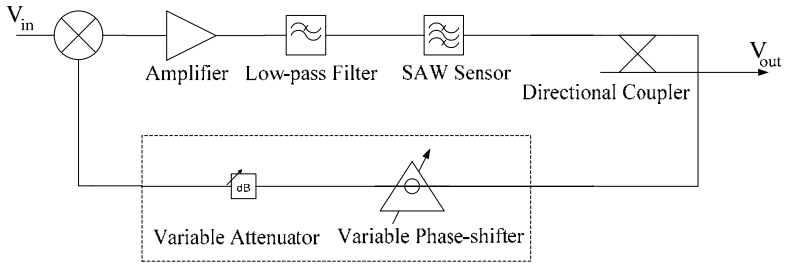

Figure 5. Schematic diagram of oscillator circuit.

Using reflectance measurements on the Agilent 8753ES vector network analyzer, the fabricated SAW sensor was seen to have a loss of around 20 dB at center frequency of 198 MHz, with a (wrapped) phase lag of 180º. The amplifier had a frequency-independent gain of about 28 dB. The assembled circuit had a phase shortfall of 15 degrees. No attenuator was found needed. The final design uses a voltage-controlled variable phase shifter (Mini-Circuits JSPHS-150). Figure 6 shows the power spectrum of the oscillator circuit output. A home-built phase shifter was used for this test. As can be seen from the figure, the oscillator circuit is able to lock on to the center frequency of the SAW sensor, and the output from the directional coupler is at a power level of -10 dBm.

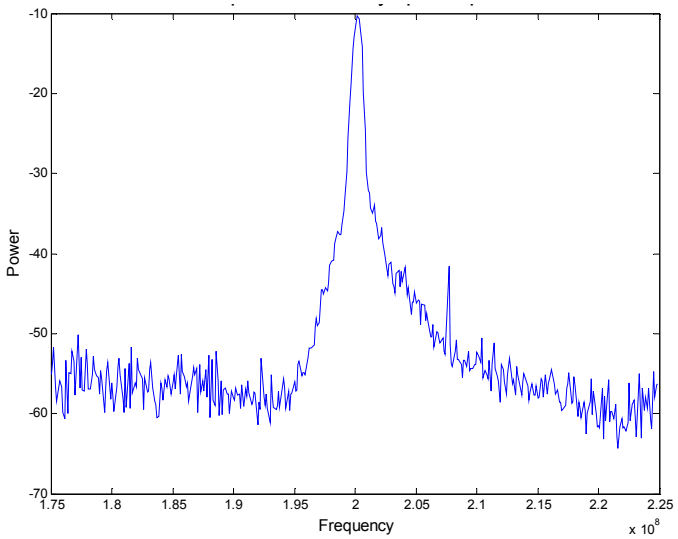

Figure 6. Power spectrum plot of phase-shifted oscillator.

Square-Law Frequency Mixers for Dual Delay Lines -- In a dual delay line scheme, one SAW delay line is deposited with a sensing layer and acts as the measurement device. The other serves as an environmental reference, primarily, ambient temperature compensation. Both delay lines are identical in design (except for the sensing layer), and their respective center frequencies are tracked by individually oscillator circuits. To achieve ambient temperature adjustment, we need to track the difference between the individual center frequencies. This is achieved by a combination of a square-law radio frequency mixer, and a low pass filter. The frequency mixer we used (Mini-Circuits ZX05-1) consisted of two inputs – a local oscillator (LO) input, and a low-power radio frequency (RF) input. We use an amplifier (ZJL-3G Mini-Circuits) to amplify one of the coupler outputs (~-10 dBm) to meet the input power requirements of the LO input (7 to 10 dBm). The output of the other coupler was fed directly to the RF input. We used SLP-5 from Mini-circuits for the low pass filter stage. This filtered output will be then fed to a frequency counter (Agilent 5334B) to record the variations in differential frequency with time. The frequency counter has been interfaced to a Dell PC together with the rest of the test-bed instrumentation to continuously log data.

Nanomaterial Synthesis

Nanomaterial Pd was synthesized in several ways. Initially, we sought to reproduce the technique used by Penner and co-workers, that of step-edged deposition. This was successful, and yielded nanoparticles and nanowires (Figure 7).

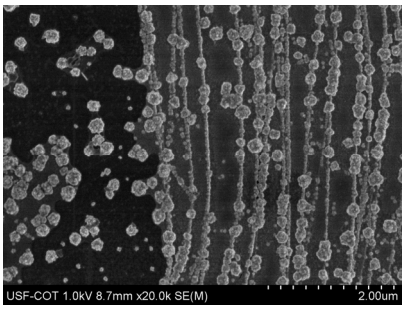

Figure 7. Pd nanowires from step edged deposition on graphite.

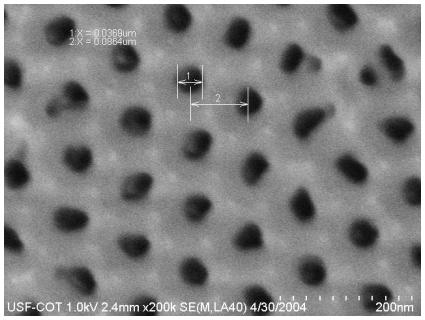

Figure 8. Fabricated alumina template of 37 nm pores.

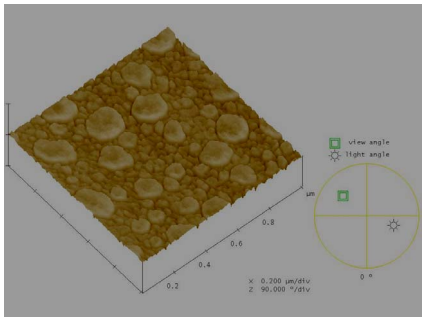

Figure 9. AFM image of Nanocrystalline Pd using sputtering.

Due to difficulties in scale-up in synthesis with this technique, we chose to utilize synthesis in alumina templates. These templates were successfully fabricated by anodization of aluminum in our group. A template made with 37 nm pores is shown in Figure 8. Current efforts are towards the deposition of Pd nanowires in these templates. Later efforts will be towards the deposition of Pd alloys in these templates.

To proceed ahead with the hydrogen sensor development, we utilized nanocrystalline Pd deposited in our own optimized sputter process. A 32 nm grain size was achieved as shown in the AFM image in Figure 9. This structure, and grain size were also established in X-ray measurements.

Theoretical Studies

Molecular dynamics simulations of nanowires and nanoclusters of Pd and Pd alloys were carried out to understand the structural, melting and surface segregation properties of these nanomaterials as a prelude to simulations of their interactions with hydrogen in sensing applications. These studies helped us in the processing of the materials, in choosing the alloying metal, and in understanding the role of nano-size on sensing. Numerous results are being presented in several publications and are not elaborated here. As an example, the dependence of melting points of Pt-Pd clusters of two sizes as a function of composition is shown in Figure 10. Please email PI for preprints and reprints. For typical results, see Sankaranarayanan *et al.* (2005).

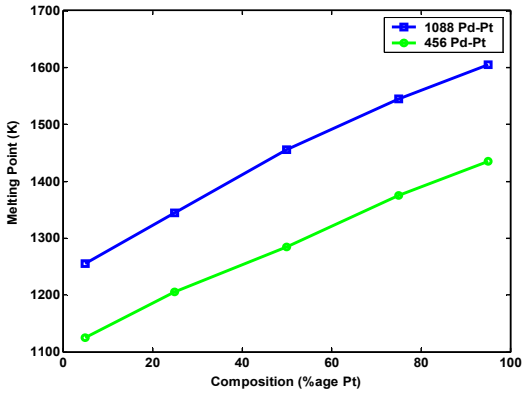

Figure 10. Melting point variations with composition for $(Pd_x\text{-}Pt_{(1-x)})_{456}$ (circles) and $(Pd_x\text{-}Pt_{(1-x)})_{1088}$ (squares).

Problems Encountered in the Research

On the device fabrication front, we encountered difficulties with the electron beam lithography, where the stage drifts not allowing us to connect the IDT structures to the bonding pads. As a consequence we are unable to test our hypothesis on the advantages to be gained by utilizing higher frequency devices.

On the sensing layer fabrication front, we faced problems of electrodeposition of nanowire materials into alumina templates. This is an electrochemistry issue which will be worked out eventually, and lead to the first reported fabrication of Pd nanowires in templated synthesis. We are facing the problem of electron beam and thermal evaporators getting contaminated with the phthalocyanine materials, necessitating the fabrication of a separate evaporator. Alternative techniques of Langmuir-Blodgett films were tried and resulting hydrogen sensors were successful, however, the phthalocyanine films contained fatty acids (a necessity in LB

techniques). This reduced the signal strength of the resulting sensors, with similar characteristics as from evaporated films.

We faced the problem of oscillator circuit skipping slowing down progress towards a field hydrogen sensor. This is a result of the delay-line design on the SAW device. This is being addressed with newer designs and with the frequency measurement being replaced by a phase measurement. We are currently developing circuits for such measurements.

In Year II, we aimed to fabricate moderate (200 MHz) and higher (900 MHz) SAW devices in $LiNiO_3$ and rather high frequency (100 MHz) TSM devices in quartz. We succeeded in two of these three objectives. While we could draw the structures and process them in the desired substrate for the GHz devices, we found stage drifts in the converted SEM ebeam lithography tool prevented us from fabricating functioning structures. The 200 MHz SAW devices combined with synthesized nanomaterials were demonstrated in successful tests as hydrogen sensors with a few seconds of response time. Improvements in response times, recovery times, limits of detection and sensitivity are envisioned with further development of devices and sensing materials. The 100 MHz TSM device was utilized to construct a very successful hydrocarbon sensor, exhibiting superior sensitivity and limit of detection. Both results for the SAW hydrogen sensor and for the TSM hydrocarbon sensor were disclosed separately, and a patent is already filed for the SAW sensor. Oscillator circuits were designed and constructed for the 200 MHz SAW sensor to achieve a field device. It is found that better stability (a few tens of Hz) is achievable with these circuits over wide temperature ranges for the dual delay-line configuration, enabling inexpensive field devices. However, the current design of the SAW tended to make the circuit skip, and phase measurements are planned as possibly superior, with circuits under design currently.

Nanomaterial synthesis, especially of transition metal nanowires has been advanced as a result of this research. Fabrication of nanoporous alumina, nanoparticles and nanowires of Pd are specific achievements.

Theoretical work utilizing molecular dynamics simulation has led to significant understanding of the surface melting, surface segregation and structural behavior of the nanomaterials we utilize in constructing superior hydrogen sensors with SAW devices. Pd-coated nanorods, carbon nanotubes and tobacco mosaic viruses, are planned for experimentation as possibly better sensing materials for hydrogen detection. Similar metal and oxide coated carbon nanotubes are planned for tests in sensing of other gases.

Pd-TMV based SAW Sensor for Hydrogen Detection

In this work, we have demonstrated a hydrogen sensor that utilizes palladium nanoparticle (2 nm diameter) coated mutated, tobacco mosaic virus (TMV, 300 nm length and 18 nm diameter) that responded and recovered to hydrogen challenges in the 0.2 to 2.5 percent volume in synthetic air and an inert nitrogen atmosphere. 99% response and recovery were seen in 3-6 seconds. A new 315 MHz SAW resonator device was utilized operated in a newly designed and fabricated oscillator circuit. Results were repeatable and robust over weeks of testing. This is the fastest responding and recovering hydrogen sensor at room temperature to our knowledge. Collaborations with researchers at the University of Maryland (mutating the virus to accept nanoparticles) and Purdue (synthesis of Pd/TMV composite) are part of this work. One response curve is shown below:

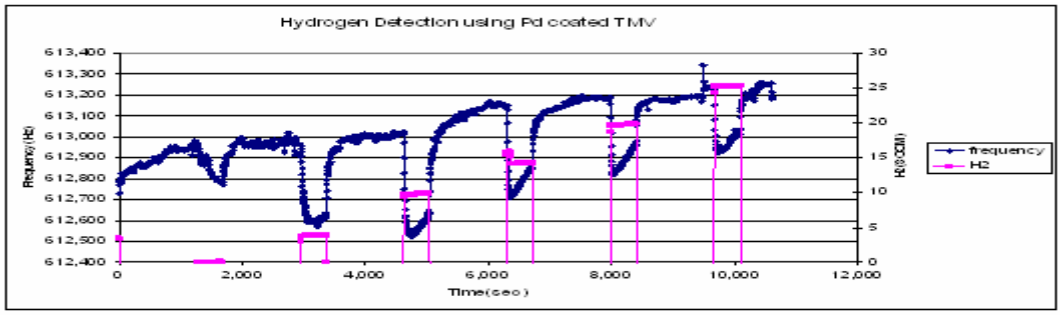

Figure 11. Respose of a Pd-TMV coated SAW resonator of 315 MHz frequency to hydrogen challenges at room temperature.

Current work is towards the utilization of Pd-coated single walled carbon nanotubes as alternative materials to this above TMV. We are utilizing physical vapor deposition techniques to coat the SWNTs with Pd.

Thickness Shear Mode Hydrocarbon Sensor

We have utilized high frequency thickness shear mode acoustic wave devices, developed utilizing inverse MESA techniques in collaboration with MTronPTI of Orlando, Florida, to demonstrate high sensitive hydrocarbon sensors that are suitable for any organic vapor. Shown below in Figure 12 are example response characteristics of a 96 MHz device in comparison to lower frequency 10 and 20 MHz devices to demonstrate sensitivity gains. This test was repeated with a number of organics and similar results were found. Further work carried out to discriminate vapors by measuring equivalent circuit parameters of the TSM devices. Figure 13 shows results of resistance shift in the equivalent circuit model vs. frequency shift, indicating that vapor discrimination by such multiple property measurements is promising.

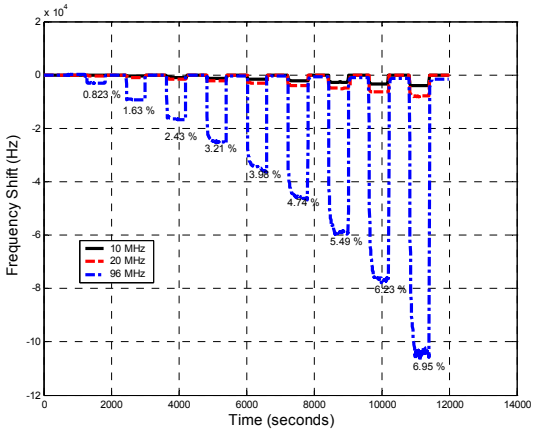

Figure 12. Response of poly(isobutylene) coated TSM devices of 10, 20 and 96 MHz resonance frequency to benzene challenges at different concentrations.

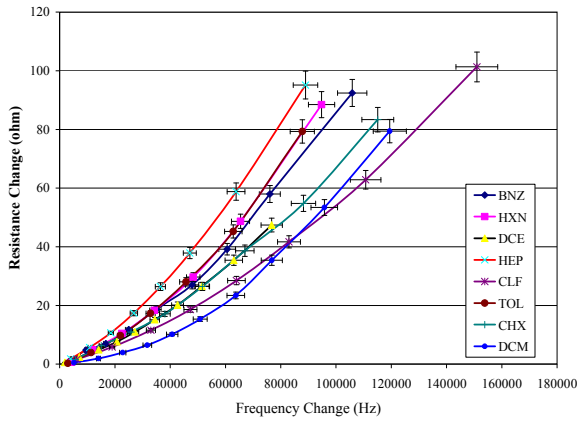

Figure 13. Possibility of vapor discrimination with the 96 MHz TSM device.

Current work is towards utilization of detailed equivalent circuit modeling of the sensor to achieve vapor discrimination.

Shear-horizontal SAW Device and Testing

New designs for a hexagonal SH-SAW device have been completed and the device fabricated. Shown below is the device layout, which is now fabricated and tested.

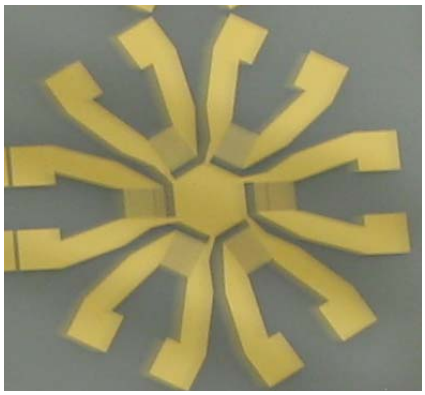

Figure 14. Optical micrograph of a fabricated SH-SAW hexagonal device with the sensing region shorted.

Measured S_{21} parameters and velocities of the acoustic wave along the three propagating paths have shown that three slightly different frequencies are being generated along the three propagating paths, allowing for multi-parameter extraction from the sensing film that sits in the propagating path (central hexagon) between the interdigital transducers. Test fixtures for liquid phase and gas phase testing of these devices have been designed and constructed. Sensor testing is underway.

Multiple-scale Simulations

Simulations at electronic structure, molecular dynamics and finite element levels are underway to support the experimental work. For example, finite element simulations of acoustic waves in

piezoelectric materials that correspond to the experimental arrangement yield insights into sensor response mechanisms when nanomaterials are utilized as sensing layers. Molecular dynamics simulations are useful in designing bi-metallic nanoclusters and wires for hydrogen and other gas sensor materials in SAW applications. Electronic structure calculations using density functional theory (DFT) are allowing us to understand the charge transfer mechanisms in the metal coated carbon nanotube, and TMV materials. Many results obtained in these areas are reflected in the publications and presentations listed later in this report. One example of how DFT is used in novel sensing material design is shown by the following results for the formation of chemical bonding between Pd and CNT. The favored site for a Pd atom on a CNT is established by these DFT calculations, and further results for charge transfer when a hydrogen molecular is brought to it will go towards helping design of the sensing nanomaterial.

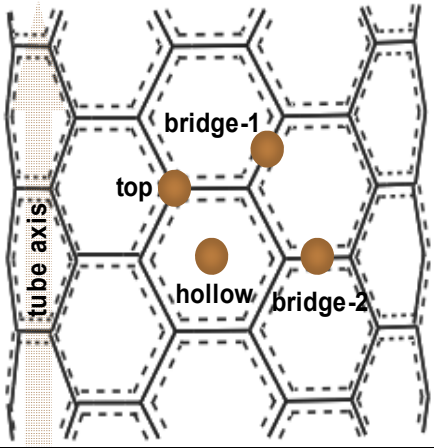

	***E*total(*eV*) (USPP)**	***E*ad (*eV*)**	**dPd-C (*Å*)**	***μ* (*μB*)**
Pd single atom	-1.52212853	/	/	0.0002
Bare SWNT(6,6)	-658.677420	/	/	0.0000
Hollow	-661.186981	-0.9874	2.1695	0.0000
Top	-661.591214	-1.3917	2.0859	0.0000
Bridge1	-661.611183	-1.4116	2.0443	0.0000
Bridge2	-661.433295	-1.2337	2.0304	0.0000

Figure 15. Favored site of a Pd atom on a SWNT.

Conclusions

Results of this research can be summarized as (1) the setting up of an acoustic wave sensors laboratory with full testing capability, (2) the development of several candidate prototypes for hydrogen sensors, (3) the development and evaluation of various nanomaterial sensing layers for hydrogen detection and sensing at room temperature in a surface acoustic wave sensor

configuration, (4) the development of a high frequency (100 MHz) thickness shear mode organic vapor sensor demonstrating superior sensitivity, (5) multiple-scale modeling to understand sensor mechanisms and (6) the development of a novel hexagonal multi-frequency surface acoustic wave sensor, useful in chemical and biological sensor applications. In particular, specific to the original mission of this project, robust and fast-responding hydrogen sensors were demonstrated in the laboratory tests that utilize nanomaterial sensing layers.

References

1. Walter, E., Favier, F., & Penner, R. (2002). Palladium mesowire arrays for fast hydrogen sensors and hydrogen-actuated switches. Anal. Chem., 74(7), 1546-1553.

2. Ballantine, D., et al. (1997). Acoustic wave sensors: theory, design, and physico-chemical applications. Applications of modern acoustics. San Diego, CA: Academic Press.

3. Kong, J., Chapline, M., & Dai, H. (2001). Functionalized carbon nanotubes for molecular hydrogen sensors. Adv. Mater. 2001, 13(18),1384-1386.

4. Jakubik, W., et al. (2003). Palladium and phthalocyanine bilayer films for hydrogen detection in a surface acoustic wave sensor system. Sensors and Actuators B, 2003. 96(1-2), 321-328.

October 2007

Thermo Catalytic H_2 Production via Oxygen-Free Methane Aromatization

J. Wolan, E. Stefanakos, A. Kababji
University of South Florida

Research Period: April 2004 to September 2007

Summary

Novel bimetallic catalysts prepared by incipient wetness co-impregnation of a ZSM-5 and H-ZSM-5 zeolite supports were formulated and tested for use in methane non-oxidative aromatization to hydrogen and aromatic species. A novel 100% hydrogen-selective custom designed catalytic membrane reactor was utilized. In this design, no separation of products is required as hydrogen is selectively permeated through an internal membrane. *In-situ* Fourier transform infrared spectroscopy (FTIR) analysis of the reactants and products as well as X-ray photoelectron spectroscopy (XPS) of fresh, activated, spent, unpromoted and promoted metal/ZSM-5 catalysts have been performed. This catalytic system has been designed to be selective for hydrogen production over benzene and thus is considered a novel technology as researched catalytic systems of this type are designed to be selective toward production of benzene.

Introduction

The ability to generate hydrogen from a biomass compatible process is a very attractive technology. The process developed is a direct gas to liquid process; a very effective way of using natural gas reserves which are currently under-utilized. The most important benefit to NASA is that this process is highly selective to pure hydrogen production with no green-house gas by-products. The bimetallic catalyst developed is molybdenum promoted H-ZSM-5 zeolite modified with various transition metal ions (TMI). These catalysts are prepared by the incipient wetness co-impregnation of the ammonium form of the zeolite, calcined in air at 500˚C, reduced and activated following an in-house developed procedure.

In this study, the focus is on the production of hydrogen rather than the aromatic products which also includes ethylene, ethane, toluene and unreacted methane. The overall chemical reaction is shown below. The process is considered highly endothermic, operating in the temperature range between 600-850°C.

$$6CH_4 \xrightarrow{Mo/HZSM-5} C_6H_6 + 9H_2 (\Delta H = 523 kJ/mol)$$

The large activation energy required leads to very high temperature reactions; this can affect the catalyst performance adversely through sintering and/or coking of the catalyst bed. Therefore, catalyst design, fabrication and pretreatment are critical.

Experimental

Two test-bed reactors have been built: the catalytic reactor (CR) to investigate the production of benzene along other hydrocarbons and the catalytic membrane reactor (CMR) with 100% selectivity to hydrogen production. A catalytic membrane reactor block diagram is shown below connected to the FTIR (figure1). Literature review estimates methane to benzene conversion in the catalytic reactor (CR) mode to be 4%, and for the (CMR) mode to be 9% (equilibrium conversion is 5%) [1]. The thermodynamic equilibrium conversion of methane is 18% at 750°C. Another advantage of using the membrane catalytic reactor (CMR) is the significant increase in conversion to benzene beyond thermodynamic conversion.

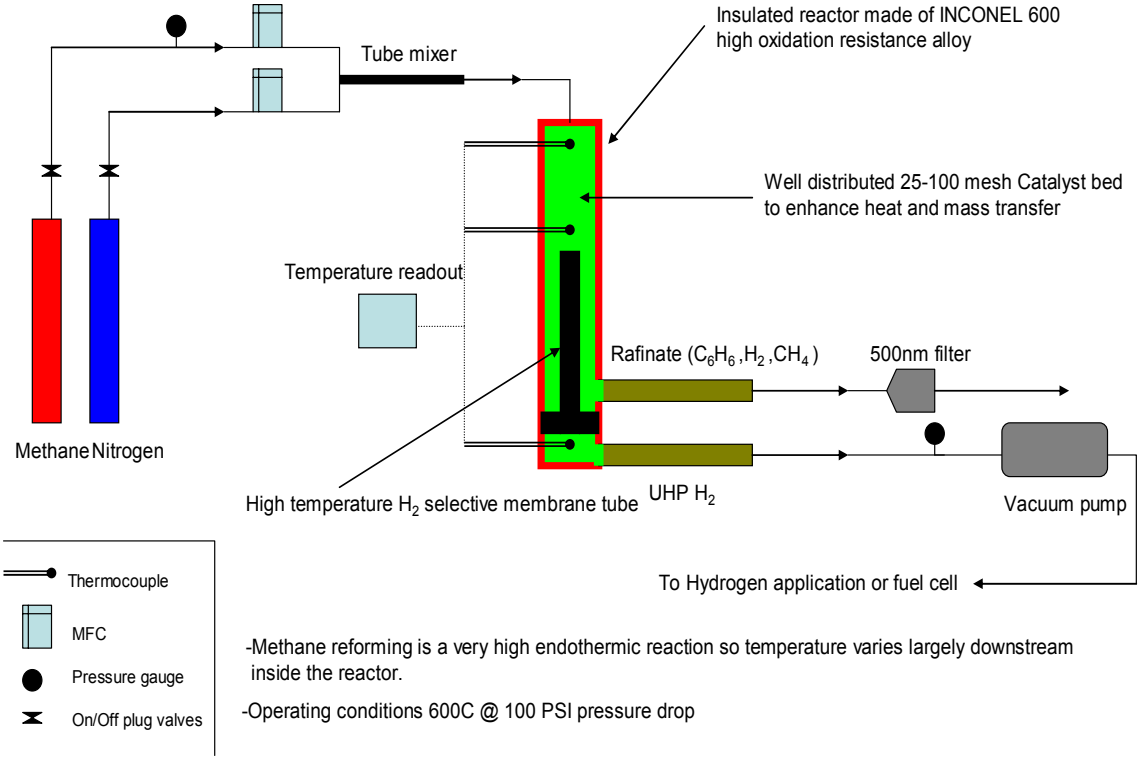

Figure 1: Schematic of the catalytic membrane reactor (CMR). Reactor is 24" tall, contains one high temperature thick-walled membrane tube backed by inconel 750X and coated with 5 μm Pd for higher temperature resistance. Side arms are 12" stainless steel.

Two membrane reactors were purchased from REB research Inc, MI. As shown in Table 1, one was used for catalyst screening at low temperatures while the other had a thicker membrane for high temperature experiments. The membrane reactor will simplify product separation and increase the yield and turnover. This reactor is non-equilibrium based (i.e., not thermodynamically limited), provides *in-situ* product separation, is portable and robust. These reactors have been operated in parallel to screen different catalyst samples for inherent catalytic activity using the catalytic reactor (CR) and test promising (screened) catalytic materials for the production of hydrogen using the catalytic membrane reactor (CMR).

Table 1: The membrane reactor specifications.

	Screening membrane reactor used to study catalyst performance	Upscale large membrane reactor (results attached)
membrane OD (mm)	2	3.2
membrane height (mm)	28	152.4
membrane material	Helical shaped Pd membrane to increase surface area	Helical shaped Pd membrane to increase surface area. Pd membrane thickness = 5 μm to increase high temperature resistivity.
Membrane surface area (mm^2)	176	1520
Reactor shell material	Inconel 600	Inconel 600
Reactor shell OD (mm)	0.25	12.7
Reactor shell Thickness (mm)	2	3.2
Reactor shell height (mm)	50.8	228.6

In the early stages of the reaction, the reduction of MoO_3 by methane creates the MoC_x species which is considered the active phase for the methane dehydrogenation and oligomerization into C_2H_y species (y<4) [2]. At the same time, the Brönsted acid sites of the HZSM-5 zeolite are responsible for the aromatization of the C_2 species. The Brönsted acid sites are the driving force for the MoO_x migration into the zeolite channels.

If the number of Brönsted acid sites per unit cell is too small, (when the SiO_2/Al_2O_3 ratio is higher than 250), the MoO_x species cannot migrate into the channels. The ZSM-5 zeolite used in preparing the studied catalyst systems had a SiO_2/Al_2O_3 =23. The MoO_x species that do migrate into the channels interact with the Brönsted acid sites and anchor on the framework aluminum of the zeolite through oxygen bridges. This species is the precursor of the active center, which is responsible for the initial rupture of C-H bond of methane aromatization reaction. During the induction period of the reaction, this species will be transformed to lattice molybdenum carbide, which is responsible for further activation of methane. If this transformation process is performed before the reaction, the temperature needed for methane activation and benzene formation will be greatly lowered (760 and 847 K, respectively). Further studies show that it is reasonable to distinguish the MoOx species into two parts: one is associated and the other is nonasscociated with the Brönsted acid sites [2]. Mo_2C and/or MoO_xC_y, which are possibly active species for CH_4 activation, are formed during the induction period. Second, the formation of the active intermediates, the CH_x species, follows the activation of CH_4 on Mo_2C and/or MoO_xC_y. The last one to be formed is inert coke, which leads to the deactivation of the catalyst. The carbonaceous species on the outer surface of Mo/HZSM-5 tend to develop into nanotubes, while those inside the channels form aromatics due to the pore size restriction [2].

The preparation and activation process of the catalyst was developed based on literature review and experimentation. All catalyst systems prepared are listed in table 2. The preparation process consisted of the following steps:

- Four types of catalysts were prepared by incipient wetness co-impregnation of the ammonium form of the zeolite. The zeolite (purchased from zeolyte Int.) has a surface area of 425 m^2/g with a Si/Al=23. The mixture was air dried overnight and heated at 200˚C for 2 hours and finally calcined for 4 hours at 600˚C.
- After loading, the membrane reactor and catalyst were purged with Ar from ambient slowly to 600˚C in one hour then stayed another 3 more hours.
- Temperature was increased to 700˚C and the gas is switched to air for 30 minutes.
- Temperature was decreased to 300˚C under Ar.
- The catalyst was reduced at 300˚C for 30 min using H_2.

Table 2: Catalyst systems developed and their preparation objective.

Catalyst formula	Objective
Mo/ZSM-5 or Mo/H-ZSM-5	original & reference
α or β-SiC/3wt%Mo/H-ZSM-5	Improved temperature distribution and heat conduction
(Pt or Ru)-Mo/ZSM-5 (bimetallic)	improving conversion and stability
(Co, Cu, Fe, Cr, Pd)/Mo/ZSM-5 (bimetallic)	Catalyst performance optimization

The reaction conditions for the prepared 0.5wt%Pd-3wt%Mo-ZSM-5 catalyst system for example are as follows:

- Amount of catalyst loaded in the reactor = 1.5 g.
- CH_4 flow rate = 100 sccm, no N_2 make up.
- Pressure upstream 1.4 bars, ΔP across the reactor = 0.1bar
- Space velocity = 4700/hr based on 1.6” bed height and using 20-80 mesh catalyst particles.
- Reaction temperature range: 500˚ C up to 700˚C
- Reactor maximum operating temperature not to exceed 700˚C across the membrane.
- Reaction total time on methane stream has been up to 4 hrs.
- Calcination, activation by air and reduction by hydrogen are done prior to introducing methane.

Results and Discussion

FTIR was used to evaluate the raffinate product, and screen for greenhouse by-products. Figure 2 shows a FTIR spectrum of the raffinate stream from the membrane reactor at 700˚C. The catalyst used was Mo/ZSM-5. The lower spectrum shows that lower space velocities (controlled methane stream and pressure) result in high benzene production. However greenhouse gases

were also produced. The region between 2000 up to 2400 wavenumbers represents the greenhouse gases (CO and CO_2). To eliminate the production of greenhouse gases, the catalyst was optimized which included a change in pretreatment conditions. Figure 3 shows an *in-situ* FTIR spectrum of the membrane reactor raffinate output at 700˚C for a Mo/ZSM-5 catalyst system. The spectrum shows methane and aromatic peaks. No greenhouse gases were present. Traces of CO_2 were formed after the catalyst active phase MoO_3 reacted with the hydrocarbon “methane”.

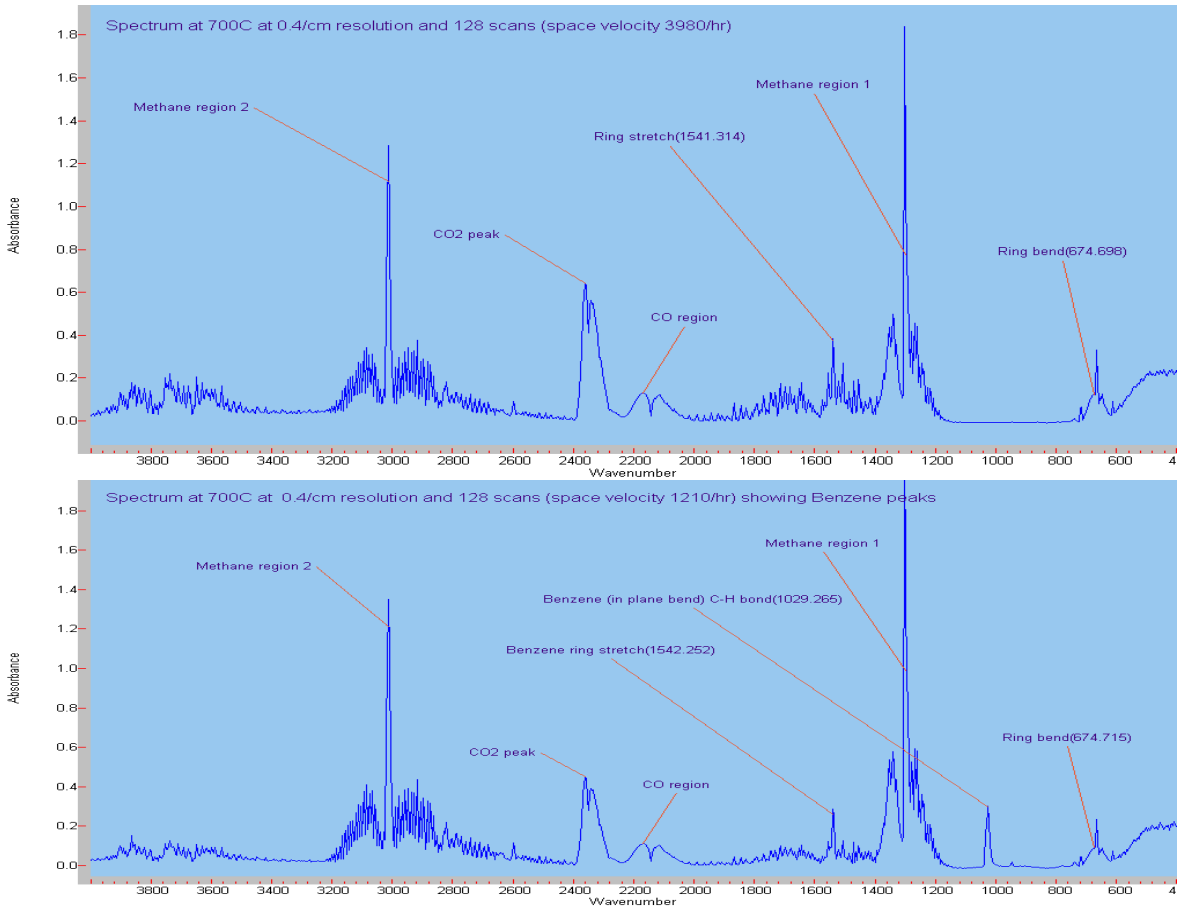

Figure 2: FTIR spectra of the catalytic reactor product stream at 700˚C. The lower spectrum shows that lower space velocities (controlled methane stream and pressure) result in better benzene peaks absorption (concentration). However green house gases were produced.

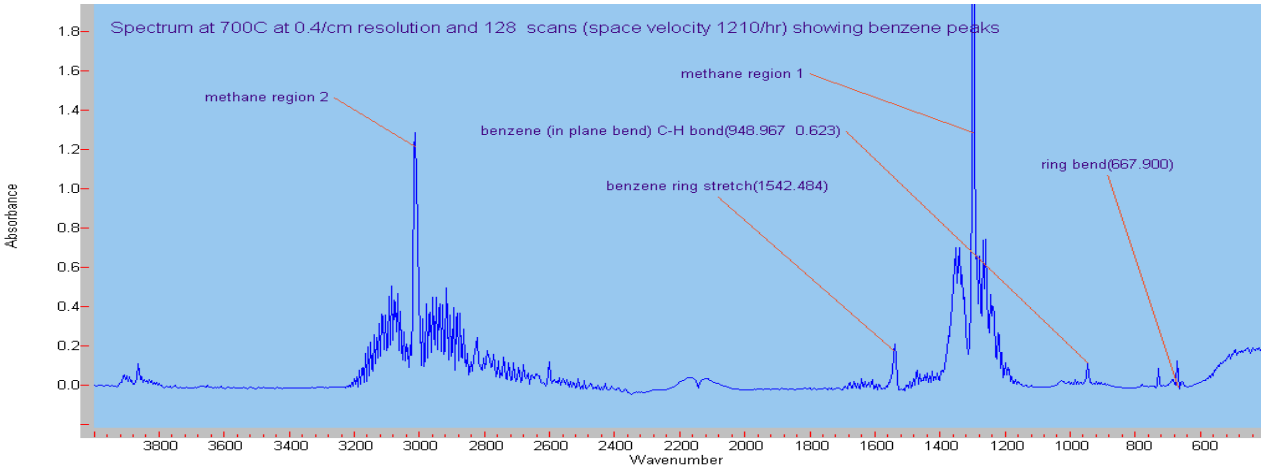

Figure 3: FTIR spectrum showing major benzene and other hydrocarbons peaks along unconverted methane at 700°C. Note the reduction in green house gases!

Figure 4 is a Gas Chromatograph GC output signal of both sides of the membrane reactor showing hydrogen in the membrane side and methane and nitrogen (the carrier gas) on the raffinate side of the reactor. The reactor was coated with additional 5μm of Pd for higher temperature runs, and for this type of columns, the carrier gas peak will always appear in the output signal. The area under the peak is relative to species concentration.

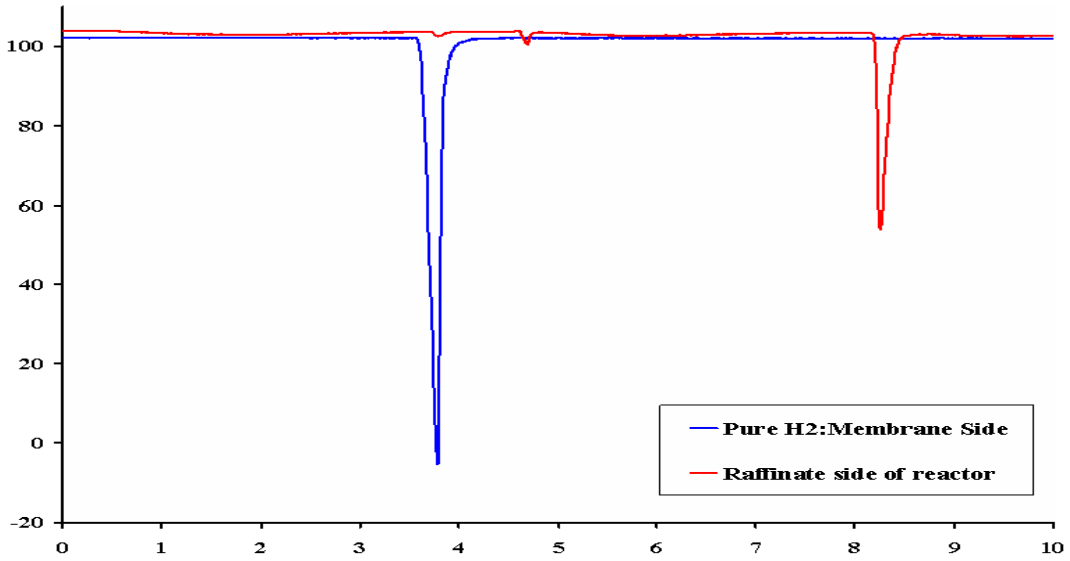

Figure 4: GC qualitative analysis of both effluent streams; the membrane and raffinate sides of the reactor. Nitrogen was the carrier gas.

XRD analysis of 0.5wt%Pd-3wt%Mo-ZSM5 bimetallic catalyst showed no structure changes occurring during the preparation procedure (i.e. the Mo atoms replacing the ammonium cations

in the zeolite) as shown in figure 5 which also shows the effect of 24 hours of reaction on this system at 700˚C. The catalyst structure seems to change due to coke formation at this high temperature, resulting in significant reduction in the catalyst activity.

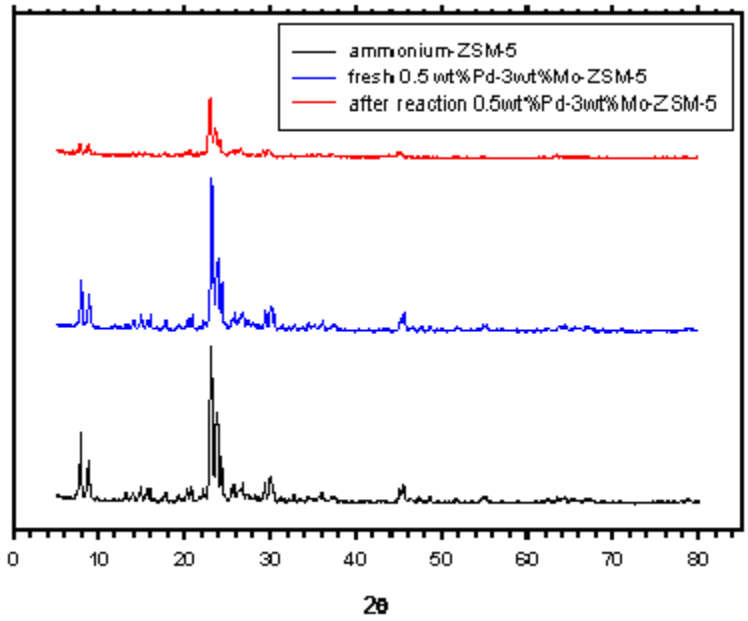

Figure 5: XRD analysis of a 0.5wt%Pd-3wt%Mo-ZSM5 bimetallic catalyst as a fresh ammonium zeolite, prepared catalyst after activation and after reaction.

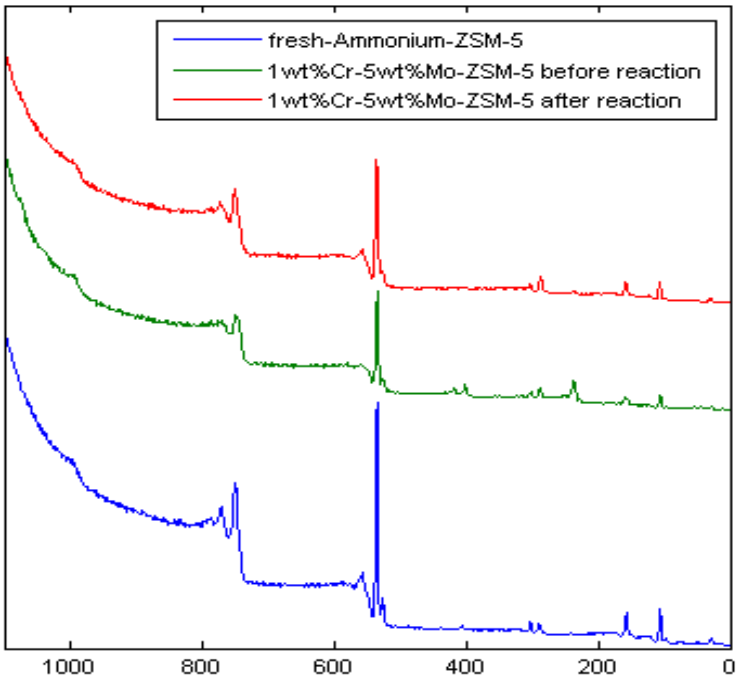

Figure 6: XPS survey analysis of a 1wt%Cr-5wt%Mo-ZSM-5 bimetallic catalyst system as a fresh ammonium zeolite, prepared catalyst after activation and after reaction.

Figure 6 shows XPS surveys of a 1wt%Cr-5wt%Mo-ZSM-5 bimetallic prepared catalyst system. XPS was used to qualify elemental peaks of Si, Al and their atomic ratio. It was also used to identify other elements in the catalyst systems prepared like the (TMI) used as well as C, Mo, O and N peaks. The changes in peaks intensity specially C, Mo and O helps understand the change in catalyst activity and coke formation as well as the formation of active catalyst phases like the MoO_x during and after reaction.

Preliminary Hydrogen Production Rate Results

- At 500˚C up to 550˚C and after 1hr on stream, H_2 production rate was 36 sccm (based on 100sccm methane flow rate).
- At 600˚C up to 650˚C and after 1hr 40 min total time on stream, H_2 production rate was about 10 sccm (based on 100 sccm methane flow rate).

- Membrane selectivity to H_2 is approximately 100%; the calculated selectivity data for different catalyst systems is shown below.

- Aromatic compounds including benzene, toluene, ethane, ethylene and cyclohexane rates of production have not been determined (product separation required). However aromatic conversion results are presented. CO and CO_2 conversion vs. temperature curves are also presented for different catalyst systems prepared.

Selectivity and Conversion Results for Different Catalyst Systems

This section presents results of running different prepared catalysts. Selectivity of hydrogen as well as methane conversion are calculated as parameters to evaluate the catalyst performance. Selectivity to greenhouse gas production is also presented.

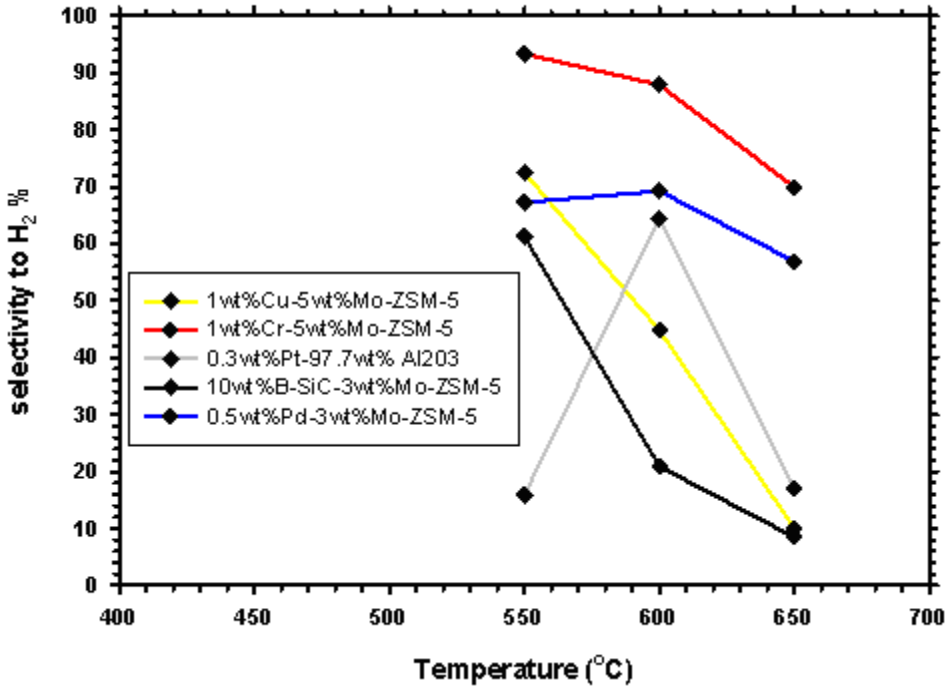

Figure 7: Selectivity to H_2 vs. Temperature based on GC peak area for different catalyst systems.

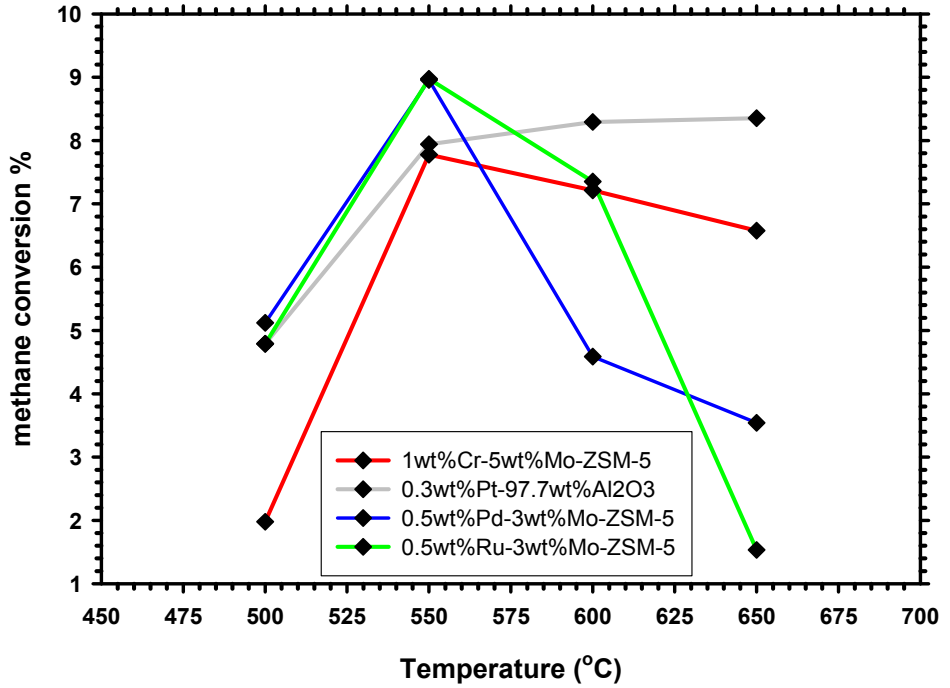

Figure 8: Methane conversion % vs. Temperature calculated based on FTIR methane absorbance peak areas for different catalyst systems.

Figure 7 shows selectivity to H_2 vs. temperature based on GC species peak areas for different catalyst systems. Samples were collected at the membrane side of the reactor and the space velocity was 434/hr. The best selectivity obtained was 96% using a Cr promoted catalyst system at 550˚C. All catalyst systems prepared showed rapid loss of selectivity to hydrogen production with increasing temperature and time. Coke formation was noticed on all catalyst surfaces after reaction. Mixing the catalyst with β-SiC to improve heat distribution and decrease hot spotting was investigated. No significant increase in selectivity or life-time of the catalyst was observed. The alumina supported catalyst showed a sharp increase in selectivity to hydrogen followed by sharp loss of activity.

Figure 8 shows percentage methane conversion vs. temperature based on FTIR methane absorbance peak areas for different catalyst systems. Samples were collected at the raffinate side of the reactor. The space velocity was 434/hr. The highest methane conversion obtained was 9% using Pd and Ru promoted zeolite systems at around 550˚C. At 600˚C, the maximum methane conversion achieved was 8.5% using the Pt-alumina supported catalyst. For the Ru or Cr/zeolite system, that number dropped to around 7.5% which is still higher than the equilibrium conversion of 5% [1] indicating that the membrane reactor shifted the reaction equilibrium.

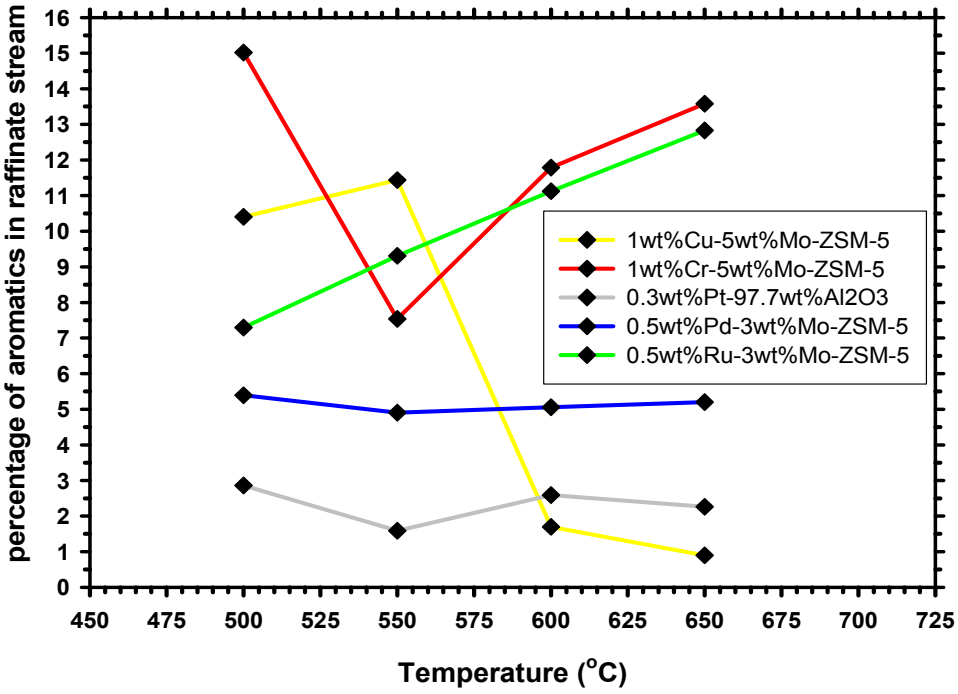

Figure 9: Aromatic percentage in raffinate stream vs. Temperature based on FTIR absorbance peak areas for different catalyst systems. Space velocity = 434/hr.

Figure 9 shows the aromatic percentage in the raffinate stream vs. temperature based on FTIR absorbance peak areas for different catalyst systems. The space velocity was 434/hr. Further stream purification or an MS-GC system analysis would be required to quantify specific aromatic species.

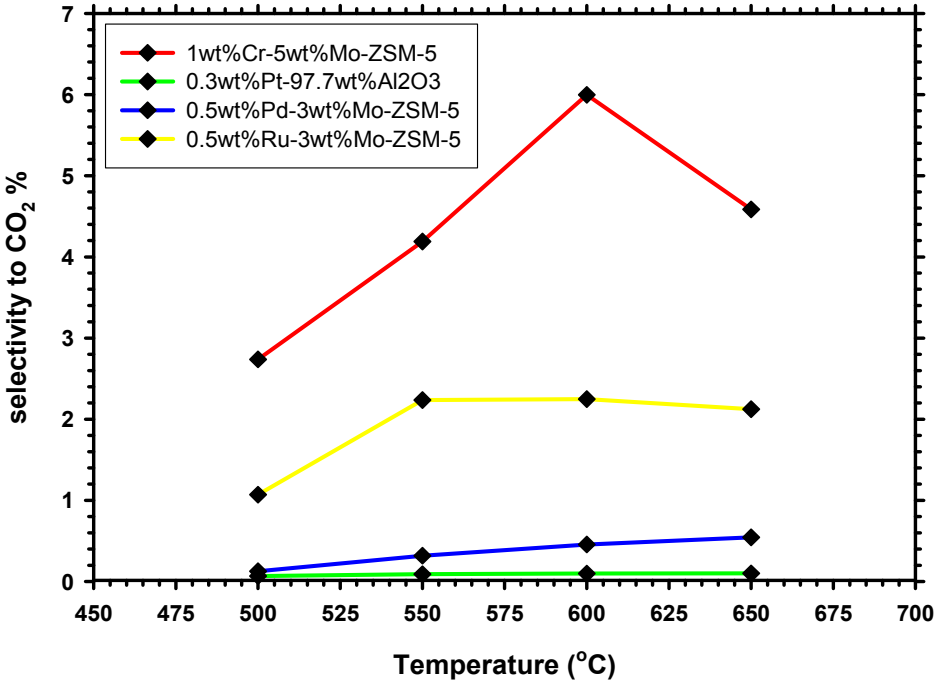

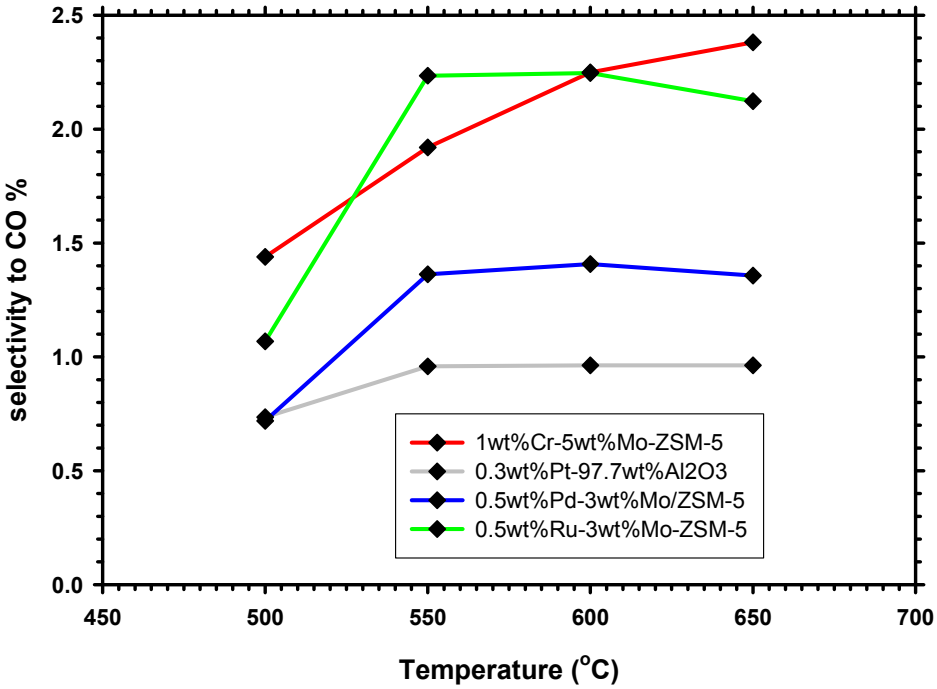

Figure 10 and 11: Selectivity to CO_2 and CO production respectively vs. Temperature based on FTIR absorbance peak areas for different catalyst systems.

In Figures 10 and 11, the commercial Pt-alumina supported catalyst showed very low CO_2 production which is very important for ultra pure nonoxidative operations. CO production in

general was lower than CO_2 production. However, operating between 500˚C and 550˚C would limit the amount of both CO and CO_2 produced.

References

Iliuta, M., & al Larachi, F. (2002). Ind. Eng. Chem. Res. 41, 2371-2378.

Zhang, et al. (2003). J Natural gas Chem., 12.

Final Report for Florida A & M University

- Modeling and Optimization of Fuel Cell systems for Aircraft Applications - Ordonez, J., Lungo, C.

Modeling and Optimization of Fuel Cell Systems for Aircraft Applications

J. Ordonez and C. Luongo
Florida Agricultural and Mechanical University-Florida State University

Research Period: March 2005 to September 2007

Abstract

This project is aimed at increasing the level of confidence and existing design know-how for the implementation of fuel-cells on aircraft. A first phase, 2005-2006, focused on a suite of studies related to the integration of fuel cells into aircraft and the optimization of fuel cell systems: 1. SOFC-gas turbine hybrid system for aircraft applications: modeling and performance analysis, 2. The optimal shape for a unit PEM fuel cell, 3. The Constructal PEM fuel cell stack design, and 4. The implementation of fuel cell based aero-propulsion systems into advanced power simulation environments (EMTDC, RTDS). During the second phase of the project, 2006-2007, we continued with the implementation of fuel cell based aero-propulsion systems into EMTDC and RTDS in synergy with the NASA URETI for aeropropulsion, concluded a study on the internal structure of a SOFC unit, and added a new aspect on the characterization and optimization of regenerative fuel cell systems. In this executive summary we present the main aspects of these studies, a complete report (100+ pages) is available to NASA upon request.

Introduction

The idea of using fuel cells for propulsion is an ever-growing concept in today's environmentally conscious world. Fuel cells continue to have promise as a source for propulsion in electric vehicles, hybrid cars, ships, and aviation applications. In a 2004 publication, NASA indicated that fuels cells were becoming reasonably practical for propulsion in small aircraft and could be promising in future large-scale commercial aircraft [1]. Currently, Boeing is preparing to test a manned-20 kW fuel cell aircraft to demonstrate the advantages of fuel cell propulsion in airplanes [2]. In the automotive industry, companies such as General Motors, have alternative vehicle programs that demonstrate the viability of employing fuel cell-based propulsion systems [3]. Fuel cells are also being examined for use in marine applications as well; the German Navy is expected to use propulsion systems with hydrogen fuel cell technology in their future submarines [4].

In many applications, it is important to investigate the fuel cell-based power system from a system integration and power management perspective [5]. Optimizing the integration of each component into the system and understanding the overall power system compatibility is essential for a successful design. Ultimately, our *main objective* with this project is to increase the level of confidence and existing design know-how for the implementation of fuel-cells on aircraft.

Background

Fuel cells are expected to become of common use in stationary power generation and transportation systems [6-9]. Solid Oxide Fuel Cells (SOFCs) are particularly attractive for aircraft applications and especially for auxiliary power units (APU). In order to make SOFCs competitive with conventional gas turbine-based APUs, there are key challenges regarding

power density and system weight that need to be overcome. In this respect, the development of efficient optimization methodologies to increase power density and minimize system total weight is essential to the successful introduction of SOFCs into aircraft.

The efforts of this project will contribute towards the integration of hydrogen based fuel cells into aircraft applications and space exploration and have resulted in initial software developments/leveraging to assist in the characterization and assessment of regenerative, renewable fuel cell systems; with particular focus upon solid oxide cells in conjunction with high altitude and/or space applications. Matlab-Simulink, EMTDC and RTDS software modules have been produced, as well as supportive documentation that includes initial performance and reliability trends associated with pilot parametric studies.

Results and Discussion

Below a summary of each of the tasks and a highlight of the key results is presented.

Implementation of Fuel Cell based Aeropropulsion Systems into Advanced Power Simulation Environments (EMTDC, RTDS)

This effort, in synergy with the NASA URETI for aeropropulsion, resulted in the development of fuel cell power network components, which can be used to create a simulated test bed for fuel cell-based power systems. The system component models were implemented into EMTDC (a electrical network simulator). The models developed include a SOFC, a PEM, a DC to DC boost converters, a DC to AC inverters, energy storage (Fig. 1.1).

The initial simulation test bed, used to evaluate some of the models developed and their applicability into a power system network, was a small Cessna type aircraft load powertrain configuration (Figure 1.2).

Fuel Cell Power System Simulation

A power output of 119 kW (~160 HP) is used as an initial design specification for the system. The system load is a fixed pitch propeller, and the primary source for the load is a solid oxide fuel cell stack. Our intent is to study controllability, system integration, and power management. To deliver power from the fuel cell to the mechanical load, electrical converters are employed. The output terminals of the fuel cell connect to a DC-to-DC boost converter. The boost converter is used to increase the voltage level from the fuel cell to a regulated value. The boost converter is connected to an inverter, or a DC-to-AC converter, which converts DC power to usable AC power for the induction motor. Finally, a propeller is attached to the output shaft of the motor to convert the torque produced into thrust. Energy storage (i.e. a battery) is employed to provide any additional power beyond the fuel cell's capacity that would otherwise cause the system to have a voltage collapse. The battery connects to the powertrain where the DC voltage is regulated, which is at the output of the boost converter.

Since the fuel cell outputs a sloping DC voltage as its load demand increases, electrical converters are used to both maintain the DC bus voltage level, and convert DC power into AC power. In practice, these converters are electrical circuits that use intricate switching techniques to achieve a desired output. The on-off cycle of these switches typically occur in the millisecond (ms) timescale. Considering flow dynamics and thermal time constants, a fuel cell's response to load changes are typically is the second (s) timescale [10]. From a system perspective, it is not necessary to model the switching dynamics of the converters; therefore, time-average models

for the electrical converters were developed. Since it may be of a particular interest to investigate the system outputs on smaller timescales, electrical converters were also developed that incorporate fast switching dynamics.

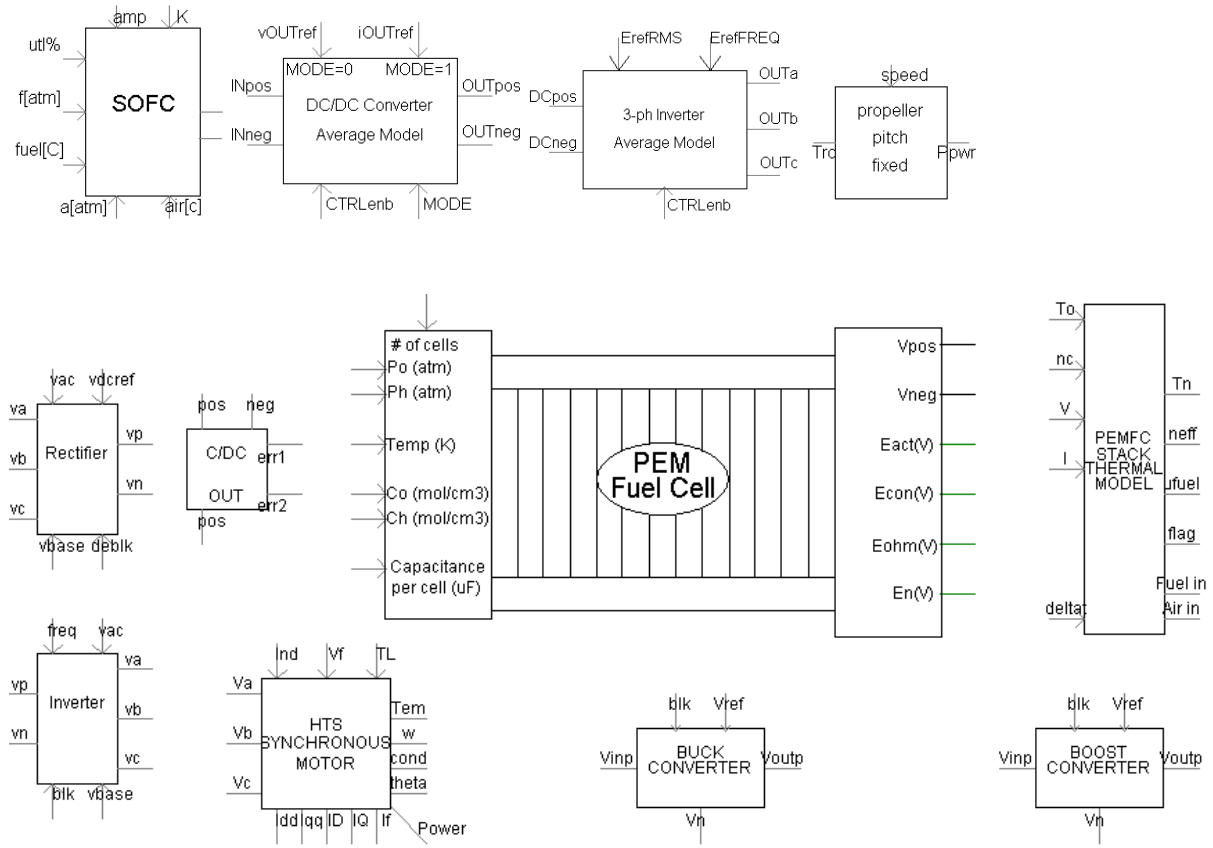

Figure 1.1. Available fuel cell power system component models: (row 1) SOFC, DC-DC boost converter average model, 3-phase Inverter average model, fixed pitch propeller (row 2) rectifier switching model, energy storage charge/discharger, PEM fuel cell, PEM Thermal model, (row 3) Inverter switching model, Motor load model, DC-DC buck converter switching model, DC-DC boost converter switching model.

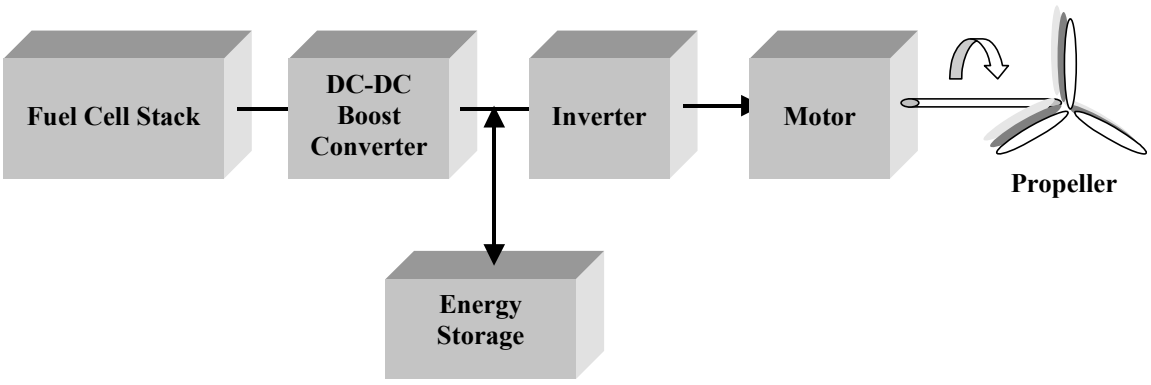

Figure 1.2 Fuel cell-based powertrain model.

System Integration Considerations

Component integration and load matching is an important aspect of power system design. The risk of instability is sufficiently reduced in verifying that a well-matched power system network exists.

Fuel Cell / Boost Converter -- Since the output of the fuel cell and the input of the boost converter are connected, care must be taken to ensure the operating point of the two components are accurately matched. To illustrate, a plot of two fuel cell characteristic curves are graphed with three boost converter input curves (Fig. 1.3). Each boost converter curve represents three different levels of power operation. Each curve is composed of a range of possible current and voltage inputs required by the converter for a voltage boost to occur. It is important to note how the boost converter curves move further away from the origin as the load demands more power. As the curves shift further away from the origin, the converter will request more current from the fuel cell. If the fuel cell is undersized, the boost converter - fuel cell connection will likely have a heighten risk of instability. It could prove useful to examine how well the fuel cell and boost converter are matched throughout a small power range centered around the system's design point.

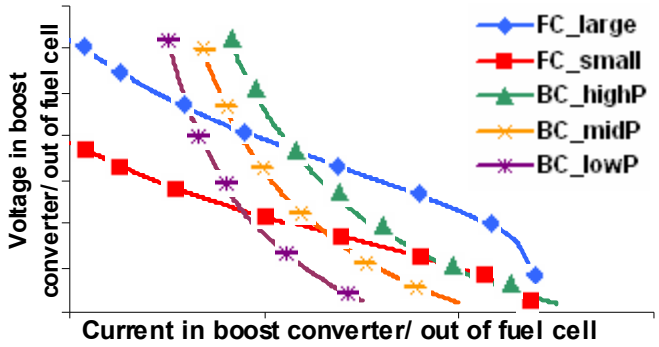

Figure 1.3. Fuel cell and boost converter integration.

Motor / Propeller -- Load matching is also very important during system design. In Fig. 1.4, a propeller torque-speed curve is graphed with an electric motor torque-speed curve.

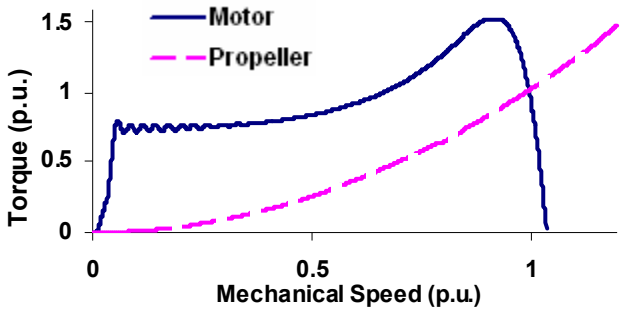

Figure 1.4. Motor and propeller integration.

The intersection of the two curves represents one operation point. For continuous range of operation, the motor will transition through many torque curves such that its point of intersection with the propeller is moving smoothly up or down the propeller's profile. To help facilitate this load following action and reduce the likelihood of stalling, a variable frequency motor drive control system is employed. The motor frequency, which is given by the inverter, is controlled using a PI controller. When the propeller demands power, the controller adjusts the frequency output of the inverter, which forces the motor's torque curve to transition to a new torque curve following along the propeller's profile.

System Start-Up -- When starting the system, the induction motor subjects the powertrain to large power requirements and fast transients. The large amount of current flow into the stator will induce the rotor to generate torque, which will cause the shaft/propeller to rotate; the large power flow required by the motor during this procedure is illustrated in Fig. 1.5. The fuel cell stack is designed to operate at 80% of its maximum power point during the cruising phase; therefore, the motor power requirement during start-up surpasses the fuel cell's capacity of 140 kW. Figure 1.5 also illustrates how the power from the fuel cell is controlled when it reaches its maximum threshold, indicating the activation of energy storage. Once the battery is activated, the boost converter is switched into current control mode to limit the power output of the fuel cell.

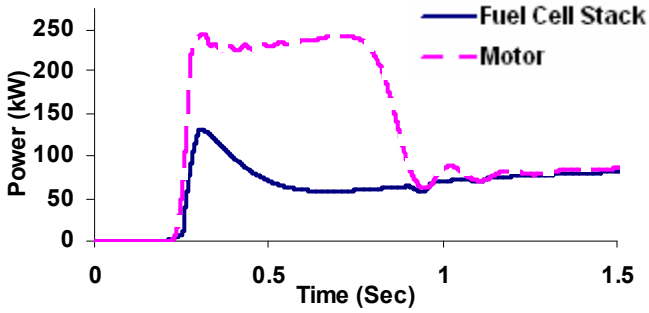

Figure 1.5. System start-up; induction motor and fuel cell stack.

In Fig. 1.5, the large and rapid increase in power being supplied to the motor occurs at 0.25 seconds. In response, the power output from the fuel cell is restricted. The power gap between the fuel cell and motor is provided by the battery. Torque generated in the motor causes the rotor to accelerate the propeller. Power flow into the motor and out of the propeller during start-up is illustrated in Fig. 1.6. At 1 second, power supplied to the motor rapidly

declines to a level just above the propeller's output near 1 second, which indicates that the rotor frequency/ propeller speed is within close proximity of the inverter supply frequency. After this event, the supply frequency is increased until the system reaches 100% rated power of 119 kW (160 HP). To help facilitate a smooth start-up, the voltage supplied to the motor is varied as a function of the frequency so that a constant voltage-frequency ratio is maintained [11]. The complete start-up time for the system to reach its rated value was 10 seconds.

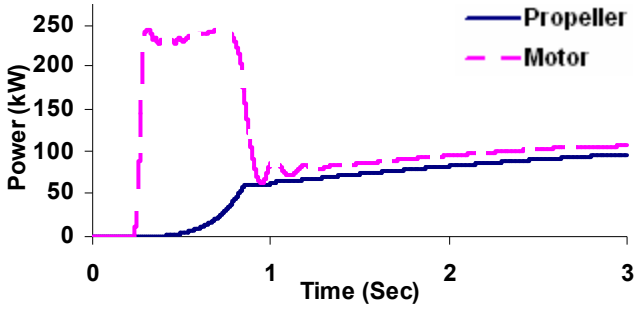

Figure 1.6. System start-up; induction motor and propeller.

Transient Load Scenario and System Response

Once the power system reaches its 100% power level, the system is subjected to the range of power levels mentioned in Table 1 in a scaled down simulation of 120 seconds. Figure 1.7(a-d) shows the power demand from the load and the response of the system. There is some overshoot observed and a time delay of 10 seconds as the system switches power levels. Notice in Fig. 1.7(d) how the power output of the fuel cell is held constant during the initial power demand (Fig. 1.7a) of 119 kW. During this phase, the boost converter is operating in a current-controlled mode which restricts current flow from the fuel cell stack. When the system's power level is decreased to a safe power level for the fuel cell stack, the PI controller in the boost converter is switched its normal voltage controlled mode. During this mode, the fuel cell stack is the sole source of power for the load. This switching event can be observed at t = 23 seconds.

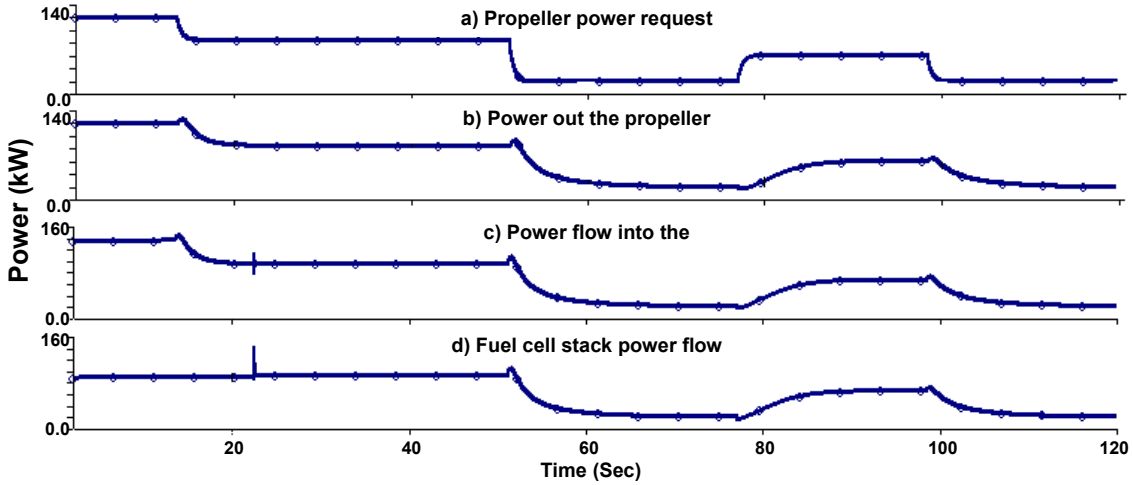

Figure 1.7. Power demand (a) and response through the fuel cell-based powertrain (b-d)

Conclusions

A library consisting of fuel cells and fuel cell power network components were development to help facilitate a simulated test bed for fuel cell-based power systems. All of the models were developed in EMTDC. The models developed include a SOFC stack, a PEM fuel cell stack, electrical converters (time-averaged models and switching models), and forms of energy storage. As a test case scenario, a fuel cell-based powertrain system was modeled and simulated to analyze the components developed and the system's performance when subjected to Cessna-like power range specifications. In this simulation, the time-based averaged models of electrical power converters were used to convert and deliver AC power to an induction motor-driven propeller from the DC output of the fuel cell stack. Preliminary results from a scaled down simulation of 120 seconds indicate that the power system transitions from one power level to the next in about 10 seconds. Current from the fuel cell stack is controlled such that its maximum power threshold is never exceeded. The fuel cell power system library is available and can be used to conduct power network studies.

As continuation effort, the implementation of all the subcomponents into RTDS (Real Time Digital Simulator) has started with the advantage of being able to perform hardware-in-the-loop experiments.

Fuel Cell (PEM/SOFC) Internal Structure Optimization [15-17]

A mathematical model and a structured procedure to optimize the internal structure (relative sizes, spacing) and external shape (aspect ratios) of a unit and stack PEM fuel cell and stack so that net power is maximized has been developed [14,15]. Initially, the optimization of flow geometry was conducted for the smallest (elemental) level of a fuel cell stack, i.e., the unit PEM fuel cell, which is modeled as a unidirectional flow system and later the optimization of flow geometry was conducted for a PEM fuel cell stack. The polarization curve, total and net power, and efficiency were obtained as functions of temperature, pressure, geometry and operating parameters. The optimization is subjected to fixed total volume. There are three levels of optimization: (i) the internal structure, which basically accounts for the relative thickness of two reaction and diffusion layers and the membrane space, (ii) the external shape of the unit cell, which accounts for the external aspect ratios of a square section plate that contains all unit PEM fuel cell components. The available volume is distributed optimally through the system so that the net power is maximized. Temperature and pressure gradients play important roles, especially as the fuel and oxidant flow paths increase, and (iii) at the stack level, we optimized the external shape, which accounts for the external aspect ratios of the PEMFC stack. The flow components are distributed optimally through the available volume so that the PEMFC stack net power is maximized. Numerical results show that the optimized single cells internal structure and stack external shape are "robust" with respect to changes in stoichiometric ratios, membrane water content, and total stack volume. The optimized internal structure and single cells thickness, and the stack external shape are results of an optimal balance between electrical power output and pumping power required to supply fuel and oxidant to the fuel cell through the stack headers and single-cell gas channels. It is shown that the twice maximized stack net power increases monotonically with total volume raised to the power 3/4, similarly to metabolic rate and body size in animal design.

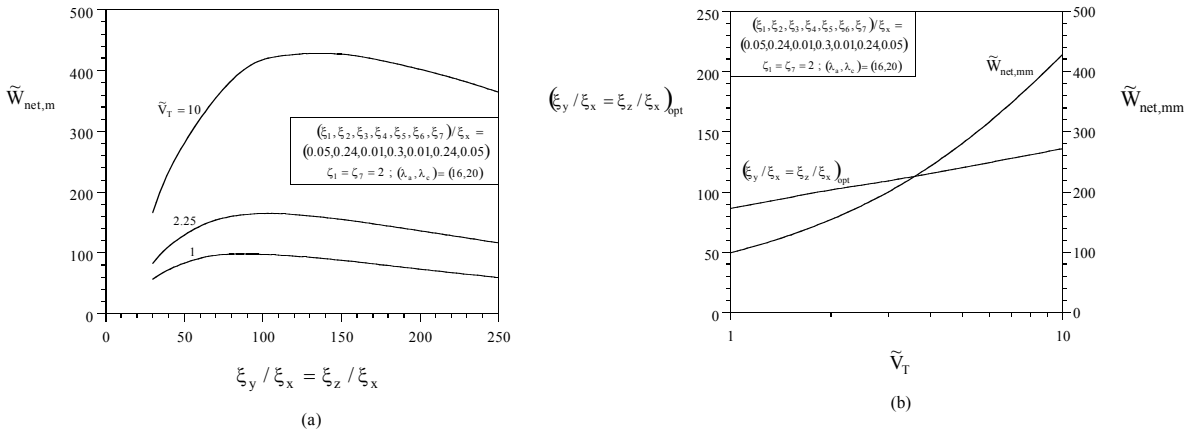

Figure 2.1. (a) The external structure optimization and the dependence on total fuel cell volume, for $\zeta_1 = \zeta_7 = 2$ and $(\lambda_a, \lambda_c) = (16,20)$, and (b) The results of the external structure optimization with respect to total fuel cell volume, $\tilde{V}_T$, for $\zeta_1 = \zeta_7 = 2$ and $(\lambda_a, \lambda_c) = (16,20)$.

The constructal development of the elemental fuel cell structure led to a new problem at larger scales: the optimization of a stack reported in [15]. The effects of internal shape on the transient response of PEM fuel cells is reported in [16], and the internal structure optimization of an SOFC in [17].

Hybrid Fuel Cell/ Gas Turbine Modeling

One of the tasks of this study addressed the thermodynamic modeling of SOFC/Gas Turbine hybrid systems and their implementation/simulation in Matlab-Simulink. Various configurations of the hybrid SOFC/GT were proposed and analyzed. A comparative study based upon performance parameters, such as SOFC power, turbine inlet temperature, and exhaust temperature was used to select the best configuration. Simple thermodynamic models for the compressor and turbine were used during the configuration selection. Once the configuration was selected, more realistic compressor and turbine models based on performance maps were incorporated into the model and used to study design and off-design performance of the hybrid system. The results were compared to the available literature.

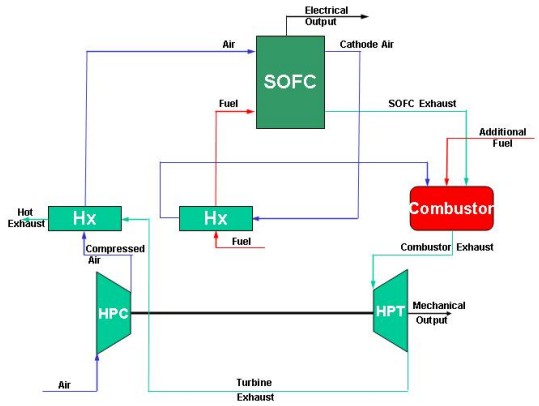

Configuration-"3"

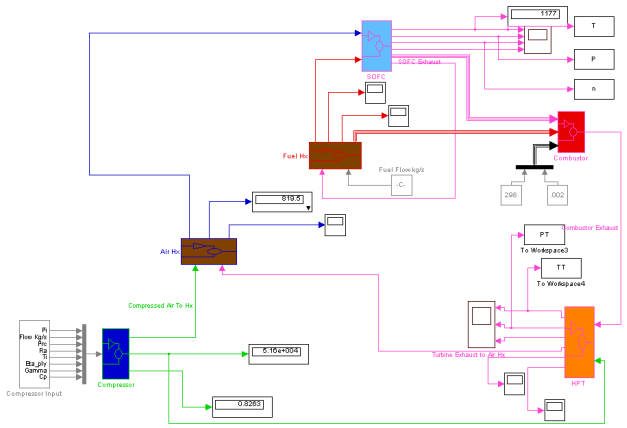

Simulink implementation

Figure 3.1. Hybrid GT/SOFC system and its implementation in Matlab-Simulink.

Table 3.1. Summarizes basic simulation results for the configuration of Figure 3.1 and its comparison with a configuration presented by [12]

	Configuration-"3"	**Reference [12]**
SOFC net power	315 kW	429 kW
Turbine power	138 kW(mechanical)	19 kW(electrical)
Cycle efficiency	56.5%	42%
Stack pressure	2.9 bar	2.9 bar
Stack temperature	856 °C	850 °C
Compressor inlet pressure	14.7 psia	14.7 psia
Compressor pressure ratio	2.88	2.88
Compressor efficiency	85%	83%
Turbine outlet pressure	17.1 psia	17.1 psia
Turbine Pressure ratio	2.47	2.37
Turbine efficiency	87%	84%

A detailed report on this effort can be found in reference [13]

Characterization and Optimization of Regenerative Fuel Cell Systems

Systems Overview -- The renewable fuel cell (RFC) subsystems, with major system subcomponents, are shown in Figures 4.1a and 4.1b. The RFC systems analyzed include reactant recirculation capabilities; i.e., the reactants are not "dead-ended." The models for each subcomponent are discussed in the following sections with the exception of the load subsystem. The load subsystem is treated as a fixed baseline power requirement. This power requirement is discussed further in the discussion of the photovoltaic array.

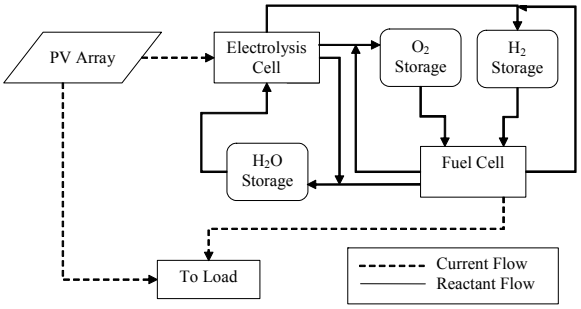

Figure 4.1a. Discrete RFC system with primary components shown.

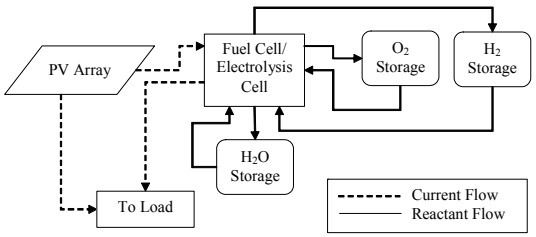

Figure 4.1b. Unitized RFC system with primary components shown.

Fuel Cell and Electrolysis Cell Models

Fuel Cell Thermal Models -- The fuel cell thermal analysis focuses upon integration of the transient energy equation, Equation (1), for a fuel cell within the SIMULINK environment. This technique is also applied to reactant partial pressures in the electrochemical model, as shown by Gemmen [18]. A basic sketch of the control volume employed is shown in Figure 4.2 below.

$$m_{cell} c_{p,stack} \frac{dT}{dt} = \dot{Q}_{gen} - \dot{Q}_{loss} + \sum_i (\dot{n}h)_{ox,in} - \sum_i (\dot{n}h)_{ox,out} \qquad (1)$$

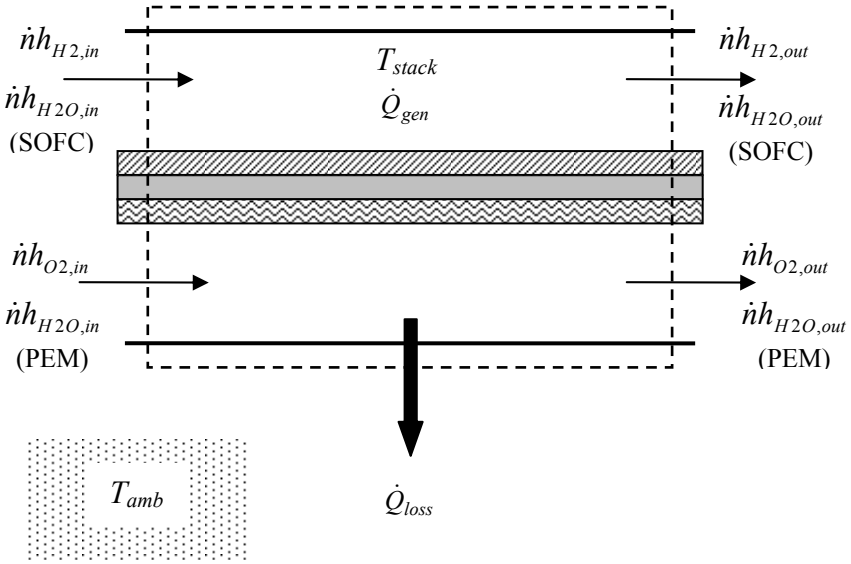

Figure 4.2. Control volume employed for fuel cell energy balance.

The terms on the right hand side of the energy equation are defined as follows:

Heat Generation: $$\dot{Q}_{gen} = i_{eff} \left[\frac{-\Delta H_{H2,oxid}(T_{stack})}{nF} - V_{cell}(T_{stack}, i) \right] \qquad (1a)$$

Heat Loss (Envelope): $\dot{Q}_{loss} = 0.02 \cdot \dot{Q}_{gen}$ (1b)

Electric Power: $\dot{W}_{elec} = i_{eff} V_{cell}\left(T_{stack}, i\right)$ (1c)

Effective Current: $i_{eff} = N \cdot i_{cell}$ (1d)

N = Number of cells in the stack (1e)

Partial Molar Enthalpy: $h_{ox,in} = h_{ox}\left(T_{inlet}\right);\ h_{ox,out} = h_{ox}\left(T_{\text{stack}}\right)$ (1f)

The heat generation term accounts for the difference between the total energy released by the electrochemical reactions and the stack power. The former is treated as a function of stack temperature only, and the latter is a function of both stack temperature and current demand (referred to in the generic sense as "*i*"). Cell voltage and electrochemical power are discussed further in the section on electrochemical models.

The cell heat loss term is calculated assuming envelope losses that are approximately 2% of the heat generation. Each model also contains the option of calculating this loss term directly via convection and radiation heat losses to the environment, with key parameters taken from established a heat transfer literature [19]. For this option a constant ambient temperature is used based upon data regarding the U.S. Standard Atmosphere [20]. This temperature is set as the mean atmospheric temperature at operational altitudes between 20 km and 30 km [21, 22]. In addition to a fixed temperature value, the option of setting temperature as a function of altitude is provided within the models. The use of a constant temperature is justified by diurnal stratospheric temperature variations of less than ±1 °C that have been demonstrated over a range of altitudes in both recent and classic meteorological literature [23-24].

Primary distinctions between the SOFC and the PEM fuel cell (PEMFC) models arise with respect to cell thermophysical properties and the influence of temperature on these properties. Temperature dependence of thermophysical properties is especially emphasized for SOFC subsystems in the present study. These properties are compiled from existing SOFC and PEMFC literature [18, 27-31] as well as standard thermal sciences texts [19, 32].

Fuel Cell Electrochemical Models -- The transient variation of reactant and product partial pressures is calculated by integrating a molar balance as given in Equation (2). As with the transient energy equation, this integration is performed in the SIMULINK environment. Initial reactant partial pressures are set based on the stack pressure and the fuel or oxidant stream concentrations of the species. This arrangement applies a bulk pressure approach to modeling mass transport within cell component layers, i.e. a constant pressure is assumed along the thickness of both the anode and the cathode.

$$\frac{dp_j}{dt} = \frac{R_u T_{stack}(t)}{V}\left(\dot{n}_{j,in} - \dot{n}_{j,out} + \frac{\nu_j i_{eff}}{2F}\right) \quad (2)$$

p_j = Partial pressure of reactant j(2a)

T_{stack} = Time dependent stack temperature (2b)

V = Volume of anode or cathode fluid passages depending on reactant(2c)

i_{eff} = Effective current (defined above) (2d)

F = Faraday's constant (2e)

$\nu_{j,}$ = Electrochemical stoichiometric coefficient (2f)

Stack voltage for the SOFC and PEMFC models is calculated as a function of temperature and reactant partial pressures. The voltage calculations for the SOFC and PEMFC models are given in Equations (3) and (4), respectively. Calculation of the Nernst potential, *E*, is outlined for both models in Equations (5) and (6).

$$V_{cell} = E - i''\,ASR_{total} - a_{act} - b_{act}\ln i'' + \frac{R_u T}{2F}\ln\left[1 - \frac{i''}{i''_{as}}\right] - \frac{R_u T}{2F}\ln\left[1 + \frac{p^o_{H2} i''}{p^o_{H2O} i''_{as}}\right] \quad (3)$$

$$V_{cell} = E - i''\,ASR_{total} - a_{act} - b_{act}\ln i'' + \frac{R_u T}{4F}\ln\left[1 - \frac{i''}{i''_{cs}}\right] + \frac{R_u T}{2F}\ln\left[1 - \frac{i''}{i''_{as}}\right] \quad (4)$$

$$E = -\frac{\Delta G}{2F} \quad (5)$$

$$\Delta G(T,p) = G_{H2O}(T, p_{H2O}) - G_{H2}(T, p_{H2}) - \tfrac{1}{2} G_{O2}(T, p_{O2}) \quad (6)$$

Curve fits for some temperature dependent properties of SOFCs have been employed based upon the data of Kim, et al [30]. For both system configurations activation losses are calculated using Equation (7). For the SOFC model, the Tafel constant a_{act} and the cell ASR are both defined using cubic polynomial curve fits produced in Matlab. The cell ASR is additionally scaled by a factor of 2.5 to reflect increased resistance (contact, interfacial, etc.) associated with the stack assembly. The Tafel constant b_{act} is calculated directly according to its definition in Equation (8).

$$\eta_{act} = a_{act} + b_{act}\ln i'' \quad (7)$$

$$a_{act} = -\frac{R_u T}{4\alpha F}\ln i_o; \quad b_{act} = \frac{R_u T}{4\alpha F} \quad (8)$$

Concentration polarization losses are calculated for the SOFC using the traditional definition of the limiting current density on the anode side, Equation (9). Cathodic concentration polarization is neglected, since the cell is assumed to be anode- supported.

$$i''_{as} = \frac{2FD_{H2-H2O}(T)}{R_u T}\frac{\varepsilon}{\tau}\frac{p_{H_2}}{t_{an}} \quad (9)$$

For the PEMFC model, the Tafel constant a_{act} is calculated directly using as shown in Equation (12). An additional multiplier of 2 is applied to this value to produce agreement between the models and cell performance results from recent literature [33]. Both anodic and cathodic concentration polarizations are calculated as shown in Equation (4). The cathodic limiting current density in this equation is found using Equation (10).

$$i''_{cs} = \frac{4FD_{O2-O2}(T)}{R_u T}\frac{\varepsilon}{\tau}\frac{p_{O_2}}{t_{ca}}\left(\frac{p}{p - p_{O_2}}\right) \quad (10)$$

Electrolysis Cell Thermal Models -- The same general strategy for fuel cell thermal modeling is applied to generate the electrolysis cell thermal models. However, to account for electrical work *applied to* the SOEC, the signs for the electrical power and voltage are reversed in the

energy balance and heat generation terms. The resulting SOEC equations are given below. The heat generation term accounts for heat supplied to the initially endothermic reaction by ohmic heating within the cell. The heat generation agrees qualitatively with published studies of SOEC thermal behavior. Specifically heat generation is negative for low current densities, zero when thermally neutral operation is reached, and increases to a positive value at higher current densities [34]. Equation (11) is a restatement of Equation (1), and Equation (12) is a slight revision of Equation (1a).

$$m_{cell} c_{p,stack} \frac{dT}{dt} = \dot{Q}_{gen} - \dot{Q}_{loss} + \sum_i \left(\dot{n}h\right)_{ox,in} - \sum_i \left(\dot{n}h\right)_{ox,out} \tag{11}$$

$$\dot{Q}_{gen} = i_{eff} \left[\frac{-\Delta H_{H2,prod}(T)}{nF} + V_{cell}(T,i) \right] \tag{12}$$

The thermal properties used for the fuel cell models are also used for the electrolysis cell models. Furthermore, in the case of a discrete PEMRFC system, the PEM electrolysis cell (PEMEC) is assumed to have the same geometric configuration as the PEMFC.

The case of a discrete SORFC system is not considered in the models presented. Primarily, such systems are not considered because in practical applications thermal cycling of the SOFC and SOEC stacks could exacerbate cell degradation, leading to decreased performance and shortened cell lifetime. Furthermore, supplying stack heating requirements for a discrete SORFC system presents a challenge. Specifically, it has been determined that raising the stack temperature from an ambient temperature to an operational temperature of 1073 K would require at a minimum ~5% of the hydrogen supply needed for one day (12 to 15 hours) of fuel cell operation. This ratio is calculated by comparing the result of Equation (13) to the lower heating value (LHV) of hydrogen, -241830 J/mol.

$$Q_{heating} = m_{cell} c_{p,stack} \Delta T_{stack} \tag{13}$$

Electrolysis Cell Electrochemical Models -- As with the corresponding thermal models, the electrolysis cell electrochemical models bear many similarities to the fuel cell electrochemical models. Key distinctions between these models can be seen in Equations (14) through (19). For both the solid oxide and PEM models' ohmic losses and activation losses are added to increase the stack voltage. Additionally, the change in Gibbs free energy for the electrolysis reaction reflects a reversal of the reactant and product species for the hydrogen oxidation reaction. For the SOEC, the reversal of steam and hydrogen pressures in the final term of the stack voltage, Equation (14), reflects that steam is the consumable species and therefore governs the concentration polarization behavior of the SOEC. This fact is also apparent in the anode limiting current density for the SOEC, Equation (18).

$$V_{cell} = E + i'' ASR_{total} + a_{act} + b_{act} \ln i'' - \frac{R_u T}{2F} \ln\left[1 - \frac{i''}{i''_{as}}\right] + \frac{R_u T}{2F} \ln\left[1 + \frac{p^o_{H2O} i''}{p^o_{H2} i''_{as}}\right] \tag{14}$$

$$V_{cell} = E + i'' ASR_{total} + a_{act} + b_{act} \ln i'' - \frac{R_u T}{2F} \ln\left[1 - \frac{i''}{i''_{cs}}\right] - \frac{R_u T}{2F} \ln\left[1 - \frac{i''}{i''_{as}}\right] \tag{15}$$

$$E = \frac{\Delta G}{2F} \tag{16}$$

$$\Delta G(T,p) = G_{H2}(T,p_{H2}) + \tfrac{1}{2} G_{O2}(T,p_{O2}) - G_{H2O}(T,p_{H2O}) \tag{17}$$

$$i''_{as} = \frac{2FD_{H2-H2O}(T)}{R_u T} \frac{\varepsilon}{\tau} \frac{p_{H_2O}}{t_{an}} \tag{18}$$

$$i''_{cs} = \frac{2FD_{O2-H2O}(T)}{R_u T} \frac{\varepsilon}{\tau} \frac{p_{H_2O}}{t_{ca}} \left(\frac{p}{p - p_{H_2O}} \right) \tag{19}$$

Photovoltaic (PV) Array and Insulation

The extraterrestrial solar flux for the latitude and longitude corresponding to Atlanta, Georgia has been calculated for several days of the year. Methods employed within NREL's HOMER program [35] have been used for these calculations. An atmospheric attenuation of 15% has been assumed for the operational altitudes. Similar values are assumed in existing NASA literature on high altitude long endurance (HALE) airships [22]. Accounting for attenuation, the solar flux incident on the horizontal array ($G_{incident}$) is found using Equation (20).

$$G_{incident} = G_{et}(1 - \tau) \tag{20}$$

Here G_{et} is the extraterrestrial solar flux, and τ is the atmospheric attenuation. The solar power produced by the array will be calculated by multiplying the incident solar flux by an appropriate efficiency for the PV array (η_{PV}). Per the specifications for the Helios Prototype, η_{PV} is set at 19%. However, lower efficiencies can be set within the model if desired.

The calculation of current available from the PV array has been established to account for the division of total PV array power among five RFC subsystems. The selection of five RFC systems is based on the NASA Helios Prototype aircraft architecture [21].

Current demand for the fuel cell system is based upon a fuel cell stack with a maximum operational voltage of 52.5 V ($V_{FC,,max}$). This current demand is calculated for a single fuel cell stack based on a 21 kW baseline load. This arrangement is outlined in Equation (21). $\dot{W}_{PV}(t)$ is the total power produced by the entire PV array, and N_{stack} is the number of fuel cell stacks. The absolute value of the power requirement is used in Equations (21) and (22) to maintain a positive current sign convention for both modes of operation.

$$i_{FC/EC} = \frac{\left| \dot{W}_{PV}(t) - \dot{W}_{baseline} \right|}{N_{stacks} \cdot V_{FC/EC,\max}} \tag{21}$$

The time dependence of the PV array power in Equation (25) stresses the presence of a variable power supply tied to the available insolation, which allows for the accommodation of transitional operation between fuel cell and electrolysis cell modes. During such transitional periods (e.g. dusk or dawn), both the PV array and fuel cell contribute toward the system power requirements. Any additional system power requirements that cannot be supplied by the fuel cell or PV array are assumed to come from a battery back-up. Detailed analysis of this battery back-up system is not included in the current models. However, a basic back-up power requirement is

calculated based on the application load voltage (52.5 V) and any unmet fuel cell current demand. This back-up is assumed to be used only when the fuel cell is operating at zero voltage.

The current supplied to a single electrolysis cell is calculated based on a 100V ($V_{EC,,max}$) electrolysis cell stack. It is assumed that five 100 V electrolysis cell stacks are connected in parallel to the PV array (also 100 V) [36, 37]. The parallel configuration is assumed because it will create a lower equivalent resistance when compared to a series configuration, as demonstrated below. The overall configuration of the PV array, electrolysis cell, and load connection is shown in Figure 4.3. It is assumed that power conditioning hardware will allow the application load to operate at 52.5 V (the fuel cell voltage) while it is connected to the PV array.

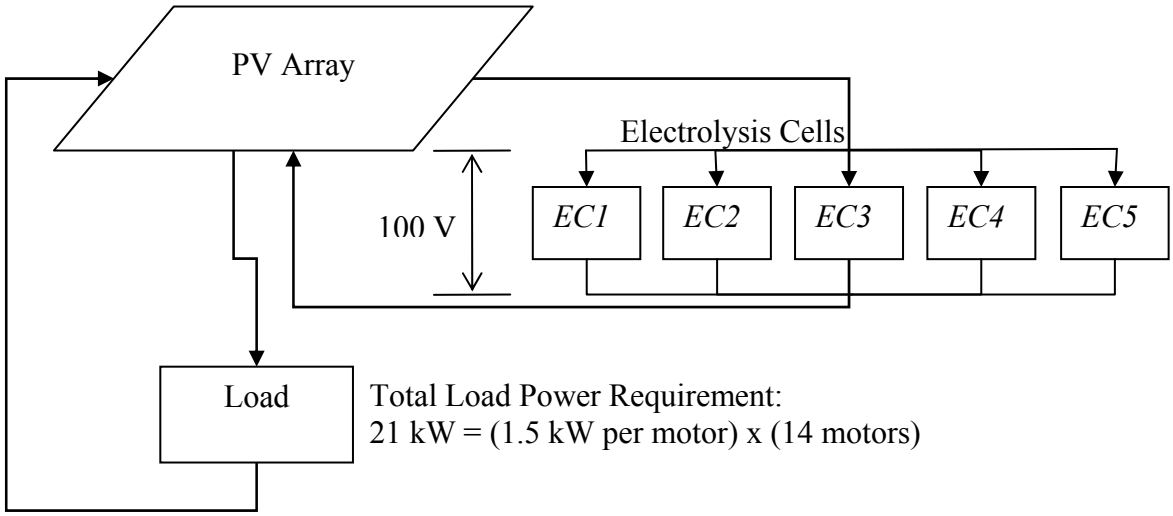

Figure 4.3 PV array, electrolysis cells, and load electrical connections.

Hydrogen and Oxygen Storage

Hydrogen and oxygen are modeled as ideal gases, and the storage tanks are treated as being maintained at the ambient temperature. The tank pressure is calculated by integrating the change in gas pressure, as defined in Equation (27).

$$\frac{dp_j}{dt} = \frac{R_u T_{amb}}{V} \dot{n}_j \qquad (27)$$

The gas change rate, $\dot{n}_j$, is set based on whether the system is operating in fuel cell mode or electrolysis cell mode. As described above, these operational modes are selected based on the relation between the baseline power load and insolation. For tank discharge in fuel cell mode, a multiplier of (-1) is applied to indicate mass flow out of the tank. The molar flowrate is a prescribed value, based on the assumption that reactant flow can be controlled to meet the cells' current demand. This flow is also influenced by NOS parameters that can be defined by the model user.

Water Storage

The water tank must be maintained above a minimum temperature of 273-274 K to prevent freezing. It is assumed that the tank is pressurized to the fuel cell stack pressure, and that the stack pressure has a minimum value of one atmosphere. An ancillary pumping load is calculated based on pressurizing the water to supply the electrolysis cell. This calculation is shown in Equation (28). Here v_{H2O} indicates the specific volume of water as a function of the storage tank temperature and pressure.

$$\dot{W}_{pump} = \frac{\dot{m}_{H2O} \cdot v_{H2O}(T_{tank}, p_{tank}) \cdot (p_{EC} - p_{tank})}{\eta_{pump}} \tag{28}$$

Model Tests and Key Results

Fuel Cell System Comparisons -- An initial performance comparison of the SOFC and PEMFC cell models was completed with respect to *V-i"* characteristics and stack sizes. Simulated polarization curves are shown in Figure 4.4. The SOFC model agrees well with published data [30, 38-40], as does the PEMFC model [33]. However, it should be noted that open-circuit voltages produced by the SOFC model are higher than the calculated Nernst potential values, which range from ~0.87 V to ~0.95 V. This overestimate of cell voltage has been found to be the case for both the SOFC models produced and classic published models [30]. As can be seen, the SOFC system demonstrates superior performance, primarily a result of higher temperature operation.

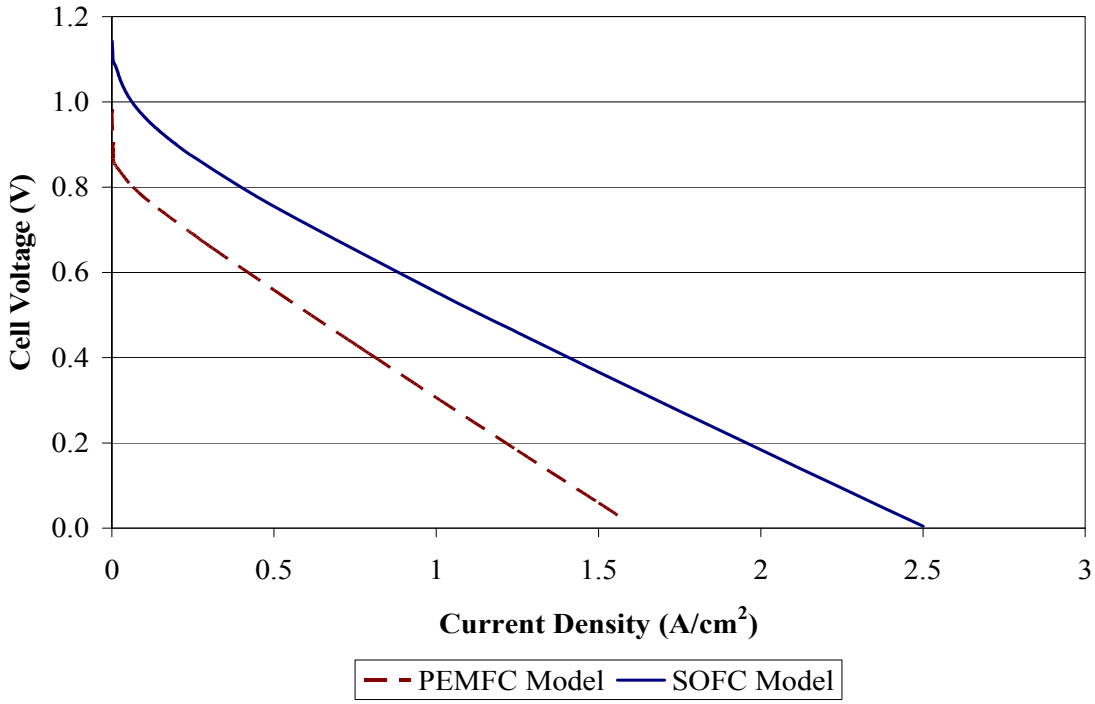

Figure 4.4. Simulated polarization curves for the SOFC and PEMFC systems.

To investigate the fuel cell stack sizes needed to produce the system baseline power requirement two sunset, or fuel cell cold start, tests were run on the PEMFC and SOFC models. The sunset test scenario considered involves ramping to current demand from zero to approximately 85 A over thirty minutes. The constant current is maintained until the fuel cell reaches a steady temperature and the maximum power production. Both sunset tests were run at a baseline stack pressure 345 kPa (~50 psi). This pressure is representative of pressures reported for the fuel cell operation of existing RFC systems [37]. Ambient temperature was set at 221.6 K, which corresponds to an elevation of 25 km [20].

From the sunset tests it was determined that an 86 cell SOFC stack and a 144 cell PEMFC stack would meet the baseline load. Results for the sunset tests are shown in Figures 4.5 and 4.6. Electrochemical light-off for the SOFC and PEMFC is indicated by the production of electrical power by each stack in Figures 4.5 and 4.6, respectively. The SOFC requires a greater amount of time to reach light-off conditions and begin producing power. When considered in combination with the SOFC thermal cycling issues, this lag in the onset of power production further justifies the emphasis placed on a unitized SORFC configuration (and the exclusion of the discrete configuration).

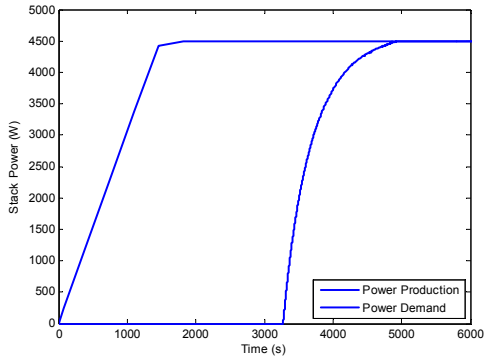

Figure 4.5. SOFC stack power profile from sunset test (cold start at 275 K).

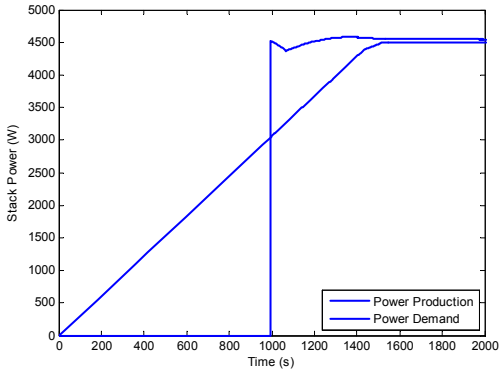

Figure 4.6. PEMFC stack power profile from sunset test (cold start at 275 K).

Full Day Tests of RFC Systems

Four full day test insolation scenarios were run for each of the three RFC configurations: unitized SORFC, unitized PEMRFC, and discrete PEMRFC. All tests were run at constant temperature. The SORFC system was maintained at 1073 K using the constant temperature operation option available in the models developed. Similarly the unitized and discrete PEMRFCs were maintained at 350 K. For all cases the system pressures were given baseline values. A common fuel cell operating pressure of 345 kPa and an electrolysis cell pressure of 2.75 MPa were used. These pressures correspond to pressures quoted in existing RFC literature [37, 41, 42].

Representative profiles of the production and consumption of electrical power are shown in Figures 4.7-4.9 for the three RFC configurations. The reactant storage profile for the SORFC system is shown in Figure 4.10. For each configuration, the Day 90 scenario is shown first because it was the scenario used to set the system PV array size. For the SORFC and discrete PEMRFC a PV array area of 200 m^2 was found to be sufficient. For the unitized PEMRFC, an

area of 250 m^2 was set. For days with lower insolation input, it was found that these PV array sizes would need to be increased. Since the current work serves as a preliminary system comparison, further consideration of array sizing was left for future investigations. In addition to the comparison of power and reactant production and consumption, the key parameter of system mass can be considered. As shown in Table 1, the unitized SORFC system could offer a significant mass savings over the PEMRFC systems.

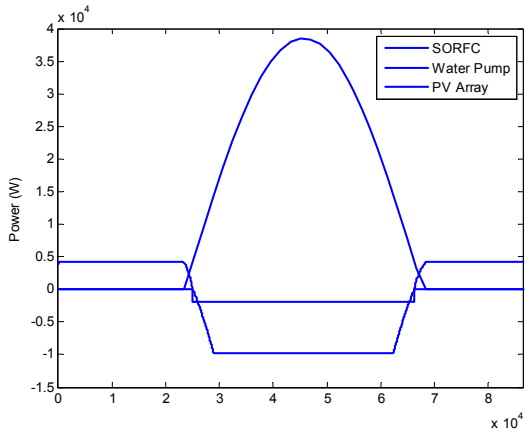

Figure 4.7. Unitized SORFC power profiles for Day 90 full day test.

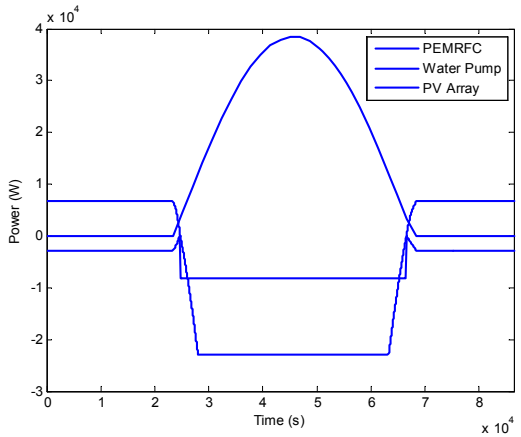

Figure 4.8. Unitized PEMRFC power profiles for Day 90 full day test.

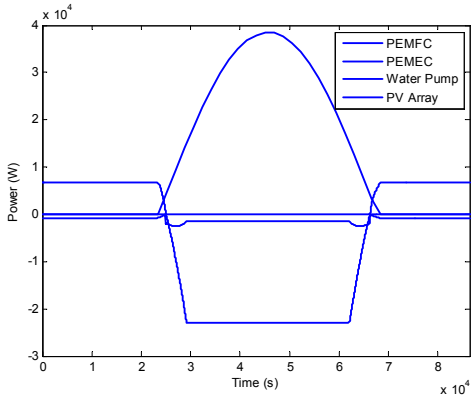

Figure 4.9. Discrete PEMRFC power profiles for Day 90 full day test.

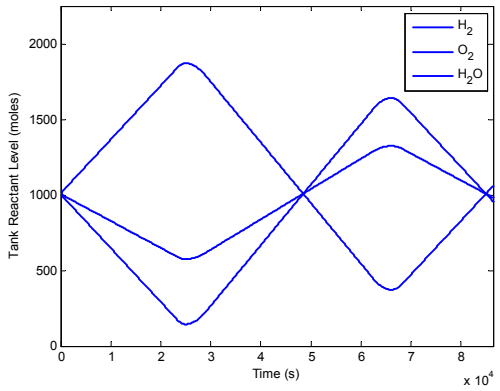

Figure 4.10. Unitized SORFC reactant storage profiles for Day 90 full day test.

Table 1. Overview of RFC system component masses (estimated based on [22, 31]).

Configuration	Stack Mass (kg)	PV Area (m^2)	PV Mass (kg)**	
			Low	High
Solid Oxide	34.8	200	24	260
Unitized PEM*	62.3	250	30	325
Discrete PEM*	124.6	200	24	260

* Stack mass estimated from values reported in [Osczipok]

** Low value represents a thin film array; high value represents a standard satellite array with mounting hardware [Collozza]

i) A library consisting of fuel cells and fuel cell power network components were development to help facilitate a simulated test bed for fuel cell-based power systems. All of the models were developed in EMTDC. The models developed include a SOFC stack, a PEM fuel cell stack, electrical converters (time-averaged models and switching models), and forms of energy storage. As a test case scenario, a fuel cell-based powertrain system was modeled and simulated to analyze the components developed and the system's performance when subjected to Cessna-like power range specifications. In this simulation, the time-based averaged models of electrical power converters were used to convert and deliver AC power to an induction motor-driven propeller from the DC output of the fuel cell stack. Preliminary results from a scaled down simulation of 120 seconds indicate that the power system transitions from one power level to the next in about 10 seconds. Current from the fuel cell stack is controlled such that its maximum power threshold is never exceeded. The fuel cell power system library is available and can be used to conduct power network studies.

   As continuation effort, the implementation of all the subcomponents into RTDS (Real Time Digital Simulator) has started with the advantage of being able to perform hardware-in-the-loop experiments.

ii) Guidelines for the optimization of fuel cells (PEM and SOFC) internal structure have been developed. The available volume is distributed optimally through the system so that the net power is maximized. At the stack level, we optimized the external shape, which accounts for the external aspect ratios of the PEMFC stack. The flow components are distributed optimally through the available volume. Numerical results show that the optimized single cells internal structure and stack external shape are "robust" with respect to changes in stoichiometric ratios, membrane water content, and total stack volume. The optimized internal structure and single cells thickness, and the stack external shape are results of an optimal balance between electrical power output and pumping power required to supply fuel and oxidant to the fuel cell through the stack headers and single-cell gas channels.

iii) Models have been developed and implemented in the Matlab-Simulink environment to guide the selection of hybrid fuel cell /gas turbine system configuration. A comparative study based upon performance parameters, such as SOFC power, turbine inlet temperature, and exhaust temperature was used to select a configuration among few candidates. Simple thermodynamic models for the compressor and turbine were used during the configuration selection. Once the configuration was selected, more realistic compressor and turbine models based on performance maps were incorporated into the

model and used to study design and off-design performance of the hybrid system. The results compare well with the available literature.

iv) The modeling of renewable fuel cell (RFC*) system* subsystems has been addressed. The models presented focus on the application of RFC subsystems to high altitude aircraft operations. Primary subcomponents modeled included fuel and electrolysis cells (both discrete and unitized), reactant/product storage, and a photovoltaic (PV) array. These subcomponents were integrated into complete RFC system models to conduct a preliminary comparison of PEMRFC and SORFC via parametric studies.

The parametric studies presented focused on fuel cell stack performance and size and the full day (24 hour) operation of RFC subsystems similar to those proposed for use in high altitude aircraft applications. Additional sunset tests were run to analyze the cold start performance of polymer electrolyte membrane and solid oxide fuel cells (PEMFCs and SOFCs, respectively). The results presented highlight the production and consumption of both electrical power and reactant species (hydrogen, oxygen, and water). Consideration is also given to system size characteristics, specifically with respect to photovoltaic (PV) array area and the number of cells required for a given fuel or electrolysis cell configuration. Related component weights are included in these considerations.

Solid oxide cells were found to have performance disadvantages that prohibit dedicated galvanic and electrolytic cell configurations, specifically with respect to thermal management. Furthermore, the thermal cycling experienced in discrete RFC configurations could prove detrimental to the reliability of the solid oxide cells. However, under a unitized configuration, it has been found that SORFCs can be competitive with PEMRFCs. Specifically, the SOFC simulated produced superior polarization performance and offered a reduced stack size (number of cells). For the unitized RFC systems this translates to a significant potential savings in system mass that is associated with the SORFC system.

Patents, Publications, Presentations and Students from Research

Patents

None

Publications

J. C. Ordonez , S. Chen , J. V. C. Vargas , F. G. Dias , J. E. F. C. Gardolinski , D. Vlassov, “Constructal Flow Structure for a Single SOFC,” International Journal of Energy Research, 2007 (In press)

T. Brinson, W. Ren, J.C. Ordonez, C.A. Luongo, T. Baldwin “Fuel Cell-Based Powertrain System Modeling and Simulation for Small Aircraft Propulsion Applications”. ASME 5th International Conference on Fuel Cell Science and Technology, Abstracts on, Brooklyn, NY, June 2007

G. Kopasakis (NASA-GRC), T. Brinson , S. Credle (FAMU) “A Theoretical Solid Oxide Fuel Cell Model for System Controls and Stability Design” Accepted to ASME Journal of Fuel Cell Science 2007.

N. Srivastava, Modeling of Solid Oxide Fuel Cell/ Gas Turbine Hybrid Systems, M.S. Thesis, Department of Mechanical Engineering, FAMU-FSU College of Engineering, Florida State University, Tallahassee, FL 2006.

S. Chen, J.C. Ordonez, and J.V.C. Vargas, "Transient Operation and Shape Optimization of a Single PEM Fuel Cell," Journal of Power Sources, 162(1), (2006) 356-368.

J.V.C. Vargas, J.C. Ordonez, A. Bejan. Constructal PEM fuel cell stack design. International Journal of Heat and Mass Transfer, Volume 48, Issues 21-22, October 2005, Pages 4410-4427.

J.V.C. Vargas, J.C. Ordonez, A. Bejan, S.C. Amico, The optimal shape for a unit PEM fuel cell, Third International Conference on Fuel Cell Science, Engineering and Technology, May 23-25, 2005, Ypsilanti, Michigan

Other papers, which are not in the main topic of the research, resulted from our look at the incorporation of PV cells systems with fuel cells:

A.M. Morega, J.C. Ordonez, P.A. Negoias, M. Morega, and R. Hovsapian, Optimal electrical design of spherical photovoltaic cell, Comsol Users conference, Prague, 2006

A.M. Morega, J.C. Ordonez, A.P. Negoias and R. Hovsapian, Spherical Photovoltaic Cells – A Constructal Approach to their Optimization

Presentations

June 18-20, 2007
• T. Brinson, “Fuel Cell-Based Powertrain System Modeling and Simulation for Small Aircraft Propulsion Applications, ASME 5th International Conference on Fuel Cell Science and Technology, Abstracts on, Brooklyn, NY, June 2007

September 25-29, 2006
• J.V. C. Vargas and J.C. Ordonez, “Modeling and Optimization of Renewable and Hybrid Fuel Cell Systems for Space Power and Propulsion,” Annapolis, Maryland.

November 1-4, 2005
• J.C. Ordonez, “Modeling/Optimization of Fuel Cell Systems,” Florida Solar Energy Center, Cocoa, Florida, FL

May 10-11, 2005
• J.C. Ordonez “Modeling/Optimization of Fuel Cell Systems,” Florida Solar Energy Center, Cocoa, Florida, FL

May 23-25, 2005
• J.C. Ordonez, “The optimal shape for a unit PEM fuel cell,” Third International Conference on Fuel Cell Science, Engineering and Technology, May 23-25, 2005, Ypsilanti, Michigan

May 2005
•J.C. Ordonez, “Fuel Cell Structure Optimization,” Department of Mechanical Engineering, Federal University of Parana, Brazil.

May 2005

•J.C. Ordonez, “Internal Structure Optimization of a PEM Fuel Cell,” Pontificia Universidade Catolica do Rio de Janeiro, Brazil.

Students

Postdoctoral fellows:
W. Wechsatol (2005), currently Assistant Professor at KMUTT, Thailand.
Bing Lu (2006)
Graduate Students:
Doctoral students:
T. Brinson (2008), G, Nelson (Georgia Institute of Technology), P. Chinda (2009 at KMUTT, Thailand).
Master students:
S. Chen (2006), N. Srivastava (2006), T. Tracy (2008), N. Anthony (2008)
Undergraduate Students Research Interns:
2007: Nicholas Azadian, Melanie Turenne, Kristin Scheel, Quinn Straub
2006: Michael Erhardt, Anita Lazic, Noel Aguilar, Steven Gerhard
2005: Sladana Lazic, Michael Erhardt, Estrella Kim, Ivan Lee, Anita Lazic, Luis Sanchez, Asefeh Hemmati

References

1. Sehra, A., Whitlow Jr., W., 2004, “Power and Propulsion for 21st Century Aviation,” Progress in Aerospace Sciences, pp. 199-235.
2. Fuel Cell Bulletin 2007, “Flight Test on Way for Boeing Fuel Cell Airplane,” Fuel Cell Bulletin, 2007 (5), pp. 2-3.
3. Hemholt, R., Eberle, U., 2007, “Fuel Cell Vehicles: Status 2007,” *Journal of Power Sources* 165, pp. 833-843.
4. Fuel Cell Bulletin 2006, “*German Navy Orders Two More Fuel Cell Subs*,” *Fuel Cell Bulletin*, 2006 (11), p. 6.
5. Brooks, N., Baldwin, T., Brinson, T., Ordonez, J.C., Luongo, C.A, 2004, “Analysis of Fuel Cell Based Power Systems Using EMTDC Electrical Power Simulator,” *Proc. of The Thirty-Sixth Southeastern Symposium on System Theory*, March 14-16, 2004, Atlanta, GA.
6. Williams, M.C., Strakey, J.P., and Surdoval W.A,The U.S. Department of Energy, Office of Fossil Energy Stationary Fuel Cell Program, *Journal of Power Sources*, Volume 143, Issues 1-2, 27 April 2005, Pages 191-196
7. Song, S., Douvartzides,S. and Tsiakaras, P., Exergy analysis of an ethanol fuelled proton exchange membrane (PEM) fuel cell system for automobile applications, *Journal of Power Sources*, May 2005.
8. Cantoni, U. Alternative fuels utilization in fuel cells for transportation, Society of Automotive Engineers, SAE, Paper 931816, 1993.
9. Sattler, G. Fuel cells going on-board, *Journal of Power Sources*, Volume 86, Issues 1-2, March 2000, Pages 61-67.
10. Gemmen, R.S., Johnson, C.D., 2005, “Effect of Load Transient on SOFC Operation – Current Reversal on Loss of Load,” *Journal of Power Sources* 144, pp. 152-164.
11. Chapman, S.J., 1999, *Electric Machinery Fundamentals*, 3rd ed., WCB/McGraw-Hill, Limited, New York, pp.424-426.
12. Freeh, J.E., A Presentation on Solid Oxide Fuel Cell/Gas Turbine Hybrid Systems for Auxiliary Power, Center for Advanced Power System, April 19, 2005.

13. Srivastava, N. Modeling of Solid Oxide Fuel Cell/ Gas Turbine Hybrid Systems, M.S. Thesis, Department of Mechanical Engineering, FAMU-FSU College of Engineering, Florida State University, Tallahassee, FL 2006.
14. Vargas, J. V. C., Ordonez, J.C., Bejan, A. Constructal flow structure for a PEM fuel cell, *International Journal of Heat and Mass Transfer*, Vol. 47 (19-20) (2004) 4177–4193.
15. Vargas, J. V. C., Ordonez, J.C., Bejan, A. Constructal PEM fuel cell stack design. *International Journal of Heat and Mass Transfer*, Volume 48, Issues 21-22, October 2005, Pages 4410-4427.
16. Chen, S., Ordonez, J.C., and Vargas, J.V.C. "Transient Operation and Shape Optimization of a Single PEM Fuel Cell," *Journal of Power Sources*, 162(1), (2006) 356-368.
17. Ordonez, J.C., Chen, S.' Vargas' J.V.C, Dias' F.G, Gardolinski, J.E.F.C, Vlassov, D. "Constructal Flow Structure for a Single SOFC," *International Journal of Energy Research*, 2007 (In press)
18. Gemmen, R.S., Analysis for the effect of inverter ripple current on fuel cell operating condition. *Journal of Fluids Engineering*, 2003. 125: p. 576-585.
19. Incropera, F.P., DeWitt, D.P., Fundamentals of Heat and Mass Transfer. 5th ed. 2002, New York: John Wiley and Sons.
20. U.S. standard atmosphere, 1976, N.O.A. Administration, Editor. 1976, National Oceanic and Atmospheric Administration.
21. Curry, M. NASA Fact Sheet: Helios Prototype. 2005 [cited; Available from: http://www.nasa.gov/centers/dryden/news/FactSheets/FS-068-DFRC.html.
22. Colozza, A., Initial Feasibility Assessment of a High Altitude Long Endurance Airship. 2003, NASA.
23. Tsuda, T., et al., Observations of diurnal oscillations with a meteor wind radar and radiosondes in Indonesia. *Journal of Geophysical Research*, 1997. 102(D22): p. 26217-24.
24. Mohanakumar, K., et al., Middle atmospheric thermal structures in Eastern and Western Hemispheres over a solar cycle. *Planetary and Space Science*, 1987. 35(1): p. 21-6.
25. Harris, M.F.,Finger, F.G., Teweles, S., Diurnal Variation of Wind, Pressure, and Temperature in the Troposphere and Stratosphere over the Azores. *Journal of the Atmospheric Sciences*, 1962. 19(2): p. 136-149.
26. Chiu, W.C., The Diurnal Temperature Variation of the Lower Stratosphere Over The United States. *Journal of the Atmospheric Sciences*, 1959. 16(4): p. 354-363.
27. Darling, R.M., Meyers, J.P., Mathematical model of platinum movement in PEM fuel cells. *Journal of the Electrochemical Society*, 2005. 152(1): p. 242-247.
28. Gemmen, R.S., Johnson, C.D., Effect of load transients on SOFC operation - current reversal on loss of load. *Journal of Power Sources*, 2005. 144(1): p. 152-64.
29. Haynes, C.L., Ford, J.C., A simulation of solid oxide fuel cell electrochemical light off phenomena, in 2005 ASME Summer Heat Transfer Conference. 2005, ASME: San Francisco, CA.
30. Kim, J.W., et al., Polarization effects in intermediate temperature, anode-supported solid oxide fuel cells. Journal *of the Electrochemical Society*, 1999. 146(1): p. 69-78.
31. Oszcipok, M., et al., Portable proton exchange membrane fuel-cell systems for outdoor applications. *Journal of Power Sources*, 2006. 157(2): p. 666-673.
32. Reid, R.C., Prausnitz, J.M., Sherwood, T.K., The Properties of Gases and Liquids. 3rd ed. 1977, New York: McGraw-Hill.
33. Liu, H., Zhou, T., Cheng, P. Transport Phenomena Analysis in Proton Exchange Membrane Fuel Cells. *Journal of Heat Transfer*, 2005. 127(12): p. 1363-1379.
34. Hawkes, G.L., et al. CFD Model of a Planar Solid Oxide Electrolysis Cell for Hydrogen Production from Nuclear Energy. in The 11th International Topical Meeting on Nuclear

Reactor Thermal-Hydraulics (NURETH-11). 2005. Popes' Palace Conference Center, Avignon, France.
35. Lambert, T., Lilienthal, P., HOMER: Optimization Model for Distributed Power. 2005, National Renewable Energy Lab, International Programs: Golden, CO.
36. Burke, K.A. and Jakupca, I., Unitized Regenerative Fuel Cell system gas dryer/humidifier analytical model development. 2004. Providence, RI, United States: American Institute of Aeronautics and Astronautics Inc., Reston, VA 20191, United States.
37. Bents, D.J., et al., Hydrogen-Oxygen PEM Regenerative Fuel Cell Energy Storage System. 2005, NASA.
38. Chan, S.H., Xia, Z.T., Polarization effects in electrolyte/electrode-supported solid oxide fuel cells. *Journal of Applied Electrochemistry*, 2002. 32(3): p. 339-47.
39. Chung, B.W., et al., Development and Characterization of a High Performance Thin-Film Planar SOFC Stack. *Journal of the Electrochemical Society*, 2005. 152(2): p. A265-A269.
40. Yakabe, H., et al., 3-D model calculation for planar SOFC. *Journal of Power Sources*, 2001. 102(1-2): p. 144-154.
41. Barbir, F., Molter, T., Dalton, L., Efficiency and weight trade-off analysis of regenerative fuel cells as energy storage for aerospace applications. *International Journal of Hydrogen Energy*, 2005. 30(4): p. 351-357.
42. Smith, W., Role of fuel cells in energy storage. *Journal of Power Sources*, 2000. 86(1-2): p. 74-83.

APPENDIX A

An, Linan
Professor
University of Central Florida
4000 Central Florida Boulevard
Orlando, FL 32816
407-823-1009
lan@pegasus.cc.ucf.edu

Baik, Jong
Senior Research Engineer
Florida Solar Energy Center
1679 Clearlake Road
Cocoa, FL 32922-5703
321-638-1532
jbaik@fsec.ucf.edu

Basarkar, Mangesh
Research Associate
Florida Solar Energy Center
1679 Clearlake Road
Cocoa, FL 32922-5703
321-638-1417
mbasarker@fsec.ucf.edu

Bhansali, Shekhar
Associate Professor
University of South Florida
4202 E. Fowler Avenue
Tampa, FL 33620
813-974-3593
bhansali@eng.fsu.edu

Bhethanabotla, Venkat
Professor
University of South Florida
4202 E. Fowler Avenue
Tampa, FL 33620
813-974-2116
bhethana@eng.usf.edu

Block, David
Program Director
Florida Solar Energy Center
1679 Clearlake Road
Cocoa, FL 32922-5703
321-638-1001
block@fsec.ucf.edu

Bokerman, Gary
Asst in Hydrogen
Florida Solar Energy Center
1679 Clearlake Road
Cocoa, FL 32922-5703
321-638-1428
gbokerman@fsec.ucf.edu

Bonville, Len
Assistant in Fuel Cell Research
Florida Solar Energy Center
1679 Clearlake Road
Cocoa, FL 32922-5703
321-638-1703
lbonville@fsec.ucf.edu

Captain, Janine
NASA/KSC
Organization: YA-C3
Kennedy Space Center, FL 32899
321-867-6970
Janine.Captain@nasa.gov

Chen, Quanfang
Assistant Professor
Unviersity of Central Florida
4000 Central Florida Boulevard
Orlando, FL 32816
407-823-2152
qchen@mail.ucf.edu

Cho, Hyoung-Jin
Assistant Professor
University of Central Florida
4000 Central Florida Boulevard
Orlando, FL 32816
407-207-7245
joecho@mail.ucf.edu

Choi, Pyoungho
Assistant Professor
Florida Solar Energy Center
1679 Clearlake Road
Cocoa, FL 32922-5703
321-638-1436
pchoi@fsec.ucf.edu

Chow, Louis
Professor
University of Central Florida
ENG2, P. O. Box 162450 - ENGR I
219, Mechanical, Materials and
Aerospace Engineering
Orlando, FL 32816-2450
407-823-3666
lchow@mail.ucf.edu

Dhere, Neelkanth
Program Director
PV Division
Florida Solar Energy Center
1679 Clearlake Road
Cocoa, FL 32922-5703
321-638-1442
ndhere@fsec.ucf.edu

Eckert, Juergen
Los Alamos National Lab
P. O. Box 1663
Los Alamos, NM 87545
505-665-2374
juergen@lanl.gov

Eddauodi, Mohamed
Assistant Professor
University of South Florida
4202 E. Fowler Drive
Tampa, FL 33620
813-974-9622
eddaoudi@cas.usf.edu

Elbaccouch, Mohamed
Research Engineer
Alstom Power, Inc.
1409 Centerpoint Boulevard
Knoxville, TN 37932-1962
865-560-1758
Mohamed.elbaccouch@power.alstom.
com

Fenton, James
Director
Florida Solar Energy Center
1679 Clearlake Road
Cocoa, FL 329220-5703
321-638-1002
jfenton@mail.ucf.edu

Fowler, James “Randy”
Lab Manager
Florida Solar Energy Center
1679 Clearlake Road
Cocoa, FL 32922-5703
321-638-1224
rfowler@fsec.ucf.edu

Gu, Lixing
Principle Research Engineer
Florida Solar Energy Center
1679 Clearlake Road
Cocoa, FL 32922-5703
321-638-1411
gu@fsec.ucf.edu

Hall, Penny
Program Assistant
Florida Solar Energy Center
1679 Clearlake Road
Cocoa, FL 32922-5703
321-638-1018
penny@fsec.ucf.edu

Ham, Chan
Assistant Research Scholar
University of Central Florida
4000 Central Florida Boulevard
Orlando, FL 32826
407-658-5598
cham@mail.ucf.edu

Hampton, Michael
Associate Professor
University of Central Florida
4000 Central Florida Boulevard
Orlando, FL 32816
407-823-2136
mhampton@mail.ucf.edu

Henzmann-Smith, Adrienne (retired)
Coordinator, Public Affairs
ahenz@netzero.net

Huang, Cunping
Research Associate
Florida Solar Energy Center
1679 Clearlake Road
Cocoa, FL 32922-5703
321-638-1505
chuang@fsec.ucf.edu

Hussaini, Mohamed
Professor
Florida State University
218 Love Building
Tallahassee, FL 32310
850-644-0601
myh@csit.fsu.edu

Justak, J.
Advanced Technologies Group
377 E. Butterfield Road
Suite 900
Lombard, IL 60148
630-964-9700

Kapat, Jay
Professor
University of Central Florida
4000 Central Florida Boulevard
Orlando, FL 32816
407-823-2179
jkapat@mail.ucf.edu

Kunz, Russell
Assistant in Fuel Cell Research
Florida Solar Energy Center
1679 Clearlake Road
Cocoa, FL 32922-5703
321-638-1252
rkunz@mail.ucf.edu

Linkous, Clovis
Senior Research Scientist
Florida Solar Energy Center
1679 Clearlake Road
Cocoa, FL 32922-5703
321-638-1447
calink@fsec.ucf.edu

Luongo, Cesar
Professor
Florida A & M University
A241 NHMFL FSU
1800 E. Paul Dirac Drive
Tallahassee, FL 32310-3706
850-644-1095
luongo@magnet.fsu.edu

Malocha, Don
Professor
University of Central Florida
4000 Central Florida Boulevard
Orlando, FL 32816
407-823-2414
malocha@pegasus.cc.ucf.edu

Mohajeri, Nahid
Senior Research Engineer
Florida Solar Energy Center
1679 Clearlake Road
Cocoa, FL 32922-5703
321-638-1525
nmohajeri@fsec.ucf.edu

Muradov, Nazim
Principle Research Scientist
Florida Solar Energy Center
1679 Clearlake Road
Cocoa, FL 32922-5703
321-638-1448
muradov@fsec.ucf.edu

Ordonez, Juan
Assistant Professor
FAMU-FSU College of Engineering
2525 Pottsdamer Street
Tallahassee, FL 32310
850-644-8405
ordonez@eng.fsu.edu

Peterson, B.
ASRC Aerospace
P. O. Box 21087
Kennedy Space Center, FL 32899

Rahman, Muhammad
Associate Professor
University of South Florida
4202 E. Fowler Avenue
Tampa, FL 33620
813-974-5625
rahman@eng.fsu.edu

Ramasamy, Karthikeyan
Research Associate
Florida Solar Energy Center
1679 Clearlake Road
Cocoa, FL 32922-5703
321-638-1518
karthikeyan@fsec.ucf.edu

Rosario, Luis
Instructor
University of South Florida
4202 E. Fowler Avenue
Tampa, FL 33620
813-974-2280
rosariol@eng.usf.edu

Schleith, Susan
Coordinator, Energy Education
Florida Solar Energy Center
1679 Clearlake Road
Cocoa, FL 32922-5703
321-638-1017
susan@fsec.ucf.edu

Seal, Sudipta
Associate Professor
University of Central Florida
4000 Central Florida Boulevard
Orlando, FL 32816
407-823-5277
sseal@pegasus.cc.ucf.edu

Self, William
Assistant Professor
University of Central Florida
4000 Central Florida Boulevard
Orlando, FL 32816
407-823-4262
wself@mail.ucf.edu

Slattery, Darlene
Senior Research Chemist
Florida Solar Energy Center
1679 Clearlake Road
Cocoa, FL 32922-5703
321-638-1449
dkslatt@fsec.ucf.edu

Smith, Frank
MEMC Pasadena, Inc.
P. O. Box 2012
Pasadena, TX 77501-2012
713-740-1420

Space, Brian
Professor
University of South Florida
4202 E. Fowler Avenue
Tampa, FL 33620
813-974-9841
bspace@mail.usf.edu

Srivastava, Rajiv
Chemical Engineering Program
Manager
Florida International University
HCET, EC 2100, 10555 West Flagler
Street
Miami, FL 33174
305-348-6621
Rajiv.Srivastava@fiu.edu

Stefanakos, Elias
Professor
University of South Florida
4202 E. Fowler Avenue
Tampa, FL 33620
813-974-4413

Sundaram, Kalpathy
Professor
University of Central Florida
4000 Central Florida Boulevard
Orlando, FL 32816
407-823-5326
sundaram@mail.ucf.edu

T-Raissi, Ali
Director
Advanced Energy Research Division
Florida Solar Energy Center
1679 Clearlake Road
Cocoa, FL 32922-5703
321-638-1446
ali@fsec.ucf.edu

Vaidyanathan, Raj
Associate Professor
University of Central Florida
4000 Central Florida Boulevard
Orlando, FL 32816
407-882-1180
raj@mail.ucf.edu

Van Sciver, Steven
Professor
Florida State University
300-Magnet Lab, Mail Code 2740,
1800 E. Paul Dirac Drive
Tallahassee, FL 32310-3706
850-644-0998
vnsciver@magnet.fsu.edu

Wolan, John
Associate Professor
University of South Florida
4202 E. Fowler Avenue
Tampa, FL 33620
813-974-6250
wolan@eng.usf.edu

Wu, Thomas
Associate Professor
University of Central Florida
4000 Central Florida Boulevard
Orlando, FL 32816
407-823-5357
tomwu@mail.ucf.edu

Zaworotko, Michael
Professor
University of South Florida
4202 E. Fowler Avenue
Tampa, FL 33620
813-974-4129
zaworo@cas.usf.edu

REPORT DOCUMENTATION PAGE	Form Approved OMB No. 0704-0188

1. REPORT DATE *(DD-MM-YYYY)*	2. REPORT TYPE	3. DATES COVERED *(From - To)*
01-02-2009	Final Contractor Report	March 2002-March 2008

4. TITLE AND SUBTITLE
Hydrogen Research at Florida Universities

5a. CONTRACT NUMBER

5b. GRANT NUMBER
NAG3-2751

5c. PROGRAM ELEMENT NUMBER

6. AUTHOR(S)
Block, David, L.; T-Raissi, Ali

5d. PROJECT NUMBER

5e. TASK NUMBER

5f. WORK UNIT NUMBER
WBS 561581.02.08.03.11.03

7. PERFORMING ORGANIZATION NAME(S) AND ADDRESS(ES)
Florida Solar Energy Center
1679 Clearlake Road
Cocoa, Florida 32922-5703

8. PERFORMING ORGANIZATION REPORT NUMBER
E-16586

9. SPONSORING/MONITORING AGENCY NAME(S) AND ADDRESS(ES)
National Aeronautics and Space Administration
Washington, DC 20546-0001

10. SPONSORING/MONITORS ACRONYM(S)
NASA

11. SPONSORING/MONITORING REPORT NUMBER
NASA/CR-2009-215441

12. DISTRIBUTION/AVAILABILITY STATEMENT
Unclassified-Unlimited
Subject Categories: 25, 28, 33, and 34
Available electronically at http://gltrs.grc.nasa.gov
This publication is available from the NASA Center for AeroSpace Information, 301-621-0390

13. SUPPLEMENTARY NOTES

14. ABSTRACT
This final report describes the R&D activities and projects conducted for NASA under the 6-year NASA Hydrogen Research at Florida Universities grant program. Contained within this report are summaries of the overall activities, one-page description of all the reports funded under this program and all of the individual reports from each of the 29 projects supported by the effort. The R&D activities cover hydrogen technologies related to production, cryogenics, sensors, storage, separation processes, fuel cells, resource assessments and education. In the span of 6 years, the NASA Hydrogen Research at Florida Universities program funded a total of 44 individual university projects, and employed more than 100 faculty and over 100 graduate research students in the six participating universities. Researchers involved in this program have filed more than 20 patents in all hydrogen technology areas and put out over 220 technical publications in the last 2 years alone. This 6 year hydrogen research program was conducted by a consortium of six Florida universities: Florida International University (FIU) in Miami, Florida State University (FSU) and Florida A&M University (FAMU) in Tallahassee, University of Central Florida (UCF) in Orlando, University of South Florida (USF) in Tampa, and University of Florida (UF) in Gainesville. The Florida Solar Energy Center (FSEC) of the University of Central Florida managed the research activities of all consortium member universities except those at the University of Florida. This report does not include any of the programs or activities conducted at the University of Florida, but can be found in NASA/CR-2008-215440-PART 1-3.

15. SUBJECT TERMS
Hydrogen; Cryogenic fluids; Cryogenic storage; Thermodynamics; Sensors; Hydrogen production; Fuel cells

16. SECURITY CLASSIFICATION OF:			17. LIMITATION OF ABSTRACT	18. NUMBER OF PAGES	19a. NAME OF RESPONSIBLE PERSON
a. REPORT	b. ABSTRACT	c. THIS PAGE			STI Help Desk (email:help@sti.nasa.gov)
U	U	U	UU	702	19b. TELEPHONE NUMBER *(include area code)* 301-621-0390